

INDIAN JOURNAL OF PHYSICS

VOL 53, SERIES A

AND

PROCEEDINGS

OF THE

Indian Association for the Cultivation of Science, Vol. 62

(Published in Collaboration with the Indian Physical Society)

Printed by Bishnupada Chowdhury, at Print Home, 209A, Bidhan Sarani, Calcutta
and Published by the Registrar, Indian Association for the Cultivation
of Science, Jadavpur, Calcutta 700 082

1979

AUTHOR INDEX

Vol. 53A (1979)

(L) Indicates Letters to the Editors

Author	Subject	Page
<i>A</i>		
Abdel Aziz N. E.	A study of the rate of diffusion of some gases in thin layers of gold	292
Acharya H. N.	On some aspect of photoconducting properties of PbS films	6
Agarwal M. K.	Studies of growth and microstructure on WSe ₂ single crystals	349
Agarwal S. C.	Electronic polarizabilities and sizes of alkaline earth and chalcogenide ions	362
Agarwala R. P.	See Anand M. S.	35
Agrawal S. C.	See Shanker Jai	554
Ahmed N. A.	X-ray line broadening study of nickel oxide(L)	454
Anand M. S.	State III recovery in neutron irradiated tungsten	35
Arora S. K.	Spherulitic growth of BaWO ₄ and SrWO ₄ in gels	612
<i>B</i>		
Bahadur Harish	Some new findings on the effect of nuclear and X-irradiation on the oscillating characteristics of quartz crystals	239
Bamane Jagan G.	Electrical properties of CoSnTe ₃ in the thin films state	213
Banerjee Ratnabali	Some theoretical considerations on the Hall effect anomaly in nickel oxide (L)	468
Bansal L. K.	See Kumar Vinod	485
Barua A. K.	See Banerjee Ratnabali	468
Barua B. P.	Energy contributions to the second-order shear elastic constants of dilute Au-Ni alloys	621

Author	Subject	Page
Basu P. K.	Lattice scattering mechanism in quantized inversion layers in silicon	110
Bhanumatti Mrs. A.	See Rao K. Sambasiva	641
Bhargava Bharat	Thermally stimulated discharge currents in polystyrene thin films	47
Bhattacharjee S.	See Mukherjee P. S.	118
Bhattacharyya S. N.	See Kanrar A.	520
Bhuniya R. C.	Electrical conductivity and optical absorption in electrolytically coloured pure and doped KCL crystals	309
Bhushan S.	Effect of strength and frequency of the field on some rare earth activated zinc oxide electroluminors	333
Biswas A. B.	See Palanna O. G.	208
Biswas A. B.	See Bamane Jagan G.	213
Bose D. N.	See Govindacharyulu P. A.	191
Bose H. N.	See Acharya H. N.	6
Bose H. N.	See Subrahmanyam A.	30
Bose H. N.	See Mukherjee M. L.	61
Bose (Miss) P.	Electric and magnetic properties of potassium nickel periodate (L)	637
C		
Chakrabarty B. C.	Diffusion of gallium into silicon	83
Chakraborty Dipak	Evaluation of the relation between extinction coefficient of infrared radiation and mechanical Q of quartz single crystals	406
Chakraborty K. G.	Biquadratic coupling in antiferromagnetic lattices	479
Chand P.	See Gupta M. P.	472
Chand P.	See Gupta M. P.	473
Chandra Ram	Surface wave instabilities in InSb-GaAs semiconductor plasmas : The temperature effects	181
Chatterjee Aparesh	See Majumdar Harashit	367

Author	Subject	Page
Chatterjee Chandana	Structure of sulfonamide drug-sulfisozazole (L)	648
Chaudhuri Bijay K.	See Ganguli Suvra	644
Chitra S.	See Sivasankar V. S.	26
<i>D</i>		
Daryan R. S.	See Mathur S. C.	450
Dattagupta J. K.	See Chatterjee Chandana	648
Dattagupta J. K.	See Podder A.	652
Dayal R.	Electron paramagnetic resonance study of Mn^{2+} doped $Zn(ClO_4)_2 \cdot 6H_2O$	514
Deb S. K.	See Neogy C.	324
Deshmukh D. D.	See Shah S. S.	136
Deshpande P. D.	Crystal data on $MgNbCuO_4$ (L)	557
Deshpande V. V.	See Dharmadhikari D. M.	459
Deshpande V. V.	See Deshpande P. D.	557
Dharmadhikari D. M.	Structural study of ZnY_2O_4 (L)	459
Dubey Sri Kant	Bonds in solids ; unified treatment	579
<i>E</i>		
Ekbote S. N.	CESR studies of high T_C $A-15$ Nb_3Ge films in normal and superconducting states	626
<i>F</i>		
Farag N.	See Abdel Aziz N. E.	292
Fernandez A. M.	The dielectric properties of cadmium iodide crystals	573
<i>G</i>		
Ganguli Suvra	Comments on the microscopic theory of ferroelectric phase transition with transvers Ising-model (L)	644
George A. M.	See Virkar A. N.	435
Ghosh C.	Optical properties of multialkali photocathodes	14
Ghosh P. K.	cathodoluminescence of point defects in polycrystalline CaS	203

Author	Subject	Page
Ghosh U. S.	See Kanrar A.	520
Ghule M. H. M.	See Swami N. K.	431
Giri N. C.	See Tiwari T. N.	565
Girila N. K.	Work hardening phenomena in single crystalline alloys and screw dislocation dipole cluster (L)	441
Govindacharyulu P. A.	Silver iodide-growth, electrical and optical properties	191
Goyal S. C.	See Kumar V.	303
Goyal S. C.	See Kumar Vinod	485
Gupta Arunava	See Shukla A. K.	299
Gupta M. P.	The crystal structure of bis-salicylato, diaquo calcium(II), $\text{Ca}(\text{C}_7\text{H}_6\text{O}_3)_2 \cdot 2\text{H}_2\text{O}$ (L)	460
Gupta M. P.	The crystal structure of monoadipato tetraaquo cobalt (II) $\text{Co}(\text{C}_6\text{H}_8\text{O}_4)_2 \cdot 4\text{H}_2\text{O}$ (L)	471
Gupta M. P.	The crystal structure of strontium maleate, tetrahydrate $\text{Sr} \cdot \text{C}_4\text{H}_2\text{O}_4 \cdot 4\text{H}_2\text{O}$ (L)	472
Gupta M. P.	The crystal structure of manganese adipate, dihydrate $\text{Mn}(\text{C}_6\text{H}_8\text{O}_4)_2 \cdot 2\text{H}_2\text{O}$ (L)	473
Gupta M. P.	The crystal structure of 5-7 dimethoxy indane 1-one $\text{C}_{11}\text{H}_{10}\text{O}_3$ (L)	474
Gupta R. K.	U-centre modes in mixed alkali halides	426
Gupta T. K.	Studies on the characteristics and fabrication of high voltage Si-diodes	57
Gupta S. K.	See Ekbote S. N.	626

H

Haridasan T. M.	See Ramachandran K.	97
Haridasan T. M.	See Kalyani S.	107
Haridoss S.	See Radhakrishna S.	103

I

Iyengar P. K.	See Jaggi N. K.	67
Iyer Ravi Chandran	Potential energy function for alkali hydride molecules (L)	465

Author	Subject	Page
<i>J</i>		
Jaggi N. K.	Mossbauer spectroscopy study of the ternary alloys Co_2FeSa and Fe_2CoCa : Site preferences of Co and Fe	67
Jain V. C.	See Shanker Jai	420
Jain V. K.	EPR of Mn^{2+} in $\text{M}''\text{M}'_2(\text{SeO}_4)_2 \cdot 6\text{H}_2\text{O}$ ($\text{M}'' = \text{Mg, Zn}$ and $\text{M}' = \text{NH}_4\text{Rh}$) single crystals	318
Jain Vimal Kumar	Electron paramagnetic resonance of VO^{2+} in $\text{RbH}_3(\text{SeO}_3)_2$ single crystals (L)	461
Jain Vimal Kumar	Electron paramagnetic resonance of Mn^{2+} in $\text{NaH}_2\text{PO}_4 \cdot 2\text{H}_2\text{O}$ single crystals	491
Joshi S. K.	See Kumar Vijay	197
<i>K</i>		
Kalyani S.	Localized modes due to U-centre pairs in RbCl	107
Kanrar A.	An ultrasonic pulse echo apparatus and velocity of compressional ultrasound in polymer glass	520
Kar Leela	See Mitta G. B.	158
Karkhanavala M. D.	See Virkar A. N.	435
Kaza Balakrishna Rao	See Bhushan S.	333
Khan D. C.	See Sharma J. K.	20
Khanna K. N.	Monovacancy resistivity in noble metals (L)	639
Khawas B.	X-ray study of L-isoleucine HCl, L- β -phenylalanine HCl and DL-methionine 2HCl (L)	559
Khawas B.	Unit cell and space group of L- β -phenylalanine 2HCl (L)	563
Kishk S. S.	See Abdel Aziz N. E.	292
Kota V. K.	See Reddi M. Satyanarayana	267
Krishnamurthy B. S.	See Kubakaddi S. S.	127
Kubakaddi S. S.	Infrared free-carrier absorption in non-polar semiconductors ; scattering by two-short wavelength phonons	127

Author	Subject	Page
Kulkarni D. K.	See Dharmadhikari D. M.	459
Kulkarni D. K.	See Deshpande P. D.	557
Kulkarni S. V.	Alkali hydride molecules and their properties	616
Kumar Deepak	See Kumar Vijay	197
Kumar V.	Strain derivatives of the static dielectric constancy of silver and thallium halide crystals	303
Kumar Vijay	Surface segregation in gold-silver alloys	197
Kumar Vinod	The effect of anharmonicity on the optical properties of silver and thallium halide crystals	485
Kumar Vijay	See Lal Krishnan	78
Kushwaha S. S.	See Singh S. P.	538

L

Lal Krishan	An instrument for study of diffuse X-ray scattering very close to reciprocal lattice points and some illustrative results	72
Lal Krishnan	A comparative study of perfection of CVD grown Czochralski grown α -Al ₂ O ₃ single crystal by X-ray diffraction topography	78
Lashkari A. K. G.	See Shanker Jai	420

M

Machwe V. G.	See Mehta A. S.	395
Majumdar Harashit	Fragment excitation and prompt neutron distribution in fission	367
Mallick Biswanath	See Talapatra Gautam Buddha	356
Mani K. K.	Trends in the valence force constants of crystals containing first-row atoms	41
Mathur B. K.	See Mitra G. B.	148
Mathur O. N.	See Srivastava A. P.	91

Author	Subject	Page
Mathur S. C.	Effect of solid dilution on the crystal field spectra of nickel ion in single crystals (L)	450
Mehta A. S.	X-ray diffraction analysis of CaS : Nd phosphors	395
Misra N. K.	Impurity diffusion in bismuth single crystals	100
Misra T.	On the structure of diquo bis (acetate) nickel (II) complex (L)	448
Misra T. N.	See Talapatra Gautam Buddha	356
Mitra A. K.	Ideal strength of some monovalent metals with a pseudopotential model	144
Mitra G. B.	Extinction in the case of aggregate of distorted crystallites	148
Mitra G. B.	A preliminary study of the changes in X-rays reflected by a piezoelectric crystals when subjected to an oscillatory electric field	158
Mitra T. K.	The excited states of abound polaron	231
Mohan S.	See Naidu B. S.	138
Mondal B. M.	See Kanrar A.	520
Mukherjee M. L.	Formation of colloid centres in pure and doped KCl single crystals	61
Mukherjee P. S.	High temperature phases in fibrous tremolite	118
Mukhopadhyay D.	Hot-electron conduction in cadmium selenide	528
Mukhopadhyay P.	See Saha Sankari	550

N

Nagireddy K.	See Agarwal M. K.	349
Naidu B. S.	Effect of post-deposition heat treatment on the electrical resistance and structure of termanium films	138
Nanda P. K.	See Misra T.	448
Narlikar A. V.	See Ekbote S. N.	626
Neogy C.	A new method of finding Born-Mayer parameters of inert gases in ionic solids	324
Nigam Rajendra P.	See Rao K. Sambasiva	641

Author	Subject	Page
<i>P</i>		
Pal S. K.	The Morse potential and a simple theoretical model for the thermal expansion studies in pure metals	225
Palanna O. G.	Studies on the electrical and magnetic properties of 3d transition metal vanadates	208
Pandey A. N.	See Bhushan S.	333
Pandey B. M.	See Anand M. S.	35
Pandey S. L.	See Saxena R. N.	257
Patel A.	See Misra T.	448
Patel H. B.	See Agarwal M. K.	349
Pathak P. D.	Debye temperature of silver and aluminium and the anharmonic parameters of their potential functions	283
Phadke Shireesh D.	Carrier trapping in plasma polymerized ferrocene films	389
Podder A.	Crystals structure of phenylpropanolamine hydrochloride (L)	652
Prakash Om.	See Rajput B. S.	274
Prasad A.	See Chakrabarty B. C.	83
Prashad R.	See Bahadur Harish	239
<i>R</i>		
Radhakrishna S.	See Sivasankar V. S.	26
Radhakrishna S.	Spontaneous current emission (SCE) from metal-polymer-metal systems	103
Rajput B. S.	Second quantization of generalized electro-magnetic fields	274
Raju R. D. Ratna	See Reddi M. Satyanarayana	267
Ram P.	See Gupta M. P.	474
Ramachandran K.	Effect of dielectric screening on the Lo phonons in SnTe	97
Ramani R.	See Mani K. K.	41
Ramaniah K.	Venkata K-conversion coefficients of some transitions in the ^{152}Eu decay (L)	655

Author	Subject	Page
Ramanjaneyulu A.	See Ramaniah K. Venkata	655
Rathore R. P. S.	Lattice excitation in alkali metals	409
Rao K. Sambasiva	Surface layer effects on the spontaneous polarization of NH_4HSO_4 (L)	641
Rao K. Suryanarayana	See Shanbhag Prakash V.	553
Rao K. R. P. M.	See Jaggi N. K.	67
Rao K. V.	See Subrahmanyam A.	30
Ray B. K.	Interband Faraday rotation in germanium at the L point	496
Ray G. P.	See Mitra T. K.	231
Reddi M. Satyanarayana	On the goodness of the pseudo quantum numbers	267
Reddy P. Jayarama	See Naidu B. S.	138
Reddy K. Venkata	See Ramaniah K. Venkata	655
Roy D. K.	On the properties of degenerate semiconductors	588

S

Saadalah F. A.	See Youssef T. H.	605
Saha A. P.	See Gupta M. P.	640
Saha N. N.	See Chatterjee Chandana	648
Saha N. N.	See Poderr A.	652
Saha Sankari	On the probable radiative and other two-body decays of the upsilon and tests of QCD (L)	550
Samantray B. K.	See Mitra G. B.	148
Sangwal K.	See Arora S. K.	612
Sastry C. V.	See Tiwari T. N.	565
Saxena R. C.	See Mehta A. S.	395
Saxena R. N.	Structure and dielectric measurements of thin films of Bi_2O_3	257
Saxena U.	Electron microscope studies of phase transformation erbium oxide films	I
Sekkina M. M. Abou	Hall effect and thermoelectric-power studies on stoichiometric antimony tritelluride (L)	444

Author	Subject	Page
Venkateswarlu Putcha	See Jain V. K.	318
Venkateswarlu Putcha	See Jain Vimal Kumar	461
Vijayashree G.	See Mukherjee P. S.	118
Virkar A. N.	Study of the phase transition U_8O_{8-x} to $U_8O_{8.1+x}$ by electrical conductivity measurement	435

Y

Youssef T. H.	Relaxation spectrum of deformed (Al+21% Zn) alloy	605
---------------	---	-----

SUBJECT INDEX

Vol. 53A (1979)

(L) Indicates Letters to the Editors

Subject	Author	Page
<i>Nuclear Physics</i>		
On the goodness of the pseudo quantum numbers	M. Satyanarayana Reddi, V.K. Kota and R. D. Ratna Raju	267
Fragment excitation and prompt neutron distribution in fission	Harashit Majumdar and Aparesh Chatterjee	367
K-conversion coefficients of some transitions in the ^{162}Eu decay (L)	K. Venkata Ramaniah, A. Ramanjaneyulu and K. Venkata Reddy	655
<i>Particle Physics and Field Theory</i>		
Second quantization of generalized electromagnetic fields	B. S. Rajput and Om Prakash	274
On the probable radiative and other two-body decays of the upsilon and tests of QCD (L)	Sankari Saha and P. Mukhopadhyay	550
Chiral $\text{SU}(4) \times \text{SU}(4)$ breaking : masses and coupling constants of pseudoscalar mesons	T. N. Tiwari, C. V. Sastra and N. C. Giri	565
<i>Solid State Physics</i>		
Debye temperature of silver and aluminium and the anharmonic parameters of their potential function	P. D. Pathak and (Miss) N. P. Shah	283
A study of the rate of diffusion of some gases in thin layers of gold	N. E. Abdel Aziz, S. S. Kishk and N. Farag	292
Anderson transition in $\text{La}_{1-x}\text{Sr}_x\text{VO}_3$	A. K. Shukla and Arunava Gupta	299
Strain derivatives of the static dielectric constant of silver and thallium halide crystals	V. Kumar and S. C. Goyal	303
Electrical conductivity and optical absorption in electrolytically coloured pure and doped KCl crystal	R. C. Bhuniya	309

Subject	Author	Page
EPR of Mn^{2+} in $M''M'_2(SeO_4)_3 \cdot 6H_2O$ ($M'' = Mg, Zn$ and $M' = NH_4Rb$)	V. K. Jain, T. M. Srinivasan and Putcha Venkateswarlu	318
A new method of binding Born-Mayer parameters of inert gases in ionic solids	C. Neogy and S. K. Deb	324
Effect of strength and frequency of the field on some rare earth activated zinc oxide electroluminors	S. Bhushan, A. N. Pandey and Balakrishna Rao Kaza	333
Studies of growth and microstructures on WSe_2 single crystals	M. K. Agarwal, H. B. Patel and K. Nagireddy	349
Host-crystal field effect on the electronic absorption spectrum of tetracene guest in mixed crystals	Gautam Buddha Talapatra, Biswanath Mallik and T. N. Misra	356
Electronic polarizabilities and sizes of alkaline earth and chalcogenide ions	S. C. Agrawal, O. P. Sharma and Jai Shanker	362
Carrier trapping in plasma polymerized ferrocene films	Shireesh D. Phadke	389
X-ray diffraction analysis of $CaS:Nd$ phosphors	A. S. Mehta, V. G. Machwe, M.C. Tiwari and R. C. Saxena	395
Lattice properties of alkali hydrides	B. N. Thakur and K. P. Thakur	401
Evaluation of the relation between extinction coefficient of infrared radiation and mechanical Q of quartz single crystals	Dipak Chakraborty	406
Lattice excitation in alkali metals	R. P. S. Rathore	409
Volume dependence of the electronic dielectric constant in cuprous and silver halides under the effect of pressure and temperature	Jai Shanker, V. C. Jain and A. K. G. Lashkari	420
U-centre modes in mixed alkali halides	R. K. Gupta and A. K. Singh	426
Effect of doping density on the efficiency of a Schottky barrier solar cell	N. K. Swami and H. M. Ghule	431
Study of the phase transition U_3O_8-x to $U_3O_{8.1+x}$ by electrical conductivity measurement	A. N. Virkar, A. M. George and M. D. Karkhanavala	435

Subject	Author	Page
Work hardening phenomena in single crystalline alloys and screw dislocation dipole cluster (L)	N. K. Girda	441
Hall effect and thermoelectric-power studies on stoichiometric antimony (L)	M. M. Abou Sekkina	444
On the structure of diaquo bis (acetyl acetate) nickel (II) complex (L)	T. Misra, A. Patel and P. K. Nanda	448
Effect of solid dilution on the crystal field spectra of nickel ion in single crystals (L)	S. C. Mathur and R. S. Daryan	450
X-ray line broadening study of nickel oxide (L)	N. A. Ahmed	454
Structural study of ZnY_2O_4 (L)	D. M. Dharmadhikari, D. K. Kulkarni and V. V. Deshpande	459
The crystal structure of bis-salicylato, diaquo calcium (II). $\text{Ca}(\text{C}_7\text{H}_6\text{O}_3)_2 \cdot 2\text{H}_2\text{O}$ (L)	M. P. Gupta and A. P. Saha	460
Electron paramagnetic resonance of VO^{2+} in $\text{RbH}_3(\text{SeO}_3)_2$ single crystal (L)	Vimal Kumar Jain and Putcha Venkateswarly	461
Potential energy function for alkali hydride molecules (L)	Ravi Chandran Iyer and L. K. Sharma	465
Some theoretical considerations of the Hall effect anomaly in nickel oxide (L)	Ratnabali Banerjee and A. K. Barua	468
The crystal structure of mono adipato tetraaquo cobalt (II), $\text{Co}(\text{C}_6\text{H}_8\text{O}_4)_2 \cdot 4\text{H}_2\text{O}$ (L)	M. P. Gupta and S. K. Sinha	471
The crystal structure of strontium maleate, tetrahydrate, $\text{Sr} \cdot \text{C}_4\text{H}_4\text{O}_4 \cdot 4\text{H}_2\text{O}$ (L)	M. P. Gupta and P. Chand	472
The crystal structure of manganese adipate, dihydrate $\text{Mn}(\text{C}_6\text{H}_8\text{O}_4)_2 \cdot 2\text{H}_2\text{O}$ (L)	M. P. Gupta and P. Chand	473
The crystal structure of 5-7 dimethoxy indane 1-one, $\text{C}_{11}\text{H}_{10}\text{O}_3$ (L)	M. P. Gupta and P. Ram	474

Subject	Author	Page
Biquadratic coupling in antiferromagnetic lattices	K. G. Chakraborty	479
The effect of anharmonicity on the optical properties of silver and thallium halides	Vinod Kumar, L. K. Bansal and S. C. Goyal	485
Electron paramagnetic resonance of Mn^{2+} in $NaH_2PO_4 \cdot 2H_2O$ single crystals	Vimal Kumar Jain	491
Interband Faraday rotation in germanium at the L point	B. K. Ray	496
Electronic paramagnetic resonance study of Mn^{2+} doped $Zn(ClO_4)_2 \cdot 6H_2O$	R. Dayal	514
An ultrasonic pulse echo apparatus and velocity of compressional ultrasound in polymer glass	A. Kankar, U. S. Ghosh, S. N. Bhattacharyya and B. M. Mandal	520
Hot-electron conduction in cadmium selenide	D. Mukhopadhyay	528
Effect of dielectric functions on calculation of lattice dynamics of hexagonal metal	S. P. Singh and S. S. Kushwaha	538
Application of the shell model to the pressure dependence of the dielectric constants of alkali halides (L)	O. P. Sharma H. P. Sharma and Jai Shanker	546
On the electronic absorption spectra of 3-chloroparatoluidine (L)	Prakash V. Shanbhag, M. A. Shashidhar and K. Suryanarayana Rao	553
Correlation between ionic radii, nuclear charges and ionisation potentials (L)	Jai Shanker and S. C. Agrawal	554
Crystal data on $MgNbCuO_4$ (L)	P. D. Deshpande, D. K. Kulkarni and V. V. Deshpande	557
X-ray study of L-isoleucine HCl, L- β -phenylalanine HCl and DL-methionine $2HCl$ (L)	B. Khawas	559
Unit cell and space group of L- β -phenylalanine $2HCl$ (L)	B. Khawas	563
The dielectric properties of cadmium iodide crystal	A. M. Fernandez and O. N. Srivastava	573

Subject	Author	Page
Bonds in solids : unified treatment	Sri Kant Dubey	579
On the properties of degenerate semi-conductors	D. K. Roy and R. Y. Thakur	588
Relaxation spectrum of deformed (Al ₄ 21% Zn) alloy	T. H. Youssef and F. A. Saadallah	605
Spherulitic growth of BaWO ₄ and SrWO ₄ in gels	S. K. Arora and K. Sangwal	612
Alkali hydride molecules and their properties	S. V. Kulkarni and L. K. Sharma	616
Energy contributions to the second-order shear elastic constants of dilute Au-Ni alloys	B. P. Barua and S. K. Singh	621
CESR studies of high T _c A-15 Nb ₃ Ge films in normal and superconducting states	S. N. Ekbote, S. K. Gupta and A. V. Narlikar	626
Debye-Waller factor of copper (L)	S. Tolpadi	631
Improved digital solar aspect sensor for space vehicles	G. K. M. Thutupalli	635
Electric and magnetic properties of potassium nickel periodate (L)	Miss P. Bose	637
Monovacancy resistivity in noble metals	K. N. Khanna	639
Surface layer effects on the spontaneous polarization of NH ₄ HSO ₄ (L)	K. Sambasiva Rao, Rajendra P. Nigam and Mrs. A. Bhanumatti	641
Comments on the microscopic theory of ferroelectric phase transition with transverse Ising-model (L)	Suvra Ganguly and Bijay K. Chaudhuri	644
Structure of sulfonamide drug-sulfisoxazole (L)	Chandana Chatterjee, J. K. Dattagupta and N. N. Saha	648
Crystals structure of phenylpropanolamine hydrochloride (L)	A. Podder, J. K. Dattagupta and N. N. Saha	652
 <i>Proceedings of International Symposium on Solid State Physics, Calcutta, 1977</i>		
Electron microscope studies of phase transformation erbium oxide films	U. Saxena and O. N. Srivastava	1
On some aspects of photoconducting properties of PbS films	H. N. Acharya and H. N. Bose	6

Subject	Author	Page
Optical properties of multialkali photo-cathodes	C. Ghosh and B. P. Verma	14
Magnetization of density of Fe^{++} in KFeF_3 and RbFeF_3	J. K. Sharma and D. C. Khan	20
Electric field gradient at impurity sites in ionic crystals	V. S. Sivasankar, S. Chitra and S. Radhakrishna	26
Effect of D. C. biasing field on the dielectric constant of rutile single crystals	A. Subrahmanyam, K. V. Rao and H. B. Bos	30
State III recovery in neutron irradiated tungsten	M. S. Anand, B. M. Pande and R. P. Agarwala	35
Trends in the valence force constants of crystal containing first-row atoms	K. K. Mani, R. Ramani and R. P. Singh	41
Thermally stimulated discharge currents in polystyrene thin films	Bharat Bhargava and A. P. Srivastava	47
Studies on the characteristics and fabrication of high voltage Si-diodes	T. K. Gupta	57
Formation of colloid centres in pure and doped KCl single crystals	M. L. Mukherjee and H. N. Bose	61
Mossbauer spectroscopy study of the ternary alloys Co_3FeSb and Fe_2CoCa : Site preference of Co and Fe	N. K. Jaggi, K. R. P. M. Rao and P. K. Iyengar	67
An instrument for study of diffuse X-ray scattering very close to reciprocal lattice points and some illustrative results	Krishan Lal and Bhanu Pratap Singh	72
A comparative study of perfection of CVD grown Czochralski grown $\alpha\text{-Al}_2\text{O}_3$ single crystals by X-ray diffraction topography	Krishnan Lal, Vijay Kumar and Ajit Ram Verma	78
Diffusion of gallium into silicon	B. C. Chakrabarty and A. Prasad	83
TSD study of pyrene picrate charge transfer complex	A. P. Srivastava and O. N. Mathur	91
Effect of dielectric screening on the Lo phonons in SnTe	K. Ramachandra and T. M. Haridasan	97
Impurity diffusion in bismuth single crystals	N. K. Misra and V. S. Venkatasubramanian	100

Subject	Author	Page
Spontaneous current emission (SCE) from metal-polymer-metal systems	S. Radhakrishna and S. Haridoss	103
Localized modes due to U-centre pairs in RbCl	S. Kalyani and T. M. Haridasan	107
Lattice scattering mechanism in quantized inversion layers in silicon	P. K. Basu	110
High temperature phase in fibrous tremolite	P. S. Mukherjee, S. Bhattacharjee and G. Vijayashree	118
Infrared free-carrier absorption in non- polar semiconductors : scattering by two-short wavelength phonons	S. S. Kubakaddi and B. S. Krishnamurthy	127
Temperature dependence of phonon- magnon bound state	S. S. Shah and D. D. Deshmukh	136
Effect of post-deposition heat treatment on the electrical resistance and structure of germanium films	B. S. Naidu, S. Mohan and P. Jayarama Reddy	138
Ideal strength of some monovalent metals with a pseudopotential model	A. K. Mitra and P. K. Sengupta	144
Extinction in the case of aggregate of distorted crystallites	G. B. Mitta, B. K. Samantray and B. K. Mathur	148
A preliminary study of the changes in X-rays reflected by a piezoelectric crystals when subjected to an oscillatory electric field	G. B. Mitra and Leela Kar	158
Eigenvalues and eigenvectors of the exchange interaction Hamiltonian of Heisenberg	N. D. Sen Gupta	168
Surface wave instabilities in InSb-GaAs semiconductor plasmas : the temperature effects	Ram Chandra and J. S. Verma	181
Silver iodide-growth, electrical and optical properties	P. A. Govindacharyulu and D. N. Bose	191
Surface segregation in gold-silver alloys	Vijay Kumar, Deepak Kumar and S. K. Joshi	197
Cathodoluminescence of points defects in polycrystalline CaS	P. K. Ghosh and V. Shanker	203

Subject	Author	Page
Studies on the electrical and magnetic properties of 3d transition metal vanadates	O. G. Palanna, A. L. Shashimohan and A. B. Biswas	208
Electrical properties of CoSnTe_3 in the thin films state	G. Jagan Bamane and A. B. Biswas	213
The Morse potential and a simple theoretical model for the thermal expansion studies in pure metals	S. K. Pal and S. P. Sen Gupta	225
The excited states of a bound polaron	T. K. Mitra and G. P. Ray	231
Some new findings on the effect of nuclear and X-irradiation on the oscillating characteristics of quartz crystals	Harish Bahadur and R. Prasad	239
Structure and dielectric measurements of thin films of Bi_2O_3	R. N. Saxena, S. L. Pandey and Sooraj Singh	257
Erratum		477

INDIAN JOURNAL OF PHYSICS

VOL. 53, SERIES B

AND

PROCEEDINGS

OF THE

Indian Association for the Cultivation of Science, Vol. 62

(Published in Collaboration with the Indian Physical Society)

Printed by Bishnupada Chowdhury, at Print Home, 209A, Bidhan Sarani, Calcutta
and Published by the Registrar, Indian Association for the Cultivation
of Science, Jadavpur, Calcutta 700 032

1979

AUTHOR INDEX

Vol. 53B (1979)

(L) *Indicates Letters to the Editors*

Author	Subject	Page
<i>A</i>		
Abou-Chacra R.	See Chamoun E.	7
Ansari A. K.	Infrared absorption spectrum of pyrogallol	136
<i>B</i>		
Basu D.	Probability of charge transger in alpha particle-hydrogen atom collision	273
Bedewi F. Fl.	Amplitude modulation in cosmic-ray and K_p -index 27-day variations	49
Bhardwaj S. K.	See Rawat T. S.	66
Bhat C. M.	See Pushpalata B. R.	80
Bhatnagar T. N.	See Sharma S. R.	150
Bhattacharya D. M.	See Basu D.	273
Bondyopadhyaya R.	Nonlinear Poynting flux for a gravitating magnetised plasma and radio emission from astrophysical bodies	15
<i>C</i>		
Chamoun E.	Direct measuring method of the anisotropic collisions	7
Chandra S. K.	See Bondyopadhyaya R.	15
Chandra Suresh	Intensities of the forbidden lines within the ground configurations of SX	76
Chattopadhyay S.	See Das R.	297
<i>D</i>		
Das R.	Rotational isomerism of some aliphatic esters	297
Daskhan M.	Photodetachment cross section of negative hydrogen	183

Author	Subject	Page
Devi Mrs. Ananda	See Sanyal Nitish K.	221
Dixit L.	See Rawat T. S.	66
Dixit Lalji	See Kaila (Miss) Rama	109

F

Farag A. A.	See Bedewi F. Fl.	49
-------------	-------------------	----

G

Ghosh A. S.	See Guha Sunanda	163
Ghosh A. S.	See Daskhan M.	183
Ghosh S. N.	See Singh M. P.	266
Ghoshal Swadesh Kumar	Vibrational and rotational level spacings of Van der Waals molecules and related thermodynamic functions : Ar ₂ molecule	124
Goel R. K.	See Sanyal Nitish K.	282
Goned A.	See Bedewi F. Fl.	49
Guha S.	Parametric excitation of acoustic waves in piezoelectric solid state magnetoplasma	228
Guha Sunanda	e ⁻ -Li scattering by simplified form of FSA	163
Gupta G. P.	See Prasad R.	101
Gupta G. P.	Charge sheath around electrodes immersed in plasma	237
Gupta P. L.	See Kaila (Miss) Rama	109

H

Husain Javed	Angular dependence of polarization of the radiation following photoionization and photodissociation	263
--------------	---	-----

J

Jha B. L.	See Verma M. P.	258
Jha R.	Application of INDO-method to study the structure of halogen substituted ethylenes	117
Jyoti B. G.	See Mummigatti V. M.	260

Author	Subject	Page
<i>K</i>		
Kaila (Miss) Rama	The molecular polarizability and intermolecular interaction potential function of adamantane	109
Kastha G. S.	See Das R.	297
Khosa P. N.	Joule heating of the ionosphere	199
<i>M</i>		
Mukundan T. S.	See Walvekar A. P.	224
Mummigatti V. M.	RKRV Franck Condon factors and r-centroids for the ($D^2\Sigma^+ - X^2\Sigma^+$) transition of AlO (L)	260
Murthy L. C. S.	Production of radio-frequency oscillations in A/C silent discharge	155
<i>P</i>		
Pal B.	See Rawat T. S.	66
Patel Ganesh	PKRV curves for A and X state of MgH and MgD molecules (L)	159
Paul J. C.	Modified Paschen's law under the influence of electric and cross magnetic field in air, nitrogen and hydrogen	85
Paul J. C.	Effect of magnetic field on mean free path and viscosity and its influence at low pressure gaseous discharge	96
Prasad R.	Nonlinear theory of whistler wave modulation	101
Pushpalata B. R.	Quadrupole coupling constants of 3P_1 and 1P_1 levels of Mg^{24} , Zn^{67} and Kr^{83} and 3D and 1D levels of Zn^{67}	80
<i>R</i>		
Raghuwanshi S. S.	Three body problem for hyperbolic and Coulomb potentials	1
Rai D. K.	See Ram Ram Samujh	56
Rai D. K.	See Singh R. B.	144
Rai S. B.	See Ram Ram Samujh	56

Author	Subject	Page
Raizada B. B.	See Rawat T. S.	66
Ram Ram Samujh	A precise vibrational analysis of the A-X system of aluminium monochloride molecule	56
Rao K. Suryanarayana	See Shanbhag Prakash V.	140
Rao K. Suryanarayana	See Shanbhag P. V.	248
Rawat T. S.	Vibrational potential functions, exact force constants of F_2 -species, isotopic shifts and mean amplitudes of vibration of ortho silicates and germanates	66
Roy K.	See Dashkhan M.	183
S		
Sanyal Nitish K.	Vapour absorption spectra of 4, 7-dichloro-quinoline in the near ultraviolet region	221
Sanyal Nitish K.	Infrared absorption spectra of 2, 4, 6-triamino-pyrimidine	282
Sarkar P. C.	A comparative study of Peacock, Heidborn and Muller's method and kinetic constant method for the solution of third order eigenvalue problem in molecular dynamics	278
Sen P. K.	See Guha S.	228
Sengoden V.	Potential constants and centrifugal distortion constants of IOF_6 , $ReOF_6$ and $OsOF_6$ (L)	255
Sengodan V.	Vibrational analysis of monomeric trihalides of scandium subgroup	288
Sengupta Sankar	See Ghoshal Swadesh Kumar	124
Shanbhag Prakash V.	Infrared and ultraviolet absorption spectra of morpholine	140
Setty P. S. V.	Production of radio-frequency oscillations in A/C silent discharge	155
Shanbhag P. V.	Ultra-violet absorption spectrum of 2-aminopyrimidine (L)	248
Sharma B. K.	A new method of estimation of limiting solid volume and related properties of simple non-polar liquids	174
Sharma L. K.	See Raghuwanshi S. S.	1

Author Index

v

Author	Subject	Page
Sharma S. N.	See Sanyal Nitish K.	282
Sharma S. R.	Longitudinal wave propagation in a relaxing plasma	150
Shashidhar M. S.	See Shanbhag Prakash V.	140
Shashidhar M. A.	See Shanbhag P. V.	248
Sheth Bidhanchandra I.	See Patel Ganesh	159
Singh A. N.	See Jha R.	117
Singh B.	Meridional neutral air winds and its effects on F_2 -region of the ionosphere during quiet and magnetically disturbed periods	213
Singh G. C.	See Sarkar P. C.	278
Singh R. B.	Vibrational spectra of 2-chloro-6-nitro toluene	144
Singh M. P.	Vertical drift velocity in the topside F layer during Aug. 27 1972 flare	266
Singh R. N.	See Singh R. P.	24
Singh R. N.	See Prasad R.	101
Singh R. N.	See Khosa P. N.	199
Singh R. N.	See Gupta G. P.	237
Singh R. P.	Comparative study of electromagnetic wave generation from the magnetosphere	24
Singh R. P.	See Singh B.	213
Singh S.	On the virial coefficients of H_2O (L)	250
Srinivasacharya K. G.	See Sengoden V.	255
Srinivasacharya K. G.	See Sengoden V.	288
Srivastava U. S. L.	See Sarkar P. C.	278
Srivastava S. L.	See Sanyal Nitish K.	221

T

Tripathi G. N. R.	On the ground state frequencies of some monosubstituted pyridenes	130
Tripathi Sita Ram	See Tripathi G. N. R.	130

U

Upadhy K.	See Ram Ram Samujh	56
Upadhyay Sachindra Nath	Calculation of scattering amplitudes by the eikonal approximation method for a modified Gaussian potential	190

Author	Subject	Page
<i>V</i>		
Verma M. P.	New bands of $A^2\pi - X^2\Sigma^+$ system of BeCl (L)	258
Verma P. K.	See Ansari A. K.	136
<i>W</i>		
Wahab S. A.	See Bedewi F. Fl.	49
Walvekar A. P.	Electronic transition moment variation in ($B^2\Sigma - X^2\Sigma$) band system of YO	224
Yashvir	See Sharma S. R.	150

SUBJECT INDEX

Vol. 53B (1979)

(L) Indicates Letter to the Editors

Subject	Author	Page
<i>Atomic and Molecular Physics</i>		
Three body problem for hyperbolic and Coulomb potentials	S. S. Raghuwanshi and L. K. Sharma	1
Direct measuring method of the anisotropic collisions	E. Chamoun and R. Abou-Chacra	7
The molecular polarizability and intermolecular interaction potential function of adamantane	Rama Kaila, Lalji Dixit and P. L. Gupta	109
Application of INDO-method to study the structure of halogen substituted ethylenes	R. Jha and A. N. Singh	117
Vibrational and rotational level spacings of Van der Waals molecules and related thermodynamic functions : Ar ₂ molecule	Swadesh Kumar Ghoshal and Sankar Sengupta	124
e ⁻ -Li scattering by simplified form of FSA	Sunanda Guha and A. S. Ghosh	163
PKRV curves for A and X state of MgH and MgD molecules (L)	Ganesh Patel and Bidhanchandra I Sheth	159
A new method of estimation of limiting solid volume and related properties of simple non-polar liquids	B. K. Sharma	174
Photodetachment cross section of negative hydrogen	M. Daskhan, K. Roy and A. S. Ghosh	183
Calculation of scattering amplitudes by the eikonal approximation method for a modified Gaussian potential	Sachindra Nath Upadhyay	190
On the virial coefficients of H ₂ O (L)	S. Singh	250

Subject	Author	Page
<i>Atomic and Molecular Physics</i>		
Angular dependence of polarization of the radiation following photoionization and photodissociation	Javed Husain	263
Vertical drift velocity in the topside F layer during Aug 27, 1972 flare	M. P. Singh and S. N. Ghosh	266
Probability of charge transfer in alpha particle-hydrogen atom collision	D. Basu and D. M. Bhattacharya	273
A comparative study of Peacock, Heidborn and Muller's method and kinetic constant method for the solution of third order eigenvalue problem in molecular dynamics	P. C. Sarkar, G. C. Singh and U. S. L.	278
Potential constants and centrifugal distortion constants of IOF_6 , ReOF_6 and OsOF_6 (L)	V. Sengoden and K. G. Srinivasacharya	255
<i>Atmospheric Physics and Space Physics</i>		
Nonlinear poynting flux for a gravitating magnetised plasma and radio emission from astrophysical bodies	R. Bondyopadhaya and S. K. Chandra	15
Comparative study of electromagnetic wave generation from the magnetosphere	R. P. Singh and R. N. Singh	24
Amplitude modulation in cosmic-ray and K_p -index 27-day variations	F. Fl, Bedevi, A. Goned, S. A. Wahab and A. A. Farag	49
Joule heating of the ionosphere	P. N. Khosla and R. N. Singh	199
Meridional neutral air winds and its effects on F_2 -region of the ionosphere during quiet and magnetically disturbed periods	B. Singh and R. P. Singh	213
<i>Optics and Spectroscopy</i>		
A precise vibrational analysis of the A-X system of aluminium monochloride molecule	Ram Samujh Ram, S. B. Rai, D. K. Rai and K. N. Upadhyaya	56

Subject	Author	Page
Vibrational potential functions, exact force constants of F_2 -species, isotopic shifts and mean amplitudes of vibration of ortho silicates and germanates	T. S. Rawat, L. Dixit, B. B. Raizada B. Pal and S. K. Bhardwaj	66
Intensities of the forbidden lines within the ground configurations of SX	Suresh Chandra	76
Quadrupole coupling constants of 3P_1 and 1P_1 levels of Mg^{2+} , Zn^{2+} and Kr^{83} and 3D and 1D levels of Zn^{67}	B. R. Pushpalata and C. M. Bhat	80
On the ground state frequencies of some monosubstituted pyridenes	G. N. R. Tripathi and Sita Ram Tripathi	130
Infrared absorption spectrum of pyrogallol	A. K. Ansari and P. K. Verma	136
Infrared and ultraviolet absorption spectra of morpholine	Prakash V. Shanbhag, M. A. Shashidhar and K. Suryanarayana Rao	140
Vibrational spectra of 2-chloro-6-nitro toluene	R. B. Singh and D. K. Rai	144
PKRV curves for A and X state of MgH and MgD molecules (L)	Ganesh Patel and Bidhanchandra L. Sheth	159
Longitudinal wave propagation in a relaxing plasma	S. R. Sharma, T. N. Bhattacharya and Yahovir	150
Production of radio-frequency oscillations in A/C silent discharge	L. C. S. Murthy and P. S. V. Setty	155
Vapour absorption spectra of 4, 7-dichloroquinoline in the near ultraviolet region	Nitish K. Sanyal, S. L. Srivastava and Mrs. Ananda Devi	221
Electronic transition moment variation in $(B^2\Sigma - X^2\Sigma)$ band system of YO	A. P. Walvekar and T. S. Mukundan	224
Ultra-violet absorption spectrum of 2-aminopyrimidine (L)	P. V. Shanbhag, M. A. Shashidhar and K. Suryanarayana Rao	248
New bands of $A^2\Pi - X^2\Sigma^+$ system of $BeCl$ (L)	M. P. Verma and B. L. Jha	258
RKRV Franck Condon factors and r-centroids for the $C^2\Sigma^+ - X^2\Sigma^+$ transition of AlO (L)	V. M. Mummigatti and B. G. Jyoti	260

Subject	Author	Page
Infrared absorption spectra of 2, 4, 6-triaminopyrimidine	Nitish K. Sanyal, R. K. Goel and S. N. Sharma	282
Vibrational analysis of monomeric trihalides of scandium subgroup	V. Sengodan and K. G. Srinivasa-charya	288
Rotational isomerism of some aliphatic esters	R. Das, S. Chattopadhyay and G. S. Kastha	297
<i>Plasma Physics</i>		
Modified Paschen's law under the influence of electric and cross magnetic field in air, nitrogen and hydrogen	J. C. Paul	85
Effect of magnetic field on mean free path and viscosity and its influence at low pressure gaseous discharge	J. C. Paul	96
Nonlinear theory of whistler wave modulation	R. Prasad, G. P. Gupta and R. N. Singh	101
Parametric excitation of acoustic waves in piezoelectric a solid state magneto-plasma	S. Guha and P. K. Sen	228
Charge sheath around electrodes immersed in plasma	G. P. Gupta and R. N. Singh	237
<i>Book Reviews</i>		302

CONTENTS

Indian Journal of Physics **Vol. 53A, Nos. 1 & 2** **January & March, 1979**

	<i>Pages</i>
SAXENA U. AND SRIVASTAVA O. N. Electron microscope studies of phase transformation in erbium oxide films	1—5
ACHARYA H. N. AND BOSE H. N. On some aspects of photoconducting properties of PbS films	6—13
GHOSH C. AND VARMA B. P. Optical properties of multialkali photocathodes	14—19
SHARMA J. K. AND KHAN D. C. Magnetization of density of Fe^{++} in KFeF_3 and RbFeF_3	20—25
SIVASANKAR V. S., CHITRA S. AND RADHAKRISHNA S. Electric field gradient at impurity sites in ionic crystals	26—29
SUBRAHMANYAM A., RAO K. V. AND BOSE H. N. Effect of D. C. biasing field on the dielectric constant of rutile single crystals	30—34
ANAND M. S., PANDE B. M. AND AGARWALA R. P. Stage III recovery in neutron irradiated tungsten	35—40
MANI K. K., RAMANI R. AND SINGH R. P. Trends in the valence force constants of crystal containing first-row atoms	41—46
BHARGAVA BHARAT AND SRIVASTAVA A. P. Thermally stimulated discharge currents in polystyrene thin films	47—56
GUPTA T. K. Studies on the characteristics and fabrication of high voltage Si-diodes	57—60

	<i>Pages</i>
MUKHERJEE M. L. AND BOSE H. N.	
Formation of colloid centres in pure and doped KCl single crystals	61—66
JAGGI N. K., RAO K. R. P. M. AND IYENGAR P. K.	
Mössbauer spectroscopy study of the ternary alloys Co_2FeSb and Fe_2CoCa : Site preferences of Co and Fe	67—71
LAL KRISHAN AND SINGH BHANU PRATAP	
An instrument for study of diffuse X-ray scattering very close to reciprocal lattice points and some illustrative results	72—77
LAL KRISHAN, KUMAR VIJAY AND VERMA AJIT RAM	
A comparative study of perfection of CVD grown Czochralski grown $\alpha\text{-Al}_2\text{O}_3$ single crystals by X-ray diffraction topography	78—82
CHAKRABARTY B. C. AND PRASAD A.	
Diffusion of gallium into silicon	83—90
SRIVASTAVA A. P. AND MATHUR O. N.	
TSD study of pyrene picrate charge transfer complex	91—96
RAMACHANDRAN K. AND HARIDASAN T. M.	
Effect of dielectric screening on the Lo phonons in SnTe	97—99
MISRA N. K. AND VENKATASUBRAMANIAN V. S.	
Impurity diffusion in bismuth single crystals	100—102
RADHAKRISHNA S. AND HARIDOSS S.	
Spontaneous current emission (SCE) from metal-polymer-metal systems	103—106
KALYANI S. AND HARIDASAN T. M.	
Localized modes due to U-centre pairs in RbCl	107—109
BASU P. K.	
Lattice scattering mechanism in quantized inversion layers in silicon	110—117
MUKHERJEE, P. S., BHATTACHERJEE S. AND VIJAYASHREE G.	
High temperature phases in fibrous tremolite	118—126

KUBAKADDI S. S. AND KRISHNAMURTHY B. S.	
Infrared free-carrier absorption in non-polar semiconductors : scattering by two-short wavelength phonons	127—135
SHAH S. S. AND DESHMUKH D. D.	
Temperature dependence of phonon-magnon bound state	136—137
NAIDU B. S., MOHAN S. AND JAYARAMA REDDY P.	
Effect of post-deposition heat treatment on the electrical resistance and structure of germanium films	138—143
MITRA A. K. AND SENGUPTA P. K.	
Ideal strength of some monovalent metals with a pseudopotential model	144—147
MITRA G. B., SAMANTRAY B. K. AND MATHUR B. K.	
Extinction in the case of aggregate of distorted crystallites	148—157
MITRA G. B. AND LEELA KAR	
A preliminary study of the changes in X-rays reflected by a piezoelectric crystal when subjected to an oscillatory electric field	158—167
SEN GUPTA N. D.	
Eigenvalues and eigenvectors of the exchange interaction Hamiltonian of Heisenberg	168—180
CHANDRA RAM AND VERMA J. S.	
Surface wave instabilities in InSb-GaAs semiconductor plasmas : The temperature effects	181—190
GOVINDACHARYULU P. A. AND BOSE D. N.	
Silver iodide-growth, electrical and optical properties	191—196
KUMAR VIJAY, KUMAR DESPAK AND JOSHI S. K.	
Surface segregation in gold-silver alloys	197—202
GHOSH P. K. AND SHANKER V.	
Cathodoluminescence of point defects in polycrystalline CaS	203—207

PALANNA O. G., SHASHIMOHAN A. L. AND BISWAS A. B.	
Studies on the electrical and magnetic properties of 3d transition metal vanadates	208—212
BAMANE JAGAN G. AND BISWAS A. B.	
Electrical properties of CoSnTe_2 in the thin film state	213—224
PAL S. K. AND SEN GUPTA S. P.	
The Morse potential and a simple theoretical model for the thermal ex- pansion studies in pure metals	225—230
MITRA T. K. AND RAY G. P.	
The excited states of a bound polaron	231—238
BAHADUR HARISH AND PARSHAD R.	
Some new findings on the effect of nuclear and X-irradiation on the oscillating characteristics of quartz crystals	239—256
SAXENA, R. N, PANDEY S. L. AND SINGH SOORAJ	
Structure and dielectric measurements of thin films of Bi_2O_3	257—266

Electron microscope studies of phase transformation in erbium oxide films

U Saxena and O N Srivastava

Physics Department, Banaras Hindu University, Varanasi-221005 (India).

1. Introduction

Industrial demand of thin film capacitors for the use in microminiaturized electronic components has greatly stimulated the investigations on rare earth metal oxide films. Recent investigations have shown that vacuum evaporated rare earth metal oxide films have excellent dielectric and semiconducting properties. Although several investigations have been carried out regarding the electrical and magnetic properties of these films, studies in relation to the structural crystallography, defect structure, the existence of intermediate phases and their transformation to other phases, are rather sparse. In view of the fact that physical properties depend crucially on the structure, microstructure and defect substructure of the films, it is imperative to study the structural aspects of these films. The present communication deals with the structural transformations in erbium oxide films. In particular the phase changes involving (i) amorphous \rightarrow crystalline, (ii) crystalline \rightarrow crystalline, short range and long range ordered variants have been studied.

2. Results and Discussion

Thin films of erbium oxide were prepared by the usual method of thermal evaporation in vacuum. The films employed in the present investigations had the thicknesses ranging between 500 and 600 Å. For studying the structural transformations, these films were pulse annealed in the electron microscope with a pre-calibrated (Srivastava and Srivastava 1975) focussed electron beam, for durations spread over 30-40 seconds. The annealing temperatures employed were about 300 and 900°C.

The electron microscope studies of as-grown films revealed that they have amorphous character. This was evidenced by broad halo type diffraction rings obtained from those films. On pulse annealing at about 300°C, an amorphous \rightarrow crystalline transformation is found to commence. Figure (1) exhibits this transformation. The featureless area represents the amorphous region whereas the area crisscrossed by the extinction contours, corresponds to the crystalline region.

Initially the crystallization is set off at several random nucleation centres. But, once the local crystallization is induced, the exothermic transformation raises



Figure 1. Transmission electron micrograph showing electron beam induced amorphous \rightarrow crystalline transformation. The featureless region represents the amorphous phase whereas the surrounding area crisscrossed by extinction contours corresponds to the crystalline region.

the temperature at the interface and thus the crystallization boundary propagates. The crystalline phase grows in spheruletic form (Figure 2) which shows that the heat transfer takes place in spherically symmetric mode. This crystalline



Figure 2. Dark field electron micrograph showing the spheruletic growth of crystalline region in the amorphous matrix.

phase has been found to correspond to a f.c.c. phase (Figure 3), similar to that obtained by directly oxidising the metal films (Murr 1967, Semiletov *et al* 1976), with a lattice parameter $a = 5.09 \pm 0.05 \text{ \AA}$. However, the lattice parameter has been found to vary by about 2% from specimen to specimen, which suggests that the obtained phase is nonstoichiometric.

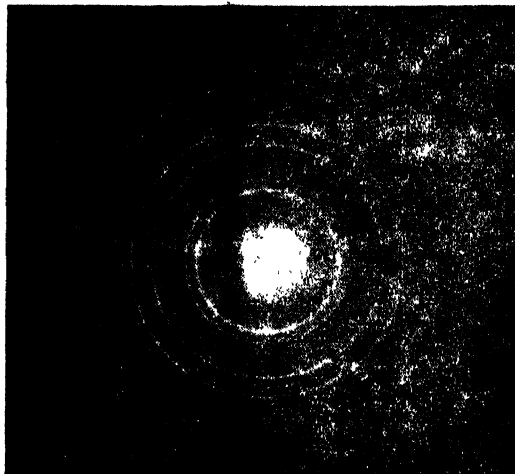


Figure 3. Powder diffraction pattern of the f.c.c. phase of erbium oxide film. The lattice parameter is found to be $a = 5.09 \pm 0.05 \text{ \AA}$.

In the present case, the nonstoichiometry is thought to arise due to oxygen vacancies. This is so, since pulse annealing of oxide samples in the electron microscope is known to produce oxygen vacancies (Bist *et al* 1972, Brusill 1961, Iijima, 1975). Also, since the oxygen ions have a much bigger size than the corresponding metal ions, the observed variation in lattice parameter becomes intelligible in terms of the existence of oxygen vacancies. The present phase can thus be designated as ErO_x . Since both the monoxide ($x = 1$) and dioxide ($x = 2$) and in between phases are known to exist for rare earth metal oxides, x , in the present case probably has the value $1 \leq x \leq 2$. Therefore, the f.c.c. phase cannot be strictly called as the monoxide, it can at best, be termed as a defect monoxide. It is, however, not possible to assign a unique structure to f.c.c. phase. Intensity calculations reveal that both ZnS (corresponding to $x = 1$) and CaF_2 (corresponding to $x = 2$) give a good fit for the observed intensities (Semiletov *et al* 1976). But the existence of the said nonstoichiometry suggests that f.c.c. phase is nearly ZnS type but tending towards CaF_2 type.

When the f.c.c. phase was further pulse annealed at higher temperature ($\approx 900^\circ\text{C}$), large single crystals grew which revealed interesting structural features. Single crystal diffraction patterns from this phase revealed that

besides the diffraction spots from the f.c.c. phase, intense diffuse streaks also appeared. Since pulse annealing is known to produce oxygen loss, the diffuse streaks seem to represent the short range ordering of oxygen vacancies. The diffuse intensity appears to be situated on a complicated surface in the reciprocal space of f.c.c. phase. Analysis of this surface is being currently investigated.

After repeated pulse annealing for longer durations (about 100 seconds) the ordering of oxygen vacancies takes place and the streaks tend to disappear, giving rise to sharp superlattice reflections. These superlattice reflections were found to arise from a b.c.c. phase which is nearly identical with the bulk phase. Representative diffraction patterns exhibiting the foregoing features are shown in figures 4 and 5. Diffraction patterns in other orientations also revealed the

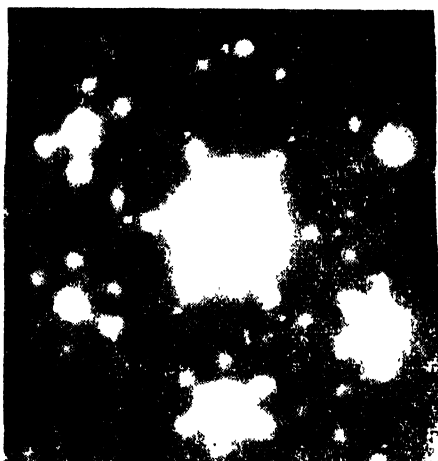


Figure 4. Diffraction pattern of the single crystal region of erbium oxide in [111] orientation. In addition to the intense f.c.c. spots, the presence of diffuse streaks can be noticed. These arise due to short range ordering of oxygen vacancies.

said characteristics. It should be mentioned here that even after the formation of the superlattice, a small amount of disorder in oxygen vacancies always persists which is manifested in the form of faint diffuse streaks when the diffraction patterns are taken at a slightly tilted position. This fact further supports the idea that the basic f.c.c. phase is neither ZnS type nor the CaF_2 type but lies in between the two.

The correspondence between the superlattice and the bulk Er_2O_3 phase indicates that the as-grown ErO_x has $1.5 < x \leq 2$ and when the reduction takes place producing the stoichiometry $x \approx 1.5$, the bulk like b.c.c. phase of $\text{ErO}_{1.5}$, i.e., Er_2O_3 gets formed. The present observations suggest that the high temperature (900°C) pulse annealing produces adequate amount of oxygen loss for the formation of the phase with $x \approx 1.5$.

It is worthwhile mentioning that the transformations amorphous \rightarrow crystalline (f.c.c.) \rightarrow crystalline (b.c.c.) have been observed to occur as a function of film thickness also. The thin films ($\leq 700^\circ\text{C}$) correspond to the amorphous phase while the thick films ($\geq 1100 \text{ \AA}$) to the crystalline b.c.c. phase. The films of



Figure 5. Single crystal diffraction pattern corresponding to figure 4. The sharp superlattice spots are due to ordering of oxygen vacancies.

intermediate thicknesses revealed the presence of mixed phases, in which initially the f.c.c. phase appeared with an amorphous phase, then individually and finally with b.c.c. phase. The heating of the film during their formation is believed to be the cause of thickness dependent transformation. This transformation was noticed while trying to monitor the transformations through the measurements of dielectric properties (Saxena and Srivastava 1976). The measurement of dielectric constant does reveal the amorphous \rightarrow crystalline (f.c.c.) \rightarrow crystalline (b.c.c.) transformation. These observations lend strong evidence to the pulse annealing induced transformations.

References

- Srivastava M M and Srivastava O N 1975 *Thin Solid Films* **29** 275
- Murr L E 1967 *Phys. Stat. Solidi* **24** 135
- Semiletov S A, Imamov M R, Ragimli N A and Man I L 1976 *Thin Solid Films* **32** 325
- Bist B M S, Kumar J and Srivastava O N 1972 *Phys. Stat. Solidi* **14** 197
- Brusill L A 1961 *Proc. Roy. Soc. A* **311** 267
- Iijima S 1975 *Acta Cryst.* **A31** 784
- Saxena U and Srivastava O N 1976 *Thin Solid Films* **33** 185

On some aspects of photoconducting properties of PbS films

H N Acharya and H N Bose

Department of Physics, Indian Institute of Technology, Kharagpur-721302.

1. Introduction

Thin films of lead sulphide have been used as infrared detectors for many years. Copious data has accumulated on the methods of preparation, structure and electronic properties of the thin films of lead chalcogenides. However, the manufacture of the most sensitive detectors is still considered as an art than science, and the mechanism of photosensitivity in these layers is still poorly understood. The controversy regarding the mechanism of photoconductivity has been highlighted by recent workers (Bode *et al* 1966, Said and Zempl 1976). It is felt that this controversy regarding the mechanism of photoconductivity might be a result of the fact that different investigators actually studied structurally different films. It was thus considered worthwhile to undertake investigations on films of known structure prepared under controlled conditions for understanding the mechanism of photoconduction in these films. Considering the different aspects of the problem a programme (Acharya 1971) of study of thin films of lead chalcogenides has been undertaken in our laboratories. This has been specifically aimed at obtaining a proper understanding of the electronic transport properties of lead chalcogenides. The work reported here constitute a part of that project.

The essential role of oxygen in sensitizing PbS films has been stressed by several workers; the mechanism of photoconduction in these films proposed by Petritz *et al* are also based on the same idea. According to majority carrier model (Petritz *et al* 1957) photoconductivity of PbS like films is due to increase of majority carrier concentration, the minority carriers created by photons being quickly trapped. It has not been possible to identify the nature of trapping mechanisms, although both surface and bulk trapping are considered possible. The exhaustive work by Sorrows (1958) lead to the estimation of density of traps. He concluded that the majority carrier life time predominate in photoconductive process and that the rate limiting process is that of transfer of charge from space charge region to traps. Sorrows predicted from the kinetics of charge transfer process that for films having particle size less than 0.1 micron the photo effect time constant should be equal to the field effect time constant. The prediction, however, could not be verified by Sorrows for want of necessary information about the particle size of the films used by him.

In present paper we report (a) the results of measurement of temperature variation of conductance of photosensitive films in darkness as well as under illumination; (b) studies on a.c., d.c. field effect and photoeffect relaxation on PbS samples whose structure are known from electron microscopic and X-ray diffraction studies. The results confirm the prediction of Sorrows about the equality of photoconductive and field effect time constants, and also indicate that surface traps are responsible for trapping of minority carriers.

2. Experimental

The films were prepared on glass substrates by a chemical method reported by Acharya and Bose (1971). The film thickness was measured by weighing technique. The conductance was measured using ohmic electrodes of colloidal graphite. The conductance of samples was measured under darkness and under steady illumination from liquid air temperature to 300°K. A tungsten filament lamp was used as a source of light; the intensity of light was measured using a calibrated Eppley thermopile. D.C. field effect studies were carried out with a circuit shown in figure 1. The a.c. field effect response and photoeffect response

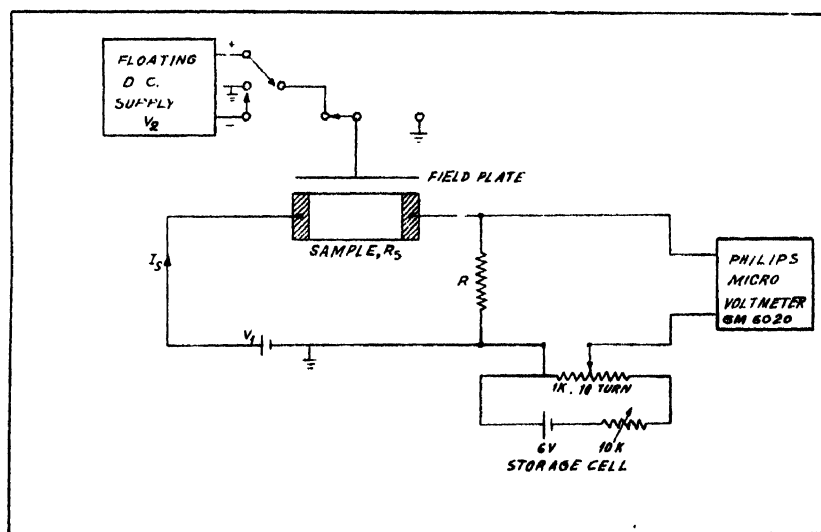


Figure 1.

to light pulses was measured by a circuit similar to that used by Sorrows (1958). The experimental arrangement is shown in figure 2.

Experimental results

The results of measurement of dark conductance under constant light for a typical sample are shown in figure 3. The figure shows $\log 1/R$ against $(1/T)$ from liquid nitrogen to room temperature.

The relaxation of conductance change induced by the application of external transverse electric field for a insensitive film is shown in figure 4. The relaxation

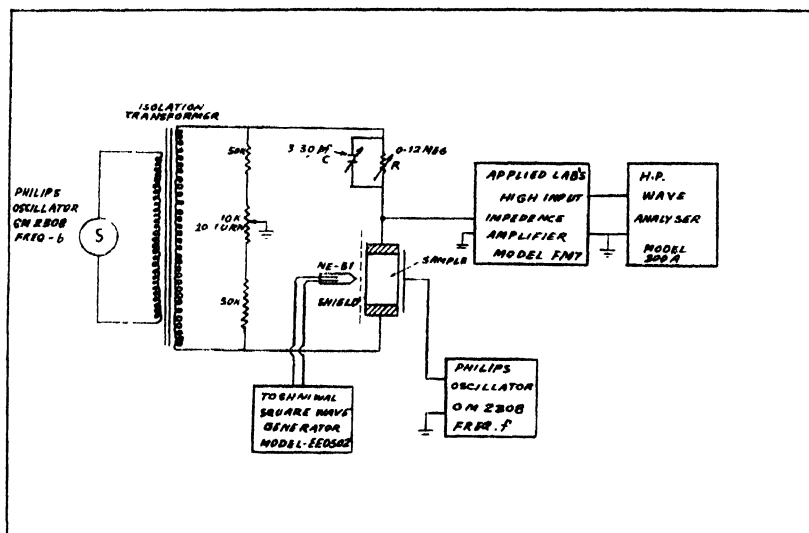


Figure 2.

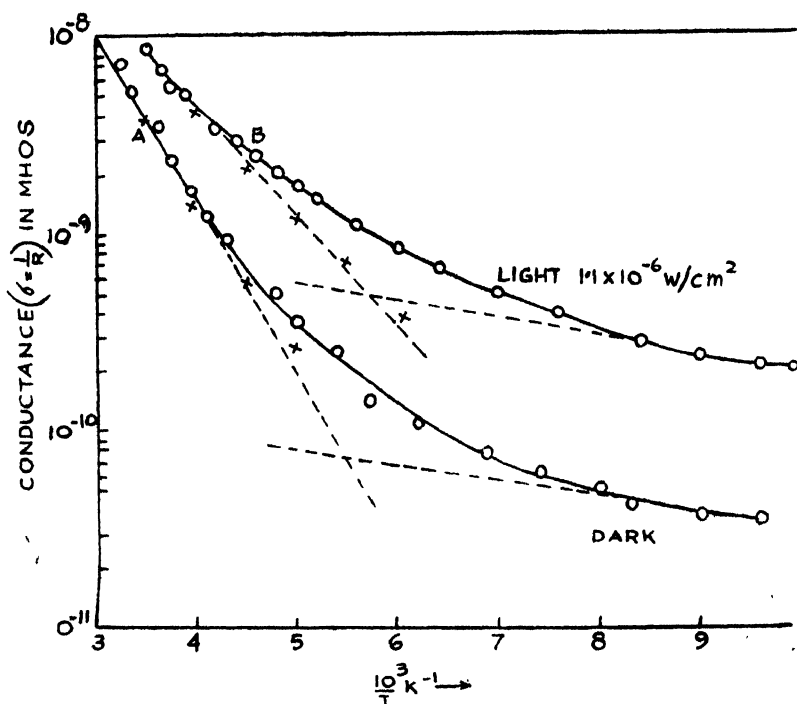


Figure 3.

of conductance induced by a transverse d.c. field along with the relaxation of photoconductivity for a sensitive sample is shown in figure 5. The variation of field effect, and photo effect response as a function of frequency are shown in figures 6 and 7 respectively. The field effect time constant and photoeffect time constant estimated by using the technique suggested by Sorrows are found

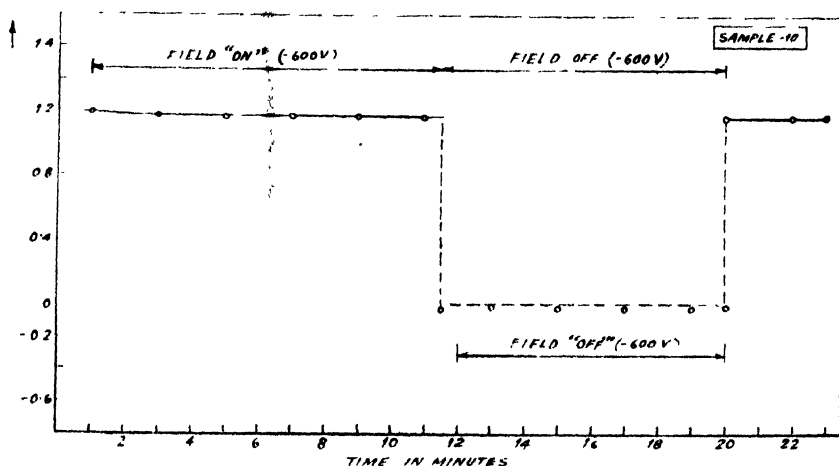


Figure 4.

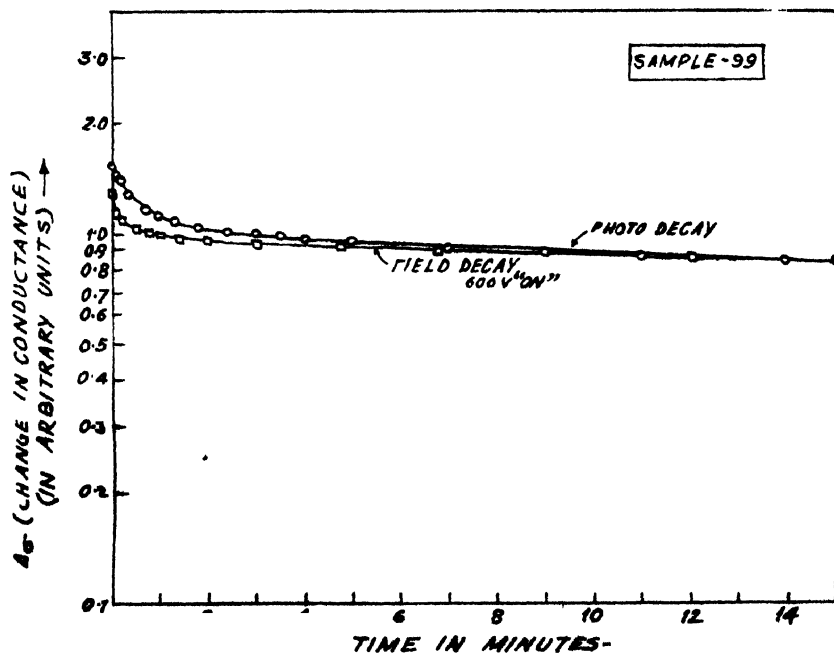


Figure 5.

to be $320 \mu s$ and $360 \mu s$ respectively which may be taken as practically equal within the limits of experimental error.

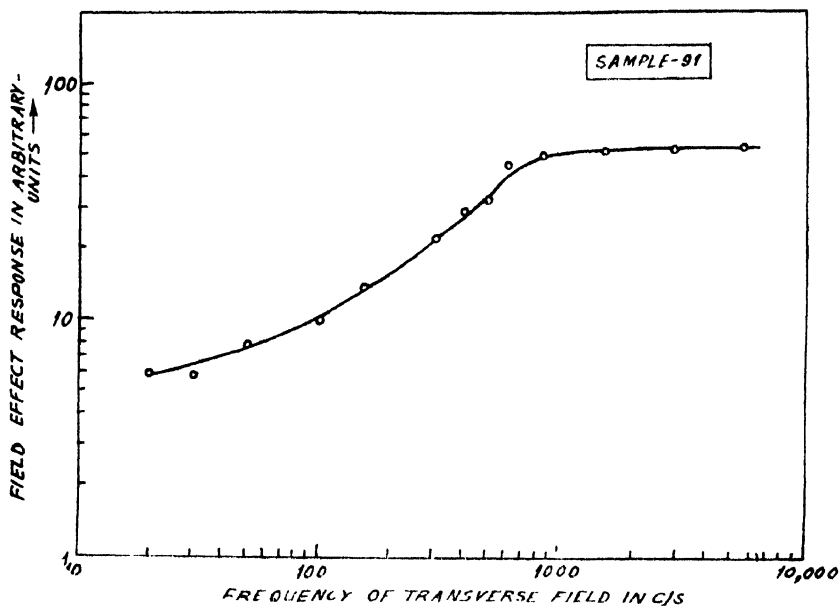


Figure 6.

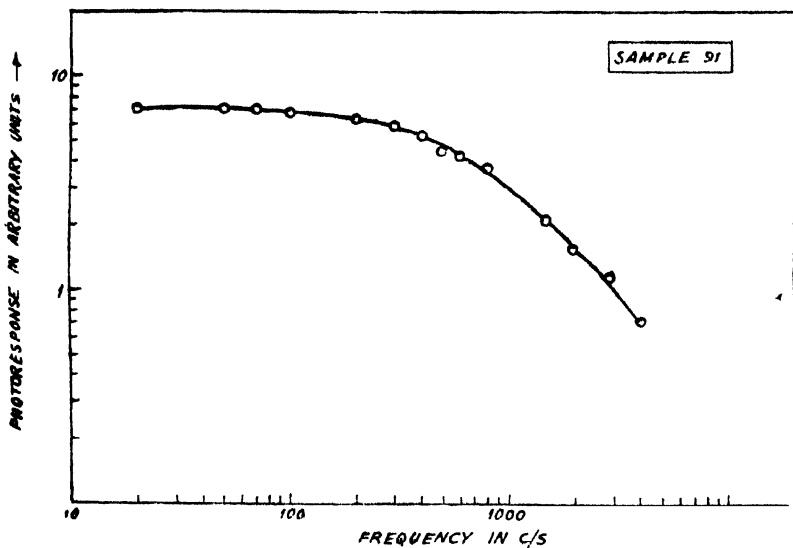


Figure 7.

The electron microscopic examination and X-ray diffraction studies (Acharya and Misra 1971) revealed that the film consist of crystallites of sizes varying from

60 to 100 Å.U. interspersed with minute gaps possibly covered with very thin layers of the material. The films in general show island structure with considerable fluctuation in thickness.

3. Discussion

Assuming the basic correctness of the model proposed by Petritz *et al* the resistance of the films may be considered to be due to a large number of barriers between crystallites in series. We, however, assume that each of such barriers has a shunt path. It is then possible under suitable assumptions, to show that the film conductance is approximately given by

$$\sigma \approx \frac{1}{R} = a_0 p_0 \mu_{p_0} + a p \mu_p e^{-\frac{q\phi}{KT}} \quad (1)$$

where a and a_0 may be considered as constants for all practical purposes, p_0 is the carrier concentration in the shunt path material, p is the concentration in the grains forming barriers of height ϕ and μ_p is the mobility in the grains.

It can be seen that the experimental curves of $\log \sigma$ vs $1/T$ are not straight lines over the entire temperature range. It seems that several activation energies are involved in the conduction process. To a first degree of approximation experimental curves can be analysed as sum of two exponential terms.

$$\begin{aligned} \sigma &= \sigma_{10} e^{-\frac{E_1}{KT}} + \sigma_{20} e^{-\frac{E_2}{KT}} \\ &= \sigma_1 + \sigma_2; \quad \text{where } \sigma = 1/R. \end{aligned} \quad (2)$$

Comparing relation (1) and (2) we are lead to the conclusion that the conductance of the films can be roughly approximated to the presence of intercrystalline barriers along with shunt paths

Following Petritz the conductance due to barriers is given by

$$\sigma_1 = \sigma_{10} e^{-\frac{(0.11 + E_B)}{KT}} \quad (3)$$

where E_B is the barrier height between the grains and 0.11 eV represents the height of trapping states (oxygen) above valence band. The shunt path conductance should then account for the second term $\sigma_2 = \sigma_{20} e^{-\frac{E_2}{KT}}$ in the relation (2). The results of present investigation tabulated in Table 1 show that E_B is reduced by illumination.

It has been found that E_2 is practically independent of illumination although σ_2 is considerably increased under light. The observed increase in σ_2 can be easily understood as an increase in p_0 , the carrier concentration. The exponen-

Table 1. Effects of light on the barrier height for a few typical PbS films

Sample No.	Amount of light falling on the sample in W/cm ²	Particle size perpendicular to planes		Barrier height E_B in eV
		(111)	(200)	
87	Dark	70 A.U.	50 A.U.	0.11
87	3×10^{-6}	70 A.U.	50 A.U.	0.02
91	Dark	100 A.U.	100 A.U.	0.13
91	1.1×10^{-6}	100 A.U.	100 A.U.	0.04
89	10^{-5}	60 A.U.	60 A.U.	0.09
89	3×10^{-5}	60 A.U.	60 A.U.	0.05

tial factor $\exp(-E_2/KT)$ can be caused by the temperature variation of the corresponding mobility $\mu p_0 = \mu_0 e^{-\frac{E_2}{KT}}$. In other words the photoconductance in the PbS films studied here can be explained by taking into account both the "barrier" as well as "number" modulation mechanisms. The relative predominance of the mechanisms being dependent on the nature of the sample and temperature range. One of the significant results of the field effect and photo effect relaxation studies reported here lies in the equality of slow as well as fast field effect relaxation constants with those of photoeffect relaxation. In the present work the X-ray study shows that the particle size $d_c = 10^{-6}$ cm is less than $L_D = 10^{-5}$ cm and for such samples the equality of the relaxation time constants of the field effect and photoconductivity is predicted by the analysis of Sorrows (1958).

Since the fast as well as slow time constant for photo-response and field effect relaxation are of the same magnitude, same trapping states are likely to be involved in both the cases. The field effect phenomena are known to be due to the exchange of carriers between the space charge layer and the surface states, (either on the oxide-crystal interface or on the outside surface of oxide layer); we are thus led to believe that the trapping states in photoconducting PbS films are also to be traced to the same origin.

4. Conclusions

The majority carrier model of Petritz (1957) with some modification can account for most of the experimental results of the present study. The modulation of conductance due to modulation of barrier height E_B in Petritz model occurs at least for films studied here. The field effect study shows that the minority

carrier traps are really surface states on the oxide-crystal interface or on the outside surface of the oxide layer

References

- Bode D E 1966 *In Physics of Thin Films* edited by Hass G and Thun R H, Vol III, Academic Press, New York p 275
- Said M S and Zerni J N 1976 *J. Appl. Phys.* **47** 866
- Acharya H N 1971 *Ph.D. Thesis* I.I.T., Kharagpur
- Acharya H N and Bose H N 1971 *Physica Status Solidi (a)* **6** K43
- Acharya H N and Misra N K 1971 *J. Phys. (D) : Appl. Phys.* Vol 4
- Petriz R L, Lummis F L, Sorrows H E and Woods J F 1957 *In Semiconductor Surface Physics* Ed Kingston R H (University Pennsylvania Press)
- Sorrows H E 1958 *Ph.D. Thesis* Catholic University of America; Navord report 6164 (1958)

Optical properties of multialkali photocathodes

C Ghosh and B P Varma

Optoelectronics Section, Bhabha Atomic Research Centre, Bombay-400086.

1. Introduction

In photoemission, the photoelectrons are emitted due to the absorption of photons in the solid. The optical properties of the solid is, therefore, an important factor which determines its photoemission. The optical transitions which lead to photoemission in the visible and near ultraviolet regions are essentially interband transitions between the valence and conduction bands. The transition strength which reflects the total number of transitions taking place per unit time is dependent on the nature of the transition. This can be calculated from the optical constants and hence it is possible to infer about the nature of optical transitions from them. The nature of the optical transition can, however, be best understood with the help of photoelectron spectroscopy.

The multialkali photocathode $\text{Na}_2\text{KSb}(\text{Cs})$ is having the highest photoemission among the conventional photoemitters. It is almost invariably used in all devices using photoemission. In spite of its widespread application, there has been little investigation into the physical processes which give rise to photoemission. This paper describes our investigation relating to the optical properties and optical transitions in such photocathodes.

2. Experiment

Very high sensitivity photocathodes ($\sim 300 \mu\text{a/lm}$) have been processed with a technique developed earlier in this laboratory (Varma and Ghosh 1974). This is prepared by reacting different metals like antimony, potassium, sodium and cesium in high vacuum (10^{-4} torr). The photocathode is prepared in the form of thin film on a glass or quartz substrate. For the study of optical properties, they were processed in "cells" with quartz windows. The optical properties were determined by measuring the transmission and reflection values of the cathode. This was carried out with Cary 14 and Carl Zeiss M4Q III spectrophotometers respectively. The optical constants were calculated in the usual way using Fresnel's formula (Heavens 1955). The figure 1 shows a plot of the real and imaginary parts of complex dielectric constant against photon energy. The relative optical transition strengths (Spicer and Eden 1968) $(\hbar\nu)^2\epsilon_2$ is calculated at each photon energy (figure 2).

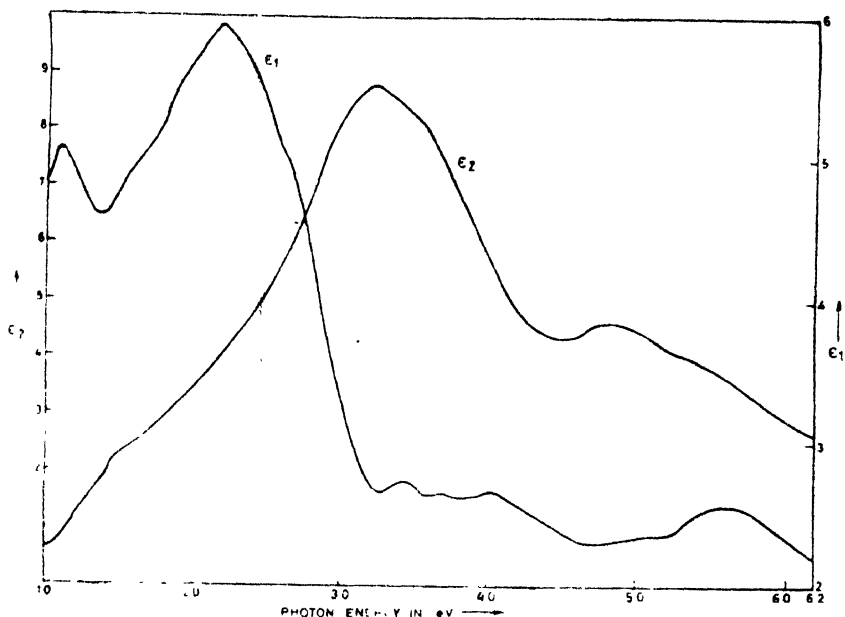


Figure 1. Plot of real (ϵ_1) and imaginary part (ϵ_2) of complex dielectric constant Vs. photon energy.

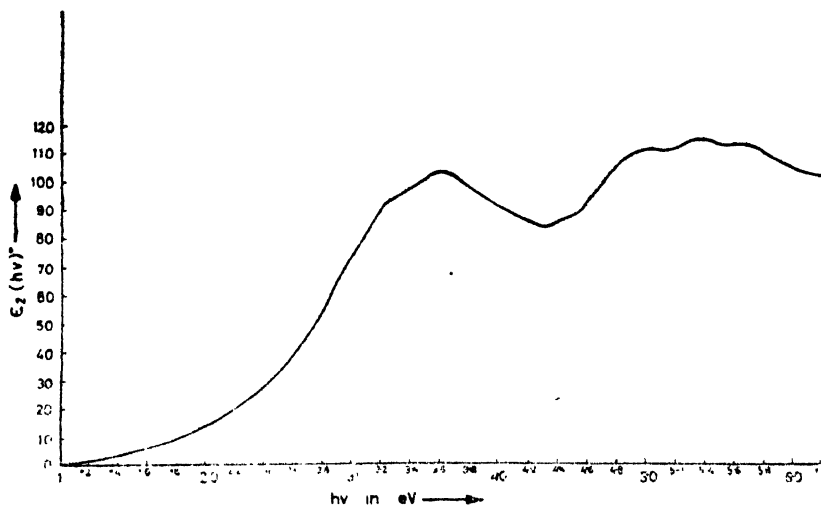
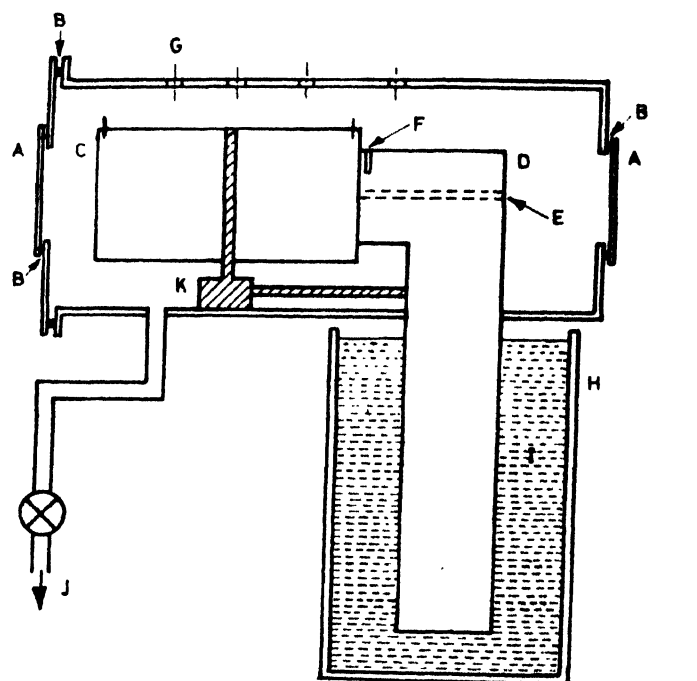


Figure 2. Plot of relative optical transition strength $(h\nu)^2 \epsilon_2$ Vs. photon energy.

For measurement of reflection and transmission at low temperature, a cryostat of cold finger type was constructed. A copper block which acted as the cold finger was dipped in liquid nitrogen to get a temperature of 90°K. Light

was passed through a small slot in the copper block (figure 3) to measure transmission values through the cathode.



- | | |
|----------------------------|---------------------------------|
| A GLASS WINDOW | B O RING SEAL |
| C PHOTOTUBE | D COPPER BLOCK |
| E 1 mm DIA. SLOT | F THEROMO COUPLE INSERTION SLOT |
| G ELECTRICAL FEED THROUGHS | H DEWAR |
| I LN ₂ | J TO ROTARY PUMP |
| K CLAMPING MECHANISM | L DETECTOR SIDE |
| M MONOCHROMATOR SIDE | |

Figure 3. Schematic diagram of the cryostat.

A photoelectron spectrometer was built to make measurements in the visible and near ultraviolet region. The energy resolution of the spectrometer was better than 175 MeV. The lower limit of integral current for analysis was about 2×10^{-13} amps. Figure 4 shows a few energy distribution curves obtained with multialkali photocathodes in a small range of photon energy.

3. Results and discussion

The plot of optical transition strength against photon energy (figure 2) shows the existence of two peaks around 3.6 and 5.4 eV and a valley between the peaks

at a value of about 20% of the higher peak. A fast rise in the transition strength after a photon energy of about 2.3 eV is seen. A sharp rise in transition strength and many structures in the ultraviolet region suggests that the transitions might

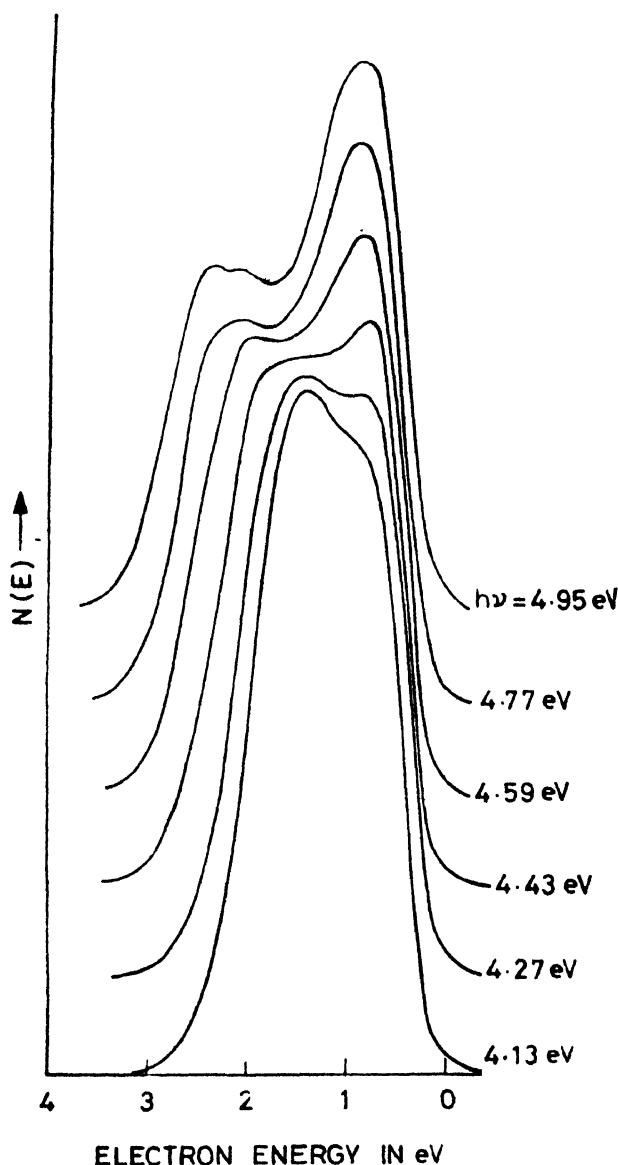


Figure 4. A few energy distribution curves from multialkali photocathodes.

be predominantly direct in nature (Eden 1967). The indirect or photon assisted transitions are unlikely to have any significant contribution in the ultraviolet region where absorption is very high. But non-direct transitions may have

considerable contribution as had been observed in Cs_3Sb and Cs_3Bi (Wooten 1973, Derbenwick *et al* 1974). The presence of indirect type of transition is more probable at longer wavelengths, particularly in the threshold wavelength region of photoemission. If the indirect type of transitions are present, the probability of such transitions would decrease by a factor of 3 or 4 at low temperature of about 90°K (Spicer 1963) due to reduction of phonon density.

The measurement of reflection and transmission was made in the cryostat system both at low and room temperature. The absorption at room temperature was compared to that at 90°K . The absorption constant at low temperature remained constant within 1% of the value at room temperature which was the limit of accuracy of the measurement. Therefore, it could be concluded that the indirect or phonon assisted transitions were not having any significant contribution in the interband transitions in this material.

The photoelectron spectroscopy was used to know whether non-direct transition is having any significant contribution. It arises due to localisation of the photogenerated hole in the valence band such that the associated wavefunction would contain all k 's if Bloch functions are used (Spicer 1967). In such transitions, some of the structures in the energy distribution curves such as peaks, shoulders, dips etc. which are obtained with a particular photon energy would move in the energy scale when the photon energy is changed. The shift in the position of the structures in the energy scale would be equal to the change of photon energy if the structures are due to the effective density of states in the valence band. This is called the equal increment rule (Berglund and Spicer 1964). On the other hand, if the structures are due to the effective density of states in the conduction band they would remain fixed at one position in the energy scale and would not move. This is so because the conservation of crystal momentum is not an important selection rule and only the effective density of states determines the energy distribution of the photoelectrons.

If the position of peaks, shoulders, valleys etc. are plotted against photon energy, the structures due to valence band would be parallel to $E = h\nu$ line and those due to the conduction band would appear parallel to $h\nu$ axis for non-direct transitions. If the transitions are of direct nature, none of these would be observed. We have plotted the peak, shoulder and valley positions obtained from energy distribution curves against $h\nu$ in figure 5. Only one shoulder which later transformed into a peak was parallel to $h\nu$ axis. But this was the peak arising due to electron-electron scattering of the high energy electrons. No other structure showed the behaviour expected for the case of non-direct transitions. Therefore it could be concluded that the interband transitions occurring in multialkali photocathodes are of direct nature.

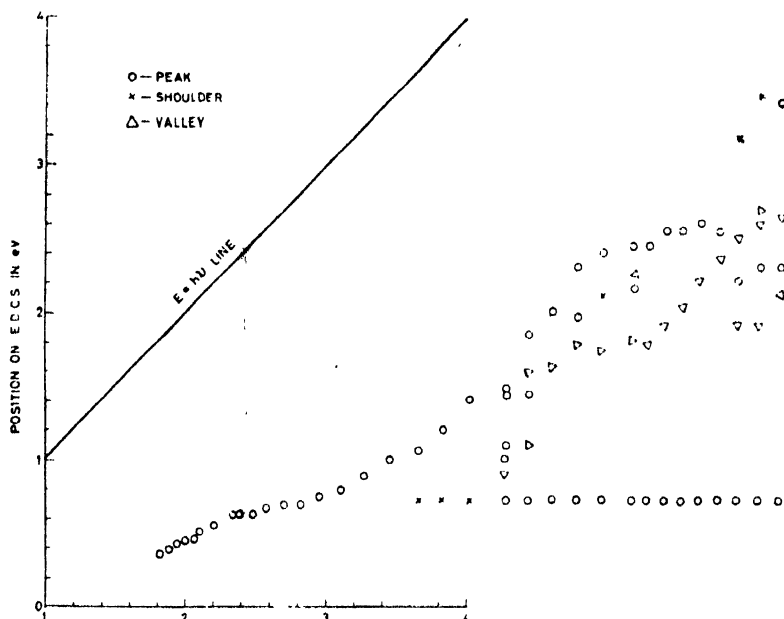


Figure 5. Plot of peak shoulder and valley positions in energy scale Vs. photon energy.

4. Conclusions

The study of the optical properties of the high sensitivity multialkali photocathode suggests that the interband transitions between the valence and conduction band is of direct nature. Comparison of optical absorption at room temperature to that of low temperature at 90°K showed that the indirect transitions do not have any significant contribution. Finally the direct nature of transitions is confirmed by photoelectron spectroscopy.

References

- Varma B P and Ghosh C 1074 *Patent No.* 142173 (1974)
 Heavens O S 1955 *Optical properties of thin solid films* Butterworths London p 92
 Spicer W E and Edon R C 1968 *Proc. 9th International Conf. on Physics of Semiconductors*, Moscow Vol 1 p 65
 Edon R C 1967 *Ph.D. Thesis*, Stanford University
 Wooten F 1973 *J. Appl. Phys.* **44** 1112
 Derbenwick G F, Pierce D T and Spicer W E 1974 *Methods of Expt. Phys.* **11** 67
 Spicer W E 1963 *Phys. Rev. Letters* **11** 243
 Spicer W E 1967 *Phys. Rev.* **154** 385
 Bergland C N and Spicer W E 1964 *Phys. Rev.* **136** A1030 and A1044

Magnetization density of Fe^{++} in KFeF_3 and RbFeF_3

J K Sharma

Department of Physics, St. John's College, Agra-282002

and

D C Khan

Department of Physics, Indian Institute of Technology, Kanpur-208016.

1. Introduction

The neutron magnetic form factor offers a direct means of obtaining a detailed picture of total magnetisation density distribution due to unpaired electrons of the unfilled 3-d shell of a transition metal ion in a crystal. In the present work, this quantity has been theoretically calculated for Fe^{++} in two of its compounds, namely KFeF_3 and RbFeF_3 . Halpern and Johnson (1939) derived an expression for magnetic form factor in case of magnetic moments due to electron spin only. Trammell (1953) extended the method of Halpern and Johnson for the cases where the orbital moment is not completely quenched. The Trammell approach, which emphasizes the Fourier-Transform like relationship between form factor and charge density distribution of magnetic electrons, has been used to consider the effect of unquenched orbital magnetic moment in these compounds. This approach has been preferred to a recent approach of Johnston and Rimmer (1969) which is more amenable to computer calculations, due to its simplicity and straight-forwardness in case of unpolarised neutron scattering from uniaxial magnetic spin distribution, as in the case of these compounds.

2. Spin structure of KFeF_3 and RbFeF_3

Both KFeF_3 and RbFeF_3 have perovskite structure (Davidson *et al* 1973) with cubic stackings of KF_3 or RbF_3 layers and octahedral anion holes filled by Fe^{++} ions. Slight distortions from cubic symmetry occur at Neel Temperature for both. The neutron diffraction studies for both materials indicate that magnetic unit cell is eight times the crystallographic unit cell. The anti-ferromagnetic ordering is of G type with six nearest neighbour spins coupled antiparallel. In both cases a single crystal develops a domain structure when cooled below T_N . In KFeF_3 , neighbouring domains have their distortions along different $\langle 111 \rangle$

directions and all $\langle 111 \rangle$ distortions are equally probable. In RbFeF_3 spins are in $\langle 100 \rangle$ direction.

3. Theory

The differential scattering cross-section for elastic magnetic scattering of unpolarised neutrons in solid angle $d\Omega$ is (Halpern and Johnson 1939)

$$\frac{d\sigma}{d\Omega} = \left(\frac{\gamma e^2}{mc^2} \right)^2 \sum_{q,q'} P_q \left| \sum_{\mathbf{n}} e^{i\mathbf{K} \cdot \mathbf{n}} \langle q' | \mathbf{T}_{\mathbf{n}} | q \rangle \right|^2 \quad (1)$$

where $|q\rangle$ and $|q'\rangle$ are initial and final states of the crystal having same energy. $\mathbf{K} = \mathbf{k} - \mathbf{k}'$ is the difference between initial and final wave vectors \mathbf{k} and \mathbf{k}' of the neutron, P_q is the probability of the state $|q\rangle$ being occupied, \mathbf{n} is the lattice vector and $\gamma = -1.91$ is the gyromagnetic ratio of the neutron, $\mathbf{T}_{\mathbf{n}}$ is the interaction of the neutrons with the electrons of the ions at the site \mathbf{n} and is given by,

$$\mathbf{T}_{\mathbf{n}} = \mathbf{K} \times \mathbf{Q}_{\mathbf{n}} \times \mathbf{K} \quad (2)$$

where

$$\mathbf{Q}_{\mathbf{n}} = \sum_j \{ e^{i\mathbf{K} \cdot \mathbf{r}_j} \mathbf{s}_j + \frac{1}{4} [l_j f(\mathbf{K} \cdot \mathbf{r}_j) + (\mathbf{K} \cdot \mathbf{r}_j) l_j] \}$$

and we have,

$$f(\mathbf{K} \cdot \mathbf{r}_j) = 2 \left[\frac{d}{dx} \left(\frac{e^x - 1}{x} \right) \right]_{x = i\mathbf{K} \cdot \mathbf{r}_j} \quad (4)$$

l_j and \mathbf{s}_j are the orbital angular momentum and spin respectively of the j -th electron of the ion at the lattice site \mathbf{n} .

4. Derivation of form factor

We assume that $|q\rangle$, the wave function of the magnetic unit cell, can be written as a product of state vectors referring to individual ions (Heitler London approximation), i.e.

$$|q\rangle = |q_1\rangle |q_2\rangle |q_3\rangle \dots |q_8\rangle$$

The magnetic unit cell may be decomposed in two ferromagnetic sublattices with spins along $+Z$ and $-Z$ directions. Since each sublattice unit cell consists of four atoms with parallel spin, eq. (1) reduces to the form,

$$\frac{d\sigma}{d\Omega} = \left(\frac{4\gamma e^2}{mc^2} \right)^2 \sin^2 \omega \left| \langle \psi_{\text{Fe}^{++}} | \mathbf{Q} | \psi_{\text{Fe}^{++}} \rangle \right|^2 \quad 2\pi i(\mathbf{h} + \mathbf{k} + \mathbf{l})^2 \quad (6)$$

where $|\psi_{\text{Fe}^{++}}\rangle$ is the ground state wave function of Fe^{++} in KFeF_3 and ω is the angle between \mathbf{K} and \mathbf{Q} at $\mathbf{K} = \mathbf{G}$, the reciprocal, lattice vector. \mathbf{Q} is given by eq. (3).

Comparing (6) with semi classical expression of Van Laar (1968), the magnetic form factor is given by,

$$f_{Fe^{++}} = \frac{|\langle \psi_{Fe^{++}} | Q | \psi_{Fe^{++}} \rangle|}{|\langle \psi_{Fe^{++}} | Q | \psi_{Fe^{++}} \rangle|_{K=0}} \quad (7)$$

5. Calculation of form factor

(a) For Fe^{++} in $KFeF_3$:—

The ground state wave function for Fe^{++} in $KFeF_3$ is given by (Davidson *et al* 1973)

$$\begin{aligned} |\psi_{Fe^{++}} \rangle &= 0.922 |M_s = 2, M_e = -1 \rangle - 0.371 |M_s = 1, \\ &M_e = 0 \rangle + 0.116 |M_s = 0, M_e = 1 \rangle \end{aligned} \quad (8)$$

when trigonal distortion is neglected and the structure is assumed to be cubic) Transforming the pseudo angular momentum eigen functions in (8) to 5D state functions (Mahendra and Khan 1971), we get,

$$\begin{aligned} |\psi_{Fe^{++}} \rangle &= -0.922 |M_s = 2, M_L = 1 \rangle - \frac{0.371}{\sqrt{2}} \\ &(|M_s = 1, M_L = 2 \rangle - |M_s = 1, M_L = -2 \rangle) \\ &+ 0.116 |M_s = 0, M_L = -1 \rangle. \end{aligned} \quad (9)$$

(i) Calculation of spherically symmetric part :—

Expressing the right hand side of (9) in terms of one electron wave functions (Appendix C of Mahendra and Khan 1971), we calculate (7) for Q_z only, since Q_x and Q_y do not contribute to spherically symmetric part of the form factor (Mahendra and Khan 1971). Simplifying, we get,

$$\begin{aligned} f_{Fe^{++}}(K) &= \frac{1}{2.239} [0.876 \langle 2 | e^{iK.r} | 2 \rangle + 0.492 \langle 1 | e^{iK.r} | 1 \rangle + 0.456 \langle 0 | \\ &e^{iK.r} | 0 \rangle + 0.415 \langle 1 | f(K.r) | 1 \rangle] \end{aligned} \quad (10)$$

Using results of Appendix (E) of Mahendra and Khan (1971), for

$$\langle dm | e^{iK.r} | dm \rangle \text{ and } \langle dm | f(K.r) | dm \rangle,$$

we have,

$$\begin{aligned} f_{Fe^{++}}(K) &= \frac{1}{2.239} [1.824 \langle j_0 \rangle + 0.415 \langle g_0 \rangle + \frac{2}{7} (5\pi)^{1/2} / 20 (0.348 \langle j_2 \rangle - \\ &0.415 \langle g_2 \rangle) + \frac{2}{7} (\pi)^{1/2} / 40 (1.644 \langle j_4 \rangle - 1.660 \langle g_4 \rangle)] \end{aligned} \quad (11)$$

Retaining only spherically symmetric part of $Y_{1m}(K)$, we get,

$$f_{Fe^{S_{++}}}(K) = \frac{1}{2.239} [1.824 \langle j_0 \rangle - 0.124 \langle j_2 \rangle + 0.264 \langle j_4 \rangle + 0.415$$

$$(\langle g_0 \rangle - 1/2 \langle g_2 \rangle) + 0.356(\langle g_2 \rangle - 3/4 \langle g_4 \rangle)] \quad (12)$$

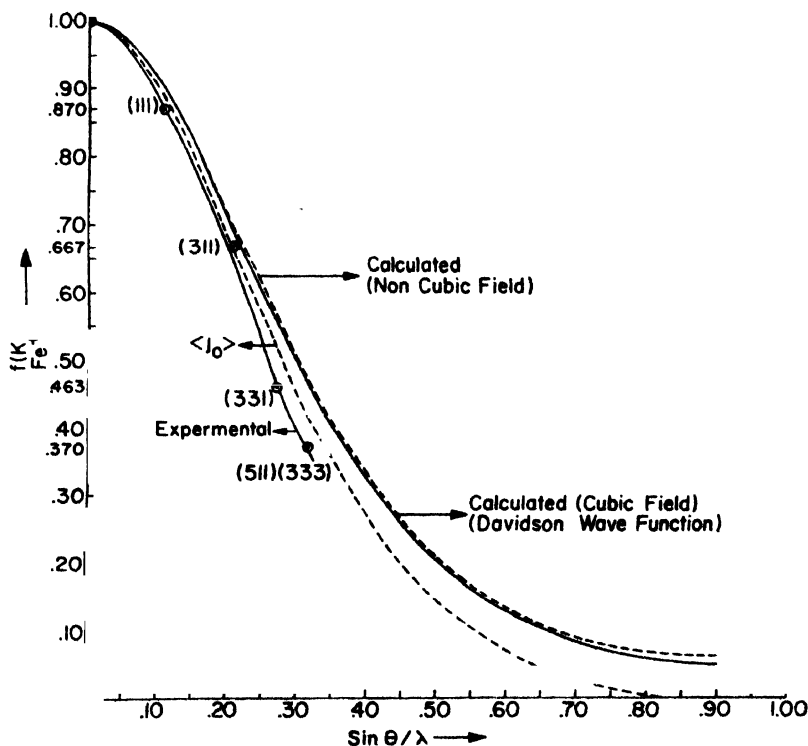
Using relation between $\langle g_L \rangle$ and $\langle j_L \rangle$

$$\langle g_{L-1} \rangle - \frac{L}{L+1} \langle g_{L+1} \rangle = \frac{2}{L+1} \langle j_{L-1} \rangle + \langle j_{L+1} \rangle \quad (13)$$

we get,

$$f_{Fe^{S_{++}}} = \langle j_0 \rangle + 0.209 \langle j_2 \rangle + 0.277 \langle j_4 \rangle. \quad (14)$$

Using Watson and Freeman (1961) values of $\langle j_L \rangle$ for Fe^{++} , $f_{Fe^{S_{++}}}$ is plotted against $\frac{\sin \theta}{\lambda}$ along with the free ion form factor $\langle j_0 \rangle$. (figure 1



Magnetic Form Factor For Fe^{++} in $KFeF_3$

Figure 1.

(ii) Calculation of the non spherical part :

Both $\langle \psi_{Fe^{++}} | Q_x | \psi_{Fe^{++}} \rangle$ and $\langle \psi_{Fe^{++}} | Q_y | \psi_{Fe^{++}} \rangle$ which are completely non spherical are evaluated. $\langle \psi_{Fe} | Q_z | \psi_{Fe} \rangle$ also has a non spherical part which is obtained by substituting cubic part of $Y_{Lm}(K)$ in (11). It turns out that the non-spherical part is very small so that the magnetization distribution in this case is almost spherical.

(b) Fe^{++} in $RbFeF_3$:

In case of $RbFeF_3$, the ground state wave function is given by (Wertheim *et al* 1967)

$$|\psi_{Fe^{++}}\rangle = 0.774|2, -1\rangle - 0.547|1, 0\rangle + 0.316|0, 1\rangle \quad (15)$$

A similar calculation carried out with this wave function yields a spherical form factor,

$$f_{Fe^{S++}} = \langle j_0 \rangle + 0.186 \langle j_2 \rangle + 0.219 \langle j_4 \rangle. \quad (16)$$

This is also plotted against $\frac{\sin \theta}{\lambda}$ along with the free ion form factor $\langle j_0 \rangle$.

Here also, the non-spherical part comes out to be negligibly small. (figure 2)

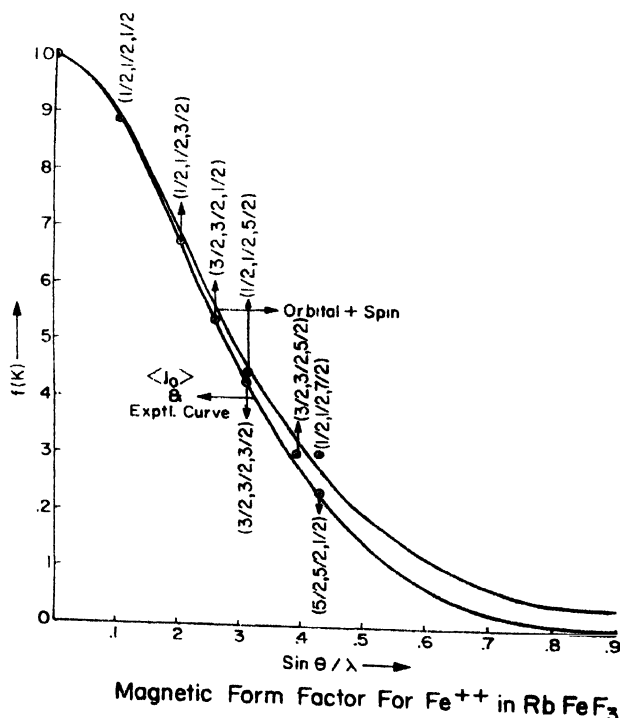


Figure 2.

6. Conclusion

The theoretical curves in both these cases exhibit an expansion of the form factor (i.e. a contraction of magnetization density) as compared to the free ion curve when the orbital effect is included. The experimental curve in case of $KFeF_3$ (Scatturin *et al* 1961) shows a contraction of about 10% from the free ion curve whereas it almost coincide with the $\langle j_0 \rangle$ curve in $RbFeF_3$ (Franklin *et al* 1971). In case of some similar compounds of other transition metal ions ($KCoF_3$ and $KNiF_3$) the authors have shown (Sharma and Khan) that inclusion of orbital part explains a part of the difference between the experimental and theoretical form factors. In case of Fe^{++} , however, it seems that covalency, that is the sharing of electrons between metal ion and ligand F^- ions plays an important role and makes a Mn^{++} like negative contribution (Freeman and Ellis 1970) to the form factor. Calculations for the inclusion of this covalency effect are in progress.

References

- Halpern O and Johnson M H 1939 *Phys. Rev.* **55**, 898
 Trammell G T 1953 *Phys. Rev.* **92**, 1387
 Johnston D F and Rimmer D E 1969 *J. Phys.* **C2**, 1151
 Davidson G R, Eibschutz M and Guggenheim H G 1973 *Phys. Rev.* **B8**, 1864
 Van Laar B 1968 *Ph.D. Thesis* (University of Loiden)
 Mahendra A and Khan D C 1971 *Phys. Rev.* **B4**, 3901
 Watson R E and Freeman A J 1961 *Acta. Cryst.* **14**, 27
 Wertheim G K, Guggenheim H T, Williams H J and Buchanan D N E 1967 *Phys. Rev.* **158**, 446
 Scatturin V, Cerliss L, Elliot N and Hastings S 1961 *Acta. Cryst.* **14**, 19
 Wang F Y Franklin, Cox D E and Kestigian M 1971 *Phys. Rev.* **B3**, 3946
 Sharma J K and Khan D C 1976 *Phys. Rev.* **14** 4184
 Freeman A J and Ellis D E 1970 *Phys. Rev. Letters* **24**, 516

Electric field gradient at impurity sites in ionic crystals

V S Sivasankar, S Chitra and S Radhakrishna

Department of Physics, Indian Institute of Technology, Madras-600036

1. Introduction

In alkali halides, the F -center, consisting of an electron trapped at an anion vacancy, has a very high local symmetry. Consequently, the excited state ($2p$) does not split. However, in the presence of other defect(s) in the vicinity, the symmetry is considerably lowered leading to splitting of the excited state. In such cases the p_x , p_y and p_z functions are oriented along the principal axes of the crystalline electric field gradient tensor. Additively coloured alkali halides, when optically bleached with F -light, give rise to F_{z1} band. The constituents of the center responsible for this band are an F center, a suitable divalent substitutional cation impurity and the associated charge compensating cation vacancy (Radhakrishna and Chowdari 1972). In this paper results of a calculation of the EFG tensor at the F_{z1} electron site in cesium chloride are reported. Three different models of the center are considered. F center is taken as the origin in all these models and the corresponding positions of the impurity and the vacancy are as follows :

Model	Impurity			Vacancy		
1	1/2,	1/2, -1/2		1/2,	1/2,	1/2
2	1/2,	1/2,	1/2	1/2,	1/2,	3/2
3	1/2,	1/2,	3/2	1/2,	1/2,	1/2

2. Theory

The contributions to the field gradient come from two sources : the charges and the effective dipoles around the site under consideration. The effective dipoles at the respective lattice points are given by

$$\mu_{\text{effective}} = \alpha E \mu_{(\text{effective charges})} \quad (1)$$

where E is the electric field arising from the neighbouring charges and effective dipole moments and α is the polarisability of the ion at the field point. The components of the electric field at a point (x, y, z) due to an ideal point charge e

at (0, 0, 0) and due to an ideal point dipole \mathbf{m} at (0, 0, 0) are given by (Boncher 1962) :

$$E_{\text{charge}} = e \frac{x}{r^3} ; \quad (2)$$

$$E_{\text{dipole}} = \frac{3x^2 - r^2}{r^5} m_x + \frac{3xy}{r^5} m_y + \frac{3xz}{r^5} m_z \quad (3)$$

with similar expressions for the y - and z -components, where $r = (x^2 + y^2 + z^2)^{1/2}$.

The components of the $\mathbf{E} \cdot \mathbf{F} \cdot \mathbf{Q}$ tensor are obtained by differentiation of eq. (2, 3) so that

$$q_{xx} = \delta E_x / \delta x; \quad q_{xy} = \delta E_x / \delta y = q_{yx}; \quad \text{etc.} \quad (4)$$

The general formulae can thus be written as follows :

Contribution of charges :

$$q_{xx} = (e/r^3)(1 - (3x^2/r^2)); \quad q_{xy} = -3exy/r^5. \quad (5)$$

Contribution of dipoles :

$$q_{xx} = \frac{3}{r^7} (r^2 - 5x^2)(xm_x + ym_y + zm_z) + \frac{6xm_x}{r^5}; \quad (6)$$

$$q_{xy} = \frac{3}{r^5} (xm_y + ym_x) - \frac{15xy}{r^7} (xm_x + ym_y + zm_z). \quad (7)$$

Cyclic permutation of x, y, z gives the other components.

3. Calculation

The main features of the calculations are schematically shown in figure 1. The F_{z1} electron site is chosen as the origin. The coordinates of all the lattice points inside a sphere (A) of radius 20 Å centered on the origin are reproduced. Associated with each lattice point are the charge and the polarisability of the respective ion. At all the sites inside a sphere (B) of radius 10 Å centered on the origin, the induced dipole moments due to all charges inside a sphere (C) of radius 10 Å centered on that point are calculated. Using these values the induced dipole moments at lattice points inside a sphere (D) of radius 5 Å, centered on the origin, due to the dipoles inside a sphere (E) of radius 5 Å, centered on that point are calculated. With the new values for the points inside the sphere (D) and the old values for those inside the sphere (B) but not in (D), the induced dipole moments at points inside the sphere (D) are recalculated. This cycle is

repeated until the desired accuracy is obtained, that is, the values obtained in one cycle differ from those in the preceding cycle by less than a suitable chosen value ($\sim 10^{-5}$, in our calculation).

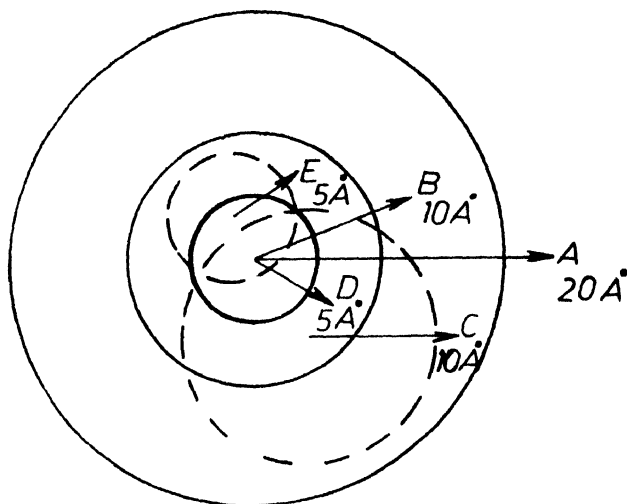


Figure 1. Schematic diagram showing the main features of the calculation.

Now we have a spherical lattice of radius 5 \AA and centered on the F_{z1} electron such that each of the lattice points inside this sphere is characterized by its co-ordinates, charge of the respective ion and the effective dipole moment. The contributions of the charges and of the effective dipoles to EFG are separately calculated and added up. The matrix corresponding to the EFG tensor is diagonalized by a unitary transformation. The numerical calculation is carried out using IBM 370/155.

3. Results

The trace ($q_{xx} + q_{yy} + q_{zz}$) of the symmetric second rank matrix is found to be zero. The components of q , the eigenvalues and eigen vector matrix are listed in Table I, for CsCl for the three models. The eigenvalues are presented in the decreasing order, and represent the principal values of q , and the columns of the eigenvector matrix give the orientations of the principal axes with respect to the crystalline a, b, c axes. The order in which the components of q are presented in Table I is as follows :

$$q_1 = q_{xx}; q_2 = q_{yy}; q_3 = q_{zz}; q_4 = q_{zx}; q_5 = q_{zy}; q_6 = q_{xz}. \quad (8)$$

The lattice constants are taken from Landolt-Bornstein (1923) Tables. The Tesman, Kahn and Shockley (1953) values for the electronic polarisabilities of

ions are used. The value of the polarisability of the trapped electron is assumed to be that of hydrogen atom ($= 0.67$) (Molekulstruktur (1934).

Table 1. Elements of the q tensor (q_1, \dots, q_6), the principal values (q_{11}, q_{22}, q_{33}), in units of 10^{14} esu, and the eigenvector matrix for CsCl for different models. The impurity is Ca^{2+} .

Model 1					
$q_1 =$	0.00298	$q_2 =$	0.00391	$q_3 =$	-0.00138
$q_4 =$	0.21512	$q_5 =$	0.21785	$q_6 =$	-0.00159
$q_{11} =$	0.30773	$q_{22} =$	0.00308	$q_{33} =$	-0.30464
	0.50301		0.71155		-0.49057
	0.50212		0.70259		-0.50421
	0.70345		0.00730		0.71070
Model 2					
$q_1 =$	0.00272	$q_2 =$	0.10334	$q_3 =$	-0.00168
$q_4 =$	-0.10998	$q_5 =$	-0.10537	$q_6 =$	-0.00103
$q_{11} =$	0.11084	$q_{22} =$	0.10164	$q_{33} =$	-0.21249
	-0.70678		0.41341		0.57405
	-0.01326		-0.81907		0.57353
	0.70730		0.39775		0.58439
Model 3					
$q_1 =$	0.00277	$q_2 =$	0.10706	$q_3 =$	-0.00077
$q_4 =$	0.10426	$q_5 =$	0.10798	$q_6 =$	-0.00199
$q_{11} =$	0.21289	$q_{22} =$	-0.10325	$q_{33} =$	-0.10964
	0.57959		-0.79762		0.16692
	0.57982		0.25971		-0.77224
	0.57260		0.54437		0.61301

4. Discussion

In all the models the site under investigation possesses a mirror-plane symmetry. However, when the effect of induced dipoles is included even this symmetry vanishes. If contribution of charges alone to q were taken, one of the principal axes is found to be perpendicular to the mirror plane with the other two lying in the plane. For q_{total} no such axis or plane could be identified.

This program can be adopted for the calculation of EFG at impurity sites in ionic crystals. Following a recent report (Radhakrishna and Chowdari 1974) on the observation of F_{21} centers in cesium halides, the results of the present calculation are being made use of in calculating the energy levels of F_{21} center in cesium halides.

References

- Radhakrishna S and Chowdari B V R 1972 *Phys. Stat. Solidi* **14** 11
 Boncher C J F 1962 *Theory of Electric Polarization* (Elsevier Publishing Co, Inc. Houston, Texas)
 Landolt-Bornstein 1923 *Physikalisch-Chemischen Tabellen* (Jullius Spring, Verlag, Berlin)
 Tesman J R, Kahn A H and Shockley W 1953 *Phys. Rev.* **92** 890
 Molekulstruktur, Stuart 1934 (Springer-Verlag, Berlin)
 Radhakrishna S and Chowdari B V R 1974 *Proc. Intnl. Conf. on Colour Centers Sendai, Japan*

Effect of D. C. biasing field on the dielectric constant of rutile single crystals

A Subrahmanyam, K V Rao and H N Bose

Physics Department, Indian Institute of Technology, Kharagpur.

Abstract. This paper reports the results of measurements of the effect of d.c. biasing field on the dielectric properties of rutile single crystals in the frequency range of 10^2 - 10^7 Hz at 30°C and 60°C . The dielectric constant K of rutile crystal at 30°C along the C axis decreases from 140 at 10^2 Hz to 88 at 10^5 Hz beyond which it is found to be frequency independent. The value of K remains practically unchanged when the crystal is heated to 60°C . The frequency dependent part of the dielectric constant obtained for comparatively low frequencies is obviously due to space charge polarisation.

Dielectric constant of rutile at room temperature increases with the biasing field, shows a peak around 75 V/cm and then gradually decreases. Though the d.c. field corresponding to the peak apparently does not change with the frequency of measurement, the K values are considerably frequency dependent at any given biasing field and decrease appreciably with increasing frequency. Measurements on the effect of raising the temperature of the crystal to 60°C show that the biasing field for the peak value of the dielectric constant decreases to 50 V/cm; the K values are lower in this case compared to their corresponding values at room temperature. The results can be explained in a general way by assuming barrier formation due to space charge layer on the surface of the crystal.

1. Introduction

The effect of space charge fields on the dielectric properties of barium titanate crystals has been studied to some extent (Drougard and Schlosser 1961, Jona and Shirano 1962). Application of a d.c. field is found to affect these space charge layers considerably. Recent studies carried out in our laboratory (Gon 1975, Gon *et al* 1975) on the influence of d.c. biasing field on the dielectric properties of barium titanate crystals at different frequencies and temperatures have indicated the possibility of using this as a method of investigating into the behaviour of space charge layers; the effect being comparatively pronounced in crystals of high dielectric constant, it is considered worthwhile to study such crystals by this method. Though some work was reported on the study of dielectric properties of rutile single crystals (Von Hippel 1965, Lal and Srivastava 1969) (a solid with a dielectric constant of 88), the influence of d.c. biasing fields on these properties has not been studied well. In the present paper are reported the

results of measurements of the effect of d.c. biasing fields on the dielectric properties of rutile crystals in the frequency range of 10^2 – 10^7 Hz at 30°C and 60°C .

2. Experimental

The samples of rutile single crystals used in the present investigation were grown by flame fusion method and obtained as gift from the Laboratory for Insulation Research, Massachusetts Institute of Technology, U.S.A. Flame photometric measurements and chemical analysis carried out on these samples showed the impurity concentration to be less than 3 ppm. The crystals after grinding and polishing had approximate dimensions of $1.5 \times 1 \times 0.15$ cm³. Silver paint was applied for electrodes on either side of the samples.

The dielectric measurements were taken on a GR 716 type capacitance bridge in the frequency range 10^2 to 10^5 Hz (Westphal 1963), and on a Marconi Circuit Magnification Metre type TF 329G in the range 10^6 – 10^7 Hz using the resonance curve principle (Rao 1961). The accuracy of the measurement in the dielectric constant is 2%.

The sample holder used in the present investigations consisted of three plates, one above the other. D.C. field is applied across the top and the bottom plates, the sample being included between the central and the bottom plate. A mica sheet fully covered the region between the top and the central plate. A dry battery of 90 V was used to apply the biasing field. The voltage across the sample could be easily measured externally and the d.c. field calculated.

The temperature of the sample was raised by proper blowing of hot air on to the arrangement.

3. Results

The dielectric constant K of rutile crystal at room temperature (30°C) along the c -axis is shown in figure 1; K decreases from 140 at 10^2 Hz to 88 at 10^5 Hz beyond which it is found to be frequency independent. The value of K remains practically unchanged when the crystal is heated to 60°C . The dielectric loss, $\tan \delta$, is found to be less than 0.002 beyond 10^3 Hz (it was 0.005 at 10^2 Hz); as such, no effort was made to pursue the study on dielectric loss.

Dielectric constant at 30°C and at 60°C as a function of d.c. biasing field at different frequencies is presented in figures 2 and 3 respectively. K at room temperature increases with the biasing field, shows a peak around 75 V/cm and then gradually decreases. Though the d.c. field corresponding to the peak apparently does not change with the frequency of measurement, the K values are considerably frequency dependent at any given biasing field and decrease appreciably with increasing frequency. Measurements on the effect of raising the temperature of the crystal to 60°C show that the biasing field for the peak

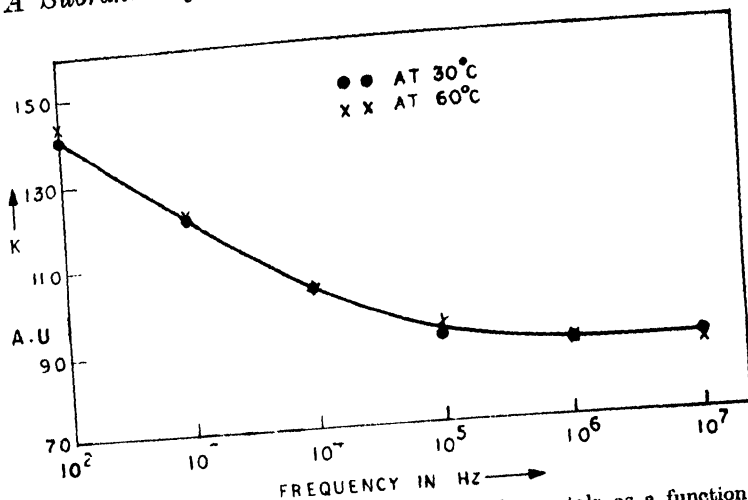


Figure 1. Dielectric constant (K) of rutile single crystals as a function of frequency at 30°C and 60°C.

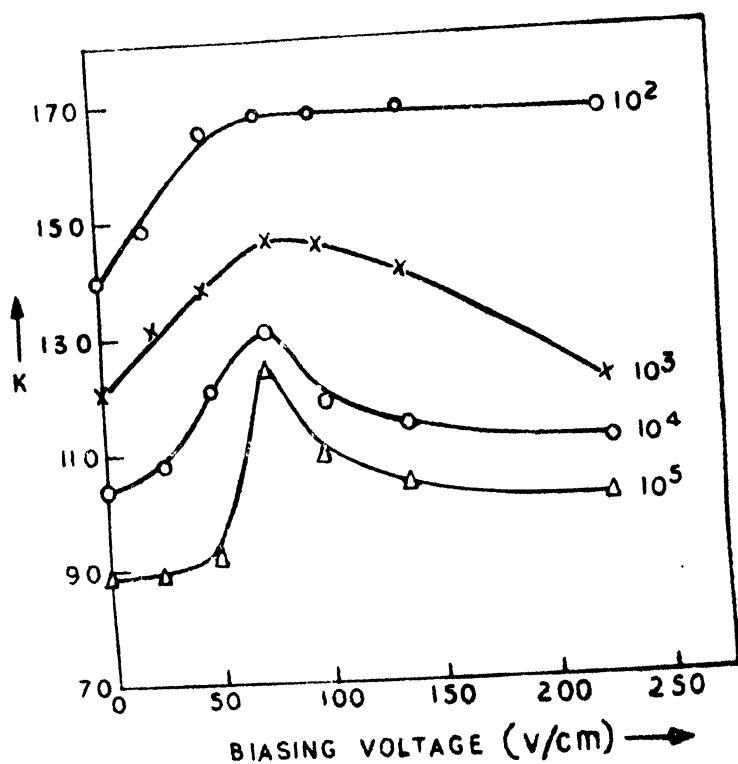


Figure 2. Dielectric constant (K) at 30°C for rutile single crystals as a function of d.c. biasing voltage at different frequencies.

value of the dielectric constant decreases to 50 V/cm (at 10^2 Hz, this value is higher); the K values are lower in this case than the corresponding values at room temperature.

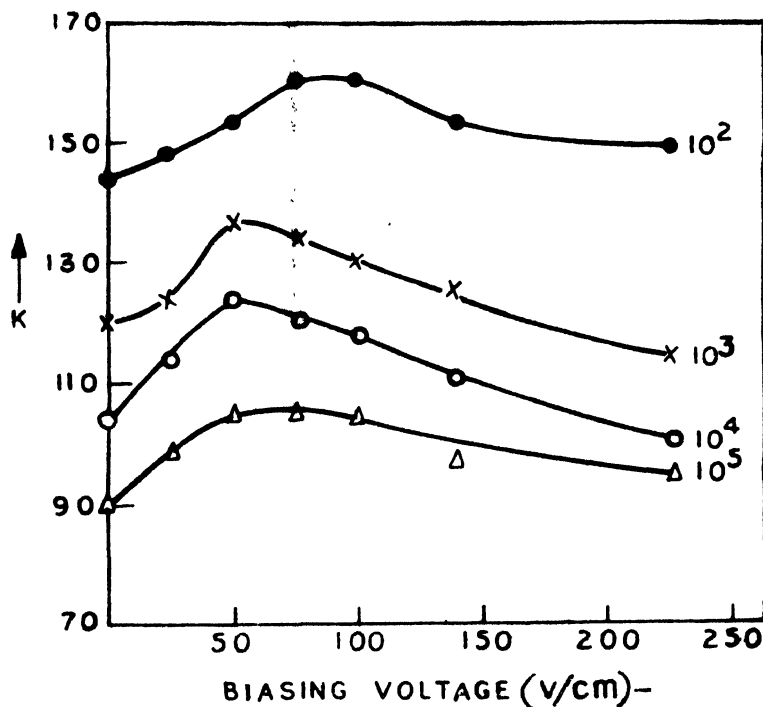


Figure 3. Dielectric constant K at 60°C of rutile single crystals as a function of d.c. biasing voltage at different frequencies.

4. Discussion

The dielectric constant of a material is composed of four types of polarisations: electronic, ionic, dipolar and space-charge. At low frequencies all the four contributions are present. In fact, the nature of the variation of dielectric constant with frequency indicates the nature of the effective polarisation for the material.

The space charge contribution will depend on the purity and perfection of the crystals. Its influence is negligible at very low temperatures and is noticeable in the low frequency region. The dipolar orientational effect can sometimes be seen in materials even upto 10^{10} Hz. The ionic and electronic polarisations always exist below 10^{13} Hz.

Recollecting our data we may ascribe the larger values of the dielectric constant of rutile crystals at low frequencies to space charge polarisation due to crystal defects (Rao and Smakula 1965, Agrawal and Rao 1970). However,

the concentration of such defects is apparently low as evidenced by the moderately low dielectric loss values.

It appears possible to understand the present results in a general way by assuming barrier formation due to space charge layer on the surface of the crystal. The results seem to suggest that under d.c. biasing fields, the loosely bound charge carriers are freed and augment the space charge layers already present on the surface of the crystal (due to the defects initially present in the crystal). The barrier thus formed seems to reach a critical height around a certain biasing field; beyond this, the charge carriers may cross over the barrier and reduce its effective height, leading to a decrease in dielectric constant. At elevated temperatures (for example, 60°C), the leakage of charge carriers across the barrier becomes more prominent. Our results seem to indicate that such leakage not only decreases the K values at 60°C in comparison to the corresponding values at 30°C but also brings down the d.c. biasing field for the critical height of the barrier.

Further work in progress now on these crystals, it is expected, will throw considerable light on the nature etc. of the space charge layers.

Acknowledgements

The authors are thankful to Mr. W. B. Westphal, Laboratory for Insulation Research, Massachusetts Institute of Technology, U.S.A. for kindly sparing the crystals used in the present work.

References

- Drougard M E and Schlosser H 1961 *J. Appl. Phys.* **32** 1227
- Jona F and Shirane G 1962 *Ferroelectric crystals* (Pergamon Press, Oxford)
- Gon H B 1975 *Ph.D. Dissertation I.I.T. Kharagpur*
- Gon H B, Rao K V and Bose H N 1975 *Ind. J. Pure and Appl. Phys.* **13** 401
- Von Hippel A R 1965 *Tables of Dielectric Materials Lab. for Ins. Res. M.I.T., U.S.A.*
- Lal H B and Srivastava K G 1969 *Canadian J. Phys.* **47** 3
- Westphal W B 1963 *Tech. Rep. Labor. Inst. Res. MIT USA* 182 10
- Rao K V 1961 *J. Phys. Chem. Solids* **20** 193
- Rao K V and Smakula A 1965 *J. Appl. Phys.* **36** 2031
- Agrawal M D and Rao K V 1970 *J. Phys. C : Solid State* **3** 1120

Stage III recovery in neutron irradiated tungsten

M S Anand, B M Pande and R P Agarwala

Chemistry Division, Bhabha Atomic Research Centre, Trombay,
Bombay-400085.

Abstract. The recovery of defects in well and partially annealed tungsten has been studied using electrical resistivity technique. The irradiation was carried out at reactor ambient temperature (~ 343 K) to a fluence of 1×10^{18} n/cm². The isochronal annealing studies of the defects show a III stage recovery at $\sim 0.17 T_m$ (T_m is the melting point of tungsten). The recovery in well and partially annealed tungsten samples was calculated to be $130 \mu\Omega$ cm and $250 \mu\Omega$ cm respectively. The greater recovery in partially annealed samples conforms to the intrinsic defects migrating in this stage.

1. Introduction

The transition metals like tungsten, molybdenum etc. are technologically important. Study of defects in these metals is necessary to understand their effect on their mechanical properties. The defects introduced by neutron irradiation or cold working anneal in fixed temperature ranges called the stages. There is a general agreement for defects migrating in various stages except in stage III which has been assigned either to intrinsic defects (Schilling and Sonnenberg 1973, Goedeme *et al* 1976, Stals *et al* 1972, Keys and Moteff 1970) or interstitial impurities (Rosenfield 1964).

Present study on recovery in stage III of neutron irradiated tungsten has been undertaken to investigate the nature of the defects migrating in this stage. Tungsten specimens having different dislocation densities have been irradiated to a fluence of 1×10^{18} n/cm² and the effects of different defects concentration on the stage III annealing has been discussed.

2. Experimental

Thin foils of 99.98 wt.% pure tungsten* were prepared as reported earlier (Anand *et al* 1973). The samples were annealed at 1973 K for 2 hours in vacuum of 10^{-6} torr. These samples are called well annealed samples. Some of the samples were annealed at 780 K and 1200 K for 2 hours to get different dislocation densities. All these samples were irradiated to a fast neutron fluence of 1×10^{18} n/cm² at a temperature of 343 K. Isochronal annealing of the samples was

* Supplied by Fansteel Metallurgical Corporation, U.S.A.

carried out using a constant heating rate of 40 K/hr. in the temperature range of 373–800 K as described earlier (Pande *et al* 1975). Figure 1 shows the ρ

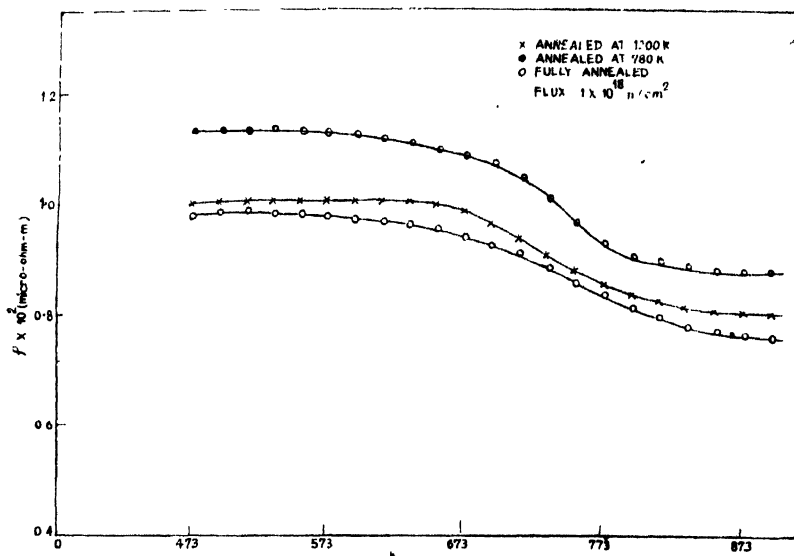


Figure 1. The resistivity versus temperature plot for three types of samples.

(resistivity of the sample) vs T (temperature) plots for the three samples. The derivative plots $\left(\frac{\Delta\rho}{\Delta T} \text{ vs } T \right)$ are given in figures 2 and 3 for well annealed and 780 K annealed sample. There is a clear peak around $0.17 T_m$ (where T_m is the melting point of tungsten). The isothermal annealing of the irradiated samples has also been carried out in the temperature range of 613–633 K to find the migration energy near the peak temperature. The migration energy (Goodeme 1971) has been calculated to be 1.69 ± 0.25 eV.

3. Discussion

In the present studies, it is observed that the resistivity in partially annealed samples (annealed at 780 K) is more compared to the well annealed samples. However, the recovery in the samples annealed at 1200 K is less than that of the samples annealed at 780 K but greater than that of well annealed samples. The enhancement of the recovery in partially annealed samples is similar to the observation made by Johnson (1973a, 1973b) for niobium and by Stals *et al* (1973) in molybdenum. The dislocation density in partially annealed samples is higher than in well annealed samples. It has recently been seen by Cornelis *et al* (1973) that in neutron irradiated molybdenum, the higher dislocation density ensures an appreciable increase in defect production at the reactor ambient temperature.

A number of investigators assign stage III annealing to the migration of intrinsic defects (Schultz 1969), on the other hand this stage is also sometime referred to arise due to the migration of interstitial impurity like carbon. Carbon has migration energy close to the migration energy of the defects migrating in

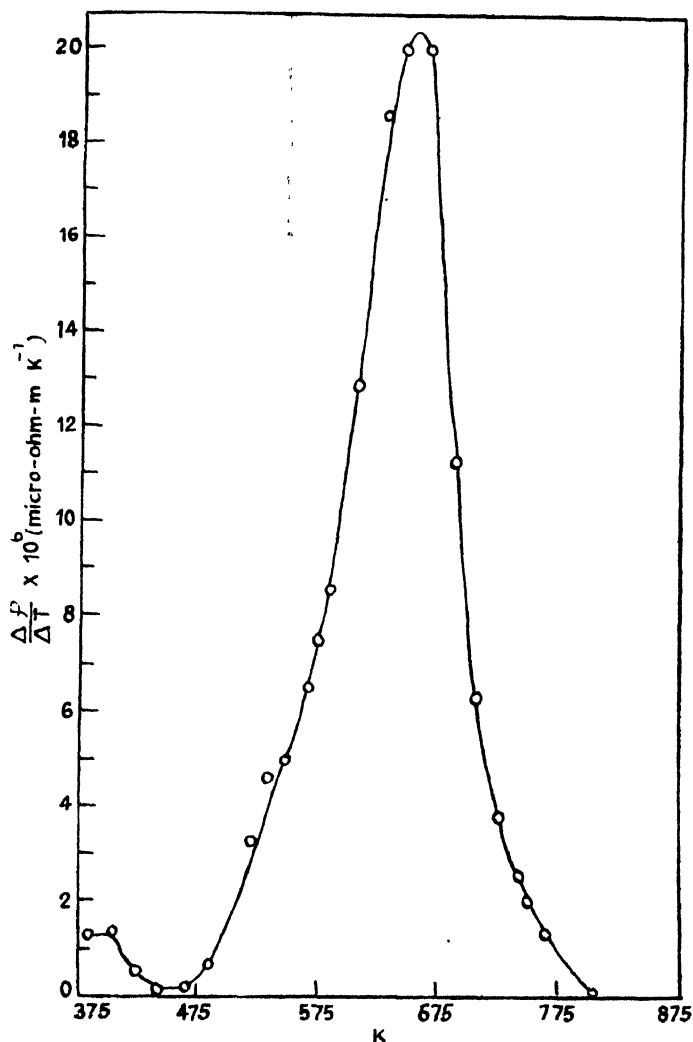


Figure 2. The derivative plot for the well annealed sample.

stage III (Fujita and Damask 1964). It may be pointed out that total interstitial impurity content in the present study does not exceed 3.6×10^{-2} at % even if it is considered that all impurities present are interstitial. Taking $2.5 \mu\Omega$ cm/at % as a reasonable value for the resistivity increase in tungsten for the impurities (Schultz 1969), the total resistivity contribution in the present

case would be $\sim 0.090 \mu\Omega \text{ cm}$. This value is much less than the recovery observed in the present study.

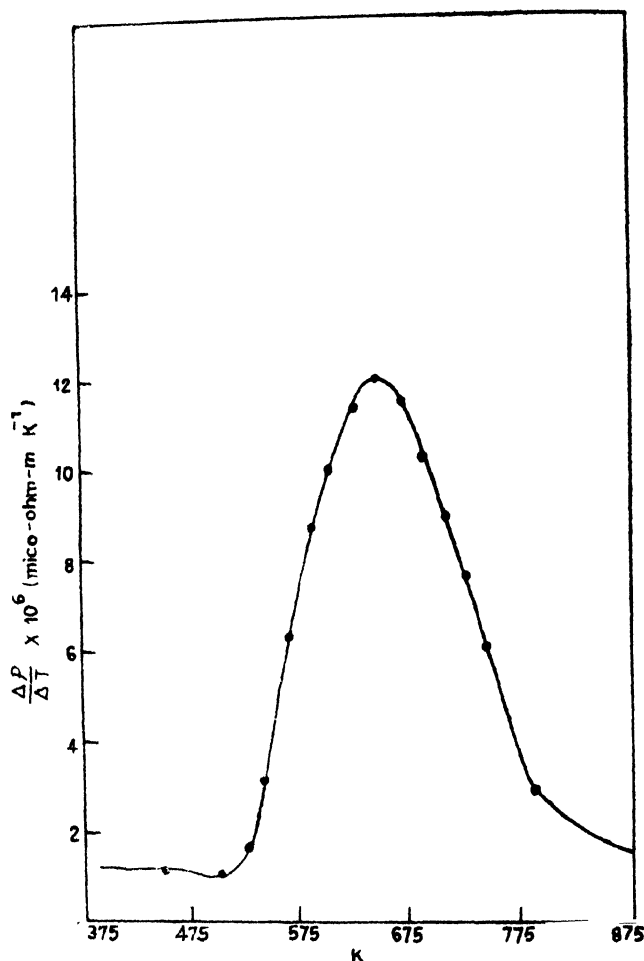


Figure 3. The derivative plot for the partially annealed sample (annealed at 780 K).

Stanley *et al*'s (1972) argument that enhanced recovery in partially annealed samples could be due to the saturation of dislocations by the interstitial impurity atoms does not justify in the present case, because of the low impurity content. It is difficult to account for the recovery entirely due to impurities. Similarly the observation of Evans *et al* (1970) on the increased defect production due to the presence of impurity is also not applicable here. Further more, Schultz (1969) has shown that in samples with controlled carbon content this stage is intrinsic. Similarly Kullman *et al* (1966) in decarborised tungsten observed

stage III at the usual temperature. Therefore it appears unlikely that carbon or another impurity in tungsten induces stage III recovery. From the above, it is clear that most probable defect migrating in stage III in tungsten, is an intrinsic defect (vacancy or self interstitial).

Present results are similar to the observation of Takamura *et al* (1971) who studied the low temperature recovery of neutron irradiated tungsten and the effect of doping on stage I annealing. These workers studied the isochronal recovery of tungsten after 6 hours of neutron irradiation (flux 1×10^{12} n/cm²) on three types of specimens (a) well annealed, (b) irradiation doping for 64 hours and annealed at 673 K for one hour, (c) 112 hour doping and annealed at 116 K for one hour. These workers observed that the recovery in stage I has been enhanced by irradiation doping. The effect of doping did not disappear when the specimens were annealed just after stage III but on annealing after Vth stage this effect vanished. These observation of Takamura *et al* (1971) also showed that the enhancement of recovery in stage I was not associated with the defects migrating in stage III but with those found after stage III. The interstitials got annihilated at vacancies and thereby giving a recovery. If the vacancies were the migrating defects in stage III there would have been also number of sinks for interstitials to get annihilated and as such the recovery after 673 K would have been less. But the enhanced recovery after 673 K rules out the vacancy migration in stage III.

In the present case, it is seen that stage III recovery is more in case of specimens annealed at 780 K compared to well annealed and those annealed at 1200 K. If the vacancies were the predominant defect migrating in stage III, the recovery should have been less in 78 K annealed samples. However it is seen that the recovery is more in 775 K annealed specimens. The above observations of different recovery in stage III is difficult to explain unless it is assumed that the self interstitials are the migrating defects in this stage.

The migration energy (E_m) in stage III has been calculated on the basis of the change of slope method (Goedeme 1971) in the temperature range of 613–633 K and it comes to be $1.69 \text{ eV} \pm 25 \text{ eV}$. No attempt has been made to calculate E_m before and after the stage, however the specimens were given an annealing treatment at 523 K for one hour before starting isothermal annealing. The migration energy is smaller than the calculated migration energy of vacancies in tungsten on the basis of self diffusion and energy of formation of vacancies data in tungsten. Taking self diffusion (SD) values of tungsten as 5.2–6.6 eV (Daunberg 1961, Andelin *et al* 1965) and energy of formation (E_F) as 3.3 eV (Schultz *et al* 1965), the migration energy (E_m) was calculated to be ($E_m = E_{SD} - E_F$) 1.9 to 3.3 eV. The migration energy of 1.69 eV observed in the present study is different from the migration energy of vacancies. This also does not support the view that vacancies are responsible for this stage.

References

- Schilling W and Sonnonberg K 1973 *J. Phys. F.* **3** 322
- Goedeme G, Pande B M, Stals L and Nihoul J 1976 *Rad. Effect* **3** 275
- Stals L, Goedeme G and Nihoul J 1972 *Defects in Refractory Metals* R De'Batist, J Nihoul and Stals, L opage 23
- Keys L K and Motoff J 1970 *J. Nucl. Materials* **34** 260
- Rosenfield A R 1964 *Acta Met.* **12** 341
- Anand M S, Pande B M and Agarwala R P 1973 *Phys. Stat. Sol. (a)* **17** 311
- Pande B M, Anand M S and Agarwala R P 1975 *Radiation Effects* **24** 173
- Goedeme G 1971 *Thesis, Katholieke Universiteit Leuven*
- Johnson A A 1973a *Scripta Met.* **7** 1
- Johnson A A 1973b *Scripta Met.* **7** 15
- Stals L, Nihoul J, Cornelis J and Meester P De 1973 *Phys. Stat. Sol. (a)* **18** 383
- Cornelis J, Meester P De, Stals L and Nihoul J *Phys. Stat. Sol.*
- Schultz H 1969 *Mater. Sci. Eng.* **3** 189
- Fujita F E and Damask A C 1964 *Acta. Met.* **12** 331
- Stanley J T, Williams J M, Brundage W E and Wechsler M S 1972 *Acta. Met.* **20** 191
- Evans J H 1970 *Acta. Met.* **18** 499
- Kuhlmann H H and Schultz H 1966 *Acta. Met.* **14** 798
- Takamura S, Hanada R, Okuda S and Kimura H 1971 *J. Phys. Soc. Japan* **30** 1091
- Daunberg W 1961 *Metall.* **15** 977
- Andelin R L, Knight J D and Kahn M 1965 *Trans. AIME* **233** 19
- Schultz H 1965 *Lattice defects in quenched metals* Ed R M J Cotterill *et al* 761

Trends in the valence force constants of crystal containing first-row atoms

K K Mani, R Ramani and R P Singh

Indian Institute of Technology, Bombay-400076.

1. Introduction

In earlier papers (Mani and Ramani 1974, Ramani and Mani 1974, Ramani *et al* 1977), we have studied the applicability of valence force fields (VFF's) to the study of the lattice dynamics of graphite and BeO, simultaneously examining the question of force constant transference in these crystals. The present work arose out of an attempt to make a similar study for BN. This substance crystallises both in a hexagonal form akin to the graphite structure and in a cubic zinc-blende structure. The ionicity of BN is intermediate between the two crystals already studied, which makes it of interest to study.

The available experimental data on BN are scanty; only the optical frequencies have been measured in both cubic (Brafman *et al* 1968) and hexagonal (Geick *et al* 1966) forms. It is, therefore, worthwhile to examine the trends in the microscopic elastic constants and the force constants of all I-row crystals, in order to predict internally consistent values for the lattice dynamical data of BN.

Similar trends in zinc-blende structure crystals have earlier been examined by Martin (1970), using the Keating (1966) model. The elastic constants and the force constants showed a simple linear variation with the Phillip's ionicity parameter f_i (Phillips 1969), for a large number of crystals. However, crystals containing I-row atoms showed considerable deviations. The present work is an extension of Martin's work to I-row crystals.

2. Dynamics of Hexagonal BN

A rigid-ion model is used to describe the Coulomb forces in the semi-ionic crystals. The dynamic effective charge ze is a parameter in the model, which is determined from the optic-mode splitting. Its value for BN (hex) is $z = 0.338$. The valence force constants (VFC's) are defined only between atoms in a given layer. The set of VFC's include a out-of-plane bond bending force constant k_θ in addition to the usual set of VFC's defined by Martin (1970), (namely k_r , k_θ , k_{rr} and $k_{r\theta}$). Two constants α_4 and γ_4 describe the inter-plane interaction. The constant γ_4

is scaled from its value in graphite, assuming Van der Waal's interactions between the planes.

We note that a satisfactory description of the dynamics of graphite was given by VFC's transferred from naphthaleno. In the case of hexagonal BN, we use data from the borazine molecule (Subhedar and Thyagarajan 1974). The optical frequencies calculated with this input data are compared with the experimental measurements in Table 1. The agreement is rather good, particularly if we consider the fact that the model uses only one adjustable parameter.

Table 1. Force constants (in 10^5 dyne cm^{-1}) and optical frequencies^(a) (in cm^{-1}) for hexagonal BN, compared with similar information for graphite^(b).

	Hexagonal BN	Graphite
k_r	4.8359	4.789
k_θ	0.4265	0.8955
k_{rr}	0.0	0.342
$k_{r\theta}$	0.0	0.1319
k_δ	0.1562	0.1562
α_4	0.0	0.0063
γ_4	0.4751	0.0572
z	0.338	0.0
Γ_2^-	872 (828)	640
$\Sigma(T)$	829 (783)	640
Γ_6^-	1421 (1367)	1575 (1675)
$\Sigma(L)$	1466 (1610)	1575 (1575)
$\Gamma_6^{+(1)}$	1421 (1370)	1575 (1588)
$\Gamma_6^{+(2)}$	48	42 (50)
$\Gamma_3^{+(1)}$	712	640
$\Gamma_3^{+(2)}$	500	126 (127)
Δ (%)	6.0	8.0

^(a) Number in parenthesis indicate the measured frequencies for BN (Geick *et al* 1966).

^(b) Mani and Ramani (1974).

3. Dynamics of Cubic BN

In the cubic structure, the optical frequencies predict an effective charge of $z = 0.927$. The elastic constants for the crystal have not been measured. We, therefore, first examine the trends in the elastic moduli of diamond, BeO and LiF. The effective cubic moduli (Martin 1972) have been used for BeO. The linking parameter is chosen to be Phillips ionicity parameter f_i (Phillips 1969), to be consistent with Marin (1970)'s work. The simplest variations with f_i , with an rms deviation less than 10%, are used to predict the elastic constants of cubic BN. These predicted constants are listed in Table 2.

Table 2. Elastic constants (in 10^{11} dyne cm^{-2}) for cubic BN, predicted from an interpolation scheme.

c_{11}	c_{12}	c_{44}	Martin ratio
71	17	38	1.002

We can think of an alternate scheme in which one infers how the VFC's change with ionicity. It is found that the VFC's in general vary at least quadratically with f_i . However, we may expect that the ratios k_θ/k_r , k_{rr}/k_r and $k_{r\theta}/k_r$ will be linear functions of f_i , to a good approximation. This scheme predicts the following ratios in cubic BN :

$$k_\theta/k_r = 0.084; \quad k_{rr}/k_r = 0.027; \quad k_{r\theta}/k_r = 0.058. \quad (1)$$

The Keating model used by Martin (1970) is essentially a simplification of the VFF model, with two parameters α and β , defined by,

$$\alpha = k_r/3 - k_\theta/4; \quad \beta = 3k_\theta/2. \quad (2)$$

The Keating model postulates the following additional interrelations :

$$k_{r\theta}/k_\theta = 1/\sqrt{8}; \quad k_{rr}/k_\theta = 1/8. \quad (3)$$

Martin found that the ratio β/α varied linearly with $(1-f_i)$. If we assume this result, we get the following ratios for the VFC's :

$$k_\theta/k_r = 0.084; \quad k_{rr}/k_r = 0.01; \quad k_{r\theta}/k_r = 0.03 \quad (4)$$

If we assume the ratios of VFC's predicted in equation (1) or equation (4), the dynamics of BN is solely determined by the constant k_r . We obtain three different estimates of k_r by the following arguments :

a) We assume that the dimensionless constant $k_r/(e^2/r_0^3)$ is a linear function of f_i . Interpolating between diamond⁽¹¹⁾ and BeO⁽³⁾ we obtain the following value for BN :

$$k_r = 3.21 \times 10^5 \text{ dyne cm}^{-1} \quad (5)$$

b) We note that the ratio of k_r for graphite (Mani and Ramani 1974) and diamond (McMurry *et al* 1967) is nearly the same as the inverse ratio of r_0^3 for the two structures. If we extend this result to the two structures of BN, we get the following value of k_r for cubic BN :

$$k_r = 3.73 \times 10^5 \text{ dyne cm}^{-1} \quad (6)$$

c) We postulate a simple electrostatic model of the bond, visualising it as being formed due to a concentration of electronic charge in between the atoms constituting the bond. This charge is considered to be spherical. It is midway between the two atoms in diamond and shifts towards the more positive core in the case of partially ionic crystals. Further, the magnitude of the charge decreases with the ionicity of the bond and vanishes in the case of totally ionic crystals like LF. We denote the charge on the bond by $-q_e$ and the charges on the atoms linked by the bond by q_1e and q_2e . Elementary electrostatics then yields,

$$k_r = 2e^2[2q(q_1+q_2+2\sqrt{q_1q_2})-q_1q_2]/a \quad (7)$$

where $q = -(q_1+q_2)/4$ for tetrahedral coordination. The bond charge is taken to remain constant when there is a change in bond-length. If we now assume, for a $A^N B^{8-N}$ crystal, that $q_1 = N$, $q_2 = (8-N)-z$, or vice versa, the qualitative requirements on the bond-charge are satisfied. Equation (7) now allows us to express k_r for any crystal in terms of k_r for diamond, giving

$$k_r = 2.86 \times 10^5 \text{ dyne cm}^{-1}, \quad \text{for BN}; \quad (8)$$

$$k_r = 2.32 \times 10^5 \text{ dyne cm}^{-1}, \quad \text{for BeO}. \quad (9)$$

The value in equation (9) agrees well with the value of $2.3 \times 10^5 \text{ dyne cm}^{-1}$ obtained by Ramani *et al* ⁽³⁾ for BeO.

These three estimates of k_r , in conjunction with the two sets of ratios of VFC's in equations (1) and (4), leads to six different sets of VFC's for cubic BN. The optical frequencies and the elastic constants calculated with these sets are given in Table 3.

Table 3. Bond-stretching for constant k_r (in $10^5 \text{ dyne cm}^{-1}$), optical frequencies (in cm^{-1}) and elastic constants (in $10^{11} \text{ dyne cm}^{-2}$) for cubic BN, using both Keating and VFF models.

	Keating model			VFF model		
k_r	3.206	3.731	2.863	3.206	3.731	2.863
ω_{LO}^e	1430	1523	1366	1319	1401	1262
ω_{TO}^e	1222	1330	1146	1090	1188	1020
c_{11}	62	72	56	65	75	58
c_{12}	5	7	3	8	11	6
c_{44}	21	26	17	23	29	20
Martin ratio	0.630	0.670	0.590	0.660	0.720	0.620

(a) Experimental values are : $\omega_{LO} = 1304 \text{ cm}^{-1}$,
 $\omega_{TO} = 1056 \text{ cm}^{-1}$ (Brafman *et al* 1968).

4. Discussion

In the absence of experimental data on the elastic constants, we look for internal consistency checks to determine favourable sets. On such check is a relation obtained by Martin (1970) for zinc-blende structure crystals.

$$\frac{2c_{44}(c_{11}+c_{12}-c')}{(c_{11}-c_{12})(c_{11}+3c_{12}-2c')+0.831c'(c_{11}+c_{12}-c')} = 1 \quad (10)$$

where, c' is connected with the effective charge. We can view equation (10) as an empirical one. This relation is satisfied to within 10% by the measured elastic constants of 14 cubic crystals. The left-hand side of equation (10), which we call the Martin ratio, works out to be 1.002 for diamond and 0.974 for BeO. Since cubic BN has an ionicity in between, we may expect that the Martin ratio must be nearly 1 for BN. If this criterion is applied, then among the different sets of elastic constants presented in Tables 2 and 3, the most probable set turns out to be (in units of 10^{11} dyne cm^{-2});

$$c_{11} = 71; \quad c_{12} = 17; \quad c_{44} = 38. \quad (11)$$

We find, from Table 3, that none of the microscopic models predict elastic constants that satisfy the Martin's relation (Martin 1972). However, this is not a serious draw-back, as the Martin's relation is only a justification for a two-parameter description of the elastic properties. That is, the elastic constants obtained from any arbitrary choice of α and β will satisfy the Martin's relation, even though they may lead to an elastically unstable crystal. For example, we repeated our calculations with a value of $k_\theta = 0.577 \times 10^5$ dyne cm^{-1} , estimated by Van Vechten (1974), along with the three values of k_r in equations (5), (6) and (8). All the sets yielded negative values for the elastic constant c_{12} , even though the Martin relation was satisfied.

It is significant that though the values of k_θ used in our calculations are substantially smaller than the one predicted by Van Vechten (1974), they yield elastically stable crystals. It has been long recognised that the bond-bending forces in I-row crystals are stronger due to the more complete sp^3 hybridization in these crystals. What has been insufficiently emphasized is the significance of angle-angle interactions in these solids. A satisfactory description of the dynamics of I-row crystals can be achieved only with a more general VFF than the one used here. The Keating model is not even a good first approximation in these cases, and a VFF such as the one we have used is superior to the Keating model in I-row crystals. Hence an alternate set of elastic constants of BN (cubic) is obtained from VFF-models :

$$c_{11} = 72 \pm 5; \quad c_{12} = 11 \pm 2; \quad c_{44} = 27 \pm 3. \quad (12)$$

The calculated bulk modulus of BN is 33 ± 2 (10^{11} dyne cm^{-2}). This value lies within the limits of 27 and 42 (10^{11} dyne cm^{-2}), predicted by Gielisse *et al* (1967) using various arguments.

5. Conclusions

Trends with ionicity in the elastic moduli of I-row crystals have been studied. These have been utilised to predict the elastic constants of cubic BN. The elastic constants have been calculated using a VFF model and a Keating model. Two different sets of elastic constants for cubic BN, have been suggested depending whether the Martin relation is expected to be satisfied or not. The dynamics of hexagonal BN has been shown to be satisfactorily described by the force constants transferred from the borazine molecule.

References

- Mani K K and Ramani R 1974 *Phys. Stat. Solidi* (b) **62** 659
 Ramani R and Mani K K 1974 *Pramana* **3** 171
 Ramani R, Mani K K and Singh R P *Phys. Rev.* **B16** (to be published).
 Brafman O, Longyel G, Mitra S S, Gielisse P J, Plendl J N and Mansur L C 1968 *Sol. St. Comm.* **6** 523
 Geick R, Perry C H and Rupprecht G 1966 *Phys. Rev.* **146** 543
 Martin R M 1970 *Phys. Rev.* **B1** 4005
 Keating P N 1966 *Phys. Rev.* **145** 637
 Phillips J C 1973 *Bonds and Bands in Semiconductors* (Academic Press, New York); the f_i values used are from Van Vechten J A 1969 *Phys. Rev.* **187** 1007
 Subhedar M K and Thyagarajan G G 1974 *Ind. J Pure Appl. Phys.* **12** 498
 Martin R M 1972 *Phys. Rev.* **B6** 4546
 McMurtry H L, Solbrig A W Jr, Boyter J K and Noble C 1967 *J. Phys. Chem. Solids* **28** 2359
 Van Vechten J A 1974 *Phys. Rev.* **B10** 4222
 Gielisse P J, Mitra S S, Plendl J N, Griffis R D, Mansur L C, Marshall R and Pascoe E A 1967 *Phys. Rev.* **155** 1039

Thermally stimulated discharge currents in polystyrene thin films

Bharat Bhargava and A P Srivastava

Solid State Physics Laboratory, University of Saugar, Saugar (M.P.).

Abstract. Thermally stimulated discharge currents have been studied in solution grown thin polystyrene films polarised at 130°C under influence of different field strengths (2-10 kV/cm), thickness (2000-10000 Å). The TSD spectra have been used to calculate relaxation time, activation energy in polystyrene films. Two relaxation peaks have been observed at 77°C and 112°C. The occurrence of 112°C peak is explained in term of space charge injection from electrode and ionic effect. The occurrence of 77°C peak has been shown to be due to release of trapped charges due to local movements of polystyrene molecular chains.

1. Introduction

The knowledge of polarisation behaviour of polymeric material is of considerable importance due to their applications in a number of devices as electrets. Polymer electrets have been examined by various authors (Davies and Lock 1973, Perlman 1971, Pillai *et al* 1972, Gross 1944, Gerson and Rohrbaugh 1955, Jain *et al* 1973, Lilly *et al* 1970, Pillai *et al* 1973) using different techniques, but the nature of the polarisation in such electrets is far from clear. Usually the results of electret charge measurements are explained in terms of Gross's two charge theory (Gross 1949), which favours the coexistence of heterocharge and homocharge. The heterocharge formation has been shown due to the volume polarisation of electrets.

Thermally stimulated discharge (TSD) current measurements have been shown to be important technique to understand the volume polarisation behaviour of polymer electrets. Perlman and Creswell (1971), Turnhout (1971) and others (Bucci and Fieschi 1964) have used this method for qualitative analysis of electrets. TSD measurements have been reported in a number of polar and non-polar polymeric materials. Little work has been reported on TSD measurements on polystyrene, a non-polar polymer. However no systematic work is reported on thin ($< 1\mu$) polystyrene films. In the present paper solution grown thin polystyrene films are studied as a function of field and film thickness. The studies are aimed to understand the internal polarisation behaviour of non-polar polymeric material.

2. Experimental

Thin polystyrene films were deposited by the isothermal solution immersion technique from a solution of polystyrene in cyclohexanone maintained at about 60°C. The film thickness ranged from 2000 to 10000 Å. The gold electrodes were vacuum evaporated through a mask of 30 gauge copper wire to yield a film width of 0.03 cm.

Polystyrene films were subjected to a high d.c. electric field ranging from 2.5 kV/cm to 10 kV/cm at polarising temperature 130°C for certain fixed time. The samples were cooled under the influence of the electric field. After some arbitrary time of 5 minutes, the samples were heated to 180°C with a linear rate of 4°C/min in a closed chamber evacuated to a pressure of about 2×10^{-5} torr. The thermally stimulated currents were recorded on X-Y recorder with the help of a GRC model 1230 A electrometer in usual manner. TSD thermographs were recorded under different conditions of field and film thickness.

3. Results

The TSD currents for thin polystyrene films of different thicknesses polarised under same conditions (5 kV/cm at 130°C) are shown in figure 1. In each case the spectrum shows two peaks at about 79°C and 120°C. Conventionally these peaks may be termed as β and α respectively in order of increasing temperature. The peak position was found to be independent of film thickness. A slight change in the peak position in different cycles may, however, be due to a small change in the heating rate.

It has been found that the total charge released to the external circuit, as indicated by the area of the curves of figure 1, increases with the film thickness as shown in figure 2. TSD currents for thin polystyrene films polarised under different polarising fields are shown in figure 3. The TSD spectrum shows two peaks at 77°C and 112°C respectively for 2.5 kV/cm field strength. The results show that the position of the α peak shifts to higher temperature side with the increasing field strength. In β peak position, however, no appreciable change is observed. It is interesting to note that the magnitude of the α peak shows large variations with increasing field values but the magnitude of the β -peak does not show much change with field. The peak current is observed to increase with the field. A linear relationship is observed between the peak current and polarising field as shown in figure 4. For the α peak, however, no such relationship is observed but the peak current shows a linear relationship with $(E_p)^{1/2}$ applied field as shown in figure 5.

Following the analysis of Garlick and Gibson's initial rise method (Garlick and Gibson 1948) the plots of $\log J$ vs. $1/T$ for the TSD curves at different field values are shown in figures 6 and 7 for α and β peaks respectively. The summary

of the estimated activation energies associated with different processes and corresponding relaxation time at different fields are tabulated in Table 1. As can be seen from the results the values of activation energy vary between 1.03 to 1.15 eV for different field values for the α peak. However, no systematic variation with field is observed. The relaxation time τ_0 is calculated to be

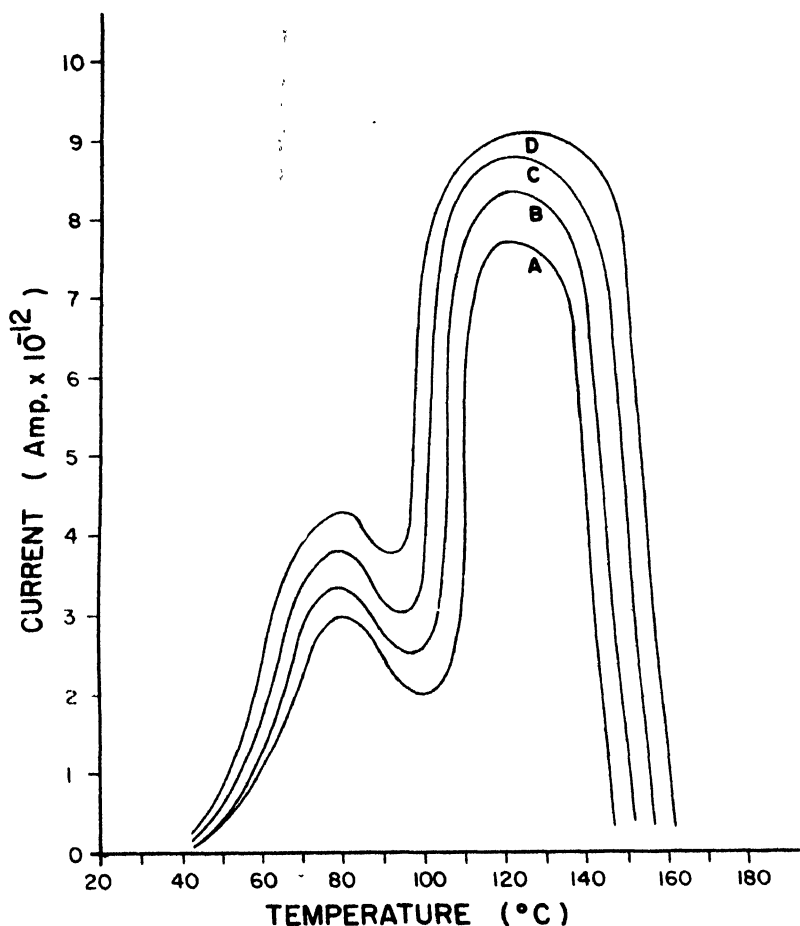
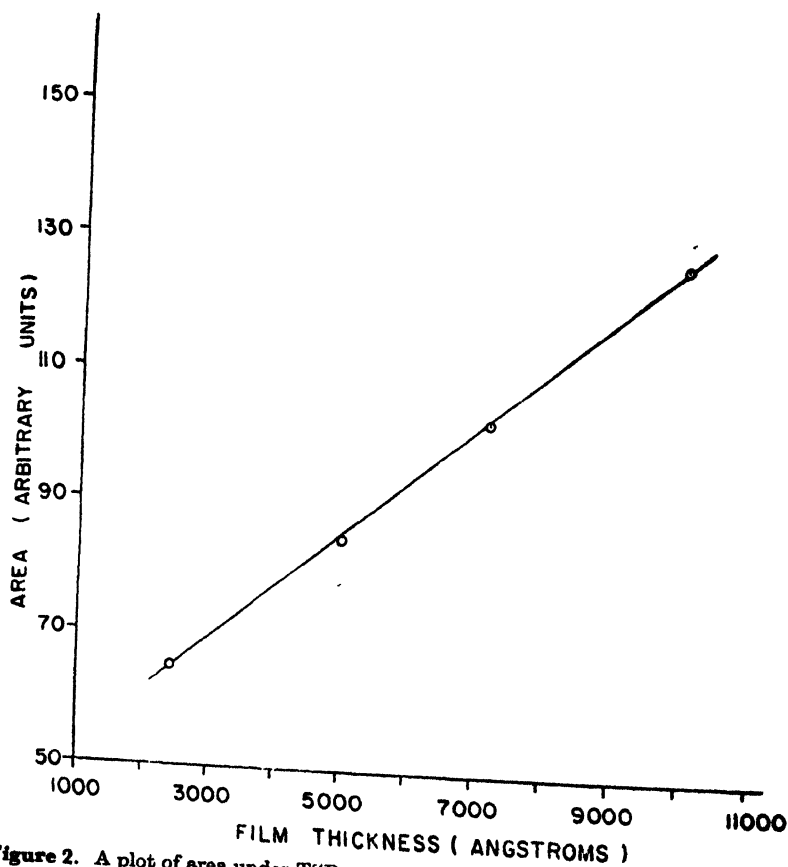


Figure 1. TSD currents for thin polystyrene films of different thicknesses (A—2500, B—5000, 7200 and 10000 Å) at 130°C temperature and 5 kV/cm polarising field.

2.45×10^{-15} sec. at 2.5 kV/cm field. These results are in agreement with Perlman's results (Perlman 1972). For the β peak the values of activation energy vary from 0.46 to 0.24 eV with the increasing polarising field. A regular decrease in the activation energy is observed with the increasing field as shown in Table 1.

Table 1. Summary of the results from the analysis of TSD peaks using initial rise method.

Relaxation process	E_p kV/cm	T_m °C	E eV	τ_0 Sec.	τ_m Sec.	τ_{300} Sec.
α	2.5	112	1.15	2.45×10^{-16}	2.77	5.10×10^4
	5.0	120	1.03	2.00×10^{-14}	3.22	4.01×10^4
	7.0	127	1.04	2.61×10^{-14}	3.30	7.73×10^4
	10.0	136	1.10	9.13×10^{-15}	3.27	2.75×10^5
β	2.5	77	0.46	1.36×10^{-7}	5.70	72.7
	5.0	79	0.31	3.05×10^{-8}	8.34	63.4
	7.0	80	0.26	1.95×10^{-8}	1.02	45.5
	10.0	82	0.24	4.30×10^{-8}	1.12	46.2

**Figure 2.** A plot of area under TSD curves Vs. film thickness for films polarised under 5 kV/cm field at 130°C.

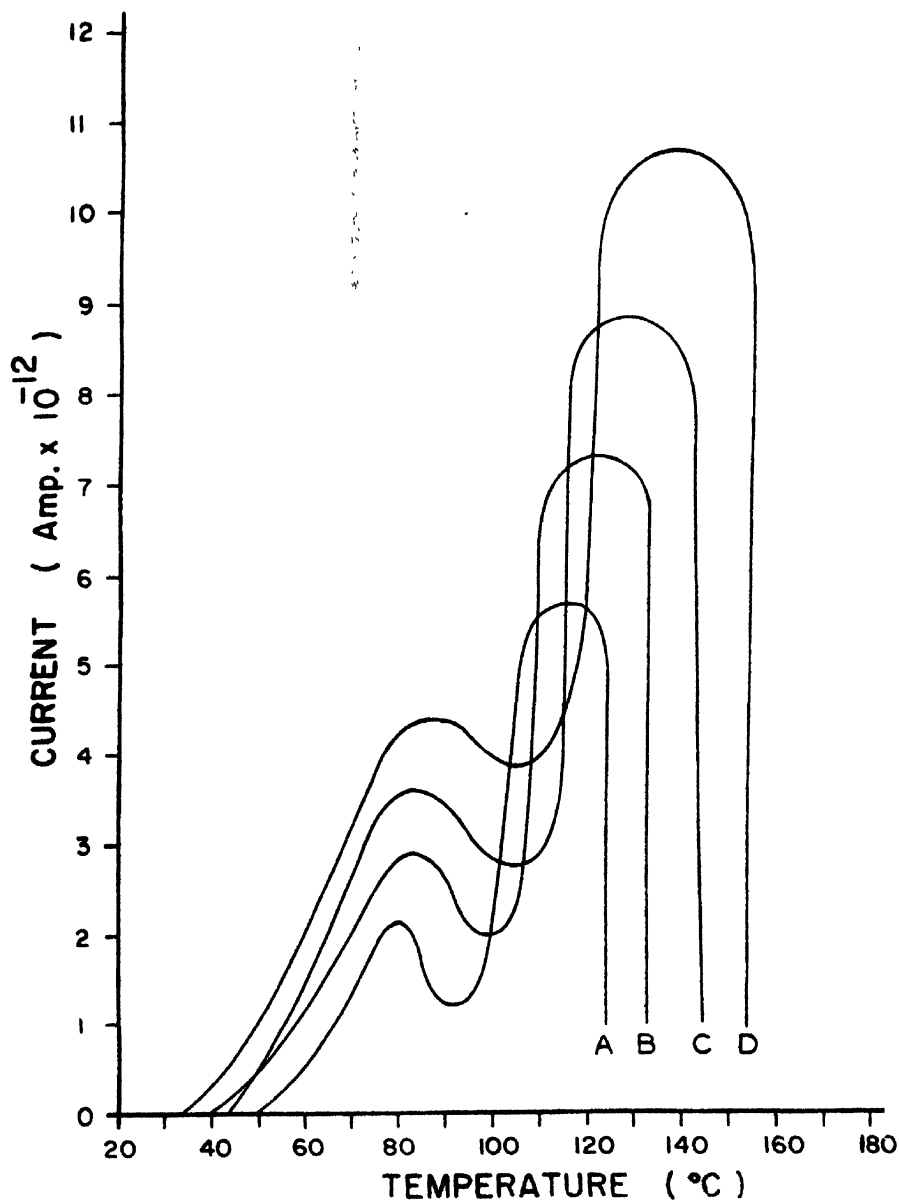


Figure 3. TSD currents for 5000 Å thick film polarised at 130°C under different field strength (A—2.5, B—5.0, C—7.0 and D—10 kV/cm).

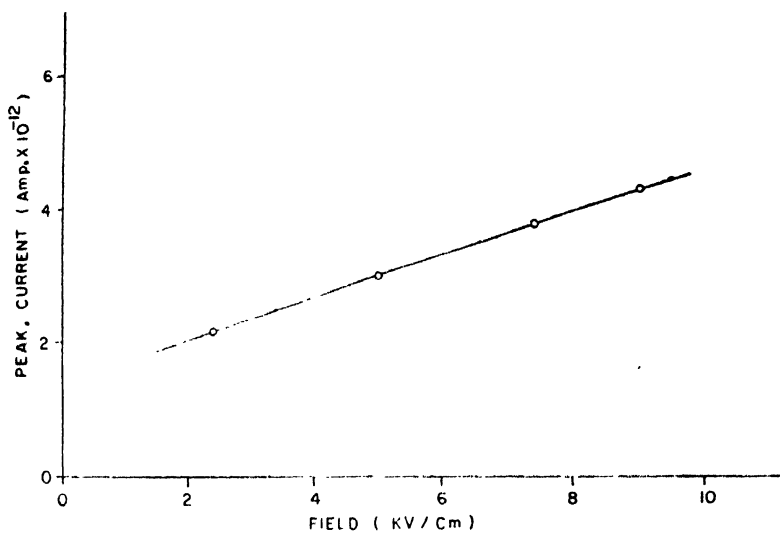


Figure 4. Peak current Vs. applied field for the β peak.

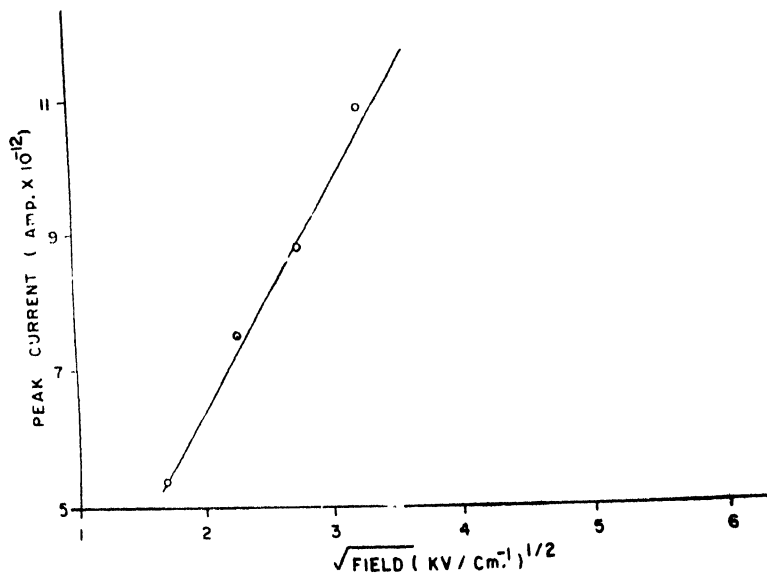


Figure 5. Peak current Vs. square root of applied field for the α peak.

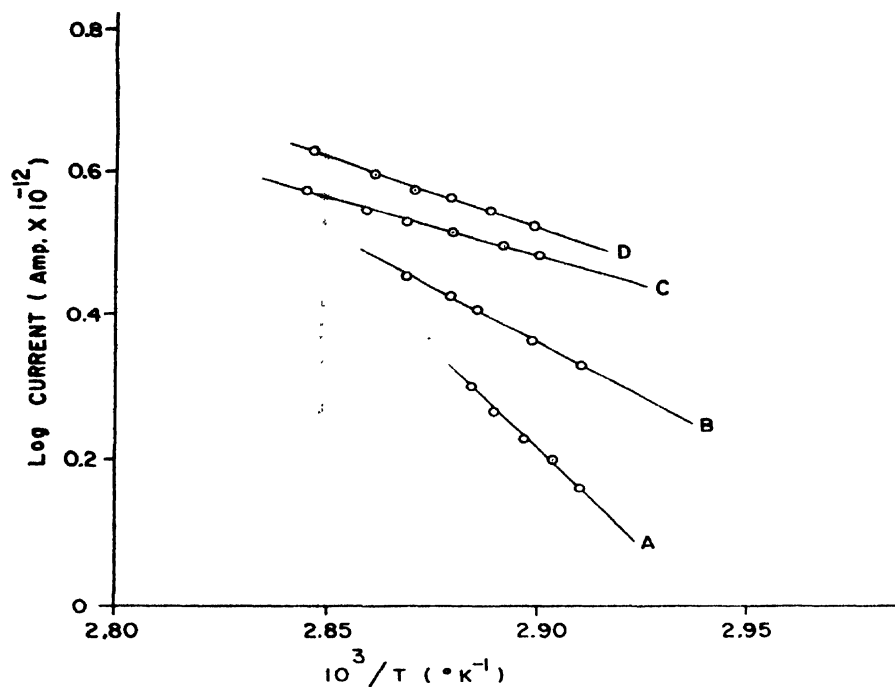


Figure 6. $\log I$ Vs. $1/T$ for β peak at different fields.

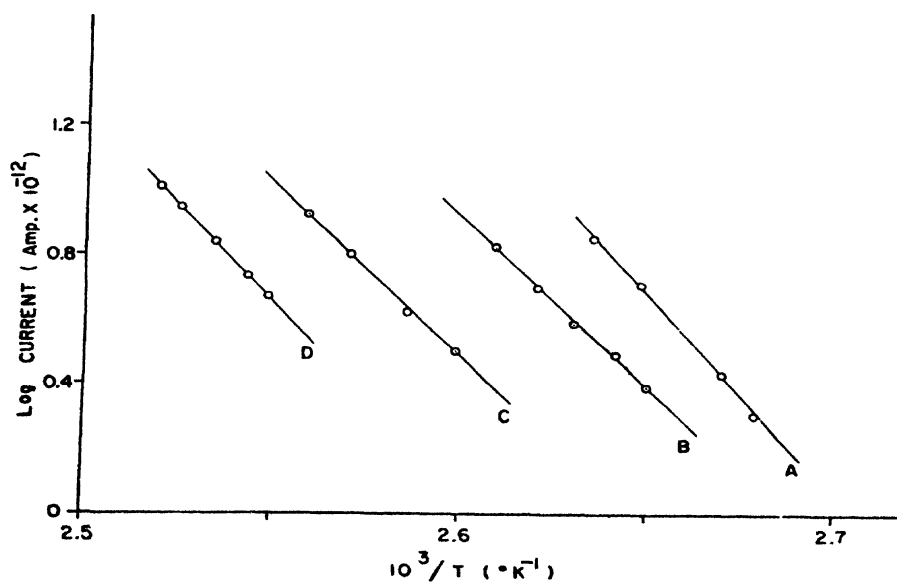


Figure 7. $\log I$ Vs. $1/T$ for α peak at different fields.

4. Discussion

The TSD currents in polymeric materials (Blli *et al* 1974, Pillai *et al* 1971, Jain and Pillai 1968) may be produced by the dipole alignment, ions trapped at the defects or dislocations in crystalline regions, space-charge build up by the migration of ions over microscopic distances and the space charge injected from the electrodes. The first two processes result in a uniform volume polarisation which is a heterocharge. The third one gives a non-uniform heterocharge while the fourth results in non-uniform heterocharge or homocharge depending on the electrode work function and material.

For thin polystyrene films the TSD results show that β peak occurs at about 77°C and is independent of field strength. However, the peak current shows a linear increase with increase in field as shown by the plot of peak current Vs. E_p . This relationship favours an uniform polarisation process. In polystyrene which is a non-polar material, the possibility of permanent dipole alignment is ruled out. However, the polarisation process may be assumed to be due to the local movement of molecular chains causing the release of trapped charge. The variation of activation energy with field value also favours local movement of polymeric chains. Usually such low values of activation energies are associated with local chain movements. The observed small changes in magnitude of β peak with thickness also favours local chain movements in polystyrene thin films. Such local chain movements of polymer chains have been proposed for dielectric—loss relaxation also.

The α peak has been observed above the glass transition temperature of the polymeric material. Its position shifts with increasing field value. It does not show a linear relationship when a curve is plotted between peak current and field. However, a linear relationship is observed for peak current Vs. (field)[†] suggesting a space charge effect. The origin of the space charge in polystyrene films can possibly be due to the injection of charge carriers from electrode (Gutmann and Lyons 1967), the charge trapped in the amorphous crystalline interface of the polymer or the microscopic ion displacement (Froiman and Fridkin 1956). Gerson and Rohrbaugh (1955) have suggested that charges in some dielectric materials suffer microscopic displacement during polarisation process and therefore get trapped. When the specimen is heated to observe TSD currents, the trapped charges are released and recaptured. The recapture time is small as compared with the life time in traps. The rate of decay of the polarisation should depend on the rate of release from the traps. The activation energy associated with this process is expected to be high (Chen 1969). It is likely that charge carriers are ions and in amorphous materials the activation energy associated with ionic traps are generally high (Jonscher 1967). The values of activation energy have been estimated to be about 1.0 to 1.15 eV for

the α process. Though the estimated values of activation energy are in good agreement with expected values for ionic traps, the possible origin of heterocharge formation due to space charge injection from electrode material can not be ruled out. The observed field dependence of the peak current for α process also favours space-charge due to injection from electrode. The electronic conduction studies in thin polystyrene films also favours the injection of carriers from electrode under the influence of high field and temperature. The observed thickness dependence also favours the space charge effect. The observed high values of activation energy, however, could not be fully explained in terms of space charge due to injection from electrodes.

From the preceding discussions it may be concluded that the heterocharge formation in polystyrene films electrode is possibly due to the space charge accumulation. This space charge could be due to either the injection of carriers from electrodes or ionic traps present at amorphous-crystalline interface. No dipolar polarisation has been observed in thin polystyrene films.

Acknowledgment

The authors are thankful to Dr. A. R. Verma, Director, National Physical Laboratory, New Delhi for providing the experimental facilities for the work. One of the authors (BB) is thankful to C.S.I.R., of India, New Delhi for the financial support.

References

- Davies D K and Lock P J 1973 *Electrets, charge storage and transport in dielectrics* Ed by Perlman M M *Electrochem. Soc. N.J.* p 285
- Perlman M M 1971 *J. Appl. Phys.* **42** 2645
- Pillai P K C, Jain K and Jain V K 1972 *Phys. Stat. Solidi (a)* **13** 341
- Gross B 1944 *Phys. Rev.* **66** 57
- Gerson P and Rohrbaugh J H 1955 *J. Chem. Phys.* **23** 2381
- Jain K, Rastogi A C and Chopra K L 1973 *Phys. Stat. Solidi (a)* **20** 167
- Lilly A C, Stewart L L Jr and Henderson R M 1970 *J. Appl. Phys.* **41** 2007
- Pillai P K C, Jain K and Jain V K 1973 *Ind. J. Pure Appl. Phys.* **11** 597
- Gross B 1949 *J. Chem. Phys.* **17** 866
- Perlman M M and Creswell R A 1971 *J. Appl. Phys.* **42** 531
- Turnhout J Van 1971 *Polymer J. (Japan)* **2** 173
- Bucci C and Fieschi R 1964 *Phys. Rev. Letters* **12** 16
- Garlick C F J and Gibson A F 1948 *Proc. Phys. Soc.* **60** 574
- Perlman M M 1972 *J. Electrochem. Soc.* **119** 892
- Blbi Al, Carchano H, Guastovino J, Chatain D, Gautier P and Lacabonn C 1974 *Thin Solid Films* **21** 313

Pillai P K C, Jain K and Jain V K 1971 *Phys. Letters* **35A** 403

Jain V K and Pillai P K C 1968 *Physica Status Solidi (a)* **28** 415

Gutmann F and Lyons L E 1967 *Organic Semi-Conductors* (John Wiley & Sons, Inc, New York) p 620

Froiman A I and Fridkin V M 1956 *Sovt. Phys. Cryst.* **1** 263

Gerson R and Rohrbough J H 1955 *J. Chem. Phys.* **23** 12

Chen R 1969 *J. Appl. Phys.* **40** 2 520

Jonscher A K 1967 *Thin Solid Films* **1** 213.

Studies on the characteristics and fabrication of high voltage Si-diodes

T K Gupta

Department of Physics & Meteorology, Indian Institute of Technology,
Kharagpur-721302.

1. Introduction

High voltage silicon diodes are now being used in tripler of a television set, and can be fabricated in the laboratory at a very cheap cost. As these high voltage silicon diodes are used extensively for commercial purposes, one should take care of the quality of the devices along with their availability at a competitive price. This paper deals with the basic techniques for fabrication of silicon diodes along with a study of their electrical characteristics and the quality of the device.

2. Experimental

1.5 inch diameter, circularly cut single crystal of silicon, having resistivity 20-30 ohm-cm obtained from M/s. Monsanto Co., U.S.A. are used for in the present investigation. As cleaning is one of the most important part of this process technology it is done very carefully. The wafers are cleaned with hydrofluoric acid solution and rinsed in deionised (DI) water. DI-water rinsed wafers are cleaned ultrasonically by acetone, trichloro ethylene, and methyl alcohol. Lastly these samples are cleaned in chromic acid solution and rinsed in DI water.

Ammonium phosphate dopant mixed slowly in DI-water kept in a beaker. This will be *n*-type dopant. Boric acid is mixed in ethyl alcohol, which will be our *p*-type dopant for the diffusion of impurities in the diode fabrication. These premixed dopants are then sprayed on the surface of the silicon samples with *n*-type dopants on the *n*-side. Dopants-sprayed wafers are baked in a 200°C oven for half an hour. Fifty numbers of these wafers are placed together with *p*-side of the next wafer. These wafers are then pushed inside the central zone of a three zone control furnace. The central zone temperature is kept at 1250°C \pm 0.5. Diffusion is carried for sixteen hours. After sixteen hours of operation, these wafers are taken out of the furnace by slowly lowering down the temperature of the furnace. These dopants-diffused wafers are soaked in hydrofluoric acid solution and rinsed in DI water.

Platinum film available from M/s. Emulsiton Co., U.S.A. is spun for ten seconds and baked in a 200°C oven for fifteen minutes. These baked wafers are then pushed inside a diffusion furnace kept at a temperature of 940°C with nitrogen flow. After one and half hour of treatment, these wafers are cleaned with hydrofluoric acid solution and rinsed with DI-water. The cleaned wafers are now etched with premixed $\text{HNO}_3\text{-HF-CH}_3\text{COOH}$ in 2:1:10 proportion, and again rinsed in DI-water. These wafers are then dipped in nickel solution, commercially available, under the trade name ENPAT, from M/s. Transene Co., U.S.A. This solution is used for making ohmic contacts to silicon with nickel.

Fourteen unplated wafers with two plated ones as end pieces are placed with *p*-side up. Aluminium foil cleaned in methanol is placed on the *p*-side of the wafers. Alloying is done at a temperature of 735°C. This stack of wafers is etched again, and second nickel plating is done. Bright gold solution, supplied by M/s. Transen Co., U.S.A. is used for gold plating on silicon. The stack is dipped in the solution for fifteen minutes. The gold plated wafer stack is now ready for taking leads from the appropriate ends.

3. Results and discussion

The volt-ampere relationship $I = I_0[\exp(V/nV_T) - 1]$ shows the dependence of I with temperature. I_0 is the diode reverse-saturation current. This reverse saturation current will increase with increasing temperature. Theoretical calculations have shown that the variation of I_0 with T is 8 percent/°C for silicon (Jacob and Christos). Our fabricated diodes which may be used commercially in tripler of TV set is passed through the electrical test, in which rectifying fly back pulses of 11 KV, at current load of 2 mA, is passed at an ambient temperature of 130°C for 15 seconds. The results are satisfactory with no thermal runaway.

Figure 1 shows the reverse voltage vs. leakage current through diode. The reverse saturation current I_0 at the break down voltage is found to be 70.0 micro ampere approximately for the fabricated high voltage silicon diode. The break down voltage is found to be 22 KV. So, diode can be used safely upto a reverse voltage of 11 KV.

Figure 2 shows the forward voltage vs. current relation, when applied to the silicon diode. For a constant current flow of 10 mA, it has been observed that the minimum voltage shown is 15 volts and maximum is 21 volts respectively.

As cleanliness of the silicon wafers are very important, cleaning should be done very carefully, otherwise uncleaned wafers may damage the surface during diffusion (Mary). Pulling and pushing of wafers in the furnace are required to be done very carefully. Very fast pulling or pushing may damage the wafers, and ultimately the devices. After the diffusion operation is over all the wafers

are tested separately, so that there should not be any crack or damage. Using four-point resistivity probe, sheet resistances are measured on both the sides; wafers with different sheet resistance of the surface are avoided. Nickel plating should be more or less uniform with no bare silicon surface left. De-ionised water used should be the order of 18 megohm-cm resistivity.

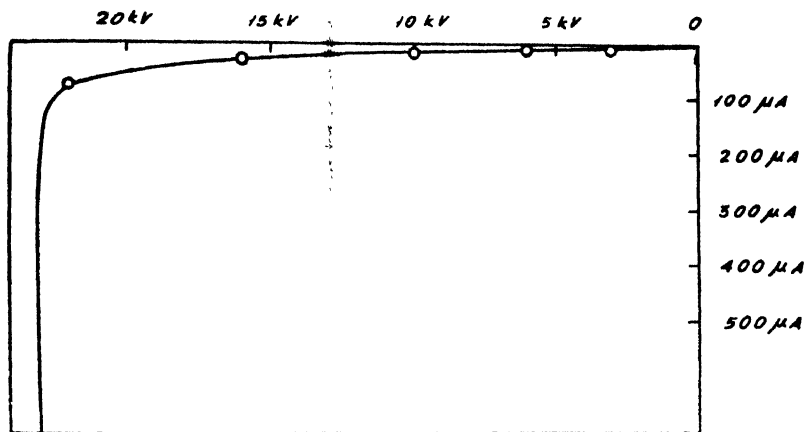


Figure 1

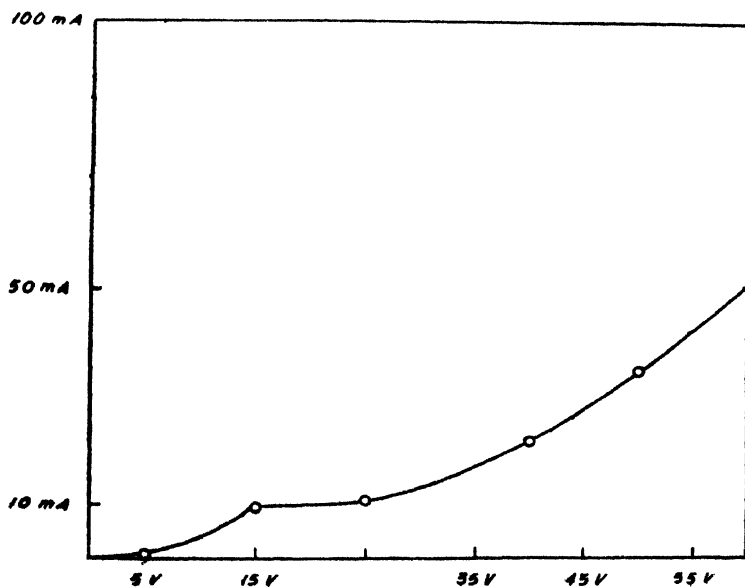


Figure 2

Acknowledgment

A part of the work has been supported by Rotary International Scholarship. Thanks to the Engineering and Research Department, Zenith Radio Corporation, Chicago, U.S.A. for providing laboratory facilities. Author is indebted to his guide Dr. G. E. Weibel, Director of Research, and Dr. Karl Busen for their guidance and valuable suggestions. Author is indebted to Mr. V. P. Oneil, Manager, Silicon Device Research, who by his years long experience has guided and suggested the methods and procedures. Author is also indebted to Prof. H. N. Bose, Head of the Department, Department of Physics and Meteorology, I.I.T., Kharagpur for his valuable suggestions, guidance and taking interest throughout my work. Lastly, he is thankful to Dr. A. K. Chaudhuri for his encouragement from time to time.

References

- Jacob Millman and Christos C Halkias *Integrated Electronics* International Student Edition, Chapt. 19 p 752
- Mary L Long *Spin on Polymers from Laboratory to High Volume Production* Texam Instrument Inc.

Formation of colloid centres in pure and doped KCl single crystals

M L Mukherjee and H N Bose

Department of Physics, Indian Institute of Technology, Kharagpur.

Abstract. The present investigation consists of the studies on the formation of colloid centres in KCl single crystals, both pure and doped with anionic and cationic impurities. Heat-treatment of electrolytically coloured KCl crystals between 110°C and 300°C induces a gradual increase of the colloid band peaking at about 725 nm at the cost of the existing *F*-band. Electrolysis destroys the typical Pb-band in KCl: Pb and $(\text{NO}_3)^-$ and $(\text{NO}_2)^-$ bands in KCl: KNO_3 single crystals. Further heat-treatment of these samples do not produce any colloid band; instead optical absorption decreases throughout the wavelength region between 240 and 1000 nm. From these measurements it is concluded: (i) that formation of colloid centres in electrolytically coloured KCl is possible by heat-treatment even at as low a temperature as 110°C; (ii) that both anionic and cationic impurities play a vital role in the formation of colloid centres and their presence tends to suppress the formation of colloids.

1. Introduction

Colloid bands in alkali halides have been studied by Scott *et al* (1951, 1953) in some details. They investigated the conditions for the formation of colloids from *F* centres in additively coloured crystals and the optical and thermal properties of these centres. According to them, these centres are due to colloidal metals of particle size of the order of 5 μ , and the equilibrium, or the saturation value of *F*-centre concentration, depends on the temperature of heat treatment, which was between 300°C and 500°C in their experiments. A definite shift of the peak of the colloid band toward longer wavelength with the higher treatment temperature has been observed (Doyle 1958). Compton observed that the presence of $(\text{OH})^-$ impurity is required for the formation of colloid band under gamma or cathode ray irradiation: however, its presence was not necessary to form the band in additively coloured crystal (Compton 1957).

Kaiser (1952) has observed colloid centres in films of alkali halides additively coloured by simultaneous evaporation of the salt and excess metal. A wide band is observed which presumably consists of colloids of various particle size, along with *F* and *M* centres.

Here in this paper we intend to study the formation of colloid centres in electrolytically coloured crystal by heat treating at relatively low temperatures (between 250°C and 110°C) and also the effect of deliberately added cationic and anionic impurities on the formation of colloid centres.

2. Experimental

Pure and impurity doped single crystal of KCl are grown from BDH Analar grade salts by Kyropoulos method. The amount of impurity added to the melt is indicated in the parenthesis. A Philips sealed tube (Cu-Target) has been used for X-irradiation. A Beckman model DU spectrophotometer has been used for measuring absorptions. Electrolytic colouration in pure and doped KCl are produced by usual method of placing the sample between a flat platinum anode and a sharp cathode, and heating at a temperature of about 650°C. Samples are handled in dim red light to avoid formation of long wavelength bands due to optical bleaching of *F*-centres.

3. Results

In figure 1 the effect of heat treatment on the absorption spectra of pure KCl coloured electrolytically has been shown. The sample in this case is coloured

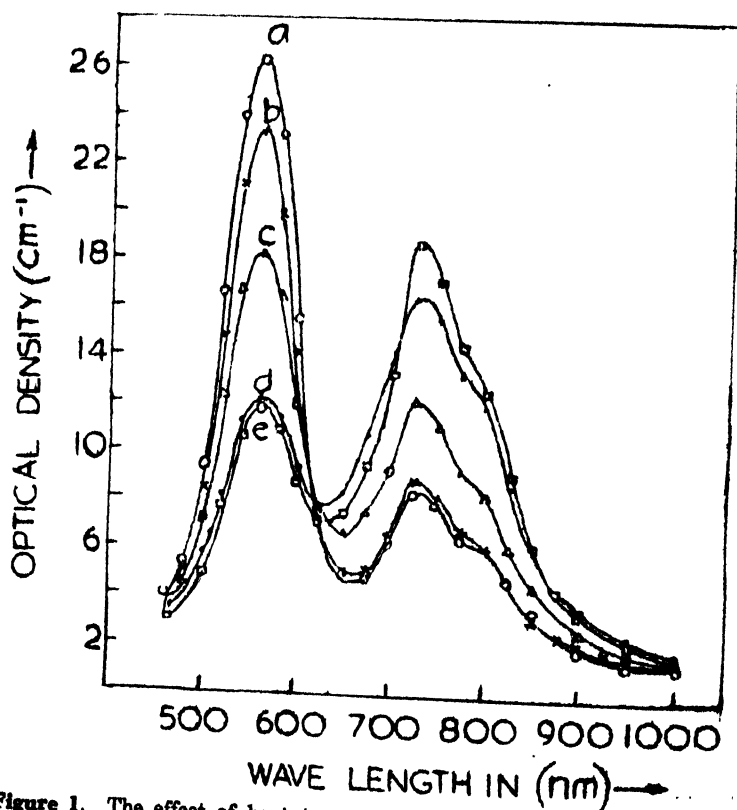


Figure 1. The effect of heat treatment on the absorption spectra of pure KCl coloured conjointly by electrolysis and X-rays (30 kV, 15 mA, 45 minutes); Curves (a), (b), (c), (d) and (e) are obtained after heating the sample at 110°C, 140°C, 170°C, 210°C and 250°C respectively for 30 minutes each.

first by electrolysis and then by X-rays and the optical absorption is measured at room temperature after the sample is kept at 110°C, 140°C, 170°C, 210°C and 250°C for half an hour successively and quenched. The colloid band build up gradually at the cost of the *F*-band. It is to be noted that there is no change of the absorption maximum of the colloid band due to higher treatment temperature.

Figure 2 depicts the absorption spectra of KCl : Pb (2.4×10^{-2} mol%) before and after electrolysis. The sharp Pb-band at 273 nm is destroyed on electrolysis and a typical *F*-band of low intensity is developed, as well as the back ground absorption increases. When this is heated at 300°C for half an hour and quenched, the colloid centres are not formed; instead the optical absorption diminishes throughout the whole range of wavelength between 240 nm and 1000 nm.

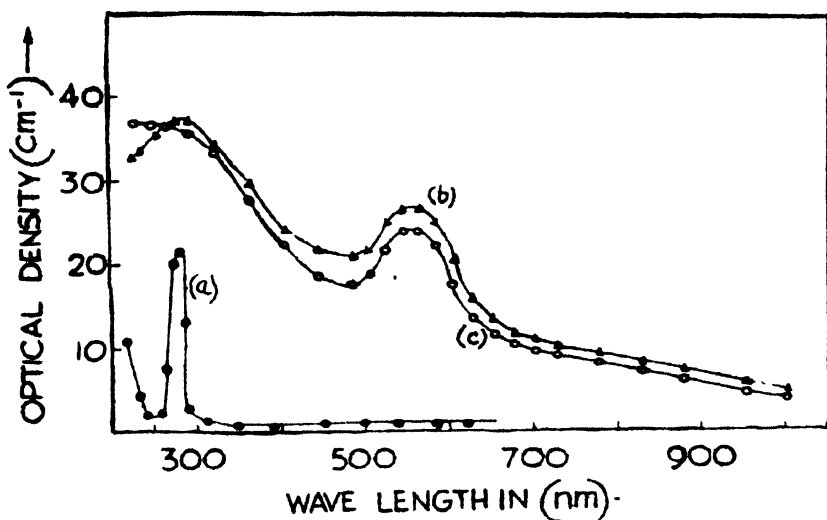


Figure 2. The effect of heating at 300°C for one hour on the absorption bands produced by electrolysis of KCl : Pb crystal. The curve (a) gives the spectra before electrolysis, (b) after electrolysis while (c) gives the spectra after heat treatment.

Upon doping the KCl lattice with KNO_3 (5×10^{-2} mol %) two absorption bands at 7.1 and 7.7 μm in the infrared region is found to develop. These are due to $(\text{NO}_3)^-$ and $(\text{NO}_2)^-$ ions (Wardzynski 1958). Electrolysis destroys these bands to a large extent leaving few centres in the uncoloured portion of the crystal (figure 3). The absorption spectra in the visible region of this sample is given in figure 4 (open circle). The change produced in the absorption spectra by heating it at 300°C for half an hour is quite appreciable. The *F*-band as well as the long wavelength band is diminished in intensity and no colloid band appears to be produced by such heat treatment.

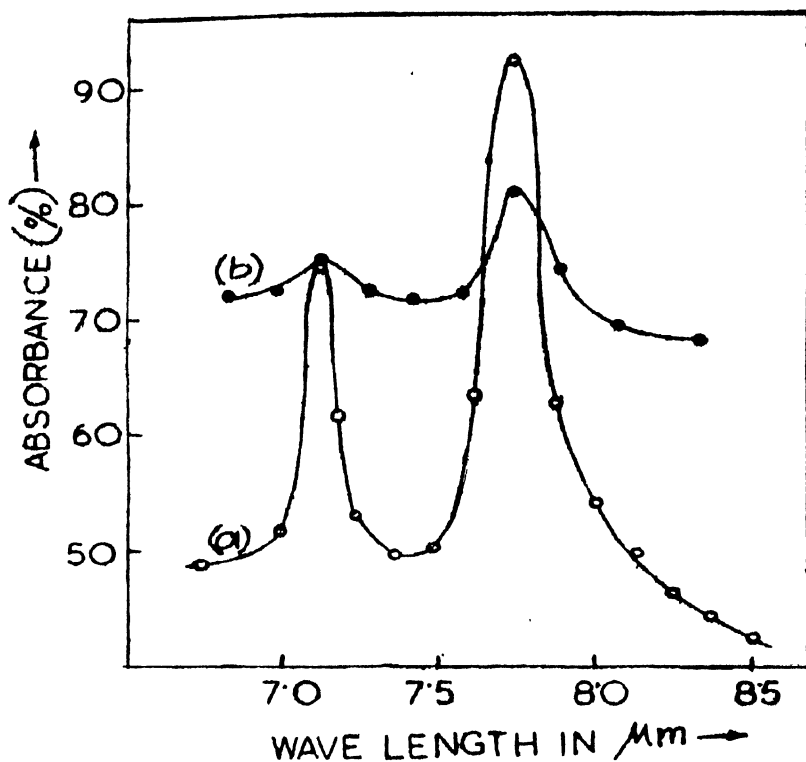


Figure 3. Infrared absorption spectra of as grown (a) and electrolytically coloured (b) $\text{KCl}:\text{KNO}_3$ crystal. A small portion of (b) was left uncoloured due to irregularity in colouration by electrolysis.

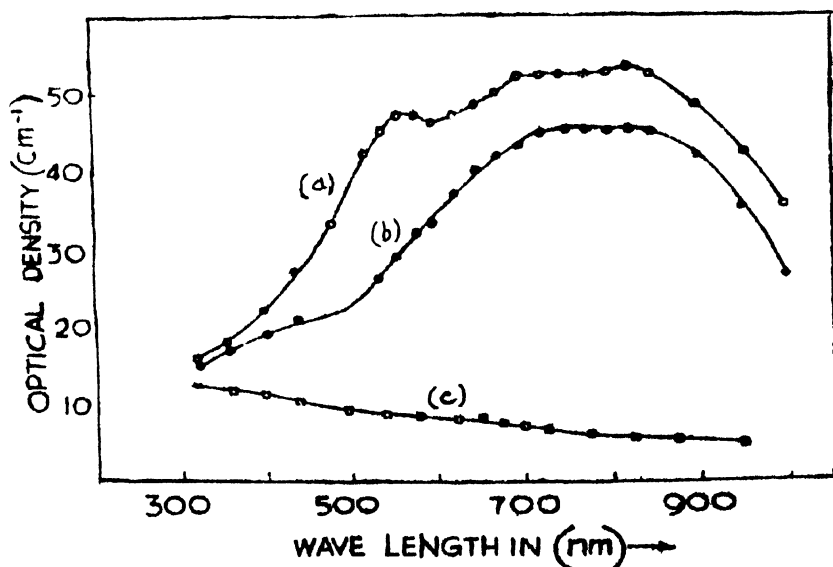


Figure 4. Curve (a) is the absorption spectra of electrolytically coloured $\text{KCl}:\text{KNO}_3$ crystal; (b) is obtained after heat treatment at 300°C ; (b) yields (c) after the sample is heated at 600°C for one hour and quenched.

4. Discussion

It is generally accepted that colloids are formed by heat treating additively coloured alkali halides at a temperature of about 300°C (Scott *et al* 1951, 1953). Figure 1 shows that even at a low temperature of 110°C colloids may be formed in electrolytically coloured KCl crystals. Moreover, if heat treatment is carried out in the low temperature region of 110°C to 250°C, no shift of the absorption maximum of the colloid band is observed. This means that no change in the size distribution of colloidal centres takes place in this temperature range. It may be noted that the shift of absorption maximum observed by Scott *et al* (1951, 1953) is due to heat treatment at higher temperatures.

The absorption band at 273 nm in figure 2 is due to Pb^{++} centres occupying potassium ion sites. On electrolysis, some or most of the Pb^{++} ions capture electrons and are converted to Pb^0 or Pb^- (Topa and Yuste 1970) and as a result the absorption band is destroyed. The presence of these neutral lead and other centres disturb the formation of colloid centres upon heat treatment.

On electrolysis of KCl with anionic impurities, F^- centres, are produced. In the case of KNO_3 doping, the complex ions, $(\text{NO}_3)^-$ and $(\text{NO}_2)^-$, irreversibly decomposed into neutral atoms or molecules (Mukherjee and Bose 1966) possibly oxygen and nitrogen, some of which may remain entrapped in microspores or other suitable lattice defects. These species cannot contribute to electrical conductivity (Mukherjee 1973) and may be looked upon as gaseous substance dissolved in the crystal. Thus the crystal contains a large number of defects, some of which are likely to be of macroscopic type. Excess metal atoms in the presence of high concentration of lattice defects can possibly coalesce into aggregates or colloids responsible for the broad band in the long wavelength region of 650 nm to 950 nm (figure 4). The wide band (650 nm to 950 nm) observed in electrolytically coloured KCl crystal may be produced by the superposition of a number of known bands. It is interesting to point out that there is a striking similarity between these absorption bands with those reported by Kaiser (1952) for the evaporated specimens of KCl containing excess potassium. It is rather tempting to believe that the absorption bands in the two cases are of similar origin. It is of course possible that metallic oxides (such as K_2O) have been produced during electrolysis and these products along with the excess potassium and other defects are responsible for this absorption bands. Kaiser has reported a decrease in the intensities of the bands on aging. In the present investigation also the long wavelength bands show a decrease on heating at about at 300°C. Further formation of colloids do not take place at the cost of F^- centres.

References

- Scott A B, Smith W A and Thompson M A 1953 *J. Phys. Chem.* **57** 757
Scott A B and Smith W A 1951 *Phys. Rev.* **83** 982
Doyle W T 1958 *Phys. Rev.* **111** 1067
Compton W D 1957 *Phys. Rev.* **107** 1271
Kaiser R 1952 *Zeits. f. Physik.* **132** 482
Wardzynski W 1958 *Acta Phys. Polon.* **17** 29
Topa V and Yuste M 1970 *Phys. Stat. Sol. (a)* **3** 131
Mukherjee M L and Bose H N 1966 *Phys. Stat. Sol.* **16** 591
Mukherjee M L 1973 *Ind. J. Pure Appl. Phys.* **11** 252

Mössböuer spectroscopy study of the ternary alloys Co_2FeGa and Fe_2CoGa : site preferences of Co and Fe

N K Jaggi, K R P M Rao and P K Iyengar

Bhabha Atomic Research Centre, Trombay, Bombay-400085.

Introduction

The Co-Ga alloys have Cs-Cl structure at stoichiometry. It has been assumed (Wachtel *et al* 1975, Sollmyer *et al* 1971, Rao *et al* 1975) in the past that in compounds having more than 50.7 atomic percent Co, the excess Co atoms (denoted as Co_x) go preferentially to the Ga sites. It is conjectured (from the analysis of susceptibility, that only those Co_x atoms which have two or more Cox (Sellmyer *et al* 1971) in NN unit cells have magnetic moments. These localized magnetic moments are randomly distributed on Ga sites. Hence for small concentration of Co_x , the alloys can be reasonably expected to show spin-glass properties at low temperatures. Similar behaviour can then be expected even in the case of Co-Ga containing small amounts of Fe atoms, provided the Fe atoms also preferentially occupy the regular Ga sites. Mössbauer spectroscopy and neutron diffraction studies of the alloys Co_2FeGa and Fe_2CoGa have been undertaken to get information on the possible site-preferences of iron and cobalt atoms, and the local environment effects.

Experimental

The alloys Co_2FeGa and Fe_2CoGa were prepared in an induction furnace, by melting at 1200°C for half an hour and then furnace cooling. Later they were powdered and annealed at 900°C for 3 days.

For source measurement 1.5 mci of Co^{57} was diffused in a thin slice of Co_2FeGa using standard techniques. $\text{K}_4\text{Fe}(\text{CN})_6$ absorber containing 0.2 mgm/cm^2 Fe^{57} was used to record the emission spectrum. A Co^{57} in Pd source was used for absorber measurements. All isomer shifts are quoted with respect to natural iron.

Results

Neutron diffraction study of the powdered samples showed the crystal structure in both the cases to be Heusler, with a lattice constant (5.71 \AA), nearly double that of Co-Ga. No precipitation of second phase was observed.

Magnetisation measurements have shown that both the alloys are strongly ferromagnetic. Curie temperature of the alloy Co_2FeGa was found to be 1150°K , while that of Fe_2CoGa was more than 1050°K .

Co_2FeGa : The absorption spectrum of unannealed Co_2FeGa sample showed a slightly broadened six-finger pattern, which could be resolved into two sextets corresponding to the same hyperfine field (HF) but different isomer shifts (IS).

The annealed sample gave a spectrum with narrower lines (figure 1) corresponding to a singlet-site-behaviour, with an HF of 310 kOe and IS of 0.05 ± 0.03 mm/sec. at room temperature (300°K). The spectrum recorded at liquid N_2 temperatures nearly the same as that obtained at RT, except for an increase of HF to 315 kOe and IS to 0.20 mm/sec due to their usual temperature dependence.

Source measurements on Co_2FeGa gave a single sextet corresponding to a HF of 217 kOe and IS of 0.26 mm/sec (figure 1).

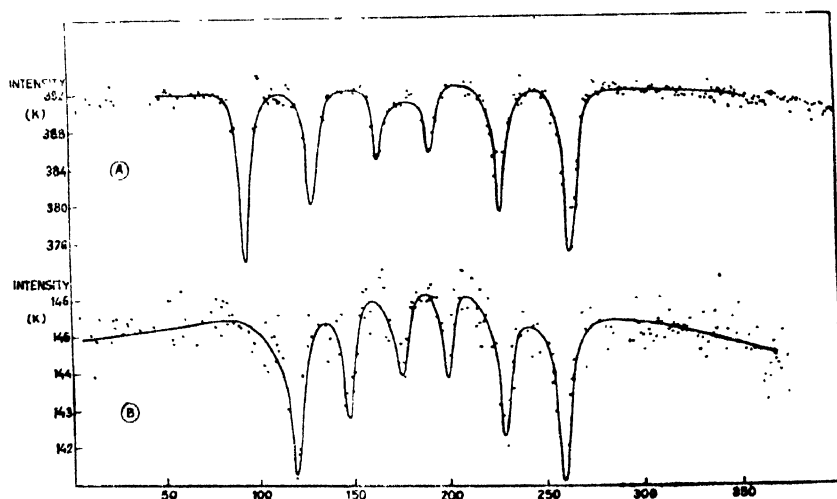


Figure 1. (A) Co_2FeGa . Absorber spectrum. 0.0586 mm/sec. channel.
(B) Co_2FeGa . Source measurement. 0.0496 mm/sec. channel.

Fe_2CoGa : The unannealed sample gave a complex spectrum which could be very clearly resolved into two sextets. One (referred to as L) has a HF of 310 kOe and IS of 0.09 ± 0.03 mm/sec. The other (referred to as S) has a HF of 235 kOe and IS of 0.26 mm/sec (± 0.05 mm/sec.) at RT. The intensity ratio of the two components (i.e., L , S) for the unannealed sample was nearly 2 : 1.

On annealing the sample, the intensities of the two components become nearly equal, without affecting any other parameter (figure 2).

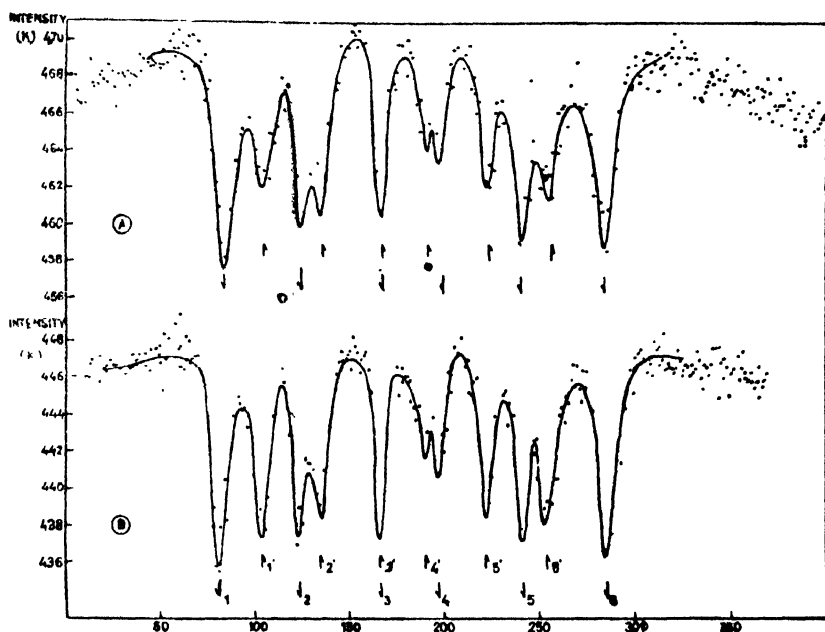


Figure 2. (A) Fe₂CoGa. Absorber spectrum before annealing.
(B) Fe₂CoGa. Absorber spectrum after annealing.
Both 0.0498 mm/sec. channel.

Discussion

The unit cell of the Co-Ga structure, when doubled, can be viewed as a Heusler structure (X_2YZ) with Co at A, C sites and Ga at $B(D)$ sites.

The sextet L corresponding to a larger HF of 310 kOe at RT can be associated with Fe atoms at $B(D)$ sites, where they have all the nn atoms as transition metal atoms, Co or Fe. Hence within the systematics, they can be expected to have large moments. Comparing the HF and IS of this alloy with that in b.c.c. Fe, we expect a moment of about $2 \mu_B$ on Fe atoms.

The other sextet with smaller HF of 200 kOe can be associated with Fe atoms at (A, C) sites, which does not have all transition metal atoms as nn . The smaller HF indicates a smaller magnetic moment of about $1.5 \mu_B$ on these Fe atoms. This correspondence between sextets and sites is further corroborated by the results of previous measurements on Fe₃Ga (Kawamiya *et al* 1972) and Fe₃Si (Stearns 1968). It was found in them that Fe atoms at B site have HF 300 kOe and IS of 0.05 mm/sec, while Fe at (A, C) site has HF 200 kOe and IS of 0.25 mm/sec.

Co_2FeGa : In this alloy, all of the iron atoms go to the $B(D)$ site, as indicated by a single sextet observed. The broadening observed in the unannealed sample is attributed to a small amount of disorder between $B-D$ sites. This disorder annealed out on heat treatment, as indicated by narrowing of the lines. The absence of $B-D$ disorder in the annealed sample was confirmed by the substantial intensity of the odd superlattice reflection (111) in the neutron diffraction measurement of the powdered sample.

The above inferred magnetic moment of $\sim 2 \mu_B$ on Fe atoms was confirmed by polarised neutron diffraction measurements to be $2.1 \mu_B$.

Source measurement clearly shows that all of the diffused Co^{57} occupies exclusively the (A, C) sites, as indicated by a single sextet corresponding to a smaller HF of 217 kOe. This result appears to be in direct contrast to the previous assumption (Wachtel *et al* 1975, Sellmyer *et al* 1971, Rao *et al* 1975), that all of the excess cobalt prefers to occupy the $B-D$ sites.

The Fe-Fe distance of 4.1 \AA is too large for any significant direct overlap to occur. On the otherhand it is unlikely that the indirect RKKY interactions between Fe alone can give rise to a T_c of 1150°K . Our source measurements show a moment of $\sim 1.5 \mu_B$ on Fe atoms at the Co sites (A, C) . Presumably the cobalt atoms themselves may carry an appreciable magnetic moment. Since the Co-Fe distance is only 2 \AA , it is likely that the direct overlap of the d -orbitals of the two atoms is responsible for the strong ferromagnetism observed.

Fe_2CoGa : The two sextets clearly show that Fe atoms are present both at (A, C) and $B(D)$ sites. Thus, it is concluded that all B sites are first occupied by Fe, and then the remaining Fe atoms start occupying the A, C sites, as indicated by the measurements on Co_2FeGa and Fe_2CoGa put together.

This possibly explains why regular Heusler alloys of the type Fe_2YZ do not exist. The cation distribution in the case of the alloy Fe_2CoGa , can be nominally written as $(\text{FeCo})\text{FeGa}$. The small difference in intensity can be due to insufficient annealing, composition not being exactly Fe_2CoGa , or a much stronger site-preference of Fe for the $B(D)$ site resulting in vacancies at (A, C) sites. From our measurement it is seen that as the number of Ga neighbours increases, the HF (and hence the magnetic moment) decreases and the IS shift increases (Table 1) similar to that reported by Hauffman (1976).

The difference of 18 kOe in the HF at A, C site, between Co_2FeGa and Fe_2CoGa , although the site has the same nn environment, may be due to transferred hyperfine field contribution from nnn sites. The HF at B site is however the same whether one has 8Co nn (as in Co_2FeGa) or 4Fe, 4Co (as in Fe_2CoGa) or 8Fe (as in Fe_3Ga). The decreasing moment on Fe atoms with increasing number of Ga neighbours can be understood as due to partial filling of the d -band

Table 1

Alloy	Site	No. of Ga	No. of trans. metal atoms	HF/RT KOe	IS/RT mm/sec
Co ₂ FeGa	B(D)	0	8 (8Co)	310	$\cdot 05 \pm \cdot 03$
	A, C	4	4 (4Co)	220	$\cdot 26 \pm \cdot 03$
Fe ₂ CoGa	B(D)	0	8 (4Co, 4Fe)	310	$\cdot 09 \pm \cdot 03$
	A, C	4	4 (2Co, 2Fe)	235	$\cdot 28 \pm \cdot 03$
Co Ga ³	A	8	0	0	$\cdot 58 \pm \cdot 05$

of the Fe atoms by electron-transfer from the neighbouring electronegative gallium atoms. As the number of *d*-electrons on the Fe atoms increases, the shielding of the 3s electrons becomes more effective, the electron density at the nucleus decreases, and consequently the IS increases, as is found experimentally. This seems to be in agreement with a recent band calculation (Morrizini 1974) on isostructural CoAl, where it was found that there is a net charge transfer from Al to Co atoms, whenever Co has Al as near neighbours.

Acknowledgments

The authors wish to thank Mr. A. K. Grover and Mr. R. G. Pillay of T.I.F.R. for making the magnetization measurements and Mr. M. R. L. N. Murthy for making the samples. The authors also wish to thank Dr. N. S. Satya Murthy for his keen interest and encouragement.

References

- Wachtel E *et al* 1975 *J. Phys. Chem. Solids* **36** 221
 Sellmyer D J *et al* 1971 *Phys. Lett.* **36A** 349
 Rao K R P M *et al* 1975 *Phys. Stat. Sol. (a)* **30** 397
 Kawamiya N *et al* 1972 *JPSJ* **33** 1318
 Stearns M B 1968 *Phys. Rev.* **168**(2) 588
 Huffman G P 1976 *MMM—Intermag Conference*
 Morrizini 1974 *Phys. Rev.* **B10** 4856

An instrument for study of diffuse X-ray scattering very close to reciprocal lattice points and some illustrative results

Krishan Lal and Bhanu Pratap Singh

National Physical Laboratory, Hillside Road, New Delhi-12

Abstract. We have developed a triple crystal X-ray diffractometer for making high resolution measurements of diffuse X-ray scattering very close to the reciprocal lattice points (relps). Two perfect silicon single crystals are used to monochromate and collimate X-ray beam from a microfocus X-ray source. These monochromators can well resolve the $K_{\alpha 1}$ and $K_{\alpha 2}$ component of the characteristic radiation. By using a special collimator the $K_{\alpha 1}$ beam is isolated and used as the exploring beam for diffuse X-ray scattering studies. This beam besides being highly monochromated has a divergence of a few sec of arc in the horizontal plane. With this exploring beam perfect single crystals have been observed to give diffraction curves with half widths very close to the theoretically expected values. Measurements of diffuse X-ray scattering can therefore be made extremely close to the relps. Some illustrative results of measurement of diffuse X-ray scattering made on perfect silicon single crystals by using this instrument are also reported. These measurements have been made using Mo $K_{\alpha 1}$ radiation around 111 relp of (111) single crystals in symmetrical Bragg configuration.

1. Introduction

If all the atoms in a crystal occupy their assigned positions, very sharp diffracted X-ray peaks are expected when the Bragg condition is exactly satisfied. Any small deviation from the assigned positions of the atoms does not lead to any change to the peak position of the Bragg peak but leads to additional scattered intensity close to the Bragg peak. This scattering is known as diffuse X-ray scattering. Study of diffuse X-ray scattering has been used to deduce elastic constants of single crystals (Ramachandran and Wooster 1951, Wooster 1962, Phatak *et al* 1972, Chandra and Hemkar 1973), phonon spectra of single crystals (Cole and Warren 1952, Walker 1956) and structure of lattice imperfections (Spalt *et al* 1973, Larson and Schmatz 1974). Recently, this technique has also been used to study piezoelectrically excited phonons (Mohling *et al* 1970, Carlson *et al* 1971, Le Roux *et al* 1975).

The X-ray diffuse scattering data obtained by using the conventional experimental techniques (Ramachandran and Wooster 1951, Wooster 1962,

Phatak *et al* 1972, Chandra and Hemkar 1973, Cole and Warren 1952) suffers from several uncertainties. There is a significant contribution to the observed diffuse scattering due to instrumental errors arising out of the finite divergence and lack of full monochromatization in the exploring X-ray beam. The contribution of instrumental errors is usually very large. Besides the instrumental errors mentioned above the resolution of the data obtained in K space is also limited by the minimum angular rotation available with the turntable of the diffractometer. Most of the time $1/100$ th of a degree of arc has been used as the minimum angular rotation. Recently, rotations of about 1 sec. of arc have been reported (Mohling *et al* 1970). We have developed a new technique for measurement of diffuse X-ray scattering at high resolution. This technique employs a triple crystal X-ray diffractometer developed by us. In this paper we briefly describe this technique and illustrate the use of this technique with an example.

2. Experimental description of the instrument and some results

In the triple crystal diffractometer a highly monochromated and collimated X-ray beam of very small dimension has been used as the exploring beam. A schematic diagram of this system is shown in figure 1. A Hilger Y-31 microfocuss X-ray generator has been used as a source of X-rays. Both point and line focus sources

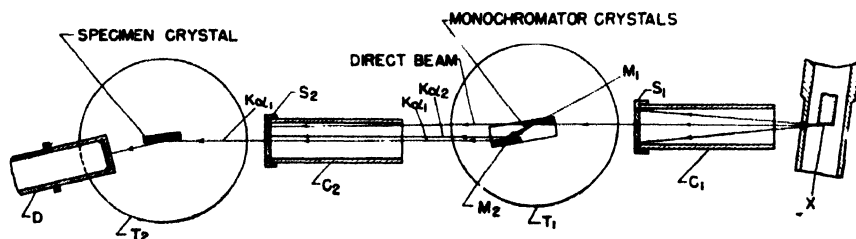


Figure 1. A schematic diagram of the triple crystal X-ray diffractometer. X is the focal spot of the X-ray generator; C_1 is a collimator having one end open and a vertical slit S_1 on the other end; M_1 and M_2 are two monochromator crystals with faces parallel to (111) and parts of the same block; T_1 is the turntable used to align M_1 , M_2 ; C_2 is another collimator having one end open and a vertical slit S_2 on the other end and used to stop all other radiation except the $K_{\alpha 1}$ beam; T_2 is the turntable used to align the specimen crystal and D is the scintillation counter used as an X-ray detector.

have been used. The X-ray beam from the generator is collimated with the help of a collimator C_1 which has a fine slit S_1 at one of its ends. The X-ray beam emerging out of C_1 falls on monochromator M_1 , which is mounted on a turntable T_1 . In fact M_1 and M_2 are two monochromator crystals which are parts of the same crystal block and are in (1, -1) configuration. When M_1 is adjusted for diffraction of collimated X-ray beam, the condition of diffraction

from M_2 is automatically satisfied. The dispersion attainable with those monochromators is very high. The diffracted beam consists of well resolved $K_{\alpha 1}$ and $K_{\alpha 2}$ beams when line focus source is used. With point focus X-ray source either $K_{\alpha 1}$ or $K_{\alpha 2}$ beam is obtained. Figure 2 shows photographs of the diffracted and the residual direct beams recorded with point as well as line focus sources. The diffracted beams and the residual direct beam pass through a second collimator C_2 . The position of C_2 is so adjusted that only $K_{\alpha 1}$ X-ray beam is allowed

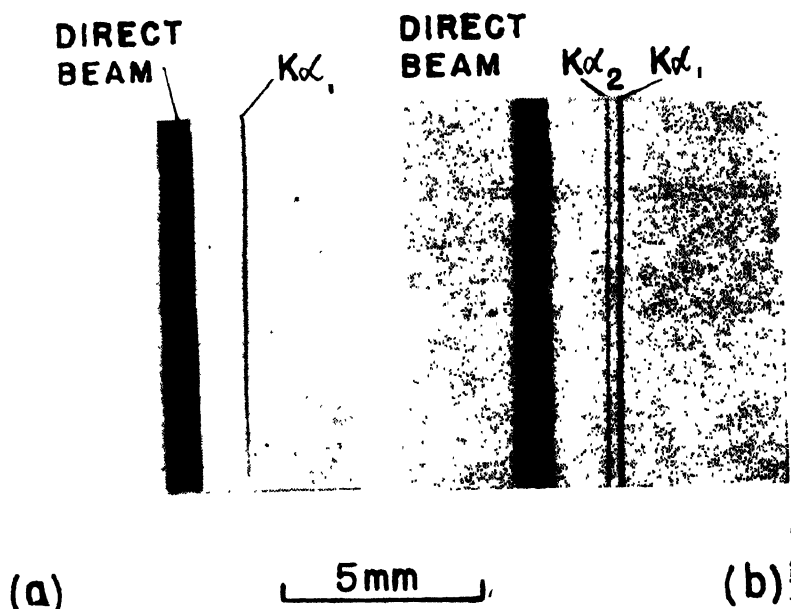


Figure 2. (a) A photograph of the monochromated X-ray beam due to $K_{\alpha 1}$ component and the residual direct beam. A spot focus source ($40 \mu\text{m}$ on the anode) was used. The film was held perpendicular to the X-ray beams between M_2 and the specimen crystal. Note the sharp $K_{\alpha 1}$ beam. (b) A photograph of the two monochromated X-ray beams due to $K_{\alpha 1}$ and $K_{\alpha 2}$ components of the characteristic radiation and the residual direct beam. A line focus X-ray source was used. The film was held perpendicular to the X-ray beams between M_2 and the specimen crystal.

to pass through slit S_2 fixed at one end of C_2 . The other beams are stopped by S_2 . The $K_{\alpha 1}$ beam emerging out of S_2 is used as the exploring beam for the specimen crystal. The specimen crystal is mounted on a standard two arc goniometer which in turn is mounted on a turntable T_2 . A scintillation counter is mounted on a radial arm of T_2 . It is possible to rotate the crystal and the detector by a few sec of arc. The position of the crystal can be measured within one second of arc.

The high degree of collimation and monochromaticity of the exploring X-ray beam leads to very narrow diffraction curves. Figure 3 shows a typical diffraction curve of a (111) silicon single crystal recorded for 111 reflection in symmetrical Bragg geometry. The shape and half width of this curve is fairly close to the theoretically expected values. The diffuse X-ray scattering measurements are performed around this peak.

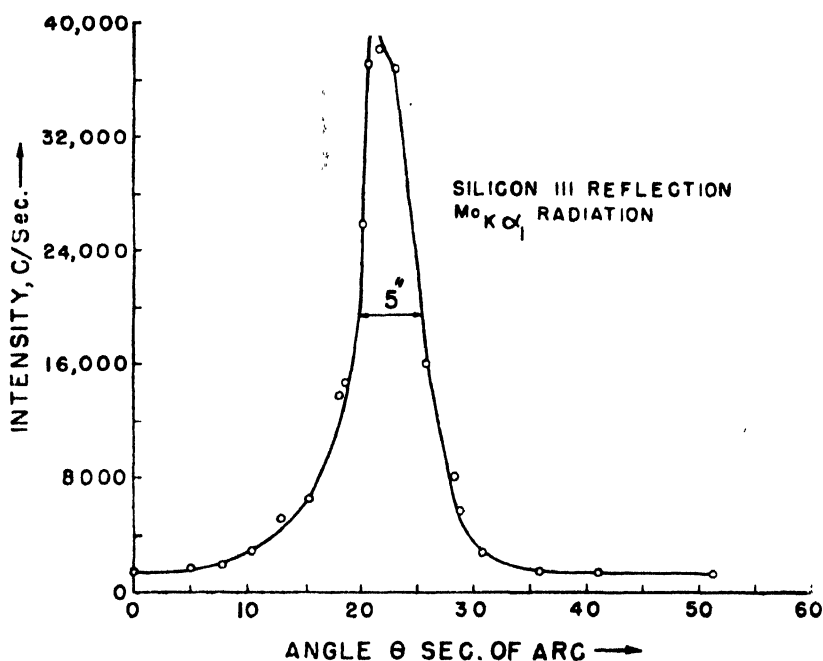


Figure 3. A typical diffraction curve of a perfect (111) Si single crystal recorded in symmetrical Bragg geometry for 111 reflection, on the triple crystal diffractometer. The observed half width of this curve (5 sec of arc) is very close to the theoretically expected half width for this reflection. MoK α_1 radiation has been used.

For diffuse scattering measurements the crystal and detector are mis-set by predetermined angles in order to explore the region around a reciprocal lattice point. Figure 4 shows a plot of intensity of diffuse X-ray scattering as a function of $1/K^2$ for measurements obtained with a dislocation free (111) silicon single crystal around 111 relp along $[111]$, $[\bar{1}\bar{1}\bar{1}]$, $[0\bar{1}1]$ and $[01\bar{1}]$. K is the vector that joins the elemental volume of reciprocal space under investigation to the reciprocal lattice points. It is seen from this figure that the slope of the lines for K parallel or antiparallel to reciprocal lattice vector (rel vector) is larger than that for the lines with K perpendicular to the rel vector. Also there is anisotropy in the intensity of diffuse scattering when one explores along two directions 180°

to each other. Since the half width is 5 sec of arc diffuse scattering measurements are made at $|K|$ as small as $1.78 \times 10^3 \text{ cm}^{-1}$ and successive measurements are made at an interval of $3.96 \times 10^2 \text{ cm}^{-1}$. This has been possible because of high resolution attainable by the triple crystal X-ray diffractometer. In these measurements there are no instrumental uncertainties.

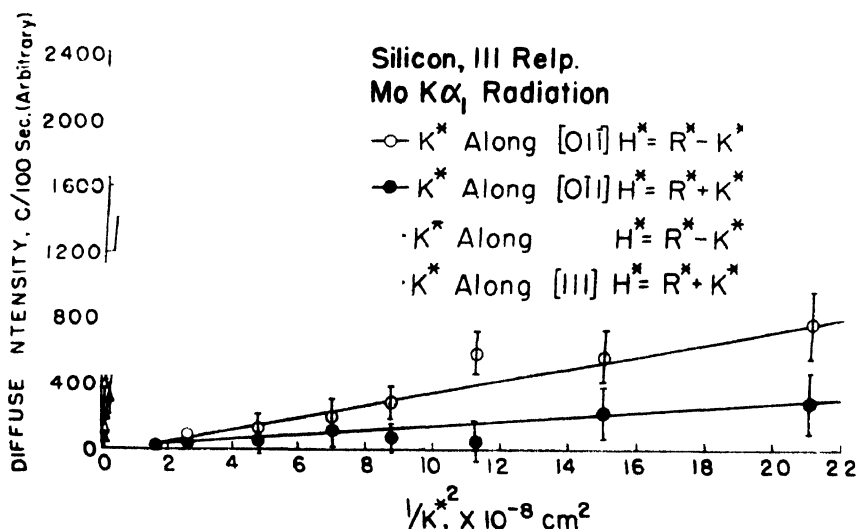


Figure 4. A typical high resolution intensity of diffuse scattering I vs $1/K^2$ plot for a (111) silicon crystal.

These results show that it is not possible to use conventional theory of thermal diffuse X-ray scattering to understand this data. Apparently the observed intensity of diffuse X-ray scattering is due to thermal diffuse scattering as well as Huang scattering. However, it is obvious that as a new high resolution technique this can be very useful in exploring the reciprocal space very near reciprocal lattice points. We are using this technique for detailed investigations of diffuse X-ray scattering in perfect silicon single crystals. Details of these results will be published separately.

Acknowledgment

The authors are grateful to Dr. Ajit Ram Verma for many valuable discussions.

References

- Ramachandran G N and Wooster W A 1951 *Acta Cryst.* **4** 431
- Wooster W A 1962 *Diffuse X-ray Reflections from Crystals* (Clarendon Press, Oxford)
- Phatak S D, Srivastava R C and Subbarao E C 1972 *Acta Cryst.* **A28** 227
- Chandra S and Hemkar M P 1973 *Acta Cryst.* **A29** 130
- Cole H and Warren B E 1952 *J. Appl. Phys.* **23** 335
- Walker C B 1956 *Phys. Rev.* **97** 654
- Spalt H, Lohstoler H and Peisel H 1973 *Phys. Stat. Sol. (b)* **56** 469
- Larson B C and Schmatz W 1974 *Phys. Rev.* **B10** 2307
- Mohling W, Muller G O, Peibst H and Schaurer E 1970 *Phys. Stat. Sol. (a)* **2** 725
- Carlson D G, Segmuller A, Mosekilde E, Cole H and Armstrong J A 1971 *Appl. Phys. Lett.* **18** 330
- Le Roux S D, Colella R and Bray R 1975 *Phys. Rev. Lett.* **35** 230

A comparative study of perfection of CVD grown and Czochralski grown α -Al₂O₃ single crystals by X-ray diffraction topography

Krishan Lal, Vijay Kumar and Ajit Ram Verma

National Physical Laboratory, Hillside Road,
New Delhi-110012

Abstract. Results of study of perfection of (0001) α -Al₂O₃ single crystals grown by chemical vapour deposition (CVD) and Czochralski method are reported. The diffraction curves of Czochralski grown crystals were observed to consist of several peaks separated by a few minutes of arc from each other and extending over several minutes of arc. This observation reveals the presence of low angle boundaries in these crystals. Topographs of this type of crystals were recorded by aligning them for most intense diffraction peak in their diffraction curve. These topographs also show the presence of low angle boundaries. The angles of mis-set between adjoining subgrain were determined. The value of the angle is approximately 2 minutes of arc. Therefore, it is seen that these crystals are not perfect crystals. The perfection of CVD grown α -Al₂O₃ crystals was found to vary with distance from the seed. Regions surrounding the seed were found to be imperfect like the Czochralski grown crystals. Those regions which were away from the seed were found to be nearly perfect crystals. These contain few isolated dislocations. These dislocations were characterised by using *g.b.* contrast analysis. Most of these dislocations were found to be edge type with Burgers vector *b* along $[\bar{2}110]$ and line vector \hat{n} along $[0110]$.

1. Introduction

α -Al₂O₃ single crystals are being widely used as substrate materials for single crystal thin films, as laser materials and in other industrial applications. Besides the purity of these materials, perfection also has a significant influence on the device performance. The perfection of single crystal thin films depends strongly upon the perfection of the substrate single crystal. α -Al₂O₃ single crystals have been usually grown by Verneuil method and Czochralski method. Recently, these crystals have been grown from Vapour phase by using chemical vapour deposition (CVD) method. In this paper we report results of study of perfection of CVD grown as well as Czochralski grown α -Al₂O₃ crystals by transmission X-ray diffraction topography.

2. Experimental

The CVD grown crystals used in this investigation were obtained from Dr. J. J. Cuomo of the IBM Thomas J. Watson research centre, York Town Heights,

New York. The Czochralski grown crystals were obtained from Dr. P. Thoma of the Physikalisch-Technische Bundesanstalt, Braunschweig and Berlin, West Germany. All the wafer were cut perpendicular to [0001].

The X-ray topography camera and the microfocus X-ray generator used in this investigation have been developed in the NPL. The details of the X-ray diffraction topography camera have been described elsewhere¹. Verma *et. al.* 1974. The microfocus X-ray generator is a demountable type system with continuously running vacuum Lal *et. al.* 1975. In this investigation line focus source has been used. $\text{MoK}\alpha_1$ and $\text{AgK}\alpha_1$ radiations have been used.

Most of the topographs have been recorded on Ilford L_4 nuclear emulsion plates with $50\mu\text{m}$ thick emulsion. For preliminary work Kodak Periapical dental X-ray films have been used.

3. Results and discussion

The idea of state of perfection of a single crystal can be had from its diffraction curve. Nearly perfect single crystals are expected to give well defined peaks due to $\text{K}\alpha_1$ and $\text{K}\alpha_2$ components of the characteristic radiation³. Diffraction curves were recorded for all the crystals that were investigated. Czochralski grown crystals gave diffraction curve consisting of several peaks. Figure 1 shows a typical

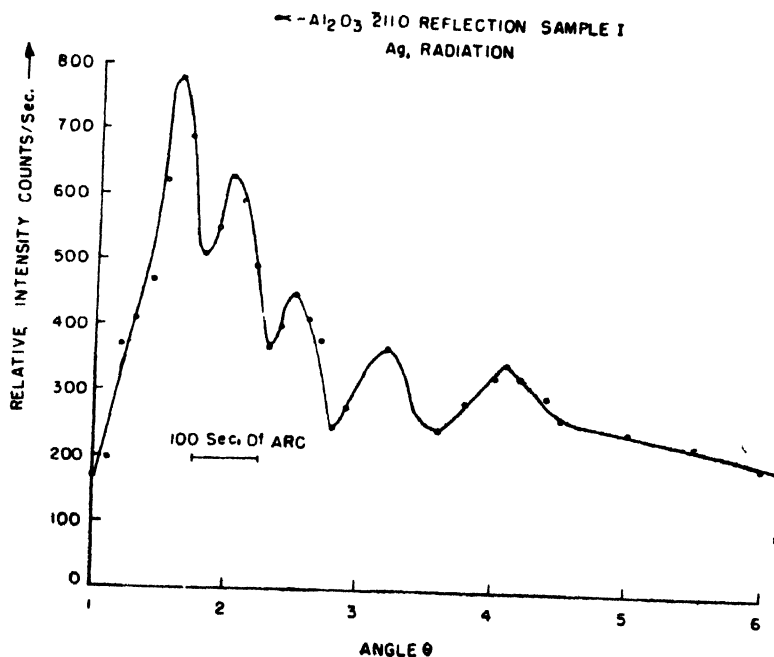


Figure 1. A typical diffraction curve of a Czochralski grown (0001) $\alpha\text{-Al}_2\text{O}_3$ single crystal wafer recorded using $\bar{2}110$ reflection with $\text{AgK}\alpha$ radiation.

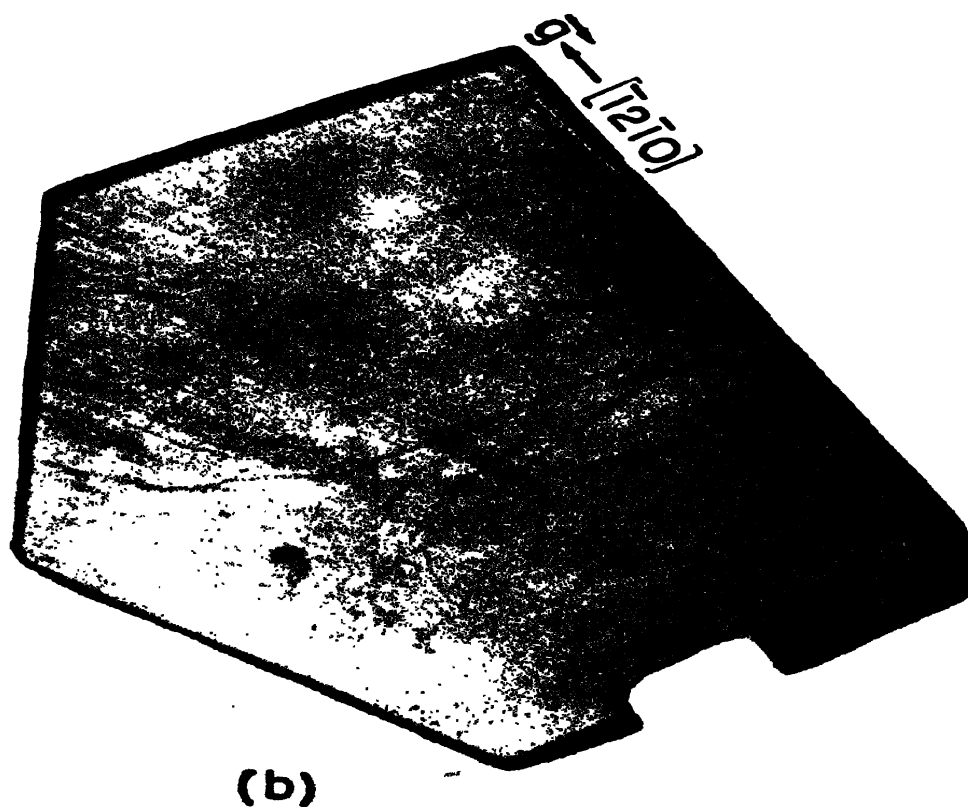
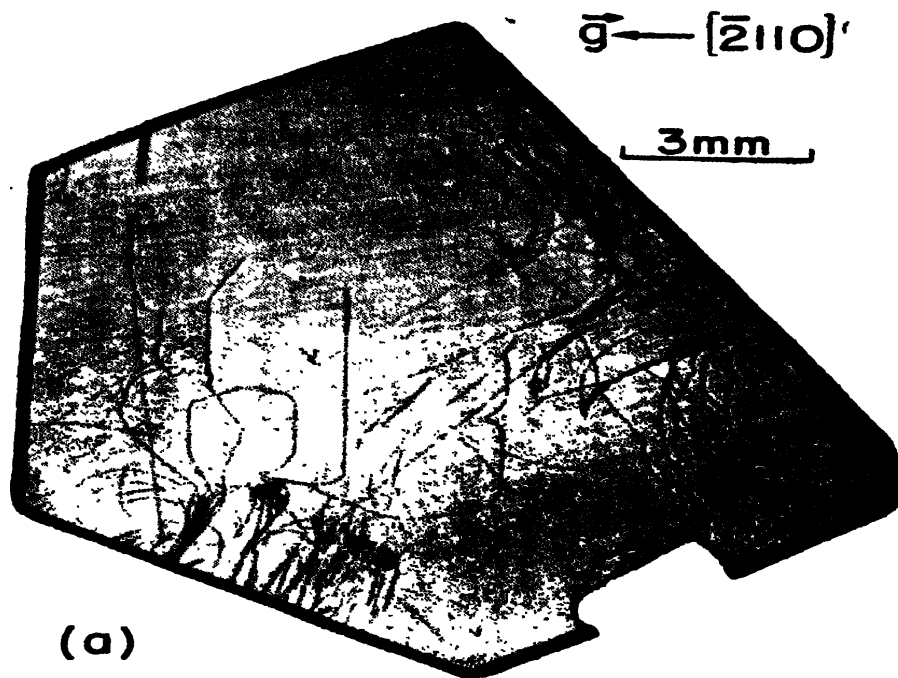
diffraction curve of a Czochralski grown wafer. The various peaks in this curve are separated from each other by a few minutes of arc. This suggests that low angle boundaries are present in these crystals.

To confirm the presence of low angle boundaries, we have recorded X-ray topographs of these crystals. Figure 2 shows a typical set of topographs of a Czochralski grown wafer. After recording the topograph of Figure 2a the crystal ; was mis-set by two minute of arc around a vertical axis and the topograph shown in Figure 2b was recorded. It can be seen that these topographs correspond to rather imperfect crystals. Low angle boundaries can be seen in some regions. This result is consistent with the diffraction curve shown in Figure 1. The appearance of the region marked A is different in Figure 2a and Figure 2b. In Figure 2a it appears as excessively black whereas in Fig. 2b this appears as white. This shows that the region of the



Figure 2. A typical set of projection topographs of a Czochralski grown (0001) α - Al_2O_3 single crystal wafer. $[\bar{2}110]$ diffraction vector and $\text{AgK}\alpha$, radiation were used

Figure 4. Projection topographs of a CVD grown (0001) α -Al₂O₃ single crystal wafer recorded with MoK α ₁ radiation. Diffraction vector was parallel to $[2\bar{1}10]$ and $\{\bar{1}\bar{2}\bar{1}0\}$ in (a) and (b) respectively



Caption see next page

crystal corresponding to A is misoriented with respect to the surrounding regions by about two minutes of arc. Indeed by aligning the crystal for different peaks in Figure 1 different subgrains can be photographed.

In the CVD grown crystals the perfection of a region was found to strongly depend upon the distance of this region from the seed. At the seed crystal interface a lot of strain was observed Lal & Kumar. However, regions of these crystals away from the seed portion were found to be nearly perfect. In this paper we will briefly describe the results of study of perfection of the perfect portions.

Figure 3 shows a typical diffraction curve of a CVD grown nearly perfect single crystal. Well resolved diffraction peaks due to $K\alpha_1$ and $K\alpha_2$ components of the characteristic radiation are observed. The peaks due to $K\alpha_1$ and $K\alpha_2$ are fairly sharp. This shows that this crystal is fairly perfect.

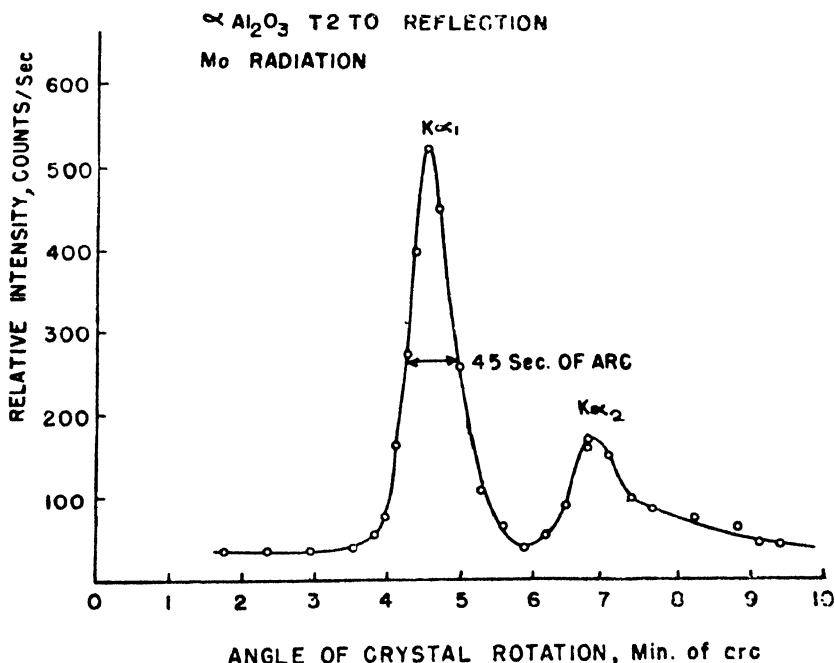


Fig. 3. A typical diffraction curve of a CVD grown (0001) α - Al_2O_3 single crystal wafer recorded using $\bar{1}2\bar{1}0$ reflection with $\text{MoK}\alpha$ radiation

Transmission X-ray topographs of nearly perfect CVD grown wafers were recorded in symmetrical Laue geometry with diffraction vector along different directions. Figures 4a and 4b are typical projection topographs of a good CVD

grown wafer recorded with diffraction vector \mathbf{g} parallel to $[\bar{2}110]$ and $[\bar{1}2\bar{1}0]$, respectively. For recording both these topographs the wafers were aligned for $K\alpha_1$ radiation. In this crystal evidently no low angle boundaries are observed. On the other hand several straight lines parallel to $[01\bar{1}0]$ are observed in Figure 4a. A large region of the topograph is free of any structure. The straight lines mentioned above are found to be dislocations. Since the line vector n of these dislocations is perpendicular to the diffraction vector \mathbf{g} , these lines cannot be due to screw dislocation, since $\mathbf{g} \cdot \mathbf{b}$ will vanish. Here \mathbf{b} is the Burgers vector of the dislocation. However, for a edge dislocation \mathbf{b} is perpendicular to \hat{n} . If we assume these lines to be edge dislocations \mathbf{g} is perpendicular to \hat{n} and therefore maximum contrast is expected (Verma *et al* 1974, Lal 1976, & Lang 1970). These arguments suggest that these lines are due to edge dislocations. Their Burgers vector is expected to be along $[\bar{2}110]$. To confirm this result several topographs with \mathbf{g} along different directions were recorded. Figure 4b shows a topograph in which \mathbf{g} is along $[\bar{1}2\bar{1}0]$. Since this direction is close to $[01\bar{1}0]$, \mathbf{g} is nearly parallel to n and therefore, the vertical lines observed in Figure 4a have nearly disappeared in this topograph. This confirms our conclusion that these lines are due to edge dislocations. Slip system of $\alpha\text{-Al}_2\text{O}_3$ has been worked out (Belt 1967). $[\bar{2}110]$ is one of the slip directions in this system (Belt 1967) and therefore, our results are quite consistent with these results. Czochralski grown $\alpha\text{-Al}_2\text{O}_3$ has been investigated for perfection earlier also (May & Shah 1969). These investigations have also shown that Czochralski grown crystals have high dislocation density. The present results show that CVD grown crystals contain few dislocations (Figure 4). Large regions in Figure 4 are practically dislocation free.

This investigation shows that CVD grown crystals cut away from the seed are more perfect than the Czochralski grown crystals and perhaps the most perfect $\alpha\text{-Al}_2\text{O}_3$ crystals.

References

1. Belt R. F. 1967 *J. Am. Ceram. Soc.* **50**, 588.
2. Lal Krishan, Kumar Vijay & Pahwa D. R. 1975 Presented at National Conference on Crystallography held at NPL New Delhi—Dec 4-6.
3. Lal Krishan 1976 *J. Phys. Education* **4**, 1.
4. Lal Krishan & Kumar Vijay 1978 *J. Electrochem. Soc.* (in press).
5. May C. A. & Shah J. S. 1969 *J. Material Science* **4**, 179.
6. Verma Ajit Ram, Lal Krishan, Pahwa D. R. Kumar Vijay & Aggarwal Keshav 1974 *Indian J. Pure & Appl. Phys.* **12**, 350.

Diffusion of gallium into silicon

B C Chakravarty and A Prasad

Division of Materials, National Physical Laboratory, Hillside Road, New Delhi-12.

Abstract. A comparative study has been carried out of the diffusion of gallium into bare silicon and into oxide covered silicon. The junction depth and the doping profiles were determined by anodically sectioning the diffused wafers. The surface concentration is found to be higher in case of bare silicon and contrary to the published results of Nakajima and Ohkawa no enhancement in junction depth is observed for diffusion of gallium into silicon through oxide at 1100°C.

1. Introduction

Gallium and aluminium are the two group III impurities which diffuse readily through silicon dioxide. Their diffusion coefficient in silicon dioxide is 3-6 orders of magnitude greater than most common donor and acceptor impurities like boron, phosphorus, arsenic and antimony (Ghezzi and Brown 1973). Therefore, gallium and aluminium get diffused into silicon even when silicon is covered with silicon dioxide. While this makes them generally unacceptable for planar technology, they have their own usefulness in the high power field, where the emphasis is on deep diffusions.

Gallium diffuses into silicon through silicon dioxide are carried out both by open tube and sealed capsule techniques. A question of common interest to both the open tube and closed capsule techniques is—what is the effect of the silicon dioxide layer on the two primary parameters of a diffusion, viz., the surface concentration and junction depth? A good deal of work has been reported (Wagner and Povilonia 1974) on the open tube diffusion of gallium into silicon through silicon dioxide. In case of open tube diffusion, it has been found that the diffusing species are gallium oxide (Wagner and Povilonia 1974), Ga_2O and the oxide is found to retard the diffusion process as evidenced by the marginal reduction of junction depth (Wagner and Povilonia 1974, Grove *et al* 1964) and surface concentration (Grove *et al* 1964) due to the presence of the oxide coating. Closed capsule diffusion of gallium into silicon covered with a layer of silicon dioxide has been reported by Nakajima and Ohkawa (1972). They used an evacuated quartz capsule and sufficient elemental gallium to establish a saturated gallium vapour atmosphere inside the sealed capsule.

Diffusions were carried out at a temperature of 1000°C for 60 minutes. The surface concentration was determined by four point probe method and the junction depth was determined by angle lapping the diffused wafers and then delineating the junction by staining the bevelled samples chemically. They reported an enhancement of about 20–40% of the junction depth in the (111) direction caused by the presence of the oxide. Their junction depth was of the order of 0.5 microns. The surface concentration was higher for bare silicon than for the oxide covered one.

We carried out closed capsule diffusions of gallium into bare silicon and into silicon through silicon dioxide at a temperature of 1100°C for 10 minutes which yielded a junction depth of 7080 Å for both bare and oxide covered slices. It was observed that neither angle lapping nor grooving is accurate enough to determine small changes in the depth of such a shallow junction. In order to overcome this difficulty a high resolution anodic oxidation method has been employed to determine the junction depths and doping profiles. This method has two distinct advantages. Firstly, with sufficient care, this method allows measurements to be made to an accuracy in oxide thickness of ± 100 Å corresponding to a silicon layer thickness of ± 36 Å. Secondly, the successive layers removed are parallel to the surface and to themselves.

2. Theory

Let us consider a one dimensional diffusion model where the interface of silicon dioxide and silicon is taken to be at $x = 0$. The concentration of gallium at the interface is assumed to be N_0 . Because of the very high diffusion coefficient of gallium in silicon dioxide, the concentration of gallium at the interface is always maintained at N and is independent of the oxide thickness. The diffusion of gallium into a semi-infinite region through the $x = 0$ plane is given by Fick's law of diffusion

$$\frac{\partial N(x, t)}{\partial t} = D \frac{\partial^2 N(x, t)}{\partial x^2} \quad (x > 0) \quad (1)$$

where $N(x, t)$ is the concentration of diffusing species and is a function of time t and distance x from the $x = 0$ plane, D is the diffusion coefficient of gallium in silicon. The boundary and initial conditions are respectively given by

$$N(0, t) = N_0 \quad (2)$$

and

$$N(x, 0) = 0 \quad (3)$$

The solution (Burger and Donovan 1967) of the diffusion equation (1) under the above conditions is

$$N(x, t) = N_0 \operatorname{erfc} \frac{x}{2(\bar{D}t)^{1/2}} \quad (4)$$

whence the junction depth is

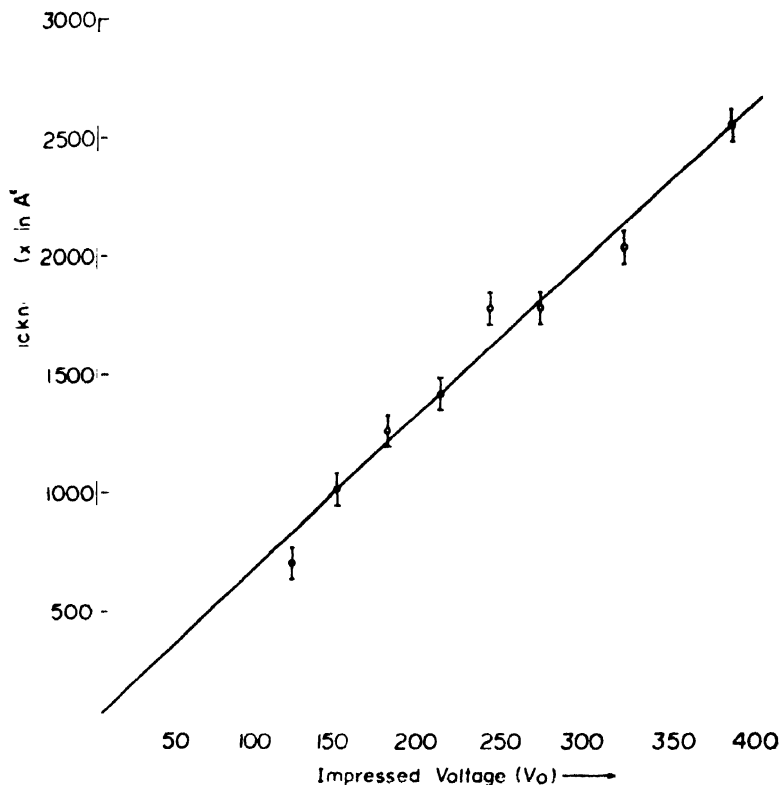
$$x_j = 2(Dt)^{1/2} \operatorname{erfc}^{-1} \left(\frac{N_b}{N_0} \right) \quad (5)$$

Here N_b is the non-diffusing background concentration.

3. Experimental Details

A single crystal of n -type conductivity and 40 ohm-cm resistivity was used as the starting material. Slices cut parallel to the (111) plane were lapped flat and polished mechanically. The slices were thermally oxidized in wet oxygen at 1100°C to form an oxide thickness of about 0.5 microns on the surface. This surface oxide was stripped in HF to remove the surface damages caused by lapping and polishing. Some of the slices so freed from surface damages were reoxidized at the same temperature for different times to form oxide thicknesses ranging from 0.5 to 1.00 microns. Both oxidized and bare slices along with a dot of 5N pure elemental gallium were sealed in a quartz capsule, evacuated to about 10^{-6} mm of Hg pressure. The quantity of gallium was sufficient to establish a saturated vapour pressure of about 10^{-3} mm of Hg inside the capsule at the temperature of diffusion. Diffusions were carried out at 1100°C for 10 minutes.

Attempts were made to determine the junction depth both by angle lapping and grooving followed by chemical staining. It was, however, found as reported by Wagner and Povilonis (1974) that the edges of the stain were too diffused to yield any reliable results. So, these techniques were abandoned in favour of anodic sectioning of the diffused wafers. For this purpose anodic oxidation of the diffused wafers were carried out at constant voltages in an anodization cell made of perspex (Jain *et al*). The forming solution was ethyleneglycol + 0.04(N) KNO_3 . To evaluate the thickness of oxide formed at a particular impressed voltage, the cell is calibrated in terms of oxide thickness formed vs. the impressed voltage. The method of oxide thickness determination at a particular impressed voltage is as follows:—the wafer is introduced in the cell and a fixed voltage less than the maximum forming voltage (which for this particular solution is found to be 380 V) is impressed across the cell. The slice is withdrawn only after the current through the cell falls down below a predetermined minimum value, say, 2 mA as in our case. The slice is then thoroughly cleaned, and the oxide colour is compared with a standard interference colour chart. By this technique the accuracy obtained in oxide thickness determination is about $\pm 100 \text{ \AA}$. A calibration curve for oxide thickness vs impressed voltage is plotted (figure 1). For our set up, an increase of 1 volt in impressed voltage gave an increment of about 6 \AA in oxide thickness. The calibration curve so established is used for evaluating the diffused wafers.

**Figure 1**

Once the diffused wafer is anodized at a particular voltage, the oxide thickness is found from the calibration curve and then the oxide is stripped in HF. The thickness of silicon layer removed in each anodization step is only a fraction of the total oxide thickness. We have found this fraction to be 0.36 by taking the density of the anodic oxide as 1.8 gm cm^{-3} (Wolf 1969). The sheet conductivity after each step is found with the help of a four point probe. The type is also noted by a hot-probe type tester. As the junction is approached (indicated by the rectifying actions shown in the four-point probe readings) the sectioning is done at lower voltages in order to remove silicon layers of smaller thickness. In this way the junction can be detected with an accuracy of $\pm 50 \text{ \AA}$.

4. Results and discussion

The variation of sheet conductivity with depth is given in figure 2. From these curves the doping profiles are plotted for both oxide covered and bare silicon. These are shown in figure 3. It has been found that for different oxide thicknesses, the doping profiles are identical. Therefore, the curve for only one oxide

thickness viz., 0.7 micron is shown. As shown in figure 3, the surface concentration for the oxide covered slice is $1.4 \times 10^{19} \text{ cm}^{-3}$ and that for the bare one is $1.8 \times 10^{19} \text{ cm}^{-3}$. This result is in conformity with the findings of Nakajima and Ohkawa (1972) that the surface concentration is higher for bare silicon than for the oxide covered one. The marginal reduction in the surface concentration

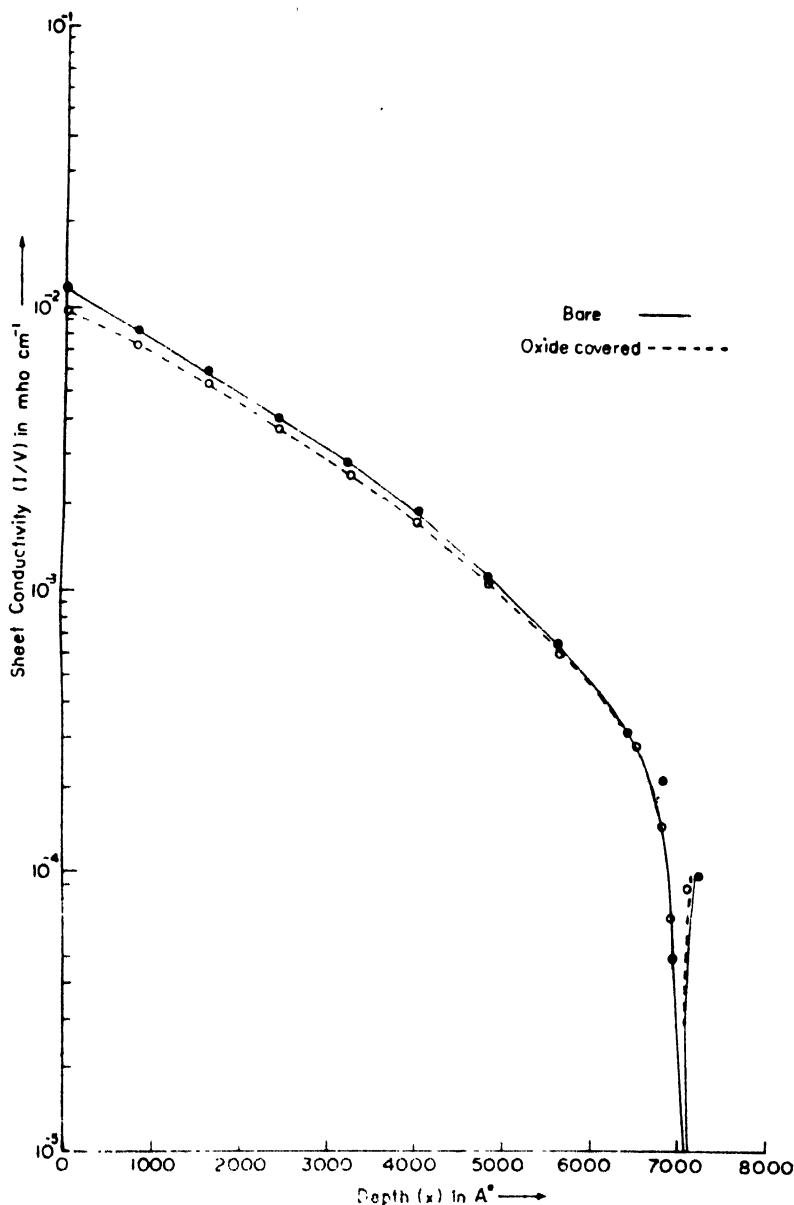
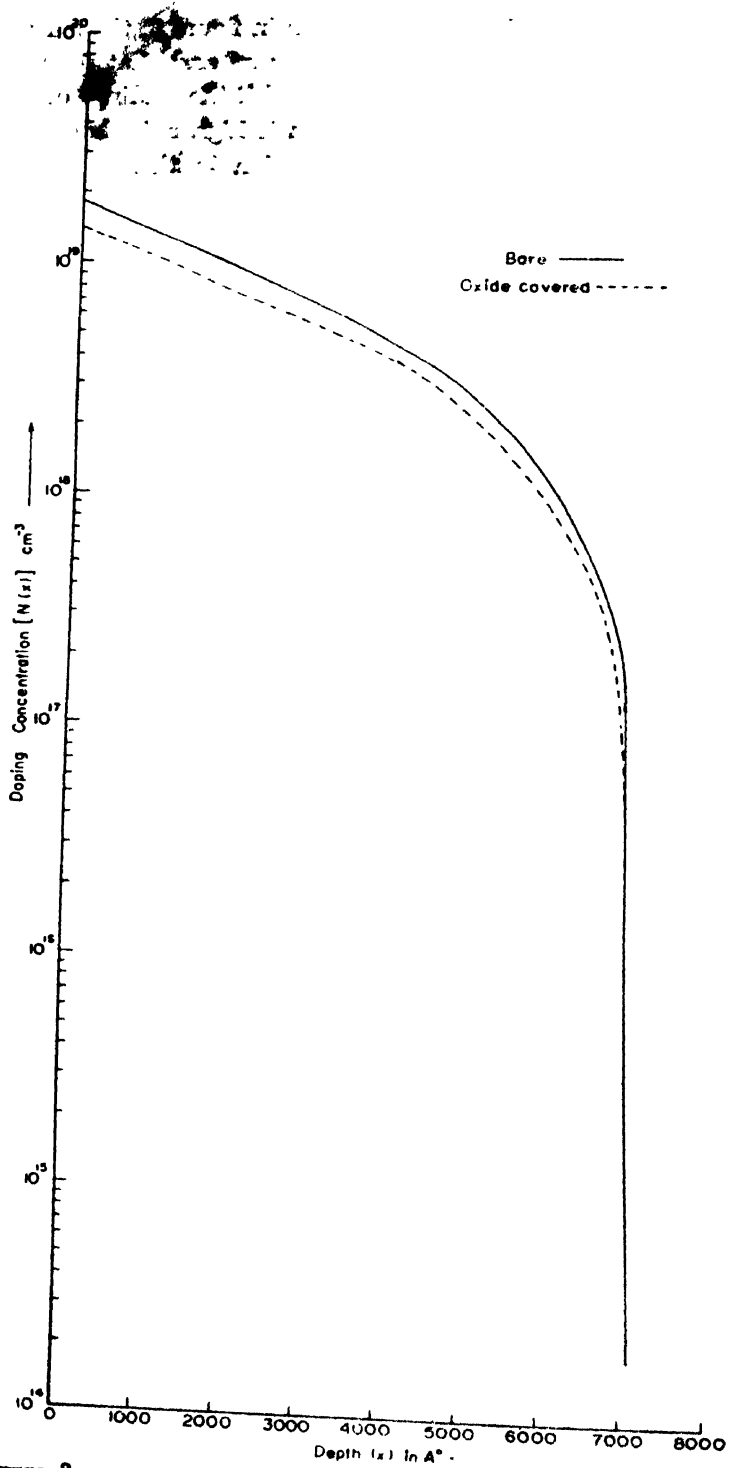


Figure 2

**Figure 8**

could be due to reduction of the effective gallium vapour pressure at the silicon dioxide/silicon interface.

The junction depth for both bare and oxide covered silicon is found to be 7080 Å. This shows that as far as the junction depth is concerned the effect of the oxide is nil at 1100°C. This is apparently at variance with the findings

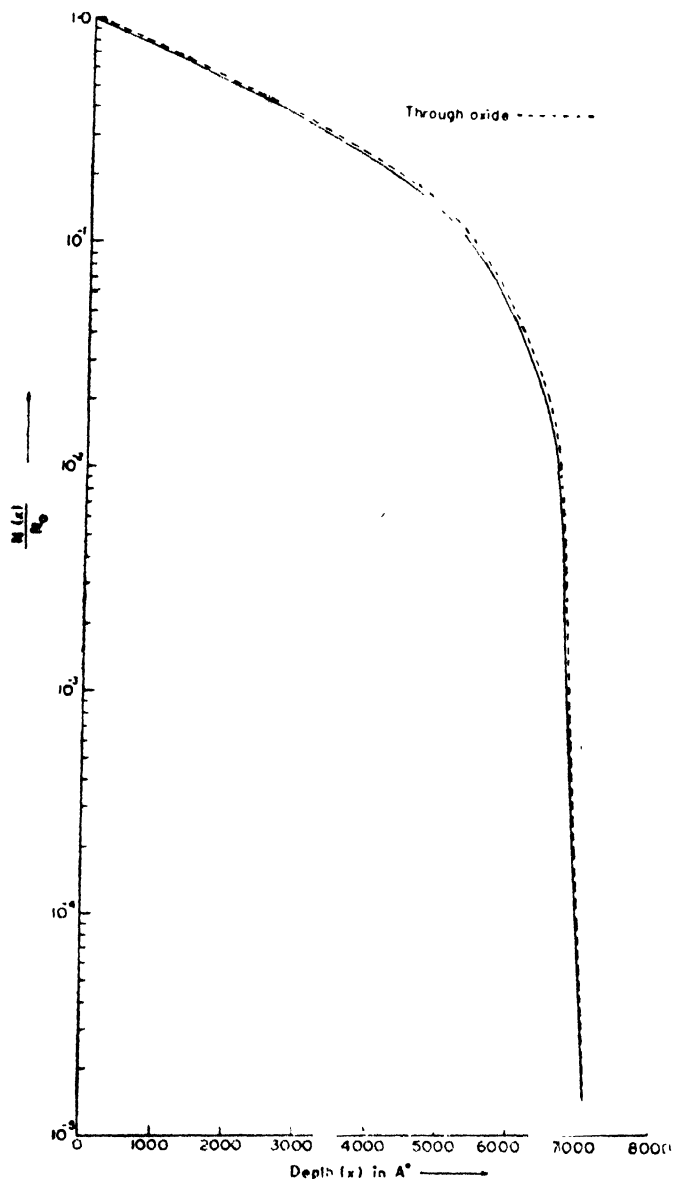


Figure 4

of Nakajima and Ohkawa (1972) that at 1000°C, the junction depth is enhanced by the presence of oxide. An enhancement in the junction depth would imply an increase in the diffusion coefficient and consequent decrease in the activation energy. In order to explain these apparently contradictory results we propose a tentative physical model whereby the silicon dioxide/silicon interface is strained which causes lowering of the crystal potentials and so also the activation energy. However, at higher temperatures these strains are relieved due to changes in the oxide structure and so the activation energy is unchanged. The diffusion coefficient of gallium in silicon at 1100°C is calculated by using equation (5) and is found to be $2.10 \times 10^{-13} \text{ cm}^2 \text{ sec}^{-1}$ for oxide covered silicon and $2.06 \times 10^{-13} \text{ cm}^2 \text{ sec}^{-1}$ for the bare slice. As expected, the diffusion coefficients do not show any significant variation.

The normalized profiles for diffusion into bare silicon and into silicon through silicon dioxide are shown in figure 4. They are almost superimposed. This shows that there is no difference in the shape of the doping profiles of the two diffusions and so both of them follow the same mathematical profile.

5. Conclusions

- (1) The surface concentrations at 1100°C are $1.4 \times 10^{19} \text{ cm}^{-3}$ for oxide covered silicon and $1.8 \times 10^{19} \text{ cm}^{-3}$ for bare silicon.
- (2) The junction depth for both oxide covered and bare silicon is 7080 Å.
- (3) Variation in the oxide thickness does not cause variation in the junction depth.
- (4) The shapes of doping profiles are the same for both oxide covered and bare silicon.

References

- Ghezzi M and Brown D M 1973 *J. Electrochem. Soc.* **120** 146
 Wagner S and Povelonis E I 1974 *J. Electrochem. Soc.* **121** 1487
 Grove A S, Leistiko O Jr and Sah C T 1964 *J. Phys. Chem. Solids* **25** 985
 Nakajima Y and Ohkawa S 1972 *Japan J. Appl. Phys.* **11** 1742
 Burger R M and Donovan R P 1967 *Fundamentals of Silicon Integrated Device Technology*
 Vol 1 Prentice-Hall Inc. Englewood Cliffs NJ
 Jain G C, Prasad A and Chakravarty B C 1979 *J. Electrochem. Soc.* **126** 88
 Wolf H F 1969 *Silicon Semiconductor Data* Pergamon Press

TSD study of pyrene picrate charge transfer complex

A P Srivastava and O N Mathur

Solid State Physics Laboratory, Saugar University, Saugar (M P.).

1. Introduction

Thermally stimulated discharge (TSD) technique, is now being extensively used to understand low frequency dielectric relaxation mechanism in large number of semi-insulators (Van Turnhout 1975). Some workers have used it to analyse electret mechanism in some materials (Jain *et al* 1973, Pillai *et al* 1972, Gross *et al* 1975, Sessler and West 1976). In this paper we describe the results of TSD study of 1 : 1 charge transfer (CT) complex of Pyrene and picric acid. The composition, purity and CT interaction in Pyrene picrate CT complex have been established by elemental, X-ray analysis and IR and UV spectra respectively (Mathur 1976).

2. Experimental Details

Pyrene obtained from M/S Fluka Switzerland was subjected to large number of zone refining runs in a specially designed zone refining unit (Saraf and Srivastava 1976), till a colourless zone was separated. This achieved the removal of tetracene an impurity difficult to remove by usual chemical techniques (Rose and Rose 1961). The melting point of zone refined Pyrene was found to lie in the range of 150.3 to 150.5°C, which agreed well with that reported for pure pyrene (Weast *et al* 1964). Picric acid was purified by repeated crystallisation from its solution in the mixture of 1 : 2 ethanol and water. The melting point of thus purified picric acid was checked and found to be 120°C. 30 gms of zone refined pyrene was dissolved in 400 ml of 1 : 1 mixture of benzene and alcohol and filtered hot in a flask. 37.5 gms of picric acid was dissolved in the same solvent and filtered in the same flask, which was heated till a clear solution resulted. Pyrene picrate got precipitated as a red solid mass on cooling the solution to room temperature. Pyrene picrate was further purified by repeated crystallisation from its solution. The needle shaped crystals, thus obtained were washed with ethanol to remove excess of picric acid.

The sample of pyrene picrate was got analysed in microanalytical laboratory of I.I.T., Kanpur and experimental values of the percentage of the various elements compared well with those obtained from its empirical formula $C_{16}H_{10}C_6H_3(NO_2)_3OH$. The purity of the pyrene picrate was checked by record-

ing its IR spectra (Mathur 1976). UV spectra showed an intense charge transfer band at 3390 \AA , while d values obtained from X-ray diffraction, when compared with those reported for pyrene (Kommandeur and Hall 1961) showed the shift of the electron cloud of the donor towards the acceptor.

The crystals of pyrene picrate were pressed into a circular discs of uniform thickness of 1 mm by subjecting them to a pressure of 5000 kg/cm^2 , in a specially designed, ultrasonically cleaned die. The discs were, then, polarised in an electrode assembly (Srivastava and Singh 1972) at different temperature under different fields. To do this, the electrode assembly was kept for four hours at the desired temperature in a precalibrated thermostat. The temperature of the sample was recorded with the help of the thermocouple whose one end was placed in contact with the electrode assembly. The electric field was applied to the sample for four hours at the desired constantly maintained temperature with the help of Keithley model 246 power supply. The electrode assembly and the sample were allowed to cool with the field applied to room temperature. As soon as the sample attained the room temperature the field was switched off and the electrodes were kept short circuited for 12 hours. The sample thus polarised was then short circuited through Keithley 600 B electrometer amplifier. The temperature of the sample was then raised at the constant rate and the value of TSD current was noted after every two minutes in the beginning and then after every five minutes till the sample was completely depolarised.

The samples were polarised at 75 , 80 and 85°C under the polarising fields of 12, 14, 16 and 18 kV/cm .

3. Results and Discussion

TSD thermograms of samples polarised at 85°C and at fields varying from 12 to 18 kV/cm are shown in figure 1. All the curves are characterised by two peaks. The position of peaks seem to be independent of the polarising field. From the shape of the curves, it appears that they are formed by the superposition of the two curves, one extending from $t = 0$ to about $t = 20$ mts and the other slightly less than 20 minutes to the rest of the value of t . The activation energies for the two processes were calculated by plotting $\log J$ vs. $1/T$ (figure 2) and using initial rise method (Garlick and Gibson 1948). The procedure of least squares was adopted to calculate the slopes. The values of activation energies were found to be 0.66 eV and 1.78 eV for the first and second peaks respectively for all the TSD curves. A linear relation between peak current and polarising field was observed for both the peaks as shown in figure 3. The current maxima for the first peak occurs at lower temperature when the heating rate is reduced. The intensity of the peak seems to be lowered down by about the same factor which is the ratio of inverse heating rates. This seems

to agree with the theoretical prediction of Mc Crum *et al* (1967) that first peak is due to bulk polarisation. The low value of activation energy of 0.66 eV for the first peak does not find favour with dipolar mechanism. The activation energy (0.66 eV) is surprisingly the same as found by electrical conductivity-temperature dependence of polycrystalline and single crystal pyrene picrate (Srivastava and Mathur). Pyrene picrate is a weak CT complex as shown by the order of electrical conductivity (10^{-12} – $10^{-13} \Omega^{-1} \text{cm}^{-1}$) and UV spectra

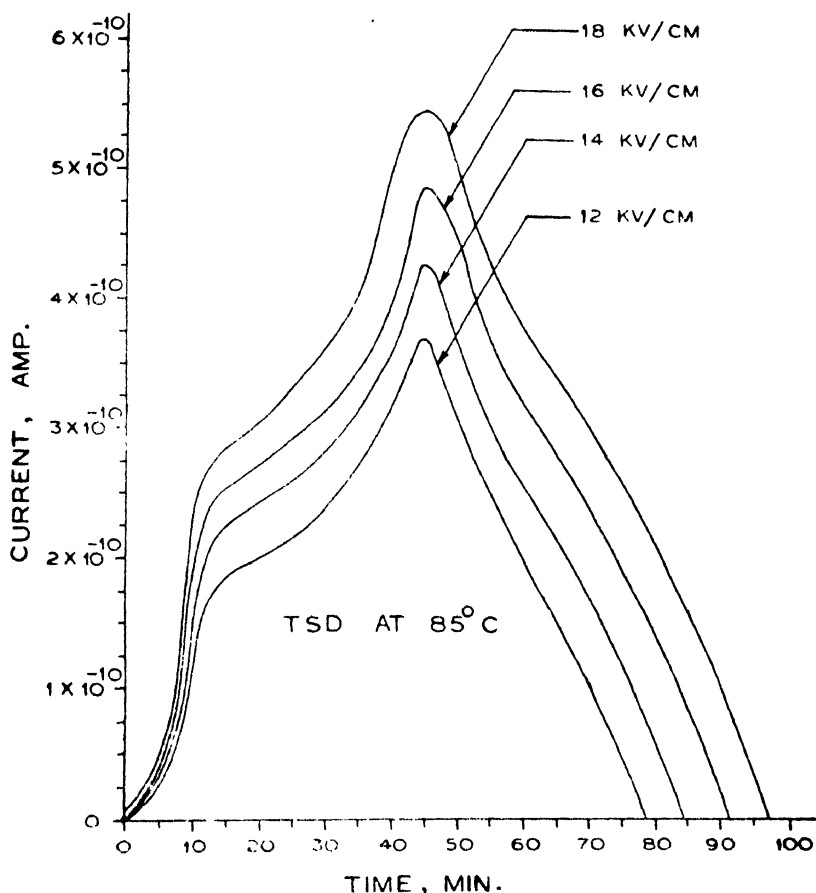


Figure 1. TSD thermograms of 1:1 Pyrene picrate CT complex polarised at 85°C at fields ranging from 12 to 18 kV/cm.

(Mathur 1976). It has been reported in the literature (Gutmann 1969) that charge transfer in a weak CT complex occurs through sterically favourable alignment between donor and acceptor neighbouring molecules. Such alignment would occur by a process of hindered rotation of molecules carrying induced

ionic effect giving rise to uniform polarisation analogous to dipolar mechanism. Such an induced ionic effect is connected with electronic mechanism because of trapping of charges by neutral molecules. This seems to account for low activation energy for the first process.

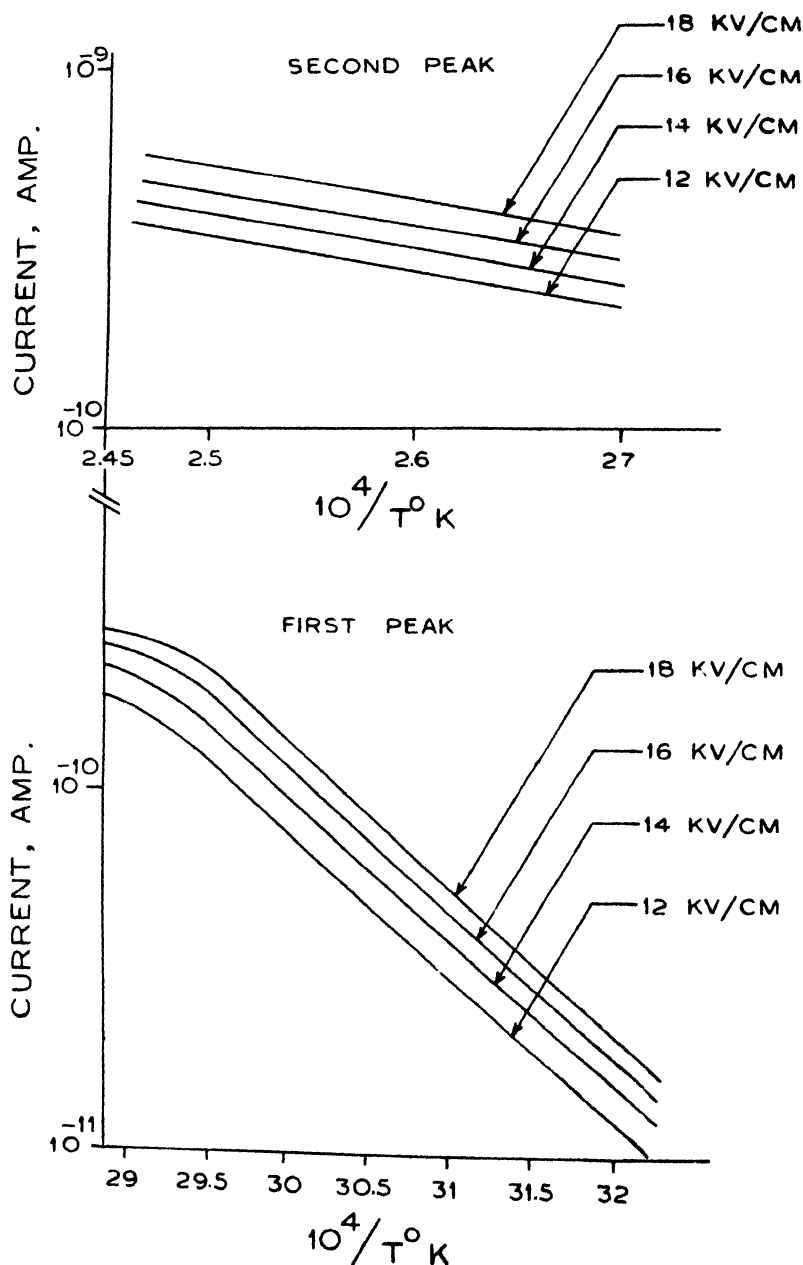


Figure 2. Garlick and Gibson plots for both the peaks ($\log J$ Vs. $10^4/T$).

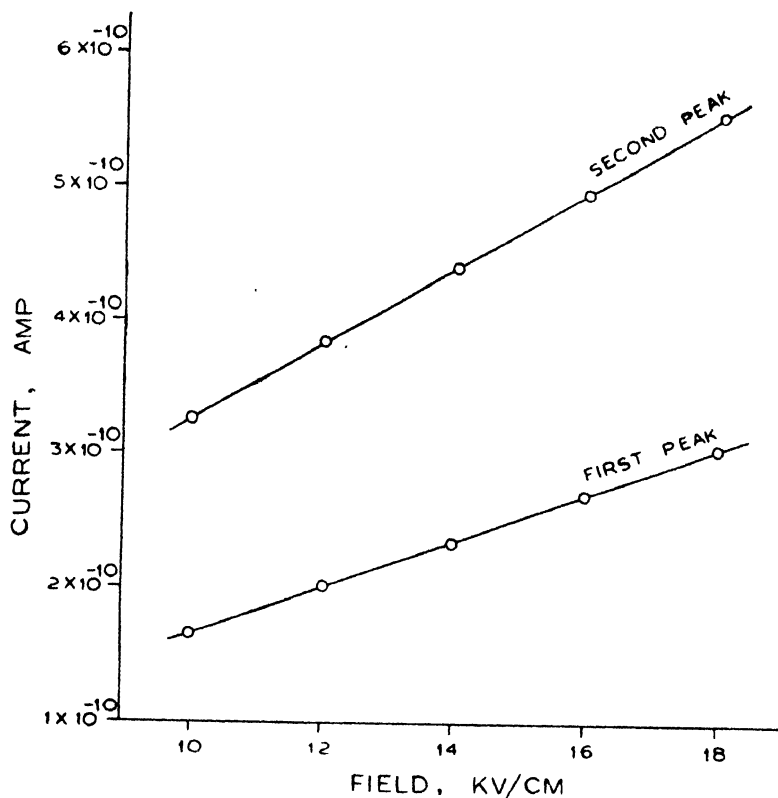


Figure 3. Plots of peak current Vs. polarisation field for both the peaks for samples polarised at 85°C.

The second peak may be due to Maxwell-Wagner charging as has been reported for many material studied in the pellet form (Van Turnhout 1975). The value of activation energy 1.78 eV and amount of charge released (1.0 to $4.0 \mu\text{C}/\text{cm}^2$) agree well with those calculated from theoretical models (Van Turnhout 1975) for M-W process.

Acknowledgment

The authors are thankful to Prof. J. D. Ranade, Prof. and Head of the Physics Department, Saugar University, Saugar for providing facilities for experimental work.

References

- Van Turnhout J 1975 *Thermally stimulated discharge of polymer electrets* (Elsevier Scientific Pub Co New York)
- Jain K, Rastogi A C and Chopra K L 1973 *Phys. Stat. Sol. (a)* **20** 167
- Pillai P K C, Jain K and Jain V K 1972 *Physics Letters A39* 315

- Gross R, Sessler G M and West J E 1975 *J. Ap. Phys.* **46** 4674
- Sessler G M and West J E 1976 *J. App. Phys.* **47** 3480
- Mathur O N 1976 *Studies in Electric and Photo-conduction mechanism of organic molecular crystals of Pyrene picrate with special reference to persistent internal polarisation effect—* Ph.D. Thesis, APS University, Rewa
- Saraf K K and Srivastava A P 1976 *Indian J. Tech.* **14** 337
- Rose A and Rose E (Eds) 1961 *Condensed Chemical Dictionary* Reinhold p 797
- Weast R C, Selby S N and Hodgman C D (Eds) 1964 *Hand Book of Chemistry and Physics* p C 517 (Chemical Rubber Co Ohio)
- Kommandour J and Hall P R 1961 *J. Chem. Phys.* **34** 129
- Srivastava A P and Singh R 1972 *Indian J. Pure and Appl. Phys.* **10** 286
- Garlick C F J and Gibson A F 1948 *Proc. Phys. Soc* **60** 574
- Mc Crum N G, Read B E and Williams G 1967 *An elastic and dielectric effects in polymeric solids* (Wiley & Sons)
- Srivastava A P and Mathur O N *Communicated to Indian Journal of Pure and Applied Physics*
- Gutinann F 1969 *Japan J. Appl. Phys.* **8** 1417

Effect of dielectric screening on the LO phonons in SnTe

K Ramachandran and T M Haridasan

Physics Department, Madurai University, Madurai-625021

1. Introduction

SnTe has a simple structure of the rocksalt in its paraelectric phase. Several investigations have been made in the past on the possibility of ferroelectric transitions in this crystal. It is found (Watari and Malsubatra 1975) that the transition temperature very much depends on the charge carrier concentration p in this semiconducting crystal. Recent Raman scattering experiment (Brillson *et al* 1974) revealed that the transition can be anywhere between 4° and 14°K for a $p = 2.0 \times 10^{20}/\text{cm}^3$. Investigations were also carried out on the mixed system of GeTe and SnTe (Bierly *et al* 1963), and it was found that the transition temperature is also a function of the composition of mixing. Apart from the 'soft mode phonon' in SnTe the interest from the point of view of lattice dynamics in the crystal comes from the LO phonon dispersion. The dispersion relations (ω versus q) was measured by Pawley *et al* (1966) on the narrow band gap semiconductor SnTe in [100] direction. Similar to the earlier observation on SnTe they found an abrupt decrease of LO phonons as $q \rightarrow 0$. This fact and the experimental observations of a peak in the neighbourhood of Brillouin zone in [100] direction were ascribed by them as arising due to this dielectric screening by the charge carriers. Due to the approximate nearness of the frequencies of the plasmons and LO phonons in SnTe, the dielectric screening is quite prominent here as in PbTe. However, no estimate of this screening has been reported so far and in this paper we represent the results of such an estimate on a simple dielectric screening function. The effect of screening on the LO phonons is discussed here on that basis.

2. Method of Calculations

First the lattice dynamics of this crystal in paraelectric phase was attempted on the basis of a shell model, the parameters of which were fitted from the known reststrahlen frequencies (Brillson *et al* 1974), dielectric constants and compressibilities (Hausch *et al* 1968). Only the nearest neighbour short range interaction is assumed in the calculations.

For estimating the corrections to LO phonons due to screening as in PbTe we used the relation

$$\omega^2(q) = \omega_T^2 + \frac{(\omega_L^2 - \omega_T^2)}{\epsilon(q, \omega)}$$

where ω_T and ω_L are the respective transverse and longitudinal phonon frequencies and $\omega(q)$ is the corrected phonon corresponding to the screened longitudinal phonon. In the absence of detailed knowledge of the band structure, one can adequately use the Thomas Fermi dielectric function its simplest form

$$\epsilon(q, 0) = 1 + \frac{k_s^2}{q^2}$$

for very small values of $q (q \ll k_s)$ since $\omega_{\text{plasmon}} \gg \omega_{\text{lattice}}$. However when $\omega_L \gg k_s$, the LO modes go to ω_L and hence the dispersion relation for the LO modes shows a marked decrease in frequency as q decreases.

The Thomas-Fermi dielectric function is given by

$$\epsilon(q, 0) = 1 + \frac{k_s^2}{q^2} \left[0.5 + \frac{k_F}{2q} \left(1 - \frac{q^2}{4k_F^2} \right) \log \left(\frac{q+2k_F}{q-2k_F} \right) \right]$$

where the screening radius $k_s^2 = 4\pi n e^2 / (2/3) E_F$ can be calculated from the charge concentration n and Fermi energy E_F . Fermi energy and k_F (Fermi radius) can be calculated from the n value which is obtained from the Hall effect measurements (Ziman 1965).

Since Pawley *et al* (1966) have not reported the n values of their sample used for measurement, we have estimated $\epsilon(q, 0)$ for two possible concentrations and with then ω_{L0} corrected for screening is evaluated as a function of q in [100] direction.

3. Results and Discussion

The shell model used could reproduce fairly the TO phonon dispersion. Thus the lattice dynamical model is thought to be adequately satisfactory. The LO phonons corrected for dielectric screening as a function of q is plotted in figure 1 along with the experimental results. It is found that the curve for $n = 2.45 \times 10^{17} \text{ cm}^{-3}$ lies much above the experimental curve, whereas for $n = 1.3 \times 10^{20} \text{ cm}^{-3}$ lies just above. In the absence of exact n value of the experimental sample of Pawley *et al*, we are unable to make an exact comparison. However, we find both qualitative features namely, (1) the abrupt fall of LO phonon near $q = 0$, (2) the peak of LO for small q value followed by a flat region, (3) relatively negligible screening of LO phonon for large q value.

Work is in progress of estimation of many of the interesting physical properties of the crystal using this model.

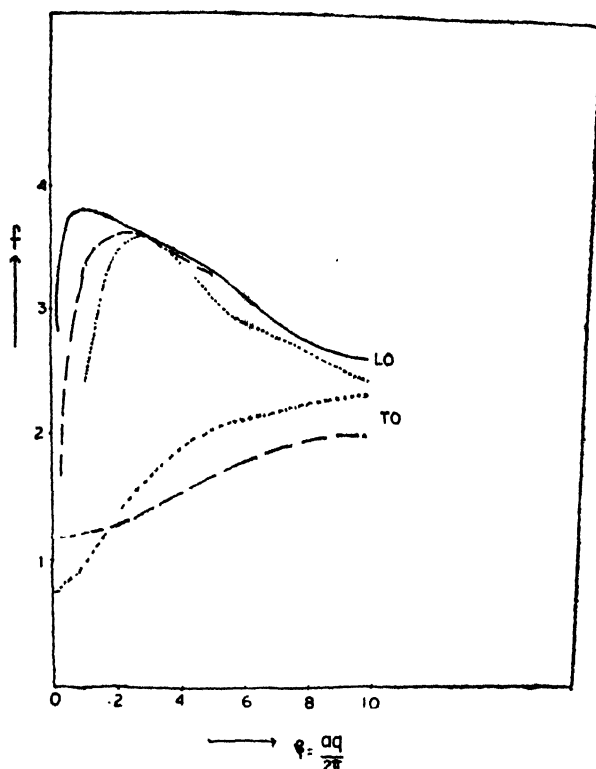


Figure 1.
Dispersion Relation of SnTe along (100). f in 10^{12} CPS
 ————— $n = 2.45 \times 10^{17} \text{ cm}^{-3}$
 - - - - - $n = 1.30 \times 10^{20} \text{ cm}^{-3}$
 Experimental observations

Acknowledgment

We thank Prof. K. S. Chandrasekaran for his encouragement.

References

- Wadari S and Mabsubatra T 1975 *Prog. Theo. Phys.* **53** 1214
 Brillson L J, Burstein E and Muldawer 1974 *Phys. Rev.* **B9** 547
 Bierly J N, Muldawer L and Beckman O 1963 *Acta. Met.* **11** 447
 Pawley G S, Cochran W, Cowley R A and Dolling G 1966 *Phys. Rev. Letters* **17** 753
 Cowley R A and Dolling G 1965 *Phys. Rev. Letters* **14** 549
 Kawamura H, Murase K, Nishikawa S, Nishi S and Katayama S 1975 *Solid State Commun.* **17** 341
 Hausch G, Sanger M G and Lushes E 1968 *Z. Ang. Phys.* **25** 251
 Ziman J M 1965 *Introduction to principle of the theory of solids* (Cambridge University Press)

Impurity diffusion in bismuth single crystals

N. K. Misra and V. S. Venkatasubramanian

Department of Physics, Indian Institute of Science, Bangalore-560012.

Non-Fickian types of diffusion have attracted some interest (Petroplous & Roussis 1967) and typical of such phenomena is diffusion (both self and impurity modes) in bismuth crystals. Here, one obtains profiles of limited penetration in which the tracer concentration exhibits an exponential dependence on depth and an essential independence on the time of anneal. These features cannot be explained on the basis of a Fischer (1951) type analysis based on grain boundary diffusion, or dislocation (pipe) diffusion. Ellis & Nachtrieb (1969) have correlated their data on the tracer penetration with the presence of mechanical twins in which the diffusing species undergoes kinetic trapping. It would be desirable to have further measurements to corroborate this behaviour and possibly help to elucidate the nature of the trapping process. In the present paper, we describe the measurements of impurity diffusion of ^{86}Rb , ^{90}Sr , ^{133}Ba and ^{137}Cs in single crystals of bismuth, and interpret the results on the basis of considerations outlined above.

Single crystals of three nines purity bismuth were prepared by the Bridgman method. The central portion of the ingot was analysed by spark source mass spectrometry and the total impurity content was less than 50 ppm. The crystals were oriented by X-ray methods, cut and polished first mechanically etched, and then annealed and reched. Our work confirms the observation of Ellis & Nachtrieb that although great care is taken in surface preparation it is impossible to eliminate the mechanical twins and retain the necessary flatness.

The preparation of the diffusion samples was carried out by an ion-implantation technique. The ion implantation set-up consists of an ion source, a Wien filter and a post acceleration chamber where the mass separated ions from the Wien filter could be accelerated upto 50 kV. A surface ionization source was employed. About 10^{12} – 10^{13} ions were implanted resulting in surface activities $\sim 10^4$ cpm. (The range of 40 KeV Sr^{90} ions in Bi is ~ 200 Å). After implantation, the samples were annealed in a furnace at temperatures in the range (220°–265°C) with a temperature control of $\pm 0.5^\circ\text{C}$, for specified times of anneal. After the diffusion anneal, tracer penetration profiles were determined by the electrolytic method of (Styris & Tomizuka 1963, McTeggart 1956, Morrison & Blackburn 1966), layers of known thickness being removed and residual activities being

measured. Cathodic etching of the substrate crystals was also carried out in the post-acceleration chamber in a number of cases.

A typical penetration profile is shown in Figure 1. (Cs^{137} in Bi). The plot of ($\log C$) vs x is linear in contradiction with Fick's Law for volume diffusion that predicts a linear variation of ($\log C$) with x^2 for a "thin" source. Nor are the laws of grain boundary diffusion obeyed as the profiles are independent of the time of anneal, as also of crystal orientation, and temperature within the range studied. The order of magnitude of the penetration distances is also far less than that on a grain boundary mechanism such as prevails in polycrystalline samples—a point that has been verified for self-diffusion (Ellis & Nachtrieb 1969). It would thus appear reasonable following Ellis & Nachtrieb (1969) to interpret the results in terms of a modified Fischer analysis using a kinetic trapping term as summarized below :

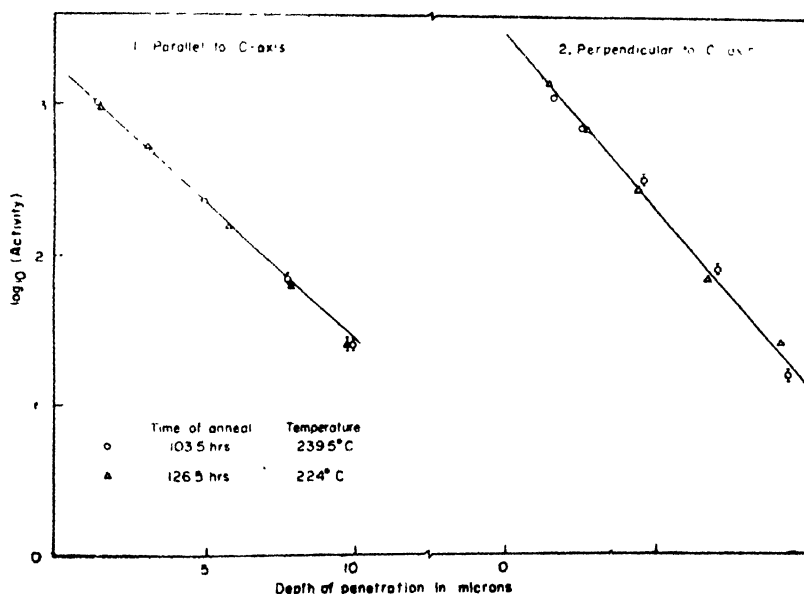


Figure 3. Penetration profiles for diffusion of Cs in Bismuth.

The modified diffusion equation

$$\partial C / \partial t = D'(\partial^2 C / \partial y^2) - kC$$

has a thin-layer solution,

$$C_m = \frac{s}{\sqrt{\pi D' t}} e^{-y^2 / 4 D' t} e^{-kC}$$

so that the concentration of trapped material,

$$C_t(y, t) = \int_0^t k C_m(y, t) dt$$

If the values of D' and k are such that the tracer concentration is immobilized at the value corresponding to $t = \infty$,

$$C_t(y, \infty) = \int_0^{\infty} \frac{ks}{\sqrt{\pi D'}} e^{-y^2/4D't} e^{-kt} t^{-1/2} dt$$

$$= s\sqrt{k/D'} e^{-y^2/4D'}$$

This yields a profile, independent of time, whose slope yields $y_1 = \ln 2/\sqrt{k/D'}$ = effective half-length for trapping at a twin boundary, i.e., the migration length for which the effective probability of trapping is 0.5. The table below gives y_1 for ^{86}Rb , ^{90}Sr , ^{133}Ba , and ^{137}Cs .

Table

Element	^{86}Rb	^{90}Sr	^{133}Ba	^{137}Cs	^{210}Bi (self-diffn.)
$y_1 (\times 10^{-4} \text{ cm})$	1.0	0.6	0.71	1.2	0.85

The general agreement of these values with those reported by Ellis & Nachtrieb (1969) and the reproducibility of the non-Fickian diffusion profiles suggests that this peculiar feature is associated with diffusion in Bi crystals that essentially proceeds via grain boundaries with kinetic trapping and release.

References

- Potropolous J. H. & Roussis P. P. 1967 *J. Chem. Phys.* **47**, 1491.
 Fisher J. C. 1951 *J. Appl. Phys.* **22**, 74.
 Ellis W. P. & Nachtrieb N. H. 1969 *J. Appl. Phys.* **40**, 472.
 Styris D. L. & Tomizuka C. H. 1963 *J. Appl. Phys.* **34**, 1001.
 McTeggart W. J. 1956 *Electrolytic and Chemical Polishing of Metals* (Pergamon)
 Morrison H. M. & Blackburn D. A. 1966 *J. Sci. Instrum.* **43**, 655.

Spontaneous current emission (SCE) from metal-polymer-metal systems

S. Radhakrishna and S. Haridoss

Department of Physics, Indian Institute of Technology, Madras-600036.

Abstract. A spontaneous current has been observed when a metal-polymer-metal structure is heated. Polymers studied include poly ethylene (PE), poly vinyl chloride (PVC), polystyrene (PS) and polytetra fluoro ethylene (PTFE) of which the studies on PVC are discussed in detail. Apart from the short-circuit current, open-circuit voltage across the metal-polymer-metal system has also been recorded and the use of such a structure as a dry cell has been discussed. In the light of the experimental results, the various possibilities that can account for such a phenomenon are explained.

1. Introduction

Extensive studies on polymers using thermally stimulated currents (TSC) have been made, because of the relevance of dielectric studies on molecular mobilities and relaxation times, which are often of direct concern in mechanical behaviour. A background current from the virgin polymer sample in a TSC measurement has always been observed in many cases (Barnes *et al* 1969, Ramican & Fleming 1972). Recently spontaneous currents from poly ethylene tetrathalate (PET) are reported (Ieda *et al* 1975). While studying TSC in poly vinyl chloride (PVC), we have observed a spontaneous current above 310°K even from an unpolarised sample. In this paper we present the results of systematic investigations made on PVC in comparison to those on poly ethylene (PE), poly styrene (PS) and poly tetra fluoro ethylene (PTFE).

2. Experimental

PVC resins supplied by Chemplast, India were used in the experiments. These were made into discs of diameter 1.3 cm and thickness 0.5 mm. Electrodes were prepared by evaporative coating of the different metals over the polymer thin specimens. The current and voltage measurements were made by placing the sample in a chamber whose temperature can be increased at a linear rate. Keithley 610 C electrometer was used for all the measurements. The temperature was monitored using an iron-constantan thermocouple.

3. Results and discussions

The short-circuit currents measured for different electrode systems are shown in Figure. 1. The sign of the current was different for different samples and the

magnitude also varied from sample to sample for the same electrode system. In the case of Zn-PVC-Zn and Ag-PVC-Ag there was a reversal of the sign of the current. However in all the metal-PVC-metal systems studied, the general features observed are :

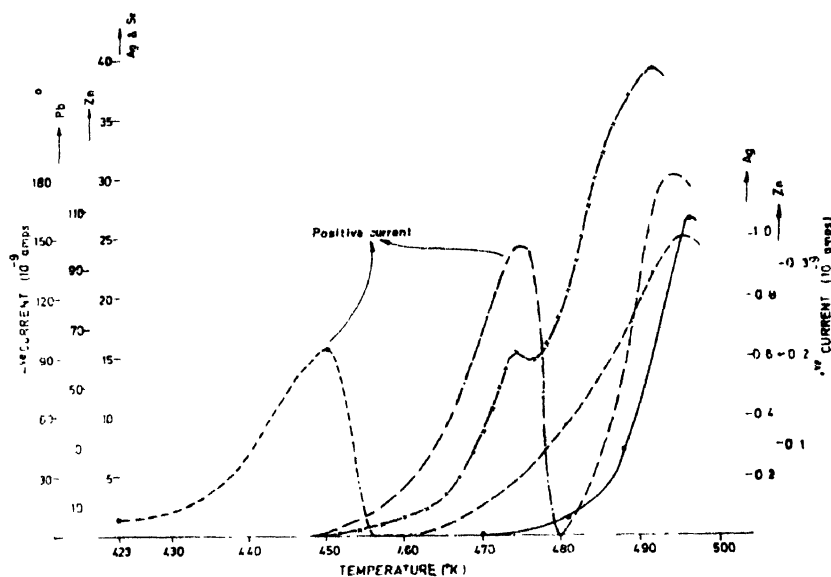


Figure 1. Electrodes' performance : S.C.E. in metal-PVC-metal systems
 - - - - Ag, - · - · - Zn, - × - × - Sn, ——— Pb.

- (1) initial increase of the current is from 290°C – 310°K with a little change from sample to sample;
- (2) the current reaches a maximum value at 493°K the peak position is almost the same for all the systems and it is independent of heating rate;
- (3) there is no change in the observations when the experiment is done in nitrogen atmosphere;
- (4) the current magnitude increases from about 10^{-12} at RT to 10^{-7} amp at 490°K ;
- (5) the phenomenon is not reversible; on cooling the system at the same rate no current is recorded. Also the thermal treatment of the sample broadens the peak slightly;
- (6) an open-circuit voltage of ~ 0.4 – 0.6 V is obtained; this corresponds to the maximum value at 493°K ;
- (7) the activation energy of the short circuit current varies from 2.0 eV to 3.7 eV.

In order to check that this spontaneous current emission is not due to impurities present in the specific sample, experiments were done on samples of various grades and on commercially available PVC sheets also. In all these cases the same features were observed. Similar studies on PS, PE, PTFE, which belong to the polyolefine series, show that there is an abrupt increase in current for PS and PE very near to their melting temperatures; in the case of PTFE no such current was observed in the region $RT - 500^{\circ}\text{K}$.

Similar currents were observed in metal-PET-metal systems by Ieda *et al* (1975). In this case the variation of the short circuit current was related to the electrical conduction in the bulk of PET; ion species supplied by the oxidation reduction reaction at electrodes were assumed to be responsible for such a phenomenon, though the details of how the reaction takes place were not discussed. The effect of magnetic field on the spontaneous currents from PVC in the temperature range $RT-420^{\circ}\text{K}$ was reported (Deshpande & Khare 1976). No clear cut explanation was given in this case also. Irradiation of polymers with high energy γ -rays was found to produce polarisation (Murphy & Gross 1964) which was treated as space charge resulting from the production and absorption of Compton electrons. In PTFE spontaneous currents were observed by Bucci *et al* (1966) at temperatures lower but closer to room temperature; the process was attributed to the rotation of molecular complexes belonging to the polymer chain. There is yet another instant in the literature where such current peaks were observed. Fresh virgin samples of a thiazine cast slabs yielded spontaneous current curves (Guttman & Keyzer 1969). This was suggested to be due to the presence of micro-regions of glassy material causing persistent interboundary polarisation; however the process was found to be removed by prolonged annealing of the sample at an elevated temperatures.

In the present case, as the currents observed are not reversible they cannot be due to pyroelectricity. Care has been taken to avoid currents due to any possible temperature gradient in the system. As the experiments done in Nitrogen atmosphere did not show any change, the possibility of oxidation reduction reaction at the polymer-metal interface at the elevated temperatures can be ruled out. Also no interboundary polarisation can be expected in the case of PVC. However taking into account the ferroelectric nature of PVC suggested by Reddish (1966), the onset of the motion of the C-Cl molecular dipoles can be thought of as giving rise to a displacement current. As the current peaks are observed at a point where carbonisation of the material takes place one can attribute the phenomenon to the carbonisation process. The orders of the current are too high to be accounted for by contact electrification. Spontaneous increase of currents in the case of PE and PS near their melting points suggests a possibility to think in terms of Costa Ribeiro effect. However no definite conclusion can be drawn about the origin of the currents observed.

The possibility of making use of this phenomenon for the plastics dry cell has been suggested by Ieda *et al* (1975). In the present case, though the open circuit voltage is 0.6 V the temperature region in which this is obtained is not very suitable for making use of metal-PVC-metal system as a dry cell. Because the thermal degradation of PVC will make the life time of such a cell shorter. However search can be made for suitable plastics to be used as dry cells making use of the phenomenon of spontaneous current emission (SCE).

References

- Barnes J. E. Hoeker F. E. & Kovan L. 1969 *Radiation Res.* **40**, 235.
Bucci C., Fieschi R. & Guidi G. 1966 *Phys. Rev.* **148**, 816.
Deshpande G. K. & Khare M. L. 1976 *Ind. J. Pure and Appl. Phys.* **14**, 311.
Gutmann F. & Keyzer H. 1969 *J. Chem. Phys.* **50**, 550.
Ieda M., Sawa G., Nakamury S. & Nishio Y. 1975 *J. Appl. Phys.* **46**, 2796.
Murphy P. V. & Gross B. 1964 *J. Appl. Phys.* **35**, 171.
Ramican & Fleming 1972 *J. Poly. Sci.* **10**, 1979.
Roddish W. 1966 *Polymer Preprints* **6**, 571.

Localized modes due to U-centre pairs in RbCl

S Kalyani and T M Haridasan

Physics Department, Madurai University, Madurai-625021

1. introduction

Three infrared action localized modes have been reported recently by DeSouza *et al* (1970) for U centre pair in RbCl. A theoretical explanation of these modes have already been made by us on the basis of Greens function approach (Kalyani and Haridasan 1976). In that work we have taken the defect space to be consisting of only the two defect atoms and two of their nearest neighbours, each of which happens to be a common neighbour to either of the two defects. This assumption was made for simplifying the problem and to make it manageable on a hand calculator. Physical intuition justifies such a simplification especially for the localized modes since only the defect atoms have displacements for such modes. However, to make the situation more realistic, one should take into account both the defects and all their first neighbours, since the perturbation may normally be carried on to such a defect space. With this in mind, we have estimated the localized modes due to U-centre pairs in RbCl in this enlarged defect space and the results are reported there.

2. Method of calculation

The method of Greens function is employed here and the details of the theory can be seen in the book of Maradudin *et al* (1966). The localized modes can be found by working out the values of the determinant $|I - g(\omega)\delta l(\omega)|$ for different ω values and picking out the ω 's for which this determinant is zero. Here $g(\omega)$ is the matrix constituted by the lattice Greens functions of the host lattice and $\delta l(\omega)$ is the perturbation brought about by the impurities. Since we assume that only nearest neighbours are involved in the perturbation, in this particular case the total number of atoms are 12 in number with two defects and 10 host atoms and the order of matrix is (36×36) . In earlier calculation the defect space was only (12×12) and block diagonalisation of this by group theory yielded (2×2) determinants which could be readily calculated with hand calculations. However in the present case we evaluated the determinant using IBM 370 computer at IIT, Madras.

The coordinates of the atoms in the defect space are given below :

1) (000)(H)	2) ($\bar{1}\bar{1}0$)(H ⁻)	3) (100)	4) ($0\bar{1}0$)
5) ($\bar{1}00$)	6) (010)	7) (001)	8) ($00\bar{1}$)
9) ($2\bar{1}0$)	10) ($1\bar{2}0$)	11) ($1\bar{1}\bar{1}$)	12) ($11\bar{1}$)

in units of r_0 half the lattice constant.

So the relevant independent Greens functions are

$$g(\begin{smallmatrix} 0 & 0 \\ + & + \end{smallmatrix}, \omega), g(\begin{smallmatrix} 0 & 0 \\ - & - \end{smallmatrix}, \omega), g(\begin{smallmatrix} 0100 \\ + & - \end{smallmatrix}, \omega), g(\begin{smallmatrix} 0111 \\ + & - \end{smallmatrix}, \omega), g(\begin{smallmatrix} 0200 \\ + & + \end{smallmatrix}, \omega) \text{ and } g(\begin{smallmatrix} 0200 \\ - & - \end{smallmatrix}, \omega).$$

Since $g(\begin{smallmatrix} 0210 \\ + & - \end{smallmatrix})$ is very small compared to others they have been neglected in the present calculations. All these Greens functions have been taken from the compilations of Haridasan *et al.* They have evaluated those for $\omega/\omega_L = 0.01$ to 3.99 at intervals of 0.02, using eigen value and eigen vectors of Shell model fitted to the experimental phonon curves. ω_L is the maximum frequency of the lattice. Then $\delta l(KK', \omega) = cM\omega^2\delta_{kk'}\delta_{ll'} - \Delta\phi(\begin{smallmatrix} l' \\ kk' \end{smallmatrix})$ where c is the mass defect parameter $\left[\frac{M_u - M_H}{M_u}\right]$, $\delta_{ll'}$ will be nonzero only when $r(l')$ is (000) or ($\bar{1}\bar{1}0$), namely at the two defect sites. $\Delta\phi(\begin{smallmatrix} l' \\ kk' \end{smallmatrix})$ was expressed in terms of change in Kellerman's parameters ΔA and ΔB . No relaxation around the defect is assumed and hence $\Delta B = 0$. Thus, $\delta l(KK', \omega)$ could be expressed in terms of c and ΔA . ΔA was obtained by fitting it to reproduce the U-centre frequency due to single impurity. With this ΔA , the (36 × 36) determinant was evaluated for ω/ω_L values starting from 1.01 to 3.99 IBM 370 computer.

3. Results and discussions

The values of ω/ω_L for which the determinant is zero were picked and ω values corresponding to localized modes were calculated. Due to the fact at these limits of ω/ω_L from 1.01 to 3.99, all the Greens functions are very small, the determinant values themselves were quite small and hence care should be taken in picking out the modes. Values of localized modes so obtained are tabulated below along with similar results from the simpler model of the earlier calculation. The identification of each mode with a ω value to a particular irreducible representation is in principle possibly by working out $g(\omega)\delta l(\omega)$ for that ω value and diagonalising it. The eigen vectors corresponding to eigen value 1 gives the displacement vectors of that mode. However, this is a very time consuming process with diagonalisations of (36 × 36) matrix, at least 6 times. So in the present work this was not attempted, and only a comparison with earlier results was used in determining the representation of the modes.

Localized modes due to U-Centre pairs in RbCl.

Table I

Mode	Model containing		Experiment (freq. in cm^{-1})
	4 nearest neighbours (freq. in cm^{-1})	all nearest neighbours (freq. in cm^{-1})	
B_{1u}	522	461	515
B_{2u}	448	467	482
B_{3u}	391	454	445
A_{1g}	396	457	--
B_{1g}	455	471	--
B_{2g}	522	464	--

The results as can be seen from the table reveals that the present elaborate model is in fact not needed in accounting for the localized modes. Even the over-simplified model with less labour and time achieves this purpose. However for the resonant modes where the host atoms also have displacements, the present model looks to be more appropriate. But a calculation later (Kalyani and Haridasan (1976) by the present authors also indicated that even for resonant modes the earlier model is quite sufficient. Thus one finds that the simplified model of the basis of physical intuition is quite sufficient in the explanation of both localized and resonant modes due to U-centre pairs in alkali halides.

References

- Souza M De, Gongara A D, Algerter M and Luty F 1970 *Phys. Rev. Letters* **25** 1426
 Kalyani S and Haridasan T M 1976 *Chemical Physics Letters* Sept Issue
 Maraduddin A A 1966 (Edited by Seitz) *Solid State Physics* **18** 289
 Haridasan T M, Gupta R K and Ludwig W (unpublished)
 Kalyani S and Haridasan T M 1976 *Paper communicated to Solid State and Nuclear Physics Sympo (DAE) Ahmedabad*

Lattice scattering mechanism in quantized inversion layers in silicon

P K Basu

Centre of Advanced Study in Radio Physics & Electronics, 92, Acharya
Prafulla Chandra Road, Calcutta-700 009

Abstract. When a large bias is applied to the gate of a Metal-oxide-semiconductor-field-effect-transistor, the motion of the carriers in the inversion channel becomes quantized in the direction of the gate field. The lattice scattering mechanism, which limits the mobility of two-dimensional electron gas formed in such layers at high temperature ($> 150^\circ\text{K}$), is the subject of investigation in the present paper. Scattering due to deformation-potential-acoustic phonons is fairly well studied. Less attention has been given to the study of the optical and intervalley phonon scattering mechanism. A review of the work done in this area is first made and the shortcomings of the existing works are discussed. The expression for the relaxation time for scattering by high energy optical phonons of degenerate two-dimensional gas is then derived. The theory is then applied to the study of transport in (100)-oriented silicon surface. The temperatures of the different phonons participating in the intervalley transitions are determined for this purpose. By adjusting the coupling constants of the intervalley and optical phonons the experimental curve showing the dependence of the effective mobility on temperature is reproduced. It is found that using the above coupling constants the dependence of mobility on gate-voltage may be explained quite well.

1. Introduction

An n -type inversion layer is produced at the surface of a p -type semiconductor, when the conduction band at the surface is sufficiently bent to cross the Fermi level (Figure 1). This inversion may be created very conveniently by applying a bias to the gate of a Metal-Oxide-Semiconductor-Field-Effect-Transistor (MOSFET). When the gate bias is strong, the width of the potential well along the direction perpendicular to the surface is small compared to the wavelength of the electrons. The motion of the electrons is thus quantized, but the electrons are free to move in a plane parallel to the surface (Stern and Howard 1967, Stern 1972). The electrons thus form a two-dimensional electron gas (2DEG).

MOSFET's with a Si/SiO₂ system are widely used to study this quantization phenomena. If the silicon surface is (100)-oriented, then the two conduction band valleys along [100]-direction in bulk Si give rise to the two lowest subbands E_0 and E_1 , both of which are two-fold degenerate (Stern and Howard

1967). The next higher subband E_2 is due to four valleys along [010] and [001] directions and is fourfold degenerate with elliptic constant energy contours. The values of E_1 and E_2 are, however, very close to each other (Stern 1972) and in the following discussion we will assume the energy values to be equal. Figures 1 and 2 depict the situation for the (100)-oriented silicon surface

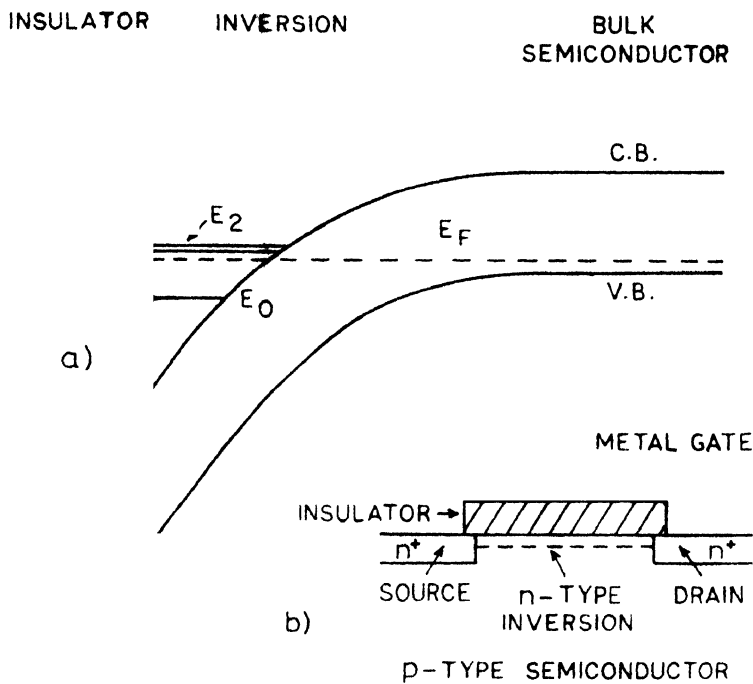


Figure 1. (a) Energy band diagram for the case of strong inversion in a semiconductor. E_F is the Fermi level, E_0 , E_1 and E_2 are the three lowest subbands for a (100)-oriented silicon surface. (b) Schematic metal-insulator semiconductor structure used for inversion layer experiments.

Transport in the 2DEG formed in silicon inversion layers has been studied by many workers (Cheng and Sullivan 1973a, 1973b, 1973c, 1974; Ezawa *et al* 1974; Fang and Fowler 1968, 1970; Sah *et al* 1972; Ning and Sah 1972, 1974). It is generally accepted that phonon scattering in addition to the scattering due to surface roughness and by surface-oxide-charges is the relevant scattering mechanism for the study of transport parameters in the inversion layer (Cheng and Sullivan 1973c). Moreover phonon scattering has been found to be the dominant scattering mechanism at higher temperatures (Sah *et al* 1972).

Scattering involving deformation-potential acoustic phonons in an inversion layer has been studied fairly well by different workers (Ezawa *et al* 1974, Wu and Thomas 1974). This type of scattering predicts a temperature variation

as T^{-1} for the mobility, whereas the experimental curve (Fang and Fowler 1968) follows a $T^{-1.5}$ law. It has been suggested (Sah *et al* 1972) that scattering involving energetic phonons should be included to explain the stronger temperature dependence of mobility. Sah *et al* have obtained the expression for mobility limited by energetic-phonon scattering for a nondegenerate 2DEG. Their theory is not directly applicable for the case of strong inversion in which most of the electrons lie in the lowest subband E_0 , below the Fermi level and obey degenerate statistics. Furthermore, Sah *et al* considered the zone-centre optical phonon only. The inter-subband transition in silicon may however involve other phonons too. Another objection to the work of Sah *et al* (Basu 1976) is that they derived the deformation potential constants for optical phonons by assuming Mathiessen's rule which may lead to considerable error.

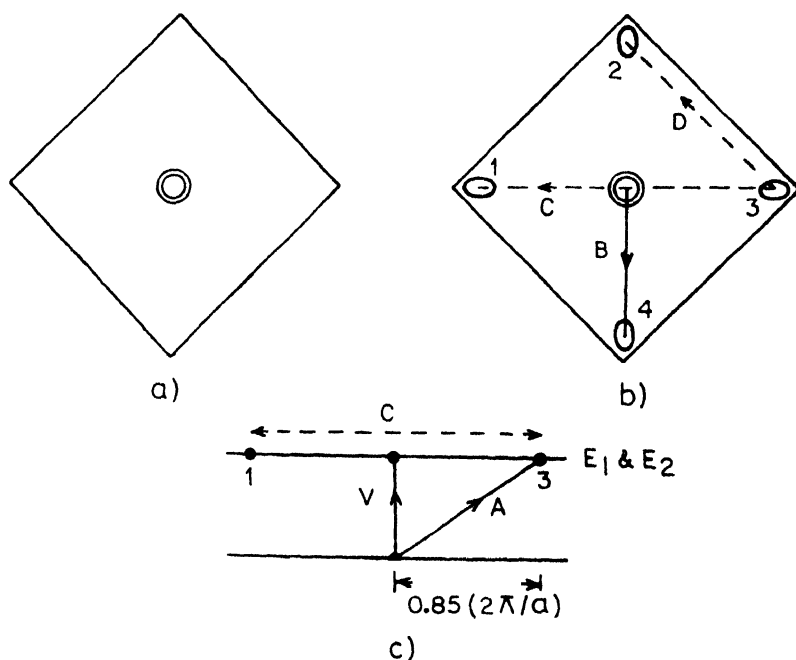


Figure 2. Schematic representation of constant energy contours and Brillouin zones for the (100)-surface of Si: (a) constant energy circles of E_0 layer, (b) constant energy contours for E_1 and E_2 layers. The radii of the circumscribed circles about the Brillouin zones are $2\pi/a$. The possible transitions from E_1 and E_2 subbands (B) and the intervalley transitions (C and D) within E_2 subbands are indicated. (c) Possible transitions from E_0 to E_1 (V) and E_0 to E_2 (A) subbands

In the present study we derive an expression for the relaxation time for energetic phonon scattering for a degenerate 2DEG and then apply it for the calculation of mobility for (100)-oriented surface. The temperature of the

phonons involved in the intersubband transitions are determined for this purpose and the corresponding deformation potential constants that reproduce the experimental mobility data are estimated.

2. Theory

The distribution function $f(\mathbf{k})$ for the degenerate 2DEG is expanded as

$$f(\mathbf{k}) = f_0(E) + k \cos \theta g_0(E) \quad (1)$$

where \mathbf{k} is the two-dimensional crystal momentum, f_0 is the equilibrium Fermi distribution, θ is the angle between \mathbf{k} and the electric field along source-drain direction, and E is the energy of the electrons.

Eq. (1) and the expression for squared matrix element for transition from \mathbf{k} to \mathbf{k}' by involving a phonon of energy $\hbar\omega_R$, viz.

$$|M(\mathbf{k}, \mathbf{k}')|^2 = (Z_R^2 \hbar \omega_R / 2A\rho Z_{av} u_l^2) (N_R + \frac{1}{2} + \frac{1}{2}) \times \delta(E_{\mathbf{k}} - E_{\mathbf{k}'} \pm \hbar\omega_R) \quad (2)$$

are then substituted in the Boltzmann equation and after usual integration over the phonon q -space (Nag 1972) one gets for the relaxation time

$$\tau^{-1} = \frac{Z_R^2 \hbar \omega_R m_D}{2\rho \hbar^3 u_l^2 Z_{av}} \{ (N_R + 1) f_0(E + \hbar\omega_R) + N_R f_0(E - \hbar\omega_R) u(E - \hbar\omega_R) \\ + (N_R + 1) [1 - f_0(E - \hbar\omega_R)] u(E - \hbar\omega_R) + N_R [1 - f_0(E + \hbar\omega_R)] \}. \quad (3)$$

In eq. (2) and (3) Z_R is the optical-phonon deformation potential constant, A is the area of the surface, ρ the density, u_l the sound velocity, m_D the density-of-states effective mass, Z_{av} is the average separation of the electrons from the surface and N_R is the phonon occupation number. u is the step function [$u(<0) = 0$, $u(>0) = 1$]

The relaxation time for intervalley or intersubband scattering may be expressed in a similar fashion. The expression for the relaxation time for transition from E_0 to E_2 via a phonon of energy $\hbar\omega_t$ is

$$\tau_{02}^{-1}(\omega_t) = \frac{Z_t^2 \hbar \omega_t m_{D2}}{2\rho \hbar^3 u_l^2 Z_{av}} \{ (N_t + 1) f_0(E + \hbar\omega_t) u(E + \hbar\omega_t - \Delta) \\ + N_t f_0(E - \hbar\omega_t) u(E - \hbar\omega_t - \Delta) + (N_t + 1) [1 - f_0(E - \hbar\omega_t)] u(E - \hbar\omega_t - \Delta) \\ + N_t [1 - f_0(E + \hbar\omega_t)] u(E + \hbar\omega_t - \Delta) \} \quad (4)$$

with

$$\Delta = E_1 - E_0.$$

For the estimation of phonon temperatures we consider the three subbands E_0 , E_1 and E_2 only and also assume that $E_1 = E_2$. Under this assumption the different intersubband transitions are as indicated in figure 2. The four-degenerate

rate valleys in the E_2 subband have their extreme $0.85 k_{max}$ away from the centre (Fehor 1959). Transitions C and D occurring amongst these four valleys are umklapp processes. From the figure it is straightforward to calculate the phonon wavevectors. The corresponding temperatures are then estimated with the help of phonon dispersion curves (Brookhouse 1959, Dolling 1965). The wavevectors and temperatures of different phonons are listed in table 1. To make the analysis less cumbersome, we take an average of all the phonons expected to participate in the intersubband transitions. For the E_0 and E_1 layers we consider, in addition to acoustic phonon scattering, scattering by 215°K and 740°K phonons. For the E_2 layer we include 140°K and 170°K phonons also to account for the intervalley transitions within the subband. The relaxation times relevant for these three subbands are

Table 1 Wave vector and temperature of the phonons involved in intra- and inter-subband scattering in (100)-oriented silicon surface.

Process	Wave vector	Direction	Phonon temperature ($^\circ\text{K}$) for modes			
			TA	LA	LO	TO
V	0	740	740
A	$0.85 (2\pi/a)$	100	215	525	620	680
B	$0.85 (2\pi/a)$	100	215	525	620	680
C	$0.3 (2\pi/a)$	100	135	225	720	720
D	$\sqrt{2} \times 0.15 (2\pi/a)$	110	110	175	725	725

$$\tau_0^{-1} = \tau_{ac0}^{-1} + \tau_{op0}^{-1} + \tau_{(215^\circ\text{K})0}^{-1}$$

$$\tau_1^{-1} = \tau_{ac1}^{-1} + \tau_{op1}^{-1} + \tau_{(215^\circ\text{K})1}^{-1} \quad (5)$$

$$\tau_2^{-1} = \tau_{ac2}^{-1} + \tau_{op2}^{-1} + \tau_{(215^\circ\text{K})2}^{-1} + \tau_{(140^\circ\text{K})2}^{-1} + \tau_{(170^\circ\text{K})2}^{-1}.$$

The relaxation time for acoustic phonon scattering is

$$\tau_{acj}^{-1} = \left\{ \frac{m_D i^2 Z_A^2 k_B T}{\rho \hbar^3 u_l^2 Z_{av}} \right\} \times 1 \text{ for } E_0 \quad (6)$$

$$\times u(E - \Delta) \text{ for } E_1 \text{ and } E_2$$

where Z_A is the acoustic deformation potential constant.

The overall effective mobility now takes the form

$$\mu_{eff} = \frac{e}{N_{inv}} \sum_j n_j < \tau_j > / m_{aj} \quad j = 0, 1, 2 \quad (7)$$

where $\langle \rangle$ denotes average over the proper distribution, m_e is the conductivity effective mass and N_{inv} , the total number of inversion layer electrons per unit area is related with the surface field F_s and dielectric constant ϵ_{sc} of silicon, by

$$N_{inv} = F_s / \epsilon_{sc} \quad (8)$$

N_{inv} may also be expressed as

$$N_{inv} = \frac{g_v k_B T}{\pi \hbar^2} \sum_j m_D j \ln \left[1 + \exp \left(\frac{E_F - E_j}{k_B T} \right) \right] \quad (9)$$

where g_v is the valley degeneracy factor. The subband energies E_j occurring in eq. (8) are related with the surface field by

$$E_j = (\hbar^2 / 2m_z)^{1/3} [3/2\pi e F_s (j + 3/4)]^{2/3}, \quad j = 0, 1, 2, \dots \quad (10)$$

where m_z is the mass along the direction of surface field.

Finally the average value of inversion layer thickness is

$$Z_{av} = \sum_j 2n_j E_j / 3eF_s N_{inv} \quad (11)$$

3. Results and Discussions

We have attempted to reproduce the mobility-temperature data for an effective gate voltage = 32 V obtained by Fang and Fowler (1968) by using the above expressions and the following values of parameters :

$g_v = 2$ for E_0 and E_1 subbands and $g_v = 4$ for E_2 subband, $m_D = 0.19 m_0$ for E_0 and E_1 , $m_D = 0.417 m_0$ for E_2 , $m_c = 0.19 m_0$ for E_0 and E_1 and $= 0.314$ for E_2 , $m_2 = 0.916 m_0$, $\rho = 2.33$ gms/cm³, $u_l = 8.476 \times 10^5$ cm/sec, $\epsilon_{sc} = 11.8 \epsilon_0$, $Z_A = 7.65$ eV.

The surface field for an effective gate voltage of 32 V is first calculated and then the values of N_{inv} , E_0 , E_1 and E_F are obtained from eq. (7)-(10) by numerical solution.

For the calculation of mobility we have treated the optical-deformation-potential constants as adjustable parameters. To make calculations easier we have considered only two adjustable parameters : one for 740°K (Z_1) and another the same for all other phonons viz., 140°K, 170°K and 215°K (Z_2). We have found that if we select $Z_1 = 17$ eV and $Z_2 = 4.5$ eV, then the calculated mobility values show a $T^{-1.5}$ dependence and the high-temperature part of the experimental curve can be explained satisfactorily (Figure 3). The calculated values do not, however, agree with the experiment for $T < 100^\circ\text{K}$, because in that range scattering by surface-oxide-charges plays a dominant role.

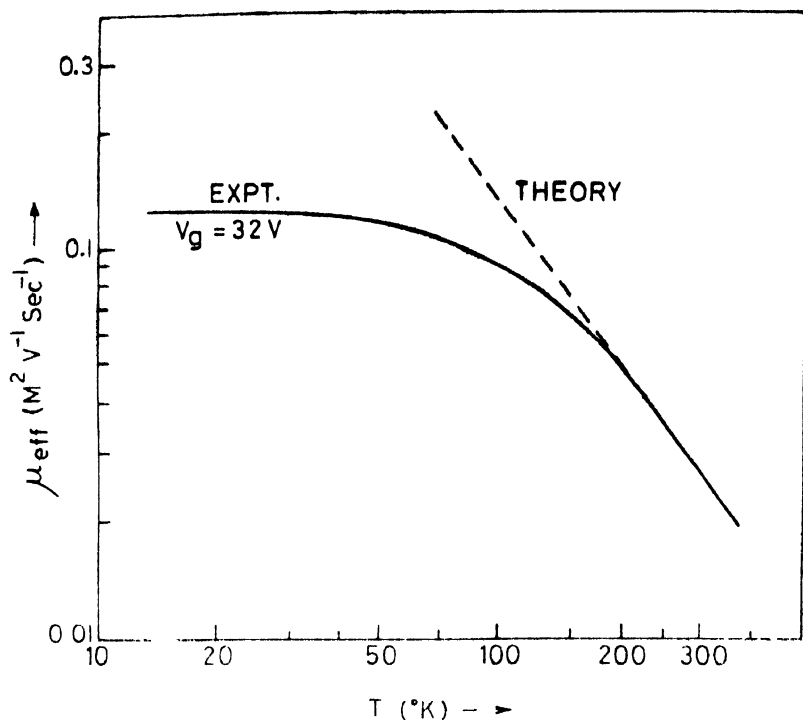


Figure 3. Effective mobility versus temperature of electrons in the (100)-oriented silicon inversion layer for an effective gate voltage of 32 V.

The mobility values at 250°K for different gate voltages calculated with $Z_1 = 17$ eV and $Z_2 = 4.5$ eV are compared with the experimental data in figure 4. The agreement is found to be quite good. In figure 4 we have also included

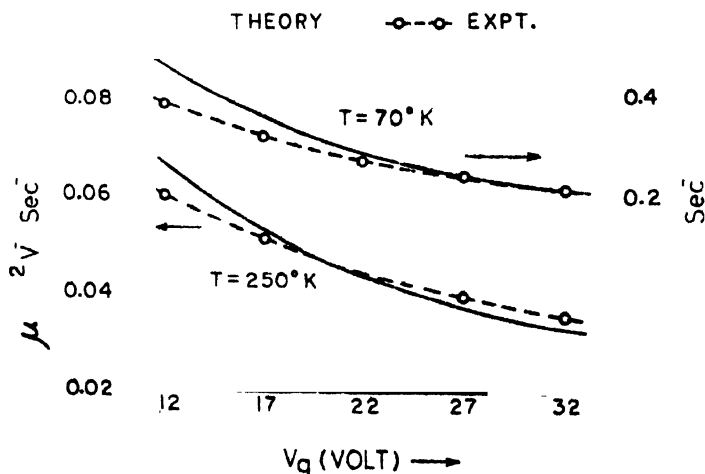


Figure 4. Effective mobility vs. gate voltage at 70°K and 250°K.

similarly calculated values for 70°K. For the sake of comparison we have included the values obtained by extrapolating the experimental curves to 70°K and again the agreement is quite satisfactory. Considering the various approximations involved in the present study, we may therefore conclude that the scattering model used in the present work can satisfactorily explain the lattice-scattering mobility in silicon inversion layers at high temperatures.

Acknowledgments

The author is grateful to Professor B. R. Nag for his encouragements and to D. Roychoudhury for many helpful discussions.

References

- Basu P K 1976 *Indian J. Pure Appl. Phys.* **14** 767
 Brockhouse B N 1959 *Phys. Rev. Letters* **2** 256
 Cheng Y C and Sullivan E A 1973a *Surface Sci.* **34** 717
 Cheng Y C and Sullivan E A 1973b *J. Appl. Phys.* **44** 923
 Cheng Y C and Sullivan E A 1973c *J. Appl. Phys.* **44** 3019
 Cheng Y C and Sullivan E A 1974 *J. Appl. Phys.* **45** 187
 Dolling G 1965 *Inelastic Scattering of Neutrons in Solids and Liquids*, International Atomic Energy Agency, Vienna, p 249
 Ezawa H, Kawaji S and Nakamura K 1974 *Japan J. Appl. Phys.* **13** 126
 Fang F F and Fowler A B 1968 *Phys. Rev.* **169** 619
 Fang F F and Fowler A B 1970 *J. Appl. Phys.* **41** 1825
 Foher G 1959 *J. Phys. Chem. Solids* **8** 486
 Nag B R 1972 *Theory of Electrical Conduction in Semiconductors*, Pergamon, London
 Ning T H and Sah C T 1972 *Phys. Rev.* **B6** 4605
 Ning T H and Sah C T 1974 *Phys. Rev.* **B9** 527
 Sah C T, Ning T H and Tschopp L L 1972 *Surface Sci.* **32** 561
 Storn F and Howard W E 1967 *Phys. Rev.* **163** 816
 Stern F 1972 *Phys. Rev.* **B5** 4891
 Wu C Y and Thomas G 1974 *Phys. Rev.* **B9** 1724

rate valleys in the E_2 subband have their extreme $0.85 k_{max}$ away from the centre (Fehér 1959). Transitions C and D occurring amongst these four valleys are umklapp processes. From the figure it is straightforward to calculate the phonon wavevectors. The corresponding temperatures are then estimated with the help of phonon dispersion curves (Brookhouse 1959, Dolling 1965). The wavevectors and temperatures of different phonons are listed in table 1. To make the analysis less cumbersome, we take an average of all the phonons expected to participate in the intersubband transitions. For the E_0 and E_1 layers we consider, in addition to acoustic phonon scattering, scattering by 215°K and 740°K phonons. For the E_2 layer we include 140°K and 170°K phonons also to account for the intervalley transitions within the subband. The relaxation times relevant for these three subbands are

Table 1 Wave vector and temperature of the phonons involved in intra- and inter-subband scattering in (100)-oriented silicon surface.

Process	Wave vector	Direction	Phonon temperature ($^\circ\text{K}$) for modes			
			TA	LA	LO	TO
V	0	740	740
A	$0.85 (2\pi/a)$	100	215	525	620	680
B	$0.85 (2\pi/a)$	100	215	525	620	680
C	$0.3 (2\pi/a)$	100	135	225	720	720
D	$\sqrt{2} \times 0.15 (2\pi/a)$	110	110	175	725	725

$$\tau_0^{-1} = \tau_{ac0}^{-1} + \tau_{op0}^{-1} + \tau_{(215^\circ\text{K})0}^{-1}$$

$$\tau_1^{-1} = \tau_{ac1}^{-1} + \tau_{op1}^{-1} + \tau_{(215^\circ\text{K})1}^{-1} \quad (5)$$

$$\tau_2^{-1} = \tau_{ac2}^{-1} + \tau_{op2}^{-1} + \tau_{(215^\circ\text{K})2}^{-1} + \tau_{(140^\circ\text{K})2}^{-1} + \tau_{(170^\circ\text{K})2}^{-1}.$$

The relaxation time for acoustic phonon scattering is

$$\tau_{acf}^{-1} = \left. \frac{m_{Df}^2 Z_A^2 k_B T}{\rho \hbar^2 u_l^2 Z_{av}} \right\} \begin{array}{l} \times 1 \text{ for } E_0 \\ \times u(E - \Delta) \text{ for } E_1 \text{ and } E_2 \end{array} \quad (6)$$

where Z_A is the acoustic deformation potential constant.

The overall effective mobility now takes the form

$$\mu_{eff} = \frac{e}{N_{inv}} \sum_j n_j \langle \tau_j \rangle / m_{ej} \quad j = 0, 1, 2 \quad (7)$$

where $\langle \rangle$ denotes average over the proper distribution, m_e is the conductivity effective mass and N_{inv} , the total number of inversion layer electrons per unit area is related with the surface field F_s and dielectric constant ϵ_{sc} of silicon, by

$$N_{inv} = F_s / \epsilon_{sc} \quad (8)$$

N_{inv} may also be expressed as

$$N_{inv} = \frac{g_v k_B T}{\pi \hbar^2} \sum_j m_D j \ln \left[1 + \exp \left(\frac{E_F - E_j}{k_B T} \right) \right] \quad (9)$$

where g_v is the valley degeneracy factor. The subband energies E_j occurring in eq. (8) are related with the surface field by

$$E_j = (\hbar^2 / 2m_z)^{1/3} [3/2\pi e F_s (j + 3/4)]^{2/3}, \quad j = 0, 1, 2, \dots \quad (10)$$

where m_z is the mass along the direction of surface field.

Finally the average value of inversion layer thickness is

$$Z_{av} = \sum_j 2n_j E_j / 3e F_s N_{inv} \quad (11)$$

3. Results and Discussions

We have attempted to reproduce the mobility-temperature data for an effective gate voltage = 32 V obtained by Fang and Fowler (1968) by using the above expressions and the following values of parameters :

$g_v = 2$ for E_0 and E_1 subbands and $g_v = 4$ for E_2 subband, $m_D = 0.19 m_0$ for E_0 and E_1 , $m_D = 0.417 m_0$ for E_2 , $m_e = 0.19 m_0$ for E_0 and E_1 and $= 0.314$ for E_2 , $m_z = 0.916 m_0$, $\rho = 2.33$ gms/cm³, $u_l = 8.476 \times 10^5$ cm/sec, $\epsilon_{sc} = 11.8 \epsilon_0$, $Z_A = 7.65$ eV.

The surface field for an effective gate voltage of 32 V is first calculated and then the values of N_{inv} , E_0 , E_1 and E_F are obtained from eq. (7)–(10) by numerical solution.

For the calculation of mobility we have treated the optical-deformation-potential constants as adjustable parameters. To make calculations easier we have considered only two adjustable parameters : one for 740°K (Z_1) and another the same for all other phonons viz., 140°K, 170°K and 215°K (Z_2). We have found that if we select $Z_1 = 17$ eV and $Z_2 = 4.5$ eV, then the calculated mobility values show a $T^{-1.5}$ dependence and the high-temperature part of the experimental curve can be explained satisfactorily (Figure 3). The calculated values do not, however, agree with the experiment for $T < 100^\circ\text{K}$, because in that range scattering by surface-oxide-charges plays a dominant role.

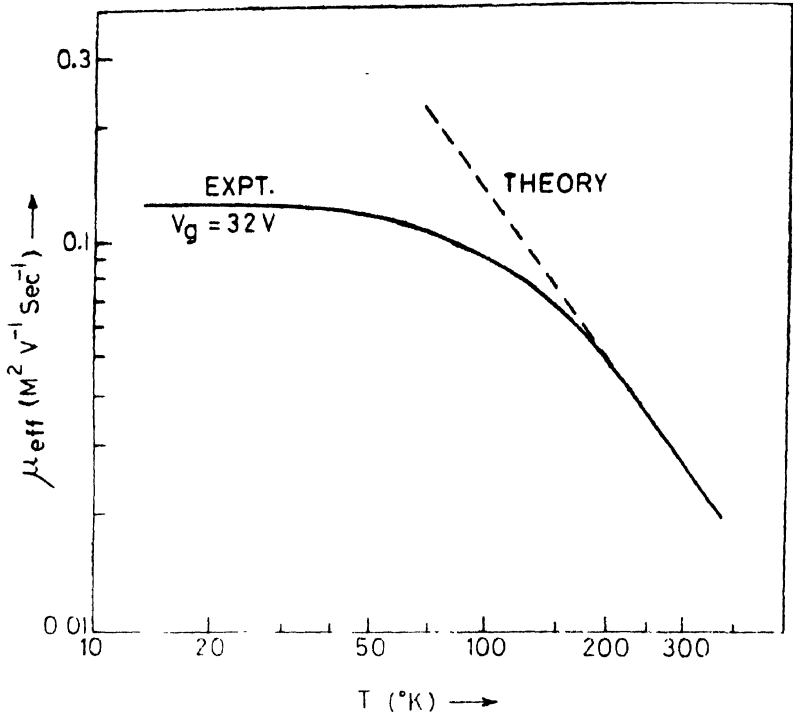


Figure 3. Effective mobility versus temperature of electrons in the (100)-oriented silicon inversion layer for an effective gate voltage of 32 V.

The mobility values at 250 K for different gate voltages calculated with $Z_1 = 17$ eV and $Z_2 = 4.5$ eV are compared with the experimental data in figure 4. The agreement is found to be quite good. In figure 4 we have also included

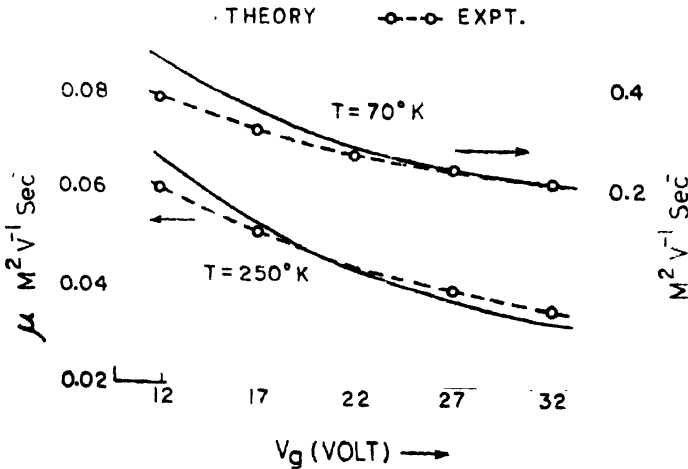


Figure 4. Effective mobility. vs. gate voltage at 70°K and 250°K.

similarly calculated values for 70°K. For the sake of comparison we have included the values obtained by extrapolating the experimental curves to 70°K and again the agreement is quite satisfactory. Considering the various approximations involved in the present study, we may therefore conclude that the scattering model used in the present work can satisfactorily explain the lattice-scattering mobility in silicon inversion layers at high temperatures.

Acknowledgments

The author is grateful to Professor B. R. Nag for his encouragements and to D. Roychoudhury for many helpful discussions.

References

- Basu P K 1976 *Indian J. Pure Appl. Phys.* **14** 767
Brockhouse B N 1959 *Phys. Rev. Letters* **2** 256
Cheng Y C and Sullivan E A 1973a *Surface Sci.* **34** 717
Cheng Y C and Sullivan E A 1973b *J. Appl. Phys.* **44** 923
Cheng Y C and Sullivan E A 1973c *J. Appl. Phys.* **44** 3619
Cheng Y C and Sullivan E A 1974 *J. Appl. Phys.* **45** 187
Dolling G 1965 *Inelastic Scattering of Neutrons in Solids and Liquids*, International Atomic Energy Agency, Vienna, p 249
Ezawa H, Kawaji S and Nakamura K 1974 *Japan J. Appl. Phys.* **13** 126
Fang F F and Fowler A B 1968 *Phys. Rev.* **169** 619
Fang F F and Fowler A B 1970 *J. Appl. Phys.* **41** 1825
Fohr G 1959 *J. Phys. Chem. Solids* **8** 486
Nag B R 1972 *Theory of Electrical Conduction in Semiconductors*, Pergamon, London
Ning T H and Sah C T 1972 *Phys. Rev.* **B6** 4605
Ning T H and Sah C T 1974 *Phys. Rev.* **B9** 527
Sah C T, Ning T H and Tschopp L L 1972 *Surface Sci.* **32** 561
Storn F and Howard W E 1967 *Phys. Rev.* **163** 816
Storn F 1972 *Phys. Rev.* **B5** 4891
Wu C Y and Thomas G 1974 *Phys. Rev.* **B9** 1724

High temperature phases in fibrous tremolite

P S Mukherjee, S Bhattacharjee and G Vijayasree

Department of Physics, I.I.T., Kharagpur 721302

Abstract. A specimen of Indian asbestos characterised as Tremolite has been heated to temperatures 760°C, 860°C, 950°C, 1040°C which are around the peaks in the D.T.A. curve. These samples were then subjected to X-ray diffraction and electron microscopic studies for identification of the different phases and the accompanying structural changes. The results showed the start of a new phase transformation at temperature around 860-960°C-thereafter with lattice contraction. These results are quite in good agreement with electron microscopic and D.T.A. results.

1. Introduction

Tremolite is the simplest and structurally least complicated of all amphiboles built of double silicate chains. The fibrous varieties called asbestos, are widely used in science and industry in various forms especially as insulators, both thermal and electrical. Although several works (e.g. Zussman 1959, Papiko *et al* 1969) have been reported on the structure of tremolite, high temperature studies especially on the fibrous varieties appears to have been quite few. One of the earliest attempts was made by Wittels (1951, 1952) by thermal method and more recently Sueno *et al* (1973) studied the thermal structural expansion of tremolite by X-ray method. However, none of these workers studied the asbestiform of tremolite. Because of the wide applications and uses of the fibrous amphiboles at high temperatures and the non-availability of adequate data on its various high temperature phases, a detailed investigation in this direction has been considered to be highly desirable. As such, we have undertaken a systematic study of a fibrous variety of tremolite amphibole for reasons as mentioned above by X-ray, electron microscope and thermal methods. The present work is the third in the series of such work and reports the results of a detailed study of the different high temperature phases formed around the temperatures indicated by the thermograms.

2. Experimental

The present work is also based on the same specimen of fibrous tremolite from Bihar whose preliminary structural analysis and data on dielectric properties have already been reported (Mukherjee and Bhattacharjee 1976), Vijayasree *et al* (1976). The samples of asbestos were finely grounded and passed through a sieve of 325 mesh and heated to temperatures 760, 860, 960 and 1040°C in an electric

furnace for four hours each. Each of samples was cooled in a dessicator and then taken for study.

(i) *Differential Thermal Analysis*

D.T.A. of the sample was carried out to record the temperatures around which changes take place by adopting a method as described by Mitra and Bhattacharjee (1969). The results of the measurement have already been reported (Vijaysree *et al* 1976). The D.T.A. reveals a broad and slowly rising exotherm starting from about 860°C with maximum at 930°C-immediately followed by a sharper endotherm with peak around 960°C.

(ii) *X-ray Methods*

Fibre photographs of the tremolite fibres were taken in a cylindrical camera of diameter 5.73 cm fitted with a suitable sample holder especially designed and fabricated for this purpose. The holder can be mounted on a goniometer head and fibre can be stretched and tilted by a suitable arrangement. Photographs were taken using this camera by the usual rotation method.

Powder photographs of the samples were also taken for proper identification of different phases by using a 11.46 cm precision Debye-Scherrer camera. Nickel filtered CuK_α radiation was used.

(iii) *Electron Microscopic Study*

For studying the different morphological changes accompanying heating, each of the heated samples was subjected to electron microscopic study. Electron micrographs of the samples were taken in an A.E.I.EM6 (London) electron microscope by employing the method as described by Mitra (1963).

3. Results and discussions

(i) The weak and broad exothermic peak (860°C) in the D.T.A. curve is indicative of an exothermic reaction taking place in the sample around this temperature range. This may be attributed to the slow oxidation of the small amount of ferrous iron present in the sample (Mukherjee and Bhattacharjee 1976) without accompanying any structural change as observed by Wittels (1952). The sharp endotherm at 960°C indicates the occurrence of a phase change in the temperature range which is due to the loss of structural water along with structural breakdown of tremolite into pyroxenes (diopside and enstatite) and silica as discussed by Vijaysree *et al* (1976).

(ii) X-ray powder photographs of the samples heated to temperatures 760, 860, 950, 1040°C are shown in Fig. 1. X-ray patterns at room temperature and 760°C do not show any change and all the lines including three characteristic lines of tremolite at 3.12, 2.71, 8.38Å are present in both the photographs. At 860°C the d values of almost all the lines decrease showing thereby that a thermal

contraction of the lattice in all direction has started around this temperature. This corresponds to the starting of the exotherm in the D.T.A. curve. Hence it may be said that the slow oxidation at this temperature range as discussed earlier is accompanied by a lattice contraction in all direction. However, the contraction is not uniform in all direction.

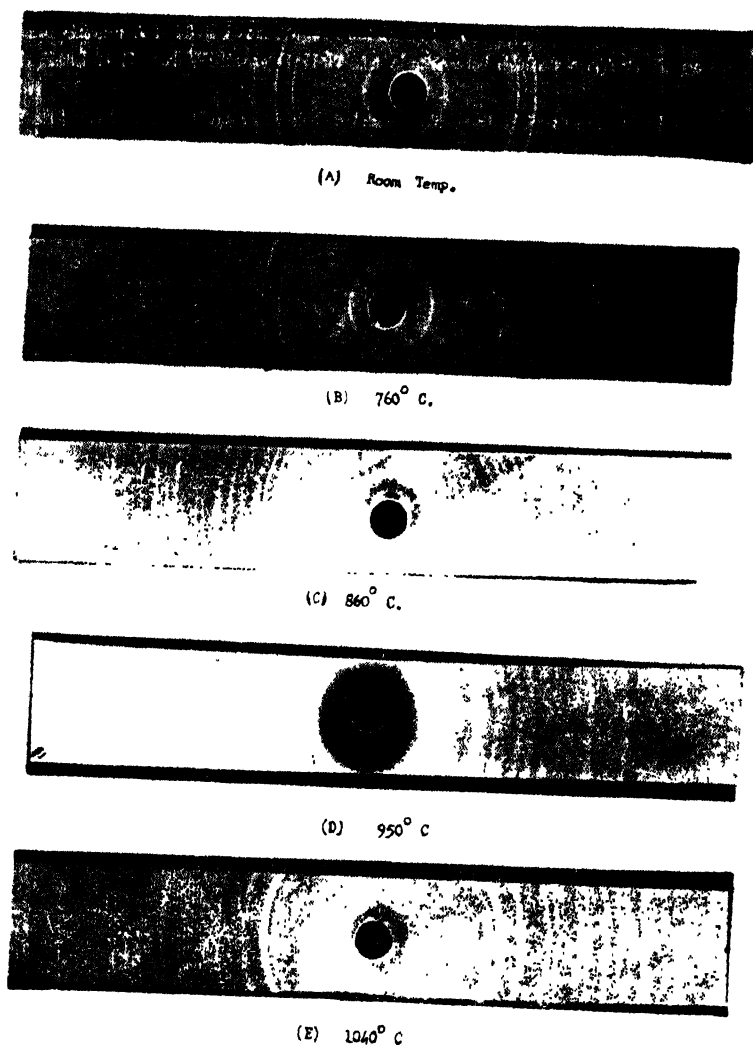


Fig. 1. Powder photographs at (A) Room temperature (B) 760°C (C) 860°C (D) 950°C (E) 1040°C

At 950°C a significant change is observed in the pattern. The strongest characteristic line of tremolite at 8.33Å disappears completely and new lines at 3.165, 2.878, 2.490Å, characteristic of enstatite and at 2.97 and 2.54Å characteristics of diopside appear. This clearly indicates that at this temperature range a phase transformation has taken place with the breakdown of tremolite into enstatite and diopside and the loss of structural water. This results are supported by the D.T.A. observation. The disintegration products are also crystalline as is evident from the powder pattern. This process continues even upto 1040°C with further contraction of the lattice and slight broadening of the lines showing thereby that the new phases are relatively less crystalline.

(iii) Fig 2 shows that the fibre photographs of the samples heated at 30°C (room temperature), 760, 860, 950 and 1040°C.

A close inspection of the photographs reveals that the streaks become slightly broader and elongated in the meridional plane giving a pattern close to Debye-Scherrer rings at 760°C. This is typical of a fibre with azimuthal randomness. Hence it does not show any apparent structural change in conformity with the D.T.A. and powder data as discussed above. The streaks become sharper at 950°C indicating an increase in crystallinity. However, at 1040°C the sharpness of the spots become relatively less showing thereby that the new phase is poor in crystallinity as indicated by the powder photographs. C values obtained from the fibre photographs gradually decreases upto 860°C, thereafter abruptly increases upto 1040°C. This is due the formation of new phases as shown by powder data and discussed above. The C values are very close to the C value of diopside.

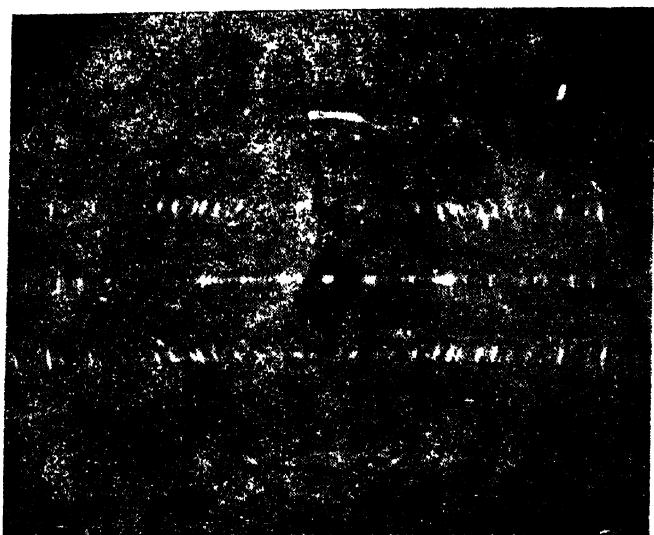
(iv) The electron micrographs (Fig. 3) show that the length of the fibrils decrease with temperature upto 860°C above which the fibres break down into almost spherical particles at 960°C—the temperature at which transformation takes place.

4. Conclusion

From the different experimental observations it may be concluded that the tremolite fibres break down into poorly crystalline reaction products viz. enstatite and diopside around 960°C. These reaction products remains as a part of the original powder and the transformation is accompanied by lattice contraction. The transformation is not very sharp and is not complete even at 1040°C.

Acknowledgment

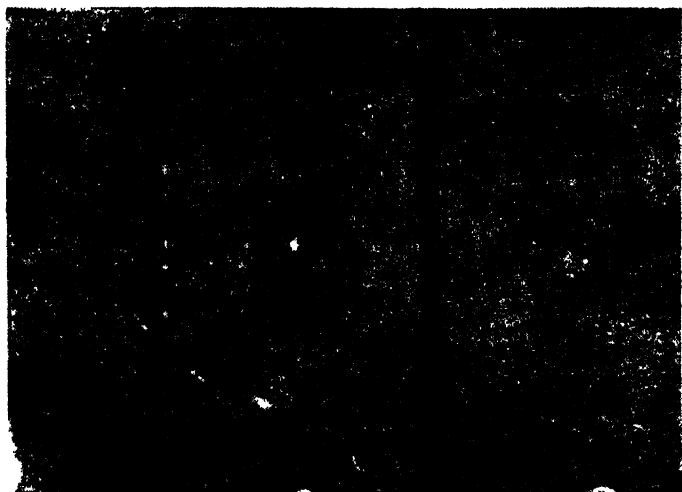
The authors express their sincere thanks to Prof. G. B. Mitra and Dr. G. D. Nigam for their encouragement and kind interest in the present work.



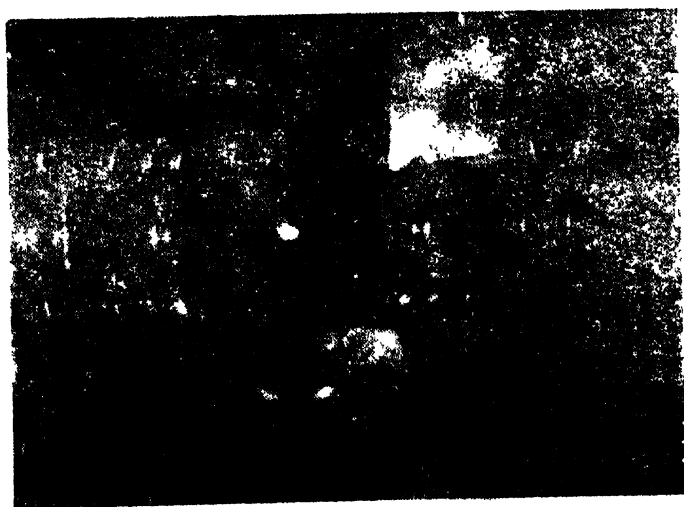
(A) Room Temp.



(B) 760° C



(C) 860° C.



(D) 950° C.



(E) 1040° C

Figure. 2. Fibre Photographs at (A) Room temperature (B) 760°C (C) 860°C (D) 950°C (E) 1040°C



(A) Room Temp. X
6000

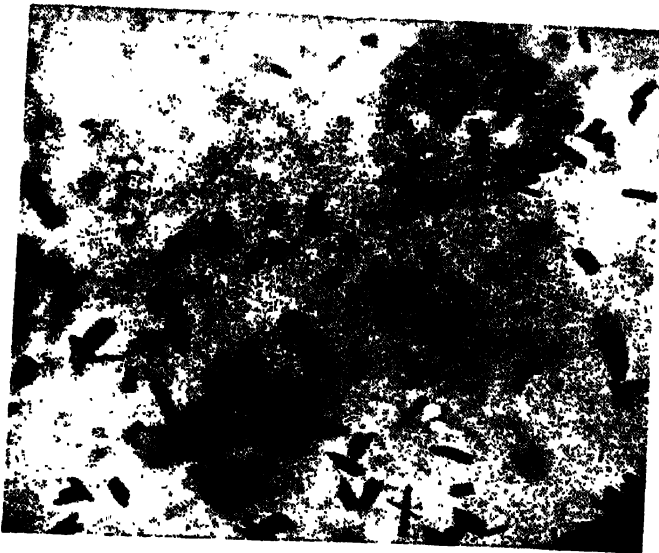
Figure. 3. Electron micrographs at :
(A) Room temperature X 6000



(B) 760° C X
10,000

(B) 760°C

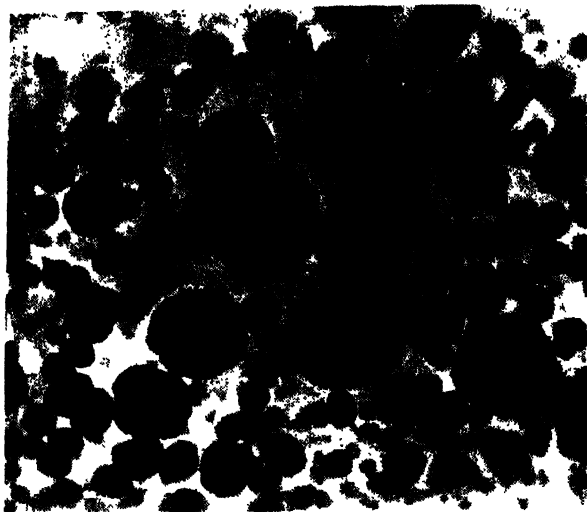
× 10,000



(C) 860° C X 13,000

(C) 860°C

× 13,000



(D) 950° C X 10,000

(D) 950° C

10,000

References

- Mitra G. B. and Bhattacharjee S. 1969 *Am. Min.* **54**, 1409.
 Mukherjee P. S. and Bhattacharjee S. 1976 *Ind. J. Earth Sc.* (Communicated)
 Papike J. J. Malcolm Ross and Joan R. Clark 1969 *Mindral Soc., American Spec. Pap.* **2**, 117.
 Sueno S. Papike J. J. Commerson M. and Prewitt C. T. 1973 *Amer. Min.* **58**, 649.
 Vijayashree G. Bhattacharjee S. and Mukherjee P. S. 1976 *Indian Journal of Physics* (under publication)
 Wittels M. 1951 *Amer. Min* **36**, 851
 Wittels M. 1952 *Amer. Min.* **37**, 28.
 Zussman J. (1956) *Acta Cryst.* **12**, 309.

Infrared free-carrier absorption in non-polar semiconductors; scattering by two-short wavelength phonons.

S. S. Kubakaddi and B. S. Krishnamurthy

Department of Physics, Karnatak University, Dharwar, Karnataka.

Abstract. The infrared free carrier absorption per electron (α/n) has been calculated in silicon and germanium considering the electron-two short wavelength phonon mechanism besides the usual electron-one phonon mechanisms following the perturbation theory for an ellipsoidal energy surface with the parabolic band model. In silicon, it is found that the calculated $(\alpha/n)_{total}$ almost agrees with that due to Long's model in magnitude and is closer to the lattice mechanism limited experimental data than the other known one-phonon models. The $(\alpha/n)_{total}$ variation with the incident wavelength is found to be $\lambda^{1.6}$ which is some what less steeper than the experimentally observed variation $\lambda^{1.8}$. Similar calculations in germanium indicates that the electron-one phonon of the acoustic type is the most dominant process and the two-phonon process is comparatively significant, over the other one-phonon processes.

1. Introduction

It is well known that the free carrier absorption (FCA) arises through scattering by impurities and lattice vibrations. The FCA depends on both band structure and scattering processes. Therefore, studies of FCA have been exploited to gain knowledge of carrier-lattice interactions in semiconductors.

Recently, it has been demonstrated by the present authors (1975, 1976a, 1976b) that the electron—two short wavelength phonon interaction contributes substantially to the transport properties such as the zero field mobility, warm electron coefficient etc., besides the usual carrier-one phonon processes. However, in such descriptions either one needs to solve the Boltzmann transport equation or one has to assume model electron distribution functions such as displaced Maxwellian as has been assumed by the present authors (1975, 1976a, 1976b) in transport calculations. But FCA studies directly leads to an understanding of the scattering mechanisms without recourses to the steady state electron distribution function.

Ganguly and Ngai (1973) have calculated FCA due to electron-two non-polar optical phonons in polar semiconductors such as InSb and found that the agreement between the experiment and theory of FCA was better than those due to electron-one phonon models. No such calculations exists as yet in non-polar semiconductors which takes cognizance of carrier-two phonon interaction.

It is the aim of the present paper to examine the importance of the carrier-two phonon interaction in non-polar semiconductors like silicon and germanium in FCA. The two-phonons under consideration are of short wavelength region such that their wave vector sum $\mathbf{q} + \mathbf{q}' = \mathbf{Q}$ is in the long wavelength region. Then, it is possible to define the two-phonon deformation potential in analogy with the usual one-phonon deformation potential

2. Calculation of the absorption coefficient

In the presence of an infrared radiation field of wavelength λ , the intraband electronic transitions are phonon assisted transitions owing to the energy and momentum conservation requirements and are describable with in the second-order perturbation theory. The transition probability per unit time of such transitions is given by

$$W = \sum_{\mathbf{q}\mathbf{q}'} (2\pi/\hbar) |\langle N_{\mathbf{q}}, N_{\mathbf{q}'}, \mathbf{k}' | H_{2p} | N_{\mathbf{q}}, N_{\mathbf{q}'}, (\mathbf{k} + \mathbf{p}) \rangle| \\ \times \frac{|\langle 0_{\mathbf{p}}, (\mathbf{k} + \mathbf{p}) | H_r | 1_{\mathbf{p}}, \mathbf{k} \rangle|^2}{(E_{\mathbf{k}} - E_{\mathbf{k} + \mathbf{p}} + \hbar\nu)} \left\{ \delta(E_{\mathbf{k}} - E_{\mathbf{k}}) \right\} \quad (1)$$

where \mathbf{p}, \mathbf{k} (initial value) and \mathbf{k}' (final value) are respectively, the photon and electron wave vectors, ν is the photon frequency; N_i ($i = \mathbf{q}$ and \mathbf{q}') is the equilibrium phonon distribution function. In eq (1) H_r and H_{2p} are, respectively, electron-radiation and electron-two short wavelength phonon interaction terms whose matrix elements are the following

$$\langle 0_{\mathbf{q}}, \mathbf{k}' | H_r | \mathbf{k}, 1_{\mathbf{p}} \rangle = -\frac{e\hbar}{mc} \left(\frac{c^2\hbar}{\nu\epsilon V} \right)^{\frac{1}{2}} e_{\mathbf{p}} \tilde{\alpha}(\mathbf{k} - \mathbf{k}_0) \delta_{\mathbf{k}', \mathbf{k}} \quad (2)$$

and

$$\langle N'_{\mathbf{q}}, N'_{\mathbf{q}'}, \mathbf{k}' | H_{2p} | N_{\mathbf{q}}, N_{\mathbf{q}'}, (\mathbf{k} + \mathbf{p}) \rangle = \frac{\hbar\alpha[F(N_{\mathbf{q}}N_{\mathbf{q}'})]^{\frac{1}{2}}}{2\rho Va^2(\omega\omega')^{\frac{1}{2}}} \quad (3)$$

where ϵ is the optical dielectric constant; c is the velocity of light; m is the bare electronic mass; $\tilde{\alpha} = (m^3/m_t^2m_l)$ is the second rank tensor expressed in terms of m_t and m_l the transverse and longitudinal effective masses of the electron; \mathbf{k}_0 is the wave vector corresponding to the energy minimum of a valley; V is the volume and a is lattice constant of the crystal; ω and ω' are the circular frequencies of the two-phonons of short wavelength region under consideration; and

$F(N_{\mathbf{q}}, N_{\mathbf{q}'})$ denotes the product of distribution functions of the two-phonons which assumes the following form :

$$\left. \begin{array}{l} \text{Both phonons emitted : } F(N_{\mathbf{q}}, N_{\mathbf{q}'}) \Longrightarrow (N_{\mathbf{q}} + 1)(N_{\mathbf{q}'} + 1) \\ \text{Both phonons absorbed : } F(N_{\mathbf{q}}, N_{\mathbf{q}'}) \Longrightarrow (N_{\mathbf{q}})(N_{\mathbf{q}'}) \\ \text{One phonon emitted and} \\ \text{the other absorbed : } F(N_{\mathbf{q}}, N_{\mathbf{q}'}) \Longrightarrow (N_{\mathbf{q}})(N_{\mathbf{q}'} + 1) \end{array} \right\} (4)$$

Inserting eqs. (2) to (4) in eq. (1), we get

$$\begin{aligned} W = & \frac{(\hbar \alpha e / m \rho)^2}{8 \pi v^3 \epsilon a^4 \omega \omega'} \times \sum_{\mathbf{q}, \mathbf{q}', s} [e_p \cdot \hat{\alpha}(\mathbf{k} - \mathbf{k}')]^2 \cdot \\ & \times \{ N N' \delta [E_{\mathbf{k}'} - E_{\mathbf{k}} - \hbar \nu - \hbar(\omega + \omega')] \\ & + (N + 1)(N' + 1) \delta [E_{\mathbf{k}'} - E_{\mathbf{k}} - \hbar \nu + \hbar(\omega + \omega')] \\ & + N(N' + 1) \delta [E_{\mathbf{k}'} - E_{\mathbf{k}} - \hbar \nu - \hbar(\omega - \omega')] \\ & + (N + 1)N' \delta [E_{\mathbf{k}'} - E_{\mathbf{k}} - \hbar \nu + \hbar(\omega - \omega')] \} \end{aligned} \quad (5)$$

where s denotes the various types of phonon involved in the scattering processes. In simplifying eq. (5) we assume that ω and ω' are independent of phonon wave vectors. This particularly true, of both Ge and Si in the short wavelength region for some of the branches of the phonon dispersion, in as much as the dispersion curves for those branches are relatively flat (Brockhouse and Lyengar 1957, Brockhouse 1959). We shall now obtain an average transition probability per unit time \bar{W} by averaging W over the equilibrium distribution of electrons which is assumed to be of Maxwellian form. Making use of the well known Herring-Vogt transformation (1956) integration over \mathbf{k} , $\mathbf{Q} = \mathbf{q} \perp \mathbf{q}'$ are performed with the use of δ -function properties. Then, we get

$$\begin{aligned} \bar{W} = & \frac{n \sqrt{2} c^2 \alpha_1 m^{\frac{1}{2}}}{9 \rho^2 a^4 (\text{dot } \hat{\alpha})^{\frac{1}{2}} \hbar k_B^{\frac{1}{2}} \epsilon \pi^{\frac{1}{2}}} \\ & \times [1 - (\gamma - 1)/3\gamma] (T^{3/2} N N' \alpha_{\Xi}^2 q_{\Xi}^3) / v^3 \Theta_{\Xi}^2 \\ & \times \exp(z_{\pm}) \{ z_{\pm}^2 K_2(z_{\pm}) + z_{\pm}^2 K_2(z_{\pm}) + 2 z_{\pm}^2 K_2(z) \} \end{aligned} \quad (6)$$

where n is the electron density in a valley, $\alpha_1 = (m_i/m^{\frac{1}{2}})$; $\gamma = (m_1/m_i)$, $z = (\hbar v/k_B T)$, $z_{\pm} = z \pm (\theta_{\Xi}/2T)$, $\theta_{\Xi} = \hbar v_{\Xi}/k_B$, T is the lattice temperature Ξ is the two-phonon critical point and it is assumed that $\omega = \omega' = (\omega_{\Xi}/2)$ and $K_2(z)$ is the modified Bessel's function. The eq. (6) is the basic result of the present investigation.

The absorption coefficient per electron due to the two-phonon process is simply related to eq. (6) is given by

$$(\alpha/n) = (\bar{W}e^{\frac{1}{2}}/cn)(1 - e^{-2s}). \quad (7)$$

3. Application to silicon and germanium

In order to compare the calculated absorption coefficient with an experiment it is required to find the total absorption coefficient per electron $(\alpha/n)_{total}$, by considering the various allowed one-phonon and two-phonon processes given in the tables 1 and 2 for silicon and germanium, respectively. The (α/n) for one-phonon processes are available in literature and are borrowed from Meyer (1958[†], Spitzer and Fan (1957) and added to eq. (7) which leads to $(\alpha/n)_{total}$. The expressions $(\alpha/n)_{total}$ and (α/n) for various individual processes have been calculated numerically for both Si and Ge making use of the relevant coupling coefficients and material parameters given in table 1 and 2. The results of the calculations are displayed in figures (1 to 4).

Now let us consider the case of Si. The $(\alpha/n)_{total}$ due to the present work (curve 1) is shown in figure 1 along with the lattice mechanism limited experimental values as deduced by Basu and Nag (1972) based on the experimental

Table 1. Scattering mechanisms and material parameters used in the present work for silicon^a.

Scattering mechanisms	Coupling constants	Equivalent phonon temperature
1. <i>Intravalley Process</i>	$\Xi_u = 8.6 \text{ eV}$...
acoustic phonons	$\Xi_a = -0.4 \text{ eV}$...
2. <i>Intervalley Process</i>	$(DK)_i$ in eV cm^{-1}	$\theta_i(K)^b$
<i>g</i> -one phonon process	5×10^7	130
<i>f</i> -one phonon process	1×10^8	530
<i>f</i> -one phonon process	1×10^8	580
<i>f</i> -one phonon process	4×10^8	690
3. <i>Two-phonon process</i>	D in eV	$\theta \Xi = (K)^c$
$2TA(\Xi = XX)$	850	420
$2TO(\Xi = XX)$	7900	1340

$(m_i/m) = 0.1905$, $(m_l/m) = 0.9163$, $s = 9.037 \times 10^5 \text{ cm s}^{-1}$,
 $\rho = 2.33 \text{ gm cm}^{-3}$, $a = 5.4307 \times 10^{-8} \text{ cm}$, $\xi_L = 1.33$, $\eta_L = 1.15$,
 $\zeta_L = 1.07$.

a. Present authors (1976b)

b. Eaves *et al* (1975)

c. Brockhouse (1959)

Table 2. Scattering mechanisms and material parameters used in the present work for Germanium^a.

Scattering mechanisms	Coupling constants	Equivalent phonon temperature
Acoustic intra-valley	$\Xi_v = 19 \text{ eV}$, $\Xi_p = -8.5 \text{ eV} \dots$	
Optical intravalley	$(DK) = 3 \times 10^8 \text{ eV cm}^{-1}$	430 K
Optical Intervalley	${}_o(DK) = 6 \times 10^7 \text{ eV cm}^{-1}$	315 K
Two-phonon process	D in eV^{-1}	
$2TA$ (= XX)	5×10^2	240 K
$2TO$ (= LL)	11.5×10^3	802 K

$\rho = 5.32 \text{ gm cm}^{-3}$, $m_t = 0.082m$; $m_l = 1.6 m$; $s = 5.4 \times 10^8 \text{ cm s}^{-1}$;
 $a = 5.66 \times 10^{-8} \text{ cm}$; $\xi_{\perp} = 1.31$, $\eta_{\perp} = 1.31$, $\zeta = 1.01$.

d. The two-phonon deformation potentials selected in the present work also fits the zero field mobility and warm electron coefficient (see Kubakaddi and Krishnamurthy 1976a).

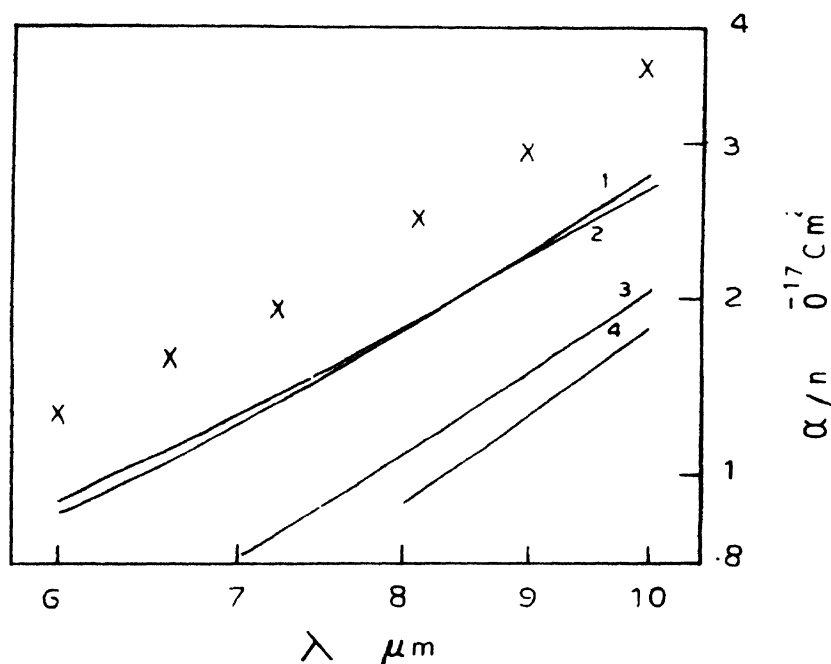


Figure 1. Wave length dependence of $(\alpha/n)_{total}$ for lattice scattering mechanisms in Si. X : Lattice scattering limited experimental points as deduced by Basu and Nag (1972) from the experimental data of Spitzer and Fan (1957). Curves 1 to 4 are, respectively, due to Present work, Long's model, Folland, Costato and Reggiani; and Dumke's model.

work of Spitzer and Fan (1957). We have also shown the calculated curves due to Basu and Nag (1972) based on the other one-phonon models* such as Long's Folklund, Dunke and Costato and Reggiani. It is interesting to note that $(\alpha/n)_{total}$ due to the present work almost agrees with Long's model and is closer to the experimental observation than other one-phonon models in magnitude. However, $(\alpha/n)_{total} \propto \lambda^{1.6}$ (curve 1, figure 1) where as all other curves in figure 1 exhibits nearly $\lambda^{1.8}$ behaviour. This is understandable. From figure 2 we notice that $(\alpha/n)_{acoustic} \propto \lambda^{1.87}$ (curves 3 and figure 2), $(\alpha/n)_{2p} \propto \lambda^{1.5}$ (curve 7, figure 2) which are the dominant processes. Hence, the inclusion of a two-phonon mechanism to obtain the $(\alpha/n)_{total}$ clearly reduces the index of λ anywhere between 1.87

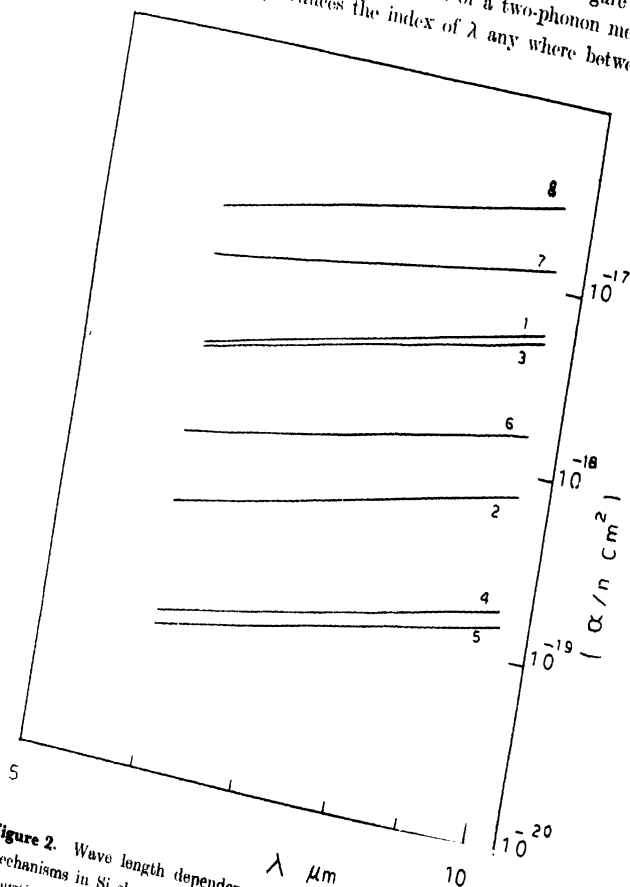


Figure 2. Wave length dependence of (α/n) for various lattice scattering mechanisms in Si shown in table 1. Curves 1 to 8 are, respectively, due to acoustic, 130 K, 420 K (27.4), 530 K, 580 K, 690 K, 1340 K (270) and $(\alpha/n)_{total}$.

* For details of other one-phonon models see table 1 of Basu and Nag (1972).

and 1.5 which in the present case happen to be 1.6. Nevertheless, the dependence of (α/n) on λ may improve if a realistic calculation is made incorporating the non-parabolicity of the band structure which seems to be considerable particularly for FCA where there exists the possibility of carriers being excited to non-parabolic region of the band in the wavelength range under consideration. In fact, the recent calculations of Das and Nag (1976) in semiconductors such as GaP, AlSb and PbTe, show that the index of the wave length for each scattering mechanism increase with the decrease of the energy gap. The enhancement of index of the case of GaP is ≈ 0.1 for phonon scattering. We expect much more pronounced enhancement in semiconductors like InSb, Si and Ge in view of the relatively smaller energy gap in these materials. Then, inclusion of non-parabolicity may be favourable in improving the value of the index from 1.6 towards the expected value 1.8 and consequently the other models, shown in figure 1, may disagree for similar reasons.

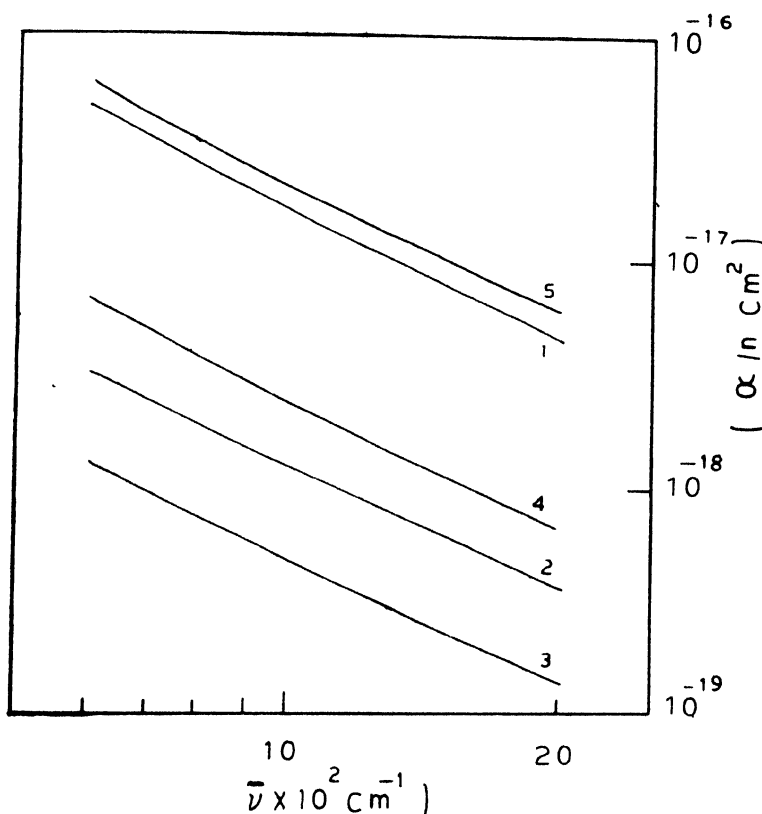


Figure 3. Wave number dependence of calculated $(\alpha/n)_{\text{total}}$ for lattice scattering mechanisms in Ge. Curve 1 : Present work, and Curve 2 : $(DK)_{\text{Intra}} = 6 \times 10^8$ eV cm^{-1} (one-phonon model only) $\theta = 430$ K (Chattopadhyaya and Nag 1972).

A few words about the phonon equivalent temperatures and coupling parameters used in the present work will be in order. It should be noted that the phonon equivalent temperatures used in the Long's model are averages over the phonon branches whereas in the present work these are evidenced by the magneto-phonon (Eaves *et al* 1975) and second-order Raman scattering (Renucci *et al* 1975) experiments. The deformation potential Ξ_u for uniaxial stress which we have selected, is in agreement with that used by Loggins and Little John (1971) to explain the stress dependences of relaxation time. The various coupling constants D_i for the one-phonon intervalley processes are in reasonable agreement with those existing in the literature. The two-phonon deformation potential constants D_{Ξ} used in the present work are not just selected at random to obtain the best fit but agrees with those deduced from non-resonant Raman scattering experiments (Orbach and Stepleton 1972) and differs from those deduced from second-order resonant Raman scattering (Renucci *et al* 1975) and magneto-phonon (Eaves *et al* 1975) experiments. Furthermore the D_{Ξ} values given in table 1 also fits the zero field mobility as well as the warm electron coefficient in Si as was shown by the present authors (1976b).

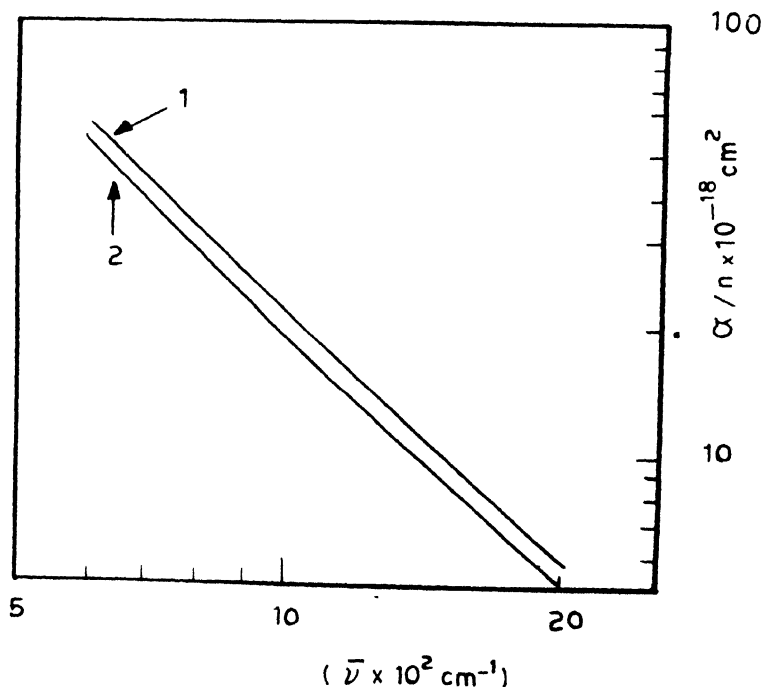


Figure 4. Wave number dependence of calculated (α/n) for various lattice scattering mechanisms given in table 2 for Ge. Curves 1 to 5 are, respectively, due to acoustic, 240K (2TA), 430 K, 802 K (2TO) and $(\alpha/n)_{total}$.

In figure 3 we have shown for Ge $(\alpha/n)_{total}$ vs wave number $\tilde{\nu}$ of the incident radiation for the present model (see curve 1) and other one-phonon model in which the intra-valley coupling constant $(DK) = 6 \times 10^8 \text{ eV cm}^{-1}$ (Chattopadhyaya, and Nag 1972). In figure 4 the various one-phonon and the two-phonon (α/n) 's together with $(\alpha/n)_{total}$ of the present model are shown. From figure 4 we notice that the acoustic phonon mechanism is the most dominant process and the two-phonon process contributes somewhat larger than the other one-phonon processes. However, the (α/n) dependence on λ is mainly controlled by $(\alpha/n)_{acoustic}$ (curve 1) in as much as $(\alpha/n)_{total} \propto \lambda^{1.82}$ (curve 5) and $(\alpha/n)_{acoustic} \propto \lambda^{1.86}$ and $(\alpha/n)_{2p} \propto \lambda^{1.5}$ (curves 2 and 4). In order to facilitate an experimental comparison one needs to incorporate the non-equivalent intervalley scattering of electrons from $\langle 111 \rangle$ to $\langle 100 \rangle$ valleys whereas in the present investigation equivalent valley scattering among $\langle 111 \rangle$ alone is considered.

In conclusion, it may be pointed out that the carrier-two phonon mechanisms contribute significantly to the FCA in non-polar semiconductors and are of comparable magnitude to that due to one-phonon mechanisms.

Acknowledgment

One of us (SSK) is grateful to the CSIR, New Delhi for the award of a research fellowship.

References

- Basu P K and Nag B R 1972 *Phys. Status. Solidi* **b53** K61
 Brockhouse B N and Iyengar P K 1957 *Phys. Rev.* **111** 747
 Brockhouse B N 1959 *Phys. Rev. Letters* **2** 256
 Chattopadhyaya D and Nag B R 1972 *Phys. Rev.* **B6** 1390
 Das A K and Nag B R 1976 (Private communication)
 Eaves L, Houlst R A, Stradling R A, Tidey R J, Portal J C and Askenazy S 1975 *J. Phys.* **C8** 1034
 Ganguly A K and Ngai K L 1973 *Phys. Rev.* **B8** 5654
 Herring C and Vogt E 1956 *Phys. Rev.* **101** 944
 Kubakaddi S S and Krishnamurthy B S 1975 *Phys. Letters* **A54** 389, 1976a *Phys. Letters* **A58** 352, 1976b *Phys. Status. Solidi* (In press)
 Loggins Jr C D and Littlejohn M A 1971 *J. Appl. Phys.* **42** 865
 Meyer H J G 1958 *Phys. Rev.* **112** 298
 Orbach R and Stapleton H J 1972 *Electron Paramagnetic Resonance* Edited by Geshwind S (Plenum NY)
 Renucci J B, Tyte R N and Cardona M 1975 *Phys. Rev.* **B11** 3885
 Spitzer W and Fan H Y 1957 *Phys. Rev.* **108** 268

Temperature dependence of phonon-magnon bound state

S. S. Shah and D. D. Deshmukh

Department of Physics, Marathwada University, Aurangabad-431002.

1. Introduction

In a magnetic system it is necessary to consider the simultaneous presence of both the excitations i.e., phonons and magnons. This study has become more important with the theoretical and experimental findings about the bound state with these excitations (Nagai *et al* 1973, Torrance *et al* 1973). It was observed that phonon and magnon form a bound state. Hence we have shown the possibility of bound state for the two-magnon one-phonon process from the energy considerations. In addition we feel that this bound state should exhibit temperature dependence. Using two particle Green's function we have seen the possibility of the phonon-magnon bound state and the variation of binding energy with the temperature.

2. Formulation of the problem

Here we formulate the problem of phonon-magnon bound state for general magnetic systems (Shah *et al* 1976). We consider the two magnon-one phonon interaction for which the hamiltonian can be written as

$$H = \sum_k W_k^m b_k^\dagger b_k + \sum_q W_q^p a_q^\dagger a_q + \sum_{k,q} \phi_{kq} b^\dagger_{k-q} b_k (a_q^\dagger - a_{-q}) \quad (1)$$

where W_k^m , W_q^p are the magnon and phonon energies, b_k^\dagger , b_k and a_q^\dagger , a_q are the creation and annihilation operators for magnons and phonons respectively and ϕ_{kq} is the phonon-magnon coupling coefficient. Values of coupling co-efficient are known from the literature (Sinha *et al* 1962, Ghatak 1972).

Now we define two particle Green's function as follows

$$G = \ll b_k(t) a_q(t); b_{k'}^\dagger(t') a_{q'}^\dagger(t') \gg. \quad (2)$$

Constructing the equation of motion for this Green's function using the above hamiltonian and taking the energy fourier transform, we get

$$(E - W_k^m - W_q^p) G = \frac{(1 + N_k^m + N_q^p)}{2\pi} + \phi_{kq} (1 + N_q^p + N_k^m) \ll b_{k+q}; b_k^\dagger a_{q'}^\dagger \gg. \quad (3)$$

Again we set up equation of motion for the Green's function $\ll b_{k'+q}; b_{k+a_q}^+ \gg$ to get

$$(E - W_{k+q}^m) \ll b_{k+q}; b_{k'+a_q}^+ \gg = \ll \phi_{kq} b_k(a_{-q} - a_q); b_{k'+a_q}^+ \gg. \quad (4)$$

We repeat the above procedure to solve the two Green's functions involved in eq. (4). Substituting the values of Green's functions so obtained into eq. (4), we get

$$\begin{aligned} & \left[E - W_{k+q}^m - \frac{\phi_{kq}^2 (N_k^m - N_q^p)}{(E - W_k^m + W_q^p)} \right] \ll b_{k+q}; b_{k'+a_q}^+ \gg \\ & = -\phi_{kq} \ll b_k a_q; b_{k'+a_q}^+ \gg. \end{aligned} \quad (5)$$

Substituting eq. (5) in eq. (3) we finally get the desired Green's function

$$i \left[\frac{(1 + N_k^m + N_q^p)}{2\pi} \left[\frac{E - W_k^m - W_q^p + \frac{\phi_{kq}^2 (1 + N_k^m + N_q^p)}{\phi_{kq}^2 (N_k^m - N_q^p)}}{E - W_{k+q}^m - \frac{\phi_{kq}^2 (N_k^m - N_q^p)}{(E - W_k^m + W_q^p)}} \right] \right] \quad (6)$$

It is clear from the above Green's function that the pole of this Green's function corresponds to the energy of the phonon-magnon bound state.

3. Results and discussion

In order to simplify the calculations we take $N_k^m \simeq N_q^p$ which is fairly true at the very low temperatures. Thus the binding energy is given by

$$\frac{\phi_{kq}^2 (1 + N_k^m + N_q^p)}{(E - W_{k+q}^m)}.$$

The denominator of this term should be positive for the formation of bound state, i.e., $E > W_{k+q}^m$. The temperature dependent part is associated with the terms N_k^m and N_q^p . Their explicit forms at very low temperature can be written as

$$N_k^m = e^{-Dk^2/kT} \text{ and } N_q^p = e^{-hw_q/kT}.$$

With suitable choice of ϕ_{kq} the binding energy can be obtained.

References

- Ghatak S. K. 1972 *Phys. Rev.* **B5**,
 Nagai et al 1973 *Phys. Rev. Lett.* **31**
 Shah et al 1976 *Proceedings of Indian Science Congress*.
 Sinha et al 1962 *Phys. Rev.* **127** 432.
 Torrance et al 1973 *Phys. Rev. Lett.* **31**.

Effect of post-deposition heat treatment on the electrical resistance and structure of germanium films

B. S. Naidu, S. Mohan and P. Jayarama Reddy

Department of Physics, S. V. U. College, Tirupati-517502

Thin films of germanium (330 to 1750 Å) were prepared by evaporating specpure (JM) germanium from resistance heated tungsten baskets onto well cleaned goldseal glass slides, maintained at room temperature. The pressure in the vacuum chamber was $\sim 10^{-6}$ torr during deposition. The deposition rates were controlled by a quartz crystal thickness monitor and were maintained around 30 Å/sec. The film thickness was measured using Fizeau's multiple beam interference technique. Thick silver electrodes were predeposited onto the substrate and connections made through pressure contact system to enable resistance measurements in vacuum immediately after film formation. The in-situ measurements of film resistance were made as a function of temperature with a Keithley 620 Electrometer during the annealing cycles. When the films were heated slowly to around 150°C and then cooled to room temperature, there was a slight rise in resistance. But, further heating to temperatures higher than 150°C, resulted in a marked fall in resistance. This significant decrease in resistance was observed at temperatures less than 300°C in thicker films where as it was not seen below 300°C in thinner films, thereby showing a strong thickness dependence. Structural observations carried out with the Hitachi HU11E transmission electron microscope indicated that this large change in resistance was due to crystallisation and the structure changing from amorphous to crystalline state.

1. Introduction

The influence of deposition parameters on the structure of germanium films and the effect on the transport properties have been investigated by various workers (Mott and Davis 1971, Grigorovici 1972). The factors that are found to affect the film structure are film substrate combination which decides the lattice mismatch, surface contamination of the substrate, substrate temperature during deposition, rate of deposition and impurity content, vacuum conditions, film thickness and post deposition heat treatment. It has been shown that amorphous structure results if the film is formed on an amorphous substrate maintained at ordinary or low temperature due to the low adatom mobilities at these temperatures. Now if these films are heat treated two things can happen (a) annealing of defects leading to an ideal amorphous state and (b) structural transformation at some high temperature.

In the present work we report the effect of post-deposition heat treatment on the structure and electrical resistance of germanium films formed on goldseal glass substrates maintained at room temperature. The purity of the material (germanium), the deposition rate and vacuum conditions are maintained to be the same for all the films investigated. The structural observations as revealed in the electrical resistance data are supported by the electron diffraction patterns.

2. Experimental

Specpure (JM) germanium is evaporated from resistance heated tungsten baskets onto well cleaned goldseal glass slides maintained at room temperature in a vacuum of 10^{-6} torr. Four films are formed at a time, one for resistance measurement, two for structural observations and the other for thickness measurement. The distance between the source and the substrate has been arranged in such a way that four films could be formed which are of equal thickness. The deposition rates are controlled by a quartz crystal thickness monitor and are maintained around $30 \text{ \AA}/\text{sec}$. Thick silver electrodes predeposited onto the substrate make contacts with the films. Electrical connections are made by spring loaded pressure contact system from which connecting leads are taken out of the vacuum chamber to enable resistance measurements immediately after the film formation. After formation the film is allowed for natural aging (until the resistance has reached a stable value). Then the substrate temperature is gradually raised simultaneously following the variation in film resistance. A chromel-alumel thermocouple fixed onto the film side of the substrate measures the substrate temperature. The in situ measurement of film resistance is made as a function of temperature with a Keithley 620 Electrometer. After natural aging, the films are heated slowly to around 150°C and then cooled to room temperature. Once again the films are heated slowly to temperatures higher than 150°C .

Tolansky's multiple beam interference technique is employed for thickness measurement. The thickness of the film is determined to an accuracy of $\pm 10 \text{ \AA}$.

The structure of the films, after the annealing cycles, are observed under a transmission electron microscope Hitachi HU11E operated at 100KV.

3. Results and discussion

The insitu variation of films resistance with temperature for two typical films is shown in figures 1 and 2. ABC represents the first annealing cycle which results in an increase in resistance due to annealing of some defects. CBDE represents second annealing to a higher temperature. In Fig. 1 the resistance is increased where as in Fig. 2 it is decreased after the second annealing. This behaviour indicates that the first film continues to be amorphous with some more defects getting annealed out where as the second one undergoes structural change (as shown by the steep fall in resistance during CBD) from amorphous state to poly-

crystalline state. The electron diffraction pattern taken on this film (Figure 3) after the first annealing and the second annealing cycles clearly support the above conclusion. All the films with thickness $< 1000 \text{ \AA}$ are found to behave similar to the one shown in Fig. 1 where as all the thick films ($t > 1000 \text{ \AA}$) exhibit the behaviour shown in Fig. 2. The temperature region in which this structural transformation has taken place is found to be $250^\circ\text{--}300^\circ\text{C}$ for films $t > 1000 \text{ \AA}$. It may be that if the thin films ($t > 1000 \text{ \AA}$) are heated to much higher temperatures crystallinity may set in.

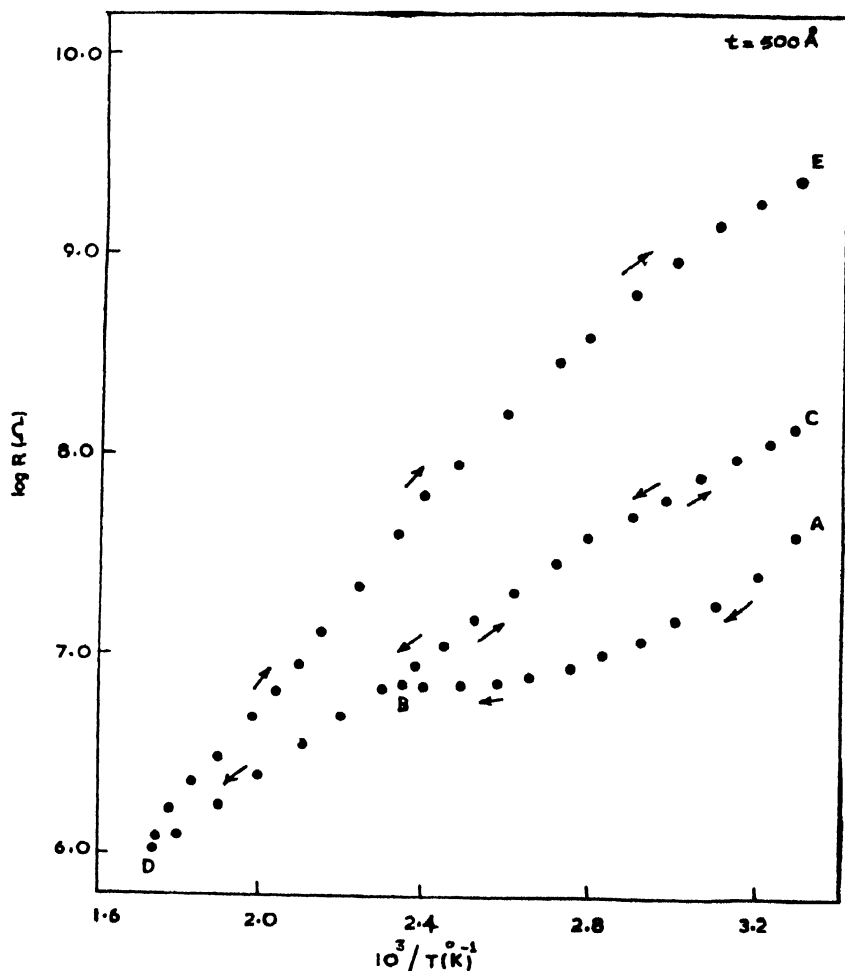


Figure 1. Log R vs $1/T$ curves for a film of thickness 500 \AA

Theye *et al* (1973) showed that the germinium films ($100\text{--}1000 \text{ \AA}$) formed on glass substrates at room temperature were amorphous in nature and that heat treatment upto 400°C did not alter the nature of the films. As the films were heated successively to increasing temperatures within 400°C , more and more

defects were eliminated and the films tend to an ideal amorphous state. These films ($t < 1000\text{\AA}$) however showed transition when heated to 420°C . But as Theye *et al* limited their investigations to only 1000\AA , whether the transition would be observed at the same temperature in thicker films could not be established. Walley and Jaoscher (1967) deposited germanium films ($350\text{--}4500\text{\AA}$) on corning 7059 glass and observed the transformation in the range $450^\circ\text{--}500^\circ\text{C}$.

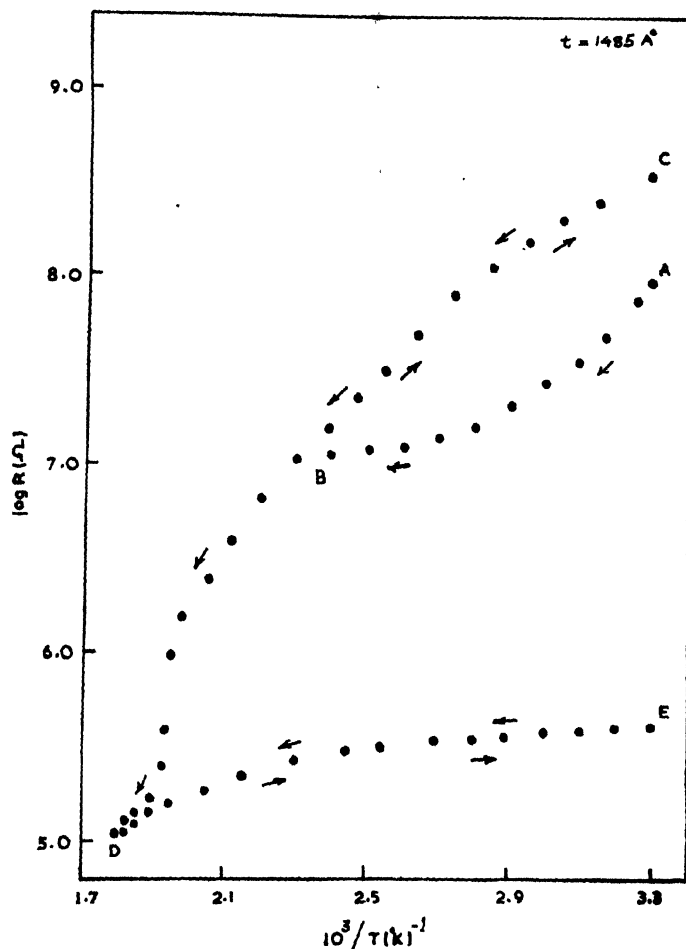


Figure 2. $\log R$ vs $1/T$ curves for a film of thickness 1485\AA

Chopra and Bahl (1970) observed a steep fall in resistance at 450°C in germanium films (1000\AA to 7μ) formed on glass substrates. The transformation was complete within a temperature increment of 25°C . Chik *et al* (1976) studied the temperature dependence of resistivity of germanium films ($100\text{--}3800\text{\AA}$) deposited on glass slides and observed the recrystallisation to take place in the temperature range $300^\circ\text{--}360^\circ\text{C}$.

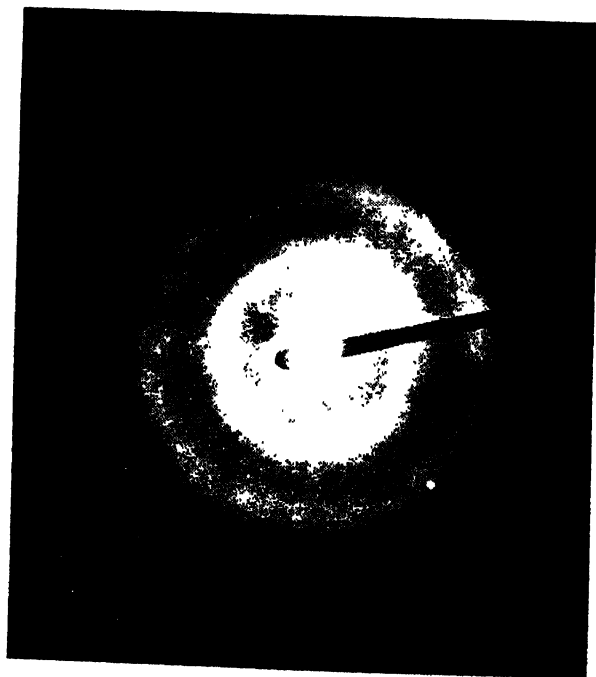
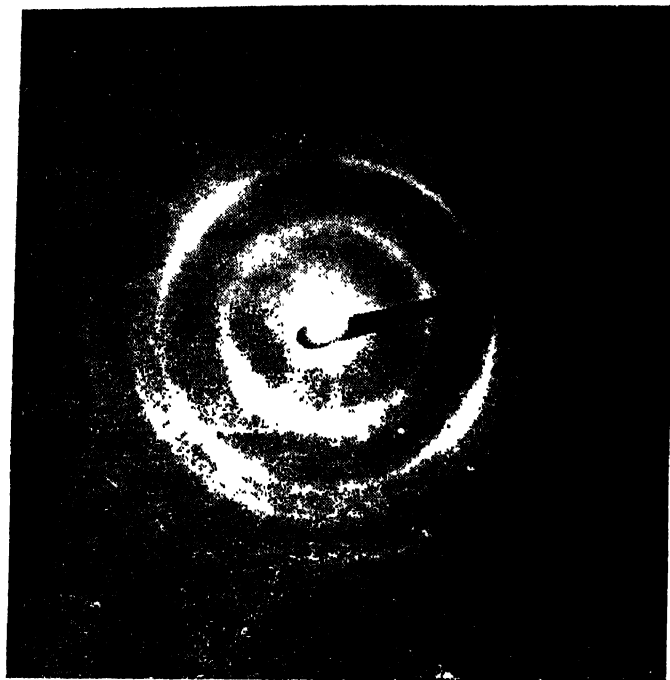


Figure 3. SAD of a film of thickness 1485Å (a) after first annealing (b) after second annealing

A comparison of our results with those of the above workers reveal that the transformation is taking place at relatively lower temperatures in our films ($t > 1000\text{\AA}$). Also in films $t < 1000\text{\AA}$ no such transformation is observed even though the deposition conditions are maintained to be the same. This clearly shows that the degree of amorphous nature is dependent on thickness also. In the case of thicker films ($t > 1000\text{\AA}$) the initial layers of germanium might have helped in creating conditions for autoepitaxy.

Further investigations to obtain ideal amorphous films and to investigate structural changes by heat treatment for the entire range of thickness ($100\text{-}2000\text{\AA}$) are under progress.

Acknowledgments

One of the authors (PJR) is thankful to UGC for the sanction of a research scheme to carry out this work. The authors are also thankful to Dr. R. V. Krishnan, Electron microscope laboratory, N.A.L., Bangalore for helping them with the electron microscope work.

References

- Chik K. P. and Pui-Kong Lim 1976 *Thin Solid Films* **35**, 45.
- Chopra K. L. and Bahl S. K. 1970 *Phys Rev.* **B1**, 2545.
- Grigorovici R. 1971 *Thin Solid Film* **9**, 1.
- Mott N. F. and Davis E. A. 1971 *Electronic processes in non crystalline materials*, Clarendon Press, Oxford
- Theye M. L., Gandais M. and Fisson S 1973 *Phys. Stat. Sol. (a)* **17**, 643.
- Walley P. A. and Jonscher A. K. 1968 *Thin Solid Films* **1**, 367.

Ideal strength of some monovalent metals with a pseudopotential model

A K Mitra

Department of Physics, Regional Engineering College, Durgapur-9, West Bengal

and

P K Sengupta

Department of Physics, University of Burdwan, Burdwan, West Bengal

Abstract. By ideal strength is meant the theoretical upper limit to the mechanical strength of a perfect crystal of the metal. The mechanical stability of a homogeneously deformed lattice, under a uniaxial stress, is studied by applying the Born stability criterion, i.e., by investigating the effect of superposition, on the primary deformation, of arbitrary, very small, homogeneous deformations. As a model of interatomic interactions, the pseudopotential formalism which provides a fairly realistic quantum-mechanical estimation of the energy of the ion-electron system is used in contrast to the simplified empirical interatomic potential functions so far used by other authors, and an effective two-body central-force ion-ion interaction potential is obtained. The energy-wave-number characteristic is computed by using Ashcroft bare ion form factor (based on a local pseudopotential approximation) in conjunction with a modified Hartree dielectric function (representing the screening of the bare ion by the conduction electron gas) which includes exchange and correlation effects and takes into account the orthogonality correction for the charge-density of a conduction state. Calculations of ideal $< 100 >$ uniaxial tensile and compressive strengths are performed for body-centered-cubic lattices of the three alkali metals, sodium, potassium and lithium. Agreement with experimental observations invariably improves.

1. Introduction

Few authors (Macmillan 1969, Milstein 1971) have made attempts to apply the stability criteria developed by Max Born (1940) to study the mechanical stability of metal crystals in the presence of applied forces and deformations, and to calculate the ultimate strength of metallic solids in a more appropriate manner. Also the earlier authors used simple interatomic potential models which were but poor representations of the state of affairs within a metal. In the present work the pseudopotential theory (Harrison 1966) which is a quite rigorous quantum-mechanical model for a metal has been used and an effective interionic

potential function derived. The structure-dependent part of the total energy of the crystal so obtained consists of an ion-ion coulomb energy and an ion-electron-ion band-structure energy. The latter has been calculated with the Ashcroft Model Potential (Ashcroft 1968) and the Hubbard-Sham (Hubbard 1958, Sham 1965) dielectric screening function including the orthogonality correction of Animalu and Heine (1965). The Born stability criteria have been examined for the deformed lattice at various applied stresses and the strengths in tension and compression calculated. Specific calculations have been performed with the three monovalent simple metals, sodium, potassium and lithium when a stress is applied along $\langle 100 \rangle$ crystal axis.

2. The born stability criteria

For a crystal lattice homogeneously deformed under applied forces to be stable, the total system (crystal plus applied forces) potential energy must be at a minimum. So if on the primary deformation is superposed an additional arbitrary, but very small, homogeneous deformation, the total system potential is increased.

That is,

$$\sum_i \sum_j \left(\frac{\partial^2 E}{\partial a_i \partial a_j} \right)_0 \delta a_i \delta a_j > 0 \quad (1)$$

for stability, provided that

$$\left(\frac{\partial E}{\partial a_i} \right)_0 = F_i^0$$

are the forces acting on the lattice in the initial state.

3. Effective interaction between ions in pseudopotential formalism

An ion-ion pair interaction potential based on pseudopotential theory has the form

$$V(r) = \frac{Z^2 e^2}{r} + \frac{\Omega_0}{\pi^2} \int_0^\infty v(q) \frac{\sin qr}{qr} q^2 dq, \quad (2)$$

where

$$v(q) = -\frac{\Omega_0 q^2}{8\pi e^2 [1 - f(q)]} \cdot |w_b(q)|^2 \frac{\epsilon(q) - 1}{\epsilon(q)} \quad (3)$$

Z is the effective valence and $G(q)$ is the energy-wave-number characteristic. $\epsilon(q)$ is the modified Hartree dielectric screening function corrected for exchange and correlation effects, present in an interacting conduction electron gas, and is expressed as

$$\epsilon(q) = 1 + [1 - f(q)] \frac{2K_F m e^2}{\pi \hbar^2 q^2} \left\{ 1 + \frac{4K_F^2 - q^2}{4K_F q} \ln \left| \frac{2K_F + q}{2K_F - q} \right| \right\}, \quad \dots \quad (4)$$

with

$$f(q) = q^2/2(q^2 + K_F^2 + q_s^2), \quad (5)$$

where $q_s^2 = 2K_F/\pi a_0$, is a screening length, a_0 being the Bohr radius.

In Ashcroft local pseudopotential model, the bare-ion form-factor is calculated to be

$$w_b(q) = -\frac{4\pi Ze^2}{\Omega_0 q^2} \cos(qr_c), \quad (6)$$

r_c being a suitable ion-core radius.

4. Calculations for uniaxial stresses

Starting with the equilibrium value when all F_i are zero, the lattice parameter a_1 is incremented by steps. In each state, the applied stress is calculated and the validity of (1) examined. The point at which any one stability criterion is first violated indicates entrance into the region of instability and the corresponding maximum stress denotes the theoretical tensile strength of the metal under given test conditions. In a similar manner, the theoretical compressive strength of the metal could be determined.

5. Results and Discussion

The results of our calculations are shown in Table 1 below.

Table 1. Ideal strength of bcc alkali metals in tension and compression

Uniaxial tension and Compression	Metal	Equilibrium lattice parameter in a.u.	Max. stress or theoretical strength $\times 10^{-8}$ dynes/cm ²	Max. strain
<100> tension	Li	6.5800	3.9	0.0113
	Na	8.2500	4.2	0.0157
	K	9.8600	5.3	0.0189
<100> Compression	Li	6.5800	-2.6	-0.0038
	Na	8.2500	-9.7	-0.0085
	K	9.8600	-7.8	-0.0069

No experimental observations on the strength of these particular metals were available to us. In fact, we doubt whether there has been any strength measurement with the alkali metals of reliable accuracy.

Yet we chose them for our calculations because these simple metals with non-overlapping ion-cores satisfy the conditions of the pseudopotential theory very well and are most suitable for being treated with the said theory. Nevertheless, our calculated tensile strength values are comparable with the experimental

tensile strength measured with another bcc metal Fe under similar conditions by Brenner (1956). With modified pseudopotential form factors to include the effects of overlapping *d*-bands, calculations may be done for useful noble and transition metals. Presently we are trying to do it.

Acknowledgment

The authors convey their thanks to the University of Burdwan for providing the necessary fund for computations.

References

- Animalu A O E and Heine V 1965 *Phil. Mag.* **12** 1249
Ashcroft N W 1968 *J. Phys.* **C1** 232
Born M and Fürth R 1940 *Proc. Cam. Phil. Soc.* **36** 454
Brenner S S 1956 *J. Appl. Phys.* **27** 1484
Harrison W A 1966 *Pseudopotentials in the Theory of Metals*, Benjamin, New York
Hubbard J 1958 *Proc. Roy. Soc.* **A243** 336
Macmillan N H 1969 *Ph.D. Thesis*, Cambridge University
Milstein F 1971 *Phys. Rev.* **B3** 1130
Sham L J 1965 *Proc. Roy. Soc.* **A283** 33

Extinction in the case of aggregate of distorted crystallites

G B Mitra, B K Samantaray and B K Mathur

Department of Physics, Indian Institute of Technology, Kharagpur-721302.

Abstract. One of the important factors affecting the measured intensity of X-rays diffracted by matter is what is known as extinction. Apart from interactions involved in primary and secondary extinctions, there is a third type of interaction in powder diffraction, between the incident beam and the beams diffracted from all preceding grains. Applying Zachariasen's mathematical technique (Zachariasen 1967, *Acta. Cryst.* 23, 558-564), an expression has been arrived at for the intensity diffracted by a powder specimen taking into account the above interaction. This expression also allows for primary and secondary extinction. The treatment has been extended to aggregates of crystallites containing defects of various types and corresponding expressions have been derived.

1. Introduction

One of the important factors affecting the measured intensity of X-rays diffracted by matters is what is known as extinction. In case of usual calculations the intensity of the incident X-ray beam arriving at different points of the diffracting matter is assumed to be the same. However, it is quite easy to see that in actual cases, this assumption can not be taken to be valid. The intensity of the incident X-rays while traversing various points in matter go on decreasing due to parts of X-rays being diffracted away in other directions and also go on fortifying and replenishing itself due to waves diffracted in the direction of its propagation due to multiple diffraction of waves originally diffracted in other direction. Thus, the incident wave and all the diffracted waves form a coupled system. A rigorous mathematical solution of this problem is highly complicated and generally a two beam approximation is made. This means that the wave diffracted in the direction H is due to the incident wave and the wave diffracted in the direction H interacting between themselves. The effect of waves diffracted in other directions e.g., H_1 , H_2 , H_3 etc. are considered negligible for calculating the wave in the direction H . This formalism was first of all used by Darwin who derived an expression for the waves reflected by a column of identical planes stacked parallelly and in regular sequences. The incident beam, as it travels deeper and deeper amidst the identically spaced planes is taken to be depleted at each plane due to the plane diffracting according to Bragg's law and is also strengthened by the Bragg reflection at the other side of the diffracting plane.

This presupposes a perfect crystal with all its atoms arranged properly as per its lattice and space group symmetry. If I_d be the intensity of the resultant diffracted wave and I_k that calculated assuming no interaction between the incident and diffracted waves, then

$$I_{d_1} = I_k y_1 \quad (1)$$

where y is known as the coefficient of extinction. If I_d and I_k concern waves diffracted by a single crystalline domain consisting of a regular stacking of periodically arranged atomic planes, y is said to be the coefficient of primary extinction and the phenomenon of coupling between the incident and diffracted waves is called primary extinction.

However, comparison with experiments for single crystals shows that the actually measured intensity $I_{measure}$ agrees more with I_k than with I_{d_1} . This was explained by Darwin (1922) by assuming that a single crystal consists of differently oriented small domains of crystals forming a mosaic. Depending on the sizes of the mosaic blocs, y will have appreciable or negligible values. Due to the space incoherence caused by misorientation between the different blocks, the intensities diffracted by the different blocks are added. If each block has the same size—say an average size and if each block receives the same intensity and assuming negligible primary extinction (since the number of diffracting layers in each block is small) so that $y_1 = 1$, we may write

$$I_d = NI_k \quad (2)$$

where N is the number of mosaic blocks irradiated and I_k the intensity diffracted by each block assuming no primary extinction. The incident wave, while transversing a distance T in the single crystal will encounter $n = T/d$ (with d the average size of the mosaic blocks) domains. Each domain will receive an incident intensity, depleted by intensities diffracted away by the preceding domains or blocks and supplemented by multiple diffraction by other blocks. Thus, the assumption of each block receiving and therefore scattering in a particular direction, the same intensity which leads us to eq. (2) above is not valid. In this case, again, there will be interaction between the primary beam incident on the crystal and the diffracted beams and we shall obtain

$$I_{d_2} = NI_k y_2 \quad (3)$$

where I_{d_2} is the intensity diffracted in the given direction taking into account this second type of interaction and y_2 is called the coefficient of secondary extinction and this type of interaction is known as secondary extinction.

It is quite obvious that in a given single crystal both primary as well as secondary extinctions may be operative. However, till recently, very little work was done to correct for or estimate the nature and extent of extinction in

crystals. Recently, however, much interest is taken to explore this effect. However, all effort seems to be concentrated on correction of extinction in single crystals only. Very little work has been done to investigate extinction in polycrystalline specimens. It, again, is obvious that there will be a third type of interaction between the incident and diffracted waves in polycrystals. Each crystallite will receive an incident beam whose intensity is modified by the diffractions due to the preceding crystallites. Diffractions due to preceeding crystallites may be subjected to both primary as well as secondary extinctions. So, we may call this type of interaction, a third type of extinction or 'tertiary' extinction. Qualitatively, this tertiary extinction is of the same type as secondary extinction and its effect will be to modify the secondary extinction. Quantitatively, however, there are two marked differences, viz.

(1) while the angle of misorientation between mosaic blocks in secondary extinction is very small, of the order of seconds, often—the angle of misorientation between crystallites in an aggregate of polycrystals will be quite large. In fact, all angles from 0 to 2π are expected with equal probability.

(2) The interaction is weak and may be taken to consist of depletions of the incident beam intensity due to scattering by previous crystallites without any fortification or supplementation by multiple scatterings in the direction of the incident beam. The tertiary extinction is thus equivalent to an increase in the effective absorption coefficient. However, quantitatively, the diffracted intensity will be different if this phenomenon is not taken into account.

The phenomenon of the tertiary extinction has not been studied by any previous author. Even the existence of this special type of interaction has not been noticed by previous workers. The aim of the present work is to explore the consequences of this factor on the integrated intensity and the line profile.

Darwin (1922) showed that secondary extinction resulted in an apparent increase in the absorption factor and obtained an expression for the correction factor for primary extinction arising in a perfectly crystalline slab having infinite lateral dimensions. Waller (1926) and Ekstein (1951) have also deduced expressions for extinction. While the formulae due to Darwin (1922) and Waller (1926) are valid for integrated intensity, Ekstein (1951) equation holds good for intensity at the Bragg angle only. Besides these, Ewald (1916), Laue (1931) and following them a large number of workers have dealt with this problem of interaction between incident and diffracted waves from different point of views. Zachariasen (1967) has developed a general theory of X-ray diffraction in a finite crystal on the basis of an approximate treatment of the coupling between incident and diffracted beams which is claimed to be valid over the entire range from perfect to ideal mosaic crystals. Zachariasen's (1967) work was initially acclaimed and put to great use and was even extended to anisotropic extinction cases by Coppens and Hamilton (1970). Soon, however, shortcomings to Zachariasen's

theory were pointed out mainly by the experimental work of Cooper and Rouse (1970). Becker and Coppens (1974, 1975) reconsidered the problem and gave a general approximate solution which resembles the Zachariasen's formalism to a great extent. Starting from the dynamical theory of Taupin (1964) and Takagi (1962, 1969, 1975), Kato (1975) and Zigan (1975) formulated a rigorous theory which takes into account both primary and secondary extinction and also lattice defects in general terms of a correlation length. For powder cases, very little work has been carried out so far. Mitra and Chattopadhyay (1975) have discussed the previous works and have developed a method for correcting the integrated intensities of powder patterns using Zachariasen's formulae. They have satisfactorily applied the same in the case of several f.c.c. metals and alloys.

According to Zachariasen's theory (1967) of extinction, y the extinction factor which is the ratio of the integrated intensity of the diffracted beam and its kinematical approximation, is given as,

$$y = (1 + 2K_L\chi_0)^{-1} \quad (4)$$

$$\chi_0 = \beta Q_0 \left[i + \frac{\bar{T} - i}{\sqrt{1 + (\beta/g)^2}} \right]$$

$$\beta = \frac{2}{3} \frac{t_1}{\lambda}$$

$$Q_0 = \left(\frac{e^2}{mc^2} \right)^2 \frac{N^2 A^2 \lambda^2}{\sin^2 2\theta} \quad (5)$$

$$K_L = \frac{1 + \cos^2 2\alpha \sin^4 2\theta}{1 + \cos^2 2\alpha \sin^2 2\theta}$$

where $\bar{T} = -\frac{1}{A} \frac{dA}{d\mu}$ is the mean path through the crystal, μ the coefficient of

linear absorption, A the transmission factor, t the mean path through perfect crystal domain, t_1 the mean thickness of the domain measured normal to the incident beam and parallel to the plane of incidence, $0.664/g$ is the full width at half maximum of the angular distribution function of the mosaic blocks, N the number of unit cells per unit volume, F is the structure factor of the diffracting plane, α the Bragg angle corresponding to the reflecting plane of the monochromator crystal, e , m the charge and mass of the electron, c the velocity of electromagnetic radiation in vacuum. Eq. (5) consists of two terms, the first term represents the secondary extinction. For spherical domain of diameter D where $i = t_1 = 3/4D$ and if $(\beta/g) \gg 1$ then eqn. (4) can be written as

$$y = 1 - \frac{3}{8} \frac{D^2}{\lambda} Q_0 K_L - g \bar{T} Q_0 K_L.$$

As long as the absorption is quite small, Lang assumed $D = 0.7D'$, where D' is the diameter of the imperfect crystal mosaic which is assumed spherical. The above equation becomes,

$$g = 1 - \frac{3}{8} \frac{D^2}{\lambda} Q_0 K_L = 0.7D' Q_0 K_L. \quad (6)$$

In the Becker and Coppens (1974) formalism, \tilde{t} is to be substituted by $\tilde{t} \sin 2\theta/\lambda$.

2. The model

A, B, C etc. are grains of the polycrystal traversed by the ray PQ (figure 1) and so oriented with respect to it as to give rise to a particular Bragg reflection, H_1 .

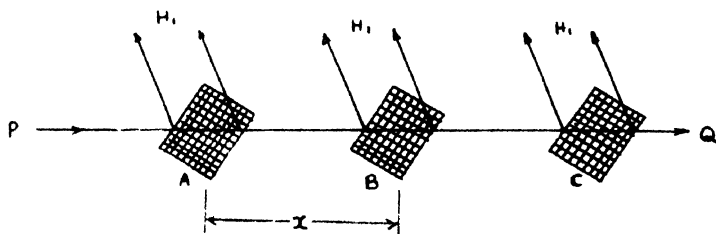


Figure 1. Schematic diagram of the model.

In between a pair of such grains, there are other grains (not shown in the figure) which do not take part in this particular Bragg reflection but merely act as absorbers of the incident radiation. Some of these grains will be so oriented as to give rise to other Bragg reflections (H_2, H_3, \dots , etc.) consistent with the space group of the crystal. The incident beam will be modified during transmission through the specimen not only by the absorption by the specimen material but also by diffraction at different directions by differently oriented grains. The diffracted beam along any particular direction will also be modified by similar process as well as by the modification of the incident beam. This interaction is, therefore, a multiple beam process. As in similar theories of dynamical diffraction, we retain the two beam approximation and shall assume that the reflection (H_1) is modified only by the diffraction (H_0) in the forward direction and is not influenced by other reflections (H_2, H_3, \dots , etc.).

Let the average separation along the path of the incident ray PQ of the grain oriented for the reflection be x . In the absence of any preferred orientation, x will be same for the reflections (H_1, H_2, \dots, H_n). Let the grain size be t while the sample thickness is T . Each grain is a mosaic of perfectly crystalline domain of size D and a misorientation factor g as defined by Zachariasen (1967). Each mosaic block diffracted power for unit volume and intensity for the particular reflection (H_1) considered. We start from the dynamical theory of Taupin

(1964) and Takagi (1962, 1969, 1975) which takes into account the local distortion of the lattice $\mathbf{U}(\mathbf{r})$ resulting in a space modulation of the amplitude of the wave in the crystal. Let \mathbf{K} be the wave vector of the incident wave, \mathbf{K}_0 and \mathbf{K}_H the wave vectors of the transmitted and diffracted waves, subject to the condition

$$\mathbf{K}_H = \mathbf{K}_0 + \mathbf{H}.$$

The displacement vectors \mathbf{D}_0 and \mathbf{D}_H of the two waves are

$$\mathbf{D}_0 = \mathbf{D}_{00}(\mathbf{r})e^{-2ni(\mathbf{K}_0 \cdot \mathbf{r} - \nu t)}$$

$$\mathbf{D}_H = \mathbf{D}_{H0}(\mathbf{r})e^{-2ni(\mathbf{K}_H \cdot \mathbf{r} - \nu t)}$$

Let t_1 and t_2 be the oblique coordinates of a point inside the crystal parallel to the incident and diffracted directions respectively. Let ξ_H be the H th Fourier component of the electrical susceptibility of the ideal perfect crystal given by

$$\xi_H = -\frac{e^2}{mc^2} \frac{\lambda^2}{4\pi^2 V} F_H$$

where F_H is the crystal structure factor of the crystal for the reflection H .

The Taupin-Takagi equation for the component of \mathbf{D} of a certain type of polarisation is given by

$$\frac{\partial}{\partial t_1} \mathbf{D}_0 = -i\pi K c \xi_H \mathbf{D}_H$$

$$\frac{\partial}{\partial t_1} \mathbf{D}_H = -i\pi K c \xi_H \mathbf{D}_0 + 2\pi i \beta'_H \mathbf{D}_H$$

with

$$\beta'_H = \frac{K_H - K}{K} = \frac{1}{K} \frac{\partial}{\partial t_2} (\mathbf{H} \cdot \mathbf{U}(\mathbf{r}))$$

and c the component appropriate for the given polarisation.

Starting from these equations, Kato (1975) derived the following equations

$$\frac{\partial I_0}{\partial t_1} = -[2\alpha\{\text{Re}(\xi_H \xi_{\bar{H}}) + \mu\}]I_0 + 2\alpha|\xi_{\bar{H}}|^2 I_H$$

$$\frac{\partial I_H}{\partial t_1} = -[2\alpha\{\text{Re}(\xi_H \xi_{\bar{H}}) + \mu\}]I_H + 2\alpha|\xi_H|^2 I_0$$

Here I_0 and I_H are average intensities over the domain containing the distortion, and α the correlation length which can be identified with the domain size in the direction under consideration. It is easily seen that

$$\begin{aligned} \text{Re}[\xi_H \xi_{\bar{H}}] &= |\xi_H|^2 = |\xi_{\bar{H}}|^2 \\ &= \left(\frac{e^2}{mc^2} \right)^2 \frac{\lambda^4}{(4\pi^2 V)^2} |F_H|^2 \end{aligned}$$

for wave lengths for which Friedel's law holds good. Comparing the above equation with the Zachariasen's (1967) equations,

$$\frac{\partial I_0}{\partial t} = -(\sigma + \mu)I_0 + \sigma I_H$$

$$\frac{\partial I_H}{\partial t} = -(\sigma + \mu)I_H + \sigma I_0$$

we find that

$$\sigma = \alpha Q$$

with

$$Q = \frac{1}{2} \left(\frac{e^2}{mc^2} \right)^2 \frac{\lambda^4}{(4\pi)^2} \frac{d^2}{\alpha^2}.$$

For a direction $(H + \epsilon)$ where ϵ is a slight departure in reciprocal space from the reciprocal lattice point, we have

$$\sigma(\epsilon) = \frac{\sin^2 \frac{\pi}{\lambda} \frac{\alpha}{d} \epsilon}{\sin^2 \frac{\pi}{\lambda} \epsilon}$$

Thus, we have been able to keep to Zachariasen's formalism with significances of terms modified in the light of Taupin-Takagi theory. Then eqns. (4) and (5) become applicable with significance of Q and α modified as above. When secondary extinction is present, due to angular misorientation between the domains, σ will be modified into

$$\bar{\sigma} = Q\bar{\alpha} \exp(-\pi_{\alpha}'^2 \epsilon^2) \quad (7)$$

with

$$\alpha' = \sqrt{2}g\alpha/\sqrt{\alpha^2 + 2g^2}. \quad (8)$$

3. Derivation of the intensity equation

Let I_0 be the intensity incident at the specimen surface i.e., at $T_1 = 0$, where T_1 is the distance in the specimen along the incident beam. A grain at a distance T_1 from the surface will receive at intensity

$$I'_0 = I_0 \exp(-\mu T) \exp \left(-\bar{\sigma} \frac{T_1}{\bar{x}} t \right) \quad (9)$$

due to absorption by the specimen mentioned of the thickness T_1 of the material and due to diffraction by T_1/\bar{x} grains each of size t and average diffracting power $\bar{\sigma}$ and on the basis of first order approximation in the solution of the differential equations describing the coupled transmission—diffraction process in each grain as described by Zachariasen (1967).

Let I''_0 and I'' be the transmitted and diffracted intensities by a grain T_1 and T_2 along the incident and diffracted beam directions respectively from the specimen surface. Then

$$\frac{dI''_0}{dT_1} = -(\mu + \bar{\sigma})I''_0 + \bar{\sigma}I'' \quad (10)$$

$$\frac{dI''}{dT_1} = -(\mu + \bar{\sigma})I'' + \bar{\sigma}I''_0 \quad (11)$$

with solution

$$I'' = I''_0 \exp(-\bar{\sigma}T_1)[1 - \exp(-\bar{\sigma}T_2)]. \quad (12)$$

If N be the total number of grains along a length T of the specimen, n of which are oriented for the reflection H_1

$$\bar{n}x = T$$

and n/N is the probability that a grain is so oriented such that (Compton and Alison 1935)

$$\frac{n}{N} = \frac{1}{2}j \cos \theta \cdot \Delta\theta \quad (13)$$

where $\Delta\theta$ is the angular spread through which the diffraction is possible and is given by

$$\Delta\theta = \frac{\epsilon_{MAX}}{d \cos \theta} \lambda \quad (14)$$

where ϵ_{MAX} is the range in reciprocal space around the particular lattice point, corresponding to the reflection H_1 , over which diffraction is appreciable, j is the multiplicity factor.

Hence, we have

$$P(\epsilon) = I_0 \bar{\sigma} V \frac{1}{V} \int e^{-\mu(T_1+T_2)} e^{-\bar{\sigma}\{(1+\beta)T_1+T_2\}} dV \quad (15)$$

where

$$\beta = \frac{j\lambda\epsilon_{MAX}}{2d}$$

Eqn. (15) can be written as

$$P(\epsilon) = I_0 \bar{\sigma} V \frac{A}{1 + \bar{\sigma}T} \quad (16)$$

where

$$A = \frac{1}{V} \int e^{-\mu(T_1+T_2)} dV \quad (17)$$

and

$$\bar{T} = \frac{\frac{1}{V} \int \{(1+\beta)T_1 + T_2\} e^{-\mu(T_1+T_2)} dV}{\frac{1}{V} \int e^{-\mu(T_1+T_2)} dV} \quad (18)$$

Eqn. (16) can be expanded to include all cases of particle size, strain stacking fault etc. through $\bar{\sigma}$.

4. Effect of particle size strain and stacking and twinning faults

Eqn. (7) for $\sigma(\epsilon)$ can be written as

$$\begin{aligned} \sigma &= \frac{Q\alpha \sin^2 \frac{\pi}{\lambda} \frac{\alpha}{d} \epsilon}{\sin^2 \frac{\pi}{\lambda} \epsilon} \\ &= Q\alpha \sum_{m=-M}^M (M - |m|) \cos 2\pi m\epsilon \end{aligned} \quad (19)$$

where $M = \alpha/d$, with d the lattice spacing. Substituting the average value $\langle F_p F_p^* \rangle_{p-m}$ for $|F|^2$ in eqn. (9), we can write

$$\sigma(\epsilon) = \frac{e^4}{m^2 c^4} \frac{\lambda^4}{8\pi^2 V^2} \frac{d^2}{\alpha^2} \sum_{m=-M}^M (M - |m|) \langle F_p F_p^* \rangle_{p-m} \cos 2\pi m\epsilon \quad (20)$$

Writing $A_m^D = (M - |m|)$ and $A_m^S = \langle F_p F_p^* \rangle_{p-m}$ we have

$$\sigma(\epsilon) = \frac{e^4}{m^2 c^4} \frac{\lambda^4}{8\pi^2 V^2} \frac{d^2}{\alpha^2} \sum_{m=-M}^M A_m^D A_m^S \cos 2\pi m\epsilon \quad (21)$$

$$= \text{Const} \sum_{m=-M}^M A_m \cos 2\pi m\epsilon. \quad (22)$$

Thus, eqn. (22) defines the line profile. Since in making measurements with line profiles, one deals with A_m/A_0 , the constant cancels out and one can proceed as usually.

The effect of extinction combining the three types described above is accounted for with the help of eqn. (16) which can be written as

$$P(\epsilon) = I_0 \sigma V A (1 - \sigma \bar{T} + \dots). \quad (23)$$

In actual procedure, one uses an iterative method. During the first iteration, one proceeds assuming no extinction and determines M the particle size and the strain and fault parameters. With these values $\bar{\sigma}$ is determined and substituted in eqn. (23) and the correction terms for each value of $P(\epsilon)$ of the line profile in (ϵ) is obtained. These corrected values of $P(\epsilon)$ are now used in redetermination of the Fourier coefficient from which the integral width, variance, fourth moment etc. can be determined.

It may be pointed out that σ and \bar{T} are both averaged out quantities assuming different particle sizes. σ is of the nature of absorption coefficient and can be calculated for different particle sizes by using the technique due to Mitra and Wilson (1960) according to whose eqn. (42), we have

$$\sigma = \langle \sigma \rangle = \frac{1}{4T} \sum_{i \neq j} (\sigma_i - \sigma_j)^2 M_{ij} \quad (24)$$

where $\langle \sigma \rangle = \sum_i p_i \sigma_i$ with p_i the proportion of particles with scattering power σ_i . σ_i can be determined from $\sigma_i a_i = \frac{\sigma}{a} a_i a = \frac{\sigma a_i}{a} a$ so that $\sigma_i = \frac{\sigma a_i}{a}$ and a is assumed to be equal for all particles. T is the total sample thickness crossed by the X-ray beam and M_{ij} is the second moment $\langle \xi_i \xi_j \rangle$ and ξ_i is the deviation from its mean value of any part length that it may be convenient to separate. \bar{T} is given by eqn. (23) where μ is the averaged out μ according to Mitra-Wilson (1960) formalism given by

$$\bar{\mu} = \langle \mu \rangle = \frac{1}{4T} \sum_{i \neq j} (\mu_i - \mu_j)^2 M_{ij}. \quad (25)$$

Here again $\mu_i = \frac{\mu}{a} a_i$ as in the case of σ_i .

Acknowledgments

The authors would like to thank Prof. A. McL. Mathiesen, C.S.I.R.O., Australia; Prof. N. Kato, Nagoya University, Japan; Prof. P. Becker, Centre National De La Recherche Scientifique, Paris and Prof. J. R. Schneider, Hahn-Meitner Institut for Kernforschung, Berlin for many valuable suggestions.

References

- Becker P and Coppens P 1974 *Acta Cryst.* **A30** 129
- Becker P and Coppens P 1975 *Acta Cryst.* **A31** 148
- Compton A H and Allison S K 1935 *X-rays in theory and Experiment* (D. van Nostrand N Y) p 414
- Cooper M J and Rouse K D 1970 *Acta Cryst.* **A26** 213
- Coppens P and Hamilton W C 1970 *Acta Cryst.* **A26** 71
- Darwin C G 1922 *Phil. Mag.* **43** 800
- Ekstein H 1951 *Phys. Rev.* **83** 721
- Ewald P P 1961 *Ann. Physik* **49** 1 117
- Koto N 1975 *Xth International Union of Crystallography Congress Amsterdam*
- Laue M von 1931 *Ergele. Exakt. Naturw.* **10** 133
- Takagi S 1962 *Acta Cryst.* **15** 1311
- Takagi S 1969 *J. Phys. Soc. Japan* **26** 1239
- Takagi S 1975 *International Summer School on X-rays Limoges*
- Taupin D 1964 *Bull. Soc. Trans. Min. Cryst.* **87** 469
- Waller L 1926 *Ann. Phys. Lpz.* **79** 261
- Zachariasen W H 1967 *Acta Cryst.* **23** 558
- Zigan F 1975 *Xth International Union of Crystallography Congress Amsterdam*

A preliminary study of the changes in X-rays reflected by a piezoelectric crystal when subjected to an oscillatory electric field

G. B. Mitra and Leela Kar

Department of Physics, Indian Institute of Technology, Kharagpur.

1. Introduction

When piezoelectric crystals are subjected to oscillatory electrical fields, a thickness vibration in the crystal sets in. This vibration is maximum at a given frequency called the resonant frequency. The resonance frequency depends on the thickness of the crystal as well as the crystallographic direction of the thickness of the crystal slab besides depending on the nature of the crystal. This thickness vibration must correspond to atomic vibrations of the same frequency as the resonance frequency traversing the crystal and must result in modifications of X-rays coherently diffracted by the crystal besides causing other changes like changes in Debye-Waller factor and T.D.S. and D.D.S. The frequency of the resulting vibrations is so low compared to that of X-rays (e.g., 10^4 Hz for piezoelectric vibrations compared to 10^{18} Hz for X-rays) that the probing X-ray photons will "see and report" the atomic arrangements in the crystal to be modulated by the thickness vibration. Hence the X-ray diffraction pattern is expected to be noticeably modified by the externally imposed electric field.

The first investigators of this phenomena were Fox and Carr (1931) who reported an increase in intensity of the reflected spots when subjected to electric oscillations. The observed increase in intensity was probably due to reduction in extinction but in those days a Debye-Waller type of reduction in intensity was expected. Warren and Krutter (1933) sought to explain the increase in intensity by assuming that, given a slight rocking, various planes were brought into proper orientation for reflection of a given wave length. Langer (1933) dismissed Warren's explanation with some very logical arguments, giving his own interpretation in terms of misorientations of the 'Zwicky blocks' in mosaic crystals under oscillation. In fact, by assuming a certain degree of misorientation, he was able to give a quantitative estimation of this increase which, according to his treatment, worked out to be as much as 30 times for a relative misorientation of $8'$. However, Fox and Cork (1931) had already reported that the reflected intensity in the Bragg position remained unchanged under piezoelectric oscillations negating the 'Zwicky block' idea of Langer (1933). They proceeded

to explain the observed change in intensity as a chance result of reduction of extinction and modification of the absorption coefficient. Colby and Harris (1933) also working with quartz report that though an increase in intensity was observed at the peak, the diffuse scattering in the background remained unchanged under oscillating conditions. They argue that there is no reason why a change in the primary extinction effect should not alter the diffuse scattering intensity while they are of opinion that secondary extinction effects should not influence the same. They, therefore, conclude that since the diffuse scattering remains unaltered, the increase in intensity of X-ray reflections due to piezoelectric oscillations is attributable only to a reduction of the secondary extinction effect. It was argued that a complementary change should occur in the transmitted beam intensity. However, there remains a controversy regarding this point because, though Fox and Frederick (1938) report just such a change, Jauncey and Deming (1935) were unable to reproduce this observation. Nisikawa, Sumoto and Sakisaka (1931) also report an increase in reflected intensity due to piezoelectric oscillations explaining it in terms of inhomogeneous strains setting in within the crystal. A similar effect was observed by them on application of (a) a thermal strain caused by a temperature gradient in a certain direction, (b) a non-uniform mechanical stress producing heterogeneous strain. No such effect was observed on application of a uniform electrical field. Similar increase in intensity in neutron diffraction patterns have been reported by Parkinson and Moyer (1961) and by Klein, Prager, Wagenfeld, Ellis and Sabine (1967).

Reviewing the entire work in this field, it is evident that no conclusive, unanimously accepted result of the application of oscillatory electric fields on piezoelectric crystals is available. From the consideration of vibrations a reduction in intensity is expected. Reduction in crystal perfection due to oscillation need not necessarily result in an increase in intensity of the order observed. Moreover, there has been a report of intensity remaining unchanged in the tail region of the intensity distribution curve. Because of this controversy and because since the late thirties no experimental work in this field has been reported—while, in the meantime, an enormous amount of improvement in the measurement of intensities has been achieved—the present work of re-examining the whole issue has been undertaken. It is proposed to present here experimental results on modification of intensity of X-rays reflected from a given set of planes of given slab of quartz when subjected to resonant vibrations due to an externally impressed oscillatory electric field. It is further proposed to present a suitable theory to explain the observed results.

2. Experimental Arrangements

A rectangular slab of a uniformly thick quartz single crystal giving a strong (101) reflection was chosen for the present experiment. A Debye-Sears (1932) type

of experiment in which the crystal was made to vibrate parallel to its thickness by applying a suitable oscillatory electric field was carried out. This vibrating crystal was placed in a transparent vessel containing carbon tetrachloride which became stratified because of the vibrations transmitted to it from the crystal resulting in a virtual grating of grating constant equal to the wavelength of the transmitted vibrations. Optical measurement of the 'grating constant' gave the wavelength of the vibrations which combined with the knowledge of the velocity of sound in the liquid medium (for carbon tetrachloride—830 m/sec.) gave the frequency of oscillations to be 0.687 mega Hertz. The oscillator was of push-pull tuned plate type capable of yielding frequencies in the range of 0.08 to 2.00 mega Hertz and a very stable output.

In order to study the effect of piezoelectric oscillations on the X-ray reflections, out put from the oscillator was connected to two suitable probes consisting of two brass plates cut in the shape shown in figure 1(a). Since proper mounting is very essential for stable resonance conditions to be obtained, the crystal placed between the two brass plate probes was held rigidly within a case made of perspex by means of four adjustable screws. This type of 'corner clamping' has the advantage of suppressing flexural modes. This also leaves an air gap between the crystal and the probes which is desirable since it reduces damping. Also, a better resonance condition may be obtained with such an arrangement.

The entire arrangement was mounted with the help of a specially hard wax on to the goniometer which was fabricated specially for the present purpose. An arrangement for rotating the crystal about a vertical axis by a desired amount was provided.

X-rays were obtained from a Norelco unit using copper target. A preliminary run was made on a Philips diffractometer obtaining the complete diffraction pattern of the quartz plate over the entire angular range. Of the two sharp peaks obtained corresponding to (101) and (202) reflections—the former, being a very strong reflection, was chosen for the present investigation. The peak angle was found to be 13.4° in

The crystal in its mount was placed on the goniometer with its 'b' axis vertical. Copper K radiation monochromatised by reflection from a calcite crystal were made to fall on the quartz crystal through a hole in the probe plate—the crystal being placed in the reflection Bragg position. The reflected X-rays were recorded with the help of a geiger counter while at rest and while under the application of an oscillating resonant electric field. This was repeated for different values of the angle, on either side of the peak value of 13.4° . In this way, X-ray reflections over an angular range of 8° to 22° were obtained at intervals of 1° . The 'b' axis was conveniently chosen to be the rotation axis. The off-Bragg angle positions were converted to the corresponding reciprocal space

positions and the reflected intensity at each position in reciprocal space around the reciprocal lattice point was determined and plotted. Figure 2 shows the plots for the crystal without and with the oscillatory resonating electric field.

3. Results and Discussions

From figure 2 showing the intensity distribution in reciprocal space for the 101 reflection, the following salient points may be noted :

1) In the absence of the oscillating electrical field, the intensity distribution is a smooth curve showing only one maximum corresponding to the (101) reflection, as expected under normal conditions.

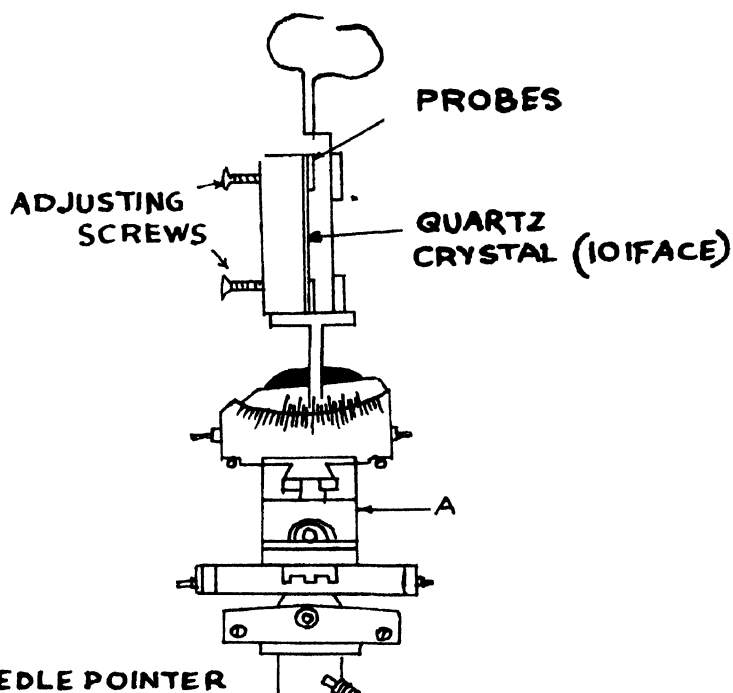
2) In the presence of the oscillating field, however, the intensity distribution assumes an oscillatory nature. It is seen that intensity corresponding to a specific point in the reciprocal space may either increase or decrease from its original value under non-oscillating conditions, giving rise to other subsidiary peaks and troughs besides that corresponding to the main peak corresponding to the (101) reflection. Also there is evidence that some positions of the intensity distribution may remain quite unchanged.

3) The distribution in the presence of oscillations is not symmetrical, showing that there does not exist an isotropy in the intensity space.

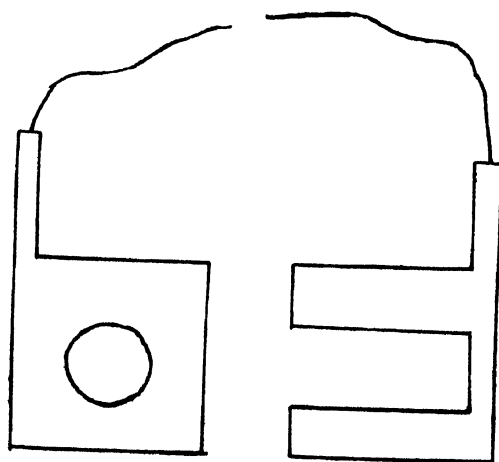
4) It is observed that the main peak is slightly displaced due to the externally impressed oscillatory field. This is to be expected since increase in oscillatory modes is equivalent to a change in temperature and due to anharmonicity effects of the potential there will be an expansion similar to that of thermal expansion. However, in the present case, the change being very small—no attempt has been made to measure the shift and study its significance. With higher frequencies and larger amplitude of the perturbing wave the shift may be more predominant and such studies have been planned as a future project.

These results, therefore, contradict the observations of the earlier workers who reported a marked increase of reflection intensity in the peak region due to the effect of piezoelectric oscillations. Also, the observations due to Colby and Harris (1933) that the background region remains unaffected by the oscillations does not appear to hold true.

The results, though not totally unexpected, are rather surprising. A diminution in intensity was expected as a result of the increase in the Debye-Waller factor. Weigle and Bleuler (1942) gave a theoretical treatment on the basis of a mechanical wave traversing the atomic positions and predicted an oscillatory background less than that for the crystal without the oscillatory electric field. A diminution in extinction is also expected which would increase the intensity when the crystal is subject to the externally impressed electrical field. But both an increase and a decrease with respect to the original intensity in the absence of the oscillations is not accounted for or predicted by the existing

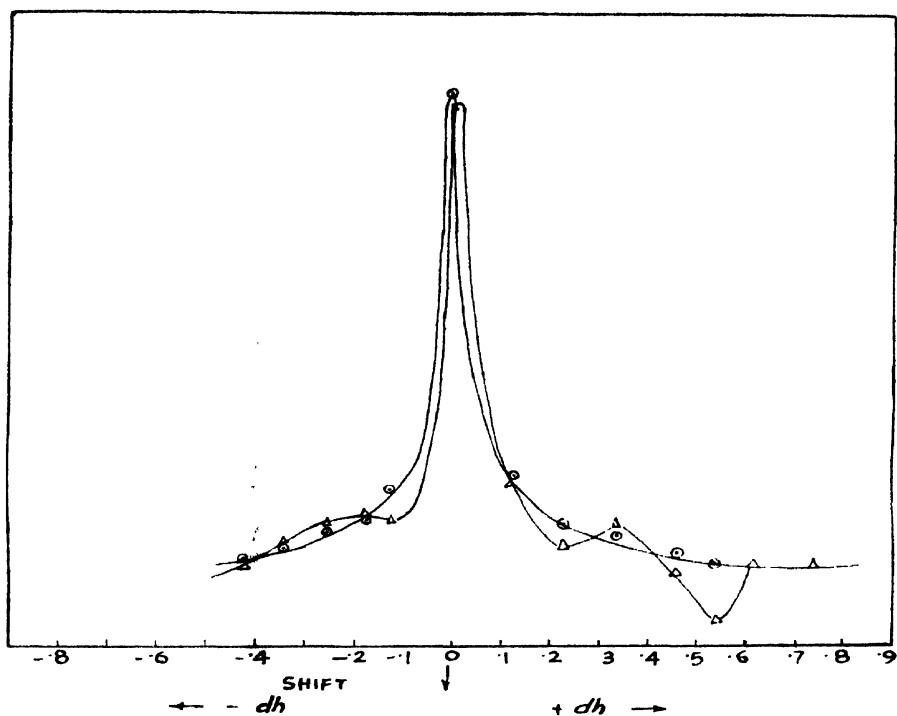


NEEDLE POINTER
CIRCULAR SCALE
GONIOMETER CONSTRUCTED
AS AN IMPROVEMENT
NECESSARY FOR THE
PRESENT INVESTIGATION

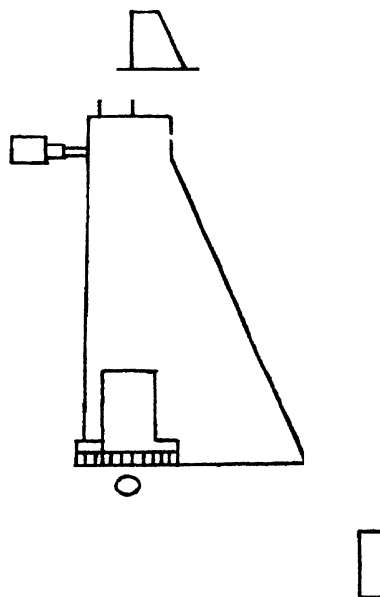


DETAILED DIAGRAM SHOWING
THE PROBES.

EN ARBITRARY TS



THE (101) POINT
SHIFT IN THE RECIPROCAL CO-ORDINATE, h



ORIGINAL CRYSTAL HOLDER
FOR LAUE METHOD

theories. Kuriyama and Miyakawa (1969) developed a theory based on the dynamical theory of diffraction which predicted in general a diminution in extinction and thus an increase in intensity when the external electric field is applied. Expression for the scattered intensity contains both dynamical as well as kinematical terms—each set of terms predominating under certain conditions. The expression in its existing form is not amenable to numerical computation and from qualitative considerations, it is difficult to predict its variation in reciprocal lattice space. Thus a more explicit theory is called for to explain the observed intensity variations in X-ray scatterings when the crystal is under piezoelectric oscillations.

3. Development of a Kinematical Theory

A treatment similar to but more generalised than that given by Weigle and Bleuler (1942) has been attempted here. The position vector describing the j -th atom in the $(n_1n_2n_3)$ th unit cell of the crystal may be written as

$$\mathbf{r}_j = n_1\mathbf{a} + n_2\mathbf{b} + n_3\mathbf{c} + \mathbf{x}_j + \mathbf{y}_j + \mathbf{z}_j \quad (1)$$

where n_1, n_2, n_3 are integers; a, b, c the unit cell repetition distances along the three crystallographic axes; x_j, y_j, z_j the position coordinates of the j -th atom within the $(n_1n_2n_3)$ th unit cell. In the presence of the piezoelectric vibrations, \mathbf{r}_j is modified and may be expressed as

$$\mathbf{r}_j' = \mathbf{r}_j + U(\mathbf{r}_j) \quad (2)$$

where $U(\mathbf{r}_j)$ has components like $\mathbf{A}_0 \sin(\omega t - \mathbf{k} \cdot n_1\mathbf{a}) + \mathbf{X}_{j_0} \sin(\omega t - \mathbf{k} \cdot \mathbf{x}_j)$ in the X -direction, the first term taking care of the modification of the lattice constants while the second accounting for the displacement of the j -th atom in the unit cell. Amplitude terms like \mathbf{A}_0 and \mathbf{X}_{j_0} will depend upon the Miller indices of the vibrating planes and it is likely that they will also vary from unit cell to unit cell. This latter variation has not been taken into consideration. Weigle and Bleuler (1942) and Kuriyama and Miyakawa (1969) have both neglected even the lattice term and have overlooked the variation of \mathbf{X}_{j_0} from unit cell to unit cell. The intensity of X-rays reflected from such a crystal in the direction \mathbf{h} is given by

$$I(\mathbf{h}) = R(\mathbf{h}) \cdot R^*(\mathbf{h}) \quad (3)$$

with

$$R(\mathbf{h}) = \sum_j f_j \exp i\mathbf{h} \cdot \mathbf{r}_j' \quad (4)$$

Defining

$$F(\mathbf{h}) = \sum_j f_j \exp i[\mathbf{h} \cdot \{\mathbf{x}_j + \mathbf{y}_j + \mathbf{z}_j\}] \quad (5)$$

and using the relation

$$\exp(-ip \sin \theta) = \sum_{-\infty}^{\infty} J_n(p) \cdot \exp(-in\theta). \quad (6)$$

We have,

$$I(\mathbf{h}) = \sum_j F^2(\mathbf{h}) \cdot \frac{\sin^2 \left(N_1 \frac{\pi}{\lambda} \mathbf{a} \cdot \mathbf{h} \right)}{\sin^2 \left(\frac{\pi}{\lambda} \mathbf{a} \cdot \mathbf{h} \right)} \cdot \frac{\sin^2 \left(N_2 \frac{\pi}{\lambda} \mathbf{b} \cdot \mathbf{h} \right)}{\sin^2 \left(\frac{\pi}{\lambda} \mathbf{b} \cdot \mathbf{h} \right)} \cdot \frac{\sin^2 \left(N_3 \frac{\pi}{\lambda} \mathbf{c} \cdot \mathbf{h} \right)}{\sin^2 \left(\frac{\pi}{\lambda} \mathbf{c} \cdot \mathbf{h} \right)}$$

$$\sum_{n_1} \sum_{n_2} \sum_{n_3} \sum_{m_1} \sum_{m_2} \sum_{m_3} J_{n_1}^2 \left(\frac{2\pi}{\lambda} \mathbf{h} \cdot \mathbf{X}_{f_0} \right) \cdot J_{n_2}^2 \left(\frac{2\pi}{\lambda} \mathbf{h} \cdot \mathbf{Y}_{f_0} \right) \cdot$$

$$J_{n_3}^2 \left(\frac{2\pi}{\lambda} \mathbf{h} \cdot \mathbf{Z}_{f_0} \right) \cdot J_{m_1}^2 \left(\frac{2\pi}{\lambda} \mathbf{h} \cdot \mathbf{a} \right) \cdot J_{m_2}^2 \left(\frac{2\pi}{\lambda} \mathbf{h} \cdot \mathbf{b} \right) \cdot$$

$$J_{m_3}^2 \left(\frac{2\pi}{\lambda} \mathbf{h} \cdot \mathbf{c} \right) \quad (7)$$

where $m_1 m_2 m_3$ are integers like $n_1 n_2 n_3$ and have the same significance namely labelling the unit cell.

Eq. (7) shows that both the structure factor term and the interference term are modified by the piezoelectric vibrations. Since the values of $J_n(x)$ are always less than unity except for $J_0(0)$ which equals unity, it appears that the presence of the piezoelectric wave has an effect of multiplying the usual intensity term by a factor oscillatory in nature but always a fraction less than unity. Thus, this kinematical treatment fails to accommodate an increase in intensity although an oscillatory nature of the reflected intensity is predicted.

5. Dynamical theory of X-ray reflection by piezoelectrically oscillating crystals

The only previous work is due to Kuriyama and Miyakawa (1969) which can not explain the observed nature of the intensity distribution. So we proceed to consider the problem afresh. We shall use the Taupin-Takagi (1964, 1962, 1969, 1975) theory for a distorted crystal leading to the following equations due to Kato (1975)

$$\frac{\partial \langle I_0 \rangle}{\partial t_1} = -\{2\tau \operatorname{Re}(\chi_h \chi_{\bar{h}}) + \mu\} \langle I_0 \rangle + 2\tau |\chi_{\bar{h}}|^2 \langle I_h \rangle$$

$$\frac{\partial \langle I_h \rangle}{\partial t_2} = -\{2\tau \operatorname{Re}(\chi_h \chi_{\bar{h}}) + \mu\} \langle I_h \rangle + 2\tau |\chi_h|^2 \langle I_0 \rangle$$

where $\langle I_0 \rangle$, $\langle I_h \rangle$ are the average intensities of the diffracted beam in the forward direction and the diffraction direction \mathbf{h} respectively in the two beam approximation, averages being carried out over all the unit cells; τ is a correlation length which may be taken to be the same as the domain size of a mosaic block in the crystal; μ the linear absorption coefficient; and χ_h the h -th order

Fourier transform of the electric susceptibility of the crystal and in the case of the vibrating crystal is given by

$$\chi_{\mathbf{h}} \chi_{\bar{\mathbf{h}}} = \left(\frac{e^2}{mc^2} \right)^2 \frac{1}{4\pi^2 v^2} F_{\mathbf{h}}^2 \sum_{n_1} \sum_{n_2} \sum_{n_3} J_{n_1}^2 \left(\frac{2\pi}{\lambda} \mathbf{h} \cdot \mathbf{X}_{f_0} \right) \times J_{n_2}^2 \left(\frac{2\pi}{\lambda} \mathbf{h} \cdot \mathbf{Y}_{f_0} \right) J_{n_3}^2 \left(\frac{2\pi}{\lambda} \mathbf{h} \cdot \mathbf{Z}_{f_0} \right). \quad (8)$$

Writing $\sigma = 2\tau(\chi_{\mathbf{h}} \chi_{\bar{\mathbf{h}}})$ and $\langle I_0 \rangle = I_0$ and $\langle I_{\mathbf{h}} \rangle = I_{\mathbf{h}}$ we have the equations due to Zachariassen (1967) viz.

$$\left. \begin{aligned} \frac{\partial I_0}{\partial t_1} &= -(\mu + \sigma)I_0 + \sigma I_{\mathbf{h}} \\ \frac{\partial I_{\mathbf{h}}}{\partial t_2} &= -(\mu + \sigma)I_{\mathbf{h}} + \sigma I_0 \end{aligned} \right\} \quad (9)$$

with boundary conditions

$$\left. \begin{aligned} I_0 &= I_0 & \text{at } t_1 &= 0 \\ I_{\mathbf{h}} &= 0 & \text{at } t_2 &= 0 \end{aligned} \right\} \quad (10)$$

μ can be written as

$$\mu = \left[\sum_i \left(\frac{\mu}{\rho} \right)_i \right] \left[\rho_0 + \xi_m \sin \left(\omega t - \frac{2\pi}{\lambda} \mathbf{h} \cdot \mathbf{r} \right) \right] \quad (11)$$

in the presence of the piezoelectric vibrations.

The solution of eqs (9) and (10) is given by

$$\begin{aligned} P(\mathbf{h}) &= \int \frac{\partial I_{\mathbf{h}}}{\partial t_2} dV \\ &= I_0 v \sigma \phi(\sigma) \end{aligned} \quad (12)$$

where $P(\mathbf{h})$ is the total power diffracted in the direction \mathbf{h} , v the volume of the crystal and

$$\phi(\sigma) = -\frac{1}{v} \int_v \exp -(\mu + \sigma)(t_1 + t_2) dV. \quad (13)$$

Combining eq. (13) with eq. (11) we have

$$\begin{aligned} \phi(\sigma) &= \frac{1}{v} \sum_m \int_v J_m[\mu_0 \xi_m(t_1 + t_2)] \exp \left[-im \left(\frac{2\pi}{\lambda} \mathbf{h} \cdot \mathbf{r} - \omega t \right) \cdot (t_1 + t_2) \right. \\ &\quad \left. \left\{ 1 - (\mu + \sigma)(t_1 + t_2) + \frac{(\mu + \sigma)^2(t_1 + t_2)^2}{2} \right\} \right] dV \end{aligned} \quad (14)$$

with $\mu_0 = \sum_i \left(\frac{\mu}{\rho} \right)_i$ which is a constant for the given material.

Thus the power diffracted by a vibrating crystal is found to be dependent on Bessel functions of arguments containing the variables t_1 and t_2 —which means that the diffracted powers increases or decreases with the direction of diffraction h . It may be noted that this is what is exactly observed in practice. Though the argument of J_m and hence the diffracted power is seen to vary-with angle of diffraction, the variation is not symmetrical, lending assymetry to the intensity distribution and showing the obviously present anisotropy in quartz. Thus it is seen that while the kinematic theory is unable to explain the observed intensity distribution in X-ray reflection from piezoelectrically vibrating crystals, the Dynamical theory is able to explain it at least qualitatively. Eqs. (7) and (14) are to be numerically evaluated in order to make any quantitative comparison.

Lastly, it is to be admitted that the present work is a preliminary work and much remains yet to be done. Other reflections from quartz and reflection from other piezoelectric crystals are to be investigated at different frequencies and different amplitudes of vibration. On the theoretical side, a more rigorous dynamical theory and numerical calculations of the derived intensity expressions are to be carried out. Then probably we shall gain entrance to the threshold of the mysteries of atomic origin of piezoelectric effects. Work has been undertaken to achieve this end.

Reference

- Colby M Y and Harris S 1933 *Phys. Rev.* **43** 562
 Dabey and Sears 1932 *Nat. Acad. Sci. Proc.* **18** 409
 Fox G N and Carr P H 1931 *Phys. Rev.* **31** 1622
 Fox G N and Cork J M 1931 *Phys. Rev.* **31** 420
 Fox G N and Frederick J R 1938 *Phys. Rev.* **53** 135
 Jauncey G E M and Deming J N 1935 *Phys. Rev.* **48** 462
 Kato N 1975 *Acta Cryst.* **A318** 225
 Klein A G, Prager P, Wagenfield H, Ellis P J and Sabine T M 1967 *Appl. Phys. Letters* **10** 203
 Kuriyama M and Miyakawa T 1969 *J. Appl. Phys.* **40** 1697
 Nishikawa S, Sumoto I and Sakisaka Y 1931 *Phys. Rev.* **38** 1078
 Parkinson T F and Moyer M W 1966 *Nature* **211** 400
 Takagi S 1962 *Acta Cryst.* **15** 1311
 Takagi S 1969 *J. Phys. Soc. Japan* **26** 1239
 Takagi S 1975 *Int. Summer School in X-ray Dynamical Theory, Limoges*
 Taupin D 1964 *Bull. Soc. Trans. Min. Cryst.* **87** 469
 Warren B E and Kurtter H M 1933 *Phys. Rev.*
 Weigle J and Bleuler K 1942 *Helvetica Physica Acta* **15** 445
 Zachariasen W H 1967 *Acta Cryst.* **23** 558

Eigenvalues and eigenvectors of the exchange interaction Hamiltonian of Heisenberg

N D Sen Gupta

Tata Institute of Fundamental Research
Bombay 400 005

The object of the paper is to develop a method to obtain successively eigenvalues and eigenvectors of the general exchange interaction Hamiltonian of Heisenberg. The method consists of generalising the usual Bloch spin wave solution of single spin excitation. It is noted that the result can be extended to any number of finite steps of interaction. Further, procedure to obtain successively the eigen-values and eigenfunctions with multiple spin deviations are discussed. The symmetry properties of the eigenstates with same number of spin deviations from all spin down and spin up states are studied.

1. Introduction

The object of this paper is to obtain methods to arrive at exact eigenvalues and eigenfunctions of the exchange interaction Hamiltonian of Heisenberg. Shortly after Heisenberg's formulation (1928) of the theory of ferromagnetism, Bloch (1930) obtained a simple set of exact eigenfunctions of the exchange Hamiltonian, the so-called spin-waves. These are suitable super-position of states with only one spin excitation. Immediately after Bloch, Bethe (1931) attempted to generalize Bloch's results. This was followed by Hulthen (1938) who obtained exact eigenvalues and eigenvector for very small values of the number atoms in a chain. In order to account for the multiple spin excitation in general Holstein and Primakoff (1940) introduced the idea of spin-deviation in their investigation on ferromagnets. Dyson (1956) while developing the general theory of Spin-wave interaction, introduced states which are apparently natural generalization of Bloch's single excitation spin-waves. These states are not orthogonal and are much more numerous than the total number of linearly independent states. This leads to the introduction of undeserving kinematical interaction between the spinwaves, though the resulting dynamical interaction is weak.

Instead of working with states introduced *ad hoc* it is worthwhile to study the nature of the exact eigen functions of the relevant Hamiltonian. This is the motivation of the paper. We start with a modest beginning with a simple case to emphasize the algebraic method followed here. We consider systems with spin $\frac{1}{2}$, in the absence of external magnetic field. The presence of external magnetic

field does not introduce any basic difficulty only the computation becomes a little involved. We show how to obtain step by step eigenfunctions with successive higher number of spin excitations. They being the eigenfunction of a hermitian operator, are necessarily orthogonal. The algebra of the operators is the total matrix algebra of 2^N dimension, N is the number of elements in the elementary cell, or the number of basic elements in the spin chain. In this context, it is interesting to note an important observation by Onsager (1943) that 'the quaternion algebra which is the direct product of N simple quaternion algebras is equivalent to the complete matrix algebra of 2^N dimension'. However we work directly with the spin operators and make use of their algebraic properties only. Thus we avoid the explicit representation which will make the problem unwieldy.

In the next Section after stating the problem, we derive some important relations which help the calculations considerably. The classification of the eigenfunction and their basic properties are considered in Section 3. Some simple properties of the eigenfunction for the special case of isotropic system are also discussed in this Section. The eigenfunctions and eigenvalues with multiple spin excitations are obtained in Section 4. The last section is devoted to remarks, on the method followed in the paper and its possible generalizations to other more complicated physical problems.

2. Formulation and preliminary results

Let the Hamiltonian be expressed as

$$\mathcal{H} = - \sum_{j,k=1}^N J_{jk} (\sigma_j^x \sigma_k^x + \sigma_j^y \sigma_k^y + g \sigma_j^z \sigma_k^z) \quad (1)$$

g is the asymmetry parameter and $g = 1$ corresponds to the isotropic case. The exchange interaction coefficients J_{jk} are symmetric and depend only on the difference $|j-k|$ i.e.

$$J_{jk} = J_k, \text{ and } J_{j(j+\beta)} = a_\beta. \quad (2)$$

The suffixes j, k runs from 1 to N . The periodic boundary condition leads to

$$J_{j(k+N)} = J_{jk}, \sigma_{j+N} = \sigma_j. \quad (3)$$

The spin operators satisfy the relation

$$(\sigma_j^\mu)^2 = 1 \text{ and } \sigma_j^\mu \sigma_k^\nu - \sigma_k^\nu \sigma_j^\mu = 2\delta_{jk} \epsilon_{\mu\nu\theta} \sigma_j^\theta. \quad (4)$$

The matrix $\{J_{jk}\}$ can be written as

$$\{J_{jk}\} = \sum_{\beta=1}^{N-1} a_\beta \Omega^\beta, (a_\beta = a_{-\beta}, J_{jj} = 0) \quad (5)$$

The only non-vanishing elements of the matrix Ω are $\Omega_{j(j+1)} = 1$ for $j = 1, 2, \dots, N-1$ and $\Omega_{NI} = 1$. The group $(\Omega^n; n = 1, 2, \dots, N)$ is isomorphic to the cyclic group of N roots of unity. We need not restrict the interactions only to the next neighbour, in which case all a_β excluding a_1 and $a_{N-1} = a_{-1}$ are zero.

The eigenvalues of $\{J_{jk}\}$ are

$$\lambda^{(n)} = \sum_{\beta=1}^{N-1} a_\beta \omega^{n\beta}, \quad (\omega = e^{i2\pi/N}; \quad n = 1, 2, \dots, N) \quad (6)$$

and the corresponding normalized eigen vectors are $\{\omega^{jn}/\sqrt{N}\}$. Though $\{J_{jk}\}$ is a real symmetric matrix yet we express eigenvectors in complex conjugate pairs, as it is convenient for future calculations. In fact

$$\lambda^{(n)} = 2 \sum_{\beta=1}^{(N-1)/2} a_\beta \cos \frac{2\pi n \beta}{N} \quad (\text{for } N \text{ odd}) \quad (7)$$

$$= 2 \sum_{\beta=1}^{2/N-1} a_\beta \cos \frac{2\pi n \beta}{N} + (-1)^n a_{N/2} \quad (\text{for } N \text{ even}) \quad (8)$$

and

$$\lambda^{(n)} = \lambda^{(N-n)} = \lambda^{(-n)}. \quad (9)$$

The complex conjugate pair of eigenvectors belong to this pair of degenerate eigenvalues. Thus

$$J_{jk} = \sum_{n=1}^N \lambda^{(n)} \frac{\omega^{n(j-k)}}{N} \quad (10)$$

and the Hamiltonian (1) is

$$\mathcal{H} = -\frac{1}{N} \sum \lambda^{(n)} \omega^{n(j-k)} (4\sigma_j^+ \sigma_k^- + g \sigma_j^z \sigma_k^z), \quad (11)$$

$$\text{where } \sigma_j^+ = \sigma_j^x + i\sigma_j^y \quad \text{and} \quad \sigma_j^- = \sigma_j^x - i\sigma_j^y. \quad (12)$$

We further introduce the operators

$$\sigma_j^{(u)+} = \sum_{j=1}^N \omega^{uj} \sigma_j^+, \quad \sigma_j^{(v)-} = \sum_{j=1}^N \omega^{vj} \sigma_j^-, \quad \text{and} \quad \sigma_j^{(w)} = \sum_{j=1}^N \omega^{wj} \sigma_j^z, \quad (13)$$

$u, v, w = 1, 2, \dots, N$. They satisfy the following commutation relations

$$\left. \begin{aligned} \sigma_j^{(u)} \sigma_j^{(v)+} - \sigma_j^{(v)} \sigma_j^{(u)+} &= 2\sigma_j^{(u+v)} \\ \sigma_j^{(u)} \sigma_j^{(v)-} - \sigma_j^{(v)} \sigma_j^{(u)-} &= -2\sigma_j^{(u+v)} \\ \sigma_j^{(u)+} \sigma_j^{(v)} - \sigma_j^{(v)} \sigma_j^{(u)+} &= \sigma_j^{(u+v)} \end{aligned} \right\} \quad (14)$$

Let ϕ^- and ϕ^+ represents the states with all spins up and down respectively, so that

$$\text{and} \quad \sigma_j^z \phi^- = -\phi^-, \quad \sigma_j^z \phi^+ = \phi^+. \quad (15)$$

Further

$$\sigma_j^x \phi^- = -N \delta_{Nu} \phi^-, \quad \sigma_j^x \phi^+ = N \delta_{Nu} \phi^+ \quad (16)$$

and

$$\sigma^+ \phi^+ = 0, \quad \sigma^- \phi^- = 0. \quad (17)$$

Again

$$\prod_{r=1}^N \sigma^+ \phi^- = C \phi^+ \quad \text{and} \quad \prod_{r=1}^N \sigma^- \phi^+ = C \phi^-. \quad (18)$$

where

$$C = \sum_p \exp. \frac{i2\pi}{N} \cdot \left(u_{n_1} j_1 + u_{n_2} j_2 + \dots + u_{n_N} j_N \right).$$

(n_1, n_2, \dots, n_N) are any permutation P of $(1, 2, \dots, N)$,

with all j_r distinct. Finally

$$\prod_{r=1}^{N+1} \sigma^+ = 0 \quad \text{and} \quad \prod_{r=1}^{N+1} \sigma^- = 0. \quad (19)$$

The Hamiltonian (10) may now be expressed in the form

$$\mathcal{H} = \frac{1}{N} \sum_{n=1}^N \left(\lambda \begin{pmatrix} n \\ n \end{pmatrix} \begin{pmatrix} n \\ -n \end{pmatrix} \sigma^+ + g \sigma^z \begin{pmatrix} n \\ -n \end{pmatrix} \right). \quad (20)$$

It should be mentioned that all the subscripts and superscripts are modulo N and $-k \equiv N-k$ for any k .

It is easy to check that the Hamiltonian satisfies the following commutation relations,

$$\sigma^+ \mathcal{H} - \mathcal{H} \sigma^+ = \frac{4}{N} \sum_{n=1}^N \left(\begin{pmatrix} n \\ n \end{pmatrix} \begin{pmatrix} n \\ -n \end{pmatrix} \right) \sigma^+ \sigma^z \begin{pmatrix} n \\ -n \end{pmatrix} \quad (21)$$

$$\sigma^- \mathcal{H} - \mathcal{H} \sigma^- = -\frac{4}{N} \sum_{n=1}^N \left(\begin{pmatrix} n \\ n \end{pmatrix} \begin{pmatrix} n \\ -n \end{pmatrix} \right) \sigma^- \sigma^z \begin{pmatrix} n \\ -n \end{pmatrix} \quad (22)$$

$$\sigma^z \mathcal{H} - \mathcal{H} \sigma^z = \frac{8}{N} \sum_{n=1}^N \left(\begin{pmatrix} n \\ n \end{pmatrix} \begin{pmatrix} n \\ -n \end{pmatrix} \right) \sigma^+ \sigma^- \begin{pmatrix} n \\ -n \end{pmatrix} \quad (23)$$

We need further the commutation relations

$$\frac{(k)}{\sigma^2} \prod_{t=1}^m \sigma^+ - \prod_{t=1}^m \sigma^+ \frac{(k)}{\sigma^2} = 2 \sum_{r=1}^m \frac{(u_r+k)}{\sigma^+} \prod_{t=1}^m \sigma^+ \quad (24)$$

$$\frac{(k)}{\sigma^2} \prod_{t=1}^m \sigma^- - \prod_{t=1}^m \sigma^- \frac{(k)}{\sigma^2} = -2 \sum_{r=1}^m \frac{(u_r+k)}{\sigma^-} \prod_{t=1}^m \sigma^-, \quad (25)$$

$$\frac{(k)}{\sigma} \prod_{t=1}^m \sigma^+ - \prod_{t=1}^m \sigma^+ \frac{(k)}{\sigma} = \sum_{r=1}^m \frac{(u_r)}{\sigma^+} \frac{(u_r+k)}{\sigma^2} - \sum_{r,s=1}^m \frac{(u_r+u_s+k)}{\sigma^-} \prod_{t=1}^m \sigma^+ \quad (26)$$

$$\frac{(k)}{\sigma^+} \prod_{t=1}^m \sigma^- - \prod_{t=1}^m \sigma^- \frac{(k)}{\sigma^+} = \sum_{r=1}^m \frac{(u_t)}{\sigma^+} \frac{(u_r+k)}{\sigma^2} - 2 \sum_{r,s=1}^m \frac{(u_r+u_s+k)}{\sigma^-} \prod_{t=1}^m \sigma^-. \quad (27)$$

' dash on the product sign of right hand side of the above relations means that the corresponding factors are omitted and similarly two dashes means corresponding two factors and are omitted.

These formulae can be easily established by the method of induction. Their validity for $m = 1$ and $m = 2$ can be easily verified. Lastly due to the linear independence of the states,

$$\left. \begin{array}{l} \text{from } \sum_{n=1}^N B_u^{(u)} \sigma^+ \phi^- = 0 \text{ follows } B_u = 0 \\ \text{and from } \sum_{n=1}^N B_u' \sigma^- \phi^+ = 0 \text{ follows } B'_u = 0 \end{array} \right\} \quad (28)$$

Again,

$$\left. \begin{array}{l} \sum_{u,v=1}^N B_{uv} \sigma^+ \sigma^+ \phi^- = 0 \\ \text{with } B_{uv} \text{ symmetric in } u \text{ and } v \text{ implies} \\ B_{uv} = \frac{1}{N} \sum_{p=1}^N B_{p(u+v-p)} \end{array} \right\} \quad (29)$$

and similarly

$$\sum_{u,v=1}^N B'_{uv} \sigma^- \sigma^- \phi^+ = 0$$

implies

$$B'_{uv} = \frac{1}{N} \sum_{p=1}^N B'_{p(u+v-p)}. \quad (30)$$

The following identities between $\sigma^{(u)}$, $\sigma^{(v)}$ and $\sigma^{(s)}$ are to be noted

$$\left. \begin{aligned} \sum_{v=1}^N \frac{(u-v)}{\sigma^+} \frac{(w-v)}{\sigma^-} &= 0, \quad \sum_{v=1}^N \frac{(u-v)}{\sigma^-} \frac{(w-v)}{\sigma^+} = 0 \\ \sum_{v=1}^N \frac{(u-v)}{\sigma^2} \frac{(u+v)}{\sigma^2} &= N^2 \delta_{us}. \end{aligned} \right\} \quad (31)$$

Further

$$\left. \begin{aligned} \sum_{u=1}^N \frac{(u)}{\sigma^2} \frac{(k-u)}{\sigma^+} &= N \sigma^+ \\ \sum_{u=1}^N \frac{(u)}{\sigma^2} \frac{(k-u)}{\sigma^-} &= -N \sigma^- \\ \sum \frac{(k+u)}{\sigma^+} \frac{(l-u)}{\sigma^-} &= \frac{1}{2} N (1 + \frac{(k+l)}{\sigma^2}). \end{aligned} \right\} \quad (32)$$

In virtue of the eqs. (29), (30) and (31), it follows that in equations,

$$\left. \begin{aligned} \sum_{u=1}^N B_u \frac{(M-u)}{\sigma^+} \frac{(u)}{\sigma^-} \phi^- &= 0 \text{ with } B_u = B_{M-u} \\ \sum_{u=1}^N B'_u \frac{(M-u)}{\sigma^-} \frac{(u)}{\sigma^+} \phi^+ &= 0 \text{ with } B'_u = B'_{M-u}, \end{aligned} \right\} \quad (33)$$

we can take without any loss of generality

$$\sum_{u=1}^N B_u = 0, \quad \sum_{u=1}^N B'_u = 0. \quad (34)$$

So that eqs. (33) implies

$$B_u = 0 \quad \text{and} \quad B'_u = 0. \quad (35)$$

Next, from the relation

$$\left. \begin{aligned} \sum_{v, u=1}^N D_v B_u^v \frac{(M-v)}{\sigma^+} \frac{(v-u)}{\sigma^+} \frac{(u)}{\sigma^+} \phi^- &= 0 \\ B_u^v &= B_{v-u}^v, \quad \sum_{u=1}^N B_u^v = 0 \text{ and } \sum_{v=1}^N D_v B_u^v = 0, \end{aligned} \right\} \quad (36)$$

it follows that

$$D_{M-q} B_p^{M-q} + D_{M-p} B_q^{M-p} + D_{p+q} B_p^{p+q} = 0. \quad (37)$$

Similarly from

$$\left. \begin{aligned} \sum_{u, v=1}^N D'_v B'_u{}^v \frac{(M-v)}{\sigma^-} \frac{(v-u)}{\sigma^-} \frac{(u)}{\sigma^-} \phi^+ &= 0 \\ \text{with} \\ B'_u{}^v &= B'^v{}_{v-u}, \sum_{v=1}^N B'_u{}^v = 0 \text{ and } \sum_{v=1}^N D'_v B'_u{}^v = 0, \end{aligned} \right\} \quad (38)$$

it follows that

$$D'_{M-q} B'_p{}^{M-q} + D'_{M-p} B'_q{}^{M-p} + D_{p+q} B'_p{}^{p+q} = 0 \quad (39)$$

for any p, q .

3. Classification of the states, their properties and spin waves

The Hamiltonian (1) commutes with σ^z , i.e. total magnetic moment, it is convenient to classify the eigen states of the Hamiltonian according to the eigen values of σ , (Lieb and Mathis 1962).

Since

$$\left. \begin{aligned} \text{and} \\ \frac{(N)}{\sigma^z} \frac{(k)}{\sigma^+} &= \frac{(k)}{\sigma^+} \frac{(N)}{(\sigma^z+2)} \\ \frac{(N)}{\sigma^z} \frac{(k)}{\sigma^-} &= \frac{(k)}{\sigma^-} \frac{(N)}{(\sigma^z-2)}, \end{aligned} \right\} \quad (40)$$

it follows that

$$\frac{(N)}{\sigma^z} \prod_{r=1}^m \frac{(u_r)}{\sigma^+} \phi^- = (2m-N) \prod_{r=1}^m \frac{(u_r)}{\sigma^+} \phi^- \quad (41)$$

and

$$\frac{(N)}{\sigma^z} \prod_{r=1}^m \frac{(u_r)}{\sigma^-} \phi^+ = (N-2m) \prod_{r=1}^m \frac{(u_r)}{\sigma^-} \phi^+. \quad (42)$$

Thus eigen functions of \mathcal{H} are suitable linear combinations of states in equation (41) and (42) with fixed m . We represent by ϕ_m^- and ϕ_m^+ such states with m operators σ^+ on ϕ^- and σ^- on ϕ^+ respectively, m may take values $0, 1, \dots, (N-1)/2$ for N odd. In case of N even, for $m = N/2$, ϕ_m^- and ϕ_m^+ are same class of states, we should consider only one of them in addition to ϕ_m^- and ϕ_m^+ with $m = 0, 1, \dots, (N/2-1)$. Both ϕ_m^- and ϕ_m^+ represents states which are linear superposition of with m spin reversals. We could have considered states only ϕ_m^- or ϕ_m^+ with $m = 0, 1, \dots, N$. But we prefer the former as, to each eigen states ϕ_m^- of \mathcal{H} there corresponds an eigenstate ϕ_m^+ of \mathcal{H} with the same eigenvalue.

(i) *Symmetry properties of the eigenstates with same number of spin-deviation*

Let

$$X = \prod_{j=1}^N \sigma_j^x, \quad (43)$$

it has the following properties

$$X^2 = I \quad (44)$$

$$X\phi^- = \prod_{j=1}^N (\sigma_j^+ + \sigma_j^-)\phi^- = \prod_{j=1}^N \sigma_j^+\phi^- = \phi^+ \quad (45)$$

and

$$X\phi^+ = \phi^- \quad (46)$$

$$X \overset{(u)}{\sigma}^+ = \overset{(u)}{\sigma}^- X, \quad X \overset{(u)}{\sigma}^- = \overset{(u)}{\sigma}^+ X \quad (47)$$

finally

$$X\mathcal{H} = X\mathcal{H} \quad (48)$$

Now let ϕ_m^- be an eigenstate of \mathcal{H} , which may be expressed as

$$\phi_m^- = \sum_{u_r} B(u_1, \dots, u_m) \overset{(u_1)}{\sigma}^+ \overset{(u_2)}{\sigma}^+, \dots, \overset{(u_m)}{\sigma}^+ \phi^- \quad (49)$$

so that

$$X\phi_m^- = \sum_{u_r} B(u_1, \dots, u_m) \overset{(u_1)}{\sigma}^- \overset{(u_2)}{\sigma}^-, \dots, \overset{(u_m)}{\sigma}^- \phi^+ = \phi_m^+ \quad (50)$$

Hence from

$$\mathcal{H}\phi_m^- = \xi_m \phi_m^-, \quad (51)$$

follows

$$\mathcal{H}\phi_m^+ = \xi_m \phi_m^+, \quad (52)$$

and conversely from eq. (52) follows eq. (51) ϕ_m^- and ϕ_m^+ are symmetrical states with respect to the same number of spin deviation from all spin down and all spin up.

(ii) *Enumeration of eigenstates and matrix elements of $\overset{(u)}{\sigma}^+ \overset{(v)}{\sigma}^-$ and $\overset{(s)}{\sigma}^z$.*

The number of linearly dependent states ϕ_m^- and ϕ_m^+ with m spin deviations are $N/(m!(N-m)!)$ each. Taken together they account for $2N!/(m!(N-m)!)$ eigenstates of \mathcal{H} . The sum over all permissible value of leads to 2^N states.

Let $\phi_m^-(\alpha)$ and $\phi_m^-(\beta)$ be the eigenstates of \mathcal{H} with eigenvalues $\xi_m^{(\alpha)}$ and $\xi_m^{(\beta)}$ respectively. $\alpha = 1, 2, \dots, N!/(m!(N-m)!)$ and $\beta = 1, 2, \dots, N!/(m!(N-m)!)$.

From eq. (40), follows

$$\overset{(N)}{\sigma}^z \phi_m^-(\alpha) \cdot \overset{(u)}{\sigma}^+ \phi_n^-(\beta) = \phi_m^-(\alpha) \cdot \overset{(u)}{\sigma}^+ (\overset{(N)}{\sigma}^z + 2) \phi_n^-(\beta)$$

i.e.,

$$(n+1-m) \phi_m^-(\alpha) \overset{(u)}{\sigma}^+ \phi_n^-(\beta) = 0 \quad (53)$$

Thus the matrix elements are nonvanishing only when $m = n+1$, the relation is exactly the same with $\phi_m^-(\alpha)$ and $\phi_m^+(\beta)$. Similarly the relation for $\sigma^-^{(u)}$ is

$$(n-1-m)\phi_m^-(\alpha)\sigma^- \phi_n^-(\beta) = 0. \quad (53')$$

But the corresponding relation for $\sigma^z^{(v)}$ is

$$(m-n)\phi_m^-(\alpha)\sigma^z \phi_n^-(\beta) = 0 \quad (54)$$

Thus $\sigma^z^{(v)}$ connects the states with same type of spin deviation states.

(iii) *All spin down and spin up states.*

It is clear from the expression (20) of the Hamiltonian that both ϕ^- and ϕ^+ are eigenstates of \mathcal{H} , in fact,

$$\mathcal{H}\phi^- = -Ng \lambda \phi^-, \quad \mathcal{H}\phi^+ = -Ng \lambda \phi^+. \quad (55)$$

(iii)(b) *Spin wave with single spin deviations*

Applying the commutation relation (21) on ϕ^- , one obtains with the help of equation (16),

$$(\mathcal{H} - Ng \lambda) \sigma^+ \phi^- = 4(g \lambda - \lambda) \sigma^+ \phi^- \quad (56)$$

Hence, $\sigma^+ \phi^- / \sqrt{N}$ is a (normalised) eigenstate with eigen value $\{(N+g)\lambda - 4\lambda\}$ with $p = 1, 2, \dots, N$. Similarly from the identity (22), it follows that the eigen state corresponding to one spin deviation from all spin up states is $\sigma^- \phi^+ / \sqrt{N}$ with same eigen value. They are the simple spin-waves of Bloch and are $2N$ in number.

(iv) *Isotropic case*

In this case i.e., with $g = 1$ it is well known that σ^+ and σ^- also commute with the Hamiltonian. So that from the above single spin-deviation states $\sigma^+ \phi^- / \sqrt{N}$ by operating with $(\sigma^+)^m$, $m = 1, 2, \dots, N-1$ one obtains $N-1$ other states with fixed σ^+ . They belong to the same eigenvalue namely $(N+4)\lambda - 4\lambda$. They can also be generated by starting from $\sigma^- \phi^+ / \sqrt{N}$ and operating with $(\sigma^-)^m$, $m = 1, 2, \dots, N-1$.

4. Spin wave with multiple spin deviations

I) *Spin waves with two spin deviations*

The commutation relations (21) and (22) immediately suggest that the eigenfunctions with two spin deviations are of the form

$$\phi_2^- = \sum_{u=1}^N B_u \sigma^+ \sigma^+ \phi^-, \quad (M = 1, 2, \dots, N) \quad (57)$$

with

$$B_u = B_{M-u} \quad \text{and} \quad \sum_{u=1}^N B_u = 0. \quad (58)$$

From equation (21), it follows that

$$\begin{aligned} & \sum \left\{ \mathcal{K} + (N-8)g \lambda + 4 \left(\lambda + \frac{(N)}{\lambda} \right) \right\} \left\{ B_u \sigma^+ \frac{(M-u)}{\sigma^+} \frac{(u)}{\sigma^+} \phi^- \right. \\ & \left. = -\frac{8g}{N} \sum_{u=1}^N b_u \frac{(M-u)}{\sigma^+} \frac{(u)}{\sigma^+} \phi^- \right. \end{aligned} \quad (59)$$

where

$$b_p = \sum_{n=1}^N \frac{(p-n)}{\lambda} B_n = b_{M-p}. \quad (60)$$

Now if we choose B_u such that

$$\sum_{u=1}^N \left[\left\{ (N-8)g \lambda + 4 \left(\lambda + \frac{(u)}{\lambda} \right) - \xi_2 \right\} B_u + \frac{8g}{N} b_u \right] \frac{(M-n)}{\sigma^+} \frac{(u)}{\sigma^+} \phi^- = 0 \quad (61)$$

then ϕ_2 is an eigen vector of \mathcal{K} with eigenvalue ξ_2 . It follows from equation (29) that B should satisfy the equation,

$$\begin{aligned} & \left\{ (N-8)g \lambda + 4 \left(\lambda + \frac{(u)}{\lambda} \right) - \xi_2 \right\} B_u + \frac{8g}{N} b_u = \frac{8}{N} b_N \\ \text{i.e.} \quad & \left[\left\{ (N-8)g \lambda + 4 \left(\lambda + \frac{(u)}{\lambda} \right) - \xi_2 \right\} \delta_u \right. \\ & \left. + \frac{4g}{N} \left\{ \frac{(u-n)}{\lambda} + \frac{(M-u-n)}{\lambda} - \lambda - \frac{(n)}{\lambda} \right\} \right] B_u = 0. \end{aligned} \quad (62)$$

In virtue of equ. (58) all the above equations for B_n are not independent. When N is odd for a fixed M there are only $(N/2-1)$ independent equations so that from the secular equation (62) follows $(N/2-1)$ eigen states of type (57). Again when N is even for M odd the number of independent equation is $(N/2-1)$ and for M even the number is $N/2$. Thus the total number of eigen states of the form (57) is $N(N-1)/2$. From eqs. (51) and (52), it follows that

$$\phi_2^+ = \sum_{u=1}^N B_u \frac{(M-u)}{\sigma^-} \frac{(u)}{\sigma^-} \phi^-, \quad (M = 1, 2, \dots, N) \quad (63)$$

is also an eigen state of \mathcal{K} with the same eigenvalue. This can also be established by proceeding exactly in the same manner with two spin deviations from all spin up states.

Each eigen value ξ_2 is at least two fold degenerate. Thus what is important is the spin deviation and not the background states, e.g. all spin up or down state. All these states (57) and (62) together give $N(N-1)$ linearly independent states. They account for all the states in the two $N(N-1)/2$ dimensional subspace of σ^2 with eigenvalue, $(4-N)$ and $(N-4)$. The normalised eigen states of \mathcal{K} , with eigenvalues ξ_2 are

$$\phi_2^-(M, \alpha) = \sum_{u=1}^N B_u(M, \alpha) \begin{matrix} (M-u) & (u) \\ \sigma^+ & \sigma^+ \end{matrix} \phi^- / 2\sqrt{2N}, \quad (64)$$

with $M = 1, 2, \dots, N$ and $\alpha = 1, 2, \dots, (N-1)/2$ (or $N/2$ or $N/2-1$). $B_u(M, \alpha)$ are solutions of the secular equation (62) with eigen value ξ_2 and so normalized that

$$\sum_{u=1}^N B_u(M, \alpha), B_u(N, \beta) = \delta_{\alpha\beta}, \quad (65)$$

$\phi_2^-(M, \alpha)$ are orthogonal also, i.e.,

$$\phi_2^-(M, \alpha), \phi_2^-(N, \beta) = \delta_{MN} \delta_{\alpha\beta} \quad (66)$$

II) Spin waves with three spin deviations

We proceed in the same manner as in the case of two spin deviations and try to obtain eigen states of \mathcal{K} , with constants C_v such that

$$\phi_3^- = \sum_v C_v \phi_2^-(\alpha(v)) = \sum_{v,u} C_v B_u(\alpha(v)) \begin{matrix} (M-v) & (v-u) & (u) \\ \sigma^+ & \sigma^+ & \sigma^+ \end{matrix} \phi^- \quad (67)$$

ϕ_2^- are eigen states of \mathcal{K} with two spin deviations belonging to eigenvalues $\xi_2(v, \alpha)$ and

$$\sum_u C_v B_u(v, \alpha) = 0. \quad (68)$$

From the commutation relation (21), one obtains

$$\begin{aligned} (\mathcal{K} - \xi_2(v, \alpha)) \phi_3^- + \sum_{u,v} \left\{ 4 \begin{pmatrix} (M-v) & (N) \\ \lambda & -g \lambda \end{pmatrix} C_v B_u(v, \alpha) + \frac{8g}{N} \right. \\ \left. \sum_{n=1}^N \lambda \begin{pmatrix} (n) \\ C_{v-n} (B_u(v-n, \alpha) + B_{v-u}(v-n, \alpha)) \right\} \begin{matrix} (M-v) & (v-u) & (u) \\ \sigma^+ & \sigma^+ & \sigma^+ \end{matrix} \phi^- = 0. \end{aligned} \quad (69)$$

Thus ϕ_3^- may be an eigen function of \mathcal{K} , with eigenvalue ξ_3 . if one can choose ξ_3 such that

$$\sum_{u,v} A(M, v, u) \begin{matrix} (M-v) & (v-u) & (u) \\ \sigma^+ & \sigma^+ & \sigma^+ \end{matrix} \phi^- = 0 \quad (70)$$

where

$$A = \left[\{ \xi_3 + \xi(v, \alpha) - 4 \binom{M-v}{\lambda} \binom{N}{-g \lambda} \} C_v B_u(v, \alpha) \right. \\ \left. - \frac{8g}{N} \sum_{n=1}^N \lambda \binom{n}{\lambda} C_{v-n} \{ B_u(v-n, \alpha) + B_{v-u}(v-n, \alpha) \} \right]. \quad (71)$$

It follows from eqs. (36) and (37) that

$$A(M, M-v, u) + A(M, M-u, v) + A(M, u+v, u) = 0. \quad (72)$$

These are linear homogeneous equations for C_v and the compatibility conditions determine the eigen values ξ_3 . In virtue of eq. (68) and symmetry of the eq. (80) in u, v , all the equations in (80) are not independent. It is not very difficult to show that total number of linearly independent states $\phi_3^-(M)$ given by (67) with $M = 1, 2, \dots, N$, which can be constructed from the solution of equation (80), is $N(N-1)(N-2)/6$. They form an orthonormal set in this subspace of three spin deviations from all spin down state. From relations (51) and (52),

$$\phi_3^+ = \sum C_v B_u(v, \alpha) \binom{M-v}{\sigma^-} \binom{v-u}{\sigma^-} \binom{u}{\sigma^-} \phi^-. \quad (73)$$

are exactly similar eigen states for three spin deviations from all spin up states. Proceeding in the same manner one can obtain eigenstates with $m+1$ spin deviations when eigen states with m spin deviations are known.

5. Discussion

In the conclusion we wish to make the following observations.

(i) The problem of obtaining the eigen states and eigen values is reduced to the solution of eqs (62, (80) and similar equations for higher spin deviations. For small values of $N < 9$. These can easily be solved algebraically. Hulthen (1938) have given explicit solutions for $N = 4$, for nearest neighbour interaction. Exact solution of these equations are involved but approximate eigenvalues and hence the eigen states may be quite easily obtained for large N .

(ii) The method used in the paper is not restricted to nearest neighbour interaction. All finite long range interactions may be considered. In this context it may be mentioned that our analysis shows that many results which are usually referred only to nearest neighbour interactions are valid for long range interactions also. Dyson considered long range interaction but with the same strength. i.e., α_p 's in eq (2) are taken the same. We have not imposed this stringent restriction. This has the added importance that our results are not confined to linear chain. In order to apply the results to crystals one has to suitably group together the terms with different set of constants.

(iii) Finally, the presence of external magnetic field does not basically change the nature of the states. Because, in virtue of the eq (14), the commutation relations (21), (22) and (23) are simply modified by the addition of a constant to one term in \mathcal{K} . Further the symmetry relation of the eigen states with same number of spin deviations from all down or all up spin states, is also maintained with due modification. It is easy to see from eqs (46)-(48), that if

$$\mathcal{K}(H)\phi_m^-(H) = \xi_m(H)\phi_m^-(H), \quad (74)$$

then

$$\mathcal{K}(-H)\phi_m^+(H) = \xi_m(H)\phi_m^+(H), \quad (75)$$

where H is the strength of the external magnetic field. Thus $\phi_m^+(-H)$ is a eigen state with m spin deviations from all spin down state with eigen value $\xi_m(-H)$ correspond to $\phi_m(-H)$ with m spin deviation states from all spin up state with eigen value $\xi_m(H)$.

References

- Bethe H 1931 *Zeit f Physik* **71**, 205
 Bloch F 1930 *Zeit f. Physik* **61** 206
 Dyson F J 1956 *Phys. Rev.* **102** 1230
 Heisenberg W 1928 *Zeit f. Physik* **49** 619
 Holstein T and Primakoff H 1940 *Phys. Rev.* **58** 1098
 Hulthen L 1938 *Ark. Met. Astr. Fys.* Na **11**
 Lieb E and Mattis D 1962 *J. Math. Phys.* **3** 749
 Onsager L 1943 *Phys. Rev.* **65** 117

Surface wave instabilities in InSb-GaAs semiconductor plasmas: The temperature effects*

Ram Chandra

Physics Department,
Indian Institute of Technology, New Delhi-29

and

J S Verma

Physics Department,
Birla Institute of Technology and Science,
Pilani (Rajasthan)

Abstract. The surface wave instabilities in n -InSb and n -GaAs (having two valleys) semiconductor plasma structure is studied in presence of strong electric fields where the carrier collision frequency becomes the temperature dependent. The way of introducing the temperature dependence of the collision frequency is the same as have been used in the earlier work (Kaushik *et al* 1975; Ram Chandra & Verma 1976). Using the quasi-hydrodynamic approximation and solving the Maxwell's equations together with the linearized equation of motion, the dispersion relation for the system is derived and is solved numerically with the help of IBM-1130 computer. It is found that one of the root increases with the heating electric field. It is also found that one root of the dispersion relation changes sharply as the magnetic field increases while rest of the roots are little affected.

1. Introduction

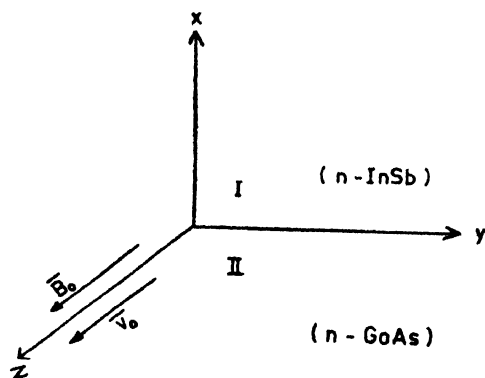
There has been a great interest in the past few years to study the electromagnetic waves and instabilities in semiconductor plasmas (Ram Chandra and Verma 1975, 1976,a,b,c Bok and Nozieres 1963, Bartelink 1967, Hsieh 1972). Hsieh (1972) has reported the results for the wave propagation and instabilities in InSb magneto-plasma in the presence of a weak longitudinal electric field and hence using field independent carrier collision frequency. However the above treatment is not applicable in the presence of hot carriers due to electric field where the carrier collision frequency becomes field dependent. Recently Kaushi *et al* (1975) have studied the effect of strong electric field E_0 on wave instabilities and propagation parameters using the temperature dependence of the collision frequency in a magnetoactive InSb plasma at both room temperature and liquid nitrogen temperature.

*This work was in progress when the first author (RC) was at the International Centre for Theoretical Physics, Trieste (Italy) during early 1976.

In the present paper we have studied the surface wave instabilities in n -InSb and two valley n -GaAs semiconductor plasma structure in the presence of strong electric field E_0 . The way of introducing the temperature dependence of the collision frequency is same as have been discussed in the earlier work (Ram Chandra and Verma 1976, Kaushik *et al.* 1975). Making use of quasi-static approximation, a dispersion relation for the system is derived. The dispersion relation is then solved for the complex propagation constant with the help of IBM-1130 computer for the different values of the heating electric field.

2. Analysis

The geometry of the problem analysed is shown in Fig. 1. The medium I is the n -InSb semiconductor plasma and the medium II is the n -GaAs polar semiconductor plasma in which we have assumed that there exist two streams of carriers (Steele and Vural 1969). The directions of the carrier drift and the propagation are along the z -axis which is also the direction of applied static magnetic field B_0 . We are going to make the quasi-static approximation and the variation of all r.f. fields of the form $\exp[j(\omega t - kz)]$. Furthermore the system is assumed to be uniform in the y -direction and therefore all the partial derivatives with respect to y vanish.



Making use of the Maxwell's equations together with the linearized equation of motion and following Steele and Vural (1969), the scalar potential ϕ_I [$\mathbf{E} = \nabla\phi$] in the medium I can be shown to satisfy the following equation

$$\frac{\partial^2 \phi_I}{\partial x^2} - \beta_I^2 \phi_I = 0 \quad (1)$$

and in the medium II, the equation

$$\frac{\partial^2 \phi_{II}}{\partial x^2} - \beta_{II}^2 \phi_{II} = 0 \quad (2)$$

where

$$\beta_I^2 = \left[\frac{\epsilon_{I1} - \alpha_1}{\epsilon_{I1} - \alpha_1'} \right] k^2, \quad \beta_{II}^2 = \left[\frac{\epsilon_{I2} - \alpha_2 - \alpha_3}{\epsilon_{I2} - \alpha_2' - \alpha_3'} \right] k^2,$$

$$\alpha_i = \frac{\omega p_i^2}{(\omega - kv_i)(\omega - kv_i - j\nu_i)}$$

$$\alpha_i' = \frac{\omega p_i^2(\omega - kv_i - j\nu_i)}{(\omega - kv_i)[(\omega - kv_i - j\nu_i)^2 - \omega_{ci}^2]}$$

Here $i = 1$ for n -InSb semiconductor plasma, $i = 2$ for the lower stream of the electrons in n -GaAs plasma and $i = 3$ for the upper stream. ωp_i and ω_{ci} are respectively the plasma frequency and the cyclotron frequency of the electrons. ϵ_{I1} is the frequency independent lattice dielectric constant of the medium I and ϵ_{I2} is the frequency dependent lattice dielectric constant of the medium II which is given by

$$\epsilon_{I2} = \frac{\epsilon^\infty \omega^2 - \epsilon^0 \omega_T^2}{\omega^2 - \omega_T^2}$$

where ϵ^∞ and ϵ^0 are the high and low frequency dielectric constants respectively and ω_T is the transverse optical phonon frequency.

The collision frequency ν is given by

$$\nu = \nu_0(T_e/T_0)^{\frac{1}{2}} \quad (3)$$

where T_e is the effective carrier temperature due to the heating electric field; E_0 , T_0 is the lattice temperature and ν_0 the collision frequency when $T_e = T_0$. The effective temperature can be calculated by the procedure outlined by Kaushik *et al* (1975).

After writing the solutions of eqs (1) and (2) in the respective media and applying the proper boundary conditions at the interface $x = 0$, one can arrive at the following dispersion relation

$$\sum_{i=1}^5 C_i k^i + C_0 = 0 \quad (4)$$

where

$$C_8 = v_1^4(a_{75} - \epsilon a_{67})$$

$$C_7 = a_{15}a_{75} - \epsilon a_{22}a_{67} + v_1^4(a_{76} - \epsilon a_{68})$$

$$C_6 = a_{16}a_{75} + a_{15}a_{76} - \epsilon(a_{23}a_{67} + a_{22}a_{68}) + v_1^4(a_{77} - \epsilon a_{64})$$

$$C_5 = a_{17}a_{75} + a_{16}a_{76} + a_{15}a_{77} - \epsilon(a_{24}a_{67} + a_{23}a_{68} + a_{22}a_{69}) + v_1^4(a_{78} - \epsilon a_{70})$$

$$C_4 = a_{27}a_{75} + a_{17}a_{76} + a_{16}a_{77} - \epsilon(a_{19}a_{67} + a_{24}a_{68} + a_{23}a_{69} + a_{22}a_{70}) + v_1^4(a_{79} - \epsilon a_{71})$$

$$C_3 = a_{27}a_{78} + a_{17}a_{77} + a_{16}a_{78} + a_{15}a_{79} \\ - \epsilon(a_{19}a_{68} + a_{24}a_{69} + a_{23}a_{70} + a_{22}a_{71})$$

$$C_2 = a_{27}a_{77} + a_{17}a_{78} + a_{16}a_{79} \\ - \epsilon(a_{19}a_{69} + a_{24}a_{70} + a_{23}a_{71})$$

$$C_1 = a_{27}a_{78} + a_{17}a_{79} - \epsilon(a_{19}a_{70} + a_{24}a_{71}),$$

$$C_0 = a_{27}a_{79} - \epsilon a_{19}a_{71},$$

$$a_{15} = (3j\nu_1 - 4\omega)v_1^3, \quad a_{16} = v_1^2(6\omega^2 - 9j\nu_1\omega - 3\nu_1^2 - \omega c_1^2),$$

$$a_{17} = v_1(9j\nu_1\omega^2 + 6\omega\nu_1^2 - 4\omega^3 - j\nu_1^3 - j\nu_1\omega c_1^2 + 2\omega\omega c_1^2),$$

$$a_{19} = a_{18}a_{11}/\omega, \quad a_{18} = \omega a_{12} - a_{11}p_1^2(\omega, a_{11} = \omega(\omega - j\nu_1),$$

$$a_{21} = \omega^2 - \nu_1^2 - \omega c_1^2 - 2j\nu_1\omega, \quad a_{22} = (3j\nu_1 - 4\omega)v_1^3,$$

$$a_{23} = a_{11}a_{20}/\omega - v_1a_{21}, \quad a_{20} = (3\omega - 2j\nu_1)v_1^2,$$

$$a_{21} = v_1[\omega p_1^2 - a_{12} + 2\omega(j\nu_1 - \omega)], \quad a_{27} = a_{11}a_{12},$$

$$a_{24} = a_{11}a_{21}/\omega - v_1a_{18}, \quad a_{67} = v_2^2a_{35}a_{56}, \quad a_{35} = a_{26}^2 - \omega c_3^2,$$

$$a_{26} = \omega - j\nu_3, \quad a_{56} = (\omega \epsilon_{l2}a_{26} - \omega p_3^2)v_2^2, \quad a_{25} = \omega - j\nu_2,$$

$$a_{68} = v_2^2a_{57}a_{35} + a_{56}a_{54}, \quad a_{57} = v_2(\omega + a_{25})[\omega p_3^2 - \epsilon_{l2}\omega a_{26}],$$

$$a_{54} = -2v_2a_{25}a_{35}, \quad a_{69} = v_2^2a_{58}a_{35} + a_{57}a_{54} + a_{56}a_{34}a_{35},$$

$$a_{58} = \epsilon_{l2}\omega^2A_{25} - \omega(a_{26}\omega p_2^2 + a_{25}\omega p_3^2), \quad a_{34} = a_{25}^2 - \omega c_2^2,$$

$$A_{25} = a_{25}, \quad a_{70} = a_{54}a_{58} + a_{57}a_{34}a_{35}, \quad a_{71} = a_{58}a_{34}a_{35},$$

$$a_{75} = -a_{60}a_{28}, \quad a_{60} = v_2^3(\omega p_3^2a_{26} - \epsilon_{l2}\omega a_{35}), \quad a_{28} = v_2a_{26},$$

$$a_{76} = -a_{61}a_{28} + a_{60}A_{25}, \quad a_{61} = v_2^2(\omega + a_{25})[\epsilon_{l2}a_{35} - \omega p_3^2a_{26}],$$

$$a_{77} = -a_{62}a_{28} + a_{61}A_{25}, \quad a_{78} = -a_{63}a_{28} + a_{62}A_{25},$$

$$a_{62} = v_2(a_{34} + 2\omega a_{25})(\omega p_3^2a_{26} - \omega \epsilon_{l2}a_{35}) + \omega v_2\omega p_2^2a_{35},$$

$$a_{63} = \omega[\epsilon_{l2}\omega a_{34}a_{35} - \omega p_2^2a_{25}a_{35} - \omega p_3^2a_{26}a_{34}],$$

$$a_{79} = a_{63}A_{25},$$

and

$$\epsilon_l = (\epsilon_{l2}/\epsilon_{l1})^2.$$

In arriving at the dispersion relation (4), we have assumed that the drift velocity of the electrons v_3 in the upper stream vanishes and consequently provides the stationary background plasma.

Table 1. The variation of the roots of the dispersion relation for different ω .

$$\frac{\omega_{p2}}{\omega_t} = 1.2 = \frac{\omega_{p3}}{\omega_t}, \quad B_0 = 100\text{KG and } \nu_2 = \nu_3 = 0$$

$E_d(\text{esu})$	T_e/T_0	$\omega(\text{rad. sec}^{-1})$	$k_1 = \alpha_1 + j\beta_1$		$k_2 = \alpha_2 + j\beta_2$		$k_3 = -\alpha_3 - j\beta_3$	
			α_1	β_1	α_2	β_2	α_3	β_3
0.90	1.5	2×10^8	0.145×10^1	0.644×10^0	0.995×10^{-3}	0.721×10^{-2}	0.493×10^{-2}	0.493×10^{-2}
		4	0.193	0.121×10^1	0.159	0.546	0.496	0.497
		6	0.235	0.170	0.217	0.475	0.497	0.498
		8	0.277	0.218	0.246	0.439	0.498	0.498
		10	0.319	0.267	0.263	0.418	0.4198	0.498
		12	0.360	0.317	0.275	0.404	0.498	0.499
		14	0.402	0.366	0.283	0.394	0.498	0.499
		16	0.443	0.415	0.289	0.386	0.499	0.499
		18	0.498	0.465	0.294	0.380	0.499	0.499
		20	0.526	0.514	0.298	0.375	0.499	0.499

Table 2. The effect of heating electric field on the roots of the dispersion relation for three values of ω_{p3} at a fixed frequency $\omega = 2.0 \times 10^9 \text{ rad. sec}^{-1}$, $B_0 = 100 \text{ KG}$, $\omega_{p2} = 1.2 \omega_T$ and $v_2 = v_3 = 0$

$E_0(\text{esu})$	$\frac{T_e}{T_0}$	$k_1 = \alpha_1 + j\beta_1$	$\omega_{p3} = 1.2 \omega_T$ α_2	$k_2 = \alpha_2 + j\beta_2$ β_2
0.90	1.5	0.526×10^1	0.514×10^1	0.298×10^{-2}
1.20	2.0	0.109×10^2	0.119×10^2	0.351
1.60	2.5	0.281	0.315	0.327
1.80	4.0	0.200	0.222	0.340
1.90	5.0	0.170	0.187	0.340
2.00	6.0	0.153	0.168	0.327

Table 2. (contd)

$k_1 = \alpha_1 + j\beta_1$ α_1	$\omega_{p3} = 3.3 \omega_T$ $k_2 = \alpha_2 + j\beta_2$ α_2	$k_1 = \alpha_1 + j\beta_1$ β_1	$\omega_{p3} = 5.2 \omega_T$ $k_2 = \alpha_2 + j\beta_2$ α_2	β_2
0.330×10^3	0.570×10^2	0.328×10^{-2}	0.33×10^{-2}	0.913×10^2
0.776	0.873	0.331	0.335	0.216×10^3
0.215×10^3	0.236×10^3	0.332	0.334	0.332
0.154	0.166	0.332	0.334	0.333
0.130	0.139	0.332	0.334	0.333
0.117	0.125	0.332	0.334	0.333

3. Results and discussion

The resulting dispersion relation (4) is of eighth degree in complex wave number $k(k = \alpha + j\beta)$ and therefore it is very difficult to solve it analytically. We have solved it numerically with the help of IBM-1130 computer for different cases.

The mechanism of obtaining the growing surface wave modes is such that the product $\alpha\beta$ must always be positive and thus the power is extracted by the wave from the medium which causes the convective instability.

The following numerical values of the different parameters have been used. For n -InSb: $\epsilon_{t1} = 17.5$, $m_1 = 0.013m_0$, $n_0 = 2 \times 10^{16} \text{ cm}^{-3}$, $\nu_0 = 2.2 \times 10^{12} \text{ sec}^{-1}$ at 290°K . For n -GaAs: $\epsilon^0 = 12.0$, $\epsilon^\infty = 10.9$, $f_T (= \omega_T/2\pi) = 8.2 \times 10^{12} \text{ sec}^{-1}$, $m_2 = 0.072m_0$, $m_3 = 0.36m_0$ and $\omega_{p2}/\omega_T = 1.2$ which corresponds to the electron concentration of $8.2 \times 10^{16} \text{ cm}^{-3}$. The results have been obtained for different values of ω_{p3}/ω_T .

Let us first consider the case $\nu_2 = \nu_3 = 0$. Table 1 shows the variation of the roots with the frequency for a fixed value of E_0 at $B_0 = 100 \text{ KG}$. Only those roots for which the product $\alpha\beta$ is positive are shown. It is found that the two roots k_1 and k_3 grow with the frequency.

The effect of increasing electric field on the roots of the dispersion relation for three different values of ω_{p3} at $B_0 = 100 \text{ KG}$ and $\omega = 2 \times 10^9 \text{ rad. sec}^{-1}$ is shown in Table 2. It is found that for all these values of ω_{p3} there exists one root k_1 which increases with the heating field. It is also found that for a particular value of the heating field, k_1 increases with the increasing values of ω_{p3} .

Tables 3, 4 and 5 show the effect of magnetic field for $\omega_{p3} = 1.2\omega_T$, $3.3\omega_T$ and $5.2\omega_T$ respectively at $E_0 = 1.6 \text{ (esu)}$, $\omega = 10^9 \text{ rad. sec}^{-1}$ and $\omega_{p2} = 1.2\omega_T$. It is found that there exists at least one root k_1 which increases sharply with the

Table 3. The effect of applied magnetic field on the roots of the dispersion relation $\omega = 10^9 \text{ rad. sec}^{-1}$, $E_0 = 1.6 \text{ esu}$, $\omega_{p3} = \omega_{p2} = 1.2\omega_T$ and $\nu_1 = \nu_2 = 0$

$B_0(\text{KG})$	$k_1 = \alpha_1 + j\beta_1$		$k_2 = -\alpha_2 - j\beta_2$		$k_3 = -\alpha_3 - j\beta_3$	
	α_1	β_1	α_2	β_2	α_3	β_3
1	0.888	0.167×10^{-1}	0.264	0.104	0.115×10^{-1}	0.392×10^{-1}
3	0.933	0.732	0.205×10^{-2}	0.311×10^{-2}	0.297	0.301
5	0.101×10^1	0.203×10^0	0.461	0.475	0.299	0.300
8	0.157	0.837	0.494	0.496	0.299	0.300
10	0.229	0.167×10^1	0.497	0.498	0.299	0.3000
15	0.728	0.743	0.499	0.499	0.299	0.300
20	0.207×10^2	0.229×10^2	0.499	0.299	0.299	0.300

magnetic field for all these values of ω_{p3} . The other roots k_2 and k_3 are little affected by the magnetic field.

Table 4. The effect of applied magnetic field on the roots of the dispersion relation.

$\omega = 10^9(\text{rad. sec}^{-1})$, $E_0 = 1.6(\text{esu})$, $\omega_{p3} = 3.3\omega_p$, $\omega_{p2} = 1.2\omega_T$ and $\nu_1 = \nu_2 = 0$

$B_0(\text{KG})$	$k_1 = \alpha_1 + j\beta_1$		$k_2 = -\alpha_2 - j\beta_2$		$k_3 = -\alpha_3 - j\beta_3$	
	α_1	β_1	α_2	β_2	α_3	β_3
1	0.910	0.446×10^{-1}	0.233×10^{-1}	0.191×10^{-1}	0.275×10^{-1}	0.312×10^{-1}
3	0.114×10^1	0.347×10^0	0.461×10^{-2}	0.474×10^{-2}	0.299	0.300
5	0.162	0.954	0.494	0.496	0.299	0.300
8	0.479	0.472×10^1	0.499	0.499	0.299	0.300
10	0.102×10^2	0.110×10^2	0.499	0.499	0.299	0.300
15	0.483	0.544	0.499	0.499	0.299	0.300
20	0.151×10^3	0.171×10^3	0.499	0.499	0.299	0.300

Table 5. The effect of applied magnetic field on the roots of the dispersion relation

$\omega = 10^9(\text{rad. sec}^{-1})$, $E_0 = 1.6(\text{esu})$, $\omega_{p3} = 5.2\omega_T$, $\omega_{p2} = 1.2\omega_T$ and $\nu_1 = \nu_2 = 0$

$B_0(\text{KG})$	$k_1 = \alpha_1 + j\beta_1$		$k_2 = -\alpha_2 - j\beta_2$		$k_3 = -\alpha_3 - j\beta_3$	
	α_1	β_1	α_2	β_2	α_3	β_3
1	0.447×10^0	0.923×10^{-1}	0.613×10^{-2}	0.486×10^{-2}	0.290×10^{-1}	0.304×10^{-1}
3	0.123×10^1	0.497×10^0	0.484	0.489	0.299	0.300
5	0.242	0.200×10^1	0.497	0.498	0.299	0.300
8	0.103×10^2	0.113×10^2	0.499	0.499	0.299	0.300
10	0.241	0.269	0.499	0.499	0.299	0.300
15	0.119×10^3	0.134×10^3	0.499	0.499	0.299	0.300
20	0.380	0.425	0.499	0.499	0.299	0.300

The variation of the roots of the dispersion relation for three different values of ω_{p3} at $\omega_{p2} = 1.2\omega_T$ and $B_0 = 100\text{KG}$ is shown in Table 6 for the case when $\nu_2 \neq 0$ and $\nu_3 \neq 0$. The results are shown for $\nu_2 = 0.4$, $\omega_{p2}, \nu_3 = 0.4\omega_{p3}$ and $\nu_2 = \omega_{p2}, \nu_3 = \omega_{p3}$, for the first seven roots only. It is found that there exist two roots k_1 and k_5 which show the convective instability for $\omega_{p2} = \omega_{p3} = 1.2\omega_T$, the growth rate decreases with increasing values of ν_2 and ν_3 for the mode k_1 while it increases for the mode k_5 . At higher values of ω_{p3} both the roots decrease with the collision frequency.

Acknowledgments

The author (RC) is thankful to the CSIR (India) for the financial assistance. He is also thankful to the Director, Prof. Abdus Salam, for providing the kind hospitality during his stay at the International Centre for Theoretical, Physics, Trieste (Italy) where this work was in progress.

References

- Bartelink D. J. 1967 *Phys. Rev.* **15B** 400
Bok J. and Nozières P. 1963 *J. Phys. Chem Solids* **24** 709
Hsieh H. C. 1972 *Phys. Rev.* **B6** 4160
Kaushik S. C. Sharma R. P. Arora A. K. and Guha S. 1975 *J. Phys. Chem. Solids* **36** 529
Ramechandra and Verma J. S. 1976 *Int. J. Electron* **42** 181
Ram Chandra and Verma J. S. 1976a *Indian J. Pure and Appl. Phys.* **14** 441
Ram Chandra 1977 *Int. J. Electron* **42** 511
Ram Chandra and Verma J. S. 1976c *Private Communication*
Ramechandra and Verma J. S. 1975 *Indian J. Phys.* **49** 831

Silver iodide-growth, electrical and optical properties

P A Govindacharyulu and D N Bose*

Electrical Communication Engineering Department, Indian Institute of Science, Bangalore.

1. Introduction

The optical and electrical properties of some of the silver halides have been studied in considerable detail, specially because of their importance in photography (Brown 1967). While silver chloride and bromide are thus well understood, comparatively little information is available on silver iodide primarily due to the difficulty in growing good single crystals. This is because β - α transition at 147°C rules out growth from the melt. Recently methods have been developed for the growth of β -AgI crystals from solutions and in silica gels (Suri *et al* 1970) enabling the detailed study of their properties.

Silver iodide presents some interesting differences with other silver halides. At room temperature it exists in the stable wurzite structure (β -AgI) or in the meta-stable sphalerite structure (γ -AgI), while the other halides have the NaCl structure. At 147°C β -AgI undergoes a phase transition to a b.c.c. structure (α -AgI) which exhibits fast ion conduction. The present study of ionic conductivity, photoconductivity and drift mobility was carried out on single crystal β -AgI and has led to the determination of defect creation and migration energies and understanding of carrier transport and band-structure.

2. Growth

Single crystals of β -AgI were grown in the form of platelets and pyramids by slow dilution of KI-AgI complex in silica gel at 40°C. AgI is insoluble in water but highly soluble in aqueous solutions of KI or HI, the solubility decreasing rapidly with dilution. This forms the principle of the growth method. An acid gel was formed by reacting sodium metasilicate with a mixture of KI and acetic acid. The gel was allowed to set for a day. A concentrated solution of KI was first diffused into the gel followed by a solution of AgI in KI for a period of two weeks. The supernatant liquid was then diluted with water at intervals of one week. The system was kept at 40°C throughout. Dilution led to the decomplexing of the KI-AgI complex formed originally in the gel and the growth

* Presently at Materials Science Centre.
Indian Institute of Technology, Kharagpur.

of two types of crystals, hexagonal platelets upto 8 mm. and pyramids upto 4 mm. in diameter respectively. 0.8 mole per cent doping with copper could be achieved during growth, but no other impurities could be similarly incorporated. Compositional characterisation using spectrographic analysis revealed trace impurities less than 20 ppm of Si, K, Fe and Cu.

3. Ionic conductivity

Samples cleaved from hexagonal pyramids with silver paint contacts were used for measurements at 10 Hz near and above room temperature and with d.c. at low temperatures. Conductivity was measured both parallel and perpendicular to the *c*-axis on undoped and copper-doped specimens and also on specimens soaked in CdCl₂ solution and annealed at 80°C to provide cadmium doping. The activation energies E_1 and E_2 obtained from plots of $\log \sigma T$ vs $1/T$ at high and low temperatures respectively are given in Table 1.

Table 1

Crystal and direction	E_1 (eV)	E_2 (eV)
Parallel to <i>c</i> -axis		
Undoped	0.73 (0.79)	0.41 (0.62)
Copper-doped	0.74 (0.79)	0.44 (0.49)
Cadoniuim-doped	0.73	0.50
Perpendicular to <i>c</i> -axis		
Undoped	0.58 (0.59)	0.38 (0.39)
Copper-doped	...	0.39-0.43
Cadmium-doped	...	0.50

The values obtained by Cochrane and Fletcher (1971) are given in brackets. From table 1, the Frenkel defect formation energy $h_f = 2(E_1 - E_2)$ is found to be 0.64 eV. Divalent cadoniuim is known to introduce silver vacancies and hence the activation energy for silver vacancies $h_{m_v}(c) = 0.50$ eV while from the results on undoped specimens the interstitial migration energy $h_{m_i}(c) = 0.41$ eV. In particular the interstitial mobility is found to be given by

$$\mu_i = \frac{8.3 \times 10^2}{T} \exp \left(-\frac{0.41}{kT} \right)$$

and is 4.0×10^{-7} cm²/V-sec at 300°K.

The effect of copper doping has been found to reduce the lattice parameter by 0.44% and hence the slight increase in activation energies could be due to motion in a contracted lattice. Cochrane and Fletcher (1971) had assumed that copper existed in the divalent state which would obviously give rise to the creation of silver vacancies. The present conductivity measurements do not support this conclusion. E.S.R. studies from 77°K to 300°K in copper-doped

crystal further showed that less than 1 copper atom in 1000 could be in the Cu^{++} state since no signal corresponding to Cu^{++} could be detected. The basic difference between Cd^{++} and Cu^{++} is in the high second ionisation potential of Cu^+ , 20.28 eV compared with 16.91 eV for Cd^+ , which thus favours the Cu^+ state.

4. Photoconductivity

The excitation spectra of photoconductivity in undoped and copper-doped $\beta\text{-AgI}$ are shown in figure 1. Peak response was found to occur at 2.88 eV for undoped and at 2.81 eV for copper-doped specimens at 260°K. These values as well as

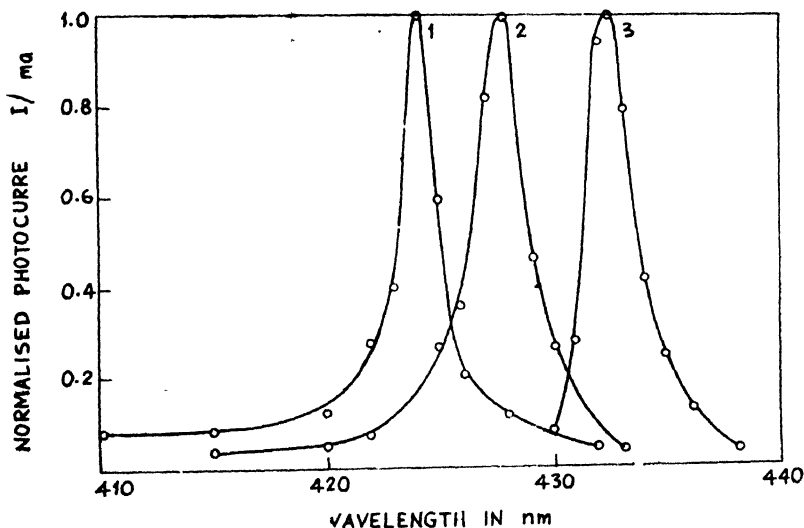


Figure 1. Spectral response curves of photo-conductivity.

1. Pure $\beta\text{-AgI}$ at 147°K
2. Pure $\beta\text{-AgI}$ at 222°K
3. Copper-doped $\beta\text{-AgI}$ (0.8 mole percent) at 141°K.

the temperature dependence agree well with the absorption edge energies measured by Suri and Henisch (1971) on single crystals but differ from the results of Cardona (1963) obtained on evaporated thin films. The comparison is given in Table 2.

No additional structure was found for copper-doped specimens suggesting that as CuI-AgI forms a solid solution, a decrease in band-gap occurs without formation of localised states.

The anisotropy in photoconductivity with the incident radiation polarised parallel or perpendicular to the c -axis is very similar to that observed in other compounds such as CdS with wurzite structure. This is due to the nature of

the valence band which is split into a Γ_9 and two Γ_7 levels. The anisotropy is measure of the energy difference between the Γ_9 and the upper Γ_7 level at $k = 0$. The valence band structures of AgCl and AgBr as discussed by Brown are quite different, with the maximum displaced from $k = 0$ and exhibits no splitting. Band-structure calculations (Smith 1976) leave no doubt that the conduction band minimum in all these compounds is at $k = 0$.

Table 2.

	This work	Suri and Henisch (1971)	Cardona (1963)
Photoconductivity Peak/ Absorption edge (eV)	2.88 (260°K)	2.85 (260°K)	2.95 (4°K)
Pure specimens			
Copper-doped (0.8 mole percent)	2.81 (260°K)	2.79 (260°K)	...
Shift due to copper doping (eV)	0.07	0.06	0.004 (4°K)
Temperature dependence of band-gap (eV/°K)	4×10^{-4}	2.8×10^{-4}	0.4×10^{-4}
Anisotropy Pure specimens (eV)	0.01	0.016	0.036

Thus β -AgI probably has a direct band-gap like CdS with the valence band maximum at $k = 0$ unlike AgCl and AgBr.

5. Drift Mobility

Drift mobility was measured by direct observation of the transit-time of holes excited by a 0.5 μ sec duration argon flash (Govindacharyulu and Bose 1977). Pulsed drift fields were used to avoid ionic polarisation. The charge of the drifting carrier which was positive was determined unambiguously by the polarity of the applied field, electron life-times being too small to allow mobility measurements. Transittimes were measured for a range of applied voltages, and the mobility μ_d obtained by plotting τ_t vs $1/V$, since $\mu_d = L^2/V\tau_t$, where L = specimen length. The variation of μ_d between $T = 260$ – 320°K is shown in figure 2 and shows a traplimited behaviour given by

$$\frac{\mu_d}{\mu_m} = \frac{1}{1 + \frac{g_t}{g_0} \frac{N_t}{N_v} e^{-E_t/kT}}$$

where μ_m = microscopic mobility, g_t/g_0 = ratio of the statistical weights for full and empty trapping states = 2, N_v = valence band density-of-states, N_t = trap

concentration and E_t = trap depth. By curve-fitting it is found that $N_t = (3 \times 10^9 - 5 \times 10^9)/\text{cm}^3$ and $E_t = 0.52 - 0.50$ eV. At 300°K , $\mu_a = 12$ $\text{cm}^2/\text{V}\cdot\text{sec}$. This value is much larger than those found in AgCl and AgBr which are typically less than 1 $\text{cm}^2/\text{V}\cdot\text{sec}$ and is probably due to both the more covalent nature of β -AgI giving weaker hole-lattice coupling (coupling constant $\alpha = 1.8$ for β -AgI, 4.1 for AgCl and 4.0 for AgBr) and also to a lower hole effective mass.

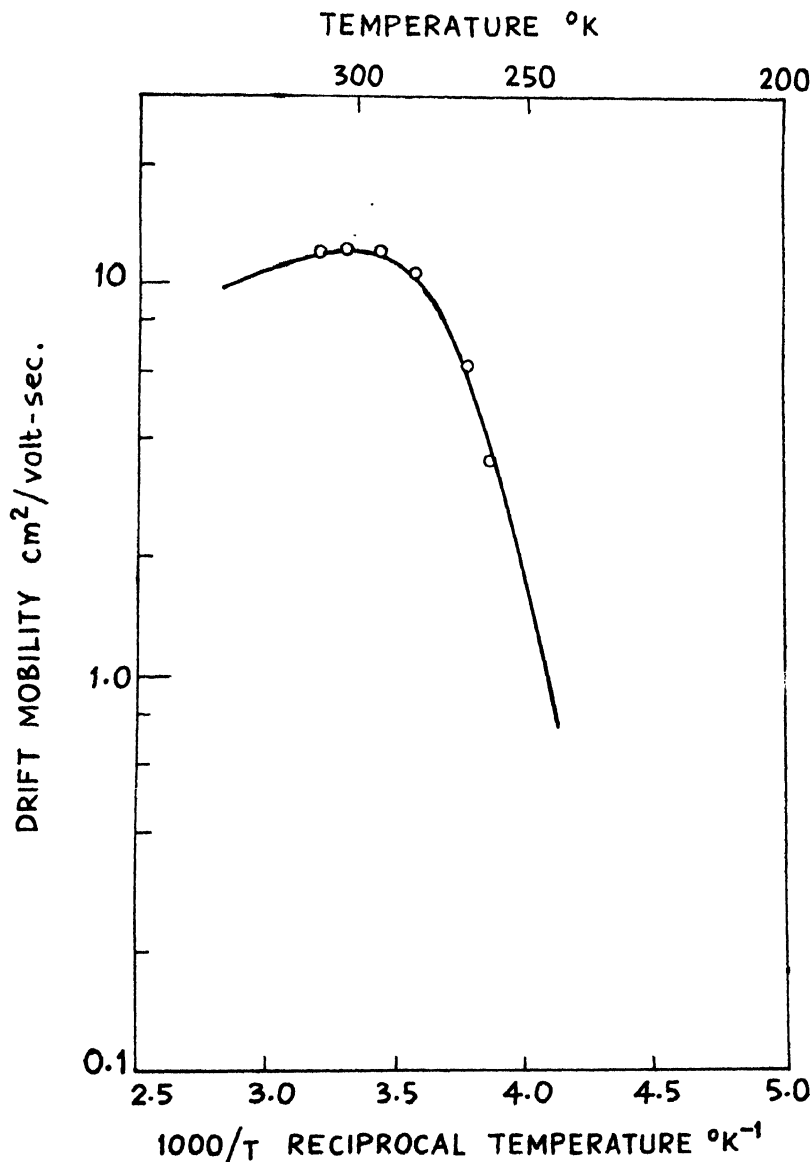


Figure 2. Drift mobility of holes as a function of reciprocal temperature. Solid line is the computed variation of mobility using $E_t = 0.52$ eV and $N_t = 3 \times 10^9 \text{ cm}^{-3}$,

6. Trap Depths

The decrease of steady-state photoconductivity with decreasing temperature confirmed the presence of deep hole traps at 0.50 eV found previously from drift mobility experiments. When the specimen was biased for electron injection $\log I$ vs $1/T$ plot showed an electron trap of depth 0.28 eV. This trap was also responsible for an increase in photoconductivity due to holes below 200°K. Finally transient photoconductivity measurements were carried out (Bose and Govindacharyulu 1976) and showed the presence of shallow hole traps at 0.14 eV. The concentration and capture cross-section of the three sets of traps are given in Table 3.

Table 3

Trap	Energy	Conc.	Cross-section
Hole	0.50–0.52 eV	$(3-5) \times 10^9/\text{cm}^3$	10^{-11} cm^2
Hole	0.14 eV	$7 \times 10^{16}/\text{cm}^3$	10^{-16} cm^2
Electron	0.28 eV		

The deep hole trap with large cross-section is expected to be a multivalent Coulomb trap due to a double charged anion or impurity complex. The shallow electron and hole traps which have large concentration could be associated with silver ion interstitials and vacancies respectively. In addition there must be recombination centres whose nature remains undetermined. It was found possible to sensitise the crystals and increase photoconductivity through an increase of hole life-time by annealing in iodine at 80°C. Heating above the transition temperature of 147°C on the other hand found to cause a drastic decrease in lifetime due to creation of additional trapping centres.

Acknowledgment

One of the authors (P.A.) would like to thank the C.S.I.R. for the award of a Junior Research Fellowship.

References

- Brown F C 1967 *Physics of Solids*, W A Benjamin Inc, New York
- Suri S K, Henisch H K and Faust J W Jr 1970 *J. Cryst. Growth* **6** 213
- Cochrane G and Fletcher N H 1971 *J. Phys. Chem. Solids* **32** 2557
- Suri S K and Henisch H K 1971 *Phys. Stat. Sol.* (6) **44** 627
- Cardona M 1963 *Phys. Rev.* **129** 69
- Smith P V 1976 *J. Phys. Chem. Solids* **37** 589
- Govindacharyulu P A and Bose D N 1977 *J. App. Phys.* **48** 1381
- Bose D N and Govindacharyulu P A 1976 *Proc. 13th Int. Conf. on Physics of Semiconductors*, Rome

Surface segregation in gold-silver alloys

Vijay Kumar

Department of Physics, University of Roorkee
Roorkee-247672 and
Department of Physics, D.B.S. College, Dehradun*
and

Deepak Kumar and S. K. Joshi

Department of Physics, University of Roorkee
Roorkee-247672

1. Introduction

Recently, Overbury and Somarjai (1976) have studied the surface composition of Au-Ag alloys at 800°K using Auger electron spectroscopy (AES). They have compared their experimental data with the monolayer regular solutions theory. They find that the monolayer regular solution theory predicts much more segregation for Ag at the surface than is found experimentally. The heat of mixing in these alloys and the difference in the heats of vapourisation of pure Au and Ag is quite large (see Hultgren 1963). Further there is experimental evidence based on X-ray diffraction (Averbach 1965), which shows that there is considerable short-range order in these alloys. Thus it is expected that the monolayer regular solution model will not be appropriate for Au-Ag alloys.

Recently Kumar, Mookarjee and Kumar (1976) (to be referred as I) in the text) have developed a theory of surface segregation for nonideal solid solutions. This theory predicts the variation of concentration with layers as one moves from top surface layer to the bulk, and has accounted for various features of surface segregation like temperature dependence etc., quite successfully. However, in the above theory the short range order was not taken into account. In this paper, firstly we extend the theory of I to take into account the short range order in Guggenheim-Fowler approximation (Guggenheim 1952). Secondly we use a more realistic procedure to determine the two thermodynamic parameters required in the theory. Previously, these parameters were taken to be constants. We now use the method of Averbach (1965) and the data of Hultgren (1963) to calculate these. In this way we are able to take into account to some extent the vibrational contributions to free energy, which are otherwise neglected in the model. The theory is explicitly applied to Ag-Au alloys.

*Present address

2. The model and its free energy

We consider a semi-infinite solid binary alloy in thermodynamic equilibrium. For details of the model, we refer the reader to I. Following the notation of I, we write for the configuration energy

$$U_N(N_{AA}, N_{AB}) = \epsilon_{AA}N_{AA} + \epsilon_{AB}N_{AB} + \epsilon_{BB}N_{BB} \quad (1)$$

where N_{AA} gives the number of AA nearest neighbour pairs etc. in the given configuration. We divide the semi-infinite system lattice into layers parallel to over planar surface, and number the layers $\alpha = 0, 1, 2, \dots, \xi$, $\lambda = 0$ denoting the surface. Let N^λ , N_A^λ , N_B^λ denote the total number of sites in the λ -th layer, number of A atoms in the λ -th layer and number B atoms on the λ -th layer respectively. Since the energy depends on the nearest neighbour atom pairs, let $N_{AA}^{\lambda\lambda}$, $N_{BB}^{\lambda\lambda}$, $N_{AB}^{\lambda\lambda}$ denote the pairs within the λ -th layer, and $N_{AA}^{\lambda, \lambda+1}$, $N_{BA}^{\lambda, \lambda+1}$, $N_{BB}^{\lambda, \lambda+1}$ denote the pairs when the two neighbours are in λ -th and $(\lambda+1)$ th layer. Next we introduce the short range order parameters in the usual manner of solid solution theory (Guggenheim 1952) we write

$$N_{AB}^{\lambda\lambda} = 2x_\lambda y_\lambda \alpha_\lambda N^{\lambda\lambda} \quad (2a)$$

$$N_{AA}^{\lambda\lambda} = x_\lambda (1 - \alpha_\lambda y_\lambda) N^{\lambda\lambda} \quad (2b)$$

$$N_{BB}^{\lambda\lambda} = y_\lambda (1 - \alpha_\lambda x_\lambda) N^{\lambda\lambda} \quad (2c)$$

where $x_\lambda = N_A^\lambda / N^\lambda$ and $y_\lambda = N_B^\lambda / N^\lambda$. Since the concentration x_λ is to vary with λ , we shall require two more short range order parameters to obtain similar expressions for interlayer pairs. Thus, we have

$$N_{AB}^{\lambda, \lambda+1} = x_\lambda y_{\lambda+1} \beta_\lambda N^{\lambda, \lambda+1} \quad (3a)$$

$$N_{AA}^{\lambda, \lambda+1} = x_\lambda (1 - \beta_\lambda y_{\lambda+1}) N^{\lambda, \lambda+1} \quad (3b)$$

$$N_{BB}^{\lambda, \lambda+1} = y_\lambda (1 - \beta'_\lambda x_{\lambda+1}) N^{\lambda, \lambda+1} \quad (3c)$$

$$N_{BA}^{\lambda, \lambda+1} = y_\lambda x_{\lambda+1} \beta'_\lambda N^{\lambda, \lambda+1} \quad (3d)$$

The two parameters β_λ and β'_λ are not independent. The relation between them follows from the constraint

$$N_{AA}^{\lambda, \lambda+1} + N_{BA}^{\lambda, \lambda+1} = Z_1 N_A^{\lambda+1} \quad (4)$$

where Z_1 denotes the number of nearest neighbours between two successive layers. The Eq. 4 gives

$$x_\lambda - x_{\lambda+1} = \beta_\lambda x_\lambda y_{\lambda+1} - \beta'_\lambda y_\lambda x_{\lambda+1} \quad (5)$$

The configurational entropy is given by

$$S = k \log P_N$$

where P_N is the number of configurations having a pre-assigned number of N_A^λ , N_B^λ , N_{AA}^λ , etc. In the spirit of Guggenheim-Fowler approximation, we write P_N as

$$P_N = \prod_{\lambda=0}^{\xi} \frac{N^{\lambda\lambda}!}{N_{AA}^{\lambda\lambda}! N_{AB}^{\lambda\lambda}! N_{BA}^{\lambda\lambda}! N_{BB}^{\lambda\lambda}!} \times \frac{N^{\lambda,\lambda+1}!}{N_{AA}^{\lambda,\lambda+1}! N_{AB}^{\lambda,\lambda+1}! N_{BA}^{\lambda,\lambda+1}! N_{BB}^{\lambda,\lambda+1}!} \\ \times \left(\frac{N_A^\lambda! N_B^\lambda!}{N^\lambda!} \right)^{Z_\lambda - 1} \quad (6)$$

where Z_λ denotes the number of nearest neighbours for an atom in λ -th layer. Substituting eqs. (2) and (3) in eqs. (1) and (6), we obtain

$$U = \sum_{\lambda=0}^{\xi} N^\lambda \left[\frac{Z_0 + 2Z_1}{2} \epsilon_{BB} + (Z_0 + Z_1) B x_\lambda + B Z_1 x_{\lambda+1} \right. \\ \left. + e \{ Z_0 x_\lambda y_\lambda \alpha_\lambda + Z_1 (x_\lambda y_{\lambda+1} \beta_\lambda + y_\lambda x_{\lambda+1} \beta'_\lambda) \} \right] \quad (7)$$

$$S = k \sum_{\lambda=0}^{\xi} N^\lambda \left[-\frac{Z_0}{2} \{ x_\lambda (1 - y_\lambda \alpha_\lambda) \ln x_\lambda (1 - y_\lambda \alpha_\lambda) + 2 x_\lambda y_\lambda \alpha_\lambda \ln x_\lambda y_\lambda \alpha_\lambda \right. \\ \left. + y_\lambda (1 - x_\lambda \alpha_\lambda) \ln y_\lambda (1 - x_\lambda \alpha_\lambda) \} - Z_1 \{ x_\lambda (1 - y_{\lambda+1} \beta_\lambda) \ln x_\lambda (1 - y_{\lambda+1} \beta_\lambda) \right. \\ \left. + x_\lambda y_{\lambda+1} \beta_\lambda \ln x_\lambda y_{\lambda+1} \beta_\lambda + y_\lambda x_{\lambda+1} \beta'_\lambda \ln y_\lambda x_{\lambda+1} \beta'_\lambda \right. \\ \left. + y_\lambda (1 - \beta'_\lambda x_{\lambda+1}) \ln y_\lambda (1 - \beta'_\lambda x_{\lambda+1}) \} + (Z_\lambda - 1) \{ x_\lambda \ln x_\lambda + y_\lambda \ln y_\lambda \} \right] \quad (8)$$

Here Z_0 denotes the number of intralayer nearest neighbours so that $Z = Z_0 + 2Z_1$, and

$$\epsilon = \epsilon_{AB} - \frac{\epsilon_{AA} + \epsilon_{BB}}{2}, \quad B = \frac{\epsilon_{AA} - \epsilon_{BB}}{2} \quad (9)$$

The quantities x_λ , α_λ and β_λ are now obtained by minimising the free energy $F = U - TS$ with the constraint that the overall concentrations in the alloys are fixed. Mathematically, this constraint is

$$\sum_{\lambda=0}^{\xi} N^\lambda x_\lambda = Nx. \quad (10)$$

The minimisation procedure leads to the following equations

$$\frac{Z_1 \epsilon}{kT} (\beta_\lambda y_{\lambda+1} - x_{\lambda+1} \beta'_\lambda + y_{\lambda-1} \beta'_{\lambda-1} - x_{\lambda-1} \beta_{\lambda-1}) + \frac{Z_1 B + \eta}{kT} \\ + \frac{Z_0}{2} \ln \frac{1 - y_\lambda \alpha_\lambda}{1 - x_\lambda \alpha_\lambda} + Z_1 \left\{ \ln \frac{1 - y_{\lambda+1} \beta_\lambda}{1 - x_{\lambda+1} \beta'_\lambda} + y_{\lambda+1} \beta_\lambda \ln \frac{y_{\lambda+1} \beta_\lambda}{1 - y_{\lambda+1} \beta_\lambda} \right. \\ \left. - x_{\lambda-1} \beta_{\lambda-1} \ln \frac{y_\lambda \beta_{\lambda-1}}{1 - y_\lambda \beta_{\lambda-1}} + y_{\lambda-1} \beta'_{\lambda-1} \ln \frac{x_\lambda \beta'_{\lambda-1}}{1 - x_\lambda \beta'_{\lambda-1}} - x_{\lambda+1} \beta'_\lambda \ln \frac{x_{\lambda+1} \beta'_\lambda}{1 - x_{\lambda+1} \beta'_\lambda} \right\} \\ - \left(Z_\lambda - \frac{Z_0}{2} - Z_1 - 1 \right) \ln \frac{x_\lambda}{y_\lambda} = 0 \quad (11a)$$

$$\alpha_\lambda = \frac{-1 + \sqrt{1 + 4\gamma x_\lambda y_\lambda}}{2\gamma x_\lambda y_\lambda} \quad (11b)$$

$$\beta_\lambda = \frac{-\{1 + \gamma(x_{\lambda+1} - x_\lambda)\} + [\{1 + \gamma(x_{\lambda+1} - x_\lambda)\}^2 + 4\gamma x_\lambda y_{\lambda+1}]^{\frac{1}{2}}}{2\gamma x_\lambda y_{\lambda+1}} \quad (11c)$$

where η is the Lagrangian multiplier for the constraint of Eq (9) and $\gamma = (e^{2\epsilon/kT} - 1)$. Noting the fact that the surface segregation occurs only in few top layers, we can determine η , by requiring a fixed concentration in the bulk. Thus η is determined by the equation

$$\eta \mid \frac{BZ}{kT} = \left(\frac{Z}{2} - 1\right) \ln \frac{x_b}{y_b} - \frac{Z}{2} \ln \frac{1 - y_b \alpha_b}{1 - x_b \alpha_b} \quad (12)$$

where the subscript b refers to bulk values.

3. Numerical results

As discussed in I, B is equal to the difference in the heats of vapourisations of metals A and B . The quantities ϵ and α are obtained from the data on heats of mixing of the alloys. We employ the method of Averbach (1965) to determine these quantities. ϵ turns out to be a slowly varying function of x_b and temperature.

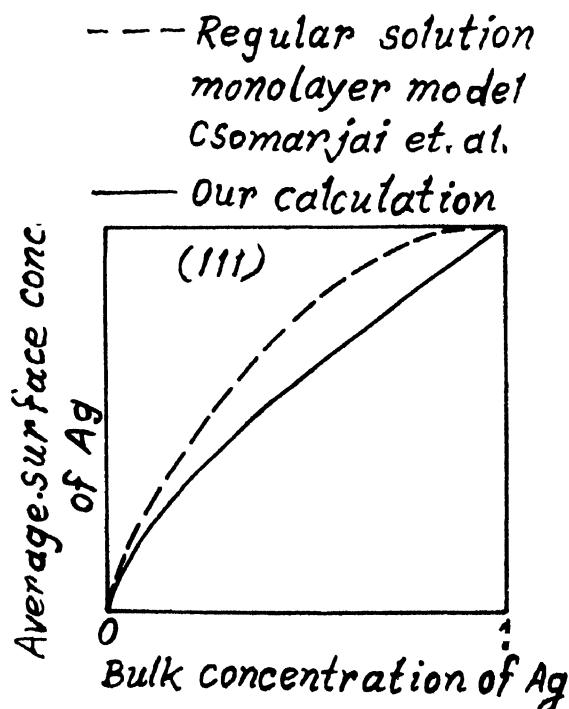


Figure 1. Plots of the surface concentration $m_\lambda = x_\lambda - y_\lambda$ vs bulk concentration ($m = x - y$) (—), (---) and (-.-) denotes respectively the first layer, second layer and the third layer compositions $T = 800^\circ\text{K}$

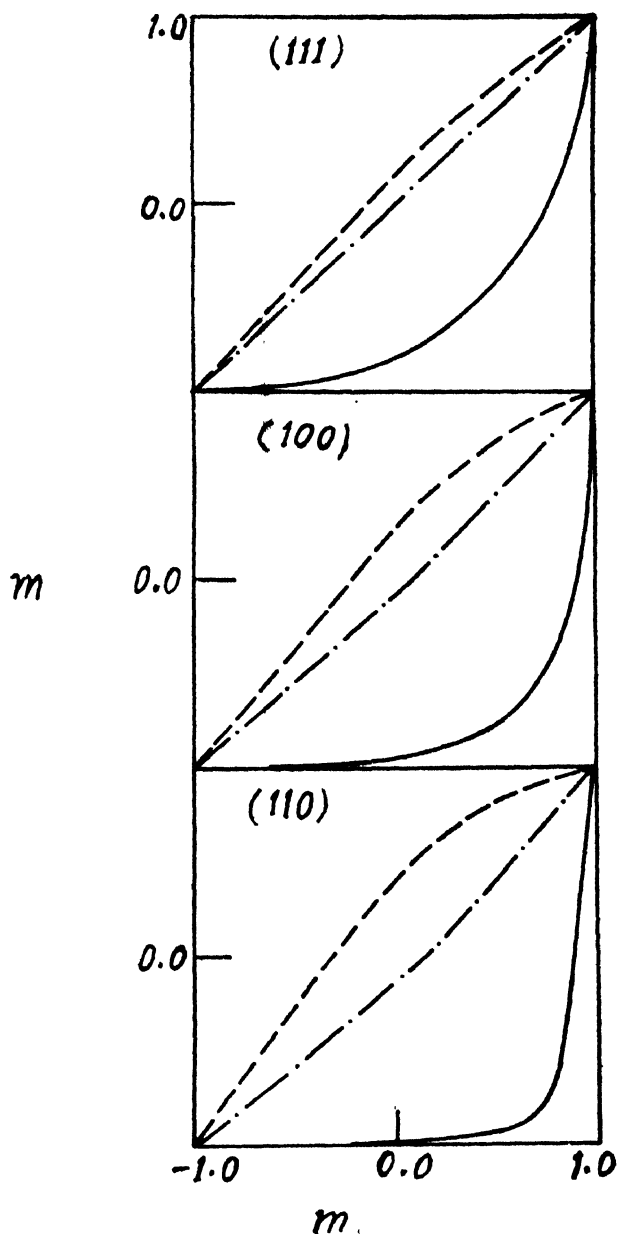


Figure 2. Plot of the surface compositions of Ag vs bulk Ag concentration. The full line denotes the averaged surface concentration of Ag which is the mean over the first three layers and the broken lines denotes the corresponding result obtained from regular solution monolayer model.

The temperature dependence of ϵ is easily understood as being due to vibrational contributions to heat of mixing. The concentration dependence is presumably related to the three body forces and long range forces in the alloys. Using the data tabulated by Hultgren *et al* (1963), we find $N\epsilon \simeq -260^\circ\text{cal/mol}$ and $NB = -1670 \text{ cal/mol}$ at 800°K . The numerical solutions for eqs. (11) are obtained following the method of I. We assume that x_i etc. assume bulk values within first three layers. Then we write eqn. 11 for the first three layers and solve them simultaneously. Here, we report the results in the absence of short-range order. The complete solution of eq (11) is in progress. Our calculation shows that a rather heavy enrichment of Ag occurs at the top layer. However, the variation of concentration with layers is not monotonic, for in the second layer, there is a slight enrichment of Au. In the third layer again enrichment of Ag occurs. This sort of oscillation is to be expected as ϵ is negative for these alloys, so that unlike pairs have lower energy. The results are shown in Fig. 1. Our results for the segregation on the top layer are much higher than those observed experimentally by AES. However, we content that an AES experiment probes not just the top layer but one or two layers more beneath the top layer. So for comparisons sake, we should calculate the average concentration over first few layers. The Fig. 2 shows the average of Ag concentration on first three layers and its comparison with the results of monolayer model. Our results are closer to experimental values.

References

- Averbach B. L. 1965 *Energetics in Metallurgical Phenomena*, Vol II Edited by W. M. Mueller (Gordon and Breach, New York)
- Guggenheim E. A. 1952 *Mixtures* (Oxford Press, London 1952).
- Hultgren R., Orr R., Anderson P. and Kelle K. 1963 *Selected Values of Thermodynamics Properties of Metals and Alloys* (Wiley, New York).
- Kumar D., Mookerjee A. and Kumar V. 1976 *J. Phys* **F6**, 725.
- Overbury S. H. and Somorjai G A 1976 *Surf. Sci.* **55**, 209.

Cathodoluminescence of point defects in polycrystalline CaS

P. K. Ghosh and V. Shanker

Materials Division, National Physical Laboratory, Hill Side Road, New Delhi-110012

1. Introduction

Early 1976, we had published an extensive work (Shanker *et al* 1976) on EPR of point defects in polycrystalline CaS, prepared by reduction of calcium sulphate in pure H_2 or H_2S . This method is expected to minimize contamination problems associated with the widely used method of reduction of calcium sulphate by carbon in air (see for example, Ghosh and Jain 1974). EPR of these samples in the temperature range of -100°C to -180°C , reveals a strong resonance signal a_0 , only under ultraviolet excitation. Above -100°C , this signal has an activation energy for thermal quenching of about 0.18 eV. It has been attributed to a sulphur vacancy with one electron raised from the lattice. We have also detected the presence of F' centres in CaS created by prior excitation by X-rays. The F' centre resonance signal has no appreciable thermal quenching, nor does it require ultraviolet excitation for its revelation. EPR of F' centres in CaS has been earlier reported by Auzins and coworkers (1963). We report, in the present paper, cathodoluminescence studies of the same CaS samples in the temperature range of 30°C to -100°C , carried out with a view to identifying omission of these centres.

Pure CaS is nearly nonluminescent under ultraviolet radiation from a mercury lamp. It possesses an optical band gap of about 4.8 eV (2600 Å). It is, therefore, difficult to excite this material with ultraviolet from normal sources, mercury lamp or vacuum ultraviolet, because the content of relevant u.v. energy is rather small. Absorption by air and normal window material further lowers this energy. This limitation is overcome by electron beam excitation.

2. Experimental

Demountable Cathodoluminescence Unit

Figure 1 shows a demountable vacuum chamber made of glass, in which the sample is excited by a high energy (~ 15 KeV) electron beam. Electrons are generated from a hot tungsten filament F , heated by a 6 volt controllable power supply FS. A variable bias from a 200 volt power supply GS is applied to grid G to control the beam current. A 0-20 KV, negative EHT supply is connected to the grid (or the filament). The glass chamber is coated with a conducting

aquadag coating AQ on the inside, leaving about 3 cms at the top. Anode baseplate B carries a copper rod C with one end inside the vacuum chamber; its outside end is dipped in liquid air for cooling. The inside end of C is faced at an angle of 45° and carries the sample. The aquadag coating and baseplate are earthed through an ammeter which measures the beam current. Parallel earth connections are avoided. Electrons are initially accelerated at the gap between the filament and aquadag coating AQ and fall thereafter at a constant energy towards the sample. A magnetic focussing coil FC focusses the electron beam to an approximately circular spot of about 1 mm diameter at the sample.

The O rings and gaskets used for the assembly and mounting of the baseplate are all made of teflon. The baseplate is supported by a wooden cylinder, which contains the dewar flask, by adjustable legs for fine tightening against the ground glass flange of the vacuum chamber. With this arrangement, we could reach down to a temperature of -100°C , beyond which the vacuum sealing at the baseplate breaks.

The sample is applied at the end of the copper rod in the form of a fine paste made with water (or some organic solvent). No binder is used. After the solvent dries off, the sample sticks to the copper surface by virtue of its fine particle size. When a high beam current is used, contamination from copper may take place at the heated spot. In such cases, we have used thin cover slips or some organic binder as an insulating layer between the sample and copper. A copper-constantan thermocouple is attached to the surface where it is also in contact with the sample. The thermocouple leads are connected to two insulated terminals fixed to the baseplate.

3. Results

For details of sample preparation, we would refer to our earlier work (Shanker *et al* 1976). It should suffice here to mention that CaS obtained by H_2 or H_2S reduction of CaSO_4 is designated as CaS H-60 or CaS HS-60 respectively, the number denoting the firing time in minutes. Any subsequent treatment, e.g., firing in N_2 with NaCl (4 mole %) shall be indicated as CaS H60 : NaCl . Here we shall describe the results on three such samples, X-irradiated, NaCl incorporated and vacuum heated CaS H120 denoted simply as CaS : X-ray , CaS : NaCl and CaS : vac.heated . EBH denotes electron beam heating.

An EHT of 15 KeV has been used for all our measurements. Beam current used is in the region of $150 \mu\text{A/cm}^2$. Electron beam heating starts beyond $240 \mu\text{A/cm}^2$.

The cathodoluminescence output of the sample is received through a window in the chamber, focussed by a lens onto the slit of a Hilger-Watts constant deviation monochromator and detected by an EMI 9658B photomultiplier. A correc-

tion for the dispersion of the system is made with the help of a calibrated tungsten filament lamp.

Table 1 gives the peak of spectral response, relative brightness and decay time at the corresponding peak wavelength of seven samples. The luminescence efficiency is very low in pure samples, CaS H-120, CaS H-180 and CaS HS-180, the excitation being well within the saturation region, where emission intensity increases sublinearly with the beam current. In this region, energy is dissipated by nonradiative means e.g., Joule heating. The reason for such low output is probably low concentration of emitting centres, high concentration of quenching centres or both. Compared to ZnS (self-activated or otherwise) the efficiency is two to three orders of magnitude lower.

Table 1.

Sample	Emission peak Å	Relative Brightness	Decay secs
CaS H-120	5800	1.5	
	5000	1.5	
CaS H-180	5800	3.3	
	5000	2.5	
CaS HS-180	5800	1.0	1.5 $\times 10^{-6}$
	5000	1.5	
CaS Vac. heated	5800	20.0	
	5000	19.0	
	4250	12.0	
CaS EBH	4250	33.0	
CaS NaCl	4250	85.0	4.0×10^{-6}
Ca X-ray	5800	100.0	3.0×10^{-6}

During room temperature measurements, occasionally, a sample would be heated to incandescence at a beam current in excess of $300 \mu\text{A}/\text{cm}^2$. The heated spot, after cooling, exhibited a more efficient blue emission peaking at 4250 Å . CaS : NaCl shows the same type of emission.

Thermal Quenching of Luminescence

Figure 2 shows temperature variation of luminescence of a partially reduced sample CaS H-15 down to -90°C . At room temperature, there is a very weak emission at 6300 Å . With lowering of temperature, a blue emission peaking at 4900 Å comes up with increasing brightness. At low temperature the slope of the intensity vs. $1/T$ is about 0.18 eV . Ideally, the total energy (area under the emission curve) is to be plotted. But due to low brightness near room temperature, it was not possible to do area calculation accurately. Furthermore, it was not possible to maintain a constant temperature for as long a time as was

required for a complete spectral distribution curve at each temperature. We have plotted the readings of the photomultiplier output at 4900 Å with changing temperature. The lack of area calculation has resulted in the lowering of slope near room temperature.

4. Discussion

Figure 2 also shows the temperature variation of EPR signal a_0 of the same sample viz., CaS H-15 (see Shanker *et al* 1976). The activation energy for thermal quenching of EPR signal is also about 0.18 eV, the same as that for luminescence in the temperature range of interest. This seems to point to the fact that the EPR and luminescence centre are one and the same. The configurational model used to explain EPR results (Shanker *et al* 1976) would also apply to luminescence of the centre. It is not certain at present whether quenching is inherently associated with sulphur vacancy or occurring at a different centre. It is quite possible that the 5000 Å peak would shift to 4900 Å at higher brightness. Low temperature measurements on fully reduced samples are in progress to confirm this.

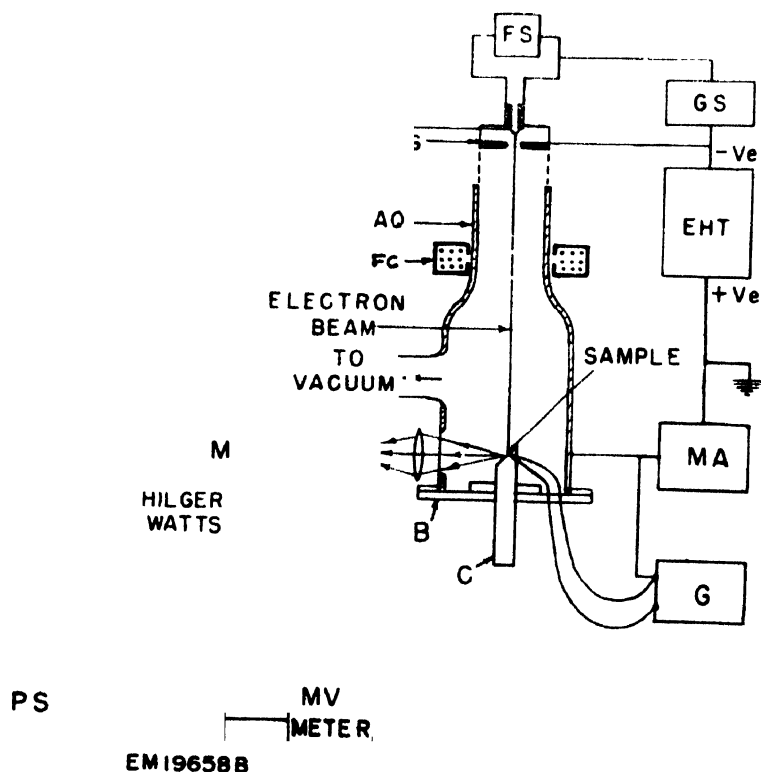


Figure 2

The strong 5800 Å emission of X-irradiated CaS points directly to an F' centre emission. This is easily distinguishable from Mn emission in CaS by decay time, which is about 4 ms in the latter case. However, EPR of the same X-irradiated sample does not indicate any change in the density of state under ultraviolet excitation. The emission may be from a different centre created by X-rays. Pending the results of some more investigation that are being carried out, it is difficult to offer a satisfactory model for this emission.

Finally, the strong 4250 Å emission is possibly due to a sulphur vacancy also, since electron beam heating is likely to increase the concentration of sulphur vacancies. The doubt as to the nature of this centre, raised by the fact that the emission peaks are different, should be resolved when temperature variation of this emission are studied. This is being carried out at present.

References

- Shanker V. Ghosh P. K. and Reddy T. R. S. 1976 *Indian J. pure Appl. Phys.* **14** 193.
Ghosh P. K. and Jain K. L. 1974 *Indian J. Pure Appl. Phys.* **12** 188.
Auzins P. Orton J. W. and Wertz J. E. 1963 *Paramagnetic resonance* vol. 1 edited by Low W (Academic Press Inc, New York) 90.

Studies on the electrical and magnetic properties of 3d transition metal vanadates

O G Palanna, A L Shashimohan and A B Biswas

Solid State Laboratory, Department of Chemistry, Indian Institute of Technology, Bombay-400076.

Abstract. Vanadates of the type $(MO)_nV_2O_5$ (where $M = Mn, Co, Ni, Cu$ and Zn , and $n = 1, 2$ and 3) have been prepared, and their electrical and magnetic properties are reported here. The compounds exhibit hopping type conduction, which occurs due to cation or anion vacancies. Cooperative magnetic phenomena, if any, have not been observed at 80-340 K, although the susceptibility obeys Curie-Weiss law. $Co_3V_2O_8$ has a positive (ferro-) Weiss constant while all others show negative (antiferro-) values.

1. Introduction

V_2O_5 reacts with metal oxides, MO ($M = Mn-Zn$) to form vanadates of the general formula $(MO)_nV_2O_5$, where $n = 1$ to 5 (Clark and Morley 1975, Brisi 1957). Here, attention is specifically focussed on the meta- (MV_2O_6) , pyro- $(M_2V_2O_7)$ and ortho- $(M_3V_2O_8)$ vanadates only.

Generally, the meta forms have Brannerite- $(ThTi_2O_6)$ type crystal structure while the pyro- are thortveitite $(Sc_2Si_2O_7)$ type and ortho-vanadates are orthorhombic. Petrogosa *et al* (1973) have reported the room temperature magnetic moments for $M_2V_2O_7$ as : $M = Mn$ (5.56), Co (4.85), Ni (2.88) and Cu (1.75) BM respectively; and according to Fuoss *et al* (1970) $Co_3V_2O_8$ becomes ferro-magnetic at $T < 10$ K.

From the above literature survey it is evident that information on the electrical and magnetic properties of the vanadates is very scanty. In this paper, the salient features of our experimental data on these materials are reported. Other details are described by Palanna *et al* (1977).

2. Results and discussion

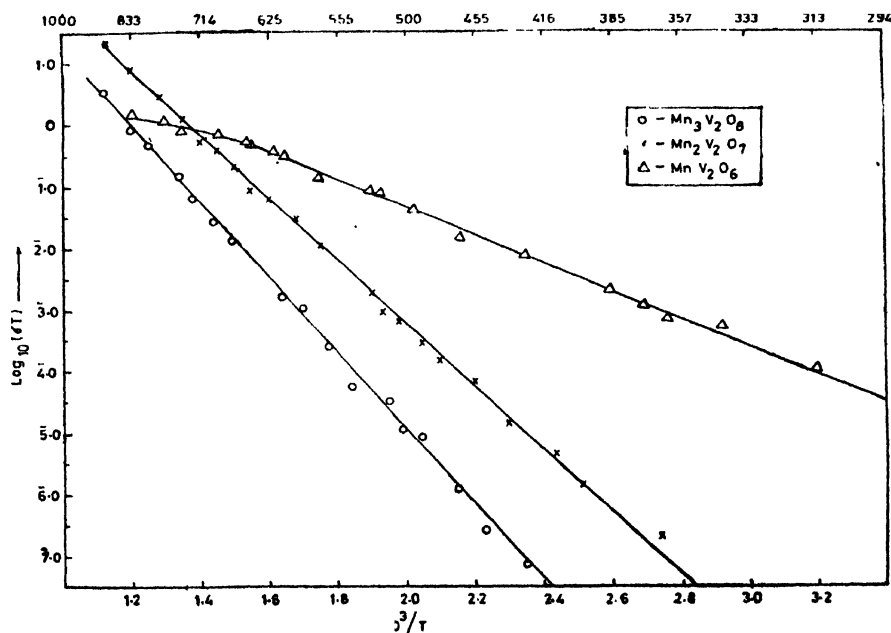
Table 1 and figures 1 to 4 illustrate the representative data regarding the electrical and magnetic behaviour of these compounds.

The temperature dependence of electrical conductivity obeys the relation.

$$\sigma = (\sigma_0/T) \cdot \exp \left(-\frac{\Delta G^*}{kT} \right)$$

Table 1. Electrical and Magnetic data for $(\text{MO})_n\text{V}_2\text{O}_5$ compounds

M	n	Type of conduction α	χ_M at 300 K	μ_{eff} (BM)
Mn	1	n to p type	1.6×10^{-2}	6.00
Co	1	n type	1.0×10^{-2}	4.19
Ni	1	n type	5.1×10^{-3}	3.52
Cu	1	n type	1.57×10^{-3}	1.95
Zn	1	n type	diamagnetic	
Mn	2	p type	2.6×10^{-2}	3.94
Co	2	p type	2.75×10^{-2}	4.10
Ni	2	p type	9.2×10^{-3}	2.36
Cu	2	n type	2.36×10^{-3}	1.20
Zn	2	n type	diamagnetic	
Mn	3	p type	3.4×10^{-2}	3.00
Co	3	p type	3.6×10^{-2}	3.21
Ni	3	p type	1.35×10^{-2}	1.91
Cu	3	n type	3.5×10^{-3}	1.00
Zn	3	n type	diamagnetic	

**Figure 1.** $\text{Log}(\sigma T)$ vs $1/T$ for Mn-vanadates.

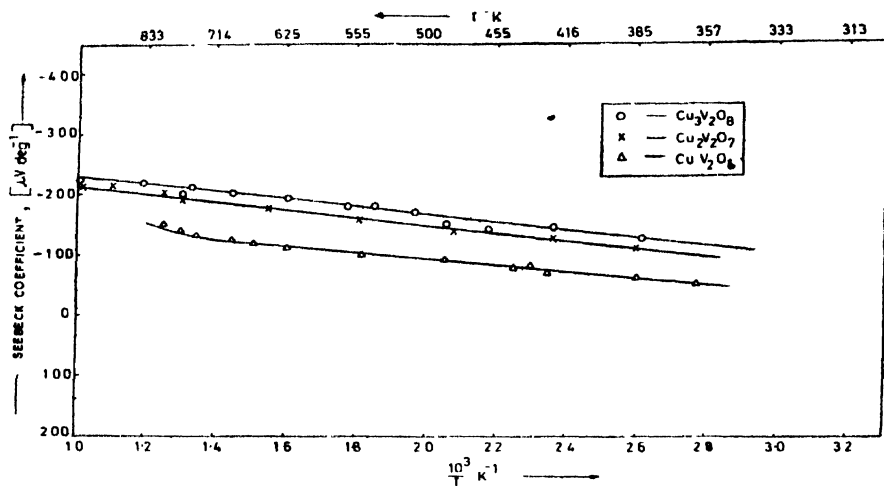


Figure 2. α vs $1/T$ for Cu-vanadates

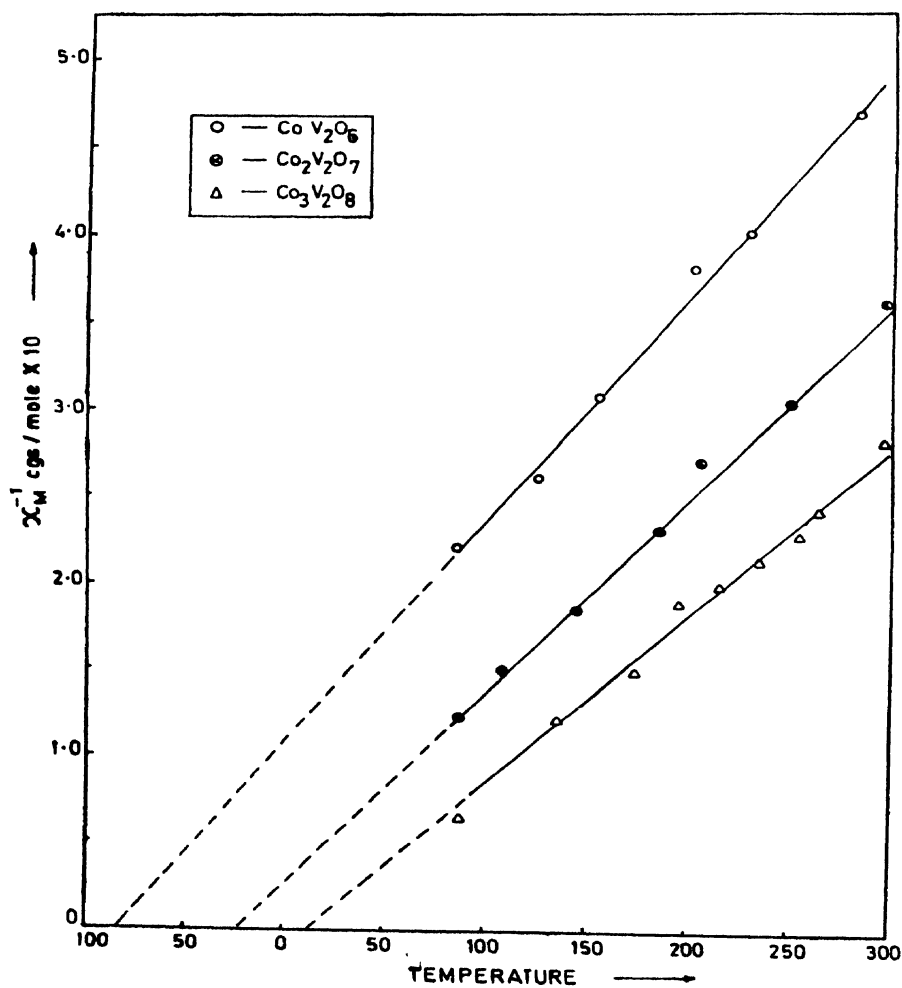


Figure 3. $1/\chi_M$ vs T for Co-vanadates.

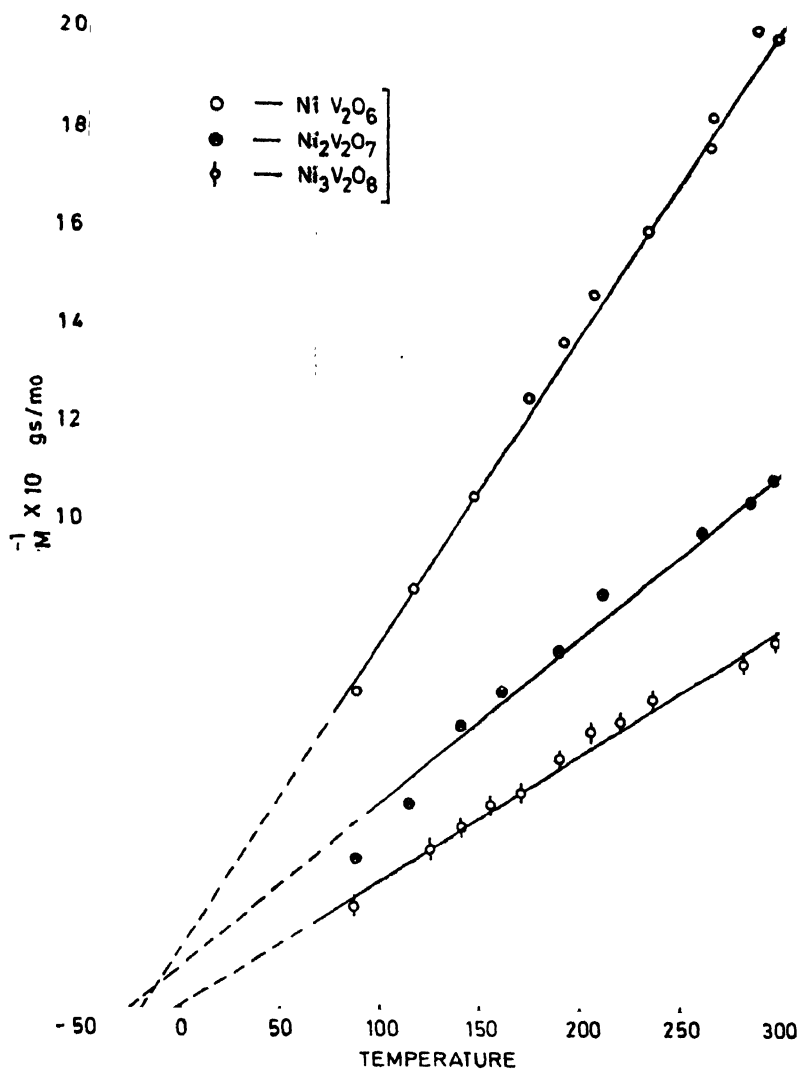


Figure 4. $1/\chi_M$ vs T for Ni-vanadates.

where σ_0 = a constant, T = absolute temperature and ΔG^* = free energy of activation for electrical conduction. Furthermore, the Seebeck coefficient, α , is nearly invariant with temperature. These observations may be interpreted to indicate a thermally activated hopping mechanism for electrical conduction. The latter itself is deemed to occur due to small deviations from stoichiometry, which may be either cation or anion vacancies. In order to determine the exact nature of defects in these materials it will be necessary to conduct experiments under various partial pressures of oxygen. We hope to do these in future.

The reciprocal of magnetic susceptibility, χ , is plotted against absolute temperature in figure 3, from which it may be noted that,

$$\chi = \frac{C}{T \pm \theta},$$

which is nothing but Curie-Weiss law. The sign of θ , the Weiss constant, is negative in all cases indicating antiferromagnetic interactions, although $\text{Co}_3\text{V}_2\text{O}_8$, with a positive (ferro-type) θ is an exception. The effective magnetic moments at $T = 300 \text{ K}$ show a decreasing tendency with increasing n in $(\text{MO})_n\text{V}_2\text{O}_5$. This may be due to the influence of the M-O-M and M-O-O-M exchange interactions, which are supposed to be predominant in these vanadates (Fuess *et al* 1970).

Acknowledgment

ALS thanks CSIR (New Delhi) for financial assistance.

References

- Clark G M and Morley R 1975 *J. Therm. Anal.* **7** 289
Brisi C 1957 *Ann. Chim.* **47** 106; 1958 **48** 263, 270
Pedregosa J C *et al* 1973 *Z. Krist.* **137** 211
Fuess H *et al* 1970 *Acta. Cryst.* **B26** 2036
Palanna O G *et al* 1977 *Proc. Ind. Acad. Sci.* **86A** 455

Electrical properties of CoSnTe_2 in the thin film state

Jagan G Bamane and A B Biswas

Thin Film Laboratory, Department of Chemistry, Indian Institute of Technology, Powai, Bombay-400076

Abstract. A study of thin films of CoSnTe_2 ($\text{CoTe} : \text{SnTe}$), prepared under a dynamic pressure of $< 10^{-5}$ torr using a flash evaporation technique is reported. The thickness dependence of resistivity, Seebeck coefficient and Hall mobility have been investigated in the temperature range of 90–600 K. The charge carriers are observed to be holes and the system shows metallic type of conduction. CoTe is reported to be metallic and SnTe a semiconductor with a complex two band structure. This anomalous behaviour of the mixed system is a reflection of the complex band structure and of a distortion of the spherical Fermi surface.

1. Introduction

Transition metal compounds such as chalcogenides, in the thin film state, play a dynamic role in microelectronics. Semiconducting properties of binary and ternary transition metal chalcogenides have been extensively studied mostly in the bulk state. CoTe was reported to be metallic (Dudkin and Dyul'dina 1959, Bither *et al* 1968, Kazuo Kanematsu 1962) and SnTe semiconducting (Rogers 1968, Burke and Riell 1969, Phillip *et al* 1966) with a complex band structure. The energy band gap would depend on the composition of their solid solution. Thus the mixed system is expected to provide tailor-made and cross-over zero band gap values of interest for device applications. However, the properties of $\text{Co}_x\text{Sn}_{1-x}\text{Te}$ either in the bulk or thin film state seem to have not been reported in the literature.

The present investigation is concerned with a study of the electrical and galvanomagnetic properties of thin films of CoSnTe_2 ($\text{CoTe} : \text{SnTe}$) at different thicknesses and temperatures.

2. Experimental

Cobalt, tin and tellurium (each 99.999%) in the atomic ratio of 1 : 1 : 2 and weighing about 20.0 grams were sealed in a quartz tube at a pressure of $< 10^{-5}$ torr. It was then heated for 60 hours at 900°C and quenched to liquid nitrogen temperature. The compound thus formed was pulverised (200–300 mesh), characterized by X-ray diffraction and used for the preparation of thin films in the thickness range from 300 to 2500 Å under a dynamic pressure of $< 10^{-5}$ torr.

At high temperature required for thermal evaporation, these compositions may dissociate and the constituents would have considerable difference in their vapour pressures. Thus the condensate and the parent composition would differ in stoichiometry. With a view to minimize this effect, a unit for flash evaporation of the material was fabricated and used to maintain the same stoichiometric composition of the film. A powder dropper was employed with a provision of auto-controlling the time and rate of fall of CoSnTe_2 powder on to a heated tungsten strip boat maintained at about 2000°C . Magnetically rotatable special turret assembly was fabricated and employed to carry six substrates where films of different thicknesses could be deposited alternatively at different substrate temperatures in a single pump down only. The assembly also allowed annealing of all the films simultaneously in situ.

Microscope glass slides, ultrasonically cleaned in pure acetone and degassed at $\sim 300^\circ\text{C}$ for 30 minutes were used as substrates. A typical deposition rate was $\sim 10 \text{ \AA/sec}$. The film thickness was measured using a quartz crystal thickness monitor, calibrated with a multiple beam interferometer. After deposition, the films were finally annealed at 300°C for seven hours in situ.

The D.C. resistance was measured using the four probe method. Electrical contacts were made with Pt-Au paste or indium (99.99%) solder and these showed ohmic behavior as tested through I-V measurements. Resistivity (ρ) measurements from 90 to 300 K were carried out inside a chamber by first creating a pressure of $< 10^{-3}$ torr and then introducing a purified nitrogen gas into a working chamber to serve as a conducting medium for heat transfer. The chamber containing the sample was then slowly immersed in a liquid nitrogen flask. The temperature was controlled within $\pm 1^\circ\text{C}$ using a proportional temperature controller, which was monitored with a chrome—alumel thermocouple attached at the side of the film. A small heater was also mounted on the back side of the substrate. All the measurements above room temperature (300 to 600 K) were carried out at a dynamic pressure of $< 10^{-5}$ torr. The temperature coefficient of resistance (TCR) measurements were carried out between room and ice temperature (300 to 273 K) at a pressure of $< 10^{-3}$ torr.

For Hall effect studies, measurements under different magnetic fields upto 23 Kilo-oersteds were carried out. The ratio of length to the width of each film was kept nearly equal to three (Colombani and Huet 1959). All measurements were taken from 90 to 600°K and also by changing the polarity of the magnet and the direction of the electric field. The experimental procedure was more or less the same as in resistivity measurements.

For the thermo-electric power (TEP) measurements, the film was held between two freshly polished copper blocks, each insulated by teflon block at top. A microheater with mica insulation was incorporated in one of the blocks for

obtaining temperature gradient in the sample, and resulting Seebeck e.m.f. measurements were carried under a dynamic pressure of $< 10^{-5}$ torr.

3. Results and discussion

X-ray powder diffraction patterns of deposited thick films were found to correspond to the intensity and d spacing values of the bulk compound. No extra line due to either pure Co or Sn or Te or their oxide or any impurity from the evaporating strip was noticed.

A linear increase of resistance with temperatures ranging from 30 to 220°C is illustrated in figure 1 for two films having thicknesses of 320 and 750 Å. Measurements made during heating and cooling cycles and also after a period of 50 hours follow nearly the same path which indicates that neither phase transition nor any appreciable oxidation has occurred in the films.

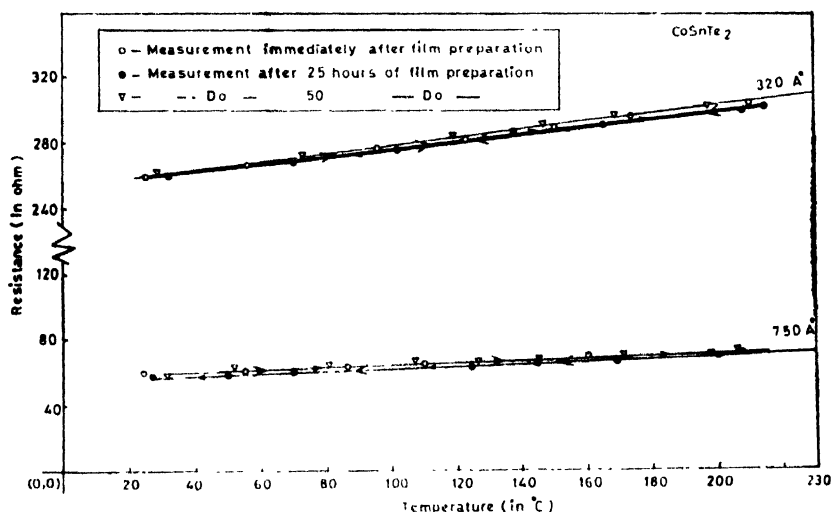


Figure 1 : Variation of resistance with temperature.

Figure 2 shows the variation of $\log \sigma$ (conductivity) vs. $1/T$ in the range 90 to 600 K for films of different thicknesses (400, 800, 1100 and 2300 Å). Little change was observed initially upto about 200 K followed by a significant fall above this temperature in all cases. Similar type of behaviour for thin films of bismuth has been observed by Baba *et al* (1976).

Table 1.

Film thickness in Å	Activation Energy	Activation Energy
	ΔE in eV (90–200 K)	ΔE in eV (200–600 K)
400	0.0015	0.017
800	0.0015	0.018
1100	0.0015	0.020
2300	0.0015	0.020

The activation energies, calculated for different films and for two temperature ranges are present in Table 1 using the relation

$$\sigma = \sigma_0 e^{-\Delta E/kT} \quad (1)$$

where

σ —the electrical conductivity

σ_0 —the residual conductivity

ΔE —the activation energy

k —the Boltzmann constant

T —the temperature in degree Kelvin.

The nature of the figure 2 and the very low values of activation energy suggest the metallic behavior of the film.

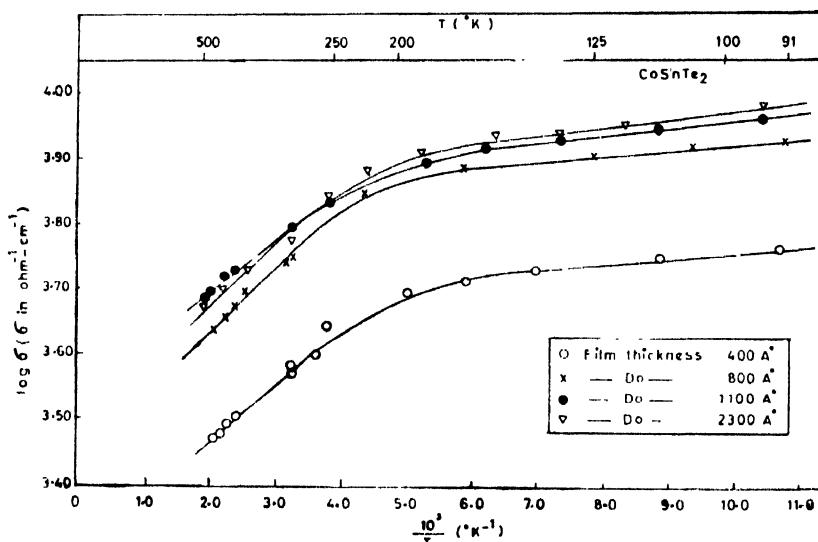


Figure 2 : Temperature dependence of the conductivity.

Thickness Dependence of Room Temperature ρ and TCR

Variation of ρ and TCR each as a function of film thickness have been plotted respectively in figure 3 and figure 4. It may be seen from figure 3 that a sharp rise in the resistivity has occurred from 2.18 to $4.18 \times 10^{-4} \Omega\text{-cm}$ upto 550 \AA and then it remains almost constant upto 2300 \AA .

Correspondingly, the TCR is observed to increase sharply from $1.10 \times 10^{-3}/^\circ\text{C}$ (for 300 \AA film thickness) and then remains nearly constant afterwards upto 2300 \AA . The TCR is positive and again confirm the metallic behavior of the films.

A sharp rise in resistivity below 550 \AA may be ascribed to the films having semicontinuous network structure providing in a small number of the conduction paths. The theoretical requirement for plane and parallel boundary surfaces and continuous film layer is not realized in this region.

The increase of resistivity is because of the reduction of some of the carrier mean free path (mfp) by grain boundary scattering and by the termination at the film surface when it becomes comparable to the film thickness. This is also known as "size effects" and was considered by Fuchs (1938), Sondheimer (1952) and Lucas (1965).

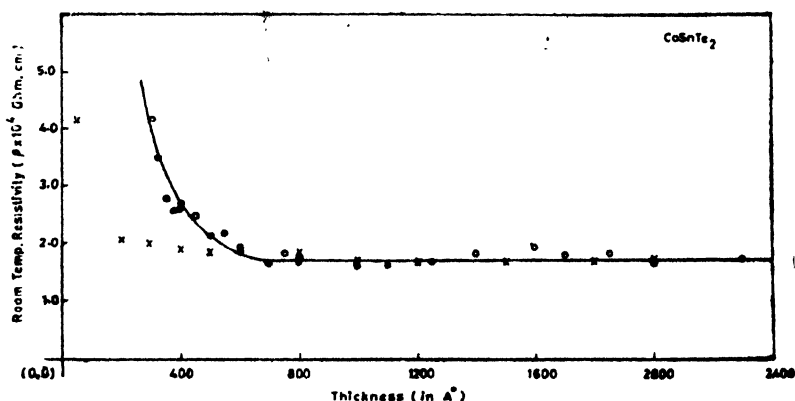


Figure 3 : Room temperature resistivity versus film thickness. Open circles are experimental points and crosses represent the theoretical values on Fuchs theory with $P = 0$ and $l = 100 \text{ \AA}$.

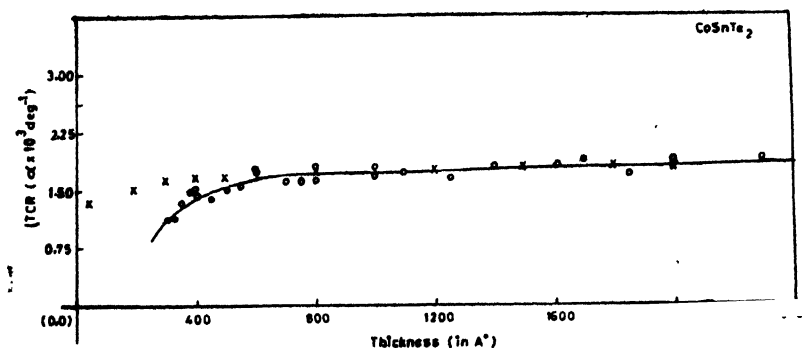


Figure 4 : Temperature coefficient of resistance versus film thickness. Open circles are experimental points and crosses represent the theoretical values on Fuchs theory with $P = 0$ and $l = 100 \text{ \AA}$.

According to Fuchs,

$$\rho = \rho_0[1 + 3/8k(1-P)] \quad \text{for } k \gg 1 \quad (\text{in case of thin films})$$

and

$$\rho = \rho_0 \frac{4}{3} \left(\frac{1-P}{1+P} \right) \cdot \frac{1}{k \log(1/k)} \quad \text{for } k \ll 1 \quad (\text{in case of thick films})$$

where

ρ_0 —the bulk resistivity

$k=d/l$

d —the film thickness

l —mfp (in bulk material)

P —the fraction of electrons undergoing specular (elastic) reflection at film surface.

These expressions predict an increase of resistivity as film thickness diminishes. Our results are in accordance with this theory.

Similarly the TCR in thin films is given approximately as

$$\alpha_{film} = -1/\rho \cdot d\rho/dT \\ - \frac{\alpha_{bulk}}{(1 + \log l/d)} \quad \text{for } d < l \quad (\text{in case of thin films})$$

and

$$\alpha_{film} = \frac{\alpha_{bulk}}{1 + 3/8 \cdot l/d(1-P)} \quad \text{for } d > l \quad (\text{in case of thick films})$$

We may assume $P = 0$, in accordance with the currently accepted convention for the polycrystalline films (Chopra and Bobb 1964). Also, for the best fit with the experimental resistivity data as noted in figure 4, Fuchs theory requires a value of 100 Å for the mfp.

The crosses in figures 3 and 4 represent the theoretical values on Fuchs theory with $P = 0$ and $l = 100$ Å. However, the values calculated from the conductivity and Hall coefficient comes out to be 340 Å. This discrepancy may be attributed to the diffusive scattering of charge carriers and also nonfulfilment of the conditions postulated in the theoretical derivation in that the Fermi surface may not have spherical symmetry and the relaxation time be not unambiguously definable.

Mayadas and Shatzkes (1970) have proposed a model for the size effect by taking into account the contribution from grain boundary scattering which was expressed as a function of electron 'mfp', grain size and a coefficient of reflection,

R of electron from the boundaries. If R is small, then electrons pass freely from one grain to the next without scattering so that

$$\rho_g/\rho_0 = 1 \quad (2)$$

where

ρ_g —the grain boundary resistivity

ρ_0 —the bulk resistivity.

This is due to the fact that the average grain size is approximately equal to film thickness so that as the latter increases, the contribution from grain boundary scattering decreases. Our results presented in figures 3 and 4 are in accordance with this theory.

Thermo-electric Power (TEP) Measurements

A linear variation of Seebeck voltage with temperature difference upto 45°C between hot and cold junctions for films of thickness 225 and 2800 Å is shown in figure 5.

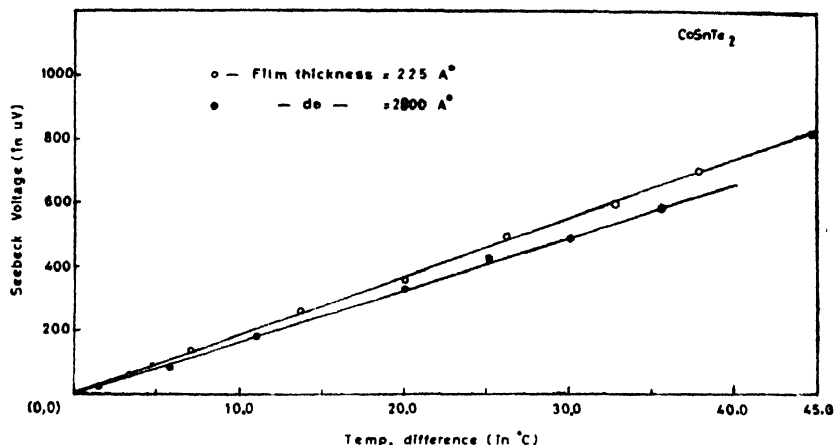


Figure 5 : Seebeck voltage versus temperature difference.

Figure 6 shows the dependence of Seebeck coefficient (S) on film thickness. S appears to increase steadily from $15.0 \mu\text{V}/^\circ\text{C}$ (for 225 Å film thickness) upto $20.0 \mu\text{V}/^\circ\text{C}$ (~ 500 Å film thickness) and then remains nearly constant upto 2800 Å.

The TEP was observed to be positive which indicates that the majority charge carriers are holes. This behavior appears anomalous to that of the free electron theory of metals where electrons are usually taken as carriers. However, it is known that metals such as Zn, Cd and Ag show p -type character. If the transport carriers are holes, the spherical Fermi surface is distorted in each octant of a sphere. This is in some way connected with the fact that Fermi surface is

distorted to the extent of contacting the Brillouin zone boundary (Pippard 1957, Shoenberg 1960). It is also suggestive of the existence of not a single band but a two band system with an energy gap between bands similar to that observed in *p*-type SnTe (Chernik *et al* 1965, Hein 1966, Andreev 1967, Kaidanov *et al* 1967).

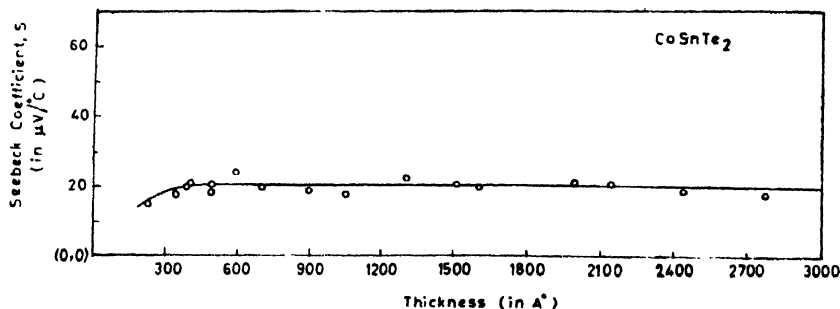


Figure 6 : Seebeck coefficient versus film thickness.

Hall effect measurements

The Hall coefficient (R_H) is found to be positive for all the films and at all temperatures. This again supports the existence of *p*-type charge carriers. Figure 7 shows the dependence of R_H with film thickness. The R_H was observed to decrease from 38 to $22.0 \times 10^{-12} \text{ V.H.cm.}^{-1} \text{ Gauss}^{-1}$ at small film thicknesses (below 550 Å film thickness) and then remains nearly constant upto 2300 Å .

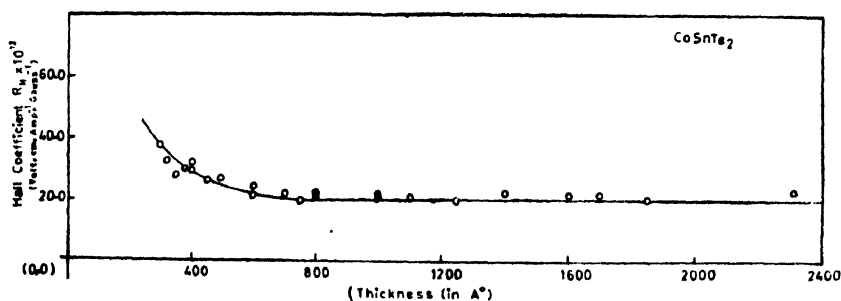


Figure 7 : Hall coefficient versus film thickness.

The relation defining the hole concentration (p) and the Hall mobility (μ_H) for these results are

$$p = \frac{1}{R_H e}$$

and

$$\mu_H = R_H \sigma$$

where

e —the electron charge,

σ —the electrical conductivity.

Figure 8 shows a linear variation of Hall voltage with magnetic field for different film thicknesses (300, 500, 1000, 1500 and 2300 Å) upto 23.0 Kilo-oersteds. This behavior is similar to that observed by Colombani and Huot (1959) in bismuth thin films except for higher fields (25 to 35 Kilo-oersteds).

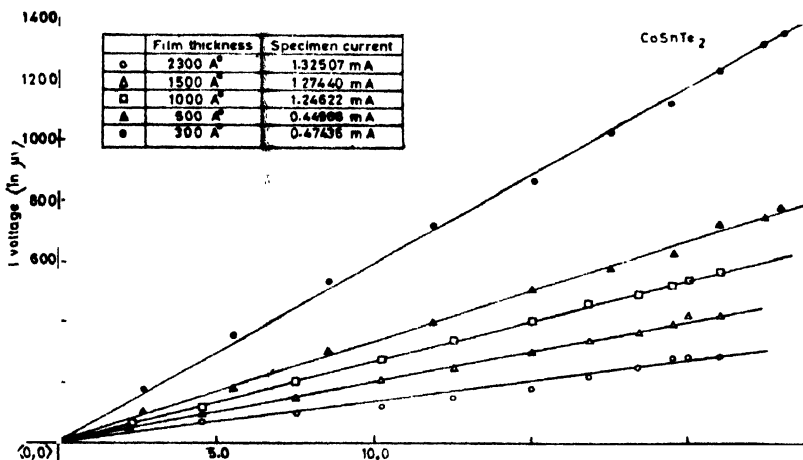


Figure 8 : Hall voltage versus magnetic field.

There was no appreciable change in the electrical resistance with an applied magnetic field upto 24 Kilo-oersteds for various films. Room temperature μ_H was observed to increase steadily from 9.0 upto 12.5 $\text{cm}^2 \cdot \text{V}^{-1} \cdot \text{sec}^{-1}$ (below 550 Å film thickness) and then remains constant upto 2300 Å as shown in figure 9. The hole concentration for the studied film thickness was found to vary from 5.4 to $10 \times 10^{19}/\text{c.c.}$

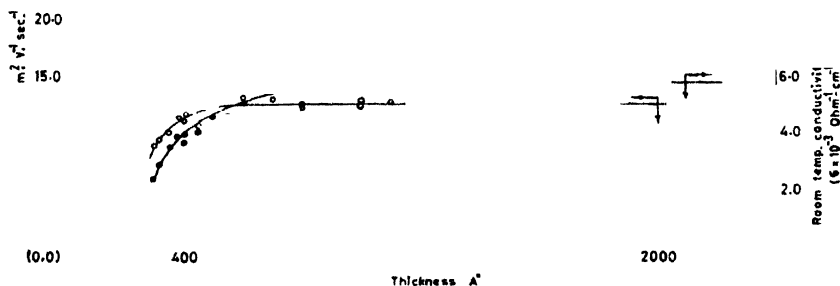


Figure 9 : Hall mobility versus film thickness.

Figures 10 and 11 show the temperature dependence of the μ_H and p . It is seen that p remains more or less constant and the change in conductivity is due to the change in μ_H . This is also suggestive of the metallic type of conduction. It is seen from figures 2 and 10 that there is change of slope in $\log \sigma$ vs $1/T$ curve around 200°K which is also associated with the change of slope in $\log \mu_H$ vs. $1/T$ curve.

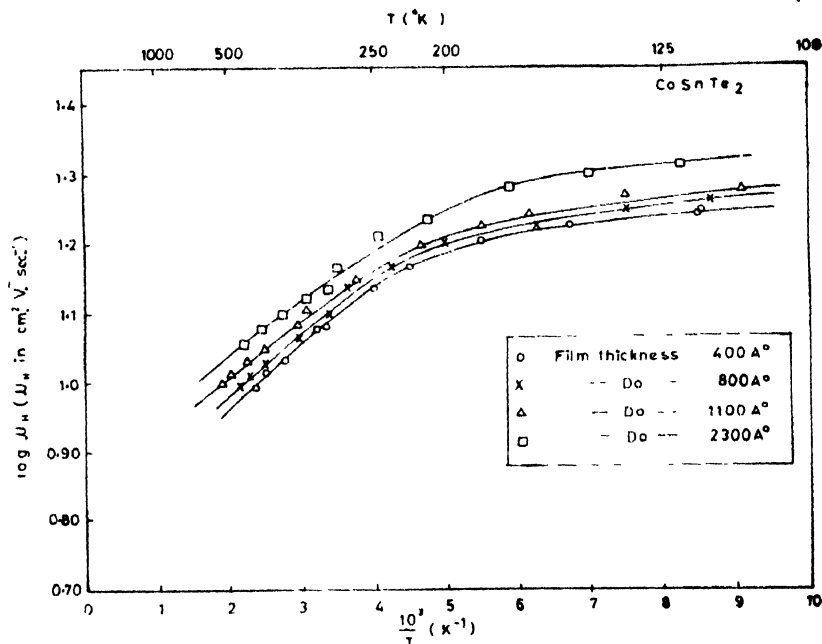


Figure 10 : Temperature dependence of the Hall mobility.

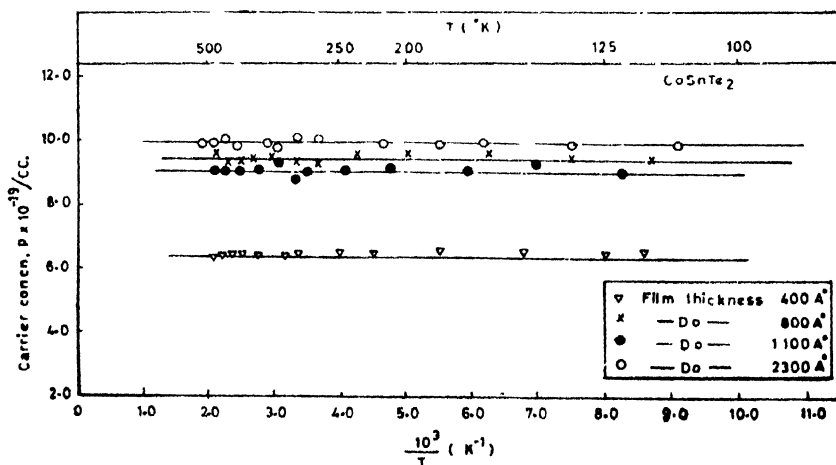


Figure 11 : Temperature dependence of the carrier concentration 'P'.

The low mobility values may be ascribed to the presence of structural and chemical defects in large concentration.

Using the following formulae applicable for bulk material :

$$\text{relaxation time, } \tau = \sigma \cdot m / m \cdot e^2$$

$$\text{Fermi energy, } E_F = (\hbar^2 / 2m)(3\pi^2 n)^{2/3} = \frac{1}{2} m U_F^2$$

$$\text{mean free path, } l = \tau U_F$$

$$\text{carrier wave length, } \lambda = \frac{h}{(2m E_F)^{1/2}}$$

$$\text{mobility, } \mu = e\tau / m$$

where U_F is the appropriate electron velocity and other symbols having their usual meanings, we have calculated the various electrical parameters from the measured data for a sufficiently thick films as representative of the bulk and presented in Table 2.

Table 2.

E_F in eV	μ_F cm/sec	τ in sec	l in Å	λ in Å	μ cm ² /V sec
0.076	1.6×10^7	2.14×10^{-13}	3.4×10^2	45.0	376.0

Finally, it may be noted that an appreciable scatter has been observed in the experimental data even though films were prepared under apparently similar conditions. In practice there would be lack of precise control of many of the pertinent parameters such as deposition rate, substrate and source temperatures, geometry inside vacuum chamber, total and residual gas pressure, source design, heat shields and angle of incidence of vapour stream. In view of the above, the observed scatter of data are considered to remain within a reasonable limits.

References

- Dudkin L D and Dyul'dina K A 1959 *Zhur. Neorg. Khim.* **4** 2313
 Bither T A *et al* 1968 *Inorg. Che.* **7**(11) 2208
 Kazuo Kanematsu 1962 *J. Phys. Soc. Japan* **17** 85
 Rogers L M 1968 *Brit. J. Appl. Phys. Ser 2* **1** 845
 Burke J R and Riedl H R 1969 *Phys. Rev.* **184** 830
 Phillip J *et al* 1966 *Tr. Mezhdunar. Konf. Fiz. Nizkikh Temp.* **10th.** **3** 257
 Colombani A and Huet P 1959 *Structure and Properties of thin films* eds Neugebauer C A, Newkirk J B and Vermilyea D A (Wiley, N Y) p 253
 Baba S, Sugawara H and Kinbara A 1976 *Thin Solid Films* **31** 329
 Fuohs K 1938 *Proc. Cambridge Phil. Soc.* **34** 100

- Sondheimer E H 1952 *Adv. Phys.* **1** 1
Lucas M S P 1965 *J. Appl. Phys.* **36** 1632
Chopra K L and Bobb L C 1964 *Acta Met.* **12** 807
Mayadas A F and Shatzkes M 1970 *Phys. Rev.* **B1** 1382
Pippard A B 1957 *Phil. Trans.* **A250** 325
Shoenberg D 1960 *Phil. Mag.* **5** 105
Chernik I A *et al* 1965 *Fiz. Tver. Tela.* **7(8)** 2524
Hein R A 1966 *Phys. Lett.* **23(7)** 435
Andreev A 1967 *Fiz. Trend. Telva.* **9(5)** 1560
Kaidanov V *et al* 1967 *Fiz. Tekh. Poluprov.* **1(6)** 869

The Morse potential and a simple theoretical model for the thermal expansion studies in pure metals

S. K. Pal and S. P. Sen Gupta

Department of General Physics & X-rays,
Indian Association for the Cultivation of Science,
Calcutta-700 032

Abstract. Following Midha and Nanda (1975), a simple theoretical model has been presented, to calculate in a straight forward manner from a single expression, the linear thermal expansion coefficient (α_l) in cubic metals over a wide range of temperature. The model incorporates the use of Morse type interaction potential for the nearest and also next-nearest neighbour cases and the Debye frequency spectrum for the Gruneisen parameter γ . The application has been made on two f.c.c. metals Cu and Au in the temperature range $\sim 300^\circ\text{K}$ to $\sim 1200^\circ\text{K}$, and a satisfactory agreement, within nearly 5%, has been observed in this temperature range for both the cases considering next-nearest neighbour interactions and specific (relatively high) γ value.

Recently, Midha & Nanda (1975) have derived a simple equation of state for metals based upon a theoretical model in which the electronic free energy has been assumed to vary slowly with volume, and the static contribution of the lattice to the free energy arises from an interaction given by Lennard-Jones-Devonshire (LJD) type of pair potential while the lattice vibrations are considered in the harmonic approximation. The theoretical results for the thermal expansion have been found to be surprisingly good in respect of copper in the temperature range $20\text{-}600^\circ\text{K}$. Although the approach is quite simple which proceeds from thermodynamical considerations, the evaluations of various parameters, involved in the derived expressions, as well as the expansion coefficient have been found to be quite cumbersome and are not explicit. In view of this, we have here considered a rather simplified approach, in the light of Midha & Nanda (1975), to calculate the linear thermal expansion coefficient in cubic metals in a straight-forward manner over a wide range of temperature from a single generalized expression. In our present approach, two aspects have been considered namely,

- (i) the use of Morse type pair potential for the nearest and next-nearest neighbour interactions because of the widespread application of this potential in pure metals and alloys (ordered and disordered) in depicting various crystal properties (harmonic and anharmonic), structure and defects (Roy *et al* 1972, Roy *et al* 1974, MacMillan & Kelly 1973, Yamamota & Doyama 1974); and

- (ii) the use of Debye frequency spectrum for the entire range of temperature (low and high).

The application of the derivation has been made on two pure metals (f.c.c.) copper and gold in the range of temperature $\sim 300^\circ\text{K}$ to $\sim 1200^\circ\text{K}$ using experimental lattice constants data (Mitra & Mitra 1963, Pearson 1958, Merryman & Kampter 1965).

Following Midha & Nanda (1975), the total free energy of a metal is given by

$$F = F_{\text{interaction}} + F_{\text{zero-point}} + F_{\text{thermal}} + F_{\text{electronic}} \quad (1)$$

and

$$F_{\text{interaction}} = \frac{NDZ}{2} \left[e^{-2\alpha(r_{ij}-r_0)} - 2e^{-\alpha(r_{ij}-r_0)} \right] \quad (1a)$$

where D, α, r_0 are the potential parameters for the Morse type pair potential (Roy, Manna & Sen Gupta 1972, 1974), $r_{ij} = 2^{1/6}v^{1/3}$ (v : volume per atom) for the nearest neighbour interaction in f.c.c. structure.

$$F_{\text{zero-point}} = \frac{1}{2} \sum_{i=1}^{3N} \hbar \nu_i \quad (1b)$$

$$F_{\text{thermal}} = kT \sum_{i=1}^{3N} \ln \left(1 - e^{-\hbar \nu_i / kT} \right) \quad (1c)$$

where eqns. (1b) and (1c) are considered in the harmonic approximation, and N, K, T denote total number of atoms, Boltzmann's constant and temperature in $^\circ\text{K}$ respectively.

So, total free energy atom

$$\begin{aligned} F = F_T/N &= \frac{DZ}{2} \left[e^{-2\alpha(r_{ij}-r_0)} - 2e^{-\alpha(r_{ij}-r_0)} \right] \\ &+ \frac{1}{2N} \sum_{i=1}^{3N} \hbar \nu_i + \frac{kT}{N} \sum_{i=1}^{3N} \ln \left(1 - e^{-\hbar \nu_i / kT} \right) + \frac{F_e}{N} \end{aligned} \quad (2)$$

where Z = co-ordination number of the lattice.

Now, using thermodynamic relation namely, $p = -(\partial F / \partial v)_T$ and considering negligible variation of $(\partial F / \partial v_e)$ over a substantial temperature and pressure, Midha & Nanda 1975 we got the following equation of state from (2):

$$\begin{aligned} pv &= \frac{DZ}{6} \left[2mv^{1/3} \left(e^{mv^{1/3} + \alpha r_0} \right) - lv^{1/3} \left(e^{lv^{1/3} + 2\alpha r_0} \right) \right] \\ &+ \frac{1}{N} \sum_{i=1}^{3N} \gamma \hbar \nu_i \left[\frac{1}{2} + 1 / \left(e^{\hbar \nu_i / kT} - 1 \right) \right] \end{aligned} \quad (3)$$

where $\alpha = -2^{2/3}\alpha$, $m = -2^{1/3}\alpha$ and $\gamma = \left(-\frac{\delta \ln \nu}{\delta \ln v} \right)$, the Gruneisen constant.

The volume thermal expansion coefficient is ($p \simeq 0$) :

$$\alpha_v = \frac{6Kv^{1/3} \sum_{i=1}^{3N} \gamma \frac{e^{\hbar\nu_i/kT}}{(e^{\hbar\nu_i/kT} - 1)^2} (\hbar\nu_i/kT)}{\left[Lm' e^{(mv^{1/3} + \alpha r_0)} - Ll' e^{(lv^{1/3} + r_0)} \right]} \quad (4)$$

where

$$l' = l + v^{-1/3}, \quad m' = m + v^{-1/3} \quad \text{and} \quad L = \frac{2^{2/3} \alpha D Z}{3}$$

As we shall try to confine ourselves in the Debye form of frequency distribution, we take simple Debye approximation, i.e.,

$$\sigma(\omega) = \sigma(\omega_D), \quad \text{for } \omega \leq \omega_D \quad \left. \vphantom{\sigma(\omega)} \right\} \omega_D : \text{Cut of circular frequency,}$$

$$0, \quad \text{for } \omega > \omega_D$$

where $\sigma(\omega)$ mode density of frequency $= \frac{3v\omega^2}{2\pi^2 C_s^3}$, C_s the

velocity of sound and $\omega = 2\pi\nu$.

In this Debye spectrum, which is entirely determined by the limiting frequency ω_D , the Gruneisen constant γ is independent of mode frequency and given by (Slater 1963)

$$\gamma = \left(-\frac{\delta \ln \nu_D}{\delta \ln v} \right) \quad (5)$$

Thus,

$$\alpha_v = \frac{6\gamma kv^{1/3} \int_0^{\omega_D} \left(\frac{\hbar\omega}{kT} \right)^2 \frac{e^{\hbar\omega/kT}}{(e^{\hbar\omega/kT} - 1)^2} \sigma(\omega) d\omega}{v_0 L \left[m' e^{(mv^{1/3} + \alpha r_0)} - l' e^{(lv^{1/3} + 2\alpha r_0)} \right]} \quad (6)$$

or,

$$\alpha_v = \frac{18\gamma kv^{1/3} . 3(T/\theta_D)^3 \int_0^{\theta_D/T} \left\{ (\beta\hbar\omega)^4 \frac{< e^{\beta\hbar\omega} >}{(e^{\beta\hbar\omega} - 1)^2} \right\} d(\beta\hbar\omega)}{v_0 L.X} \quad (7)$$

where $\beta = 1/kT$, $\theta_D = \hbar\omega_D/k$, the Debye temperature and

$$X = \left[m' e^{(mv^{1/3} + \alpha r_0)} - l' e^{(lv^{1/3} + 2\alpha r_0)} \right]$$

So, the linear thermal expansion coefficient α_1 , for the nearest neighbour case is given by :

$$\alpha_1 = \frac{6\gamma k v^{1/3} I(x)}{v_0 L X} \quad (8)$$

where $x = \beta \hbar \omega$ and $I(x) = 3(T/\theta_D)^3 \int_0^{\theta_D/T} \frac{e^x x^4 dx}{(e^x - 1)^2}$

Considering the next-nearest neighbour interaction in the interaction potential (eq. 1a), the linear thermal expansion coefficient α_2 is given by :

$$\alpha_2 = \frac{6\gamma k v^{1/3} I(x)}{v_0 (L\bar{X} + M\bar{Y})} \quad (9)$$

where $Y = \left[m_1' e^{(m_1 v^{1/3} + \alpha r_0)} - l_1' e^{(l_1 v^{1/3} + 2\alpha r_0)} \right]$

$$L = -4ZD/3, \quad l_1 = -2^{5/3}\alpha, \quad l_1' = l_1 + v^{-1/3}$$

$$M = -4ZD/3, \quad m_1 = -2^{2/3}\alpha, \quad m_1' = m_1 + v^{-1/3}$$

Thus above eqs. (8) and (9) lead to the evaluations of linear thermal expansion coefficients for the entire range of temperature concerned for the respective cases of nearest and next-nearest neighbour interactions.

In applying eqs. (8) and (9) to calculate the linear thermal expansion coefficients (α_i) for Cu from 303-1144°K and for Au from 298-1275°K considering nearest and next-nearest neighbour interactions, we have taken respective γ values from two different approaches of Slater (1963). In one case, γ can be obtained from compressibility data using the relation $\gamma_1 = -\frac{2}{3} + \frac{P_2}{P_1}$ where $P = P_0 + P_1 \left(\frac{V_0 - V}{V_0} \right) + P_2 \left(\frac{V_0 - V}{V_0} \right)^2$, and in the other case γ may be evaluated from the Morse potential parameters α and r_0 using the relation $\gamma_2 = \frac{\alpha r_0}{2} + \frac{1}{3}$. Table 1 lists the respective values for γ and the potential parameters (Roy *et al* 1972), used in the evaluation of expansion coefficients for Cu and Au. The values of the parameter

Table 1. Morse potential parameters and Gruneisen's Constant γ for f.c.c. Cu and Au

Material	nearest-neighbour			Morse Potential parameters next-nearest neighbour			Gruneisen's constant		
	D (ergs/atom $\times 10^{12}$)	α (\AA^{-1})	r_0 (\AA)	D (ergs/atom $\times 10^{12}$)	α (\AA^{-1})	r_0 (\AA)	γ_1	γ_2 (nearest)	γ_2' (next-nearest)
Cu	0.94332	1.432	2.5444	0.77988	1.3980	2.6230	1.90	2.15	2.16
Au	1.01374	1.6523	2.8759	0.89181	1.630	2.9214	3.03	2.71	2.713

r_0 differ slightly here from the earlier ones (Roy *et al* 1972), as r_0 's have now been obtained from a least-squares fit of experimental r - T values (Mitra and Mitra 1963, Slater 1963, Merryman & Kamptner 1965). Tables 2 and 3 show the cal-

Table 2. Coefficients of linear thermal expansion (α_{l_i}) from nearest neighbour consideration

Temperature °K	Copper			Temperature °K	Gold		
	α_{l_1} (calc.) $\times 10^6/^\circ\text{K}$ ($\gamma_2 = 2.15$)	α_{l_1} (calc.) $\times 10^6/^\circ\text{K}$ ($\gamma_1 = 1.90$)	α_{l_1} (expt.) $\times 10^6/^\circ\text{K}$ (least-sq. fitted)		α_{l_1} (calc.) $\times 10^6/^\circ\text{K}$ ($\gamma_2 = 2.71$)	α_{l_1} (calc.) $\times 10^6/^\circ\text{K}$ ($\gamma_1 = 3.03$)	α_{l_1} (expt.) $\times 10^6/^\circ\text{K}$ (least-sq. fitted)
303	17.6	15.5	16.7	298	12.5	13.9	11.9
403	18.5	16.2	17.5	385	12.8	14.3	12.6
503	19.0	16.7	18.3	469	13.0	14.5	13.3
603	19.6	17.2	19.2	585	13.3	14.9	14.2
703	20.1	17.6	20.0	775	13.9	15.6	15.7
803	20.6	18.1	20.8	883	14.3	16.0	16.6
944	21.3	18.8	21.9	973	14.6	16.4	17.4
1044	21.9	19.3	22.7	1081	15.0	16.8	18.3
1144	22.5	19.8	23.5	1183	15.5	17.3	19.1
				1275	16.0	17.9	19.8

Table 3. Coefficients of linear thermal expansion (α_{l_n}) from next-nearest neighbour consideration

Temperature °K	Copper			Temperature °K	Gold		
	α_{l_2} (calc.) $\times 10^6/^\circ\text{K}$ ($\gamma_2 = 2.16$)	α_{l_2} (calc.) $\times 10^6/^\circ\text{K}$ ($\gamma_1 = 1.90$)	α_{l_2} (expt.) $\times 10^6/^\circ\text{K}$ (least-sq. fitted)		α_{l_2} (calc.) $\times 10^6/^\circ\text{K}$ ($\gamma_2 = 2.713$)	α_{l_2} (calc.) $\times 10^6/^\circ\text{K}$ ($\gamma_1 = 3.03$)	α_{l_2} (expt.) $\times 10^6/^\circ\text{K}$ (least-sq. fitted)
303	17.8	15.7	16.7	298	12.8	14.3	11.9
403	18.7	16.4	17.5	385	13.1	14.6	12.6
503	19.3	17.0	18.3	469	13.3	14.9	13.3
603	19.8	17.4	19.2	585	13.7	15.4	14.2
703	20.4	17.9	20.0	775	14.3	16.0	15.7
803	20.8	18.3	20.8	883	14.7	16.4	16.6
944	21.6	19.0	21.9	973	15.0	16.8	17.4
1044	22.2	19.5	22.7	1081	15.5	17.3	18.2
1144	22.8	20.0	23.5	1183	15.9	17.8	19.1
				1275	16.4	18.3	19.8

culated and least-squares fitted experimental values of linear thermal expansion coefficient for Cu (Mitra & Mitra 1963, Slater 1963) and Au (Merryman & Kampter 1965) in the above-mentioned temperature ranges for the respective cases of nearest and next-nearest neighbour interactions.

It may be seen from both Tables 2 and 3 that the overall agreement between the calculated and experimental values of α_l is quite satisfactory in the wide range of temperature concerned, the agreement being more satisfactory for the case of next-nearest neighbour interaction and for higher γ values irrespective of mode of obtaining γ either from compressibility or potential parameter data. Thus, the value of γ is quite critical in the evaluation of α_l , and demands the use of γ from a realistic approach. The disagreement in the α_l values for the above cases has been found to lie in the range of 5% except for Au where the disagreement is slightly larger in the lower temperature for higher γ value. It may further be seen that higher γ value yields, for both the cases of Cu and Au, slightly higher values for α_l (calc.) initially which become less at higher temperatures when the contributions from vacancy concentrations also come into play. This may imply the necessity of considering the variation of γ with temperature (Lokunsa 1963). However, considering the limitations of our present approach based on a phenomenological model, it appears that this simple theory can, to a large extent, satisfactorily explain the lattice expansion behaviour in f.c.c. metals over a wide range of temperature, and Morse type pair potential function can also be successfully applied if the respective parameters are obtained in a consistent manner.

Acknowledgements

The authors are grateful to Prof. A. K. Barua for his active interest in the problem. The authors are also thankful to Dr. D. Roy for helpful discussion on the problem.

References

- Lokunsa I. E. 1963 *Soviet Phys. Solid State* **5**, 798.
- Macmillan N. H. & Kelly A. 1973 *Materials Sc. Engg.* **12** 79.
- Merryman R. G. & Kampter C. P. 1965 *J. American Ceramic Society* **48**, (4) 202.
- Midha Y. R. & Nanda V. S. 1975 *J. Appl. Phys.* **46** 3710.
- Mitra G. B. & Mitra S. K. 1963 *Ind. J. Phys.* **37**, 462.
- Pearson W. B. 1958 *A Handbook of Lattice spacings and Structures of Metals & Alloys* (Pergamon Press).
- Roy D., Manna A. & Sen Gupta S P 1972 *J. Phys. F : Metal Phys* **2**, 1092.
- Roy D., Manna A. & Sen Gupta S. P. 1974 *J. Phys. F : Metal Phys.* **4** 2145.
- Slater J. C. 1963 *Introduction to Chemical Physics* (McGraw Hill, paper back edn. New York) chaps. 14-27.
- Yamamoto R., Doyama & M. 1974 *J. Phys. Chem. Solids* **35**, 759.

The excited states of a bound polaron

T. K. Mitra and G. P. Ray*

Department of Theoretical Physics

Indian Association for the Cultivation of Science

Calcutta-700 032

The excited states of an electron bound to an impurity in an ionic crystal are investigated by second order RSPT. Interaction of the localised electron with the longitudinal optical phonons of the host material is treated within the standard framework of the Fröhlich polaron theory. The second order perturbation effect is obtained analytically following a procedure developed earlier by Mitra. The first excited states are treated in this way, numerical estimates are obtained and compared with those of others. It is found that (i) the degeneracy of the first excited states in the absence of the interaction with the longitudinal optical phonons is removed, on including the interaction, to a higher degree than that obtained by others and (ii) the numerical values of the phonon induced energy shift are different (smaller) from those obtained by other authors. This latter result, consistent with the spirit of the perturbation theory, is discussed with reference to the parameters of a real solid.

1. Introduction

The problem of an electron bound to an impurity centre (the bound polaron) in an otherwise perfect polar semiconductor has lately received considerable attention. Early calculation (Platzman 1962) based on the Fröhlich Hamiltonian, modified to include a term due to the Coulomb impurity, were aimed at obtaining approximately the ground state energy. Since then a number of authors (Mitra 1972, Larsen 1974, Engineer and Tzoar 1972) have investigated the problem for intrinsic and practical reasons. Recent activity (Engineer and Tzoar 1973, Bajaj 1976) has been extended to excited states as well as the ground state. The traditional method of calculation has been perturbative (other methods to a lesser extent), but even lowest order perturbation theory was not amenable to analytical treatment and further approximations had to be introduced. The validity and applicability of such approximations have been amply discussed in the literature. Very recently however, second order Raleigh Schrodinger perturbation theory (RSPT) has been applied in a nearly exact manner—numerically by Engineer and Tzoar (1972, 73, referred herein after as ET) and analytically by one of us (Mitra 1972). In the latter work (referred to as I hereinafter) the author inadvertently overlooked the somewhat similar analysis of ET. In the present paper

*Honorary worker at the Department of Theoretical Physics, Indian Association for the Cultivation of Science Calcutta-700 032.

the approach of I is adopted and developed more generally to obtain an expression for the energy shift of a general level due to interaction with the longitudinal optical phonons (assumed dispersionless, for simplicity). Numerical values are obtained for the ground (1s) and the first excited states (2s, 2p). In Section II we present the analytical formulation (briefly reported in I) of the problem. Results are then obtained for the ground and the first excited levels and compared with other available numerical values in Section III. A discussion of method and results, with special reference to the new features of our results, is presented in Section IV.

2. Mathematical formulations

The modified Fröhlich Hamiltonian for the problem

$$H = H_e + H_{ph} + H_{e-ph} + H_{e-I} \quad (1)$$

where

$$H_e + H_{e-I} = p^2/2m - Ze^2/c_{\infty}r \quad (2)$$

$$H_{ph} = \hbar\omega \sum_{\mathbf{q}} (b_{\mathbf{q}} + b_{\mathbf{q}}^\dagger) \quad (3)$$

$$H_{e-ph} = \frac{iu}{\sqrt{V}} \sum_{\mathbf{q}} \frac{1}{q} (b_{\mathbf{q}} e^{i(\mathbf{q} \cdot \mathbf{r})} - b_{\mathbf{q}}^\dagger e^{i(\mathbf{q} \cdot \mathbf{r})}) \quad (4)$$

$$u = \hbar\omega(4\pi\alpha)^{1/2}(\hbar/2m\omega)^{1/4} \quad (5a)$$

$$\alpha = \frac{e^2}{\hbar} \left(\frac{1}{\epsilon_\infty} - \frac{1}{\epsilon_0} \right) \left(\frac{m}{2\hbar\omega} \right)^{1/2} \quad (5b)$$

in the usual notation. Besides the usual natural parameter α , it has of late been customary to introduce a second parameter $R = \beta^2$ (β as defined here differs by a numerical factor of 2 from β as defined by other authors, for example by ET) which is the ratio of the ground state energy of (2) and the dispersionless longitudinal optical phonon energy $\hbar\omega$. In terms of these two parameters the energy shift in second order RSPT is obtained, as in I,

$$\Delta E_n = \sum_{n'} A(n') f(n') \quad \dots \quad (6)$$

where now ΔE_n is the shift of a general level n and not just the ground level, and $f(n')$, $A(n')$ are given by

$$f(n') = \frac{1}{\hbar\omega} \left[1 + \beta^2 \left(\frac{1}{n^2} - \frac{1}{n'^2} \right) \right]^{-1} \quad (7)$$

$$A(n') = \int d^3\mathbf{r}_1 d^3\mathbf{r}_2 \frac{1}{|\mathbf{r}_1 - \mathbf{r}_2|} \psi_n^+(\mathbf{r}_1) \psi_{n'}'(\mathbf{r}_2) \psi_{n'}^+(\mathbf{r}_1) \psi_n(\mathbf{r}_2) \quad (8)$$

The important point to note here is that the structure of $A(n')$ is identical to that encountered in atomic physics in the calculation of the correction to the atomic levels due to electrostatic interaction between the electrons (Condon and Shortley 1970). There $A(n')$ is split into a product of an angular part whose values are available in Condon and Shortley and a radial part which has been conveniently reduced by us. Thus

$$A(n') = A_{nn'} = \sum_{k=|M|}^{\infty} C_k^2(lm, l'm') R^k(nl n'l', n'l' nl) \quad (9)$$

where

$$C_k^2(lm, l'm') = \frac{2}{2k+1} \left\{ \int_0^\pi \Theta(k, m-m') \Theta(lm) \Theta(l'm') \sin \theta d\theta \right\} \quad (10)$$

where (10) is taken from Condon and Shortley, the Θ 's are related to the Legendre functions as follows,

$$\Theta(lm) = (-1)^m \left\{ \frac{(2l+1)(l-m)!}{2(l+m)!} \right\}^{\frac{1}{2}} \sin^m \theta \frac{d^m}{d(\cos \theta)^m} P_l(\cos \theta) \quad (11)$$

with

$$m-m' = M \quad (12a)$$

$$k+l+l' = 2g, \quad g \text{ integer} \quad (12b)$$

$$|l-l'| \leq k \leq l+l' \quad (12c)$$

and a typical matrix element due to the radial parts of the wave functions ψ in (8) is given by

$$\begin{aligned} & R^k(nl n'l', n'l' nl) \\ &= \int_0^\infty dr_1 R_{nl}(r_1) R_{n'l'}(r_1) \left\{ \frac{1}{r_1^{k+1}} \int_0^{r_1} r_2^k dr_2 + r_1^k \int_{r_1}^\infty \frac{dr_2}{r_2^{k+1}} \right\} R_{n'l'}(r_2) R_{nl}(r_2) \end{aligned} \quad (13)$$

Expression (13) has been reduced by us to the analytical form

$$\begin{aligned} R^k(nl n'l', n'l' nl) &= \sum D(nl n'l' p_1 p_2 p_1' p_2') \{ |s_2+k+1| |s_1-k| \\ &- \sum_{j_1} \frac{1}{2^{s_1+j_1+k} j_1!} |s_2+k+1| |s_1-k+j_1| \\ &+ \sum_{j_2} \frac{1}{2^{s_1+j_2+k+1} j_2!} |s_2-k| |s_1+j_2+k+1| \} \end{aligned} \quad (14)$$

where

$$\begin{aligned} & D(nl n'l', p_1 p_2 p_1' p_2') \\ &= \frac{Z}{a_0} \frac{1}{n+n'} F_{nl p_1} F_{nl p_2} F_{n'l' p_1'} F_{n'l' p_2'} \end{aligned} \quad (15a)$$

$$F_{nlp} = (-1)^{p+1} \lambda_n p^{+l+1} \frac{\{(n+l)!(n-l-1)!\}^{\frac{1}{2}}}{n^{\frac{1}{2}}\{(n-l-1-p)!(2l+1+p)!p!\}} \quad (15b)$$

$$\lambda_n = 2n'/(n+n') \quad (15c)$$

$$\beta = 0 \text{ to } n-l-1; \quad p' = 0 \text{ to } n'-l'-1 \quad (15d)$$

$$j_1 = 0 \text{ to } s_2+k \quad (15e)$$

$$j_2 = 0 \text{ to } s_2-k-1 \quad (15f)$$

$$s_1 = p_1+p_1'+l+l'+2 \quad (15g)$$

$$s_2 = p_2+p_2'+l+l'+2 \quad (15h)$$

3. Results.

The apparently formidable looking expression (14) is very easily handled by the computer. Numerical values are then obtained for (6) using (7), (8), (9) and (14). In table I values of $A(n')$ are given for successive values of n' (given n) to show explicitly the rapid fall of $A(n')$ with n' . Fig. 1 is based on table I. In table 2 our

Table 1. Values of $A(n')$ for the states cited, as obtained by the present theory

$A(n')$				
n	$n' = 1$	$n' = 2$	$n' = 3$	$n' = 4$
$1s$	0.625000	0.0731595	0.0205993	0.0085458
$2s$	0.0219478	0.2382812	0.0524913	0.0198705
$2p_0$	0.0170705	0.2460937	0.0518366	0.0196697
$2p_{\pm}$	0.0170705	0.4101562	0.0762978	0.0282819

values of $-\Delta E/\alpha\hbar w$ are collected for $1s$, $2s$, $2p_0$ and $2p_{\pm}$. We have a new feature, not reported by any of the other authors, in that the p level degeneracy is partially removed. In the same table 2, numerical values of $1s$, $2s$, $2p$ (unsplit) as obtained by other authors, are displayed for comparison. Our values are consistently smaller than those of others. These discrepancies as well as a discussion of the methods are taken up in the next section.

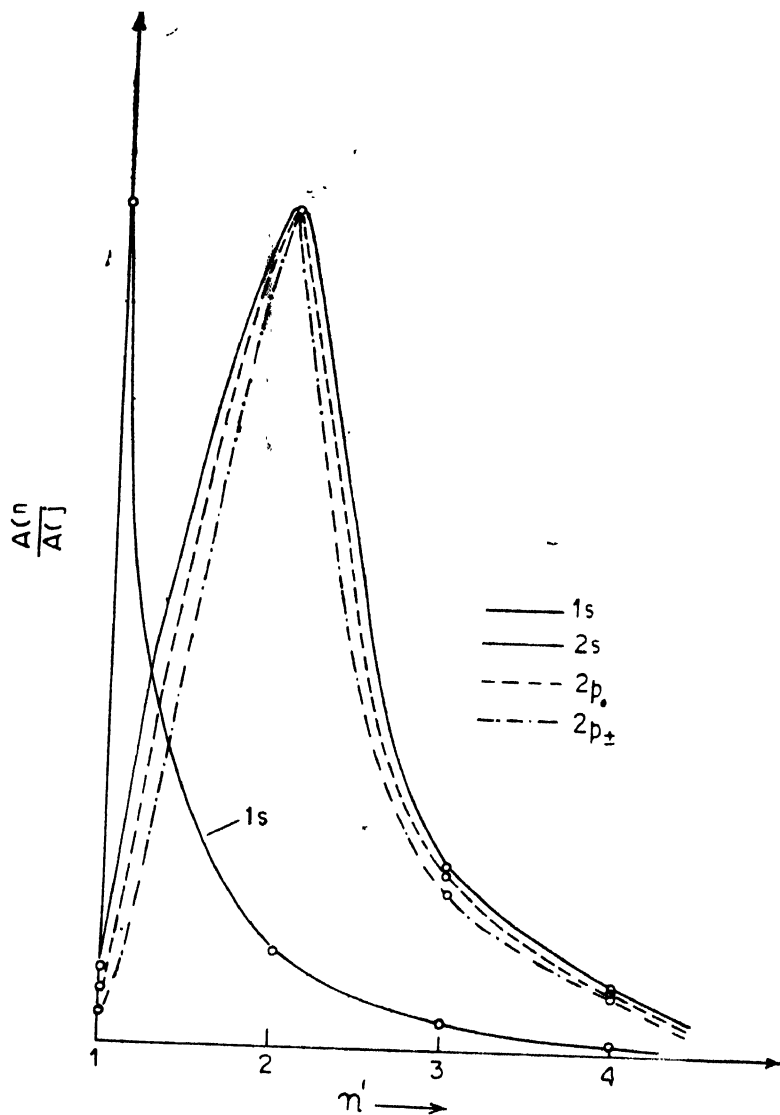


Figure 1. Figure based on Table 1 to show the sharp fall of $A(n')$ with n'

4. Discussion of method and results.

Since our calculation is based on straight forward perturbation theory, we shall confine our discussion to perturbative approaches only. After Fröhlich's (1954) pioneering work on the free polaron the first attempt to consider the possibility of a bound polaron was due to Platzman. In this approach the second order perturbation term is modified to consist of a term similar to the free polaron (at the bottom of the conduction band) and a remainder series which is cut off arbitrarily. In the absence of an alternative this approach and its variants

Acknowledgments

The authors are grateful to Prof. N. C. Sil for hospitality at his department and to Dr. S. Chatterjee for computational help.

References.

- Bajaj K K and Clark T D 1973 *Phys. Stat. Solidi* **56** 211 and references therein
Bajaj K K and Aldrich C 1976 *Solid St. Commn.* **18** 641
Condon E O and Shortley G H 1970 *The Theory of Atomic Spectra* (Cambridge)
Engineer M H and Tzoar N 1972 *Phys. Rev.* **B5** 3029
1973 *Phys. Rev.* **B3** 3356
Fröhlich H 1954 *Adv. Phys.* **3** 325
Hostler L and Pratt R H 1963 *Phys. Rev. Lett.* **10** 469
Lemmens L F *et al* 1975 *Phys. Rev.* **B12** 4316
Larsen D M 1974 *Phys. Rev.* **B9** 823 and references therein
Mitra T K 1972 *Phys. Lett.* **A42** 223
Platzman P M 1962 *Phys. Rev.* **125** 1961
Sak J 1971 *Phys. Rev.* **B3** 3356

Some new findings on the effect of nuclear and X-irradiation on the oscillating characteristics of quartz crystals

Harish Bahadur and R Parshad

National Physical Laboratory
New Delhi-110012

Abstract. Natural AT-cut quartz crystals irradiated with fast neutrons, gamma rays and X-rays (30 kV) were examined for their frequency characteristics compared to those of the virgin crystals. The neutron source was $^{241}\text{Am-Be}$ having flux equal to 2.67×10^6 neutrons/second/cm² and the gamma ray sources were ^{137}Cs and ^{60}Co having dose rates of 30mr/second and 23.5 r/second respectively.

The neutron irradiation at lower accumulated doses ($\sim 2 \times 10^{10}$ nvt) produced only a temporary negative shift of the resonance frequency (~ 15 parts per million), the frequency reaching the pre-irradiation value after about an hour long mechanical oscillations of the quartz crystal. Varying time intervals were kept between the termination of irradiation and the generation of the mechanical oscillations, this fact producing only a negligible effect on the temporary frequency shifts. High accumulated doses ($\sim 15 \times 10^{10}$ nvt) produced, along with the temporary shift, also a negative permanent change in frequency (~ 50 parts per million). At lower doses negative frequency so produced, was followed by positive frequency shifts as a result of prolonged irradiation. The gamma-irradiated crystals showed the typical smoky colouration at higher accumulated doses ($\sim 1.5\text{M Rads}$) exhibiting the typical EPR signal of the E_2' -center at room temperature.

In both the cases of neutrons and gamma irradiated crystals, the temporary frequency shifts could be eliminated by temperature annealing before the start of the generation of mechanical oscillations.

In the X-irradiated crystals there was, in contrast, only a permanent frequency shift. The X-irradiated crystals like gamma irradiated showed, negative and positive frequency shifts (the latter for increased doses) and the typical smoky colouration and the associated EPR signal.

That mechanical oscillations or thermal treatment anneal the frequency shows that at least some portion of the nuclear displacements caused by neutrons (by the recognized knock-on process) and the gamma rays (by the Coulomb interaction of the Compton electrons with nuclei) have low activation energy. The present work also shows that gamma rays produce, as may be expected, effects common to those produced by neutrons and those produced by X-rays.

A theory for positive frequency shift by X-and gamma-irradiated synthetic and natural quartz crystals is proposed. Evidence has been offered to show that apart from precursors of the A-centers, the alkali ions in the quartz crystal lattice have alternate placings (called moorings) mostly in the c-channel. On

irradiation, electrons released from the precursors of the *A*-centers are captured at the moorings for the alkali ions, resulting in the destruction of the anelasticity of alkali ion centers at the moorings and the consequent increase of elasticity and so the frequency. In synthetic crystals, due to the large concentration of the moorings and their associated alkali ions, the positive frequency shifts starts from the commencement of the irradiation. In natural crystals, the alkali ions released from the *A*-centers by irradiation, are caught at the moorings forming electron traps and centers of anelasticity. Thus for increased radiation doses, the concentration of the moorings increases enough to give the positive frequency shifts observed.

The present work also indicates that in crystals, neutrons, gamma and X-rays irradiation produces, as detected by Scanning Electron Microscope, microscopic cracks in the crystal, which will produce their own associated frequency effect.

1. Introduction

Following Frondel (1945), considerable work (Chi 1957, Bechmann 1958, Berman *et al* 1950, Johnson & Pease 1954, Arnold 1956, Arnold 1957, Arnold 1954, Wittles & Sherrill 1954, Primak *et al* 1953, Kinchin & Pease 1955, Primak & Szymanski 1956, Dienes 1953, King 1959, King 1959, Bolser & Hicklin 1963, Poll & Ridgway 1966, Fraser 1968, Flanagan & Wrobel 1969, Capone *et al* 1970) has been done on the irradiation of quartz crystals with nuclear radiations like neutrons and gamma rays, X-rays and high energy electrons. This paper describes the irradiation results of the authors done on natural rectangular AT-cut quartz crystals of dimensions $3.8 \times 2.8 \times 0.39$ cm³ of fundamental frequency in the region of 1.87 MHz. The irradiation was done by fast neutrons, gamma rays and X-rays. The neutron source was a doubly encapsulated ²⁴¹Am-Be of 100 mCi strength. The source following the well known α -*n* reaction, emitted neutrons at the flux of 2.67×10^5 neutrons/cm²/sec. The associated background gamma dose rate was feeble (~ 0.25 mr/h at one meter from the source). The gamma ray sources were (a) ¹³⁷Cs of 4.5 mCi strength having a dose rate of 30 mr/sec at the surface of the container and (b) ⁶⁰Co of 1000 Ci strength having dose rate of 23.5 Rads/second.

The X-ray generator was a Phillips tube operated at 30 kV and 12 ma (Cu target). While for neutron and gamma ray irradiation, the whole crystal was uniformly exposed to the radiation field, for X-rays only the area equal to the area of the window (0.5 cm²) of the X-rays generator could be exposed. As would be expected this experimental limitation of the reduced area of exposure, gave no fundamental difficulties because it was experimentally verified that by exposing the same crystal to X-rays at different surface locations in turn, gave only an integrated effect of the results produced by exposing the crystal at only one window area on its surface.

The effects of irradiation looked for were the frequency offset and stability compared to the oscillating behaviour of the unirradiated quartz crystals obtained in a conventional oscillator circuit. The crystal oscillating circuit used was a modified Colpitts (Shea 1957), the frequency being measured by a standard frequency counter (HP model 5245L).

The electrodes for the quartz crystal for piezoelectric excitation were of steel having the same surface area as that of the quartz crystals (the crystals having no metallic film over them) but had raised corners so that the electrodes touched the quartz crystals only at these corner areas, leaving an air gap of the order of 0.2 mm between the non-touching areas of the crystal and the electrodes. For irradiation, the crystals were taken out from the electrode assembly and the post-irradiation frequency was measured after replacing the crystal back within the electrodes. The crystals used were AT-cut thickness shear devices of fundamental frequency in the region of 1.87 MHz. The uncertainty in the frequency measurements was found to be of the order of ± 10 Hz and was due to the departure from exact reproducibility of electrode placing in the act of taking out the crystal for irradiation and replacing the crystal again between the electrodes. The precision in the frequency measurement was ± 1 Hz, the frequency being measured digitally. Thus only those irradiation effects which gave a frequency offset of much more than 10 Hz were taken significant for interpretation of results.

2. Experimental Results

The experimental results obtained for neutron, gamma rays and X-rays would be given separately in the following paragraphs.

Neutron Irradiation

It was noticed that after the irradiated crystal is put back in the oscillator circuit, the quartz crystal oscillations pass through a stage of initial instability, before the frequency reached a stable final value. This characteristic of neutron irradiation does not seem to have been clearly documented so far in literature. This initial instability persists for about an hour or so. In this context it is instructive to note that the fact of existence of a period of initial instability and its duration is, to a large extent, independent of the time of idle keeping of the quartz crystal after irradiation. This observation indicates the significant contribution of the mechanical oscillations of the quartz crystal themselves in culminating the period of initial instability. The stabilization time could be reduced or even eliminated, if, after irradiation and before making the crystal oscillate (in the oscillator circuit), an initial warming of the crystal was done (for about fifteen or twenty minutes).

As the accumulated neutron doses were varied, the frequency offset obtained, after the initial stability had terminated, passed through three stages. In the

first stage, for low neutron dosage ($\sim 5 \times 10^{10}$ nvt) there was no observable permanent or steady offset, there being, as mentioned already, only a decrease of frequency stability for about an hour or so. Figure 1 shows a typical behaviour of such a crystal, irradiated by 7×10^{10} nvt. In the second stage, when the doses

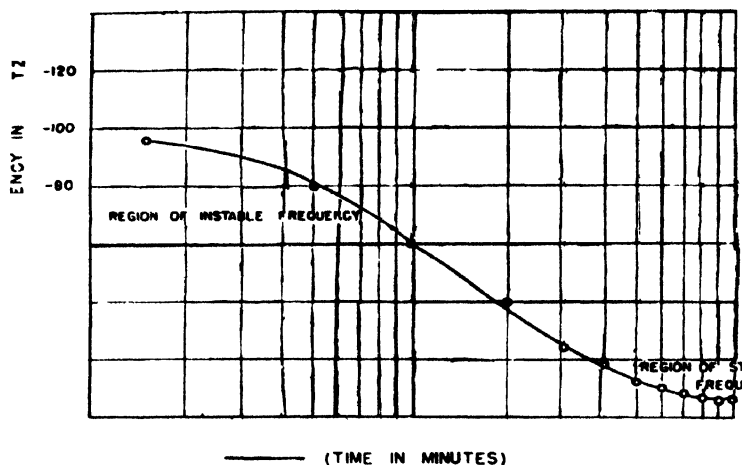


Figure 1. Frequency behaviour of an AT-cut quartz crystal resonator irradiated by hot neutrons with a dose of 7×10^{10} nvt.

were increased, a steady negative frequency offset was obtained, the magnitude of the offset increasing with dose. In the third stage, after a still further accumulated dose, the offset became positive, in line with the earlier observations reported in the literature (Belser & Hicklin 1961, King & Fraser 1961). Figure 2 depicts the results for this typical character of frequency versus neutron doses. Different neutron doses corresponding to points A, B...F, were given to a crystal specimen and the accompanying steady frequency shifts are mentioned obtained after the culmination of region of frequency instability.

No colouring of the quartz crystal was observable with the eye for all the accumulated dose used. This fact was supported by there being almost no change in the ultraviolet and optical absorption spectra for the pre-and post-irradiated quartz crystal. This observation corresponded with the fact that no EPR spectra could be recorded for the neutron irradiated crystal.

Gamma Irradiation

As mentioned earlier the gamma ray sources were ^{137}Cs and ^{60}Co . The quartz crystals irradiated by ^{137}Cs were given varying doses from 20 Röntgens to 10.5K Röntgens and those irradiated by ^{60}Co were given varying doses from 2000 Rads to 88K Rads.

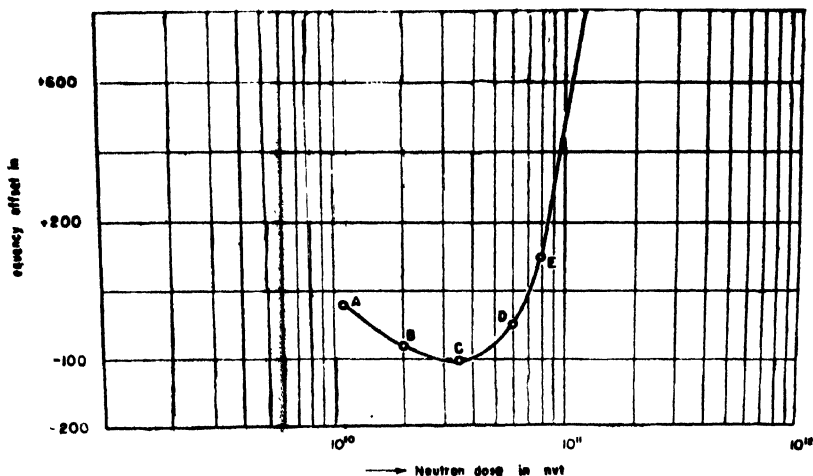


Figure 2. Steady frequency offsets of an AT-cut quartz crystal irradiated by hot neutrons in stages. Accumulated doses at point A = 2×10^{10} nvt, B = 20×10^{10} nvt, C = 36×10^{10} nvt, D = 60×10^{10} nvt, E = 80×10^{10} nvt, F = 4×10^{11} nvt.

The nature of results on the frequency behaviour of quartz crystals under gamma irradiation was of the same pattern as that obtained for irradiation with neutrons, except that during the period of initial instability the change of frequency with time was not linear as in the case of neutron irradiation. Figure 3 depicts a

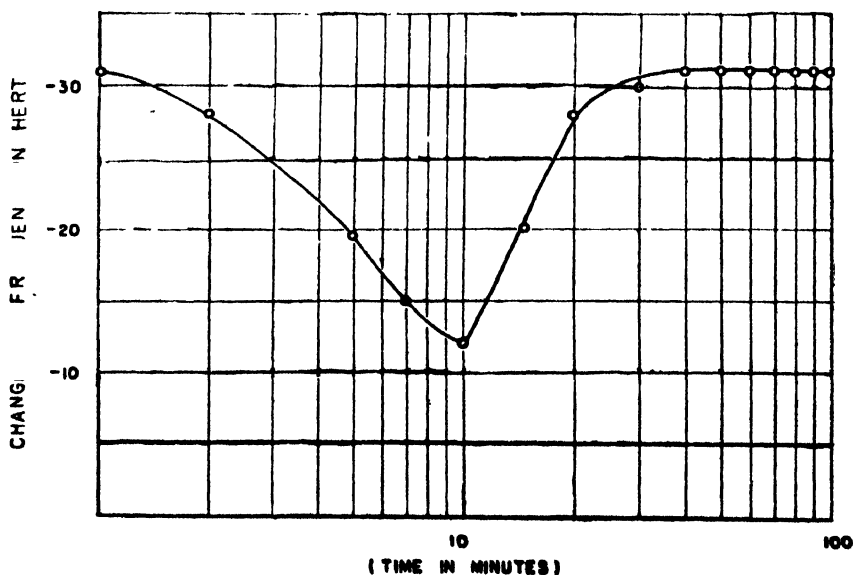


Figure 3. Frequency behaviour of an AT-cut quartz resonator irradiated by gamma ray with a dose of 2000 Rads using ^{60}Co

representative example for the frequency characteristic of a crystal irradiated with 2000 Rads from ^{60}Co . Figure 4 depicts such a characteristics of a crystal irradiated with 350 Röntgens from ^{137}Cs . Figure 5 depicts the complete general characteristic of a quartz crystal, irradiated in stages, showing that first there occurs a negative offset in frequency, followed by an increasing negative offset

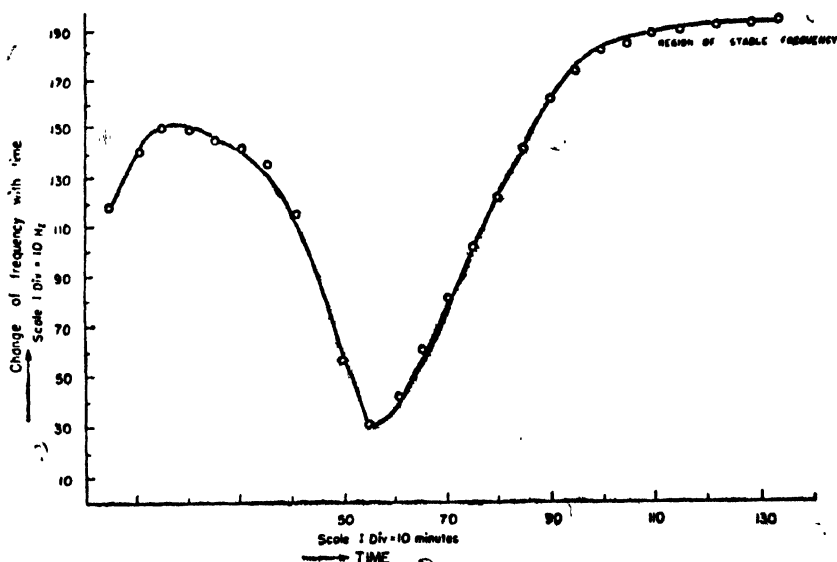


Figure 4. Frequency behaviour of an AT-cut quartz crystal resonator irradiated by gamma rays with a dose of 350 Roentgens using ^{137}Cs .

and afterwards showing a positive trend, the frequency finally reaching a positive offset with still further increase of accumulated doses. Figure 6 depicts the steady frequency offset character as a function of different accumulated doses for the crystal whose complete frequency characteristics (including the regions of initial frequency instability) are shown in figure 5.

Correspondingly, for the lower gamma ray doses ($\sim 2\text{-}10\text{K}$ Rads) there was no darkening produced as observed visually, but yet the permanent shift in the frequency was produced. Also, the crystals did not show any EPR signal when irradiated for these doses. As in the case of neutron irradiation, for these lower doses, the absorption curves in the ultra-violet and optical spectrum for the pre- and post-irradiated quartz crystals almost coincided.

For the crystals darkened by the gamma irradiation (doses $\sim 1\text{M}$ Rads), EPR spectra could be recorded in the Varian Associate's EPR Spectrometer at room temperature. Figure 7 represents a typical EPR spectrum obtained.

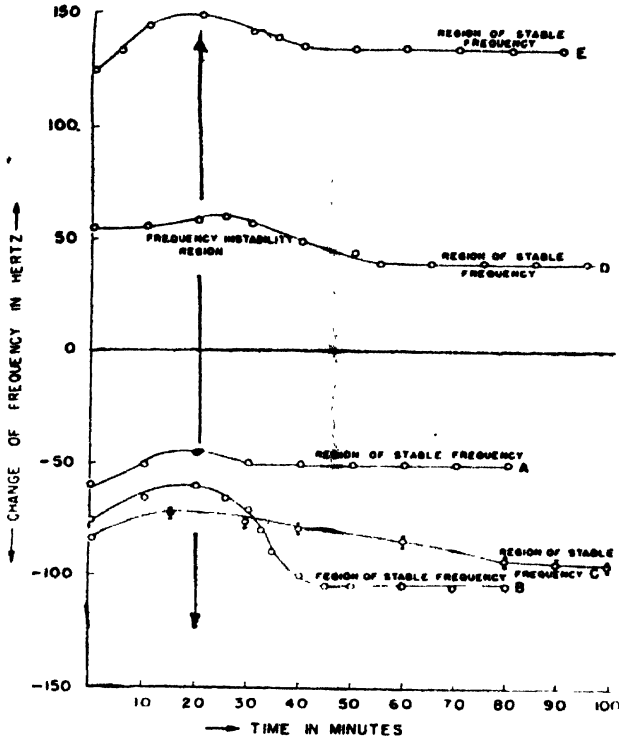


Figure 5. Frequency behaviour of an AT-cut quartz crystal irradiated by gamma rays in stages. Accumulated doses at A = 8000 Rads, B = 16000 Rads, C = 40000 Rads, D = 64000 Rads and E = 88000 Rads

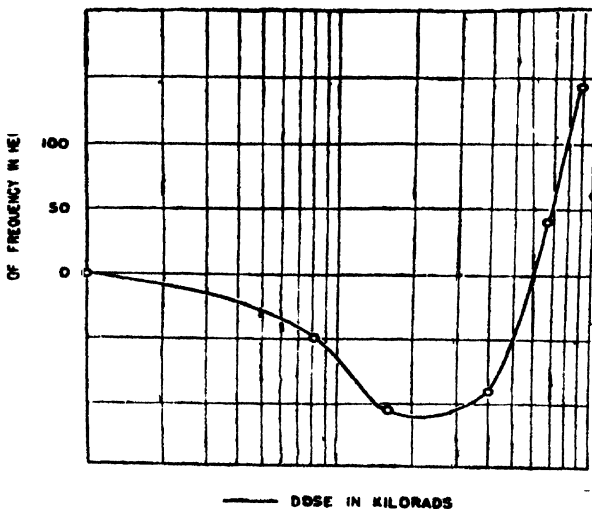


Figure 6. Steady frequency offsets of an AT-cut quartz resonator (whose complete frequency characteristics have been shown in fig. 5) irradiated in stages. Accumulated doses at points A, B ... F are those mentioned in fig. 5



Figure 7. EPR spectrum of an AT-cut quartz crystal irradiated by gamma rays (dose = 1M Rads) Observed at 300°K

X-Irradiation

For X-irradiation the nature of results were different from those of neutrons and gamma rays. The important difference was that X-irradiated crystals did not exhibit any instability in the beginning of their mechanical oscillations. The frequency offset obtained was always steady and was a function of the period

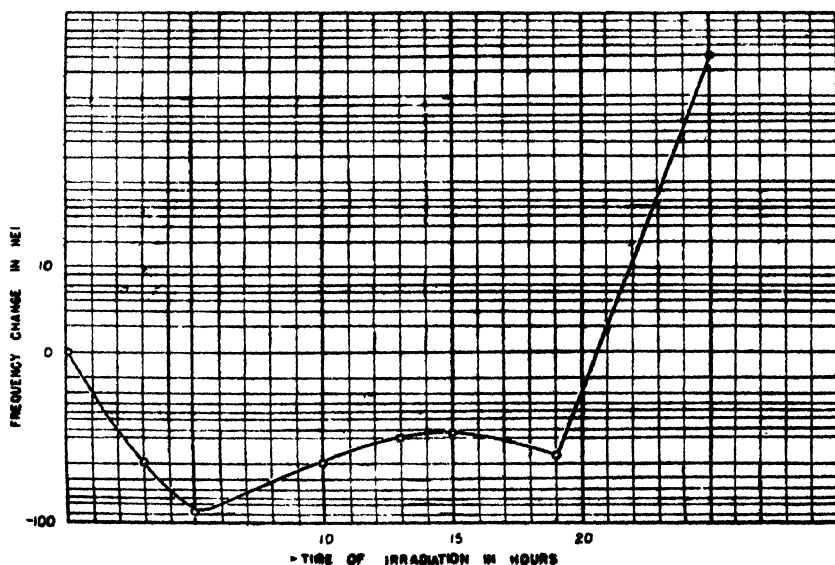


Figure 8. Frequency character of an AT-cut quartz crystal on being irradiated by X-rays (35kV, 12ma) in a stages at different accumulated doses

of exposure to the X-rays i.e. the accumulated dose. The variation of the offset with dose was of the same broad nature as that obtained in the case of gamma rays. Figure 8 gives the results.

The X-irradiated crystals gave characteristic EPR spectra at room temperature (300°K) as depicted in Figure 9. It will be noticed that the signal is a multiple line structure, in contrast to the single line obtained for gamma irradiation.

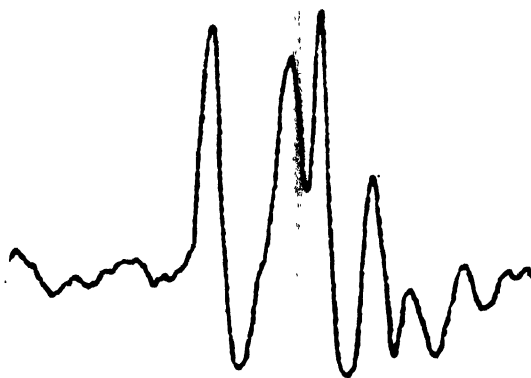


Figure 9. EPR Spectrum of an AT-cut quartz crystal irradiated by X-rays (35kV, 12ma) for 5 hours

3. Discussion of Results

The present study gives a number of new results, all of which it will be difficult to explain at the present stage of the work. However, we will take up some of the broad results obtained and offer explanations for them.

First, it should be noticed that gamma irradiation gives features common to those given individually by neutron irradiation and X-irradiation. Thus, both neutron and gamma irradiations give initial instability in frequency. As mentioned already, this instability is removed either by initial warming of the quartz crystals before they are put into mechanical oscillations or by the mechanical oscillations themselves when the quartz crystals are allowed to vibrate in an oscillating circuit for sufficient time. This conclusion follows from the fact, that as mentioned earlier instability in the frequency caused initially when the quartz crystals are first put into oscillations, is independent of the time of idle keeping of the quartz crystals in the interval between the termination of irradiation and the generation of their mechanical oscillations by means of a crystal oscillator circuit.

The effect of neutron and gamma irradiation in causing initial frequency instability is probably due to the nuclear displacements caused by neutron and gamma irradiation, an appreciable fraction of which (displacements) have low activation energies. Thus by mechanical oscillations or heat activation these

displaced nuclei of low activation energies cross the potential barriers involved for regaining their original lattice positions. Those nuclei which have been displaced sufficiently enough from their original positions in the un-irradiated sample will not come back by mere heating or through mechanical oscillations and will produce a permanent frequency offset. Some of these displaced nuclei will form centers for dislocation in the crystal.

It may be mentioned here that in literature only a positive frequency shift by neutron irradiation of AT-cut crystals has been reported (Bolser & Hicklin 1961, King & Fraser 1961). The neutron doses used by the earlier authors have been a number of orders of magnitude higher than those used by us. The present observations show that starting from low values of neutron doses, the frequency first decreases and for increased doses begins to increase, the latter fact being in line with the observations reported earlier in literature. The above suggests two opposing effects of neutron irradiation in the quartz crystal lattice.

No clear cut mechanism has been provided so far in literature for the positive frequency shift noticed with neutron irradiation. As has been mentioned earlier, the present work reports both kinds of changes of frequency and therefore the fundamental mechanism for causing these frequency changes must be quite complex.

In the following is presented a general consideration for the explanation of the frequency changes caused by gamma and X-irradiations. Explanation for effects of neutron-irradiation will not be taken up in this paper. Before taking up the theory, it may be mentioned that an added complexity involved in the detailed explanation of the experimental results of change of frequency is the evidence of minute surface cracks, obtained by examining the surfaces of virgin and irradiated crystals under scanning electron microscope. Figure 10-14 show the surface microstructures obtained for unirradiated and irradiated samples. Thus for a complete fundamental and detailed mechanism of the effect of neutron irradiation, the production of microscopic cracks in the sample would have to be taken into account. However, in the present work the role of the cracks in causing change of frequency would be neglected.

X- and Gamma Irradiation

In the following will be taken up the effect of gamma and X-rays in causing the change of frequency of quartz crystals. A mechanism for the negative change in frequency caused by gamma and X-irradiation has already been proposed in literature (King 1959, Fraser 1968). It will be our purpose in the following paragraphs to advance an overall mechanism which would explain the positive change of frequency for X- and gamma irradiation. Before we do so, it would be in order to mention as to what mechanism has already been advanced to explain the negative frequency shift for X- and gamma irradiation of quartz crystals. This

mechanism will form a background for the mechanism we would offer for explaining the positive frequency shift.

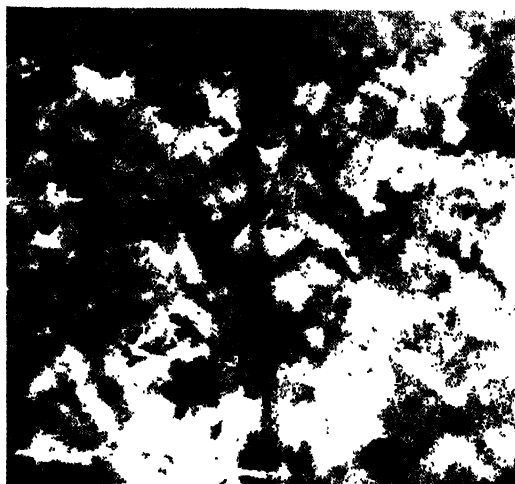


Figure 10. SEM micrograph of a virgin quartz crystal. Magnification = 850

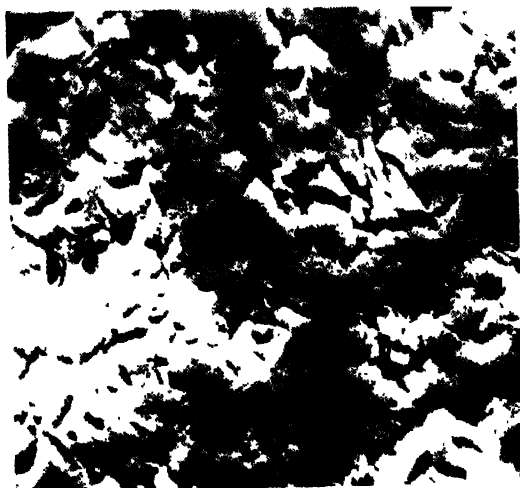


Figure 11. SEM micrograph of the quartz crystal (whose surface in the virgin state is shown in fig. 10) irradiated by X-rays (30kV, 12ma, 10 hours) Magnification = 850

The explanation is in terms of the Al^{3+} impurities in the quartz crystal. The Al^{3+} ions substitutionally displace the Si^{4+} atoms in the quartz lattice. For forming the covalent bonds with Si^{4+} , an Al^{3+} takes an extra electron to become

isoelectronic with Si^{4+} . For charge neutrality, a positive ion (H^+ , Li^+ or Na^+) is captured to be in the neighbourhood of Al^{3+} at an interstitial site, in the *c*-axis channel. This Al impurity center is often called X^{Al} P-center where *X* stands for H^+ or any of the alkali ions. (King 1959, Fraser 1968).

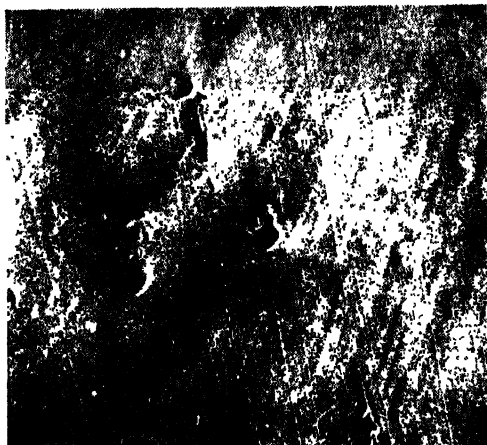


Figure 12. SEM micrograph of a virgin quartz crystal. Magnification = 650



Figure 13. SEM micrograph of the gamma irradiated (600k Rads) quartz crystal. Magnification = 1600

The steady negative change of frequency in natural quartz is supposed to be due to the release of cations thus released which attach themselves to some other places in the *c*-axis channel most probably dislocations or Ge impurities and become

electrontraps. The Al^{3+} center in the absence of the X^+ , due to the existence of the lone electron, becomes paramagnetic, showing the characteristic EPR signal. The centers so created are called *A*-centers and have a characteristic optical absorption band ($460\text{m}\mu$ and $620\text{m}\mu$) in the visible region (Fraser 1968 Ditchburn *et al* 1955). It has been shown (King 1959, Fraser 1968) that the *A*-centers

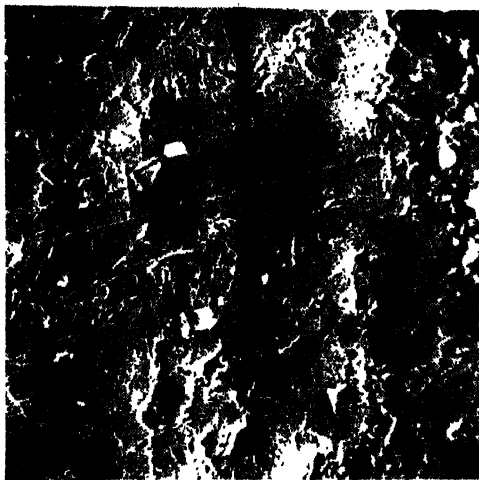


Figure 14. SEM micrograph of the quartz crystal irradiated by fast neutrons ($14 \times 10^{10} \text{nvt.}$). Magnification = 2800

given an anelastic effect and are thus responsible for decrease of elasticity and so the attendant negative frequency shift on irradiation. The decrease of elasticity is in line with Bottoms' findings (Bottom 1947) of decrease of all elastic constants with X-irradiation. Enough experimental evidence has been collected to show that the acoustic absorption due to anelastic behaviour, the intensity of the EPR spectrum and the intensity of the optical absorption are correlated (King 1959, Fraser 1968, Ditchburn *et al* 1955, Bottom 1947, Brien & Pryce 1955), thus all these effects arising from the same source (*A*-centers).

It has been mentioned above that in the case of natural crystals, the frequency change caused by X- or gamma-irradiation is negative. In contrast, in synthetic unswept quartz crystals the frequency change is positive and in the case of swept synthetic crystals, there is hardly any change of frequency by irradiation (Capone *et al* 1970). No satisfactory explanation has been offered for these effects taken together so far except to infer that the presence of the Na^+ ions at X^{Al} P sites probably cause lattice distortion to cause the positive change of frequency (Fraser 1964, King & Sander 1972). This inference is apparently taken to be supported by the authors earlier (Fraser 1968, King & Sander 1972), by the fact that there

are no Na^+ ions in the swept synthetic crystals, those ions having been replaced by H^+ by electrolysis of quartz crystals at high enough temperatures ($\sim 500^\circ\text{C}$). We will show in following paragraph that this influence is not tenable.

In the following is being offered an explanation of the positive change of frequency in synthetic crystals for all X- or gamma-ray doses and in natural crystals for increased doses.

We will first attempt to show that apart from the $\overset{\text{Al}}{\text{X}}\text{P}$ sites, Na^+ and other cations can exist in other sites also, most probably in the *c*-channel and other minor channels in the quartz crystal. The evidence for our supposition is presented in the following paragraphs.

(1) King (1959) has shown that synthetic crystals produce two kinds of anelasticities. In the first kind, an acoustic absorption peak for a quartz resonator of 5 MHz is produced at 50°K before irradiation. After irradiation, the 50°K peak almost disappears, the 100°K absorption mentioned previously appearing. Since the relative magnitudes of the 50°K absorption maxima produced for different crystals have no relationship with the relative magnitudes of the 100°K maxima, King was led to conclude that there is no relationship between the 50°K and 100°K defects. This conclusion becomes all the stronger, since in natural crystals, the 50°K peak is very much reduced but the 100°K peak is comparable to that in the synthetic crystals.

From the above, since the 100°K defect is associated with the $\overset{\text{Al}}{\text{X}}\text{P}$ center, there has to be another site for the 50°K loss peak. Incidentally King's observations also negated Fraser's assumption (Fraser 1964) mentioned earlier that the 50°K peak is associated with lattice distortion due to Na^+ at the $\overset{\text{Al}}{\text{X}}\text{P}$ sites, for if this were so, the amplitudes of 50°K peak and 100°K peak would have been associated.

(2) Fraser (1964) showed that injection of Na^+ ions in natural quartz crystals by electrolysis, produced a prominent 50°K acoustic absorption which is present in synthetic quartz. This fact shows that since the Al^{3+} defects are already associated with their cations in the natural or synthetic crystal, the Na^+ ions injected into the natural quartz and giving rise to 50°K absorption have occupied sites other than $\overset{\text{Al}}{\text{X}}\text{P}$. It also follows that these other sites are occupied by Na^+ ions in the normal way in synthetic crystals, since on the one hand the concentration of Na in synthetic crystals is much more than in natural crystals and also because synthetic crystals show the 50°K peak prominently.

(3) Fraser (1964) was led to conclude that there are different kinds of sites for alkali ions in quartz. He prepared synthetic quartz crystals grown in Li-doped nutrient solutions. This solution of course had Na due to Na_2CO_3 in it. He found that though the room and low temperature characteristics were changed

(showing that Li had been taken up by the crystals) the high temperature behaviour (of the acoustic loss) of the doped crystals remained unchanged and indicated the presence of Na.

(4) Dielectric investigations have shown that the low temperature dielectric loss is due to the cations at the $\text{X}^{\text{Al}}\text{P}$ center, flipping between the two minima in the potential curve for the center (Devos & Volger 1970, Stevels & Volger 1962) but the high temperature dielectric loss is due to the migration of cations in the *c*-channel (Show & Gibbs 1964).

(5) King and Fraser (1961, 1962) have shown that electrolysis (i.e. subjecting quartz to a field of 1.2 kV/cm in a furnace at about 500°C) of both natural and synthetic quartz removes the acoustic loss existing at high temperatures. Since the loss is due to the movement of charge carriers, which movement is possible in the *c*-channel (Verhoegen 1952), the improvement in the quartz shows that alkali ions are present in the *c*-channel before electrolysis.

From all the above, we conclude that the alkali cations can exist at two different kinds of sites, one the $\text{X}^{\text{Al}}\text{P}$ Centers and the other existing in the channels. In these channels the cations would be pinned at dislocations, Ge and other defects, called 'moorings' by Stevels and Volger (1962)

From all the above we are led to conclude that though the 100°K acoustic absorption peak produced after irradiation, is associated with the anelastic behaviour of the $\text{X}^{\text{Al}}\text{P}$ defect, the pre-irradiation 50°K absorption is associated with the presence of cations at moorings. This deduction gets support from the work of Brown (1960) and Jones & Brown (1962) on synthetic crystals, who have shown that density of defects in quartz depends on the growth rate and that there is correlation between growth rate and the height of the 50°K loss peak. In other words, the greater is the growth rate, the greater would be the moorings (defects) at which the cations can be trapped for forming the 50°K defects.

For the explanation of our experimental results, we first note that the cations at the moorings would, due to their positive charge, form electron traps. We make the assumption that when the moorings capture electrons, produced by irradiation, the 50°K absorption loss is eliminated. Due to the removal of the anelastic behaviour associated with the absorption peak, the elasticity increases, leading to increase of resonance frequency. Thus there will be two simultaneous processes existing for change of frequency with irradiation. Due to the generation of anelasticity associated with the 100°K absorption peak on irradiation, the frequency would decrease and due to the disappearance on irradiation of the anelastic behaviour associated with 50°K absorption, the frequency would increase. We here assume that the positive change of frequency caused by the destruction of 50°K defect (electron trapping by the cation at the moorings) is greater than the negative change of frequency caused by the formation of A-center.

At this stage we are in a position to explain the irradiation behaviour of synthetic and natural quartz crystals on the premises made above.

Synthetic Crystals

Due to the fact that there is a large concentration of imperfection sites in synthetic quartz at which sites the Na^+ ions can be attached for forming electron traps, the over all effect of frequency change is to give a positive offset. Though by now, no irradiation experiments have been done on natural quartz injected with Na^+ ions, it may be inferred from all the above, that on irradiation, there may be positive change of frequency from the very commencement of irradiation, or at least, the range of dose of the ionizing radiations, for which the negative offset takes place would be reduced.

Natural Crystals

In the natural crystals, due to the relatively large concentration of $\text{X}^{\text{Al}}\text{P}$ defects accompanied by a small concentration of cations at the moorings in the *c*-channel, the net irradiation effect would be of a negative frequency offset at the lower radiation doses caused by A-centers. All along, as the radiation dose increases, more and more of the cations would come away from the $\text{X}^{\text{Al}}\text{P}$ defects to the moorings, due to the formation of A-centers out of them (P-defects). These new cations at the moorings would produce the positive frequency offset. Thus it is straightforward to deduce that with increased radiations the frequency offset after being negative in the beginning, will change sign, in the way experimentally observed.

4. Conclusion

The physical basis of a theory, in terms of alternative sites for alkali cations in quartz crystals has been given which explains the two opposing kinds of changes in frequency of quartz crystals produced as a function of irradiation doses of X-rays and gamma rays. The irradiation removes alkali cations from the Al^{3+} defect centers, this process giving rise to decrease of frequency. At the same time, the alkali cations present at moorings in the quartz crystal *c*-channels and others, capture electrons produced by irradiation, this process leading to increase of frequency. Of the cations present at the moorings, some are those which are present in the quartz crystal inherently or have been injected in the lattice by electrolysis and the others are those set free from the Al^{3+} defect centers by irradiation.

Apart from the general common features mentioned above for the two kinds of radiations, there would be of course individual differences among them in causing the respective changes of frequency. This would be due to the facts mentioned above that X-rays are only ionizing and gamma rays ionizing and can also cause nuclear displacements. Future work should unravel the exact role of these differences in causing the frequency changes.

Acknowledgments

For the present studies the cooperation extended by Dr. Jagdish Bahadur (Nuclear Research Laboratory, I.A.R.I., New Delhi) for irradiating the quartz crystals by $^{241}\text{Am-Be}$ and ^{137}Cs , Dr. A. Nagarathnam (Inst. Nuclear Medicine and Allied Sciences, New Delhi) for irradiating quartz crystals by ^{60}Co , Dr. S. K. Gupta (National Physical Laboratory, New Delhi) for recording EPR Spectra, Dr. L. M. Tiwari (Ind. Inst. Tech. Delhi) for permitting the use of their X-ray generator is highly appreciated. Courtesy of Dr. Allen Hepworth and Mr. V. K. Lall (Ind. Inst. Tech. Delhi) for their help in examination of surface microstructures of virgin and irradiated quartz crystals under Scanning Electron Microscope and also Mr. N. C. Goel (NPL)'s help in getting the samples prepared for examination in SEM is gratefully acknowledged and appreciated. Thanks are also due to Mr. S. B. Manamohanam (NPL) for his help in recording ultraviolet and optical absorption characteristics.

One of the authors (HB) thanks the Department of Atomic Energy, Government of India for the award of research fellowship to him.

References

- Fronnel C. 1945 *Amer. Mineralogist* **30**, 432.
 Chi A. R. 1957 *Physics Rev.* **107**, 1524.
 Bechmann R. 1958 *Nucleonics* **16**, 122.
 Berman R. K. emons P. G., Simon F. E. & Fry T. M. 1950 *Nature* **166** 764
 Johnson F. B. & Pease R. S. 1954 *Phil. Mag.* **45** 651.
 Arnold G. W. 1956 *Proc. Ann. Freq. Control Symp.* **10**, 61.
 Arnold G. W. 1957 *Proc. Ann. Freq. Control Symp.* **11**, 112.
 Arnold G. W. 1954 *Jour. Chem. Phys.* **22**, 1259.
 Wittlos M. & Sherrill F. A. 1954 *Phys. Rev.* **93**, 1117.
 Primak W, Fuchs L. H. and Day P 1953 *Phys Rev.* **92**, 1064.
 Kinchin G. H. and Pease R.S 1955 *Reports Prog. Phys* **19**, 1.
 Primak W. and Szymanski H. 1956 *Phys. Rev.* **101** 1268.
 Dienes G. J 1953 *Phys. Rev.* **91**, 1283.
 King J. C. 1959 *Phys. Rev.* **109**, 1552.
 King J C. 1959 *Bell Syst. Tech. Jour* **38** 575.
 Belser R. B. & Hicklin W H 1963 *Proc. Ann. Freq. Control Symp.* **17** 127.
 Poll R. A. & Ridgway S. L 1966 *IEEE Trans. Nucl. Sci.* **NS-13** 130 Dec.
 Fraser D. B. 1968 *Physical Acoustics* (Ed W. P. Mason) Acad. Press **V** 59.
 Flanagan T. M. and Wrobel T. E. 1969 *IEEE Trans. Nucl. Sc.* **NS-16** 130 Dec.
 Capone B. R, Kahan A, Brown R N and Buckmelter J R 1970 *IEEE Trans. Nucl. Sc.* **NS-17** 217
 Shoa R. F. 1957 *Transistor Circuit Engg* (John Wiley and Sons Inc New York) p 234
 Belser R. B. & Hicklin W. H. 1961 *Proc. Ann. Freq. Control Symp.* US Army Electronics Command NJ (USA) **15** 138
 King J. C. & Fraser D B 1961 *Proc. Ann. Freq. Control Symp.* **15** 2
 Ditchburn R. W., Mitchell E. W. J, Paige E G S, Custers J F, Dyor H. B. & Clark C. D. 1955 *Defects in Crystalline Solids*, Bistol Conference, Physical Soc., London, p 92

- Bottom V. E. 1947 *Phys. Rev.* **71**, 476.
- Brien M. C. M. O' & Pryce M. H. L. 1955 *Defects in Crystalline Solids*, Bristol Conference Phys. Soc (Lond) p 88
- Brien M. C. M. O' 1955 *Proc. Royal Soc. (Lond)* **A231**, 404,
- Fraser D. B. 1964 *Jour. Appl. Phys.*, **35**, 2913.
- King J. C. and Sander H. H. 1972 *IEEE Trans. Nucl. Sc.* **NS-19**, 23.
- DeVos W. J & Volger J 1970 *Physica* **47**, 13.
- Stevens J. M & Volger J. 1962 *Philips Res. Reports* **17** 283.
- Snow E. H. & Gibbs P. 1964 *Jour. Appl. Phys.* **35**, 2368.
- King J. C. 1962 *Proc. Inst. Electr. Engrs. (Lond)* 109B Suppl. **22**, 1.
- Verhoeven J 1952 *Amer. Mineralogist* **37** 637
- Brown C. S. 1960 *Proc. Phys. Soc. (Lond)* **75**, 459.
- Jones C. K. & Brown C. S. 1962 *Proc. Phys. Soc. (Lond)* **79**, 930.

Structure and dielectric measurements of thin films of Bi_2O_3

R N Saxena, S L Pandey and Sooraj Singh

Physics Department, Bareilly College Bareilly (U.P.)-243001

and

S K Sharma

National Physical Laboratory, Hillside Road, New Delhi 110012

Abstract. Thin films of Bi_2O_3 have been prepared by oxidation of bismuth films in atmospheric conditions. The structure of these films has been investigated by electron microscopy and electron diffraction. Dielectric measurements of the films have been carried out using sandwich structure and the variation of capacitance and loss factor have been studied as a function of temperature, frequency and thickness. The observed results are reported and explained suitably in the present paper.

1. Introduction

It is well known that oxide dielectric films are used extensively in active as well as passive devices in the field of micro circuitry. So the study of the dielectric properties of the insulating materials in thin film forms has become a subject of recent investigations. A vast variety of materials having amorphous as well as crystalline structure, has been used as the dielectric medium. Usually the amorphous material show remarkable insulating properties and insensitivity to impurities (Mott 1967). Most of the work on thin insulators has been carried out in amorphous films, particularly metal oxides (Chopra 1969). These films are mechanically and chemically very stable.

Although amorphous Bi_2O_3 films have been studied earlier (Doyle 1958), but very little information is available about the behaviour and dielectric properties of crystalline $\alpha\text{-Bi}_2\text{O}_3$ films (rhombic phase). In the present investigation the authors have studied dielectric properties of thin films of Bi_2O_3 and the structure of these films. Preliminary results obtained in the course of investigation are reported in the present paper.

2. Experimental Details

(a) Preparation of films

For the present investigation, glass slides were used as substrates and for structure study the films were prepared onto NaCl crystals. Thin films of Bi_2O_3

were prepared by oxidation (Doyle 1958, Hapase *et al* 1967) of vacuum deposited Bi films. The glass slides were cleaved in the usual way (Holland 1956) and a strip shaped thick electrode of aluminium (~ 8000 A.U.) was deposited on to the glass substrate and it was followed by the deposition of bismuth films under vacuum of the order of 10^{-5} Torr. while depositing Bi films freshly cleaved rocksalt pieces was also kept by the side of glass slide for the simultaneous deposition of bismuth films. The glass slides with bismuth films on top of aluminium electrode was heated in an oven at 175°C for several hours (50 to 100 hours) in atmospheric condition. In this way the top surface of Bi-films was oxidised into rhombic yellow Bi_2O_3 layers. It has been found that in case of thick Bi films, the oxidation was not complete even after prolonged heating. The thickness of Bi_2O_3 films was varied from 1300 to 2750 A.U. A thick counter electrode of aluminium (~ 800 A.U.) was deposited over Bi_2O_3 layers in a coplanar sandwich structure as shown in figure 1. using appropriate mark. Sandwiched area of the dielectric between the electrodes was of the order of 0.8 cm^2 (Chopra 1969). The thin film capacitors so formed with rhombic yellow Bi_2O_3 as dielectric were investigated.

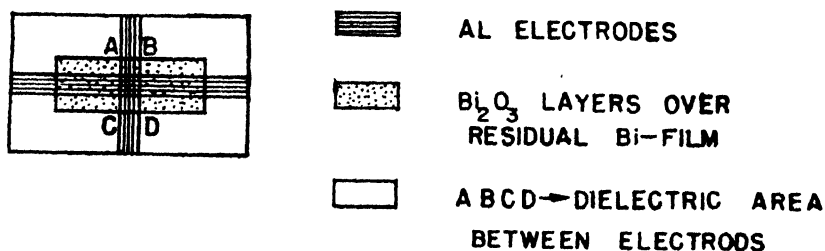


Figure 1. The diagram showing the schematic arrangement for depositing various thin films.

These capacitors were mounted and fixed on a suitable base and the leads were connected with the electrodes with the help of silver paint. It was found that the (leads + electrode) resistance was $< 1\Omega$ and the effective lead capacity $< 2\text{ pf}$. This was sufficient to minimise the losses at higher frequencies (McLean 1967). For making different depositions the vacuum was broken each time.

(b) Measuring Instruments used

Marconi Universal Bridge model TF 2700 has been used for measuring the capacity and losses at different frequencies (200 Hz to 20kHz) and at temperatures from room temperature to 130°C by null detection method. The universal bridge was fed with both external and internal generators.

The dielectric thicknesses were calculated by capacitance formula $C = KA/4\pi t$, assuming the dielectric constant for Bi_2O_3 films to be 18 as reported by Young (1961) for layers of Bi_2O_3 prepared by anodic oxidation.

The breakdown voltage was found with the help of a microvolt meter, model MV001 supplied by M/s. SES Roorkee, by measuring the voltage across a $10\ \Omega$ resistance which was placed in series with a $50\text{K}\Omega$ resistance and the film capacitor as shown in figure 2.

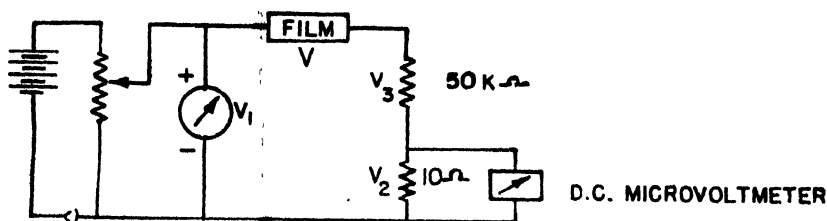


Figure 2. The diagram shows the circuit used for measuring the break down voltage.

The breakdown voltage has been calculated from the relation

$$V = \{V_1 - 5V_2 \text{ in mV}\} \text{ volts.} \quad (i)$$

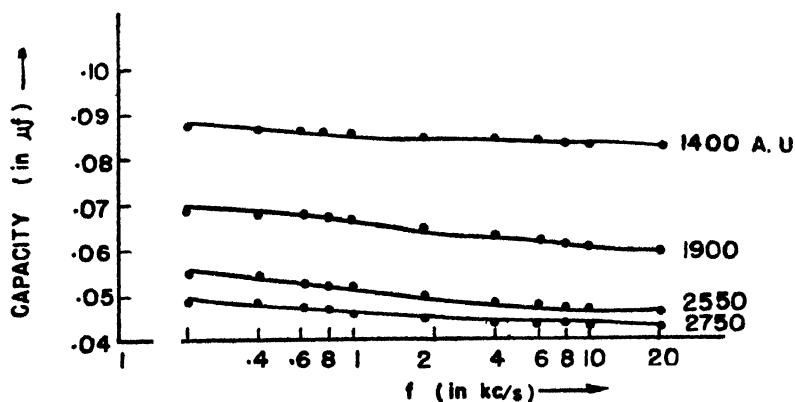
From the above circuit, the currents of the order of even 10^{-7} amps. could be measured. All the observations have been made at atmospheric pressure.

For making electron microscopy and electron diffraction investigations. Philips EM 200 electron microscope has been used. The films of Bi_2O_3 (500–1000 Å) formed on NaCl were floated on the distilled water and picked up on the grids and were studied with the electron microscope.

3. Results

(a) Structure of Bi_2O_3 films

The films of Bi deposited simultaneously onto the rocksalt substrates were oxidised at the same time while making the dielectric films for the capacitors. The Bismuth films so oxidised on examination with electron microscope showed polycrystalline structure. Figures 3, 4 show the electron micrographs and electron diffraction pattern of the Bi_2O_3 films. All the films examined above 500 Å were found to be continuous. On calculating the d -values for the various lines observed in the diffraction pattern, the films showed rhombic structure ($\alpha\text{-Bi}_2\text{O}_3$) corresponding to ASTM card No. 14-699, thus confirming that the oxidation conditions used in the present investigation are the correct and required conditions for forming $\alpha\text{-Bi}_2\text{O}_3$ dielectric films.



CAPACITY VARIATION WITH FREQUENCY

Figure 3. The curves show the variation of capacitance with frequency.

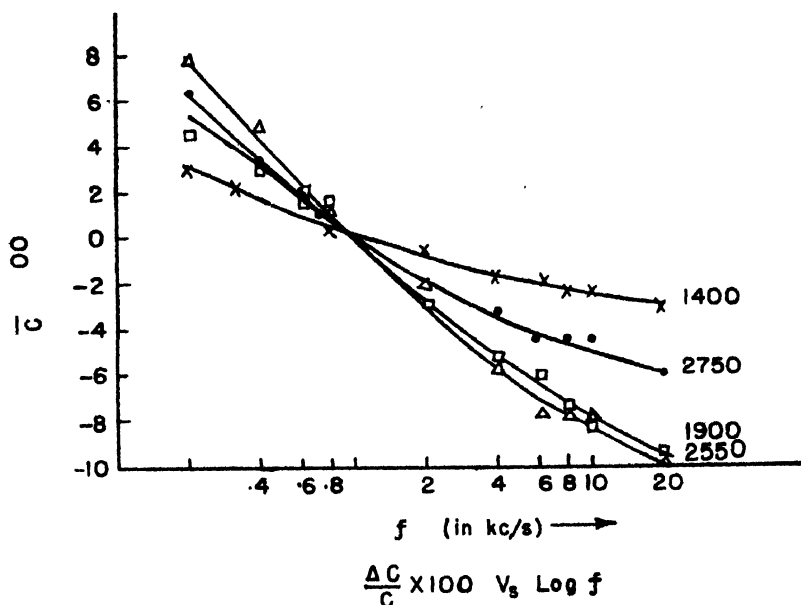


Figure 4. The curves show the variation of $\frac{\Delta C}{C} \times 100$ with frequency.

(b) Dielectric properties

The unannealed films first showed a marked fall in its capacitance and loss factor ($\tan \delta$), which became very slow after a few days. But complete stable conditions could not be achieved even after a long period, due to the aging effects as usually observed. However, after repeated annealing of the capacitor at 175°C for 2 hours each time and leaving it to settle down for one day after each annealing, it was found to have almost stable values.

(i) Capacitance and loss variation with frequency

The variation of capacitance and the losses for a frequency range (200 Hz to 20 kHz) was studied and it was found that for all the thicknesses of the dielectric (1300–2750) value of the capacitance decreases with the increase in frequency as shown in figure 5. Below 1 kHz upto 200 Hz the change in value of the capacitance $\left(\frac{\Delta C}{C} \times 100\right)$ was around 8%, while in higher frequency range (1 kHz to 20 kHz) it was around 10% as shown in figure 6.

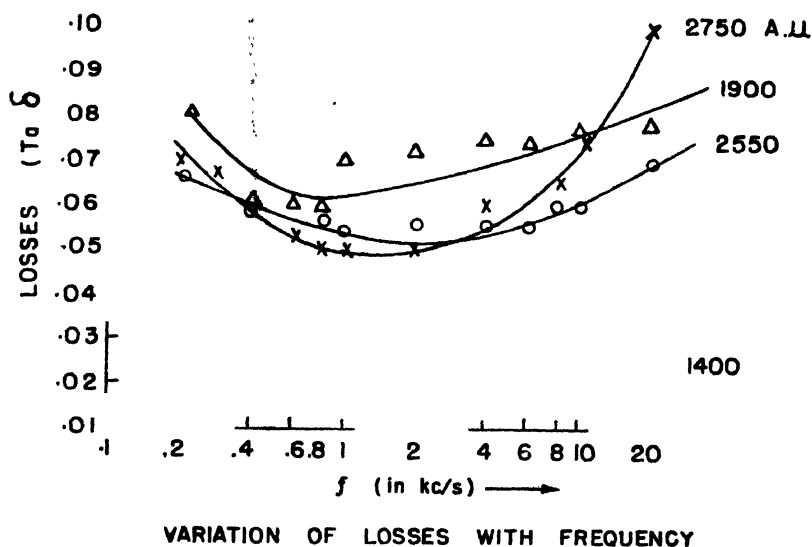


Figure 5. The curves depict dependence of loss factor ($\tan \delta$) with frequency.

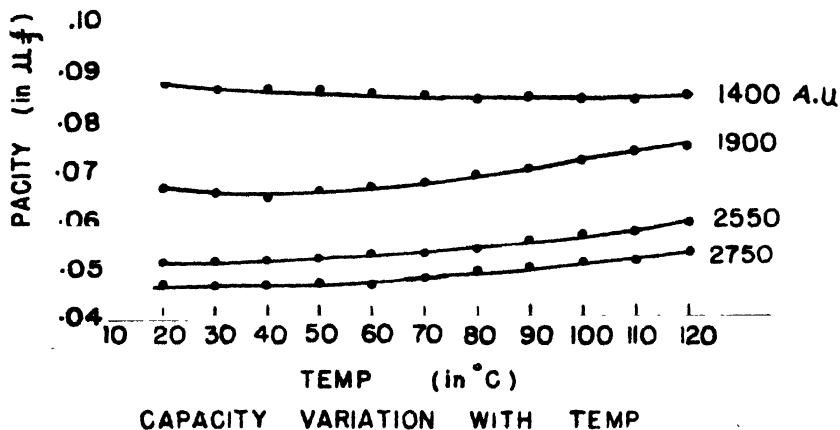


Figure 6. The curves in the figure show the variation of capacitance with temperature.

For the respective thicknesses, we obtained that the loss factor, $\tan \delta$, attained a minimum value at certain frequency range on the lower frequency side, figure 7. It was also observed that $\tan \delta$ for layers of thicknesses (1900 to 2750 A.U.) was nearly of the same order, while for a thinner layer (1400 A.U.) it was quite low.

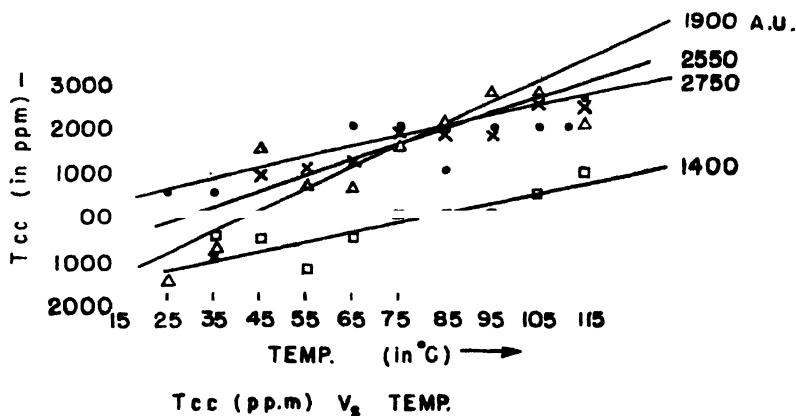


Figure 7. The curves depict the variation of T.C.C. with temperature.

(ii) Effect of temperature on capacitance and losses

It was observed that the capacitance and losses both are quite sensitive to the temperature variation. The effect of temperature on capacitance and loss factor was studied at 1 kHz frequency. It was found that for thinner dielectric layers capacitance first decreased (negative T.C.C.) with temperature and then increased with it (positive T.C.C.). But for thicker ones the capacitance increased earlier with temperature, as shown in figures 8 and 9. T.C.C. for these films varied from -1000 to 2800 ppm/°C which is quite high as compared to other good dielectrics.

Unlike the capacitance, losses showed an increase with temperature for all the dielectric thicknesses (figure 10).

(iii) Break down Intensity

We measured the break down voltages for different thicknesses of Bi_2O_3 and then calculated the breakdown intensities. It was observed that the thicker films of Bi_2O_3 had lower breakdown intensities obeying the relation $F_b \propto t^{-\beta}$ where F_b is the breakdown intensity, t the thickness of dielectric and β is a constant. In the present case $\beta = 0.78$ (figure 11). Similar results have been suggested (Forlani and Minnaja 1964) and reported by other workers (Forlani and Minnaja 1969, Bundenstein and Hayes 1967, Goswami and Goswami 1974) also, for different dielectrics. Figure 11 shows the variation of $F_b V_b t$. The slope of the straight line is negative.

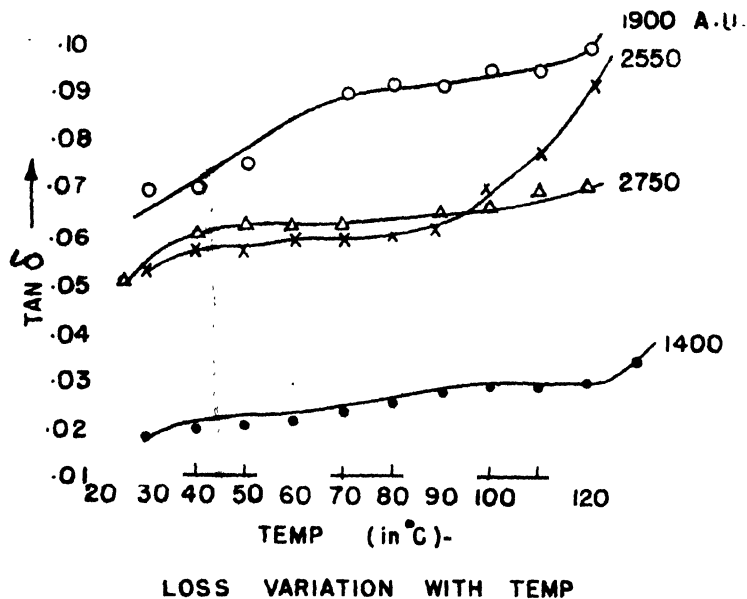


Figure 8. The curves in the figure show the losses with temperature.

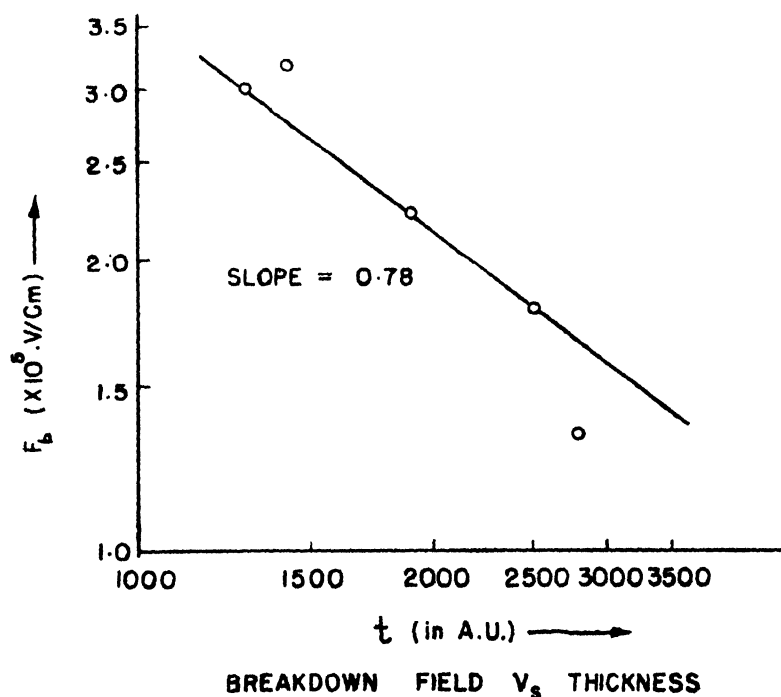


Figure 9. The curve shows the variation of $\log F_b$ versus t (the thickness). The curve shows a straight line having a slope equal to -0.78 .



3-ELEMENT CAPACITOR SYSTEM

EQUIVALENT CIRCUIT

Figure 10. (a) 3-element circuit of the capacitor.
(b) Its equivalent circuit.

4. Discussion

From the above results it is observed that the dielectric behaviour of Bi_2O_3 is quite similar to those of Nb_2O_5 or ZnS , as reported by Goswami and Goswami (1973, 1974). So the dielectric properties of Bi_2O_3 layers could also be explained on the basis of Goswami model which assumed the dielectric capacitor to consist of three elements, figure 12(a), viz., (i) an inherent capacity element C which remains constant for all frequencies and temperatures, (ii) the dielectric film resistance R in parallel with C , and (iii) a series lead resistance r , due to connecting leads etc. They also assumed R to vary with temperature as $R = R_0 e^{\Delta E/kT}$ the lead resistance r being almost constant and that $R \gg r$.

The measured equivalent capacity and the equivalent series resistance of 3-element circuit of figure 12(a) are given by

$$C_s = C + \frac{1}{\omega^2 R^2 C} \quad (\text{ii})$$

$$R_s = r + \frac{R}{1 + \omega^2 R^2 C^2} \quad (\text{iii})$$

and hence

$$\begin{aligned} \tan \delta &= \omega C_s R_s \\ &= \omega r C + \frac{1}{\omega R C} + \frac{r}{\omega R^2 C} \end{aligned}$$

or

$$\tan \delta = \omega r C + \frac{1}{\omega R C} \quad \text{as } R \gg r \quad (\text{iv})$$

from equation (iv), we find a loss minimum to occur at a frequency, given by

$$\omega_{\min} = \frac{1}{\sqrt{r R C^2}}$$

Thus the loss minimum in $\tan \delta$ Vs frequency curve could be explained satisfactorily. The increase in $\tan \delta$ at lower and higher frequencies could be well explained with the help of equation (iv). At lower frequencies $\frac{1}{\omega R C} \gg \omega r C$ and so $\tan \delta = \frac{1}{\omega R C} \propto \frac{1}{\omega}$ while at higher frequencies $\omega r C \gg \frac{1}{\omega R C}$ and therefore,

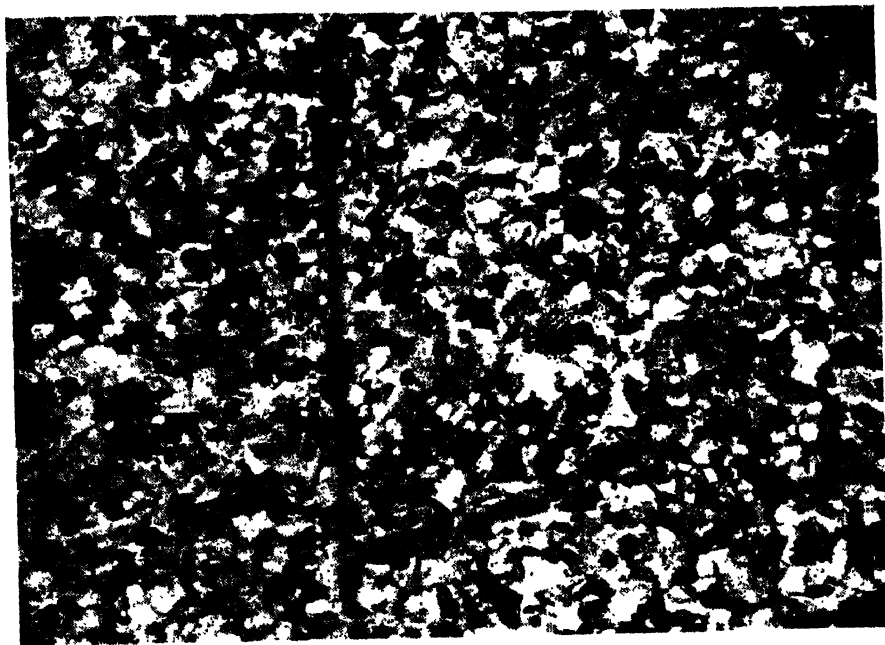


Plate 1. The electron micrograph of thin Bi_2O_3 film showing Poly crystalline structure.

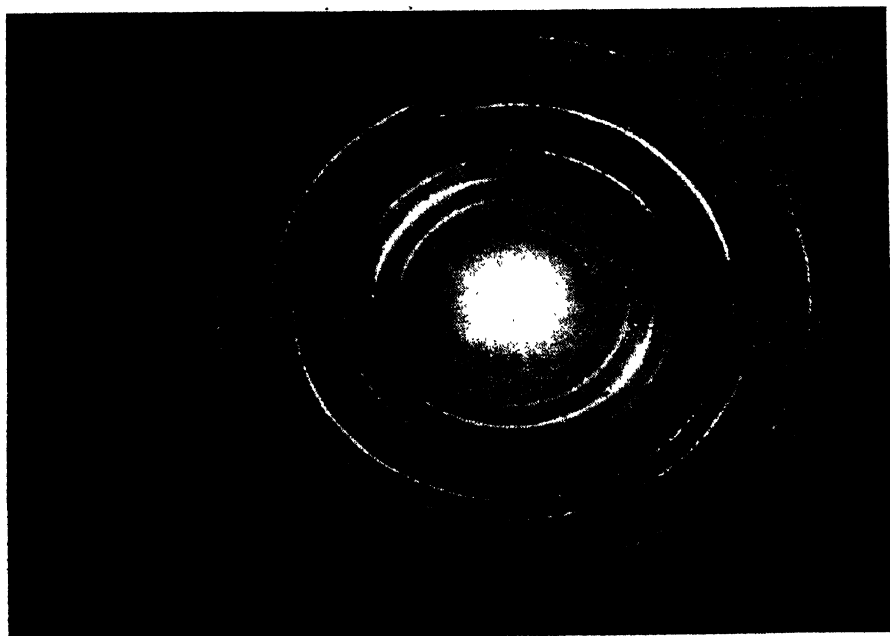


Plate 2. Electron diffraction pattern of thin Bi_2O_3 film showing rhombic structure.

$\tan \delta = \omega R \sin \delta$. Since the value of R of Bi_2O_3 films decrease with temperature, the values of $\tan \delta$ will increase at higher temperatures.

The variation of capacitance Vs frequency and temperature could also be explained with the help of equation (ii)

$$C_s = C + \frac{1}{\omega^2 R^2 C}$$

It is evident from the above equations that the measured capacity C_s should decrease with frequency, as has been observed in the present investigation. Similarly the value of R decreases with the temperature, C_s will increase with the temperature. Similar behaviour has been shown by thicker films of Bi_2O_3 , while thinner ones first exhibit a decrease in capacity with temperature and then increases with further increase in temperature, thus showing both negative and positive TCC. This effect is expected to be due to slight porosity in thinner dielectric films and requires further investigation.

Very recently we have carried out some dielectric measurements at lower pressure and have found that the capacitance decreases slightly with frequency while the losses are reduced to nearly 50% of the value attained at atmospheric pressure.

Further work on the dielectric measurements, growth of Bi_2O_3 layers is in progress and it is proposed to carry out detailed work on the investigation with a wide range of film thickness. The measurements will also be carried out under different controlled pressures.

5. Conclusion

Capacitance and losses of Bi_2O_3 films are quite sensitive to frequency and temperature variation. These characteristics could be explained quite well with the help of Goswami model of 3-element capacitor-resistance circuit. The field strength required for breakdown of Bi_2O_3 films is of the same order, as for other dielectrics.

References

- Mott N F 1967 *Advan. Phys.* **16** 49
- Chopra K L 1969 *Thin Film Phenomena* **8** 466
- Doyle W P 1958 *J. Phys. Chem. Solids* **4** 144
- Hapase M G, Tore V B and Biswas A B 1967 *I.J.P.A. Phys.* **5** 401
- Holland L 1956 *Vacuum Deposition of Thin Films* 84
- Mclean D A 1967 *IEEE Inter Conv. Record* p t. 7, *Electron devices, Materials and Microwave Components* p 108
- Young L 1961 *Anodic Oxide Films* p 12 Academic Press Inc. New York
- Forlani F and Minnaja N 1964 *Phys. Stat. Solidi* **4** 311
- Forlani F and Minnaja N 1969 *J. Vac. Sc. Technol.* **6** 518
- Bundenstein P P and Hayes P J 1967 *J. Appl. Phys.* **38** 2837
- Goswami A P and Goswami A 1974 *I.J.P.A. Phys.* **12** 26
- Goswami A and Goswami A P 1973 *Thin Solid Films* **16** 175

STATEMENT OF THE OWNERSHIP AND OTHER PARTICULARS ABOUT THE
INDIAN JOURNAL OF PHYSICS AND PROCEEDINGS OF THE INDIAN ASSO-
CIATION FOR THE CULTIVATION OF SCIENCE, VOL. 53A & B, 1979)

Form IV
(See Rule 8)

1. Place of publication : .. Indian Association for the Cultivation of Science, 2 & 3, Raja Subodh Mallick Road, Jadavpur, Calcutta 700032
 2. Periodicity .. Monthly
 3. Printer's Name .. Sri Haradhan Chakrabarti
Whether Citizen of Indian Indian
Address Eka Press,
204/1 B. T. Road, Calcutta-700035
 4. Publisher's Name (1) Sri Samarendra Nath Sen (Upto 30.9.78)
(2) Sri M. K. Ghosh (From 3.10.78)
Whether Citizen of India Indian
Address Registrar, Indian Association for the Cultivation of Science, 2 & 3, Raja Subodh Mallick Road, Jadavpur, Calcutta 700032.
 5. Editors' Name
Whether citizen of India
Address
- | | | |
|--|--|---|
| <p>1. Dr. D. N. Basu,
Indian,
Director,
Indian Association
for the Cultivation of
Science 2 & 3, Raja
Subodh Mallick Road,
Calcutta-700032.</p> | <p>4. Prof. A. Bose
Indian
Indian Association for the
Cultivation of Science
2 & 3 Raja Subodh
Mallick Road,
Calcutta-700032</p> | <p>8. Prof. D. N. Kundu
Indian,
Director, Saha Institute
of Nuclear Physics
92, Acharya Prafulla Ch.
Road
Calcutta-700009</p> |
| <p>2. Prof. J. N. Bhar,
Indian
Head of the Dept. of
Radiophysics and
Electronics
University College of
Technology
92, Acharya Prafulla
Ch. Road,
Calcutta-700009</p> | <p>5. Prof. S. D. Chatterjee
Indian,
91, Ballygunj Place
Calcutta-700019.</p> | <p>9. Prof. C. K. Majumdar
Indian,
Department of Pure
Physics University
College of Science
92, Acharya Prafulla Ch.
Road
Calcutta-700009</p> |
| <p>3. Dr. V. G. Bhide
Indian,
Director, National
Physical Laboratory
Hillside Road,
New Delhi-110012</p> | <p>6. Prof. K. L. Chopra
Indian,
Department of Physics
Indian Institute of
Technology Hauz Khas,
New Delhi-110029</p> | <p>10. Dr. A. P. Mitra
Indian,
Head, Radio Science
Division National
Physical Laboratory
Hillside Road,
New Delhi-110012</p> |
| <p>7. Prof. Krishnaji
Indian,
Pro-Vice Chancellor
Senate House
Allahabad University
Allahabad U.P.</p> | | |

- | | | |
|---|---|---|
| <p>11. Prof. B. R. Nag
Indian,
Institute of Radiophysics
& Electronics University
College of Technology
92, Acharya Prafulla Ch.
Road
Calcutta-700009</p> | <p>13. Dr. T. Pradhan
Indian
Director, Institute of
Physics
A/105 Saheed Nagar
Bhubaneswar Orissa</p> | <p>15. Dr. R. Ramanna
Indian,
Scientific Advisor to the
Minister of Defence
Central Secretariate
South Block
New Delhi</p> |
| <p>12. Dr. B. D. Nagchaudhuri
Indian,
8, Tughlag Road
Delhi-11</p> | <p>14. Prof. G. N. Ramachandran
Indian
Institute Professor of
Biophysics Indian
Institute of Science
Molecular Biophysics
Unit
Bangalore-560012</p> | <p>16. Prof. U. R. Rao
Indian,
Indian Scientific Satellite
Project
A 1-6 Peenya Industrial
Estate
Peenya 562140
Bangalore</p> |
| <p>17. Prof. P. Venkateswarlu
Indian
Department of Phys/cs
Indian Institute of
Technology
Kanpur-16 U.P.</p> | <p>18. Prof. A. K. Barua
Indian,
(Hon.) Secretary,
Board of Editors
Indian Journal of Physics
Indian Association for
the Cultivation of
Science,
2 & 3, Raja Subodh
Mullick Road
Calcutta-700032.</p> | |

Name and address of individuals who own the newspaper and partners or shareholders holding more than one per cent of the total capital.

Indian Association for the Cultivation of Science 2 & 3, Raja Subodh Mallick Road Jadavpur, Calcutta-700032.

I, Sri Mahadev Kumar Ghosh, hereby declare that the particulars given above are true to the best of my knowledge and belief.

Dated : 20.2.79

Sd/- M. K. GHOSH
Signature of Publisher

Three body problem for hyperbolic and Coulomb potentials

S. S. Raghuwanshi and L. K. Sharma

Department of Applied Physics, Govt. Engineering College, Jabalpur-482 011.

Received 25 May 1976, revised 26 May 1977.

The method proposed by Eyges (1961) for finding ground state eigen values, and eigen functions for a system of three identical particles between any pair of which there is an attractive interaction does not provide accurate solution for hyperbolic and coulomb potential functions. However, it has been shown that Eyges method gives sufficiently satisfactory solutions not only for a single exponential potential but even for a more general exponential potential, thereby showing that his method fits in well for the exponential type of potentials.

1. Introduction

Eyges (1961) has proposed an approximate method which has an explicit advantage over the variational method that in the former one can estimate the errors of the approximations that it is necessary to make. Eyges considered the quantum mechanical problem of finding the ground state energy-eigen values and eigen functions for a system of three identical particles in which identical attractive forces act between each pair. The method was tested for a simplest exponential potential satisfactorily. Further, Eyges claimed that more complicated problems could also be solved along similar lines. From the graph between $g(k)$ and (k) , Eyges drew a conclusion that first iterate which is closer to the zeroth order iterate could be taken as approximate value of the function.

The object of this note is to contradict the claim made by Eyges that proceeding along similar lines more complicated problems could be solved. This is shown by taking specifically hyperbolic potential functions which have already been solved completely by Sharma (1970) and Coulomb potential. It has been shown that by applying Eyges technique the accuracy actually diminishes for such types of potentials. It has however, been shown that Eyges method gives satisfactory results not only for a single exponential potential but for the triple exponential potentials also. In actuality the first iterate for hyperbolic and Coulomb potentials do not lie as nearer the zeroth order iterate as that for the simplest exponential potential solved by Eyges.

2. Basic Equations

Eyges (1961) has given following expressions for the solution of the Schrodinger wave equation and found for the first iterate of wave function :

$$\phi_0^{(1)} = \frac{1}{(k^2 + K^2 + 3/4\kappa^2)} \left[f(k, \kappa) + \sum_{l=0}^{\infty} \sum_{m=0}^{\infty} (2l+1) F_{lm}(k, \kappa) \right] \quad (1)$$

As the contributions of the higher F_{lm} to the series for $\phi_0^{(1)}$ fall off rapidly with l and m and thus an approximation of truncating the series is made keeping only F_{00} and F_{11} . With this approximation and for $m, l = 0$, equation (1) takes the form :

$$\phi_0^{(1)} = \frac{1}{(k^2 + 3/4\kappa^2 + K^2)} \left[f(k, \kappa) + F_{00}(k, \kappa) \right] \quad (2)$$

Eyges proposed a test for his method by introducing another function $g(k)$ which he defined as follows :

$$g(k) = \left[1 + 2 \frac{\phi_0(\frac{1}{2}k, k)}{\phi_0(k, 0)} \right]^{1/2} \quad (3)$$

Further $g(k)$ was plotted against k . Hence for different values of parameter ' K ' graphs between $g(k)$ and k were obtained.

3. Hyperbolic Potential

Now we apply Eyges (1961) method to following hyperbolic potential function

$$V(r) = -V_0 \cosh(\alpha r). \quad (4)$$

Following Gradshteyn and Ryzhik (1965) and Morse and Feshbach (1953) we get

$$f(k, \kappa) = -\left(\frac{\pi^2 V_0}{\alpha^2}\right) \left[\frac{4\beta}{\rho^2 - 4\beta^2} \right] \quad (5)$$

$$F_{00}(k, \kappa) = \left(\frac{\pi^2 V_0}{\alpha^2}\right) \left(\frac{1}{3k_0\kappa_0}\right)$$

$$\log \frac{[(\alpha+1)^2 + (k_0 + 3/2K_0)^2][(\alpha-1)^2 + (k_0 - 3/2K_0)^2]}{[(\alpha+1)^2 + (k_0 - 3/2K_0)^2][(\alpha-1)^2 + (k_0 + 3/2K_0)^2]} \quad (6)$$

Utilizing above values of $f(k_1\kappa)$ and $F_{00}(k_1\kappa)$ one gets the following value of $g(k)$ for the potential given in eq. (4)

$$g(k) = \left[1 + \frac{[(K_0^2 + 3/4k_0^2)K_0\{(k_0^2 + K_0^2 + 1)^2 - 4K_0^2\}]}{(K_0^2 + 3k_0^2)[(K_0^2 + k_0^2 + 1)^2 - (K_0^2 + 3/4k_0^2)]} \right. \\ \left. - \frac{K_0[(k_0^2 + K_0^2 + 1)^2 - 4K_0^2] \ln \frac{[(\alpha+1)^2 + (7/4k_0)^2][(\alpha-1)^2 + (5/4k_0)^2]}{[(\alpha+1)^2 + (5/4k_0)^2][(\alpha-1)^2 + (7/4k_0)^2]}}{6(K_0^2 + 3k_0^2)k_0^2} \right]^{1/2} \quad (7)$$

It may be of interest to note that a similar expression with only parametric difference can be obtained for $g(k)$ for the potential $V(r) = -V_0 \sinh(\alpha r)$.

For testing the accuracy of the Eyges method on the hyperbolic potential function $V(r) = -V_0 \cosh(\alpha r)$, a graph between $g(k)$ and k is plotted. The following table gives the values of $g(k)$ for different values of K_0 , and k_0 .

Table 1.

k_0	$K_0 = 1$	$K_0 = 2$	$K_0 = 4$
	$g(k)$	$g(k)$	$g(k)$
0	1.000	1.850	4.300
1	1.795	2.138	2.910
2	1.730	9.940	2.390
4	1.300	1.114	1.670

In figure 1, the function $g(k)$ has been plotted. We find that for a given K_0 , the first order iterate is a function which in general first rises from its value at the origin and for $K_0 = 2$ and $K_0 = 4$, these iterates cut the zeroth order iterate in two points separately. Further, first order iterate for $K_0 = 2$ also rises but more sharply than the first order iterates for $K_0 = 1$ and $K_0 = 0.5$, then drops suddenly and cuts the zeroth order iterate in a point C.

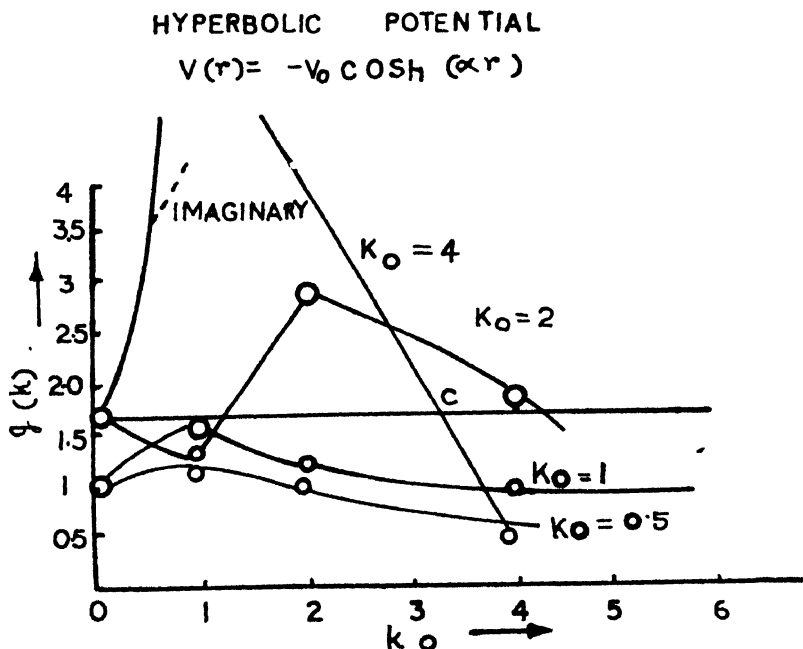


Figure 1. The curves give $g_{hyp}(k)$ as evaluated from the first iterate and its dependence on k_0 for different values of K_0 .

4. Coulomb Potential

Next we consider the coulomb potential

$$V(r) = A/r. \quad (8)$$

Proceeding on similar lines one obtains the following value of $g(k)$ for this type of potential

$$g(k) = \left[1 + 2 \frac{\{(16K^2 + 61k^2)^{\frac{1}{2}} - 4(K^2 + k^2)^{\frac{1}{2}}\} \{(4K^2 + 13k^2)^{\frac{1}{2}}\}}{\{(4K^2 + 13k^2)^{\frac{1}{2}} - 2(K^2 + k^2)^{\frac{1}{2}}\} \{(16K^2 + 61k^2)^{\frac{1}{2}}\}} \right]^{1/2} \quad (9)$$

values of $g(k)$ for different values of K and k have been shown in Table 2.

Table 2.

k	For $K = 1$	For $K = 2$
	$g(k)$	$g(k)$
0	$\sqrt{3}$	$\sqrt{3}$
1	1.67	1.74
2	1.73	1.70
3	1.72	1.64
4	1.74	1.68

In figure 2, a plot between $g(k)$ and k is given which shows that :

(1) Graphs for $K = 1$ and $K = 2$ lie on either sides of the zeroth iterate.

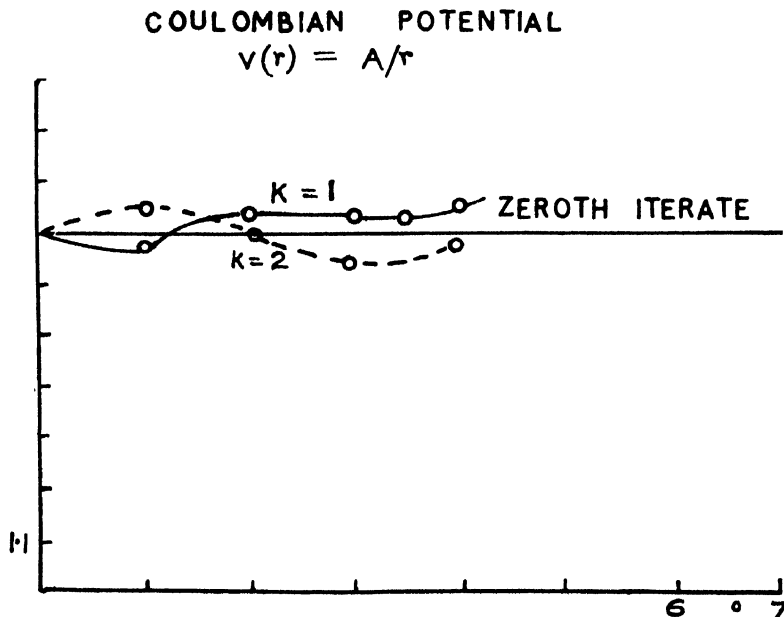


Figure 2. The curves for $g_{\text{coul}}(k)$ as evaluated from the first iterate.

(b) In both graphs maximum and minimas are found which are of course not observed in case of corresponding graphs for exponential potential.

(c) The curves are found to intersect with each other. This intersection of various iterates is also observed in the case of hyperbolic potentials.

5. Triple Exponential Potential

Here we show that Eyges (1961) method gives accurater esults not only for single exponential potential but for a general exponential potential as well. For showing this we take the following triple exponential potential

$$V(r) = Be^{-2\alpha r} + Ce^{-3\alpha r} + De^{-4\alpha r}. \quad (10)$$

The above mentioned potential has already been solved exactly by Sharma (1971).

The value of $g(k)$ for this potential is given as :

$$g(k) = \left[1 + \frac{2}{3} \{ k_0^2 + (1 + K_0)^2 \} \left\{ \frac{1}{1/4k_0^2 + \{1 + \beta(\kappa_0)\}^2} + \right. \right. \\ \left. \left. + \frac{4}{3k_0^2} \ln \frac{\{1 + \alpha(\kappa_0)\}^2 + 4k_0^2}{\{1 + \alpha(\kappa_0)\}^2 + k_0^2} \right\} \right] \quad (11)$$

In figure 3, a graph between $g(k)$ and k_0 for different K_0 has been plotted. This graph resembles exactly the graph for single exponential potential and

EXPONENTIAL POTENTIAL

$$V = - (Be^{-2\alpha r} + Ce^{-3\alpha r} + De^{-4\alpha r}) = Ee^{-r/d}$$

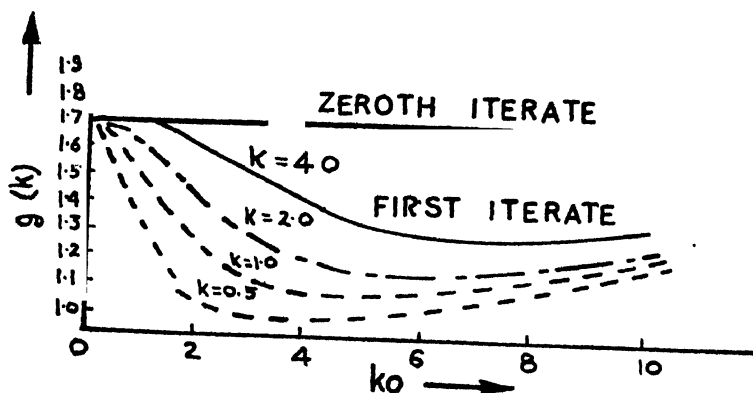


Figure 3. Function $g_{exp}(k)$ as evaluated from the first iterate.

thus arguing on the lines of Eyges one can infer that this method fits in very well for generalized exponential potentials.

On comparing the graphs for the exponential hyperbolic and Coulomb potentials figures 1, 2 and 3, we find that for hyperbolic and coulomb potential, the curves do not satisfy the conditions swchich exist for the exponential type of potentials i.e., the curves for the latter potential for first order iterates and for different values of parameter K_0 start from $g(k) = \sqrt{3}$ and then gradually recede. However, in the case of hyperbolic and coluomb potentials, first iterates do not start from the same point for $k_0 = 0$. Further, the shape of the curves do not have the same form and moreover they intersect with each other and also all the first order iterates are found to intersect with the zeroth order iterate with a peculiarity that for the hyperbolic potential the iterate for $K_0 = 2$ cuts the zeroth order iterate at two points. Eyges (1961) has discussed and justified existence of all I order iterates for $g(k)$ lying between 0 and $\sqrt{3}$ for the three body problem. As this conclusion is not observed for hyperbolic and coulomb potentials, thus it can be inferred that the claim made by Eyges that this method could be applied to more complicated potentials could not be held valid for the potentials considered by us in this paper.

Acknowledgment

One of the authors (S.S R.) is indebted to the Council of Scientific and Industrial Research for the award of a research Fellowship.

References

- Eyges L 1961 *Phys. Rev.* **121**, 1744
 Gradshteyn I S Ryzhik I M 1965 *Tables of Integrals, Series and Products*, Academic Press, N.Y.
 Morse P M and Feshbach H 1953 *Methods of Theoretical Physics*, Vol. I, McGraw Hill Book Co., N.Y.
 Sharma L K 1970 *Proc. Indian Nat. Sci. Acad.* **36A**, 23
 Sharma L K 1971 *Indian J. Phys.* **45**, 1

Direct measuring method of the anisotropic collisions

E. Chamoun and R. Abou-Chagra

Faculty of Science, Hadeth, Beirut, Lebanon.

Received 30 September 1977, revised 8 March 1978.

Abstract. We propose a simple model for the study of anisotropy. It is found that the analysis of the anisotropy can be made by a direct examination of the alignment signal. Experimentally, a HeI target was excited by a beam of Na^+ ions, and a rate of anisotropy was found to be 4%.

1. Introduction

The study of collisions between excited atoms and atoms in the ground states, is done in the case of statistically isotropic collisions in space, (Omont 1965). The existence of a privileged direction of collisions led to the work of Chamoun *et al* (1977) on new phenomena related to the anisotropic collisions. Their work was achieved without knowing the rate of anisotropy which meant an unpredictable order of magnitude of the signals expected from secondary effects. Hence the importance of the rate of anisotropy especially as we are generally dealing with very small signals.

We propose to show here the existence of the anisotropy by a direct study of its effect on the aligning signal. This kind of study is easy to achieve in many cases of collisions as it only uses simple geometrical considerations. Thus we study the Hanle effect (Hanle 1926), of the linear signal corresponding to different directions of detection and external magnetic field, in terms of the average relaxation coefficients of the density matrix. By a comparison of the Hanle curves with some experimental data we detect the rate of anisotropy.

2. Theoretical Calculation

We detected the linearly polarised light emitted by the relaxing level in the 0_x direction (Figure 1) and whose polarisation direction is parallel ($I_{||}$), normal (I_{\perp}), or at $\pm 45^\circ$ from the 0_z axis. This was done in the presence of two static magnetic fields, H_x along 0_x and H_z along 0_z .

We developed the density matrix of the excited state over a basis of irreducible tensors T_q^k , Fano (1959), and we neglect the coupling alignment-orientation

terms as well as the coupling terms with higher order tensors. Thus the collision leads to the evolution of the density matrix

$$\left\{ \frac{d\rho_q^2}{dt} \right\}_{coll} = -\Gamma_q^2 \rho_q^2 \text{ with } \Gamma_q^2 (q = 0, 1, 2)$$

= average relaxation coefficients of the density matrix.

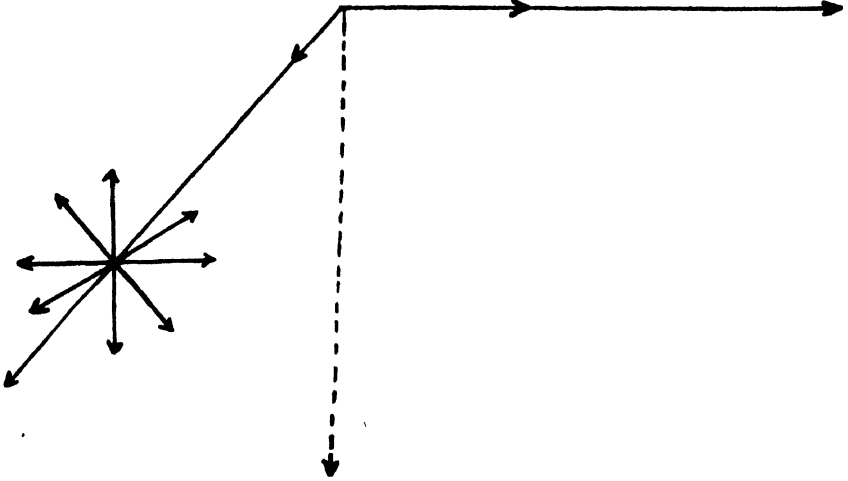


Figure 1. A scheme showing the detection direction with respect to the magnetic field, for different polarisation directions.

The variation of the total density matrix is

$$\frac{d\rho_q^k}{dt} - \gamma\rho_q^k - i[\mathcal{M}, \rho]_q^k - \Gamma_q^k \rho_q^k \equiv 0$$

with $-\gamma\rho_q^k$ = spontaneous evolution term

$-i[\mathcal{M}, \rho]_q^k$ = evolution term due to the coupling of the excited level with the external magnetic field.

The signal of the rectilinear light is calculated in the tensorial space by the formula of D'yakonov (1965)

$$I_{k',\lambda} = (-)^{j_0+j_1} I_0 \sum_{k=0}^2 \sqrt{2j_1+1} \sqrt{2k+1} \begin{Bmatrix} 1 & 1 & k \\ j_1 & j_1 & j_0 \end{Bmatrix}$$

$$\times \sum_{q=-k}^{+k} (-)^q \rho_q^k \phi_q^k(\mathbf{e}_{k,\lambda})$$

Where $I_{\mathbf{k}', \lambda}$ is the intensity of the emitted light in the direction $\mathbf{k}'(\theta, \phi)$ and polarisation λ . The detailed algebra gives;

$$I_{||} - I_{\perp} = \frac{K[2\omega_x^2\omega_z^2 - \omega_x^2\Gamma_1^2\Gamma_2^2 - (\omega_z^2 + \Gamma_1^2)(4\omega_x^2 + \Gamma_2^2)]}{\Gamma_0^2[4\omega_x^2\omega_z^2 - 2\omega_x^2\Gamma_1^2\Gamma_2^2 - (\omega_z^2 + \Gamma_1^2)(4\omega_x^2 + \Gamma_2^2) - \omega_x^4]}$$

$$\frac{K[2\omega_x^2\omega_z^2 - \omega_x^2\Gamma_1^2\Gamma_2^2 - (\omega_z^2 + \Gamma_1^2)(4\omega_x^2 + \Gamma_2^2)]}{-3\omega_x^2[\Gamma_2^2(\Gamma_1^2\Gamma_2^2 + \omega_x^2) + 4\omega_x^2\Gamma_1^2]}$$

and

$$I_{45} - I_{-45} = \frac{2K\omega_x[\Gamma_2^2\omega_x^2 + \Gamma_1^2(4\omega_x^2 + \Gamma_2^2)]}{\Gamma_0^2[4\omega_x^2\omega_z^2 - 2\omega_x^2\Gamma_1^2\Gamma_2^2 - (\omega_z^2 + \Gamma_1^2)(4\omega_x^2 + \Gamma_2^2) - \omega_x^4]}$$

$$\frac{2K\omega_x[\Gamma_2^2\omega_x^2 + \Gamma_1^2(4\omega_x^2 + \Gamma_2^2)]}{-3\omega_x^2[\Gamma_2^2(\omega_x^2 + \Gamma_1^2\Gamma_2^2) + 4\Gamma_1^2\omega_x^2]}$$

with

$$K = I_0 \begin{Bmatrix} 1 & 1 & 2 \\ 1 & 1 & 0 \end{Bmatrix} \sqrt{6} \rho_0(0)2$$

$\rho_0(0)^2$ = term of the density matrix of the linear excitation

$$\omega_x = \mu_B g_J H_x,$$

$$\omega_z = \mu_B g_J H_z$$

μ_B = Bohr magneton,

g_J = Landé factor.

Let us consider two cases

a) $H_z = 0$, H_x = sweeping magnetic field.

The plot of $I_{||} - I_{\perp}$ in terms of H_x gives an absorption Hanle curve of amplitude $A_1 = \frac{K}{\Gamma^2}$ and of width $\Delta = 2 \sqrt{\frac{\Gamma_0^2 \Gamma_1^2 \Gamma_2^2}{\Gamma_0^2 + 3\Gamma_2^2}}$. Similarly $I_{45} - I_{-45}$ gives a dispersion Hanle curve of amplitude $A_2 = \frac{2K}{\Gamma_0^2 \Gamma_1^2} \sqrt{\frac{\Gamma_0^2 \Gamma_1^2 \Gamma_2^2}{\Gamma_0^2 + 3\Gamma_2^2}}$ and of width $\Delta = 2 \sqrt{\frac{\Gamma_0^2 \Gamma_1^2 \Gamma_2^2}{\Gamma_0^2 + 3\Gamma_2^2}}$.

We check that in the case of isotropic collisions, $\Gamma_1^2 = \Gamma_0^2 = \Gamma_2^2 = \Gamma$, the two curves have the same amplitude $A_1 = A_2 = K/\Gamma$ and the same width $\Delta = \Gamma$ as it ought to be.

This leads to a method of checking the existence of the anisotropy by comparison of the amplitudes of these two curves :

$$R = \frac{A_2}{A_1} = \frac{2}{\Gamma_1^2} \sqrt{\frac{\Gamma_0^2 \Gamma_1^2 \Gamma_2^2}{\Gamma_0^2 + 3\Gamma_2^2}}$$

If this ratio R (equal to 1 in the case of isotropy) is different from 1 in the case under consideration, it implies the existence of anisotropy. This simple method is not very meaningful, it only indicates the existence of an anisotropy. Furthermore it can be sometimes misleading because the relaxation coefficient may be different but divided up in such a way that $R = 1$. Experimentally, we need for this method a high stability of the experimental parameters. For these reasons we shall consider the following case.

b) We fix H_z as a parameter and vary H_x , we get for $I_{||}-I_{\perp}$ and $I_{45}-I_{-45}$ as functions of H_x (or ω_x), two curves similar to those of Brossel and Bittor (1952). These curves possess double bumps for large values of H_x and they correspond, in a fixed frame reference, to what we get in a rotating frame for the resonance experiment. For this reason we shall call these curves the pseudo-Brossel curves and denote $I_{||}-I_{\perp}$ by B_{90} and $I_{45}-I_{-45}$ by B_{45} . Then we have solved numerically the root equations of B_{90} and B_{45} , which allowed us to deduce the half-width of these curves which we have denoted by $\Gamma_{B_{90}}$ and $\Gamma_{B_{45}}$. On a reduced scale graph we plotted

$$\left[\frac{\Gamma_{B_{90}}}{\Delta} \right]^2 \text{ and } \left[\frac{\Gamma_{B_{45}}}{\Delta} \right]^2 \text{ in terms of } \left[\frac{H_x}{\Delta} \right]^2$$

(Figure 2), where Δ is the width of the Hanle curve in the case (a). This plotting was done in two theoretical cases : firstly, the isotropic case, $\Gamma_0^2 = \Gamma_1^2 = \Gamma_2^2 = \Gamma$,

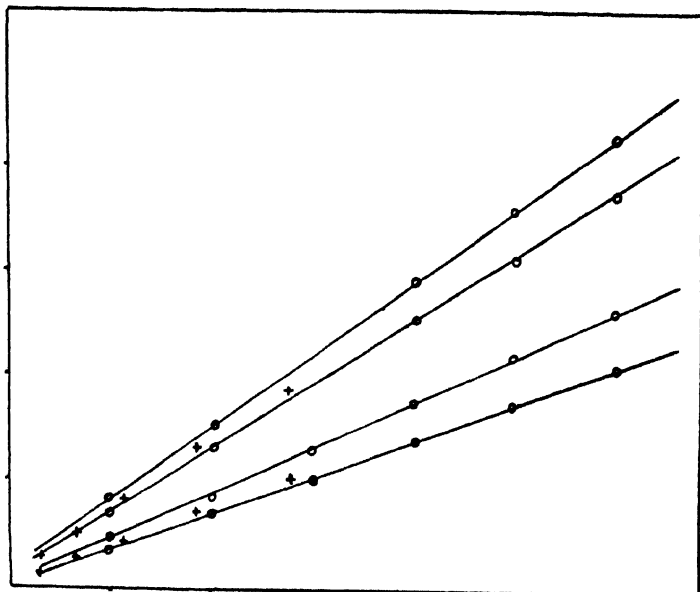


Figure 2. Numerical curves (1) B_{90} isotropic, (2) B_{90} anisotropic \perp Van Der Waals, (3) B_{45} isotropic, (4) B_{45} anisotropic \perp Van Der Waals. + experimental points.

with $\Delta = \text{Hanle width} = \Gamma$ (lines (1) and (3) in Figure 2; secondly the ideal anisotropic case where we have assumed that the anisotropy direction is along O_y , and the interaction of an excited atomic level with an atom in the ground state is of the van Der Waals type (lines (2) and (4) in Figure 2). in the later case

$$\Gamma_0^2 = 0.61, \Gamma_1^2 = \Gamma_2^2 = 0.78, \text{ and } \Delta = 2\sqrt{\frac{L_0^2 \Gamma_1^2 \Gamma_2^2}{\Gamma_0^2 + 3\Gamma_2^2}} = 0.79, \text{ (Lombardi 1969).}$$

3. Experimental

Experimentally, we have excited a target of HeI enclosed into a cell at a pressure $P_{He} = 1.17 \cdot 10^{-1}$ Torr, by an accelerated beam of ions Na^+ (Sames at 70KeV). The beam excites the target atoms and get excited itself. The atoms of the target recoil under the effect of the shock in a plane almost perpendicular to the direction of the beam; and these atoms relax by collision with other atoms

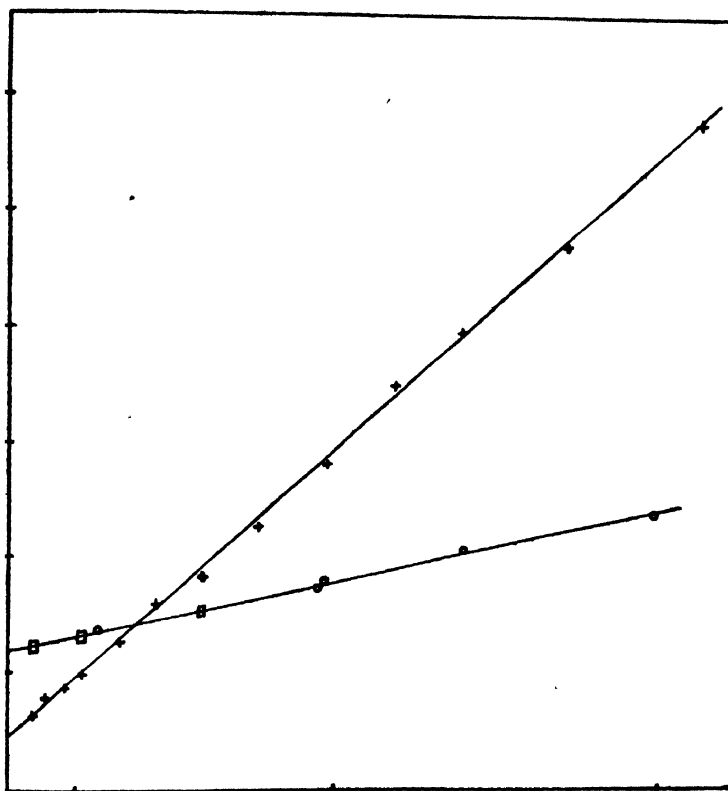


Figure 3. Width of the level as a function of the pressure of HeI for $\lambda = 4922 \text{ \AA}$.

- (1) \square High frequency discharge, 0 electronic bombardment with $\tau = 3.12 \cdot 10^{-8}$ sec. (lifetime of the excited level)
- (2) $+Na^+ \rightarrow HeI$ (70 keV) $\therefore \langle v \rangle_{\text{recoil}} = 4.26 \langle v \rangle_{\text{thermal}}$.

of HeI (into the cell in the ground state; by doing so they emit a linearly polarised light. The study was done on the ray 4922\AA (level 4^1D_2 of HeI) for which we found the collision cross section about four times greater than the electronic cross section by comparison of the slopes of lines (1) and (2) in Figure 3.

For the transverse magnetic field H_x , we have included the earth field component H_e (the other components were compensated by special directed coils which was measured to be $H_{er} = 0.23$ gauss. The Hanle-width Δ was found to be 9.82 gauss and the result were stocked in a multi-channel (16 cycles with 1 cycle = 100 sec.).

Figure 4 shows the experimental curves B_{45} and B_{90} for different values of the transverse magnetic field.

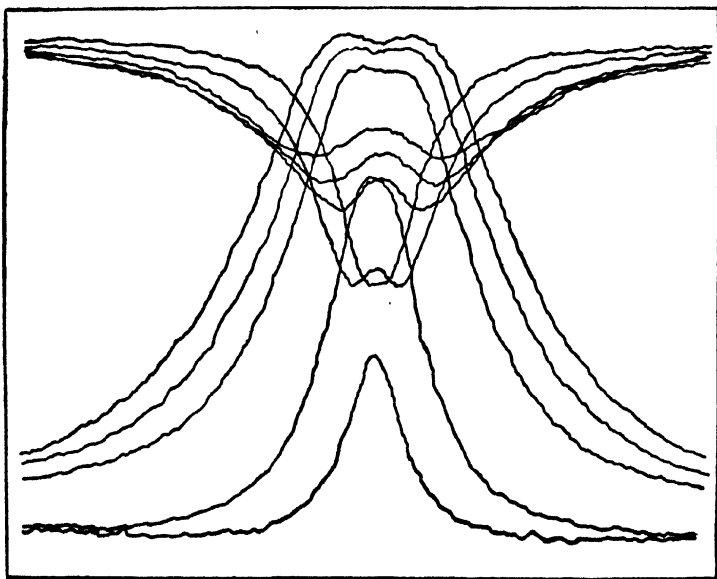


Figure 4. Experimental pseudo-Brossel curves B_{45} and B_{90} for

- | | |
|--------------------------|--------------------------|
| (1) $H_x = 2.72$ gauss, | (2) $H_x = 5.45$ gauss, |
| (3) $H_x = 10.88$ gauss, | (4) $H_x = 13.62$ gauss, |
| (5) $H_x = 16.36$ gauss. | |

Consequently we have fitted the experimental curves by Brossel curves of the form $\frac{a+bx^2}{1+cx^2+dx^4}$. Thus we have deduced numerically the values of $\Gamma_{B_{90}}$ and $\Gamma_{B_{45}}$ and we have plotted, on the same graph of reduced scale, $\left[\frac{\Gamma_{B_{90}}}{\Delta}\right]_{exp}$ and $\left[\frac{\Gamma_{B_{45}}}{\Delta}\right]_{exp}$ in terms of $\left[\frac{H_x}{\Delta}\right]^2$; these values are indicated by (+) on (Figure 2), and by comparison of the experimental with the theoretical results of (Figure 2)

we notice that in this experiment a collision anisotropy is present and is evaluated to 4% of the ideal anisotropy.

4. Discussion

This work is done here in a particular case of beam and target. However, it has a much wider range of application. Furthermore, the case studied here is not ideal because, for the level 4^1D_2 of Helium, the collisions He^*-He are not van Der Waals collisions at long distances. This point is checked by a comparison of the collisions cross section with the radial wave function of the $4d$ electron of the atom HeI (Figure 5). Thus, collisions between He^* and other rare gases would give an experimental curve closer to the theoretical one, Van Der Waals, and consequently a higher rate of anisotropy which corresponds better to the reality.

A further advantage of this method is that it can be used to match certain experimental curves with previously worked theoretical curves for a given interaction potential, which throws some light on the kind of interaction, yet unknown.

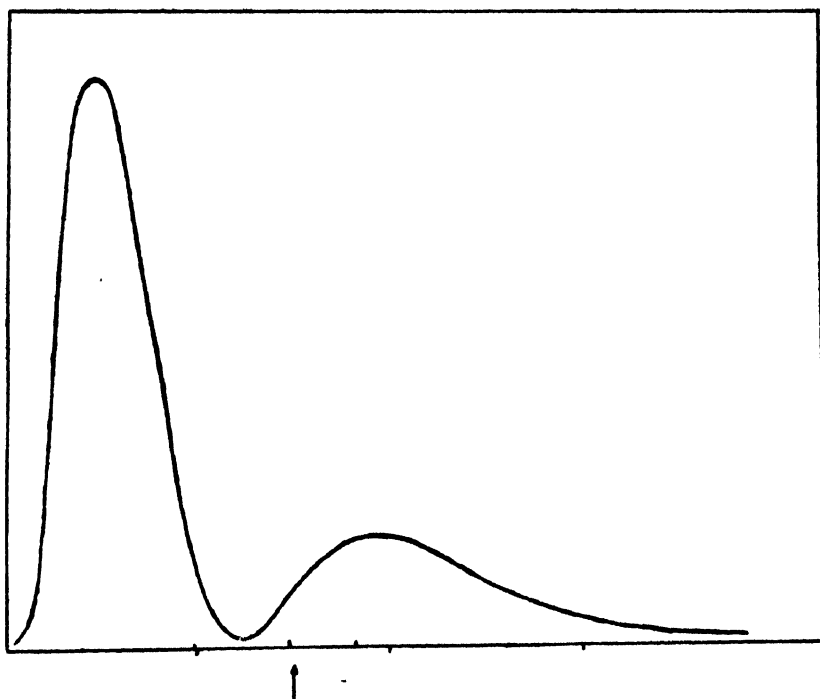


Figure 5. The radial wavefunction $|\psi|^2$ of the electron $4d$ in the HeI atom. The vertical scale is arbitrary. The horizontal axis contains two scales: the lower one is taken in units of a_0 , and the upper one is the cross-section.

References

- Brossel J and Bitter F 1952 *Phys. Rev.* **80**, 308.
Chamoun E, Lombardi M, Carré M. and Gaillard M L 1977 *J. de Physique* **38**, 591.
D'yakonov M I 1965 *Sov. Phys. JETP* **20**, 1484.
Fano U and Racah G 1959 *Irreducible tensorial sets*, Academic Press, N. York.
Hanle W 1926 & *Phys.* **35**, 346.
Lombardi M 1969 *These de Doctoratèes Sciences Grenoble*, France.
Omont A, 1965 *J. de Phys.* **26**, 26.

Nonlinear Poynting flux for a gravitating magnetised plasma and radio emission from astrophysical bodies

R Bondyopadhaya

Department of Mathematics, Jadavpur University, Calcutta-700 032

and

S K Chandra

Department of Mathematics K. C. College, P.O. Hetampur
Birbhum, West Bengal-731129

Received 7 March 1977, revised 2 December 1977

Abstract. Perturbation method of Lindstedt has been applied to obtain the amplitude dependent Poynting flux of first order and second order approximations of a transverse wave in a magnetised and gravitating plasma fluid medium. It is observed that the effect of gravitation, pressure and external magnetic field are present in the second order approximation and not in the first order. At a large distance from the centre of the spherical system, the flux will flow along the radial direction only. It has been suggested that the second order Poynting flux may be the mechanism for radio emission from radio sources like radio source in the jet of M87 galaxy.

1. Introduction

Poynting flux is a very important aspect of any plasma medium. Several authors (Field 1956, Erickson and Cronyn 1965, Bondyopadhaya 1976, Chakraborty 1973, etc.) have derived the expressions for it for different media. In the present paper, we have considered the nonlinear wave propagation in a magnetised plasma under the influence of gravitation and pressure, and have found out the average Poynting flux upto the second order of approximations. We have used spherical polar co-ordinates because it could be very useful in many astrophysical problems. It is observed that the effects of gravitation, pressure and the external magnetic field are present not in the first order but in the second order approximations (may be in all other orders greater than two). At a large distances from the centre ($r \rightarrow \infty$), it is observed that the Poynting flux moves along the radial directions only, in both the order of approximations and in such case if the external magnetic field is negligible, there will be no flow of energy in any of the directions. However, the method used to find out the field components is a multiple-scale method, namely Lindstedt method (Minorsky 1969, Chandra and Bondyopadhaya 1974, etc.)

The possible applications of the theory of Poynting flux in astrophysical context has been discussed by a number of authors (Field 1956, Bondyopadhaya 1976, etc.). In the present, the most interesting part is the occurrence of magnetic field in the second order approximation which opens up the great possibility of emission of radio flux from highly magneto-active plasma body e.g. hot regions in the galaxy, radio-sources, etc.

2. Basic equations

Let us consider one electron component weakly relativistic plasma fluid under the influence of gravitation and external magnetic field. We assume that the medium is at rest equilibrium before perturbation and the collisional phenomenon is negligible. For convenience we introduce the spherical polar co-ordinate. We express the energy momentum equation as

$$\left(\frac{\partial}{\partial t} + \mathbf{v} \cdot \nabla\right) \frac{\mathbf{v}}{\left(1 - \frac{v^2}{c^2}\right)^{\frac{1}{2}}} + \frac{e\mathbf{E}}{m} + \frac{1}{\rho} \Delta p + \frac{e}{mc} [\mathbf{v} \times \mathbf{H}] + \text{grad } \phi = 0 \quad (1)$$

Together with this we have the usual equation of continuity, the Maxwell's equations and the Poisson's equation

$$\begin{aligned} \frac{\partial n}{\partial t} + \text{div}(n\mathbf{v}) &= 0 \\ \text{curl } \mathbf{H} &= \frac{1}{c} \frac{\partial \mathbf{E}}{\partial t} - \frac{4\pi en\mathbf{v}}{c} \\ \text{curl } \mathbf{E} &= -\frac{1}{c} \frac{\partial \mathbf{H}}{\partial t} \\ \text{div } \mathbf{E} &= -4\pi(n - n_0) \\ \text{div } \mathbf{H} &= 0 \\ \nabla^2 \phi &= 4\pi G \rho_t \end{aligned} \quad (2)$$

where $\rho_t = \beta\rho$, ρ_t is the average total density, β is a constant, G is the gravitational constant, ϕ is the gravitational potential, n is the electron density after perturbation, n_0 is the uniform background ion density, \mathbf{v} is the electron velocity, \mathbf{E} and \mathbf{H} are the electric and magnetic field intensities and c is the velocity of light.

3. Perturbation

Let us define the perturbation in the form

$$\mathbf{F} = \sum_i e^i \mathbf{F}_i(a, \psi) \quad (3)$$

where F may represent and field variables E or H or v or n or p or ρ ($=mn$). We further consider the situation where unperturbed velocity or electric field does not exist. We also take the equation of state as

$$p = 3nXT = mV_e^2 n \quad (3.1)$$

and in our problem 'only one degree of freedom' is excited by the field so, $V_e^2 = \frac{3XT}{m}$ where V_e is the root mean square electron's velocity, X is the Boltzmann constant, p_0 , H_0 are pressure and magnetic field before perturbation and H_0 acts along the azimuthal direction of the spherical polar co-ordinates, a is the amplitude of electric and ψ is the phase.

In general, the variables in the eqn. (3) having ϵ as co-efficients are functions of space and time. If we use eq. (3) in eqs. (1) and (2), we get nonlinear equations containing secular terms which grow up indefinitely when $t \rightarrow \infty$ and thus destroy the convergence of the series. Our aim in this paper is to deal with stable configuration, and hence definitely to convergent perturbation. Therefore, what we have to do is to eliminate the secular terms. In fact, the elimination of secular terms in each step of the approximation rendered the perturbation method a practical tool in the actual computation of successive approximations. The method of Lindstedt is particularly suitable for our purpose which has been used in plasma medium by Chandra (1974), Chandra and Bandyopadhyaya (1974). In essence the method we are going to consider is the initial value problem and the basic principle of this method is to express time variable in power series as

$$t + \lambda = s \left(1 + \sum_{i=1} \epsilon^i \alpha_i \right) \quad (4)$$

where λ is independent of time but adjusts the phase and α_i 's are dimensionless constants in space and time, such that $\alpha_n < \alpha_{n+1}$. These constants will be so chosen that the terms yielding secular behaviour after integration could be removed. One may note that in relation (4) the time scale t has been replaced by the series of time scale s , $\alpha_1 s$, $\alpha_2 s$, However, evidently the time derivatives are given by

$$\frac{\partial r}{\partial t} = \frac{1}{(1 + \epsilon \alpha_1 + \epsilon^2 \alpha_2 + \dots)^r} \frac{\partial r}{\partial s}, \quad (r = 1, 2, \dots) \quad (5)$$

4.1. First order approximation of Poynting flux

Let the solution of the first order approximation of the electric vector propagating along the cross-radial direction be

$$E_{1\theta} = a \cos \psi \quad (6)$$

where $\psi = kr - \omega s$ and a is real constant. This assumption does not reduce the generality of the analysis because, physically such harmonic solution does exist. By using eq. (3) in the eqs. (1) and (2), the other components of the field vectors in the first order approximation have been found to be the following

$$v_{1r} = -\frac{\Omega_0 e a \cos \psi}{m(\omega^2 - \omega_p^2 - \Omega_0^2)}, \quad v_{1\theta} = \frac{ea(\omega^2 - \omega_p^2) \sin \psi}{m\omega(\omega^2 - \omega_p^2 - \Omega_0^2)}, \quad v_{1\phi} = 0$$

$$E_{1r} = \frac{\Omega_0 a \omega_p^2 \sin \psi}{\omega(\omega^2 - \omega_p^2 - \Omega_0^2)}, \quad E_{1\theta} = 0$$

$$H_{1r} = 0, \quad H_{1\theta} = 0, \quad H_{1\phi} = \frac{ea}{r\omega} \sin \psi + \frac{cak}{\omega} \cos \psi$$

$$n_1 = 0 \text{ and } p_1 = 0 \quad (7)$$

where $\omega_p = (4\pi e^2 n_0 / m)^{1/2}$ is the plasma frequency, and $\Omega_0 (= eH_0 / mc)$ is the gyro frequency.

Now the Poynting flux associated with these fields is given by

$$S = \frac{c}{4\pi} [\text{Re } \mathbf{E} \times \text{Re } \mathbf{H}] \text{ ergs cm}^{-1} \text{ sec}^{-1} \quad (8)$$

Using the eq. (7), the first order approximation of the energy flux along the three mutually perpendicular directions comes out to be

$$\begin{aligned} \langle S_{1r} \rangle &= (c^2/8\pi)(k/\omega)a^2 \\ \langle S_{1\theta} \rangle &= -(ce^3/2m)(n_0/\omega^2)(\Omega_0/r)(\omega^2 - \omega_p^2 - \Omega_0^2)^{-1}a^2 \\ \langle S_{1\phi} \rangle &= 0 \end{aligned} \quad (9)$$

where $\langle \rangle$ stands for average over time period $2\pi/\omega$.

We observe that in the absence of any external magnetic field (H_0) or at a great distance from the central region of the medium ($r \rightarrow \infty$) the flow of energy occurs only along the direction of wave propagation and this is independent of magnetic field and density of the medium. Further, the effect of gravitation and the pressure are not present in this linear approximation.

4.2. Second order approximation of the Poynting flux

The equations of second order approximations must involve second harmonic terms only, and hence α_1 must be zero, otherwise it would give rise to the secular solution. But even then, derivation for the second order approximation of the field variables, appears to be very much laborious as well as complicated. For

simplicity, let us concentrate our attention to the phenomenon occurred at a large distance from the centre so that we can have $r \rightarrow \infty$. Then safely we can take

$$V_e^2 \left(\frac{\partial^2}{\partial r^2} + \frac{2}{r} \frac{\partial}{\partial r} - \frac{2}{r^2} \right) \simeq V_e^2 \frac{\partial^2}{\partial r^2} \quad (10)$$

Consequently, the solutions of the second order approximation reduces, by using eqs. (1), (2) and (3), to

$$\begin{aligned} v_{2r} &= -M \cos 2\psi, \quad v_{2\theta} = \frac{Q}{2\omega} \sin 2\psi, \quad v_{2\phi} = 0 \\ E_{2r} &= \frac{m\omega^2 p}{2e\omega} M \sin 2\psi, \quad E_{2\theta} = \frac{m\omega^2 p Q \cos 2\psi}{4e(\omega^2 - c^2 k^2)}, \quad E_{2\phi} = 0 \\ H_{2r} &= 0, \quad H_{2\theta} = 0, \quad H_{2\phi} = \frac{c\omega p^2 m k Q \cos 2\psi}{4\omega e(\omega^2 - c^2 k^2)} \end{aligned} \quad (11)$$

$$n_2 = -n_0(k/\omega)M \cos 2\psi, \quad p_2 = -V_e^2 \rho(k/\omega)M \cos 2\psi$$

where

$$\begin{aligned} M &= 3(e/m)^2 \alpha^2 (k/\omega) (\omega^2 - c^2 k^2) (\omega^2 - \omega_p^2 + \Omega_0^2) (\omega^2 - \omega_p^2 - \Omega_0^2)^{-1} \\ &\quad \cdot [(4\omega^2 - \omega_p^2 + \omega_g^2 - 4V_e^2 k^2) (4\omega^2 - 4k^2 c^2 - \omega_p^2) - 4\Omega_0^2 (\omega^2 - k^2 c^2)]^{-1} \\ Q &= 4\Omega_0 (\omega^2 - c^2 k^2) (4\omega^2 - 4c^2 k^2 - \omega_p^2)^{-1} [(e/m)^2 (k/\omega) \alpha^2 (\omega^2 - \omega_p^2 - \Omega_0^2)^{-1} \\ &\quad + M] \end{aligned}$$

and

$$\omega_g^2 = 4\pi G \beta \rho_0$$

Therefore the Poynting flux in the second order approximation is given by

$$\mathbf{S}_2 = (c/4\pi) [\text{Re } \mathbf{E}_2 \times \text{Re } \mathbf{H}_2]$$

or

$$\langle S_{2r} \rangle = (\pi c^3 e^2 / 8) n_0^2 (k/\omega) (\omega^2 - c^2 k^2)^{-2} Q^2$$

$$\langle S_{2\theta} \rangle = 0$$

and

$$\langle S_{2\phi} \rangle = 0 \quad (12)$$

where Q has already been defined.

The following important observations could be made from the above results in eq. (12).

(i) Similar to first order approximation, second order energy flux propagates only along the wave propagation at large distance from the system. This is, however, a well known result.

(ii) The Poynting flux is dependent on both the gravitational potential and the pressure. (Note that their effects were absent in the first order approximation). But, in general, the gravitational effect is not significant because $\omega \gg \omega_g$. Only in certain resonating cases the effect of gravitation could be significant e.g. if $4\omega^2 + \omega_g^2 = \omega_p^2 + 4V_e^2 k^2$.

(iii) The Poynting flux is proportional to the square of the field strength if $\Omega_0 \ll \omega$ and it disappears in the absence of any external magnetic field.

(iv) The relativistic effect is absent even in the second order approximation. Its effect may be found in the field equation of the third order approximation or above (Sluijter and Montgomery 1965).

(v) The Poynting flux depends on the Plasma frequency and hence on the electron density of the medium. If $\omega \gg \omega_p$, the second order approximation of Poynting flux is proportional to the square of the number density. In the first order approximation, however, the Poynting flux, at large distances, independent of number density of the medium. (Eq. 9).

However, to have a handy formula, so that one can use that easily for the explanation of physical phenomena, let us make some assumptions for simplification,

$$\omega \sim ck (\omega \neq ck), \quad \omega \gg \omega_p, \quad \omega \gg \Omega_0, \quad \omega \gg \omega_g, \quad \omega \gg V_e k$$

Then

$$M \sim (\sqrt{3e/4m})^2 (k/\omega^3) a^2$$

$$Q \sim (22/3) \Omega_0 M$$

and hence

$$\begin{aligned} \langle S_{2r} \rangle &\sim 0.15 (c^2 e^2 / 11 m^2) (\omega_p^4 \Omega_0^2 a^4 k^3 / \omega^{11}) \\ &\sim 10^{56} (n_0^2 H_0^2 a^4 / \omega^8) \text{ ergs cm}^{-2} \text{ sec}^{-1}. \end{aligned}$$

5. Application of the theory

A mechanism of Radio Emission from astrophysical radio sources.

The derived expression for Poynting flux indicates that in body where the electron density and magnetic field are weak the first order Poynting flux is much greater than the second order and the first order itself is not very significant. For example, even if we suppose that the electric field intensity a as high as $\sim 3.5 \times 10^{-3}$ e.s.u. (see e.g. Zheleznyakov 1970, p. 594-7), the wave length of the radiation corresponds to short wave ~ 1 meter ($\omega \sim 2 \times 10^8$ c/s), the steady magnetic field is \sim normal magnetic field of sun ~ 1 gauss, and the electron number density \sim electron density in upper coronal region $\sim 10^7$ cm $^{-3}$. Then we have

$$\langle S_{1r} \rangle \sim 1.5 \times 10^4 \text{ ergs cm}^{-2} \text{ sec}^{-1} \sim 3 \times 10^{-7} \text{ L.}$$

$$\langle S_{2r} \rangle \sim 1.42 \times 10^{-14} \text{ ergs cm}^{-2} \text{ sec}^{-1} \sim 2.4 \times 10^{-25} \text{ L.}$$

where

$$L. = \text{flux from sun} = 5 \times 10^{10} \text{ ergs cm}^{-2} \text{ sec}^{-1}.$$

This estimation clearly justifies our statement above. Thus we arrive at the conclusion that, if, at all the Poynting flux from sun's upper coronal region is to be significant, then electric field intensity must be ~ 5 e.s.u. and the first order flux ($< S_{1r} >$) itself will be comparable with the observed luminosity.

But the situation will be quite different in magnetically active and high density region. For example, near photosphere and at the sunspot region $n_0 \sim 10^{13} \text{ cm}^{-3}$ and $H_0 \sim 3 \times 10^3$ gauss (See e.g. Zheleznyakov 1970, Chap. 1) so that

$$< S_{1r} > \sim 1.5 \times 10^5 \text{ ergs cm}^{-2} \text{ sec}^{-1}$$

$$< S_{2r} > \sim 1.1/10^5 \text{ ergs cm}^{-2} \text{ sec}^{-1}$$

The Poynting flux in the second order approximation is now comparable to that in the first order but the flux strength is still not comparable with the observed total flux from Sun.

The significant radio flux could be obtained from the astrophysical bodies which contain very strong magnetic field and high electron density medium (hence which are very active). Radio source, radio galaxies, Quasars (?), Pulsars and other neutron stars may be considered as such entities.

Let us discuss a probable real situation. It is known that there exists a *jet* coming out of the nucleus of the galaxy M87 (NGC4486) which emits strong radio waves. We now see how far the present theory can explain this emission. Before that let us note that this *jet* is in plasma state, polarised (having strong magnetic field), the central region of this galaxy consists of a variable X-ray source and a small radio source, and emits H_α and [OII] lines, the average velocity of gas clouds in the jet is 1066 Km/Sec., the jet has mass $\sim (2.5) \times 10^6 m_\odot$, the energy released is $\sim 3 \times 10^{43}$ ergs/sec. (Shklovskii 1972, Burbidge *et al* 1965). Almost all the authors agree that this jet has been formed due to the explosions of plasma bolb in the nucleus of M87. We may hypothesise that this explosion is somewhat similar process as solar burrrts in the sunspot. A number of justification for this hypothesis could be set although few difficulties are there. But in the present paper we are not concerned with that we only show that sunspot type region in the nucleus of M87 could produce observed radio flux. Let us take the value $a \sim 3.5 \times 10^{-2}$ e.s.u., $n_0 \sim 10^{13} \text{ cm}^{-3}$, $H_0 \sim 3 \times 10^7$ gauss, then

$$< S_{2r} > \sim 1.1 \times 10^{17} \text{ ergs cm}^{-2} \text{ sec}^{-1}$$

$$< S_{1r} > \sim 1.5 \times 10^4 \text{ ergs cm}^{-2} \text{ sec}^{-1}.$$

Now if the source dimension is $\sim 40R_\odot$, then

$$< S_{2r} > \sim 1.1 \times 10^{17} \times 6.28 \times 10^{22} \times (40)^2 \text{ ergs sec}^{-1}$$

$$\sim 10^{-3} \text{ ergs sec}^{-1}$$

which is of the order of radio flux observed from the radio source in M87.

Actually dimension of radio source may be much larger. Therefore with weaker magnetic field also we can obtain the very strong flux. The Quasars ($\sim 10^3 R$), radio flux strength is $\sim 10^{42-45}$ ergs Sec^{-1} (See Lang 1975, p. 573). Thus it is not unlikely that the mechanism of radio emission in Quasars may be second order Poynting flux with significantly strong magnetic field.

A nice example for the application of the theory is Neutron stars (particularly Pulsar)'s radiation. Its plasma density and magnetic field can safely be taken as $\sim 10^{13} \text{ cm}^{-3}$ and $\sim 10^{13}$ gauss at least over some discrete region if not all over the surface where from the radio-energy of strength $\sim 10^{14-17}$ ergs $\text{cm}^{-2} \text{ sec}^{-1}$ radiates (see e.g. Gold 1968, Chieu 1970). The electric field strength required for such flux is $\sim 8 \times 10^{-6}$ e.s.u. only.

This theory, we feel really a good achievement in the sense over the controversy still existing regarding the mechanism of radio emission from sources in Neutron stars Galaxies and Quasars.

6. Remarks

- (i) Since, there is a lot of ambiguities about the Physics in Quasars and not in galaxies, we feel safe in applying our theory for the case of galaxy and not for the case of Quasars.
- (ii) The theory developed here could be utilised for many hitherto unexplained mechanism for radio emission from astrophysical bodies. The detailed discussion will be communicated later.
- (iii) The immediate extension could be made in finding out poynting flux for small values of.
- (iv) It could be noted that the second order flux is completely longitudinal while the first order flux has both longitudinal and transverse. This has been possible because the starting solution we have taken is transverse. If we would take that solution as longitudinal then the first order would come out as mixed and second order as purely longitudinal.
- (v) The values of electric field, number density and magnetic field used for the plasma jet of M87 are so chosen that it satisfy the observed flux. In fact, there is no confirmed values of those parameters at present.

Acknowledgment

We wish to express our gratitude to Dr. B. Chakraborty of the Department of Mathematics, Jadavpur University, Calcutta for his valuable discussion in the preparation of this paper, and to Referee for his valuable comments and suggestions. One of the authors Dr. R. Bondyopadhaya thanks to CSIR, New Delhi, India, for giving the scope of this work offering Post Doctoral Fellowship to him under Dr. B. Chakraborty

References

- Bondyopadhyaya R 1976 *Ph.D. Thesis, Jadavpur University, Calcutta*
Burdidge G R, Burbidge M and Sandage A R 1963 *Rev. Mod. Phys.* **35**, 947
Chakraborty B 1973 *Appl. Sci. Res.* **28** 466
Chandra S K and Bondyopadhyaya R 1974 *Ind. J. Phys.* **48** 779
Chandra S K 1974 *Czech. J. Phys.* **B-24** 1338
Chiu H Y 1970 *PASP* **82** 486
Erickson W C and Cronyn W M 1965 *Ap. J.* **142** 1156
Field G 1956 *Ap. J.* **124** 555
Gold T 1968 *Nature* **218** 731
Lang, Kenneth R 1974 *Astrophysical formulae* (Springer-Verlag New York), p. 573
Minorsky N 1969 *Nonlinear Oscillations* (D. Van Nostrand, East-West) p. 242
Sluijter F W and Montgomery D 1965 *Phys. Fluids*, **8** 551
Zheleznyakov V V 1970 in *Radio Emission From Sun and Planets*; trans. by H.S.H. Massey,
Ed. J S Hey; Pergamon Oxford.

Comparative study of electromagnetic wave generation from the magnetosphere

R P Singh

Physics Department, Faculty of Science, Banaras Hindu University
Varanasi

and

R N Singh

Physics Section, Institute of Technology, Banaras Hindu University
Varanasi.

Received 3 March 1978

Abstract The comparative features of electromagnetic radiation from various processes, namely, cyclotron, doppler-shifted cyclotron, Čerenkov and synchrotron have been studied. The radiation from a test charge particle is considered. The total incoherent power is calculated by multiplying the test charge particle power by the particle number density. However, the need for coherent radiation to account for some special features of magnetospheric radiation is stressed. The coherently radiated total power is approximately proportional to the square of particle density. Taking the measured electron density and energy spectrum, we have computed the total radiated power and direction of radiation for different processes. The polarization study of radio-frequency waves has been included. In light of these the reception of electromagnetic signals generated by various processes is discussed. The pulsating nature of electromagnetic radiations, which is characteristic of auroral zone radiation, is proposed to arise from the hydromagnetic perturbations. It is argued that these features of the radiated electromagnetic spectrum could be quite helpful in interpreting the experimental observations of natural electromagnetic noise generated in the frequency range between $\sim 100\text{Hz}$ and $\sim 10\text{MHz}$.

1. Introduction

We have studied the generation and propagation of electromagnetic waves by various processes in magnetoplasma (Singh and Singh 1968, 1969a,b, 1970). Each of these papers contain the details of one radiating process. The three basic processes considered were Čerenkov process, Doppler-shifted normal and anomalous cyclotron process, and Synchrotron process. These processes cover a wide range of electromagnetic spectrum and the magnitude of the radiated power and the direction of radiation changes from one process to another. The successful interpretation of the source of electromagnetic signals received at the ground or by rocket and satellite depends on the precise knowledge of some of these features.

Therefore, in the present paper, we propose to compare the features of the three processes which we have discussed separately.

Among these distinguishing features are the radiated power, the beamwidth and the direction of radiation. All these quantities are plotted in polar diagrams, according to the energy of the radiating particle and to the process of radiation.

A summary of experimental observations of electromagnetic radiations is included to aid the interpretation and discussion of our results. The role of beam of electrons and coherence of charged particle on radiation is outlined. The effect of geomagnetic activity and solar flare conditions is discussed. The reception of electromagnetic wave power is illustrated. It is argued that, under certain conditions, the received power could be oscillatory due to local ionospheric effects; although the wave-particle interaction in the equatorial region may also give rise to such oscillatory behaviour of precipitating charged particles and hence in the generated electromagnetic wave.

2. Experimental observations

The electromagnetic waves covering a wide frequency range generated in the ionosphere and the magnetosphere can be received at the ground by means of suitably designed receiving systems. These signals are detected in space by means of rocket—or satellite—born receiving devices. In this section, we will give a brief account of some recent experimental measurements of very low frequency and radio-frequency electromagnetic waves. In the VLF-range (4 kHz–230 kHz), Dowden (1961) made a number of measurements using the Hiss recorder and obtained an electromagnetic power of the order of 7.0×10^{-10} to $6 \times 10^{-14} \text{ W. m}^{-2} \text{ Hz}^{-1}$. Later measurements (Kleimenova *et al* 1966, Harang 1968) reported power of the order of 10^{-14} to $10^{-13} \text{ W. m}^{-2} \text{ Hz}^{-1}$ in the frequency range 0.8–10 kHz. In the recent years the VLF hiss has been recorded almost as a routine over a span of time by different groups (R. A. Holliswell, Stanford, U.S.A.; D. A. Gurnett, Iowa University, U.S.A.; R. Gendrin, France; R. L. Dowden, New Zealand; L. Harang, Oslo, Norway; T. R. Kaiser, University of Sheffield, U.K.). The maximum observed spectral density of VLF wave in the frequency range 1–20 kHz at the Byrd station using his recorder was reported to be $10^{-13} \text{ W. m}^{-2} \text{ Hz}^{-1}$ (Helms and Turtle, 1964). Gurnett (1966) has reported the satellite measurement (Injun-3, Dec. 1962—Oct. 1963) of VLF spectral density of the order of $10^{-12} \text{ W. m}^{-2} \text{ Hz}^{-1}$ in the frequency range 2–10 kHz. Analysing the Injun-3 data, Gurnett (1968) reported that the spectral density in the inner magnetosphere for 1–8.8 kHz was of the order of $10^{-12} \text{ W. m}^{-2} \text{ Hz}^{-1}$. The VLF power of the same order of magnitude was obtained by Gendrin *et al* (1970a) by a rocket measurement (0.3–2.0 kHz).

The electromagnetic noise in the high frequency range has been reported by various authors either in terms of brightness or in terms of equivalent antenna

temperature*. Dyce and Horowitz (1963) have reported the spectral density to be $4.1 \times 10^{-21} \text{ W. m}^{-2} \text{ Hz}^{-1}$ and also have shown variation along the geomagnetic latitude. Ochs (1964) using huge array of antennas operating at 30 and 50 MHz has reported the average power (averaged over a year) measured at Lima, Peru, to be $1.3 \times 10^{-20} \text{ W. m}^{-2} \text{ Hz}^{-1}$ and $7.8 \times 10^{-21} \text{ W. m}^{-2} \text{ Hz}^{-1}$ respectively. The ground based observation of Ellis (1964) is $5 \times 10^{-20} \text{ W. m}^{-2} \text{ Hz}^{-1}$ for 20 MHz. Hartz (1964) has analysed the Alouette data and has reported the spectral density to be $1.5 \times 10^{-20} \text{ W. m}^{-2} \text{ Hz}^{-1}$ for 4 MHz. Hower and Dunlap (1966) have shown that 10 MHz noise may be observed from the north at the Washington. The measurement of galactic noise reported by Fortini *et al* (1966) at MHz is of the order of $10^{-18} \text{ W. m}^{-2} \text{ Hz}^{-1}$. Recently, Vasecky (1969) has analysed satellite observations and has reported $5 \times 10^{-21} \text{ W. m}^{-2} \text{ Hz}^{-1}$ for 1.5 MHz and $1.5 \times 10^{-20} \text{ W. m}^{-2} \text{ Hz}^{-1}$ for 4.8-15 MHz.

The polarization measurement of the signal is an important tool for measuring the electron content in the ionosphere and the horizontal gradients in the electron density. Gendrin *et al* (1970a) have measured the polarization of VLF signal (0.3 kHz-2.0 kHz) and have shown that these waves propagate in the right hand circularly polarized mode. Using the simultaneous measurement at the rocket and at the ground, they have shown that there is no change of polarization of those waves and also the generation mechanism is the one which discards the generation of left-handed circularly polarized waves. Contrary to this, the radio-frequency waves, while propagating through the ionosphere, change their polarization (Ochs 1966). The ground based observations made by Ochs *et al* (1963) in radiofrequency range show an elliptical polarization which has been explained as the results of alteration of polarization while the linearly polarized wave propagates through the ionosphere. The linearly polarised wave may be generated by synchrotron process. Peterson and Hower (1966) have shown that the polarization measurement of synchrotron signal leads to the estimation of Faraday-rotation and, consequently, the electron content of the ionosphere. In the next section, we will make comparative study of power-frequency spectra for different cases.

3. Comparative study of frequency and power spectra

It is well known that the acceleration and deceleration of charged particle give rise to electromagnetic wave. The electromagnetic wave radiations from accelerated electrons are classified into four main processes. These processes of electromagnetic wave emission are interrelated and the radiation characteristics

*The correspondence between antenna temperature and power flux is made by assuming that the source radiates like a black body at the frequency which is considered. 1°K is equivalent to $3.1 \times 10^{-23} \text{ W. m}^{-2} \text{ Hz}^{-1}$ at 1 MHz and varies like f^2 .

Change drastically from one to another. The energy and pitch angle dependent classification is often made, which is given below :

(a) **Cyclotron radiation**—If the charged particle is of low energy and possesses only perpendicular velocity V_{\perp} (pitch angle 90°), then the radiation at cyclotron frequency is known as cyclotron or gyro-radiation process.

(b) **Doppler-Shifted Cyclotron Radiation**—If gyrating charged particles have low energy and pitch angle α lying between 0 - 180° , then the charged particles spiral along the magnetic lines of force and radiate electromagnetic waves whose frequency is either shifted up ($0 < \theta < 90^{\circ}$) or down ($90^{\circ} < \theta < 180^{\circ}$), θ being the angle between the propagating wave vector and magnetic field) due to their motion while radiating. If S is the harmonic number, then $S > 0$ gives the condition for normal doppler-shifted cyclotron radiation and $S < 0$, the anomalous doppler-shifted cyclotron radiation (Singh and Singh 1969b). The pitch angle dependence may be studied by the following emission equation :

$$V_P = \frac{V \cos \alpha \cos \theta}{1 - \frac{S\omega_H}{\omega}} \quad (1)$$

where α is the pitch angle, ω and ω_H are the wave frequency and gyro-frequency respectively, V and V_P are particle velocity and phase velocity of the wave. From the equation it may be seen that, if $S > 0$ and $\frac{S\omega_H}{\omega} > 1$, then for upward doppler-shifting, $90^{\circ} < \alpha < 180^{\circ}$, and for downward doppler-shifting, $0^{\circ} < \alpha < 90^{\circ}$. If $S > 0$ and $\frac{S\omega_H}{\omega} < 1$, then for upward doppler-shifting, $0^{\circ} < \alpha < 90^{\circ}$ and for downward doppler-shifting $90^{\circ} < \alpha < 180^{\circ}$, whereas for anomalous doppler-shifted cyclotron radiation ($S < 0$), for upward dopplershifting, $0^{\circ} < \alpha < 90^{\circ}$, and for downward doppler-shifting, $90^{\circ} < \alpha < 180^{\circ}$.

(c) **Cerenkov Radiation**— If the charged particle has only parallel velocity component (pitch angle 0°) which is greater than or equal to the phase velocity of the emitted wave, then the process of radiation is known as Cerenkov.

(d) **Synchrotron Radiation**— When the energy of the radiating electron is relativistic and the pitch angle lies between 0° 180° , the radiation characteristics are changed and the process is known as synchrotron process. In certain cases (Bekefi 1966), the pitch angle of the radiating electron in synchrotron mode is assumed to be 90° and in such cases the information about polarization is lost. Therefore, to get information about polarization one is obliged to consider pitch angle different from 90° (Westfold 1959).

The above four processes are believed to operate and cover a wide range of electromagnetic spectrum starting from VLF waves and extending up to radio-frequencies and microwave frequencies. The radiation characteristics of all these processes have been studied separately in details elsewhere (Singh and Singh 1968, 1969a,b 1970, Singh 1973a,b). Here, we propose to discuss the distinguishing features of the radiation process as operating in the ionosphere and the magnetosphere. The formulation of these theories is based almost on similar assumptions, namely :

- (i) The medium is permeated by a static magnetic field and the electromagnetic field vector is comparatively very small.
- (ii) The magnetoplasma is considered to be cold, collisionless, dispersive, anisotropic and neutral.
- (iii) Thermal motion of the particle has been neglected.
- (iv) The permeability of the medium is taken to be equal to that of free space, $\mu = \mu_0$
- (v) The dielectric tensor is complex and Hermitian.
- (vi) In the spatial and temporal description of the medium, the velocity effect of the spiraling particle has been neglected.

However, some of the recent observations demand the modifications of these theories to include the collisional and thermal effects. The singularity catastrophe which arises in VLF wave-power spectrum can be easily removed by accounting for the collisional and thermal effects of ambient plasma (Kurdyumov 1966, Furutani 1968).

The high frequency radiation is not affected by the collisions or thermal effects. However, the drifting plasma has shown a marked feature of suppressing certain part of the frequency spectrum (Ramaty and Lingenfelter 1967, Shukla and Singh 1970 Shukla *et al* 1974).

The theoretical formulation of these processes with above assumptions shows that the radiated power spectrum in each case has different dependence on the energy and pitch angle of the radiating particles. As an aid for the interpretation and discussions forthcoming in the following pages, we have reduced the power spectrum dependence on relevant plasma parameters.

1. *Cyclotron Radiation*—Power radiated by a single electron in cyclotron mode is given by :

$$P = 1, 5 \times 10^{-22} B^2 \beta^2 (1 + \cos^2 \theta) \text{ W.Hz.}^{-1} \quad (2)$$

where B is static magnetic field in Gauss and $\beta = v/c$.

θ is the angle between magnetic field and radiated power direction. The radiation frequency is the gyrofrequency. From above expression, it is seen that the

power per electron increases as the magnetic field and energy of the radiating electron increase. The power, P , is directly proportional to the square of the magnetic field. It is also directly proportional to the radiating particle energy.

2. *Doppler-Shifted Cyclotron Radiation*—Power radiated in the S -th harmonic is given by (Trulsen and Fejer 1970)

$$\begin{aligned} \frac{dP}{d\omega} = \sum_{modes} \frac{q^2}{v_{11}} \frac{\omega}{R} & \left[\left(\left(1 - \beta_{\parallel}^2 \epsilon_1 - \frac{s^2 \omega_H^2}{c^2 k_{\perp}^2} \epsilon_3 \right) \left(k^2 - \frac{\omega^2}{c^2} \epsilon_1 \right) - \beta_{\parallel}^2 \frac{\omega^2}{c^2} \epsilon_2^2 \right) J_s^2 \right. \\ & + \frac{2\beta_{\perp} \omega k_{\perp}}{c} \epsilon_2 \left(\frac{1 - s\omega_H \omega}{c^2 k_{\perp}^2} \right) J_s J_s' - \\ & \left. \beta_{\perp}^2 \left(\epsilon_3 k_{\perp}^2 - \epsilon_1 k_{\parallel}^2 - \frac{\omega^2}{c^2} \epsilon_1 \epsilon_3 \right) J_s'^2 \right] \end{aligned} \quad (3)$$

where ϵ_1 , ϵ_2 and ϵ_3 are the components of the cold plasma dielectric tensor (Stix 1962). J_s and J_s' are the Bessel function and its derivative of S -th order.

$$k_{\parallel} = \frac{\omega - s\omega_H}{v_{11}} \quad \text{and} \quad k_{\perp \pm} = \frac{X \pm R}{2\epsilon_1}$$

$$R^2 = \left[(\epsilon_1 - \epsilon_3) \left(k_{11}^2 - \frac{\omega^2}{c^2} \epsilon_1 \right) + \frac{\omega^2}{c^2} \epsilon_2^2 \right]^2 + \frac{4\omega^2}{c^2} k_{11}^2 \epsilon_2^2 \epsilon_3$$

and

$$X = -(\epsilon_1 + \epsilon_3) \left(k_{11}^2 - \frac{\omega^2}{c^2} \epsilon_1 \right) - \frac{\omega^2}{c^2} \epsilon_2^2$$

ω_H and ω are the cyclotron and wave frequency. From the equation it is seen that the power radiated is a complicated function of radiating particle energy, frequency of radiation, gyrofrequency and plasma frequency. Singh and Singh (1969b) have made a detailed analysis and have shown that the radiated power decreases as the energy of the radiating particle increases. The radiated power increases as the magnetic field and radiated frequency increases. The power decreases as the plasma frequency increases, showing that the effect of the medium is to decrease the effective radiated power. In eq. (3), v_{\parallel} may be written as $v \cos \phi$, which shows that, when the pitch angle of the particle increases, the radiated power increases. This is true for $S \neq 0$.

3. *Cerenkov Radiation*—Eq. (3) for $S = 0$ gives the radiated power in the Cerenkov mode. So, all of the above remarks for Doppler-shifted cyclotron radiation follow for Cerenkov radiation. McKenzie (1963) and Singh and Singh (1969a) have shown that the power radiated in Cerenkov mode for VLF waves

is inversely proportional to the plasma density and directly proportional to the square of the magnetic field. Also $\frac{dP}{d\omega} \propto E^{-1}$ and $\frac{dP}{d\omega} \propto \omega$. This dependence is in the limit $\omega_H \ll \omega_P$ and $\left(\frac{c\omega_H}{v\omega_P}\right)^2$. 1. Similar dependence has also been obtained by Gendrin and Etcheto (1970).

4. *Synchrotron Radiation*—Resolving the velocity of the radiating electrons along directions perpendicular and parallel to the projection of B in the plane normal to the instantaneous velocity of electrons, the distribution of the radiated power in these two modes is given by (Westfold 1959):

$$P_{\parallel} = 2.8 \times 10^{-26} \frac{\beta}{\gamma} \frac{f^2}{f_H^2 \sin^2 \alpha} \psi^2 (1 + \gamma^2 \psi^2)^2 K_{1/3}^2 \left(\frac{f}{3f_H \gamma^3 \sin \alpha} (1 + \gamma^2 \psi^2)^{3/2} \right),$$

$$P_{\perp} = 2.8 \times 10^{-26} \frac{B}{\gamma^3} \frac{f^2}{f_H^2 \sin^2 \alpha} (1 + \gamma^2 \psi^2)^2 K_{2/3}^2 \left(\frac{f}{3f_H \gamma^3 \sin \alpha} (1 + \gamma^2 \psi^2)^{3/2} \right)$$

$$W.H_z^{-1} \quad (4)$$

The average radiated power in these two modes, after integration over ψ (ψ is the angle between the direction of radiation and the orbital plane) is written as

$$\bar{P}_{\parallel} = 2.34 \times 10^{-25} B \sin \alpha F_{11}(f/f_c)$$

$$\bar{P}_{\perp} = 2.34 \times 10^{-25} B \sin \alpha F_{1}(f/f_c) \quad W.H_z^{-1} \quad (5)$$

where B is the ambient magnetic field in Gauss, $f_c = 4.2\gamma^3 B \sin \alpha$ in MH_z and $\gamma = E/mc^2$. Also,

$$F_{11}\left(\frac{f}{f_c}\right) = \frac{f}{2f_c} \left[\int_{f/f_c}^{\infty} K_{5/3}(\eta) d\eta - K_{2/3}(f/f_c) \right],$$

$$F_1(f/f_c) = \frac{f}{2f_c} \left[\int_{f/f_c}^{\infty} K_{5/3}(\eta) d\eta + K_{2/3}(f/f_c) \right],$$

$K_{5/3}$, $K_{2/3}$ and $K_{1/3}$ are modified Bessel function of the second kind. From the above equation (4), it is seen that the average power radiated is directly proportional to the magnetic field. The increase in energy through the function $F(f/f_c)$ for fixed B will increase the power in the beginning, and then will decrease, showing a maxima at certain energy depending upon the magnetic field and the frequency of radiation.

All these theories are formulated for single radiating charged particles. In order to get the total radiated power, the single particle power is multiplied by the number of charged particles giving rise to electromagnetic radiation in the same frequency range. Therefore, the power radiated in the magnetosphere has

to account for the energy spectrum of the charged particles and the magnetic field corresponding to this region. For the evaluation of total radiated power, we have assumed the earth's magnetic field to be a perfect dipole one. The energy and pitch angle dependence of the radiating electron flux has been assumed to be of the following form

$$J(L, \alpha, E) = J(L) \exp(-E/E_0) \sin^m \alpha_e(L) \quad (6)$$

where $\sin^m \alpha_e(L)$ gives the pitch angle distribution of electrons in the magnetosphere.

The exponential energy parameter E_0 has been assumed equal to 50 KeV (Gendrin *et al* 1970b have shown that $E_0 < 100$ KeV). The pitch angle distribution parameter, m varies with L , between 1.5 and 3 in magnetosphere (Watari and Kamiyama 1969). For simplicity, we have assumed $m = 2$ for L values 2-5. The equatorial pitch angle α_e for $L = 2$ has been assumed equal to 20° . The loss cone angle for $L = 2$ is 14.6° . All the electrons having equatorial pitch angle less than 14.6° will be precipitated into the ionosphere and will not contribute to radiation by mirroring back and forth.

The variation of pitch angle in the equatorial plane with L and along L in the non-equatorial plane has been considered, using the conservation of the first adiabatic invariant. The variation of $J(L)$ with L has been tabulated below for ready reference ($J(L_2)$ is omnidirectional) :

$$\begin{array}{ccccccc} L & 2 & 3 & 4 & & & \\ J(L) & 2 \times 10^7 & 4 \times 10^7 & 4 \times 10^6 & 6 \times 10^7 & \text{cm}^{-2}\text{sec}^{-1}. \end{array}$$

The $J(L)$ values reported here are in accordance with those reported by Vernov *et al* (1969), although they have reported $J(L)$ values for energy greater than 100 KeV, therefore, their values are smaller than the one we assume here, because we have taken all the electrons of energy greater than 1 KeV. Using the above energy spectrum and pitch angle distribution the power radiated by different processes have been tabulated for comparative study.

The radiated power from cyclotron process, for $L = 2, 3, 4$ and 5, and geomagnetic latitude, $\phi = 0^\circ, 20^\circ$ and 40° , has been tabulated in table 1. The

Table 1. Cyclotron radiation

Geomag- netic latitude	$L = 2$		$L = 3$		$L = 4$		$L = 5$	
	Frequ- ency	Power	Frequ- ency	Power	Frequ- ency	Power	Frequ- ency	Power
0°	110.0	6.0×10^{-24}	32.0	3.0×10^{-25}	14.0	3.0×10^{-27}	7.0	5.0×10^{-27}
20°	200.0	4.0×10^{-23}	60.0	2.0×10^{-24}	21.0	1.0×10^{-26}	10.0	1.0×10^{-26}
40°	800.0	2.0×10^{-21}	200.0	8.0×10^{-23}	100.0	1.0×10^{-24}	52.0	2.0×10^{-24}

frequency of radiation has been assumed to be the corresponding local gyro-frequency. The power has been expressed in $W.m^{-3}$, Hz^{-1} , the radiated frequency in kHz.

Synchrotron radiated power for $L = 2$ has been calculated and shown in Table 2. The calculation for higher L -values has not been made because it has been seen that the radiated power decreases very rapidly as L -increases in radiofrequency range (Singh and Singh 1968).

The power has been expressed in $W.m^{-3}Hz^{-1}$ and frequency in $M.Hz$.

Table 2. Synchrotron radiation

Frequency	$\phi = 0^\circ$	$\phi = 20^\circ$	$\phi = 40^\circ$
10	6.0×10^{-35}	2.0×10^{-34}	3.0×10^{-33}
30	2.0×10^{-35}	9.0×10^{-35}	5.0×10^{-34}
100	5.0×10^{-36}	6.0×10^{-35}	9.0×10^{-35}

The doppler-shifted cyclotron radiated power and Cerenkov radiated powers have been calculated and tabulated below. The calculation for Anomalous Doppler-Shifted Cyclotron radiated power has been made for $L = 2$. For normal Doppler-Shifted Cyclotron Radiation and Cerenkov Radiation, the power evaluation has been made for different L -values. As usual, the power has been expressed in $W.m^{-3}Hz^{-1}$ and frequency in kHz.

Using the experimentally measured energy spectrum appropriate for all the four processes, we have computed the total radiated power in the magnetosphere. The results presented in Tables 1-5 show that the power radiated in the cyclotron mode is maximum and in the synchrotron mode is minimum. The radiated power in the Cerenkov mode is greater than the doppler-shifted cyclotron mode, but less than the cyclotron mode. The radiated power increases in regions of high latitude as compared to the equatorial region. From Table 1, it is seen that electromagnetic waves of higher frequency is generated in the auroral region and lower frequency is generated in the equatorial region. Also the power radiated at lower L -values is large as compared to higher L -values. From Table 2, it is seen that the power radiated in the MHz frequency range is of the order of $10^{-33} W.m^{-3}.Hz^{-1}$. The radiated power decreases with increasing frequency at $L = 2$. We have made the power computation for 10, 30 and 100 MHz, which are high frequencies as compared to local gyrofrequency. The power would increase as the frequency decreases, showing a maximum around local gyrofrequency and then will decrease as frequency decreases.

Table 3. Anomalous-Doppler-shifted Cyclotron radiation ($S = -1$)

Frequency	$\phi = 0^\circ$	$\phi = 20^\circ$	$\phi = 40^\circ$
10	8×10^{-29}	10^{-27}	4×10^{-27}
30	10^{-27}	8×10^{-27}	7.0×10^{-26}
50	3×10^{-27}	7×10^{-27}	3×10^{-26}

Table 4. Normal-Doppler-shifted Cyclotron radiation ($S = 1$)

Geomagnetic Latitude	Frequency	$L = 2$	$L = 3$	$L = 4$	
0°	10	4×10^{-28}	3×10^{-28}		
	40	5×10^{-27}	...		
20°	10	3×10^{-27}	7×10^{-28}	4×10^{-30}	3×10^{-29}
	40	2×10^{-26}	5×10^{-28}
40°	10	3×10^{-26}	5×10^{-27}	3×10^{-17}	2×10^{-26}
	40	2×10^{-26}	2×10^{-26}	4×10^{-27}	...

Table 5. Cerenkov radiation ($S = 0$)

Geomagnetic Latitude	Frequency	$L = 2$	$L = 3$	$L = 4$	$L = 5$
0°	10	5×10^{-27}	3×10^{-26}	4×10^{-30}	0
	40	2×10^{-26}
20°	10	5×10^{-26}	3×10^{-25}	5×10^{-29}	5×10^{-28}
	40	2×10^{-25}	4×10^{-25}
40°	10	4×10^{-25}	4×10^{-23}	6×10^{-27}	10^{-26}
	40	2×10^{-26}	2×10^{-22}	2×10^{-26}	4×10^{-26}

The VLE power from the auroral shows an increasing tendency. From Tables 3 and 4, it is seen that the power radiated in the normal and anomalous doppler-shifted cyclotron mode is of the same order of magnitude and has the same trend of variation along geomagnetic field line. The normal doppler-shifted cyclotron radiation is concentrated in the backward hemisphere, whereas the anomalous doppler-shifted cyclotron radiation is concentrated in the forward hemisphere. The radiated power in the Cerenkov mode is slightly greater than the

The dotted line in the table shows that the corresponding frequency does not satisfy the radiation condition at the place (L, ϕ space) for the corresponding radiation process.

doppler-shifted cyclotron mode and has the same type of variation with frequency and latitude. The radiated power shows a maximum at $L = 3$ due to an enhanced hot electron density at $L = 3$, as compared to $L = 2$ or $L = 4$. Although the electron density is maximum at $L = 5$, but the radiated power per electron decreases with increased L -value, therefore, the radiated power does not show any maximum at $L = 5$, but the radiated power at $L = 5$ is greater than the radiated power at $L = 4$.

It is obvious from Tables 1-5 that the high frequency waves are mainly generated by synchrotron radiation process, whereas VLF waves are generated by one of the remaining three processes. Also it is seen that relativistic electrons are responsible for high frequency noise generation, whereas low energy (including mildly relativistic) electrons play an important role in the generation of VLF waves. It is also seen that the same frequency may be generated by different processes with different intensities. More specifically, we can say that a given frequency f_s greater than the local gyrofrequency f_h is generated more efficiently by synchrotron process and that the frequency which is equal to the gyrofrequency is generated more efficiently by cyclotron process. The frequency below the local gyrofrequency is generated either by Cerenkov process or by doppler-shifted cyclotron (Normal and anomalous) process. Thus, knowing the frequency, intensity and direction of radiated wave in the magnetosphere, one can pin down the process of generation of the electromagnetic waves. The synchrotron process has clear-cut distinguishing features. The radiation is mostly in the high frequency range and is polarized. The measurement of polarization in the high frequency region is characteristic of this process. Sometimes synchrotron radiation can also be emitted in the $k\text{Hz}$ region. This is dependent on the particle flux, the energy spectrum of the charged particles and the ambient magnetic field. If the magnetic field is small (local gyrofrequency in the $k\text{Hz}$ frequency range), then the electromagnetic waves in the $k\text{Hz}$ frequency range may be generated by synchrotron process from high latitudes as well as from equatorial regions of higher L -values. To be more specific, we find that the power radiated by a single electron of 1 MeV at 25 $k\text{Hz}$ at $L = 5$ and $\phi = 40^\circ$ is $4 \times 10^{-31} \text{W.Hz}^{-1}$. This shows that the power radiated by single electron at 25 $k\text{Hz}$ in the auroral region ($L = 5$, $\phi = 40^\circ$) is as high as the power radiated by single electron at 1 MHz , in the auroral region ($L = 5$, $y = 40^\circ$) is as high as the power radiated by single electron at 1 MHz , $L = 1, 3$, $\phi = 0^\circ$ (Singh and Singh, 1968), which means that the synchrotron process may be effective even in the $k\text{Hz}$ range from the upper magnetosphere. Wang and Kim (1970) have made calculation of synchrotron radiation from auroral zone electrons and have shown that their results are in good agreement with the auroral noise observed at College, Alaska.

The decisive radiating process and the correct measurement is capable of revealing features of the electron velocity distribution or energy spectrum of

radiating particles. The role of charged particle energy spectra on the radiation characteristics in the high frequency region was studied by Singh *et al* (1969). Such information may be derived for all the radiating processes, since in all these processes, the total power is computed by assuming a certain energy spectrum of the radiating electrons. Thus, by measuring the exact intensity of the wave and the particle density, the energy spectra may be obtained, or by knowing the energy spectra, the particle density in different energy ranges may be obtained.

4. Angular distribution of the radiated power

The polar characteristics of the radiation processes give the angular distribution of radiated power which determines the direction of maximum power radiation and helps in describing the geometry of reception. The polar characteristics of cyclotron radiation is determined by the term $(1 + \cos^2\theta)$ in eq. (2), θ being measured from the magnetic field in clockwise direction. This shows that the radiated power in the magnetic field direction is twice as compared to the power radiated in a direction perpendicular to the magnetic field. This is the case for cyclotron radiation from low energy electrons. The characteristics of cyclotron radiation from mildly relativistic electrons are completely different. The maximum radiation direction for cyclotron radiated power from mildly relativistic electrons varies with the harmonic number and with the energy of the emitting particle (Bekefi 1966, Singh 1969). The polar characteristics of doppler-shifted cyclotron radiation and Corenkov radiation is expressed as (Singh and Singh 1969b)

$$\frac{dP}{d\Omega} = - \frac{dP}{d\omega} \frac{df}{d(\cos\theta)}$$

where $\frac{df}{d(\cos\theta)}$ is obtained from the dispersion equation. It is a function of V_{11} and of the components of the dielectric tensor of the medium. The angular distribution of synchrotron radiation is obtained by changing ψ (the angle between the direction of radiation and the orbital plane) in the radiated power expression (eq. (4)). Therefore, the angular distribution of the radiated power depends on all the parameters. The radiation is concentrated in a fine beam in the direction of instantaneous velocity of the electrons. The beam width of the synchrotron radiation is given by $\theta = (mc^2/E)$, which shows that, as the energy of radiating electron increases, the radiated beam becomes sharp. The separation of radiated pulse in a certain direction is given by $\Delta T = 2\pi/\omega_H$, (ω_H is the local relativistic gyrofrequency), which shows that in a strong magnetic field, the synchrotron radiation process would be a continuous radiation process. Also ΔT becomes small, which indicates that more electromagnetic pulses are radiated per second. This is another argument for the enhancement of synchrotron and cyclotron power in the presence of enhanced magnetic field.

For the comparative study of polar diagram of different processes, we have plotted polar diagram for all the processes in one figure. We have drawn the angular variation of radiated power in the range of 0° to 180° . For 180° to 360° , there exists a symmetry. In fact, the parameter which plays a role in controlling the angular variation of the radiated power is the parallel velocity of the particle (pitch angle). For cyclotron and synchrotron radiation, V_{11} has been assumed to be equal to zero, so that the polar diagrams are also symmetric with respect to $\theta = 90^\circ$. The normalized radiated power in certain direction was obtained by dividing the angular power by the maximum radiated power. Therefore, polar diagrams shown in figure 1 give the angular variation and the relative amplitude. The polar diagram for Cerenkov radiation is independent of frequency (McKenzie 1963, Singh and Singh 1969a), whereas, for doppler-shifted cyclotron radiation (normal and anomalous), the frequency has been taken equal to 10 kHz . The frequency of synchrotron mode polar diagram is 30 MHz . The energy of the radiating particle for doppler-shifted cyclotron and Cerenkov has been assumed to be 1 keV , whereas for synchrotron mode the corresponding energy has been assumed to be 10 MeV (1 keV energy is close to experimental measurements in the ionosphere and magnetosphere, and 10 MeV is an upper limit encountered only during artificial injection of relativistic electrons). From the figure, it is seen that the electromagnetic radiation in space covers almost the entire space and the

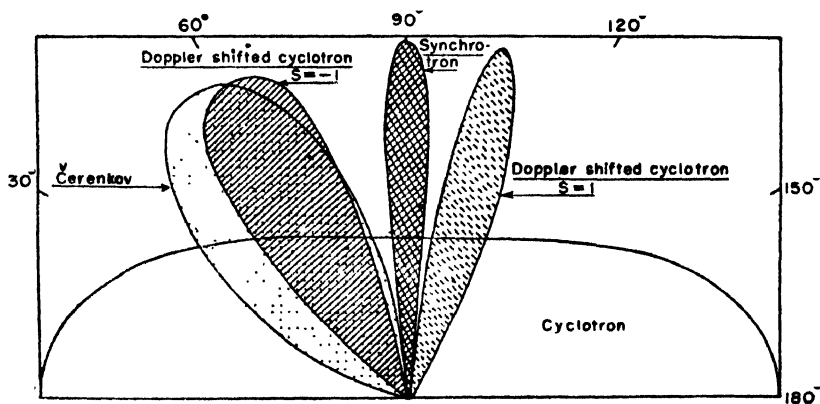


Figure 1. Normalized polar diagram of cyclotron, doppler-shifted cyclotron, Cerenkov and synchrotron radiation from a single electron ($L = 2$, $\phi = 0$)

maximum power in certain direction is characteristic of certain process of radiation. The contribution of doppler-shifted cyclotron radiation is in the forward as well as in the backward hemisphere. When the particles parallel velocity is positive, the anomalous doppler-shifted cyclotron radiation is effective in the forward hemisphere, whereas normal doppler-shifted cyclotron process is effective in the backward hemisphere. The beam width in the forward hemisphere is comparatively larger than the beam width in the backward hemisphere. The beam

width of Cerenkov radiation lies in the forward hemisphere and is comparatively larger. The angular distribution of anomalous doppler-shifted cyclotron radiation is similar to Cerenkov radiation in many respects, except of the beam width.

From the figure it is seen that the synchrotron power radiated by relativistic electrons is concentrated mainly along the instantaneous velocity vector and the beam width is narrow. From the study of polar diagram of cyclotron radiation and synchrotron radiation, it is observed that the polar diagram changes when the radiating electron energy changes from low energy to relativistic energy, which is consistent with the theory (Singh and Singh 1970). In figure 2 we have shown the variation of total radiated power from different processes. The place of radiation in space is characterized by $L = 2$ and $\phi = 0^\circ$. The radial vector represents the magnitude and direction of the maximum radiated power for each of these radiating processes. All the properties of the radiation processes which

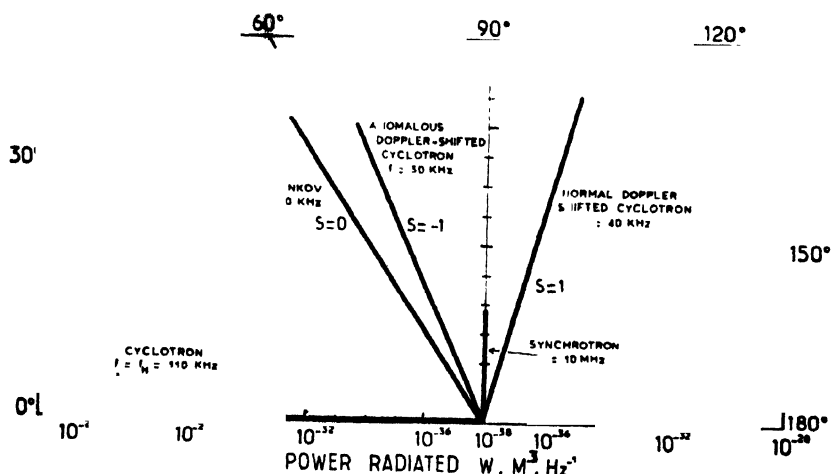


Figure 2. Vector diagram of the radiated power ($W. m^{-3}. Hz^{-1}$) for different processes. The vector direction represents the maximum power radiation which is measured with respect to ambient magnetic field direction $L = 2$, $\phi = 0^\circ$, $\alpha_s = 20^\circ$, $m = 2$, $E_0 = .50$ keV.

have been describe in the previous sections can be studied by the aid of this simple vector diagram. From the vectordigram, it is seen that the power radiated in Cerenkov and doppler-shifted cyclotron mode are approximately of the same order of magnitude, but in different directions. This characteristic of radiation process is helpful for the study of wave-particle interaction as proposed by Wang (1969) and Singh (1973a,b). Recently, Dowden (1970) has shown that the anomalous doppler-shifted cyclotron radiation is the most promising emission process of whistler precursors. To explain this, he has shown on the basis of physical arguments, that the phase bunching produced during the wave-particle interaction is helical, but we are not discussing here the backward effect of the waves upon the particles.

5. Reception of radiated power on the ground

The electromagnetic wave emitted in the magnetosphere and ionosphere may propagate in any direction depending upon the process of radiation and the direction of emission. The electromagnetic wave propagating along the geomagnetic field direction can be received on the ground at the base of the lines of force. The electromagnetic wave emitted in a direction perpendicular to the magnetic field direction may propagate towards the earth as well as away from the earth. A part of the wave which propagates towards the earth may be reflected from some layer in the ionosphere and may not be received on the ground. The counterpart which is not reflected from the ionosphere is received on the ground. The reception of such waves is discussed in this section. We confine ourselves to the discussion of detectability of electromagnetic wave on the ground emitted by different processes outlined in earlier sections.

The radiated power by the cyclotron process at the fundamental frequency is concentrated along the magnetic field direction; therefore, the power radiated by all the electrons in a magnetic tube of force will be additive. By devising suitable antenna system at the base of geomagnetic lines of force the integrated cyclotron power can be received.

From the polar characteristics of Cerenkov radiation and doppler-shifted cyclotron radiation, it is seen that the maximum power is emitted in a direction at an angle θ with the magnetic field. Such VLF waves, because of irregularities, are ducted in the magnetic field direction, and they can be received on the ground. Moreover, if the angle θ is such that $\cos \theta = 2f/f_H$, the energy is propagating strictly along the magnetic field line, even in the absence of irregularities (Gendrin 1961).

Helliwell (1965) has suggested that the quasi-periodic emissions with frequencies similar to those of micropulsations are caused by the hydromagnetic modulation of the source. To explain the amplitude modulated quasi-periodic VLF emissions, observed on the rocket, Beghin (1967) has argued that these emissions are generated by the precipitated high energy electrons, which are modulated by hydromagnetic waves (Parks *et al* 1968). Coronity and Kennel (1970) made theoretical study of modulation of VLF hiss by the hydromagnetic waves and have shown that the amplitude of the VLF emission and intensity of the associated particle flux vary exponentially with the amplitude of the hydromagnetic waves. This theory has been experimentally verified by making simultaneous observation of particles and waves by rockets (Etcheto *et al* 1971). Similar fluctuations in the high frequency electromagnetic waves (1–7 MHz) has been observed (Berky and Parthasarathy 1964). Also, such an effect could be used to explain the periodic fluctuations in the received high frequency electromagnetic power. We have proposed a mechanism of synchrotron radiation during the magnetically disturbed

periods (next section). Similar effects could also explain the pulsating and modulated VLF hiss which is often observed in the auroral zone. Recently, such a correlation between the magnetic activity and the VLF-pulsating hiss was reported by Kitamiura *et al* (1969). In the next section we have given the geometry of the reception of synchrotron radiation in the auroral zone during the severe magnetic storm. As these magnetic storms are accompanied by large amplitude hydromagnetic waves, the pulsating nature of the auroral noise in the VLF and high frequency region is explained.

6. Synchrotron radiation in the auroral zone

The high frequency wave radiated by synchrotron process is along the instantaneous velocity vector direction which is perpendicular to the magnetic field. The reception of radio wave in the equatorial plane was suggested by Dyce and Nakada (1959), where plane of a helix in the equatorial region is perpendicular to the horizontal magnetic field; therefore, the radiation emitted along the direction of instantaneous velocity can be easily received on the equatorial receiving stations. Exception to this situation arises during the severe magnetic storms, where high energy electrons are accelerated along the lines of force and they precipitate in the auroral zone. Such storms are also accompanied by large amplitude hydromagnetic waves (Gondrin 1970), which rather govern the plane of the gyrating electrons and enable the synchrotron radiation to be detected in the auroral zone. Therefore, we briefly outline the possible geometry for synchrotron radiation detection in the auroral zone.

Let us consider the energetic electrons spiralling down the lines of force at a height h , above the earth's surface (figure. 3). The magnetic line of force in this region makes an angle (D) with the vertical and the pitch angle of the electrons at height (h) is assumed to be α . Due to the large amplitude (ΔB) hydromagnetic wave, the tubes of magnetic lines of force execute a simple harmonic motion and, consequently, the plane of the electron helix also executes a corresponding oscillation in the vertical plane (keeping the plane of the helix perpendicular to the instantaneous direction of the lines of force). During half of the cycle, when ΔB increases or decreases, the resultant direction of the lines of force changes instantaneously. When the tangent to the geomagnetic field line at $P(LM)$ changes by an angle λ (determined by the amplitude of the hydromagnetic wave ΔB) and occupy a new position $L'M'$, the instantaneous plane of the helix also changes by the same angle, so as to keep itself at an angle α to the instantaneous direction. The angle between LM and $L'M'$ is given by

$$\tan \phi = \Delta B \quad (8)$$

transverse vibration in the vertical plane, the distance Sd is always directed south of the over-head radiating electrons. This simple consideration shows that the synchrotron radiations in the auroral zone is most of the time arriving at the receiving site from north. This is consistent with the observations of Egan and Peterson (1960) at Stanford and Hower and Dunlap (1966) at Washington.

7. Polarization of synchrotron radiation

Schwinger (1949) made a comprehensive study of synchrotron radiation from an accelerated charged particle and showed that the synchrotron signal is unpolarized. Using the field vector, which was not taken into account by Schwinger. Westfold (1959) reformulated the problem and showed that the synchrotron signal is elliptically polarized. The axes of polarization ellipse are parallel and perpendicular to the projection of the external magnetic field into the plane normal to the direction of observation. The axial ratio of the polarization ellipse can be written as (Westfold 1959)

$$R = \pm \frac{[1 + \gamma^2(\alpha - \theta)^2]^{\frac{1}{2}}}{\gamma(\alpha - \theta)} \frac{K_{2/3} \left(\frac{f}{3f_H \gamma^3 \sin \alpha} (1 + \gamma^2(\alpha - \theta)^2)^{3/2} \right)}{K_{1/3} \left(\frac{f}{3f_H \gamma^3 \sin \alpha} (1 + \gamma^2(\alpha - \theta)^2)^{3/2} \right)}, \quad (12)$$

where $\gamma = E/(mc^2)$, $\alpha =$ pitch angle, and θ is the angle between the magnetic field and observation direction. $K_{2/3}$ and $K_{1/3}$ are modified Bessel function of second kind and are always positive. Therefore, the axial ratio R is positive or negative according to $\alpha \gtrless \theta$. When R is positive, the sense of rotation of the ellipse is right-handed (extraordinary wave), otherwise left-handed (ordinary wave). The axial ratio variation with θ for different values of pitch angle has been shown in figure (4). From the figure it is seen that the axial ratio increases as θ increases, and becomes infinite at $\theta = \alpha$ and after that changes its direction. It may also be noted that the axial ratio is always greater than one showing that the magnitude of the power radiated in extraordinary mode is always greater than or equal to power radiated in the ordinary mode. When $\alpha < \theta$, the power radiated in the ordinary mode becomes appreciably large and the sense of polarization is reversed. Also, an increase in α leads to decrease in axial ratio, which shows that as α increase the distribution of power between the two modes becomes closer to each other. Now in the case of $\alpha = \theta$, the axial ratio becomes infinite, showing that the synchrotron signal is linearly polarized in a plane perpendicular to the magnetic field direction.

The degrees of polarization for the radiated signal is defined as the ratio of the difference of power radiated in two polarized directions to the sum of powers

radiated in two polarized directions. Using eq. (5), the degree of polarization is given as

$$P = \frac{P_{\perp} - P_{\parallel}}{P_{\perp} + P_{\parallel}} = \frac{K_{2/3}(f/f_e)}{\int_{f/f_e}^{\infty} K_{5/3}(\eta) d\eta} \quad (13)$$

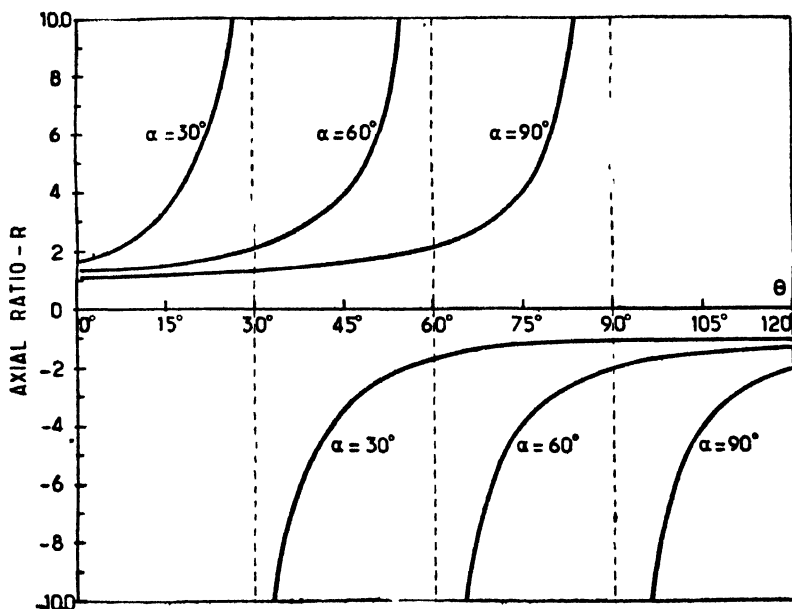


Figure 4. Variation of polarization (axial ratio) with θ (angle between magnetic field and the direction of observation) for different pitch angles ($\alpha = 30^\circ$, 60° , 90°), $E = 1$ MeV; $f_H = 100$ kHz, and $f = 100$ kHz.

Using eq. (13), we have studied the variation of degree of polarization with frequency for different electron energy. The magnetic field has been fixed ~ 0.04 gauss ($L = 2$, $\phi = 0^\circ$). From the figure 5, it is seen that, as the frequency goes on increasing, the degree of polarization increases for fixed electron energy and magnetic field. The increase in electron energy decreases the degree of polarization. Similar effect is also obtained by varying magnetic field. This shows that the effect of electron energy and magnetic field is additive. Using eq. (13) and figure 5 it is easily seen that the power radiated in extraordinary mode increases with frequency, whereas in ordinary mode decreases (keeping other parameters fixed). Also, it is seen that as energy increases, the phenomena shifts toward higher frequency side, showing that low frequency waves can be generated by low energy electrons even in synchrotron process.

The synchrotron radiation is strongly linearly polarized in the orbital plane. When such a signal passes through the ionosphere, its polarization is changed because of Faraday rotation. Thus, measuring the change in polarization of the synchrotron radiation, the electron content of the ionosphere is determined with

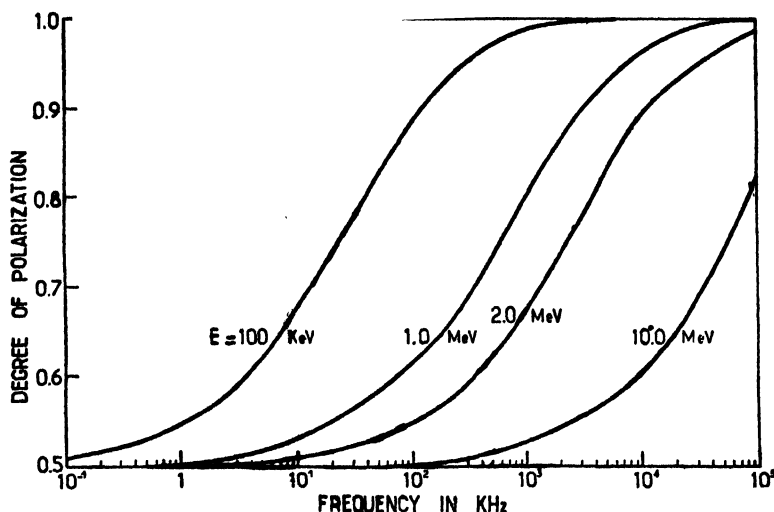


Figure 5. Variation of polarization degree with frequency for different electron energies ($E = 0.1, 1.0, 2.0$ and 10.0 MeV), $\alpha = 60^\circ$, $f_H = 300$ kHz.

precision (Peterson and However, 1966). Also, because of its strongly polarized nature, it is possible to measure separately synchrotron signal in the presence of background galactic noise (randomly polarized), even when the amplitude of the two is of the same order of magnitude. The present study of polarization of synchrotron signal is the case of single electron phenomena. The polarization of the signal, to be received at the ground or by the satellite, will depend on the energy spectra and pitch angle distribution of the electron. Further study including these effects should be made.

8. Conclusions

The four basic processes of electromagnetic wave generation, using the concept of single-particle radiation, has been worked out and it has been shown that different processes are operative in different energy ranges of radiating electrons, and also in different emitted frequency ranges. The polar diagram of cyclotron, doppler-shifted cyclotron and Cerenkov processes help the signal reception at the base of geomagnetic lines of force. Therefore, it is possible to make observations from low latitudes to high latitudes. To explain, the observed VLF intensity received at the ground, the total radiated power from the whole volume

of the radiating region is calculated. This is expressed as $P_T = \int P_r dv$, where P_r is the power radiated in unit volume and dv is the small volume element. If one considers the geomagnetic tubes of force of $1m^2$ base area, then $P_T = \int P_r dr$, where dr is the incremental length of lines of force. Generally, in magnetosphere, it is assumed that P_r , radiated power in the auroral zone, is propagating along the lines of force. Therefore, P_r may be assumed to be uniform in the geomagnetic tube, which give $P_T = P_r \cdot l$, l is the length of geomagnetic lines of force in meter. This method of evaluation of total power and comparison with observation relies upon many gross assumptions. Ball (1968) calculated the Cerenkov radiated power from artificially injected electron beams and showed that after assuming partial correlation, the power radiated increases by orders of magnitude and, therefore, it is possible to measure the generated waves by means of rockets or satellites, a conclusion which was somewhat questioned by Etcheto and Gendring (1970).

The radiation from the test charge particle and its multiplication with the number of charged particles gives a fairly good estimate of the radiated power in the tenuous, cold and collisionless magnetoplasma. However, there are times when the streaming charged particles form a partially correlated fluctuation. Under these conditions the streaming electron beam can be thought to consist of various sections radiating more or less coherently. The simple formulation in such a case has to account for the plasma current and field constituted by collective electrons obeying certain favoured distribution. The collective electron beam is supposed to have a velocity distribution characteristics of Cerenkov mode which we denote by a function $f(v_{11})$. The current density constituted by the electrons streaming along the static magnetic field is written as

$$J(r, t) = e \int v_{11} f(v_{11}) \delta(z - v_{11}t) dv_{11} \quad (1)$$

Fourier transforming the electric current and carrying out integration over dt we obtain :

$$J(\omega, k) = \frac{e}{(2\pi)^3} \int v_{11} f(v_{11}) dv_{11} e^{-i(\omega z/v_{11} + k_z z)} dz \quad (2)$$

*The following correction to our previous papers should be made :

1. Study of Cerenkov radiation from electrons in the magnetosphere and ionosphere-II. Ann. Geophys, 1969 25, 629 pages 636 lines 26-30: the line should be read as "the total Cerenkov radiated power storm the whole tube of force which can be received on the ground is $(10^{-25} \times 10^6 \times 10^6 =) 10^{-13} W. m. Hz^{-1}$. Jorgensen (1966) has reported that, for low altitudes, the VLF radiated power is $19^{-12} W. m^{-2} Hz^{-1}$.
2. Study of doppler-shifted cyclotron radiation from energetic electrons in the magnetosphere-III. Ann. Geophys, 1969 25, 639. Page 644, lines 9-10, $L=3$. where cross-sectional area on the ground is 1 m is found to be $(6 \times 10^{-25} \times 10^6 \times 10^6 =) 6 \times 10^{-13} W. m. Hz^{-1}$.

and

$$E(\omega, k) = \frac{i\omega\mu_0 e}{(2\pi)^2} \int \frac{A y}{\Delta} v_{11} f(v_{11}) dv_{11} e^{-i(\omega z/v_{11} + k_z z)} dz \quad (3)$$

We use the same notations as were used by McKenzie (1967). The rate of energy loss by the stream of electrons is thus defined as

$$\frac{dW}{dt} = - \int J \cdot E dz \quad (4)$$

Substituting for J and E in eq. (4) and carrying out Z and k integrations, we obtain an expression for the power radiated by a stream of electrons per unit path length in a small frequency range. We denote this by P_s .

$$P_s = \int P_i'(\omega, v_{11}) v_{11} f^2(v_{11}) dv_{11} \quad (5)$$

where $P_i'(\omega, v_{11})$ is the power radiated by an electron per unit path length in a small frequency range, and i specifies the direction of Cerenkov radiation cone.

$$P_i'(\omega, v_{11}) = K F_i'(\Omega) \quad (6)$$

where

$$K = \frac{e^2 \mu_0}{4\pi} \omega_H^2$$

$$\text{and} \quad F_i'(\Omega) = \frac{\Omega |(\mu_i^2 - \epsilon_1)(\alpha_{11}^2 - \epsilon_1) - \epsilon_2^2|}{|\epsilon_1(\mu_1^2 - \mu_2^2)|} \quad I_i^2 = F_i(\Omega) I_i^2$$

Now, differentiating eq. (5), we rewrite

$$\frac{dP_s}{dv_{11}} = P_i'(\omega, v_{11}) v_{11} f^2(v_{11})$$

Therefore, we find that the individual electron power should be multiplied by the square of the distribution function. This is consistent with the arguments of Panofsky and Phillips (1962), who have argued that electron beams radiate coherently and the radiated power is proportional to N^2 rather than N . Recently, Yip (1970) has also argued that the electrons in the stream radiate coherently.

The polar diagram of synchrotron radiation shows that the equatorial radiated power can be received on the equator (Singh and Singh 1968). We have shown that radiofrequency waves could also be received on the ground in the auroral region and corresponding geometry has been drawn. Of course, for the radio-frequency wave generation by synchrotron process, one needs high energy electrons. In the magnetosphere, high energy electrons are few in number. But

the proposed study may be very much useful in the case of artificial injection of relativistic electron beams. The artificial injection of low energy electron beam has been studied by Bell (1968), Etcheto and Gendrin (1970), Mead *et al* (1969). To explain the experimental observations made at College, Alaska, Wang and Kim (1970) have calculated synchrotron radiated power from auroral electrons of 30 KeV energy range and claim that their results are in good agreement with the experimental observations.

In the calculation of single particle radiation, one assumes that the parallel and perpendicular components of the particle velocity are constant. But, for the most part of the observed natural phenomena, in this frequency range, the velocity components are continuously changing during the phenomena. To take account of this, one has to consider the distribution of particles in energy and pitch angle and one has to take account of collective behaviour of the particles. The study of collective behaviour of the particle includes the study of linear and quasi-linear theory of wave-particle interaction. The role played by collective phenomena, in these processes, may be studied using the concept of amplification coefficients for the waves and diffusion coefficients for the particles. But the resonance condition which is used in the formulation of collective phenomena is the same as the radiation condition, in the individual particle radiation process. Therefore, the basic condition of the two approaches, namely individual particle and collective particle, is the same. One can use the single particle approach to study the phenomena in the first approximation, but to include the details of the time development of the phenomena, one has to use the collective approach. Therefore, the present study is justified in the first approximation. To complete the present study, we are studying the phenomena, using collective approach. The results will be presented in a forthcoming letter.

Apart from these basic processes discussed in this paper, there could be other processes which might operate in certain frequency regions. Two other competing candidates could be bremsstrahlung radiation in the high frequency region and the plasma oscillation and conversion into electromagnetic waves. The former process is a potential source of VHF and microwave radiation. The possibility of high frequency radiation by the conversion of plasma oscillation in the ionosphere has been discussed by d'Angelo (1970). However, the selection of cross-conversion coefficient seems to play a decisive role in ascertaining the role of this process and this has been chosen arbitrarily. Although the contribution of such a mechanism is likely to supplement the basic processes discussed in this paper.

Acknowledgments

We are thankful to Dr. R. Gendrin for the comments, valuable suggestions and discussions. The financial support given by Physical Research Laboratory, Ahmedabad, to one of us (R.P.S.) is gratefully acknowledged.

References

- Beghin C 1967 *Ann. Geophysique* **23** 275
- Bekefi G 1966 *Radiation Processes in Plasmas*. John Wiley & Sons, Inc.
- Bell T F 1968 *J. Geophys. Res.* **73** 4409
- Berky T F and Parthasarathy R 1964 *J.A.T.P.* **26** 936
- Coronity F V and Kennel C F 1970 *J. Geophys. Res.* **75** 1279
- D'Angelo 1970 *ESRIN-Internal Note* 102
- Dowden R L 1961 *J. Geophys. Res.* **66** 1587
- Dowden R L 1970 *CIRES Preprint* 47. University of Colorado, Boulder Colorado
- Dyoe R B and Nakada M P 1959 *J. Geophys. Res.* **64** 1163
- Dyoe R B and Horowitz S 1963 *J. Geophys. Res.* **68** 713
- Ellis G R A 1964 *Nature* **204** 17
- Etcheto J and Gendrin R 1970 *Planet-Space Science* **18** 777
- Etcheto J, Gendrin R and Lemaire D 1971 *J.G.R.* **76** 1079
- Fortini J, Garcia C, Gay M and Glover F 1966 *J.G.R.* **71** 1936
- Furutani Y 1968 *Rayonnement d'une particule chargée dans un magnetoplasma sur des modes a indice de refraction eleve*, Ph.D. Thesis, Orsay.
- Gendrin R 1961 *Planet-Space Science* **5** 274
- Gendrin R 1967 *Space Sc. Rev.* **7** 314
- Gendrin R 1970 *Space Sc. Rev.* **11** 54
- Gendrin R, Berthoumer C, Cory M, Meyer A, Sukhera B and Vigneron J 1970a *J. Geophys. Res.* **75** 6153
- Gendrin R, Etcheto J and B. de la Porte de Vaux 1970b *J.G.R.* **75** 6169
- Gurnett D A 1966 *J. Geophys. Res.* **71** 5599
- Gurnett D A 1968 *J.G.R.* **73** 1096
- Harang L 1968 *J.A.T.P.* **30** 1143
- Hartz T R 1964 *Nature* **203** 173
- Helliwell R A 1965 *Whistlers and related ionospheric phenomena*, Stanford University Press, Stanford, Calif.
- Helms W J and Turtle J P 1964 *Stanford Electronic Lab. Tech. Rept.* 30408-2
- Hower G L and Dunlop F C 1966 *J. Geophys. Res.* **71** 1512
- Jorgensen T S 1966 *J.G.R.* **71** 1367
- Kimura I 1967 *Planet Space Sc.* **15** 1427
- Kitamiura T, Jacobs J A, Watanake T and Flinly R B Jr 1969 *J. Geophys. Res.* **74** 5652
- Kurdymov V N 1966 *Soviet Phys. Tech. Phys* **10** 1370
- Kleimenova N, Troitskaya V A, Dassac M, Gendrin R, Ponsot C and Vigneron J 1966 *Ann. Geophys.* **22** 519
- McKenzie J F 1963 *Phil. Trans. Roy. Soc. London* **255** 585
- McKenzie J F 1967 *Phys. Fluids* **10** 2680
- Mead G D, Mead J M and Davis T N 1969 *Tech. Report, N.G.S.F.* no° X-641-69
- Ochs G R 1964 *J. Geophys.* **69** 1014
- Ochs G R 1966 *Radiation trapped in the earth's magnetic field*, Ed. by Billy M McCormac, 703-713
- Ochs G R, Farley D T and Boweles K L 1963 *J.G.R.* **68** 701
- Panofsky W K H and Phillips M 1962 *Classical Electricity and Magnetism*, Addison Wesley Publishing Co., Reading, Mass
- Parks G K, Coronity F V, McPherson R L and Anderson K A 1968 *J Geophys Res.* **73** 1685
- Peterson A M and Hower G L 1966 *Radiation trapped in the earth's magnetic field*, Ed. by Billy M McCormac 714-754.
- Ramaty R and Ligenfelter R E 1967 *J. Geophys R.* **72** 879

- Schwinger J 1949 *Phys. Rev.* **75** 1912
- Singh R P 1969 *Study of natural generation of electromagnetic waves in the magnetosphere and some related problems, Ph.D. Thesis, Banaras Hindu University, India*
- Singh R P 1973a *Ann. Geophys.* **29** 227
- Singh R P 1973b *Planet. Space Sci.* **21** 1268
- Singh R N and Singh R P 1968 *Ann. Geophysique* **24** 991
- Singh R N and Singh R P 1969a *Ann. Geophys.* **25** 629
- Singh R P and Singh R N 1969b *Ann. Geophys.* **25** 639
- Singh R P and Singh R N 1970 *J. Scientific Res. (B.H.U.)*
- Singh R P, Misra K D and Singh R N 1969 *Proceedings 11th Symp. on cosmic rays, Astrophysics, Geophysics and elementary particle Physics* vol. II 414
- Singh R P, Misra K D and Singh R N 1971 *J.A.T.P.* **33** 825
- Shukla P K and Singh R N 1970 *Int. J. Electronics* **29** 369
- Shukla P K, Singh R P, Singh K P and Singh R N 1974 *Int. J. Elect.* **36** 393
- Trulsen J and Fejer J A 1970 *J. Plasma Phys.* **4** 825
- Vasecky J F 1969 *J. Geophys. Res.* **74** 3628
- Vernov S N, Gorchakov E V, Kuznetsov S N, Logachev Yu. I, Sosnovets E N and Stalrovsky V G 1969 *Rev. Geophys.* **7** 257
- Watari N and Kamiyama H 1969 *Report Ionosphere and Space Research, Japan* **23** 270
- Wang C S and Kim J 1970 (Abstract) *Gupper atmospheric and electric field symposium, Boulder.*
- Westfold K C 1959 *Astrophys. J.* **130** 241
- Yip W K 1970 *Aust. J. Phys.* **23** 161

Amplitude modulation in cosmic-ray and K_p -index 27-day variations

F EL Bedewi, A Goned, S A Wahab and A A Farag

Physics Department, Faculty of Science, Ain Shams University, Cairo

Received 7 August 1978

Abstract. The 27-day amplitudes of cosmic-rays, planetary geomagnetic K_p -index, and relative sunspot numbers have been studied for the 1965-1969 period. The amplitude modulation for these parameters is found to be characterized by two basic periodicities of 130 ± 8 and 320 ± 46 days. The significance of these periodicities is discussed and their interaction with the main 27-days one and its second harmonic is investigated in relevance to additional periodic variations observed in cosmic ray intensity and geomagnetic activity.

1. Introduction

Several investigations have shown that periodicities other than the well known 27- and 13.5 day ones exist in the ranges 23-21 and 9-4 days for both cosmic rays and geomagnetic activity (Dorman and Shatashvili 1961, Shapiro and Ward 1966, Patel and Chasson 1968, Dyring *et al* 1970). A study by Abdel-Wahab and Goned (1974) of the additional periodicities of 9-4 days in K_p -index has shown that they relate to variations in the interplanetary magnetic field structure which modulate the geomagnetic activity during years of minimum and decreasing phases of solar activity. However, the additional periodicities reported for periods of increasing and maximum phases are not yet thoroughly analysed for both cosmic rays and geomagnetic activity.

In the present work, a study is made of the 27-day amplitude modulation (AM) in cosmic rays, geomagnetic and solar activities through the 1965-1969 period of increasing phase of solar activity. The aim of the study is to relate the additional periodicities to few fundamental frequencies which modulate the 27-day amplitudes and to investigate the relationship with solar sources affecting interplanetary magnetic field conditions. The data used are the mean daily cosmic-ray intensity (CR) recorded at Deep River and the daily sums of K_p -index, while the solar activity is represented by the daily values of Zurich sunspot numbers (RSN).

2. Method of Data Analysis

The day-to-day amplitudes and phases of the 27-day periodicity have been extracted applying the method of complex demodulation (see Ables *et al* 1965,

Goned and Wahab 1973). Briefly, the method consists of shifting the input time series by a frequency $\omega = 1/27$ cpd and then applying a low-pass filter to produce an output series $c(t, \omega)$. The filter used was designed according to the method given by Behannon and Ness (1965). The amplitudes and phases are then calculated from the relations

$$\begin{aligned} A_{27}(t) &= 2 |c(t, \omega)| \\ \phi_{27}(t) &= -\arg[c(t, \omega)]. \end{aligned} \quad (1)$$

Power spectra are then calculated for the amplitudes using a Hanning window to eliminate side lobes in the spectral density $p(f)$ around frequency f as much as possible. For such spectra, the frequency resolution is $\frac{1}{2}M\Delta T$, where M is the chosen maximum lag and ΔT is the sampling time interval.

3. Power Spectra of 27-day Amplitudes

Figure 1 presents the power spectra of the amplitudes $A_{27}(t)$ for the different concerned parameters, for frequencies up to 1/100 cpd. Beyond this frequency, the power drops considerably and no significant peaks are revealed. The 0.7 and 0.3 probability limits (dotted lines) of obtaining power spectral density $p(f)$ at the used resolution have been calculated following the method of Martinic *et al* (1971).

Beside the characteristic long trend densities, the important conclusions that can be drawn from Figure 1 are :

- (a) Peaks at 366 and 275 days show for the amplitudes of K_p -index and CR, respectively. Since these periodicities are most probably the result of the same mechanism and because they differ by only one lag number, the mean of their periods has been calculated as 320 ± 46 days. No similar peak is observed in RSN.
- (b) For all parameters, a broad peak covering the range 122–136 days with mean at 130 ± 8 days is revealed.

The existence of the latter period in the amplitudes of RSN indicates that the responsible mechanism is the variation in density of active sources on the solar disk. The former periodicity is absent from RSN and is thus produced by a different mechanism, possibly the variability of modulating source strength or the annual modulation due to earth's rotation.

4. The interaction between Modulation and 27-day frequencies

To interpret the observed features of 27-day variation and its AM in the different parameters, a phenomenological approach may be based on the idea of an interaction between the main 27-day frequency and some other fundamental frequencies which are independent of the solar rotation. We therefore assume

that there exists an ideal active region located on the solar disk that is capable of modulating the cosmic ray primaries by a frequency ω_1 , equal to 1/27 cpd and characterized by,

- A variable density on the solar disk which is periodic by a frequency ω_2 .
- A source activity varying with frequency ω_3 .
- All 11-year variation with frequency ω_{11} .

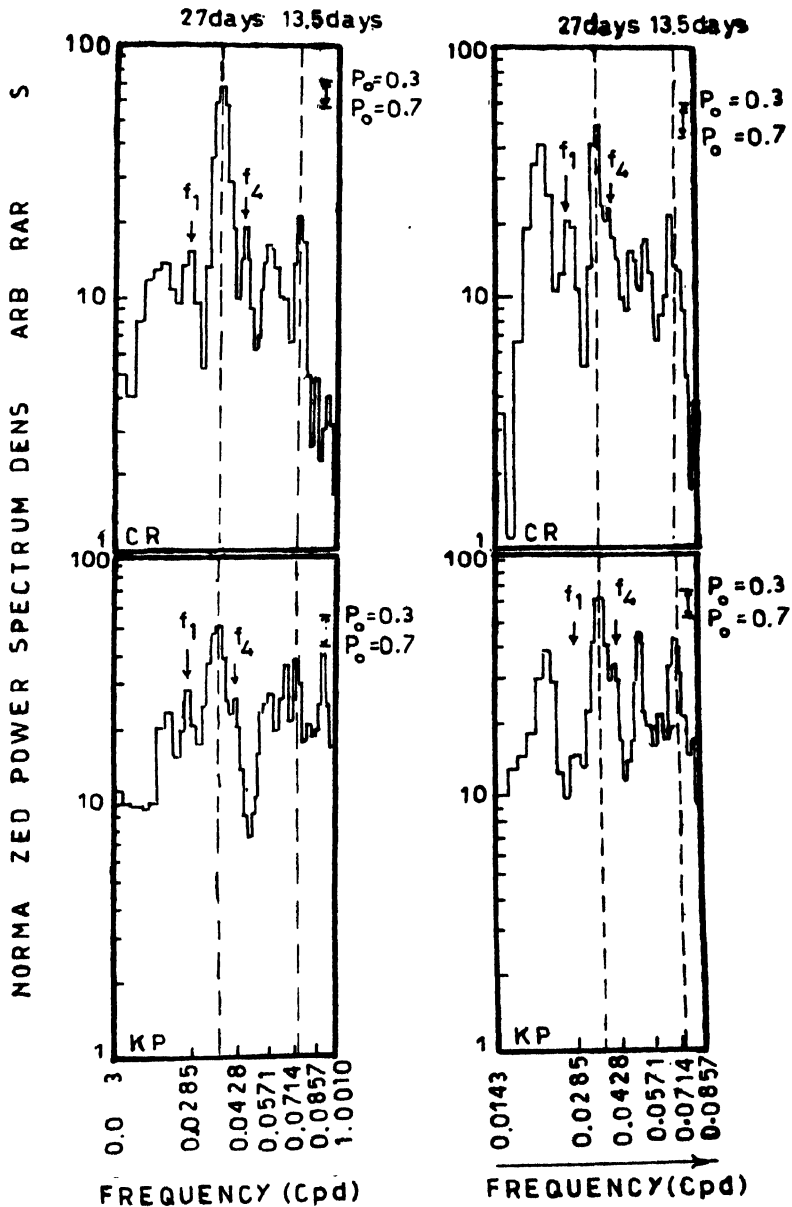


Figure 1

Accordingly, the observed cosmic-ray (or K_p -index) 27-day amplitude may be represented as :

$$A = A_0[1 + \alpha \cos(\omega_2 t + \phi_2) + \beta \cos(\omega_3 t + \phi_3) + \gamma \cos(\omega_{11} t + \phi_{11})] \cos(\omega_1 t + \phi_1) \quad (2)$$

where the ϕ 's are phases and A_0 , α , β and γ are coefficients corresponding to the different processes.

The above representation predicts six additional frequencies. With contributions smaller than the main 27-day one in CR- and K_p -parameters. Since the 11-year variation has a frequency negligible compared to ω_1 , then within power spectral resolution only four side-band frequencies would be observable in CR and K_p -index power spectra. The 27-day amplitude in RSN responds only to the variable persistence of active regions on the solar disk and only two additional frequencies are expected to appear in its spectrum.

5. Comparison of Predictions with Observations

The detected periodicities for the AM of the 27-day variation with lengths 130 ± 8 and 320 ± 46 days have been taken to correspond to the frequencies ω_1 and ω_3 in expression (2), respectively. The additional periodicities predicted in the spectra of CR and K_p -index are given in table 1. The given limits correspond to the errors in ω_1 , ω_2 and ω_3 .

Table 1. Periodicities Predicted in CR and K_p -index spectrum.

Frequency (cpd)	F_1	F_2	F_0	F_3	F_4
	0.0293	0.0339	0.0370	0.0402	0.0447
Period (days)	34.13 ± 2	29.50 ± 1.5	27.0 ± 1	24.88 ± 1	22.37 ± 1

In order to check the present predictions, power spectra have been calculated for the raw data of CR and K-index for two periods, namely 1967-1968 and 1968-1969, the division being for the purpose of checking the stationarity of the investigated periodicities over the whole increasing phase of solar activity. The obtained spectra are given in figures (2a, b) for the frequency range 0.014 to 1.0 cpd. The 27- and 13.5-day peaks as well as some additional ones are seen to be common to both CR and K_p -index spectra and to persist in both investigated periods. Of particular interest in the calculated spectra are the two peaks around the 27-day one marked f_1 and f_4 . The periodic lengths corresponding to these two peaks are given in table 2.

Comparison of tables 1 and 2 shows that in general the observed peaks f_1 and f_4 correspond, within power spectral resolution, to the predicted periodicities F_1 and F_4 , respectively. Such agreement between predictions and observations

Table 2. Periodic lengths (days) for peaks f_1 and f_4 observed in CR and K_p -index spectry (figure 2).

Investigated period		1967-1968	1968-1969
f_1	CR	35.1	35.1
	K_p	35.7	34.5
f_4	CR	23.3	24.0
	K_p	23.8	24.0

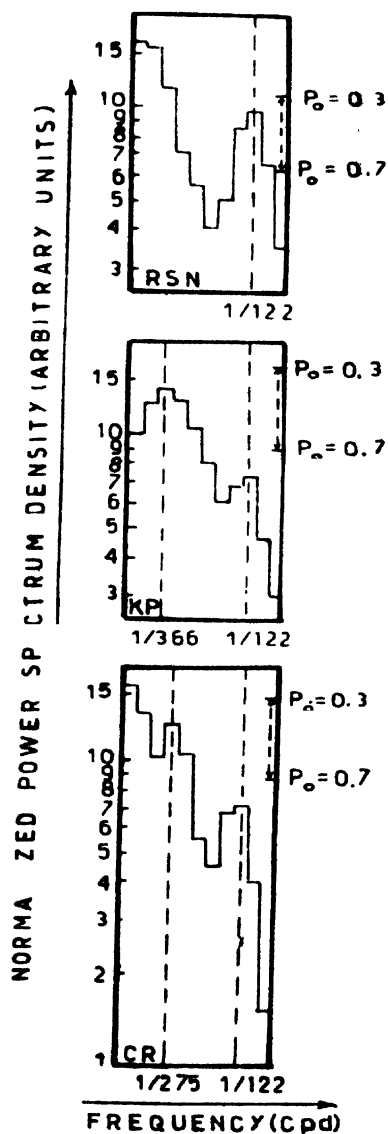


Figure 2.

may be taken as an evidence for the persistence of the 130 ± 8 day modulating periodicity. This is in agreement with the work of Dorman (1963) according to which corpuscular streams originating from dense sunspot zones can persist for several solar rotations.

In spite of the significant contribution of ω_3 to the AM of the concerned parameters, the resulting periodicities F_2 and F_3 were not observed in the spectra of figure (2). This could be due to the limitations imposed by the frequency resolution. Further investigation of this point has been done by calculating the spectra for the whole period 1965–1969, thus increasing the frequency resolution. Some evidence for the resolving of the peaks F_2 and F_3 has been obtained from this analysis, indicating the necessity of long data periods (5 years or more) for their proper identification.

With regard to the relative contribution of the frequency ω_2 to CR 27-day variation, this was calculated by taking the mean power density of f_1 and f_4 to be proportional to $(\alpha A_0/2)^2$. The resulting value of α is 1.14, i.e. the amplitude of ω_2 is 57% of the 27-day amplitude.

It should be noted that an AM in the 13.5 period similar to that of the 27-day one is expected on the basis of the present approach. In fact, some indication as to the presence of side lobes around the 13.5-day peak in the range 12.6–15.6 days is present as shown in figure (2). Quantitative analysis of these peaks will be given in a later publication.

6. Conclusions

The present analysis of the periodic variations additional to the 27- and 13.5 day periodicities in cosmic ray intensity and geomagnetic and solar activity parameters shows that they could be related to three fundamental periodic solar phenomena. These are concerned with a variable density of active spots on the solar disk with a period of 130 ± 8 days, a variable activity of spots with a period of 320 ± 46 days, i.e., a possible annual variation, together with the well known 11-year variation of solar activity. The possible interaction of these modulating frequencies with the 27- and 13.5-day main periodicities is reflected on the intensity of corpuscular streams constituting the solar wind, thus producing the observed modulation. Such mechanism is capable of interpreting additional periodicities in the ranges 34–22 days and 15.6–12.6 days in cosmic ray and K_p -index spectra.

References

- Ables J G, McCracken K G and Rao U R 1966 *Proc. 9th Int. Conf. on Cosmic Rays, London*, 1965, vol 1 pp 208
 Abdel-Wahab C and Goned A 1974 *Planet. Space Sci.* **3** 537

- Behannon K W and Ness N F 1965 *Scientific Report*. X-612-65 276 *Goddard Space Flight Centre*, Greenbelt, Maryland
- Dorman L I 1963 *Cosmic Ray Variations* Moscow, Eng. Trans. by Tech. Liaison Office, Wright. Patterson Air Force Base, Ohio.
- Dorman L I and Shatashvili L K 1961 *Results of IGY* Moscow, No. 4
- Dyring E, Hauska H and Kangedal B 1970 *Acta Phys. Hung.* Suppl. 2209
- Goned A and Wahab S 1973 *J. Nat. Sci. Math.* (W Pakistan) 13 155
- Martinic N, Lindgren S and Abdel-Wahab S 197 *Scientific Report* UU/CRG 71-2, Uppsala University
- Patel V L and Chasson R L 1968 *Canad. J. Phys.* 65 966
- Shapiro R and Ward F W 1966 *J. Geophys. Res.* 71 2385

A precise vibrational analysis of the A-X system of aluminium monochloride molecule

Ram Samujh Ram, S. B. Rai, D. K. Rai and K. N. Upadhyya

Laser and Spectroscopy Laboratory, Department of Physics, Banaras Hindu University, Varanasi-221005, India.

Received 18 March 1978.

Abstract. A high resolution spectrum of the A-X system of aluminium monochloride molecule has been obtained in the third order of a 10.6 meter concave gratings spectrograph (reciprocal dispersion $\sim 0.22 \text{ \AA/mm}$). The *R* and *Q* heads due to both the isotopic molecules AlCl^{35} and AlCl^{37} could be detected and measured precisely. Some new bands belonging to the $\Delta v = -6, -7$, and -8 sequences have been observed. The vibrational analysis for both the isotopic molecules has been carried out. It is found that the present constants for the lower state are in very good agreement with the constants reported by Wyse and Gordy (1972) from the analysis of the microwave spectrum. The vibrational constants for the excited state have been modified as compared to the values reported earlier.

1. Introduction

The spectrum of aluminium monochloride molecule has been a subject of study by several workers (Jovons 1913, 1924, Mahanti 1934, Bhaduri & Fowler 1934, Mischer 1936, Holst 1935, Chaudnury & Upadhyya 1968, Wyse & Gordy 1972). The high resolution studies of the A-X system of this molecule reported earlier by Holst (1935) and by Chaudhury & Upadhyya (1968)₂ have been shown to be in error. This prompted us to rephotograph this spectrum and reanalyse the rotational structure (Ram Samujh Ram *et al* 1977). During this study we observed that *R* and *Q* heads for both the isotopic molecules are well resolved in our spectrum. On comparison with the earlier studies of the vibrational analysis it was found that for some of the bands the earlier measurements are inaccurate and in many bands the isotopic heads are not observed. In addition several new bands belonging to the $\Delta v = -6, -7$ and -8 sequences were detected on our plates. In some bands a part of the rotational structure is overlapped to such an extent that it appears almost as a broad patch with no discernible features. These were not reported by previous workers. Therefore we re-analysed the vibrational structure of these bands using the high resolutions measurement of the *Q* heads, for both the isotopic molecules. Since a large number of bands have been observed, least square procedure could be used to

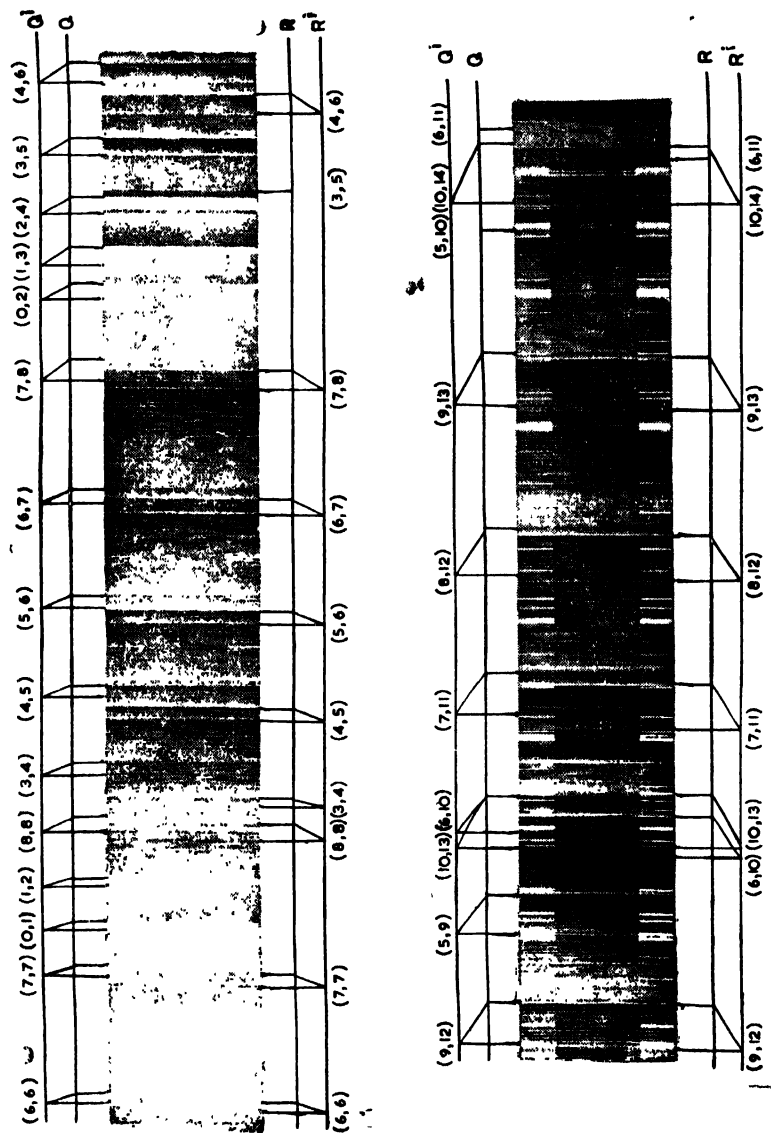


FIG.1. HIGH RESOLUTION SPECTRUM OF THE A-X SYSTEM OF AlCl_3 MOLECULE

determine the precise vibrational constants e.g. ω_e , $\omega_e x_e$, $\omega_e y_e$ and $\omega_e z_e$. Our lower state constants agree very well with the microwave constants reported by Wyse & Gordy (1972), resulting in appreciable differences between the constants for the excited state determined by us and the previously reported values. These new constants reproduce the observed wave numbers with an accuracy of $\pm 0.1 \text{ cm}^{-1}$. The details of the experimental procedure have already been given in our previous paper (Ram Samujh Ram *et al* 1977).

2. Study of the plates

The structure consists of both red and violet degraded bands. A few headless bands are also seen. It is difficult to mark the exact position of heads in the regions where there is reversal of shading.

This system is well established to be due to a $^1\Pi-1\Sigma$ transition and the structure will have two heads one *R* or *P* head and the other *Q* head. The *Q* head will lie very close to the origin. We have used natural AlCl_3 in which chlorine has two isotopes ^{35}Cl and ^{37}Cl with their percentage abundances as 75.6% and 24.4% respectively. Therefore, both the isotopic molecules Al^{35}Cl and Al^{37}Cl are expected to contribute to the spectrum. Now if both the isotopes are contributing to the spectrum, the number of heads in the structure should be four. In fact our high resolution spectrum shows the presence of four heads in most of the bands in the structure which could be easily marked in the spectrogram (see the figure 1). In the (0-0) band in which the vibrational isotopic shift will be minimum there are only two heads. The relative intensity of the *R* and the *Q* heads shows wide fluctuations. The *Q* head which will always be close to the origin appears to be the more intense one in the region where there is reversal of shading. In other regions the *R* head is more intense. The intensity of the isotopic head is almost one third of the intensity of the main head and there is no trouble in identifying it.

Vibrational Analysis and Isotopic Shift

The sequence structure is quite well developed and the vibrational analysis can be carried out in a straight forward manner. Since the position of the band origins could not be marked for all the observed bands while the *Q* head could be identified and measured accurately, we have used these for the vibrational analysis. The previous analyses have been made using the *R* heads measured from low resolution spectrogram in which the *Q* heads were not clearly resolved for all the bands.

The vibrational quantum assignment has been made in the usual way. The frequency of a transition can be given as

$$\nu_{v'',v'''} = \nu_0 + G'(v') - G''(v'') \quad (1)$$

where

$$G(v) = w_e(v + \frac{1}{2}) - w_e x_e(v + \frac{1}{2})^2 + w_e y_e(v + \frac{1}{2})^3 + w_e z_e(v + \frac{1}{2})^4 + \dots \quad (2)$$

where the different terms have their usual meanings. In order to determine the vibrational constants, the bands were arranged in the Deslandres scheme from which $\Delta G(v + \frac{1}{2})$ values for different v -values become known. These $\Delta G(v + \frac{1}{2})$ values were used in a least squares procedure to determine the vibrational constants making use of the following equation

$$\Delta G(v + \frac{1}{2}) = w_e - w_e x_e[2(v + \frac{1}{2}) + 1] + w_e y_e[3(v + \frac{1}{2})^2 + 3(v + \frac{1}{2}) + 1] + w_e z_e[2(v + \frac{1}{2}) + 1][2(v + \frac{1}{2})^2 + 2(v + \frac{1}{2}) + 1] + \dots \quad (3)$$

This equation can be represented in a simple form as

$$\Delta G(v + \frac{1}{2}) = w_e - A w_e x_e + B w_e y_e + C w_e z_e. \quad (4)$$

This equation (4) is solved by the least squares procedure for w_e , $w_e x_e$, $w_e y_e$ and $w_e z_e$ using the various ΔG values obtained from our experimental measurements. We find that for Al^{35}Cl ,

$$\Delta G(v' + \frac{1}{2}) = 453.807 - 4.753A - 0.256B + 0.003C \quad (5)$$

and

$$\Delta G(v'' + \frac{1}{2}) = 481.337 - 2.07A + 0.0057B + \dots \quad (6)$$

For Al^{37}Cl ,

$$\Delta G(v' + \frac{1}{2}) = 448.43 - 4.64A - 0.243B + 0.0092C \quad (7)$$

and

$$\Delta G(v'' + \frac{1}{2}) = 475.33 - 1.98A + 0.0037B + \dots \quad (8)$$

The molecular constants, thus obtained for both the states in both the molecules are given in Table 2.

Table 1.

v', v''	Head	Mahanti (Å)	Bhaduri and Fowler (Å)	Present		Isotopic Shift	
						obs.	calc.
				(Å)	(cm ⁻¹)	(cm ⁻¹)	(cm ⁻¹)
2, 0 *	R	2555.44	2555.46	2555.50	39119.55		
	R ⁱ		2556.07	2556.12	39110.07	9.48	
	Q	2556.35	2556.28	2556.25	39108.08		9.72
	Q ⁱ		2556.87	2556.85	39098.75	9.33	
3, 1 *	R	2559.87	2559.60	2559.56	39057.50		
	R ⁱ		2560.16	2560.10	39049.28	8.22	
	Q	2560.34	2560.16	2560.10	39049.28		8.62
	Q ⁱ		2560.75	2560.68	39040.42	8.86	
4, 2 *	R	2564.36	2564.27	2564.22	38986.53		
	R ⁱ		2564.74	2564.72	38978.93	7.60	
	Q	2564.82	2564.76	2564.72	38978.93		7.25
	Q ⁱ		2565.27	2565.21	38971.48	7.45	

v', v''	Head	Mahanti (Å)	Bhaduri and Fowler (Å)	Present		Isotopic Shift	
				(Å)	(cm ⁻¹)	obs.	calc.
						(cm ⁻¹)	(cm ⁻¹)
5, 3 *	R	2569.78	2569.63	2569.59	38905.06		
	R'		2570.02	2569.96	38899.56	5.50	
	Q	2570.03	2570.02	2569.96	38899.56		5.27
	Q'		2570.40	2570.32	38894.16	5.40	
6, 4 *	R		2575.74	2575.64	38813.68		
	R'			2575.88	38810.06	3.62	3.48
1, 0 *	R	2582.76	2583.01	2582.91	38704.44		
	R'		2583.37	2583.27	38699.05	5.39	
	Q	2584.47					4.89
	Q'		2584.70				
2, 1 *	R	2586.55	2586.72	2586.67	38648.18		
	R'		2586.98	2586.91	38644.60	3.58	
	Q	2587.77	2587.88	2587.80	38631.31		4.11
3, 2	R	2590.71	2590.81	2590.87	38585.53		
	R'		2591.02	2591.01	38582.50	3.03	
	Q	2591.55	2591.64	2591.60	38574.66		3.11
4, 3	R	2595.35	2595.42	2595.44	38517.66		
	R'		2595.52	2595.54	38516.11	1.55	
	Q	2596.00	2596.04	2596.06	38508.53		1.54
5, 4	R	2600.58	2600.67	2600.68	38440.02		
	Q	2601.06	2601.14	2601.14	38433.20		0.21
6, 5	R	2606.54	2606.68	2606.66	38351.81		
	Q	2606.92	2607.06	2607.05	38346.08		-1.75
0, 0	R	2611.02	2610.22	2610.23	38299.42		
	Q	2614.03	2614.44	2614.48	38237.05		-0.17
1, 1	R'			2614.62	38235.36	-0.74	
	R	2614.50	2614.44	2614.65	38234.62		-0.71
	Q'			2616.84	38202.63	-0.73	
	Q	2616.80	2616.77	2616.89	38201.90		
2, 2	R'			2618.09	38184.39	-1.39	
	R	2618.15	2618.10	2618.18	38183.00		-1.40
	Q'		2619.89	2619.85	38158.74	-1.42	
	Q	2619.80	2619.98	2619.94	38157.32		
3, 3	R'		2622.24	2622.20	38124.54	-2.32	
	R	2622.15	2622.40	2622.36	38122.22		-2.32
	Q'		2623.41	2623.37	38107.54	-2.34	
	Q	2623.39	2623.54	2623.53	38105.20		
4, 4	R'	2626.66	2626.74	2626.71	38059.01	-3.58	
	R	2626.92	2627.00	2627.03	38055.43		-3.51
	Q'		2627.55	2627.54	38047.11	-3.43	
	Q	2627.74	2627.82	2627.77	38043.68		

ν', ν''	Head	Mahanti (Å)	Bhaduri and Fowler (Å)	Present		Isotopic Shift	
						obs.	calc.
				(Å)	(cm ⁻¹)	(cm ⁻¹)	(cm ⁻¹)
5, 5	<i>R</i> ⁱ	2631.74	2631.83	2631.80	37985.48	-5.08	
	<i>R</i>	2632.11	2632.19	2632.15	37980.40		-5.03
	<i>Q</i> ⁱ		2632.46	2632.37	37977.26	-5.08	
	<i>Q</i>	2632.70	2632.80	2632.72	37972.18		
6, 6	<i>R</i> ⁱ	2637.54	2637.59	2637.60	37902.03	-6.97	
	<i>R</i>	2638.01	2638.10	2638.08	37895.06		-6.90
	<i>Q</i> ⁱ		2638.10	2638.01	37896.07	-6.98	
	<i>Q</i>	2638.46	2638.55	2638.50	37889.59		
7, 7]	<i>R</i> ⁱ	2644.23	2644.22	2644.23	37806.93	-9.15	
	<i>R</i>	2644.85	2644.92	2644.87	37797.78		-9.18
	<i>Q</i> ⁱ			2644.58	37801.93	-9.17	
	<i>Q</i>	2645.18	2645.25	2645.22	37792.76		
8, 8	<i>R</i> ⁱ	2651.91		2651.94	37697.02	-11.90	
	<i>R</i>	2652.76		2652.78	37685.12		-11.93
	<i>Q</i>	2653.00					
0, 1]	<i>Q</i> ⁱ		2647.08	2647.08	37766.23	-6.29	
	<i>Q</i>		2647.50	2647.52	37759.94		-5.81
1, 2	<i>Q</i> ⁱ		2649.30	2649.35	37733.87	-6.03	
	<i>Q</i>		2649.73	2649.76	37727.81		-6.23
3, 4]	<i>R</i> ⁱ	2653.58	2653.68	2653.62	37673.16	-7.65	
	<i>R</i>	2654.14	2654.21	2654.16	37665.51		-7.75
	<i>Q</i> ⁱ	2655.34	2655.54	2655.40	37647.91	-7.76	
	<i>Q</i>	2655.89	2656.03	2655.95	37640.15		
4, 5	<i>R</i> ⁱ	2658.16	2658.31	2658.24	37607.69	-8.69	
	<i>R</i>	2658.80	2658.92	2658.85	37599.00		-8.75
	<i>Q</i> ⁱ	2659.42	2659.46	2659.37	37591.71	-8.64	
	<i>Q</i>	2660.03	2660.06	2659.98	37583.07		
5, 6	<i>R</i> ⁱ	2663.26	2663.35	2663.31	37536.10	-10.19	
	<i>R</i>	2664.00	2664.08	2664.03	37525.91		-10.17
	<i>Q</i> ⁱ		2664.08	2664.07	37525.40	-10.20	
	<i>Q</i>	2664.76	2664.84	2664.77	37515.60		
6, 7	<i>R</i> ⁱ	2668.97	2669.10	2669.05	37455.38	-11.97	
	<i>R</i>	2669.81	2669.93	2669.90	37443.41		-11.96
	<i>Q</i> ⁱ			2669.58	37447.94	-11.90	
	<i>Q</i>	2670.40	2670.47	2670.42	37436.04		
7, 8	<i>R</i> ⁱ	2675.58	2675.70	2675.63	37363.27	-14.18	
	<i>Q</i> ⁱ	2676.02	2676.13	2676.02	37357.83	-14.01	-14.15
	<i>R</i>	2676.58	2676.71	2676.65	37349.09		
	<i>Q</i>	2677.00	2677.12	2677.02	37343.82		
0, 2	<i>Q</i> ⁱ		2680.29	2680.31	37298.04	-11.46	
	<i>Q</i>		2681.10	2681.13	37286.58		-11.32
1, 3	<i>Q</i> ⁱ		2682.26	2682.33	37270.23	-11.67	
	<i>Q</i>		2683.11	2683.15	37258.56		-11.87

v', v''	Head	Mahanti (Å)	Bhaduri and Fowler (Å)	Present		Isotopic Shift	
						obs.	calc.
				(Å)	(cm ⁻¹)	(cm ⁻¹)	(cm ⁻¹)
2, 4	Q^1		2684.82	2684.83	37235.28	-12.41	
	Q		2685.68	2685.72	37222.87		-12.41
3, 5	R			2686.08	37217.92		
	Q^1			2687.93	37192.31	-12.78	
	Q			2688.85	37179.53		-12.89
4, 6	R^1	2690.02	2690.13	2690.07	37162.72	-13.85	
	R	2691.04	2691.12	2691.07	37148.87		-13.90
	Q^1	2691.68	2691.80	2691.74	37139.68	-13.85	
	Q	2692.68	2692.80	2692.74	37125.83		
5, 7	R^1	2695.19	2695.31	2695.11	37093.23	-15.13	
	R	2696.30	2696.39	2696.21	37078.10		-15.23
	Q^1		2696.39	2696.21	37078.10	-15.14	
	Q	2697.34	2697.43	2697.31	37062.96		
6, 8	R^1	2700.93	2701.04	2700.97	37012.76	-16.88	
	Q^1	2701.60	2701.70	2701.64	37003.58	-16.96	-16.92
	R	2702.15	2702.26	2702.20	36995.88		
	Q	2702.82	2702.94	2702.88	36986.62		
7, 9	R^1	2707.47	2707.56	2707.50	36923.49	-19.08	
	Q^1	2707.92	2707.97	2707.93	36917.63	-18.95	-19.02
	R	2708.84	2708.95	2708.90	36904.41		
	Q	2709.32	2709.41	2709.32	36899.08		
8, 10	R^1	2715.02	2715.11	2715.08	36820.42	-21.68	
	Q^1	2715.38		2715.40	36816.08	-21.55	-21.58
	R	2716.60	2716.73	2716.68	36798.74		
	Q	2716.96	2717.10	2716.99	36794.53		
9, 11	R^1	2723.90		2723.94	36700.66	-24.62	
	R	2725.68	2625.83	2725.77	36676.04		-24.63
	Q^1			2724.19	36697.29	-24.63	
	Q	2725.98	2726.06	2726.02	36672.66		
10, 12	R			2735.56	36531.39		
	Q			2728.78	36528.48		-28.24
4, 7	R^1			2723.20	36710.63	-18.86	
	R			2724.60	36691.77		-18.96
	Q^1	2724.54		2724.60	36691.77	-19.11	
	Q	2725.98		2726.02	36672.66		
5, 8	R^1	2727.42	2727.57	2727.48	36653.03	-20.14	
	R	2728.93	2729.07	2728.98	36632.89		-20.19
	Q^1		2729.07	2728.98	36632.89	-20.13	
	Q	2730.42	2730.58	2730.48	36612.76		
6, 9	R^1	2733.30	2733.43	2733.33	36574.58	-21.79	
	Q^1	2734.21	2734.35	2734.20	36562.95	-21.61	-21.79
	R	2734.91	2735.01	2734.96	36552.79		
	Q	2735.82	2735.92	2735.81	36541.34		

v', v''	Head	Mahanti (Å)	Bhaduri and Fowler (Å)	Present		Isotopic Shift	
						obs.	calc.
				(Å)	(cm ⁻¹)	(cm ⁻¹)	(cm ⁻¹)
7, 10	R^1	2739.77	3739.90	2739.86	36487.42	-23.78	
	Q^1	2740.47		2740.42	36480.00	-23.77	-23.80
	R	2741.56	2741.69	2741.65	36463.64		
	Q	2742.25	2742.28	2742.20	36456.25		
8, 11	R^1	2747.27	2747.42	2747.36	36387.82	-26.30	
	Q^1	2747.97		2748.04	36383.05	-26.83	-26.27
	R	2749.26	2749.45	2749.35	36361.52		
	Q	2749.76	2749.83	2749.71	36356.72		
9, 12	R^1	2756.10	2756.31	2756.21	36271.05	-29.19	
	R	2758.35	2758.49	2758.43	36241.86		-29.23
	Q^1			2756.38	36268.75	-29.19	
	Q	2758.66	2758.66	2758.60	36239.56		
10, 13	R^1			2766.67	36133.88	-33.00	
	R			2769.20	36100.88		-32.75
	Q			2769.30	36099.57		
5, 9	R^1			2760.30	36217.20	-25.09	
	R		2762.34	2762.29	36192.16		-25.07
	Q^1		2762.34	2762.29	36192.16	-25.12	
	Q		2764.21	2764.13	36167.04		
6, 10	R^1		2766.17	2766.07	36141.70	-26.66	
	Q^1		2767.43	2767.29	36126.03	-26.46	-26.57
	R		2768.16	2768.11	36115.04		
	Q		2769.33	2769.30	36099.57		
7, 11	R^1		2762.69	2762.63	36056.19	-28.53	
	Q^1		2773.42	2773.32	36047.19	-28.43	-28.49
	R	2774.81	2774.88	2774.83	36027.66		
	Q	2775.64	2775.64	2775.51	36018.76		
8, 12	R^1		2780.21	2780.13	35958.93	-30.92	
	Q^1			2780.54	35953.63	-30.77	-30.86
	R	2782.37	2782.57	2782.52	35928.01		
	Q		2783.10	2782.93	35922.86		
9, 13	R^1		2789.14	2788.93	35845.47	-33.53	
	Q^1			2789.20	35842.00	-33.50	-33.73
	R	2791.51	2791.60	2791.54	35811.94		
	Q		2791.94	2791.81	35808.50		
10, 14	R^1			2799.28	35713.00	-38.55	
	Q^1			2799.46	35710.65	-38.94	-37.16
	R			2802.30	35674.45		
	Q			2802.52	35671.71		
5, 10	Q		2798.28	2798.30	35725.45		-29.85
6, 11	R^1		2799.80				
	R		2803.32	3802.59	35683.50		-31.26
	Q		2803.37	2803.30	35661.74		
7, 12	R^1		2805.92	2805.85	35629.33	-33.19	
	Q^1		2807.08	2806.75	35617.90	-33.06	-36.08
	R		2808.50	2808.47	35596.14		
	Q		2809.57	2809.34	35584.84		

v', v''	Head	Mahanti (Å)	Bhaduri and Fowler (Å)	Present		Isotopic Shift	
						obs.	calc.
				(Å)	(cm ⁻¹)	(cm ⁻¹)	(cm ⁻¹)
8, 13	R'			2814.41	35520.97	-35.55	
	R			2817.23	35485.42		-35.37
	Q			2816.78	35491.08		
9, 14	R'			2822.17	35423.30	-37.54	
	Q'			2822.45	35419.79	-37.60	-38.15
	R			2825.16	35385.76		
	Q			2825.45	35382.19		
10, 15	R'			2832.45	35294.74	-43.06	
	Q'			2832.63	35292.50	-43.43	-41.48
	R			2835.91	35251.68		
	Q			2836.12	35248.67		
6, 12	Q			2837.81	35228.11		-35.86
7, 13	R			2842.53	35169.59		-37.58
	Q			2843.78	35154.13		
8, 14 *	Q'			2847.78	35104.77	-38.68	-39.78
	Q			2850.92	35066.09		
9, 15 *	R'			2855.66	35007.89	-43.71	
	Q'			2856.04	35003.23	-42.71	-42.47
	R			2859.23	34964.18		
	Q			2859.53	34960.51		
10, 16 *	Q'			2866.11	34880.26	-48.37	
	Q			2870.09	34831.89		-45.71
8, 15	Q'			2882.17	34685.90	-43.14	-44.10
	R			2885.14	34650.08		
	Q			2885.76	34642.76		
9, 16 *	Q'			2890.24	34589.07	-47.21	-46.70
	Q			2894.19	34541.86		
10, 17 *	Q'			2900.13	34471.11	-53.75	-49.85
	Q			2904.66	34417.36		
9, 17 *	Q'			2924.71	34181.43	-51.35	-50.85
10, 18 *	Q'			2934.80	34063.91	-57.33	-53.89
	Q			2939.75	34006.56		

* These bands are measured from our low resolution spectrogram.

The ν_e value which corresponds to the separation of the minimum of the potential curve of the upper state to the minimum of the potential curve of the

lower state was obtained from the relation

$$\begin{aligned} \nu_{0,0} = \nu_e + & \left(\frac{1}{2}\omega_e' - \frac{1}{4}\omega_e'x_e' + \frac{1}{8}\omega_e'y_e' + \frac{1}{16}\omega_e'z_e' + \dots\right) \\ & - \left(\frac{1}{2}\omega_e'' - \frac{1}{4}\omega_e''x_e'' + \frac{1}{8}\omega_e''y_e'' + \frac{1}{16}\omega_e''z_e'' + \dots\right) \end{aligned} \quad (9)$$

where $\nu_{0,0}$ is the frequency of the 0-0 band. The vibrational isotopic shift as calculated by the formula

$$\begin{aligned} \Delta\nu = \nu_{v',v''} - \nu_{v',v''}^i = & (1-\rho)[\omega_e'(v'+\frac{1}{2}) - \omega_e''(v''+\frac{1}{2})] \\ & - (1-\rho^2)[\omega_e'x_e'(v'+\frac{1}{2})^2 - \omega_e''x_e''(v''+\frac{1}{2})^2] \\ & + (1-\rho^3)[\omega_e'y_e'(v'+\frac{1}{2})^3 - \omega_e''y_e''(v''+\frac{1}{2})^3] + \dots \end{aligned} \quad (10)$$

where $\rho = \sqrt{\frac{\mu}{\mu^i}}$ is the ratio of the reduced masses of the two isotopic molecules and $w_e, w_e x_e$, and $w_e y_e$ etc. are the molecular constants, has been compared with the observed isotopic shifts in Table 1.

Table 2. Constants for the A-X system of Al^{35}Cl and Al^{37}Cl molecules

Constants	Bhaduri & Fowler (1934)	Wyse & Gordy (1972)	Present
Al^{35}Cl	w_e'	449.96	453.807
	$w_e'x_e'$	4.37	4.753
	$w_e'y_e'$	-0.216	-0.254
	$w_e'z_e'$	—	0.003
	w_e''	481.30	481.337
	$w_e''x_e''$	1.95	2.071
	$w_e''y_e''$	—	0.0057
	$w_e''z_e''$	—	—
	ν_e	38254.00	38251.517
Al^{37}Cl	w_e'		448.43
	$w_e'x_e'$		4.64
	$w_e'y_e'$		-0.243
	$w_e'z_e'$		0.0029
	w_e''	475.97	475.331
	$w_e''x_e''$	2.03	1.98
	$w_e''y_e''$		0.0037

3. Analysis and Discussion

The wavelengths of different bands corresponding to the two molecules as reported by different workers have been compared in Table 1. This clearly indicates that some of the earlier measurements contained appreciable errors even as regards their positions. The marked improvement in the regularity of our $\Delta G(v+\frac{1}{2})$ values as compared to the previous work clearly indicates the

superiority of our measurements. We could mark few new bands belonging to the $\Delta v = -6$, -7 and -8 sequences which were not observed by previous workers. These are shown in Table 1. We have calculated the isotopic shifts for these bands and found that the calculated and observed isotopic shifts agree very well confirming our assignments.

The molecular constants calculated in this way have been compared to previously reported values in Table 2. One can see from the table that for the lower state our values are in close agreement with the values reported by Bhaduri & Fowler (1934) and by Wyse & Gordy (1972). For the excited state our values differ appreciably from those reported by Bhaduri & Fowler (1934). We could also determine $\omega_e''y_e''$, $\omega_e'y_e'$ and $\omega_e'z_e'$ for the first time.

The calculated and observed isotopic shift have been compared in Table 1. It is found that the two values are in good agreement. We have also verified the molecular constants for the two isotopic molecules by using the isotopic relations $\omega_e(\text{Al}^{37}\text{Cl}) = \rho\omega_e(\text{Al}^{35}\text{Cl})$, $\omega_ex_e(\text{Al}^{37}\text{Cl}) = \rho^2\omega_ex_e(\text{Al}^{35}\text{Cl})$ etc.

Acknowledgment

One of us (RSR) is thankful to the University Grants Commission, New Delhi for financial assistance during the course of this work.

References

- Bhaduri B N & Fowler A 1934 *Proc. Roy. Soc. London* **A145** 321.
 Chaudhury A K & Upadhyaya K N 1968 *Ind. J. Phys.* **42**, 544.
 Herzberg G G 1950 *Spectra of Diatomic Molecules*, D. Van Nostrand Co., Inc., N.Y.
 Holst W 1935 *Z. f. Physik* **93**, 55.
 Jevons W 1913 *Proc. Roy. Soc. London* **A89**, 187.
 Jevons W 1924 *Proc. Roy. Soc. London* **A106**, 174.
 Mahanti P C 1934 *E. f. Physik* **88**, 550.
 Meischer E. 1936 *Helv. Phys. Acta* **9**, 693.
 Ram Samujh Ram, Rai S B Ram R. S. & Upadhyaya K N 1977 *J-de Chem. Phys.* (in press).
 Wyse F C & Gordy W 1972 *J. Chem. Phys.* **56**, 2129.

Vibrational potential functions, exact force constants of F_2 -species, isotopic shifts and mean amplitudes of vibration of ortho silicates and germanates

T S Rawat*, L Dixit**, B B Raizada, B Pal and

S K Bhardwaj***

Chemical Physics Research Group ; Department of Chemistry, D.B.S. College, Dehra Dun (U.P.)-248001.

Received 4 April 1976.

Abstract Several vibrational potential functions viz., GVFF, UBFF, OVFF and L.J. potential have been utilized to perform normal co-ordinate analysis of ortho silicates and germanates. Utilising $^{28}\text{Si}/^{30}\text{Si}$ and $^{70}\text{Ge}/^{76}\text{Ge}$ isotopic shift data, unique force-fields of F_2 -species are established. Isotopic effects have also been examined on the nature of Si—O and Ge—O bond vibrations and non-bonded 0...0 distances. Results are critically discussed in terms of molecular structure and nature of metal—oxygen bonding.

1. Introduction

Some aspects of vibrational spectra of transition metal chalcogen compounds have been recently discussed by Schmidt & Muller (1974). A study on spectroscopic properties of tetrahedral oxo-anions and their isotopic species for examining the nature of internal vibrations was systematically done by them. However, normal co-ordinate analysis of very few oxometalates is performed (Sanyal *et al* 1977) due to the lack of additional spectroscopic data generally required for such studies (Mohan *et al* 1976, Alix *et al* 1975) apart from conventional constraint methods (Isotany 1975). As a matter of fact, the determination of exact force-field, corresponding to species with more than one vibrations, is not reliable unless additional data such as Coriolis coupling constants, centrifugal distortion constants, mean amplitudes of vibration, Raman intensities and isotopic-shifts in frequencies are available, Muller *et al* (1972), and Dixit *et al* (1977) have gone into details of such problems and theories and found a way out in the case of isotopic compounds by their investigations. We have also succeeded in examining tetrahydrides of III B group by using H/D isotopic-shifts (Rawat *et al* 1976) and isotopic compounds of some refractory materials (Rawat *et al* 1977).

* For all correspondence.

** Present address : Indian Institute of Petroleum, Dehra Dun.

*** Present address : Department of Chemistry, D.A.V. College, Dehra Dun.

The problem of force-fields in tetrahedral molecules has been reviewed by Basille *et al* (1977) using several potential functions but their data cannot be regarded as unique on the ground that they have not used any of the aforementioned spectroscopic data; and as such the inherent approximation in potential energy functions used, is too large to be accepted as reliable force-constants except for purposes of comparison.

The purpose of this communication is to report new results on spectroscopic constants utilizing Ledent's (1976) recent infrared and Raman data for some silicates and germanates. Vibrational data of such compounds is collected in table 1. All these compounds of general formula $A^I B^{III} X^{IV} O_4$ ($A^I = \text{Li, Na; } B^{III} = \text{Sc, In, Y and rare earths, } X^{IV} = \text{Si, Ge}$) are characterized by Olivine type structure. A good amount of X-ray work on such compounds has been reported to confirm a D_{2h}^{16} space-group (Blasse *et al* 1967) for these compounds making

Table 1. Vibrational frequencies (in Cm^{-1}) of orthosilicates and germanates of general formula $A^I B^{III} X^{IV} O_4$

Ion	$\nu_1(A_1)$	$\nu_2(E)$	$\nu_3(F_2)$	$\nu_4(F_2)$
$^{28}\text{SiO}_4^{4-}$	842.0	444.0	972.0	539.5
$^{30}\text{SiO}_4^{4-}$	831.0	443.0	957.9*	535.5
$^{76}\text{GeO}_4^{4-}$	658.5	377.5	775.5	422.0
$^{78}\text{GeO}_4^{4-}$	655.5	376.0	772.0	419.6

* computed.

use of stable isotopes of Si and Ge, Ledent (1976) has separated the fundamental vibrations as well as internal vibrations of tetrahedral XO_4^{4-} anions. More experimental data, concerning spectra of Olivine compounds, viz., As_2SiO_4 , A_2GeO_4 , $\text{AB}^{II}\text{PO}_4$ and $\text{AB}^{II}\text{AsO}_4$ have recently appeared. However, the information, regarding the nature of vibrations in tetrahedral oxo-anions of Si and Ge, are yet to be considered keeping in view the following points :

- (i) Whether the commonly used potential functions as described by Ferrarro *et al* (1977) are applicable and give reliable results consistent with unique potential functions obtainable from isotopic data reported by Ledent (1976).
- (ii) Whether perturbation theory of potential energy functions (Muller *et al* 1973) developed so far describes adequately the shifts in vibrational bonds of Olivine type of compounds and also whether the experimental observations of Ledent (1976) really fit in the frame-work of perturbation theory.
- (iii) The effect of isotopic substitution of central atoms in a tetrahedra on the bounded and non-bonded mean amplitudes.

2. Theoretical Considerations

Only the internal modes of $AB^{III}X^{IV}O_4$ structures, characterised for XO_4^{4-} tetrahedra, (Ledent 1976) which are distributed under the irreducible representation $\Gamma = A_1 + E + 2F_2$ have been considered. The forms of internal and symmetric co-ordinates, for the ions in question, are the same as described by Gans (1972). The forms of GVFF, OVFF, UBFF potential functions and L.J. Potential are the same as discussed by Basille *et al* (1977) and Krebs & Muller (1967) for XY_4 tetrahedra compounds. Under the frame-work of the above potential functions the fundamental Wilson's secular equation, relating normal frequencies with symmetrized force constants, has been solved without any approximation. Several kinematically defined approximation methods (Muller *et al* 1972) have also been utilized for obtaining symmetry force constants of F_2 -species. The form of kinetic energy matrices is the same as used in earlier investigations (Sanyal *et al* 1977). We have not studied the results of approximate forms of oscillations in more details, however, exact forms of vibrations were studied using isotopic shifts. This study was based on the fact that harmonic force-fields are unchanged due to isotopic substitution and hence Wilson's secular equation for F_2 -symmetry species, involving three principal force-constants could be uniquely solved. The analytical expressions connecting principal force constants F_{11} , F_{12} and F_{22} with two eigen values of a species are :

$$G_{11}F_{11}^2 - (\lambda_1 + \lambda_2 - 2G_{12}F_{12})F_{22} + G_{22} \cdot \frac{\lambda_1 \lambda_2}{\det|G|} + F_{12}^2 = 0 \quad (1)$$

and

$$F_{22} = \frac{\lambda_1 + \lambda_2 - 2G_{12}F_{12}}{G_{22}} - \frac{G_{11}}{G_{22}} \cdot F_{11}. \quad (2)$$

Using above equations and making use of frequencies of parent and isotopically labelled systems, exact force constants have been computed for F_2 -vibrations. This is displayed graphically in figures 1 and 2. Further, the isotopic data of Si and Ge holds good for the above method under the limiting conditions of very high substitution. The details of theory for the interpretation of observed frequency shifts, using perturbation theory, were discussed by Dixit *et al* (1974). In brief, a deduction, based on Wilson, Decius & Cross formalism relating isotopic shifts and L -matrix after simplification with $L_{12} = 0$ approximation (Muller *et al* 1972) yields :

$$\frac{\Delta\lambda_1}{\lambda_1^0} = \frac{\Delta G_{11}}{G_{11}^0} \quad (3)$$

$$\frac{\Delta\lambda_2}{\lambda_2^0} = \frac{1}{\det|G|} \left[\frac{G_{12}^2}{G_{11}} \Delta G_{11} - 2G_{12}^0 \Delta G_{12} + G_{11}^0 \Delta G_{22} \right]. \quad (4)$$

The above equations work satisfactorily, atleast for oxides and in general where the mass coupling in the two eigen values is small.

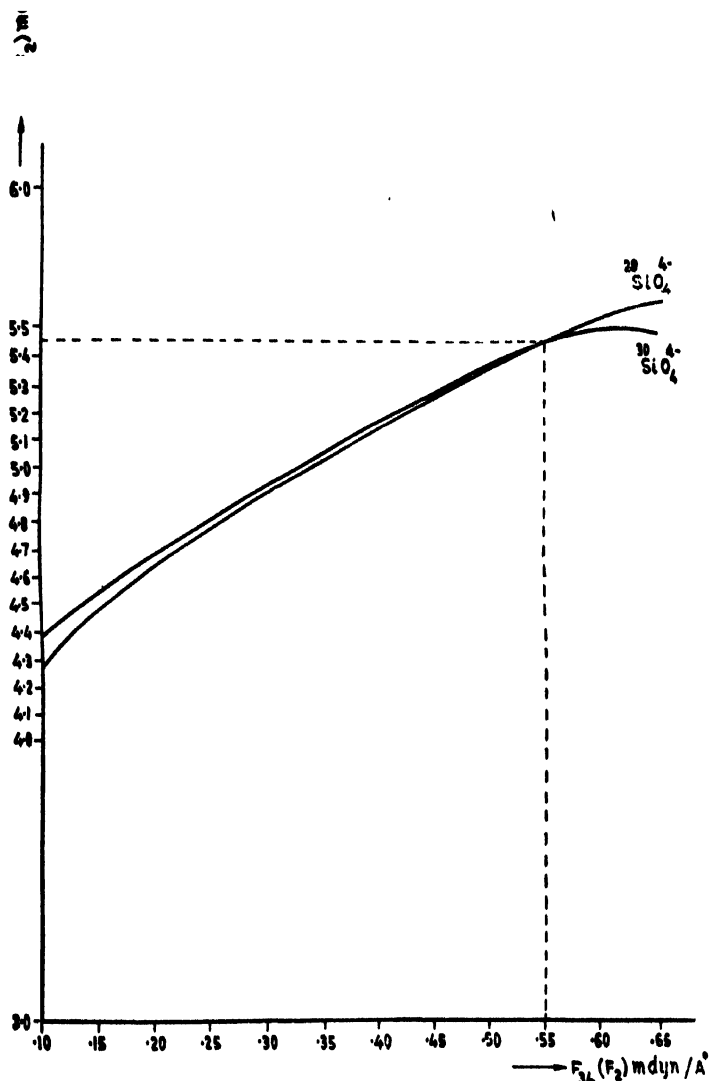


Figure 1. Force constants display for SiO_4^{4-} using $^{28}\text{Si}/^{30}\text{Si}$ isotopic shift [$F_{34}(F_2)$ vs. $F_{35}(F_2)$].

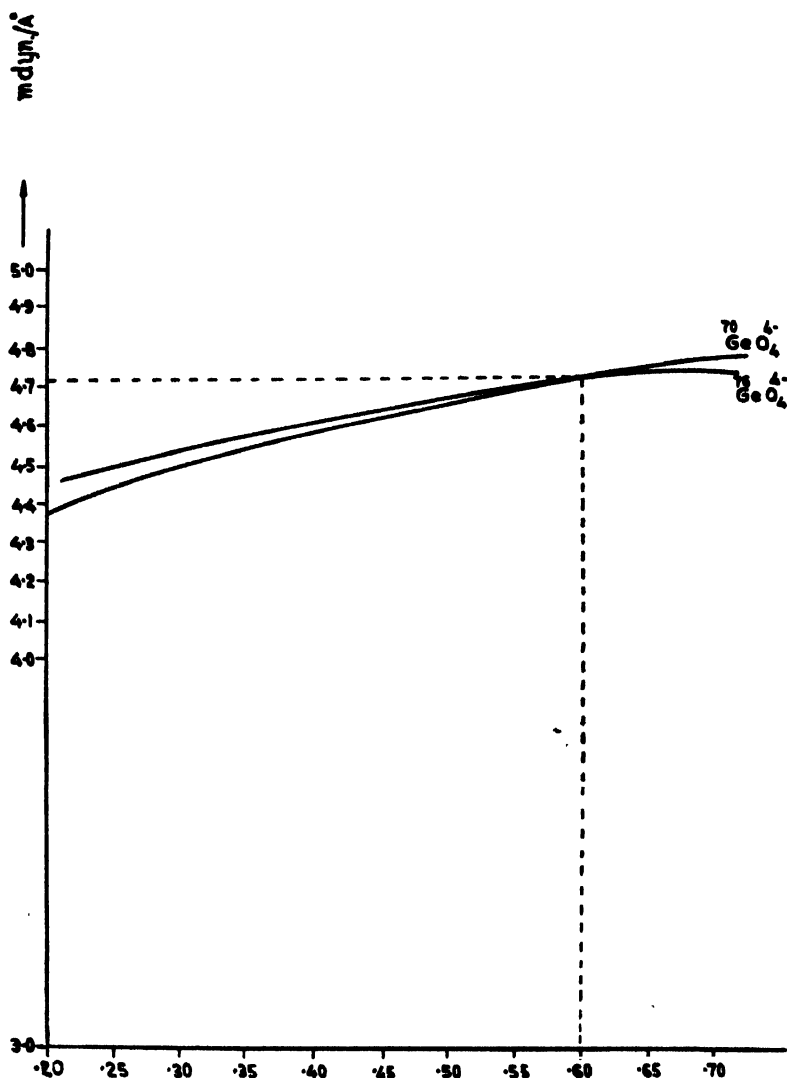


Figure 2. Force constants display for GeO_4^{4-} using $^{70}\text{Ge}/^{76}\text{Ge}$ isotopic shift [$F_{34}(S_2)$ vs. $F_{33}(F_2)$].

3. Results and Discussion

Utilizing the infrared and Raman data of SiO_4^{4-} and GeO_4^{4-} and their isotopic ions (table 1) the force constants obtained by GVFF, OVFF, UBFF and L-J. Potential methods are presented in tables 2 and 3. There is a good harmony among the magnitudes of intramolecular forces obtained from various approaches. The stretching force constant f_r , k_1 and K , the bending force constant f_a , H and k_a' and other non-bonding forces obtained by all the methods,

are comparable in the three potential functions. All the P - E functions reproduce vibration frequencies with minor deviations.

Table 2. OVFF and UBFF Constants of $^{28}\text{SiO}_4^{4-}/^{30}\text{SiO}_4^{4-}$ and $^{70}\text{GeO}_4^{4-}/^{76}\text{GeO}_4^{4-}$ (in mdyn/Å)

Ion pair	$k_1(K)$	$k'_a(3H)$	$A(F/2)$	$B/R(-F')$	Method
$^{28}\text{SiO}_4^{4-}$	3.937	1.099	0.343	0.072	(a)
	4.315	1.153	0.296	0.114	(b)
	3.538	1.011	0.393	0.061	(c)
$^{70}\text{GeO}_4^{4-}$	4.108	1.410	-0.003	-0.061	(a)
	4.199	1.237	-0.014	0.134	(b)
	3.605	1.213	0.060	0.009	(c)

(a) OVFF, (b) UBFF, (c) L.J. Potential ($A = 6.5 B/R$).

Table 3. GVFF constants (mdyn/Å) for $[^{28}\text{SiO}_4^{4-}/^{30}\text{SiO}_4^{4-}]$ and $[^{70}\text{GeO}_4^{4-}/^{76}\text{GeO}_4^{4-}]$

Method*	f_r	f_{rr}	$f_a - f_{aa}$	$f_a - f_{aa}'$	$f_{ra} - f'_{ra}$
[$^{28}\text{SiO}_4^{4-}/^{30}\text{SiO}_4^{4-}$]					
(a)	5.873	0.270	0.677	0.735	0.450
(b)	6.801	-0.039	0.893	1.167	1.460
(c)	5.461	0.407	0.677	0.735	0.225
(d)	4.542	0.713	0.795	0.971	0.000
[$^{70}\text{GeO}_4^{4-}/^{76}\text{GeO}_4^{4-}$]					
(a)	4.373	-0.095	0.510	0.572	0.189
(b)	4.596	-0.170	0.570	0.692	0.638
(c)	4.280	-0.064	0.510	0.572	0.094
(d)	4.091	-0.001	0.536	0.624	0.000

* (a) $L_{12} = 0$, (b) $L_{21} = 0$, (c) PED, (d) $F_{12} = 0$.

An examination of table 4 reveals that any of the methods, used to establish F_2 -block symmetry force constants, gives identical results with rest of the methods. However, the principal force constants calculated by $L_{12} = 0$ approximation method, are nearer to exact force constants $> L_{21} = 0$ approximation method $> \text{PFD} > \text{MVFF}$ (where interaction force constant F_{12} vanishes). Observing table 5 the observed and calculated isotopic shifts of SiO_4^{4-} due to $^{28}\text{Si}/^{30}\text{Si}$ substitution are almost the same while in case of GeO_4^{4-} , observed and calculated $\Delta\nu_3$ and $\Delta\nu_4$ are $3.5/7.2 \text{ cm}^{-1}$ and $2.5/4.6 \text{ cm}^{-1}$ respectively due to $^{70}\text{Ge}/^{76}\text{Ge}$ substitution. These results show the validity of calculations in silicate system but

Table 4. Symmetrised Force Constants* (mdyn/Å) for $^{28}\text{SiO}_4^{4-}$ and $^{70}\text{GeO}_4^{4-}$

	Method**	$F_{33}(F_2)$	$F_{34}(F_2)$	$F_{44}(F_2)$
$^{28}\text{SiO}_4^{4-}$				
$F_{11}(A_1) = 6.683$	(a)	5.604	0.636	0.735
	(b)	6.840	2.065	1.167
$F_{22}(E) = 0.619$	(c)	5.053	0.318	0.735
	(d)	3.829	0.000	0.971
	(e)	6.450	0.550	0.737
	(f)	4.756	0.409	0.899
	(g)	4.953	0.319	0.771
	(h)	4.505	0.484	0.869
$^{70}\text{GeO}_4^{4-}$				
$F_{11}(A_1) = 4.087$	(a)	4.469	0.267	0.572
	(b)	4.766	0.903	0.692
$F_{22}(E) = 0.448$	(c)	4.344	0.134	0.572
	(d)	4.092	0.000	0.624
	(e)	4.700	0.600	0.604
	(f)	4.162	0.037	0.601
	(g)	3.983	-0.108	0.627
	(h)	3.753	0.074	0.662

* All values using assignments of Ledent (1976).

** (a) $L_{12} = \infty$, (b) $L_{21} = 0$, (c) PED, (d) $F_{12} = 0$, (e) Exact force constants, (f) OVFF, (g) UBFF, (h) OVFF, ($A = 6.5 B/R$).

Table 5. Isotope shifts of F_2 -species using Muller-Mohan theory for MO_4^{4-} ions ($M = \text{Si}$ and Ge) and Verification of Teller-Redlich Product Rule

[A]		$^{28}\text{SiO}_4^{4-}/^{30}\text{SiO}_4^{4-}$		$^{70}\text{GeO}_4^{4-}/^{76}\text{GeO}_4^{4-}$	
		$\nu_3(F_2)$	$\nu_4(F_2)$	$\nu_3(F_2)$	$\nu_4(F_2)$
Observed		14.1 cm^{-1}	4.0 cm^{-1}	3.5 cm^{-1}	2.5 cm^{-1}
Calculated		(14.1) cm^{-1}	(4.8) cm^{-1}	(7.2) cm^{-1}	(4.6) cm^{-1}
[B] Class		$^{28}\text{SiO}_4^{4-}/^{30}\text{SiO}_4^{4-}$		$^{70}\text{GeO}_4^{4-}/^{76}\text{GeO}_4^{4-}$	
	Product ratio	Calc.	Obs.	Calc.	Obs.
A_1	$\frac{\nu'_1}{\nu_1} = \left[\frac{m_x}{m'_x} \right]^{\frac{1}{2}}$	0.987	0.987	1.005	1.005
E	$\frac{\nu'_2}{\nu_2} = \left[\frac{m_x}{m'_x} \right]^{\frac{1}{2}}$	0.987	0.987	1.005	1.005
F_2	$\frac{\nu'_3 \nu'_4}{\nu_3 \nu_4} = \frac{m_x}{m'_x} \left[\frac{M'}{M} \right]^{\frac{1}{2}}$	0.980	0.978	0.980	0.986

results are less satisfactory for GeO_4^{4-} system. It may be due to the mass coupling effect. Table 6 consists of calculated values of ν_3 and ν_4 frequencies using various methods. It is clear from table 5 that the results for ν_3 and ν_4 are excellent for both the systems as evidenced by the verification of Teller-Rodlich product rule. We have also calculated the frequency of a symmetric stretching vibration of $^{30}\text{SiO}_4^{4-}$ which was not observed by Lodent (1976). This comes out to be 957.9 cm^{-1} .

Table 6. Observed and calculated frequencies of F_2 -species $^{28}\text{SiO}_4^{4-}$ and $^{70}\text{GeO}_4^{4-}$ (in Cm^{-1})

		$\nu_3(F_2)$	$\nu_4(F_2)$	% Deviation	
				$\nu_3(F_2)$	$\nu_4(F_2)$
$^{28}\text{SiO}_4^{4-}$	observed	972.0	539.5		
	UBFF	972.0	539.5	0.00	0.00
	OVFF	949.2	580.0	2.37	7.51
	L-J Potential				
	($A = 6.5 \text{ B/R}$)	904.7	576.7	6.92	6.90
	GVFF				
	(from OVFF)	949.0	580.9	2.37	7.67
$^{70}\text{GeO}_4^{4-}$	observed	775.5	422.0		
	UBFF	775.5	422.0	0.00	0.00
	OVFF	771.9	425.0	0.46	0.71
	L-J. Potential				
	($A = 56. \text{ B/R}$)	733.0	446.0	5.48	5.69
	GVFF				
	(from OVFF)	733.0	446.0	5.48	5.69

The values of force constants, determined in this study, agree very well with the data based on isotopic shifts. Our study indicates that due to the $^{28}\text{Si}/^{30}\text{Si}$ substitution in SiO_4^{4-} systems, the spectral data observed by Lodent (1976) are suitable for establishing reliable force constants values. The results obtained in UBFF and OVFF calculations overall agree with GVFF symmetry force constants for both the systems (table 4). The agreement between present potential constants and those reported earlier (Dixit *et al* 1977) is good, however, the present data is more reliable than previous investigators because of the use of additional spectroscopic data. Table 7 consists of bonded and non-bonded mean amplitudes of vibration for silicates and germanates in question. The isotope effect on Ge-compounds due to $^{70}\text{Ge}/^{76}\text{Ge}$ substitution are more pronounced on Ge—O bond than in Si—O bond due to $^{28}\text{Si}/^{30}\text{Si}$ substitution in Si-compounds. And this should be so, when we examine the magnitudes of force constants of these compounds. However, this has been obtained of minor magnitude and is consistent with our previous studies (Dixit & Vorma 1977). Hence, whatever

tetrahedra (SiO_4^{4-} or GeO_4^{4-}) is considered, the mean amplitudes of bonded Si—O or Ge—O distance, at $T = 298^\circ\text{K}$, are not very much different and attains approximate value of 0.042\AA —an observation made by Muller & Schmidt (1972). In other words, the bonds ^{28}Si —O, ^{30}Si —O, ^{70}Ge —O and ^{76}Ge —O are highly charac-

Table 7. Mean amplitudes of vibration (in \AA) of SiO_4^{4-} and GeO_4^{4-}

Systems	Distance	$T = 0^\circ\text{K}$	$T = 298^\circ\text{K}$	$T = 500^\circ\text{K}$
1. $^{28}\text{SiO}_4^{4-}$	Si—O (bonded)	0.0418	0.0422	0.0446
	0...0 (non-bonded)	0.0738	0.0771	0.0849
2. $^{30}\text{SiO}_4^{4-}$	Si—O (bonded)	0.0416	0.0421	0.0445
	0...0 (non-bonded)	0.0732	0.0764	0.0844
3. $^{70}\text{GeO}_4^{4-}$	Ge—O (bonded)	0.0365	0.0428	0.0468
	0...0 (non-bonded)	0.0708	0.0770	0.0883
4. $^{76}\text{GeO}_4^{4-}$	Ge—O (bonded)	0.0414	0.0426	0.0467
	0...0 (non-bonded)	0.0703	0.0765	0.0880

eristic as regards their mean amplitudes of vibration. On the other hand, the non-bonded mean-amplitudes due to 0...0 are affected very much by isotopic substitutions. This shows that the replacement of central atom, by its isotope or another element, in a tetrahedra, affects the non-bonded mean amplitudes considerably while the bonded mean amplitudes are least affected. Conclusively, it may be said that any change brought about in the bond strength of metal—oxygen bond in a tetrahedra due to the replacement of the central atom is reflected in terms of mean amplitudes—values of non-bonded distances such that the characteristic nature of vibration of metal-oxygen bond are not lost. Bond stretching force constant for Si—O is larger than bond stretching force constant for Ge—O showing more stability of Si—O bond than Ge—O bond.

Acknowledgments

Authors are thankful to Dr. I. B. Gulati, Director, I. I. P., Dehra Dun, for his interest in the problem and constant encouragement.

References

- Alix A J P Eysel H H, Jordavnov B Kebabcioglu R Mohan N & Muller A 1975 *J Mol. Struct.* **27**, 1.
- Basille L J Ferrero J R Lobonville P & Wall M C S M V 1977 *Coord. Chem. Reviews* **11**, 21.
- Blasse G & Brill A 1967 *J Inorg. Nucl. Chem.* **29**, 2231.
- Dixit L & Verma D N 1977 *Indian J Pure Appl. Phys.* **15**, 329.
- Gans P 1972 *Vibrating Molecules*, Chapman & Hall.
- Isotany S 1975 *J Mol. Struct.* **28**, 61.
- Krebs B & Muller A 1967 *J Mol. Spectrosc.* **22**, 290.
- Ledent M T D 1976 *Spectrochim Acta* **23a**, 383.
- Mohan N, Cyvin S J & Muller A 1976 *Coord. Chem. Reviews* **21**, 221.
- Muller A Kebabcioglu R Cyvin S J & Mohan N 1972 *Detkangelige. Norske, Videnskabers, Selskab, Skrifter* No. 7.
- Muller A & Mohan N 1973 *J Chem. Phys.* **58**, 2994.
- Muller A Schmidt K H & Boran E J 1972 *Characteristic mean amplitudes of Vibrations, in Molecular Vibrations and Molecular Structures*, edited by S J Cyvin.
- Muller A Schmidt K H & Mohan N 1972 *J. Chem. Phys.* **57**, 175.
- Muller A Schmidt K H & Mohan N 1972 *J. Chem. Phys.* **57**, 1752.
- Rawat T S Dixit L & Raizada B B 1976 *Indian J. Pure Appl. Phys.* **14**, 656.
- Rawat T S Dixit L Raizada B B & Katiar A K 1977 *Indian J. Phys.* (under publication).
- Sanyal N K & Dixit L 1974 *E. Natureforsch* **29a**, 693.
- Sanyal N K Ganguli A K & Dixit L 1977 *Indian J. Pure Appl. Phys.* **15**, 17.
- Schmidt K H & Muller A 1974 *Coord. Chem. Reviews* **115**, 179.

Intensities of the forbidden lines within the ground configurations of S X

Suresh Chandra

Department of Physics, D. N. College, Gulaothi-245408

Received 7 April 1978, revised 30 August 1978.

Abstract.. Intensities of the forbidden lines of the transitions within the configurations of S X are computed for the electron densities $N_e = 10^7, 10^8, 10^9$ and 10^{10} . The populations of the states required for the calculations are obtained following the method of Zirker (1970). The results are presented in the tabular form. It is observed that for (S-D) and (D-D) transitions the line intensity decreases with the increase of electron density N_e whereas for (S-P), (P-P) and (D-P) transitions the intensity increases.

1. Introduction

The intensity of the line (in $\text{ergs cm}^{-2} \text{sec}^{-1}$) observed at the earth's distance is given by (Pottasch 1963)

$$I = 1.744 \times 10^{-17} W \int N_j A_{ji} dh \quad (1)$$

where A_{ji} (sec^{-1}) is the spontaneous transition probability, $W(\text{eV})$ the energy gap between the corresponding levels, N_j the population density of the ion in the state j and the integration is performed over the line forming region.

For the quiet regions in the transition zone (electron pressure parameter $= 6 \times 10^4$, the conductive flux factor $= 10^{12}$) equation (1) reduces to (using $N_H = 0.8 N_e$) (Chandra 1978)

$$I = 5.02 W \frac{N_E}{N_H} \int \frac{N_j}{N_1} \frac{N_1}{N_E} \frac{T^{\frac{1}{2}}}{N_e} dT. \quad (2)$$

Here the relative abundance of sulphur to hydrogen (N_E/H_H) is taken as 2.04×10^{-5} (Dupree 1972). For other values of the relative abundance the intensities might be scaled. The relative ion abundances (N_1/N_E) utilized here include the density effect and are taken from Jordan (1969). The population of the excited states relative to the ground state (N_j/N_1) are determined for a fixed temperature and electron density by the steady state equations (Zirker 1970)

$$N_j \sum_{i < j} (A_{ji} + C_{ji}) = \sum_{k < j} N_k (A_{kj} + C_{kj}) \quad (3)$$

where A 's and C 's are the radiative and collisional transition rates. The collisional excitation rates, by assuming the collision strength $\Omega(i, j)$ independent of energy, are computed with the help of the expression

$$C_{ij} = 8.63 \times 10^{-8} N_e g_i^{-1} T^{-1} \Omega(i, j) \exp(-11606 W/T). \quad (4)$$

Collisional deexcitation rates are connected with the excitation rates by

$$C_{ji} = C_{ij} g_i g_j^{-1} \exp(11606 W/T). \quad (5)$$

The photo excitation rates A_{ij} are related to the spontaneous transition probabilities by

$$A_{ij} = A_{ji} D g_j g_i^{-1} [\exp(11606 W/T_r) - 1]^{-1}. \quad (6)$$

In the present investigation the black body radiation temperature T_r is taken equal to 6000 K and the dilution factor D is 0.3.

The values of the various parameters used are displayed in Table 1 and their sources are given in the footnotes.

Table 1. Values of the parameters

Transition	W^* (eV)	A_{ji}^{**} (Sec $^{-1}$)	$\Omega(i, j)^{***}$	g_i
$^4S_{3/2} - ^2D_{3/2}$	10.2135	15.021	0.112	4
$^4S_{3/2} - ^2D_{5/2}$	10.3560	0.374	0.170	4
$^2D_{3/2} - ^2D_{5/2}$	0.1425	0.016	0.231	4
$^4S_{3/2} - ^2P_{1/2}$	15.7345	140.005	0.041	4
$^2D_{3/2} - ^2P_{1/2}$	5.5210	57.470	0.071	4
$^2D_{5/2} - ^2P_{1/2}$	5.3784	0.290	0.083	6
$^4S_{3/2} - ^2P_{3/2}$	15.9613	320.001	0.083	4
$^2D_{3/2} - ^2P_{3/2}$	5.7478	100.260	0.117	4
$^2D_{5/2} - ^2P_{3/2}$	5.6053	54.590	0.210	6
$^2P_{1/2} - ^2P_{3/2}$	0.2268	0.052	0.094	2

* Edlen B 1972 *Solar Phys.* **24** 356

** Garstang R H 1972 *Optica Pure Y. Aplicada* **5** 192

*** Czyzak S J, Aller R. H. & Euwema R N 1974 *Astrophys. J. Suppl. Ser.* **28** 465

Values of N_j/N_1 are calculated, by using the equations (3) through (6) as a function of temperature. These values along with relative ion abundances of Jordan are then used in the graphical integration of the integral in equation (2) by plotting a graph of $(N_j/N_1) (N_1/N_E) T^{1/2} N_e^{-1}$ versus T .

The computed line intensities of the forbidden lines of the transitions within the ground configurations of SX for the electron densities $N_e = 10^7$, 10^8 , 10^9 and 10^{10} are quoted in Table 2.

Table 2. Line intensities

Transition	N_e			
	10^7	10^8	10^9	10^{10}
$^4S_{3/2}—^2D_{3/2}$	8.858(−5)*	8.858(−5)	8.701(−5)	7.914(−5)
$^4S_{3/2}—^2D_{5/2}$	1.281(−4)	1.142(−4)	5.879(−5)	1.102(−5)
$^2D_{3/2}—^2D_{5/2}$	7.541(−8)	6.723(−8)	3.461(−8)	6.489(−9)
$^4S_{3/2}—^2P_{1/2}$	3.400(−5)	3.671(−5)	5.140(−5)	6.919(−5)
$^2D_{3/2}—^2P_{1/2}$	4.877(−6)	5.288(−6)	7.403(−6)	9.965(−6)
$^2D_{5/2}—^2P_{1/2}$	2.407(−8)	2.599(−8)	3.639(−8)	4.899(−8)
$^4S_{3/2}—^2P_{3/2}$	6.768(−5)	7.422(−5)	1.076(−4)	1.509(−4)
$^2D_{3/2}—^2P_{3/2}$	7.636(−6)	8.374(−6)	1.215(−5)	1.702(−5)
$^2D_{5/2}—^2P_{3/2}$	4.054(−6)	4.447(−6)	6.449(−6)	9.038(−6)
$^2P_{1/2}—^2P_{3/2}$	1.563(−10)	1.714(−10)	2.486(−10)	3.483(−10)

* The numbers in brackets are the powers of ten, e.g. 8.858(−5) = 8.858×10^{-5}

The line intensity for ($S-D$) and ($D-D$) transitions decreases with the increase of electron density N_e whereas for ($S-P$), ($P-P$) and ($D-P$) transitions the intensity increases.

The relative populations of the levels are presented in Table 3. Obviously, the population of the D and P levels increases with N_e whereas that of S level decreases for the electron densities under consideration. The population of P levels increases more rapidly than that of D levels. Since the population of S level decreases and that of P levels increases rapidly, it shows that the fraction of electrons in D levels which are collisionally excited to the P levels increases with the increase of electron density and a smaller number of electrons follow the radiative decay. Further the transitions between S and D levels are not optically allowed, the lifetimes of D levels are larger and the electrons in D levels can easily be collisionally excited to the allowed P levels. Therefore on increasing the electron density the number of de-exciting electrons in D levels decreases hence the intensity of the lines for the transitions ($S-D$) and ($D-D$) decreases. Further, the population of P levels increases, hence the intensity of the lines for the transitions ($S-P$), ($P-P$) and ($D-P$) increases with the increase of electron density.

Table 3. Relative populations of the levels at the temperature $T = 1 \times 10^6 \text{K}$.

N_i	$\frac{N_1}{\Sigma N_i}$	$\frac{N_2}{\Sigma N_i}$	$\frac{N_3}{\Sigma N_i}$	$\frac{N_4}{\Sigma N_i}$	$\frac{N_5}{\Sigma N_i}$
10^7	0.992	1.415(-4)*	8.159(-3)	3.743(-6)	3.161(-6)
10^8	0.931	1.326(-3)	6.783(-2)	3.861(-5)	3.330(-5)
10^9	0.736	1.033(-2)	2.531(-1)	4.234(-4)	3.861(-4)
10^{10}	0.566	6.959(-2)	3.555(-1)	4.443(-3)	4.182(-3)
10^{11}	0.358	1.956(-1)	3.680(-1)	3.396(-2)	4.474(-2)
10^{12}	0.205	1.710(-1)	2.628(-1)	6.652(-2)	2.949(-1)

* See note of table 2.

On further increasing the electron density the population of D levels also shows a decreasing trend and hence the intensity will decrease more rapidly for the transitions ($S-D$) and ($D-D$) and will increase for the transitions ($S-P$), ($P-P$) and ($D-P$).

Acknowledgments

I am grateful to Professor S. P. Khare and Dr. Udit Narain for their encouragements and cooperation. I am thankful to Dr. K. C. Mittal (Principal) for providing facilities. Financial support by U.G.C. is thankfully acknowledged.

References

- Chandra S. 1978 *Solar Phys.* (In press)
 Dupree A. K. 1972 *Astrophys. J.* **178**, 527
 Jordan C. 1969 *Monthly Notices Roy. Astron. Soc.* **142** 501
 Pottasch S. R. 1963 *Astrophys. J.* **137** 945
 Zirker J. B. 1970 *Solar Phys.* **11** 68

Quadrupole coupling constants of 3P_1 and 1P_1 levels of Mg^{25} , Zn^{67} and Kr^{83} and 3D and 1D levels of Zn^{67}

B R Pushpalata and C M Bhat

Department of Physics, Central College, Bangalore University, Bangalore-560001

Received 9 August 1978

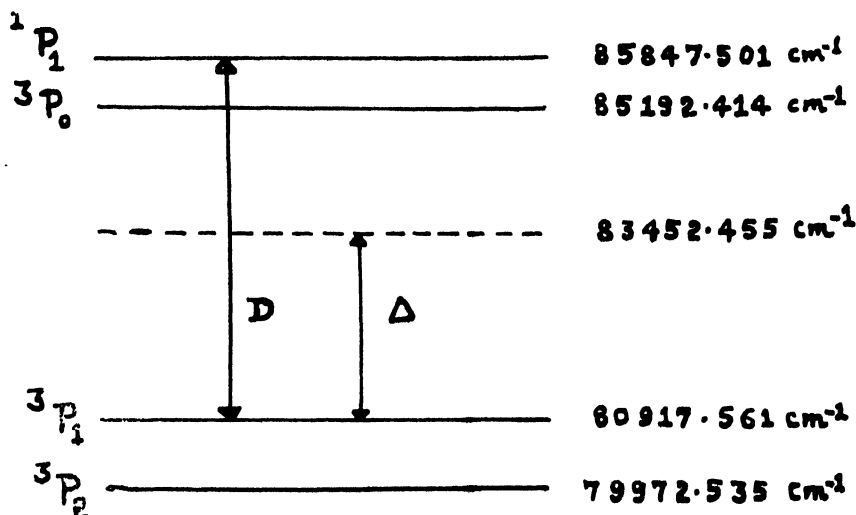
Abstract Quadrupole coupling constants (B) for the 3P_1 and 1P_1 levels of Mg^{25} , Zn^{67} , Kr^{83} and 3D and 1D levels of Zn^{67} have been calculated using the experimentally determined values of the quadrupole coupling constants of the 3P_2 levels of these atoms.

1. Introduction

Hyperfine structure of the metastable 3P states of Mg^{25} and Zn^{67} have been studied by Lurio (1962) through atomic beam resonance method and quadrupole coupling constants have been determined for 3P_2 and 3P_1 levels of Mg^{25} and 3P_2 level of Zn^{67} . Ho has calculated B (3P_1) of Zn^{67} using the data of Böckman *et al* (1957). Fausi *et al* (1963) have studied the hyperfine structure of the metastable $(4p^55s)^3P_2$ state of Kr^{83} , again through atomic beam resonance method and have determined the quadrupole coupling constant for its 3P_2 level. We have calculated the B values for 3P_1 and 1P_1 levels of Mg^{25} , Zn^{67} and Kr^{83} and 3D and 1D levels of Zn^{67} using the experimentally determined B values of 3P_2 levels of these atoms.

2. Calculations

We are interested in looking at the $(3s3p)$ configuration of Mg^{25} , $(4s4p)$ and $(4s4d)$ configurations of Zn^{67} and $(4p^55s)$ configuration of Kr^{83} . Here in Kr^{83} , there is a single hole in the otherwise closed $4p$ shell. Therefore all these configurations are simple two electron problems of the configuration type (sl) . The charge distribution of the s electron being spherically symmetric, the field gradient is only due to the single p electron or the d electron in the (sp) or (sd) type of configurations considered here. The configuration (sl) in the limit of Russel-Saunders's coupling gives rise to four terms $^3L_{I+1}$, 3L_I , $^3L_{I-1}$ and 1L_I . The energy levels arising from the configuration $4p^55s$ of Kr^{83} is shown in figure 1. The energy in wave numbers for the levels of Mg^{25} , Zn^{67} and Kr^{83} have been taken from Moore (1949, 1971).


 Figure 1. Diagrammatic energy levels of Kr^{83} atom.

Quadrupole Moment and Quadrupole Coupling constants :

The quadrupole coupling constant B is defined by the equation,

$$Q = B \cdot \frac{h}{e^2 q_J}, \quad (1)$$

where Q is the nuclear quadrupole moment and q_J is the electric field gradient.

The field gradient q_J is directly related to $\left\langle \frac{1}{r^3} \right\rangle$ and is given by,

$$q_J = \sum_{nlm} A^2_{nlm} \left[\frac{3m^2 - l(l+1)}{l(2l+3)} \right] \left(\frac{2l}{2l+3} \right) \left\langle \frac{1}{r^3} \right\rangle_{nlm} R \quad (2)$$

where

$$\left\langle \frac{1}{r^3} \right\rangle = \frac{\Delta T}{R_\infty \alpha^2 Z_l a_0^3 H_r(l, Z_l)(l + \frac{1}{2})} \quad (3)$$

ΔT is the separation between the levels $^3L_{l-1}$ and $^3L_{l+1}$; R_∞ is the Rydberg constant, α is the fine structure constant, Z_l is the effective atomic number, H_r is a relativistic correction factor and a_0 is the Bohr radius. The values of $\left\langle \frac{1}{r^3} \right\rangle$ are listed in Table 1.

The experimentally determined B values, $B(^3P_2) = 16.009$ Mc/s for Mg^{25} , $B(^3P_1) = 36.024$ Mc/s for Zn^{67} and $B(^3P_2) = -452.1697$ Mc/s for Kr^{83} have

been used for the calculation of the nuclear quadrupole moment Q of these atoms. We get the nuclear quadrupole moments as,

$$\begin{aligned} Q(\text{Mg}^{25}) &= 0.22 \, b \\ Q(\text{Zn}^{67}) &= 0.15 \, b \\ Q(\text{Kr}^{83}) &= 0.263 \, b \\ (1b &= 10^{-24} \text{ cm}^2). \end{aligned}$$

Table 1. Values of $\left\langle \frac{1}{r^3} \right\rangle a_0^3$ and other parameters required in the calculation.

	Mg^{25}	Zn^{67}		Kr^{83}
		$L = 1$	$L = 2$	
$\left\langle \frac{1}{r^3} \right\rangle a_0^3$	0.768	2.416	0.0295	17.497
Δ	0.199 cm^{-1}	2.921 cm^{-1}	0.03 cm^{-1}	2534.894 cm^{-1}
D	13180.934 cm^{-1}	14243.927 cm^{-1}	313.49 cm^{-1}	4929.940 cm^{-1}
C_1	0.5741	0.5656	0.6248	-0.1830
C_2	0.8187	0.8246	0.7807	0.9831
S_r^a	1.0096	1.0626	1.0157	1.0923

a. Kopfermann (1958).

Using eqs. (1) and (2) one can arrive at the expressions for the B values of various levels. These quadrupole interaction constants for the various levels are given by Lurio *et al* (1962),

$$B(^3L_{I+1}) = b_{I+(1)} \quad (4)$$

$$B(^3L_{I-1}) = \frac{(2I-3)(2I+2)}{2I(2I-1)} b_{I-(1)} \quad (5)$$

$$\begin{aligned} B(^3L_I) &= \frac{(2I-1)(2I+4)}{(2I+1)(2I+2)} C_1^2 b_{I+(1)} + C_2^2 b_{I-1} \\ &\quad - \frac{12C_1C_2S_r}{2I(2I+1)} \left(\frac{2I}{2I+2} \right)^{\frac{1}{2}} b_{I+(1)} \end{aligned} \quad (6)$$

$$\begin{aligned} B(^1L_I) &= \frac{(2I-1)(2I+4)}{(2I+1)(2I+2)} C_1'^2 b_{I+(1)} \\ &\quad + C_2'^2 b_{I-(1)} - \frac{12C_1'C_2'S_r}{2I(2I+1)} \left(\frac{2I}{2I+2} \right)^{\frac{1}{2}} b_{I+(1)} \end{aligned} \quad (7)$$

S_r is a relativistic correction factor.

The correction factors C_1 , C_2 , C'_1 and C'_2 are given by

$$C_1 = \sin(\theta_0 - \theta); \quad C_2 = \cos(\theta_0 - \theta);$$

$$\theta_0 = \tan^{-1} \sqrt{\frac{l}{l+1}}; \quad \theta = \sin^{-1} \sqrt{\frac{\Delta}{D}} \quad (8)$$

Δ being the deviation of 3L_I state from the position it would have had if the 3L separations obeyed a Lande Interval Rule and D is the separation between 3L_I and 1L_I levels.

Also, $C'_1 = C_2$; $C'_2 = -C_1$, and b 's are the single electron quadrupole elements defined by,

$$b_j = \frac{(2j-1)}{(2j+2)} \frac{e^2 Q}{h} \left\langle \frac{1}{r^3} \right\rangle R_j \quad (9)$$

where R_j is a relativistic correction factor.

The expression applies with a plus sign for a $p_{3/2}$ electron and with a minus sign for a $p_{3/2}$ hole. So, in case of Kr^{83} , the expression applies with a minus sign (Fausi *et al* 1963).

The various quantities required for the calculation of the B values have been calculated and are listed in Table 1. Using the values of these parameters, the quadrupole coupling constants have been calculated and are listed in Table 2 along with the experimentally determined values wherever available, for the sake of comparison.

Table 2. B values for various levels.

Configuration	Level	B values in Mc/sec
$\text{Mg}^{25} \quad 3s(^2S)3p$	3P_1	-8.054 (-8.029 ^b)
	1P_1	16.058
$\text{Zn}^{87} \quad 3d^{10}4s(^2S)4p$	3P_1	-19.488 (-18.65 ^c)
	1P_1	37.500
	$3d^{10}4s(^2S)4d$	
	3D_3	0.597
	3D_2	0.305
	3D_1	0.216
	1D_2	0.604
$\text{Kr}^{83} \quad 4p^5(^2P_{3/2})5s$	3P_1	-133.283
	1P_1	-344.210

b. Lurio (1962)

c. Fausi *et al* (1963).

A good agreement was found between the calculated values and the experimental values,

Acknowledgments

The authors would like to acknowledge the helpful discussion with Dr. (Mrs.) R. Chandramani, Department of Physics, Bangalore University. The authors are also thankful to Dr. N. G. Puttaswamy, Reader in Physics and Dr. K. N. Kuchela, Head of the Department of Physics, Bangalore University for their encouragement.

References

- Böckman, Krüger & Recknagle 1957 *Ann. Physik* **20**, 250.
Chandramani R & Devaraj N 1971 *Indian J. Phys.* **45** 145
Fausi & L Y Chow Chiu 1963 *Phys. Rev.* **129** 1214
Kopfermann H 1958 *Nuclear Moments*, Academic Press.
Lucken E A C 1969 *Nuclear Quadrupole Coupling Constants*, Academic Press.
Lurio A, Mandel M & Novick R 1962 *Phys. Rev.* **126** 1758
Lurio A 1962 *Phys. Rev.* **126** 1768
Moore C E 1948, 1971 *Atomic Energy Levels*, Vols. I and II.

Modified Paschen's law under the influence of electric and cross magnetic field in air, nitrogen and hydrogen

J C Paul

Department of Electrical Engineering,
Tripura Engineering College, Tripura-799055

Received 27 December 1977

Paschen's law is a unique law in the gaseous breakdown. But in the present investigation it has been observed that under the influence of both electric and cross-magnetic field it is not a unique function of the product P (pressure) and d (gap distance) but dependent on other parameters. A mathematical analysis for the dependence of these parameters together with experimental verification has been presented in this paper for air, nitrogen and hydrogen.

1. Introduction

When a magnetic field whose direction is at right angle to that of the electric field, is applied to a gaseous Townsend discharge, the charged particles, instead of moving in straight lines between collision, are deflected to a cyclodal path. Such deflection increases the probability of collision in the direction of the electric field resulting in an effective reduction of the electron mean free path. The reduction of the mean free path by the magnetic field can be interpreted as an apparent increase of pressure which gives rise to the equivalent pressure concept studied (Mayer 1919, Wherl 1922, Townsend 1935, Valle 1952, Smervalle 1952, Haefer 1953, Belvin and Hayden 1958, Hayden 1961) extensively in the past. Paul *et al* (1974) studied on the gaseous breakdown and Paul (1975) derived equation of effective field calculation under the influence of electric and magnetic field. In this paper Paschen's law under the influence of electric and cross-magnetic field has been investigated at different pressure region with air, hydrogen and nitrogen. Paschen's law states that sparking potential is a unique function of the product P and d , where P is the pressure and d is the gap distance. But in the present investigation it has been observed that under the influence of both electric and magnetic field it is not a unique function of the product P and d but also dependent on other parameters. A mathematical analysis for the dependence of these parameters under the influence of cross-magnetic field is presented and the experimental results amply support the theoretical prediction.

2. Theoretical analysis

Blevin and Haydon (1958) have deduced an expression for the equivalent pressure by considering the bulk properties of electron swarm in cross magnetic and electric field. The equivalent pressure as derived by them may be written as

$$P' = P[1 + c(T/P)^2]^{\frac{1}{2}} \quad (1)$$

where P = pressure without magnetic field

P' = equivalent pressure

T = flux density

$$c = \left(\frac{e}{m} \cdot \frac{\lambda}{v} \right)^2 \quad (2)$$

where m = electron mass

e = electron charge

λ = mean free path of an electron in the gas at 1 torr

v = electron velocity

The electron velocity may be written as

$$v = -\frac{e}{m} \cdot \frac{E}{\nu} \quad (3)$$

ν = collision frequency

E = electric field

Substituting the value of c from Eqn. 2 in eq. 1

$$P' = P \left[1 + \left(\frac{e}{m} \cdot \frac{\lambda}{v} \cdot \frac{T}{P} \right)^2 \right]^{\frac{1}{2}} \quad (4)$$

Rewriting the value of v from Eqn. 3 in eq. 4

$$P' = P \left[1 + \left(\frac{\lambda \nu T}{EP} \right)^2 \right]^{\frac{1}{2}} \quad (5)$$

For uniform field geometry

$$E = \frac{V}{d} \quad (6)$$

Hence substituting the value of E in eq. 5

$$P' = P \left[1 + \left(\frac{\lambda \nu T d}{VP} \right)^2 \right]^{\frac{1}{2}} \quad (7)$$

The usual breakdown voltage (Nasser 1970) is given by

$$V = \frac{BPd}{\log \left(1 + \frac{APd}{\gamma} \right)} \quad (8)$$

where A and B are constant and γ is the secondary Townsend ionization coefficient.

Under the influence of magnetic field P changes to P' , therefore substituting P' from eq. 7 in eq. 8 the following expression may be written

$$BPd \left[1 + \left(\frac{\lambda \nu T d}{VP} \right)^2 \right]^{\frac{1}{2}} \quad (9)$$

$$V = \frac{APd \left\{ 1 + \left(\frac{\lambda \nu T d}{VP} \right)^2 \right\}^{\frac{1}{2}}}{\log \left(1 + \frac{1}{\gamma} \right)}$$

Thus eq. 9 suggests that in an electric and cross-magnetic field the sparking voltage is not only a function of P and d alone as stated by Paschen, but also dependent on other parameters such as T/P , d , λ and ν .

3. Experimental set up

The testing chamber, used in the experiment, is different from a conventional one. Normally the chamber is made of metal and the electrodes are inserted through bushings. In the present experiment the discharge chamber was made of insulating materials and the electrodes were fitted on it. The gap distance between the electrodes could be varied and measured from a scale fitted outside the chamber. Parallel plate electrodes of Rogowski's profile was used. The electrodes were polished until a satisfactory and smooth surface finish was obtained. They were washed in *n*-hexane, so as to remove any grease and to limit the formation of an oxide layer on the surface. The electrodes were conditioned before carrying out the experiment. The voltage for the experiment was obtained from a 40 K.V. d.c. source with a moving coil regulator giving smooth and uniform variation in voltage. The magnetic field was produced by an electromagnet which could produce a magnetic flux density of about 1.15 tesla across the working gap. The schematic arrangement of the experimental set up which consists of a testing chamber, magnetic field with vacuum system, etc. are shown in Figure. 1.

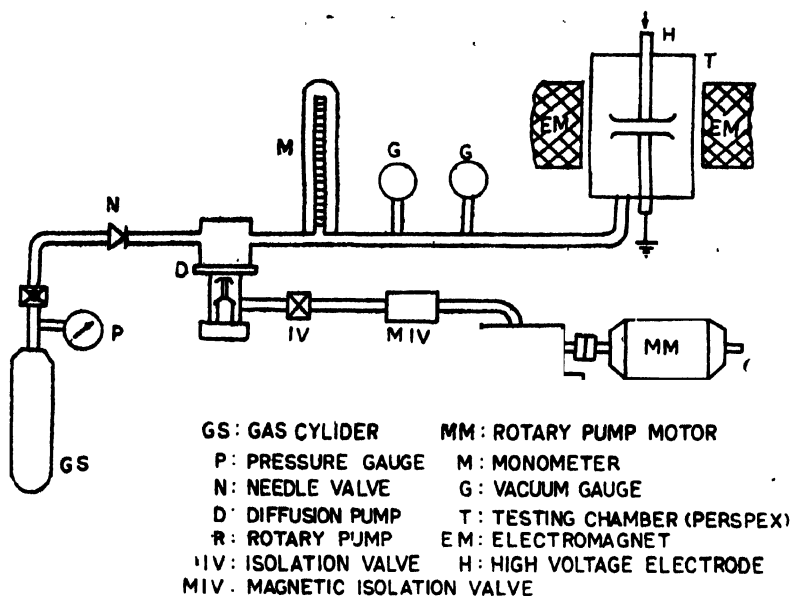


Figure 1.

4. Results

Result presented in this paper are for different values of Pd and magnetic field intensity. For a particular value of Pd and magnetic field breakdown voltage measurements were made with three different values of gap distance. Figure. 2(a) shown the Paschen's breakdown characteristics of air without the application of magnetic field. But when the cross magnetic field is applied the breakdown voltage for a particular value of Pd is correspondingly increased as can be seen in Figure. 2(b), 2(c) and 2(d). Even in the presence of magnetic field the breakdown characteristics follows Paschen's law, but changes in the values of the gap distances considerably modify the slope of the curves as is observable from Figure. 3. Results with hydrogen and nitrogen are depicted in Figure. 4 to Figure. 7 which are also similar in characteristics to that of air.

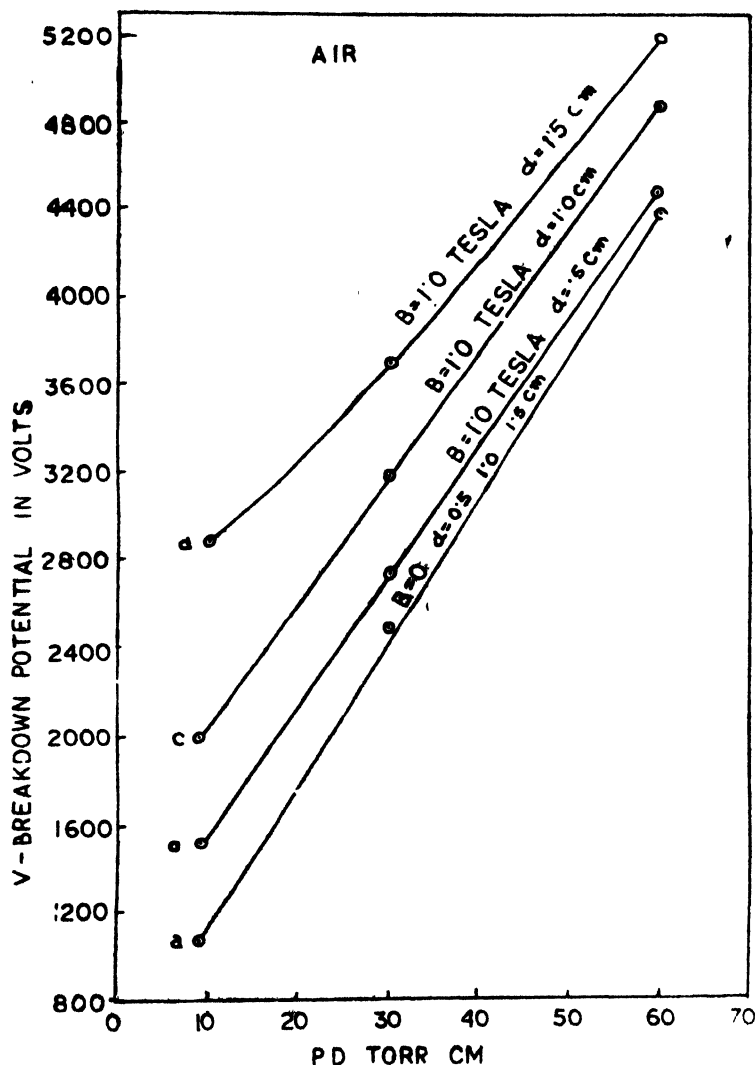


Figure 2.

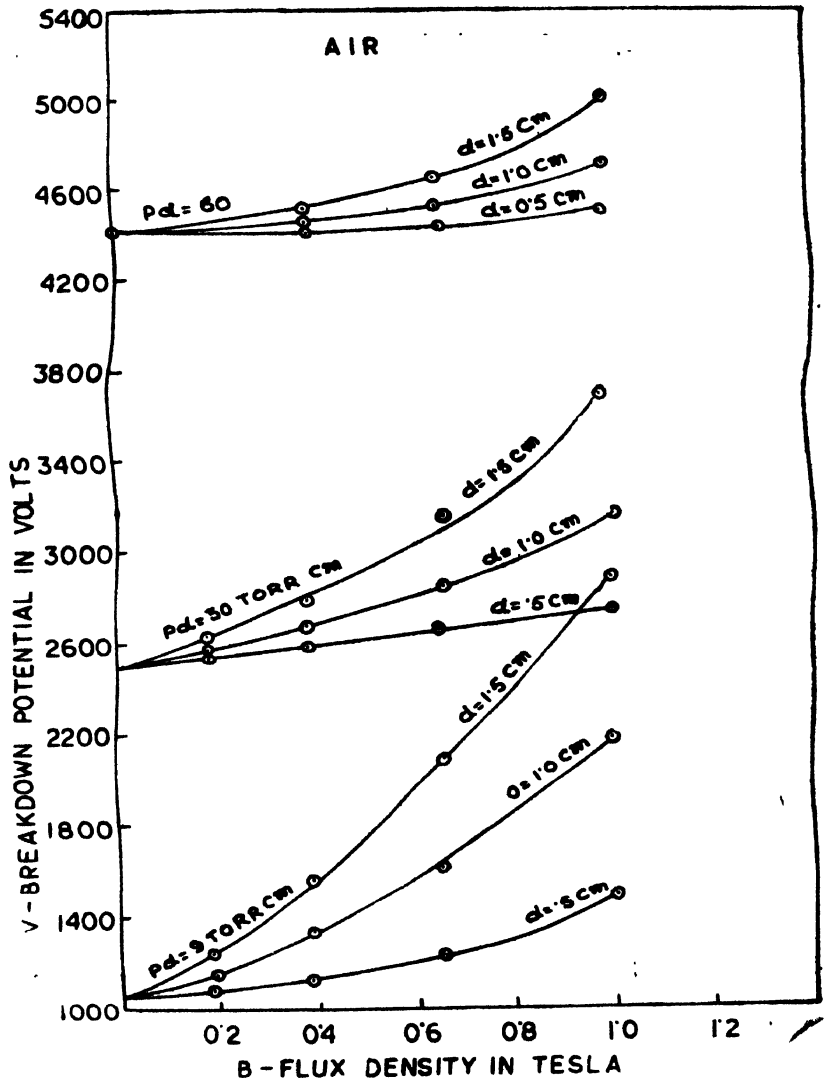


Figure 3.

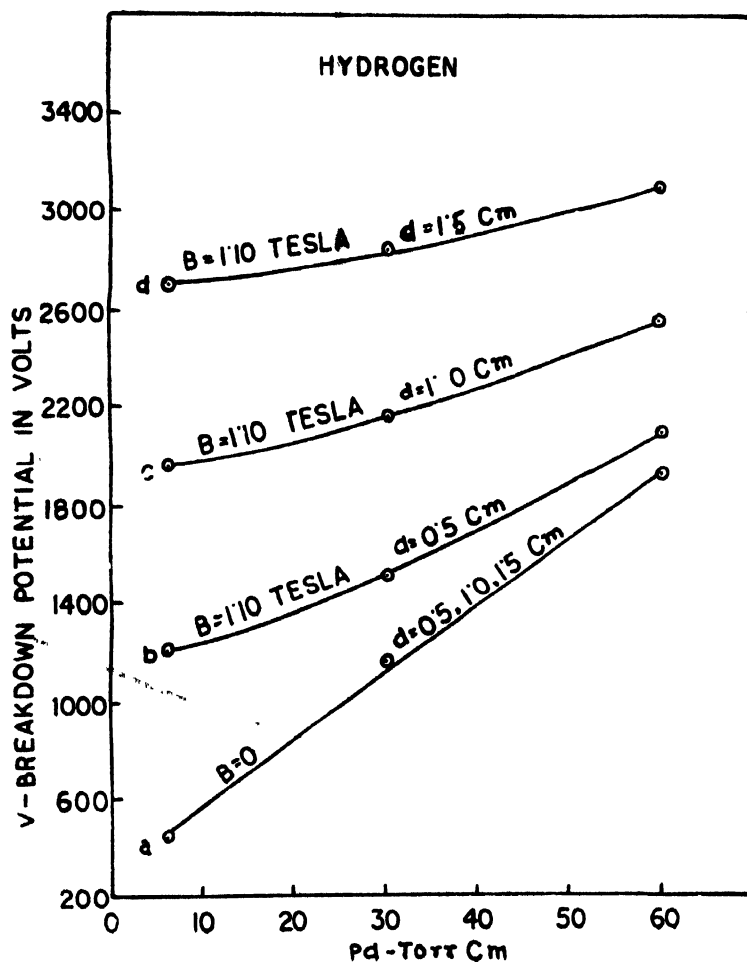


Figure 4.

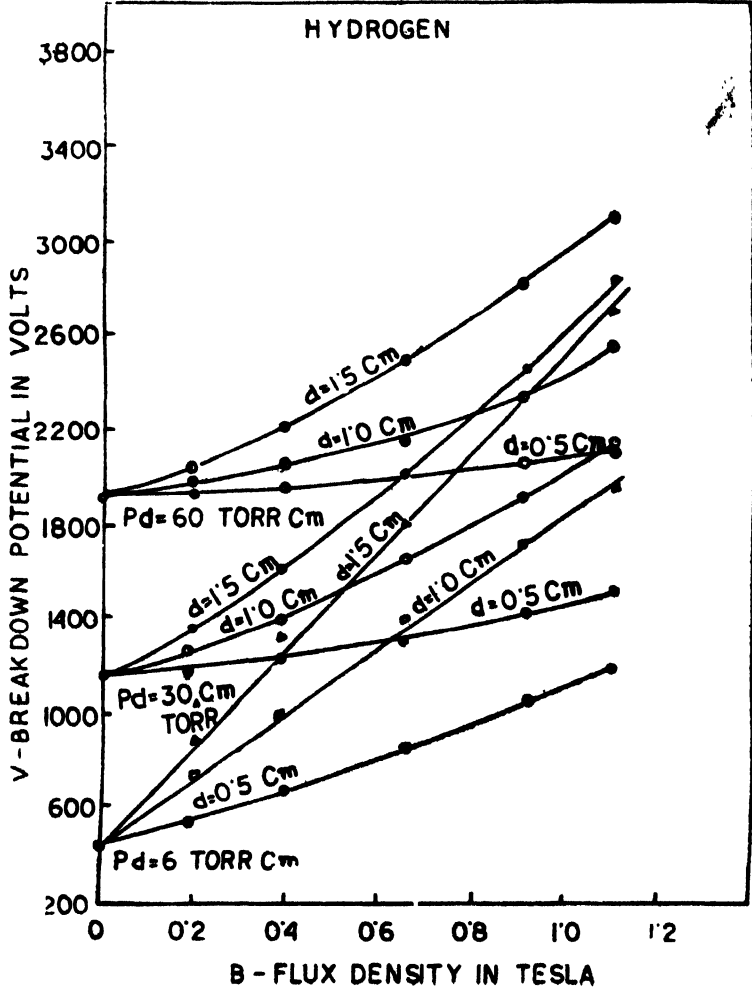


Figure 5.

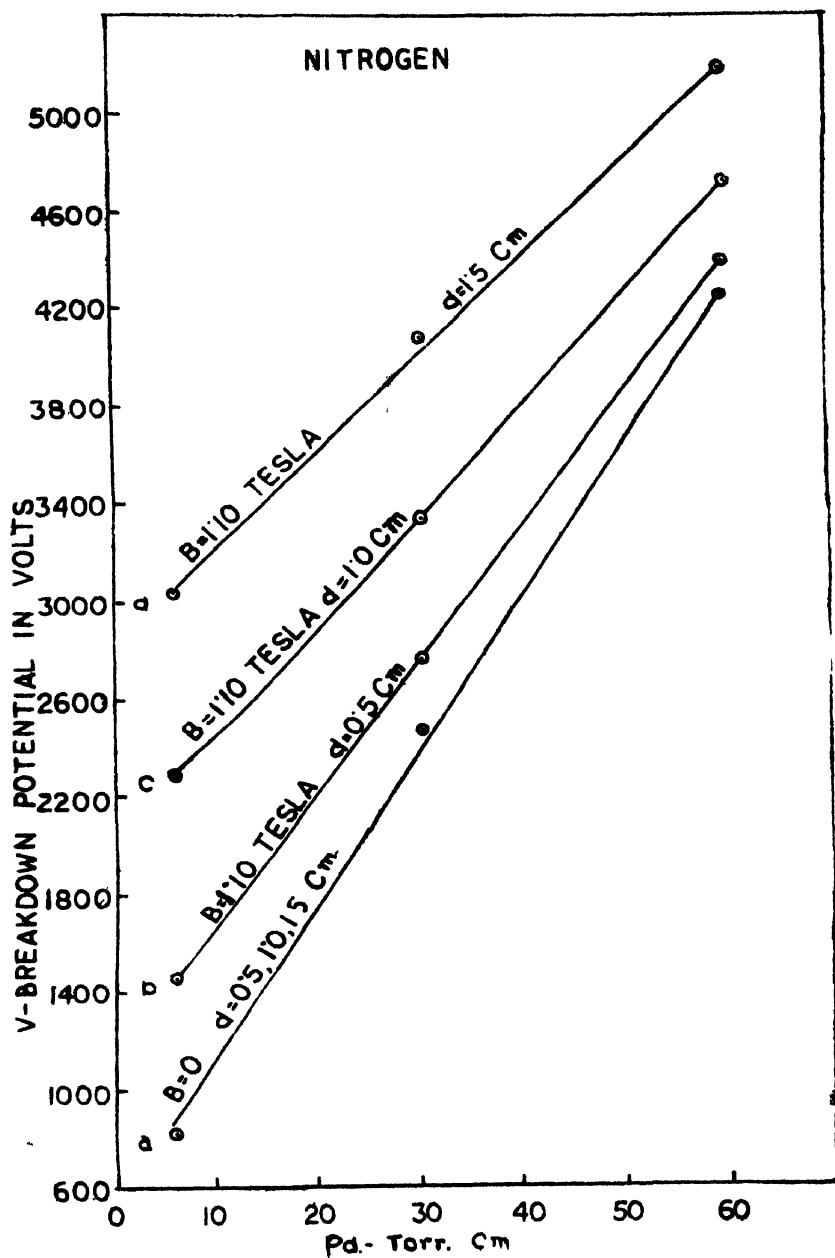


Figure 6.

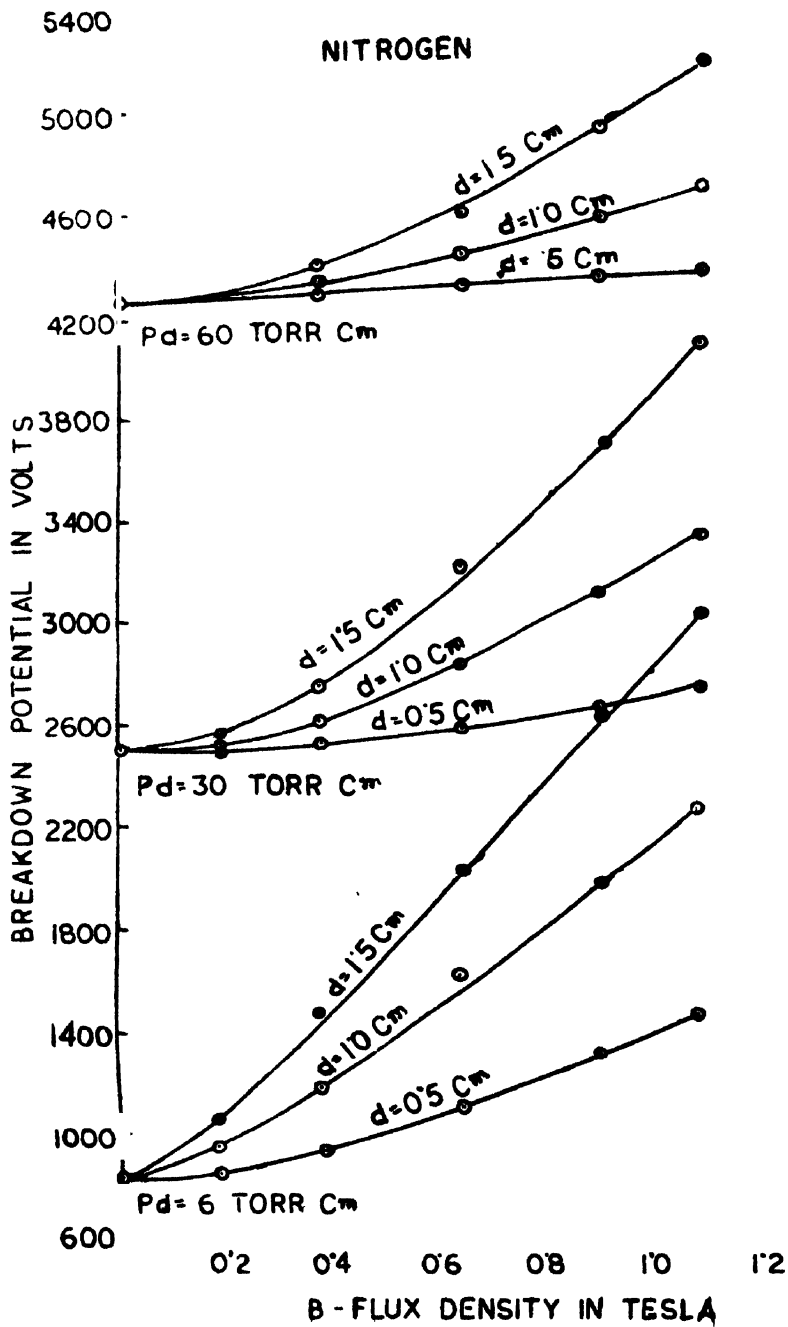


Figure 7.

5. Conclusions and Discussion

When the product Pd and magnetic field remained constant there is a large change in sparking voltage when d is varied. This shows that the path of Paschen's curve is modified with the change in gap distance. It may be concluded from the experimental results that when the gap distance is increased from one lower value to the next higher, value, keeping the product Pd and magnetic field constant, the equivalent pressure is further increased as a result of which the breakdown voltage is increased. The increase in breakdown voltage with increase in d , keeping Pd constant, under the influence of cross-magnetic field may also be explained from eq. (9). When the product P and d is constant in that case increasing the value of gap distance d means P decreases. This decrease in the value of pressure P increases the value in the numerator of 9 much faster than in the denominator. Although the other parameters are also changing with the change in p , but however, the net effect of cross magnetic field is the increase in the voltage when d is increased, keeping the product and constant. It may be further stated that this effect is not present in absence of magnetic field.

Acknowledgment

The author is grateful for the financial support provided by the Ministry of Education and Social Welfare, Government of India.

References

- Belvin H A and Haydon S C 1958 *Austral. J. Phys.* **11** 18
- Essam Nasser 1970 *Fundamental of gaseous ionization and plasma electronics* Wiley Int.
- Haydon S C 1961 *5th Int. Conf. on ionization pheno. in gases*, Munich 1
- Haefer R 1953 *Acta. Phys.* **7** 52
- Mayer E 1919 *Ann. Phys.* **58** 297
- Paul J C, Saha T N and Chakravorty B 1974 *Ind. J. Phys.* **48** 138
- Paul J C, Saha T N and Chakravorty B 1974 *Ind. J. Phys.* **48** 564
- Paul J C 1975 *Int. Conf. on H.V. Engg., Zurich*
- Somervalle J M 1952b *Proc. Phys. Soc.* **65** 620
- Townsend J S 1938 *Phil. Mag.* **26** 290
- Valle G 1952 *Nuove Oimento* **7** 174
- Wherl M 1922 *Ann. Phys.* **69** 285

Effect of magnetic field on mean free path and viscosity and its influence at low pressure gaseous discharge

J C Paul

Department of Electrical Engineering,
Tripura Engineering College Tripura-799055

Received 27 December 1977

Abstract : Conduction and breakdown at low pressure under the influence of magnetic field have been studied by several scientists, but the effect of parameters like viscosity, mean free path have not been studied much. In the present paper the effect of parameters like mean free path, viscosity, under the influence of cross-magnetic field have been considered and an equation of conduction current is obtained considering the effect of magnetic field on these parameters. The experimental results with air are presented and it has been observed that the trends of the experimental curves are in good agreement with the theoretically derived equation.

1. Introduction

Breakdown at low pressure under the influence of magnetic field has been studied by several scientists (Mayer 1919, Wehrl 1922, Townsend 1938, Valle 1952, Somer Valle 1952, Haefer 1953, Belvin & Haydan 1958, Haydan 1961, Rajan 1972). It is known that when a cross-magnetic field is applied to a gaseous discharge the electron or ions, instead of moving in straight line between collisions, are deflected, as a result of which there is an increase in collision frequency and reduction in mean free path. The reduction of mean free path by the magnetic field can be interpreted as an apparent increase of pressure which gives rise to the equivalent pressure concept and this concept has been studied by several authors as stated earlier. The effect of magnetic field on the parameters like viscosity, mean free path and their effect on conduction current has not been investigated so far in the available literature. Although Loeb (1955) has derived an equation of mobility in terms of mean free path, viscosity and radius of the charged particles, but the effect of magnetic field has not been studied by him. Further Coope and Snider (1972) although studied viscosity under the influence of magnetic field, but the effect of magnetic field on viscosity and its effect on conduction has not been dealt with. Paul *et al* (1974) studied on the gaseous breakdown and derived equations for the calculation of breakdown strength of various gases. Paul (1975) also developed equation of effective field calculation of dielectric under the influence of electric and magnetic field and very recently Paul (1979) derived an

equation of sparking potential of air, hydrogen and nitrogen under the applied electric and magnetic field. In the present paper an equation of conduction current has been presented considering the effect of parameters like mean free path, viscosity on the applied magnetic and electric field. The experimental result with air are presented and it has been observed that the trends of the experimental curves are in good agreement with the theoretically derived equation.

2. Theoretical Analysis

The equation of current density neglecting recombination and in the absence of magnetic field may be written as

$$J = \sigma E$$

$$= (n_e \sigma \mu_e + n_n q \mu_n + n_p q \mu_p) E \quad (1)$$

where J = current density

σ = electrical conductivity

E = electric field

n = number density

e = electronic charge

q = ionic charge

Considering

$$K_1 = n_e e, \quad K_2 = n_n q \quad \text{and} \quad K_3 = n_p q$$

eqn. 1 reduces to

$$J = (K_1 \mu_e + K_2 \mu_n + K_3 \mu_p) E \quad (2)$$

The equation of mobility as developed by Loeb (1955) is given by

$$\mu = q \left(1 + \frac{\lambda}{r} \right) \cdot \frac{1}{6\pi\eta r} \quad (3)$$

where μ = mean free path

η = viscosity

r = radius of the charged particles

Substituting the value of the mobility equation of ions and electron from eq. (3) in eq. (2) the current density equation may be written as

$$J = \left[K_1 e \left(1 + \frac{\lambda_e}{r_e} \right) \cdot \frac{1}{6\pi\eta_e r_e} + K_2 q \left(1 + \frac{\lambda_n}{r_n} \right) \cdot \frac{1}{6\pi\eta_n r_n} \right. \\ \left. + K_3 q \left(1 + \frac{\lambda_p}{r_p} \right) \cdot \frac{1}{6\pi\eta_p r_p} \right] E \quad (4)$$

It is further known (1975) that when a cross magnetic field is applied to a gaseous discharge then there is a reduction in mean free path. If it be assumed that the mean free path changes from λ to $\lambda - \Delta\lambda$ for a particular value of applied magnetic field, then the current density equation in presence of cross-magnetic field may, therefore, be modified as

$$J = \frac{E}{6\pi} \left[\frac{K_1 e}{\eta_e r_e} \left(1 + \frac{\lambda_e - \Delta\lambda_e}{r_e} \right) + \frac{K_2 q}{\eta_n r_n} \left(1 + \frac{\lambda_n - \Delta\lambda_n}{r_n} \right) + \frac{K_3 q}{\eta_p r_p} \left(1 + \frac{\lambda_p - \Delta\lambda_p}{r_p} \right) \right] \quad (5)$$

where $\Delta\lambda$ is the term which is due to the application for a particular value of magnetic field and $\Delta\lambda = 0$ when $B = 0$ and $\Delta\lambda$ changes with the change in the magnetic field strength. From the work of Coope and Snide (1972) it is further known that the viscosity, in the case of a gas, is a function of B/P and $1/P$ (where P is the pressure) i.e.

$$\eta = \delta(B/P, 1/P) \quad (6)$$

When the pressure is kept constant the viscosity is a function of magnetic field and the value of viscosity increases with the increase of magnetic field. Let it be assumed that the viscosity is changed from η to $\eta + \Delta\eta$ when a particular value of magnetic field is applied. Therefore, considering the effect of magnetic field on the mean free path and viscosity, the equation of current density (eq. 5) may be modified and may be written as

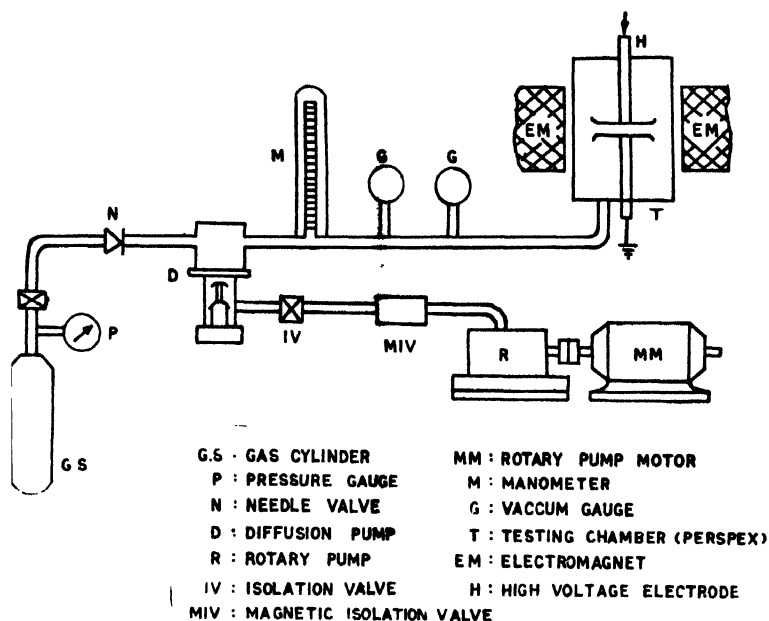
$$J = \frac{E}{6\pi} \left[\frac{K_1 e}{(\eta_e + \Delta\eta_e) r_e} \cdot \left(1 + \frac{\lambda_e - \Delta\lambda_e}{r_e} \right) + \frac{K_2 q}{(\eta_n + \Delta\eta_n) r_n} \cdot \left(1 + \frac{\lambda_n - \Delta\lambda_n}{r_n} \right) + \frac{K_3 q}{(\eta_p + \Delta\eta_p) r_p} \cdot \left(1 + \frac{\lambda_p - \Delta\lambda_p}{r_p} \right) \right] \quad (7)$$

From eq. 7 it is evident that the effect of magnetic field reduces the current density. In the absence of magnetic field the value of $\Delta\lambda$ and $\Delta\eta$ are zero, while in presence of magnetic field the mean free path, λ changes to $\lambda - \Delta\lambda$ and in the case of viscosity, η changes to $\eta + \Delta\eta$. Further the values of $\Delta\lambda$ and $\Delta\eta$ change with the change of magnetic field strength.

3. Experimental set up

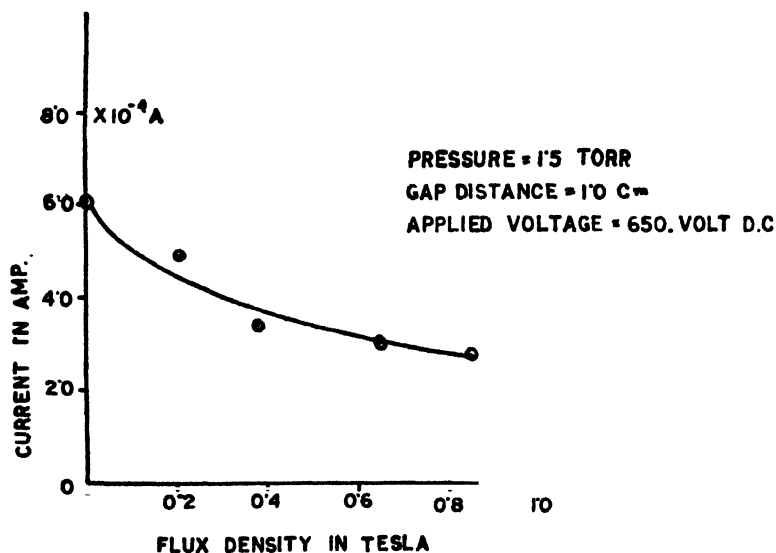
The experimental set up consists of a testing chamber and its assembly, the vacuum system, production of magnetic field and its measurement, high voltage d.c. supply, the details of which have been reported by Paul (1975, 1979) earlier. However, the experimental set up of the system is shown schematically in Fig. 1. As the purpose of the experiment was to investigate the behaviour of the conduction current as a function of magnetic field, hence the gas used in the experiment was discharged at a certain voltage for a fixed value of gap distance and the current

was adjusted to a certain value. Magnetic fields of different strength were then applied and the conduction current values were noted.

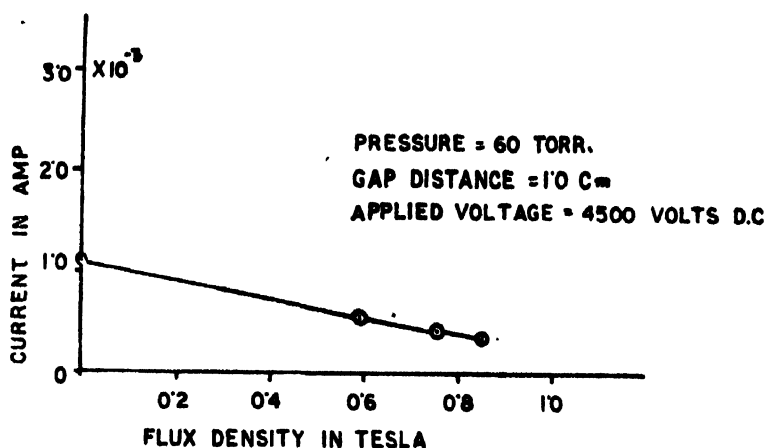


4. Results and discussion

Fig. 2 represents the behaviour of the conduction current as a function of magnetic field at a pressure of 1.5 torr for a gap distance of 1.0 cm. Fig. 3 repre-



rents the similar characteristics but at a pressure of 60 torr with the same gap distance.



It is evident from the experimental results that the effect of magnetic field reduces the conduction current. It may be concluded that the effect of magnetic field reduces the mean free path of the charged particles as a result of which the conduction current is decreased. Further the viscosity also increases due to the applied magnetic field. The net result of the cross-magnetic field is, therefore, the reduction in conduction current as it can be easily observed from eq. (7).

Acknowledgement

The author is grateful for the financial support provided by the Ministry of Education and Social Welfare, Government of India.

References

- Belvin H A and Haydon S C 1958 *Aust. J. Phys.* **11** 18
- Coope J A R and Snider R F 1972 *J. Chem. Phys.* **57** 4286
- Haefer R 1953 *Acta Phys. Austriaca* **7** 52
- Haydon S C 1961 *5th Int. Conf. on Ionization Phenomena in gases, Munich*
- Mayer E 1919 *Ann. Phys.* **58** 297
- Loeb L B 1955 *Basic process of gaseous electron*
- Paul J C, Saha T N and Chakravorty B 1974 *Ind. J. Phys.* **48** 138
- Paul J C, Saha T N and Chakravorty B 1974 *Ind. J. Phys.* **48** 560
- Paul J C 1975 *Int. Sym. on H.V. Engg. Zurich*, 361
- Paul J C 1975 *Int. Sym. on H. V. Engg. Zurich*, 608
- Paul J C 1979 *Ind. J. Phys.*

Nonlinear theory of whistler wave modulation

R Prasad, G P Gupta and R N Singh

Applied Physics Section, Institute of Technology, Banaras Hindu University,
Varanasi-221 005

Received 6 June 1978

Abstract. The general condition for modulational instability and corresponding growth rate of a large amplitude wave propagating through a dispersive medium has been discussed. The nonlinear dispersion equation arising due to consideration of relativistic electron effect for quasi longitudinal propagation of whistler wave through cold and dense magnetoplasma has been derived. Using the nonlinear dispersion equation and the general expressions the variation of frequency spectrum and growth rate of modulationally unstable whistler waves with different wave normal angles has been studied. The results thus obtained have been applied to explain the observed features of banded whistlers.

Introduction

The nonlinear response of a dispersive medium to a large amplitude electromagnetic wave propagating through it has been of recent interest. Consideration of non-linearity of the dispersive medium results in the medium property to depend on the wave field amplitude which, in turn, causes the self-trapping (Chio *et al* 1964) and the self-focussing (Akhmanov *et al* 1966) of waves propagating through the dispersive medium. Taniuti and Washimi (1968) have first considered the whistler wave modulation by low frequency density perturbation. Brinca (1972) has studied simultaneously the relativistic and ion effects on the modulational (self-trapping) instability of whistler wave propagating parallel to the static magnetic field. In the present paper, following the mathematical formalism of Brinca (1972) we have studied the effect of relativistic mass variation of electrons on the modulational instability of whistler waves. The propagation of whistler waves has been considered to be directed at an angle to the static magnetic field permeating the cold and dense plasma. We have, in general discussed the condition for modulational instability and corresponding growth rate of a wave propagating through the dispersive and nonlinear medium with the help of wellknown criterion (Karpman and Krushkal 1969) and the nonlinear Schrödinger wave equation. The nonlinear dispersion equation resulting due to relativistic electron effect for the whistler wave propagating under quasi-longitudinal approximation has been derived. Using the well known criterion (Karpman

and Krushkal 1969) the frequency spectrum for the modulationally unstable whistler waves has been discussed. It is found that the relativistic electron effect sets-in modulational instability of whistler waves for the frequency range $\omega < \frac{\omega_{ce}}{4} \cos \theta$. With a view to study the effect of wave normal angles on the modulational instability, we have computed the maximum growth rate of modulationally unstable whistlers at two ionospheric heights with different wave normal angles. It is shown that the growth rate increases with the wave normal angle and becomes considerable beyond certain wave normal angle. At $\omega = \frac{\omega_{ce}}{4} \cos \theta$, a singularity in the growth rate is obtained. When the growth rate becomes appreciably large, whistlers may break into pulsations and thus explain the observed features of banded whistlers.

2. Modulational Instability

The nonlinear evolution of modulational instability is studied with the help of nonlinear Schrödinger wave equation which is written as (Hasegawa 1975, Liu and Nishikawa 1975)

$$i \frac{\partial \Phi}{\partial \tau} + \alpha \frac{\partial^2 \Phi}{\partial \xi^2} + \beta (|\Phi|^2 - |\Phi_0|^2) \Phi = 0 \quad (1)$$

where Φ is the modulational envelop amplitude of a finite amplitude wave, Φ_0 is its initial value, α and β are coefficients defined as

$$\alpha = \frac{1}{2} \frac{\partial^2 \omega}{\partial k^2}, \quad \beta = - \frac{\partial \omega}{\partial |\Phi|^2} \quad (2)$$

$\tau = t$ and $\xi = Z - \frac{\partial \omega}{\partial k} t$ are coordinates in wave packet frame. The second term in equation (1) characterises the dispersion property of the medium and the third term in equation (1) represents the nonlinearity of the medium. According to the well known criterion (Karpman and Krushkal 1969), the modulational instability occurs only when

$$\frac{\beta}{\alpha} > 0. \quad (3)$$

A perturbation solution of the nonlinear Schrödinger wave equation is obtained by expressing the amplitude of the modulated envelop in the form

$$\Phi = \rho^{\frac{1}{2}} e^{i\sigma} \quad (4)$$

and expanding ρ and σ in a linear approximation

$$\begin{pmatrix} \rho \\ \sigma \end{pmatrix} = \begin{pmatrix} \rho_0 \\ \sigma_0 \end{pmatrix} + \begin{pmatrix} \rho_1 \\ \sigma_1 \end{pmatrix} \exp[i(\Omega\tau - K\xi)] \quad (5)$$

where Ω and K are the frequency and wave number of the modulating wave respectively. The modulating wave is a sort of wave resulting from large wavelength perturbations in the medium. The initial values appearing in equation (5) are $\rho_0 = |\Phi_0|^2$ and $\sigma_0 = 0$. Substituting the expression for Φ as given in equation (4) in equation (1) and then linearising the resulting equation with the help of perturbation scheme (5) we obtain the linear dispersion equation for the modulating wave,

$$\Omega^2 = \alpha^2 K^2 \left(K^2 - 2 \frac{\beta}{\alpha} |\Phi_0|^2 \right) \quad (6)$$

We find that for $K^2 > \frac{2\beta}{\alpha} |\Phi_0|^2$ the Ω remains real and the wave propagation is stable. However, from equation (6) we easily see that Ω becomes complex if the wave number K becomes smaller than certain critical value. This is expressed as

$$K < \sqrt{\frac{2\beta}{\alpha}} |\Phi_0| \quad (7)$$

As a consequence of Ω being complex with K satisfying equation (7) the temporal growth rate of the modulating perturbation is obtained as

$$\eta = \text{Im}\Omega = \alpha K \left(\frac{2\beta}{\alpha} |\Phi_0|^2 - K^2 \right)^{\frac{1}{2}} \quad (8)$$

The maximum growth rate η_m occurs for optimum wave number K_{opt} given by

$$K_{opt} = \sqrt{\frac{\beta}{\alpha}} |\Phi_0| \quad (9)$$

and the corresponding growth rate is

$$\eta_m = \beta |\Phi_0|^2 \quad (10)$$

It is clear from equation (10) that if the medium is linear ($\beta = 0$), the wave is

modulationally stable. For nonlinear dispersive medium, the growth rate of modulational instability is proportional to square of initial wave amplitude.

3. Nonlinear Dispersion Equation

In order to obtain the expressions for the coefficients α and β appearing in equation (2) we derive the nonlinear dispersion equation for a finite amplitude whistler wave propagating along z -axis. The static magnetic field permeating the plasma is assumed to be directed at an angle θ to the z -axis. The motion of charged particles are governed by the electric and magnetic fields of the whistler wave in addition to static magnetic field.

$$m_e \frac{d}{dt} (\gamma V) = -eE - eV \times (B_0 + B) \quad (11)$$

where E and B are described by Maxwell equations as

$$\Delta \times B = -\frac{1}{\epsilon_0 C^2} enV \quad (12)$$

$$\Delta \times E = -\frac{\partial}{\partial t} B$$

Here B_0 is the static magnetic field, E and B are the field vectors of the whistler wave, n is the electron number density, m_e is the electron mass, $\gamma = \left(1 - \frac{V^2}{C^2}\right)^{-1/2}$ is the relativistic correction factor which accounts for the relativistic variation of electron mass. We have neglected the ion motion in equation (11) which limits the lower range of the whistler wave frequency to the lower hybrid frequency. The displacement current in whistler mode propagation has been neglected. Eliminating the wave electric field from equation (11) with the help of equation (12) and using the quasi-longitudinal approximation we obtain the coupled equations

$$\frac{dH}{dt} + H \frac{\partial V_z}{\partial z} - i \frac{V_A}{\omega_{ce}} \frac{\partial}{\partial z} \left[\frac{d}{dt} (\gamma u) \right] - V_A \cos \theta \frac{\partial u}{\partial z} = 0 \quad (13)$$

$$\frac{du}{dt} + i \frac{V_A}{\omega_{ci}} \frac{d}{dt} \left(\frac{n_0}{n} \frac{\partial H}{\partial z} \right) - V_A \frac{n_0}{n} \frac{\partial H}{\partial z}$$

where $H = (B_x + iB_y)/B_0$, $u = (V_x + iV_y)/V_A$, ω_{ce} is the particle gyro-frequency and $V_A = \left(\frac{\epsilon_0 B_0^2 C^2}{n_0 m_i} \right)^{1/2}$ is the Alfvén velocity and n_0 is unperturbed

electron number density. We look for a solution of the coupled equations in terms of the following harmonic variation.

$$\begin{pmatrix} H \\ u \end{pmatrix} = \begin{pmatrix} H_0 \\ u_0 \end{pmatrix} \exp[i(\omega_0 t - k_0 z)] \quad (14)$$

where ω_0 and k_0 are the whistler wave frequency and wave number respectively. In addition, we assume

$$\begin{pmatrix} V_z \\ n \end{pmatrix} = \begin{pmatrix} 0 \\ n_0 \end{pmatrix} \quad (15)$$

Substituting equations (14) and (15) in equation (13) and rearranging result into dispersion equation for whistler waves propagating at angle with the static magnetic field under quasi-longitudinal approximation

$$\left(\frac{\omega_0}{k_0 V_A} \right)^2 = \frac{\omega_0}{\omega_{ce}} \left(\cos \theta - \frac{\gamma \omega_0}{\omega_{ce}} \right) \quad (16)$$

Substituting expressions (14) and (15) and their differentiations in equation (13) and then solving give the expression for $|u_0|^2$ as

$$|u_0|^2 = \left(\frac{k_0 V_A}{\omega_0} \right)^2 \left(1 + \frac{\omega_0}{\omega_{ce}} \right)^2 |H_0|^2. \quad (17)$$

Writing $V_y = |u_0|^2 V_A^2$ the expression for γ reduces to

$$\gamma = \left(1 - \frac{|u_0|^2 V_A^2}{C^2} \right)^{-1} \quad (18)$$

expanding the R.H.S. of equation (18) to first order and then substituting for $|u_0|$ from equation (17) we obtain the expression for γ as

$$\gamma = 1 + \frac{V_A^2}{2C^2} \left(\frac{k_0 V_A}{\omega_0} \right)^2 \left(1 + \frac{\omega_0}{\omega_{ce}} \right)^2 |H_0|^2 \quad (19)$$

Thus the factor γ is dependent on the amplitude of the wave making the dispersion relation nonlinear. Substituting equation (19) in equation (16) and assuming $\omega_0 \gg \omega_{ce}$ we obtain the nonlinear dispersion equation for the whistler wave as

$$\omega_0 = \frac{c^2 k_0^2}{\omega_{pe}^2} \left(\omega_{ce} \cos \theta - \omega_0 \right) - \frac{\omega_0^3}{2 \omega_{pe}^2} \frac{|H_0|^2}{\left(\cos \theta - \frac{\omega_0}{\omega_{ce}} \right)^2} \quad (20)$$

In the limit of $\theta \rightarrow 0$ this equation is similar to that obtained by Brinca (1972).

4. Frequency Spectrum and Growth Rate

In order to obtain the frequency spectrum and growth rate of modulationally unstable whistler waves the expressions for α and β are obtained using equation (2) and the nonlinear dispersion equation. Since equation (1) is also valid for the normalized wave amplitude, we consider Φ_0 as the normalized wave magnetic field H_0 . With the help of equations (2) and (20) the expressions for α and β are obtained as

$$\alpha = \frac{\omega_0(\omega_{ce}\cos\theta - \omega_0)(\omega_{ce}\cos\theta - 4\omega_0)}{k_0^2\omega_{ce}^2\cos^2\theta} \quad (21)$$

$$\beta = \frac{\omega_0^3}{2\omega_{pe}^2\left(\cos\theta - \frac{\omega_0}{\omega_{ce}}\right)^2} \quad (22)$$

Using equations (21), (22) and the criterion (3) we find that whistler waves propagating at angle to the static magnetic field are modulationally unstable when

$$\omega_0 < \frac{\omega_{ce}\cos\theta}{4} \quad (23)$$

This inequality gives the frequency spectrum of the modulationally unstable whistler waves. It is found that the upper limit of the frequency spectrum decreases as the wave normal angle increases. The expression for maximum growth rate is obtained using equations (10) and (22).

$$\eta_m = \frac{\omega_0^3 |H_0|^2}{2\omega_{pe}^2\left(\cos\theta - \frac{\omega_0}{\omega_{ce}}\right)^2} \quad (24)$$

Using equation (24) the maximum growth rate of modulationally unstable whistler wave with frequency $f = 10$ KHz and normalized magnetic field $|H_0| = 0.01$ has been computed. For this purpose, we have considered two ionospheric heights where the whistler wave during its propagation makes different wave normal angles with the magnetic field. The ionospheric plasma and magnetic field parameters used for computation are given in table 1.

Table 1. Ionospheric plasma and magnetic field parameters

Height	ω_{pe} (rad/sec)	ω_{ce} (rad/sec)
100 Km.	2.3×10^7	10^7
250 Km.	4×10^7	8.8×10^6

Figure 1 shows the variation of maximum growth rate with wave normal angles at two ionospheric heights. It is found that the growth rate increases with increasing values of wave normal angles at a particular ionospheric height. However, the growth rate is decreased at the same wave normal angle if the

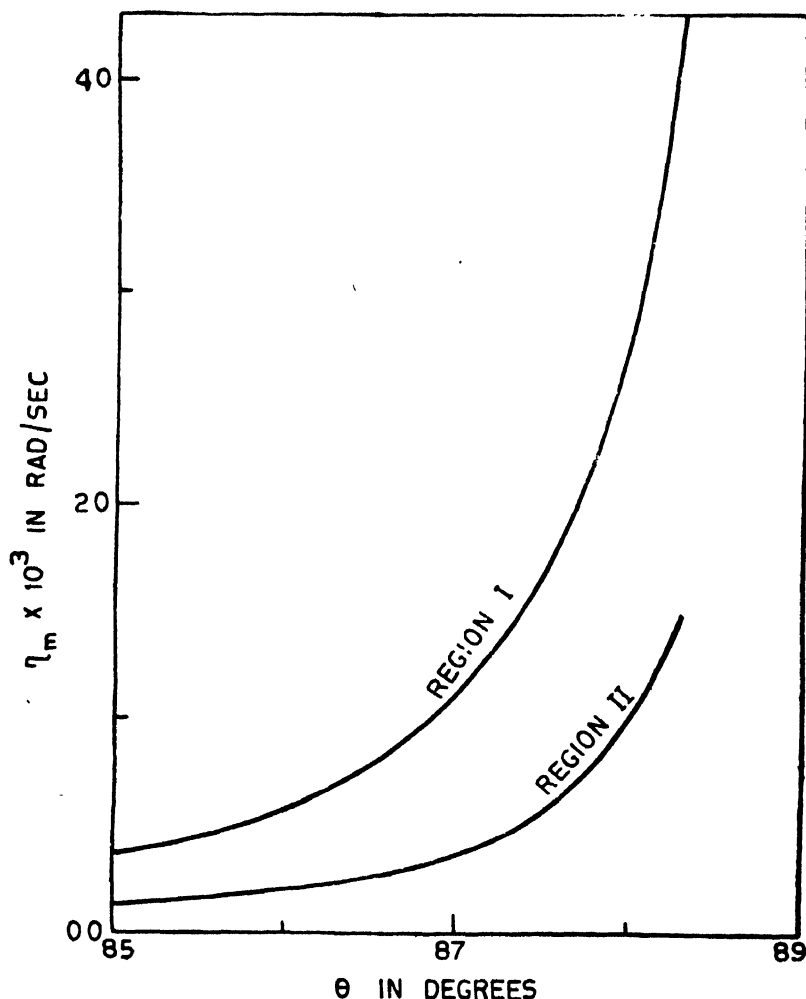


Figure 1. Variation of maximum growth rate with wave normal angles at two ionospheric heights. (Region I for 100 Km and II for 250 Km).

ionospheric height which is characterized by plasma and field parameters is increased. The maximum growth rate is significant beyond certain wave normal angles and is seen to increase rather fast near $\omega = \frac{\omega_{ce} \cos \theta}{4}$

5. Conclusions

Using the well known criterion and the nonlinear Schrödinger wave equation we have discussed the condition for the onset of modulational instability and have obtained the corresponding growth rate for a wave in general propagating through the dispersive and nonlinear medium. Accounting for the effect of relativistic mass variation of electrons we have derived the nonlinear dispersion equation for the whistler wave at an angle to the static magnetic field under quasi-longitudinal approximation. It is found that the consideration of relativistic effect of electrons induces the modulational instability for the frequency range $\omega < \frac{\omega_{ce} \cos \theta}{4}$. The variation of wave normal angles is found to affect

the upper limit of the frequency spectrum and the growth rate of modulationally unstable whistler waves. From the study of maximum growth rate at two ionospheric heights for different wave normal angles, it is shown that the growth rate becomes considerable after a certain wave normal angle. Near $\omega = \frac{\omega_{ce} \cos \theta}{4}$

the growth rate is significantly large, which may cause the whistler wave to break into smaller pulsations. Thus whistler wave energy received on the ground may not be a continuous function of frequency and may instead appear in the form of frequency bands. This explains the observed features of banded whistlers often times recorded at the low and high latitude stations.

Acknowledgment

Two of us (RP and GPG) are grateful to C.S.I.R., New Delhi for the award of research fellowships.

References

- Akhmanov S A, Sukhorukov A P and Khokhlov R V 1966 *Sov. Phys. JETP* **23** 1025
- Brinca A L 1972 *SUIPR Report No 664 Stanford*
- Chiao R Y, Garmire E and Townes C H 1964 *Phys. Rev. Lett.* **13** 479
- Hasegawa A 1975 *Plasma Instabilities and Nonlinear Effects* Springer Berlin
- Karpman V I and Krushkal E M 1969 *Sov. Phys. JETP* **28** 277
- Liu C S and Nishikawa K 1975 *Advances in Plasma Physics* **6**
- Taniuti T and Washimi H 1968 *Phys. Rev. Lett.* **21** 209

On the goodness of the pseudo quantum numbers

M. Satyanarayana Reddi* V. K. Kota and R. D. Ratna Raju

Theoretical Group, Department of Physics, Andhra University,
Waltair

Received 1 August 1977

The goodness of the pseudo Nilsson quantum numbers in the asymptotic limit is tested by calculating the single particle contribution to the quadrupole moments in the pseudo scheme. It is found that, the pseudo scheme also gives small values which are very close to the values given by the real Nilsson scheme, thus indicating the approximate goodness of the pseudo Nilsson quantum numbers.

1. Introduction

The introduction of the pseudo spin and pseudo angular momentum quantum numbers (Hecht *et al* 1969, Arima *et al* 1969) has shown a way of considerably reducing the calculational labour in the shell model basis (Adler 1969). It was further shown (Ratna Raju *et al* 1973) that associating a pseudo major oscillator shell number \tilde{N} would naturally lead to the classification of the many body Nilsson states growing out of the single particle spherical shell orbitals, according to the irreducible representations of the pseudo SU(3) group. Therefore, the goodness of the pseudo SU(3) model depends upon the goodness of the pseudo Nilsson quantum numbers to a large extent.

The approximate goodness of the pseudo Nilsson quantum numbers in the asymptotic limit to predict the magnetic moments, was studied (Ratna Raju *et al* 1973). However, a real test would be to check whether the pseudo Nilsson asymptotic quantum numbers would give only small values for the particle part of the quadrupole moments, thus preserving the largeness of the core part.

The core value is independent of the particle quantum numbers. Therefore, here we have tested to see whether the single particle values given by the pseudo scheme would agree with what the real Nilsson scheme would predict. The classification of the Nilsson orbitals as pseudo spin orbit doublets can be found in Ratna Raju (1973) and Reddi *et al* (1975).

*Present address : Regional Engineering College, Warangal-506004.

2. Method of Calculation

The Pseudo Nilsson Scheme

The quadrupole moment operator in the lab system is defined as

$$Q_{0p} = Q_p + Q_c$$

where Q_p gives the contribution coming from the individual particle motion and Q_c the contribution from the collective motion. Explicitly it is written as (Nilsson 1955)

$$Q_{0p} = \sum_p 2 \left[\frac{4\pi}{5} \right]^{\frac{1}{2}} \left(\delta_p + \frac{Ze}{A^2} \right) r_p^2 Y_0^2(\theta_p \phi_p) + \frac{3Ze}{\sqrt{5\pi}} r_0^2 \beta D_{00}^2 \quad (1)$$

where the effective charge can be taken as $\delta_p = 2$ for protons and 1 for neutrons (Greiner *et al* 1970). The summation in the first term runs over all the particles. In the real Nilsson scheme, the expectation value of Q_c can be written trivially as (Nilsson 1955)

$$\langle |Q_c| \rangle = \frac{3K^2 - I(I+1)}{(I+1)(2I+3)} Q_0$$

where

$$Q_0 = \frac{3Ze}{\sqrt{5\pi}} r_0^2 \beta$$

The commonly used deformation parameter δ is simply related to β as

$$\delta = \frac{3}{2} \sqrt{\frac{5}{4\pi}} \beta$$

The contribution from the core i.e., the collective part totally dominates the particle part and in fact all the quadrupole moments predicted by neglecting the particle part are in excellent agreement with experiment.

The core part is independent of the particle quantum numbers and as such it would give the same contribution in both the real and pseudo Nilsson schemes. However, the particle part does depend upon the individual particle quantum numbers and it is essential to see how it would behave in the pseudo scheme and to compare its contribution in the pseudo scheme with what we get in the real scheme in the asymptotic limit as well as for actual deformation. For this purpose, we decompose Q_p into irreducible components of spherical tensor operators in the real and pseudo spaces. Making use of the definition of the one-body operator in the second quantization language we can write

$$Q_{0p} = \sum_{\substack{u, u' \\ m, m'}} \langle (l' \frac{1}{2}) j' m' | 2 \left[\frac{4\pi}{5} \right]^{\frac{1}{2}} \delta_p r_p^2 Y_0^2 | (l) j m \rangle a_{j'm}^{\dagger} a_{jm} \quad (3)$$

where we have neglected the factor Ee/A^2 since it is much less than one for all cases of interest. After evaluating the matrix element, coupling the creation and annihilation operators and performing necessary transformations we obtain the final expression for the operator in the real scheme as

$$Q_p = 2\delta_p \sum_{l, l', j, j'} (-1)^{j+1} \frac{(2j'+1)(2j+1)}{5} [(2L_0+1)(2S_0+1)]^{\frac{1}{2}} \\ < j - \frac{1}{2} j' \frac{1}{2} | 2. > < n'l' || r^2 || nl > \\ \left\{ \begin{array}{ccc} l' & \frac{1}{2} & j' \\ l & \frac{1}{2} & j \\ L_0 & S_0 & J_0 = 2 \end{array} \right\} [a_{l'}^+ \times a_l]_{00}^{L_0 S_0 J_0 = 2}$$

When we make the transformation to the pseudo scheme, the real spin (4) and orbital angular momenta go over into the pseudo spin and orbital angular momenta. The ranks of the tensor operator in various spaces would also go over into the pseudo \tilde{L}_0 and \tilde{S}_0 . The final expression can be written as

$$\tilde{Q}_{0p} = 2\delta_p \sum_{n', j'} (-1)^{j+1} \frac{(2j+1)(2j'+1)}{5} [(2\tilde{L}_0+1)(2\tilde{S}_0+1)]^{\frac{1}{2}} \\ < j - \frac{1}{2} j' \frac{1}{2} | 20 > < n'l' || r^2 || nl > \\ \sum_{\tilde{l} \tilde{l}'} \left\{ \begin{array}{ccc} \tilde{l}' & \frac{1}{2} & j' \\ \tilde{l} & \frac{1}{2} & j \\ \tilde{L}_0 & \tilde{S}_0 & J_0 = 2 \end{array} \right\} [a_{\tilde{l}'}^+ \cdot a_{\tilde{l}}]_{\tilde{l}' \tilde{l}}^{\tilde{L}_0 \tilde{S}_0 J_0 = 2} \quad (5)$$

These operators are explicitly evaluated for the real $N = 3, 4$ and 5 and the pseudo $\tilde{N} = 2, 3$ and 4 shells. The results are given tables 1 and 2 respectively. The coefficients of various tensors are labelled as $C_{11}(C_{\tilde{1}\tilde{1}})$ in the tables.

In the asymptotic limit where the deformation becomes very large, the Nilsson representation $[N n_z \Lambda]$ provides a set of good quantum numbers. In the pseudo scheme also we expect the pseudo Nilsson representation $[N \tilde{n}_z \Lambda]$ to do the same. We start with the unified-model wave function for the last (odd) nucleon given by

$$\psi = \left[\frac{2I+1}{16\pi^2} \right]^{\frac{1}{2}} \sum_{l \Lambda \epsilon} \left\{ D_{MK}^I a_{l \Lambda \epsilon} \chi_{\Lambda \Sigma \Omega}^{I \frac{1}{2}} \right. \\ \left. - (-1)^{I+\frac{1}{2}} D_{M-K}^I a_{l -\Lambda -\Sigma -\Omega} \chi_{-\Lambda -\Sigma -\Omega}^{I \frac{1}{2}} \right\}$$

Table 1. Coefficients for the tensor term of Q_p

Major oscillator shell	1'	1	L_0	S_0	J_0	$C_{1'1}$
$N = 3$	1	1	2	0	2	-3.1176
	1	3	2	0	2	3.1749
	3	1	2	0	2	3.1749
	3	3	2	0	2	-3.8884
$N = 4$	0	2	2	0	2	3.3466
	2	0	2	0	2	3.3466
	2	2	2	0	2	-4.1576
	2	4	2	0	2	4.3028
	4	2	2	0	2	4.3028
	4	4	2	0	2	-5.3184
$N = 5$	1	1	2	0	2	-4.5033
	1	3	2	0	2	5.0911
	3	1	2	0	2	5.0911
	3	3	2	0	2	-5.6166
	3	5	2	0	2	5.4160
	5	3	2	0	2	5.4160
	5	5	2	0	2	-6.9041

Note : The values in the last column are in the units of

$$\left(\frac{2\hbar}{m\omega_0} \delta_p \right)$$

where

$$a_{l\Lambda\Sigma\Omega} = \sum_j C_{j\Omega}^{[0]} \langle l\Lambda\frac{1}{2}\Sigma | j\Omega \rangle$$

and

$$a_{l-\Lambda-\Sigma-\Omega} = (-1)^l a_{l\Lambda\Sigma\Omega}$$

We can calculate the expectation value of the operator given in eqn. 4 by making use of the above wave function in the usual way. To evaluate the expectation value of Q_p in the pseudo Nilsson scheme we replace the real ($l\Lambda\Sigma$) quantum numbers by the pseudo ($\tilde{l}\tilde{\Lambda}\tilde{\Sigma}$) quantum numbers. The wave function then becomes

$$\tilde{\psi} = \left[\frac{2I+1}{16\pi^2} \right]^{\frac{1}{2}} \sum_{\tilde{l}\tilde{\Lambda}\tilde{\Sigma}} \left\{ D_{M-K}^{\tilde{l}\tilde{\Lambda}} a_{\tilde{l}-\tilde{\Lambda}-\tilde{\Sigma}\Omega} \chi^{\tilde{l}\frac{1}{2}}_{\tilde{\Lambda}\tilde{\Sigma}\Omega} \right. \\ \left. (-1)^{I+\frac{1}{2}} D_{M-K}^{\tilde{l}\tilde{\Lambda}} a_{\tilde{l}-\tilde{\Lambda}-\tilde{\Sigma}\Omega} \chi^{\tilde{l}\frac{1}{2}}_{-\tilde{\Lambda}-\tilde{\Sigma}-\Omega} \right\}$$

Table 2. Coefficients for the tensor term of \tilde{Q}_p

Major oscillator shell	\tilde{l}'	\tilde{l}	\tilde{L}_0	\tilde{S}_0	J_0	$C_{\tilde{l}' \tilde{l}}$
$\tilde{N} = 2$	0	2	2	0	2	2.5582
	0	2	2	1	2	0.2349
	2	0	2	0	2	2.5582
	2	0	2	1	2	-0.2349
	2	2	1	1	2	-0.1993
	2	2	2	0	2	-3.2641
	2	2	3	1	2	-1.4068
$\tilde{N} = 3$	1	1	1	1	2	-0.0681
	1	1	2	0	2	-3.7142
	1	3	2	0	2	3.9982
	1	3	2	1	2	0.8125
	1	3	3	1	2	0.1079
	3	1	2	0	2	3.9982
	3	1	2	1	2	-0.8125
	3	1	3	1	2	0.1079
	3	3	1	1	2	-0.2822
	3	3	2	0	2	-4.6194
	3	3	3	1	2	-1.6833

Note : The values in the last column are in the units of

$$\left(\frac{2\hbar}{m\omega_0} \delta_p \right)$$

In the asymptotic limit when $[\tilde{N}n_A]$ gives a set of good quantum numbers, the $a_{\tilde{l} \tilde{\Lambda} \tilde{\Sigma} \Omega}$ coefficients turn out to be the transformation coefficients from spherical to the cylindrical basis (Sharp *et al* 1969) which can easily be evaluated. Before we calculate the expectation value of the quadrupole operator, we transform it into the body-fixed frame through the relation.

$$T^{L_0 S_0 J_0 -2} = \sum D_{0\alpha}^2 T'^{L_0 S_0 J_0 -2}$$

Table 3. Particle contribution to the total quadrupole moment

Nucleus	Spin	Nilsson Repr.		Single particle contribution		
		Real	Pseudo	Real scheme		Pseudo scheme asymptotic
				asymptotic	Actual δ	
1	2	3	4	5	6	7
⁷⁹ Br	3/2 ⁻	[301]	[$\tilde{202}$]	-0.0829	-0.0753	-0.0608
⁸¹ Br	3/2 ⁻	[301]	[$\tilde{202}$]	-0.0843	-0.0765	-0.0619
⁸⁵ Rb	5/2 ⁻	[303]	[$\tilde{202}$]	-0.1555	-0.1428	-0.1141
⁸⁷ Rb	3/2 ⁻	[310]	[$\tilde{202}$]	-0.0884	-0.0803	-0.0649
¹⁵³ Eu	3/2 ⁺	[411]	[$\tilde{312}$]	-0.0524	-0.0294	-0.0634
¹⁵⁷ Tb	3/2 ⁺	[411]	[$\tilde{312}$]	-0.0534	-0.0299	-0.0361
¹⁵⁹ Tb	3/2 ⁺	[411]	[$\tilde{312}$]	-0.0539	-0.0301	-0.0364
¹⁷⁵ Lu	7/2 ⁺	[404]	[$\tilde{303}$]	-0.4777	-0.4517	-0.3717
¹⁷⁷ Lu	7/2 ⁺	[404]	[$\tilde{303}$]	-0.4813	-0.4551	-0.3745
¹⁸¹ Tu	7/2 ⁺	[404]	[$\tilde{303}$]	-0.4886	-0.4619	-0.3802
¹⁸¹ Ta	5/2 ⁺	[402]	[$\tilde{303}$]	-0.3739	-0.3514	-0.2910
¹⁸⁵ Re	5/2 ⁺	[402]	[$\tilde{303}$]	-0.3794	-0.3565	-0.2952
¹⁸⁷ Re	5/2 ⁺	[402]	[$\tilde{303}$]	-0.3822	-0.3591	-0.2974
¹⁹¹ Ir	3/2 ⁺	[402]	[$\tilde{301}$]	-0.2170	-0.1694	-0.2080
¹⁹³ Ir	3/2 ⁺	[402]	[$\tilde{301}$]	-0.2185	-0.1706	-0.2092
⁶⁵ Zn	5/2 ⁻	[303]	[$\tilde{202}$]	-0.0650	-0.0595	-0.0477
⁶⁷ Zn	5/2	[303]	[$\tilde{202}$]	-0.0663	-0.0609	-0.0487
¹⁵⁵ Gd	3/2 ⁻	[521]	[$\tilde{422}$]	0.0200	0.0165	0.0339
¹⁵⁷ Gd	3/2 ⁻	[521]	[$\tilde{422}$]	0.0201	0.0166	0.0342
¹⁶¹ Dy	5/2 ⁻	[523]	[$\tilde{422}$]	0.0339	0.0236	0.0621
¹⁶³ Dy	5/2 ⁻	[523]	[$\tilde{422}$]	0.0342	0.0238	0.0626
¹⁶⁵ Er	5/2 ⁻	[523]	[$\tilde{422}$]	0.0345	0.0240	0.0631
¹⁷¹ Er	5/2 ⁻	[512]	[$\tilde{413}$]	-0.0700	-0.0623	-0.0665
¹⁷³ Yb	5/2 ⁻	[512]	[$\tilde{413}$]	-0.0706	-0.0628	-0.0670
¹⁷⁷ Hf	7/2 ⁻	[514]	[$\tilde{413}$]	-0.1018	-0.0889	-0.0889
¹⁸⁹ Os	3/2 ⁻	[512]	[$\tilde{411}$]	-0.0419	-0.0237	-0.0404

We can show trivially that the final expression for the expectation value of the operator is given by

$$\begin{aligned}
 & \langle [\tilde{N}\tilde{n}_z\Lambda]\Omega I K M | T^{\tilde{L}_0\tilde{S}_0J_0^{-2}} | [\tilde{N}\tilde{n}_z\Lambda]\Omega I K M \rangle \\
 &= \frac{3K^2 - I(I+1)}{(I+1)(2I+3)} \sum_{\tilde{\tau}, \tilde{\tau}'} a_{\tilde{\tau}, \tilde{\tau}}^a a_{\tilde{\tau}', \tilde{\tau}'}^a \tilde{C}_{\tilde{\tau}, \tilde{\tau}'}^C \langle \tilde{L}_0\tilde{S}_0 | Z O \rangle \\
 & \left[\frac{2\tilde{L}_0+1}{2(2\tilde{\ell}+1)} \right]^4 \langle \tilde{\ell}\tilde{\Lambda}\tilde{L}_0\tilde{S}_0 | \tilde{\ell}'\tilde{\Lambda}' \rangle.
 \end{aligned}$$

in the pseudo scheme.

Actually, the coefficients $C_{11}(C_{\tilde{\tau}, \tilde{\tau}}^C)$ of the various tensors are given in the units of $\frac{2\hbar}{m\omega_0} \delta p$. The values of $\frac{\hbar}{m\omega_0}$ which come into the calculation through the expectation value of the r^2 in the operator can simply be evaluated as

$$\frac{\hbar}{m\omega_0} = \frac{r_0^2 A^{2/3}}{N+3/2}$$

The contribution coming from the particle part in the pseudo scheme is compared with what we get in the real scheme in table 3.

3. Discussion of the Results

As can be seen from table 3, the single particle values predicted by the pseudo scheme are small, and in a great majority of the nuclei where the deformations are well defined, they are very close to the real Nilsson values in the asymptotic limit. In the table we have also compared those values with the results of a calculation considering the actual deformation for each nucleus.

Except in the case of nuclei which are represented by the pseudo Nilsson representation [422], in all other cases the values of the pseudo Nilsson scheme are very close to the real Nilsson values.

References

- Adler A. 1969 Ph.D. Thesis, University of Michigan
 Arima A. Harvey M. and Shimizu K. 1969 *Phys. Letters* **30B**, 517.
 Eisenberg J. M. and Groiner W. 1970 *Nuclear Theory* 1 (North Holland)
 Hecht K. T. and Adler A. 1969 *Nucl. Phys.* **A137**,
 Nilsson S. G. 1955 *Matt. Phys. Medd. Dan. Vid. Selsk.* **29**, No. 16.
 Ratna Raju R. D. Draayer J. P. and Hecht K. T. 1973 *Nucl. Phys.* **A202**, 433.
 Satyanarayana Reddi M. and Ratna Raju R. D. 1975 *J. Phys. Soc. Japan* **39**, 566.
 Sharp R. T. Van Baeyer H. C. and Pieper S. C. 1969 *Nucl. Phys.* **A127**, 513.

Second quantization of generalized electromagnetic fields

B S Rajput and Om Prakash

Department of Physics, Garhwal University, Srinagar (Garhwal)

Received 5 May 1977, revised 16 August 1977

Second quantization of generalized electromagnetic fields has been done in purely reduced expansions of fields in terms of Foldy-Shirokov realizations of irreducible representations of proper-orthochronous inhomogeneous Lorentz group. Expressions for Hamiltonian and momentum operator have been derived in terms of annihilation and creation operators and the Hamiltonian has been shown to consist of three parts corresponding to free field term, contribution of charge source densities, and the interaction term respectively.

1. Introduction

First exception to the arguments (Rosenbaum 1966, Zwanziger 1965, Hagen 1965) against the existence of Dirac's monopole (1931, 1948) is the work of Schwinger (1966a, 1966b), who while treating the lack of experimental support less serious, formulated a relativistically covariant quantum field theory of magnetic charges. He put forward a hypothesis concerning a magnetic model of matter in terms of hadrons and dyons (Schwinger 1970, Yan and Beden harn 1970, Kim and Korean 1972) giving some insight into the nature of hypercharge and possible time reversal mechanism. Schwinger's quantum field theory of spin $-\frac{1}{2}$ magnetic charge was extended by Zwanziger (1968, 1971) to the fields of spin $-\frac{1}{2}$ particles carrying both the electric and magnetic charges. Recently Chiang (CPT201) has shown that a consistent local Lagrangian field theory of magnetic monopoles can be constructed by using the indefinite metric and concept of shadow states (Nelson and Sudarshan 1972a, 1972b).

Considering the generalized charge as a complex quantity with electric and magnetic charges as its real and imaginary parts, we could derive (1970a, 1970b) the reduced expansions for generalized electromagnetic fields associated with spin-1 particles carrying the generalized charges. In these reduced expansions derived in terms of Lomont-Moses (1967) and Foldy-Shirokov (1956, 1958) realizations of irreducible representations of proper, orthochronous, inhomogeneous Lorentz group the asymmetry present in the reduced expansions (Rajput 1969a, 1971) for ordinary electromagnetic fields have been removed. By choosing a suitable Lagrangian density (Parkash and Rajput 1976) to yield generalized field

*On leave from Physics Department, Kurukshetra University, Kurukshetra

equations, the symmetry properties and dual invariance have been demonstrated (Parkash and Rajput 1977a) under the rotation and reflection in charge space. This Lagrangian density has also been used to derive the expression for field Hamiltonian and it has been shown (Parkash and Rajput 1977b) that the interaction between the generalized charges depends on their electric and magnetic coupling parameters.

In the present work the second quantization of generalized electromagnetic fields has been done in purely relativistic group theoretical Lorentz covariant manner on replacing in the reduced expansions of field operators the amplitudes by annihilation operators and their complex conjugates by creation operators. In this theory of second quantization, the two four-potentials have been introduced for the specification of generalized fields and the use of arbitrary and controversial string variables introduced by Zwanziger (1968, 1971) has been avoided. The commutation rules for field operators have been derived and it has been shown that in general the locality can not be achieved in these commutations and that the effect of making simultaneously the charge and current source densities vanishing is the same as that of setting the mass equal to zero. The expressions for Hamiltonian and momentum operators have been derived in terms of annihilation and creation operators and it has been shown that the total Hamiltonian consists of three parts corresponding to free field Hamiltonian, contribution of charge source densities, and the interaction term respectively.

2. Reduced expansions of field operators

Assuming the generalized charge (Rajput and Parkash 1974a) as a complex quantity with electric and magnetic charges, e and g as its real and imaginary parts i.e.

$$q = e - ig, \quad (2.1)$$

the following expressions have been derived (Parkash and Rajput 1976) for generalized electromagnetic fields associated with spin -1 generalized charges;

$$\mathbf{E}(\mathbf{x}) = \frac{\partial \mathbf{A}}{\partial t} - \nabla \phi_e - \nabla \times \mathbf{B} \quad (2.2a)$$

$$\mathbf{H}(\mathbf{x}) = \frac{\partial \mathbf{B}}{\partial t} - \nabla \phi_g + \nabla \times \mathbf{A} \quad (2.2b)$$

where the components of electric and magnetic four-potentials $\{\mathbf{A}_\mu\} = (\mathbf{A}, i\phi_e)$ and $\{\mathbf{B}_\mu\} = (\mathbf{B}, i\phi_g)$ have been introduced to avoid the use of arbitrary and controversial string variables (Zwanziger 1971). Reduced expansions of the components of these four-potentials in terms of Foldy-Shirokov realizations of proper, orthochronous, inhomogeneous Lorentz group, has already been derived in the

following term in our earlier paper (Rajput and Prakash 1976) by comparing eqns. (2.2) with the reduced expansions of generalized electromagnetic fields obtained on substituting our reduced expansions of scalar (Rajput 1969b) and vector (Rajput 1969c) fields for non-zero mass systems into Epstein's (1967) results;

$$\begin{aligned} \mathbf{A}(x) = & \frac{e}{|q|4\pi^{3/2}} \left\{ \int \frac{d\mathbf{p}}{\omega} f(\mathbf{p}) \exp[i(\mathbf{p} \cdot \mathbf{x} - \omega t)] \right. \\ & \left. + \int \frac{d\mathbf{p}}{\omega} h^*(\mathbf{p}) \exp[-i(\mathbf{p} \cdot \mathbf{x} - \omega t)] \right\} \end{aligned} \quad (2.3a)$$

and similar expression for $\mathbf{B}(x)$ with e replaced by g ,

$$\begin{aligned} \phi_e = & \frac{e}{|q|4\pi^{3/2}} \left[\int d\mathbf{p} \frac{\{\mathbf{p} \cdot f(\mathbf{p})\}}{\omega(\omega+m)^2} \exp[i(\mathbf{p} \cdot \mathbf{x} - \omega t)] \right. \\ & \left. + \int d\mathbf{p} \frac{\{\mathbf{p} \cdot h^*(\mathbf{p})\}}{\omega(\omega+m)} \exp[-i(\mathbf{p} \cdot \mathbf{x} - \omega t)] \right] \end{aligned} \quad (2.3b)$$

and the similar expression for ϕ_g with e replaced by g , where $f(\mathbf{p}) = f(m, \mathbf{p})$ is the representation of wave-function of particle of mass m and spin -1 in the basis characterized by the Hilbert space upon which the generators of inhomogeneous Lorentz group operate; $h(\mathbf{p}) = f^*(m, -\mathbf{p})$; x is the space-time four-component position vector; $c = \hbar = 1$; and $\omega(\mathbf{p}) = (m^2 + \mathbf{p}^2)^{1/2} = \omega$.

Generalized electromagnetic fields may also be written in terms of their longitudinal and transverse parts,

$$\mathbf{E}(x) = \mathbf{E}^L(x) + \mathbf{E}^T(x) \quad (2.4a)$$

$$\mathbf{H}(x) = \mathbf{H}^L(x) + \mathbf{H}^T(x) \quad (2.4b)$$

from which the reduced expansions of longitudinal and transverse parts of generalized fields may be readily derived. The transverse parts of fields are specified by two transverse vector potentials given by

$$\mathbf{A}^T(x) = \nabla \times \int D(\mathbf{x} - \mathbf{x}') \mathbf{H}^T(x') d\mathbf{x}' \quad (2.5)$$

$$\mathbf{B}^T(x) = -\nabla \times \int D(\mathbf{x} - \mathbf{x}') \mathbf{E}^T(x') d\mathbf{x}'$$

$$\text{where} \quad D(\mathbf{x} - \mathbf{x}') = \frac{1}{(2\pi)^3} \int \frac{d\mathbf{p}}{p^2} \exp(i\mathbf{p} \cdot (\mathbf{x} - \mathbf{x}')). \quad (2.6)$$

Substituting the reduced expansions of transverse fields in these equations, we get the following reduced expansions for transverse potentials:

$$\begin{aligned} \mathbf{A}^T(\mathbf{x}) = & \frac{1}{|q|4\pi^{3/2}} \left[\int d\mathbf{p} \left\{ \left[\frac{e f(\mathbf{p})}{\omega} - \frac{e \mathbf{p} \{ \mathbf{p} \cdot f(\mathbf{p}) \}}{p^2 \omega} - \frac{g \mathbf{p} \times f(\mathbf{p})}{p^2} \right] \right. \right. \\ & \times \exp\{i(\mathbf{p} \cdot \mathbf{x} - \omega t)\} \\ & + \int d\mathbf{p} \left\{ \left[\frac{e h^*(\mathbf{p})}{\omega} - \frac{e \mathbf{p} \{ \mathbf{p} \cdot h^*(\mathbf{p}) \}}{p^2 \omega} - \frac{g \{ \mathbf{p} \times h^*(\mathbf{p}) \}}{p^2} \right] \right. \\ & \left. \left. \times \exp[-i(\mathbf{p} \cdot \mathbf{x} - \omega t)] \right\} \right] \end{aligned} \quad (2.7)$$

and

$$\begin{aligned} \mathbf{B}^T(\mathbf{x}) = & \frac{1}{|q|4\pi^{3/2}} \left[\int d\mathbf{p} \left[\frac{g f(\mathbf{p})}{\omega} - \frac{g \mathbf{p} \{ \mathbf{p} \cdot f(\mathbf{p}) \}}{p^2 \omega} + \frac{e \{ \mathbf{p} \times f(\mathbf{p}) \}}{p^2} \right] \exp\{i(\mathbf{p} \cdot \mathbf{x} - \omega t)\} \right. \\ & \left. + \int d\mathbf{p} \left[\frac{g h^*(\mathbf{p})}{\omega} - \frac{g \mathbf{p} \{ \mathbf{p} \cdot h^*(\mathbf{p}) \}}{p^2 \omega} + \frac{e \mathbf{p} \times h^*(\mathbf{p})}{p^2} \right] \exp\{i(\mathbf{p} \cdot \mathbf{x} - \omega t)\} \right] \end{aligned} \quad (2.8)$$

Lagrangian density for the generalized electromagnetic fields may be written in the following form in terms of these four-potentials:

$$\begin{aligned} L = & -\frac{1}{4} [\alpha \{(\hat{A}_{\nu,\mu} - \hat{A}_{\mu,\nu})^2 - (B_{\nu,\mu} - B_{\mu,\nu})^2\} - 2\beta \{(\hat{A}_{\nu,\mu} - \hat{A}_{\mu,\nu})(B_{\nu,\mu} - B_{\mu,\nu})\} \\ & + (\alpha \hat{A}_\mu - \beta B_\mu) j_\mu - (B \hat{A}_\mu + \alpha B_\mu) k_\mu] \end{aligned} \quad (2.9)$$

where α and β are real positive parameters. This Lagrangian density has been shown in our earlier paper (Rajput and Parkash 1976) to yield the suitable generalized Maxwell field equations under the independent variations of \hat{A}_μ and B_μ .

Replacing the amplitudes $f(\mathbf{p})$ and $h(\mathbf{p})$ in the corresponding reduced expansions by annihilation operators and their complex conjugates by creation operators, we get the second quantized reduced expansions for field operators, four-potential operators and the transverse potential operators.

3. Commutation rules for field operators

Using the second quantized reduced expansions for all the field operators, their commutation rules may be derived by assuming Bose statistics for the annihilation and creation operators of generalized fields associated with spin -1 particles, such that all their commutators vanish except the following:

$$\begin{aligned} [f(\mathbf{p}, \lambda), f^*(\mathbf{p}', \lambda')] &= \omega \delta(\mathbf{p} - \mathbf{p}') \delta_{\lambda, \lambda'} \\ [h(\mathbf{p}, \lambda), h^*(\mathbf{p}', \lambda')] &= \omega \delta(\mathbf{p} - \mathbf{p}') \delta_{\lambda, \lambda'} \end{aligned} \quad (3.1)$$

Then the following equal time commutation rules for the second quantized operators $\hat{E}(\mathbf{x})$ and $\hat{H}(\mathbf{x})$ may readily be derived by using their reduced expansions;

$$[\hat{E}_i(\mathbf{x}), \hat{E}_j(\mathbf{x}')] = [\hat{H}_i(\mathbf{x}'), \hat{H}_j(\mathbf{x}')] - [\hat{E}_i(\mathbf{x}), \hat{H}_j(\mathbf{x}')] = 0 \quad (3.2a)$$

and

$$[\hat{E}_i^*(\mathbf{x}), \hat{H}_j(\mathbf{x}')] = [\hat{E}_i(\mathbf{x}), \hat{H}_j(\mathbf{x}')] \\ = -i \left[\frac{egm^2}{|q|} \delta_{ij} \Delta(\mathbf{x} - \mathbf{x}') + \epsilon_{ijk} \nabla_k \delta(\mathbf{x} - \mathbf{x}') \right], \quad (3.2b)$$

where

$$\Delta(x) = \frac{1}{(2\pi)^3} \int \frac{d\mathbf{p}}{\omega} \sin \mathbf{p} \cdot \mathbf{x}. \quad (3.3)$$

In the absence of magnetic charge (or that of electric charge) this commutation rule reduces to the usual local commutation rule derived earlier (Parkash and Rajput 1974) for the ordinary electromagnetic fields for non-zero mass system.

For the transverse electromagnetic field operators $\hat{\mathbf{E}}^T(\mathbf{x})$ and $\hat{\mathbf{H}}^T(\mathbf{x})$ we get

$$[\hat{\mathbf{E}}_i^T(\mathbf{x}), \hat{\mathbf{E}}_j^T(\mathbf{x}')] = [\hat{\mathbf{H}}_i^T(\mathbf{x}'), \hat{\mathbf{H}}_j^T(\mathbf{x})] - [\hat{\mathbf{E}}_i^T(\mathbf{x}), \hat{\mathbf{H}}_j^T(\mathbf{x}')] = 0 \quad (3.4a)$$

and

$$[\hat{\mathbf{E}}_i^T(\mathbf{x}), \hat{\mathbf{H}}_j^T(\mathbf{x}')] = [\hat{\mathbf{E}}_i^T(\mathbf{x}), \hat{\mathbf{H}}_j^T(\mathbf{x}')] \\ = \frac{im^2 eg}{|q|^2} \left[\delta_{ij} - \frac{\nabla_i \nabla_j}{\nabla^2} \right] \Delta(\mathbf{x} - \mathbf{x}') + i\epsilon_{ijk} \nabla_k \delta(\mathbf{x} - \mathbf{x}') \quad (3.4b)$$

which also reduces to usual commutation rule in the absence of magnetic charge (or electric charge). The simplification of this commutation rule and that given by eqn. (3.2) to the usual form may also be done by putting $m = 0$.

For the second quantized transverse potential operators given by eqns. (2.7) and (2.8), we get

$$[\hat{A}_i^T(\mathbf{x}), \hat{A}_j^T(\mathbf{x}')] = [\hat{B}_i^T(\mathbf{x}), \hat{B}_j^T(\mathbf{x}')] = [\hat{A}_i^{T*}(\mathbf{x}), \hat{A}_j^{T*}(\mathbf{x}')] = 0 \\ [\hat{B}_i^{T*}(\mathbf{x}), \hat{B}_j^T(\mathbf{x}')] = [\hat{A}_i^T(\mathbf{x}), \hat{B}_j^T(\mathbf{x}')] = [\hat{A}_i^{T*}(\mathbf{x}), \hat{B}_j^{T*}(\mathbf{x}')] = 0 \quad (3.5a)$$

and

$$[\hat{A}_i^T(\mathbf{x}), \hat{B}_j^T(\mathbf{x}')] = [\hat{A}_i^{T*}(\mathbf{x}), \hat{B}_j^T(\mathbf{x}')] \\ = \frac{egm^2}{|q|^2} \left[\delta_{ij} - \frac{\nabla_i \nabla_j}{\nabla^2} \right] \Delta \frac{(\mathbf{x} - \mathbf{x}')}{\nabla^2} - i\epsilon_{ijk} \nabla_k D(\mathbf{x} - \mathbf{x}') \quad (3.5b)$$

where $D(\mathbf{x}-\mathbf{x}')$ is given by eqn. (2.6). This rule also reduces to the usual local one for $g = 0$ or $e = 0$ or $m = 0$. Similarly, we get

$$[\hat{E}_i^T(\mathbf{x}), \hat{A}_j^{T*}(\mathbf{x}')] = \{i[\delta_{ij}\delta(\mathbf{x}-\mathbf{x}') - \nabla_i \nabla_j D(\mathbf{x}-\mathbf{x}')] - \frac{im^2 eg}{|q|} \epsilon_{ijk} \frac{\nabla_k}{\nabla^2} \Delta(\mathbf{x}-\mathbf{x}')\} \quad (3.6)$$

which reduce to the usual non-local commutation rules for $e = 0$ or $g = 0$ or $m = 0$. If we impose the restriction $\mathbf{p} \cdot \mathbf{f}(\mathbf{p}) = \mathbf{p} \cdot \mathbf{h}^*(\mathbf{p}) = 0$ (i.e. electric and magnetic charge source densities are made zero) in addition to $e = 0$ or $g = 0$, only then these commutation rules become local.

For the longitudinal second quantized field operators, we get

$$[\hat{E}_i^L(\mathbf{x}), \hat{H}_j^{L*}(\mathbf{x}')] = \frac{im^2 eg}{|q|^2} \frac{\nabla_i \nabla_j}{\nabla^2} \Delta(\mathbf{x}-\mathbf{x}') \quad (3.7)$$

which also reduces to the usual one for $e = 0$ or $g = 0$ or $m = 0$.

It is obvious from all these commutation rules that in the presence of both the charges on a particle, neither parallel nor perpendicular components of electric and magnetic field operators commute. It is also obvious from the commutation rules (3.4) and (3.5) that the locality can not be achieved in general in the commutation of transverse field and potential operators and that the effect of making simultaneously the charge and current source densities vanishing is the same as that of making the mass vanishing. The same conclusion has also been derived earlier (Parkash and Rajput 1973) by considering the effect of Maxwell's field equations on electromagnetic fields for non-zero mass system.

4. Hamiltonian of generalized fields

Reduced expansions of second quantized operators for the components of generalized four-potential V_μ defined as

$$V_\mu = \hat{A}_\mu - iB_\mu \quad (4.1)$$

may be readily derived from the quantized reduced expansions (2.3). These operators obviously satisfy the following wave equation :

$$\left(\nabla^2 - \frac{\partial^2}{\partial t^2} - m^2 \right) V_\mu = 0 \quad (4.2)$$

and therefore, the Hamiltonian density of the field under consideration is written as follows (Roman 1969).

$$H(x) = \sum_{\mu=0}^3 [\hat{V}^{\mu*}(x) \hat{V}_\mu(x) + \nabla \hat{V}^{\mu*}(x) \nabla \hat{V}_\mu(x) + m^2 \hat{V}^{\mu*}(x) \hat{V}_\mu(x)]. \quad (4.3)$$

Substituting the quantized reduced expansion of $V_\mu(x)$ in this equation and calculating its volume integration, we get the following expression for the field Hamiltonian :

$$H = \int d\mathbf{p} \left[\{\hat{f}^*(\mathbf{p})\hat{f}(\mathbf{p}) + \hat{h}(\mathbf{p})\hat{h}^*(\mathbf{p})\} + \frac{\{\mathbf{p} \cdot \hat{f}^*(\mathbf{p})\}\{\hat{p} \cdot \hat{f}(\mathbf{p})\} + \{\mathbf{p} \cdot \hat{h}(\mathbf{p})\}\{\hat{p} \cdot \hat{h}^*(\mathbf{p})\}}{(\omega + m)^2} \right] \quad (4.4)$$

In the absence of charge source densities we have $\mathbf{p} \cdot \hat{f}(\mathbf{p}) = \mathbf{p} \cdot \hat{f}^*(\mathbf{p}) = \mathbf{p} \cdot \hat{h}(\mathbf{p}) = \mathbf{p} \cdot \hat{h}^*(\mathbf{p}) = 0$, and then the expression (4.4) reduces to

$$H = H_\gamma = \sum_{\lambda=1}^3 \int d\mathbf{p} [f^*(\mathbf{p}, \lambda)f(\mathbf{p}, \lambda) + h(\mathbf{p}, \lambda)h^*(\mathbf{p}, \lambda)] \quad (4.5)$$

Let us introduce new creation and annihilation operators

$a^*(\mathbf{p}, \lambda)$, $b^*(\mathbf{p}, \lambda)$, $a(\mathbf{p}, \lambda)$ and $b(\mathbf{p}, \lambda)$ such that

$$\begin{aligned} a(\mathbf{p}, \lambda) &= \omega^{-1/2} f(\mathbf{p}, \lambda) \\ b(\mathbf{p}, \lambda) &= \omega^{-1/2} h(\mathbf{p}, \lambda) \end{aligned} \quad (4.5a)$$

which satisfy the following commutation rule

$$[a(\mathbf{p}, \lambda), a^*(\mathbf{p}', \lambda')] = [b(\mathbf{p}, \lambda), b^*(\mathbf{p}', \lambda')] = \delta(\mathbf{p} - \mathbf{p}') \delta_{\lambda, \lambda'} \quad (4.6)$$

Then equation (4.5) reduces to

$$H_\gamma = \sum_{\lambda=1}^3 \int d\mathbf{p} \omega [a^*(\mathbf{p}, \lambda)a(\mathbf{p}, \lambda) + b(\mathbf{p}, \lambda)b^*(\mathbf{p}, \lambda)] \quad (4.7)$$

which is the usual expression for free field Hamiltonian. Hamiltonian given by eqn. (4.4) may also be written as

$$H = H_\gamma + H_M \quad (4.8)$$

where H_γ is the free field Hamiltonian derived above, and H_M given by

$$H_M = \sum_{i,j=1}^3 \int \frac{d\mathbf{p}}{(\omega + m)^2} \omega [p_i p_j \{a^*(\mathbf{p}, i)a(\mathbf{p}, j) + b(\mathbf{p}, i)b^*(\mathbf{p}, j)\}] \quad (4.9)$$

is the contribution of temporal part of four-potential operator $\{\hat{V}_\mu\}$ or equivalently, it is the contribution of charge source densities.

Adding one more term, corresponding to the interaction between the field and four-current, to the expression (4.8), the total Hamiltonian may be written as

$$H = H_\gamma + H_M - H_I \quad (4.10)$$

where the interaction part H_I has been calculated in another paper (Parkash and Rajput 1977) from the second part of Lagrangian density (2.9) in the following form;

$$H_I(\mathbf{x}) = - \sum_{i,j=1}^3 \int d\mathbf{p} \frac{m}{\omega} \left[\frac{m}{\omega} \left\{ a^*(\mathbf{p}, i) a(\mathbf{p}, i) + b(\mathbf{p}, i) b^*(\mathbf{p}, i) \right. \right. \\ \left. \left. + \frac{2}{(\omega + m)} \{ p_i p_j [a^*(\mathbf{p}, i) a(\mathbf{p}, j) + b(\mathbf{p}, i) b^*(\mathbf{p}, j)] \} \right] \right]. \quad (4.11)$$

If charge source densities vanish, the total Hamiltonian becomes

$$H = H_f + H_I \\ = \sum_{\lambda=1}^3 \int d\mathbf{p} \frac{p^2}{\omega} [a^*(\mathbf{p}, \lambda) a(\mathbf{p}, \lambda) + b(\mathbf{p}, \lambda) b^*(\mathbf{p}, \lambda)]. \quad (4.12)$$

Finally, the momentum of the system may be calculated by choosing following momentum density in terms of the components \hat{V}_μ satisfying eqn. (4.2);

$$T^{0k}(x) = - [\hat{V}_\mu^*(x) \partial_k \hat{V}_\mu(x) + \partial_k \hat{V}_\mu(x) \hat{V}_\mu^*(x)]. \quad (4.13)$$

Substituting the reduced expansion of $\hat{V}_\mu(x)$ and integrating this expression, we get the k -th components of momentum operator,

$$\hat{P}^k = \int \frac{d\mathbf{p}}{\omega} p_k \left[\{ \hat{f}^*(\mathbf{p}) \hat{f}(\mathbf{p}) + \hat{h}(\mathbf{p}) \hat{h}^*(\mathbf{p}) \} \right. \\ \left. + \frac{\{ \mathbf{p} \cdot \hat{f}^*(\mathbf{p}) \} \{ \mathbf{p} \cdot \hat{f}(\mathbf{p}) \} + \{ \mathbf{p} \cdot \hat{h}(\mathbf{p}) \} \{ \mathbf{p} \cdot \hat{h}^*(\mathbf{p}) \}}{(\omega + m)^2} \right] \quad (4.14)$$

from which we get the following expression of momentum operator in the case of vanishing charge source densities:

$$\hat{P} = \sum_{\lambda=1}^3 \int d\mathbf{p} \mathbf{p} [a^*(\mathbf{p}, \lambda) a(\mathbf{p}, \lambda) + b(\mathbf{p}, \lambda) b^*(\mathbf{p}, \lambda)] \quad (4.15)$$

which is the usual expression for momentum operator. In this way without using the arbitrary string variables (Zwanziger 1971) and simply by introducing two four-potentials we could do the second quantization of generalized electromagnetic fields associated with spin -1 particles carrying both electric and magnetic charges.

Acknowledgement

One of the authors (O.P.) is grateful to the Council of Scientific and Industrial Research, New Delhi for the financial assistance in the form of Post Doctoral Research Fellowship.

References

- Chiang C C CPT 201 CRO-3992-157 the Centre of Particle Theory. The University of Texas at Austin
- Dirac P A M 1931 *Proc. Roy. Soc.* **A183** 60; 1948 *Phys. Rev.* **74** 817
- Epstein K J 1967 *Phys. Rev. Letter* **18** 56
- Foldy L L 1956 *Phys. Rev.* **102** 568
- Magen C R 1965 *Phys. Rev.* **140B** 804
- Kimy and Koroan J 1972 *Phys. Soc.* **5** 39
- Lomont J S and Moses H E 1964 *Jour. Math. Phys.* **5** 39
- Nelson C A and Sudashan E C G 1972a *Phys. Rev.* **D6** 3658
- 1972b *Phys. Rev.* **D9** 3678
- Rosenbaum D 1966 *Phys. Rev.* **147** 891
- Rajput B S 1969a *Ind. J. Phys.* **43** 439
- 1969b *Ind. J. Phys.* **43** 602
- 1969c *Ind. J. Pure and Appl. Phys.* **7** 720
- 1970a *Ind. J. Pure and Appl. Phys.* **8** 297
- 1970b *Ind. J. Pure and Appl. Phys.* **8** 439
- 1971 *Nuovo Cim. Lett.* **2** 712
- Rajput B S and Parkash Om 1973 *Ind. J. Phys.* **47** 641
- 1974a *Ind. J. Phys.* **48** 152
- 1974b *Ind. J. Phys.* **48** 359
- 1976 *Ind. J. Phys.* **50** 929
- 1977a *Nuovo Cimento* (Communicated)
- 1977b *Nuovo Cimento* (Communicated)
- Roman P 1969 *Introduction to Quantum Field Theory* John Wiley & Sons Inc. New York
- Shirokov Iu M 1958 *Sov. Phys. JE TP* **6** 919
- Schwinger J 1966a *Phys. Rev.* **144** 1087
- 1966b *Phys. Rev.* **151** 1048
- 1969 *Science* **165** 757
- Yan M Y and Bieden harn L C 1970 *Phys. Rev. Lett.* **24** 118
- Zwanziger D 1965 *Phys. Rev.* **140B** 804
- 1968 *Phys. Rev.* **176** 1489
- 1971 *Phys. Rev.* **3D** 880

Debye temperature of silver and aluminium and the anharmonic parameters of their potential functions

P D Pathak and (Miss) N P Shah

Physics Department, University School of Sciences, Ahmedabad-9

Received 10 January 1977, revised 28 July 1977 and 20 September 1977

Debye temperatures of silver and aluminium have been determined by X-ray diffraction using a special furnace (Pathak and Vasavada 1969) from room temperature upto about their melting points with methods due to Paskin (1957), Chipman (1960) and Maradudin and Flinn (1963). The anharmonic contribution to the Debye temperature upto about 900 K for Ag and 700K for Al is shown to arise essentially from thermal expansion. The values of the anharmonic parameters γ_0 in the potential energy function of Willis (1969) are determined and found to be -0.955×10^{-12} erg \AA^{-4} for Al and -1.285×10^{-12} erg \AA^{-4} for Ag.

1. Introduction

Variation of X-ray Debye temperature Θ_M with temperature for Ag has been investigated by many workers notably by Andriessen (1935), Boskovits *et al* (1958), Spreadborough and Christian (1959), Haworth (1960) and Simerska (1961). A similar study for Al has been carried out by Owen and Williams (1947), Chipman (1960) and Flinn and McManus (1963). We have investigated the variation of Debye temperature Θ_M with temperature for both metals upto the melting point.

2. Experimental

The experimental procedure is fully described by Pathak and Vasavada (1970). The metal powders were prepared by filing and passing them through 350 and 400 mesh sieves. The metal powders were mixed with a small amount of binding material and were annealed in argon atmosphere. The profiles of lines 311 and 331 for Ag and 331 and 420 for Al were recorded on a chart recorder and planimetered. The background was determined by a method described by Mitra and Misra (1966).

The basic equation from which the X-ray Debye temperature Θ_M is calculated is (Pathak and Trivedi 1973)

$$R = \frac{mK}{12h^2} \frac{\lambda^2}{(1-\rho) \sin^2 \theta_0} \left[\ln \frac{I}{I_0} - \ln \frac{B'}{B_0'} \right]$$

$$\frac{T_0 \psi_0}{\Theta_{M0}^2} - \frac{T \psi}{\Theta_M^2} \frac{\sin^2 \theta}{\sin^2 \theta_0} \quad (1)$$

where I and I_0 are the measured integrated intensities at temperatures T and T_0 and θ is the Bragg angle. ψ and B' are respectively given by

$$\psi = \frac{1}{x} \int_0^x \frac{udu}{e^u - 1} + \frac{x}{4}$$

$$B' = Npf^2 \frac{1 + \cos^2 2\theta}{\sin^2 \theta \cos \theta}$$

where $x = \Theta_M/T$, N is the number of unit cells irradiated, p is the multiplicity factor and f is the atomic scattering factor.

The quantity $(1-\beta)$ takes into account the one-phonon thermal diffuse scattering (TDS) contribution to the measured intensity according to Chipman and Paskin (1959). The quantity β for an f.c.c. crystal is given by

$$\beta = \frac{1}{2} \left(\frac{\pi}{3} \right)^{1/3} \frac{a \cos \theta}{\lambda} \Delta$$

where a is the lattice constant and Δ is the length of the straight line background expressed in radians.

It can be seen from equation (1) that the value of θ_M at different temperatures can be found only if Θ_M at some reference temperature T_0 (say room temperature) is known. In this investigation the value of Θ_{M0} is computed by three methods : (i) Paskin's (ii) Chipman's and (iii) Maradudin and Flinn's.

According to Paskin's (1957) method, if the temperature variation of θ_M is due to thermal expansion, the plot of $\ln(I/I_0)$ versus the reduced temperature $T' [= T(a/a_0)^{3\gamma}]$ should be a straight line and the value of θ_{M0} can be obtained from the slope of this line.

In the second method Chipman (1960) used the fact that Debye temperature versus T curves as determined from the elastic constants are approximately linear. Hence if one plots a family of θ_M versus T curves with a series of arbitrary values of θ_{M0} , one can assume that the curve with the smallest curvature is the correct one.

Maradudin and Flinn considered the effect of anharmonicity of the lattice vibrations on the Debye-Waller factor. The relation obtained by them for an f.c.c. metals is

$$\theta^{-2}{}_M = a(1 + \mu T) \quad (2)$$

In this equation the quantities a and μ are constants independent of temperature and it holds for $T > \theta_M$. For temperatures T and T_0 we can write

$$\frac{\Theta^2{}_M}{\Theta^2{}_M} = \frac{1 + \mu T_0}{1 + \mu T} \quad (3)$$

By inserting equation (3) into (1), and rearranging we get

$$\frac{R}{T_0 - T + \tau_1} = \frac{1}{\theta_{M0}^2} + \frac{\mu}{\theta_{M0}^2(1 + \mu T_0)} (T + \tau_2) \quad (4)$$

τ_1 and τ_2 are minor corrections. Plot of $R/(T_0 - T + \tau_1)$ against $T + \tau_2$ should give a straight line with intercept $1/\theta_{M0}^2$ and slope $\mu/\theta_{M0}^2(1 + \mu T_0)$. Thus θ_{M0} and hence θ_M versus T can be found.

3. Results and Discussion

The plots of $\ln(I_T/I_R)$ (I_R = intensity at room temperature) versus reduced temperature T'' ($T'' = T(a_T/a_R)^{1/3}$) for line 331 are given in Figs. 1 and 2. Debye θ_M

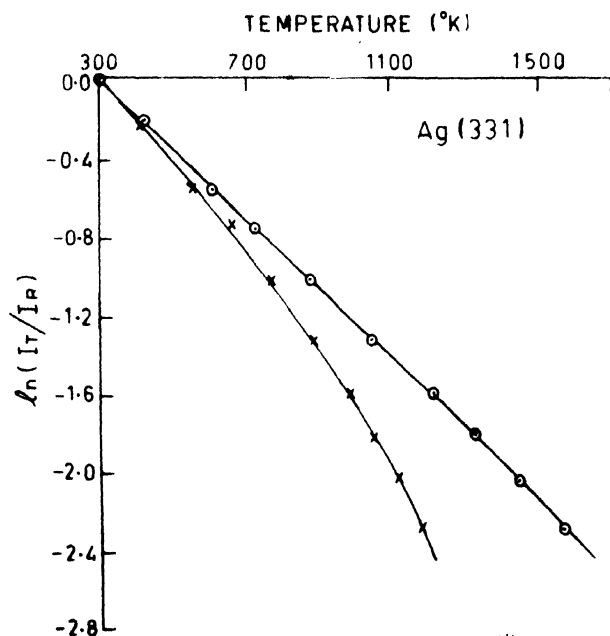


Fig. 1. Plot of temperature dependence of the quantity $\ln(I_T/I_R)$ for 331 reflexion of Ag
 X $\ln(I_T/I_R)$ versus absolute temperature
 O $\ln(I_T/I_R)$ versus reduced temperature

at different temperatures are presented in Figs. 3 and 4. The values of θ_M in the plots are averages of those corresponding to lines 311 and 331 for Ag and 331 and 420 for Al. Comparisons with other workers are shown in Fig. 5 and 6. In these figures, full line shows the results of the present investigation as obtained by Chipman's method.

Since the plots of $\ln(I_T/I_R)$ versus reduced temperature T' (Figures 1, 2) are straight lines upto about 1100K (reduced) for Ag and 800K (reduced) for Al it is evident that the anharmonic contribution to the Debye θ_M upto these temperatures comes essentially from thermal expansion.

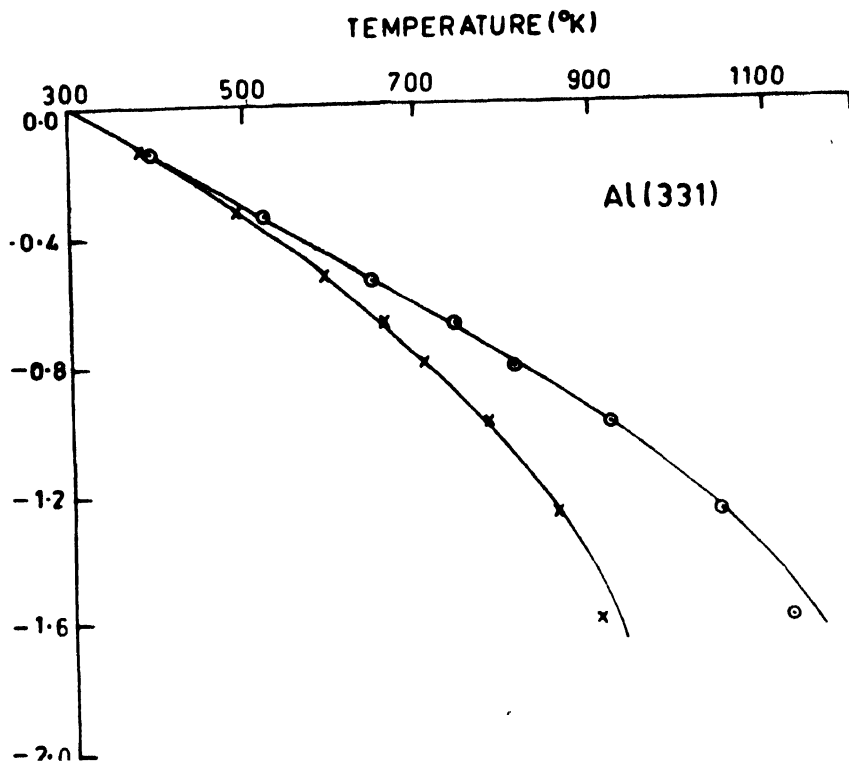


Fig. 2. Plot of temperature dependence of the quantity $\ln(I_T/I_R)$ for 331 reflexion of Al
 X $\ln(I_T/I_R)$ versus absolute temperature
 o $\ln(I_T/I_R)$ versus reduced temperature

The general expression due to Willis (1969) for the potential of the k -th atom in a cubic crystalline field is given by

$$V_K(U_1 U_2 U_3) = V_0 + \frac{1}{2} \alpha_K r^2 + \beta_K U_1 U_2 U_3 + \gamma_K r^4 + \delta_K \left(U_1^4 + U_2^4 + U_3^4 - \frac{3}{5} r^4 \right) \quad (5)$$

where $r^2 = U_1^2 + U_2^2 + U_3^2$. $\beta_K = 0$ when the atomic site coincides with the centre of symmetry. δ_K is the anisotropic term taken to be zero in the present case.

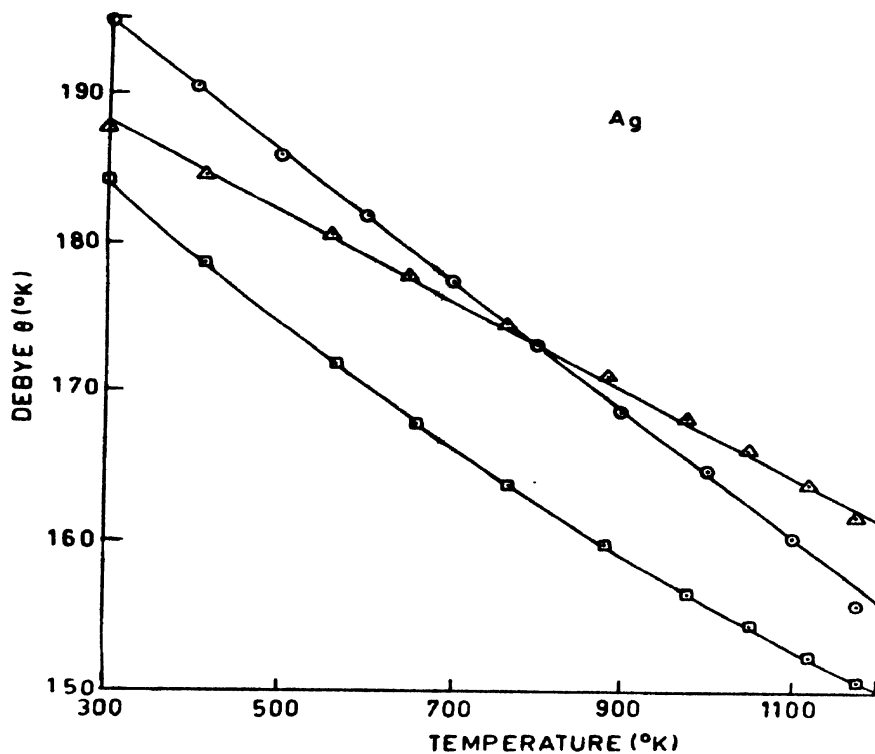


Fig. 3. Plot of Debye θ (average) versus temperature Ag: Δ Paskin's method; \odot Chipman's method; \square Maradudin and Flinn's method

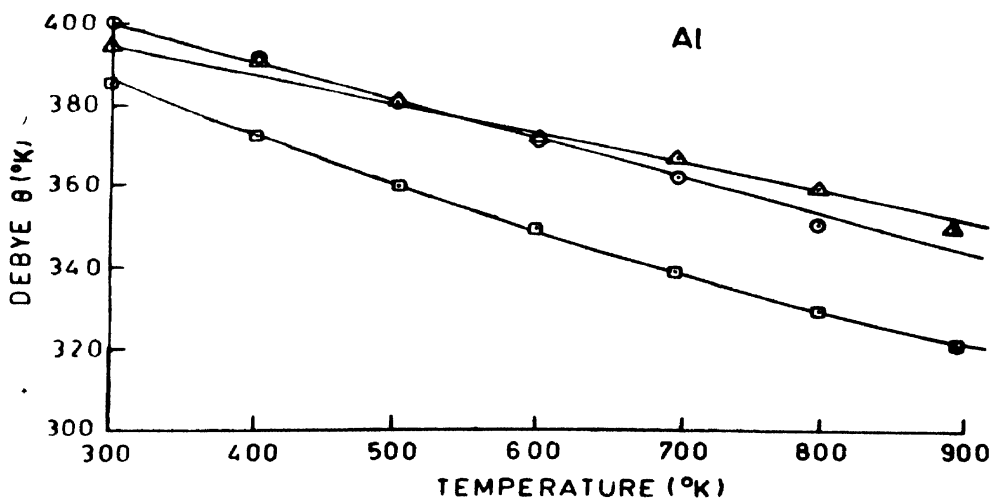
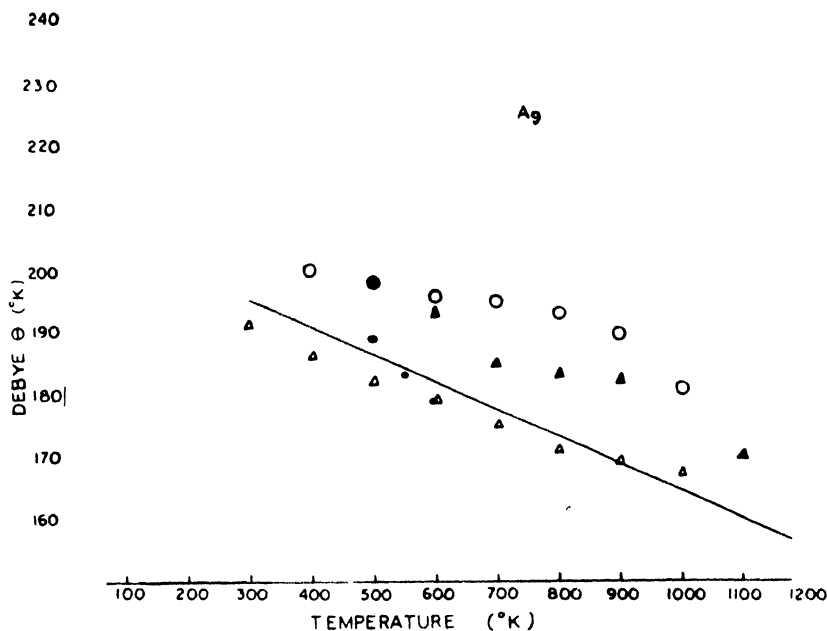
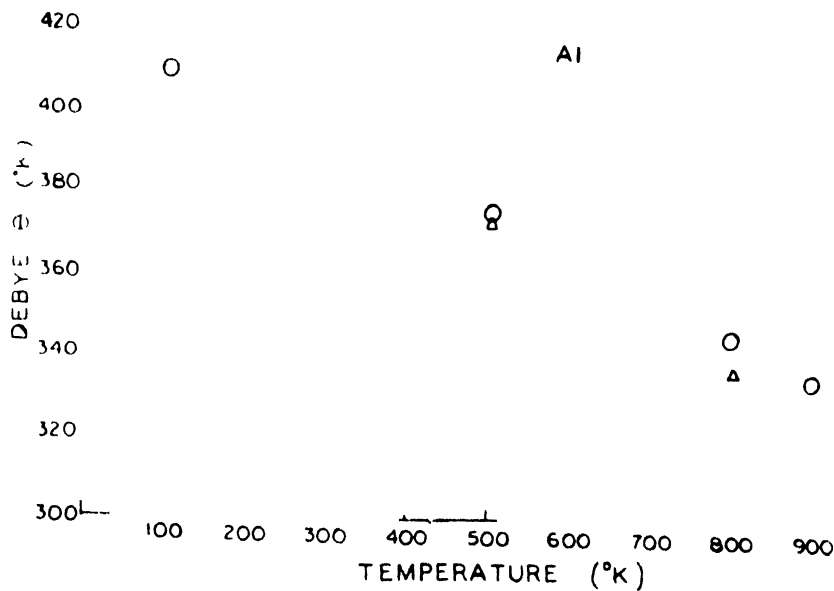


Fig. 4. Plot of Debye θ (average) versus temperature Al: Δ Paskin's method; \odot Chipman's method; \square Maradudin and Flinn's method

Fig. 5. Plot of Debye θ versus temperatureAg: ● Boskovits *et al*; O Simerska

Δ Spreadborough and Christian; ▲ Howorth;

□ Andriessen; — Present work (Chipman's method)

Fig. 6. Plot of Debye θ versus temperature

Al: ● Flinn and McManus; O Owon and Williams;

Δ Chipman; — Present work (Chipman's method)

The potential parameters α and γ are temperature dependent, their relations with temperature being given by

$$\frac{1}{\alpha} = \frac{1}{\alpha_0} (1 + 2\gamma_G \chi T)$$

or $\alpha = \alpha_0(1 - 2\gamma_G \chi T)$

with a similar expression for γ . Here α_0 is the value of α in the absence of thermal expansion and it is assumed that $2\gamma_G \chi T \ll 1$. γ_G is the Gruneisen constant and χ the volume coefficient of expansion.

Now

$$\left(\frac{\lambda}{\sin \theta} \right)^2 \ln \left(\frac{I_T}{I_R} \right) = 2 |B(T) - B(T_R)| \quad (6)$$

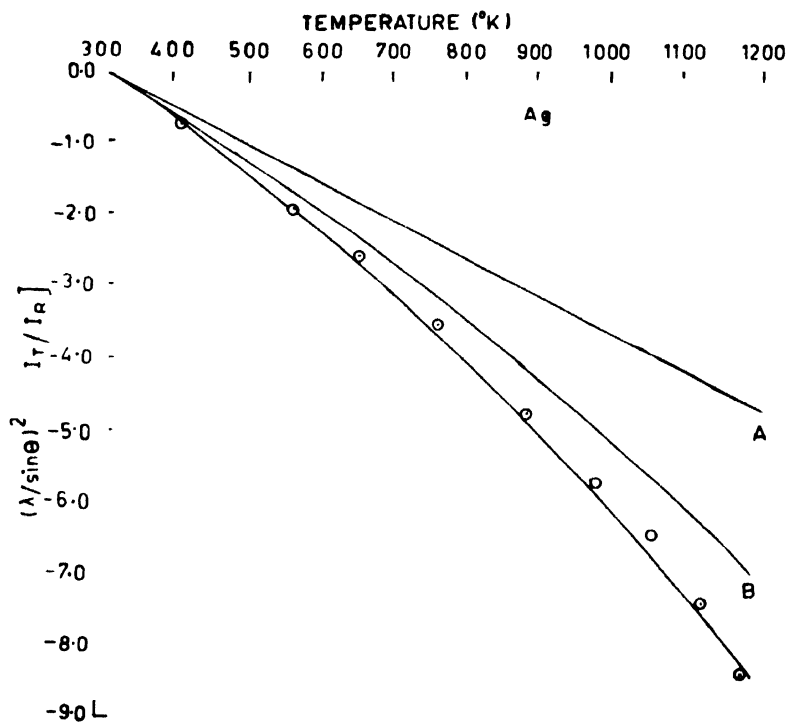


Fig. 7. Plot of logarithm of integrated intensities from Ag versus temperature. Experimental points are shown as circles. Curve A was calculated using the harmonic Debye-Waller theory. Curve B was calculated using the quasi-harmonic theory to include the effect of thermal expansion; curve C was calculated using the anharmonic theory accounting for both thermal expansion and quartic anharmonicity.

Here $B(T)$ is the Debye-Waller factor at temperature T and T_R is the room temperature. Willis (1969) has shown that

$$B(T) = B^h(T) \left[1 + T \left(2\chi\gamma_G - 20K_B \frac{\gamma_0}{\alpha_0^2} \right) \right] \quad (7)$$

where K_B is the Boltzmann constant and $B^h(T)$, the harmonic factor, is given by

$$B^h(T) = \frac{[8\pi^2 K_B T]}{\sim} \quad (8)$$

Figs. 7 and 8 represent the plots of $(\lambda/\sin \theta)^2 \ln(I_T/I_R)$ versus T . Experimental points are plotted as circles. The curve *A* corresponds to the harmonic Debye-Waller theory. Curve *B* is drawn using equation (7) in its quasi-harmonic form, that is by retaining the thermal expansion term but putting $\gamma_0/\alpha_0^2 = 0$. Curve *C* represents the anharmonic form of equation (7) with $\gamma_0/\alpha_0^2 = -0.075 \times 10^{12} \text{erg}^{-1}$ for Ag and $-0.064 \times 10^{12} \text{erg}^{-1}$ for Al. These values are chosen so as to make the anharmonic curve pass through the experimental points at highest temperatures where the influence of anharmonicity is greatest.

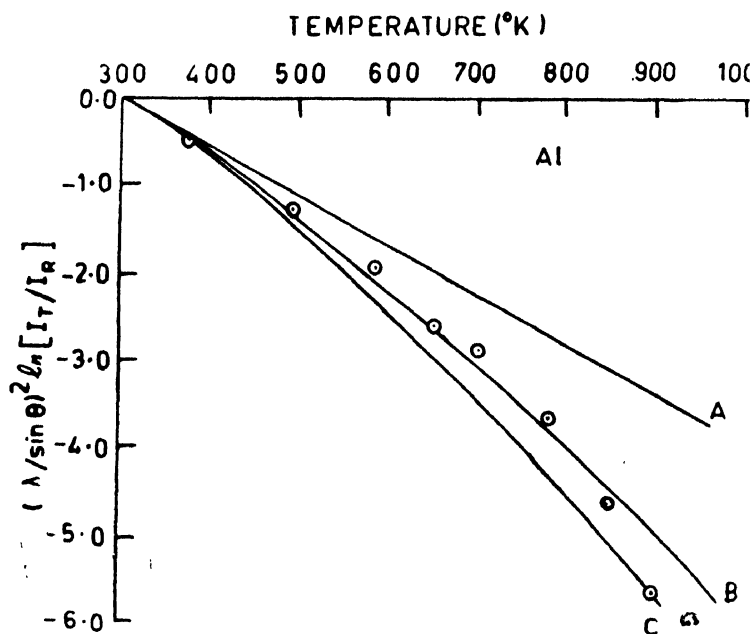


Fig. 8. Plot of logarithm of integrated intensities from Al versus temperature. Experimental points are shown as circles. Curve A was calculated using the harmonic Debye-Waller theory; curve B was calculated using the quasi-harmonic theory to include the effect of thermal expansion; curve C was calculated using the anharmonic theory, accounting for both thermal expansion and quartic anharmonicity.

The harmonic parameters α_0 were calculated from equation (8) and were found to be $4.140 \times 10^{-12} \text{erg} \text{\AA}^{-2}$ for Ag and $3.868 \times 10^{-12} \text{erg} \text{\AA}^{-2}$ for Al. These values give $\gamma_0 = -1.285 \times 10^{-12} \text{erg} \text{\AA}^{-4}$ for Ag and $-0.955 \times 10^{-12} \text{erg} \text{\AA}^{-4}$ for Al.

The value of $B(T)$ for Ag was obtained from Singh and Sharma (1971) and that for Al from Prakash and Hemkar (1974). The Gruneisen constants were taken from Kittel (1959) and the expansion coefficients from Pathak and Shah (1978).

4. Conclusion

Debye temperatures of Ag and Al are determined using X-ray technique and a specially designed furnace. The anharmonic contribution to the Debye temperature upto 900°K for Ag and 700°K for Al arises essentially from thermal expansion. The anharmonic parameter γ_0 of the potential function of Willis is determined for the two metals.

Financial assistance to one of us (NPS) by the Council of Scientific and Industrial Research is gratefully acknowledged.

References

- Andriesson R 1935 *Physica* **2**, 417.
 Boskovits J Roilos M Theodossiou A and Alexopoulos K 1958 *Acta Cryst.* **11** 845.
 Chipman D R 1960 *J. Appl. Phys.* **31** 2012.
 Chipman D R and Paskin A 1959 *J. Appl. Phys.* **30**, 1992, 1998.
 Flinn P A and McManus G M 1963 *Phys. Rev.* **132**, 2458.
 Haworth C W 1960 *Phil. Mag.* **5** 1229.
 Kittel C 1959 *Introduction to Solid State Physics* 2nd Ed. p.155.
 Maradudin A A and Flinn P A 1963 *Phys. Rev.* **129**, 2529.
 Mitra G B and Misra N K 1966 *Brit. J. Appl. Phys.* **17**, 1319.
 Owen E A and Williams R W 1947 *Proc. Roy. Soc. (London)* **A188** 509.
 Paskin A 1957 *Acta Cryst.* **10**, 667.
 Pathak P D and Shah N P 1978 *Ind. J. Phys.* **52A** 55.
 Pathak P D and Trivedi J M 1973 *Acta Cryst.* **A29**, 45.
 Pathak P D and Vasavada N G 1969 *Indian J. Phys.* **43**, 421.
 Pathak P D and Vasavada N G 1970 *Acta Cryst.* **A26**, 655.
 Prakash J and Hemkar M P 1974 *J. Phys. Soc. Jap. (Japan)* **A26**, 1608.
 Simerska M 1961 *Acta Cryst.* **14**, 1259.
 Singh N and Sharma P K 1971 *Phys. Rev.* **B3**, 1141.
 Spreadborough J and Christian J W 1959 *Proc. Phys. Soc.* **74**, 609.
 Willis B T M 1969 *Acta Cryst.* **A25**, 277.

A study of the rate of diffusion of some gases in thin layers of gold

N E Abdel Aziz and S S Kishk

National Institute of Standards, Giza, Egypt

N Farag

Physics Department, Faculty of Science, University of Cairo, Giza, Egypt

Received 5 April 1977, revised 27 September 1977

Diffusion of gases through gold layers of different thicknesses, evaporated on a porous material of Egyptian clay as support, has been investigated at room temperature and at an inlet pressure of 450 Torr. The gases used are hydrogen, nitrogen, argon, carbon dioxide, air and oxygen. It is found that the rate of diffusion of a gas through a gold layer depends on the pressure of the gas as well as its molecular weight, and also on the thickness and the area of the gold layer.

1. Introduction

Diffusion of gases through metals usually occurs if the gas is apparently soluble in the metal. This diffusion occurs as volume diffusion, grain boundary diffusion, or interface diffusion.

Smithells and Ransley (1935) studied the diffusion of gases through different metals in the form of tubes at different high temperatures. Straight lines were obtained when the logarithm of the rate of diffusion was plotted against the reciprocal of the absolute temperature. At high pressures, the rate of diffusion was found to vary linearly with the square root of the pressure. They showed that the rate of diffusion (q) of gases through metals depends on the solubility (K) of the gas within the metal, the area (A) of the metal, the diffusion constant (D), the thickness (d) of the metal, the pressure (P) of the gas, and the absolute temperature (T) according to the equation

$$q = \frac{KAD}{d} P^{1/2} T^{1/2} e^{-b_0/T},$$

where b_0 is a constant.

Seeger (1955) showed that, for diffusion along interstitial sites in face centered cubic crystals, such as gold, the following relation applies at constant absolute temperature and solubility constant

$$D = \nu a^2 e^S / k e^{-Q/kT},$$

where ν is the jump frequency of the gas atoms (it is inversely proportional to the square root of the molecular weight of the gas), a is the lattice constant, S is the entropy, Q is the activation energy, and k is the Boltzman's constant.

The authors (Farag *et al* 1977) studied the diffusion of gases through thin layers of silver. They found a proportionality between the rate of diffusion (q) and $(\sqrt{P_1} - \sqrt{P_2})$, where P_1 is the inlet pressure of the gas and P_2 is the outlet pressure.

2. Apparatus and Procedure

The apparatus used in the present work is shown in figure 1. It consists of two cylindrical tubes A & B, of pyrex glass, connected together by means of a ground joint. A polished disc (D) of Egyptian clay of suitable porosity is used as a support for the metal layer, this disc is fitted tightly to the ground joint C .

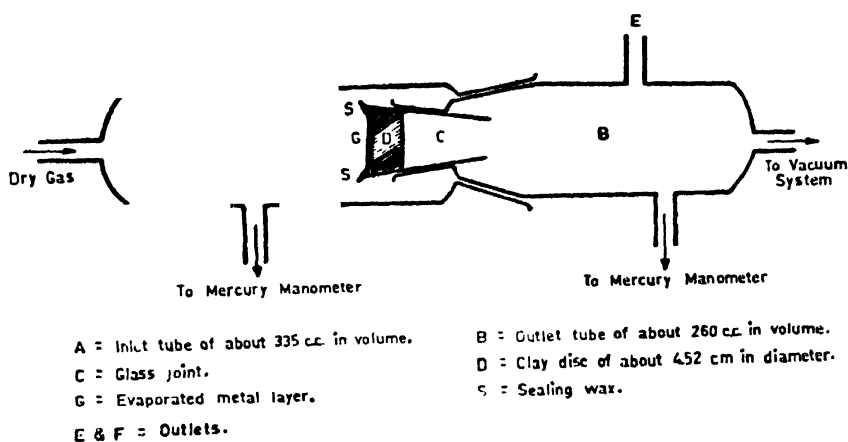


Fig. 1. The Apparatus

The apparatus is evacuated and the hydrogen gas is allowed to flow at a steady rate to the tube A till a pressure of about 450 Torr is reached, then the gas supply is stopped. The gas then diffuses through the metal layer and the clay to the evacuated tube B. Both the inlet and outlet pressures are measured successively at equal intervals of time until the pressure in each tube becomes nearly constant.

The apparatus was tested for undesirable leakages from the atmosphere; no leakage was observed. This showed that the diffusion of the gas took place through the gold layer only.

The surface of the metal layer was studied before and after diffusion by an optical microscope of magnification 800 X. Electron micrographs were also

taken using an electron microscope having a resolving power between 20 & 30 and maximum magnification of 30,000 X.

3. Results

The relation between the time and the outlet pressure was plotted for every gas and for the different thicknesses of the gold layer. Fig. 2 represents the pressure-

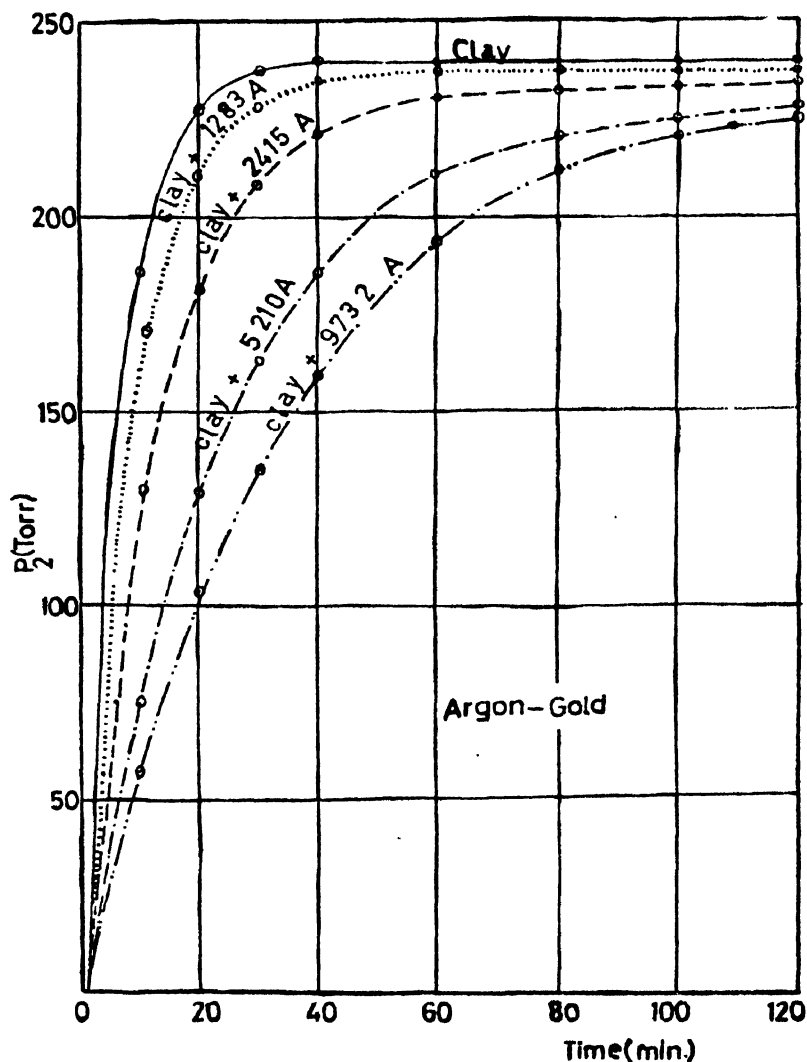


Fig. 2. The relation between the time T in minutes and the outlet pressure P_2 in Torr

time relation in the case of argon. From these curves the rate of diffusion q (Torr. min⁻¹) was calculated and a family, of curves showing the relation between

$(\sqrt{P_1} - \sqrt{P_2})$ and q was plotted for every gas and for the different thicknesses fig. 3. Straight lines were obtained showing a proportionality between q and $(\sqrt{P_1} - \sqrt{P_2})$. The slope of each line was obtained giving the value $(KAD/d_T)T$, where d_T is the total effective thickness in mm. The reciprocal of this slope $(d_T/KAD)T$ was obtained for different thicknesses and different gases.

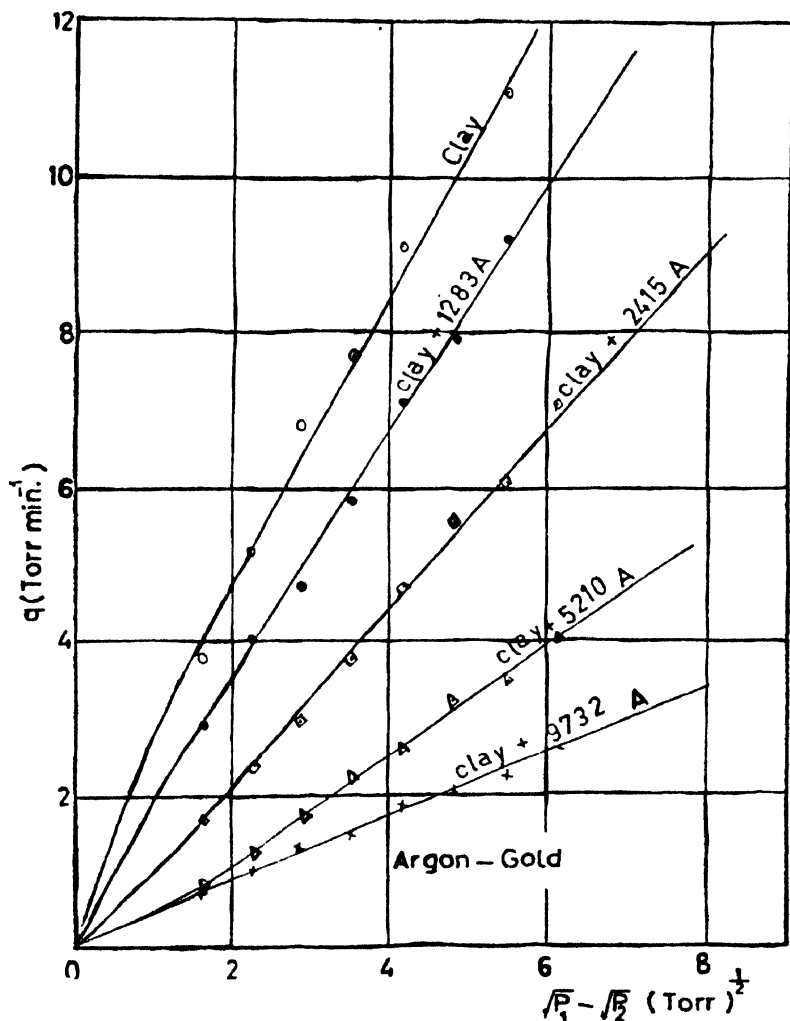


Fig. 3. The relation between $(\sqrt{P_1} - \sqrt{P_2})$ and the rate of diffusion q

The total effective thickness (d_T) was then plotted against $(d_T/KAD)T$ for different gases, straight lines were obtained as shown in fig. 4. The slope of each of these lines gave the value (KAD) which is characteristic for the gas used. Finally the value (KAD) was plotted against $1/\sqrt{M}$, where M is the molecular weight of the gas; this yielded a straight line as shown in fig. 5.

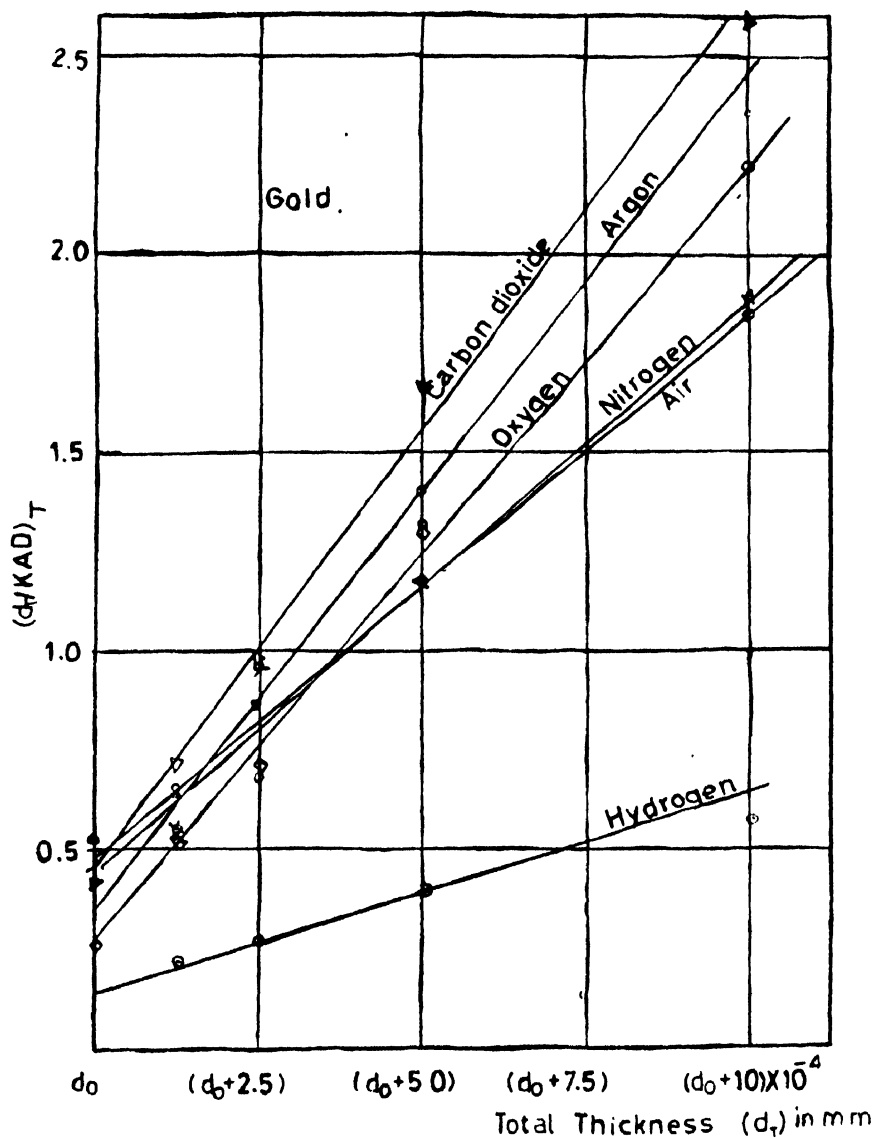


Fig. 4. The relation between the total effective thickness (d_T) and the value $(d_T/KAD)_T$

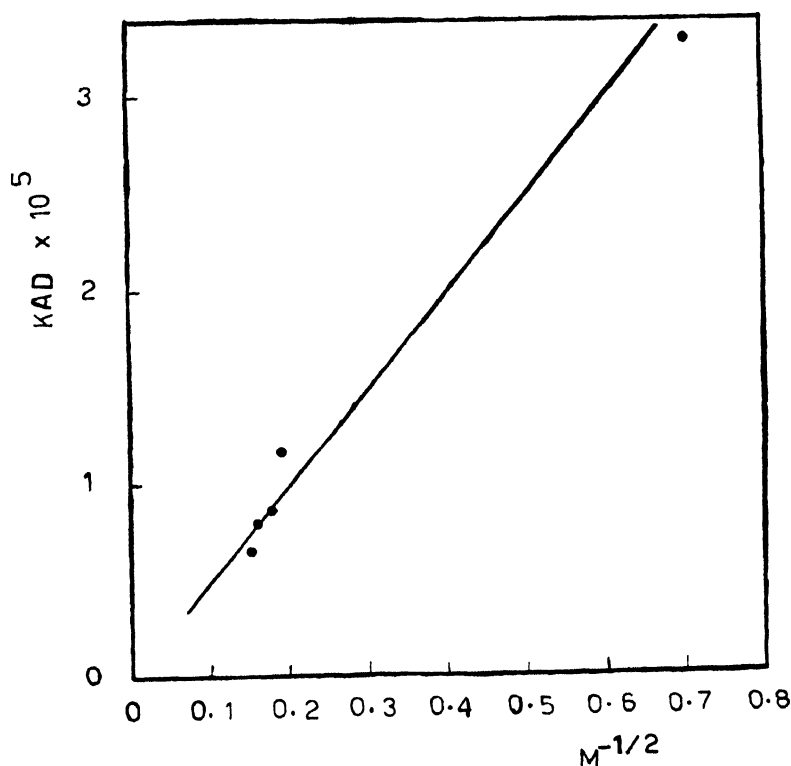
The accuracy in determining q was calculated and was found to be 5%.

4. Discussion and Conclusion

The present results show that the diffusion of a gas in a metal usually occurs as a result of the absorption of the gas into the metal from one side where the concentration is high and then released on the other side where the pressure of the

Table 1. The relation between reciprocal of square root of molecular weight of gas and KAD (gold)

Gas	Molecular weight M	$\frac{1}{\sqrt{M}}$	KAD
Hydrogen	2.0159	0.704	3.2893×10^{-5}
Nitrogen	28.0134	0.189	1.1574×10^{-5}
Oxygen	31.9988	0.178	0.8620×10^{-5}
Argon	39.9480	0.158	0.7911×10^{-5}
Carbondioxide	44.0099	0.151	0.6476×10^{-5}
Air	—	—	1.2076×10^{-5}

**Fig. 5.** The relation between the reciprocal of the square root of the molecular weight of the gas and the constant (KAD)

gas is low. This may appear from the study carried out on the surface of the metal layer by the electron microscope which shows that the pressure of the gas tends to make the metal layer more adhesive to the surface of the supporting clay. This is in agreement with the previous results (Hulbert and Konecny 1961).

The present results show that the rate of diffusion q is proportional to $(\sqrt{P_1} - \sqrt{P_2})$ for values of P_1 between 260 and 450 Torr. This agrees with the relation suggested by other investigators (Silberg and Bachman 1958).

The results obtained in the present work show also that the diffusion constant D and the solubility K of the gas are inversely proportional to $\sqrt{\bar{M}}$, where \bar{M} is the molecular weight of the gas. This may be suggested from the linear relation between the value (KAD) and $1/\sqrt{\bar{M}}$.

It appears also from the present results that the rate of diffusion of hydrogen is greater than that of nitrogen, oxygen, argon, carbon dioxide and air. This agrees with the results obtained by Landecker and Gray (1954).

References

- Farag N, Abdel Aziz N E and Kishk S S 1977 *Proc. Math. Phys. Soc. (Egypt)* **43** 105
Hurlbert R C and Konecny J O 1961 *J. Chem. Phys.* **34** 655
Landecker K and Gray A J 1954 *Rev. Sci. Instr.* **25** 1151
Seeger A 1955 *Handbuch der Physik* **7/1** 411
Silberg P A and Bachman C H 1958 *J. Chem. Phys.* **29** 777
Smithells C J and Ransley C E 1935 *Proc. Roy. Soc. (London)* **A150** 152, 172

Anderson transition in $\text{La}_{1-x}\text{Sr}_x\text{VO}_3$

A K Shukla* and Arunava Gupta

Department of Chemistry, Indian Institute of Technology, Kanpur-208016

(Received 29 August 1978)

Electrical resistivity and thermopower measurements on $\text{La}_{0.85}\text{Sr}_{0.15}\text{VO}_3$ clearly show the occurrence of Anderson transition in this material.

1. Introduction

Mott (1972) pointed out that the system $\text{La}_{1-x}\text{Sr}_x\text{VO}_3$ could be a case of Anderson transition (Rao and Shukla 1976) with a minimum metallic conductivity, the disorder arising from the random positions of La^{3+} and Sr^{2+} . This disorder is sufficient to localize the wave function at the Fermi level in the vanadium 3d band when x is small. Electron transport properties of this material reported in the literature (Dougier and Hagenmuller 1975, Sayer *et al* 1975) show some differences. Thus, the thermopower measurements of Dougier and Hagenmuller (1975) indicate that when x is between 0.05 and 0.1, the thermopower increases with decreasing temperature. However, when $x = 0.15$, the thermopower decreases with decreasing temperature suggesting variable range hopping mechanism. Thermopower measurements of Dougier and Hagenmuller (1975) were, however, carried out only upto 300K and do not show the change in mechanism from variable range hopping to excitation to mobility edge as pointed out by Mott *et al* (1975). Electrical resistivity data on $\text{La}_{1-x}\text{Sr}_x\text{VO}_3$ ($0.1 < x < 0.2$) of Sayer *et al* (1975) show that $T^{-1/4}$ hopping behaviour only at very low temperatures, although we would have expected this behaviour to hold even upto 300K in accordance with the thermopower measurements of Dougier and Hagenmuller (1975). Such correspondence between thermopower and resistivity data has indeed been found in the analogous $\text{Lu}_{1-x}\text{Sr}_x\text{CoO}_3$ system investigated by Rao and Om Parkash (1977). In view of these difficulties we considered it worthwhile investigating electron transport properties of $\text{La}_{0.85}\text{Sr}_{0.15}\text{VO}_3$ which should clearly show the Anderson transition.

2. Experimental

$\text{La}_{0.85}\text{Sr}_{0.15}\text{VO}_3$ was prepared starting with an appropriate mixture of La_2O_3 , SrO , VO_2 and V_2O_5 , all of better than 99.9% purity. SrO was obtained by de-

*Present Address : Solid State and Structural Chemistry Unit, Indian Institute of Science, Bangalore-560012.

composition of SrCO_3 at 1270K. V_2O_3 was prepared by reducing V_2O_5 in hydrogen atmosphere at 1270K for 12 hours. VO_2 was prepared by the arc method. The starting materials were thoroughly mixed and ground in a mortar. The mixture was pelletized and placed in a mortar. The mixture was pelletized and placed in a quartz tube which was connected to the vacuum line. The sample was first heated at 1270K in vacuum accompanied by periodic flushing with dry Argon. The quartz tube containing the sample was then sealed and heated in a global furnace for 52 hours at 1570K. The resulting specimen was high density sintered pellet. Four probe electrical conductivity and thermopower measurements were carried out using the apparatus fabricated in this laboratory.

3. Results and Discussion

The temperature variation of electrical resistivity of $\text{La}_{0.85}\text{Sr}_{0.15}\text{VO}_3$ is shown as a log vs $T^{-1/4}$ plot in figure 1. We see that there is a slight break in the curve

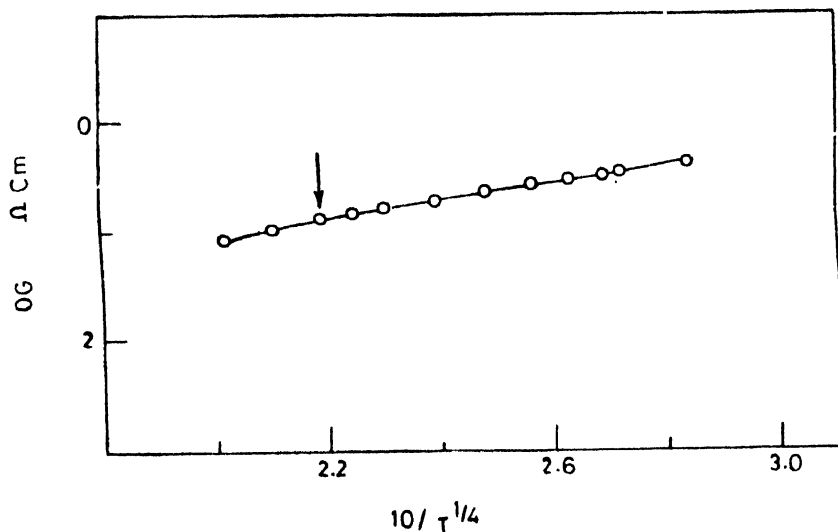


Figure 1. Plot of logarithm of resistivity ($\log \rho$) against $1/T^{1/4}$ for $\text{La}_{0.85}\text{Sr}_{0.15}\text{VO}_3$.

around 330K which may indicate a change in mechanism from variable range hopping to transport at E_c . Thermopower measurements (Figure 2) show that around this temperature there is a change in slope. This behaviour is similar to that found by Rao and Om Parkash (1977) in $\text{Ln}_{1-x}\text{Sr}_x\text{CoO}_3$ ($\text{Ln} = \text{Pr}$ or Nd). The change in slope of the thermopower—temperature plot can be understood as follows :

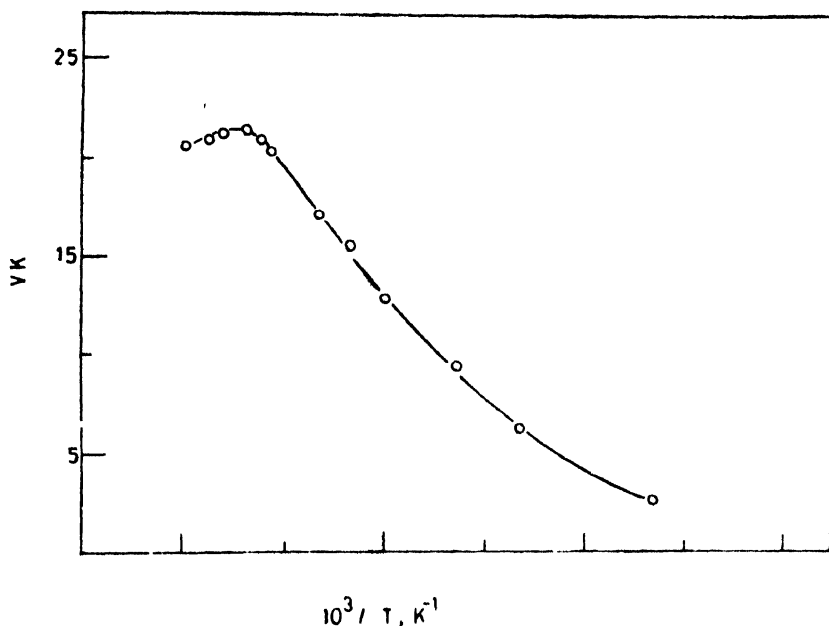


Figure 2. Plot of thermopower against reciprocal of temperature for $\text{La}_{0.85}\text{Sr}_{0.15}\text{VO}_3$.

In the hopping range, the behaviour of thermopower, S , is given by Mott and Davis (1971), as,

$$S = (\pi^3/3)(k^2T/e)(d \ln \sigma/dE). \quad (1)$$

With S increasing with increase in temperature. Substituting

$$\sigma = \sigma_0 \exp(-W/kT),$$

we obtain,

$$S = \frac{\pi^3}{3} \frac{k}{e} \left[kT \frac{d \ln \sigma_0}{dE} - \frac{dW}{dE} \right] \quad (2)$$

If the transport is at E_c , then S will decrease with increasing T as shown by Cutler and Mott (1969) :

$$S = \frac{K}{e} [\{(E_c - E_F)/kT\} + 1]. \quad (3)$$

Since, in $\text{La}_{0.85}\text{Sr}_{0.15}\text{VO}_3$ we would expect the above mechanisms to be operating. Depending on the temperature, there should be a significant change in the slope of the thermopower—temperature plot as a consequence of the change in mechanism of conduction from variable range hopping to transport at E_c . It is also

interesting that the temperature around which we find the change in slope of thermopower is close to that below which $T^{-1/4}$ law behaviour of conductivity is observed. These results confirm occurrence of Anderson transition in $\text{La}_{0.85}\text{Sr}_{0.15}\text{VO}_3$. The temperature upto which the variable range hopping regime extends is indeed surprising. It is possible that the frequency dependence of a.c. conductivity is more characteristic of Anderson localization than $T^{-1/4}$ dependence. In $\text{La}_{0.85}\text{Sr}_{0.15}\text{VO}_3$ we find the frequency dependence only at very low temperatures as also observed by Sayer *et al* (1975).

Acknowledgement

The authors thank Professor C. N. R. Rao for suggesting the problem and for guidance.

References

- Cutler M and Mott N F 1969 *Phys. Rev.* **181** 1336
Dougier P and Hagenmuller P 1975 *J. Solid State Chem.* **15** 158
Mott N F 1972 *Adv. Phys.* **21** 785
Mott N F and Davis E A 1971 *Electronic Processes in Non-Crystalline Solids* Oxford University Press
Mott N F, Pepper M, Pollitt S, Walis R H and Adkins C J 1975 *Proc. R. Soc.* **A345** 169
Rao C N R and Om Parkash 1977 *Phil. Mag.* **35** 1111
Rao C N R and Shukla A K 1976 *Indian J. Phys. Centenary Commemoration Vol.* **1** 93
Sayer M, Chen R, Fletcher R and Man Singh A 1975 *J. Phys.* **C8** 2059

Strain derivatives of the static dielectric constant of silver and thallium halide crystals*

V. Kumar** and S. C. Goyal

Department of Physics, Agra College, Agra-282002

Received 25 July 1977, revised 7 October 1977 and 27 April 1978

The theory of elastic dielectric has been applied to obtain the expressions for the strain derivatives of the static dielectric constant of the solids crystallising in CsCl type structure. The calculated values of the $\left(\frac{1}{\epsilon_0} \frac{d\epsilon_0}{dp}\right)$ have been found in excellent agreement with the experimental values for both silver and thallium halides which also provide the values of the W^0_{ijk} which may be helpful in analysing the experimental data.

1. Introduction

The study of the dielectric behaviour of the silver and thallium halides has been a subject of great interest for the last ten years. In both Phillips' (1970) and Goyal's (1976) *Ionicity Scale*, these solids have been shown as possessing low value of the fractional ionic character. The values of the static dielectric constant for thallium halide solids (TlCl, TlBr) are much larger than the values for the silver halide solids. Similarly the values of the change in ϵ_0 with pressure (Samara 1968) are very large. However, the experimental values of $\left(\frac{1}{\epsilon_0} \frac{d\epsilon_0}{dp}\right)$ (Samara 1968, Lowndes 1972) for these solids (TlCl, TlBr, AgBr) are very close to the values for alkali halides. In fact, these experimental values of $\left(\frac{1}{\epsilon_0} \frac{d\epsilon_0}{dp}\right)$ are related to the strain derivatives of the static dielectric constant W^0_{ijk} as given in Srinivasan and Srinivasan (1972) which is as follows

$$\frac{1}{\epsilon_0} \frac{d\epsilon_0}{dp} = -\frac{1}{\epsilon_0} \frac{W^0_{11,11} + 2W^0_{11,22}}{C_{11} + 2C_{12}} \quad (1)$$

Therefore, in order to study the above mentioned experimental similarities of silver and thallium halides with alkali halides, it is necessary to analyse the trends of variation in the values of W^0_{ijk} of these solids with an appropriate theory.

Recently Goyal *et al* (1977) have given the lattice theory of elastic dielectric based on Toupin's (1963) and Srinivasan's (1968) theory which studies the strain

* Work supported by U.G.C. (India).

** Department of Physics, B.S.A. College, Mathura (India).

optical constants ($P^{\infty}_{ij,kl}$) of silver and thallium halides. These solids have different type of the lattices. The former have the f.c.c. lattices while the latter possess b.c.c. lattices. However, the evaluation of the W^0_{ijkl} require the knowledge of several other elements which we need for the computation of $P^{\infty}_{ij,kl}$. We have tried to derive all the elements in the present study. The derived theory can be used to evaluate W^0_{ijkl} and $\frac{1}{\epsilon_0} \frac{dc_0}{dp}$ of the silver and thallium halides. The theoretically evaluated values of W^0_{ijkl} may be helpful in analysing the various experimental studies.

2. Theory

The strain derivatives of the dielectric constants are defined as

$$W_{ij,kl} = \frac{\partial \epsilon_{ij}}{\partial \eta_{kl}} \equiv 4\pi G_{ij,kl} \quad (2)$$

where ϵ_{ij} is the dielectric constant tensor and η_{kl} are the Lagrangian strain components. The components $G_{ij,kl}$ are the linear coefficient of variation of the components of the electrical susceptibility tensor χ_{ij} in the deformed and polarised state with the deformation parameter ϵ_{kl} which can be expressed as

$$G_{ij,kl} = \rho_{ij,kl} - G_{ij}\delta_{kl} \quad (3)$$

where

$$\begin{aligned} \rho_{ij,kl} = & -\frac{1}{v^2} \sum_{\lambda\rho} \sum_{\alpha\alpha} \sum_{\beta b} e(\lambda)\{\lambda i, \alpha\alpha\}e(\rho)\{\beta b, \rho j\}[\alpha\alpha, \beta b, kl] \\ & -\frac{1}{2}[G_{ii}\delta_{jk} + G_{ji}\delta_{ik} + G_{jk}\delta_{il} + G_{ik}\delta_{jl}] \end{aligned} \quad (3a)$$

$$G_{ij} = \frac{1}{v^2} \sum_{\lambda\rho} e(\lambda)\{\lambda i, \rho i\}e(\rho), \quad (3b)$$

The Greek letters represent the type of ion and small letters ij etc. represent the Cartesian components. In cubic crystals there are three independent values of the dielectric tensor. The corresponding $G_{ij,kl}$ factors are given by

$$G_{11,11} = -\frac{1}{v^2} \sum_{\lambda\rho} \sum_{\alpha\beta} e(\lambda)\{\lambda x, \alpha x\}[\alpha x, \beta x, xx]\{\beta x, \rho x\}e(\rho) - 3G_{11} \quad (4)$$

$$G_{11,22} = -\frac{1}{v^2} \sum_{\lambda\rho} \sum_{\alpha\beta} e(\lambda)\{\lambda x, \alpha x\}[\alpha x, \beta x, yy]\{\beta x, \rho x\}e(\rho) - G_{11} \quad (5)$$

$$G_{12,12} = -\frac{1}{v^2} \sum_{\lambda\rho} \sum_{\alpha\beta} e(\lambda)\{\lambda x, \alpha x\}[\alpha x, \beta y, xy]\{\beta x, \rho x\}e(\rho) - G_{11} \quad (6)$$

In the notation of Srinivasan and Srinivasan (1972) λ , ρ , α and β take the values 2 and 4, $e(2) = Z_2|e|$ and $e(4) = Y_2|e|$. Thus with the help of equations (2-6) the values of $W_{11,11}^0$, $W_{11,22}^0$ and $W_{12,12}^0$ can be evaluated. If λ , ρ , α and β take the values 4 only then the above equations will give the values of the strain derivatives of the high frequency dielectric constant $W_{11,11}^\infty$, $W_{11,22}^\infty$ and $W_{12,12}^\infty$ which will give the values of the strain optical constants P_{ijkl}^∞ using the relation

$$P_{ijkl}^\infty = -\frac{1}{\epsilon_\infty^2} W_{ijkl}^\infty \quad (7)$$

3. Calculations

The equations of the shear modulus and dielectric constant for NaCl and CsCl structures needed for the evaluation of the model parameters are given below :

NaCl structure

$$C_{11} - C_{12} = \frac{e^2}{4a^4} \left[-5.338 + A_1 + B_1 + \frac{(A_2 + 7B_2)}{2} \right] \quad (8a)$$

$$C_{44} = \frac{e^2}{4a^4} \left[2.556 + B_1 + \frac{(A_2 + 3B_2)}{2} \right] \quad (9a)$$

$$C_1 = \frac{4a^3}{e^2} \left[r \frac{d^3\phi_1(r)}{dr^3} \right]_{r=a} \equiv \frac{A_1^2}{B_1} \quad (10a)$$

where

$$A_1 = \frac{4a^3}{e^2} \left[\frac{d^2\phi_1(r)}{dr^2} \right]_{r=a}$$

$$B_1 = \frac{4a^3}{e^2} \left[\frac{1}{r} \frac{d\phi_1(r)}{dr} \right]_{r=a}$$

$$A_2 = \frac{4a^3}{e^2} \left[\frac{d^2\phi_2(r)}{dr^2} \right]_{r=a} \sqrt{2} \quad (11a)$$

$$B_2 = \frac{4a^3}{e^2} \left[\frac{1}{r} \frac{d\phi_2(r)}{dr} \right]_{r=a} \sqrt{2} \quad (12a)$$

CsCl structure

$$C_{11} - C_{12} = \frac{e^2}{4a^4} \left[-1.2211 + \frac{B_1}{2} + \frac{A_2}{2} \right] \quad (8b)$$

$$C_{44} = \frac{e^2}{4a^4} \left[-0.3505 + \frac{A_1 + 2B_1}{6} + \frac{B_2}{2} \right] \quad (9b)$$

$$C_1 = \frac{16a^3}{e^2} \left[r \frac{d^3\phi_1(r)}{dr^3} \right]_{r=a} \sqrt{3} \quad (10b)$$

where

$$A_1 = \frac{16a^3}{e^2} \left[\frac{d^2\phi_1(r)}{dr^2} \right]_{r=a\sqrt{3}}$$

$$B_1 = \frac{16a^3}{e^2} \left[\frac{1}{r} \frac{d\phi_1(r)}{dr} \right]_{r=a\sqrt{3}}$$

$$A_2 = \frac{8a^3}{e^2} \left[\frac{d^2\phi_2(r)}{dr^2} \right], \quad (11b)$$

$$B_2 = \frac{8a^3}{e^2} \left[\frac{1}{r} \frac{d\phi_2(r)}{dr} \right]_{r=2a} \quad (12b)$$

In view of the recent studies (Bakhshi *et al* 1977) of the interaction system in the solids under study, the short range next nearest neighbour interaction potential $\phi_2(r)$ is considered to be of van der Waal's type i.e. $\phi_2(r) = -\frac{C}{r^6} - \frac{D}{r^8}$. The expressions for the optical vibrational frequency $\omega_{T,0}$ at zone centre, Lorentz-Lorenz relations in the framework of simple shell model of Woods *et al* (1960) are given as follows

$$\frac{3}{4\pi} \frac{\epsilon_\infty - 1}{\epsilon_\infty + 2} = \frac{Y_2^2}{k_2 + (A_1 + 2B_1)\delta} \quad (13)$$

$$1 - \omega_{T,0} \left(\frac{\epsilon_0 - \epsilon_\infty}{4\pi} \right)^{1/2} \frac{3}{\epsilon_\infty + 2} \left(\frac{\mu\nu}{c^2} \right) = - \frac{Y_2(A_1 + 2B_1)\delta}{K_2 + (A_1 + 2B_1)\delta} \quad (14)$$

where $\delta = 1$ (NaCl structure)
 $\delta = 4/3$ (CsCl structure)

3. Results and Discussions

The values of the model parameters ($A_1, A_2, B_1, B_2, C_1, Y_2$ and K_2) have been determined with the help of above seven eqs. (8-14) using the experimental elastic constants from Huntington (1958), optical data from Lowndes and Martin (1969) and C and D from Bakhshi, Goyal and Jai Shanker (1977). The values of the parameter Z_2 are arbitrarily chosen. The model parameters are given in table 1.

The values of W^0_{ijk1} and $\frac{1}{\epsilon_0} \frac{d\epsilon_0}{dp}$ have been evaluated with the help of equations (1-7) using the evaluated model parameters. The computed values of W^0_{ijk1} and $\frac{1}{\epsilon_0} \frac{d\epsilon_0}{dp}$ are given in table 2.

Table 1. The values of the model parameters

Crystals	A ₁	B ₁	A ₂	B ₂	C ₁	Y ₂	Z ₂	K ₂
AgCl	9.4125	-1.6279	-1.0030	0.1404	-54.4229	-2.2879	1.2828	37.9007
AgBr	9.5297	-1.2908	-1.3623	0.1904	-70.3557	-2.7678	1.7778	51.3113
TlCl	37.0964	-2.0500	-10.1889	1.4011	-671.2891	-29.8257	27.9000	6477.8119
TlBr	40.6021	-2.1295	-11.2031	1.4849	-774.1397	-47.6202	45.7500	15584.298

Table 2. The calculated values of the $W_{ij,kl}^0$ and $\frac{1}{\epsilon_0} \left(\frac{d\epsilon_0}{dp} \right)$

Crystals	$W_{11,11}^0$	$W_{11,22}^0$	$W_{12,12}^0$	$\frac{1}{\epsilon_0} \left(\frac{d\epsilon_0}{dp} \right)_{cal.}$	$\frac{1}{\epsilon_0} \left(\frac{d\epsilon_0}{dp} \right)_{experimental}$
AgCl	196.918	- 10.838	9.043	-1.392	-1.35 ± .05
AgBr	190.042	9.299	25.025	-1.609	-1.56 ± .05
TlCl	- 15.712	281.560	299.181	-1.78	-1.81 ± 0.5
TlDr	- 85.634	288.211	308.226	-1.811	-1.77 ± .05

It is encouraging to note from table 2 that the calculated values of the $\frac{1}{\epsilon_0} \frac{d\epsilon_0}{dp}$ in silver and thallium halides are in excellent agreement with the experimental values. It is striking to note that the evaluated values of $W_{11,11}^0$ are larger than the values of $W_{11,12}^0$ and $W_{12,12}^0$ in case of the silver halides, however, in case of the thallium halides, the values of $W_{11,11}^0$ are smaller than the values of other two components. Hence, it appears that under the uniaxial strain these two halides show the distinct dielectric behaviour which is also apparent from their experimental lattice dynamical and dielectrical (Lowndes and Martin 1969) studies.

Therefore, we may conclude that although the silver and thallium halides are considered to be ionic solids, even then they show very distinct behaviour in the variation of the static dielectric constant with pressure in the different directions.

References

- Bakhshi P S, Goyal S C and Jai Shanker 1977 *J. Nucl. Eng. Chemistry* **39** 546
 Goyal S C 1976 *Solid State Commn.* **20** 269
 Goyal S C, Bakhshi P S and Jai Shanker 1977 *Solid State Commn.* **23**
 Huntington H 1958 *Academic Press N.Y. Solid State Physics* Vol. 7
 Lowndes R P 1972 *Phys. Rev.* **4667**
 Lowndes R P and Martin D H 1969 *Proc. Roy. Soc.* **A308** 473
 Phillips J C 1970 *Rev. Mod. Physics* **42** 317
 Samara G A 1968 *Phys. Rev.* **165** 959
 Srinivasan and Srinivasan K 1972 *J. Phys. Chem. Solids* **33** 1079
 Srinivasan R 1968 *Phys. Rev.* **165** 1041
 Toupin R A 1963 *Intern. J. Eng. Sci.* **1** 101
 Woods A D B, Chocharan W and Brockhouse B N 1960 *Phys. Rev.* **119** 980

Electrical conductivity and optical absorption in electrolytically coloured pure and doped KCl crystals

R. C. Bhuniya

Department of Physics, Indian Institute of Technology,
Kharagpur

Received 9 August 1977, revised 28 March 1978

Electrolytic colouration decreases the electrical conductivity of pure and Pb-doped KCl crystals in the extrinsic range. The decrease is higher in Pb-doped crystals compared to pure potassium chloride. The extrinsic conductivity of the coloured crystals decreases further upon removing the colouration. After colouration pure KCl crystal develops a strong F band and a weak but distinct M band. But in the Pb-doped crystal the F-band is very weak and no M band is formed at all. The characteristic Pb^{++} ion absorption band reduces extremely and a broad band develops in the ultraviolet. These results show that Pb^{++} ions are more efficient in trapping electrons than negative ion vacancies or inherent Ca^{++} ions of the pure crystals. The divalent cation impurities precipitate to some extent into metallic phase during electrolytic colouration.

1. Introduction

The formation of F and F' aggregate centres in alkali halide crystals by electrolytic colouration depends very much on the nature and concentration of divalent cations present in the crystal prior to colouration. Optical absorption measurements (Radhakrishna and Chowdari 1972) have shown that aggregate centres like Z_1 centres which comprise of divalent cations, cation vacancies and F centres are formed in electrolytically coloured KCl crystals doped with Ca^{++} , Ba^{++} and Sr^{++} ions. Again the divalent Pb^{++} ions of the Pb-doped crystals (Jain, Radhakrishna, Sai, 1969) and Cd^{++} ions of Cd-doped crystals have been found (Jain, Sootla, Jain, 1968) to trap electrons during colouration when their valency is reduced. The method of production of F centres by electrolytic colouration requires that the crystal should be quenched from colouring temperature. It is known (Kear and Pratt 1959) that when an uncoloured KCl crystal is quenched from such high temperature, the thermally produced and impurity induced vacancies coagulate during quenching process resulting in the formation of clusters of vacancies and dislocations. The divalent cation impurities also coagulate in the form of clusters consisting of impurity-vacancy dipoles and vacancy pairs (Bhuniya 1977). But when F centres are present in the coloured crystal, the coagulation of vacancies and impurities during quenching is likely to be different.

The coagulation of impurities will also depend on whether they trap electrons or not. The aim of the present paper is to study the conversion and coagulation of divalent cations of KCl crystals upon electrolytic colouration. Since the extrinsic conductivity of the alkali halide crystals depends very much on the presence of divalent cations in the crystal lattice so the measurement of extrinsic conductivity together with optical absorption of electrolytically coloured crystals will help the purpose.

2. Experiment

Potassium chloride crystals both pure and doped with PbCl_2 were grown in the laboratory by Kyropoulos method. The experimental details for electrolytic colouration have been given in a previous paper (Bhuniya and Mukherjee 1975). A potential difference of 140 volts per cm. was applied for colouring pure KCl crystals while for colouring the doped samples, the potential difference applied, was 160 volts per cm. Electrical conductivity of coloured and uncoloured crystals has been measured in the temperature range from 100 to 600°C both during heating and cooling. Optical absorptions of the samples have been measured in the wave length region from 220nm to 1000nm.

3. Results

The electrical conductivity of KCl crystals after electrolytic colouration is found to be less than that of the 'as grown' crystals throughout the impurity range while a small increase is observed in the intrinsic range (Fig. 1). The conductivity of the coloured crystals, at temperatures above 300°C, exhibits a fast decay with time at a particular temperature. The decay disappears at about 600°C when the conductivity of the coloured crystal attains the same value as that of the 'as grown' crystal. Upon measuring the conductivity during cooling, it is found to have the same conductivity as the crystal before colouration in the intrinsic range while the extrinsic conductivity is less than that of the 'as grown' or of the coloured crystal during heating.

The optical absorption spectrum of the electrolytically coloured KCl crystal shows the prominent F-band at 560 nm along with a weak M band at 820nm (Fig. 2). Upon annealing at temperatures above 300°C, the F band decreases and the M band disappears with the development of the colloidal band whose maximum absorption is at 780nm. The effect of electrolytic colouration on the Pb-doped crystal is also shown in the figure 2. The characteristic absorption band due to Pb^{++} ions at 273nm is considerably reduced and appears to be replaced by a broad and diffuse region of absorption on the long wavelength side of the band. The F band is also formed but not as prominently as in the case of undoped crystals and the M band is not formed at all. Heat treatment at 250°C reduces F and Pb^{++} band as well as the broad band in the neighbourhood of the

Pb^{++} band. The crystals so treated show rather pronounced absorption in the wavelength region below 240nm and in the long wavelength side of the F band.

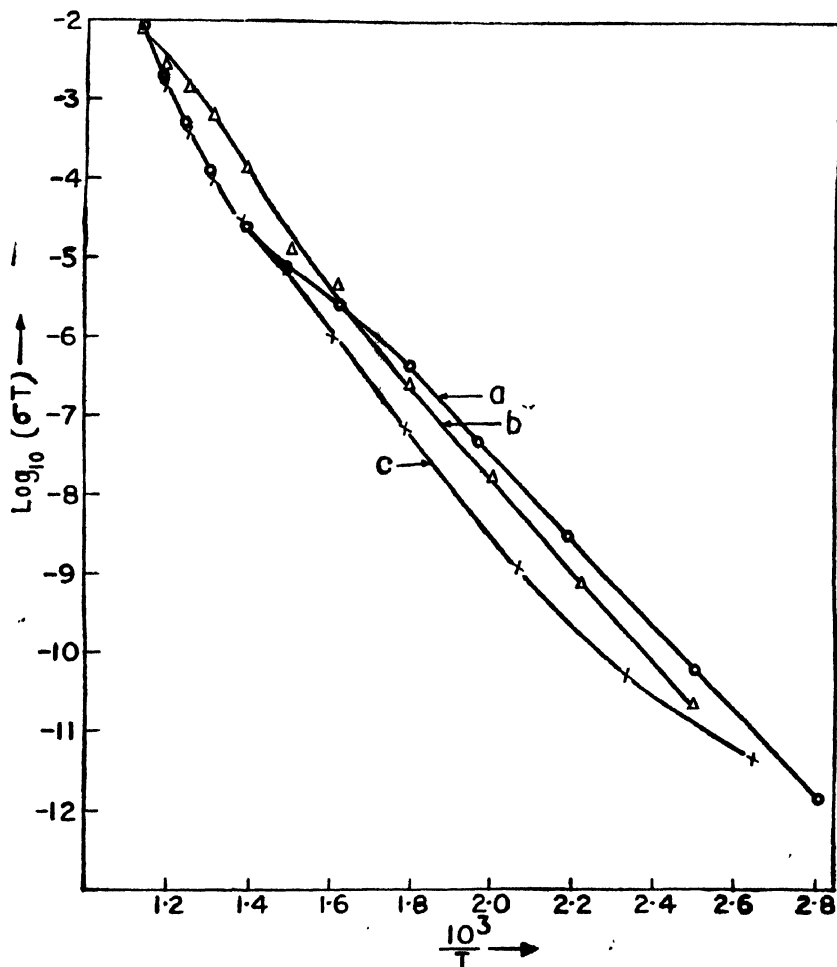


Fig. 1. Electrical conductivity of KCl crystals before and after electrolytic colouration at 650°C

- a) O O O KCl as grown
- b) $\Delta \Delta \Delta$ KCl electrolytically coloured, during heating.
- c) $\times \times \times$ KCl electrolytically coloured during cooling

The electrical conductivity of KCl crystals increases in the extrinsic region upon doping with Pb^{++} ions. Electrolytic colouration decreases the conductivity of the Pb -doped crystals very much throughout the temperature range investigated i.e. from 100 to 600°C (Fig. 3). Unlike the electrolytically coloured potassium chloride, these crystals exhibit a long period decay of conductivity at a particular temperature below 300°C. The readings for figure 3 b were taken after

allowing the current at each temperature to decay for about twenty minutes. The current has been measured as a function of time at a particular temperature in the region where it decays and is shown in the figure 4 as plots of $\log_{10} I$ vs. t . When the electrolytically coloured Pb-doped crystals are annealed at 300°C and

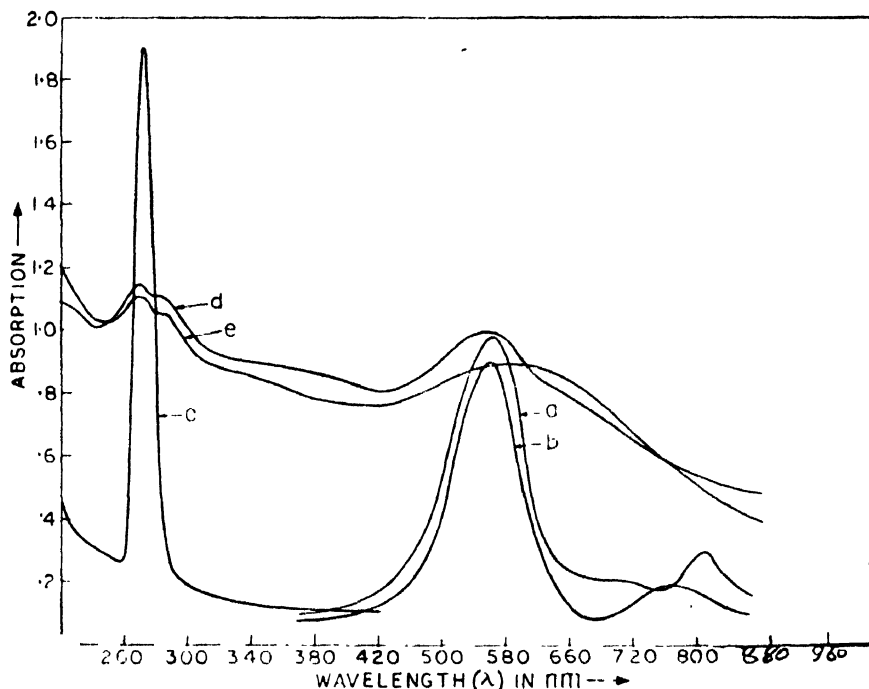


Fig. 2. Optical absorption spectra of KCl and KCl : Pb crystals after electrolytic colouration at 650°C

- a) KCl E-coloured
- b) KCl E-coloured after annealing at 300°C for one hour.
- c) KCl:Pb as grown
- d) KCl:Pb E-coloured
- e) KCl:Pb E-coloured after heating at 250°C for one hour

slowly cooled, the conductivity of the crystals is found to be much lower during cooling than during heating. It does not change further while heating the annealed crystal for the second time. The slope of the curve increases and tends to have the same value as for the rest of the curve of figure 3b which corresponds to an activation energy of 1.75 e.v. The annealing not only decreases the conductivity but also removes the long period decay exhibited by the crystals below 300°C. The conductivity of the same doped and coloured sample was measured during heating to 600°C and cooling from this temperature. During cooling, the conductivity of the sample is found to have the same value as that during heating upto 300°C. Below this temperature, the conductivity curves of the crystals

annealed from 600°C and 300°C resemble alike, the latter being slightly higher in conductivity.

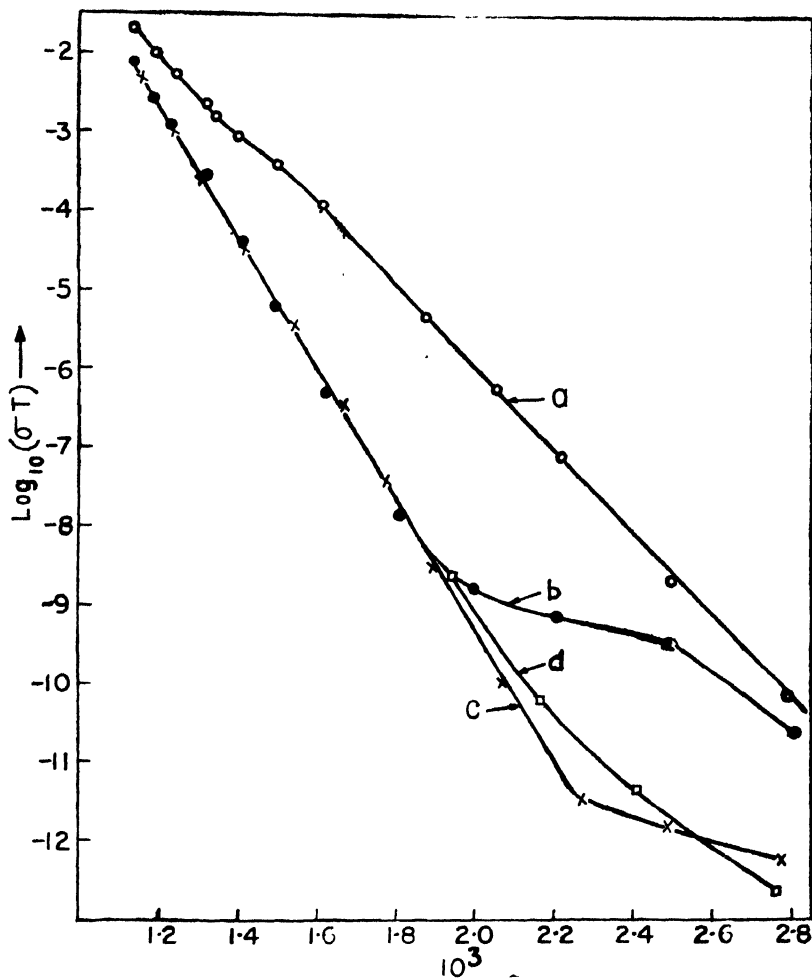


Fig. 3. Electrical conductivity of KCl:Pb crystals after electrolytic colouration at 650°C

- a) ○ ○ ○ KCl:Pb as grown
- b) ● ● ● KCl:Pb E-coloured during heating
- c) × × × KCl:Pb E-coloured during cooling from 600°C
- d) □ □ □ KCl:Pb E-coloured during cooling from 300°C

4. Discussion

At the temperature of electrolytic colouration of KCl crystal at 650°C, large number of positive and negative ion vacancies (2.2×10^{17} per c.c., calculated from the data given by Kelting and Witt 1949) are produced thermally. The negative

ion vacancies trap electrons producing F centres. So, to maintain charge neutrality an equal number of thermally produced positive ion vacancies must disappear from the crystal lattice. A fraction of the inherent divalent cations also trap electrons when their valency is reduced. The positive ion vacancies cor-

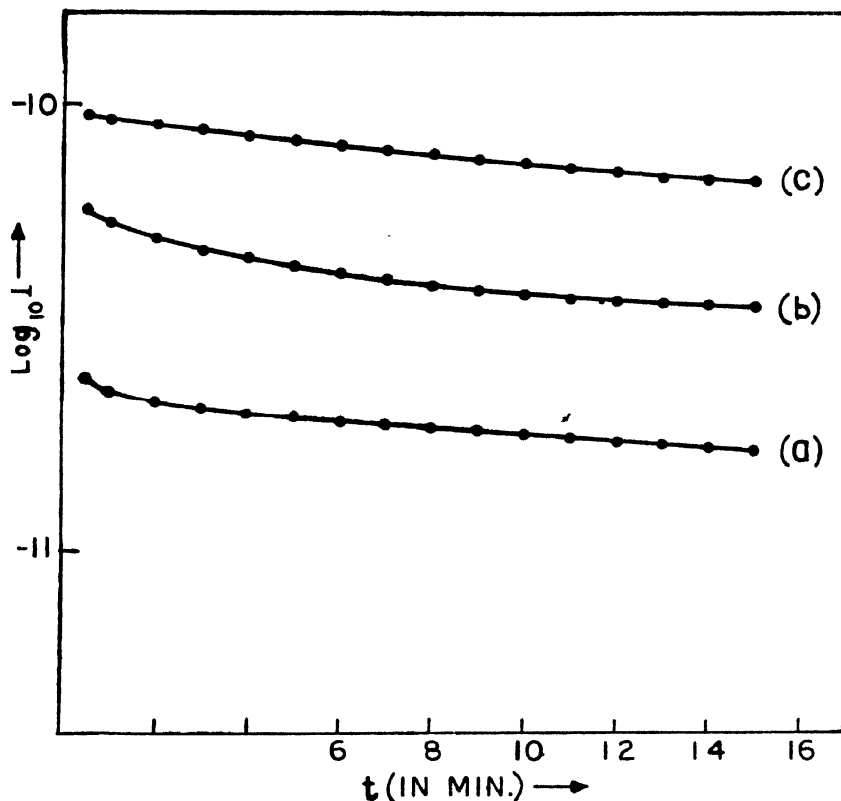


Fig. 4. Decay of current in electrolytically coloured KCl:Pb crystal at different temperatures

- a) 130°C
- b) 180°C
- c) 230°C

responding to the impurity ions which have trapped electrons must also move out of the crystal. The disappearance of the cation vacancies takes place quickly due to their high mobility at such temperatures. When the colouration of the crystal is complete at 650°C, it contains a large concentration of F centres, a fraction of the divalent cations with valency reduced and the rest in the form of dissociated impurity vacancy dipoles. During the quenching process most of the F centres remain isolated (1.5×10^{17} per c.c. calculated from the present experiment using Smakula formula) while a fraction of them coagulate amongst themselves leading to the formation of different types of F aggregate centres viz. *M.R.N*

etc. of which M centres produce the strongest absorption band at 820nm. Aggregation of F centres with divalent cation impurities and cation vacancies gives rise to Z type of centres. Since their numbers are small and their absorption maxima fall on the long wave length side of the F band, they do not produce any distinct absorption band in the absorption spectrum. That divalent cation impurities and cation vacancies are trapped during quenching after colouration can be seen from the observation that although they remain separated in the coloured crystal they do not coagulate during subsequent annealing producing a decay of current as is observed in the quenched crystal (Bhuniya 1976). Since some of the divalent cations trap electrons during colouration, so the concentration of impurity induced positive ion vacancies decreases in the coloured crystal which decreases its conductivity in the extrinsic range. The higher value of the conductivity of the coloured crystal during heating compared to its value during cooling may be due to two reasons. Firstly the divalent cation impurities of the coloured crystal are converted into monovalent or metallic phase by the capture of electrons produced by the ionisation of F and F -aggregate centres during the heating process. Secondly, the electrons produced by the ionisation of F and F -aggregate centres will also provide a contribution to the conductivity of the coloured crystal (Jain and Sootha, 1968). The F -centres coagulate above 300°C to form colloids. The electrons produced by the thermal ionisation of colloids contribute to current at such temperatures so that the intrinsic conductivity increases (Jain and Sootha 1968).

The inherent divalent cation impurities of the undoped KCl crystal are mostly Ca^{++} ions. Upon electrolytic colouration, the relative decrease of Pb^{++} ions of the Pb-doped crystal is much more than that of Ca^{++} ions of the undoped crystal which is seen by the relative decrease of their conductivity. The decrease of Pb^{++} ions can also be seen from the observation that the Pb^{++} ion band at 273nm reduces extremely after electrolytic colouration. The thermally produced anion vacancies are of the same order of magnitude (2×10^{17} per c.c.) in both Pb-doped and undoped KCl crystals at the temperature of electrolytic colouration viz. 650°C . But the concentration of F centres is much more in the latter (1.5×10^{17} per c.c.) than in the former (8.5×10^{16} per c.c.). This shows that Pb^{++} ions are better traps for electrons than negative ion vacancies or Ca^{++} ions. The Pb^{++} ions of the Pb-doped crystal also trap electrons during X-irradiation converting into centres like Pb^+ and Pb^0 (Sonder and Sibley 1964) when the Pb^{++} ion band decreases. These centres at temperatures above 200°C loose the trapped electrons and convert into Pb^{++} ions when the Pb^{++} ion band regains (Sonder and Sibley 1964). Since the Pb^{++} ion band of the electrolytically coloured Pb-doped crystal does not regain upon thermal treatment at temperatures above 200°C , it is likely that the Pb impurities of the crystal are not in the form of isolated Pb^+ and Pb^0 centres. The low concentration of F centres indicates that only a small

fraction of thermally produced anion vacancies trap electrons compelling an equal number of cation vacancies to disappear during electrolytic colouration. As the bulk of the thermally produced vacancies remain in the crystal during colouration, they form clusters consisting of impurity vacancy dipoles and vacancy pairs which will be continually formed and destroyed. These defect sites are the easy path of electrons during colouration when Pb^{++} ions will trap electrons forming Pb^+ , Pb^0 and Pb^- centres. Since the clusters may contain a number of Pb^{++} ions, these centres will remain coagulated. Further coagulation will take place during quenching so that most of these centres will be in the colloidal phase in the coloured crystal although a few of them can remain isolated. The broad absorption band in the ultraviolet may be due to the colloidal phase of Pb^+ , Pb^0 and Pb^- centres. Annealing from high temperatures removes the broad band of the ultraviolet and develops a band due to metallic lead (Topa *et al* 1969, Jain *et al* 1969). For the development of the metallic lead from Pb^+ centres, the latter have to trap electrons during annealing from some excess electron centres like F and Pb centres. Since the concentrations of such centres are small and the coloured crystal still contains some Pb^{++} ions, so the trapping of electrons by Pb^+ ions during annealing is extremely negligible. Hence the metallic lead must be formed from the colloids of Pb^0 and Pb^- centres and the absorption in the wavelength region from 240nm to 420nm which decreases upon annealing seems to be due to colloids of Pb^0 , Pb^- centres.

A small fraction of Pb^{++} ions, even after colouration, remain isolated as well as in the form of clusters with vacancies. The isolated impurity ions form clusters with vacancies during subsequent annealing at lower temperatures. The decrease of the Pb^{++} ion band of the coloured crystal after annealing at 250°C shows that the Pb^{++} ions of the crystal trap electrons released from F centres or Pb^- centres during annealing. The impurity ions convert into Pb^+ centres (Pb^0 and Pb^- centres will not be formed as their formation requires the presence of high concentration of free electrons in the crystal) when the clusters turn into aggregate centres consisting of Pb^+ ions and vacancies. These aggregate centres develop an absorption band at 215nm (Jain *et al* 1969). In the present experiment absorption could not be measured below 220 nm and the increase of absorption in the wavelength region below 240nm of the coloured crystal after annealing seems to be due to the development of the band of these aggregate centres. During annealing colloids of Pb^0 grow further in size and precipitate as metallic lead while those of Pb^- loose electrons forming colloids of Pb^0 which may also precipitate in the metallic phase.

The decay of the electrical conductivity of the electrolytically coloured Pb-doped crystal at temperatures below 300°C can be divided into two regions. In the lower temperature region formation of clusters by coagulation of free impurity ions and cation vacancies gives rise to the decay. At higher temperatures, the

electrons released from Pb^- and F centres will contribute to current. They will cease to contribute as soon as they are trapped by Pb^{++} or other trapping centres. The current will decay with time during annealing when Pb^- and F centres are destroyed. Moreover, because of the trapping of electrons by Pb^{++} ions, the impurity induced positive ion vacancies will diffuse out of the crystal which will make the current to decay. The same value of the conductivity during heating and cooling at temperatures above 300°C shows that excess electron centres like F and Pb^- are destroyed below this temperature.

Acknowledgment

The author is indebted to Prof. H. N. Bose for helpful discussion. Thanks are also due to Dr. M. L. Mukherjee for providing the crystals.

References

- Bhuniya R C 1976 *Ind. Phys.* **50** 572
Bhuniya R C 1977 *Czech. J. Phys.* **27**, 1164
Bhuniya R C and Mukherjee M L 1975 *Ind. J. Pure. and Appl. Phys.* **13** 366
Jain S C and Sootha G D 1968 *Phys. Rev.* **171** 1083
Jain S C, Sootha G D and Jain R K 1968 *J. Phys. C*, **1** 1220
Jain S C, Radhakrishna S and Sai K S K 1969 *J. Phys. Soc. Japan* **27** 1179
Kear B H and Pratt P L 1959 *Phil Mag.* **4** 56
Keltting H and Witt H 1949 *Z. Physik* **126** 697
Radhakrishna S and Chowdari B V R 1972 *Phys. Stat. Sol (a)* **14** 11
Sonder E and Sibley W A 1964 *Phys. Rev.* **136** 537
Topa V and Velicescu B 1969 *Phys. Stat. Sol.* **33** K29

EPR of Mn^{2+} in $M''M'_2(SeO_4)_2 \cdot 6H_2O$ ($M'' = Mg, Zn$ and $M' = NH_4, Rb$) single crystals

V K Jain and T M Srinivasan

Department of Physics, Indian Institute of Technology Kanpur
Kanpur 208016

and

Putchu Venkatoswarlu*

Herzberg Institute of Astrophysics
National Research Council of Canada
Ottawa K1S 0R6, Canada

Received 29 August 1977

The electron paramagnetic resonance of divalent Mn^{2+} ions in the Tutton salts $M''M'_2(SeO_4)_2 \cdot 6H_2O$, ($M'' = Mg, Zn$ and $M' = NH_4, Rb$) single crystals has been observed at 298K. The Mn^{2+} is found to substitute divalent cation sites. The spectra have been analysed using the spin-Hamiltonian appropriate for rhombic symmetry.

1. Introduction

The Tutton salts with the general formula $M''M'_2(XO_4)_2 \cdot 6H_2O$, where M'' is a divalent cation (Zn, Mg , or an ion of the $3d$ group), M' is a monovalent cation (K, Rb, Cs, Tl or NH_4) and $X = S, Se$, form an isomorphous series of compounds. Therefore, it is easy to prepare solid solution of paramagnetic Tutton salts in diamagnetic ones over a wide range of relative concentrations often from zero to 100 per cent. These solid solutions have been the subject of numerous electron paramagnetic resonance (EPR) investigations on iron group ions (Althshuler and Kozyrev 1964). In the present paper we report EPR study at 298K of Mn^{2+} incorporated into $Mg(NH_4)_2(SeO_4)_2 \cdot 6H_2O$ (MAScH), $MgRb_2(SeO_4)_2 \cdot 6H_2O$ (MRbSeH), $Zn(NH_4)_2(SeO_4)_2 \cdot 6H_2O$ (ZAScH) and $ZnRb_2(SeO_4)_2 \cdot 6H_2O$ (ZRbSeH) single crystals for the first time.

2. Crystal Structure

An X-ray study of the structure determination of the Tutton salts was made by Hoffmann (1931). The crystal structure of Tutton salts is monoclinic with space

*Visiting Research Officer, on leave from Department of Physics, Indian Institute of Technology Kanpur, Kanpur 208016, India.

group $P2_1/a$. The crystallographic axes (a, b, c) are approximately in the ratio (3, 4, 2) and the angle β is about 105° . There are two formula units per unit cell. The two inequivalent divalent cations in the unit cell are situated at the points (0, 0, 0) and $(\frac{1}{2}, \frac{1}{2}, 0)$ and all others are in general positions. Each divalent cation is surrounded by a slightly distorted octahedron of water molecules. Although the detailed structural studies are available only for crystals of ammonium Tutton salts, the isomorphism of the Tutton salts, however, leads one to assume that bond distances and angles in the hydration shell of divalent cation in the Tutton salts studied are not very different from those in ammonium Tutton salts.

3. Experimental

Single crystals of Tutton salts doped with Mn^{2+} were grown by slow evaporation of aqueous solution, at room temperature. The Mn^{2+} were introduced into the lattice by adding a small amount (0.1 percent by weight) of manganese sulfate. The experiments were performed on a Varian V-4502 EPR Spectrometer, operating at X-band, provided with 100kHz field modulation. As a reference for magnetic field strength the resonance line of DPPH with $g = 2.0036$ is used. The magnetic field at DPPH resonance was measured with the help of a Varian Model F-8A fluxmeter while the frequency of proton signal is measured by Systronics type 701 frequency counter.

4. Results and Discussion

For an arbitrary orientation of the magnetic field, a complex spectrum corresponding to two identical but differently oriented Mn^{2+} complexes is observed in $MAsE\cdot H$, $ZAsE\cdot H$, $MRbSe\cdot H$ and $ZRbSe\cdot H$. When the magnetic field is varied in the ac plane the EPR spectrum shows only one set of five sextets ($\Delta M = \pm 1$, $\Delta m = 0$ transitions). This is in conformity with the fact that the ac is a mirror plane perpendicular to the b axis, in which two divalent sites become equivalent. Thus, it may be concluded that the Mn^{2+} ion enters the Tutton salt lattices in the divalent sites and magnetic $Mn(H_2O)_6^{2+}$ complexes are obtained. The principal axes of the two inequivalent Mn^{2+} complexes were obtained by getting the extrema in fine structure spread. The spectrum at 298K for magnetic field along the principal z axis of one set of equivalent Mn^{2+} complexes in $ZAsE\cdot H$ is shown in Fig. 1. The angle between z axes of two inequivalent Mn^{2+} complexes in all the crystal studied is given in Table I. The results of other Tutton salts (Baleaney and Ingram 1951, Ingram 1953, Janakiraman and Upreti 1970, Kasthurirengan and Navalgund 1975) are also included in this table. Study of the spectrum's angular variation showed that the crystal field symmetry is orthorhombic. Fig. 2 shows the angular variation of the fine structure transitions ($\Delta M = \pm 1$) in the

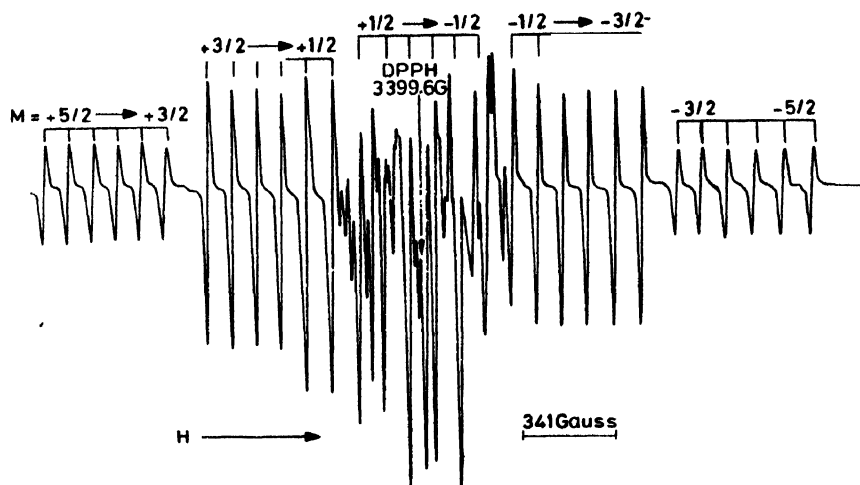


Figure 1. EPR spectrum of $\text{Zn}(\text{NH}_4)_2(\text{SeO}_4)_2 \cdot 6\text{H}_2\text{O}:\text{Mn}^{2+}$ single crystals at 298K; with H parallel to z axis of one of the magnetic complexes of Mn^{2+}

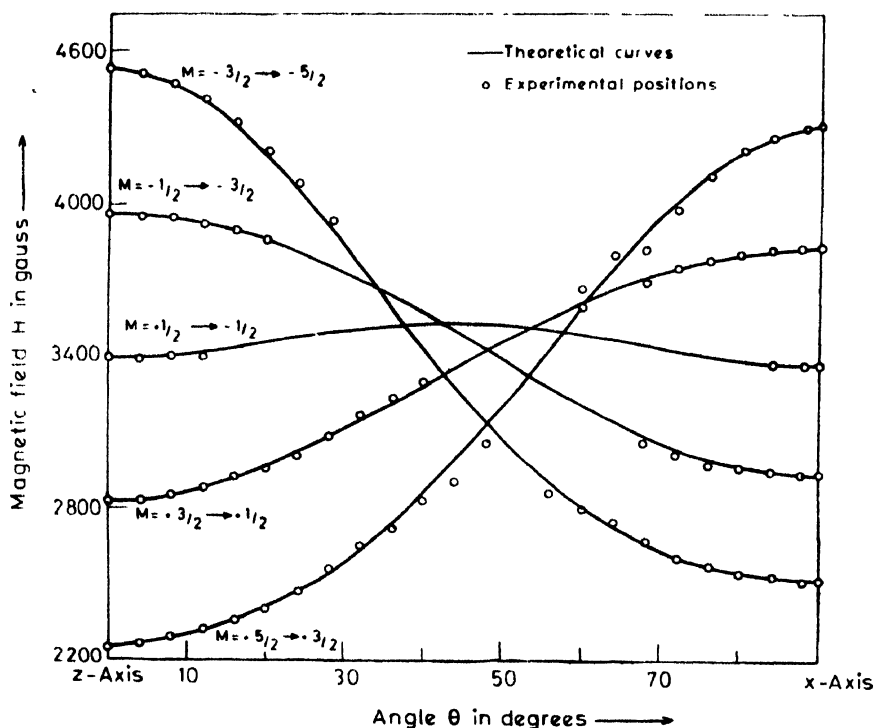


Figure 2. Angular variation of the allowed fine structure transitions in the zx plane of the one of the magnetic complexes of Mn^{2+} in $\text{Zn}(\text{NH}_4)_2(\text{SeO}_4)_2 \cdot 6\text{H}_2\text{O}$ single crystals

zx plane of the one of the Mn^{2+} complexes in $ZAsH$. Similar curves have been found for the isomorphous crystals $MAsH$, $ZAsH$, $MRbSeH$ and $ZRbSeH$. The similarity of these curves in the four host crystals is indicative that the local environment have the same symmetry, with the spectra differing only in the magnitude of the splitting. The observed orthorhombic spectra for $MAsH$, $ZAsH$, $MRbSeH$ and $ZRbSeH$ for sample temperature of 298K were fitted to a spin-Hamiltonian (Chowdari and Venkateswarlu 1968)

$$\begin{aligned}\mathcal{H} = & \beta(g_x H_x S_x + g_y H_y S_y + g_z H_z S_z) + D[S_z^2 - (1/3)S(S+1)] + E(S_x^2 - S_y^2) \\ & + (a/6)[S_x^4 + S_y^4 + S_z^4 - (1/5)S(S+1)(3S^2 + 3S + 1)] \\ & + AI_z S_z + BI_x S_x + CI_y S_y\end{aligned}$$

where the symbols have their usual meaning and for Mn^{2+} , $S = 1/2$.

Magnetic field measurements were made for the allowed lines along z and x axes. No measurements could be made along y axis since the lines are all mixed together and consequently the various transitions could not be distinguished. Therefore, it was necessary to assume that $B = C$ and $g_x = g_y$ (for Mn^{2+} g_y values and hyperfine splitting is nearly isotropic) in the calculations. Using the above spin-Hamiltonian, the Mn^{2+} EPR spectra are analysed and the values of the best fit parameters, thus obtained are listed in Table 1. For comparison, the spin-Hamiltonian parameters of Mn^{2+} in other Tutton salts (Bleaney and Ingram 1951, , Ingram 1953, Janakiraman and Upreti 1970, Kasthurirengan and Navalgund 1975) are also included in this table. The signs of the parameters (given in Table 1) are relative. Since the hyperfine splitting constant is always found to be negative for a manganese ion (Watson and Freeman 1961, Richardson *et al* 1970), this sign is taken for A in this case as well. The examination of the magnitude of the splitting of the hyperfine sextets appearing at high fields and low fields when the magnetic field is parallel to z axis, attributes a sign to parameter D (Low 1960). The sign of rhombic parameter E results from the sign of D and choice of x and y axes.

The g factor and the hyperfine coupling constant were found to be almost isotropic within the experimental error for all the crystal studied. It was recognized that nearest neighbour interactions are dominating for hyperfine splitting in contrast to other EPR parameters like D , a and g values where long range interaction can be important (Müller 1970). Therefore, the determination of hyperfine splitting constant in EPR spectra of Mn^{2+} makes it possible to evaluate the nature of bond between manganese ion and its immediate surroundings. It is instructive to compare hyperfine splitting constant of Mn^{2+} in Tutton salts studied with those of other crystals. Comparison with the values of hfs constant of Mn^{2+} in struvite (Vinokurov and Tikhvatullin 1968), GASH (Milsch and Windsch 1969), Perchlorate (Fritz and Yarmus 1968), Double nitrate (Jain and Srinivasan 1977) where it is surrounded by six water molecules also confirms that immediate neigh-

Table 1. Comparison of the spin-Hamiltonian parameters and angle α between z axes of two magnetic inequivalent Mn^{2+} complexes in Tutton salt single crystals. All the crystal field and hyperfine parameters are in units of 10^{-4} cm^{-1}

Host lattice	D	E	a	g_z	g_x	A	B	α	References
$Mg(NH_4)_2(SO_4)_2 \cdot 6H_2O$	231	60.0	3.0	—	—	90.0	90.0	60°	Ingram (1953)
$Zn(NH_4)_2(SO_4)_2 \cdot 6H_2O$	243	100.0	5.0	—	—	-91.0	-91.0	64°	Bleaney and Ingram (1951)
$Fe(NH_4)_2(SO_4)_2 \cdot 6H_2O$	-232.5	45.0	—	$2.004 \pm .001$	—	-87.8	90.8	$70^\circ \pm 5^\circ$	Janakiraman and Upreti (1970)
$ZnK_2(SO_4)_2 \cdot 6H_2O$	-245.8	67.8	8.7	2.0164	—	-82.2	-82.9	64°	Kashurirengan and Navalgrund (1975)
$Mg(NH_4)_2(SeO_4)_2 \cdot 6H_2O$	248.6 ± 1	-60.8 ± 2	5.8 ± 1	$2.004 \pm .001$	$2.006 \pm .002$	-88.0 ± 1	-88.0 ± 1	$66^\circ \pm 4^\circ$	Present work
$Zn(NH_4)_2(SeO_4)_2 \cdot 6H_2O$	264.9 ± 1	-51.5 ± 2	5.3 ± 1	$2.005 \pm .001$	$2.007 \pm .002$	-88.6 ± 1	-87 ± 1	$68^\circ \pm 4^\circ$	Present work
$MgRb_2(SeO_4)_2 \cdot 6H_2O$	-296.5 ± 1	68 ± 2	8.6 ± 1	$2.006 \pm .002$	$2.008 \pm .002$	-88 ± 1	-87 ± 1	$60^\circ \pm 4^\circ$	Present work
$ZnRb_2(SeO_4)_2 \cdot 6H_2O$	-301.6 ± 1	63 ± 2	9.1 ± 1	$2.003 \pm .001$	$2.005 \pm .002$	-88.8 ± 1	-89 ± 1	$66^\circ \pm 4^\circ$	Present work

bour of Mn^{2+} in Tutton salts is six water molecules. At the same time it is noted that the half width of Mn^{2+} absorption lines in the Tutton salts is of the order of 12 gauss, which can be explained as mainly due to local magnetic field of the proton nuclear moments in the water molecules (Abragam and Bleaney 1970).

In all the salts quoted in Table 1, the value of angles between the z axis of two inequivalent magnetic complexes and the values of the parameters D and E are very nearly of the same magnitude. This gives a qualitative idea of the local symmetry at divalent cation sites especially in the system where no detailed crystal structure is available. Qualitatively it can be concluded that the co-ordination of the octahedron of water molecules at the divalent cation is nearly the same for all the systems both as regards the symmetry as well as distances from the divalent cation. It is also noticed from Table 1, that the zinc Tutton salts have larger D values in comparison with the magnesium Tutton salts. The value of D is larger for selenate Tutton salts than for the corresponding sulfate Tutton salts. This is probably related to the larger size of the selenium (Manoogian and Leclerc 1975)—the ionic radii of Se^{6+} and S^{6+} are 0.42 Å and 0.30 Å respectively.

References

- Abragam A and Bleaney B 1970 *Electron Paramagnetic Resonance of Transition Ions*, Clarendon Press, Oxford, p 217
- Althshuler S and Kozyrev B 1964 *Electron Paramagnetic Resonance*, Academic Press, New York, Ch. 4.
- Bleaney B and Ingram D J E 1951 *Proc. Roy. Soc. (London)* **A205** 336
- Chowdari B V R and Venkateswarlu P 1968 *J. Chem. Phys.* **48** 318
- Fritz I J and Yarnus L 1968 *Phys. Rev.* **173** 445
- Hoffmann W 1931 *Z. Krist.* **78** 279
- Ingram D J E 1953 *Proc. Phys. Soc. (London)* **A66** 412
- Jain V K and Srinivasan T M 1977 *Z. Naturforsch* **23a** 665
- Janakiraman R and Upreti G C 1970 *Chem. Phys. Lett.* **4** 550
- Kasthuriangan S and Navalgund R R 1975 *Phys. Stat. Sol.(b)* **72** K1
- Low W 1960 *Paramagnetic Resonance in Solids* (Solid State Phys. Suppl. 2), Academic Press, New York
- Manoogian A and Lecero A 1975 *J. Chem. Phys.* **63** 4450
- Milsch B and Windsch W 1969 *Phys. Stat. Sol.* **31** K79
- Richardson R J, Lee S and Menne T J 1970 *Phys. Rev.* **32** 2295
- Vinokurov V M and Tukhvatullin R S 1968 *Geokhim (In Russian)* **4** 496
- Watson R E and Freeman A J 1961 *Phys. Rev.* **123**, 2027

A new method of finding Born-Mayer parameters of inert gases in ionic solids

C Neogy and S K Deb

Department of Physics, University of Kalyani, Kalyani, West Bengal, India

Received 3 October 1977

A new method has been suggested for finding the Born-Mayer repulsive parameters $\beta_{ij}b$ and ρ for the interaction between a neutral interstitial defect and the neighbouring ions, in an ionic solid from the electronic charge density overlap of the interacting atoms and ions. Thus $\beta_{ij}b$ and ρ for He and Ar in NaCl and KCl lattices are obtained. These parameters have been utilised to calculate the activation energies of interstitial defect diffusion in the host lattices. The activation energies are calculated assuming a semi continuum model and by considering contributions from electrostatic, repulsive, polarisation and van der waal's energy terms in minimising the total change of energy of the lattice, as a function of the relaxation of the nearest neighbour ions, when the defect atom occupies the cube center and the face center positions.

1. Introduction

Born (1954) has formulated a theory to describe the various properties of alkali halides with the help of a simple interaction potential energy function. For a perfect crystal this potential function consists of (i) an electrostatic term, (ii) a repulsive term and (iii) multipole interaction terms while for a defect crystal additional contribution from polarisation energy results. The least certain part of the above mentioned potential energy function is the repulsive energy term. Born, however has given an empirical form to find the repulsive interaction between two interacting ions in an ionic lattice

$$E_{ij}(r) = \beta_{ij}b \exp \{(r_i + r_j - r)/\rho\} \quad (1)$$

where b and ρ are repulsive strength and range parameters respectively, β_{ij} is called the Pauling coefficient and r_i , r_j are the ionic radii.

These b and ρ values are usually found out by utilising two equilibrium crystal properties, namely,

$$(i) \text{ equilibrium condition } \left. \frac{dU(r)}{dr} \right|_{r_0} = 0. \quad (2)$$

and (ii) compressibility at absolute zero, K_0 ,

$$\left. \frac{d^2U(r)}{dV^2} \right|_{v=v_0} = \frac{1}{K_0 V_0} \quad (3)$$

b and ρ values thus found out from pure crystal properties, construct the repulsive part of a potential which reproduces successfully many of the properties of a pure ionic crystal. But when a defect, either a neutral atom or a charged impurity, occupies an interstitial or a substitutional position, the situation becomes different. The method by which b and ρ for a pure crystal have been obtained from equilibrium crystal properties, cannot be applied for a defect crystal as, such equilibrium crystal properties of defect crystal do not exist. So, one has to take recourse to various approximations, regarding the nature of interaction between the impurity and the surrounding ions. These approximations are generally grouped in two different approaches. In one approach, the repulsive interaction between an ion and an atom is taken to be the same as that would be between two atoms in the gaseous state (Abrahamson *et al* 1961). The ion is approximated by an atom having similar electronic configurations. In the second approach the atom is approximated by an ion of zero charge in the evaluation of the Pauling coefficient and the ion-ion interaction method of Born-Mayer is applied to find the repulsive interaction between a defect atom and a host ion. b and ρ values of such interaction are taken to be the same as that between two host ions (Lidiard and Norget 1972). As an illustration, Hatcher and Dienes (1961) have assumed the repulsive parameters between Na^+ and Cl^0 to be the same as that between Na^+ and Cl^- . For a substitutional defect, Tosi and Fumi (1964) have assumed the repulsive parameters between H^- ion and a negative halogen ion to be the same as that between two halogen ions. Actually for any type of defect, b and ρ values for the defect interaction is taken to be the same as that between two host ions.

Now, Deb and Ghosh (1975) have shown that the repulsive parameters b and ρ for a pure crystal can be correlated to the overlap of the electronic charge density of the constituent ions. In this paper, we want to see the effect of extending that idea to the case of a defect crystal. Following the same principle, we present here a method of finding the repulsive interaction parameters between an ion and a defect atom from their electronic charge density overlap. To check the validity of our determined values, we have decided to calculate one physical quantity which ultimately depends on such repulsive parameters. We have therefore calculated activation energies of interstitial defect diffusion in different host lattices taking our repulsive parameters as well as taking other parameters and compared the two sets.

2. Method of calculation

Deb and Ghosh (1975) have shown how to find b and ρ values from the electronic charge density overlap for a pure crystal. It was observed that a relation exists between the Born-Mayer parameters of an alkali halide and the corresponding overlap height and the overlap spread when the free ionic charge densities of the

host ions are plotted at the ends of the equilibrium interionic separation r_0 (Fig. 1). Actually, one such correlation was obtained for the alkali chlorides and the alkali bromides. Using that correlation and the overlap height and the overlap spread for any particular ion pair, b and ρ for that ion pair can be obtained. The repulsive parameters thus obtained explains the repulsive interaction between the constituent ions of a crystal, even when they are displaced from their normal lattice sites.

Following similar type of arguments, we plot here the free ionic charge density of the anion or of the cation at one end and the free atomic charge density of the defect atom at the other end of the equilibrium interionic separation of the particular crystal and hence obtain the overlap height and the overlap spread. b and ρ values are then obtained assuming the same correlation existing between the defect atom and the host ions as was assumed between the host ions. The value of b and ρ thus obtained will explain the repulsive interaction between the host ions and the defect atom even when the defect atom occupies an interstitial position. We understand that this principle of placing a neutral defect in a normal ionic lattice site does not normally represent a physical case but still this involves in some way the physical properties of the defect atom as well as that of the host lattice (through r_0) for finding the interaction between a defect atom and the host ions.

The method by which we have calculated the activation energy of defect diffusion is the same as reported in one of our earlier paper (Neogy and Deb 1976). We shall not, therefore, describe that method here in detail. Only the principle of the method is, however, discussed.

We place the defect atom in two positions—once in a square centre position (S position) and then in a cube centre position (C position) and calculate, in each case, the change in the lattice energy (as a result of introduction of the defect atom) as a function of the radial relaxation (σ) of the nearest movable ions. In the square centre position, we have relaxed the nearest four ions and in the cube centre position, eight nearest neighbour ions are relaxed. We assume the amount of relaxation to be the same for both the type of ions, which is an approximation only. Our defect calculation includes (1) electrostatic contribution ΔE_{ES} from all the host ions in the crystal (2) polarisation energy contribution ΔE_{POL} arising as a result of the displacement of ionic charges from their normal positions giving displacement dipoles and considering the contribution from all the ions on the first sixteen neighbouring shells (3) repulsive contributions between the host ions themselves and also between the host ions and the defect atom and (4) van der Waal's energy contribution between the host ions and also between the host ions and the defect atom. As repulsive energy and van der Waal's energy are of very

short range, so we consider the contribution from the first five nearest neighbour shells. Therefore we actually calculate,

$$\Delta E_{Total}(\sigma) = \Delta E_{ES}(\sigma) + \Delta E_{POL}(\sigma) + \Delta E_{REP}(\sigma) + \Delta E_{VDW}(\sigma) \quad (4)$$

where σ is the change per unit length.

We calculate the value of ΔE_{Total} for different values of σ and find that for some value of σ , ΔE_{Total} has its minimum value for both C and S positions. Physically this means, this σ gives the amount of radial displacement of the ions in the nearest shell when the defect atom occupies sites C and S . The difference of the minimum of the ΔE_{Total} between these C and S positions gives the activation energy of the defect diffusion.

The expressions for calculating ΔE_{ES} , ΔE_{POL} and ΔE_{REP} are reported in our earlier paper (Neogy and Deb 1976). The expression for Van der Waals' energy between two atoms or ions, is,

$$E_{VDW}(r_{ij}) = -1.5 \frac{I_1 I_2}{I_1 + I_2} \cdot \frac{\alpha_1 \alpha_2}{r_{ij}^6} \quad (5)$$

where, α_1 , α_2 are the polarisabilities, I_1 , I_2 are the ionisation potentials and r_{ij} is the distance between the interacting bodies. The total change in the Van der Waal's energy is written as,

$$\Delta E_{VDW} = \Delta E_{V1} + \Delta E_{V2} \quad (6)$$

The first part gives the change in the Van der Waal's energy due to all the host ions among themselves. The second part gives the change in the Van der Waal's energy that arises from the interaction of the defect atom with the host ions. As Van der Waal's energy varies with the inverse sixth power of the distance, so, we have considered contribution from the first five neighbouring shells

$$\begin{aligned} \Delta E_{V1} = & \frac{1}{2} \sum_{i=1}^M \sum_{j \neq i}^M [E_V(|\mathbf{r}_i' - \mathbf{r}_j'|) - E_V(|\mathbf{r}_j - \mathbf{r}_i|)] \\ & + \sum_i^M \sum_{\substack{k \neq i \\ k \neq M}} [E_V(|\mathbf{r}_i' - \mathbf{r}_k|) - E_V(|\mathbf{r}_i - \mathbf{r}_k|)] \end{aligned} \quad (7)$$

and,

$$\Delta E_{V2} = \sum_i^M [E_V(|\mathbf{r}_D - \mathbf{r}_i'|)] + \sum_k [E_V(|\mathbf{r}_D - \mathbf{r}_k|)] \quad (8)$$

where M stands for no. of movable ions, K stands for unrelaxed ions, \mathbf{r}_i' , \mathbf{r}_j' denote the relaxed positions of the M movable ions and \mathbf{r}_D denote the position of the defect atom.

3. Results and discussions

The electronic charge densities of the ions Na^+ , Cl^- and K^+ and of the atoms H and Ar, are derived from the Clementi wavefunctions (Clementi and Roetti 1974). b , ρ and r_0 data for the host lattices are taken from Choudhury *et al* (1975) which have been determined from extrapolated $^\circ\text{K}$ values of the most recent elastic constant and density measurements of alkali halides. These values are given in Table 1.

Table 1. All values are in a.u.

Lattice	r_+	r_-	r_0	b	ρ
NaCl	2.267	3.061	5.271	.00497	.577
KCl	2.853	3.080	5.872	.00408	.556

The electronic polarisabilities of the ions are taken from Tossmann *et al* (1953) and the atomic polarisabilities of the atoms are taken from Pauling (1927). The first ionisation potentials of the atoms H and Ar; the second ionisation potentials of the positive ions, Na^+ and K^+ and the resonance potential for Cl^- ion are taken from American Institute of Physics Handbook (1972) and given in Table 2.

Table 2. Ionisation potentials in eV

Second ionisation potentials		First ionisation potentials		Resonance potential	
Na^+	47.29	He	24.588	Cl^-	9.02
K^+	31.81	Ar	15.760		

The overlap height (h) and the overlap spread (s)—the two parameters of the overlap region that we require are defined in fig. 1. The electronic charge densities of the Na^+ ion and the Ar atom are plotted in a graph in the manner as shown in fig. 1. The overlap height (h) and the overlap spread (s) are obtained from the graph. For obtaining the value of S , the charge density is to be truncated at 0.1 atomic unit of charge density. With the help of the following relations (Deb and Ghosh 1975)

$$\ln(\beta_{ij}b) = -3.9990 - 0.187 \ln(h^2 r_0^5) \quad (9)$$

$$\text{and} \quad \rho = 0.7750 - 0.0768s \quad (10)$$

$\beta_{ij}b$ and ρ for the interaction between Na^+ and Ar are obtained. In the eqns. (9) and (10), all the physical parameters— h , r_0 , s , ρ and $\beta_{ij}b$ are in atomic units. Similarly, $\beta_{ij}b$ and ρ for Cl^- and Ar interaction are determined. Following similar

procedure, we determine β_{ijb} and ρ values for different interactions, according to our requirement and these are given in Table 3.

Table 3. Repulsive interaction parameters from our method

Host crystal	Interacting pairs		β_{ijb} in a.u.	ρ in a.u.
NaCl	Na ⁺	and Cl ⁻	0.004972	0.5777
	Na ⁺	and He	0.009180	0.7750
	Na ⁺	and Ar	0.005657	0.6890
	Na ⁺	and Cl ⁰	0.005462	0.6730
	Cl ⁻	and He	0.005069	0.6136
	Cl ⁻	and Ar	0.003380	0.4907
	Cl ⁻	and Cl ⁰	0.003394	0.4747
KCl	K ⁺	and Cl ⁻	0.004079	0.5560
	K ⁺	and He	0.008299	0.7750
	K ⁺	and Ar	0.004545	0.6549
	Cl ⁻	and He	0.005376	0.6591
	Cl ⁻	and Ar	0.003593	0.5364

For the purpose of comparing the values obtained from our method, we have also included here the result of the calculation of interstitial Cl⁰ atom diffusion in

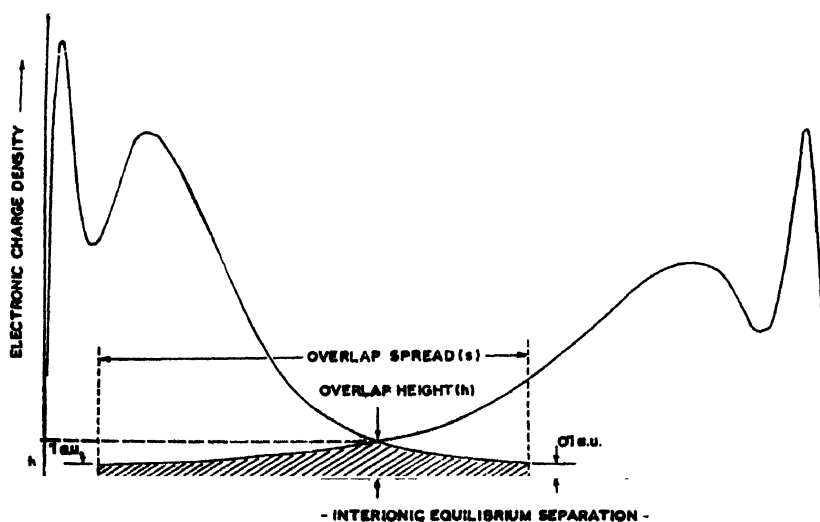


Figure 1. Schematic of the plot for estimating overlap parameters, s and h .
A, B-positions of centres of interacting pairs

NaCl from our previous paper. We have calculated the activation energies for the defect according to the following two methods :

(1) According to the first method, $\beta_{ij}b$ and ρ values for the different pairs of interaction are taken from our work from the values reported in Table 3.

(2) According to the second method, b and ρ values are taken to be the same as that for two host ions.

The activation energies, according to these methods are calculated and shown in Table 4. The calculations were done in an IBM 1130 computer in the University of Calcutta.

The diffusion of Cl^0 atom interstitially in NaCl lattice was reported by Hatcher and Dienes (1961). They calculated activation energy of such diffusion to be 0.45ev. Our values according to method (1) is 0.61ev and that due to method (2) is 0.54ev. Hatcher and Dienes observed that their value was much lower than the experimental value. So we may say that our value also represents more correctly the activation energy of Cl^0 diffusion in NaCl.

The activation energy of He diffusion in KCl was reported by Wayne (1973) to be 0.39ev. Our values according to method (1) is .36ev and that due to method (2) is 0.42ev.

Similarly our calculated values of the activation energy of Ar diffusion in KCl lattice by method (1) is 0.63ev and that due to method (2) is 0.66ev. The experimental activation energy of Ar in KCl in the high temperature region is 0.38ev and in the low temperature region it is 2.45ev (Lidiard and Norget 1972).

Next we calculate the activation energy of He in NaCl. Its value is 0.33ev both by method (1) and (2). It seems that the activation energy of He diffusion is smaller in NaCl lattice than in KCl lattice which is against our common idea that it is easier to diffuse in a larger lattice. This type of behaviour is not un common as has been shown by Lidiard and Norget (1972) who calculated the activation energy of Ar diffusion in different ionic solids. Their calculated values are shown in the Table 5.

Table 5. Activation energy

System	High temperature region	
	Exp	Calculated
KF-Ar	1.8 ev	1.3 ev
KCl-Ar	0.38 ev	0.4 ev
KBr-Ar	0.36 ev	0.2 ev
KI-Ar	0.30 ev	0.3 ev

Table 4. Activation energies of defect diffusion (all values are in a.u.)

Nature of the defect	Defect in the				Activation energy (bracketed values are in ev)			
	Square centre position		Cube centre position					
	Relaxation of the host ions	ΔE_{Total} by method (1)	ΔE_{Total} by method (2)	Relaxation of the host ions	ΔE_{Total} by method (1)	ΔE_{Total} by method (2)	by method (1)	by method (2)
He in NaCl	.225	.07938	.06667	.147	.06731	.05461	.01207 (.33ev)	.01206 (.33ev)
He in KCl	.163	.06613	.04943	.087	.05293	.03387	.01320 (.36)	.01556 (.42)
Ar in NaCl	.324	.12316	.12503	.258	.08655	.08945	.03661 (.99)	.03558 (.97)
Ar in KCl	.239	.09428	.09519	.154	.07106	.07093	.02322 (.63)	.02426 (.66)
Cl ^o in NaCl	.283	.12648	.12702	.190	.10401	.10633	.02247 (.61)	.01995 (.54)

Similarly, the activation energy of Ar diffusion in NaCl by method (1) is 0.96 eV and by method (2) is 0.97.

It is seen from a scrutiny of b and ρ values in Table 3, that the repulsive parameters between the anions and the cations of an ionic crystal, lie intermediate between the corresponding parameters between a defect atom and both the host ions. Thus, if we calculate the repulsive energy of the defect with the host ions, with our parameters, then the repulsive energy for one pair will be higher and for the other pair will be lower thus compensating and giving a net energy which may not be far different from the corresponding energy with the host ion parameters. It is for this reason that the activation energy values obtained with the new interaction parameters seem to be little different from the corresponding values with the host ion parameters though there is a substantial difference in the interaction parameters in the two approximations.

Thus, it seems, from a study of Table 4, that activation energies of different diffusion in NaCl and KCl lattices calculated by our method are quite close to the values calculated by the standard procedure described here as method (2). Activation energy, calculated by our method may yield different values from those obtained by method (2), when unequal relaxations of the host ions are assumed. This technique of getting b and ρ may not be free from all objections but it considers at least some physical property of the defect atom in finding the repulsive interaction parameters between the host ions and the defect atom.

References

- Abrahamson A A, Hatcher R D and Vineyard G H 1961 *Phys. Rev.* **121** 1959
 American Institute of Physics Handbook 1972 (3rd Edition) Ed. by Gray D E p 7-9
 Born M and Huang K 1954 in *Dynamical theory of crystal lattices*, Oxford
 Choudhury S, Roy D and Ghosh A K 1975 *Ind. J. Phys.* **49** 928
 Clementi E and Roetti C 1974 *Atomic data and nuclear data table* **14**, 177
 Deb S K and Ghosh A K 1975 *Ind. J. Phys.* **49** 528
 Hatcher R D and Dienes G J 1961 *Phys. Rev.* **124** 726
 Lidiard A B and Norget M J 1972 *Computational Solid State Physics* (Ed. by Herman F, Dutton
 N W and Koehler T R) Plenum Press
 Neogy C and Deb S K 1976 *Ind. J. Phys.* **50** 907
 Pauling L 1972 *Proc. Roy. Soc. (London)* **A114** 181
 Tessmann J T, Kahn A H and Shockley W 1953 *Phys. Rev.* **92** 890
 Tosi M P and Fumi F G 1964 *J. Phys. Chem. Solids* **25** 45
 Wayne R C 1973 *Phys. Rev.* **B8** 2958

Effect of strength and frequency of the field on some rare-earth activated zinc oxide electroluminors

S. Bhushan, A. N. Pandey and Balakrishna Rao Kaza

Department of Physics, Ravishankar University, Raipur-492002

Received 7 October 1977, revised 14 February 1978

A series of rare-earth (Dy, Yb, Nd, Sm, Pr, Gd, La and Er) doped ZnO electroluminors have been prepared in vacuum and voltage and frequency dependence of time-averaged electroluminescent brightness of these systems have been investigated. Brightness-voltage relation $B = B_0 \exp(-b/V^{\frac{1}{2}})$ is satisfied for all the electroluminors with slight deviations at lower and higher frequencies in some of the systems. At lower voltages the electroluminescent brightness is found to increase very slowly with the increase of frequency and a state of saturation is observed at higher frequencies in some of the electroluminors. At higher voltages the frequency dependence is found to be more linear. Further, the electroluminescent spectra consist of three peaks which shift towards the shorter wavelength side with the increase in the frequency of the applied field. All these phenomena have been discussed in the light of existing models.

1. Introduction

Electroluminescence is the phenomenon of light emission by luminors due to the sole action of electric field (a.c. or d.c.). Studies of the voltage, frequency and temperature dependence of time-averaged electroluminescent brightness and the brightness waveforms are the important means to understand the mechanism of electroluminescence. Electroluminescent studies of rare-earth doped ZnS (Anderson 1964), CdS (Bryant *et al* 1972) and ZnSe (Ibuki *et al* 1970) electroluminors have been done extensively, while ever since the discovery of luminescence (Destriau 1936) till recently (Bhushan *et al* 1976), the rare-earth doped zinc oxide electroluminors have received a little attention. The present paper reports the results of voltage and frequency dependence of time-averaged electroluminescent brightness for rare-earth (Dy, Yb, Nd, Sm, Pr, Gd, La & Er) doped zinc oxide electroluminors.

2. Experimental Procedure

2.1. Preparation of the Material

Zinc Oxide (from M/s. Koch-Light Laboratories 99.998%) and 99.9% pure rare-earth compounds (Nitrates of Nd, Pr, La & Sm and Oxides of Dy, Yb and Gd

from M/s. Indian Rare-earths Ltd. and Erbium Oxide from M/s. Michigan Chemicals) were taken in proper proportions and were thoroughly mixed. The mixture was fired at 1050°C in a tubular furnace under reduced pressure of about 1 Torr for one hour and was cooled slowly to room temperature. The fired content was finely ground in a Agate pestle and mortar and the homogeneity of the samples was checked under a black wood glass U.V. lamp.

2.2. Electroluminescent cell

The construction of electroluminescent cell is shown in Fig. 1. The electroluminors were mixed with Araldite resin and were deposited in a 100μ circular groove on a stainless steel plate. A mica sheet of about 30μ thickness was first placed gently and after that it was pressed by a conducting glass plate of resistivity of the order of $100\text{ohm}/\text{cm}^2$. Care was taken to remove all the air bubbles. The conducting glass plates were prepared by spraying vapours of SnO_2 on the heated surface ($\sim 500^{\circ}\text{C}$). The electroluminors are found to be highly photoconducting with a high dark current at room temperature and therefore it was not possible to prepare proper electroluminescent cell by direct sandwiching of the material between a stainless steel and a conducting glass plate.

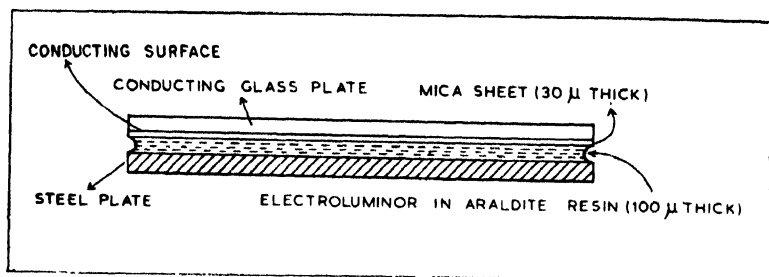


Figure 1. Construction of the Electroluminescent cell.

2.3. Experimental Arrangement

Experimental arrangement is shown in Fig. 2a & 2b. The order of the field normally required for electroluminescent excitation is between $10^3\text{V}/\text{cm}$ to $10^5\text{V}/\text{cm}$ and therefore a high voltage source is needed. To study the variation of electroluminescent light with frequency this source must give high voltages over a wide range of frequencies. Therefore, an audio oscillator coupled with a wide band amplifier (from M/s. Electronic Appliances, Roorkee), which gives voltages from 0 to 1000V for the frequency range 20 to 20KHz, was used as the electroluminescent excitation source. The light intensity was measured by a RCA IP21 photomultiplier tube which was operated by a regulated power supply (HV218 ECIL, India) at 1000V. The integrated light output from the photomultiplier tube in the form of current was measured by a polyflex galvanometer

(10^{-9} amp/mm). For the brightness Vs. voltage (or frequency) studies the arrangement shown in Fig. 2a was used. For spectral studies the light was first passed through a prism monochromator ($4000\text{--}7500\text{\AA}$) and intensity corresponding to each wavelength was noted by photomultiplier-galvanometer assembly. This arrangement is shown in Fig. 2b.

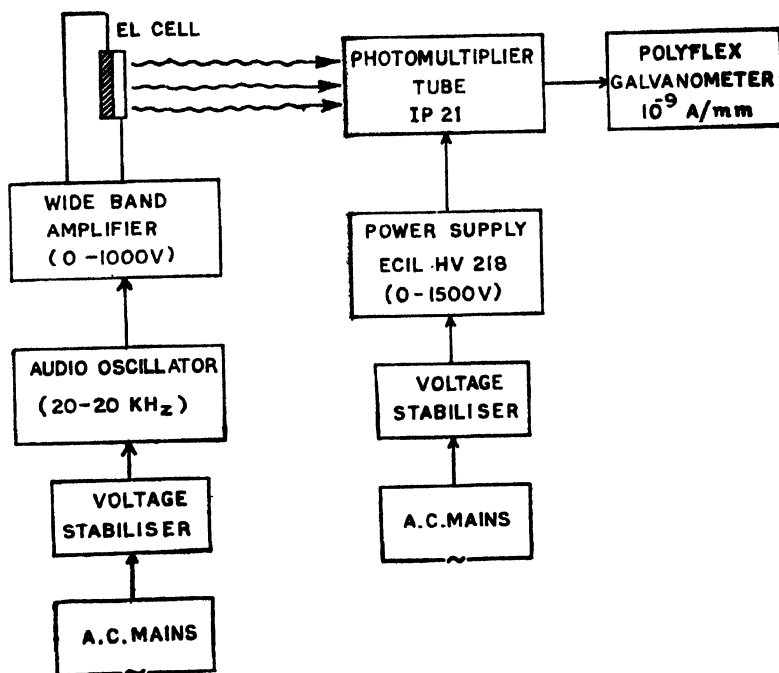


Figure 2. (a) Experimental arrangement for brightness Vs. voltage (or frequency) studies.

3. Results

3.1. Electroluminescent Spectra

Electroluminescent spectra of all the rare earth doped ZnO electroluminors consist of three bands. As an example electroluminescent spectra for ZnO:Dy (at 0.2%) is shown in Fig. 3. The detailed nature of these bands on the concentration of rare earth ions and other parameters have been separately discussed (Bhushan *et al* 1977).

3.2. Voltage Dependence of average Electroluminescent Brightness

Fig. 4 shows the log brightness Vs. $100/V^{1/2}$ plots of ZnO:Gd electroluminor and those of ZnO:Dy, ZnO:Sm, ZnO:Nd and ZnO:La electroluminors are shown in Fig. 5, 6, 7 and 8 respectively. The plots are straight line for all the systems except for ZnO:La at 100Hz and for ZnO:Nd at 2KHz. From Fig. 4 the plots

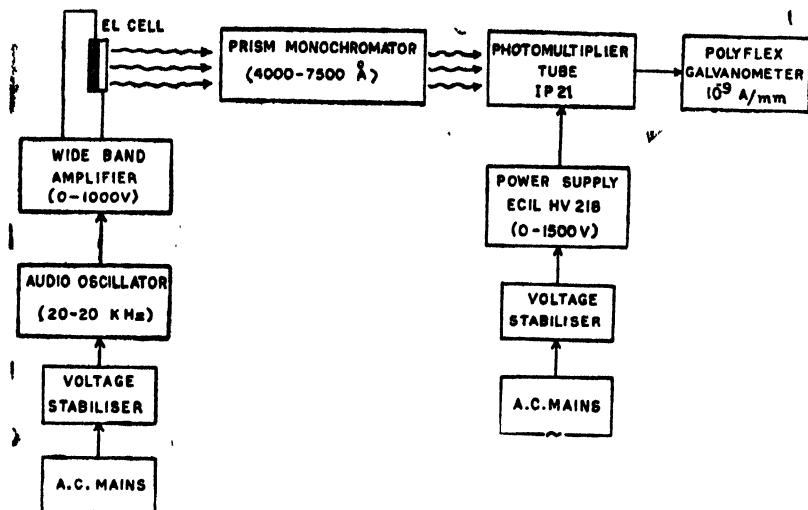


Table 2. (b) Experimental arrangement for spectral studies

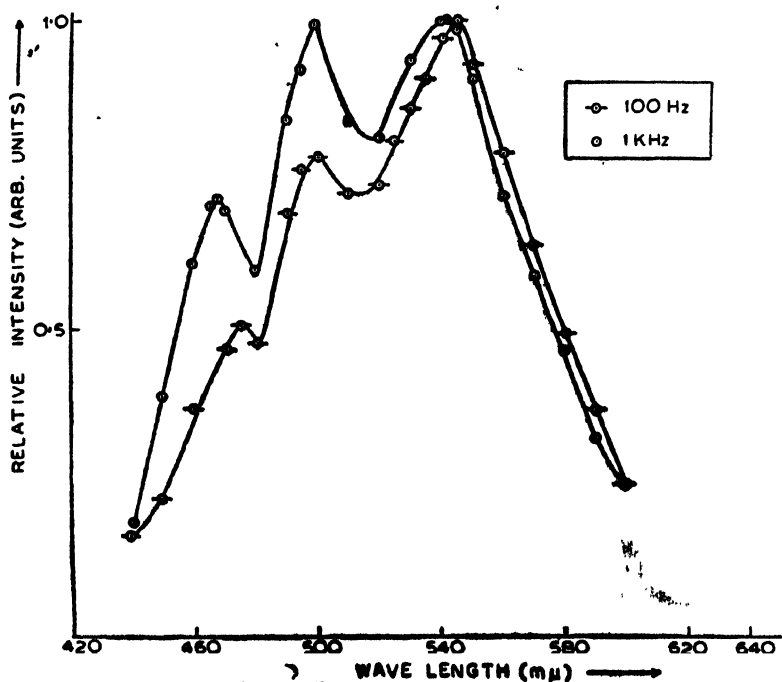


Figure 3. Electroluminescent Spectra of ZnO:Dy system (at 0.2% Dy) at two frequencies.

for ZnO:Gd system are seen to be parallel at all the frequencies. Similar nature is seen for ZnO:Yb electroluminor. The voltage dependence plots are parallel

at lower frequencies (100Hz, 500Hz & 1KHz) for ZnO:Dy and ZnO:Pr electroluminors but at higher frequency (2KHz) the slope of the plots are higher than that at lower frequencies.

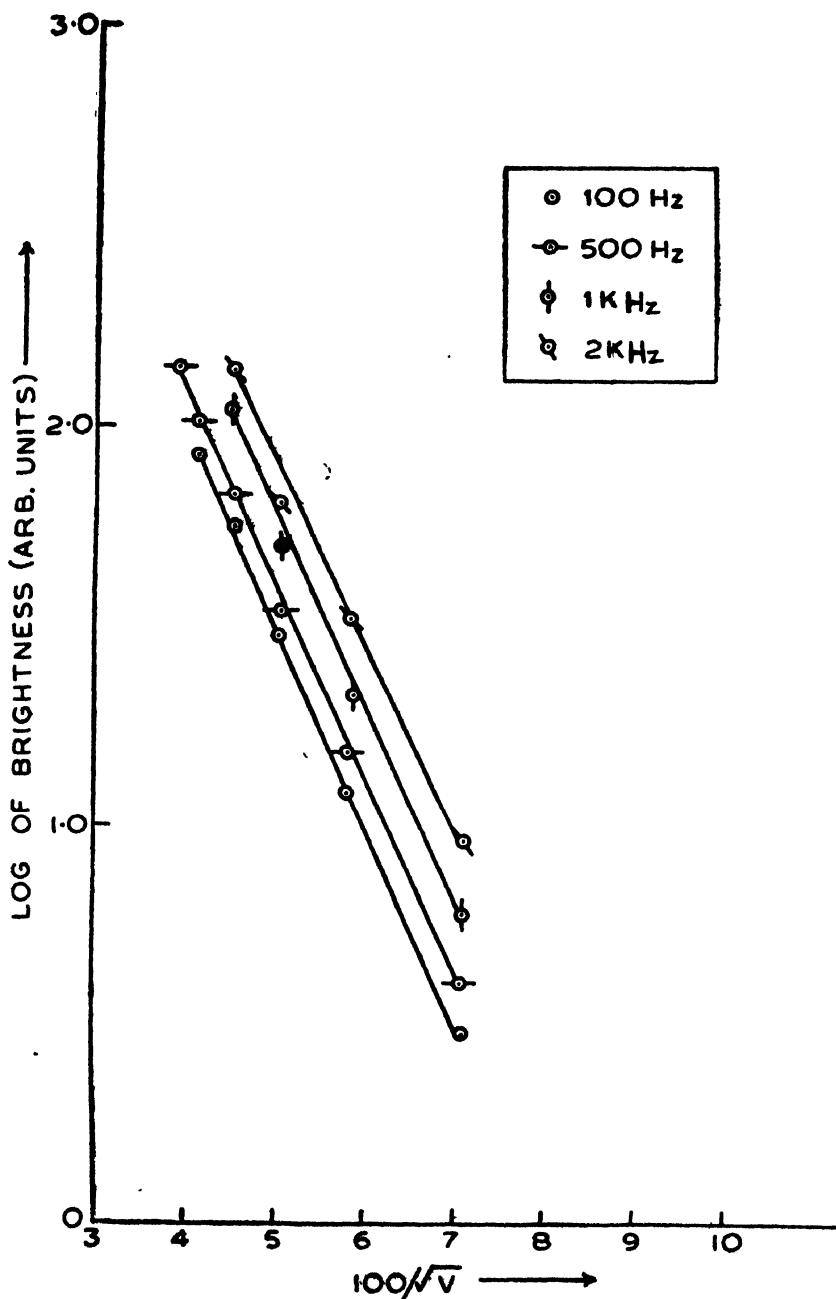


Figure 4. Dependence of Electroluminescent brightness on voltage for ZnO:Gd Electroluminor.

ZnO:Pr, ZnO:Sm and ZnO:Gd electroluminors. At lower frequencies the electroluminescent brightness increases very slowly with frequency while at higher

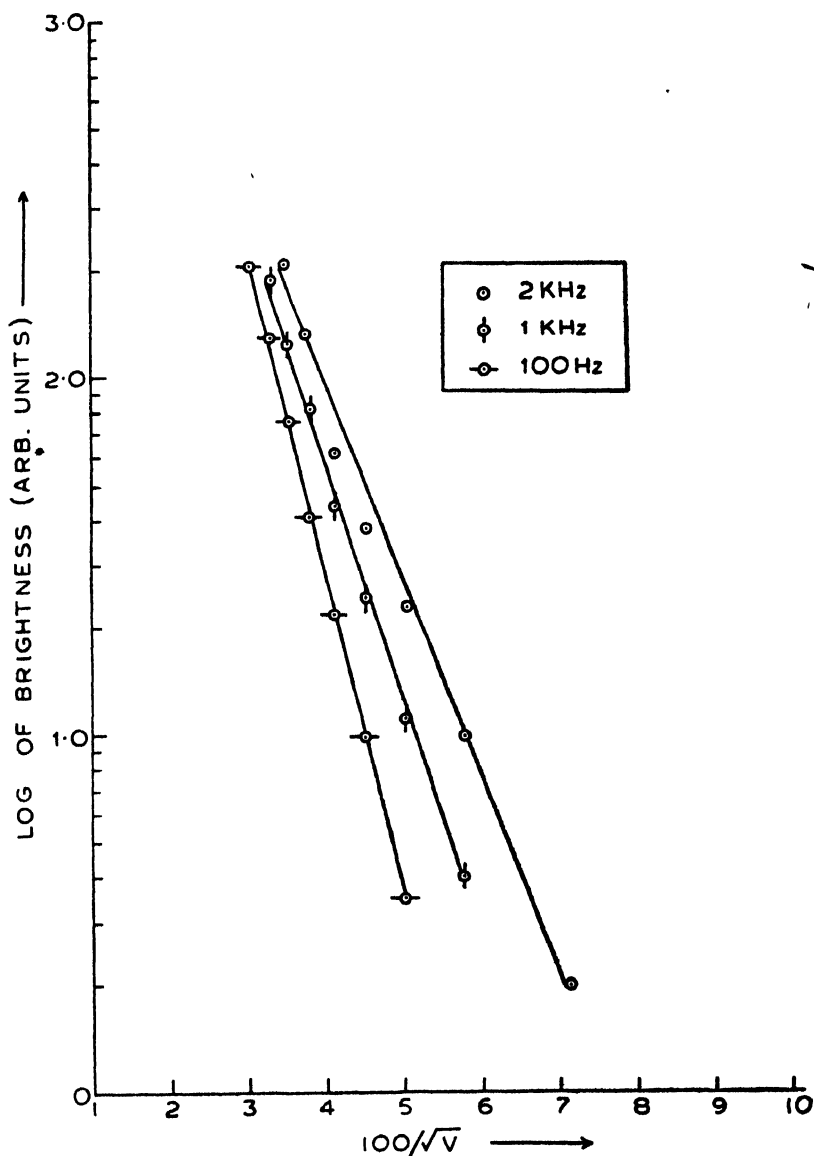


Figure 7. Dependence of Electroluminescent brightness on voltage for ZnO:Nd Electroluminor.

frequencies it is comparatively faster. In ZnO:Gd electroluminor (shown in Fig. 10) the slope of the curves at higher frequencies is much less than those of other systems.

Fig. 11 shows the frequency dependence curve of ZnO:Er electroluminor and Figs. 12 and 13 are those of ZnO:Dy and ZnO:La electroluminors respectively. In Fig. 11 the plots become linear with increasing the voltage. At 600 volts, the

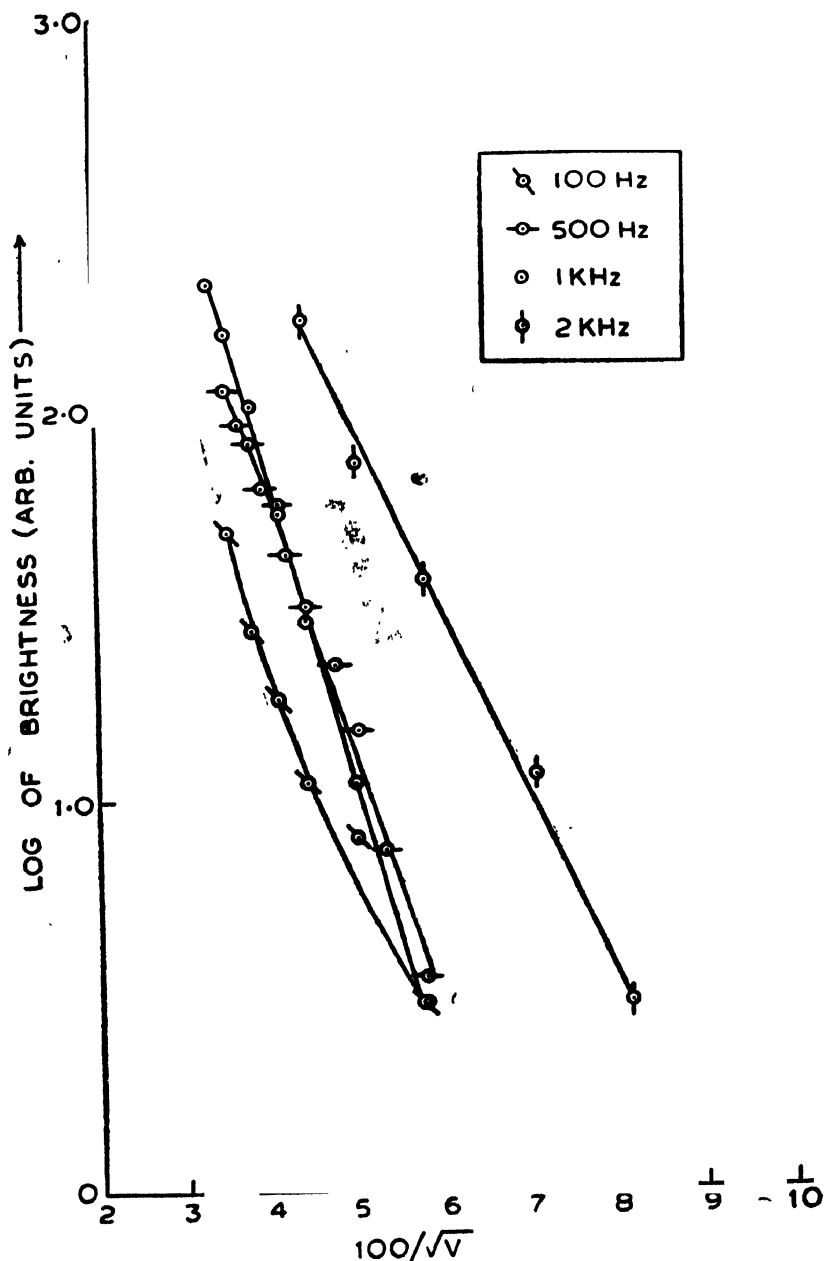


Figure 8. Dependence of Electroluminescent brightness on voltage for ZnO:La Electroluminor,

frequency dependence curve is a straight line. At lower voltage, the nature of plot is similar to that of ZnO:Gd system. In case of ZnO:La also, the increase in brightness at low frequencies is very slow (Fig. 13) but it shows the existence of saturation of intensity at higher frequencies. Similar existence of saturation of

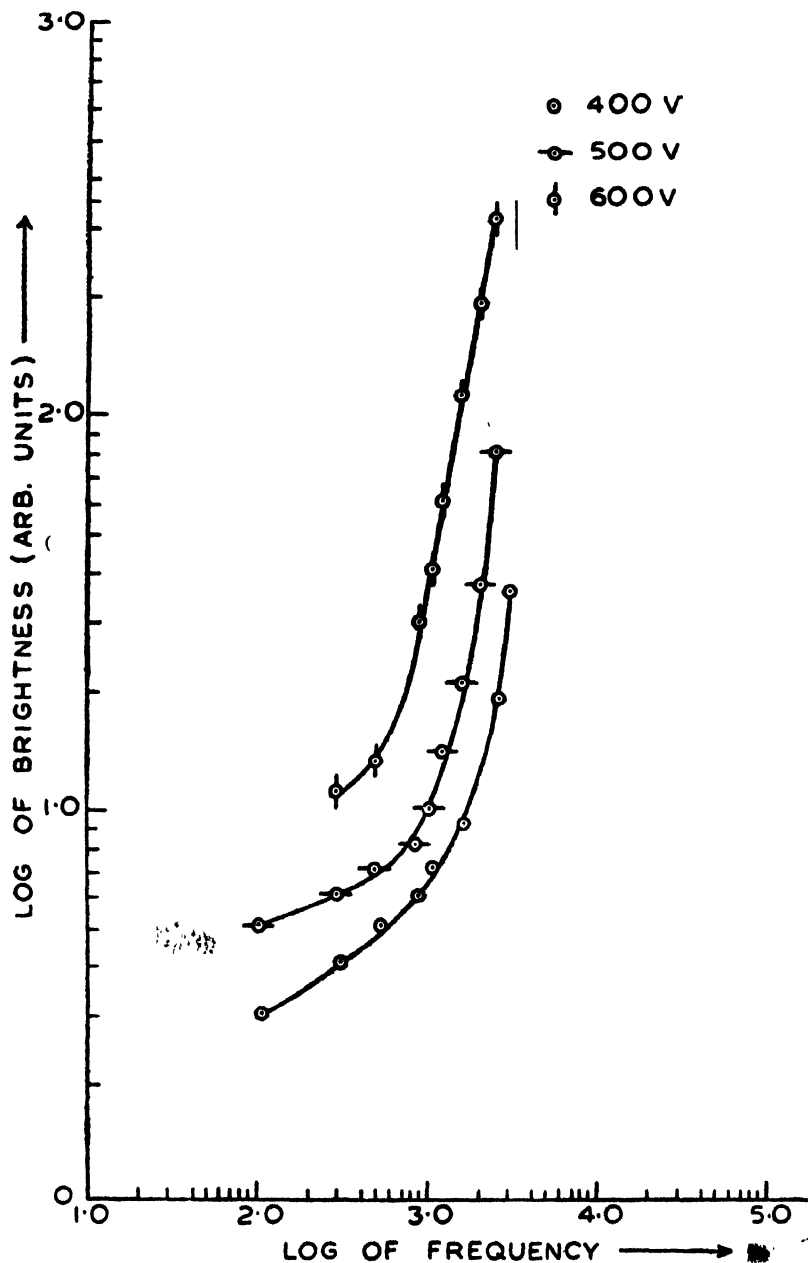


Figure 9. Dependence of Electroluminescent brightness on frequency for ZnO:Nd Electroluminor.

brightness at higher frequencies is very much clear for ZnO:Dy electroluminor in Fig. 12, whose frequency dependence curve is practically linear at low frequency side.

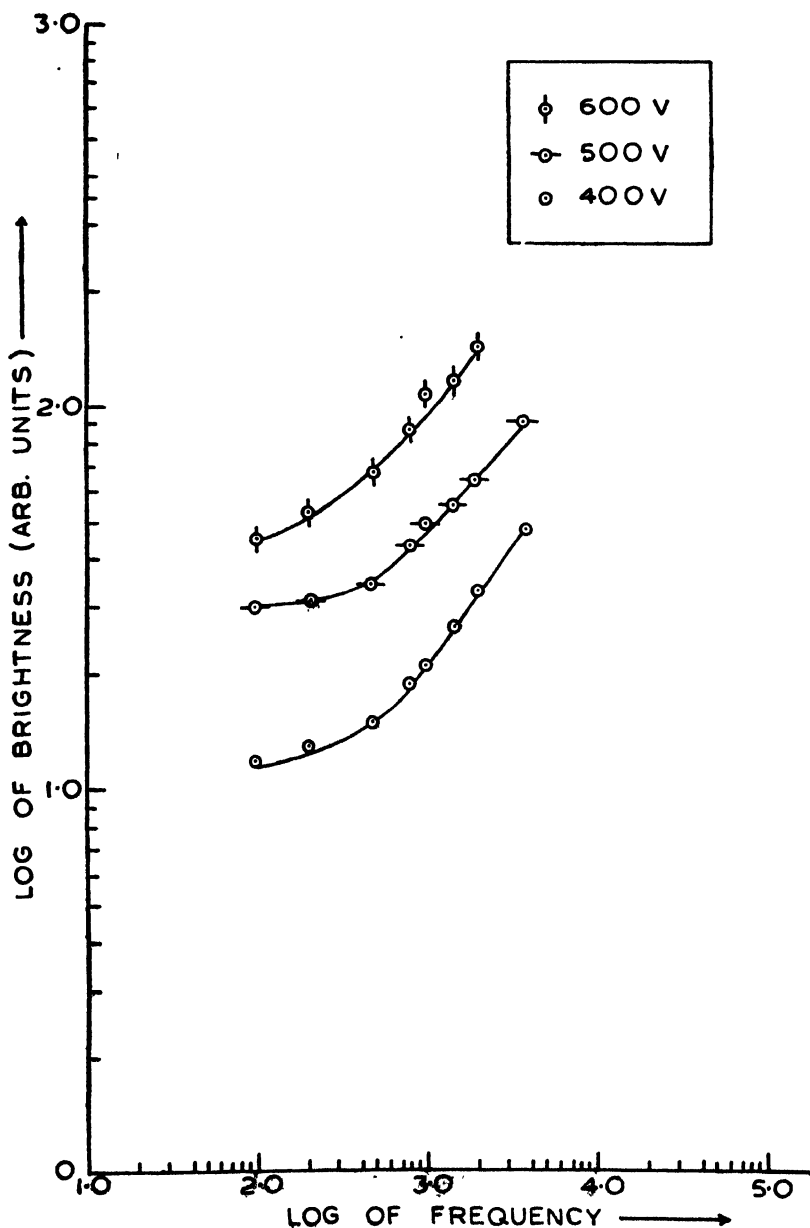


Figure 10. Dependence of Electroluminescent brightness on frequency for ZnO:Gd Electroluminor.

3.3b. Frequency Dependence of Electroluminescent Spectra

The frequency dependence of electroluminescent spectra of ZnO:Dy electro-luminor is shown in Fig. 3 All the peaks are being shifted towards shorter wave-length side and the relative intensity of peaks at lower wave length side is enhanced with increase in frequency.

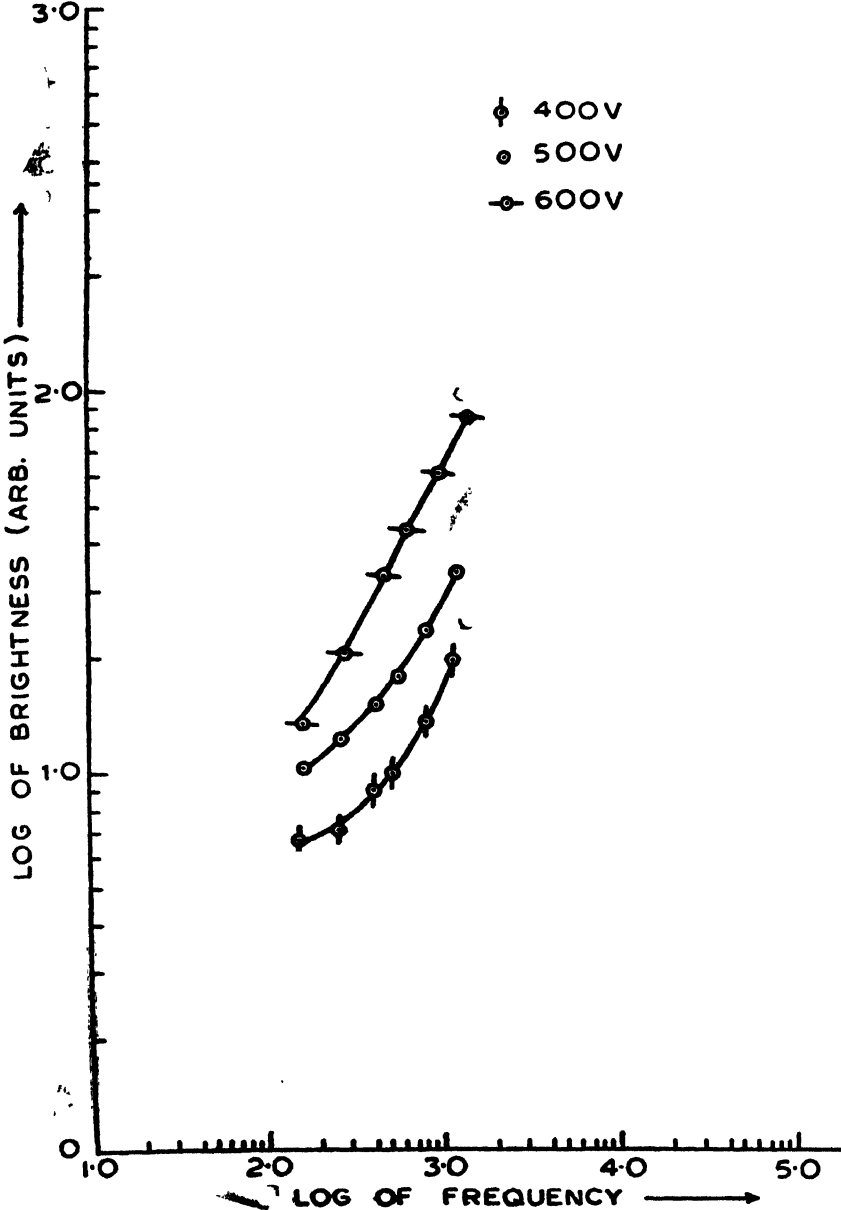


Figure 11. Dependence of Electroluminescent brightness on frequency for ZnO:Er Electroluminor,

4. Discussions

The use of mica sheet between the two electrodes exclude the possibility of 'carrier injection' (Sidalli 1959) at electrode contacts.

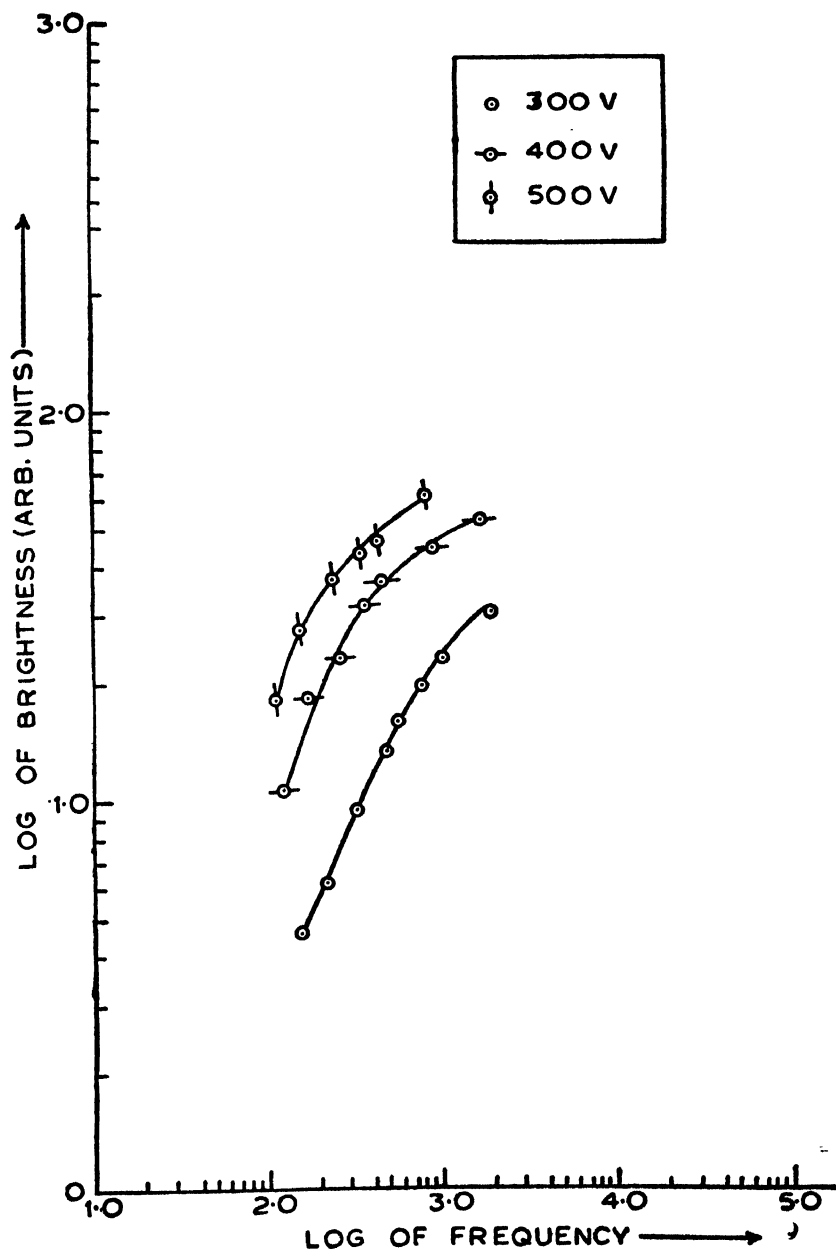


Figure 12. Dependence of Electroluminescent brightness on frequency for ZnO:Dy Electroluminor.

4.1. Voltage Dependence

Qualitatively all the electroluminors have nearly similar type of dependence i.e. practically the mean electroluminescent brightness is an increasing function of the voltage. On this basis it can be understood that initially the region in which

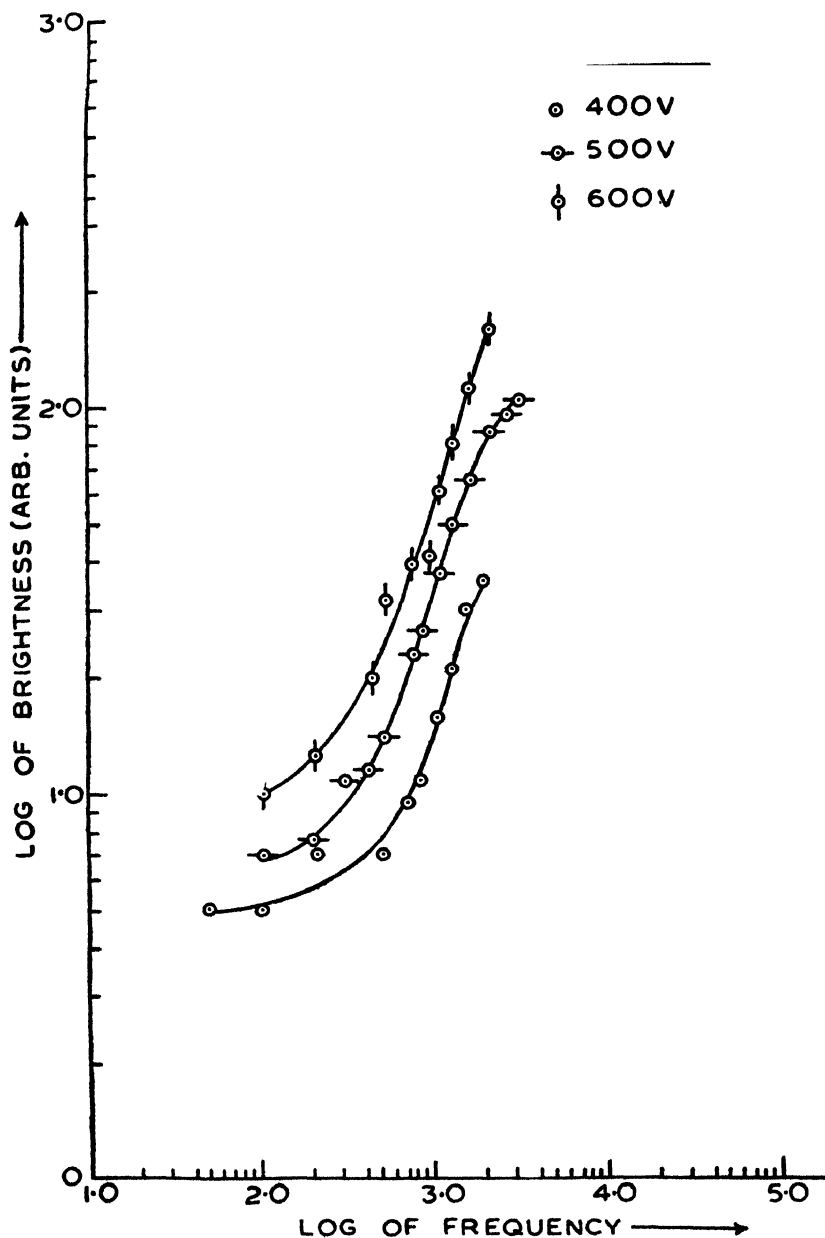


Figure 13. Dependence of Electroluminescent brightness on frequency for ZnO:La Electroluminor.

electroluminescence takes place is small, but on increasing the voltage, more and more active regions are exposed to voltage gradient above the threshold level. A number of empirical relations of this dependence have been reported to suit the individual data. Destriau originally suggested.

$$B = B_0 \exp(-b/V) \quad (1)$$

(B_0 and b are Constants)

The relation is amenable to simple theoretical interpretation (Curie 1963). A modified form of the same is

$$B = B_0 V^n \exp(-b/V) \quad (2)$$

Where n is another constant. Another relation proposed by Zalm *et al* (1957) and used widely is

$$B = B_0 \exp(-b/V^{1/2}) \quad (3)$$

Alfrey and Taylor (1955) assuming that the luminescence emission results mainly from potential barriers of Mott-Schottky type, where the field is proportional to $V^{1/2}$, have derived an equation similar to equation (3). Our experimental curves (Fig. 4 to Fig. 8) being very close in agreement with the theoretical formula (equation 3) indicate the existence of a Mott-Schottky barrier in the present system of electroluminors. The mechanism of excitation is, therefore an 'acceleration-collision' type i.e. the probability of impact ionisation to be proportional to $\exp(-C'/E)$, E being the electric field and C' a constant alongwith the fact that E itself is proportional to $V^{1/2}$ in Mott-Schottky barrier.

For systems where the electroluminescent brightness vary slowly at lower and higher frequencies it may be thought to be due to (1) irregular behaviour of frequency dependence of electroluminescent brightness at lower and higher frequencies. (2) lesser effect of voltage on luminous condensor due to polarisation effect which is more effective at lower frequencies (Curie, 1963).

4.2a. Frequency Dependence of Electroluminescent Brightness

The increase in electroluminescent brightness can be understood on the basis that emptying and refilling of electroluminescent centres take place more rapidly with increase in frequency, but when the time-period of applied a.c. cycle becomes comparable with the life time of excited electrons, the electron does not have enough time to emerge out from the trap, the time averaged brightness will not increase linearly with frequency. By considering the rate of recombination to be determined by field controlled release of electrons from trap brightness is given by (Thronton 1956)

$$B = N_0 f [1 - \exp(-A/f)] \quad (4)$$

Where N_0 has been assumed as a constant number of excited centres for each half cycle of voltage and A increases as voltage increases. At higher frequency the time-averaged brightness becomes equal to $N_0 A$ i.e. a saturation of brightness

occurs. Some plots (Fig. 9 and Fig. 10) show the occurrence of saturation within the applied frequency range and for others it may occur at still higher frequencies. The depletion of ionised activators does not occur during cycle at lower voltages and therefore N_0 is independent of frequency while at higher voltages, it is strong and N_0 becomes frequency dependent and therefore the curves become more linear at higher voltages. The non-linearity of frequency dependence at lower frequencies may be attributed to its combined effect with polarisation effect of luminous condensor.

4.2b. Frequency Dependence of Electroluminescent Spectra

In our separate publication (Bhushan *et al* 1977) we have shown that the emission of rare earth doped ZnO is due to the transition between levels of donor-acceptor pairs (Williams *et al* 1956, 1959; Shionoya 1970). The donor-levels are formed due to rare earth ions and are shallower (below the edge of the conduction band). The acceptor levels are those responsible for the emission of undoped ZnO electroluminors and are deeper. At low frequencies, since the time is sufficiently large, the transition may take place between the levels of donor-acceptors pairs. But at higher frequencies when the time becomes sufficiently low the transition does not take place via the donor levels but between the edge of the conduction band and the acceptor levels. Therefore, a shift towards higher energy or lower wavelength side is expected.

Acknowledgments

The authors are grateful to Prof. D. Sharma, Prof. S. Chandra and Dr. R. K. Thakur for their constant encouragement throughout the work. Two of the authors (ANP & BRK) are also thankful to University Grants Commission, New Delhi for financial assistance.

References

- Alfrey G F and Taylor J B 1955 *Proc. Phys. Soc. Lond.* **B68**, 775.
- Anderson W W 1964 *Phys. Rev.* **136**, A556.
- Apple E F and Williams F E 1959 *J. Electrochem. Soc.* **106**, 224.
- Bhushan S and Saleem M 1976 *Physica Status Solidi (a)* **38**, K27.
- Bhushan S Pandey A N and Kaza B R 1977 *Proc. of NP and SSP Symp. 20C. held at Poona University, from December 26-30.*
- Bryant F J Goodwin G K and Lowther J E 1972 *J. Phys. (c)* **5**, 2669.
- Curie D 1963 *Luminescence of Crystal* 1963 (Mathuen and Co. Ltd. London) 241.
- Destriau G 1936 *J. Chem. Phys.* **33**, 587.
- 1939 *Trans. Faraday Soc.* **35**, 227.
- Ibuki S Komiya H Nakada M Masui H and Kimura H 1970 *J. Lum.* **1/2** 797.
- Prener J S and Williams F E 1956 *J. Electrochem. Soc.* **103**, 342.
- Shionoya S 1970 *J. Lum.* **1/2** 17.
- Sidalli G 1959 *Vacuum* **61**, 7.
- Thronton W A 1956 *Phys. Rev.* **102** 38; 1956 **103**, 1585.
- Zalm P Diemer G and Klasens H A 1957 *J. Electrochem. Soc.* **104**, 130.

Studies of growth and microstructures on WSe_2 single crystals.

M K Agarwal, H B Patel and K Nagireddy

Department of Physics, Sardar Patel University,
Vallabh Vidyanagar 388120, Gujarat

Received 18 October 1977

Single crystals of tungsten diselenide have been grown by direct vapour transport method. The conditions of growth have been adjusted to produce crystals of fairly large size. Estimation regarding the degree of polygonisation, size of the critical nucleus, supersaturation σ and step translation rate V_s have been made from the geometry of the growth spirals observed on the as grown faces of the crystals.

1. Introduction

WSe_2 is one of a number of transition metal dichalcogenides which form in a layered structure. Recent interest in this compound has emerged from its properties as a wide band gap semiconductor (Upadhyayula *et al*, 1968). Looking at the wide potentialities, these crystals might have in solar energy conversion, it was decided to grow them with sufficient purity and perfection.

In past, chemical vapour transport has been reported as the most reliable method of growing WSe_2 single crystals. Although the chemical vapour transport method produces crystals of several mm squares in size, they suffer from the obvious disadvantage of the contamination of the crystals by the transporting agents which in the present case of WSe_2 were either iodine or bromine. There is always a possibility for bromine or iodine to enter into the crystal lattice. Since our aim of growing WSe_2 crystals was to obtain them as pure and defect free as possible, it was concluded that a method of growth which avoids the use of any transporting agent would be most satisfactory. Such a method was used by Al-Hilli and Evans (1972) to grow single crystals of certain transition metal dichalcogenides. This method is used to grow the single crystals of WSe_2 . This paper describes the growth of these crystals.

Since WSe_2 crystals grown by us have exceptionally flat faces, the surface topographic studies were made on them. The common features observed were regular polygonal hexagonal spirals. The parameters of these spirals were measured and the critical nuclear radius, the supersaturation, the step translation rate and the degree of polygonisation were determined. These observations have been described here.

2. Experimental

Crystal preparation

For the growth of the WSe_2 crystals presented in this paper, Tungsten (99.9% pure) and specpure selenium pellets were taken in stoichiometric proportions and were placed in a Quartz ampoule (length 215mm and an inner diameter 20mm). The ampoule was then evacuated to a pressure of less than 10^{-5} torr and sealed off at the neck. The ampoule was then kept in the two zone furnace and was heated as per the scheme outlined in table 1.

The resulting samples consisted of several small single crystals intergrown and several layer platelet single crystals sporadically distributed throughout the ampoule. These crystals were about 0.6mm thick and upto 18mm in length and 6.6mm in breadth. The resulting crystals are shown in fig. 2. In order to grow crystals of still larger dimensions, it was decided to repeat the above experiment in an ampoule of larger diameter. This increase in diameter of the ampoule will reduce the supersaturation, which plays an important role in the growth of the crystals. The temperature gradient was therefore increased as shown in fig. 3 to maintain the condition of supersaturation similar to that of table 1. A representative experiment was carried out in an ampoule of 215mm length and 22mm

Table 1. Procedure used for the preparation of the crystals

	Temp. °C	Time
1. 25°C to 800°C	800°C	3 days
2. 800°C to 25°C		1 day
3. Agitation in reaction tube	25°C	$\frac{1}{2}$ hour
4. 25°C to Temp. gradient shown in fig. 1	—	10 days
5. Temperature gradient to 25°C	—	1 day

inner diameter. The procedure similar to table 1 was carried out. The resulting crystals are shown in fig. 4. It can be easily seen that these crystals are certainly having larger dimensions than those shown in fig. 2.

In order to grow crystals of still larger size, it was decided to consider ampoules of still larger diameter in further experiments. To maintain necessary supersaturation the temperature gradient will also have to be correspondingly changed. This will need temperatures of the order of 1100°C to 1200°C . As the Quartz ampoules cannot withstand such a high temperature, the ampoules were kept in the temperature gradient shown in fig. 3. In all these cases the crystals did not

grow as the necessary supersaturation was not obtained. It is therefore concluded that one has to find a compromise between the diameter of the ampoules and the temperature gradients to acquire condition of supersaturation necessary to grow crystals of larger size.

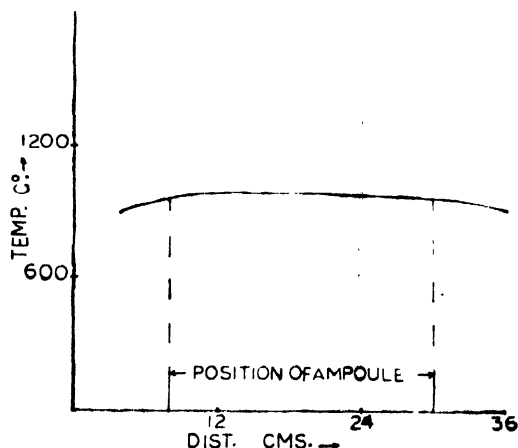


Figure 1. Line profile showing the temperature gradient in which the ampoule is kept

For characterisation, X-ray diffraction photographs of the resulting crystals were taken and it was seen that the lattice parameters of these crystals are in agreement with those reported by the previous workers.

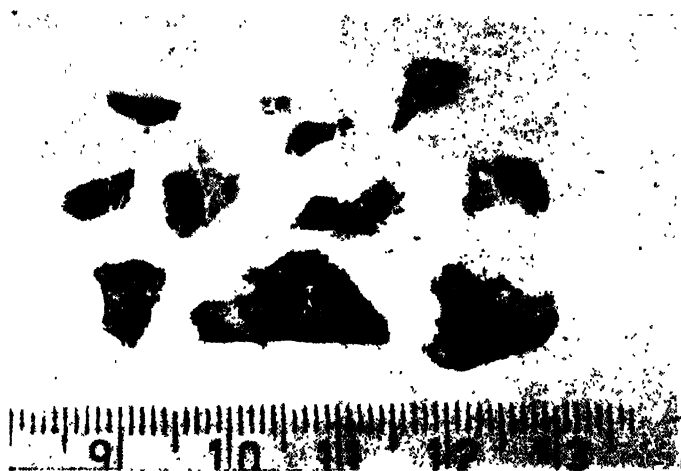


Figure 2. Single crystals of WSe₂ in mm

Observation on microstructures

On the finished faces of the as grown crystals, a large number of polygonal hexagonal spirals were seen. Fig. 5 shows a pattern which is a representative of all such polygonal spirals.

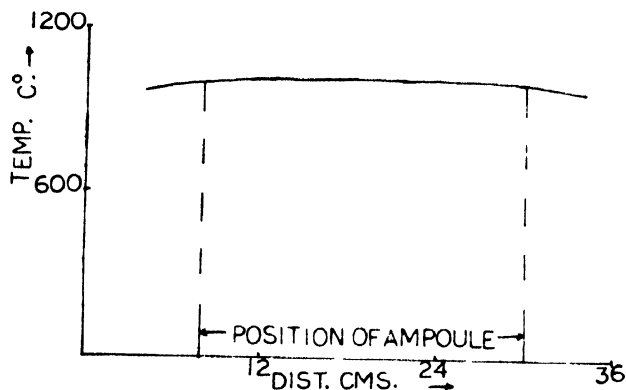


Figure 3. Line profile showing the temperature gradient in which the ampoule is kept

Degree of polygonisation

Calculations regarding the degree of polygonisation (Amelinckx and Strumane 1960) are made from a ratio of the radius of curvature R of a growth front to its distance D from the centre of the spiral. The values of R and D are plotted as shown in fig. 6. The constancy of R/D ratio is well illustrated by the straight



Figure 4. Single crystals of WSe_2 in mm

line nature of the graph. The reciprocal of the slope which is 0.963 gives the degree of polygonisation.

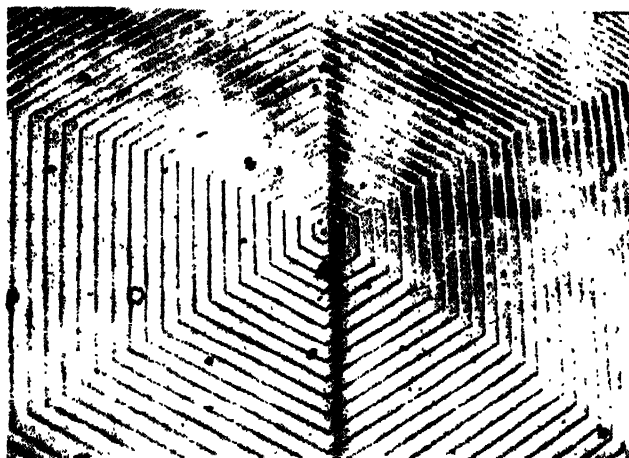


Figure 5. A polygonal spiral on the as grown face of a WSe₂ crystal

The size of the critical nucleus

The radius of the critical nucleus is given by (Verma 1953).

$$\rho_0 = 4\pi$$

where $\delta\phi$ = spacing between the neighbouring turns of the spirals.

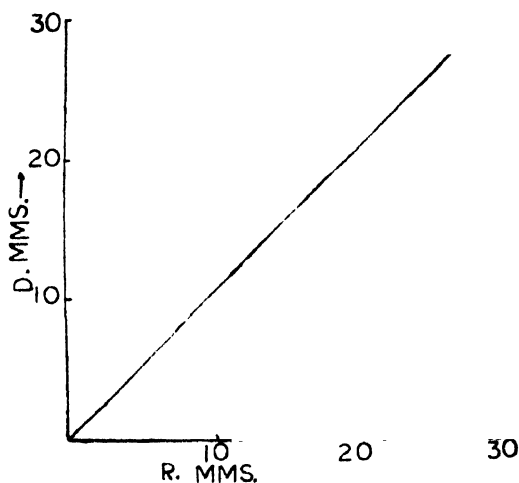


Figure 6. Radius of curvature (R) of a growth front versus its distance (D) from the centre of the spiral

The spacing between the turns of the spiral in fig. 5 is $13.6\mu\text{m}$. This gives the size of the critical nucleus as $2.166\mu\text{m}$

Super saturation (σ)

The supersaturation σ is related to the size of the critical nucleus by the relation (Guseinov *et al* 1967)

$$\sigma = e^{\frac{a\theta}{L_0 kT} - 1}$$

Where a is the interatomic distance in WSe_2 on the (0001) plane and θ is the binding energy between two nearest neighbours in the crystal,

Assuming (i) $\frac{\theta}{kT} = 5.8$ as suggested by Guseinov *et al*, (1967)

$$(ii) \quad a = 3.282 \pm .004 \text{ \AA},$$

$$(iii) \quad \frac{a}{L_0} \cdot \frac{\theta}{kT} < 1$$

we get
$$\sigma = \frac{a}{L_0} \cdot \frac{\theta}{kT}$$

which gives $\sigma = 0.08812\%$

The rate of advancement of the spiral steps is expressed by

$$V_\infty = 2x_s \sigma v e^{-\frac{6\theta}{kT}}$$

Where x_s the mean displacement of the adsorbed molecules on the crystal surface is given by

$$X_s \sim a e^{-\frac{3}{2} \frac{\theta}{kT}}$$

The frequency factor in the present case is $10^{13} \text{ sec.}^{-1}$ This gives $V_\infty = 0.09479 \frac{\mu\text{m}}{\text{hr}}$.

3. Conclusions

1. Single crystals of WSe_2 having dimensions ($17 \times 12 \times 0.4 \text{ mm}^3$) have been grown by the sublimation method.
2. A selection of the appropriate ampoule size and the temperature gradient is necessary for the growth of large size crystals.
3. The degree of polygonisation estimated from a spiral having a perfect polygonal shape is found to be 0.963.
4. An estimation regarding the size of the critical nucleus, supersaturation σ , step translation rate V_c etc. has been made. It is seen that the supersaturation at which polygonal spirals are formed is very low.

Acknowledgement

The authors are very grateful to Prof. A. R. Patel for his keen interest in this work, Mr. H. B. P. and Mr. K. N. R. wish to thank the U.G.C. for the award of fellowships. H.B.P. is also grateful to the Principal and the Management of the Arts and Science College, Bhadran for the grant of the study leave.

References

- Al-Hilli A A and Evans B L 1972 *J. Cryst. Growth.* **15** 93
Amelineckx S and Strumane G 1960 *Silicon carbide, A high Temp. semiconductor*. Edited by J R O'Connor and J Smiltens, (Pergamon Press) pp. 162
Guseinov G D and Ramuranzade A M 1967 *Phys. Status. Solidi* **23** 461
Upadhyayula L C, Loferski J J, Wold A, Giriat W and Korshaw A 1968 *J. Appl. Phys.* **39** 4736
Verma A R 1953 *Crystal growth and dislocations*, London p. 85

Host-crystal field effect on the electronic absorption spectrum of tetracene guest in mixed crystals

Gautam Buddha Talapatra, Biswanath Mallik and T. N. Misra

Optics Department, Indian Association for the cultivation of Science
Jadavpur, Calcutta-700032

Received 11 January, 1978

Abstract. The electronic absorption spectrum of tetracene molecule as guest in number of molecular crystals has been investigated. The effect of biphenyl, naphthalene, anthracene and carbazole as the host on the lowest guest electronic transition has been studied. It has been observed that the electronic transition energy of the guest differs in different hosts. The energy depression of the guest electronic transition in the host lattice from that of free molecular transition energy has been calculated and compared with the experimental values using the expression proposed by Craig *et al.* Contribution to this energy depression by nearest and distant neighbour dipole-dipole interaction between the host and the guest has been considered. The large discrepancy observed in some cases has been attributed to neglect of overlap of charge distribution between the guest and the nearest host molecule and also to higher multipole interactions.

1. Introduction

Electronic absorption and fluorescence spectra (Chaudhuri and Ganguly 1960, Akon and Craig 1967, McClure 1954, Chaudhuri 1974, Sidman 1956, Craig and Thirunamachandran 1963) of organic molecules embedded in a host lattice have been extensively studied but has mainly been concerned with the measurement of polarization of the lowest guest transition. The experimental investigations of mixed crystals have shown that there is a significant change in absolute intensities and polarization ratios of guest transitions from that expected in an oriented gas. Change in guest transition energy has also been observed. The theory of mixed crystals developed by Craig and Thirunamachandran (1963) explains these observations as due to mixing of the excited states of the guest molecules with the excited states of the surrounding host molecules. As a result of this mixing, the transfer of spectral intensity from the host transition to the guest transition takes place and the polarization ratio of guest transition in a mixed crystal changes. The present investigation deals with the effect of different host lattice on the lowest electronic transition energy of a tetracene guest molecule in a number of mixed crystals. Depression in energy of lowest guest transition from free mole

cular transition energy has been calculated for biphenyl, naphthalene, anthracene and carbazole host and compared with the experimental observation.

2. Experimental

Different host crystals used in this investigation are biphenyl, naphthalene, anthracene and carbazole. Tetracene guest and these hosts are purified by sublimation and recrystallizations. The final purification stage consists of a zone-refining step of 50 passes. Tetracene is introduced at a concentration of 10^{-3} mole/mole in different hosts. Single crystals are made by Bridgman technique. Spectral measurements are recorded by spectrophotometer Spectromom-202.

3. Result

The spectra of tetracene guest molecule in different host crystals are shown in Fig. 1. The broad spectra are obtained at room temperature. The 0-0 band of

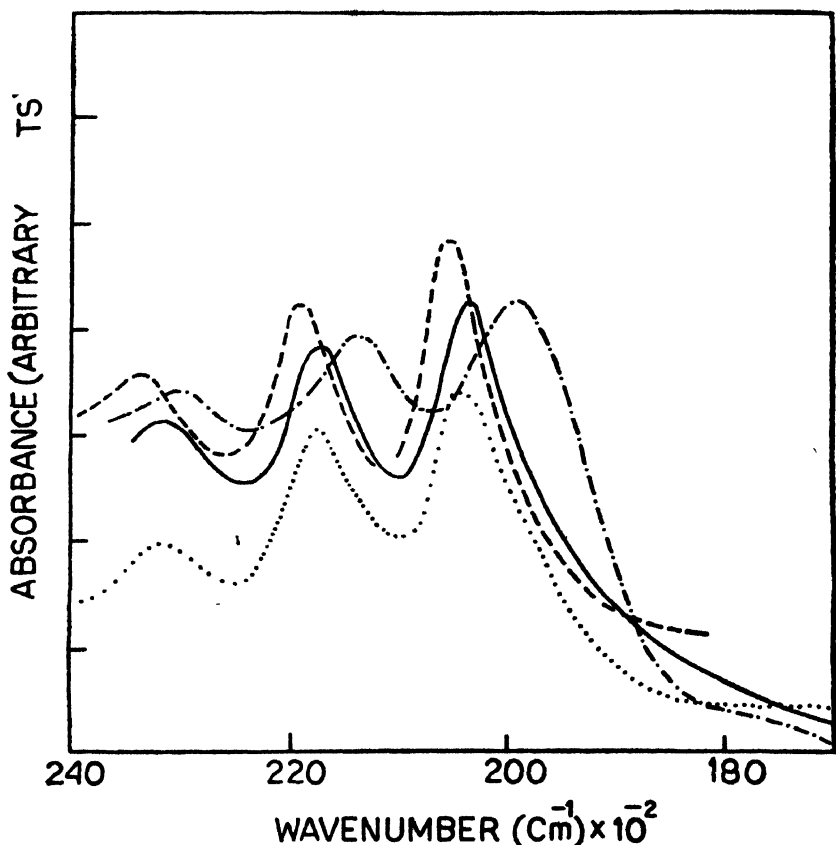


Figure 1. Absorption spectrum of tetracene guest in different host crystals (— — — — —) in biphenyl, (.) in naphthalene, (—) in anthracene, (— . — . — .) in carbazole hosts,

the lowest singlet transition of tetracene in solution is at $21,000\text{ cm}^{-1}$. This free molecular transition of tetracene is depressed in energy in crystalline hosts and appears at different positions in different hosts. It is observed that the 0-0 band of the lowest guest transition appears at 20491, 20408, 20366 and 19762 cm^{-1} in biphenyl, naphthalene, anthracene and carbazole hosts respectively.

All the other bands can be assigned in terms of the upper state fundamental 1400 cm^{-1} . It is observed that the 0-0 band of tetracene is lowered in energy to different extent in different matrix and large energy shift is observed in carbazole. The energy shift is of comparable magnitude in naphthalene and anthracene hosts. The analysis of the absorption spectra of mixed crystals is shown in Table 1 and the calculated and experimental energy depression of the first free molecular transition of tetracene in different hosts is shown in Table 2.

Table 1. Lowest energy absorption spectrum of tetracene molecule in different host crystals at room temperature (26°C)

Host	Band peak position (cm^{-1})	$\bar{\nu} - \bar{\nu}_0$ (cm^{-1})	Analysis
Biphenyl	20491	0	0, 0
	21891	1400	1400
	23296	2805	2×1400
Naphthalene	20408	0	0, 0
	21808	1400	1400
	23210	2802	2×1400
Anthracene	20366	0	0, 0
	21766	1400	1400
	23166	2800	2×1400
Carbazole	19762	0	0, 0
	21162	1400	1400
	22566	2804	2×1400

Table 2. Energy depression of the first solution absorption band ($21,000\text{ cm}^{-1}$) of tetracene molecule in different hosts.

Host	Calculated δE in cm^{-1}	Observed δE in cm^{-1}
Biphenyl ^(a)	181	509
Naphthalene ^(a)	453	592
Anthracene ^(b)	312	634
Carbazole ^(c)	832	1238

(a) Calculated over sphere of radius 25\AA

(b) Calculated over sphere of radius 30\AA

(c) Calculated over sphere of radius 35\AA

4. Discussion

It is observed that a free molecular transition is lowered in energy when the molecule is inserted in the lattice of a host crystal as a guest. The theory of the energy depression is developed by Craig & Thirunamachandran (1963). The energy depression of the guest transition due to host-guest interaction is given by

$$\delta E = \Sigma'(H_{lk}, l'k')^2 / (\Delta\omega_g^* - \Delta\omega_h^*)$$

where the denominator is the difference between the transition energies to the r -th and s -th excited states of guest and host. $H_{lk}, l'k'$ is the host-guest interaction energy and the primed sum omits $lk = l'k'$. Here the host molecule is considered at the k -th site of its l -th unit cell and the guest molecule at the site k' of the l' -th unit cell of the host.

The matrix elements $H_{lk}, l'k'$ have been calculated for these mixed crystals considering interaction between translationally equivalent and non-equivalent molecules. The nearest and distant neighbour interactions have been taken into account. The value of $H_{lk}, l'k'$ is found out from the relation (Craig and Hobbins 1955, Honma 1977)

$$H_{lk}, l'k' = e^2 |\mu_g| |\mu_h| \sum_{ij} (\delta_{ij} r_{lk}^2 - 3r_{lk}^i r_{lk}^j - 3r_{lk'}^i r_{lk'}^j) d_g^i d_h^j / r_{lk}, l'k'$$

where μ_h and μ_g are the molecular transition dipole moments of the host and the guest respectively. $d_g^i, d_h^j (i, j = x, y, z)$ are the direction cosines of the transition dipole moments μ_g and μ_h and $\bar{r}_{lk}, l'k' = \rho_k - \rho_{k'} + \sum_n l_n \alpha_n (l_n \text{ being integers})$ denotes the equilibrium position of the molecule at the k -th site of the l -th unit cell relative to the origin located at the position of the guest molecule, ρ_k describes the position vector of the k -th molecule within the unit cell and $\alpha_n (n = 1, 2 \text{ and } 3)$ are the three primitive translation vectors of the unit cell of the crystal.

Here the calculations are based on the mixing of short axis polarized 4800 Å ($|\mu| = 0.6855 \text{ Å}$) (Davydov 1962, Misra 1965) system of tetracene with (i) the 3200 Å (long axis, $|\mu| = 1.5 \text{ Å}$), 2750 Å (short axis, $|\mu| = 1.24 \text{ Å}$) 2200 Å (long axis, $f = 1.7$), 1670 Å (short axis, $f = 0.8$) system of naphthalene host. (Suzuki 1967)

ii) the 3800 Å (short axis, $|\mu| = 0.61 \text{ Å}$), 2500 Å (long axis, $|\mu| = 2.3 \text{ Å}$) 2200 Å (short axis, $f = 0.28$), 1800 Å (long axis, $f = 0.65$) system of Anthracene host (Craig 1955, Kleven's 1950).

iii) the 2474 Å (short axis, $f = 0.47$), 2005 Å (long axis, $f = 1.7$), and 1600 Å (short axis, $f = 0.6$) system of Biphenyl host. (Kleven's 1950).

iv) the 3300 Å (short axis, $f = 0.042$) & 2900 Å (long axis, $f = 0.15$) system of carbazole host. (Zwarich 1968, Siegel and Judeikis 1966, Schutt and Zimmerman 1963).

The crystal structure and the other relevant data for the calculations are given in the appendix.

Appendix

Host	Structure and space group	Unit cell dimensions	Position matrix q_{ij} from which the position of the molecules in the unit cell is obtained by the relation $P_i = \sum q_{ij} a_j$	**Direction cosines of the molecular axes with respect to the system $a, b, a \times b$
Biphenyl (Hargreaves <i>et al</i> 1962)	Monoclinic	$a = 8.12\text{\AA}$	$\begin{pmatrix} 0 & 0 & 0 \\ 0.50 & 0.50 & 0 \end{pmatrix}$	$L = \begin{pmatrix} 0.3031 & -0.0066 & -0.9529 \end{pmatrix}$
	$c_2s(P2_1, a)$	$b = 5.63\text{\AA}$		$\begin{pmatrix} 0.3031 & 0.0066 & -0.9529 \end{pmatrix}$
	$\sigma = 2$	$c = 9.51\text{\AA}$		$M = \begin{pmatrix} 0.5177 & -0.8376 & -0.1744 \end{pmatrix}$
		$\gamma = 95.1\text{\AA}$		$\begin{pmatrix} 0.5177 & 0.8376 & -0.1744 \end{pmatrix}$
Naphthalene (Davydov 1962)	Same as in Biphenyl	$a = 8.29\text{\AA}$	Same as in Biphenyl	$L = \begin{pmatrix} -0.4274 & -0.2182 & 0.8771 \end{pmatrix}$
	Biphenyl	$b = 5.97\text{\AA}$		$\begin{pmatrix} -0.4274 & 0.2182 & 0.8771 \end{pmatrix}$
		$c = 8.68\text{\AA}$		$M = \begin{pmatrix} 0.3223 & 0.8763 & 0.3567 \end{pmatrix}$
		$\gamma = 122.2^\circ$		$\begin{pmatrix} 0.3223 & -0.8763 & 0.3567 \end{pmatrix}$
Anthracene (Cricksbank 1956)	Same as in Biphenyl	$a = 8.56\text{\AA}$	Same as in Biphenyl	$L = \begin{pmatrix} -0.4960 & -0.1248 & 0.8596 \end{pmatrix}$
	Biphenyl	$b = 6.04\text{\AA}$		$\begin{pmatrix} -0.4960 & 0.1248 & 0.8596 \end{pmatrix}$
		$c = 11.16\text{\AA}$		$M = \begin{pmatrix} -0.3234 & -0.8919 & -0.3162 \end{pmatrix}$
		$\gamma = 122.9^\circ$		$\begin{pmatrix} -0.3234 & 0.8919 & -0.3162 \end{pmatrix}$
Carbazol (Zwarich 1968, Lahiri 1963)	Orthorhombic	$a = 7.76\text{\AA}$	$\begin{bmatrix} 0 & 0 & 0 \\ 0.5 & -1.032 & 0 \end{bmatrix}$	$L = \begin{bmatrix} 0 & 0 & 1 \\ 0 & 0 & 1 \end{bmatrix}$
	$D_{2h}(P_{nsm})$	$b = 19.15\text{\AA}$		
	$\sigma = 4$	$c = 5.74\text{\AA}$	$\begin{bmatrix} -0.526 & -1.532 & 0.5 \\ -0.026 & 0.5 & 0.5 \end{bmatrix}$	$\begin{bmatrix} 0 & 0 & -1 \\ 0 & 0 & -1 \end{bmatrix}$
				$M = \begin{bmatrix} 0.4803 & 0.8771 & 0 \\ 0.4803 & -0.87 & 0 \\ -0.4803 & -0.8771 & 0 \\ -0.4803 & 0.8771 & 0 \end{bmatrix}$

* σ = the no of molecules per unit cell. ** L_{ij} and M_{ij} represents the cosines of the angle between the long and short axis of the molecule at ρ_i ($i = 1, 2, \dots, \sigma$) with the j ($j = 1 (= a), 2 (= b), 3 (= a \times b)$) axis.

In the case of Naphthalene the calculated and observed values of δE are in reasonable agreement but in the other cases it differs markedly. These disagreement is probably due to the evaluation of the interaction energy by point multipole expansion since the point multipole expansion is valid only (Craig and Thirunamachandran 1963, 1964) when the condition $r_i + r_j < r_{kk'}$ is satisfied, where i and j are any two charges in the distributions of k and k' molecule, r_i and r_j are the distances from the molecular centres. In our case the above relation does not hold for some zones of the charge distribution in nearest neighbour molecules excepting the Naphthalene-tetracene mixed crystal where the calculated value of δE approaches the observed δE value.

The low calculated value of δE compared to that of experimentally observed in biphenyl, anthracene and carbazole host could be due to our neglecting the overlap of charge distribution between the nearest-neighbours & higher multipole interaction between the host and the guest. Configuration interaction of this lowest singlet state of tetracene with the ion-pair (Choi *et al* 1964) exciton states of the host may also contribute to the depression of energy.

Acknowledgment

The authors express their thanks to Prof. G. S. Kashta for his kind interest in the work. One of the authors (B.N.M.) thanks the C.S.I.R., New Delhi for a Senior Research Fellowship.

References

- Akon C. D. and Craig D. P. 1967 *Trans. Faraday. Soc.* **63** 56
 Chaudhuri M. K. 1974 *Chem. Phys. Letters* **26** 574
 Chaudhuri N. K. and Ganguly S. C. 1960 *Proc. Roy. Soc.* **A259** 419
 Choi S. Jortner J. Rice S. A. and Silbey R. 1964 *J. Chem. Phys.* **41** 3294
 Craig D. P. 1955 *J. Chem. Soc. (London)* 2302
 Craig D. P. and Hobbins P. C. 1955 *J. Chem. Soc.* 539
 Craig D. P. and Thirunamachandran T. 1963 *Proc. Roy. Soc.* **A271** 207
 Craig D. P. and Thirunamachandran 1964 *Proc. Phys. Soc.* **84** 781
 Cruickshank E. W. J. 1956 *Acta Cryst.* **9** 915
 Davydov A. S. 1962 *Theory of Molecular Excitons* (Translated by M. Kasha and M. Oppenheimer Jr). McGraw-Hill Book Company
 Hargreaves A. and Rizvi S. H. 1962 *Acta Cryst.* **15** 365
 Honma A. 1977 *J. Phys. Soc. of Japan* **42** 1129
 Klevenhans H. B. 1950 *J. Chem. Phys.* **18** 1063
 Kurahashi M., Fukuyo M., Shimada A., Furusaki A. and Nitta I. 1966 *Bull. Chem. Soc. Japan* **39**, 2564
 Lahiri B. N. 1963 *Z. Krist.* **127**, 456
 McClure D. S. 1954 *J. Chem. Phys.* **22** 1668
 Misra T. N. 1965 *Reviews on Pure and Applied Chemistry* **15** 39
 Schutt H. and Zimmerman H. 1963 *Bunsen Phys. Chem.* **67** 54
 Sidman J. W. 1956 *J. Chem. Phys.* **25** 122
 Siegel S. and Judeikis H. S. 1966 *J. Phys. Chem.* **70** 2205
 Suzuki H. 1967 *Electronic Absorption Spectra and Geometry of Organic Molecules* Academic Press
 Zwarich R. J. 1968 *Ph.D. Thesis University of British Columbia.*

Electronic polarizabilities and sizes of alkaline earth and chalcogenide ions

S. C. Agrawal*, O. P. Sharma and Jai Shanker

Department of Physics, Agra College, Agra 282002

(Received 22 September 1977, revised 14 February 1978)

An analysis of electronic polarizabilities and sizes of Ca^{2+} , Sr^{2+} , Ba^{2+} , O^{2-} , S^{2-} , Se^{2-} and Te^{2-} ions has been performed. The crystalline state values are obtained from the solution values using Ruffa's theory and polarizability radius cube relation. Calculated values present good agreement with other studies.

1. Introduction

The electronic polarizabilities and ionic radii have played a prominent role in the development of crystal physics (Pauling 1960, Tosi 1964). There have been numerous attempts (Fajans and Joos 1924, Born and Heisenberg 1924, Pauling 1927, Mayer and Mayer 1933, Sternheimer 1957, Tessman *et al* 1953, Pirenne and Kartheuser 1964, Ruffa 1963, Boswarva 1970) to evaluate the electronic polarizabilities of ions. The method of Ruffa (1963) alongwith a relation between polarizability and ionic radius (Jai Shanker *et al* 1973) has been very useful to understand the difference between free state and crystalline polarizabilities (Jai Shanker and Verma 1975, Jai Shanker and Agarwal 1976). The crystal electronic polarizabilities of alkaline earth and chalcogenide ions derived from the crystal refraction data (Boswarva 1970) differ from the free state polarizabilities in an interesting manner, being larger for cations and smaller for anions than the corresponding free state values. An analogous situation exists for ionic radii also. Fumi and Tosi (1964) and Tosi (1964) have demonstrated, by analysing the crystal data for alkali halides within the framework of the Born model, that crystal radii for cations are larger and those for anions are smaller than the free state radii. However, it does not appear to have been established experimentally that the ions exist in free state (Yamashita and Kojima 1952). The existence of ions in solutions and crystals is an experimental fact. The interionic forces in solutions are quite weak and the ions can be considered as in free state. The electronic polarizabilities of ions have been obtained by Fajans and Joos (1924) from an examination of the indices of refraction of salts in aqueous solution.

* Permanent Address : C. L. Jain College, Firozabad (U.P.)

In the present study we investigate how these polarizabilities are changed when the ions are considered in crystals. An analysis of ionic radii is also presented.

2. Analysis of the electronic polarizabilities and ionic radii

Following the energy level analysis of Ruffa (1963) we can write for the free ion polarizability

$$\alpha_f = \frac{e^2 \hbar^2 n}{m E_f^2} \quad (1)$$

where e and m are the electronic charge and mass respectively. \hbar is Planck's constant divided by 2π . E_f is an energy parameter which can loosely be referred to as being the mean excitation energy of the ion. n is the number of electrons in the ion. In the crystalline state, the energy parameter becomes modified owing to the existence of the Madelung potential and consequently the crystalline state polarizability is given by

$$\alpha_c = \frac{e^2 \hbar^2 n}{m(E_f - e V_M)^2} \quad (2)$$

Eqs. (1) and (2) yield

$$\frac{\alpha_c}{\alpha_f} = \left(\frac{E_f}{E_f - e V_M} \right)^2 \quad (3)$$

where V_M , the Madelung potential, is given by

$$V_M = \frac{AZe}{R} \quad (4)$$

where A is the Madelung constant, R the interionic separation and $Z = 2$ in crystals of alkaline earth chalcogenides.

Values of α_c for Ca^{2+} , Sr^{2+} , and Ba^{2+} ions calculated from equation (1-4) in twelve crystals are listed in Table 2. The input data are given in Table 1. Eq. (3), however, cannot be used for anions because of the contribution of excitation levels to the anion polarizability in the crystal which has no counterpart in free state. In addition, quantum states above the first ionization continuum contribute substantially to the free anion polarizability. For evaluating α_c of anions, we therefore make use of the following relation (Jaisankar *et al* 1973).

$$\frac{\alpha_c}{\alpha_f} = \left(\frac{r_c}{r_f} \right)^3 \quad (5)$$

where r_c and r_f are the ionic radii in crystalline and free states respectively. Using (α_c/α_f) as calculated from eqn. (3) and r_f from Pauling (1960), we have estimated r_c from eq. (5) for Ca^{2+} , Sr^{2+} and Ba^{2+} ions in different crystals. These are

reported in table 1. Now the values of r_e for chalcogenide ions can be deduced by subtracting the appropriate cation radius from the interionic separation R . The crystal radii thus obtained are given in Table 2. Now we evaluate α_e for chalcogenide ions from eq. (5) using the data on α_f and r_f given in Table 1.

Table 1. Values of input parameters

Crystal	$R(\text{\AA})$	$r_{f+}(\text{\AA})$	$r_{f-}(\text{\AA})$	$\alpha_{f+}(\text{\AA}^3)$	$\alpha_{f-}(\text{\AA}^3)$
CaO	2.40	0.99	1.40	0.51	2.75
CaS	2.84		1.84		8.6
CaSe	2.96		1.98		11.2
CaTe	3.17		2.21		15.7
SrO	2.57	1.13	1.40	0.86	2.75
SrS	2.94		1.84		8.6
SrSe	3.12		1.98		11.2
SrTe	3.24		2.21		15.7
BaO	2.76	1.35	1.40	1.68	2.75
BaS	3.18		1.84		8.6
BaSe	3.31		1.98		11.2
BaTe	3.50		2.21		15.7

Table 2. Values of electronic polarizabilities (in \AA^3) and sizes of ions (in \AA).

Crystal	α_{e+}	α_{e-}	r_{e+}	r_{e-}
CaO	1.16	1.33	1.30	1.10
CaS	1.00	5.68	1.24	1.60
CaSe	0.97	7.54	1.23	1.73
CaTe	0.92	11.04	1.21	1.96
SrO	1.70	1.53	1.42	1.15
SrS	1.54	5.32	1.37	1.57
SrSe	1.48	7.93	1.36	1.76
SrTe	1.45	9.91	1.34	1.90
BaO	3.50	1.11	1.72	1.04
BaS	3.12	4.85	1.66	1.52
BaSe	3.04	6.66	1.65	1.66
BaTe	2.93	9.60	1.62	1.88

3. Discussion

We observe from Table 2 that the radius and polarizability of a given ion vary slightly from one crystal to another. The additivity rule, which implies that the radius and polarizability of a given ion remain constant in different crystals, holds only in an approximate manner for the crystals under study. In table-3 we compare the average values of the calculated crystal polarizabilities with those derived by Boswarva (1970) from the experimental refraction data. For the sake of contrast we have also included in Table 3 the polarizabilities corresponding to free state. It is convincing to observe that polarizabilities of alkaline earth and chalcogenide ions calculated in the present study (Table 3) are closer to the values corresponding to experimental refraction data derived by Boswarva. This suggests that the Madelung potential existing at ionic sites is largely responsible for the change in electronic polarizabilities from free state to the crystal. A comparison of free state and crystalline polarizabilities reveals the loosening of cations and tightening of anions in crystals relative to free state. This prediction is in tune with earlier investigations (Fajans and Joos 1924, Petrashen *et al* 1960, Ledovskaya 1969).

Table 3. Comparison of average crystal polarizabilities α_c in \AA^3 with the values (a) Derived by Boswarva from experimental refraction data and (b) Corresponding to free state (Pauling)

	Ca ²⁺	Sr ²⁺	Ba ²⁺	O ²⁻	S ²⁻	Se ²⁻	Te ²⁻
Present	1.01	1.54	3.15	1.32	5.28	7.38	10.18
(a)	1.21	1.92	3.51	1.69	4.71	6.18	8.45
(b)	0.47	0.86	1.55	3.88	8.60	10.50	14.00

An important aspect of the present study is the evaluation of the crystal radii which are found to be larger and smaller by about 0.30\AA , for cations and anions respectively, than the values corresponding to free state (Table 4). These differences can be considered as a measure of the ionic deformation when the ions pass from free state to a crystal as emphasised by Tosi (1964). Studies on ionic

Table 4. Comparison of average radii r_c in \AA with the values (a) Based on the criterion of Fumi and Tosi and (b) Corresponding to free state (Pauling)

	Ca ²⁺	Sr ²⁺	Ba ²⁺	O ²⁻	S ²⁻	Se ²⁻	Te ²⁻
Present	1.24	1.37	1.66	1.10	1.56	1.72	1.91
(a)	1.29	1.43	1.65	1.10	1.59	1.68	1.91
(b)	0.99	1.13	1.35	1.40	1.84	1.98	2.21

radii performed by Fumi and Tosi (1964) reveal that the crystal radii for cations and anions are, respectively, larger and smaller by about 0.30\AA than Pauling's free ion radii. Based on this criterion of Fumi and Tosi (1964) we obtain the radii for alkaline earth and chalcogenide ions as listed in Table 4. It is encouraging to observe from there that our calculated radii present a good agreement with those of Fumi and Tosi.

References

- Born M and Heisenberg W 1924 *Z. Physik.* **23** 388.
Boswarva I M 1970 *Phys. Rev.* **B1** 1698.
Fajans K and Joos G 1924 *Z. Phys.* **23** 1.
Fumi F G and Tosi M P 1964 *J. Phys. Chem. Solids* **25** 31: **25** 45
Hartree D R 1957 *Calculations of Atomic Structure* Wiley N Y
Jai Shanker, Kumar N and Verma M P 1973 *Indian J. Pure Appl. Phys.* **11** 641.
Jai Shanker and Verma M P 1975 *Phys. Rev.* **B12**, 3449.
Jai Shanker and Agrawal S K 1976 *J. Phys. Chem. Solids* **37** 443.
Ledovskaya E M 1969 *Phys. Stat. Sol.* **31** 507.
Mayer J E and Mayer M G 1933 *Phys. Rev.* **43** 605
Pauling L 1927 *Proc Roy. Soc.* **A114** 181.
Pauling L 1960 *The Nature of the Chemical Bond* Cornell University Press Ithaca.
Petrashen M I Abarenkov L V and Kristvfel N N 1960 *Optics Spectrosc.* (N Y) **9** 276
Pirenne J and Kartheuser E 1964 *Physica* **30** 2005.
Ruffa A R 1963 *Phys Rev* **130** 1412
Sternheimer R M 1957 *Phys Rev.* **107** 1565.
Tessman J R, Kahn A H and Sockley W 1953 *Phys Rev.* **92** 890.
Tosi M P 1964 *Solid State Physics* **16** 1.
Yamashita J and Kojima M 1952 *J. Phys. Soc. Japan* **7** 261.

The molecular polarizability and intermolecular interaction potential function of adamantane

(Miss) Rama Kaila*, Lalji Dixit** and P L Gupta

Analytical Physics Section

Indian Institute of Petroleum, Dehra Dun

Received 11 November 1976, revised 6 December 1978

A study of bond contribution to the average molecular polarizability of adamantane ($C_{10}H_{16}$) has been made using delta function potential model of chemical binding. Using polarizability data and Kirkwood-Müller, London and Slater-Kirkwood formulae, the intermolecular potential function has been evaluated and discussed. It is concluded that the results for molecular constants: $A = 22.44 \times 10^{-57}$ ergs cm^6 and $B = 97.05 \times 10^{-101}$ ergs cm^{12} obtained from heat of vaporisation, I.R. and lattice-energy considerations are difficult to be interpreted in terms of polarizability data obtainable from refractive index measurements or semi-empirical quantum mechanical model for the molecule in question.

1. Introduction

The $C_{10}H_{16}$ hydrocarbon is characterised by its several isomeric forms viz. *d*-limonene, dipentene, α -pinene, β -pinene, terpinolene and adamantane. Owing to the high symmetry of adamantane, (T_d), considerable interest has been shown in the study of its spectro-chemical properties with a view to get better insight of its structure and bonding. Thus, the studies on physico-chemical properties (Lee and Slutsky 1975), form of inter-and-intra-molecular potential functions (Breitling *et al* 1971), distribution of lattice dynamical frequencies (Synder and Schachtschneider 1965, Luty 1971, Venkataraman and Sahani 1970, Stockmeyer and Stiller 1968), nature of molecular vibrations (Cyvin 1972, Cyvin *et al* 1971), gas-phase electron diffraction (Hargittai and Hedberg 1972) and other electro-optical properties (Appelquist *et al* 1969) have appeared in literature.

Adamantane is a molecular crystal like hexamino. Recent measurements indicate that above 208K, it has a cubic fcc structure while below this temperature, a tetragonal structure would be more stable. The dynamics of this molecule has been studied experimentally using slow neutron scattering by Stockmeyer

*C.S.I.R. (New Delhi) Research Fellow

**To whom the correspondence should be addressed.

and Stillor (1968). It must be pointed out that adamantane in the high temperature phase is a plastic crystal and is known to show hindered rotations amongst the equivalent configurations. Because of the large amplitudes, the rotational motions cannot be described satisfactorily within the framework of harmonic approximation.

Recently, Lee and Slutsky (1975) have used the static lattice energy derived from experimental heat of vaporisation to deduce intermolecular potential function parameters A and B which in turn have been applied to test the adequacy of assumed potentials (Hirschfelder *et al* 1954) involved in Kirkwood-Müller, London and Slater-Kirkwood deductions. After solving the simultaneous equations of cohesive energy in terms of nearest neighbour distance r and static equilibrium nearest neighbour distance r_0 , Lee and Slutsky obtained the value of A as 22.44×10^{-57} ergs cm⁶ and B as 97.05×10^{-101} ergs cm⁶ respectively. However, the same values of A computed from aforementioned deductions have been reported not to exceed 6.35×10^{-57} ergs cm⁶. This enormous difference in the magnitude of A obtained from various approaches assuming that change of phase does not significantly affect the values of these parameters, warrants further investigation of several input data like polarizabilities, diamagnetic susceptibilities etc. required in the expressions of intermolecular potential function parameter A. In the present communication, we have studied the polarizability of adamantane by computation of London dispersion energy. The polarizability would be computed quantum mechanically using the delta function potential model of chemical binding (Lippincott and Stutman 1964) and improvement in the results for A over the data of Lee and Slutsky would be examined. Accordingly it is assumed that at each nucleus there exists a potential whose magnitude is infinite at a very small interval of the coordinate of motion and for the large intervals the magnitude of potential is zero. Thus the assumed potential follows the properties of delta function i.e. $\delta x = \infty$ when $x = 0$ and $\delta x = 0$ when $x \neq 0$. However integral of potential over all the space is finite i.e. $\int_{-\infty}^{+\infty} \delta x dx = 1$ for any argument of x and equals to a parameter called delta function strength. At each nucleus, then a delta function wave function is generated representing the probability amplitude of the electron for this isolated nucleus. These delta function wave functions are then linearly combined to form molecular orbitals with the restriction that only two electrons may interact at a time and that too when bonds exist between the atoms.

2. Procedural details

2.1. Molecular polarizability

Lippincott and co-workers (1964, 1966) have proposed relevant equations to compute parallel and perpendicular components and thereby arrived at average molecular polarizabilities based on Dirac delta potential and Hylleraas (1930) and

Hasse's (1931) variational treatment. Using proper coordinate of nuclei, α_M can be expressed as :

$$\alpha_M = \frac{1}{3} [\sum_i \alpha_{11} + \sum_j 2\alpha_{11}] \quad (1)$$

where,

$$\alpha_{11} = 4nA_{12}(1/a_0)[\langle x^2 \rangle]^2 \sigma \quad (2)$$

and

$$\sum 2\alpha_{11} = ndf \frac{\sum X_j^2 \alpha_j}{\sum X_j^2} \quad (3)$$

where,

$$\langle x^2 \rangle = \frac{R^2}{4} + \frac{a_0^2}{2CR_{12}^2} \quad (4)$$

In the expressions (2) and (3) n is the bond order, A_{12} is reduced delta function strength, a_0 is Bohr's radius of atomic hydrogen, x is electronegativity and α the atomic polarizability. The summation extends over all the bonds (i) and atoms (j). The quantity $\langle x^2 \rangle$ is the expectation value of electronic position squared along the bond axis and computed from the equation (4) where R_{12} is internuclear distance and $CR_{12} = (n_1 n_2 N_1 N_2)^{1/2} \times A_1 A_2$ for a pair of bonded atoms; n_1, n_2 are the principal quantum numbers of the atoms forming the bond and N_1, N_2 are twice the value of their group number. Finally A_1 and A_2 are the delta function strengths acting on the nuclei of atoms 1 and 2. The quantity ndf is a symmetry and geometry dependent parameter derivable from the number of atoms (N) and bonds (nb) involved in molecular formation by the equation : $ndf = (3N - 2nb)$. The applicability of this model to hydrocarbon systems has been very well shown by Beran and Kevan (1968), Sanyal *et al* (1972, 73) and Dixit *et al* (1975, 76).

2.2. Intermolecular potential function

The potential energy of interaction between a pair of molecules separated by a distance r_{ij} is given by

$$U_{ij} = -Ar_{ij}^{-6} + Br_{ij}^{-12} \quad (5)$$

The corresponding cohesive energy per mol in terms of nearest neighbour distance r may be written as

$$U = \frac{N}{\sigma} [-C_6 A r^{-6} + C_{12} B r^{-12}] \quad (6)$$

where N is Avogadro's number and C_n is equal to $\sum_j (r/r_{ij})^n$ and A and B are inter-molecular potential parameters. The static equilibrium nearest neighbour distance in terms of A , B and C_{12} is given by

$$r_0^6 = 2C_{12}B/C_6A \quad (7)$$

London (1930) obtained dispersion energy expression in terms of average molecular polarizability using closer approximation as

$$A = \frac{3}{2} \alpha_1 \alpha_2 [\bar{\mathbf{E}}_1 \bar{\mathbf{E}}_2 / (\bar{\mathbf{E}}_1 + \bar{\mathbf{E}}_2)] \quad (8)$$

where $\bar{\mathbf{E}}_1$ and $\bar{\mathbf{E}}_2$ could be approximated by using ionization potentials. Utilizing this model and following Margenau's (1939) generalization for f -charges, equation (8) yields, assuming ν to be the vibrating frequency,

$$A = (3/4)\alpha^2\hbar\nu \quad (9)$$

$$A' = \frac{15}{4} [\alpha^3(\hbar\nu)^2/f e^2] \quad (10)$$

$$A'' = \frac{315}{32} [\alpha^4(\hbar\nu)^3/(f e^2)^2] \quad (11)$$

where A' and A'' represent second and third order contributions. If ν and α are known, f can be estimated. Eliminating ν , one finds

$$A = \frac{3}{4} [e^2 \hbar^2 \alpha^3 f / m_e]^\dagger \quad (12)$$

$$A' = \frac{15}{4} [\hbar^2 \alpha^2 / m_e] \quad (13)$$

$$A'' = \frac{315}{32} [\hbar^3 \alpha^2 / e m_e] (\alpha / f m_e)^\dagger \quad (14)$$

If f is identified with N , equation (12) is identical with Slater-Kirkwood (1931) model. Hence the London dispersion energies involve a series of terms in which the higher terms correspond to quadrupole-induced dipole and higher order effects, i.e.,

$$U(dts) = - \frac{A}{r^6} - \frac{A'_{11}}{r^8} - \frac{A''_{12}}{r^{10}} \quad (15)$$

Mason and Monchik (1967) pointed out that London formula ($A = 3\alpha^2/I/4$) gives results that are low; Kirkwood-Müller formula ($A = 3 mc^2\alpha x$) would yield too high results and only Slater-Kirkwood formula ($A = 3eh\alpha^{3/2}N^{1/8}/8\pi m^{1/4}$, with usual notations) would lead to remarkably accurate results. As such we have recalculated the value of A using Slater-Kirkwood approach where contributions of higher order term A' and A'' have been separately estimated along with fresh set of α -values deduced quantum mechanically.

3. Results and Discussion

The interatomic separations of carbon-carbon (secondary and tertiary both) and carbon-hydrogen bonds have been taken from the electron diffraction measure-

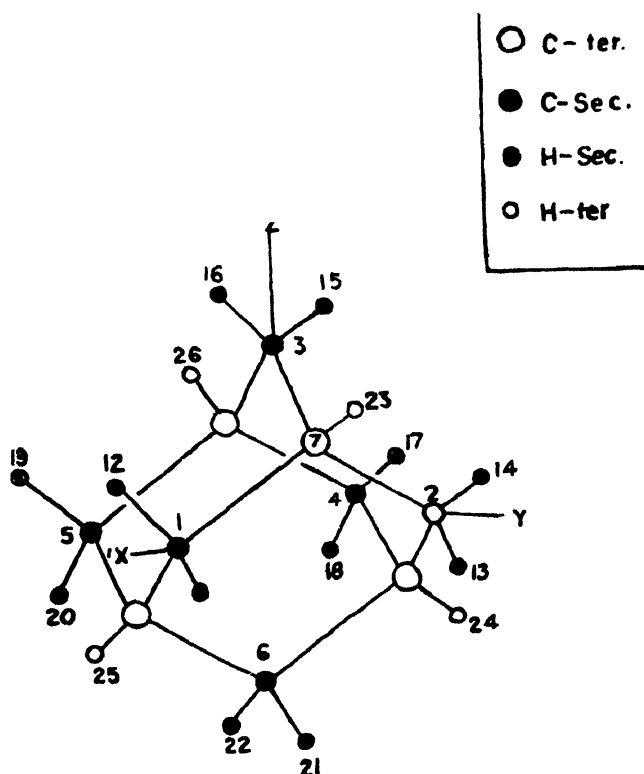


Figure 1. Model of the Adamantane molecule showing the atom numbering electron diffraction values $R(\text{C-C}) = 1.540 \pm 0.002\text{\AA}$, $R(\text{C-H}) = 1.111\text{\AA} \pm 0.004\text{\AA}$, after Hargittai and Hedberg (1972)

ments of Hargittai and Hedberg (1972). This includes $r_{\text{C-C}} = 1.540\text{\AA}$ and $r_{\text{C-H}} = 1.111\text{\AA}$ which are thermal average internuclear distances. The delta function strengths acting at the nuclei of carbon and hydrogen are $A_{\text{C}} = 9.98$ a.u. and

$A_H = 5.92$ a.u. Atomic polarizabilities of carbon and hydrogen are $\alpha_C = 10.25 \times 10^{-25} \text{ cm}^3$ and $\alpha_H = 4.07 \times 10^{-25} \text{ cm}^3$ respectively. These values of A and α are such that they give component polarizabilities of (C-C) and (C-H) bonds close to those of Denbigh's measurements (1940). Considering expectation values of electronic position squared, $\langle x^2 \rangle$, in the bond region of several interatomic configurations, we have generated component bond polarizabilities for various interatomic distances R_{12} . This includes 25 bonded distances (Figure.1) representing the tetrahedral geometry of adamantane. The reported average polarizability of adamantane as $165.0 \times 10^{-25} \text{ cm}^3$ is much lower in comparison to our computed result $218.99 \times 10^{-25} \text{ cm}^3$. Now we compare average polarizabilities of other hydrocarbons lying in the same carbon number range. All the $C_{10}H_8$ non-alternant hydrocarbons, e.g., fluorene and azulene show α_M values lying around $180 \times 10^{-25} \text{ cm}^3$ (Dixit *et al* 1976). As the number of C and H atoms per molecule increases

Table 1. Bond and molecular polarizabilities and intermolecular potential parameters of adamantane

Polarizability components	α -values $\times 10^{-25} \text{ cm}^3$	Potential parameters	Values in $10^{-57} \text{ erg cm}^6$			References
			Kirkwood formula	London formula	Slater Kirkwood formula	
$\alpha_{11}[\text{C-H}]$	6.58					
$\alpha_{11}[\text{C-C}]$	25.86	A	6.35	3.06	6.30	Lee and Slutsky (1975)
$\Sigma \alpha_{11}$	492.74		8.38	5.38	9.65	This work; without higher order corrections
$\alpha \Sigma 2\alpha_1$	163.99					
$\alpha_{M(\text{calc.})}$	218.99	A'	—	—	0.523	This work; Eqn (13) (see text)
$\alpha_{M(\text{expt})}$	165.0 ^a	A''	—	—	0.015	This work; Eqn (14) (see text)
	447.2 ^b					
	590.0 ^c	A corrected	—	—	10.188	This work; applying higher order corrections
	383.4 ^d					
A_{expt}		22.5 22.44	Bridgman piston cylinder measurements 1971) Lee and Slutsky (1975)			Breitling <i>et al</i>
B_{expt}	44.05×10^{-101} $97.05 \times 10^{-101} \text{ erg cm}^{12}$		Figures in parenthesis show computed value.			

(Internuclear distances taken from gas phase electron diffraction Hargittai and Hedberg 1972)

- Using Clausius-Mossotti equation and refractive index
- Using London formula and A values from Lee and Slutsky (1975)
- Using Kirkwood-Müller formula and A values from Lee and Slutsky (1975)
- Using Slater-Kirkwood formula and A values from Lee Slutsky (1975)

the value of α_M rises and for pyrene ($C_{16}H_{10}$) this value is found to be $290 \times 10^{-25} \text{ cm}^3$. For the hydrocarbons in the range C_{10} - C_{16} the value of α_M is expected to lie between 180 and $290 \times 10^{-25} \text{ cm}^3$. Against this, a value of $165.0 \times 10^{-25} \text{ cm}^3$ taken by Leo and Slutsky (1975) for $C_{10}H_{16}$ for the computation of parameter A seems to be on lower side. This level of value is expected for compounds with formula $C_{10}H_8$ (ignoring other effects due to phasechange). Hence fresh evaluation of the parameter A has been made by us and given in table 1. Higher order contributions to r^{-6} coefficient of London dispersion formula have also been given in the same table. Our theoretically computed coefficient of r^{-6} ($A_{calc} = 10.187 \times 10^{-57} \text{ ergs cm}^6$) would show significant improvement over those calculated by Breiting *et al* (1971) and Leo and Slutsky (1975) although even then the value is far away from the experimental value of $22.44 \times 10^{-57} \text{ ergs cm}^6$. This would mean that the results of London dispersion theory obtainable from $A_{calc} = (3/4)I\alpha^2$ could hardly be consistent with r^{-6} coefficient $A = er_m^6 n/(n-6)$, unless higher order contributions be taken into account. However, we too could not achieve satisfactory results very close to the experimental values, but the improvement is significant within the limitations of London dispersion theory. Better agreement would be possible by considering higher order contributions. This would imply that other alternatives using sublimation energy crystal lattice parameter and compressibility data and coupled with suitable potential function should be searched for achieving better results. Such a study for a series of globular hydrocarbons is in progress.

Acknowledgments

One of us (L.D.) records his sincere thanks to Prof. Nitish K. Sanyal, University of Gorakhpur, for helpful discussions and constant encouragement. Thanks are also due to CSIR (New Delhi) for financial assistance to R.K.

References

- Applequist J, Rivers P and Applequist E 1969 *J. Am. Chem. Soc.*, **91** 5705
 Breiting S M, Jonas A D and Boyed R H 1971 *J. Chem. Phys.* **54** 3959
 Beran J A and Kevan L 1968 *J. Phys. Chem.* **73** 3860
 Cyvin S J, Ra Ö and Brunvall J 1971 *Ind. J. Pure Appl. Phys.* **9** 890
 Cyvin S J 1972 *Molecular Structures and Vibrations* Elsevier Amsterdam
 Dixit L, Kapoor S K, Singh I D and Gupta P L 1976 *Ind. J. Pure and Appl Phys.* **14** 648
 Dixit L, Kapoor S K, Singh I D and Gupta P L (Unpublished)
 Denbigh K G 1940 *Trans. Faraday Soc.* **36** 936
 Hargittai I and Hedberg K 1972 *Gas Phase electron diffraction of adamantane in Molecular structures and vibrations* edited by S. J. Cyvin, Elsevier, Amsterdam
 Hirschfelder J O, Curtiss C F and Bird R B 1964 *Molecular Theory of gases and liquids*, Wiley, New York
 Hylleraas E A 1930 *Z. Phys.* **65** 209

- Hasse H R 1931 *Proc. Camb. Phil. Soc.* **26** 26, 66, 542
- Lee W Y and Slutsky L J 1975 *J. Phys. Chem.* **79** 2802
- Luty T 1971 *Acta Physica Polonica* **A40** 37, 49, 63
- Lippincott E R and Stutman J M 1964 *J. Phys. Chem.* **68** 2926
- Lippincott E R, Nagarajan G and Stutman J M 1966 *J. Phys. Chem.* **70** 78
- London F 1930 *Z. Phys. Chem.* **B11** 222
- Margenau H 1939 *Rev. Mod. Phys.* **11** 1; *Phys. Rev.* **56** 1000
- Mason E A and Monchik L 1967 *Advances in Chem. Phys.* **XII**, edited by J. C. Hirschfelder, Interscience Publishers
- Nagarajan G 1966 *Ind. J. Phys.* **40** 319
- Slater J C and Kirkwood J G 1931 *Phys. Rev* **37** 682.
- Snyder R G and Schachtschneider J H 1965 *Spectrochim Acta* **21** 169
- Stockmeyer R and Stillor H 1968, 1967 *Physica Status Solidi* **27** 269, **19** 781
- Sanyal N K, Ahmed P and Dixit L 1973 *J. Phys. Chem.* **77** 2552
- Sanyal N K, Dixit L and Pandey A N 1972 *Ind. J. Pure Appl. Phys.* **10** 329
- Venkataraman G and Sahani V C 1970 *Rev. Mod. Phys.* **42** 409

Application of INDO-method to study the structure of halogen substituted ethylenes

R Jha* and A N Singh

Department of Physics, Magadh University, Bodh-Gaya

Received 1 December 1977, revised 15 May 1979

Abstract. INDO- method of Pople and Beveridge has been applied to study the electronic structure of fluoro-ethylenes. The present study has predicted dipole moment, ionization potential, total energy, binding energy, spin density and hyperfine coupling constants. The calculated dipole moment values and ionization potentials are in good agreement with experiment. The net charge distributions are derived and shown in the figure.

1. Introduction

The fluorine substituted ethylenes have drawn the attention of a number of workers for the theoretical and experimental study of their spectra and structure. Belanzer *et al* (1969) have recorded the vacuum ultra-violet spectra of fluoro-ethylenes between $50,000\text{ cm}^{-1}$ and $80,000\text{ cm}^{-1}$. Watson and co-workers (1970) have theoretically examined the electronic transitions of ethylene derivatives using extended Hückel-scheme with Mulliken-Wolfsberg-Helmholtz parametrization.

Recently Lake and Thomson (1970) have measured photoelectron spectra of fluoro-, chloro- and chlorofluoroethylenes. Ionization potentials of these compounds have been found in the range 6 to 21 eV. Landan *et al* (1969) have done Hückel calculations on the spectra of fluoro-ethylenes but their results fail to account for the observed spectra. The vacuum ultraviolet photolysis of the difluoro-ethylenes has been done by Guillory and co-worker (1975).

Although the electronic structure of fluoro-ethylenes has been studied by several workers no unanimity has been reached on their interpretation. The theoretical study is limited to the application of preliminary π -electron approximation methods which are not able to account properly for the observed spectra. It is essential to use improved semiempirical ($\pi+\sigma$) electron approximation method and the purpose of the present calculation is to make an attempt to gain more precise information using INDO-procedure to fluorine substituted ethylenes.

* Department of Physics, S. P. Jain, College, Sasaram.

2. Procedure

The elements of Fock matrix F , in the INDO method, are

$$F_{\mu\mu} = U_{\mu\mu} + \sum_{\lambda} P_{\lambda\lambda}[(\mu\mu|\lambda\lambda) - (\frac{1}{2})(\mu\lambda|\mu\lambda)] + \sum_{B \neq A} (P_{BB} - Z_B)\gamma_{AB}$$

$\mu \rightarrow \text{atom } A$

$$F_{\mu\nu} = P_{\mu\nu}[(3/2)(\mu\nu|\mu\nu) - (\frac{1}{2})(\mu\mu|\nu\nu)]$$

$\mu \neq \nu \rightarrow \text{atom } A$

$$F_{\mu\nu} = \beta_{AB}^0 S_{\mu\nu} - (\frac{1}{2})P_{\mu\nu}\gamma_{AB},$$

$\mu \rightarrow \text{atom } A$
 $\nu \rightarrow \text{atom } B$

and

$$U_{\mu\mu} = -(\frac{1}{2})(I_{\mu} + A_{\mu}) - (Z_A - (\frac{1}{2}))\gamma_{AA}$$

$$(\mu\nu|\mu\nu) = \int \int \phi_{\mu}^{(1)} \phi_{\mu}^{(2)} \frac{1}{r_{12}} \phi_{\nu}^{(1)} \phi_{\nu}^{(2)} d\tau_1 d\tau_2 \quad \mu \neq \nu$$

the symbols having usual meaning.

Using these F matrices the equation of Hartree Fock-Roothaan (1951) was solved and the energies were computed. The present calculation was carried out using the modified version by Ansari (1974), of the program of Del Bene and Jaffe (1968). The geometry has been assumed on the basis of work by Laurie (1961).

The expression for the isotropic hyperfine coupling constant of atom N , due to Pople *et al* (1968), is given by

$$a_N = \left[\frac{4\pi}{3} g\beta\gamma_N \hbar \langle S_z \rangle^{-1} |\phi_{SN}(R_N)|^2 \right] \rho_{S_N} S_N$$

where g is the electronic g factor, β is the Bohr magneton, γ_N is the gyromagnetic ratio of N and R_N is the position vector of N .

The expectation value of the spin density operator at the nucleus of atom N is

$$\langle \psi | \rho^S(R_N) | \psi \rangle = \rho_{S_N} S_N |\phi_{SN}(R_N)|^2.$$

3. Results and discussions

The net charge distributions of halogen substituted ethylenes have been shown in figure 1. We find that fluorine atoms in all compounds bear negative charges. Each fluorine substituted ethylene is endowed with the two carbon atoms of the C = C bond, and the charges on C-atoms and hydrogen atoms are positive. The numerical value of charge on fluorine atoms in 1,1 di-fluoro-ethylene is

much larger than those in 1,2-trans-di- and 1,2-cis-di-fluoro-ethylenes. The explanation is rather trivial.

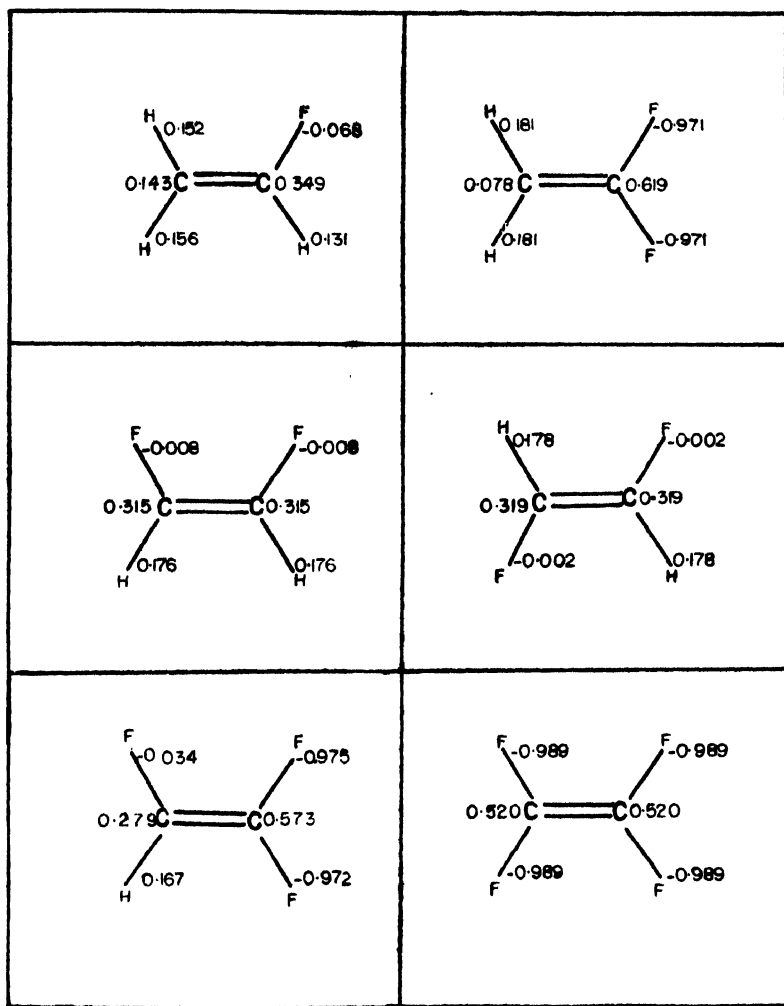


Figure 1. Net charge distributions of fluoroethylene (INDO).

Dipole moments :

The calculated dipole moments of fluorine substituted ethylenes are listed in table 1, and the observed values are included with their references. The calculated dipole moment value of mono-fluoro-ethylene agrees well with the observed value of Mirri *et al* (1961). The theoretical values of dipole moments (μ) of 1,1- and 1,2 cis-difluoro-ethylene are near the experimental values of

Roberts and Edgell (1949) and Laurie (1961) respectively. The dipole moments of 1,2-trans-di- and tetra-fluoro-ethylenes are zero because of symmetry considerations, and that of tri-fluoro-ethylene is about two and a half Debye units. To our knowledge the experimental values of dipole moments for 1,2-trans-di-fluoro-ethylene, tri-fluoro-ethylene and tetra fluoroethylene are not known.

Table 1. Dipole moment values of fluoro-ethylenes in Debye units

Molecule	$\mu(\text{obsd.})$ D	Ref.	$\mu(\text{calcd.})$ D	Method
$\text{CH}_2 = \text{CHF}$	1.427 ± 0.010	<i>a</i>	1.483	INDO
$1,1\text{-CH}_2 = \text{CF}_2$	1.366 ± 0.02	<i>b</i>	1.420	
$1,2\text{-CH}_2 = \text{CF}_2(\text{cis})$	2.420 ± 0.03	<i>c</i>	2.523	
$1,2\text{-CH}_2 = \text{CF}_2(\text{trans.})$			0.000	
$\text{CF}_2 = \text{CHF}$			2.571	
$\text{CF}_2 = \text{CF}_2$			0.000	

a : Roberts *et al* (1949); *b* : Laurie (1961); *c* : Bralsford and co-workers (1960).

Total Energy and Binding Energy :

The total energy and binding energy of fluoro-ethylenes are presented in table 2. Our INDO calculation predicts that the total energies of 1,1-di-fluoro-ethylene, 1,2-cis-di-fluoro-ethylene and 1,2-trans-di fluoroethylene are of the same order; and their binding energies are nearly equal. The numerical value of total energy varies in the order Mono-fluoro-ethylene < Di-fluoro-ethylene < Tri-fluoro-ethylene < tetra-fluoro-ethylene. The binding energy of the molecules varies in the same order except difluoro-ethylene.

Table 2. Total energy and binding energy of fluorine substituted ethylenes.

Molecule	Total Energy	Binding Energy	Method
$\text{CH}_2 = \text{CHF}$	— 43.521	— 1.726	INDO
$1,1\text{-CH}_2 = \text{CF}_2$	— 71.058	— 2.352	
$1,2\text{-CH}_2 = \text{CF}_2(\text{cis})$	— 70.978	— 2.272	
$1,2\text{-CH}_2 = \text{CF}_2(\text{trans.})$	— 70.979	— 2.273	
$\text{CF}_2 = \text{CHF}$	— 97.509	— 1.894	
$\text{CF}_2 = \text{CF}_2$	— 125.008	— 2.482	

The Lowest Ionization Potentials :

The lowest ionization potentials by Koopman's theorem are collected in table 3, which includes the observed ionization potentials obtained by Lake and Thomson (1970), Bralsford *et al* (1960) and Lifshitz and Long (1963). The first ionization potential (IP) varies in the order 1,2-cis-d.f.e. > 1,2-trans-d.f.e. > Mono-f.e. > 1,1-di-f.e. > tetra-f.e. > tri-f.e.

Table 3. The Lowest ionization potential of fluoro-ethylenes.

Molecule	Experimental			Theoretical		
	IP(eV)	Ref.	Method	IP(eV)	MO	Method
CH ₂ = CHF	10.37	a	Photoelectron	10.26	σ	INDO
	10.37	b	Photoionization	10.28	σ	
	10.45	c	Electronimpact	10.42	σ	
1,1-CH ₂ = CF ₂	10.30	b	Photoionization	10.246	π	INDO
	10.31	a	Photoelectron	10.362	π	
	10.45	c	Electronimpact	10.366	σ	
1,2-CH ₂ = CF ₂ (cis)				10.532	σ	INDO
				10.624	π	
				10.629	π	
1,2-CH ₂ = CF ₂ (trans)				10.529	π	INDO
				10.592	σ	
				10.710	σ	
CF ₂ = CHF				10.09	σ	INDO
				10.11	π	
				10.15	σ	
CF ₂ = CF ₂	10.11	a	Photoelectron	10.23	σ	INDO
	10.12	c	Electronimpact	10.35	π	
	10.12	b	Photoionization	10.39	π	

a : Lake *et al* (1970); b : Bralsford and co-workers; c : Lifshitz *et al* (1963).

The calculated first ionization potential of mono-fluoro-ethylene is close to the experimental IP of Lake and Thomson (1970), and the theoretical values of higher IPs are in a reasonably good agreement with experimental values. The calculated first ionization potential of 1,1-di-fluoroethylene agrees well with the observed IP obtained by Bralsford *et al* (1960).

From the present calculation the first ionization potentials of 1,2-cis-di-fluoro-ethylene, 1,2-trans-di-fluoro-ethylene and tri-fluoro-ethylene are predicted 10.532, 10.529 and 10.09 eV respectively. The first ionization potential of tetra-fluoroethylene is computed 10.23 eV and the observed IP is 10.11 eV. The experimental data for ionization potentials of 1,1-di-; 1,2-trans-di- and tri-fluoro-ethylenes appear to be unknown.

Spin density and hyperfine coupling constant :

The spin density and hyperfine coupling constant (h.c.c.) of the systems for the ground state have been calculated using HF orbitals, and summarized in

table 4. It is found that fluorine and carbon hyperfine coupling constants in 1,1-di-fluoro-ethylene are of the same sign, and the fluorine h.c.c. in Mono-; 1,1-di- and tetra-fluoro-ethylenes bear negative sign. The present calculation indicates that the hydrogen h.c.c. in 1,2-cis-di-fluoro-ethylene is positive and that in tri-fluoro-ethylene is negative. The study predicts the alteration of sign for carbon h.c.c. of fluoroethylenes with the exception of 1,1-di-fluoro-ethylene. The hydrogen and fluorine spin density are all positive for 1,2-cis-di-fluoro-ethylene. We cannot, however, comment, for the present, on the accuracy of those data, since the experimental values of spin density and hyperfine coupling constants for fluoro-ethylenes seem to be unknown.

Table 4. Spin density and hyperfine coupling constants of fluoroethylenes.

Molecule	Atoms	S-orbital spin density ρ	Hyperfine coupling constant A (gauss)	Method
$\text{CH}_2 = \text{CHF}$	C	0.12	7.65	INDO
	C	-0.23	- 9.24	
	F	-0.25	- 6.92	
	H	-0.01	- 0.82	
	H	0.00	0.00	
	H	-0.29	-10.00	
1,1- $\text{CH}_2 = \text{CF}_2$	C	-0.11	- 5.83	INDO
	C	-0.16	- 8.41	
	F	-0.14	- 5.64	
	F	-0.22	- 6.29	
	H	0.28	9.02	
	H	-0.30	- 9.22	
1,2- $\text{CH}_2 = \text{CF}_2(\text{cis})$	C	0.08	4.34	INDO
	C	-0.16	- 6.36	
	H	0.12	6.28	
	F	0.16	4.68	
	F	0.23	5.24	
	H	0.42	12.10	
1,2- $\text{CH}_2 = \text{CF}_2(\text{trans})$	C	-0.14	- 5.86	INDO
	C	0.19	8.29	
	F	0.34	6.23	
	H	-0.92	-10.28	
	F	-0.24	- 5.92	
	H	0.82	13.28	
$\text{CF}_2 = \text{CHF}$	C	0.30	9.09	INDO
	C	-0.26	- 8.56	
	F	-0.28	- 6.28	
	F	-0.31	- 6.41	
	H	-0.32	- 7.43	
	F	0.25	5.98	
$\text{CF}_2 = \text{CF}_2$	C	-0.24	- 6.84	INDO
	C	0.37	7.92	
	F	-0.34	- 6.97	
	F	-0.21	- 6.21	
	F	-0.16	- 5.89	
	F	-0.17	- 5.96	

Acknowledgment

We would like to thank Dr. D. K. Rai, Professor of Spectroscopy, B.H.U. for several stimulating discussions.

References

- Ansari W H 1974 *Ph.D. Thesis* Magadh University, Bodh-Gaya
Belanzer and Sandorfy 1969 *CP Letters* **3** 661
Bralsford, Harris and Price 1960 *Proc. Roy. Soc. (L)* 4258 459
Del Bene J and Jaffe H H 1968 *J. Chem. Phys.* **48** 1907
Guillory W A and Andrews G H 1975 *J. Chem. Phys.* **62** 4667
Lake R F and Thomson S H 1970 *Proc. Roy. Soc. Lond.* **A315** 323
Londan, Dubor and Medvedev 1969 *J. Phys. Chem.* **43** 3
Laurie V W 1961 *J. Chem. Phys.* **34** 291
Lifshitz C and Long F A 1963 *J. Phys. Chem. Ithaca* **67** 2463
Mirri A M, Guarnieri A and Favero P 1961 *Nuovo Cimento* **19** 1189
Pople J A, Deveridge D L and Dobosh P A 1968 *J. Am. Chem. Soc.* **90** 4201
Roberts A and Edgell W F 1949 *J. Chem. Phys.* **17** 742
Roothan C C J 1951 *Rev. Mod. Phys.* **23** 69
Watson F H, Armstrong A T and McGlynn S P 1970 *Theoret. Chim. Acta* **16** 75

Vibrational and rotational level spacings of Van der Waals molecules and related thermodynamic functions: Ar₂ molecule

Swadesh Kumar Ghoshal

Department of Physics, Ranaghat College, West Bengal

and

Sankar Sengupta

Department of Physics, Jadavpur University, West Bengal

Received 15 November 1978, revised 29 January 1979

Abstract. Vibrational and rotational level spacings for Van der Waals Ar₂ molecule by use of the Morse potential suggested by Konowalow and Hirschfelder (1961) is presented. Calculated results of vibrational energy spacing agree well with experimental and other theoretical calculations. The energy spacings of Ar₂ molecule are used to calculate the thermodynamic functions of the Van der Waals bond.

1. Introduction

Van der Waals molecules are weakly bound complexes of small atoms or molecules held together solely by intermolecular attraction. Unlike the molecules held together by chemical bond Van der Waals molecules have very low dissociation energy. Still then, Van der Waals molecules exhibit well defined vibrational and rotational energy levels. Recently both theoretical and experimental investigations are being done on these level spacings (Ewing 1975). Vacuum ultraviolet spectroscopic studies have recently yielded important information on the ground state vibrational structure and potential well depth of Ar₂ (Tanaka *et al* 1970), Kr₂ (Tanaka *et al* 1973) and Xe₂ (Freeman *et al* 1974).

Theoretical studies of the spectrum of Van der Waals molecules are mostly limited to numerical integration of the radial Schrödinger equation for complicated potentials. It will be useful if the same problem could be tackled analytically to yield explicit energy spacing expressions as preliminary source of information. Shin (1977) has formulated such expressions for the vibrational structure of Van der Waals molecules in the ground electronic state. He used W.K.B. approximation assuming Lennard-Jones potential for intermolecular interaction. W.K.B. approximation is suitable for large quantum numbers and to situations in which potential energy varies very slowly with distance. There may be some

doubt regarding its suitability in the case of floppy Van der Waals molecules. Alternatively, one can use simple Morse potential for which expression for the vibrational and rotational energy spacings can be obtained simultaneously. This feature is not present with other phenomenological potentials. Kanowalow and Hirschfelder (1961) have suggested simple and accurate Morse potential functions for non-polar molecules. Apparently, Morse potential is erroneous for very large internuclear separation. But the behaviour of the potential energy at extremely large separation may not be so much important. At moderate separation the energy of interaction contains inverse eighth power, inverse tenth power etc., dispersion terms plus second order exchange/terms. Thus, it is quite possible that the Morse potential may provide as good as or better representation of the essential features of the true potential such as Lennard-Jones and Buckingham exp-6 potentials (Buckingham 1955). In this paper we shall use Morse potential suggested by Kanowalow and Hirschfelder (1961) to establish its usefulness in determining vibrational-rotational structures of dimer in the ground electronic states. Detailed results on Ar_2 molecule will be reported here.

2. Eigenvalue expression

The shape of the energy curves for a typical diatomic molecule derived by Morse is given by

$$E = D[1 - \exp\{a(r_e - r)\}]^2 \quad (1)$$

where a is constant for a particular molecule, D is the dissociation energy and r_e the equilibrium internuclear distance. The eigenvalue expression for this potential can be written in the form usually employed in the study of observed spectra, as

$$\begin{aligned} \frac{W_{Jv}}{hC} = & \bar{\nu}_e(v + \frac{1}{2}) - x_e \bar{\nu}_e(v + \frac{1}{2})^2 + J(J+1)B_e + D_e J^2(J+1)^2 \\ & - \alpha_e(v + \frac{1}{2})J(J+1) \end{aligned} \quad (2)$$

v and J are vibrational and rotational quantum numbers respectively. Explicit expressions for $\bar{\nu}_e$, x_e , B_e , D_e can be obtained from Pauling and Wilson (1935).

3. Vibrational structure

For the Van der Waals Ar_2 molecules, the well depth of interaction is known to be 91.6 cm^{-1} from spectroscopic studies (Tanaka *et al* 1970). The corresponding value for the Morse potential as found out by Konowalow and Hirschfelder (1961) is 99.91 cm^{-1} . For Argon, the minimum distance r_e for Morse potential is 3.86 \AA . The value of r_e obtained for fitting with Lennard-Jones potential is 3.437 \AA . In table 1, we have listed the vibrational level spacing ΔG_{v+1} for Ar_2

and compared the results with experimental data by Tanaka *et al* (1970), the numerical results by Docken and Schafer (1973) who used $D = 97.83 \text{ cm}^{-1}$ and $r_e = 3.76 \text{ \AA}$ and W.K.B. results of Shin (1977). The agreement between the present calculation with experiment and results obtained by Docken and Schafer (1973) who integrated the radial Schrödinger equation numerically for a M.S.V. potential function and also by Shin (1977) is reasonably good. The values are also in reasonably good agreement with the values obtained by Colbourn and Douglas (1976) for the vibrational and rotational energy levels. They obtained their values by fitting the experimentally observed spectroscopic data together with information from long range forces and from the second virial coefficient into a potential curve. For some high value of the vibrational quantum number Morse potential yields values closer to experimental values than any other calculations. Seven vibrational levels were obtained by the present calculation similar to Docken and Schafer (1973) instead of only five levels by Shin (1977).

Table 1. Level spacings of Ar_2 ^{a)}

		ΔG_{v+1}		
	eq. (2)	expt (Tanaka <i>et al</i> 1970)	Docken and Schafer (1973)	Shin (1977)
0	23.407	25.0-26.7	25.50	25.53
1	19.736	18.6-20.8	20.14	20.40
2	16.065	14.8-16.2	15.06	15.27
3	12.394	9.2-11.3	10.63	10.12
4	8.723	5.9- 8.0	6.68	4.99
5	5.052	-	3.56	-
6	1.380	-	1.42	-
$\sum_{v=0}^4 \Delta G_{v+1}$	80.325	73.5-83.0	78.01	76.31

^{a)} All units are in cm^{-1} .

4. Rotational structure

With the use of Morse potential it is possible to determine rotational energy levels along with vibrational levels. For Ar_2 , the calculated values of $\bar{\nu}_e$, x_e , B_e , D_e and α_e are: $\bar{\nu}_e = 27.0779 \text{ cm}^{-1}$, $x_e = .06778 \text{ cm}^{-1}$, $B_e = .056647 \text{ cm}^{-1}$, $D_e = -0.9916 \times 10^{-16} \text{ cm}^{-1}$, and $\alpha_e = .00336 \text{ cm}^{-1}$. Table 2 gives wave numbers of first few lines in each P and R branch of the Fundamental absorption band centered at about 23.41 cm^{-1} and the first overtone centered at about 43.14 cm^{-1} . The pattern of vibration-rotation spectrum is same as that of

chemically bonded diatomic molecules. Again the lines in the *R* branch become closely spaced with increasing state of excitation while the lines in the *P* branch become more separated. It is interesting to observe that unlike Ne_2 (Sengupta 1978) spacings between lines are beyond the limit of resolution. The feature may be attributed to reduced anharmonicity.

Table 2. Part of the far infrared spectrum of Ar_2 molecule (in cm^{-1}).

	Line	ν	Separation $\langle \Delta \nu \rangle$	Line	$\bar{\nu}$	Separation $\langle \Delta \bar{\nu} \rangle$
<i>v</i> = 0 to <i>v</i> = 1	<i>P</i> ₍₁₎	23.297	·116	<i>R</i> ₍₀₎	23.510	·096
	<i>P</i> ₍₂₎	23.181	·1222	<i>R</i> ₍₁₎	23.606	·091
	<i>P</i> ₍₃₎	23.0579	·1303	<i>R</i> ₍₂₎	23.697	·083
	<i>P</i> ₍₄₎	22.9276	·1366	<i>R</i> ₍₃₎	23.780	·071
	<i>P</i> ₍₅₎	22.7910	·148	<i>R</i> ₍₄₎	23.851	·071
	<i>P</i> ₍₆₎	22.643	·148	<i>R</i> ₍₅₎	23.922	·066
	<i>P</i> ₍₇₎	22.495	·153	<i>R</i> ₍₆₎	23.988	·057
	<i>P</i> ₍₈₎	22.342	·162	<i>R</i> ₍₇₎	24.045	·042
	<i>P</i> ₍₉₎	22.180		<i>R</i> ₍₈₎	24.087	
<i>v</i> = 0 to <i>v</i> = 2	<i>P</i> ₍₁₎	43.030	·129	<i>R</i> ₍₀₎	43.230	·090
	<i>P</i> ₍₂₎	42.901	·130	<i>R</i> ₍₁₎	43.320	·071
	<i>P</i> ₍₃₎	42.771	·150	<i>R</i> ₍₂₎	43.391	·050
	<i>P</i> ₍₄₎	42.621	·169	<i>R</i> ₍₃₎	43.441	·050
	<i>P</i> ₍₅₎	42.452	·169	<i>R</i> ₍₄₎	43.491	·031
	<i>P</i> ₍₆₎	42.283	·188	<i>R</i> ₍₅₎	43.522	·011
	<i>P</i> ₍₇₎	42.095	·208	<i>R</i> ₍₆₎	43.533	·002
	<i>P</i> ₍₈₎	41.887		<i>R</i> ₍₇₎	43.535	

5. Thermodynamic functions of the Van der Waals bond of Ar_2

The information obtained for vibrational and rotational structures can be used to calculate the thermodynamic properties of Van der Waals bond. Knowing the energy spacings explicitly, the relevant partition function can be estimated. As the motion of Van der Waals molecules is anharmonic, the number of bound vibrational levels is not too large. It is not possible to obtain simple analytic formula for the partition function. The function must be evaluated by numerical summation.

$$Q_{\text{vib}} = \sum_{v=0}^{v_m} \exp(-\Delta E_v/RT) \quad (3)$$

where $\Delta E_v = E_v - E_0$, E_0 being the zero point energy. With the equation (3), the evaluation of thermodynamic functions becomes straight forward. The

pertinent thermodynamic functions for the vibrational motion of the Van der Waals bond are

$$(G-E_0)/RT = -\ln Q_{vib} \quad (4)$$

$$(E-E_0)/RT = Q_{vib}^{-1} \sum_v (\Delta E_v/RT) \exp(-\Delta E_v/RT) \quad (5)$$

$$C_v/R = Q_{vib}^{-1} \sum_v (\Delta E_v/RT)^2 \exp(-\Delta E_v/RT) - [(E-E_0)/RT]^2 \quad (6)$$

and

$$S/R = (E-E_0)/RT + \ln Q_{vib} \quad (7)$$

For Ar_2 the summation is over $v = 0$ to $v_m = 6$. All the relevant quantities for Ar_2 are condensed in table 3. The table shows the contribution of the vibrational and rotational motion to the thermodynamic functions for Ar_2 for three different temperatures. Table 3 also contains values of rotational partition function defined by

$$Q_{rot} = \sum_{J=0}^{J_m} (2J+1) e^{-J(J+1) \frac{hCB_e}{kT}} \quad (8)$$

Table 3. Thermodynamic Functions of Ar_2 ^{a)}

$T(K)$	Q_{vib}	$-(G-E_0)$	$(E-E_0)$	C_v	S	Q_{rot}
100	2.93	213.59	161.81	.886	3.75	370.17
200	4.47	594.68	173.10	.242	3.84	403.49
300	5.17	979.47	176.71	.111	3.85	415.50

^{a)} $-(G-E_0)$ and $(E-E_0)$ are in units of cal/mol; S and C_v are cal/mol/deg.

These data may be important for the study of thermodynamic properties of Ar_2 molecule. Here also the function must be evaluated by numerical summation ($J_m = 20$).

When we recognise the simple form of Morse potential and the simplicity of equation (2), the agreement between the present calculation and the experimental results is good. We, therefore, may state that the Morse potential function can be of practical importance in determining vibrational and rotational structure of Van der Waals Ar_2 molecules. It will be interesting to see for what Van der Waals molecule the Morse potential function fails to reproduce a experi-

mental data satisfactorily. This kind of study may throw some light as to the nature of interaction effective in Van der Waals bond.

Acknowledgment

We are indebted to U.G.C. for financial assistance.

References

- Buckingham A D 1955 *J. Chem. Phys.* **23** 412
Colbourn E A and Douglas A E 1976 *J. Chem. Phys.* **65** 174
Docken K F and Schafer P T 1973 *J. Mol. Spectro.* **46** 454
Ewing G E 1975 *Accounts Chem. Res.* **8** 185
Freeman D E, Yoshino K and Tanaka Y 1974 *J. Chem. Phys.* **61** 4880
Kanowalow D D and Hirschfelder J O 1961 *Phys. Fluid* **4** 629
Pauling L and Wilson E 1935 *Introduction to Quantum Mechanics* (McGraw-Hill Book Comp. Inc., New York) p 271
Shin H K 1977 *Chem. Phys. Letters* **47** 225
Sengupta S 1978 *Chem. Phys. Letters* **59** 423
Tanaka Y, Yoshino K and Freeman D E 1970 *J. Chem. Phys.* **53** 2012
Tanaka Y, Yoshino K and Freeman D E 1973 *J. Chem. Phys.* **59** 5160

On the ground state frequencies of some monosubstituted pyridenes

G N R Tripathi* and Sita Ram Tripathi**

Department of Physics, University of Gorakhpur, Gorakhpur

(Received 15 July 1976, revised 16 November 1976)

Abstract Vibrational analyses of the infrared spectra of isomeric pyridyl 2- 3- and 4-aldehydes have been made in the region $400-4000\text{ cm}^{-1}$ in liquid phase. The fundamental frequencies are discussed considering C_s point group for the geometry of the molecules.

1. Introduction

In continuation of our study of the vibrational spectra of monosubstituted pyridines (Tripathi & Tripathi 1976) vibrational analyses of the infrared spectra of pyridyl 2-, 3- and 4-aldehydes are proposed in this paper.

Pyridyl aldehyde molecule is obtained by replacing a hydrogen atom of pyridine ring by (-CHO) group. It was shown by Jesson *et al* (1972) that the pyridine molecule has planar structure in ground state and quasi-planar in excited state. The molecules under investigation belong to C_s point group if all the atoms of (-CHO) group lie in the plane of the ring.

2. Experimental procedure

The infrared spectra of three isomers of pyridyl aldehydes obtained from M/S K. Light Laboratory England were recorded on Beckman-IR12 infrared spectrophotometer in the frequency range $400-4000\text{ cm}^{-1}$ using KBr optics. Nearly fifty bands were observed in *o*- and *m*-isomers and sixty bands in the *para*-isomer. Detailed vibrational analysis are contained in the table 1 and assignments of the probable modes of the fundamental frequencies are given in table 2. The molecular weight of the pyridyl aldehyde and benzaldehyde is nearly the same, therefore, the ring and group sensitive vibrations of the two types of compounds should show resemblance. A comparison of the fundamental frequencies of the two type compounds along with that of formaldehyde (Herzberg 1945) and pyridine will be useful in assignments (table 3). Most of the assignments are obvious from tables 1 and 2, therefore, only a few will be discussed here.

*Present address—Department of Physics, Manchester University, Manchester, U.K.

**Department of Physics, National Degree College, Barhalganj, Gorakhpur 273001, India (To whom correspondence should be addressed).

Table 1. Vibrational assignments for pyridyl 2-, 3- and 4-aldehydes (All values are in cm^{-1})

Pyridyl 2-aldehyde				Pyridyl 3-aldehyde				Pyridyl 4-aldehyde			
Wave number	Intensity	Assignments*	Wave number	Intensity	Assignments*	Wave number	Intensity	Assignments*	Wave number	Intensity	Assignments*
(1)	(2)	(3)	(4)	(5)	(6)	(7)	(8)	(9)	(10)	(11)	(12)
405	s	ν_{16a}	410	s	ν_{13a}	405	s	ν_{16a}	405	s	ν_{16a}
430	s	ν_{16b}	425	s	ν_{16b}	430	s	ν_{16b}	430	s	ν_{16b}
495	vs	ν_{6a}	490	vs	ν_{6a}	495	vs	ν_{6a}	495	vs	ν_{6a}
650	ms	ν_{6b}	650	vs (sh)	ν_{6b}	645	s (sh)	ν_{6b}	645	s (sh)	ν_{6b}
705	ms	ν_4	700	vs (sh)	ν_4	720	w (sh)	ν_4	720	w (sh)	ν_4
740	s	ν_{10a}	755	mw	ν_{10a}	760	ms	ν_{10a}	760	ms	ν_{10a}
780	ms	ν_1	800	s	ν_1	800	vs (sh)	ν_1	800	vs (sh)	ν_1
840	w	ν_{10b}	830	vs (sh)	ν_{10b}	830	vs (sh)	ν_{10b}	830	vs (sh)	ν_{10b}
860	mw	$2\nu_{16b}$	890	mw	$\nu_{16a} + \nu_{6a}$	870	mw	$2\nu_{16a}$	870	mw	$2\nu_{16a}$
900	mw	$\nu_{16a} + \nu_{6a}$	990	mw	$2\nu_{16a}$	905	mw	$\nu_{16a} + \nu_{6a}$	905	mw	$\nu_{16a} + \nu_{6a}$
930	mw	$\nu_{16b} + \nu_{6a}$	1015	ms (sh)	ν_{12}	990	ms (sh)	ν_{12}	990	ms (sh)	ν_{12}
990	ms	ν_{12}	1050	mw	$\nu_{16a} + \nu_6$	1000	ms	$2\nu_{16a}$	1000	ms	$2\nu_{16a}$
1040	ms	ν_{16b}	1080	mw	ν_{16b}	1055	ms (sh)	ν_{16b}	1055	ms (sh)	ν_{16b}
1070	ms	$\nu_{16b} + \nu_{6b}$	1110	mw	$\nu_{16a} + \nu_4$	1075	w	$\nu_{16b} + \nu_{6b}$	1075	w	$\nu_{16b} + \nu_{6b}$
1140	ms	ν_{8a}	1185	ms (s')	ν_{6b}	1190	vs	ν_{6b}	1190	vs	ν_{6b}
1170	ms	ν_{C-CHO}	1205	vs (sh)	ν_{C-CHO}	1210	vs (s')	$3\nu_{16a}$	1210	vs (s')	$3\nu_{16a}$
1255	ms	$\nu_{16a} + \nu_{10a}$	1230	s	$\nu_{16b} + \nu_1$	1220	vs	ν_{C-CHO}	1220	vs	ν_{C-CHO}
1265	ms	$2\nu_{16b} + \nu_{16a}$	1315	s (sh)	ν_3	1260	w	$2\nu_{16b} + \nu_{16a}$	1260	w	$2\nu_{16b} + \nu_{16a}$
1295	ms	$2\nu_{16b}$	1245	mw	$\nu_4 + \nu_{6b}$	1280	mw	$2\nu_{16b}$	1280	mw	$2\nu_{16b}$
1345	ms	ν_3	1380	s (sh)	ν_{14}	1315	vs	ν_3	1315	vs	ν_3
1370	ms	ν_{14}	1400	ms	$2\nu_{14}$	1385	vs (sh)	ν_{14}	1385	vs (sh)	ν_{14}
1395	ms	$\nu_{16a} + \nu_{12}$	1415	s	ν_{13a}	1410	vs (sh)	ν_{13}	1410	vs (sh)	ν_{13}
1400	ms	$2\nu_{14}$	1460	mw	ν_{16b}	1450	mw	$2\nu_{14}$	1450	mw	$2\nu_{14}$
1420	s	ν_{13a}	1470	mw (s')	$\nu_{6b} + \nu_{10a}$	1460	mw	$\nu_{6b} + \nu_{10a}$	1460	mw	$\nu_{6b} + \nu_{10a}$
1455	ms	ν_{13b}	1520	mw	$2\nu_{16a} + \nu_4$	1480	mw	$2\nu_{16a} + \nu_4$	1480	mw	$2\nu_{16a} + \nu_4$

Table 1. (contd)

Pyridyl 2-aldehyde			Pyridyl 3-aldehyde			Pyridyl 4-aldehyde		
Wave number	Inten- sity	Assign- ments*	Wave number	Inten- sity	Assign- ments*	Wave number	Inten- sity	Assignments
(1)	(2)	(3)	(4)	(5)	(6)	(7)	(8)	(9)
1480	ms	2x ν_{10a}	1535	mW	ν_{8a}	1490	mW	18
1510	w	$\nu_{10a} + \nu_1$	1560	vs (s')	$\nu_1 + \nu_{10a}$	1500	mW	2x 18 + 6
1540	ms	$\nu_{10a} + \nu_{9b}$	1575	vs	ν_{9b}	1530	vW	2x 18 + 4
1550	ms	ν_{8a}	1625	mW	$\nu_1 + \nu_{10b}$	1560	vs (sh)	8
1570	vs	ν_{9b}	1645	ms	2x $\nu_{10b} + \nu_1$	1625	mW	1 + 1
1640	w	$\nu_{6b} + \nu_{12}$	1675	vs (s')	2x ν_{10b}	1660	s	2x 18 + 1
1660	w	2x $\nu_{10a} + \nu_{10b}$	1690	vs	$\nu_{C=O}$	1690	s	3x ν_1
1670	w	2x ν_{10b}	1830	w	$\nu_{10b} + 2x\nu_4$	1700	vs (sh)	C=O
1690	ms	$\nu_{6b} + \nu_{10b}$	1840	vW	$\nu_{10b} + \nu_{12}$	1850	mW	2x 18 + 12
1700	ms	$\nu_{C=O}$	1910	vW	$\nu_{10b} + \nu_{8a}$	1940	mW	4 + C=CHO
1730	w	$\nu_{10a} + \nu_{12}$	2600	mW	$\nu_{10a} + \nu_{8a}$	2010	mW	2x 1 + 16
2820	w	$\nu(C-H)$	2740	vW	$\nu(C-H)$	2730	ms	C-H
3040	ms	ν_{1a}	2800	w	4x ν_4	2780	w	2x 1 + 9
3060	ms	ν_{20a}	2840	ms	$\nu(C-H)$	2820	ms	(C-H)
3400	w	2x $\nu_{C=O}$	3040	w	ν_{7a}	2970	mW	3x 12
			3080	w	ν_{20a}	3020	ms	7
			3400	mW	2x $\nu_{C=O}$	3080	w	2
						3360	w	2x 3 + 4
						3380	w	2x 13 + 16

* Wilson's notations are used

s = strong, ms = medium strong, vs = very strong, w = weak,

vW = very weak, sh = sharp, s' = shoulder

 ν = stretching frequency, (-CHO) group.

Table 2. Correlation of fundamental frequencies of pyridine, benzaldehyde, pyridyl 2-, 3- and 4-aldehydes (in cm^{-1})

Modes	Species		Pyridine	Benzalde hyde Ref. 5	Pyridyl 2-alde- hyde	Pyridyl 3-alde- hyde	Pyridyl 4-alde- hyde
	C_{2v}	C_s					
ν_1	a	a'	992	828	780	800	800
ν_{14}	b_1	a'	1375	1311	1370	1380	1385
ν_{18b}	a_2	a'	1482	1489	1455	1460	1490
ν_{18a}	b_1	a'	1439	1453	1420	1415	1410
ν_{2b}	a_2	a'	1580	1595	1570	1570	1590
ν_{2a}	b_1	a'	1572	1583	1550	1535	1560
ν_{9b}	a_2	a'	1218	1166	1140	1185	1190
ν_{18b}	a_1	a'	1068	—	1040	1080	1055
ν_8	b_2	a'	—	1311	1345	1315	1315
ν_{12}	a_1	a'	1029	1000	990	1015	990
ν_{9b}	a_1	a'	605	614	650	650	645
ν_{8a}	b_2	a'	542	437	495	490	490
ν_{10a}	b_1	a''	886	852	840	830	830
ν_{10b}	a_2	a''	749	744	740	755	760
ν_6	b_1	a''	675	—	705	700	720
ν_{18b}	b_1	a''	405	—	430	425	430
ν_{18a}	a_2	a''	374	—	405	410	405
ν_{20a}	a_1	a'	3036	3033	3040	3040	3020
ν_{7b}	a_1	a'	3054	3088	3060	3080	3080

Table 3. Correlation of fundamental frequencies of pyridine, benzaldehyde, pyridyl 2-, 3- and 4-aldehydes (in cm^{-1})

Formalde- hyde	enzalde- hyde	Pyridyl 2-aldehyde	Pyridyl 3-aldehyde	Pyridyl 4-aldehyde	Assignments
1167	1166	1140	1185	1190	(C-H) bending
1743.6	1698	1700	1690	1705	$\nu(O=O)$
—	1204	1170	1205	1220	$\nu(C-CHO)$
2780	2735	—	2740	2730	$\nu(C-H)$ symmetrical
2874	2818	2820	2840	2820	($\nu C-H$) asymmetrical

3. Discussion

Ring Vibrations

Among the symmetrical ring vibrations of pyridine derivatives belonging to point group C_s , the e_{2g} (ν_{8a} and ν_{8b}) are the lowest in frequency. Generally, they appear strongly in all substituted benzenes and pyridines in modified form. The (ν_{8b}) vibration is less sensitive to substitution in comparison to ν_{8a} vibration. The ν_{8a} vibrations has been assigned to a frequency lying between 400–500 cm^{-1} in most of the pyridine derivatives. Its precise value depends upon the mass and nature of the substituent group. In substituted pyridines (Tripathi & Tripathi, 1976 and Green *et al* 1963, 1973) the ν_{8b} vibration is found to increase slightly in magnitude upon substitution. In benzaldehyde (Imanishi 1951) this was reported at 614 cm^{-1} . Three intense and sharp bands at 650, 650 and 645 cm^{-1} in *o*-, *m*- and *p*-isomers of pyridyl aldehydes have been observed and assigned as the ν_{8b} vibration. The ν_{8a} mode has been identified at 495, 490 and 495 cm^{-1} .

There are two prominent frequencies at 992 cm^{-1} (ν_1 , ring breathing) and 1010 cm^{-1} (ν_{12} , trigonal mode) in benzene molecule. These vibration intermix in substituted benzenes. In pyridine they result into two symmetrical ring vibrations having frequency around 800 cm^{-1} (ν_1) and 1000 cm^{-1} (ν_{12}). In substituted pyridines the higher of these two does not vary much. But, the lower one is sensitive to the substitution. In pyridyl 2-, 3- and 4-aldehydes the approximate trigonal (ν_{12}) are assigned at 990, 1015 and 990 cm^{-1} and ring breathing at 780, 800 and 800 cm^{-1} respectively.

In pyridine the mixed (C–C) and (C–N) stretching vibrations are seen in the region 1400–1600 cm^{-1} . However, the intense absorption peaks at 1570, 1570 and 1590 cm^{-1} and 1420, 1455, 1415, 1560 and 1410, 1490 cm^{-1} are assigned to represent the e_{2g} (ν_{8a} and ν_{8b}) and e_{1u} (ν_{13a} and ν_{13b}) modes in the three isomers respectively.

(–CHO) Group Vibrations

In *o*-, *m*- and *p*-pyridyl aldehydes the strong and sharp frequencies are measured at 1700, 1690 and 1705 cm^{-1} . They are very prominent in the spectra. In the substituted pyridines (Green *et al* 1963, 1973), when the substituent group does not contain (C = O) group, such intense frequencies have not been observed around 1700 cm^{-1} . In benzaldehyde (Imanishi 1951) and its derivatives (Jaiswal 1965) a band appears near 1700 cm^{-1} which is interpreted as (C = O) stretching mode. Therefore, the fundamental frequencies around 1700 cm^{-1} in all the pyridyl aldehydes can satisfactorily be assigned as (C = O) stretching mode. Another vibration involving (–CHO) group is stretching of (C–CHO) band. It is clear from table 2 that a fundamental near 1200 cm^{-1} in the infrared spectra of benzaldehyde (Imanishi 1951) and its derivatives appears invariably which

classified it as a characteristic vibration of (-CHO) group. The absorption peaks at 1170, 1205 and 1220 cm^{-1} in the *o*-, *m*- and *p*-pyridyl aldehydes represent the (C-CHO) stretching vibration. The reduction in the magnitude of this frequency in pyridyl 2-aldehyde is attributed to the high electronegativity of the nitrogen atom.

Three strong frequencies at 1140, 1185 and 1190 cm^{-1} are observed in pyridyl 2-, 3- and 4-aldehydes. These bands correspond to e_{2g} (ν_9), the inplane bending of benzene, which lies in the region 1150–1200 cm^{-1} . Ballaus & Wagner (1940) have reported a strong band at 1167 cm^{-1} as (C-H) bending vibration in formaldehyde. Therefore, it is difficult to say whether this (C-H) vibration belongs to pyridine or the substituent group (-CHO).

Acknowledgments

Authors are thankful to University Grants Commission, New Delhi, for financial assistance to SRT. The cooperation of Sri L. K. Dwivedi, Principal, N. D. College, Barhalganj, Gorakhpur, is also acknowledged.

References

- Ballaus, O & Wagner, J 1940 *Z. Physik. Chem.* **B45**, 165.
Green, J H S., Harrison, D J & Kipps, M R 1973 *Spectrochim. Acta* **29A**, 1177.
Green, J H S., Kynaston, W & Paisley, H M 1963 *Spectrochim. Acta* **19**, 549.
Herzberg, G 1945 *Infrared and Raman Spectra of Polyatomic molecules* (D. Van Nostrand Company, Inc., New York).
Imanishi, S 1951 *J Chem. Phys.* **19**, 389.
Jaiswal, R M P 1965 *Spectral Studies of some substituted benzaldehydes* Ph.D. Thesis, Gorakhpur University, Gorakhpur.
Jesson, J P., Kroto, H W & Ramsay, D A 1972 *J Chem. Phys.* **56**, 6257.
Tripathi, G N R & Tripathi, Sita Ram 1976 *Spectroscopy Letters* **9**, 11.

Infrared absorption spectrum of pyrogallol

A K Ansari and P K Verma

Department of Physics, Aligarh Muslim University, Aligarh-202001

Received 23 August 1977, revised 3 October 1978

Infrared spectra of catechol and resorcinol have been well studied by Hidalgo *et al* (1960) and Wilson (1974). Raman spectra of *o*-, *m*- and *p*-dihydroxybenzenes were reported by Kohlrausch *et al* (1934). No such spectral studies have been reported so far for pyrogallol which is a tri-substituted phenol. Therefore the need was felt to record the infrared absorption spectrum of pyrogallol and see the effect of one more OH group to the di-hydroxybenzene.

The chemical used was procured from B.D.H. Co., England and was used as such.

The infrared absorption spectrum of pyrogallol in the KBr pellet was recorded in the region $250\text{--}4000\text{ cm}^{-1}$ on a Perkin Elmer double beam infrared spectrophotometer (model 521) under high resolution. Scan time was 32 minutes. The frequency accuracy is $\pm \frac{1}{2}\text{ cm}^{-1}$. The infrared trace of the said compound is reproduced in the Figure 1. The assignments of all the fundamental frequencies of pyrogallol is given in the Table 1.

Pyrogallol (1, 2, 3-tri-hydroxybenzene) is a tri-substituted benzene. As an approximation we may assume each of the OH groups to behave as a single mass point and lies in the plane of the ring, then the molecule pyrogallol would belong to the point group C_{2v} . Apart from thirty normal modes of vibrations of benzene, there would be some more fundamental vibrations due to substituents.

The choice of the fundamental frequencies is based on general correlation with the spectra of benzene (Herzberg 1945) *m*- and *p*-di-hydroxybenzene (Kohlrausch 1934, 1935), *m*-fluorophenol (Tripathi 1969), 2, 6-; 3, 4-; and 3, 5-di-chlorophenols (Varadarajan *et al* 1971) and 2, 3-; 2, 4; and 2, 5-di-chlorophenols (Shrivastava 1970). Table 1 is self explanatory. We shall, therefore, discuss have only some points.

The C-OH symmetric stretching vibration has been studied by many workers (Kohlrausch 1934, 1935, Tiwari 1966). Kohlrausch *et al* have reported this frequency at 768, 748 and 829 cm^{-1} for *o*-, *m*- and *p*-di-hydroxybenzene. Present authors assign this frequency at 760 cm^{-1} for pyrogallol.

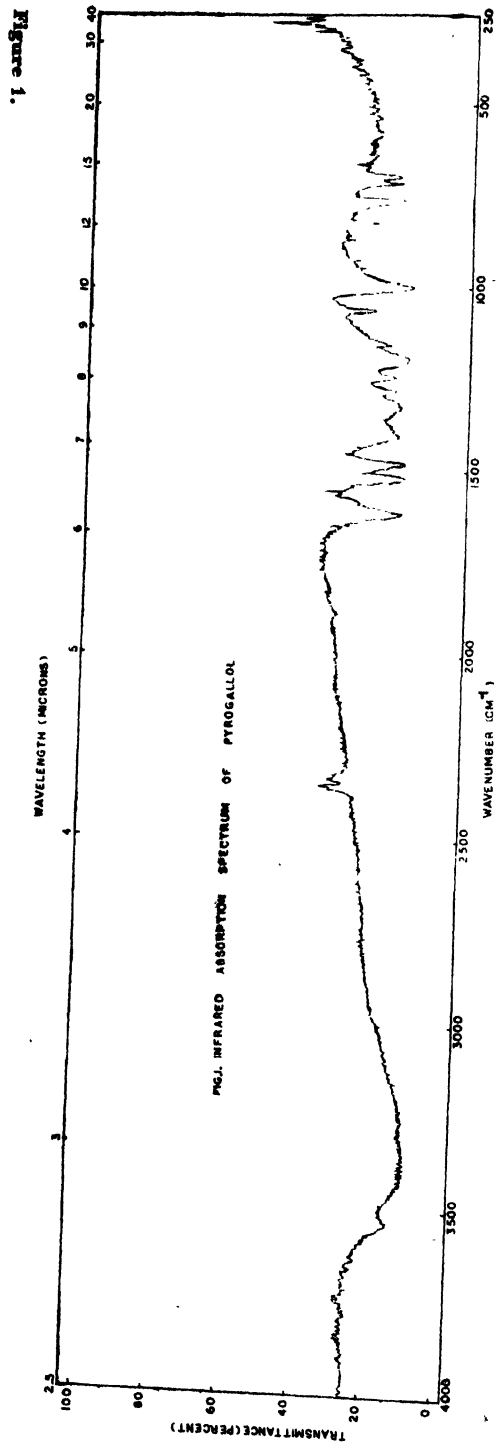


Figure 1.

Table 1. Assignments of the fundamental vibrational frequencies for pyrogallol

Infrared frequencies cm ⁻¹	Intensity	Assignments
255	s	b ₁ C-OH bending o.p.
375	w	b ₁ C-C deformation o.p.
425	ms	b ₁ C-C deformation o.p.
535	w	a ₁ C-C deformation i.p.
660	ms	a ₁ C-C deformation i.p.
715	s	b ₁ C-C deformation o.p.
760	vs	a ₁ C-OH symmetric stretching
825	a	b ₂ or b ₁ C-H bending o.p.
870	s	b ₁ C-H bending o.p.
925	s	b ₁ C-H bending o.p.
1000	s	a ₁ Ring breathing
1060	vs	a ₁ C-H bending i.p.
1155	ms	a ₁ O-H ₂ deformation i.p.
1190	bs	a ₁ C-H bending i.p.
1240	s	a ₁ C-H bending i.p.
1400	b	a ₁ C-C ring stretching
1480	vs	a ₁ C-C ring stretching
1515	vs	a ₁ C-C ring stretching
1540	ms	a ₁ C-C ring stretching
1620	s	a ₁ C-C ring stretching
3030	w	a ₁ C-H stretching
3540	ms	b ₁ O-H stretching

Note : vs = very strong, s = strong, w = weak ms = medium, strong
bs = broad strong, b = broad, i.p. = in-plane, o.p. = out-of-plane.
a₁ = totally symmetric vibrations
b₁, b₂ = Antisymmetric vibrations.

The infrared frequency observed at 255 cm⁻¹ is attributed to C-OH out of-plane bending vibration. In the Raman spectrum of *m*-fluorophenol (Tripathi 1969), the depolarized Raman frequency 240 cm⁻¹ very likely represents the C-OH out-of-plane bending vibration.

Present authors assign the O-H deformation vibration at 1155 cm^{-1} for the said molecule. This assignment is in line with the assignments made by others (Varadarajan 1971, Shrivastava 1970) for the same mode.

The infrared frequency 3540 cm^{-1} is assigned tentatively as O-H stretching frequency. Frequency for this mode has also been reported by Varadarajan (1971) and Shrivastava (1970).

It was not possible to assign the three C-H stretching frequencies in the present investigation. Only one frequency at 3030 cm^{-1} is considered due to C-H stretching mode of vibration.

The authors are grateful to Prof. M. Z. Rahman Khan for his kind interest during the course of work. We are also thankful to Mr. Nizam Ahmad, research scholar (Analytical Chemistry) for giving us the said chemical as a gift. One of us (A. K. Ansari) is thankful to UGC, New Delhi for financial assistance.

References

- Hidalgo A and Otero C 1960 *Spectrochim Acta* **16A** 528
Herzberg G *Infrared and Raman Spectra of Polyatomic Molecules*, D. Van Nostrand Co. Inc. 364 (1945)
Kohlrausch K W F and Pongratz A 1934 *Wein Ber* **143** 358; *Mh. Chem.* **65** 6
Shrivastava S L 1970 *Ind. J. Pure Appl. Phys.* **8** 237
Tripathi G N R 1969 *Ind. J. Pure Appl. Phys.* **7** 517
Tiwari S K 1966 *Ph.D. Thesis*, Banaras Hindu University
Varadarajan T S and Parthasarthy S 1971 *Ind. J. Pure. Appl. Phys.* **9** 401
Wilson H W 1974 *Spectrochim Acta* **30A** 2141

Infrared and ultraviolet absorption spectra of morpholine

Prakash V Shanbhag, M A Shashidhar and K Suryanarayana Rao

Department of Physics, Karnatak University, Dharwad-580003

Received 25 July 1978

Abstract. The infrared and ultraviolet absorption spectra of Morpholine have been recorded and analysed. The assignments of the fundamentals are discussed.

1. Introduction

Although a number of compounds analogous to 1,4-dioxane are known, only the infrared and Raman spectra of cyclohexane (Ramsay and Sutherland 1947, 1950; Beckett *et al* 1947), 1,4-dioxane (Malherbe and Bernstein 1952, Burkett and Badger 1950) and piperazine (Hendra and Powell 1960, 1962), molecules containing two identical heteroatoms, have been thoroughly investigated. Many workers have attempted assignments of observed infrared absorption and Raman bands to fundamental modes of vibration in these molecules. However, little work has been reported in the literature on molecules containing two unlike heteroatoms. In the case of morpholine the infrared (only 650 cm^{-1} upwards) and Raman spectral data have only been reported (Friedel and McKinney 1947) without the bands being analysed and assigned. In contrast to molecules containing two like hetero-atoms, it has been thought interesting and worth while to investigate the spectra of molecules with two unlike heteroatoms. As a step in this direction the infrared (from 400 cm^{-1} upwards) and ultraviolet absorption spectra of morpholine have been recorded with a view to analysing these spectra and assigning the fundamentals to the different modes of vibration of the molecule.

2. Experimental

Pure samples were distilled before use under reduced pressure. Vapour phase spectra were recorded with a medium quartz spectrograph with 10 to 200 cm-cells at -10°C to 150°C . Ilford R-40 plates were used. The accuracy of measurements has been estimated to be $\pm 5\text{ cm}^{-1}$ for sharp bands and $\pm 10\text{ cm}^{-1}$ for broad or diffuse bands. The infrared absorption spectrum of the molecule was recorded using a Perkin-Elmer model 221 double beam automatic spectro photometer equipped with KBr and NaCl optics in the pure liquid state.

3. Results and discussion

The Raman and infrared spectral data as reported in the literature and the infrared spectrum obtained by us in the liquid state are given in Table 1. The infrared spectrum was analysed with the help of the analysed infrared and Raman spectra of similar molecules. The molecule may very nearly belong to C_{2v} symmetry. The ring breathing vibration of cyclohexane, 1,4-dioxane and piperazine occurs at 802, 834 and 836 cm^{-1} . Due to the similarity of the above molecules and morpholine a band near 836 cm^{-1} may well be due to this vibration. Comparison of the Raman spectra of a range of compounds of the type

Table 1. Fundamental vibrational frequencies (in cm^{-1}) of morpholine
(Frequencies from infrared and Raman spectra of morpholine recorded earlier also given for comparison)

Infrared		Raman (Earlier work)	U.V. absorption (Present work)	Tentative assignment
Present work	Earlier work			
—	—	171 vw	178 m	ring deformation
443 m	—	446 vw	433 ms	ring deformation
475 w	—	476 w	—	ring deformation
600 s	—	—	605 m	ring deformation
810 vs	809 vs	—	—	CH_2 rock
836 vs	836 vs	832 vs	834 mw	ring breathing
850 ms	—	—	—	CH_2 rock
880 vs	888 s	—	—	ring stretch
910 s	907 s	—	—	ring stretch
1015 m	1015 m	1011 w	1013 mw	ring stretch
1035 s	1033 m	1034 m	—	CH_2 rock
1065 s	1063 m	1063 w	—	CH_2 rock
1100 vs	1097 vs	1098 m	1102 mw	ring stretch
1120 m	—	1124 vw	—	ring stretch
1145 vs	1142 vs	—	—	N-H out of plane bending
1200 s	1200 s	1200 m	—	CH_2 wag
1230 s	1226 s	—	—	CH_2 wag
1250 s	1248 s	—	—	CH_2 wag
1300 s	1302 s	1305 m	—	CH_2 wag
1320 vs	1317 vs	—	—	CH_2 twisting
1350 s	1348 s	—	—	CH_2 twisting
1395 w	1395 w	—	—	CH_2 twisting
1445 sh	—	1441 w	—	CH_2 deformation
1460 s	—	1460 w	—	CH_2 deformation
1650 m	1650 m	—	—	N-H in-plane bending
2845 vs	2848 vs	2840 ms	—	symmetric C-H stretch
2860 s	—	—	—	symmetric C-H stretch
2925 s	2928 s	2901 w	—	antisymmetric C-H stretch
2955 s	2958 s	2955 vs	—	antisymmetric C-H stretch
3300 s	3300 s	3302 vw	—	N-H stretching

vs = very strong; s = strong; ms = medium strong; m = medium;
mw = medium weak; w = weak; vw = very weak; sh = shoulder

$X(C_2H_4)_Y$, where X and $Y = CH_2, NH, S, O$ etc. given by Hibben (1939), supports the above conclusion. The bands at 895, 910, 1013, 1105 and 1120 cm^{-1} may correspond to the other ring stretching frequencies. Similar frequencies have also been observed in 1,4-dioxane, piperazine and cyclohexane and assigned to the ring stretching frequencies.

By comparison with the assignments of the modes in cyclohexane, 1,4-dioxane and piperazine one may expect to find the hydrogen bonding frequencies separated roughly into the following spectral regions :

- The bands near 1450 cm^{-1} probably due to deformation vibrations,
- wagging vibrations giving rise to bands around 1200–1300 cm^{-1} ,
- twisting vibrations giving rise to bands around 1300–1390 cm^{-1} , and
- rocking vibrations giving rise to bands around 800–1050 cm^{-1} .

The intensities of the infrared bands make a reasonable selection of fundamentals possible since all the other bands can be explained as mostly combinations. The assignment given in Table 1 though consistent with the data may, therefore, have to be regarded as tentative.

Table 2. Assignment of the prominent absorption bands of morpholine

Wave number (cm^{-1}) and Intensity	Assignment	Wave number (cm^{-1}) and Intensity	Assignment
38039 mw	0,0–1102	40105 w	0,0+1400–433
38118 mw	0,0–1023	40132 s	0,0+991
38307 mw	0,0–834	40229 s	0,0+1088
38400 w	0,0–1023–605+666	40304 ms	0,0+1595–433
38465 w	0,0–433–259	40333 w	0,0+534+666
38536 m	0,0–605	40465 w	0,0+2×666
38613 m	0,0–2×259	40541 s	0,0+1400
38708 ms	0,0–433	40620 w	0,0+793+666
38834 m	0,0–1102+793	40736 ms	0,0+1595, 0,0+2×793
38882 ms	0,0–259	40829 w	0,0+900+793
38953 m	0,0–178	40894 w	0,0+1088+666
39092 m	0,0–834+793	40934 m	0,0+793+991
39141 vs	0,0	40949 w	0,0+2×900
49241 mw	0,0+534–433	41027 w	0,0+991+900
39304 mw	0,0+991–834	41065 w	0,0+1400+534
39395 w	0,0+1088–834	41114 w	0,0+3×666, 0,0+2×991
39439 m	0,0+900–605	41192 w	0,0+1400+666
39495 m	0,0+793–433	41260 w	0,0+1088+991
39550 ms	0,0+409	41330 w	0,0+2×1088
39606 m	0,0+900–433	41442 w	0,0+1400×900
39675 ms	0,0+534	41538 w	0,0+3×797
39805 s	0,0+666	41853 w	0,0+3×900
39934 s	0,0+793	42101 w	0,0+3×991
40041 s	0,0+900		

The band system lying in the region λ 2620–2370 Å consists of some what narrow bands and are degraded to the red. The intensity of the 0,0 band confirms the transition as allowed and as π - π^* transition. The study of the temperature effect on band system has facilitated the choice of the band at 39141 cm^{-1} as the 0,0 band. With this band as 0,0 the bands with separations 178, 259, 433, 605, 834, 1032 and 1102 cm^{-1} towards its longer wavelength side are assigned as the ground state fundamentals while the strong bands with shifts 409, 534, 666, 793, 900, 991, 1088, 1400 and 1595 cm^{-1} from the 0,0 band towards its short wavelength side are identified as the excited state vibrational frequencies. On the basis of these ground and excited state frequencies all the observed bands of this molecule can be interpreted. The band data of this system of the molecule are given in table 2.

References

- Beckett C W, Pitzer K S and Spitzer R 1947 *J. Am. Chem. Soc.* **69** 2488
Burkett S C and Badger R M 1952 *J. Am. Chem. Soc.* **72** 4397
Friedel R A and McKinney D S 1947 *J. Am. Chem. Soc.* **69** 604
Hendra P J and Powell D B 1962 *Spectrochimica Acta* **18** 299
Hendra P J and Powell D B 1960 *J. Chem. Soc.* 5105
Hibben J H 1939 *The Raman effect and its chemical applications* p 296
Malherbe F E and Bernstein H J 1952 *J. Am. Chem. Soc.* **74** 4408
Ramsay D A and Sutherland G B B M 1947 *Proc. Roy. Soc. (London)* **A 90** 245, 562

Vibrational spectra of 2-chloro-6-nitro toluene

R B Singh* and D K Rai

Department of Physics, Banaras Hindu University, Varanasi-221005

Received 16 December 1978

Abstract. The infrared ($200\text{--}4000\text{ cm}^{-1}$) and Raman spectra of 2-Cl-6-NO₂ toluene in the liquid phase have been recorded. The vibrational spectrum has been analysed assuming that the molecule belongs to the C_s point group. Tentative assignments for the fundamental vibrations to the various modes of the benzene ring as well as to the internal modes of the methyl and the nitro groups have been proposed.

1. Introduction

Though the vibrational spectra of disubstituted benzenes have been extensively investigated, the study of tri-substituted benzenes, specially when the three substituents are all different, is not well developed. Varsanyi (1969) has developed a system of classifying a substituent as either light or heavy in order to systematise the assignments of observed frequencies to the different benzene modes. On this characterization tri-substitutions containing both "light" and "heavy" substituents have been rarely studied (Green and Harrison 1971). Green (1970) and Green and Harrison (1970) have studied the vibrational spectra of chloro-toluenes as well as nitro-toluenes and this prompted us to undertake the spectral study of tri-substituted benzenes containing NO₂, -Cl and -CH₃. The results of our study of the vibrational spectrum of 2-chloro, 6-nitro-toluene are presented here.

2. Experimental

The compound under investigation was obtained from Fluka A.G. and used without further purification. The colour of the compound is yellow and it has a m.p. $37\text{--}40^\circ\text{C}$.

A small amount of the compound was mixed with Nujol and the infrared absorption was recorded in the region ($200\text{--}4000\text{ cm}^{-1}$) using a Perkin-Elmer Infrared Spectrophotometer (Model 621).

The Raman spectrum was recorded on a 3-prism Steinheil glass spectrograph with a camera of aperture $f/4$. Four mercury discharge lamps running at about

* On leave from S. K. R. College Barbigha, Monghyr (Bhagalpur University).

8-10 Amp. current were used to excite the spectrum. Exposure times ranging from 1/2 hour to 4 hours on a panchromatic film (400 ASA) were needed. Five Raman lines could be recorded on the long wavelength side of the 4358 Å line of Hg which was the exciting line.

3. Results and Discussion

It is customary to treat multiatomic substituents e.g. CH_3 and NO_2 as a point mass so that all substituted benzenes have only 30 normal modes of vibration. Since the molecule under consideration belongs to the C_s point group 21 of these vibrations would be planar and 9 non-planar. In addition to these 30 ring vibrations there would be 15 additional vibrations due to the internal motion in the substituents. For a C_s point group all the vibrations, i.e. whether they are of the type a' or a'' , are both infrared and Raman active. The assignments of the observed frequencies to different modes have been made in analogy with the earlier assignments in ortho-chloro-toluene; ortho-nitro-toluene (Green 1970, Green and Harrison 1970), the 3 isomers of chloro-fluorotoluene (Green and Harrison 1971) and bromoxylenes (Singh and Prasad 1978)

(i) *Stretching vibrations* : $\nu(\text{C-H})$ and $\nu(\text{C-X})$

Benzene has six modes of (C-H) stretching vibrations denoted by the vibrational modes 2, 20a, 20b, 7a, 7b and 13 (in Wilson's notation). These have frequencies 3062 cm^{-1} (a_{1g}), 3080 cm^{-1} (e_{1g}), 3046 cm^{-1} (e_{2g}) and 3060 cm^{-1} (b_{1u}) respectively. In the trisubstituted derivatives proper superposition of these modes would give rise to three nearly pure $\nu(\text{C-H})$ vibrations while the remaining three vibrations would be substituent dependent. The earlier authors (Green 1970, Green and Harrison 1970, Singh and Prasad 1978) have shown that 2, 7a and 20b are the (C-H) vibrations, while 7b, 13 and 20a are the (C-X) vibrations. In the present work out of the three (C-H) stretching frequencies only one frequency corresponding to mode 20b could be observed at 3084 cm^{-1} . This magnitude is quite close to the magnitude of 3080 cm^{-1} observed in benzene for this mode. The three (C-X) stretching frequencies ($\text{X} = \text{Cl}, \text{NO}_2, \text{CH}_3$) have been assigned at 392 cm^{-1} , 1163 cm^{-1} (1164 cm^{-1} in Raman) and 1206 cm^{-1} respectively.

(ii) *Stretching and the Ring Breathing Vibrations* : $\nu(\text{C-C})$

The vibrational modes 8a, 8b, 19a, 19b, 14 and 1 which in benzene have the frequencies 1585 cm^{-1} (e_{2g}), 1485 cm^{-1} (e_{1u}), 1310 cm^{-1} (b_{2u}) and 992 cm^{-1} respectively are the (C-C) stretching vibrations. In general vibration 8a has a frequency below 1600 cm^{-1} whereas vibration 8b appears above 1600 cm^{-1} for the case of vicinal trisubstitution. Also in vicinal trisubstitution we have $19a > 19b$. In the present work we have assigned 8a to 1573 cm^{-1} and 8b to 1603 cm^{-1} whereas 19a and 19b are assigned to the frequencies 1463 cm^{-1} and 1453 cm^{-1} respectively. The mode 14 and 1 are assigned to the frequencies 1218 cm^{-1} and 630 cm^{-1} (634 in Raman) respectively.

Internal Vibrations of the CH₃ Group

$\nu(\text{C-H})$ frequencies for the CH_3 group lie in the range 2920–2985 cm^{-1} . In the present case ν_s and ν_{as} frequencies are assigned at 2920 cm^{-1} and 2940 cm^{-1} .

In 3-Cl-2-F toluene δ_s , δ^+_{as} , δ^-_{as} , δ^-_{as} modes of the CH_3 group are assigned to 1382 cm^{-1} , 1451 cm^{-1} , 1017 cm^{-1} , 1039 cm^{-1} respectively, where as in ortho-chloro toluene the three internal frequencies δ_s , δ^+_{as} and δ^-_{as} have been assigned at 1380 cm^{-1} , 1439 cm^{-1} and 1041 cm^{-1} respectively by Green (1970). In the present work the four internal modes δ_s , δ^+_{as} , δ^-_{as} and δ^-_{as} have been assigned the frequencies at 1383 cm^{-1} , 1430 cm^{-1} , 1013 cm^{-1} and 924 cm^{-1} respectively.

Internal Vibrations of the NO₂ Group

In ortho-nitro-toluene the stretching frequencies ν_s and ν_{as} are identified at 1349 cm^{-1} and 1525 cm^{-1} . In the present case we have taken ν_s and ν_{as} as 1358 cm^{-1} and 1530 cm^{-1} respectively.

Green and Harrison (1970) has assigned the bending vibrations β_s , β_{as} , γ_s in NO_2 group as 860 cm^{-1} , 540 cm^{-1} and 729 cm^{-1} respectively. In the present work we have taken these vibrations as 890 cm^{-1} , 558 cm^{-1} and 728 cm^{-1} .

The assignment of the other observed bands is shown in Table 2.

Table 2.

No.	cm^{-1}	Int.	Over tones and Combination bands
1	1548	s	808+ 728 = 1536
2	1713	w	694+1013 = 1707
3	1723	w	728+ 992 = 1720
4	1759	w	748+1013 = 1761
5	1788	w	694+1080 = 1774
6	1833	s	748+1080 = 1828
7	1903	s	800+1112 = 1912
8	1968	s	800+1163 = 1963
9	1993	s	2 × 992 = 1984
10	2582	w	2 × 1286 = 2572
11	2690	w	1080+1603 = 2683
12	2870	vs	2 × 1430 = 2860 2870 (in Raman)
13	3170	s	1573+1603 = 3176
14	3320	s	392+2940 = 3332
15	3550	s	466+3084 = 3550
16	3790	s	694+3084 = 3778
17	3968	s	872+3084 = 3956

s = strong
vs = very strong
w = weak

Acknowledgments

The authors are grateful to Drs. K. N. Upadhyaya, S. N. Thakur and S. B. Rai of the spectroscopy laboratory for their cooperation and encouragement during the work. They are also indebted to Professor Dr. B. M. Shukla, Head of the Department of Chemistry, Banaras Hindu University, Varanasi for permission to use the Perkin-Elmer (Model 621) Grating spectrophotometer for this work. One of us (RBS) is thankful to U.G.C., New Delhi for financial assistance.

References

- Varsanyi G 1969 *Vibrational Spectra of Benzene Derivatives* Academic Press, New York
Green J H S and Harrison D J 1971 *Spectro. Chim. Acta* **27A** 793
Green J H S 1970 *Spectro. Chim. Acta* **26A** 1913
Green J H S and Harrison D J 1970 *Spectro. Chim. Acta* **26A** 1925
Singh R N and Prasad S C 1978 *Spectro. Chim. Acta* **34A** 39

Longitudinal wave propagation in a relaxing plasma

S R Sharma, T N Bhatnagar and Yashvir*

Department of Physics, University of Rajasthan, Jaipur

Received 16 August 1978

Abstract. Effect of collisions on longitudinal wave propagation in a plasma with an initial anisotropic pressure has been considered with the help of Boltzmann equation using a simple relaxation model. The time evolution of the amplitude and phase of the wave is determined using the Laplace's transform technique. It is found that the collisional damping is significantly affected by pressure anisotropy.

1. Introduction

The study of wave propagation in an anisotropic plasma is of considerable importance for re-entry communications, ionospheric physics and thermonuclear fusion. There are several situations in which a plasma develops anisotropic pressure. In machines employing adiabatic magnetic compressions or expansions, it is frequently the case. Since the collision times are rather long the anisotropic pressure is maintained for sufficiently long times for the propagation of high frequency waves. However, with time the zero order distribution function relaxes gradually to isotropic pressure. Hence the particles of the waves see a gradually changing distribution function which should be taken into account.

Wave propagation in a plasma with anisotropic distribution has been considered by several authors (Anderson 1967, Burt *et al* 1961, Jaggi 1962, Krall 1973, Stix 1963). However, in all these treatments the role of collisions has been completely ignored. Sharma (1968) using fluid equations has investigated the effect of collisions on high frequency propagation in a plasma with anisotropic pressure. But for a proper treatment of the problem the use of Boltzmann equation is required.

In this paper we investigate high frequency longitudinal plasma waves in a relaxing plasma. The initial pressure is assumed to be anisotropic. The collisions are switched on at time $t = 0$ and the system is perturbed. We study the time evolution of the perturbation using Fourier transform in space and Laplace's transform in time.

*Department of Physics, Gyan Vigyan Mahavidyalaya, Banasthali Vidyapith, Rajasthan.

2. Basic equations and dispersion relation

We consider wave propagation along the external magnetic field in a magnetized plasma. Assuming the ions to be stationary, the distribution function of the electrons is governed by the Boltzmann equation

$$\frac{\partial F}{\partial t} + \mathbf{V} \cdot \frac{\partial F}{\partial \mathbf{r}} + \frac{e}{m} (\mathbf{E} + \mathbf{V} \times \mathbf{B}) \cdot \frac{\partial F}{\partial \mathbf{V}} = \nu(F_0 - F) \quad (1)$$

The initial distribution function F_t is supposed to be anisotropic, and these distribution functions are given by

$$F_t = \frac{n_0}{(2\pi RT_{\parallel})^{1/2} (2\pi RT_{\perp})^{1/2}} \exp \left\{ -\frac{V_{\perp}^2}{2RT_{\perp}} - \frac{V_{\parallel}^2}{2RT_{\parallel}} \right\} \quad (2)$$

and

$$F_0 = \frac{n_0}{(2\pi RT_0)^{3/2}} \exp \left\{ -\frac{V^2}{2RT_0} \right\} \quad (3)$$

where $R = \text{Boltzmann constant}/m$.

In this paper, we are interested in the longitudinal electrostatic oscillations propagating along the magnetic field. The Lorentz force term can be dropped in eq. (1) because there is no perturbed magnetic field in this mode. Hence the required kinetic equation is

$$\frac{\partial F}{\partial t} + \mathbf{V} \cdot \frac{\partial F}{\partial \mathbf{r}} + \frac{e}{m} \mathbf{E} \cdot \frac{\partial F}{\partial \mathbf{V}} = \nu(F_0 - F) \quad (4)$$

We divide the perturbed distribution function into (i) slowly varying space independent part F_1 , (ii) and rapidly oscillating perturbed part f_1 , so that

$$F = F_1(\mathbf{V}, t) + f_1(\mathbf{V}, \mathbf{r}, t)$$

with $f_1 \ll F_1$

From (4) we obtain

$$F_1 = F_0[1 - \exp(-\nu t)] + F_t \exp(-\nu t) \quad (6)$$

The perturbed distribution is governed by

$$\nu f_1 + \frac{\partial f_1}{\partial t} + \mathbf{V} \cdot \frac{\partial f_1}{\partial \mathbf{r}} + \frac{e}{m} \mathbf{E}_1 \cdot \frac{\partial F_1}{\partial \mathbf{V}} = 0 \quad (7)$$

Taking Fourier transform in space and Laplaces transform in time of eq. (7) we obtain

$$(\nu + p + i\mathbf{K} \cdot \mathbf{V})f_{\mathbf{k}}(p) = f_{\mathbf{k}}(0) - \frac{e}{m} \mathbf{E}_{\mathbf{k}}(p) \cdot \frac{\partial F_0}{\partial \mathbf{V}} - \frac{e}{m} \mathbf{E}_{\mathbf{k}}(p + \nu) \cdot \frac{\partial F_2}{\partial \mathbf{V}} \quad (8)$$

where $F_2 = F_1 - F_0$

By taking Fourier and Laplaces transform of the relevant Poissons equation, we get

$$\mathbf{k} \cdot \mathbf{E}_{\mathbf{k}}(p) = \frac{e}{i\epsilon_0} \int f_{\mathbf{k}}(p) dV \quad (9)$$

Substituting (8) in (9) and on integrating over the velocities perpendicular to \mathbf{k} , we get

$$(1 + g_0)E_{\mathbf{k}}(p) + (g_{||} - g_0)E_{\mathbf{k}}(p + \nu) = a(p + \nu) \quad (10)$$

where

$$g_{0,||} = \frac{1}{k^2 \lambda_{0,||}^2} \left[\nu A_{0,||} Z(\xi_{0,||}) - \frac{1}{2} \{1 - 2\nu A_{0,||} \xi_{0,||}\} Z'(\xi_{0,||}) \right]$$

$$A_{0,||} = \frac{i}{(2) i k \omega_{pe} \lambda_{0,||}}$$

$$a(p + \nu) = \frac{e}{i\epsilon_0} \int_{-\infty}^{+\infty} \frac{f_{\mathbf{k}}(0)}{(p + \nu + i\mathbf{k} \cdot \mathbf{V})} d^3V$$

$$\xi_{0,||} = p A_{0,||}$$

$$\lambda_{0,||}^2 = \frac{RT_{0,||}}{\omega_{pe}^2}$$

and $Z(\xi_{0,||})$ is the plasma dispersion function. Prime denotes differentiation with respect to the argument. If $\nu \ll p$ eq. (10) can be written as

$$(1 + g_{||})E_{\mathbf{k}}(p) + \nu(g_{||} - g_0)E'_{\mathbf{k}}(p) = a(p) + \nu a'(p) \quad (11)$$

If $\nu = 0$, we get

$$E_{\mathbf{k}}(p) = \frac{a(p)}{(1 + g_{||})} \quad (12)$$

Assuming ν to be small, we solve eq. (11) by iteration and we get

$$E_k(p) = 1 + \frac{\nu(g_{\parallel} - g_0)g'_{\parallel}}{(1+g_{\parallel})^2} \frac{a(p)}{(1+g_{\parallel})} + \frac{\nu(1+g_0)}{(1+g_{\parallel})^2} a'(p) \quad (13)$$

As we are interested in the time evolution of the electric field, we seek the inverse Laplace transform of eq. (13)

$$E_k(t) = \int_{p_0-i\infty}^{p_0+i\infty} \left[\left\{ 1 + \frac{\nu(g_{\parallel} - g_0)g'_{\parallel}}{(1+g_{\parallel})^2} \right\} \frac{a(p)}{(1+g_{\parallel})} + \frac{\nu(1+g_0)}{(1+g_{\parallel})^2} a'(p) \right] e^{pt} dp \quad (14)$$

Integrating the second term of the right-hand side by parts and after rearranging the terms, taking ν to be small, we get

$$E_k(t) = \int_{p_0-i\infty}^{p_0+i\infty} \frac{a(p)e^{pt}}{D(p, k, t)} dp \quad (15)$$

where

$$D(p, k, t) = (1+g_{\parallel}) + \nu t(1+g_0) + \nu g'_0 - \frac{\nu(2+g_0+g_{\parallel})g'_{\parallel}}{(1+g_{\parallel})} \quad (16)$$

The dominant modes of the electric field are given by

$$D(k, \omega, t) = 0$$

where $\omega = ip$

writing

$$D(k, \omega, t) = D_r + iD_i \quad (17)$$

and using asymptotic expansion (Fried *et al* 1961) for plasma dispersion function, we get in long wavelength limit after neglecting small exponential terms

$$D_r(\omega_r, k, t) = 1 - \frac{\omega_{pe}^2}{\omega_r^2} - 3k^2\lambda_{\parallel}^2 \frac{\omega_{pe}^4}{\omega_r^4} + \nu t \left[1 - \frac{\omega_{pe}^2}{\omega_r^2} - 3k^2\lambda_0^2 \frac{\omega_{pe}^4}{\omega_r^4} \right] \quad (18)$$

and

$$D_i(\omega_r, k, t) = \nu \left[12k^2(\lambda_0^2 - \lambda_{\parallel}^2) \frac{\omega_{pe}^4}{\omega_r^6} + \{4 + 6k^2(\lambda_0^2 - \lambda_{\parallel}^2)\} \frac{\omega_{pe}^6}{\omega_r^7} + 6k^2(\lambda_0^2 + 7\lambda_{\parallel}^2) \frac{\omega_{pe}^8}{\omega_r^9} + \left(\frac{\pi}{2} \right)^{\frac{1}{2}} \frac{t\omega_r}{k^3\lambda_0^3\omega_{pe}} \exp(\omega_r^2 A_0^2) \right] + \left(\frac{\pi}{2} \right)^{\frac{1}{2}} \frac{\omega_r}{k^3\lambda_{\parallel}^3\omega_{pe}} \exp(\omega_r^2 A_{\parallel}^2) \quad (19)$$

Putting $D_r(\omega_r, k, t) = 0$, we obtain

$$\omega_r^2 = \omega_{pe}^2 [1 + 3k^2 \{ \lambda_{||}^2 - \nu(\lambda_{||}^2 - \lambda_0^2) \}] \quad (20)$$

while ω_i is given by

$$\begin{aligned} \omega_i &= -D_r(\omega_r, k, t) \left[\frac{\partial D_r}{\partial \omega_r} \right]^{-1} \text{ when } \omega_i \ll \omega_r \\ &= 2\nu \left[1 - 6k^2(\lambda_{||}^2 - \lambda_0^2) \right. \\ &\quad + \left(\frac{\pi}{2} \right)^{\frac{1}{2}} \frac{t}{\lambda_0^3} \left\{ \frac{1}{k^3} - \frac{9k\lambda_{||}^4}{\lambda_0^3} \right\} \exp(\omega_r^2 A_0^2) \\ &\quad + \left(\frac{\pi}{2} \right)^{\frac{1}{2}} \omega_{pe} \left\{ \frac{1}{\nu k \lambda_{||}} \left(\frac{3}{2} + \frac{1}{k^2 \lambda_{||}^2} \right) - \frac{3t(\lambda_{||}^2 - \lambda_0^2)}{\lambda_{||}} \right. \\ &\quad \left. \left(\frac{9k}{\nu} + \frac{1}{k \lambda_{||}^2} \right) - \frac{9k\lambda_{||}}{\nu} \right\} \exp(\omega_r^2 A_{||}^2) \left. \right] \quad (21) \end{aligned}$$

Eq. (20) is the same as obtained by Sharma (1968) but eq. (21) differs from his expression for ω_i . With $\nu = 0$, eqs. (20) and (21) reduce to the well-known expressions (Krall and Trivelpiece 1973). It is seen that for $\lambda_{||}^2 > \lambda_0^2$, the contribution to ω_i from collisional damping decreases significantly, and the first term may become positive for sufficiently short wavelengths and the amplitude may grow with time in the absence of Landau damping. Further we see from eq. (21) that the damping decreases if $\lambda_0 < \lambda_{||}$. This decrease is due to the differential pumping of the thermal energy from one direction to the other. The contribution to Landau damping also depends on the values of $\lambda_{||}$ and λ_0 . However, it can never lead to growing oscillations. For $\nu = 0$, ω_i corresponds to the usual expression for Landau damping.

Acknowledgments

We are thankful to Prof. P. K. Kaw, Physical Research Laboratories, Ahmedabad, for a useful discussion.

References

- Anderson J T 1967 *Proc. Phys. Soc. (London)* **90** 715
 Burt P B and Harris E G 1961 *Phys. Fluids* **4** 1412
 Fried B D and Conte S D 1961 *The Plasma Dispersion Function* (Academic Press, New York and London)
 Jaggi R K 1962 *Phys. Fluids* **5** 949
 Krall N A and Trivelpiece A W 1973 *Principles of Plasma Physics* (McGraw-Hill Book Co.)
 Sharma S R 1968 *J. Phys. A (Proc. Phys. Soc.)* **1** 367
 Stix T H 1963 *The Theory of Plasma Waves*, (McGraw-Hill Book Co.)

Production of radio-frequency oscillations in A/C silent discharge

L C S Murthy and P S V Setty

Department of Physics, Central College Bangalore University,
Bangalore-1

Received 6 December 1978

Abstract. Production of radio-frequency oscillations in A/C silent discharges is reported by a number of workers in this field. The atmosphere surrounding the discharge tube has also been shown to influence considerably A/C silent discharges. It has been shown in this paper that radio-frequency oscillations of exactly the same nature and frequency are produced in a number of other simple circuits wherein no ionized gas is involved. From this a conclusion has been drawn that the gas inside the discharge tube is in no way connected with the production of radio-frequency oscillations.

1. Introduction

A survey of literature on the effect of light on A/C silent discharges through different gases and vapours shows that Radio-frequency Oscillations (Warburg *et al* 1903, Khastgir *et al* 1962, Karnik 1957) are present in these discharges. Three types of discharge tubes such as, sleeve discharge tube, semi-ozonizer and ozonizer are used in these experiments. Oscillographic patterns of these radio-frequency oscillations have also been published (Setty 1958). Further investigation has shown that the atmosphere surrounding the discharge tube has considerable influence on these discharges (Setty 1959, Setty 1960, Setty 1960). Hence the study on the production of radiofrequency oscillations was taken up under various conditions. Four different experiments were designed.

1. Sleeve discharge tube containing saturated vapour of iodine at room temperature.
2. A plain glass tube as described below
3. A high carbon resistance of the order of 100 mega ohms.
4. A metallic pointed edge.

When suitable high voltage is applied to the above mentioned apparatus radio-frequency oscillations were observed. They were exactly same in shape and frequency in all the cases. This fact suggests strongly that the gas inside the discharge tube is in no way connected with the production of radio-frequency oscillations.

2. Experimental Arrangements

1. Sleeve discharge tube containing iodine vapour. The discharge tube circuit employed is shown in Figure 1. When sufficient high A/C voltage is applied, the discharge starts and the radio-frequency oscillations in the discharge circuit are received by properly tuning a radio receiver. Tappings from the output of the intermediate frequency amplifier were taken out and fed to a Cathode ray oscillograph. The radio-frequency oscillations were clearly observed on the screen of C.R.O. which have been photographed.

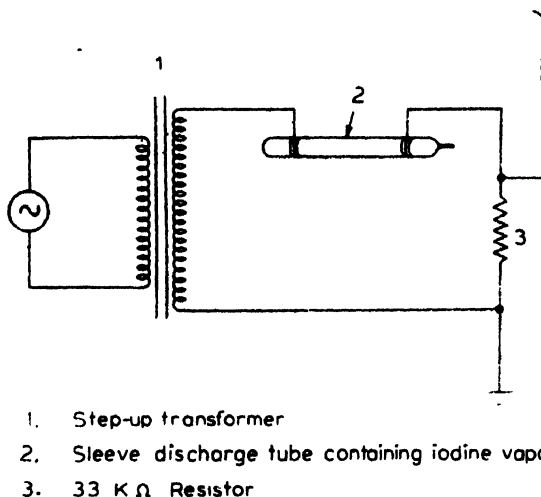


Figure 1. Circuit diagram to study the R/F Oscillations in A/C silent discharges containing iodine vapour.

2. An ordinary glass tube with a coil of copper wire wound inside and a coil of copper wire wound outside forming the two electrodes as shown in figure 2 was used in place of the discharge tube in figure 1 and the same type of radio-frequency oscillations were observed on the C.R.O. screen, when the required A/C voltage was applied.

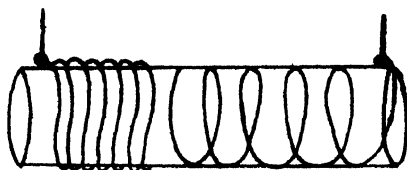


Figure 2. The ordinary glass tube used to study the R/F Oscillation in place of the discharge tube in Figure 1.

3. A very high carbon resistor of the order of 100 mega ohms ($\frac{1}{2}$ watt) is used in place of the discharge tube and the voltage was applied. Radio-frequency

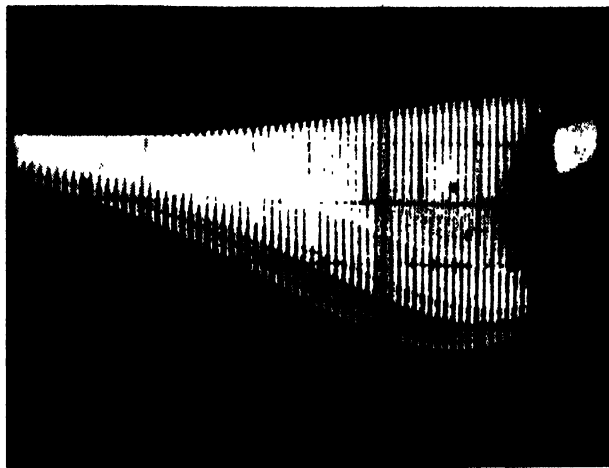


Figure 4(a). CRO patterns of R/F Oscillations observed in the case of iodine sleeve discharge tube.

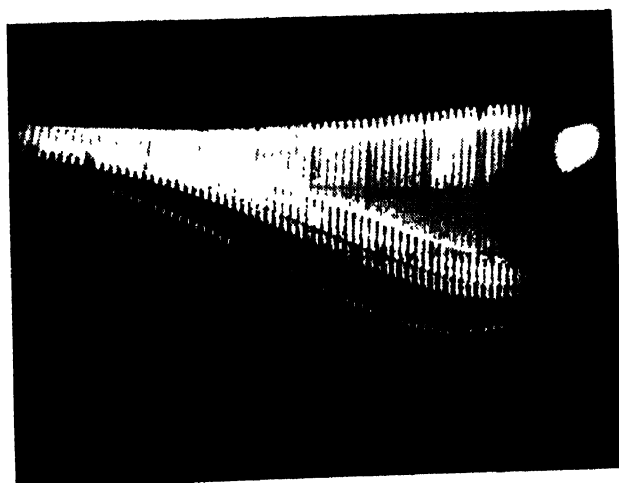


Figure 4(b). CRO patterns of the R/F oscillations observed in the case of the ordinary glass tube.

4. The radio-frequency oscillations shown in Figures 1 to 4 is one of the observed frequencies while a number of other frequencies were also available.

4. Conclusions

From the above observation it can be concluded that the iodine vapour inside the discharge tube does not produce these radio-frequency oscillations. In all the above four cases an insulator of a resistance of the order of 100 mega ohm is involved. Therefore we can say that when a high voltage is applied an electron moves with high velocity in a conductor. Such an electron when suddenly faces an insulator, its motion is obstructed. Such a sudden stoppage of the electron makes it radiate in the form of radio-frequency oscillations. The shape of the R/F oscillation observed suggests that a *vibrating electric charge* (White 1934) is continually damped by the radiation of energy in which case the shape of the damped oscillations resemble that of the C.R.O. patterns observed above.

Acknowledgment

We take this opportunity to thank Professor K. N. Kuchela, Head of the Department of Physics, Central College, Bangalore University, for his constant encouragement and interest. Our thanks are also due to U.G.C. for the financial assistance given for this work. One of the authors (L.C.S. Murthy) is grateful to Bangalore University for having been awarded a U.G.C. fellowship.

References

- Karnik M B 1957 *Indian J. Phys.* **40** 61
Khastgir S R and Setty P S V 1952 *Curr. Sci.* **21** 197
Setty P S V 1958 *Proc. Nat. Inst. Sci., India A* **24** 236
Setty P S V 1959 *Curr. Sci* **28** 195
Setty P S V 1960 *Indian J. Phys.* **34** 187
Setty P S V 1960 *J. Sci. Ind. Res.* **19B** 112
Warburg and Leithauser 1903 *Ann. der. Physik* **28** 1
White H E 1934 *Introduction to Atomic Spectra*, McGraw-Hill Book Co. Inc., New York, Page 421

Letter to the Editors

R K R V curves for A and X states of MgH and MgD molecules

Ganesh K Patel

Department of Physics, V. S. Patel College of Arts and Science,
Billimora

and

Bidhanchandra I Sheth

Department of Physics, South Gujarat University, Surat.

Received 26 May 1977, revised 25 January 1979

Spectroscopic methods are used for understanding conditions prevailing in astrophysical sources. For quantitative spectroscopic studies, knowledge of the potential energy as a function of internuclear distance is needed. It is now known that R K R V potential calculated using methods developed by Rydberg (1931, 1933), Klein (1931), Roos (1947) and Vanderlice (1959, 1960) is more reliable and the Morse potential (1929) is the most commonly used potential.

MgH and MgD systems are of some astrophysical significance. Their spectra have been observed by Guntach (1939). Astrophysical importance of MgH has been emphasised by Balfour and Cartwright (1975). We have calculated RKR curves for (A—X) band system of MgH and MgD using expressions for r_e , f_e and g_e given by Singh and Jain (1962). For MgH, we have used T_e , w_e and $w_e X_e$ given by Khan (1962) and $B_e \propto e$ given by Herzberg (1950). For MgD, we have used molecular constants given by Herzberg (1950). The results are given in tables 1 and 2 for MgH and MgD respectively.

We have compared turning points of RKR potential with those of the Morse potential. We observe that for lower levels of MgH the difference between the turning points of Morse potential and RKR curves are quite small. For higher levels, Morse potential does not seem quite appropriate for MgH. For MgD, the Morse potential is not quite appropriate. Validity of the Morse potential for a given state can be checked by using Pekeris relation (1934). For MgH, the deviation for $A^2\pi$ state is 3% and for $X^2\Sigma$ state is about 12%. For MgD, the deviation for $X^2\Sigma$ state is about 180% and for $A^2\pi$ state it is 220%. This is an agreement with our observations regarding the turning points. Thus our results for RKR curves and the deviation α_e suggest that for reliable calculations of molecular properties like r -centroids, F—C factors etc. for MgH and MgD, one must use RKR potential.

Table 1. Potential energy curves for MgH

State	<i>V</i>	<i>U+Te</i> cm ⁻¹	Turning points (Å)			
			RKR _V		Morse	
			<i>r</i> _{max}	<i>r</i> _{min}	<i>r</i> _{max}	<i>r</i> _{min}
<i>X</i> ² Σ	0	740.4	1.90	1.59	1.90	1.59
	1	2172.6	2.05	1.505	2.05	1.51
	2	3540.0	2.175	1.456	2.18	1.46
	3	4842.6	2.283	1.416	2.29	1.42
	4	6080.0	2.386	1.381	2.38	1.38
	5	7253.5	2.490	1.359	2.49	1.36
	6	8361.6	2.585	1.322	2.60	1.34
	7	9405.0	2.694	1.303	2.71	1.33
	8	10383.6	2.802	1.282	2.81	1.31
	9	11297.4	2.927	1.262	2.94	1.30
	10	12146.4	3.032	1.245	3.06	1.28
	11	12930.4	3.157	1.227	3.21	1.275
	12	13650.0	3.290	1.208	3.34	1.27
	13	14304.6	3.435	1.192	3.49	1.26
	14	14894.4	3.593	1.174	3.66	1.25
	15	15419.2	3.7676	1.154	3.77	1.25
	16	15879.6	3.960	1.135	4.05	1.25
	17	16275.0	4.192	1.111	4.30	1.24
	18	16605.6	4.462	1.084	4.54	1.24
	19	16871.4	4.796	1.052	4.88	1.24
	20	17072.4	5.238	1.011	5.22	1.235
<i>A</i> ² π	0	20025.7	1.849	1.550	1.85	1.54
	1	21560.7	1.995	1.469	1.99	1.46
	2	23031.1	2.109	1.417	2.11	1.41
	3	24438.1	2.214	1.380	2.21	1.37
	4	25781.3	2.314	1.350	2.31	1.32
	5	27060.7	2.412	1.325	2.41	1.29
	6	28276.3	2.511	1.304	2.51	1.27
	7	29428.2	2.610	1.285	2.61	1.26
	8	30516.1	2.713	1.268	2.71	1.25
	9	31540.3	2.818	1.253	1.81	1.24
	10	32500.7	2.927	1.239	2.92	1.235
	11	33397.3	3.042	1.226	3.03	1.23
	12	34230.1	3.163	1.214	3.16	1.22
	13	34999.1	3.291	1.202	3.29	1.22
	14	35704.3	3.429	1.190	3.43	1.22
	15	36345.7	3.578	1.179	3.58	1.21
	16	36923.3	3.743	1.167	3.76	1.20
	17	37434.1	3.925	1.155	3.92	1.20
	18	37884.1	4.130	1.141	4.14	1.19
	19	38273.3	4.369	1.126	4.37	1.19
	20	38595.7	4.651	1.108	4.66	1.18

Table 2. Potential energy curves for MgD

State	V	$U + T_e$ cm^{-1}	Turning points (\AA)			
			RKR		Morse	
			r_{max}	r_{min}	r_{max}	r_{min}
$X^2\Sigma$	0	534.9	1.867	1.606	1.87	1.61
	1	1580.5	1.980	1.522	1.99	1.54
	2	2594.0	2.066	1.466	2.09	1.49
	3	3575.4	2.141	1.422	2.18	1.45
	4	4524.7	2.211	1.385	2.25	1.43
	5	5441.9	2.278	1.351	2.32	1.40
	6	6326.9	2.343	1.321	2.40	1.38
	7	7179.8	2.407	1.292	2.47	1.36
	8	8000.6	2.472	1.262	2.55	1.35
	9	8789.3	2.536	1.240	2.61	1.34
	10	9545.9	2.602	1.216	2.71	1.32
	11	10270.3	2.669	1.192	2.78	1.31
	12	10962.6	2.737	1.169	2.86	1.29
	13	11622.9	2.807	1.146	2.95	1.28
	14	12250.9	2.880	1.124	3.04	1.28
	15	12846.9	2.955	1.102	3.13	1.27
	16	13410.7	3.033	1.080	3.22	1.27
	17	13942.4	3.118	1.057	3.32	1.26
	18	14472.0	3.205	1.035	3.41	1.25
	19	14909.5	3.298	1.012	3.50	1.25
	20	15344.9	3.398	0.988	3.63	1.25
$A^2\Pi$	0	19809.3	1.811	1.559	1.82	1.66
	1	20929.8	1.920	1.477	1.93	1.50
	2	22015.3	2.002	1.423	2.02	1.45
	3	23066.0	2.075	1.380	2.12	1.42
	4	24081.7	2.142	1.343	2.19	1.39
	5	25062.5	2.206	1.310	2.27	1.37
	6	26008.3	2.269	1.280	2.34	1.35
	7	26919.2	2.330	1.252	2.41	1.33
	8	27795.2	2.392	1.226	2.48	1.31
	9	28636.2	2.454	1.201	2.56	1.29
	10	29442.3	2.517	1.176	2.63	1.28
	11	30213.4	2.581	1.153	2.71	1.27
	12	30949.6	2.647	1.130	2.79	1.26
	13	31650.6	2.715	1.107	2.88	1.25
	14	32317.2	2.785	1.085	2.97	1.24
	15	32948.5	2.859	1.063	3.06	1.23
	16	33544.9	2.935	1.041	3.16	1.23
	17	34106.4	3.015	1.018	3.25	1.22
	18	34632.9	3.100	0.996	3.37	1.22
	19	35124.6	3.190	0.973	3.48	1.21
	20	35581.3	3.287	0.950	3.619	1.20

References

- Balfour W J and Cartwright H M 1975 *Chem. Phys. Lett* **32** 85
- Guntch A 1939 *Dissertation*, University of Stockholm
- Herzberg G 1950 *Spectra of Diatomic Molecule*, (D. Van Nostrand Company Inc., Princeton, U.S.A.)
- Khan M A 1962 *Proc. Phys. Soc. (London)* **A80** 523
- Klein O 1932 *Z. Phys.* **76** 226
- Morse P M 1929 *Phys. Rev* **34** 57
- Pekeris C L 1934 *Phys. Rev* **45** 98
- Rydberg R 1931 *Z. Phys.* **73** 376
- Rydberg R 1933 *Z. Phys.* **80** 514
- Rees A L G 1947 *Proc. Phys. Soc.* **59** 998
- Singh N L and Jain D C 1962 *Proc. Phys. Soc.* **79** 274
- Vanderslice J T, Mason E A, Maisch W G and Lippincott E R 1959 *J. Mol Spectrosc.* **3** 17
- Vanderslice J T, Mason E A, Maisch W G and Lippincott E R 1960 *J. Mol. Spectrosc* **5** 83.

Fragment excitation and prompt neutron distribution in fission

Harashit Majumdar

Saha Institute of Nuclear Physics, Calcutta-700009

and

Aparesh Chatterjee

Physics Department, Calcutta University, Calcutta-700009

Received 30 May 1978, revised 8 August 1978

Abstract. A modification of Renormalised Gas Model (RGM) has been attempted with special emphasis on the reformulation of the structure part of excitation energy (U_F^{RGM}) based on simple statistical arguments assuming sufficient adiabaticity of the short and the long range interactions. Fission energy distributions are re-calculated for some well known fissioning nuclei $^{235}\text{U}(n, f)$, $^{239}\text{Pu}(n, f)$ and $^{252}\text{Cf}(s, f)$. Similar calculations are also done for $^{231}\text{Pa}(n, f)$ and $^{237}\text{Np}(n, f)$ for which no experimental results for the distributions (e.g. excitation energy, prompt neutron distribution and their kinetic energy distribution) exist. All our predicted distributions utilise an assumption of the partition of intrinsic structure energy and the nuclear level density parameters. The structural energy partition is estimated here from a modified RGM estimate of the available excitation energy. The predicted distributions are in satisfactory agreement with measurements where available. In particular, the mean number of neutrons, $\bar{\nu}_F$ and the mean neutron kinetic energy $\bar{\eta}_F$ for ^{252}Cf agree well with observations.

1. Introduction

There has been a serious attempt in the last few years to understand the division of available fission energy into the kinetic and the excitation energies of the fragments. In spite of very detailed studies on different aspects of nuclear fission phenomena, this problem is still of central interest.

All attempts to solve this problem aspire to define the total energies at the saddle and scission points of the fissioning nucleus and the fragments respectively. These energies strongly depend on nuclear shell structure, as was pointed out by Strutinski (1965). They may, for example, be obtained from the energy eigenvalues of a single particle Hamiltonian (Nilsson 1955, 1968, 1969) plus pairing terms of the BCS formalism (Bardeen *et al* 1957). Dickmann and Dietrich (1969) showed that the shell effects of two static tangent fission fragments

and the pairing effects can reasonably account for the kinetic and excitation energies of the fragments. Nardi *et al* (1973) have used a realistic level density after Moretto (1970) to calculate the kinetic energies of the evaporated neutrons with the Nilsson model plus the BCS Hamiltonian. Geilikman and Zimina (1976) have calculated the total energy of a fissioning nucleus allowing for the fragment shell effects at the scission point and have estimated the fission fragment excitation energies by including a pre-scission kinetic energy of the fission degrees of freedom.

Nuclear statistical models, first introduced by Fong (1953, 1956), have also been used to tackle this energy partition problem. Kluge and Lajtai (1968, 1969) assumed isothermal equilibrium between the fragments at the scission point to predict the excitation energy of the fragments from the nuclear temperature of the system. An interacting form of Fermi gas model (Sarkar and Chatterjee 1969, 1970; Chatterjee 1970) was developed to statistically include the nuclear structure effects to go into the total energy of the system. The sum of the total nuclear energy plus self-Coulomb energy and the mutual Coulomb energy between the fragments, balanced at the saddle-scission point, were shown to contain terms which can be sorted out to give a natural description of the partition process. The present work is based on this model and is discussed in more details in the next section. Recently, Facchini and Saetta-Menichella (1974) assumed that the degrees of freedom due to intrinsic nuclear structure are in statistical equilibrium while those of fragment motion are not in equilibrium at the scission point. They were able to predict the fragment nuclear temperatures from a large set of averaging over distributions in which the merit of the assumption was not clearly brought out.

2. The RGM and its Application to Fission Phenomena

In an interacting form of the Fermi Gas Model, called the Renormalised Gas Model (RGM) (Sarkar and Chatterjee 1969, 1970, Chatterjee 1970), nuclear structure effects are introduced as suitable energy corrections on top of the Fermi surface ϵ_0 to define the nuclear ground state in a self-consistent way. As the model has been discussed in details in several papers, we very briefly summarise only the basic features.

The RGM correction terms include the single particle combinatorial energy correction f (Rosenzweig 1957), pairing gap Δ , pairing interaction E_P and ground state deformation energy E_β . The quantities Δ , E_P and E_β are calculated from the Belyaev model (Belyaev 1959). The total RGM correction is

$$\partial\epsilon = f - E_\beta - \Delta - E_P = \delta_{LR} + \delta_{SR}, \quad (1)$$

where $\delta_{LR} = f - E_\beta$ (the long range part) and $\delta_{SR} = -(\Delta + E_P)$ (the short range part).

The available fission energy at the saddle-scission point consists of the RGM correction and the nuclear potential energy surface (PES) terms. The total PES energy of a nuclear system A , consisting of Z protons and N neutrons, according to Mosel and Greiner (1968, 1969) is given by

$$E_A(\beta) = \sum_{Z,N} \left(e_i v_i^2 + \frac{\Delta^2}{G} \right) + E_{CA}(\beta), \quad (2)$$

where e_i , v_i and G have their usual meanings; E_{CA} represents the self-Coulomb energy. Assuming that the RGM correction δe is normalised with respect to PES ground state, the total energy $E_I(\alpha_I)$ of fissioning nucleus at its saddle point deformation α_I is approximately equal to the total energy of the nascent binary fragments (neck-to-neck configuration) at the scission point. It was shown that an energy balance equation can be explicitly written to have the form (Sarkar and Chatterjee 1970)

$$\begin{aligned} E_I(\alpha_I) &= E_T(\beta_T) + E_{th} \\ &= \sum_{L,H} \{ E_F(\beta_F) + \frac{1}{2} C_0 (\alpha_F - \beta_F)^2 + C' (\alpha_F - \beta_F)^3 \\ &\quad + E_{CF}(\alpha_F) - E_{CF}(\beta_F) \} + E_{r_0} - E_d + E_q, \end{aligned} \quad (3)$$

where $E_T(\beta_T)$ is the energy of the target nucleus at the ground state deformation β_T and E_{th} is the fission threshold energy to bring the fissioning nucleus to its saddle point; α_F , β_F are the fragment deformations at the scission point and the ground state, respectively; C_0 , C' are the stiffness parameters; the Coulomb interaction terms E_{r_0} , E_d and E_q , in obvious notations, are of the form (Wilets 1964) :

$$E_{r_0} = Z_L Z_H e^2 / (R_{0L} + R_{0H}), \quad (4a)$$

$$E_d = \sum_F E_{dF} = -\frac{1}{2} \sqrt{\frac{5}{\pi}} E_{r_0} (\sum R_{0F} \alpha_F) / \sum R_{0F}, \quad (4b)$$

$$E_q = \sum_F E_{qF} = \frac{3}{5} \sqrt{\frac{5}{4\pi}} E_{r_0} (\sum R_{0F}^2 \alpha_F) / (\sum R_{0F})^2. \quad (4c)$$

The energy release is defined as

$$E_R = E_I(\alpha_I) - \sum_F E_F(\beta_F) = E_K + U. \quad (5)$$

E_K is the total kinetic energy of the fragments and U is their total excitation energy. The excitation U may be further partitioned as follows :

$$U = \sum_F U_F = \sum_{L,H} [U_F^{PES} + U_F^{RGM}]. \quad (6)$$

The term U_F^{PES} contains the PES contribution plus the change in self Coulomb energy of a fragment and the quadrupole interaction E_{qF} :

$$U_F^{PES} = \frac{1}{2}C_0(\alpha_F - \beta_F)^2 + C'(\alpha_F - \beta_F)^3 + \Delta E_{CF} + E_{qF}. \quad (7)$$

The term U_F^{RGM} originates from the static structural corrections to the excitation and can be evaluated from the view point of the RGM. The initial nucleus I and the fragment nuclei F have their own RGM corrections $\partial\epsilon_I$ and $\partial\epsilon_F$ respectively. Assuming that the difference $(\Sigma\partial\epsilon_F - \partial\epsilon_I)$ appears as the excitation energy U_F^{RGM} in the conjugate fragment pairs (U_F^{RGM} for a fragment F), U_F^{RGM} was estimated very crudely from

$$U_F^{RGM} \approx \partial\epsilon_F - \frac{1}{2}\partial\epsilon_I. \quad (8)$$

From these equations the quantities solved were the saddle point deformation α_I , the scission point deformations α_F , the fission barrier, the energy release the kinetic energy and the excitation energies of the fragments.

3. Present Work

In the present work, briefly discussed earlier (Majumdar and Chatterjee 1976), we have introduced several modifications in the RGM formulation. The first modification is a more appropriate choice of Nilsson orbitals; the refined orbitals were found from an iterative method starting from the spherical Nilsson basis to the expected deformation of fragments. Secondly, the self-Coulomb energy and the mutual Coulomb interaction terms were corrected for realistic ground state deformations of the fragment. Finally, the partitioning of the structural part of the excitation energy U_F^{RGM} is assumed, instead of equation (8) used earlier, to depend on a (long range) part of nuclear interactions (shell structure and deformation) on the one hand and the 'short range' part (gap parameter and pairing interactions) on the other; we use here a new statement of the partitioning of $\partial\epsilon_I$ in particular.

These modifications are discussed in the next three subsections and were used to calculate all relevant fission energies. Some experimentally observable parameters like $\bar{\nu}_F$, $\bar{\nu}$, $\bar{\eta}_F$, $\bar{\eta}$ and \bar{E} related to the evaporated neutrons are estimated from the RGM for the first time. We have calculated the nuclear temperatures T_F and the level density parameters a_F based on our earlier work (Chatterjee *et al* 1976) to compute these quantities.

3.1 Modifications of the RGM in Energy Partition :

We express the energy balance equation in a more general form

$$E_I(\alpha_I, \beta_I, \xi_{SI}) = \sum_F E_F(\alpha_F, \beta_F, \xi_{SF}) + E_N + W, \quad (9)$$

where ξ_S now specifically includes the deformation dependent nuclear structure effects, E_N is the pre-scission kinetic energy and W is the interaction energy. It is convenient to split the first term in (9) into two parts in the form

$$\sum_F E_F(\alpha_F, \xi_{SF}) = \sum_F U_F^{RGM} + \sum_F \overline{E_F(\alpha_F, \xi_{SF})}. \quad (10)$$

The first term U_F^{RGM} is the purely structural contribution to the excitation energy of the fragments. The second term with a bar is an average value over the range of the RGM corrections. This term is now given by terms inside the curly bracket in equation (3). The stiffness parameters C_0 and C' are assumed to have a structure dependence of the form

$$C_{0F} = C_0 \left(1 + \frac{\partial \epsilon}{\epsilon_0}\right)^{-1}, \quad C'_F = C' \left(1 + \frac{\partial \epsilon}{\epsilon_0}\right)^{-1} \quad (11)$$

Proper calculation of E_N in (9) needs a detailed study of the dynamics of the fission process. But as has been pointed out by Nifeneckner *et al* (1973), ambiguous assumptions about the dynamics can be avoided if the fragment excitation energy variances are specifically known; we follow the result of their variance calculations and take $E_N \approx 0$.

The interaction term W in (9) includes terms E_{r0} , E_d , E_q of (3) plus the nuclear potential terms. From penetrability calculations from heavy ion potentials (Thomas 1959, Wilczynsky and Siwek-Wilczynska 1975), we have found that the contribution of the nuclear part is negligible compared to the sum of Coulomb terms. We therefore neglect the nuclear part.

We have replaced the Coulomb terms in (4) by E_r , E'_d , E'_q by using a radial expansion of a deformed surface over the actual ground state deformation of the fragments. The spherical basis used in the earlier work (Sarkar and Chatterjee 1970) is replaced by the more accurate form

$$\begin{aligned} E_r &= E_{r0} \left(1 + \frac{\sum A_F^{1/3} \beta_F}{\sum A_F^{1/3}}\right)^{-1} \\ E'_d &= \sum E'_{dF} = \sum_F E_{dF} (1 + \beta_F) \cdot \left(1 + \frac{\sum A_F^{1/3} \beta_F}{\sum A_F^{1/3}}\right)^{-2} \\ E'_q &= \sum E'_{qF} = \sum_F E_{qF} (1 + \beta_F)^2 \cdot \left(1 + \frac{\sum A_F^{1/3} \beta_F}{\sum A_F^{1/3}}\right)^{-3} \end{aligned} \quad (12)$$

3.2 Treatment of U_F^{RGM} :

It is desirable to replace the crude assumption for the partitioning of $\partial \epsilon_I$ in (8) into the two conjugate fragments by a more accurate description. The

fragments clearly differ in composition, in odd-evenness and pairing and in occupancy in a deformed shell. An unequal weightage of the partition of $\partial\epsilon_I$ is therefore necessary. This is done by conveniently considering separately the pairing properties (the so-called 'short range' part of the interaction) and the occupation properties of the nucleus in a deformed unfilled shell (the so-called 'long range' part). Odd-nucleon fragments get a smaller share of $\partial\epsilon_I$ than the even-even neighbours. Similarly, the midshell nuclei will have a smaller share of $\partial\epsilon_I$ compared to the nuclei near closed shell. Such fragments therefore will have a comparatively greater excitation. Recalling from (1) that the signs of two types of interactions δ_{LR} and δ_{SR} are opposite, the following reasonable assumption of U_F^{RGM} may be made :

$$U_F^{RGM} = \partial\epsilon_F - (\chi_F \delta_{LR} + \lambda_F \delta_{SR}), \quad (13)$$

where χ_F and λ_F are two fractional coefficients giving the relative weights of the long range and the short range effects respectively. Obviously

$$\sum_F \chi_F = \sum_F \lambda_F = 1. \quad (14)$$

3.3 Evaluation of χ_F and λ_F :

A self-consistent simple formalism for χ_F and λ_F should not introduce any new parameters. Our study on the variation of $(f+E_\beta)$ in a major shell shows that (i) it is symmetrical with respect to the midshell where its value is maximum and (ii) the variation is almost linear with respect to Z or N on either side of the midshell. We would therefore expect a comparatively smaller U_F^{RGM} for a fragment nearer to a closed shell than away from it. As $\chi_F \delta_{LR}$ contributes negatively to U_F^{RGM} in (13), this means that the magnitude of $\chi_F \delta_{LR}$ should be greater for a fragment in the closed shell region than that in the midshell nuclides. Writing

$$\delta_{LR} = \sum_F \partial U_I^F, \quad (15)$$

where ∂U_I^F is the contribution of δ_{LR} to the fragment F , a suitable partitioning of δ_{LR} can be achieved by the following simplest assumption

$$\partial U_I^F \propto \frac{1}{D_F} = \frac{1}{|Z_F - Z_F^S| + |N_F - N_F^S|} \quad (16)$$

where Z_F , N_F are the proton and neutron numbers of the fragment F and Z_F^S ,

N_F^S are their corresponding nearest closed shell numbers; D_F is determined from these. For two light and heavy fragments L and H , (16) gives

$$\partial U_I^L / \partial U_I^H = D_H / D_L$$

or

$$\frac{\partial U_I^L}{D_H} = \frac{\partial U_I^H}{D_L} = \frac{\delta_{LR}}{\Sigma D_F} \quad (17)$$

Hence the coefficients χ_F for the fragments, by comparing with (13), are

$$\chi_L = \frac{D_H}{\Sigma D_F}, \quad \chi_H = \frac{D_L}{\Sigma D_F} \quad (18)$$

The coefficient λ_F can be simply estimated, from the Belyaev prescription of short range interactions, from the energy-weighted form

$$\lambda_F = \frac{\Delta_F + E_{PF}}{\Sigma (\Delta_F + E_{PF})} \quad (19)$$

Combining (18) and (19) in (13), we finally get

$$U_{L,H}^{RGM} = \partial \epsilon_{L,H} - \left\{ \frac{D_{H,L}}{\Sigma D_F} \delta_{LR} + \frac{\Delta_F + E_{PF}}{\Sigma (\Delta_F + E_{PF})} \delta_{SR} \right\} \quad (20)$$

This replaces the earlier simple equation (8).

3.4 Energy Balance and Energy Release Equations :

Combining equations (3), (10), (11), (12) and (13) and recalling the simplifications and approximations introduced in the symbolic energy balance equation (9), we explicitly display here all terms and quantities in our working formula :

$$\begin{aligned} E_I(\alpha_I, \xi_{SI}) = & \sum_F \{ E_F(\beta_F) + \frac{1}{2} C_{0F}(\alpha_F - \beta_F)^2 + C'_{FF}(\alpha_F - \beta_F)^3 + \Delta E_{CF} \\ & + \sum_F \{ \partial \epsilon_F - (\chi_F \delta_{LR} + \lambda_F \delta_{SR}) \} \\ & + E_r \left(1 + \frac{\Sigma A_F^{1/3} \beta_F}{\Sigma A_F^{1/3}} \right)^{-1} \left[1 - \frac{1}{2} \sqrt{\frac{5}{\pi}} \cdot \frac{\sum_F (1 + \beta_F) A_F^{1/3} \alpha_F}{\Sigma A_F^{1/3}} \cdot \left(1 + \frac{\Sigma A_F^{1/3} \beta_F}{\Sigma A_F^{1/3}} \right)^{-1} \right. \\ & \left. + \frac{3}{5} \sqrt{\frac{5}{4\pi}} \frac{\sum_F (1 + \beta_F)^2 A_F^{2/3} \alpha_F}{(\Sigma A_F^{1/3})^2} \cdot \left(1 + \frac{\Sigma A_F^{1/3} \beta_F}{\Sigma A_F^{1/3}} \right)^{-2} \right] \end{aligned} \quad (21)$$

The scission point fragment deformations α_F^S are obtained from the optimisation condition

$$\frac{\partial}{\partial \alpha_F} [E_I(\alpha_I, \xi_{SI}) - \sum_F E_F(\beta_F)]_{\alpha_F = \alpha_F^S} = 0, \quad (22)$$

assuming that the deformations α_L and α_H are independent of each other. The energy release E_R is then given by

$$\begin{aligned} E_R &= E_I(\alpha_I, \xi_{SI}) - \sum_F E_F(\beta_F) \\ &= \sum_F \{ \frac{1}{2} C_{0F} (\alpha_F^S - \beta_F)^2 + C'_{1F} (\alpha_F^S - \beta_F)^3 + \Delta E_{CF} + E'_{qF} \} \\ &\quad + \sum_F \{ \partial \epsilon_F - (\chi_F \delta_{LR} + \lambda_F \delta_{SR}) \} + (E_r + E'_d) \\ &= \sum_F U_F^{PES} + \sum_F U_F^{RGM} + E_K. \end{aligned} \quad (23)$$

3.5 Neutron Emission from Prompt Fragments :

At the post-scission stage, the excitation energy U_F is expended in (i) prompt neutron emission, (ii) cascade γ -emission and (iii) delayed neutron emission. One has therefore to know the fraction of U_F carried away by neutrons and by γ -emission. In the RGM, the term E'_{qF} in (12) is identified with γ -de-excitation. The physical interpretation and explanation is given in the original work (Sarkar and Chatterjee 1970). The energy available for prompt neutron emission is, therefore, $U_F - E'_{qF}$.

Let us assume that all neutrons emitted from a fragment has each a binding energy \bar{B}_F and that the emitted neutron distribution is Maxwellian in the centre-of-mass system. A temperature T_F for a fragment, related to the Fermi gas temperature T_t , is usually defined as (Kluge and Lajtai 1968, 1969)

$$T_F \approx T_t \approx 1 \left| \frac{d \ln \rho(U_F)}{d U_F} \right| \simeq \sqrt{\frac{U_F}{a_F}}, \quad (24)$$

where $\rho(U_F)$ is the level density and a_F is the single particle level density parameter of the fragment. The average kinetic energy for the neutrons from a fragment is

$$\bar{\eta}_F \simeq \frac{3}{2} T_F \simeq \frac{3}{2} \sqrt{\frac{U_F}{a_F}}. \quad (25)$$

The mean number of neutrons emitted by a fragment F is clearly equal to the

ratio of the energy available for neutron emission and the sum of the average neutron binding energy and average kinetic energy of a neutron :

$$\bar{\nu}_F = (U_F - E'_{qF}) / (\bar{B}_F + \bar{\eta}_F). \quad (26)$$

The mean binding energy \bar{B}_F can be taken from binding energy tables (Wing and Varley 1964, Milton 1962). The level density parameter in (24) has been calculated by following the work of Ghosh *et al* (1973) and has been tabulated (Chatterjee *et al* 1976).

3.6 Average Quantities $\bar{\eta}$ and $\bar{\nu}$:

By definition, the average fission neutron energy $\bar{\eta}$ in the centre-of-mass system is

$$\bar{\eta} = \frac{\int \eta \nu(\eta) d\eta}{\int \nu(\eta) d\eta} = \frac{\int \int_{A_F} \eta P_F \nu_F(\eta) d\eta dA_F}{\int \int P_F \nu_F(\eta) d\eta dA_F}, \quad (27)$$

where $\nu(\eta)$ is the number of evaporated neutrons in a fission process with the kinetic energy η . In the last term the double integration is over the kinetic energy η and the fragment mass A_F ; $\nu_F(\eta)$ is the number of neutrons emitted from a fragment F with kinetic energy η . Clearly this differs from $\bar{\nu}_F$ of (26); P_F is the probability of occurrence of fragment F . The assumed Maxwellian shape for the neutron distribution, emitted from a prompt fragment F , can be expressed in the fractional form

$$\frac{\nu_F(\eta)}{\bar{\nu}_F} = \frac{2}{\sqrt{\pi}} \left(\frac{2}{3} \bar{\eta}_F \right)^{-3/2} \eta^{1/2} \exp \left(-\eta / \frac{2}{3} \bar{\eta}_F \right), \quad (28)$$

which substituted in (27) gives

$$\bar{\eta} = \frac{\int P_F dA_F \int \bar{\nu}_F \bar{\eta}_F^{-3/2} \eta^{3/2} \exp \left(-\frac{3}{2} \eta / \bar{\eta}_F \right) d\eta}{\int P_F dA_F \int \bar{\nu}_F \bar{\eta}_F^{-3/2} \eta^{1/2} \exp \left(-\frac{3}{2} \eta / \bar{\eta}_F \right) d\eta} \quad (29)$$

The variables A_F and η are assumed to be independent of each other. Integration over η in the range from 0 to α yields

$$\bar{\eta} = \frac{\int P_F \bar{\nu}_F \bar{\eta}_F dA_F}{\int P_F \bar{\nu}_F dA_F} \simeq \frac{\sum_F Y_F \bar{\nu}_F \bar{\eta}_F \Delta A_F}{\sum_F Y_F \bar{\nu}_F \Delta A_F}. \quad (30)$$

In the last equation, we have approximated the integration by a summation over a wide fragment mass range. The probabilities P_F may be replaced by their corresponding percentage yields Y_F .

The general relationship between the neutron kinetic energy E in the laboratory system to η in the c.m. system is

$$E = \eta + E_f + 2\sqrt{E_f \bar{\eta}} \cos \phi. \quad (31)$$

E_f is the kinetic energy of a neutron moving with the velocity of a fragment and may be taken numerically equal to the fragment kinetic energy per nucleon E_k/A ; ϕ is the neutron emission angle in the c.m. system.

Averaging over all ϕ and E_f gives the average fission neutron energy \bar{E} in the laboratory system as

$$E = \bar{\eta} + \bar{E}_f, \quad (32)$$

where the average \bar{E}_f is given by

$$\bar{E}_f = \frac{\sum_{\text{Pairs}, i} P_i E_{Ki} \Delta A_{Fi}}{\sum P_i A_i \Delta A_{Fi}} \simeq \frac{\sum_i Y_i E_{Ki} \Delta A_{Fi}}{A \sum Y_i \Delta A_{Fi}}, \quad (33)$$

where E_{Ki} and P_i are, respectively, the total kinetic energy for the i -th pair and the probability of its occurrence. As before, percentage yields (Y_i) may be used for P_i . The theoretical $\bar{\eta}$ in (30) has to be corrected for \bar{E}_f to give the experimental fission neutron energy \bar{E} from (32).

The average number of neutrons emitted per fission event ($\bar{\nu}$) can be estimated following the appropriate averaging procedures similar to above. The final results, starting from the general expression

$$\bar{\nu} = \int_{A_F} \int_{\eta} P_F \nu_F(\eta) d\eta dA_F / \int P_F dA_F \quad (34)$$

$$\bar{\nu} \simeq (\sum Y_F \bar{\nu}_F \Delta A_F) / \sum Y_F \Delta A_F. \quad (35)$$

4. Results

To solve the energy balance equation (21), the first step is to obtain the ground state deformations of the fragments. These deformations β_F were found from the Belyaev prescription starting from an average non-zero deformation β_F utilising the Nilsson scheme to give new deformation parameters β'_F which were then used as inputs for the iteration process to finally obtain the stationary ground state deformations β_F and the corresponding deformation energies E_{β_F} . These β_F values were used to solve for the scission point deformations α_L^S and α_H^S . From equations (7), (12), (20) and (23) of the text, we can obtain the values of U_F^{PES} , E_r , E'_a , E'_q , U_F^{RGM} and E_R , respectively.

We have made detailed calculations for the following fissioning nuclei: $^{231}\text{Pa}(n, f)$, $^{235}\text{U}(n, f)$, $^{237}\text{Np}(n, f)$, $^{239}\text{Pu}(n, f)$ and $^{252}\text{Cf}(s, f)$. Of these, the first and the third, undergoing threshold fission, are calculated for the first time. The second and the fourth refer to fission induced by thermal neutrons. Of the several observable characteristics, we particularly compare here our calculations with the following measured quantities: the total energy release E_R , the excitation energy U_F , the total kinetic energy E_K , neutron kinetic energy distribution $\bar{\eta}_F$ as a function of fragment mass A_F , the prompt neutron distribution $\bar{\nu}_F$, the average number of neutrons $\bar{\nu}$ per fission and finally the average fission neutron energy $\bar{\eta}$ (in the c.m. frame) and \bar{E} (in the laboratory frame).

Most of the results given here are in better agreement with the available experimental measurements than the earlier estimates of Sarkar and Chatterjee (1970). In figure 1, the energy release E_R , the total kinetic energy E_K and the fragment excitation energy U_F for $^{235}\text{U}(n, f)$ are plotted. Earlier results of Sarkar and Chatterjee (1970) are also included. We note that the present estimates of E_R agree closely with Wing and Varley (1964). Theoretical studies of Geilikman and Zimina (1976) predict the maximum energy release $E_R^{\text{max}} \simeq 195$ MeV at $A_H/A_L = 1.4$. We predict $E_R^{\text{max}} = 204$ MeV at $A_H/A_L \simeq 1$ in conformity with the estimate of 205 MeV of Wing and Varley (1964).

Our computed values of E_K are in better agreement with the experimental results of Apalin *et al* (1964, 1965) and Unik *et al* (1973), specially in the symmetric and the most asymmetric mass regions. Dickmann and Dietrich (1969) predicted higher kinetic energies than the experimental values (see figures 4a,b,c of their paper) using a model of two touching spheroids; by taking a distance D of about 0.9 fm between the surfaces of two aligned fragments, their predictions were in better agreement with the experimental results but yet left a lot to be desired particularly in the asymmetric region.

The excitation energies are plotted in the bottom part of figure 1. Our calculations agree well (specially for light fragments) with the results of Schmitt *et al* (1966). Theoretical studies by Dickmann and Dietrich also tried to reproduce the saw-tooth structure of U_F . But the general trend using $D = 0.9$ fm is only in qualitative agreement with the experimental results; they attributed this discrepancy due mainly to the assumption of a 'cold' scission. Geilikman and Zimina (1976) predicted the highest fragment excitation to occur at symmetric fission and the minimum excitation energy at $A_H/A_L \simeq 1.3$. Their predictions for the light fragments are higher than our values or than the experimental ones. We predict the maximum to be at $A_F \simeq 114$ and minimum to occur at $A_H/A_L \simeq 1.24$. We also predict some fine structures, e.g. local dips near fragment masses $A \simeq 84$ and 100. These are due to the closure of $N = 50$ shell for $A_F = 84$ and to the proton $2p_1$ subshell closure for $A_F = 100$.

Figure 2 shows new calculations for the neutron induced threshold fission of ^{237}Np . Here E_R values may be compared with Milton (1962) and E_K values with Bennett and Stein (1967) to conclude that the fits are fairly satisfactory.

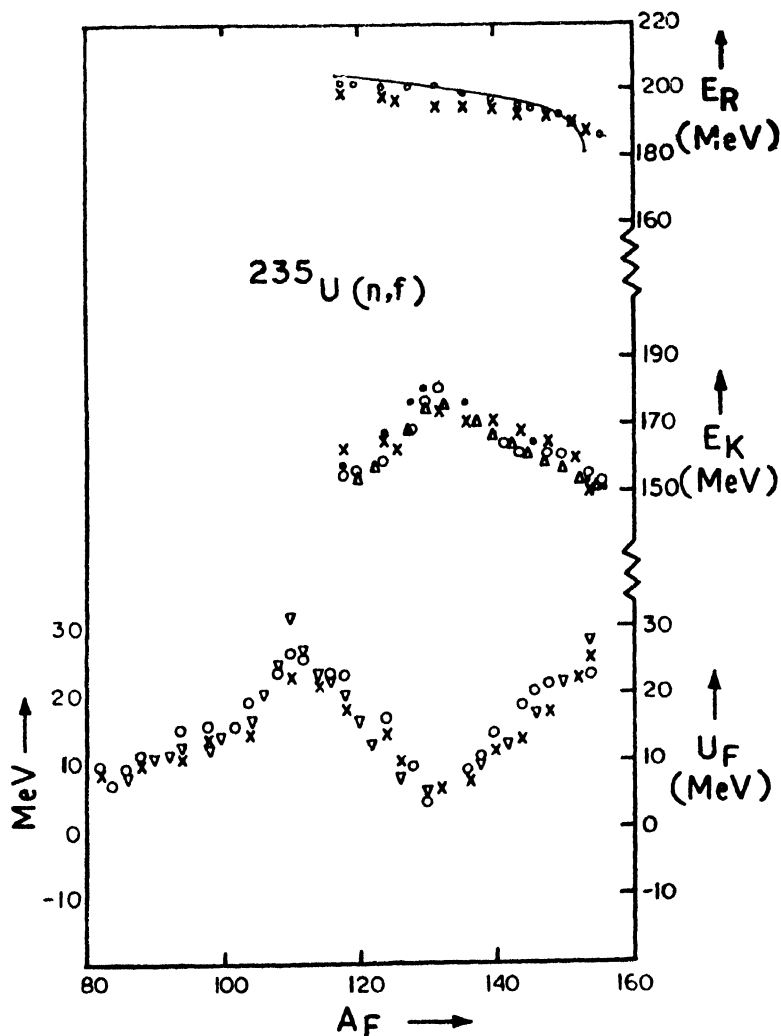


Figure 1. Fission energy distribution for $^{235}\text{U} + \text{thermal } n$.

O : Present Results, X : Sarkar & Chatterjee (1970); ∇ : Aplain *et al* (1964, 1965); Δ : Schmitt *et al* (1966); \bullet : Unik *et al* (1973); - : Wing and Varley (1964).

Our predicted saw-tooth shape in U_F and its associated fine structures are to be experimentally confirmed. Similar trends of all the three quantities for $^{231}\text{Pa}(n, f)$ and the wellknown cases of $^{239}\text{Pu}(n, f)$ and $^{252}\text{Cf}(s.f.)$ are not reproduced here.

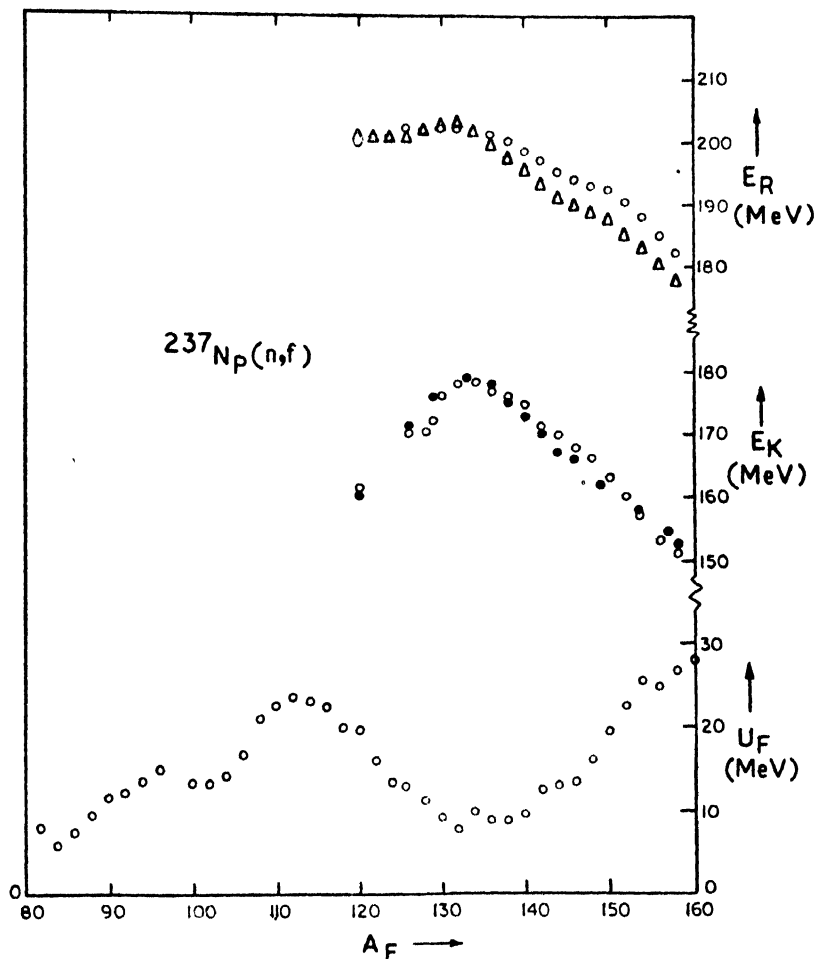


Figure 2. Fission energy distribution for neutron induced threshold fission of ^{237}Np . O : Present results; ● : Bennett and Stein (1976); Δ : Milton (1962).

Figures 3 to 7 show the calculated distribution of the number of prompt neutrons $\bar{\nu}_F$ using the procedure of Sec. 3.5. These distributions were not presented in the earlier fission work with RGM (Sarkar and Chatterjee 1969, 1970, 1971). Uniformly good agreement with experimental results, where available, are observed. For example, the neutron yield peaks for ^{238}U , ^{240}Pu and ^{252}Cf were found at the fragment mass numbers $A_F = 110$, 114 and 120, respectively, as experimentally observed (Apalin *et al* 1964, 1965, Bowman *et al* 1962, Maslin *et al* 1967, Milton and Fraser 1965, Nifenecker *et al* 1973, Signarbieux *et al* 1972). The peaks in the neutron yield curve are at higher available RGM energies near the midshells of $1g_{7/2} + (2d_{5/2}, 1h_{1/2}, 3s_{1/2})^n$. In case of $^{235}\text{U}(n, f)$, although our

maximum value of $\bar{\nu}_F$ is almost 20% greater than these found by Nifenecker *et al* (1973) and Maslin *et al* (1967), we do not have any evidence of high neutron yield values $\bar{\nu}_F = 3.5$ to 4 at $A_F = 110$ and 156 as observed by Apalin *et al* (1964, 1965). However, some fine structures, as was seen by Milton and Fraser (1965) are predicted around $A_F \simeq 90, 96$ and 101. To our knowledge, no experimental results for the neutron distribution exist for $^{231}\text{Pa}(n, f)$ and $^{237}\text{Np}(n, f)$. We predict the neutron yield peak at $A_F \simeq 114$ (see figures 6 and 7) for both. Although the overall shape is again predicted to be a saw-tooth in these two cases, there is a secondary peak in $^{237}\text{Np}(n, f)$ and there is the existence of structures in the neighbourhood of peak position in $^{231}\text{Pa}(n, f)$. It is interesting that the peak and the structures correspond closely to the symmetric fission in $^{231}\text{Pa}(n, f)$.

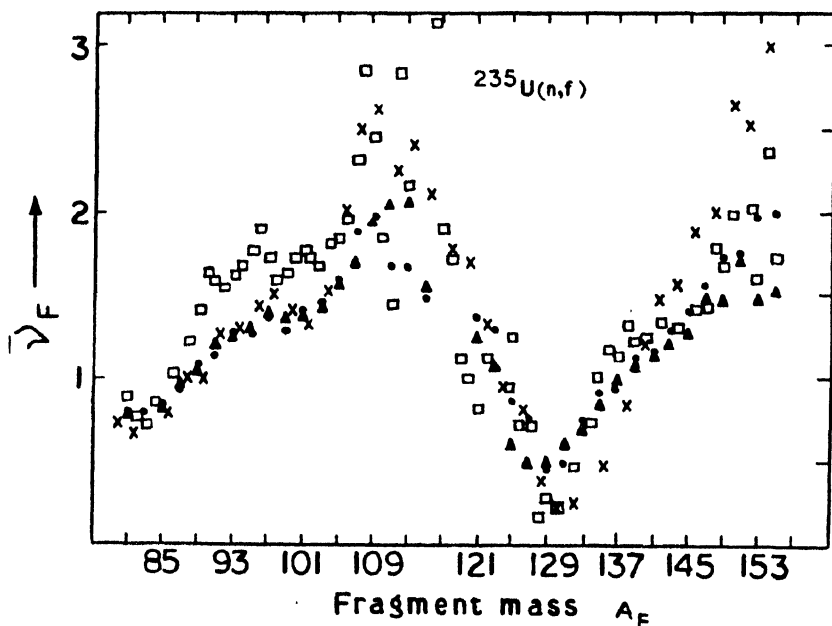


Figure 3. Distribution of prompt neutron number $\bar{\nu}_F$ as a function of prompt fragment mass A_F for the thermal neutron induced fission of ^{235}U . X : Present results; ● : Nifenecker *et al* (1973); ▲ : Maslin *et al* (1967); □ : Milton and Fraser (1965).

Figure 8 shows the variation of $\bar{\eta}_F$ with fragment mass A_F for $^{252}\text{Cf}(s, f)$. The study of this distribution was not attempted in the earlier work (Sarkar and Chatterjee 1969, 1970 and 1971). This case has been experimentally studied by Bowman *et al* (1963). Although the general trends and magnitudes approximately agree, the discrepancy in the mass region $A_F \simeq 125-145$ seems to be real.

We estimate the mean number of fission neutrons $\bar{\nu}$ from equation (35). Experimental percentage mass yield values are taken as inputs (Schmitt *et al* 1966, Bennett *et al* 1967, Unik *et al* 1973, Fraser *et al* 1963). Average fission neutron energies $\bar{\eta}$ and \bar{E} are calculated from (30) and (32), respectively. Our values for $\bar{\eta}$ and \bar{E} are compared with those of other workers in table 1.

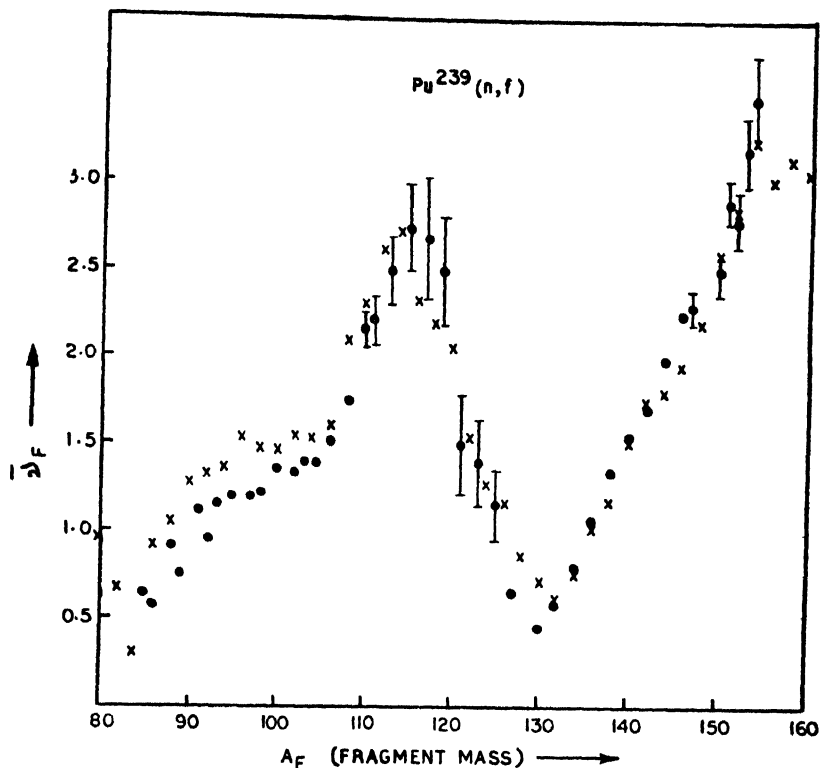


Figure 4. $\bar{\nu}_F$ vs. A_F for the thermal neutron induced fission of ^{239}Pu .
X : Present results; ● : Apalin *et al* (1964, 1965).

5. Discussion and Conclusion

In all detailed work aimed at obtaining the partition of available energy, the dynamics of the fission process contributing to a delicate balance of interactions at suitable energy points is important. The construction of the energy balance equation at such points with appropriate interactions is therefore crucial. In the energy balance equation (21) used by us, no important energy-contributing terms seem to have been left out. A direct proof is the average fit of total energy release E_R within $\sim \pm 2\%$ in all cases with experiments; the average kinetic energy fit is within $\sim \pm 1\%$ and the average excitation energy fit is within $\sim \pm 3\%$. The magnitudes and trends agree in all cases without any normalisation.

tion. Local deviations are often large but are randomly distributed in the three directly measurable quantities E_R , E_K and U_F ; large deviations in particular appear in the symmetric mass region where experimental accuracy is known

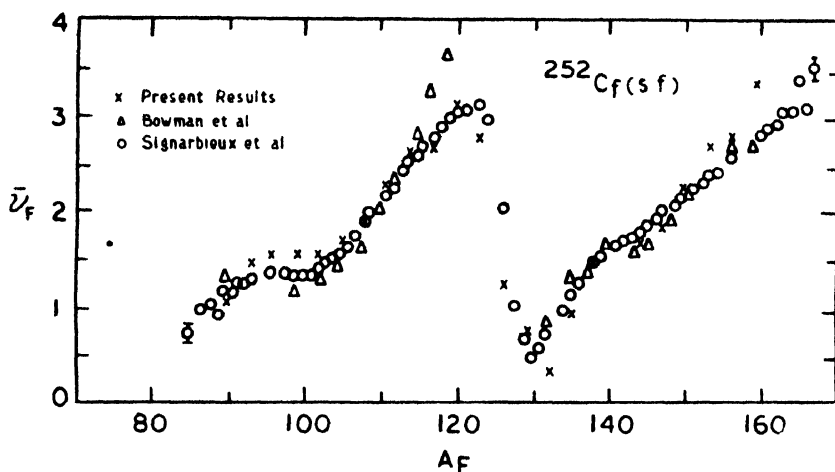


Figure 5. \bar{v}_F vs. A_F for the spontaneous fission of ^{252}Cf . X : Present results; Δ : Bowman *et al* (1963); O : Signarbieux *et al* (1972).

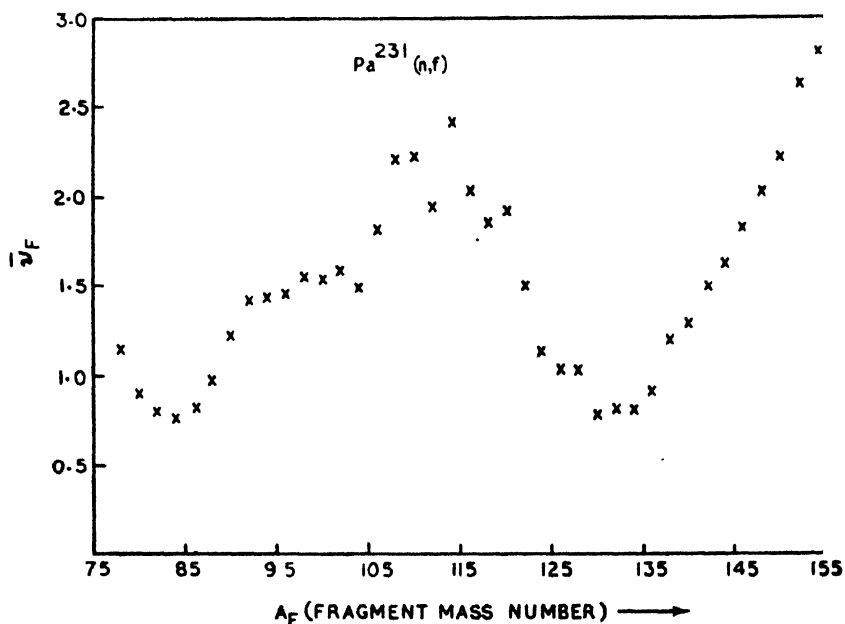


Figure 6. \bar{v}_F vs. A_F for the neutron induced threshold fission of ^{231}Pa . X : Present results.

to be poorer than the average. Our predictive accuracy of the derived quantities like $\bar{\nu}_F$ and $\bar{\eta}_F$ is within $\pm 20\%$, which is also the maximum measured discrepancy of these two parameters, between different groups of experimental workers.

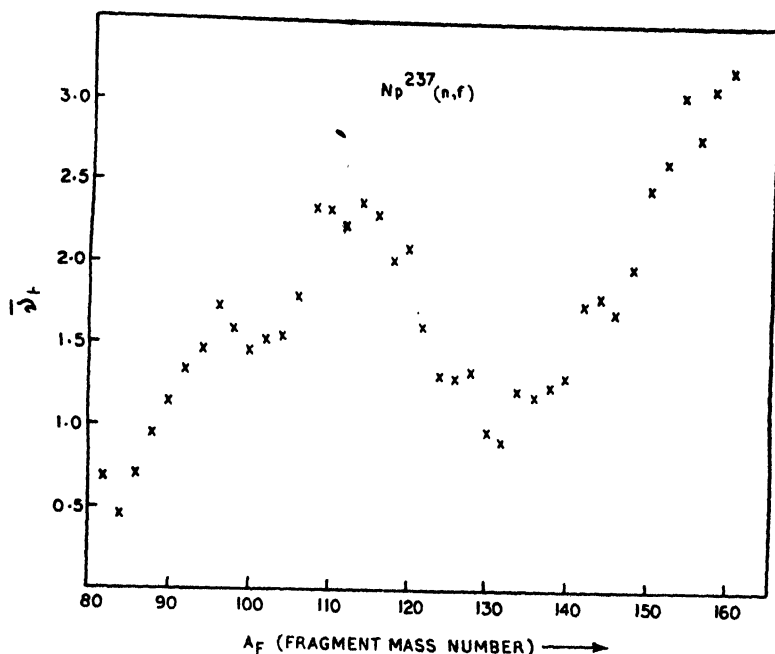


Figure 7. $\bar{\nu}_F$ vs. A_F for the neutron induced threshold fission of ^{237}Np .
X : Present results.

We consider the components of our theoretical energy terms responsible for the energy partition of the fragments. The excitation energy of a fragment, for example, consists of two parts: U_F^{RGM} and U_F^{PES} . U_F^{PES} in addition to the PES expansion terms contains a small part E'_{qF} arising from the mutual Coulomb interaction. A similar term appears in the work of Geilikman and Zimina (1976) who attribute the origin of that term to the interaction of the fragments after scission during the short non-quasistatic stage of the process. They agree with our estimate of this term to be 3–5 MeV. Dickmann and Dietrich (1969) also felt that the inclusion of a Coulomb excitation term and 'other modes' of intrinsic excitation at the scission point might improve the fits with measured excitation energies of the fragments. The gross behaviour of E'_{qF} is shown as E_{qF} in figure 2 of earlier work (Sarkar and Chatterjee 1970). E'_{qF} will have small structural fluctuations in this gross trend. The inclusion of E'_{qF} alone, however, will not improve the fit with experiments. The inclusion of intrinsic excitation energy

(mentioned by Dickmann and Dietrich) has been correctly done in our U_F^{RGM} , giving fairly satisfactory fit for all fragment masses.

The remaining Coulomb interaction terms $E_r + E'_d$ of two touching deformed fragments by our assumption give the total kinetic energy E_K of the fragments. With a choice of $r_0 = 1.40$ fm, the fit in trend and in magnitude with experimental results are shown to be within 2.5%. Since the expansion of the mutual Coulomb interaction terms to higher orders contributes negligibly to E_K , the best value of r_0 was actually adjusted to 1.40 fm.

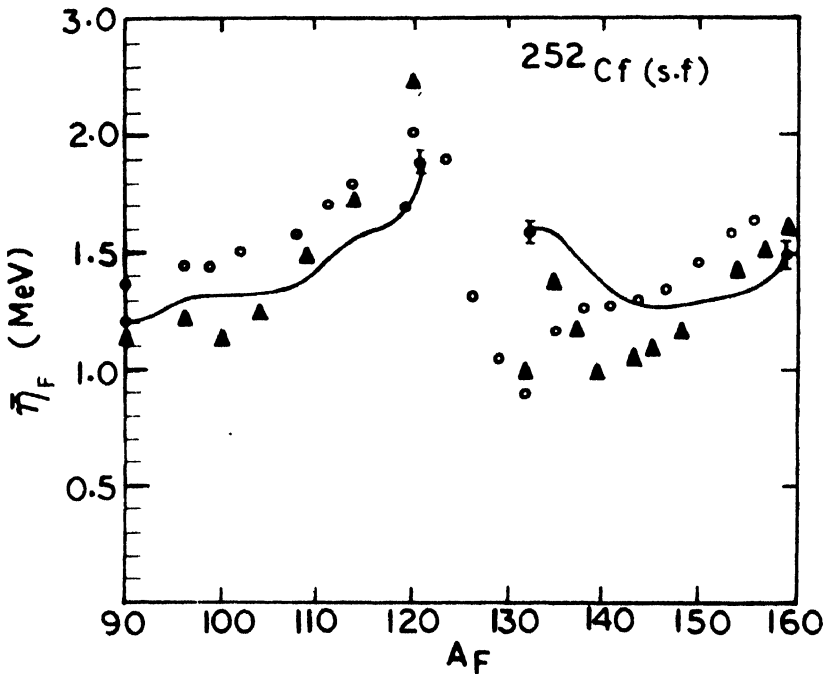


Figure 8. Average centre-of-mass prompt neutron kinetic energy $\bar{\eta}_F$ distribution as a function of fragment mass A_F for the spontaneous fission of ^{252}Cf . O : Present results; -- : Bowman *et al* (1963); Δ : Nardi *et al* (1973). Typical experimental errors are shown by full dots with error bars.

An almost constant observed number of neutrons emitted from fragments in the mass region $A_F \simeq 96$ –102 for all fissioning nuclei agrees with our notion of almost constant excitation of these fragments. The detailed study of the trend of the RGM structural corrections in the fragment mass region $A_F \simeq 93$ –108 predicts that the resultant of the combined corrections remain almost constant. Similar RGM analysis for $A_F \simeq 110$ –120 predicts the structural part to be very sharply peaked in this region.

Table 1. Calculated values of average fission neutron energy (\bar{E}) and average number of prompt neutrons ($\bar{\nu}$) per fission event and the corresponding values obtained by other workers

Target	Type of fission	\bar{E} values in MeV		$\bar{\nu}$ values	
		Present	Other workers and Expts	Present	Other workers
^{235}U	Thermal neutron induced fission	2.018	1.956 ± 0.013 (Proton recoil) ^a	2.432	2.4071 ± 0.0066^c
			2.020 ± 0.025 (He ³ spectrometer) ^a		
			1.96 ± 0.015 (combined average) ^b		
^{239}Pu	Thermal neutron induced fission	2.083	2.136 ± 0.024 (Proton recoil) ^a	3.115	2.8738 ± 0.0090^c
			2.075 ± 0.017 (He ³ spectrometer) ^a		
			2.085 ± 0.015 (combined average) ^b		
^{252}Cf	Spontaneous fission	2.245	2.155 ± 0.024 (Proton recoil)	3.761	3.756 ± 0.012^c
			2.130 ± 0.022 (He ³ spectrometer) ^a		
			2.130 ± 0.03 (combined average) ^b		
^{237}Pa	Threshold fission (neutron induced)	1.995	—	2.650	—
^{237}Np	Threshold fission (neutron induced)	2.075	—	3.109	—

^aWerle and Bluhm (1971), ^bBarnard *et al* (1965), ^cHanna *et al* (1969)

A very stringent test of the internal consistency of our exercise is the prediction of the energy release E_R for different conjugate pairs. This prediction needs a fragment composition or their charge dispersion as inputs. These are usually obtained from the standard tables of Milton (1962) and Wing and Varley (1964). All cases presented here appear in these tables. Our calculations assume the most probable isotopic charge to occur with unit probability. A variant of

our exercise in which the charge dispersion of the fragments can be predicted would allow us to predict the energy release from fragment pairs without reference to these tables. In this case our predicted energy release would be completely independent of the use of any standard mass tables.

The various experimental results for $\bar{\nu}_F$ themselves do not agree within themselves. This discrepancy, being somewhere as high as 30%, is presumably due to the different experimental setups and detectors being used. These features have been critically analysed by Nifenecker *et al* (1973). However, there is a general agreement about the local observed structures in $\bar{\nu}_F$. Our calculations, in general, reproduce these fluctuations.

In the previous section we have indicated the discrepancy in $\bar{\eta}_F$ in the mass region $A_F \simeq 125$ –145 to be real. We also predict a minimum in $\bar{\eta}_F$ at $A_F \simeq 132$, corresponding to the neutron shell closure at $N_F \simeq 82$ and proton shell closure $Z \simeq 50$. The level density parameter a_F shows a local minimum of about 50% of its maximum value at $A_F \simeq 114$, while the excitation energy U_F (also being minimum here) is as low as only 20% of U_F^{max} . The resultant ratio U_F/a_F is still a local minimum at $A_F \simeq 132$ and $\bar{\eta}_F$ follows roughly the same trend as that of U_F or a_F . The results of Nardi *et al* (1973) for $\bar{\eta}_F$ for $^{252}\text{Cf}(s.f.)$ follow our trend; in the mass regions $A_F \simeq 90$ –105 and $A_F \simeq 140$ –155 our values are systematically about 20% higher than theirs but in other regions the two calculations show reasonable agreement.

The present work affords an opportunity to re-evaluate the postulates of RGM and its application to fission phenomena. Our energy balance equation (21) contains parameters which are all pre-determined from the RGM and from the Mosel-Greiner PES. We recall that the energy release E_R is directly obtained without using a mass formula. The fact that the energy release distributions are rather accurately predicted by us without any normalisation in trend and magnitudes shows that no important energy contributing terms have been neglected in our treatment. We must emphasise that no single parameter in equation (21) was adjusted to fission data.

This predictive power of the RGM gives us a neutral opportunity to compare our work with the other important work. For example, Dickmann and Dietrich (1969) added nuclear structure effects to the LDM energy without using any single parameter adjusted to fission data. On the other hand, in RGM the nuclear structure effects are used as corrections to the free Fermi Gas Model. The RGM has been successfully applied to fast neutron reaction cross-sections (Chatterjee 1970) and in problems of nuclear level densities (Ghosh and Chatterjee 1973, Chatterjee *et al* 1976). The RGM also finds a natural application in predicting $\bar{\eta}_F$ and $\bar{\nu}_F$ in fission.

In this work, more emphasis has been given to (i) reformulation of U_F^{RGM} and (ii) the prompt neutrons characteristics in fission. We have shown in particular that a combination of the RGM and the statistical model gives satisfactory answers to prompt neutron distribution $\bar{\nu}_F$, the kinetic energy $\bar{\eta}_F$ distribution and their average values.

Acknowledgments

One of us (HM) is grateful to Prof. D. N. Kundu and Prof. S. K. Mukherjee for their interest and encouragement. We wish to thank Dr. Sudip Ghosh for helpful discussions.

References

- Apalin V F *et al* 1964 *Nucl. Phys.* **55** 249
 Apalin V F *et al* 1965 *Nucl. Phys.* **71** 546
 Bardeen J, Cooper L N and Schrieffer J R 1957 *Phys. Rev.* **108** 1175
 Barnard E *et al* 1965 *Nucl. Phys.* **71** 228
 Belyaev S T 1959 *Mat. Fys. Medd. Dan. Vid Selsk.* **31** No 11
 Bennett M J and Stein W E 1967 *Phys. Rev.* **156** 1277
 Bowman H R *et al* 1963 *Phys. Rev.* **129** 2133
 Chatterjee A, Ghosh S K and Majumdar H *Tables of Nuclear Level Density Parameters (IAEA, Vienna)* Document INDC(IND)-20/U, March 1976
 Chatterjee S 1970 *Nucl. Phys.* **A143** 277
 Dickmann F and Dietrich K 1969 *Nucl. Phys.* **A129** 241
 Facchini U and Sacetta-Menichelly E 1974 *J. Phys. London* **A7** 975
 Fong P 1953 *Phys. Rev.* **89** 332
 Fong P 1956 *Phys. Rev.* **102** 434
 Fraser J S *et al* 1963 *Canad. J. Phys.* **41** 2080
 Gailikman B T and Zimina O V 1976 *Sov. J. Nucl. Phys.* **26** 624
 Ghosh S K and Chatterjee A 1973 *Phys. Rev.* **C7** 840
 Hanny G C *et al* 1969 *Atomic Energy Rev.* **7** No 43
 Kluge G and Lajtai A 1968 *Phys. Lett.* **27B** 65
 Kluge G and Lajtai A 1969 *Phys. Lett.* **30B** 311
 Majumdar H and Chatterjee A 1976 *Proc. Nucl. Phys. & Solid State Phys. Symp.* (Ahmedabad) organised by D A R, (India) **B19** 124
 Maslin E E *et al* 1967 *Phys. Rev.* **164** 1520
 Milton J C D 1962 *Fission Energy Tables* UCRL-9883 (Rev.)
 Milton J C D and Fraser J S 1965 *Physics and Chemistry of Fission* Salzburg (I A E A, Vienna) Vol ii p 39
 Milton E E *et al* 1970 *Energia Nucleare* **17** 936.
 Moretto L G 1970 *Energia Nucleare* **17** 936
 Mosel U and Greiner W 1968 *Z. Physik* **217** 256
 Mosel U and Greiner W 1969 *Z. Physik* **222** 261
 Nardi E, Moretto L G and Thompson S G 1973 *Phys. Lett.* **43B** 259
 Nifenecker H *et al* 1973 *Physics and Chemistry of Fission* Rochester, U S A (I A F A, Vienna) Vol II p 117
 Nilsson S G 1955 *Mat. Fys. Medd. Dan. Vid. Selsk.* **29** No 16
 Nilsson S G *et al* 1968 *Nucl. Phys.* **A115** 545

- Nilsson S G *et al* 1969 *Nucl. Phys.* **A131** 1
- Rosenzweig N 1957 *Phys. Rev.* **108** 877
- Sarkar R and Chatterjee A 1969 *Phys. Lett.* **30B** 373
- Sarkar R and Chatterjee A 1970a *Phys. Rev.* **C1** 619
- Sarkar R and Chatterjee A 1970b *Phys. Lett.* **33B** 263
- Sarkar R and Chatterjee A 1971 *Phys. Rev.* **C4** 944
- Schmitt H W *et al* 1966 *Phys. Rev.* **149** 894
- Signarbioux C *et al* 1972 *J. de Physique* **C5** 33(8-9)
- Strutinski V S *et al* 1965 *Nucl. Phys.* **62** 145
- Thomas T D 1959 *Phys. Rev.* **116** 703
- Unik J P *et al* 1973 *Physics and Chemistry of Fission* Rochester (I A E A) Vienna Vol II p 19
- Werle H and Bluhm H 1971 *Proc. of Consultants Meeting on Prompt Fission Neutron Spectra* Vienna (I A E A,) p 65
- Wilczynsk J and Siwek-Wilczynska K 1975 *Phys. Lett.* **55B** 270
- Wilets L 1964 *Theories of Nuclear Fission* (Oxford Univ Press)
- Wing J and Varley J D 1964 *Argonne National Laboratory Report No. ANL-6886* (unpublished)

Carrier trapping in plasma polymerized ferrocene films

Shireesh D Phadke

Armament Research and Development Establishment, Pashan, Poona 411 021.

Received 24 April 1978

Abstract. The dark electrical conductivity of plasma polymerized ferrocene films has been investigated over the temperature range 300 to 525 K at reduced pressure of 10^{-5} torr. Temperature induced changes in the activation energy E' for ohmic conduction have been observed. From these the presence of an electron trapping level located 0.45 eV below the conduction band edge with density $(3.15 \pm 0.05) \times 10^{15} \text{ cm}^{-3}$ and a donor level of density $(1.38 \pm 0.07) \times 10^9 \text{ cm}^{-3}$ at the same depth are deduced. Above 427 = 9 K conduction process is assumed to be intrinsic.

1. Introduction

Study of electrical properties of plasma polymerized organic films have been reported earlier, Bradley and Hammes (1963). The current-voltage characteristics show space-charge-limited (SCL) conduction in these films at high fields (Phadke *et al* 1978). The study of temperature dependence of the ohmic and SCL currents is of considerable importance as it is capable of providing information about the thermal activation energy of forbidden band, the density of trapping centres and its location below the conduction band. The plasma polymerized ferrocene (PPFa) films has been the subject of such investigations because of its semiconducting nature and unusually high thermal and chemical stability.

In the present paper the author reports his investigations on PPFa for the temperature dependence of dark conductivity over a temperature range 300 to 525 K at reduced pressure and estimates the density of trapping centres and donor levels. The depth of trapping centres and donor levels is also calculated.

2. Experimental

The current measurements were carried out on Al-PPFa-Al sandwich specimen. The sandwich fabrication technique was same as described elsewhere (Bradley and Hammes 1963, Phadke 1978). The thickness of Al electrode was $\approx 2000 \text{ \AA}$ with cross over area of 100 mm^2 . The thickness of polymer films studied was between $1550\text{--}80 \text{ \AA}$, as estimated by Fizeau fringe method. For electrical

measurements the specimen was mounted on an electrically heated copper block placed in a specially designed vacuum cell and evacuated to 10^{-5} torr (Phadke 1978). The temperature was measured by means of chromel/alumel thermocouple fixed on to the specimen. The current and voltage were measured using a vibrating condensor electrometer and a VTVM. The current readings were noted at every interval of 5 K while heating as well as cooling. The electrical field of 2.5×10^3 V cm $^{-1}$ and 3.8×10^5 V cm $^{-1}$ were applied to investigate the ohmic and SCLC conditions respectively.

3. Results and Discussion

Figure 1 shows a typical $\log \sigma$ versus T^{-1} plot for Al-PPFa-Al sandwich for both, ohmic and SCL current conditions. The temperature dependence of ohmic current is identical, within experimental errors, to that of SCL current for lower temperature. While at higher temperature the dependence changes remarkably. It is clear that the ohmic process consists of three different regions each having different gradient and as such is associated with different conduction process with characteristic thermal activation energy. This type of dependence was observed in many organic materials (Yoshino *et al* 1973). Barbe and Westgate (1970) had analysed it in case of pthalocyniene and proposed a band model to account for this non-linearity. Barbe and Westgate's treatment can be applied to present study if we assume that the electrons are majority carriers. This assumption is based on the effect of oxygen on conductivity study (Phadke *et al* 1977) and secondly on the conclusions drawn by β radley and Hammes (1963) and Phadke and Karekar (1978) from their photoconductivity experiments on plasma polymerized films.

To analyse the results a set of electron traps (N_t) and donor levels (N_d) are assumed to be located at a common energy level (E_t) below the bottom of conduction band as shown in Figure 2. Now if the Fermi level (E_F) is at least a few kT below E_t and it is always a several kT above the top of valence band, then Barbe and Westgate's analysis reveals the expression for calculating the conduction electron density (n). The value of n at different temperature conditions are given as follows :

(a) at low temperature when n is much less than the trapped electrons and the thermal release of carriers from donor levels predominate (conduction process is extrinsic) then

$$n = \frac{N_c N_d}{2N_t} \exp \left(\frac{-E_c - E_t}{kT} \right), \quad (1)$$

(b) at an intermediate temperature when the thermal excitation of electron from the valence band is much more to dominate the contribution from donor

state (i.e., the conduction process is neither extrinsic nor intrinsic only, but is in a transition state. Roberts and Schimidlin (1969) has defined this as non-extrinsic and in this case

$$n = N_c \left(\frac{V_v}{2N_t} \right)^{\frac{1}{2}} \exp \left[\frac{-(E_c - E_t/2)}{kT} \right] \quad (2)$$

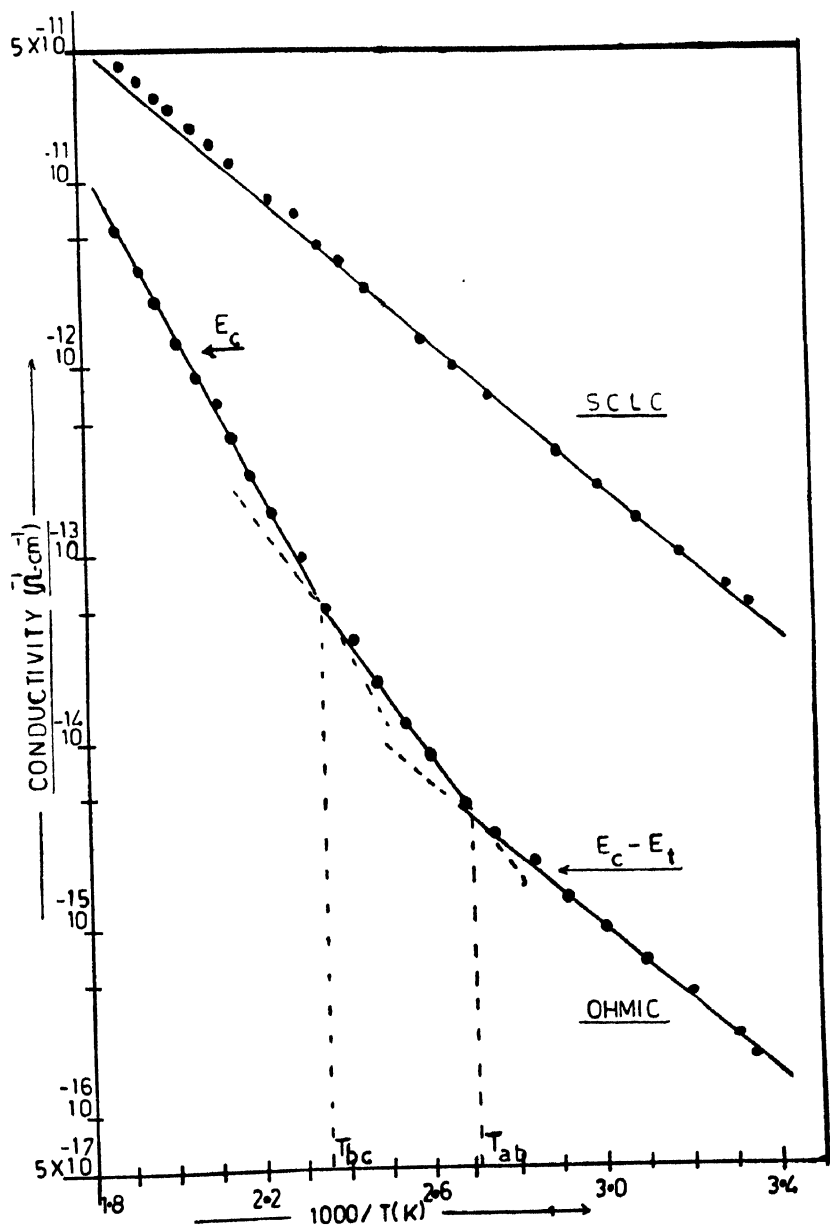


Figure 1. Conductivity—(temperature)⁻¹ variations in (PPFa) films.

(c) lastly at sufficiently high temperature when the conduction process becomes intrinsic then

$$n = (N_v N_c)^{\frac{1}{2}} \exp \left(\frac{-E_c}{2kT} \right). \quad (3)$$

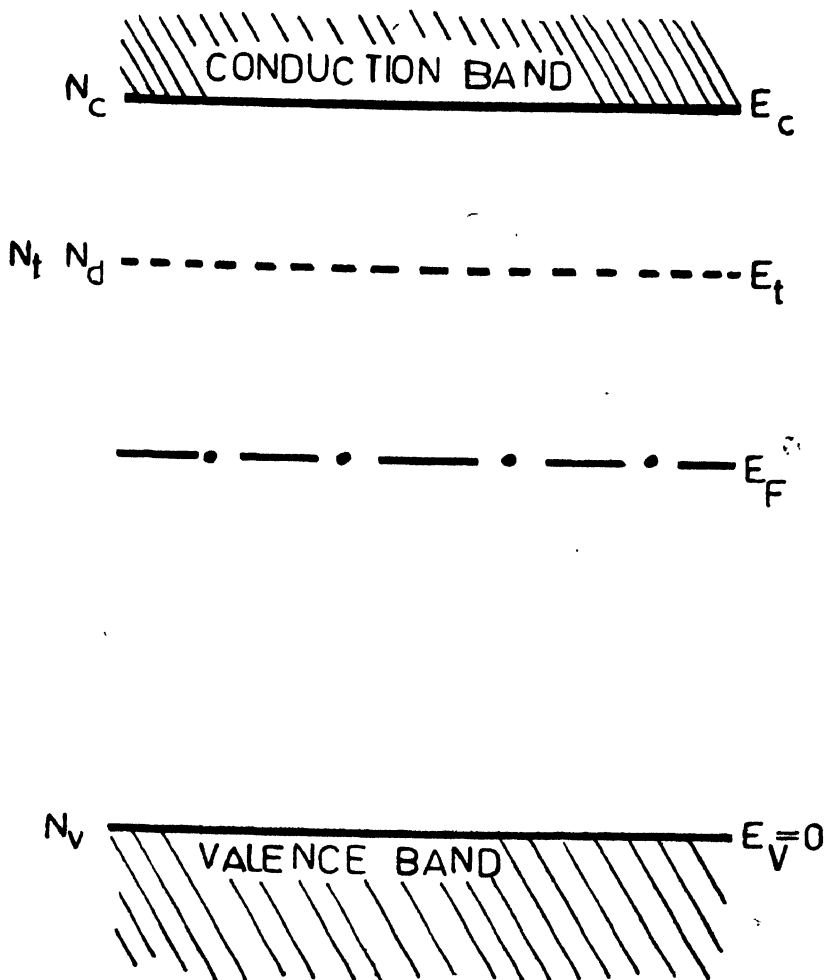


Figure 2. Band model and Trapping states for (PPFa) films.

E_v —energy corresponding to top of valence band

E_F —Fermi level

E_t —energy of the trapping and donor centres

E_c —energy corresponding to bottom of conduction band

N_v —density of states in valence band

N_d —density of donor centres

N_t —density of trapping centres

N_c —density of states in conduction band

These equations account for the three regions which appear in figure 1, each having different thermal activation energy associated with different process of conduction.

If T_{ab} denote the transition temperature from low temperature state of extrinsic process of conduction to intermediate temperature of non-extrinsic process then according to equations (1) and (2).

$$T_{ab} = \frac{E_t}{k} \cdot \frac{1}{\ln(2N_v N_t / N_d^2)} \quad (4)$$

Similarly if T_{bc} is the transition temperature from non-extrinsic process to intrinsic process of conduction then from equations (2) and (3).

$$T_{bc} = \frac{E_c - E_t}{k \cdot \ln(N_e / 2N_t)} \quad (5)$$

Thus the density of trapping centres and donor levels can readily be determined from the two equations by utilizing the experimentally observed transition temperatures T_{ab} , T_{bc} and the activation energies E_c and $E_c - E_t/2$ calculated from the wellknown relationship

$$\sigma = \sigma_0 \exp(-E/kT). \quad (6)$$

The averaged data of five samples are summarized in table 1.

If the effective density of states in the conduction band (N_c) and valence band (N_v) is taken to be 10^{22} cm^{-3} , which is of the order of molecular density (Roberts and Schmidlin 1969) in PPFa films then substituting the data from table 1, the value of N_t is about $(3.15 \pm 0.05) 10^{15} \text{ cm}^{-3}$ and N_d is about $(1.38 \pm 0.07) 10^8 \text{ cm}^{-3}$.

Table 1.

E_c	=	0.8 \pm 0.05 eV
$E_c - E_t$	=	0.45 \pm 0.05 eV
T_{ab}	=	385 \pm 11 K
T_{bc}	=	427 \pm 9 K
Film thickness	=	1550 \pm 80 Å

However the value of N_t recorded in present study differs much from the value ($N_{t_{SCLC}} = 3.25 \times 10^{12} \text{ cm}^{-3}$) reported previously (Phadke *et al* 1978), which was calculated from the space-charge-limited, current-voltage characteristics at 300 K. This deviation may be due to uncertainty in the assumed value of N_c and N_v . Unfortunately there appears to be no previous reported data on PPFa to have a cross check.

5. Conclusions

The results obtained are in accordance with proposed model in which the energy gap between bottom of conduction band and top of valence band is 0.8 ± 0.05 eV. Two temperature induced changes in the activation energy E for ohmic conduction have been observed. For $T < 385 \pm 11$ K; $E = 0.45$ eV; for 385 ± 11 K $< T < 427 \pm 9$ K; $E = 0.6$ eV and for $T > 427 \pm 9$ K; $E = 0.8 \pm 0.05$ eV. The activation energy for SCLC is 0.5 ± 0.02 eV at all temperature investigated. At temperature below 385 ± 11 K the conduction process is consistent with presence of an electron trapping centres located at 0.45 ± 0.05 eV below the bottom of conduction band of density $(3.15 \pm 0.05) 10^{15} \text{ cm}^{-3}$ and donor levels of density $(1.3 \pm 0.07) 10^8 \text{ cm}^{-3}$ at the same depth. Above 427 ± 9 K there is evidence to suppose that the conduction process is intrinsic.

Acknowledgment

The author is thankful to Dr. R. N. Karekar for timely discussions. The experimental work was carried out at Thin Film Division, Department of Physics, University of Poona.

References

- Barbe D F and Westgate 1970 *J. Chem. Phys.* **52** 4046
- Bradley A and Hammes J P 1963 *J. Electro. Chem. Soc.* **110** 15, 543
- Phadke S D, Karekar R N and Sathianandan K 1977 *Symp. Nuclear Phys. and Solid Stat. Phys. D.A.E. (India)* SUA-12
- Phadke S D 1978 *Thin Solid Film* **45** (Feb issue)
- Phadke S D and Karekar R N 1978 *Phys. State Solidi* **A48** (Feb issue)
- Phadke S D, Karekar R N and Sathianandan K 1978 *Thin Solid Films* **48** (in press)
- Roberts G G and Schmidlin F W 1969 *Phys. Rev.* **180** 785
- Yoshino K, Kaneto K, Tatsuno K and Inuishi Y 1973 *J. Phys. Soc. Japan* **35** 120

X-ray diffraction analysis of CaS : Nd phosphors

A S Mehta, V G Machwe, M C Tiwari and R C Saxena*

S. A. Technological Institute, Vidisha (M. P.)

Received 6 November 1975, revised 4 July 1978

Abstract. The CaS : Nd phosphors synthesised from gypsum are characterised by X-ray powder diffraction method. All the samples show uniform growth of only CaS lattice. The site occupied by Nd^{3+} in this lattice as substitutional, could not be ascertained by X-ray work.

1. Introduction

Inorganic solid phosphors are structure sensitive materials. In order to investigate their properties it is necessary to examine their crystal structures. According to Fonda (Fonda 1948a) lattice abnormalities may affect the emission. To know the chemistry involved in doping the phosphors with impurity, X-ray analysis is preferred over chemical analysis because the latter cannot determine the nature of crystallinity of compounds. In this paper we report briefly the crystal chemistry involved and site occupied by impurity in CaS lattice through X-ray powder diffraction analysis.

2. Phosphor preparation

A series of ten samples of CaS : Nd phosphors is prepared on the line of Bhawalkar's method (Bhawalkar 1951). The $\text{CaSO}_4 \cdot 2\text{H}_2\text{O}$ purified from mineral gypsum, activated E-Merck carbon and BDH Hypo as flux were mixed in the ratio of 5 : 1 : 1 respectively by weight along with the known weight of the activator Neodymium and fired at an elevated temperature $920 \pm 10^\circ\text{C}$ (Mohra *et al* 1975) for two hours.

3. Measurements and Results

X-ray diffraction powder pattern is taken on Orwa X-ray film of 35×355 mm using Philips Debye Scherrer powder camera with radius 57.3 mm. The aperture selected is 1 mm in diameter. A thin symmetrically cylindrical rod (about 5 mm dia.) of the phosphor specimen is prepared with the help of 'quick fix' as the cementing material, so that absorption due to Lindemann capillary is avoided. Ni-filtered CuK radiation obtained from sealed Machlett X-ray diffraction tube type-2 is used to take the photographs.

* Department of Physics, M. A. College of Technology, Bhopal (M.P.).

The measurement of the diameter between two corresponding lines around $2\theta = 0^\circ$ and $2\theta = 90^\circ$ of the two holes in the film is done by Carlzeiss Comparator (least count 0.001 mm). The error due to shrinkage is calculated (Buerger 1953) and necessary correction is applied. The lattice spacings ' d ' are calculated and are compared with the standard data given in N.B.S. Circular 539, U.S. Department of Commerce and all the lines are indexed. The exact intensity measurements are not carried out but visual intensities are recorded (Table 1 and 2). Lattice constant ' a ' for each sample, is obtained by Nelson

Table 1. Sample No. 21.

Line No.	Intensity	d Calculated	d Standard	hkl	Phase
1.	V.S.	2.778	2.848	200	CaS
2.	V.S.	1.986	2.013	220	CaS
3.	S.	1.625	1.643	222	CaS
4.	M.S.	1.403	1.423	400	CaS
5.	S.	1.265	1.273	420	CaS
6.	S.	1.152	1.162	422	CaS
7.	M.	0.9986	1.0068	440	CaS
8.	M.S.	0.9408	0.9491	600	CaS
9.	M.S.	0.8906	0.9005	620	CaS
10.	M.S.	0.8521	0.8585	622	CaS
11.	F.	0.8193	0.8220	444	CaS
12.	M.S.	0.7893	0.7897	640	CaS
V.S.	Very Strong.				
S.	Strong.				
M.S.	Medium Strong.				
F.	Feeble.				
M.	Medium.				

Table 2. Sample No. 25.

Line No.	Intensity	d Calculated	d Standard	hkl	Phase
1.	V.F.	3.089	3.178	131	Na_2SO_4
2.	V.F.	2.915	3.118	200	CaSO_4
3.	V.S.	2.843	2.846	200	CaS
4.	V.F.	2.602	2.646	220	Na_2SO_4
5.	V.F.	2.018	2.013	220	CaS
6.	V.F.	1.855	1.850	311	CaSO_4
7.	S.	1.648	1.643	222	CaS
8.	M.S.	1.416	1.423	400	CaS
9.	S.	1.275	1.273	420	CaS
10.	S.	1.167	1.162	422	CaS
11.	M.	1.001	1.0068	440	CaS
12.	M.S.	0.9410	0.9491	600	CaS
13.	M.S.	0.8941	0.9005	620	CaS
14.	M.S.	0.8553	0.8585	622	CaS
15.	F.	0.8200	0.8200	444	CaS
16.	M.S.	0.7894	0.7897	640	CaS

Intensity notations as in table 1 and V.F. = Very Feeble.

and Riley extrapolation method (Nelson and Riley 1945). The variation in 'a' values is plotted against the concentrations of activator in samples (figure 1). The 'a' values along with the ESD values (calculated by formula given in Champion and Davy 1960) are given in table 3.

Table 3. Lattice constant with ESD values and activator concentration.

Sample Nos.	Nd—Concentration in 10 gms. of $\text{CaSO}_4 \cdot 2\text{H}_2\text{O}$ by wt.	Lattice constant 'a'	ESD values
9	2.0×10^{-4} gm.	5.691	± 0.0180
11	6.0×10^{-4} „	5.675	± 0.0380
14	9.0×10^{-4} „	5.695	± 0.0380
17	3.21×10^{-3} „	5.691	± 0.0390
20	7.5×10^{-3} „	5.672	± 0.0210
21	1.0×10^{-2} „	5.688	± 0.0300
22	2.0×10^{-2} „	5.668	± 0.0220
23	4.5×10^{-2} „	4.698	± 0.0390
25	6.5×10^{-2} „	5.702	± 0.0220
27	1.0×10^{-1} „	4.715	± 0.0260

4. Discussions and Conclusions

In the present series of phosphors all the samples show the diffraction lines of CaS. Absence of extra lines indicate that the reduction of $\text{CaSO}_4 \cdot 2\text{H}_2\text{O}$ to CaS has taken place and that a homogeneous lattice of CaS is formed. Sample No. 25 Plate is in this series has a peculiar behaviour. This sample shows 131 and 220 reflections of Na_2SO_4 and 200 and 311 reflections of CaSO_4 which means that the base as well as the intermediary product of the flux used are present in the sample. The strongest line of Na_2SO_4 (IV) transforms to Na_2SO_4 (III) (metastable at room temperature) at ambient temperature. One of the possibilities of deterioration of sample No. 25 can be assigned to the shortage of Carbon in reduction. This shortage does not allow whole of the CaSO_4 to reduce to CaS. The probable equation of semireduction can be :



The resolution of $\alpha_1 \alpha_2$ doublet indicates the quality of crystal formation. If separation between $\alpha_1 \alpha_2$ is large the crystal formation is better and *vice versa*. The sample No. 25 shows minimum separation in $\alpha_1 \alpha_2$ which suggests that the crystal formation is poor, while sample No. 21 Plate 2 has maximum separation

between $\alpha_1\alpha_2$ in the series. It helps in assuming that this sample should normally be the best sample of this series. The fact is supported by the fluorescence of various samples, in which sample No. 21 exhibits intense lines (plate No. 3a) while the sample with higher concentration of activator does not exhibit such strong lines. Probably the quantity of activator added to sample No. 21 is just sufficient to have the peak emission lines. The lower the quantity of activator weaker is the intensity of fluorescence of samples and hence the lines in the spectra (sample No. 14) do not appear (plate No. 3b).

In the present course of study of phosphors the method of synthesis used by us needs justification. The formation of another phase of CaO does not at

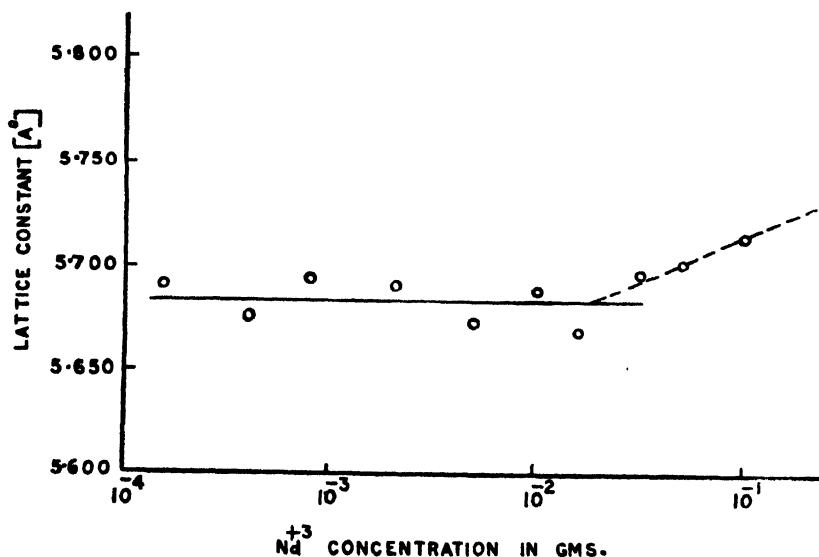
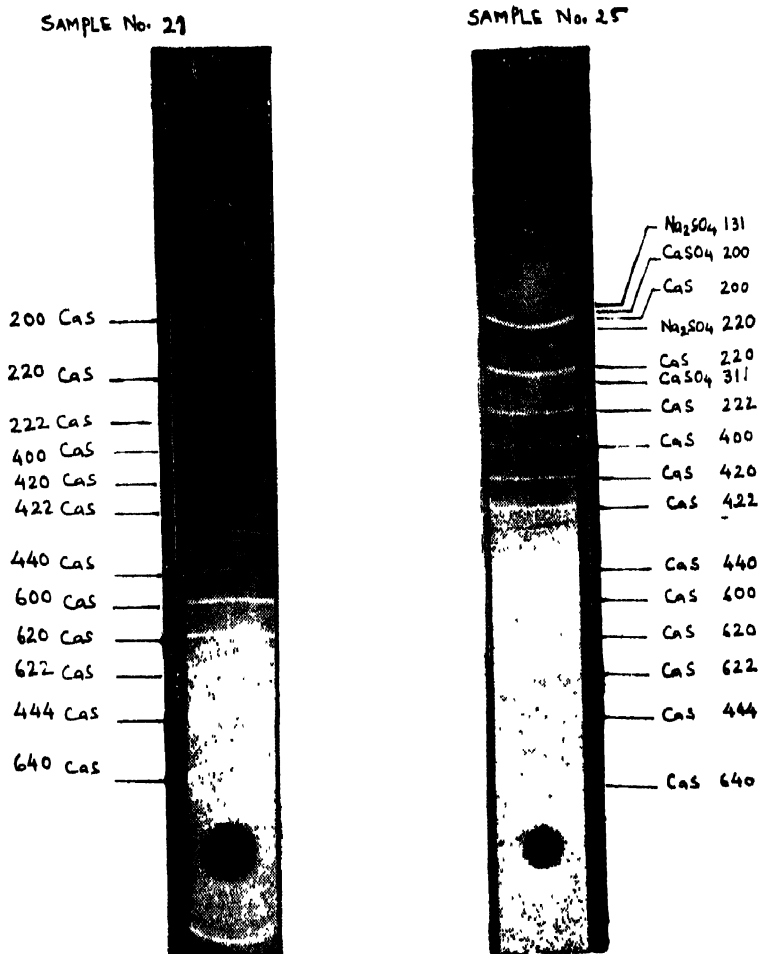


Figure 1. Lattice constant α with increasing concentration of Nd.

all take place as no diffraction lines for this are obtained. It may be due the formation of an intermediate compound Na_2SO_4 during the decomposition of the flux. It does not possibly permit oxygen in the air to be used up by CaSO_4 to get converted to CaO. X-ray diffraction plate No. 2 shows the presence of Na_2SO_4 but not of CaO. One of the authors (Machwe 1969) has confirmed the absence of CaO exactly on the lines of Tunitskaya (Tunitskaya 1953) during the spectral study of CaS:Bi phosphor prepared by the method identical to the present one.

It is important to arrive at the site of impurity atoms in the lattice. The impurity may dissolve via substitution solid solution or forming interstitial solid solution. In CaS lattice Bi does not show any variation in the values of lattice constant when doped at varying concentrations. So Saxena (Saxena



Plates 1 and 2. X-ray diffraction lines of CaS : Nd³⁺ phosphors numbered 21 and 23

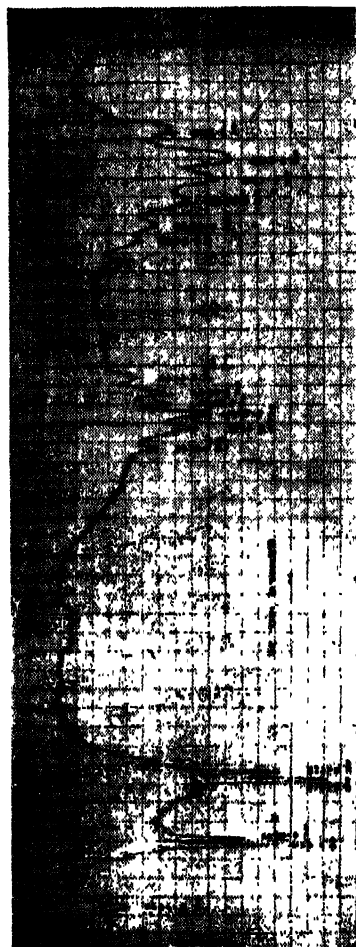
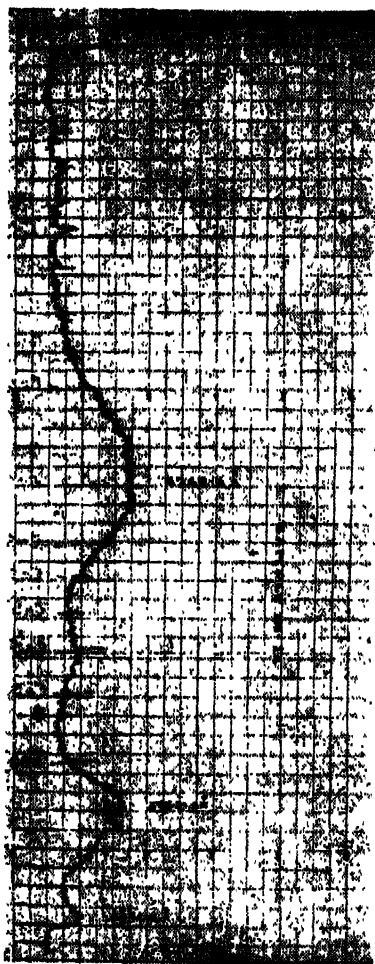


Plate 3a and 3b. Fluorescence record of phosphors No. 21 and 14.

1966) inferred that Bi occupies interstitial site which is a known fact. However, Mn^{2+} goes substitutionally in zinc-orthosilicate for Zn and thereby alters the lattice constant (Rookshy 1947). Similar change in 'a' due to the substitutional site when occupied by the activator is reported (Fonda 1948b and Diwan and Ranade 1969). The substitutional site of Mn^{2+} is confirmed by ESR-studies in CaS-lattice by Nair *et al* (Nair *et al* 1969). The ionic radii of Ca^{2+} , Nd^{3+} and S^{2-} are 0.99, 1.04 and 1.84 Å respectively, while the electronegativity values are 1.0, 1.07 and 2.5 respectively (Cotton and Wilkinson 1962). These data help in suggesting that Nd^{3+} may occupy substitutional site in CaS lattice. The suggestion of Yocom and Larch (Yocom and Larch 1965) seems to have some significance. According to him the Nd^{3+} in CaS lattice may occupy the substitutional site in place of 2Ca^{2+} atoms with a near neighbour vacancy left free for charge compensation by monovalent Na ion spared by flux used in the process. Some vacancies are detected indirectly in the form of F_2^+ and F_3 centres reported by EPR-studies in CaS lattice (Ekbote and Ranade 1972). Substitutional site for Nd^{3+} is reported in ZnS lattice (Larch 1966). The lattice 'a' value thus show a slight variation with the increase of concentration of Nd^{3+} up to 4.2×10^{-2} gm (figure 1), but the change is insignificant. For higher concentration that is up to 1×10^{-1} gm a regular rise in 'a' values (dotted line in the same figure) is observed. If samples of still higher concentration of Nd were prepared probably such a rise would have helped in inferring that Nd goes substitutionally in CaS phosphors. But at the same time higher concentration of activator produces quenching of luminescence. In other words at useful concentrations of activator for luminescence the X-ray diffraction technique, unless very accurate methods are used, seems to be a weaker tool to decide the site occupied by them. Thus without any supporting study to X-ray diffraction, it is not possible to arrive at a definite conclusion that Nd^{3+} occupies substitutional site.

Acknowledgments

The authors are thankful to late Prof. V. S. Dubey and Dr. B D Shrivastava of School of Studies in Physics, Vikram University, Ujjain for providing facilities for experimentation.

References

- Bhawalkar D R 1951 *Saugar University Journal Sagar* (India) **1** 209
Buerger M J 1953 *X-ray Crystallography* John Wiley & Sons, INC, NY 3rd print, p 401
Champion F C and Davy N 1960 *Properties of Matter* Blakie & Sons Ltd, Glasgow, London p 294
Cotton F A and Wilkinson G 1962 *Advance Inorganic Chemistry* Interscience Pub, NY, p 93
Diwan P S and Ranade J D 1969 *Saugar University Journal, Sagar* (India) **17** 23
Ekbote S N and Ranade J D 1972 *Indian J. Phys.* **46** 529

- Fonda G R 1948a *Preparation and Characteristics of Solid Luminescent Materials* John Wiley & Sons, INC, NY p 69
- Fonda G R 1948b *J. Phys. Chem.* **44** 435
- Kröger F A and Vink H J 1956 *Solid State Physics* F Seitz and D Turnbull, Academic Press, NY **3** 374
- Larch S 1966 *Proc. of International Conference on Luminescence* Budapest p 1554
- Machwe V G 1969 *Ph.D. Thesis, Saugar University, Saugar* (India) p 119
- Mehta A S, Machwe V G and Saxena R C 1975 *Indian J. Phys.* **49** 761
- Nair P G, Lingam K V and Machwe V G 1969 *Proc. Ind. Acad. Sciences* **70A** 53
- Nelson J B and Riley D P 1945 *Proc. Phys. Soc. London* **57** 160
- Rooksby H P 1947 *Proc. International Congress on Pure and Applied Chemistry, London* p 263
- Saxena R C 1966 *Ph.D. Thesis, Saugar University, Saugar* (India) p 124
- Tunitskaya V F 1953 *Dok. Akad. Nauk. S.S.S.R.* **91** 507
- Yocom P N and Larch S 1965 *Extended Abstract, Electro-Chemical Society, San Francisco Meeting* May 9 to 11 p 15

Lattice properties of alkali hydrides

B N Thakur*

Department of Physics, S. P. College, Dumka-814101

and

K P Thakur

Department of Physics, T. N. B. College, Bhagalpur University, Bhagalpur-812007.

Received 26 September 1977, revised 8 March 1978.

Abstract. From an appropriate form of the interaction potential energy function the values of the cohesive energy, force constant, compressibility, i.r. absorption frequency, Debye temperature, Grüneisen parameter, Anderson-Grüneisen parameter, and Moelwyn-Hughes parameter of alkali hydride crystals have been reported using a recent method of calculation which utilizes molecular constants known to a high degree of accuracy. The agreement between calculated and experimental values is satisfactory which further establishes the universality of the logarithmic potential for ionic crystals.

1. Introduction

The interaction potential energy function plays an important role in solid state physics. It is possible to predict a large number of properties of a crystal if the true nature of the binding between the atoms of the crystal is known. Several empirical and semi-empirical potential energy functions are available which contain either inverse power function or exponential function for the repulsive terms, but they have been severely criticised by several workers (Brumer and Karplus 1973, Dobbs and Jones 1957, Ree and Holt 1973, Thakur 1973, 1976a, Woodcock 1974). Various theoretical potential energy functions are also available, but they are inadequate for accurately reproducing experimental results. Thakur (1973, 1976a) has suggested a new potential model, which is well tested for several ionic compounds (Thakur 1973, 1974a, b, 1975a, b, c, 1976a, b, c, 1977a, Thakur and Pandey 1974, 1975). In the present paper, this new model (Thakur 1976a) has been utilised to compute the properties of alkali hydride crystals.

2. Calculation

The new logarithmic potential (Thakur 1976a) is given by

$$\phi(r) = -Ae^{2r^{-1}} - Cr^{-6} - Dr^{-8} + PCo \log(1 - pr^{-6}). \quad (1)$$

* To whom all communications should be addressed.

where A is the Madelung constant, e the electronic charge, $\phi(r)$ the potential energy of an ion pair interacting with each other and with rest of the lattice r the inter-nuclear separation, C and D are van der Waals constants and P and p are potential parameters. The contribution of the hyperpolarizability term has been neglected in equation (1) since it contributes only 0.01% to the total potential energy (Thakur 1976a). The potential parameters have been computed by the method of Kachhava and Saxena (1963). The values of C and D used in the calculations were obtained from the polarizability data of Varshni and Shukla (1963) using the method discussed by Chandra and Sharan (1967).

Knowing the potential parameters, $\phi(r_0)$ and hence the cohesive energy per mol, W , is calculated by the relation

$$W = -[N\phi(r_0) + \epsilon] \quad (2)$$

where N is the Avogadro's number, ϵ the zero point energy and r_0 the equilibrium neighbour distance in the lattice.

The value of the cohesive energy computed from equations (1) and (2) are listed in table 1 together with the experimental values and other literature values (Dass and Saxena 1965). Table 1 also presents the computed values of potential parameter p .

Following Krishnan and Roy (1951) the force constant, f is given by

$$f = -\frac{1}{3} \left[\psi''(r_0) + \frac{2}{r_0} \psi'(r_0) \right] \quad (3)$$

where $\psi(r)$ is the non Coulombic part of $\phi(r)$ and primes denote derivatives with respect to r .

From the polarization the contribution to the force constant, f , is given by (Sharma and Gupta 1963))

$$2a_2 = \frac{4}{3} \frac{\pi e^2}{V_a}$$

where V_a , is the volume of unit cell, has been neglected in equation (3) since it contributes only a little to the total value of f . Moreover if we consider a uniformly polarized sphere in the absence of an external electric field, the only forces acting are due to the $\psi(r)$ term as shown by Szigetti (1951), the Lorentz effective field F being equal to zero.

The compressibility, β , is related to the force constant

$$\beta = \frac{3k_1 r_0}{f} \quad (4)$$

Table 1. Values of interionic distance (r_0 /in 10^{-8} cm), potential parameters (p /in 10^{-48} cm⁶) and P /in kJ mol⁻¹) and cohesive energy (W /in kJ mol⁻¹) from various sources for alkali hydride crystals.

Crystals	r (exptl)	p (calc)	P (calc)	W (expt)	W (calc) equations (1 and 2)	W (calc) Born potential	W (calc) exponen- tial potential
LiH	2.042	18.817	960.6	903.7	976.2	765.8	1039.1
NaH	2.440	37.692	1096.1	800.2	823.9	692.1	883.2
KH	2.850	76.612	1133.3	710.6	700.4	625.5	760.9
RbH	3.0185	90.595	1251.5	682.7	671.5	601.9	722.2
CsH	3.188	108.119	1326.6	651.2	637.7	578.4	686.5
Average error (%)					3.2	12.7	8.7

where k_1 is the crystal structure parameter, which is 2 for f.c.c. lattices.

The i.r. absorption frequency, ν , is given by

$$\nu = \frac{(f/m)^{1/2}}{2\pi} \quad (5)$$

where m is the reduced mass being known, the Debye temperature, θ_D , is computed from the relation

$$\theta_D = \frac{h\nu}{k} \quad (6)$$

where h is Planck's constant and k , the Boltzmann constant.

The values of f , β , ν and θ_D obtained according to equations (3) to (6) are reported in Table 2. The table 2 also contains the Grüneisen parameter (γ) calculated from the relation

$$\gamma = \frac{r_0 \phi'''(r_0)}{6\phi''(r_0)} \quad (7)$$

where $\phi''(r)$ and $\phi'''(r)$ refer to the second and third derivatives of $\phi(r)$ respectively.

The values of Anderson-Grüneisen parameter, δ , computed from the second relationship of Chiang (1967) connecting γ and δ are also listed in table 2.

The Moelwyn-Hughes parameter, which is merely the pressure derivative of the isothermal bulk modulus of elasticity at constant temperature, plays a very important role in solid state physics (Thakur 1976b, 1977a). The application of thermodynamic principles to crystal stability and compressibility condi-

tions of an interaction potential energy function yields the following expression for the Moolwyn-Hughes parameter (Thakur 1976b)

$$C_1 = \left[\frac{dB}{dP} \right]_T = 1 - \frac{r_0^3 \beta}{27V} \phi'''(r_0) \quad (8)$$

where B is the isothermal bulk modulus of elasticity, P the pressure and V the molar volume.

The computed values of C_1 according to equation (8) are also presented in Table 2.

Table 2. Calculated values of force constant (f /in Nm^{-1}), compressibility (β /in $10^{-11}\text{m}^2\text{N}^{-1}$), i.r. absorption frequency (ν_0 /in 10^{12}Hz), Debye temperature (θ_D /in $^\circ\text{K}$), Grüneisen parameter (γ /dimensionless), Anderson-Grüneisen parameter (δ dimensionless) and Moolwyn-Hughes parameter (C_1 /dimensionless) for alkali hydride crystals according to potential (1).

Crystals	f	β	ν_0	θ_D	γ	δ	C_1
LiH	59.38	2.06	32.08	1540	1.20	2.40	3.40
NaH	37.83	3.87	24.45	1173	1.33	2.66	3.66
KH	24.66	6.93	19.57	939	1.39	2.78	3.78
RbH	21.28	8.51	18.05	866	1.43	2.86	3.86
CsH	18.41	10.39	16.76	804	1.46	2.92	3.92

3. Discussion

Much less is known about the hydride crystals. Hydrides belong to a peculiar group of ionic crystals in which polarisability and ionic radius of hydride ion changes as we pass from LiH to CsH. No single potential energy function reproduces experimental data for all hydrides. The present communication adds a little to the physics of these hydride crystals by predicting the values of the parameters W , f , β , ν , θ_D , γ , δ , and C_1 . The computed values of W (in Table 1) compare well with the cyclic data. Although no experimental values of f , β , ν , and θ_D for hydrides are available in the literature still it is found that they obey the same rule as is obeyed by alkali metal halides (Thakur 1976b, 1977a, b; Thakur and Thakur 1976) i.e., the plot of f against r_0 is a straight line, the plot of $\log \beta$ against $\log r_0$ is a straight line, and the plots of ν and θ_D against reduced mass are straight lines. Thus we conclude that our computed values of f , β , ν and θ_D are acceptable. The experimental values of γ , δ and C_1 for these crystals are also not available in the literature. It is found that the present values of γ vary in a narrow band about the value $\gamma = 1.3$ for these crystals. For alkali metal halides and alkaline earth chalcides the values of γ vary round the value

$\gamma = 2$ and $\gamma = -3$, respectively (Thakur and Pandey 1975). Actually the values of γ depend upon the specific volume and they increase, as a rule, as we move towards the heavier crystals. Thus it can be said that the present values of γ which follow this rule are acceptable.

Acknowledgment

The authors thank Professor K. P. Sharma for encouragement and facilities provided in the department.

References

- Brumer P and Karplus M 1973 *J. Chem. Phys.* **58** 3903
Chandra M and Sharan B 1967 *Proc. Phys. Soc.* **91** 257
Chang Y A 1967 *J. Phys. Chem. Solids* **28** 697
Dass L and Saxena S C 1965 *J. Chem. Phys.* **43** 1747
Dobbs E R and Jones G O 1957 *Rep. Prog. Phys.* **20** 516
Kachhava C M and Saxena S C 1963 *Phil. Mag.* **8** 1429
Krishnan K S and Roy S K 1951 *Proc. R. Soc. London* **A207** 447
Ree F H and Holt A C 1973 *Phys. Rev.* **B8** 826
Sharma M N and Gupta S S 1963 *Indian J. Phys.* **37** 33
Szigeti B 1951 *Proc. Roy. Soc. London* **204** 51
Thakur K P 1973 *Indian J. Pure Appl. Phys.* **11** 549
Thakur K P 1974a *J. Inorg. Nucl. Chem.* **36** 2171
Thakur K P 1974b *Indian J. Chem.* **12** 376
Thakur K P 1975a *Acta Cryst.* **A31** 540
Thakur K P 1975b *Curr. Sci. India* **44** 45
Thakur K P 1975c *Acta. Phys. Polonica* **A48** 419
Thakur K P 1976a *Aust. J. Phys.* **29** 39
Thakur K P 1976b *Acta Cryst.* **A32** 363
Thakur K P 1976c *J. Inorg. Nucl. Chem.* **38** 1433
Thakur K P 1977a *Aust. J. Phys.* **30** 325
Thakur K P 1977b *Acustica* **37** 118
Thakur K P and Pandey J D 1974 *J. Chem. Phys.* **71** 850
Thakur K P and Thakur L 1976 *Indian J. Chem.* **A14** 97
Varshni Y P and Shukla S C 1963 *Rev. Mod. Phys.* **35** 130
Woodcock L V 1974 *J. C. S. Faraday II* **70** 1405

Evaluation of the relation between extinction coefficient of infrared radiation and mechanical Q of quartz single crystals

Dipak Chakraborty*

Institut für physikalische Chemie der Universität Münster,
4400 Münster, Schlossplate 4, West Germany.

Received 28 November 1977

Abstract. Some members of the International Electrotechnical Commission (1973) have justified the use of the wave number 3500 cm^{-1} to evaluate mechanical Q not properly. Proper consideration reveals that the wave number 3590 cm^{-1} or any other wave number in the 3400 cm^{-1} region of ir spectrum could be used for this purpose.

1. Introduction

It is well-known that quartz single crystals give rise to a complex ir spectrum consisting of upto sixteen distinct absorption bands in the 3400 cm^{-1} region. In 1966, Rudd *et al* found that the mechanical Q of quartz was related to the extinction coefficient (α) of a particular wave number 3500 cm^{-1} which happens to be one of the above mentioned absorption bands. Mechanical Q of quartz was evaluated by that of AT-cut resonator (5 MHz) processed from the material under consideration. The standard method (*viz.* transmission technique, logarithmic decrement technique or resonance response band width technique) was utilised for evaluating it. Extinction Coefficient was obtained from the formuly :

$$\alpha_{3500} = \frac{10 \log T_{3800} - 10 \log T_{3500}}{\text{thickness (cm)}},$$

where T_{3800} and T_{3500} are transmittances at 3800 cm^{-1} and 3500 cm^{-1} respectively.

This type of relation could be obtained because of the presence of some impurities like hydrogen (Ballman and Rudd 1965) which lowered mechanical Q of quartz and also because the hydrogen content of the crystals could be identified and determined by its ir absorption spectra. This type of relation evidently helped to avoid the comparatively complex method of evaluating mechanical Q by standard methods, and also made it possible to obtain mechanical Q value with considerable accuracy within a few seconds.

The purpose of writing this note is to discuss the justification of selecting the wave number 3500 cm^{-1} from the ir spectrum for this purpose.

* Present address : Central Glass & Ceramic Research Institute, P.O. Jadavpur University, Calcutta-700032, India.

2. Discussion

Although Rudd *et al* (1966) recommended the relation Q Vs α_{3500} , they commented that the wave number 3590 cm^{-1} could also be used to test the relationship between mechanical Q and extinction coefficient (α). However, they observed that a better correlation with sample possessing a very high Q existed at 3500 cm^{-1} . Sawyer (1972) found also the relationship Q Vs α_{3500} . Toyocom (1970) has suggested a relationship Q Vs α_{3590} . International Electrotechnical Commission (1973) faced difficulties in selecting the wave number for this purpose. Some members of International Electrotechnical Commission (1973) have suggested the use of 3500 cm^{-1} . The justification given by them for not using the wave number 3590 cm^{-1} was that this band was associated with Li impurity in combination with OH. In support of their statement they referred to the work of Dodd and Fraser (1965). But it is to be pointed out that according to Dodd and Fraser (1965) the band at 3585 cm^{-1} was associated with Li in combination with OH in the case of natural quartz only and not in the case of synthetic quartz. In the case of synthetic quartz the band at 3585 cm^{-1} was independent of alkali impurities. Since the relation Q Vs α is practically applicable to evaluate mechanical Q of synthetic quartz, it appears that the supporters for the wave number 3500 cm^{-1} have referred incorrectly to the work of Dodd and Fraser (1965) in support of their statement. Moreover, it will not also be proper to accept the idea that the band at 3585 cm^{-1} in the case of synthetic quartz should be associated with alkali impurities in combination with OH simply because it is so in the case of natural quartz. This is substantiated by the fact that the bands at 3440 and 3400 cm^{-1} were associated with alkali impurities in combination with OH in the case of natural quartz but the same bands were found to be independent of alkali impurities in the case of synthetic quartz. The occurrence of the very absorption band at 3585 cm^{-1} in the spectrum of natural quartz is still doubtful, because no other worker has observed this band in the case of natural quartz (Bambauer 1961, Bambauer *et al* 1961, Brown and Kahan 1975, Chakraborty and Lehmann 1976a, Dodd and Fraser 1965, Kats 1962, Staats and Kopp 1974, Wood 1960). Therefore the justification for not using the band at 3585 cm^{-1} for evaluating mechanical Q is not proper. On the other hand, some other members of International Electrotechnical Commission (1973) supported the use of 3585 cm^{-1} because they obtained the relation Q Vs α_{3585} and found it suitable for evaluating mechanical Q .

The position of the wave number 3585 cm^{-1} can be fixed up in their chart easily because it is a specific sharp absorption band. This facilitates easy and accurate evaluation of α_{3585} and hence from the practical point of view it is more logical to use Q Vs α_{3585} .

** This band shifts to 3585 cm^{-1} at 78K.

Chakraborty and Lehmann (1976b) showed that OH associated with the bands at 3585, 3520, 3440, 3400 and 3355 cm^{-1} was linearly proportional to the total OH content of the crystals. It can be easily derived from this work that extinction coefficient of these bands are linearly related to the hydrogen content of the crystals. The reason is that OH associated with a specific band can be obtained by multiplying extinction coefficient with the band width which is a constant for that band and a constant factor (1976b). It was also noted that mechanical Q was inversely proportional (approximately linearly) to hydrogen content of synthetic quartz. Therefore it was concluded that absorption coefficient of any of the above mentioned bands could be used to indicate mechanical Q , because each of these bands bore same type of relationship with mechanical Q . This is also substantiated by the fact that few workers used Q Vs α_{3500} and some others used Q Vs α_{3585} relation.

Hence, it can be concluded from the discussion that the justification for using the band at 3500 cm^{-1} to evaluate mechanical Q was not properly made. It seems highly probable that any of the absorption bands in the 3400 cm^{-1} region of ir spectrum could be used to indicate mechanical Q . Also from the practical point of view it is recommended that a band with sharp absorption peak should be used to evaluate mechanical Q .

Acknowledgments

The author wishes to thank Prof. Dr. G. Lehmann of Münster University, West Germany and Dr. J. Mukherjee, Central Glass & Ceramic Research Institute, Calcutta, India for their interest in the work.

References

- Ballman A A and Rudd D W 1965 *The Western Electric Engineer* **IX** 1
- Bambauer H U 1961 *Schweiz. Min. Petr. Mitt.* **41** 335
- Bambauer H U, Brunner G O and Laves F 1961 *E. Elektrochem.* **56** 135
- Brown R N and Kahan A 1975 *J. Phys. Chem. Solids* **36** 467
- Chakraborty D and Lehmann G 1976a *Phys. Stat. Sol.* **A34** 467
- Chakraborty D and Lehmann G 1976b *J. Sol. State Chem.* **17** 305
- Dodd D M and Fraser D B 1965 *J. Phys. Chem. Solids* **26** 673
- International Electrotechnical Commission, Technical Committee 49 (Secretariat) August 1973
- Kats A 1962 *Philips Res. Repts.* **17** 201
- Rudd D W, Houghton E E and Carroll W J 1966 *The Western Electric Engineer* **X** 1
- Sawyer B 1972 *IEE Trans. Sonics Ultrasonics* **SU-19** 32
- Staats P A and Kopp O C 1974 *J. Phys. Chem. Solids* **35** 1029
- Toyocom Technical Bulletin 1970 June 30 **4**
- Wood D L 1960 *J. Phys. Chem. Solids* **13** 326

Lattice excitation in alkali metals

R P S Rathore

Department of Physics, R. B. S. College, Agra

Received 28 November 1977, revised 20 March 1978

Abstract. Dispersion relations for the lattice excitations along the high symmetry directions have been investigated theoretically using a central pair potential (CPP) model incorporating the electron-response for bcc monovalent metals. The model expresses the ion-ion interaction as the first and the second derivatives of CPP potentials coupling the nearest and the next nearest neighbouring ions of bcc structure. The long range electron ion interaction have been described on the lines suggested by Sharma-Joshi scheme, which is well suited for the alkali metals because of validity of the small core approximation. The lattice stability has been preserved under the ionic pressure which is counterbalanced by that due to conduction electrons. Binding energy, pressure and bulk modulus produced by the short-range electron response to the ionic motion have been discussed in the light of some theoretical formalisms. The simple model explains very well the cross over of L and T branches along the direction $[\zeta 00]$. The phonon frequencies for the alkali metals yielded by the model show good agreement to the experimental ones.

1. Introduction

Lattice dynamical behaviour of cubic metals have been phenomenologically investigated (Goel *et al* 1974, Rathore 1975, Rathore and Verma 1976, Singh and Hemkar 1975, 1976, Behari and Tripathi 1970, 1972) using non central force models incorporating both types of angular forces *viz* the de-Launay (1956) type and the Clark *et al* (1964) type. Recently the present author (Rathore and Verma 1977a) have shown that there is hardly any justification for the inclusion of the angular forces in the interaction system of simple metals like the alkalis. Moreover it has been established that the angular-force parameters merely express the electron pressure, which has been ignored in all these studies. Further it has been verified that the CPP forces (Maradudin *et al* 1963) are equivalent (Rathore 1977a) to those contained in the axially symmetric model (Lehman *et al* 1962) or Bhatia model (1955) for describing the ionic interaction. In the present communication, the electron response to the ionic motion has been investigated in some details leading to the consideration of the following interactions in metals.

(a) The presence of conduction electrons in metals screens the ion-ion interaction upto a few neighbours. In view of this fact the first and second derivative of central pair-wise potentials coupling only the first two neighbours have been used to derive the elements of dynamical matrix representing the ion-ion interaction in bcc structure.

(b) The electron-response to the ionic motion give rise to the kinetic, potential and correlation-energies, which being volume dependent cause electron pressure ignored so far.

(c) The longe-range electron-ion interaction has been described on the lines suggested by Sharma-Joshi (1963) which although does not satisfy the symmetry requirements but its coupling-coefficients falls off desirably because of the presence of the Bardeens function (1937). Further the quantum mechanical analysis of Finnis 1974 supports the validity of this scheme, which is well suited for point-ions.

The first derivative of CPP goes to describe the unpaired (Brovman and Kagan 1974) ionic interaction. The lattice stability so far not being dealt adequately, is maintained by equating the ionic pressure with that due to the electrons, which bears a definite ratio with the corresponding bulk modulus. This ratio is derived by ascertaining best fit to the experimental data on phonon-dispersion. Theoretical analysis to reproduce these ratios for different alkali metals has also been worked out in the present communication.

The model using the three known values of elastic constants and one cone boundary frequency, derives the dispersion relations in alkali metals which are in good agreement with the experimental data. The inclusion of short and long-range electron response to the ionic motion in the CPP scheme on one hand accounts satisfactorily for the Cauchys discrepancy while on the other hand makes the elastic and frequency relations consistent with the experimental situations. It may be noted that the crossing over of L and T modes along the direction $[\zeta 00]$ could be explained so simply in terms of the above mentioned short ranged electron-response.

2. Theory

The first (α_1, α_2) and the second derivatives (β_1, β_2) of the CPP coupling the nearest (ϕ_1^I) and the next nearest (ϕ_2^I) neighbouring ions can be defined as

$$\begin{aligned}\alpha_1 &= \frac{1}{r} \frac{\partial \phi_1^I}{\partial r}, & \alpha_2 &= \frac{1}{r'} \frac{\partial \phi_2^I}{\partial r'} \\ \beta_1 &= \frac{\partial^2 \phi_1^I}{\partial r^2}, & \beta_2 &= \frac{\partial^2 \phi_2^I}{\partial r'^2}\end{aligned}\tag{1}$$

where r and r' are the respective separation of nearest and next nearest neighbouring ion from the central one. The elements of dynamical matrix ($D_{\alpha\beta}^I$) describing the ionic interaction in CPP scheme may be written as

$$D_{\alpha\beta}^I = 8/3(\beta_1 - \alpha_1)S_\alpha S_\beta C\gamma \quad (\text{bcc}) \quad (2)$$

$$D_{\alpha\alpha}^I = 8/3(\beta_1 + 2\alpha_1)(1 - C_\alpha C_\alpha C\gamma) + 2\beta_2 S_\alpha^2 + 2\alpha_2(2 - C_\beta' - C\gamma')$$

where $\alpha, \beta = x, y, z$, $C_\alpha = \cos(\frac{1}{2}aq_\alpha)$, $S_\alpha = \sin(\frac{1}{2}aq_\alpha)$ and $C_\alpha' = \cos(aq_\alpha)$. a is the cube edge and q_α the α -component of the phonon wave vector \mathbf{q} .

The volume interaction may be expressed on the lines outlined by Sharma-Joshi (1963) scheme as

$$D_{\alpha\beta}^E = (\alpha^3/2)K_e q_\alpha q_\beta G^2(x) \quad (\text{bcc}) \quad (3)$$

$$D_{\alpha\alpha}^E = \frac{\alpha^3}{2}K_e q_\alpha^2 G^2(x)$$

where $x = qro$, ro is the radius of the Wigner-Seitz sphere, K_e the bulk modulus of the electron-gas and G is the Bardeen (1937) function, which introduces a type of symmetry in the expression with the result the Sharma-Joshi (1963) scheme satisfies the condition of rotational invariance for all wave vectors except for long wave vectors where the deviation is not more than five per cent for alkali metals. The scheme yields good results for cases where small core approximation is valid and the conduction electron describe the Fermi-surface which are not far from spherical.

The secular determinant expressing the phonon frequencies (w) in high symmetry directions may be written as

$$|D - mw^2I| = 0 \quad (4)$$

where m is the mass of the ion and I the unit matrix of order 3. Elements of total dynamical matrix ($D_{\alpha\beta}$) is the sum of those contributed by the ion-ion ($D_{\alpha\beta}^I$) and the electron-ion ($D_{\alpha\beta}^E$) interaction.

On comparing the equation (4) in long wave limit to Christoffel elastic equation (Love 1944) one gets

$$\begin{aligned} aC_{11} &= 2/3(2\alpha_1 + \beta_1) + 2\beta_2 + aKe \\ aC_{12} &= 2/3(\beta_1 - 4\alpha_1) - 2\alpha_2 + aKe \quad (\text{bcc}) \\ aC_{44} &= 2/3(2\alpha_1 + \beta_1) + 2\alpha_2. \end{aligned} \quad (5)$$

It is evident from these relations that the Cauchy's discrepancy is partly due to the first derivatives of the CPP potentials and partly due to the electron bulk modulus (Ke) viz.

$$aC_{12}-aC_{44} = -4(\alpha_1+\alpha_2)+aKe \quad (\text{bcc}) \quad (6)$$

It is worth mentioning that the values of C_{11} , C_{12} and C_{44} used as input data are experimentally determined under to condition of static equilibrium (Thomas 1971) of the crystal. Therefore the satisfaction of the condition of lattice stability becomes the pre-requisite to all such studies. The practical constraint for the lattice-stability may be expressed as

$$PI+Pe = 0 \quad (7)$$

where PI is the ionic pressure, which may be derived as

$$PI = \frac{\partial \Phi^I}{\partial \Omega} = 2(\alpha_1+\alpha_2) \quad (8)$$

where

$$\Phi^I = \phi_1^I + \phi_2^I. \quad (9)$$

The electron pressure Pe may be derived using the relation

$$Pe = -\partial \Phi^e / \partial \Omega \quad (10)$$

where Φ^e is the total electron-energy, which comprises of the kinetic (or Fermi) potential (or exchange) and correlation energies. The kinetic part of the energy may be written as

$$\phi_{kin} = \frac{\hbar^2 K_F^2}{2m_e} \quad (11)$$

where m_e is the mass of the bound electron and K_F the fermi wave vector.

It is interesting to note that an accurate explicit binding in metal is expressed by Bohm-Pines (Ziman 1964) screening. This fact has also been reported recently by Moruzzi *et al* (1977). Considering that the screened Coulombian interaction is responsible for the binding of the electrons, the potential energy of these electrons may be derived as

$$\phi_{pot} = -\frac{3e^2}{r_e} [(K_e r_e)^{-2} - \exp(-K_e r_e) \{ (K_e r_e)^{-2} - (K_e r_e)^{-1} \}] \quad (12)$$

where K_e is the screening parameter and r_e the electron spacing. It may also be noted that the electron-electron correlation energy given by Nozières and Pines (1958) interpolation procedure agree well with those given by Singwi *et al* (1968, 1970) and Vasistha and Singwi (1972) using mean field theory. Following Nozières and Pines (1958) one gets the expression for the correlation energy

$$\phi_{corr} = \left[-\frac{0.458\beta^2}{r_e} + \frac{0.866\beta^3}{r_e^{3/2}} - \frac{0.98\beta^4}{r_e^2} + 0.019\frac{\beta^4}{r_e} + 0.706\frac{\beta^5}{r_e^{5/2}} \right] \text{(NP)} \quad (13)$$

where β is related to long wave length momentum transfers. Gellman and Brueckner (1957) expression for ϕ_{corr} may be written as

$$\phi_{corr} = 0.622 \ln(r_e) - 0.096 \quad \text{(GB)} \quad (14)$$

These volume dependent electron energies may be used to derive the electron pressure P^e , which is related to the electron bulk modulus as

$$K_e = -\Omega \delta P^e / \delta \Omega. \quad (15)$$

The numerical analysis of the dispersion frequencies has inferred that the electron pressure (P^e) bears a definite ratio with the electron-bulk modulus (K_e) i.e.,

$$K_e = \sigma P^e. \quad (16)$$

Assuming that the electron provides wholly the kinetic energy and the potential energy takes care of the screening effect, the proportionality constant assumes the value 1.67 which has been used by the present author (Rathore and Verma 1977, Rathore 1977b) and also by some other workers (Upadhyaya *et al* 1975, Kulshrestha and Upadhyaya 1976, Sharma 1976) to describe the dispersion relations in cubic metals.

The phonon-frequencies derived on the basis of the present model provide the best fit to the experimental data for the following values of σ ,

$$\begin{aligned} \sigma &= 1.8 \quad \text{for Li} \\ \sigma &= 1.04 \quad \text{for Na} \\ \sigma &= 1.4 \quad \text{for K} \\ \sigma &= 1.1 \quad \text{for Rb.} \end{aligned} \quad (17)$$

Four of the model parameters are evaluated using equations (5), (7), (16) and (17). the fifth model parameter is evaluated by the knowledge of a zone boundary

frequency for T -mode at the point (100). The required relation may be expressed as

$$m\omega_T^2[100] = \frac{16}{3}(2\alpha_1 + \beta_1). \quad (18)$$

3. Results and discussion

The input data and the computed model parameters for alkali metals are shown in tables 1 and 2 respectively.

The computed dispersion relations for Li, Na, K and Rb are shown in figures 1, 2, 3 and 4 respectively by continuous lines. Theoretical curves reported in a recent study (Rai and Hemkar 1977) are shown by dashed-lines. Experimental points closely follow the computed curves of the present model. Like

Table 1. Input data for alkali metals

Metal	C_{11}	C_{12}	C_{44}	a Å	m 10^{-24} gms	ν_T 10^{12} Hz	Reference	
	10^{12} dyne/cm ²						elastic constants	frequency
Lithium	0.1481	0.1248	0.1077	3.48	11.519	8.50	Nash and Smith (1959)	Smith <i>et al</i> (1968)
Sodium	0.0808	0.0664	0.0586	4.24	38.163	3.58	Diederich and Trivisonno (1966)	Woods <i>et al</i> (1962)
Potassium	0.0410	0.0341	0.0261	5.228	64.909	2.26	Marguardt and Trivisonno (1965)	Cowley <i>et al</i> (1966)
Rubidium	0.0342	0.0288	0.0206	5.605	141.880	1.24	Gutman and Trivisonno (1967)	Copley <i>et al</i> (1973)

Table 2. Computed model parameters

Metal	α_1	α_2	β_1	β_2	ake
	10^4 dyne/cm				
Lithium	-0.03045	-0.08052	0.8698	0.1818	-0.3843
Sodium	-0.01626	-0.0008974	0.4079	+0.6395	-0.03556
Potassium	-0.01342	-0.02688	0.3043	0.07175	-0.11414
Rubidium	-0.01709	-0.03983	0.2428	0.08914	-0.1257

the other phenomenological studies the theoretical curves due to Rai and Hemkar (1977) do not explain the cross over in $[\zeta 00]$ direction. while the present curves for Li, Na, K and Rb do so at reduced wave vector $\zeta = 0.7, 0.8, 0.7$ and 0.07 respectively. The amount of these degeneracies are 9.64%, 0.6%, 7% and 0.5% for Li, Na, K and Rb respectively whereas the amount of assymetry inherent to Sharma-Joshi (1963) theory in these regions are respectively 3.6%, 0.3%,

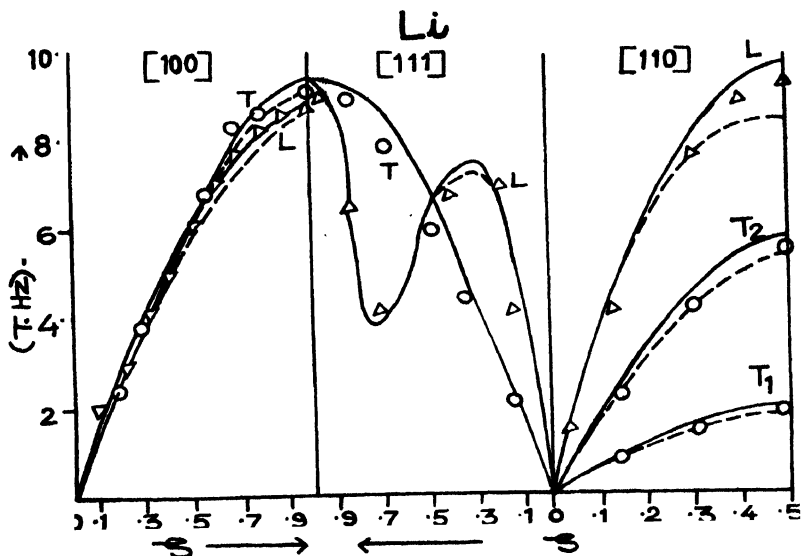


Figure 1.

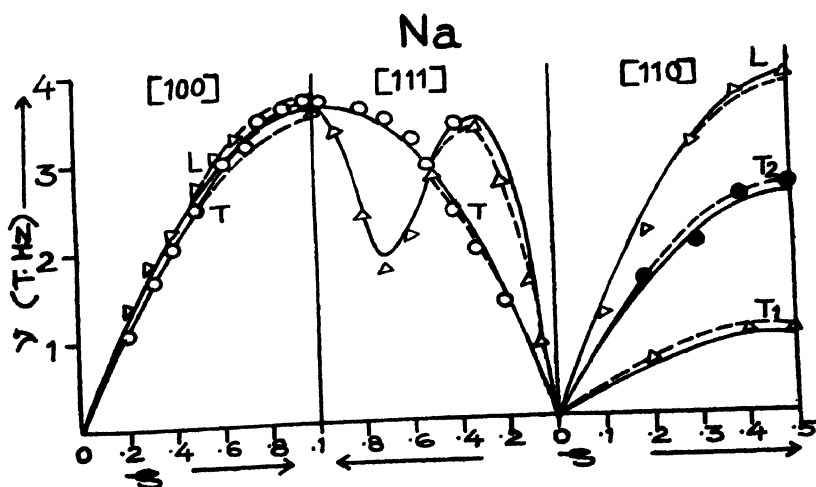


Figure 2.

4.5% and 0.2%. It is thus evident that the cross over is definitely explained by the model under report. The binding energies (B.E.) pressures (P^e) and bulk moduli (K_e) are computed on the basis of the formalisms given by Gellman and Brueckner (1957), Noziers and Pines (1958), Bohm Pines (Ziman 1964) and Thomas-Fermi (1927, 1928). The kinetic part of the energy given by the

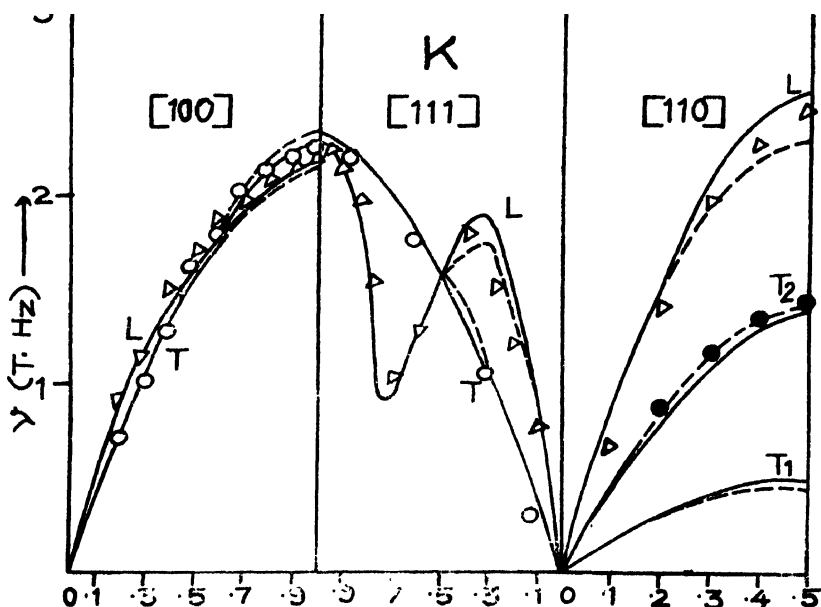


Figure 3.

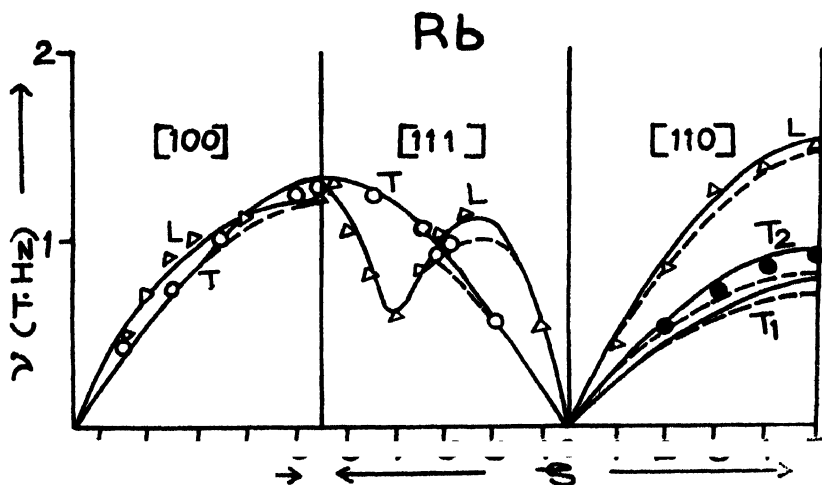


Figure 4.

Table 3. Binding energies, pressure and bulk modulus for the electrons in alkali metals (in atomic mass units).

Scheme	Li				Na			
	B.E.	P_e	K_e	σ	B.E.	P_e	K_e	σ
Gellman and Brueckner	-0.0951	+0.003151	+0.00807	1.93	-0.101	+0.0009961	+0.001974	1.98
Nozières and Pines	-0.1014 to	+0.003523 to	+0.007828 to	2.2 to	-0.1156 to	+0.000851 to	+0.002281 to	2.68 to
	-0.1132	0.03148	+0.05995	1.9	-0.1319	+0.01027	+0.01977	1.92
Bohm-Pine	-1.325	-0.03902	-0.0238	1.57	-0.9157	-0.0152	-0.02477	1.62
Thomas-Fermi	-0.2594	+0.008433	+0.01415	1.63	-0.1729	+0.00313	+0.006762	1.46

Table 3. (Contd.) Binding energies, pressure and bulk modulus for the electrons in alkali metals (in atomic mass units).

Scheme	K				Rb			
	B.E.	P_e	K_e	σ	B.E.	P_e	K_e	σ
Gellman and Brueckner	-0.0925	+0.00282	+0.005907	2.02	-0.0877	+0.001856	+0.000376	2.01
Nozières and Pines	-0.1167 to	+0.0009032 to	+0.0005137 to	2.69 to	-0.1151 to	+0.0000085 to	+0.000287 to	3.35 to
	-0.1347	+0.003037	+0.005976	1.97	-0.1695	+0.002009	+0.004	1.99
Bohm-Pine	-0.6138	-0.0551	-0.0091	1.65	-0.5367	-0.003954	-0.006409	1.61
Thomas-Fermi	-0.1120	+0.001084	+0.001822	1.60	-0.0969	+0.0007611	+0.001288	1.59

equation (11) has been added to ϕ_{pot} given by the equation (12) to give the total energy used with Bohm-Pines and Thomas-Fermi schemes. The fermi (ϕ_f) and the exchange energy (ϕ_x) given by the following expressions are added to ϕ_{corr} to give the total energy used with the Nozières and Pines (1958) and Gellmann and Brueckner (1957) schemes.

$$\phi_f = 2.21/r_e \quad (19)$$

$$\phi_x = -0.916/r_e.$$

These values for B.E., P^e and K_e are enlisted in table 3. The values of the proportionality constant (σ), thus derived theoretically may be compared with the model values given by the equation (17). It may be verified that the Bohm-Pine scheme gives the fair values of BE, P^e and K_e , which are comparable with those given by the present model.

Acknowledgment

Author's sincere thanks are due to Dr. M. P. Verma for his supervision of the present work.

References

- Bhatia A B 1955 *Phys. Rev.* **97** 363
 Bardeen J 1937 *Phys. Rev.* **52** 688
 Behari J and Tripathi B B 1972 *J. Phys. Soc. Japan* **33** 1207
 Behari J and Tripathi B B 1970 *Aust. J. Phys.* **23** 311
 Brovman E G and Kagan Yu M 1974 *Soviet Phys. Uspekhi* **17** 125
 Cowley K A, Woods A D B and Dolling G 1966 *Phys. Rev.* **150** 487
 Clark B C, Gazis D C and Wallis R F 1964 *Phys. Rev.* **134** A1486
 Copley J R D and Brockhouse B N 1973 *Can. J. Phys.* **5** 657
 DeLaunay J 1956 *Solid State Phys.* Ed Soitz and D Turnbull (Academic New York) **2** 276
 Diederich M E and Trivisonno J 1966 *J. Phys. Chem. Solids* **27** 637
 Fermi E 1928 *Physik Z.* **48** 73
 Finnis M W 1974 *J. phys. F.* **4** 1645
 Gellmann M and Brueckner K A 1957 *Phys. Rev.* **106** 364
 Gutman E J and Trivisonno J 1967 *J. phys. Chem. Solid* **28** 805
 Goel C M, Pandey B P and Dayal B 1974 *Phys. Stat. Solidi b.* **68** 625
 Kulshrestha O P and Upadhyaya J C 1976 *Ind. J. Pure Appl. Phys.* **14** 253
 Love A E H 1944 *Mathematical theory of elasticity* (Dover, New York) p 299
 Lehman G W, Wolfram T and Dewames R E 1962 *Phys. Rev.* **129** 2483
 Moruzzi V L, Williams A R and Janak J F 1977 *Phys. Rev.* **B15** 2854
 Maradudin A A, Montroll E W and Weiss G H 1963 *Solid state phys. supp.* **3** (Academic, New York.)
 Marguardt W R and Trivisonno J 1965 *J. Phys. Chem. Solid* **26** 273
 Nozières P and Pines D 1958 *Phys. Rev.* **111** 442
 Nash H C and Smith C S 1959 *J. Phys. Chem. Solid* **9** 113
 Rathore R P S 1975 *Ind. J. Phys.* **49** 858

- Rathore R P S and Verma M P 1976 *Ind. J. Phys.* **50** 605
- Rathore R P S and Verma M P 1977a *Ind. J. Pure Appl. Phys.* **15** 1
- Rathore R P S 1977a *Ind. J. Pure Appl. Phys.* **15** 730
- Rathore R P S and Verma M. P. 1977b *Ind. J. Pure Appl. Phys.* **15** 467
- Rathore R P S 1977b *Ind. J. Phys.* **51A** 108
- Rai R C and Hemkar M P 1977 *Phys. Stat. Solid* **79(b)** 289
- Sharma S S 1976 *Agra University Thesis*
- Singh V P and Hemkar M P 1975 *Phys. Lett.* **A54** 24
- Singh V P and Hemkar M P 1976 *Phys. Lett.* **A58** 409
- Smith H G, Dolling G, Nicklow R M, Vijay Raghvan P R and Wilkinson M K 1968 *Neutron in elastic scattering IAEA* (Vienna) **1** 149
- Sharma P K and Joshi S K 1964 *J. Chem. Phys.* **39** 2633
- Singwi K S, Tosi M P, Land R H and Sjolander A 1968 *Phys. Rev.* **176** 589
- Singwi K S, Sjolander A, Tosi M P and Land R H 1970 *Phys. Rev.* **B1** 1044.
- Thomas J F Jr 1971 *Scripta Metallurgica* **5** 787.
- Thomas L H 1927 *Proc. Camb. Phil. Mag.* **23** 542
- Upadhyaya J C, Sharma S S and Kulshrestha 1975 *Phys. Rev.* **B12** 2236
- Vasistha P and Singwi K S 1972 *Phys. Rev.* **B6** 875
- Woods A D B, Brockhouse R H, March R N, Steware A T and Bowers R 1962 *Phys. Rev.* **128** 1112
- Ziman J M 1964 *Principles of the theory of solids* (Cambridge Univ press, London)

Volume dependence of the electronic dielectric constant in cuprous and silver halides under the effect of pressure and temperature

Jai Shanker, V C Jain* and A K G Lashkari**

Department of Physics, Agra College, Agra-282002

Received 4 January 1978, revised 27 April 1978

Abstract. The volume dependence of the electronic dielectric constant in CuCl, CuBr, AgCl and AgBr crystals has been calculated using the Clausius-Mossotti dielectric model. The results are compared with the experimental values derived from the data on photoelastic constants and temperature dependence of the electronic dielectric constant. Values of the strain polarizability parameter, strain derivative of the electronegativity parameter and temperature derivative of polarizability have been reported for the crystals under study.

1. Introduction

Cuprous and silver halides are partially ionic crystals whose rather unusual behaviour has attracted the attention of numerous investigators. The present paper deals with the variation of electronic dielectric constant ϵ with the change in volume V in CuCl, CuBr, AgCl and AgBr crystals. For cuprous halides the photoelastic constants have recently been measured by Biegelsen *et al* (1976). The volume dependence of ϵ , at constant temperature, can be estimated from the relation

$$\frac{V}{\epsilon} \left(\frac{\partial \epsilon}{\partial V} \right)_T = - \frac{\epsilon}{3} (p_{11} + 2p_{12}) \quad (1)$$

where p_{11} and p_{12} are the photoelastic constants. For silver halides the data on p_{11} and p_{12} are not available. However, the values of $\frac{V}{\epsilon} \left(\frac{\partial \epsilon}{\partial V} \right)_P$ in these crystals can be obtained from the temperature dependence of ϵ using the following transformation

$$\frac{V}{\epsilon} \left(\frac{\partial \epsilon}{\partial V} \right)_P = \frac{1}{\beta \epsilon} \left(\frac{\partial \epsilon}{\partial T} \right)_P \quad (2)$$

Attached to :

* Department of Physics, Paliwal Degree College, Shikohabad (U.P.).

**Government P. G. College, Morena (M.P.).

where $\beta = \frac{1}{V} \left(\frac{\partial V}{\partial T} \right)_P$ is the volume thermal expansion coefficient. A theoretical estimate of $\frac{V}{\epsilon} \left(\frac{\partial \epsilon}{\partial V} \right)_T$, on the other hand, can be made from the Lorentz-Lorenz relation

$$\frac{\epsilon-1}{\epsilon+2} = \frac{4\pi}{3V} \alpha \quad (3)$$

where α and V are, respectively, the polarizability and volume per ion pair. Volume derivative of equation (3) yields (Burstein and Smith 1948)

$$\frac{V}{\epsilon} \left(\frac{\partial \epsilon}{\partial V} \right)_T = - \frac{(\epsilon-1)(\epsilon+2)}{3\epsilon} \quad (4)$$

In deriving equation (4), the polarizability has been assumed to remain constant under changing volume. Values of $\frac{V}{\epsilon} \left(\frac{\partial \epsilon}{\partial V} \right)_T$ obtained from equation (4) are consistently higher in magnitude than the experimental values (Table 1). This implies the invalidity of the assumption that the polarizability of ions are constant under changing volume.

Table 1. Values of the strain derivatives of electronic dielectric constants

Crystal	$V \left(\frac{\partial \epsilon}{\partial V} \right)_T$ and $V_c \left(\frac{\partial \epsilon}{\partial V} \right)_P$		Value of $\frac{V}{\epsilon} \left(\frac{\partial \epsilon}{\partial V} \right)_T$ calculated from	
	Experimental			
	$V \left(\frac{\partial \epsilon}{\partial V} \right)_T$	$V_c \left(\frac{\partial \epsilon}{\partial V} \right)_P$	Equation (4)	Equation (5)
CuCl	-0.77	—	-1.40	-0.70
CuBr	-0.69	—	-1.68	-0.75
AgCl	—	-0.44	-1.49	-0.94
AgBr	—	-0.43	-1.75	-0.86

2. Volume dependence of polarizabilities

If one considers the variation of polarizabilities with volume then equation (3) yields

$$\frac{V}{\epsilon} \left(\frac{\partial \epsilon}{\partial V} \right)_T = - \frac{(\epsilon-1)(\epsilon+2)}{3\epsilon} (1-\lambda) \quad (5)$$

where λ the strain polarizability parameter is

$$\lambda = \frac{V}{\alpha} \left(\frac{\partial \alpha}{\partial V} \right)_T = \frac{1}{3} \frac{R}{\alpha} \left(\frac{\partial \alpha}{\partial R} \right)_T \quad (6)$$

R is the interionic separation. We have recently suggested a method (Sharma *et al* 1976, Jai Shanker *et al* 1977) according to which $\left(\frac{\partial \alpha}{\partial R}\right)_T$ can be expressed as follows

$$\left(\frac{\partial \alpha}{\partial R}\right)_T = (\alpha_{\text{O}} - \alpha_{\text{Q}}) \frac{1}{e} \left(\frac{\partial e^*}{\partial R}\right)_T \quad (7)$$

where α_{O} and α_{Q} are the free ion polarizabilities of cation and anion respectively. e^*/e is the effective charge parameter introduced by Szigeti (1950). The strain derivative of the effective charge parameter can be obtained from the relation (Lowndes and Martin 1970)

$$\frac{R}{e} \left(\frac{\partial e^*}{\partial R}\right)_T = \left[\frac{R}{\rho} - \frac{2\rho}{R-2\rho}\right] \left(\frac{e}{e} - 1\right) \quad (8)$$

where ρ is the Born repulsive hardness parameter. We calculate λ for CuCl, CuBr, AgCl and AgBr with the help of equations (6) to (8). The input data used in calculation have been compiled in table 2. The resulting values of λ are given in table (3). Values of $\frac{V}{e} \left(\frac{\partial \epsilon}{\partial V}\right)_T$ have been obtained from equation (5) using calculated values of λ . These are included in table 1 for the sake of comparison.

Table 2. Values of the input data used in calculations

Crystal	$R(\text{\AA})$	$\rho(\text{\AA})$	ϵ	$\alpha(\text{\AA}^3)$	e/e^*	$\alpha_{\text{Q}}(\text{\AA}^3)$	$\alpha_{\text{O}}(\text{\AA}^3)$	f
CuCl	2.35 ^a	0.26 ^b	3.73 ^c	4.63 ^c	0.67 ^f	1.22 ^g	3.66 ^h	0.75 ⁱ
CuBr	2.46 ^a	0.27 ^b	4.48 ^c	5.87 ^c	0.69 ^f	1.22 ^g	4.77 ^h	0.74 ⁱ
AgCl	2.77 ^a	0.28 ^b	3.97 ^d	5.33 ^e	0.68 ^d	1.72 ^h	3.66 ^h	0.86 ⁱ
AgBr	2.88 ^a	0.28 ^b	4.68 ^d	6.59 ^e	0.67 ^d	1.72 ^h	4.77 ^h	0.85 ⁱ

(a) Slater (1965)

(b) Bakhshi *et al* (1977)

(c) Van Vechten (1969)

(d) Lowndes and Martin (1969)

(e) Tessman *et al* (1953)

(f) Lawaetz (1971)

(g) Pirenne and Kartheuser (1964)

(h) Pauling (1927)

(i) Phillips (1970)

Table 3. Values of the Strain polarizability parameters, strain derivative of the electronegativity parameter, and temperature derivative of polarizability.

Crystal	λ	$\frac{R}{C} \left(\frac{\partial C}{\partial R} \right)_T$	$\frac{1}{\beta\alpha} \left(\frac{\partial \alpha}{\partial T} \right)_P$
Cu3I	0.50	0.95	—
CuBr	0.55	0.67	—
AgCl	0.37	0.45	0.27
AgBr	0.51	0.04	0.20

3. Discussion

The cuprous halides are tetrahedrally coordinated compounds with stronger covalent bond than that of silver halides (Phillips 1970). The photoelastic behaviour of cuprous as well as silver halides is similar to that exhibited by alkali halides (Aggarwal and Szigeti 1970) in the sense that their electronic or high frequency dielectric constant increases with pressure. Following Phillips-Van Vechten dielectric theory one can write (Van Vechten 1969)

$$\frac{V}{\epsilon} \left(\frac{\partial \epsilon}{\partial V} \right)_T = \frac{2}{3} \frac{(\epsilon-1)}{\epsilon} \left[-1.5 + 2.48(1-f) - f \frac{R}{C} \left(\frac{\partial C}{\partial R} \right)_T \right] \quad (9)$$

where f is the fractional ionic character and C is the electronegativity parameter. Theoretical calculation of $\left(\frac{\partial C}{\partial R} \right)_T$ turns out to be rather difficult. However, after inspecting experimental values of $\left(\frac{\partial \epsilon}{\partial V} \right)_T$ for various ionic crystals, Van Vechten (1969) arrived at the interesting conclusion that

$$\frac{R}{C} \left(\frac{\partial C}{\partial R} \right)_T \simeq 0 \quad (10)$$

is a characteristic feature of highly ionic crystals. The above criterion (equation 10) is best obeyed by alkali halides. Significant deviations from this rule are, however, expected for those crystals which are partially covalent. We have evaluated $\frac{R}{C} \left(\frac{\partial C}{\partial R} \right)_T$ from equation (9) for the crystals under study. These values should, however, not be considered highly accurate. Firstly these are derived in an empirical manner. Secondly the uncertainties in the calculated values of $\frac{V}{\epsilon} \left(\frac{\partial \epsilon}{\partial V} \right)_T$ may directly affect the magnitudes of $\frac{R}{C} \left(\frac{\partial C}{\partial R} \right)_T$. Still we

can approximately find out how far equation (10) is obeyed by cuprous and silver halides. It is observed from table 3 that values of $\frac{R}{C} \left(\frac{\partial C}{\partial R} \right)_T$ are smaller for silver halides than those for cuprous halides. This is in conformity with Van Vechten's prediction since silver salts possess lower values of ionicities as compared to those for cuprous salts.

It is apparent from table 1 that the values of $\frac{V}{\epsilon} \left(\frac{\partial \epsilon}{\partial V} \right)_T$ calculated from equation (5) are in better agreement with experimental values than those obtained from equation (4). This shows the importance of considering the variation of polarizability with volume in the theory of strain derivative of electronic dielectric constant. The agreement between calculated and experimental values of $\frac{V}{\epsilon} \left(\frac{\partial \epsilon}{\partial V} \right)_T$ is good for the cuprous halides. It should be remarked that the cuprous halides are only known tetrahedrally coordinated binary semiconductors to have negative value of $\frac{V}{\epsilon} \left(\frac{\partial \epsilon}{\partial V} \right)_T$. On the other hand, $\frac{V}{\epsilon} \left(\frac{\partial \epsilon}{\partial V} \right)_T$ is positive for tetrahedral crystals like ZnO, ZnS, CdS and GaAs (Vedam and Davis 1969, Cardona 1972).

We observe from table 1 that for silver halides the calculated values of $\frac{V}{\epsilon} \left(\frac{\partial \epsilon}{\partial V} \right)_T$ differ substantially from the values of $\frac{V}{\epsilon} \left(\frac{\partial \epsilon}{\partial V} \right)_P$. One can seek an explanation for this difference by emphasising the fact that $\frac{V}{\epsilon} \left(\frac{\partial \epsilon}{\partial V} \right)_P$ includes also a contribution arising from the temperature dependence of polarizability at constant volume. Following Vedam *et al* (1975) we can write

$$\frac{V}{\epsilon} \left(\frac{\partial \epsilon}{\partial V} \right)_P = - \frac{(\epsilon-1)(\epsilon+2)}{3\epsilon} \left[1 - \lambda - \frac{1}{\beta\alpha} \left(\frac{\partial \alpha}{\partial T} \right)_V \right] \quad (11)$$

Equations (5) and (11) yield

$$\frac{V}{\epsilon} \left(\frac{\partial \epsilon}{\partial V} \right)_P = \frac{V}{\epsilon} \left(\frac{\partial \epsilon}{\partial V} \right)_T + \frac{(\epsilon-1)(\epsilon+2)}{3\epsilon\beta\alpha} \left(\frac{\partial \alpha}{\partial T} \right)_V \quad (12)$$

Thus the difference between $\frac{V}{\epsilon} \left(\frac{\partial \epsilon}{\partial V} \right)_P$ and $\frac{V}{\epsilon} \left(\frac{\partial \epsilon}{\partial V} \right)_T$ as apparent from table 1 can be ascribed to the temperature dependence of polarizability at constant volume. Using our calculated values of $\frac{V}{\epsilon} \left(\frac{\partial \epsilon}{\partial V} \right)_T$ we have obtained $\frac{1}{\beta\alpha} \left(\frac{\partial \alpha}{\partial T} \right)_V$ for AgCl and AgBr. It is evident from table 3 that the variation in polarizability

with temperature is positive for these crystals. It will be pertinent to remark here that Vedam *et al* have also obtained positive values of $-\frac{1}{\beta\alpha} \left(\frac{\partial\alpha}{\partial T} \right)_V$ for a number of other compounds. It should be mentioned that the temperature dependence of polarizability at fixed volume is a useful quantity in the study of the anharmonic behaviour of crystals.

Acknowledgment

The work has been supported financially by the U.G.C., New Delhi. Authors are grateful to the referee for his valuable comments.

References

- Aggarwal K G and Szigeti B 1970 *J. Phys.* **C3** 1097
 Bakhshi P S, Goyal S C and Jai Shanker 1977 *J. Inorg. Nucl. Chemistry* **39** 546
 Biegelsen D K, Zesch J C and Schwab C 1976 *Phys. Rev.* **B14** 3578
 Burstein E and Smith P L 1948 *Phys. Rev.* **74** 229
 Jai Shanker, Sharma P O and Lashkari A K G 1977 *Phil. Mag.* **35** 1671
 Lawaetz P 1971 *Phys. Rev. Lett.* **26** 697
 Lowndes R P and Martin D H 1969 *Proc. Roy. Soc.* **A308** 473
 Lowndes R P and Martin D H 1970 *Proc. Roy. Soc.* **A316** 351
 Pauling L 1927 *Proc. Roy. Soc.* **A114** 181
 Phillips J C 1970 *Rev. Mod. Phys.* **42** 317
 Pirenne J and Kartheuser E 1964 *Physica* **30** 2005
 Sharma H P, Jai Shanker and Verma M P 1976 *Phil. Mag.* **34** 163
 Slater J C 1965 *Quantum Theory of Molecular and Solids Vol. 2* (McGraw-Hill, U.S.A.)
 Szigeti B 1950 *Proc. Roy. Soc.* **A204** 51
 Tessman J R, Kahn J H and Schockley W 1953 *Phys. Rev.* **92** 890
 Van Vechten J A 1969 *Phys. Rev.* **182** 891
 Vedam K, Kirk J L and Achar B N N 1975 *J. Solid State Chemistry* **12** 213
 Vedam K and Davis T A 1969 *Phys. Rev.* **181** 1196

U-centre modes in mixed alkali halides*

R K Gupta and A K Singh

Department of Physics, University of Jodhpur, Jodhpur-342 001

Received 27 January 1978

Abstract. The localized mode due to U-centre in various alkali halides containing additive cation impurity at one of the six neighbouring sites have been computed by considering the vibrations of the U-centre and additive cation impurity. Using group theory analytical expressions have been derived for the doubly degenerate E mode and the non-degenerate A_1 mode, in terms of the change in nearest neighbouring overlapping force constant ΔA and the Green function G of the perfect crystal. The theoretical results have been compared with the experimental measurements.

1. Introduction

The first experimental observation on the local modes due to U-centre in mixed alkali-halides was made by Schafer (1960) in (KCl : Rb+H) system. More detailed results were obtained by Mirkin and Reshina (1966) and by Barth and Fritz (1967). Recently Gupta and Singh (1977) have reported the primary results of the computation of these modes in (KBr : Rb+H) system by Green function technique. In the present paper we report the detailed theoretical results for (NaCl : K+H), (RbBr : K+H), (RbCl : K+H) and (KBr : Na+H) systems. It is hoped that this investigation will be useful in understanding the changes that has taken place in crystal due to the substitution of the impurity at the cation site

2. Method of Calculation

It is well known that the local vibrations due to U-centres in alkali-halides are triply degenerate due to cubic symmetry of these crystals. However, when one of the six nearest neighbour cation is replaced by an additive cation impurity, the O_h symmetry of the system changes to C_{4v} site symmetry and the triply degenerate mode splits-up into a doubly degenerate E mode and a non-degenerate A_1 mode.

* This paper was presented in 65th Session of the Indian Science Congress, Ahmedabad (1978), where only abstract has been published.

For the computation of these modes we consider the vibrations of the hydride ion and cation impurity only. The modes of vibrations are given by

$$\Gamma_6 = 2E + 2A_1. \quad (1)$$

These modes have been obtained by the Green function method (1967) using determinantal equation

$$|\mathbf{I} - \mathbf{GJ}| = 0 \quad (2)$$

where G is the Green function matrix of the perfect lattice and J is the perturbation matrix as a result of the defects which contain both mass changes and changes in the short-range interactions. The short-range interactions are represented by Kellermann's coefficients A and B (1940). For simplicity we have taken the changes in B as zero by assuming that there is no relaxation around the defect and consider the changes in short-range force constant A only. We use the following notations

$$\left. \begin{aligned} \Delta A &= A(\text{cation defect}^+ - \text{H}^-) - A(\text{perfect lattice}) \\ \Delta A_1 &= A(\text{cation defect}^+ - \text{H}^-) - A(\text{perfect lattice}) \\ \Delta A_2 &= A(\text{cation defect}^+ - \text{Anion}^-) - A(\text{perfect lattice}) \\ \Delta A_3 &= \Delta A_1 - \Delta A. \end{aligned} \right\} \quad (3)$$

Here $A(\text{cation defect}^+ - \text{H}^-)$ represents the A parameter for (cation defect⁺ - H⁻) bond etc. In this case $|\mathbf{I} - \mathbf{GJ}|$ is a (6×6) matrix. Using group theory, symmetry coordinates were constructed and the (6×6) matrix was block diagonalised into various irreducible representations. We obtain the following determinants for A_1 and E modes.

A_1 mode

$$\begin{vmatrix} D_0 & D_1 \\ D_2 & D_3 \end{vmatrix} = 0 \quad (4)$$

E mode

$$\begin{vmatrix} d_0 & d_1 \\ d_2 & d_3 \end{vmatrix} = 0 \quad (5)$$

here

$$\begin{aligned}
 D_0 &= 1 - g_0 J_0 + g_2 \Delta A_1 \\
 D_1 &= g_2 J_1 - g_0 \Delta A_1 \\
 D_2 &= g_2 J_0 - g_1 \Delta A_1 \\
 D_3 &= 1 - g_1 J_1 + g_2 \Delta A_1 \\
 d_1 &= 1 - g_1 j_1 \\
 d_1 &= g_3 j_0 \\
 d_2 &= g_3 j_1 \\
 d_3 &= 1 - g_0 j_0.
 \end{aligned} \tag{6}$$

$$\left. \begin{aligned}
 J_0 &= (M_{anion} - M_H)w^2 + \Delta A + \Delta A_1 \\
 J_1 &= (M_{cation\ perfect} - M_{cation\ defect})w^2 + \Delta A_1 + \Delta A_2 \\
 j_0 &= (M_{anion} - M_H)w^2 + 2\Delta A \\
 j_1 &= (M_{cation\ perfect} - M_{cation\ defect})w^2 + 2\Delta A_2
 \end{aligned} \right\} \tag{7}$$

and the g_0 act are the Green function elements given by

$$\left. \begin{aligned}
 g_0 &= G_{xx}(000, -; 000, -; w^2) \\
 g_1 &= G_{xx}(000, +; 000, +; w^2) \\
 g_2 &= G_{xx}(000, -; 100, +; w^2) \\
 g_3 &= G_{yy}(000, -; 100, +; w^2)
 \end{aligned} \right\} \tag{8}$$

It can be seen from these equations that the expressions for various modes involve parameter ΔA , ΔA_1 , ΔA_2 and the Green function G of the perfect crystal. The Green functions computed on the bases of neutron fitted shell model of Raunio and Rolandson (1970) were used in our calculations.

3. Results

The computed results using the above expressions are displayed in Tables 1, 2, 3 and 4. The parameter ΔA , ΔA_1 , ΔA_2 are in units of $e^2/2V$ of the perfect lattice. It has been found from the computation that the variation of ΔA_2 does not change the values of these modes. However, the variation of ΔA_1 changes the vibrational frequencies of the non-degenerate A_1 mode but this variation does not affect the frequencies of doubly degenerate E mode. The variation of ΔA changes very much. the vibrational frequencies of E mode, however a small

variation of the frequencies of A_1 mode is also observed. As expected the value of ΔA_3 comes out to be negative if we replace the cation by a lighter impurity and positive if we replace by a heavier impurity. In Tables 1, 2, 3 and 4, ν_1 refer to the frequency of doubly degenerate E mode and ν_2 non-degenerate A_1 mode.

Table 1. Local-mode frequencies of hydride ions in mixed (NaCl:K+H) system (in cm^{-1})

ΔA_1 in units of $e^2/2V$ of NaCl	ΔA in units of $e^2/2V$ of NaCl						Experimental	
	$\Delta A = -5.3$		$\Delta A = -5.5$		$\Delta A = -5.7$			
	ν_1	ν_2	ν_1	ν_2	ν_1	ν_2	ν_1	ν_2
-0.3	529.9	703.1	519.4	697.8	498.4	692.6		
-0.5	529.9	697.8	519.4	692.6	498.4	682.1	514.0	686.0
-0.7	529.9	692.6	519.4	682.1	498.4	676.9		
-0.9	529.9	687.3	519.4	676.9	498.4	671.5		

Table 2. Local-mode frequencies of hydride ions in mixed (RbBr:K+H) system (in cm^{-1})

ΔA_1 in units of $e^2/2V$ of RbBr	ΔA in units of $e^2/2V$ of RbBr						Experimental	
	$\Delta A = -5.6$		$\Delta A = -5.8$		$\Delta A = -6.0$			
	ν_1	ν_2	ν_1	ν_2	ν_1	ν_2	ν_1	ν_2
-6.8	448.3	412.0	437.9	406.6	425.0	401.7		
-7.1	448.3	404.2	437.9	396.4	425.0	391.8	443.0	388.0
-7.4	448.3	393.9	437.9	388.7	425.0	383.5		
-7.7	448.3	386.1	437.9	378.3	425.0	373.2		

Table 3. Local-mode frequencies of hydride ions in mixed (RbCl:K+H) system (in cm^{-1})

ΔA_1 in units of $e^2/2V$ of RbCl	ΔA in units of $e^2/2V$ of RbCl						Experimental	
	$\Delta A = -5.4$		$\Delta A = -5.6$		$\Delta A = -5.8$			
	ν_1	ν_2	ν_1	ν_2	ν_1	ν_2	ν_1	ν_2
-6.6	508.0	472.9	497.5	465.8	483.4	458.8		
-6.9	508.0	462.3	497.5	455.3	483.4	451.7	493.0	432.0
-7.2	508.0	455.3	499.5	448.3	483.4	441.2		
-7.5	508.0	444.7	497.5	437.7	483.4	434.0		

Table 4. Local mode frequencies of hydride ions in mixed (KBr : Rb+H) system (in cm^{-1})

ΔA_1 in units of $e^2/2V$ of KBr	ΔA in units of $e^2/2V$ of KBr						Experimental	
	$\Delta A = -5.7$		$\Delta A = -5.9$		$\Delta A = -6.1$			
	ν_1	ν_2	ν_1	ν_2	ν_1	ν_2	ν_1	ν_2
-2.8	438.6	515.3	428.6	511.9	415.2	508.6		
-3.1	438.6	508.6	428.6	501.9	415.2	498.6	426.0	494.0
-3.4	438.6	501.9	428.6	495.3	415.2	488.6		
-3.7	438.6	491.9	428.6	488.6	415.2	481.9		

The computed results have been compared with the experimental results. Looking to the simplicity of the model, the results are quite satisfactory. Model can be further improved by considering the defect space consisting of H^- ion and all its nearest neighbour. In that case the problem will be a little more complicated and one needs large number of Green functions. These calculations are in progress and will be communicated in due course of time.

Acknowledgments

We are thankful to Prof. A. N. Nigam. One of us (AKS) is thankful to Jodhpur University for the grant of U.G.C. Fellowship.

References

- Barth W and Fritz B 1967 *Phys. Stat. Sol.* **19** 515
 Gupta R K and Singh A K 1977 *Phys. Lett.* **59A** 489
 Kellermann E W 1940 *Phil. Trans. Roy. Soc.* **A238** 513
 Ludwig W 1967 *Springer Tracts in Modern Phys.* **43** Springer, New York;
 Maradudin A A 1966 *Solid State Phys.* (Edited by Seitz and Turnbull) Vol **18**
 Mirlin D N and Reshinya I I 1966 *Fiz. Tver. Tela* **8** 152
 Raunio G and Rolandson S 1970 *Phys. Rev.* **B2** 2098
 Schaefer G 1960 *J. Phys. Chem. Solids* **12** 233

Effect of doping density on the efficiency of a Schottky barrier solar cell

N K Swami and H M Ghule

Physics Group, Birla Institute of Technology and Science, Pilani-333031 (Rajasthan)

Received 30 June 1978

Abstract. It is known that the doping density greatly affects various parameters such as the depletion region width, diffusion length, minority carrier life time, diode quality factor and mobility of the electrons of a Schottky barrier solar cell. All these factors play an important role in determining the efficiency of such a cell. We have studied the variations of the short circuit current and efficiency of the cell with donor density. The interfacial layer thickness appears as a parameter in our calculations. The cell efficiency initially increases with the doping density and after attaining a maximum value starts decreasing.

1. Introduction

In recent years studies on Schottky barrier solar cells (SBSC's) have increased considerably. One drawback with SBSC's is that they give low open circuit voltage V_{OC} . V_{OC} is however improved (Stirn and Yeh 1975, Ponpon and Siffert 1976) when an insulating layer is present between the metal and the semiconductor. The thickness of the interfacial layer δ is not the only factor affecting the efficiency η of a SBSC. Doping density is also very important. We report here results based on a number of calculations incorporating the dependence of various factors like the minority carrier life time, diffusion length, depletion region width, resistivity of the sample and diode quality factor with doping density.

2. Theory

On illuminating a SBSC (Au-n Si system), a voltage V is developed, a part V_i of which appears across the interfacial layer while the rest $V_s (= V - V_i)$ appears across the depletion region of the semiconductor of width w . The total current through the device is given by

$$I = I_{Ph} - (I_n + I_h), \quad (1)$$

where I_{Ph} is the photogenerated current. I_{Ph} is given by (Anderson *et al* 1974)

$$I_{Ph} = e\phi \left(1 - \frac{e^{-\alpha w}}{1 + \alpha L_p} \right) \quad (2)$$

where e is the electronic charge, ϕ is the photon flux (number/cm²sec), α is the

absorption coefficient for Si and $L_P (= \sqrt{D_P \tau_P})$ is the diffusion length of the minority carrier, D_P and τ_P are the diffusion coefficient and minority carrier life time for holes respectively.

I_n and I_h are the dark current components due to electrons and holes respectively. I_h is given by (Sze 1969)

$$I_h = \frac{ep_n D_P}{L_P} \left[\exp \left(\frac{eV}{kT} \right) - 1 \right] \quad (3)$$

where p_n is the equilibrium hole concentration in the bulk of the semiconductor, k is the Boltzmann's constant.

Using Strikha's Theory (Strikha 1964) I_n is given by

$$I_n = A^* T^2 \exp \left(- \frac{e\phi_{B_n}}{kT} \right) \frac{4E_s^0 \mu_n / (4E_s^0 \mu_n + \bar{T}_r \bar{v})}{\left[\exp \left(\frac{eV_s}{kT} \right) - \exp \left(- \frac{eV_t}{kT} \right) \right]} \quad (4)$$

where A^* is Richardson's constant, E_s^0 is the electric field in semiconductor across the boundary, ϕ_{B_n} is the barrier height, \bar{v} is the effective recombination velocity in the depletion region, μ_n is the mobility of electrons, \bar{T}_r is the transmission coefficient for electrons (Strikha 1971) through the interfacial layer, which is usually taken as 1 in most of the papers.

Taking into account the series resistance R_s (Dubey 1976) and the diode factor n , I is given by

$$I = I_{Ph} - I_0 [e^{e(V+IR_s)/nkT} - 1] \quad (5)$$

where $n = 1 + \frac{\epsilon_s \delta}{\epsilon_i W}$, (ϵ_s and ϵ_i are the permittivities of semiconductor and interfacial layer respectively).

From equation (5), we can get short circuit current I_{sc} ($= V = 0$), open circuit voltage V_{oc} ($= I = 0$), V_{mp} (Voltage for maximum power), I_{mp} (current for maximum power), fill factor F ($= I_{mp} \cdot V_{mp} / I_{sc} \cdot V_{oc}$) and efficiency ($= \frac{P_{mp}}{P_{in}}$) of the cell.

3. Results and discussion

The donor density affects the minority carrier life time according to the relation (Fossum 1976).

$$\tau_P = \frac{3.9 \times 10^{-4}}{1 + N_D / N_{D0}} \quad \text{where } N_{D0} = 7.1 \times 10^{15} \text{ cm}^{-3}.$$

It is clear that increase of N_D decreases the minority carrier life time which in turn affects the short circuit current. Figure 1 shows that the short circuit

current remains almost constant upto the donor density $10^{15}/\text{cm}^3$, but thereafter it decreases with N_D . One reason for this behaviour is the decrease in the minority carrier life time and diffusion length ($L_P = \sqrt{D_P \tau_P}$) of the carriers. Another factor which is responsible for the decrease in short circuit current is the decrease in the depletion region width w resulting in a decrease in the number of carriers generated in the depletion region.

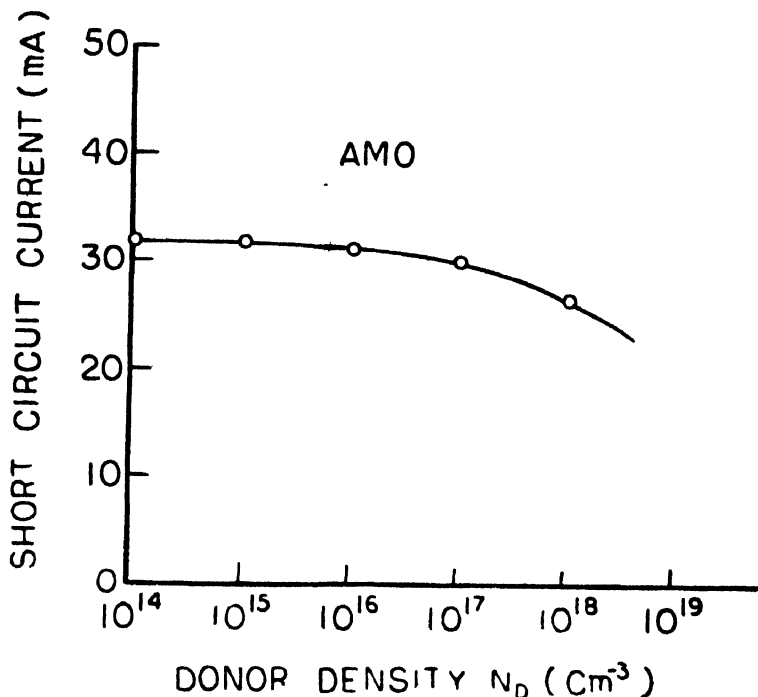


Figure 1. Variation of short circuit current of the SBSC with donor density for AMO illumination.

In figure 2 we have shown variation of efficiency η of the SBSC. The graph 2 shows the efficiency η of the cell first increases with N_D , it becomes maximum and thereafter it decreases with donor density. The primary reasons for increase in the efficiency are increase in the diode quality factor n and increase in the open circuit voltage. However, after $10^{17}/\text{cm}^3$ the decrease in I_{sc} becomes stronger than increase in the diode quality factor and the open circuit voltage with N_D and this results in a decrease in the efficiency of the SBSC. At high doping the saturation current I_0 also becomes very large and this also gives rise to decrease in efficiency.

We have not considered in our calculations the Schottky barrier lowering. It also affects the open circuit voltage at higher doping. The variation of μ_n , D_P , with N_D was taken from Si data Book (Wolf 1969). In our calculations, the graphs are obtained for Au, -n Si system with $\phi_{Bn} = 0.8$ eV, and the value for P_{in} for AMO sunlight is $135 \text{ mw}/\text{cm}^2$.

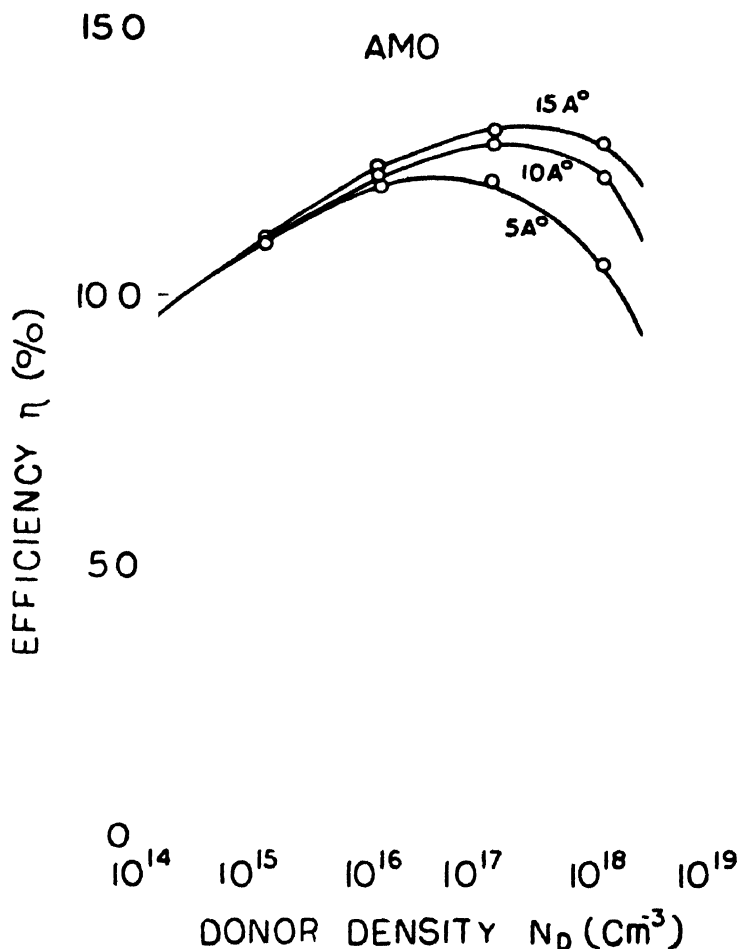


Figure 2. Variation of efficiency of the SBSC with donor density for AMO illumination.

Acknowledgment

The authors wish to thank Prof. V. K. Tewary, Dean, Research and Consultancy Division, B.I.T.S. for his keen interest and encouragement. One of the authors (N.K.S.) expresses his sincere thanks to the U.G.C. for the financial support.

References

- Anderson W A, Delahoy A E and Milano R A 1974 *J. Appl. Phys.* **45** 3913
- Dubey P K 1976 *Appl. Phys. Lett.* **29** 435
- Fossum J G 1976 *Solid State Electronics* **19** 269
- Ponpon J P and Siffert P 1976 *J. Appl. Phys.* **47** 3248
- Stirn R J and Yeh Y C M 1975 *Appl. Phys. Lett.* **27** 95
- Strikha V I 1964 *Radio Engg. and Electronics Phys.* **9** 552
- Strikha V I 1971 *Soviet Physics Semiconductors* **4** 1705
- Sze S M 1969 *Physics of Semiconductor Devices* Chapter 8, John Wiley & Sons, Inc.
- Wolf H F 1969 *Silicon Semiconductor Data* Oxford Pergamon Press p 45-47

Study of the phase transition U_3O_{8-x} to $\text{U}_8\text{O}_{21+z}$ by electrical conductivity measurement

A N Virkar, A M George and M D Karkhanavala

Chemistry Division, Bhabha Atomic Research Centre, Trombay, Bombay-400085

Received 7 August 1978

Abstract. Electrical conductivity of U_3O_{8-x} has been measured in the temperature interval of 850 to 1275 K in air using the four-probe technique. The plot of logarithm of conductivity versus reciprocal temperature during heating consists of two nearly parallel straight lines with a discontinuity in the temperature range of 1111-1190 K. In this temperature interval the conductivity is nearly constant, thereby showing the existence of a biphasic region. During subsequent thermal cycling the samples do not show any discontinuity in conductivity. From the existing literature on U_3O_{8-x} it is found that the two equilibrium phases in the biphasic region are U_3O_{8-x} and $\text{U}_8\text{O}_{21+z}$.

1. Introduction

A number of intermediate oxide phases exist between UO_2 and UO_3 , some of them are found to show several polymorphic forms (Cordfunke 1969). U_3O_8 shows a high degree of non-stoichiometry (Gronvold 1948, Randle and McDonald 1948, Hockstra and Katz 1955, Sata 1955, Blackburn 1958, Ackermann and Chang 1973, Rachev 1964) and hence, the region extending from $\text{UO}_{2.60}$ to $\text{UO}_{2.667}$ is quite interesting. Regarding the composition of U_3O_8 phase, there has been considerable differences of opinion. A variety of structures were reported by Kovba (1967) corresponding to the composition range $\text{UO}_{2.50}$ to $\text{UO}_{2.67}$. Numerous studies of its non-stoichiometric structure and thermal and thermodynamic behaviour have been made by number of workers (Anderson 1958). Kiukkola (1962) obtained thermodynamic data by measuring the electromotive force on galvanic cells at temperatures 1073 to 1273 K and concluded that the lower composition limit of U_3O_{8-x} is between 2.61 and 2.625. The composition of U_3O_{8-x} phase, in general, lies in the range 2.60 to $\text{UO}_{2.667}$. The upper limit of U_3O_8 appears to be the stoichiometric composition.

Biltz and Muller (1957) found that as the temperature increased above 873 K, U_3O_8 slowly began to lose oxygen at oxygen pressure of $0.1332 \times 10^4 \text{ N/m}^2$ until at 1653 K the composition was found to be $\text{UO}_{2.2}$. Warde and Johnson (1955) also showed that U_3O_8 lost oxygen above 863 K and converted to UO_2 .

in the range 1423 to 1673 K. In recent years, there have been increasing evidences for the possibility of the existence of more than one phase in the previously assumed single phase region of U_3O_8 .

The thermogravimetric and electrical conductivity studies on non-stoichiometric U_3O_{8-x} by Matsui *et al* (1974), in the temperature range $1038 \leq T \leq 1268$ K and in the pressure interval $0.1013 \times 10^2 \text{ Nm}^{-2} \leq PO_2 \leq 0.1013 \times 10^6 \text{ Nm}^{-2}$, suggested the presence of six phases within U_3O_{8-x} phase separated by second or higher order transitions in the composition range $O/U = 2.63$ to 2.66 .

Ackermann *et al* (1973) previously assumed that U_3O_8 region is homogeneous but recently they observed orthorhombic to hexagonal transition at 623 K; the hexagonal form being stable upto 1148 K. Another transformation from hexagonal to a pseudo-orthorhombic phase was reported to initiate above 1148 K which was found to be over at 1203 K (Ackermann *et al* 1977). At the same time, Dharwadkar and Chandrasekharaiah (1973), in their study on the thermal stability of U_3O_{8-x} by micro-thermogravimetric measurements, reported a sharp phase transition from U_3O_{8-x} to U_8O_{21+z} phase between 1123 to 1223 K with rapid reversible oxygen loss. Similarly high temperature X-ray diffraction patterns above and below the transition temperature showed splitting and broadening of certain reflections. On thermal cycling these measurements showed hysteresis (Dharwadkar 1975). Malinin and Tolmachen (1968) observed an enthalpy change of 400 cal. at 1143–1193 K by the differential thermal analysis (DTA).

The electrical conductivity of the U_3O_8 has been studied by many investigators (Le Blanc and Sachse 1930, 1931, George and Karkhanavala 1963, Singh and Karkhanavala 1966). Investigations on electrical conductivity made by Matsui and coworkers (1974) using four probe method showed changes in slopes corresponding to phase transitions. But the reversibility of these phases on thermal cycling is not clear from their work.

Ishii and coworkers (1970) studied the electrical conductivity below and above 1125 K but they started with the phase U_5O_{13+z} . They employed the electrical conductivity measurements for the study of the phase diagram of Uranium-oxygen system around U_3O_8 region. Two transformations, one orthorhombic to hexagonal and the other U_5O_{13+z} (please refer to following page) to U_3O_{8-x} phase, were indicated from the $\log \sigma$ vs $1/T$ plots obtained for different compositions.

From the above review of the electrical conductivity data, it is clear that the electrical conductivity was studied mostly upto the temperature of 1123 K. As in the recent years there have been increasing evidences of phase transitions (≥ 1125 K) in U_3O_8 , the present investigations were made to study these transitions and their reversibility.

2. Experimental

U_3O_8 powder (nuclear pure grade) was compacted to pellets of 16 mm diameter and 3 mm thickness at 155 kg/cm² and sintered in one atmosphere of oxygen for one week at 1200 K. U_3O_8 pellets of 92% theoretical density and O/U ratio 2.667 were obtained.

The four-probe method was used to measure the electrical conductivity of these specimens in air from 850 to 1275 K. Details of the apparatus used have been described elsewhere (George and Gopalakrishnan 1975).

3. Results and discussions

Typical temperature dependence of the electrical conductivity of a few samples in air is shown in figure 1. The values as given in the plot on three samples, are

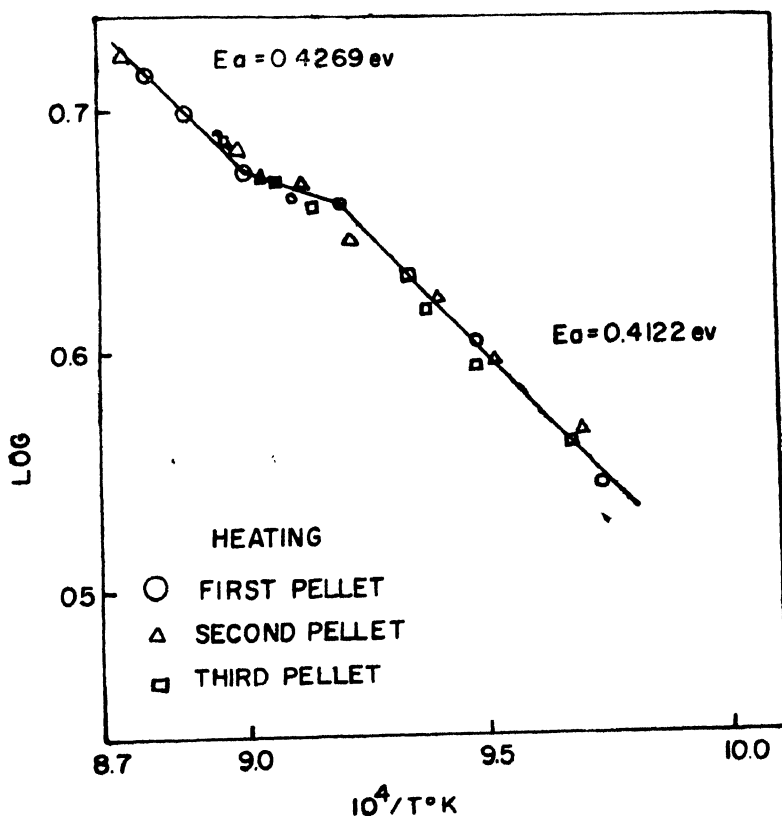


Figure 1. U_3O_8 - U_8O_{21+z} transformation during heating.

found to agree well within the limits of experimental error. The temperature independent region in all the three cases falls between 1111-1190 K during the

heating cycle. Below and above this region, the activation energies are found to be 0.412 eV and 0.427 eV respectively. However, on thermal cycling the samples do not show the conductivity discontinuity as given in figure 2. During

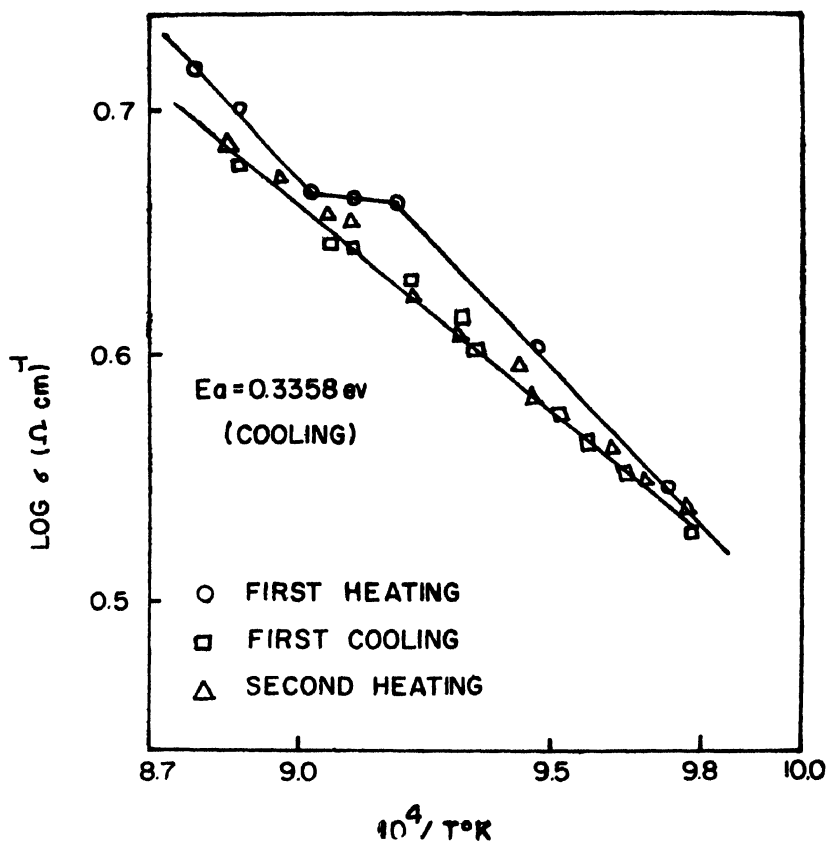


Figure 2. U_3O_8 - $\text{U}_8\text{O}_{21+x}$ transformation during the thermal cycling.

the first heating the constant conductivity region is clearly seen; on (first) cooling this region is not sufficiently pronounced. On subsequent thermal cycling the conductivity does not seem to show this discontinuity. The activation energy for conductivity during thermal cycling is found to be 0.336 eV.

The temperature region where discontinuity in conductivity is observed is in good agreement with the phase transition observed by micro-thermogravimetric and X-ray diffraction study (Dharwadkar and Chandrasekharaiah 1975, Ackermann *et al* 1977). The fact that in this temperature region conductivity is nearly constant, clearly shows that more than one phase coexists in equilibrium. Analyses of the existing literature (Ishii *et al* 1970) lead to the conclusion that these phases are U_3O_{8-x} and $\text{U}_8\text{O}_{21+x}$.

Ishii *et al* (1970) studied from electrical conductivity measurement the phase transition of U_8O_{21+z} (they referred it as U_5O_{13+z}) to U_3O_{8-x} phase. It was found that their heating and cooling curves could not be superimposed due to the oxidation of U_8O_{21+z} phase to the oxygen-rich U_3O_{8-x} phase during heating which once formed remains stable on cooling. On the other hand if the starting material is U_3O_8 the same will loose oxygen in air on heating leading to the formation of oxygen-deficient U_8O_{21+z} .

In the careful X-ray studies Ackermann *et al* (1977) and Dharwadkar (1975) have found that this transition is a reversible process. Dharwadkar *et al* (1975) have shown that on heating the rate of oxygen loss during the transition is much faster than the rate of oxygen pick-up during the reverse process of cooling. In the present electrical conductivity measurements, U_3O_8 sample on heating shows a transition to an oxygen deficient phase U_8O_{21+z} . The oxygen deficient phase formed in this way can take oxygen during cooling process. But as the rate of gain of oxygen during cooling is slow which is clear from the thermogravimetric study, the extent to which a sample will readjust its composition homogenously upon cooling may be difficult to predict.

One point should be noted here that in the present study, the electrical conductivity measurements are carried out on highly dense pellets ($> 92\%$ T.D.). While both the above groups of authors have carried out experiments on powder, it is prominently seen in our results that the transition induced in the oxide consequent to or subsequent to the loss of oxygen is not reversible. Hence, kinetics of oxygen diffusion in and out of the samples are totally different from that of powders used in other experiments. Hence, our results are not directly comparable with those obtained by the authors cited above. But if sufficient time is given for cooling the sample may recover the composition.

Thus the phase transition observed in this study provides additional evidence regarding the existence of more than one phase in the previously assumed single phase region of U_3O_8 . The mechanisms of these transitions, nevertheless, demands further investigations.

Acknowledgments

Thanks are due to Dr S. R. Dharwadkar for determination of O/U ratios of the experimental samples. One of the authors (A. N. Virkar) thanks the Department of Atomic Energy for a fellowship.

References

- Ackermann R J and Chang A T 1973 *J. Chem. Thermodynamics* **5** 873
- Ackermann R J, Chang A T and Sovell C A 1977 *J. Inorg. Nucl. Chem.* **39** 751
- Anderson A F 1958 *Acta Cryst.* **11** 612

- Biltz W and Muller H 1957 *Chemistry of Uranium* Ed by Katz and Rabinowitch, National Nuclear Energy Series, Mauhattan Project Tech. Sec., Vol. 5, Chap. 11, page 249
- Blackburn P E 1958 *J. Phys. Chem.* **62**, 897
- Cordfuke E H P 1969 *Chemistry of Uranium*, Elsevier Publishing Co., New York
- Dharwadkar S. R. 1975 *Ph.D. Thesis submitted to the University of Bombay* September 1975
- Dharwadkar S R and Chandrasekharaiiah M S 1975 *J. Thermal Analysis* **7** 219
- George A M and Gopalakrishnan I K 1975 *J. Phys. E. Sci. Instr.* **8** 13
- George A M and Karkhanavala M D 1963 *J. Phys. Chem. Solids* **24** 1207
- Gronvold F and Haraddsen 1948 *Nature* **68** 162
- Hockstra R R, Siegal S, Fuchs L H and Katz J J 1955 *J. Phys. Chem.* **59** 136
- Ishii T, Naito K and Oshima K 1970 *J. Nucl. Materials* **35** 335
- Kinkkola K 1962 *Acta Chem. Scand.* **16** 327
- Kovba L M 1967 *Radiokhimiya* **9** 134
- Le Blane and Sachse H 1930 *Ber. Verhandl. Sachs. Akad. Wiss, Leipzig* **82** 155
- Le Bland and Sachse H 1931 *Z. Phys.* **82** 887
- Malinin G V and Tolmachen Y M 1968 *Radiokhimiya* **10** 362
- Mitsui T, Tsuji T and Naito K 1974 *J. Nucl. Sci. and Tech.* **11** 216 317
- Rachev V V, Kovba L M and Ippolitova E A 1964 *Dokl. Akad. Nauk. SSSR* **159** 1371
- Randle R E, Baenziger N C, Wilson A S and McDonald R A 1948 *J. Am. Chem. Soc.* **99**
- Sata T 1955 *Bull. Tokyo Inst. Tech.* **59** 136
- Singh N and Karkhanavala M D 1966 *Phys. Stat. Sol.* **17** 501
- Warde J M and Johnson J R 1955 *J. Franklin. Inst.* **260** 455

Letters to the Editors

Work hardening phenomena in single crystalline alloys and screw dislocation dipole clusters

N K Gilra

Physics Department, University of Science and Technology,
Kumasi, Ghana

Received 27 January 1977, revised 19 August 1977

In recent years, it has been shown by Sadananda and Marchinkowski (1972, 1973) that unlike screw dislocation could not pass each other due to the formation of dipoles or multipoles if it is assumed that they are constrained not to cross slip by invoking. These configurations have been extensively observed in ordered alloys by Lakso and Marcinkoski (1969) and Leamy *et al* (1969). The formation of these dipoles is helpful in explaining the work hardening of ordered and disordered single crystalline alloys. In the present communication, we deduce the formula for the flow stress and the work hardening coefficient for the model crystal with homogeneous array of long screw dislocation dipole clusters.

Here we consider a regular grid of screw dislocation dipoles along the Z axis (Figure 1a). Two such dipoles are illustrated in figure 1b. We define the flow stress τ_G as the $(\sigma_{yz})_{\max}$.

The distance d between the dipoles is equal to $1/\sqrt{t(a)}$ where $t(a)$ is the density of dipoles (dipole clusters).

For the isotropic case and 45° equilibrium configuration ($\rho = 1.5h$), the stress component of the screw dipole (σ_{yz}) given by Gilra (1977) is

$$\sigma_{yz} = -D \frac{h}{\rho^2} (\cos 2\phi - \sin 2\phi) \quad (1)$$

where $D = \frac{Gb}{2\pi}$, G is the shear modulus and $\rho = \sqrt{x^2 + y^2}$

For $y = d/2$, $\rho_1 = \rho_2$ and $\phi_2 = 2\pi - \phi_1$, the sum of the stresses coming from both the dipoles is

$$\sigma_{yz} = -\frac{Dh}{\rho^2} \cos 2\phi \quad (2)$$

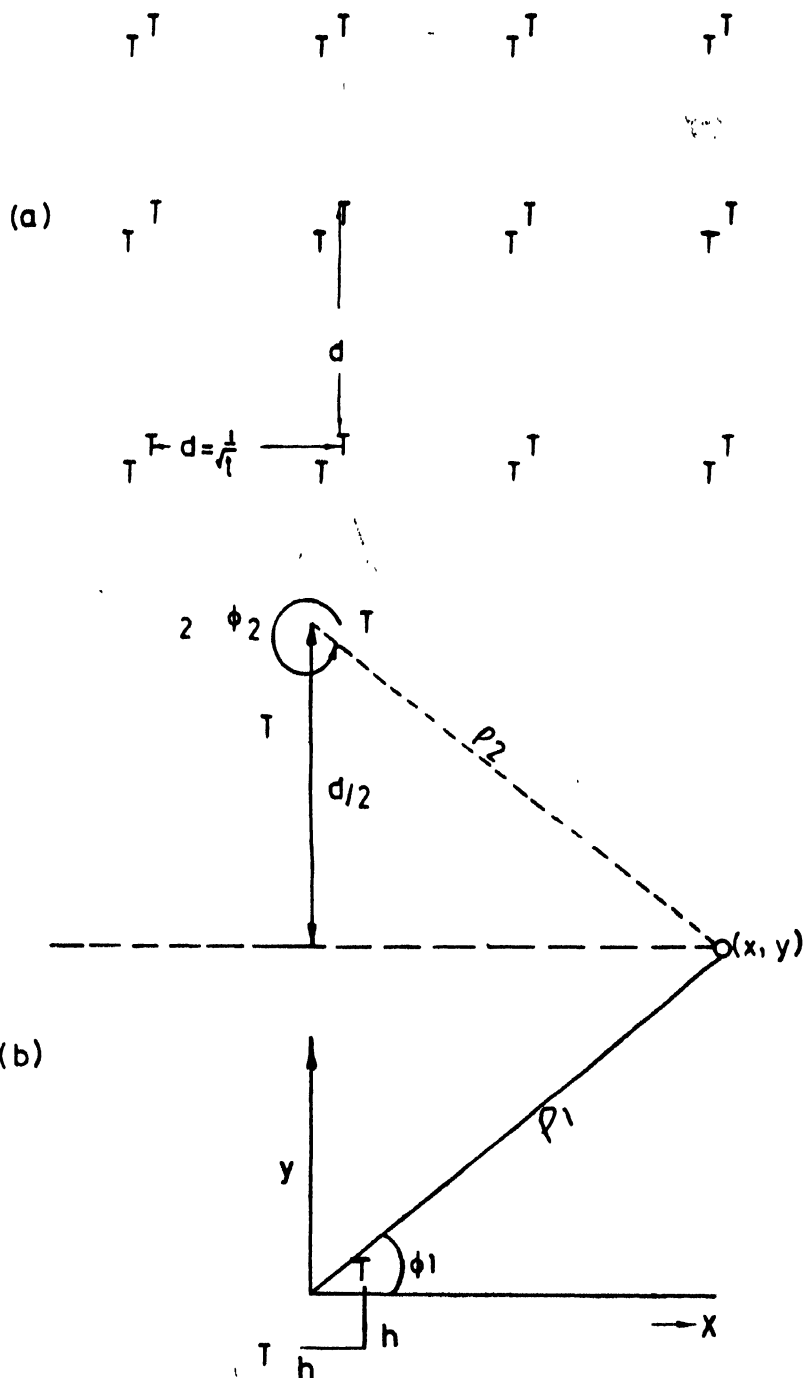


Figure 1(a) Regular grid of screw dislocation dipoles along z axis

(b) Two screw dislocation dipoles

$$\text{Thus } \tau_G = (\sigma_{yz})_{\max} = \frac{2Gb}{\pi} \ln(a) \quad (3)$$

By taking approximation of these configuration clusters by super configuration, valid for $\rho > 4d$, we obtain

$$\tau_G = \frac{2Gbn}{\pi} \ln(a) \quad (4)$$

where n is the order of the super configuration. For any array, the following expressions are obtained.

$$\frac{d\tau_G}{dn} = \frac{2Gb}{\pi} \ln(a) \quad (5)$$

$$\text{and} \quad \frac{da}{dn} = LbN \quad (6)$$

where $L = d$, is the mean free path of screw dislocation and $N = t(a)$ is the density of obstacles.

Therefore, work hardening coefficient (θ) is given as

$$\theta = \frac{d\tau_G}{da} = \frac{2G}{\pi} \ln(a) \quad (7)$$

Thus, the change of the work hardening coefficient depends directly on the change of the number of dipoles or dipole clusters t along the stress-strain curve.

Acknowledgement

The author is thankful to Professor P. A. Dziwornook for the constant encouragement during this work.

References

- Gilra N K 1977 *Ind. J. Phys.*
- Lakso G E and Marcinkowski M J 1969 *Trans AIME* **245** 1111
- Leamy H J, Kayser F X and Marcinkowski M J 1969 *Phil. Mag.* **20** 763, 769
- Sadananda K and Marcinkowski M J 1972 *J. Appl. Phys.* **43** 2609
- Sadananda K and Marcinkowski M J 1973 *Mat. Sci. Eng.* **11** 51

Hall effect and thermoelectric-power studies on stoichiometric antimony tritelluride

M M Abou Sokkina

Department of Chemistry, Faculty of Science
Tanta Univ, Tanta, Egypt, ARE

Received 3 February 1977, revised 15 August 1977

Hall effect and thermoelectric-power measurements find their great interest in determining whether the material is *p*- or *n*-type, the number of current carriers and carrier mobility.

Hall effect of antimony tritelluride polycrystals was previously measured (Parrott 1960, Eichler 1964, Liebe 1965) indicating a *p*-type conduction mechanism. On the other hand, Love (1965) investigated the Hall effect on single crystal specimen perpendicular to the (*c*) axis up to 150°C. Values of 9×10^{-2} cm³/amp.sec, 8.3×10^{19} /c.c. and 380 cm²/V-sec. were also given for Hall coefficient, carrier concentration and Hall mobility respectively.

With regard to the thermoelectric-power relatively few authors (Liebe 1965, Håken 1910, Rönnlund 1965) investigated this property. It was found to decrease strongly with the height of the intercrystalline barriers and surface states (Tyushev 1976).

The aim of the present work was to evaluate the Hall effect and the thermoelectric behaviour of stoichiometrically adjusted antimony tritelluride in continuation with other physical measurements (Hanafi 1975, Alzewel 1975), a problem which has not yet been tackled before in detail.

Stoichiometric antimony tritelluride was freshly prepared by the master alloying technique (neutralization of the excess component) under vacuum (10^{-5} mm Hg). The correct stoichiometry was controlled by both chemical and X-ray analyses. Thin films on glass substrate and rectangular blocks of the obtained sample were made and kept in vacuum desiccator for the purpose of Hall effect and thermoelectric-power measurements.

Measurements of Hall effect was performed on thin film due to the very low resistivity (2×10^{-4}), (Black 1957) of this compound and on rectangular blocks (1.6 cm \times 0.4 cm \times 0.13 cm) of the investigated specimen (prepared by pressing at 0.5 ton/cm²). D.C. current, supplied from dry battery was used. All potentials were measured by means of K₃-potentiometer (Leeds and Northrup type), connected to a moving scale galvanometer (Carl Zeiss Jena type) of sensitivity 10^{-6} volt.

The experimental arrangement and measuring technique of the thermoelectric power was that previously devised by Andrews (1974) with little modification and were carried out in the temperature range of 30°C up to 300°C.

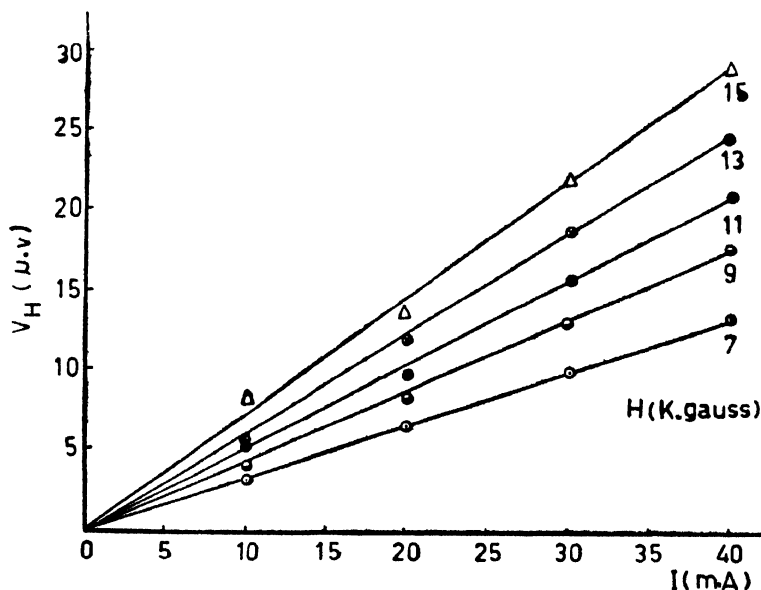
The above measurements were repeated several times in order to attain a reliable and reproducible data.

The Hall coefficient R_H in $\text{cm}^3/\text{Coulomb}$ is calculated from the relation

$$R_H = 10^8 V_H \cdot t / IH$$

where V_H is the measured Hall voltage in volts, t the thickness in cm., H the magnetic field in gauss and I the current in amperes.

Figs. (1 and 2) show the obtained Hall voltage V_H (μV) against current I (mA) at different magnetic strengths for the compressed specimen and thin film specimen respectively. It is clear that a linear relation for the change of (V_H) values as a

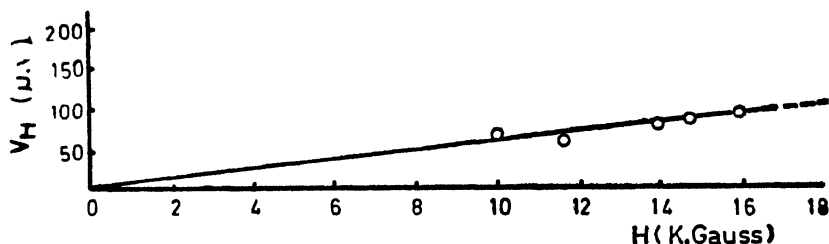


Hall voltage V_H against the current I of antimony tritelluride disc at different magnetic field H .

Figure 1.

function of current (I) was obtained. The positive sign of the Hall coefficient R_H was determined from the polarities of I , H and V_H . This indicates that the positive holes are the predominant charge carriers in this semiconductor. Thus, the material possesses a p -type conduction mechanism in conformity with that previously given by Parrott and Penn (1960).

The calculated value of R_H for the compressed specimen is $3.6 \times 10^{-2} \text{ cm}^3/\text{colomb}$.



Hall voltage V_H against the magnetic field H of antimony tritelluride thin film at a current of 0.09 mA.

Figure 2.

The number of current carriers can be determined using the following relation

$$n = A \cdot \frac{1}{R_H e}$$

where e is the electron charge $= 1.6 \times 10^{-19}$ coulomb and A is taken $3\pi/8$. A value of $2 \times 10^{19}/\text{c.c.}$ is evaluated for the number of charge carriers which is relatively small in comparison with that previously given (Black *et al* 1957) ($10^{20}/\text{c.c.}$).

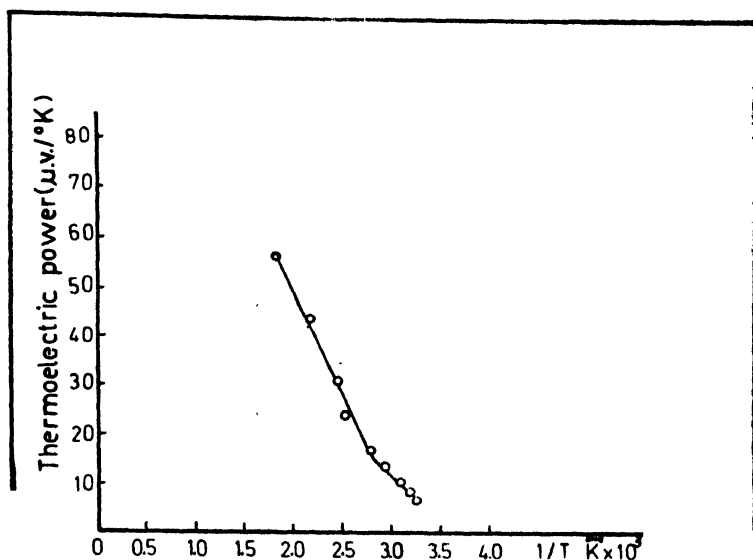
The calculation of hole mobility (μ) is done using $\mu_p = 0.5R_H/\rho$, where ρ is the specific resistivity. This resulted in a value of $80 \text{ cm}^2/\text{V-sec}$.

Thus, the differences between the number of current carriers (n) and their mobility (μ) presented by different authors including those obtained in the present work may be attributed to difference in exact stoichiometry and/or origin, nature and previous thermal history of the specimens prepared by the different authors.

The temperature dependence (K^{-10}) of the thermoelectric power ($\mu\text{V}/K$) is shown in Fig. (3) from which it can be seen that there is a discontinuity in the curve at $\simeq 420^\circ\text{K}$ which is the knee temperature in the $\log \sigma$ vs $1/T$ relation (Alzewel *et al*, 1975). This is in good conformity with similar observation as previously made by Anderson (1960) on cuprous oxide.

It was stated that in this compound, the concentration of holes is small and the p -type e.m.f. slightly changes on firing (Kokosh 1960). Donor impurities first of all lower the concentration of holes and increase the positive thermal e.m.f. If the diffusion of impurity is sufficient, the thermoelectric (Kokosh 1960) power rapidly decreases. The same author found that the thermal e.m.f. and number of current carriers for antimony tritelluride are higher when excess tellurium metal is present in combination with antimony tritelluride. Accordingly, we can attribute the difference between the various author values including

ours to the presence of different concentrations of excess tellurium. The present value is the least one indicating the least concentration of excess tellurium and hence the most stoichiometric prepared one.



The thermoelectric power of antimony tritelluride as a function of temperature.

Figure 3.

Since the prepared material possesses a considerable thermoelectric power along with very low electrical resistivity, it can be used as thermoclements in industry up to 300°C without deterioration.

References

- Alzewel K A, Abou Sekkina M M and Hanafi Z M 1975 *Z. Phys. Chem.* **94** 235
 Anderson 1960 Cited in Ioffe, A F 311, *Physics of Semiconductors* Inforsearch Limited, London
 Andrews J P 1947 *The Proceedings of the Physical Society* **59** 990
 Black J, Conwell E M, Seigle L and Spencer C W 1957 *J. Phys. Chem. Solids* **2** 240
 Eichler W and Nicke H 1964 *Wiss. Z. Martin-Luth. Univ. Muth. Nat. Reihe* **13** 1
 Haken W 1910 *Ann. Physik.* **32** 291
 Hanafi Z M, Alzewel K A, Ebrahim E M H and About Sekkina M M 1975 *Z. Phys. Chem.* **94** 291
 Harman T C, Paris B, Miller S E and Goering H L 1957 *J. Phys. and Chem. Solids* **2** 181
 Kokosh G V and Sinani S S 1960 *Soviet Phys. Solid State* **2** 1012
 Leve L 1965 *Ann. Physik.* **15** 179
 Parrott J E and Penn A W 1960 *Proc. Intern. Conf. Brussels* **2** 836
 Ronnlund B, Beckman O and Levy H 1965 *J. Phys. Chem. Solids* **26** 1281
 Smirnov I A, Andrev A A and Kutasov V A 1968 *Fiz. Tverd. Tela* **10** 1782 (Soviet Phys. of Solid State)

no condition (1952). Therefore the possible space group assigned to the sample is P_{222} or P_{mm2} or P_{mmm} .

Acknowledgment

The authors express their sincere thanks to Dr. T. Ratho, Head of the Dept. of Physics, R. E. College, Rourkela for his valuable suggestions.

References

- Azaroff L V and Buerger M J 1958 *Powder Method*, The Maple Press Company, New York, PA. McGraw Hill Book Co.
- D'eye R W M and Wait E 1960 *X-ray powder Photography in Inorganic Chemistry*, London Butterworths Scientific Publications printed in Northern Ireland, at the University Press, Belfast
- Henry N F M, Lipson H and Wooster W A 1951 *The Interpretation of X-ray, Diffraction Photographs*, London, McMillan & Co. Ltd., New York, St. Martins Press. Ito, T., 1950, X-ray Studies in Polymorphism. Maruzen, Tokyo
- International table for X-ray Crystallography* Vol. 1. The Keynock Press, England (1952), p 102-165
- Lipson H 1949 *Acta Cryst.* 2 43

Indian J. Phys. 53A, 450-453 (1979)

Effect of solid dilution on the crystal field spectra of nickel ion in single crystals

S C Mathur and R S Daryan

Department of Physics, Indian Institute of Technology,
New Delhi-110029

Received 21 September 1977

A considerable amount of work on the magnetic behaviour of the hydrated salts of nickel have been carried out (Krishnan *et al* 1933, Krishnan and Mookherji 1938, Bose 1948, Guha 1951, Bose *et al* 1958, Dreisch and Trommer 1937, Kiss *et al* 1941, Owen *et al* 1957, Hartmann and Muller 1958, Mookherji and Chhonkar 1960). The results so obtained reveal that magnetic and optical behaviour of Ni^{++} ion in crystals may be explained in several details by assuming the Ni^{++} ion in crystals to be under the influence of a strong and generally asymmetric crystalline electric field, arising out of the charges immediately surrounding the Ni^{++} ion as well as from the direct and induced effects of the charges outside this primary cluster. Under the influence of such a ligand field the ground state of $Ni^{++}(3F)$

splits into a singlet and two triplets with the increasing order of energy. The next higher state $3p$ with the same parity lies at about 15840 cm^{-1} (Owen 1955) above it (Fig. 1).

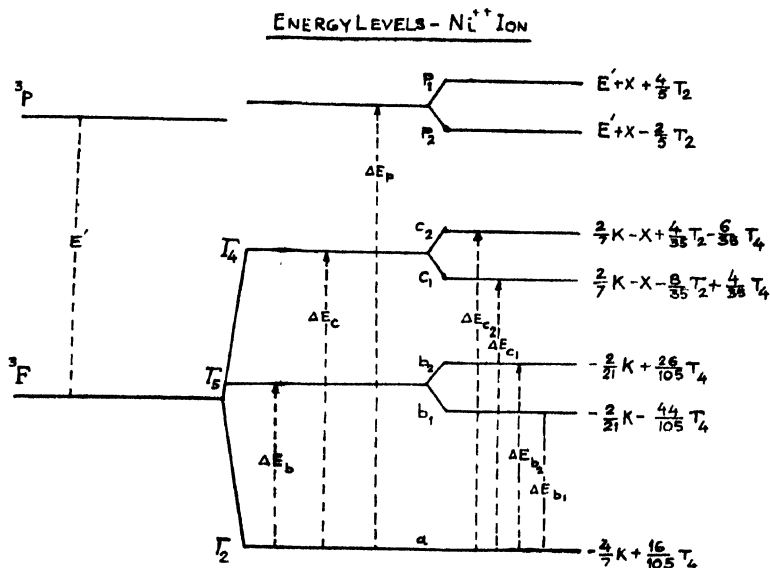


Figure 1.

Leifer and Ballhausen (1959), Owen *et al* (1957) and Engelman (1961) theoretically treated the absorption spectra of Ni^{++} ions in crystals and found that the number of levels, their relative separations and their intensities are in good accord with that what one should expect to occur with a crystal field of cubic symmetry. One direct consequence of such a cubic field will mean complete magnetic isotropy of the water cluster surrounding the Ni^{++} ion, but this is not supported by the experimental findings of Krishnan and Mookherji (1938), Bose *et al* (1958) and by our results also on the nickel ion in single crystals. Recently Bose and Chatterji (1963) have explained theoretically the absorption spectra of Mookherji and Chhonkar (1960) by taking the Ni^{++} ion under the influence of a crystal field of predominantly cubic in symmetry on which a small orthorhombic component and spin-orbit coupling were superimposed.

Therefore, in nickel Tutton salts, one should consider the nickel ion under the influence of a tetragonally distorted octahedral crystal field. One should obtain at least five absorption peaks in the visible and near infrared region. Mookherji and Chhonkar (1960) and Dreisch and Trommer (1937) have shown that the nickel salt crystals have three absorption maxima in the visible region centered at about 0.395 , 0.650 , and 0.720μ respectively. Low (1958) has obtained four absorption maxima in case of Ni^{++} ion in a crystal of MgO , three in the visible region and one broad band in the near infrared region. In our case we observed

four absorption maxima in the diluted crystals of Nickel Tutton salts (Fig. 2) but as we increase the dilution of the nickel ion in crystals by solid dilution the resolution increases and we observed five absorption maxima in the visible and near infrared region centered at about 0.394, 0.660, 0.720, 1.125, and 1.270 μ respectively (Mathur and Daryan 1978) (Figs 3-4).

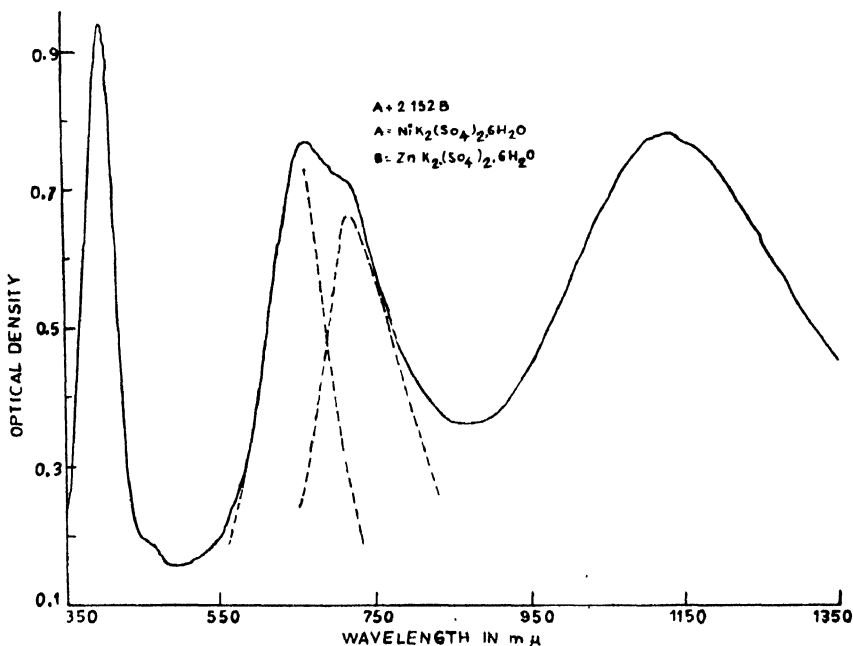


Figure 2.

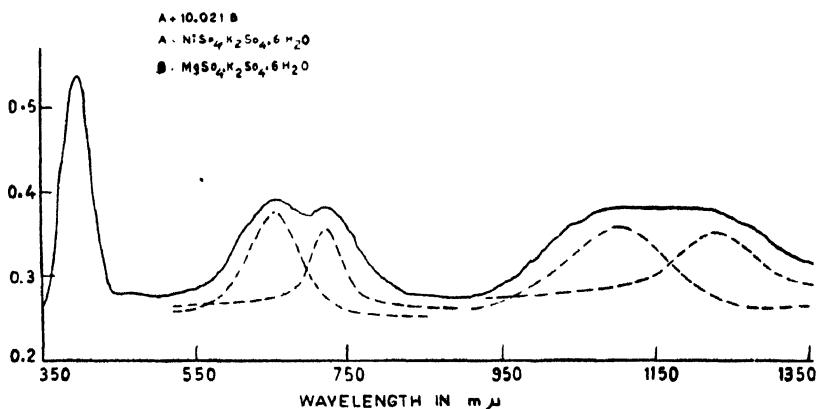


Figure 3.

Further work on the experimental calculations on the absorption spectra of nickel ion is in progress. Here, following Owen's (1955) energy expressions for the different energy levels in case of nickel ion we calculate the different crystal

field parameters and the effect of solid dilution on them. In the present studies the nickel ion salts are not purely ionic because a rough estimate shows that the

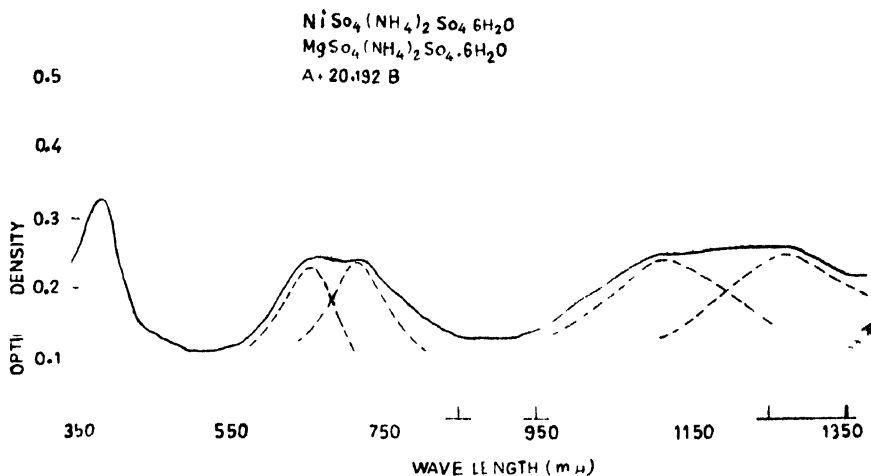


Figure 4

covalency factor is always less than unity and it changes with dilution. From our optical data we calculate the magnetic anisotropy, magnetic moment and splitting factor for different crystals at different dilution. A rough estimate shows that these measured values are in good agreement with the directly measured values by the magnetic measurements (1948). Details will be published soon.

Acknowledgment

One of us (R.S.D.) acknowledges the financial assistance given by CSIR, India.

References

- Bose A 1948 *Ind. J. Phys.* **22** 483
 Bose A and Chatterji R 1963 *Proc. Phys. Soc. (London)* **82** 23
 Bose A Mitra S K and Datta S K 1958 *Proc. Roy. Soc. (London)* **A248** 153
 Dreisch Th. and Trommer W 1937 *Z. Physik Chem.* **B37** 40
 Engelman R 1961 *Trans. Faraday Soc.* **57** 236
 Guha B C 1951 *Proc. Roy. Soc. (London)* **A206** 353
 Hartmann H and Muller 1958 *Discussions Faraday Soc.* **26** 49
 Kiss A V *et al* 1941 *Anorg. Allgem. Chem.* **254** 356
 Krishnan K S, Chakravarty N C and Banerjee S 1933 *Phil. Trans.* **232** 99
 Krishnan K S and Mookherji A 1938 *Phys. Rev.* **54** 533
 Lieher A D and Ballhausen C J 1959 *Ann. Phys. (Y.Y.)* **2** 123
 Low S 1958 *Phys. Rev.* **109** 247
 Mathur S C and Daryan R S 1978 (to be published)
 Mookherji A and Chhonkar N S 1960 *Ind. J. Phys.* **34** 363
 Owen J 1955 *Proc. Roy. Soc. (London)* **A227** 183
 Owen J, Halmes O G and McClure D S 1957 *J. Chem. Phys.* **26** 1686

X-ray line broadening study of nickel oxide

N A Ahmed

Physics Dept. National Research Centre, Dokki, Cairo

Received 4 October 1977

A considerable work has been carried out on the coloured oxides such as CoO , NiO , CdO in trying to explain the cause of the variation in colours of the differently prepared oxides.

Lo Blanc *et al* (1930) attributed the variation in colour of nickel oxide to the presence of oxygen. Bahatnagar (1934), Foex (1949), Kutsiva (1961) and Shirakov (1961) on measuring the magnetic susceptibility of nickel oxide prepared by different methods attributed the variation in the colour of the oxide to either excess of nickel ions or to absorbed oxygen.

X-ray study of nickel oxide was done by Yasumitsu (1948, 1954), Francois (1950) and Tourky *et al* (1970). All the previous authors found that the only difference in the diffraction patterns of the different coloured oxides is the increase of line broadening passing from green to black. Francois attributed the difference in colour to difference in particle size while Tourky attributed it to micro-strain. No quantitative determination of the particle size and strain was carried out by these authors, and it is the aim of this work to determine quantitatively by precise methods the values of particle size and strain in order to find out the reason for the difference of colours.

Four samples of NiO were prepared by heating Nickel carbonate in air at 500° , 650° , 800° and 1000°C for three hours each. The colour of the obtained compound passes from black to green. X-ray diffraction of the four samples showed that the compound is NiO , and that the only difference between the patterns is the line broadening. Spectroscopic analysis showed that all forms passes the same traces (in p.p.m) of impurities. Four reflections were chosen to study their line profiles namely (111), (222), (200), (400). A Seifert diffractometer was used to record the profile of reflections using low speed of scanning (10 cm for 1° of θ). The sample prepared at 1000°C was considered as a strain free sample containing no broadening due to small particle size, from which the instrumental broadening was determined. The breadth of the diffracted lines was determined using two methods, the variance (Wilson 1962) and the Fourier analysis (Warren and Averbach 1950).

a. Variance method

According to Wagner (1965) the true variance is the sum of the particle size variance and the strain variance

$$\frac{W(2\theta) \cos \theta}{\lambda \Delta 2\theta} - \frac{1}{2\pi^2 D_{(hkl)}} + 4\langle \epsilon \rangle^2 \frac{\sin \theta \tan \theta}{\Delta 2\theta \cdot \lambda}$$

The true variance ($W(2\theta)$) is the difference between the variance of the observed intensity W_h and the aberration function W_θ .

Fig. 1 shows the relation between $W(2\theta) \cos \theta / \lambda \Delta 2\theta$ and $\sin \theta \tan \theta / \lambda \Delta 2\theta$ for the two zones [111] and [100] of all oxides. Table 1. gives the calculated particle size $D(hkl)$ and mean strain $\langle \epsilon \rangle$. The calculations were performed on the computer ICL 1905 using a programme written by the author.

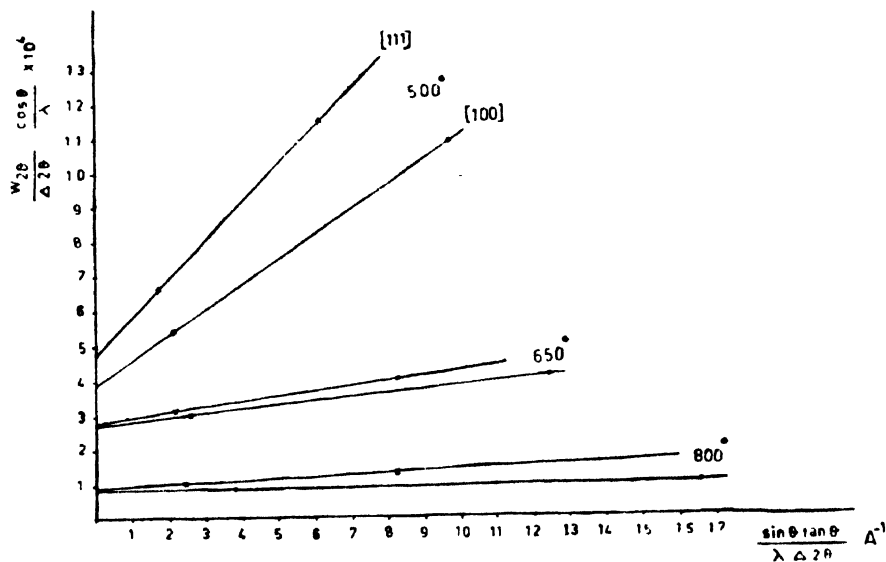


Figure 1.

Table 1

Temp. of preparation	$D \text{ \AA}$		$\epsilon \times 10^3$	
	[111]	[100]	[111]	[100]
500°C	110	130	5.40	4.30
650°C	181	190	2.1	1.91
800°C	540	600	0.43	0.39

b. *Fourier Analysis*

As shown by Warren (1958), the profile of a powder pattern peak corrected for instrumental broadening can be expressed in terms of a Fourier series.

$$p'(s) = K \sum_{n=-\infty}^{\infty} C_n \exp[-2\pi i n a_g(s-s_0)]$$

for cubic crystals we have

$$\ln A(L) = \ln A^{PF}(L) - h_0^2 [2\pi^2 L^2 (\langle \epsilon_L^2 \rangle - \langle \epsilon \rangle^2) / a^2]$$

If the Fourier coefficient $A(L)$ are plotted on a semi-log paper as a function of h_0^2 a straight line is obtained for elastically isotropic materials. For anisotropic material one can, only use the different orders of reflections from the same zone. The intercepts of the $A(L)$ vs h_0^2 curves are equal to the particle size coefficients $A^{PF}(L)$. If these are plotted as a function of L , the initial slope of the $A^{PF}(L)$ vs. L curve is a direct measure of the particle size D .

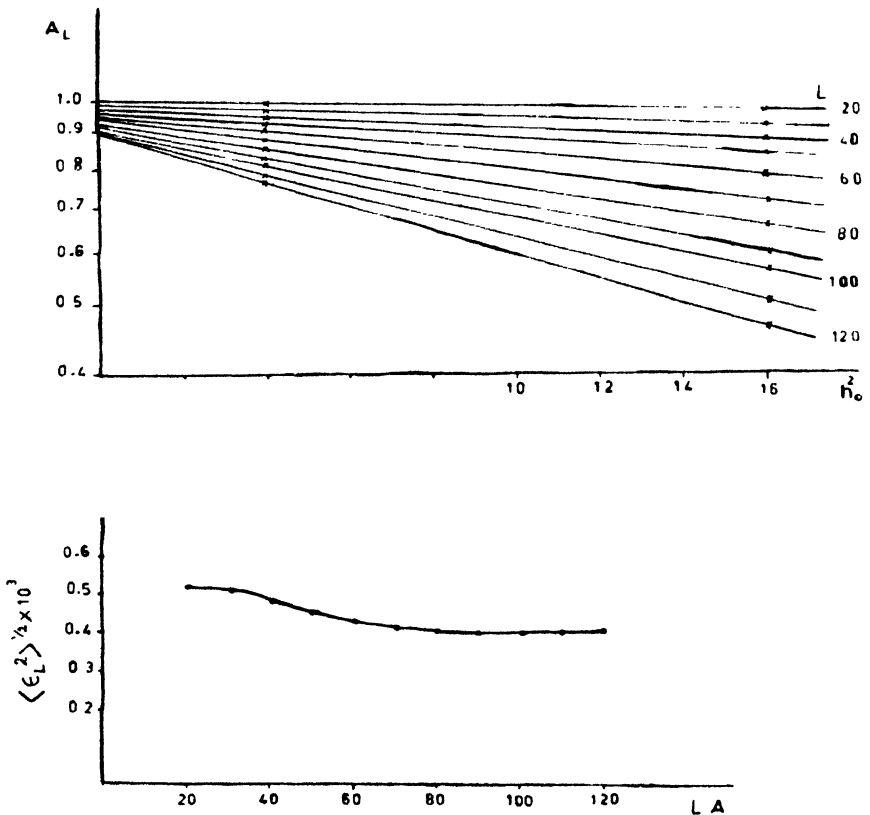


Figure 2.

A programme was written by the author to determine the Fourier coefficient and correct it for instrumental broadening according stokes (1948). Examples of the curves obtained from which the effective particle size and root mean squared strain are determined are shown in Figs 2, 3.

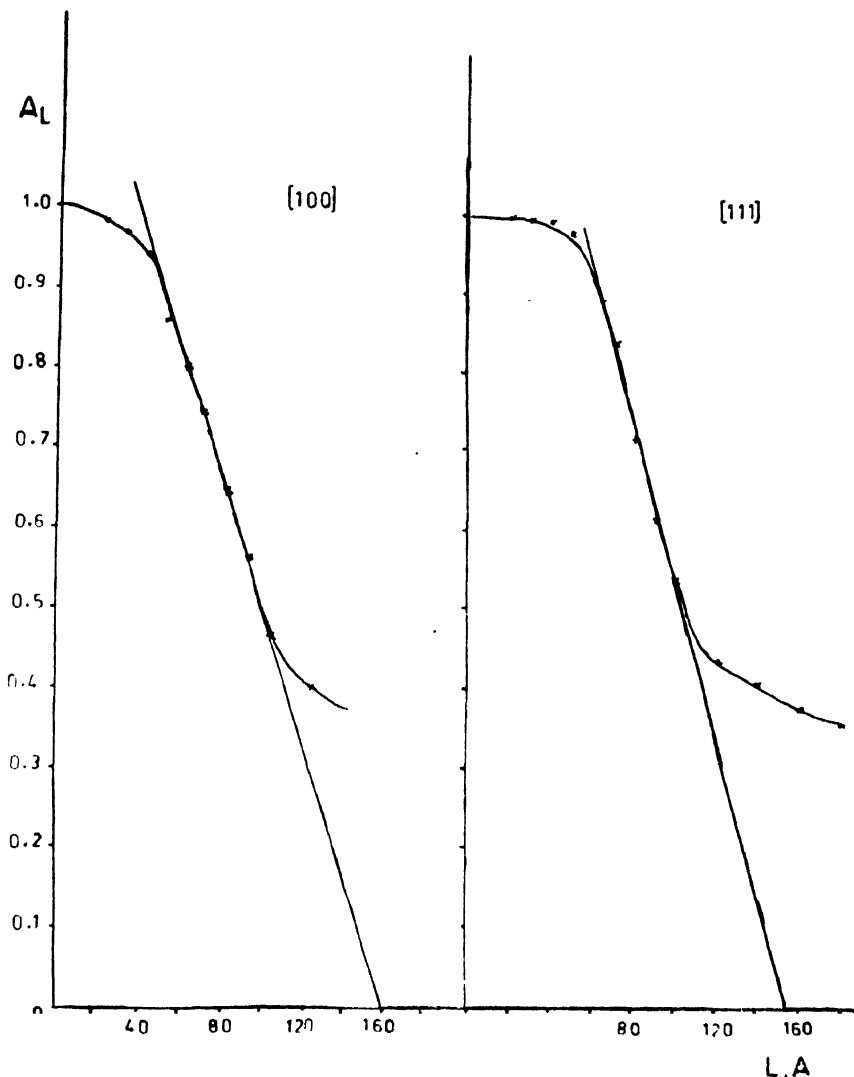


Figure 3.

Results are given in Table 2.

As the lattice defects affect the lattice constants, they were measured from the high order reflections and are given in Table 3. The density which must be taken into consideration is also measured for the different oxides (Table 3).

It was shown by Halder and Mitra (1963) and Guillatt and Brett (1970) that the variance method of analysis gives results very close to Fourier analysis. However some differences are found in the present results between the two methods.

Table 2

Temp. of preparation	$D\text{\AA}$		$\epsilon \times 10^3$	
	[111]	[100]	[111]	[100]
500°C	105	140	4.2	3.9
650°C	158	160	1.8	1.2
800°C	500	720	0.45	0.40

Table 3

Temp. of preparation	$a\text{\AA}$	$\rho\text{gm/cm}^3$
500°C	4.1708	5.803
650°C	4.1728	6.170
800°C	4.1754	6.428
1000°C	4.1767	6.666

The values of particle size (Tables 1, 2) increase as the temperature of preparation increases. This result is expected as it is known that crystals grow bigger at high temperatures. The values of strain decrease as the temperature of preparation increases. This is also expected as it means that the lattice growing at higher temperatures is more perfect. But it is shown that the difference between the particle size of the black oxide (prepared at 500°C) and the grey oxide (prepared at 650°C) is much smaller than the difference in strain. This leads to the conclusion that the variation in colour of the different oxides is most probably due to variation in strain. The small variation in unit cell dimension, compared to density variation indicates that the defect present is Nickel vacancies. This conclusion agrees with the observation of Deren *et al* (1961) of change of colour from black to green with decrease of oxygen. The values of a and ρ approach the theoretical values ($a = 4.1769\text{\AA}$ and $\rho = 6.67\text{gm/cm}^3$) at 1000°C. This indicates that the green oxide prepared at 1000°C is the stoichiometric one.

References

- Bahatnagar S S and Gurbachan 1934 *J. Ind. Chem. Soc.* **11** 603
 Deron J J. Habor and Sloczynski 1961 *Sci. Ser. Sci. Chem. Polon.* **9**, 245.
 Foex M and Charlott H 1949 *Compt. Rend.* **228**, 1519.
 Francoois J 1950 *Compt. Rend.* **230**, 1282.
 Guilliatt I F and Brett N H 1970 *Phil. Mag.* **21**, 172, 671.
 Kussiva L N 1961 *Dok. Akad. Nauk USSR* **138** 409.
 Le Blance M and Sachso H 1926 *Z. Electrochem.* **32**, 58,
 Shirakov Yu G and Kirillov 1961 *Z. khim. i khim. Tek.* **4**, 599.
 Stokes A R 1948 *Proc. Phys. Soc. (London)* **B61**, 382.
 Tourky A R Hanafi Z and Salem T M 1970 *Zeit. phys. Chem.* **243**, 145.
 Wagner C N J 1965 *Local Atomic Arrangement studied by X-ray Diffraction* by J B Cohen and J E Hilliard. Gordon and Breach Science. Pub., New York, London, Paris.
 Warren B E 1958 *Prog. Metal Phys.* **8**, 147.
 Warren B E and Averbach B L 1950 *J. Appl. Phys.* **21** 295.
 Yasumitsu S and Nishcyama Z 1948 *Men. Inst. Sci. Ind.* **630**, 1954 *J. Phys. Soc. Japan* **9**, 521.

Indian J. Phys. **53A**, 459-460 (1979)

Structural study of ZnY_2O_4

D M Dharmadhikari, D K Kulkarni and V V Deshpande

Department of Chemistry & Physics, Institute of Science, Nagpur

Received 18 January 1978, revised 19 September 1978

A literature survey shows that, no work has been done on the compound ZnY_2O_4 . We have undertaken this study as it was expected that this compound would crystallize in ZnFe_2O_4 structure (Bradburn and Rigby 1953) (spinel) as Y^{+3} ions have ionic radii (Goldschmidt 1927) suitable (Romeign 1953) for spinel lattice.

The compound has been prepared by intimately mixing together the two reacting oxides of AR grade in equimolecular proportions and then was heated in a platinum boat in an electrically operated furnace at 1200°C for 80 hours in air. The compound was then slowly cooled in a furnace.

The formation of compound was checked by X-ray diffractometer using filtered chromium radiation. All the lines show a single phase. Our crystallographic data are included in Table 1. This data has been analysed. It showed that the crystal system is neither a cubic nor a tetragonal. Only the data fits well to orthorhombic cell. Indexing has been done by the method described by Henry *et al* (1961). The cell dimensions a, b, c are $7.86 \pm 0.01 \text{ \AA}$, and $9.03 \pm 0.01 \text{ \AA}$ respectively, with face-centered Bravais lattice.

Table 1. Crystallographic data of ZnY_2O_4

<i>d</i> obs (in Å)	<i>d</i> cal (in Å)	<i>h k l</i>
3.096	3.096	0 2 2
2.960	2.960	2 0 2
2.888	2.888	2 2 0
2.566	2.562	1 3 1
2.145	2.134	0 4 0
1.831	1.873	2 4 0
1.761	1.774	4 2 0
1.549	1.549	0 4 4
1.515	1.523	5 1 1
1.431	1.441	2 4 4
1.390	1.398	4 2 4

$$a = 7.86 \pm 0.01 \text{ Å}$$

$$b = 8.53 \pm 0.01 \text{ Å}$$

$$c = 9.01 \pm 0.01 \text{ Å}$$

The compound crystallize in an orthorhombic structure and not in spinel lattice which may be due to large difference of electronegativities of Y^{+3} and Fe^{+3} ions.

References

- Bradburn T S and Rigby G R 1953 *Trans. Brit. Cer. Soc.* **52** 417
 Goldschmidt V M 1927 *Chem. Berichte* **60** 1263
 Henry N F M, Lipson H and Wooster W A 1961 *The interpretation of X-ray diffraction photographs* Macmillan & Co. Ltd, London
 Romeign F C 1953 *Philips Research Report* **8** 304

Indian J. Phys. **53A**, 460-461 (1979)

The crystal structure of bis-salicylato, diaquo calcium (ii), $\text{Ca}(\text{C}_7\text{H}_5\text{O}_3)_2\cdot 2\text{H}_2\text{O}$

M P Gupta and A P Saha

Department of Physics, Ranchi University.

Received 24 April 1978

The crystal structure of the title compound was investigated as part of a larger programme of studying hydrogen bonded crystalline solids and oxygen ligands around metal.

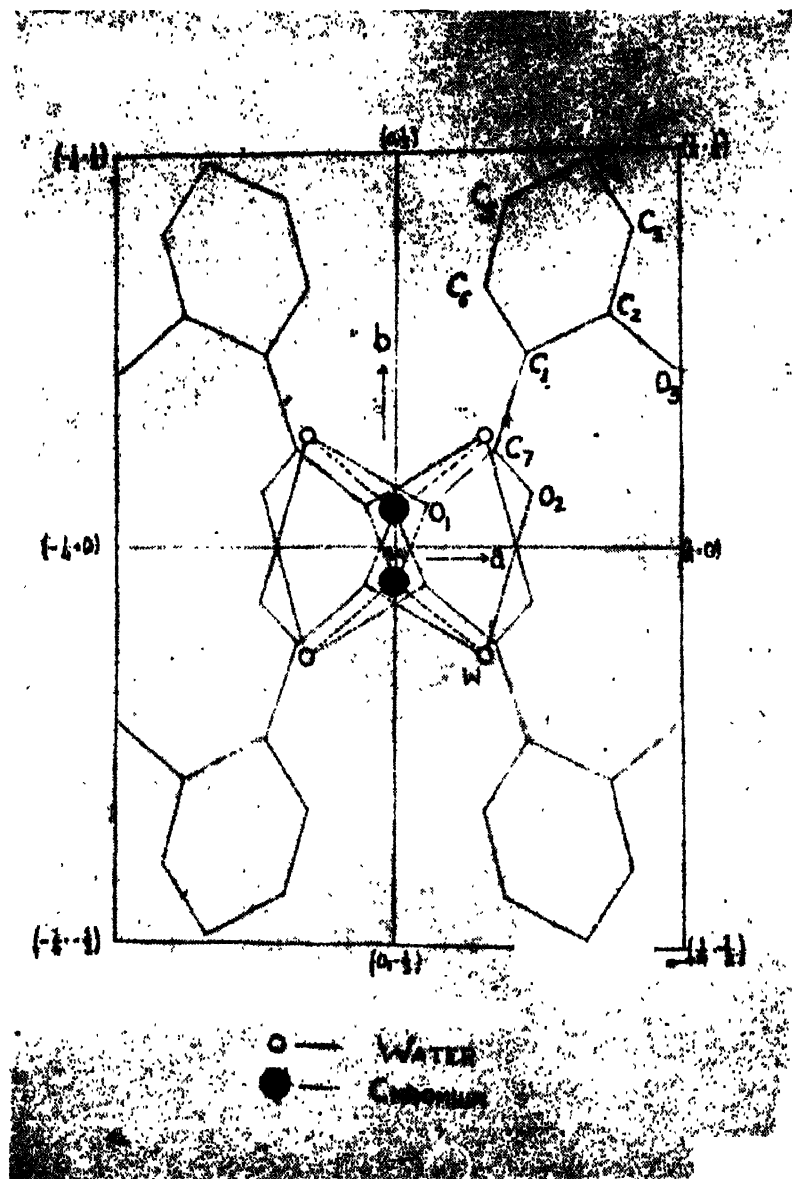


Figure 1.

Crystal Data : Monoclinic with $a = 16.48$, $b = 11.48$ and $c = 7.62$ Å, $\beta = 91.3^\circ$, $D_{obs} = 1.62$, $D_{cal} = 1.67$, $Z = 4$, space group C_c or $C2/c$. C_c is ruled out from structure analysis. 604 reflexions were collected by Weissenberg photography intensities estimated visually and data processed in the usual manner.

Crystal Structure : The structure was solved by heavy-atom technique, Ca-atom occupying special position on two-fold axes. A view of the structure looking down [001] is given in figure 1. The metal is 6-fold co-ordinated, average metal oxygen distance being (2.00 Å) as normally found for Ca-O linkages. The geometry of the salicylate anion is normal. Apart from metal-oxygen ionic linkages the water molecule provides hydrogen bonding in the structure, hydrogen bonds being 2.87 Å and 2.88 Å. Further work to refine the structure by least-squares analysis is in progress.

Indian J. Phys. **53A**, 461-464 (1979)

Electron paramagnetic resonance of VO^{2+} in $RbH_3(SeO_3)_2$ single crystals

Vimal Kumar Jain and Putha Venkateswarlu

Department of Physics, Indian Institute of Technology Kanpur,
Kanpur-208 016, U.P.

Received 11 July 1978

Rubidium trihydrogen selenite, $RbH_3(SeO_3)_2$, belongs to the family of alkali trihydrogen selenite whose properties are under intense study at the present time. Rubidium trihydrogen selenite is an improper ferroelectric (Gladkii *et al* 1976a, 1976b, 1977) which undergoes a phase transition of the first kind, close to a transition of second kind (Gladkii *et al* 1976a), at $T_c = 153$ K. At phase transition, symmetry undergoes a change from $P2_12_12_1$ to $P2_1$ and the length of the unit cell doubles along the c axis, and the spontaneous polarization appears along the b axis (Aknazarov *et al* 1975). This compound, due to its interesting properties, has been subjected to various physical investigations by many workers (Shuvalov *et al* 1970, Ivanov *et al* 1971, Gesi *et al* 1973, Gufan and Shuvalov 1975, Shuvalov *et al* 1975, Sannikov and Levanyuk 1977, Fitgerland and Grimm 1977). Sergeev and Falaleev (1975) observed the electron paramagnetic resonance (EPR) of γ -irradiated $RbH_3(SeO_3)_2$ single crystals. Their study has shown a

line splitting below the Curie point. Previously, we have studied the EPR of Mn^{2+} in $\text{RbH}_3(\text{SeO}_3)_2$ (Jain and Venkateswarlu 1978) single crystals. We have extended our studies to VO^{2+} doped rubidium trihydrogen selenite single crystals. In this paper we report our initial results which indicate that the VO^{2+} can be incorporated into the crystal at specific sites. We have determined the spin-Hamiltonian parameters from the observed spectra.

The crystal structure of $\text{RbH}_3(\text{SeO}_3)_2$ in the paraelectric phase is orthorhombic with four formula units per unit cell (Torbis *et al* 1972, Tellgren *et al* 1973, Aknazarov *et al* 1975). The space group is $D_2^4 (P2_12_12_1)$. The lattice constants (Tellgren *et al* 1973) are : $a = 5.9192 \text{ \AA}$, $b = 17.9506 \text{ \AA}$, and $c = 6.2519 \text{ \AA}$. The rubidium ion in the lattice is surrounded by eight oxygen atoms forming a distorted cube. The $\text{Rb}^+\text{-O}$ distances are between 2.934 \AA and 3.192 \AA . The unequal O-Rb-O angle ranging from 61.22° to 94.54° .

Single crystals of $\text{RbH}_3(\text{SeO}_3)_2$ doped with VO^{2+} were grown at 283 K by slow evaporation of an aqueous solution of one mole of Rb_2CO_3 and four moles of SeO_2 to which vanadyl sulfate (0.5% by weight) was added. The $\text{RbH}_3(\text{SeO}_3)_2 : \text{VO}^{2+}$ crystals have poor facets. The crystals grow very slowly and took about two to three months. A Varian V-4502 EPR spectrometer with a 9-inch magnet and 100 kHz field modulation was used to record the spectra. As a reference for magnetic field strength, the resonance line of DPPH with $g = 2.0036$ was used.

The EPR signal consisted of a number of overlapping angular dependent eight line hyperfine patterns, each produced by ions located at a specific site. These eight line patterns result from the hyperfine coupling of a single unpaired electron with a ^{51}V (99.8% abundant, $I = 7/2$) nucleus. At least three chemically different sites having differing intensities were observed. In addition, for an arbitrary orientation of the crystal, there are four magnetically inequivalent orientations which become equivalent in pairs, when the magnetic field is in the ac plane away from the axes. Finally when the field is along the crystallographic axes all symmetry related sites become magnetically equivalent. Nevertheless, in these directions three distinct hyperfine patterns of differing intensities were observed, corresponding to three chemically distinct sites. Multiple sites have frequently been observed in VO^{2+} doped materials previously (Borcherts and Kikuchi 1964, Pandey and Venkateswarlu 1975, Jain and Srinivasan 1977, Kohin *et al* 1978, Jain 1970).

The VO^{2+} EPR spectra could be analysed using the usual spin-Hamiltonian for an orbitally non-degenerate electron;

$$H = \beta S.g.B + \hbar c S.A.I,$$

where the hyperfine tensor A is measured in units of cm^{-1} , and the other terms have their usual meaning. The quadrupole and nuclear Zeeman interactions

are ignored, as these terms are sufficiently small to be neglected. Within the accuracy of the experiment, both g and hyperfine tensors were found to be nearly axially symmetric, permitting use of the perturbation theory results first given by Bleaney (1951). His expression for the magnetic field position B_m for the m th hyperfine line is

$$B_m = B_k - ma - \frac{a_{\perp}^2(a_{\parallel}^2 + a^2)}{4a^2G} [I(I+1) - m^2] - \frac{a_{\perp}^2 a_{\parallel} m (2M-1)}{2aG} - \frac{\left[\left(\frac{g_{\perp} g_{\parallel}}{g^2} \right) (a_{\perp}^2 - a_{\parallel}^2) m \sin 2\theta \right]^2}{8a^2G}$$

Here, B_k is the klystron frequency expressed in Gauss ($B_k = \frac{h\nu}{g\beta}$), g is the effective g factor ($g^2 = g_{\parallel}^2 \cos^2 \theta + g_{\perp}^2 \sin^2 \theta$), and $a = \frac{hcA}{g\beta}$ is the effective hyperfine splitting in Gauss (a_{\parallel}, a_{\perp} are similarly defined in terms of A_{\parallel}, A_{\perp} the hyperfine tensor components), where $g^2 A^2 = g_{\parallel}^2 A_{\parallel}^2 \cos^2 \theta + g_{\perp}^2 A_{\perp}^2 \sin^2 \theta$. The electronic transition occurs between the states $M, M-1$ with the nuclear quantum number m fixed. θ is the angle between the external magnetic field and the symmetry axis (z axis).

Values for the Hamiltonian parameters can most conveniently be obtained by observing a given hyperfine pattern and rotating the crystal until the splitting is maximized. This correspond to the axial direction as $|a_{\parallel}| > |a_{\perp}|$. The perpendicular components of g and A tensors can then be determined by rotating the crystal in a plane perpendicular to the symmetry axis (z axis). All spectra were observed to be axially symmetric within the experimental error. In their pioneering work on VO^{2+} ions, Borcherts and Kikuchi (1964) carefully analysed the very small departure from axial symmetry in VO^{2+} doped Zn Tutton salts, however, our line widths (~ 20 Gauss) prevent the great precision required in observing these deviations. Previous work has, in general, shown axial symmetry in the spin-Hamiltonian parameters.

Table 1. Spin-Hamiltonian parameters for VO^{2+} ions in $RbH_2(SeO_3)_2$ at 298 K. A values are in units of 10^{-4}cm^{-1} .

Parameters	Site I	Site II	Site III
g_{\parallel}	1.920 ± 0.002	1.926 ± 0.002	1.923 ± 0.002
g_{\perp}	1.974 ± 0.002	1.988 ± 0.004	1.990 ± 0.004
A_{\parallel}	177 ± 0.05	174.7 ± 2	173 ± 2
A_{\perp}	70.3 ± 1	71 ± 3	78 ± 3
Relative Intensity	14	6	2

The Hamiltonian parameters observed for all three sites are given in Table 1. We were unable to determine the orientations of g and A tensors relative to crystallographic axes due to the poor facets of the crystals. Therefore, no attempt at present could be made to correlate the known metal-oxygen directions with V-O bond directions. It is seen from the table that the principal values of g and A tensors are approximately what one would expect for a VO^{2+} centre. A calculation of the constants P ($P = 2\gamma\beta\beta_N < r^{-3} >$, is the direct dipolar term and accounts for the dipole-dipole interaction of the electron moment and nuclear moment) and χ (Fermi contact term) using the equations given by Kivelson and Lee (1964) and spin-Hamiltonian parameters of Table 1 yielded $P = 113.0 \times 10^{-4} \text{ cm}^{-1}$ and $\chi = 0.84$ for $\text{RbH}_3(\text{SeO}_3)_2 : \text{VO}^{2+}$.

EPR experiments were also carried out at low temperatures through the phase transition temperature of $\text{RbH}_3(\text{SeO}_3)_2$. But there was no appreciable change in the spectrum.

Acknowledgments

The authors wish to thank Professor Roger P. Kohin of Clark University, Worcester, Massachusetts for helpful discussions.

References

- Aknazarov S Kh, Shekhtman V Sh and Shuvalov L A 1975 *Soviet Phys. Crystallogr.* **19** 804
 Bleaney B 1951 *Phil. Mag.* **42** 441
 Borcherts R H and Kikuchi C 1964 *J. Chem. Phys.* **40** 2270
 Fitgerland W J and Grimm H 1977 *Solid State Commun.* **22** 749
 Gesi K, Ozawa K and Makita Y 1973 *J. App. Phys. Jpn.* **12** 1963
 Gladkii V V, Zheludev I S, Magatev V K and Shuvalov L A 1976a *Soviet Phys. Crystallogr.* **21** 344
 Gladkii V V, Magataev V K and Zheludev I S 1976b *Ferroelectrics* **13** 343
 Gladkii V V, Kirikov V I, Magataev V K and Shuvalov L A 1977 *Soviet Phys. Solid State* **19** 167
 Guffan Yu M and Shuvalov L A 1975 *Soviet Phys. Solid State* **17** 381
 Ivanov N R, Tukhtasunov I T and Shuvalov L A 1971 *Soviet Phys. Crystallogr.* **15** 647
 Jain V K and Srinivasan T M 1977 *Z. Naturforsch.* **32a** 1068
 Jain V K and Venkateswarlu P 1978 *Can. J. Phys.* **56** 80
 Jain V K 1978 *J. Chem. Phys.*
 Kivelson D and Lee S K 1964 *J. Chem. Phys.* **41** 1896
 Kohin R P, Zakelz J and Jain V K 1978 *J. Chem. Phys.* **68** 778
 Pandey S D and Venkateswarlu P 1975 *J. Magn. Reson.* **17** 137
 Sannikov D G and Levanyuk A P 1977 *Soviet Phys. Solid State* **19** 67
 Sergeev N A and Falaleev O V 1975 *Bull. Acad. Sci. (Phys. Ser.) USSR* **39** 714
 Shuvalov L A, Ivanov N V, Gordeeva N R and Kirpichnikova L F 1970 *Soviet Phys. Crystallogr.* **14** 554
 Shuvalov L A, Ivanov N R, Shirokov A M, Boiko A A, Kirpichnikov L F, Gordeeva N V, Baranov A I, Fonskova A, Ryabkin V S, Babayants V A and Aknazarov S Kh 1975 *Soviet Phys. Solid State* **20** 206
 Tellgren R, Ahmed D and Liminga R 1973 *J. Solid State Chemistry* **6** 250
 Torbis A B, Darydova T S and Simonov V I 1972 *Soviet Phys. Crystallogr.* **17** 81

Potential energy function for alkali hydride molecules

Ravi Chandran Iyer and L K Sharma

Department of Applied Physics, Government Engineering College,
Jabalpur-482011, (M.P.)

Received 3 August 1978, revised 19 September 1978

In spite of the fact that alkali hydride crystals appear to be quite simple chemical compounds, it has been possible only to obtain a meagre experimental information regarding their various physical properties owing to their reactive nature. This is precisely the reason why the theoretical estimates of various properties of these hydride is done. In this direction efforts have already been made by Varshni and Shukla (1963), Dass and Saxena (1965a, b, 1970), Thakur and Sarkar (1975) and Dass and Kachhava (1977).

The usual form of representing the inter-ionic potential in the molecular state is :

$$\phi(r) = \frac{-e^2}{r} + V(r), \quad (1)$$

where $\phi(r)$ is the interaction energy between two ions separated by a distance r , $-e$ the electronic charge and $V(r)$ is the overlap term. This term usually involves two potential parameters. In this note, we have used the overlap term $V(r)$ of the form :

$$V(r) = Ae^{-k \cdot r}, \quad (2)$$

for calculating the values of rotational constant α_e , the vibrational constant $\omega_e x_e$ and the binding energy D_t of various alkali hydride molecules.

It is interesting to note that a similar overlap term was used by Goyal and Shankar (1972) for determining the cohesive energy of alkali halide crystals and their results agreed with the corresponding experimental values to within 5%.

The two potential parameters A and k involved in the overlap term $V(r)$ can be determined from the equilibrium conditions and the knowledge of the force constants as illustrated by Herzberg (1955).

Utilizing well known relations (Varshni and Shukla 1957) the values of α_e , $\omega_e x_e$ and D_t have been computed for various alkali hydride molecules. These values have been listed in Table 1. Experimental values of various molecular

Table 1. Comparative study of the various values of α_e , $\omega_e x_e$ and D_1 .

Molecules	α_e (cm^{-1})				$\omega_e x_e$ (cm^{-1})				D_1 (Kcal/mole)			
	Experi- mental	Present calcula- tion	Born Mayer potential	VS-II potential	Experi- mental	Present calcula- tion	Born Mayer potential	VS-II potential	Experi- mental	Present calcula- tion	Born Mayer potential	VS-II potential
LiH	0.2132	0.2319	0.1362	0.2636	23.20	23.53	18.36	25.56	165.1	145.12	153.5	142.6
NaH	0.1353	0.1412	0.0982	0.1484	19.72	18.58	15.17	19.00	150.3 ± 4.6	129.39	134.9	129.0
KH	0.081	0.0963	0.0713	0.0945	14.30	15.23	12.87	15.13	127.2 ± 3.5	113.12	116.9	113.5
RbH	0.072	0.0819	0.0639	0.0816	14.21	14.44	12.35	14.22	119.6 ± 4.6	108.79	112.1	109.3
CsH	0.057	0.0724	0.0578	0.0718	12.79	13.70	11.83	13.43	115.4 ± 6.4	104.43	107.3	105.0

constants like k_e , r_e , μ , B_e , ω_e , α_e , $\omega_e x_e$ and D_e for different alkali hydride molecules have been taken from Gray (1972).

For our investigation a simplified two term potential function comprising only the Coulomb and the overlap term has been selected due to the simple reason that alkali hydride molecules possess NaCl type of symmetric structure for which the Van der Waals and polarization forces can be neglected.

Further, the inclusion of these two forces (due to nonavailability of correct experimental values of polarizability in the molecular environment and hence of Van der Waals constant) may lead to distorted results. This fact is amply demonstrated in the calculation of α_e and $\omega_e x_e$ for Rittner and VS-I potentials (Dass 1976) where both the above mentioned forces are included in the interaction. The results of these calculations are highly unsatisfactory.

The values of α_e obtained in the present study for various molecules have been found to be more satisfactory than for the Born-Mayer (1932), Rittner (1951) and VS-I (Varshni and Shukla 1961) and VS-II (Varshni and Shukla 1963) potentials. The values of $\omega_e x_e$ for the potential considered in this note are superior to those calculated by Gohel (1970) for a three parameter modified Rittner potential function. For the values of D_e however, our potential is only superior to VS-II, but the values of D_e for the other two potential energy functions too do not agree with the corresponding experimental values completely though this disagreement being only within 10%. In our case also the disagreement is of the same order.

Acknowledgments

The authors are grateful to Prof. M. C. Sen for encouragement. One of the authors (R.C.I.) thanks C.S.I.R., New Delhi for the award of a Junior Research Fellowship.

References

- Born M and Mayer J E 1932 *E. Physik* **75** 1
- Dass Lachhman and Saxena S C 1965a *J. Chem. Phys.* **43** 1747
- Dass Lachhman and Saxena S C 1965b *Ind. J. Pure Appl. Phys.* **3** 494
- Dass Lachhman and Saxena S C 1970 *Proc. Ind. Nat. Sci. Acad.* **36** 31
- Dass Lachhman and Kachhava C M 1977 *Proc. Ind. Nat. Sci. Acad.* **43** 110
- Dass Lachhman 1976 *Ph.D. thesis* unpublished, Deptt. of Phys. University of Rajasthan, Jaipur
- Gohel V B 1970 *Ind. J. Pure Appl. Phys.* **8** 139
- Goyal S C and Shankar J 1972 *Curr. Sci.* **41** 859
- Gray D E 1972 *American Institute of Physics Hand Book* (Third Edition)
- Herzberg G 1955 *Molecular Spectra and Molecular Structure-I, Spectra of Diatomic Molecules*, D. Van Nostrand Company Inc (NY)
- Rittner E S 1951 *J. Chem. Phys.* **19** 1030
- Thakur K P and Sarkar G K 1975 *Ind. J. Pure Appl. Phys.* **13** 717
- Varshni Y P and Shukla R C 1963 *Rev. Mod. Phys.* **35** 130
- Varshni Y P and Shukla R C 1957 *Rev. Mod. Phys.* **29** 664
- Varshni Y P and Shukla R C 1961 *J. Chem. Phys.* **35** 582

Some theoretical considerations on the Hall effect anomaly in nickel oxide

Ratnabali Banerjee and A K Barua

Department of General Physics & X-rays,
Indian Association for the Cultivation of Science, Calcutta-700032

Received 23 August 1978

An interesting phenomenon in nickel oxide is the sign reversal of the Hall mobility (μ_H) at about 600K (T_s). This sign reversal of μ_H as reported by Bosman, van Daal and Knuvers (1965) did not reflect itself in the resistivity and Seebach coefficient. They studied the Hall mobility and the resistivity as functions of the concentration of Lithium dopant and temperature. The experiments were performed on polycrystalline samples under atmospheric pressure. The most remarkable feature of this experiment is that the sign reversal temperature of the Hall mobility is more or less the same for all the four samples having different dopant concentrations.

More recently Friedman *et al* (1975) have studied resistivity of single crystals of NiO at different oxygen partial pressures as a function of temperature. The increase in oxygen partial pressure is in a way equivalent to the presence of Li acceptors. The sign reversal of the Hall mobility was also observed in this case but contrary to the observation of van Daal and Bosman (1967) with different Li dopant concentrations, T_s was found to be higher at lower oxygen pressure.

De Wit (1972) has attempted to explain the sign reversal of the Hall mobility in terms of the existence of *n*-type inclusions in the matrix of NiO by an extension of the theory of Airapetiants (1958). It was thus possible to explain qualitatively the sign reversal in the Hall mobility. The near independence of T with respect to the dopant concentration, however, could not be explained. Friedman *et al* (1975) tried to explain unsuccessfully the variation of T_s with oxygen partial pressure in terms of two types of carriers.

In this note we have attempted to explain qualitatively the above mentioned features of T_s in terms of the concept of the existence of *n*-type inclusions, NiO being a *p*-type semiconductor. In the experiment of Van Daal and Bosman (1967), Li dopant introduces holes so that the resistivity should decrease with increase in Li concentration. This is actually observed for the four samples studied. However, a very small amount of *n*-type inclusions in the matrix of

NiO will affect the Hall mobility and it has been shown that sign reversal is possible by this mechanism and is most likely when $\sigma_m = \sigma_i$, σ_m and σ_i being the conductivity of the matrix and inclusions respectively.

In view of the experimental observations and the above mentioned points we suggest that Li used as dopant may contain a small amount of impurity which effectively increases *n*-type inclusions. The Li dopant will introduce holes and its effects will be counteracted by the *n*-type inclusions introduced by impurities. It may be argued that the percentage of dopant in the first place is very small and the percentage of the inclusions introduced by impurities in the dopant will be insignificant. However, it is known that less than 0.1 at % of Li can lower the resistivity of NiO by five orders in magnitude. Therefore, a very small concentration of inclusions due to the introduction of the dopant may have a drastic effect.

From the formulae given by de Wit (1972) we have calculated σ_i for the different samples, at three temperatures. At low temperatures, σ -values obtained by van Daal and Bosman (1967) were supposed to be due to holes only, the inclusions being more effective at the higher temperatures. The values of σ_i for the four samples are shown in Table 1.

Although these values of σ_i are not likely to be quantitatively satisfactory, a few conclusions may however be drawn from them. At $T = T_N$, the Neel temperature, the σ_i values increase monotonically with the increase in Li con-

Table 1. Results obtained from different samples of NiO studied.

Temperature	Sample	Li (at %)	σ_i ($\Omega^{-1}\text{cm}^{-1}$)	Conclusion
T_N (523K)	IV	< 0.001	0.0140	$\sigma_i(\text{IV}) < \sigma_i(\text{I})$
	I	0.005	0.0188	$< \sigma_i(\text{II})$
	II	0.01	0.0281	$< \sigma_i(\text{III})$
	III	0.09	0.8140	
Turning Point (600K)	IV	< 0.001	0.0631	$\sigma_i(\text{IV}) > \sigma_i(\text{I})$
	I	0.005	0.0398	$\sigma_i(\text{IV}) = \sigma_i(\text{II})$
	II	0.01	0.0631	$\sigma_i(\text{IV}) < \sigma_i(\text{III})$
	III	0.09	15.8495	
800K	IV	< 0.001	3.8531	$\sigma_i(\text{IV}) > \sigma_i(\text{I})$
	I	0.005	0.2569	$\sigma_i(\text{IV}) > \sigma_i(\text{II})$
	II	0.01	0.8503	$\sigma_i(\text{IV}) < \sigma_i(\text{III})$
	III	0.09	176.8135	

centration whereas if there were no n -type inclusions introduced with it, σ_i would have remained unchanged. At higher temperatures, σ_i initially decreases with dopant concentration and then increases. This is due to the opposite effects of introducing Li dopant and n -type inclusions and is a function of the temperature and concentration dependence of the physical parameters responsible.

In the experiment of Friedman *et al* (1975), which has been performed on single crystals of NiO, resistivity values decrease with increase of oxygen partial pressure. This is due to the fact that oxygen effectively introduce holes in NiO, although it is far less effective than Li dopant. For the temperature dependence of Hall mobility, μ_H is higher at lower oxygen partial pressures.

This can easily be explained as the Hall coefficient R_H varies inversely as the hole concentration and thus decreases with increase in pressure whereas the conductivity behaves in the opposite way. The behaviour of H , which is a product of R_H and σ , depends upon the dominating factor. Thus, in this case, the first, i.e. R_H , is predominant. (In the experiment of van Daal and Bosman it is the other way round with σ dominating under the effect of Li as dopant). The Hall mobility of the inclusions balance the Hall mobility due to the holes at T_s . Since the effect of the former is more pronounced at higher temperatures, at lower oxygen partial pressures it will balance the Hall mobility due to holes at higher temperatures than in the case of higher oxygen partial pressures.

From the above discussion it is seen that it may be possible to explain the behaviour of T_s for both the experiments of van Daal and Bosman (1967) and Friedman *et al* (1975). However, to test the suggestions made further experiments should be done simultaneously at different Li dopant concentrations and oxygen partial pressures.

References

- Airapetiants C V 1958 *Sov. Phys. Tech. Phys.* **2** 429
 Bosman A J, Van Daal H J and Knijvers G F 1965 *Physics Lett.* **19** 372
 de Wit H J 1972 *J. Appl. Phys.* **43** 908
 Friedman F, Weichman F L and Tannhauser D S 1975 *Phys. Stat. Sol. (a)* **27** 273
 Van Daal H J and Bosman A J 1967 *Phys. Rev.* **158** 736

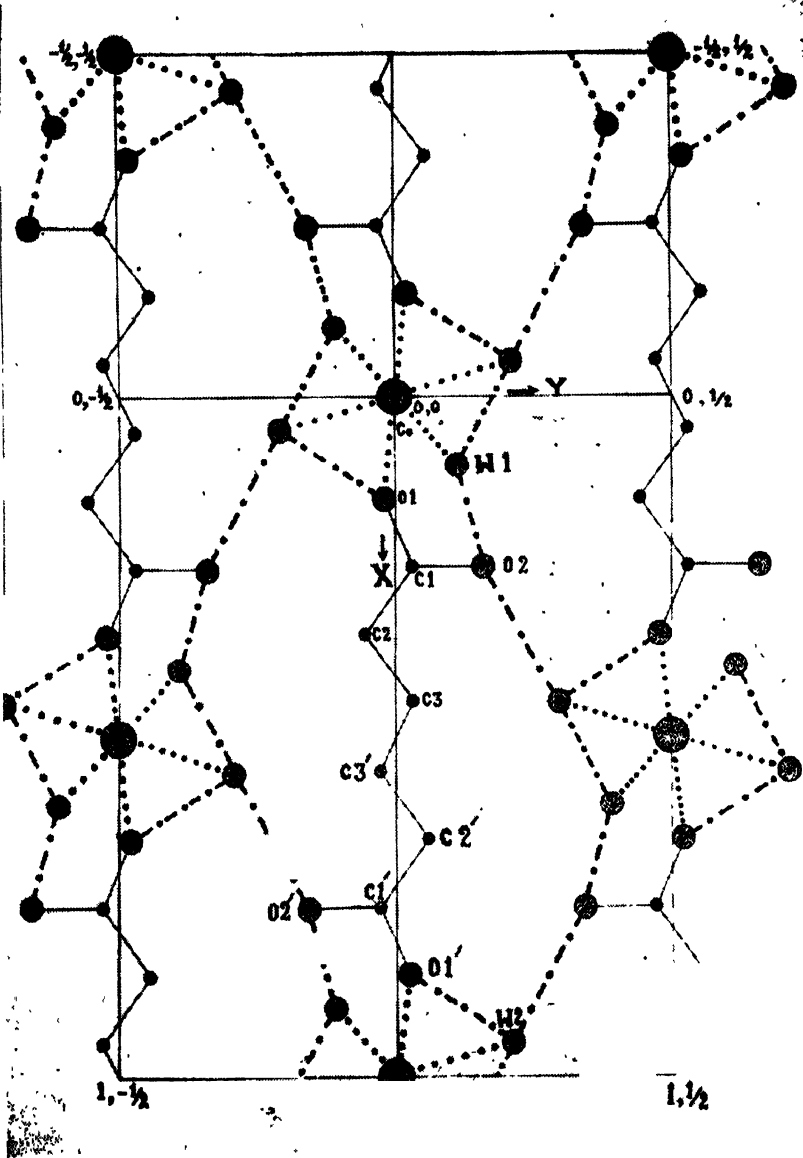


Figure 1.

The crystal structure of mono adipato tetraaquo cobalt (ii), $\text{Co}(\text{C}_6\text{H}_8\text{O}_4), 4\text{H}_2\text{O}$

M P Gupta and S K Sinha

Department of Physics, Ranchi University, Ranchi-834008

Received 11 August 1978

The title compound was studied by unravel the oxygen ligand around the metal and to study the scheme of hydrogen bonds in the crystal.

Synthesis: The compound was prepared by reaction of stoichiometric amount of adipic acid and cobalt carbonate and the crystals were grown out of water solution. The shape of the crystal is like thin elongated plates.

Crystal data: Monoclinic with $a = 11.70$, $b = 9.77$, $c = 4.79 \text{ \AA}$, $\beta = 99^\circ 48'$, $D_{\text{obs}} = 1.69 \text{ gm/cc}$, $D_{\text{calc}} = 1.70 \text{ gm/cc}$, $Z = 2$, space group $P2_1/a$.

430 reflexions were collected using single crystal Weissenberg photography, intensities estimated visually and data processed applying usual corrections and brought to approximate absolute scale by statistical method.

Structure determination and comments: The structure was solved by heavy atom technique. The metal ion and adipate anion occupy the special positions of centres of symmetry. The water molecules occupy general positions.

A view of the crystal structure looking down $[001]$ is shown in figure 1. In the structure, the metal is six-fold coordinated by oxygen atoms, metal-oxygen distances ranging from 2.07 to 2.09 \AA . The dimensions of adipate anion are normal. The structure is held together by metal-oxygen ionic linkages and hydrogen bonds via the water molecules, hydrogen bonds ranging from 2.64 to 2.90 \AA .

However, great interest lies in the location of the hydrogen atoms and in establishing the true scheme of hydrogen bonds in the structure. To locate the hydrogen atoms further work to refine the structure is currently in progress.

The crystal structure of strontium maleate, tetrahydrate, $\text{Sr.C}_4\text{H}_2\text{O}_4.4\text{H}_2\text{O}$

M P Gupta and P Chand

Department of Physics, Ranchi University, Ranchi-834008.

Received 17 August 1978

This compound was studied to unravel the scheme of hydrogen bonds and co-ordination of oxygen atoms around the strontium atoms.

Crystal data: Monoclinic with $a = 11.29(2)$, $b = 6.98(2)$, $c = 12.50(3)$ Å, $\beta = 118.4^\circ$, $D_o = 2.04$, $D_c = 2.08$ g.cm⁻³, $Z = 4$, space group $P2_1/c$.

810 unique reflexions with non-zero values of intensity were collected by single crystal Weissenberg photography and their intensities values estimated visually. Diffraction data were brought to approximate absolute scale by statistical methods.

Structure determination and comments: The structure was solved from a 3-dimensional Patterson using heavy-atom technique. A view of the crystal structure down [010] is given in figure below. In the crystal, the interatomic forces are: (a) ionic (metal-oxygen) with values ranging from 2.46 to 2.75 Å giving eight-fold co-ordination around strontium, (b) hydrogen bonds through the water molecules (distances ranges from 2.51 to 3.10 Å) and van-der Waals.

The maleate anion is non-planar with one of its carboxyl groups rotated out of the plane of the three carbon atoms by a large amount ($\simeq 80^\circ$). This is an usual feature found in a number of maleates with both the carboxyl groups ionized. The geometry of the anion is also comparable to a number of maleates reported in the literature with both COOH groups ionized.

As location of the hydrogen atoms is of great importance to establish the true nature of hydrogen bonds, further work is in progress.

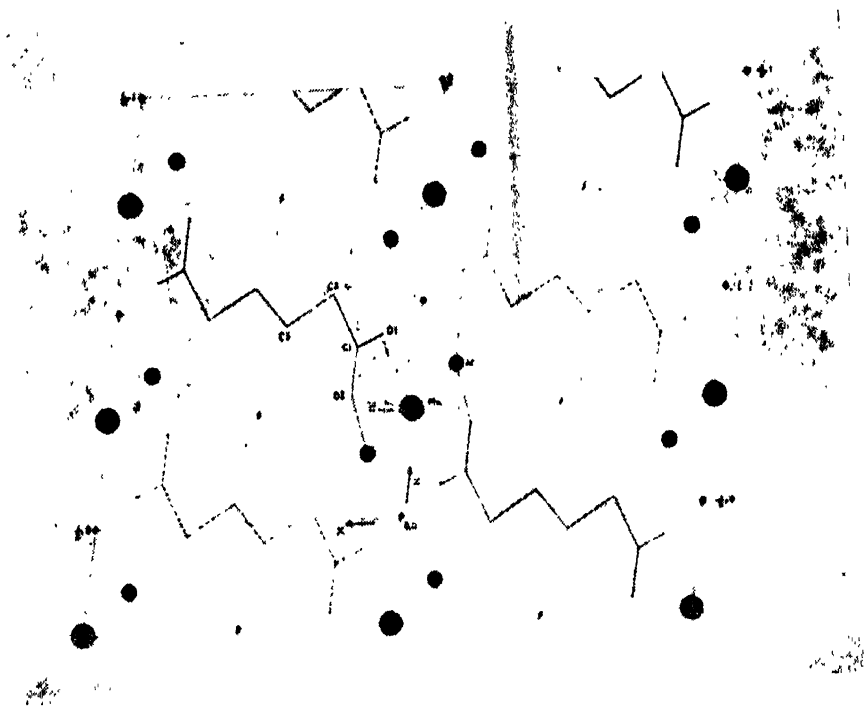


Figure 1.



The crystal structure of manganese adipate, dihydrate $\text{Mn}(\text{C}_6\text{H}_8\text{O}_4)\cdot 2\text{H}_2\text{O}$

M P Gupta and P Chaud

Department of Physics, Ranchi University, Ranchi-834008.

Received 17 August 1978

The title compound was investigated to study the hydrogen bonding and co-ordinating behaviour of oxygen atoms around the metal.

Crystal data : Monoclinic with $c = 10.95(2)$, $b = 5.42(1)$, $a = 16.32(3)$ Å, $\beta = 98.6^\circ$, $D_o = 1.59$, $D_c = 1.63$ g.cm⁻³, $Z = 4$, formula units of $\text{Mn}(\text{C}_6\text{H}_8\text{O}_4)\cdot 2\text{H}_2\text{O}$, space group $C2/c$ or Cc . Complete structure determination confirms the space group to be $C2/c$.

470 unique reflexions with non-zero values of intensity were collected by single crystal Weissenberg photography, intensities estimated visually and data brought to approximate absolute scale by statistical methods.

Structure determination and comments : The structure was solved by heavy-atom technique. As there are only four manganese atoms in the unit cell in the space group $C2/c$, they occupy special positions on the two-fold symmetry axis. A view of the crystal structure down $[010]$ is given in figure below. In the crystal, the linkages are : ionic (metal-oxygen), hydrogen bonds (through water molecule with values of 2.68 and 2.70 Å). The Mn-O distances range from 2.12 to 2.22 Å giving a six-fold co-ordination.

As the hydrogen bonds, at this stage of analysis, come out to be on the short side, further work to refine the structure is in progress to locate the hydrogen atoms.

The crystal structure of 5-7 dimethoxy indane 1-one, $C_{11}H_{10}O_3$

M P Gupta and P Ram

Department of Physics, University of Ranchi, Ranchi-834008.

Received 6 September 1978

The crystal and molecular structure of the title compound was investigated to establish the stereochemistry of the molecule.

Crystal data: Monoclinic with $a = 8.71(2)$, $b = 9.67(2)$, $c = 11.12(3)$ Å, $\beta = 91.1^\circ$, $D_o = 1.34$, $D_c = 1.35$ g.cm $^{-3}$, $Z = 4$, space group $P2_1/n$.

427 unique reflexions with non-zero values of intensity were collected by single crystal Weissenberg photography using $CuK\alpha$ radiation and intensities estimated visually. Because of large thermal motion in the crystal higher $\sin \theta$ reflexions were mostly not recorded. They were brought to approximate absolute scale by statistical methods.

Structure determination and refinement: The structure was solved using Patterson maps and packing considerations. Trial co-ordinates derived from projections were refined by the method of full-matrix least-squares using the programme of Busing, Martin and Levy (1962). Unit weight was given to all observed reflexions and only individual isotropic thermal parameters were used in the refinement. The present conventional R factor for the data is 0.15. Hydrogen atoms in the structure could not be located from a difference Fourier map. Table 1 below gives the atomic parameters of the non-hydrogen atoms in the crystal. Tables 2(a) and (b) give the bond lengths and angles in the molecule.

Comments: Figure 1 (with numbering scheme of atoms in the molecule) gives a view of the crystal structure as looking down the (100) axis in the crystal. The geometry of the molecule is as expected with no abnormal values for the bond lengths and angles. These values are also comparable with that found for a number of similar molecules.

The crystal structure is held together mostly by van-der Waals forces.

Atoms O1, O2, O3 and carbon atoms C1 to C11 are nearly in the same plane, maximum deviation from this plane being 0.31 Å (atom O3), 0.10 Å (atom C9), 0.11 Å (atom C11). Thus the molecule is only approximately planar.

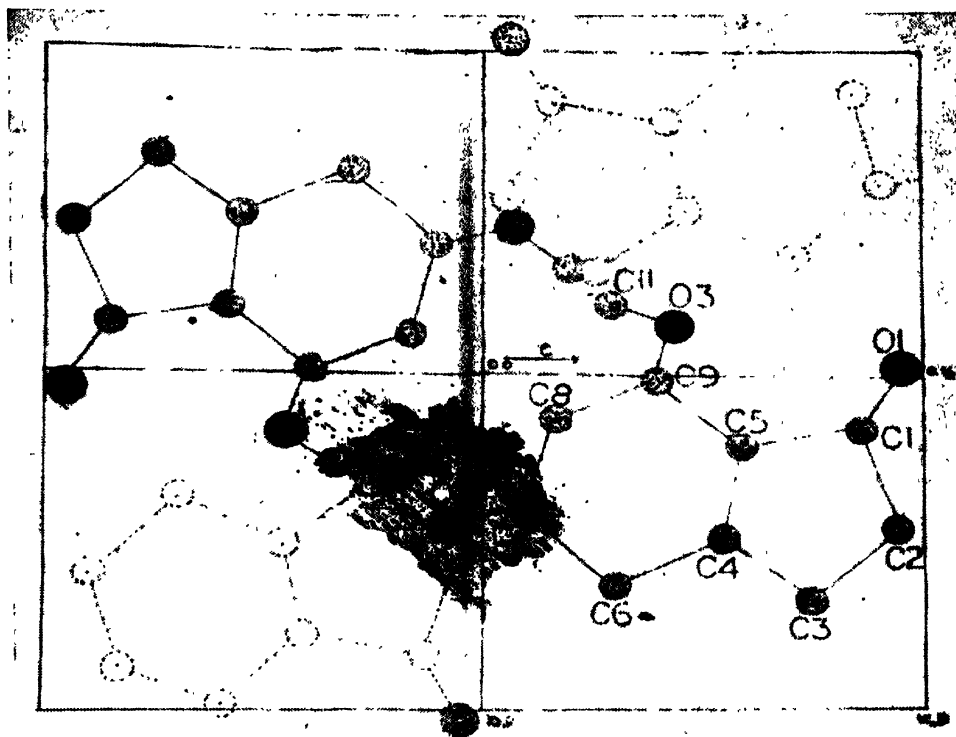


Figure 1. Crystal structure down the [100

Table 1. Atomic parameters ($\times 10^4$).

Atom	x/a (σ)	y/b (σ)	z/c (σ)
O1	2249(8)	-212(14)	643(12)
O2	2257(2)	516(18)	-416(14)
O3	2691(20)	-1053(16)	2292(13)
C1	2251(21)	951(17)	4212(14)
C2	2274(22)	2372(18)	4759(15)
C3	2277(30)	3437(29)	3792(26)
C4	2258(25)	2489(22)	2720(16)
C5	2307(39)	1085(28)	3060(26)
C6	2192(21)	-3190(18)	1419(16)
C7	2343(29)	2017(24)	563(22)
C8	2244(22)	636(19)	895(14)
C9	2163(22)	81(20)	2008(15)
C10	2233(29)	1970(24)	-1388(22)
C11	2221(25)	-1804(25)	1141(20)

Table 2(a). Bond lengths.

Atoms

O1—C1	1.23(2)
C2—C1	1.54(2)
C2—C3	1.49(3)
C3—C4	1.55(3)
C4—C5	1.44(2)
C4—C6	1.39(2)
C6—C7	1.42(2)
C7—C8	1.43(2)
C8—C9	1.35(2)
C7—O2	1.31(2)
C9—O3	1.34(2)
C11—O3	1.33(4)
C10—O2	1.32(2)

Table 2(b). Bond angles

Atoms involved

O1—C1—C2	138.3(1.2)
O1—C1—C5	114.5(1.0)
C2—C1—C5	107.0(1.0)
C1—C2—C3	109.8(1.0)
C2—C3—C4	101.8(1.1)
C3—C4—C5	110.5(1.0)
C4—C5—C1	110.5(1.4)
C1—C5—C9	133.3(1.5)
C9—C5—C4	116.1(1.2)
C5—C4—C6	131.1(1.0)
C4—C6—C7	107.2(1.2)
C6—C7—C8	125.9(1.0)
C7—C8—C9	122.1(1.0)
C8—C9—C5	116.6(1.1)
C8—C7—O2	118.3(1.0)
C6—C7—O2	115.9(1.0)
C7—O2—C10	136.8(1.5)
O3—C9—C8	123.8(1.8)
O3—C9—C5	113.1(1.2)
C9—O3—C11	117.6(1.2)
C3—C4—C6	118.1(1.4)

References

- Busing W R, Martin K O and Levy H A 1962 *ORFLS Report ORNL-M-305 Oak Ridge National Laboratory, Oak Ridge, Tennessee*. The CDC 3600 version incorporates modifications by W C Hamilton, J A Ibers, C K Johnson and S Srikanta.

ERRATUM

Chiral symmetry breaking and quarks (current and constituent) II

P. Sinha and V. P. Gautam

Indian J. Phys. 52A, 9-28 (1978)

The factor $2M$ occurring in eq. (21b) should read as $2M_N$.

In eq. (27) \approx sign is missing after m_π/m_K .

In the first and second line after eq. (27) and in the unnumbered eq. after eq. (27)

\approx sign is missing after $\sigma_{NN}^{\pi\pi}$, σ_{NN}^{KK} and $\frac{\sqrt{2+c}}{\sqrt{2-\frac{1}{2}c}}$ respectively.

In eq. (28) \approx sign is missing after $\frac{m_\pi^2}{m_K^2}$.

Eq. (32) should read as

$$f_+(0) = (f_K^2 + f_\pi^2 - f_\pi^2)/2f_K f_\pi \approx 0.97.$$

In eq. (37) \approx sign is missing after $\frac{f_{K^+m_{K^+}}}{f_{K^0m_{K^0}}}$.

Eq. (40) should read as

$$f_{\pi^0} \approx 1.03 f_{\pi^+}.$$

The correct signs of the terms containing m_s^2 in eqs. (43) and the eq. following it, should be opposite to those appearing there.

m_P^2 in eq. (46a) and $\overline{m_P^2}$ in eq. (48) should read as m_P^2 .

Eq. (52) should read as

$$(\Delta m_{\pi^+}^2 - \Delta m_{\pi^0}^2)_{JJ} = (m_{\pi^+}^2 - m_{\pi^0}^2) - \frac{1}{6f_\pi^2} (f_\pi m_\pi + 2f_K m_K)^2 d^2.$$

The term $m_{\pi^0}^2$ in the eq. following eq. (52) should be replaced by $\Delta m_{\pi^0}^2$

The second unnumbered relation after eq. (53) should read as $f_{K^0} \approx f_K^0$

The left hand side of eq. (55) should read as t/s .

The line after eq. (56) should read as, in consistency with our interpretation of c_{GMOR} .

e^- -Li scattering by simplified form of FSA

Sunanda Guha and A S Ghosh

Department of Theoretical Physics,
Indian Association for the Cultivation of Science, Jadavpur, Calcutta-700032.

Received 24 April 1978, revised 15 September 1978

Abstract. Simplified form of Fixed-Scatterer Approximation as proposed by Ghosh has been used to investigate the elastic scattering of electrons by Lithium atoms in the energy region $E = 10$ to 200 eV. Results of the differential and elastic integrated cross-sections have been calculated in this energy region and comparisons have been made with the recent experimental results of Williams *et al* at energies 10, 20 and 60 eV only.

1. Introduction

The measurement of differential cross-section for the elastic and inelastic e^- -Li scattering by Williams *et al* (1976) gives a scope to the theoretical workers to justify their approximations in a better way. No other differential measurement has so far been reported for elastic e^- -Li scattering. Agreement between the purely elastic integrated cross-sections and the existing theoretical results (Burke and Taylor 1969, Walters 1973, Sarkar *et al* 1973, Inokuti and McDowell 1974) are not very encouraging.

The aim of this paper is to obtain the purely elastic integral and differential cross-sections of e^- -Li scattering using the simplified form of fixed scatterer approximation as proposed by Ghosh (1977). In this paper Ghosh has written explicitly the necessity of employing this approximation in the framework of fixed scatterer approximation (FSA) and has also discussed in detail the difference between the present form and the simplified form of second Born approximation as proposed by Massey and Mohr (1934). The formalism of Ghosh yields reliable results (Ghosh 1977) for elastic and inelastic processes at high energies for e^- -H scattering. In the case of e^\pm -He scattering, results (Daskhan and Ghosh 1978) obtained using this formalism are also very encouraging. FSA assumes the static configuration of the target atom. Ghosh has retained upto the double scattering term assuming the fact that at intermediate and high energies higher order terms won't contribute appreciably. The effect of exchange has been taken into account explicitly following Ghosh (1978). Inclusion of exchange in the framework of FSA always improves the results. In the present calculations we have used the one electron wave function as used by Walters (1973). It has been pointed out by Mathur (1972) that the difference between the

scattering parameters by using one or three electron wavefunction of Li atom is not very appreciable at intermediate and high energies. He has arrived at this conclusion by using the Glauber approximation. It may be mentioned that Glauber's method for multiple scattering is an approximate method of fixed scatterer approximation. Keeping this thing in mind we have selected the one electron wave function for the Lithium atom. Here we have calculated the purely elastic integral and differential cross sections from 10 to 200 eV.

2. Theory

We can write the Schrödinger's equation for e^- -Li scattering in FSA as

$$(E - E_B - T_1)\psi_{\mathbf{k}_i}^+(\mathbf{r}_1, \mathbf{r}_2) = V(\mathbf{r}_1, \mathbf{r}_2)\psi_{\mathbf{k}_i}^+(\mathbf{r}_1, \mathbf{r}_2) \quad (1)$$

where the total wave function of the system, $\psi_{\mathbf{k}_i}^+(\mathbf{r}_1, \mathbf{r}_2)$ is expressed as the product of the target wave function $\phi_t(\mathbf{r}_2)$ and the incident wave $F_{\mathbf{k}_i, \mathbf{r}_2}^+(\mathbf{r}_1)$ in the FSA, is

$$\psi_{\mathbf{k}_i}^+(\mathbf{r}_1, \mathbf{r}_2) = \phi_t(\mathbf{r}_2)F_{\mathbf{k}_i, \mathbf{r}_2}^+(\mathbf{r}_1) \quad (2)$$

with \mathbf{k}_i is the incident momentum and $V(\mathbf{r}_1, \mathbf{r}_2)$ is the perturbed potential. Here E_B is the binding energy of the target atom and T_1 , the K.E. part. The equation (1) takes the form

$$(E - E_B - T_1)F_{\mathbf{k}_i, \mathbf{r}_2}^+(\mathbf{r}_1) = V(\mathbf{r}_1, \mathbf{r}_2)F_{\mathbf{k}_i, \mathbf{r}_2}^+(\mathbf{r}_1). \quad (3)$$

Here the function $F_{\mathbf{k}_i, \mathbf{r}_2}^+(\mathbf{r}_1)$ which has a parametric dependence on the target electron coordinate \mathbf{r}_2 , satisfies the usual boundary condition.

The corresponding Lippmann-Schwinger equation is given by

$$F_{\mathbf{k}_i, \mathbf{r}_2}^+(\mathbf{r}_1) = |\mathbf{k}_i\rangle + \frac{2}{8\pi^3} \int d\mathbf{k}'' \frac{|\mathbf{k}''\rangle \langle \mathbf{k}''| V(\mathbf{r}_1, \mathbf{r}_2) | F_{\mathbf{k}_i, \mathbf{r}_2}^+(\mathbf{r}_1) \rangle}{k_i^2 - k''^2 + i\epsilon} \quad (4)$$

Equation (4) in the FSA is exact uptill now. $F_{\mathbf{k}_i, \mathbf{r}_2}^+(\mathbf{r}_1)$ on the right hand side of equation (4) is now replaced by a plane wave i.e., two terms are retained. Thus the function $F_{\mathbf{k}_i, \mathbf{r}_2}^+(\mathbf{r}_1)$ takes the form with proper normalisation

$$\langle \mathbf{k}_f | V | F_{\mathbf{k}_i, \mathbf{r}_1}^+(\mathbf{r}_1) \rangle = \langle \mathbf{k}_f | V | \mathbf{k}_i \rangle + \frac{1}{4\pi^3} \int d\mathbf{k}'' \frac{\langle \mathbf{k}_f | V | \mathbf{k}'' \rangle \langle \mathbf{k}'' | V | \mathbf{K}_i \rangle}{k_i^2 - k''^2 + i\epsilon} \quad (5)$$

The direct scattering amplitude from the initial state $|\mathbf{i}\rangle$ with momentum \mathbf{k}_i to the final state $\langle \mathbf{f}|$ with momentum \mathbf{k}_f is given by

$$f_{fs}^{FSA}(\hat{\mathbf{k}}_f, \hat{\mathbf{k}}_i) = f^S + f^D \quad (6)$$

where

$$f^S = -\frac{1}{2\pi} \int e^{i\mathbf{q}\cdot\mathbf{r}_1} \left(-\frac{1}{r_1} + \frac{1}{r_{12}} + V_c \right) \phi_f^*(\mathbf{r}_2) \phi_i(\mathbf{r}_2) d\mathbf{r}_1 d\mathbf{r}_2$$

and

$$f^D = \frac{1}{8\pi^4} \phi_f^*(\mathbf{r}_2) \phi_i(\mathbf{r}_2) \int d\mathbf{k}'' \frac{\langle \mathbf{k}_f | V | \mathbf{k}'' \rangle \langle \mathbf{k}'' | V | \mathbf{k}_i \rangle}{k''^2 - k_i^2 - i\epsilon} d\mathbf{r}_1 d\mathbf{r}_2. \quad (7)$$

The calculation of f^S which is nothing but the first Born terms is straightforward. The final expression for f^D is lengthy and the type integrals by which one can get the final expression for f^D are given in Appendix I. The corresponding rearrangement amplitude is

$$g_{fi}^{FSA}(\hat{k}_f, \hat{k}_i) = -\frac{\mu_f}{2\pi} \langle \phi_f(\mathbf{r}_1, \mathbf{r}_2) | \mathbf{k}_f | V | \phi_i(\mathbf{r}_2, \mathbf{r}_1) F_{\mathbf{k}_i, \mathbf{r}_2}^+(\mathbf{r}_1) \rangle. \quad (8)$$

We now calculate the exchange amplitude for e^- -Li scattering in which both the initial and final states are in the ground state. In the present case, the function $F_{\mathbf{k}_i, \mathbf{r}_2}^+(\mathbf{r}_1)$ takes the form

$$F_{\mathbf{k}_i, \mathbf{r}_2}^+(\mathbf{r}_1) = e^{i\mathbf{k}_i \cdot \mathbf{r}_1} + \frac{1}{\pi^2} \int d\mathbf{k}'' \frac{1}{|k'' - k_i|^2 (k''^2 - k_i^2 - i\epsilon)} e^{i\mathbf{k}'' \cdot \mathbf{r}_1} [1 - e^{i(\mathbf{k}_i - \mathbf{k}'') \cdot \mathbf{r}_2}] \quad (9)$$

Equation (8) may then be written as

$$g_{fi}^{FSA}(\hat{k}_f, \hat{k}_i) = g^S + g^D \quad (10)$$

where g^S is nothing but the Oppenheimer amplitude and it can be easily calculated. The double scattering term of the exchange amplitude g^D is given by

$$g^D = -\frac{1}{2\pi^3} \int \phi_i^*(\mathbf{r}_1) e^{-i\mathbf{k}_f \cdot \mathbf{r}_2} \left(-\frac{1}{r_2} + \frac{1}{r_{12}} \right) \phi_i(\mathbf{r}_2) \frac{e^{i\mathbf{k}_i \cdot \mathbf{r}_1} [1 - e^{i(\mathbf{k}'' - \mathbf{k}_i) \cdot \mathbf{r}_2}]}{|\mathbf{K}'' - \mathbf{K}_i|^2 (k''^2 - K_i^2 - i\epsilon)} \times d\mathbf{K}'' d\mathbf{r}_1 d\mathbf{r}_2 \quad (11)$$

The final expression for g^D is also very lengthy and the type integrals from which the final expression can be obtained are given in Appendix II.

The wave function used for the ground state of lithium atom is

$$\phi_{2s}(\mathbf{r}) = A e^{-0.65r} + B \phi_{1s}$$

where

$$\phi_{1s}(\mathbf{r}) = \left(\frac{(2.7)^3}{\pi} \right)^{\frac{1}{2}} e^{-2.7r}$$

and the constants A and B are so chosen that ϕ_{2s} is orthogonal to ϕ_{1s} and also normalised. It may be mentioned that we have included the core potential V_c , in the Born and Oppenheimer terms and V takes the form

$$V = -1/r_1 + 1/r_{12} + V_c,$$

V_c can be obtained following Walters (1973) and

$$V_c = -2(1/r_1 + 2.7/2)e^{-5.4r}$$

In the calculation of Double scattering terms we have neglected the core potential V_c , for it has been found that the inclusion of V_c in the double scattering terms will not affect the cross-sections appreciably.

3. Results and Discussion

A. Differential cross-sections :

Figures 1 to 3 represents our results with and without exchange for the differential cross-sections along with the recent measured values of Williams (1976). The results of Guha and Ghosh (1979) using polarised orbital method (POM) are also inserted in the same figure for comparison. For low incident energy

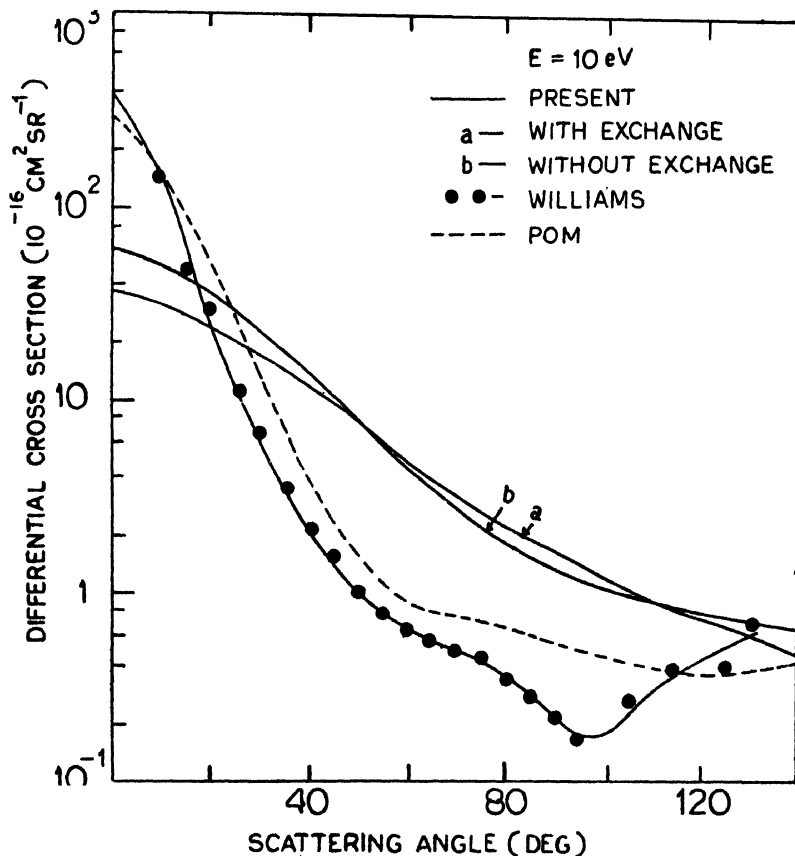


Figure 1

the present curves with and without exchange fail to reproduce either qualitative or quantitative agreement with the measured values. At 20 eV, the present differential results are somewhat similar to those of POM values as well as experimental findings. The present curve, however, fails to reproduce the shallow minimum as given by the measured values. From figure 3 it is evident that the present computed results for the incident energy 60 eV yield the qualita-

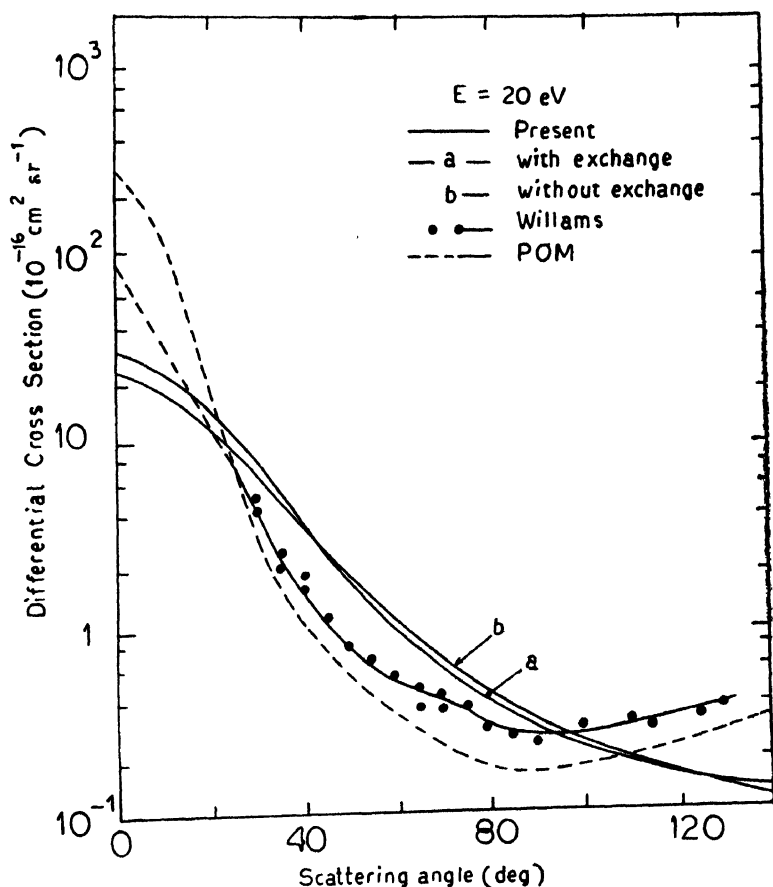


Figure 2.

tive feature of the experimental curve though the magnitudes are not same. Near the forward direction, present values, with and without exchange, are close to the experimental findings. The results of the POM are not very much different from the present results at 60 eV except very near the forward direction. We have calculated the values of the differential cross-sections with and without exchange at different energies from 10 to 200 eV. From the results it

is clear that the effect of exchange is not negligible even at the incident energy 200 eV. At low energies, the present values show marked difference with those of FBA results. With the increase of energy, the difference decreases as expected; at $E = 200$ eV, the two set of results are within 5 %.

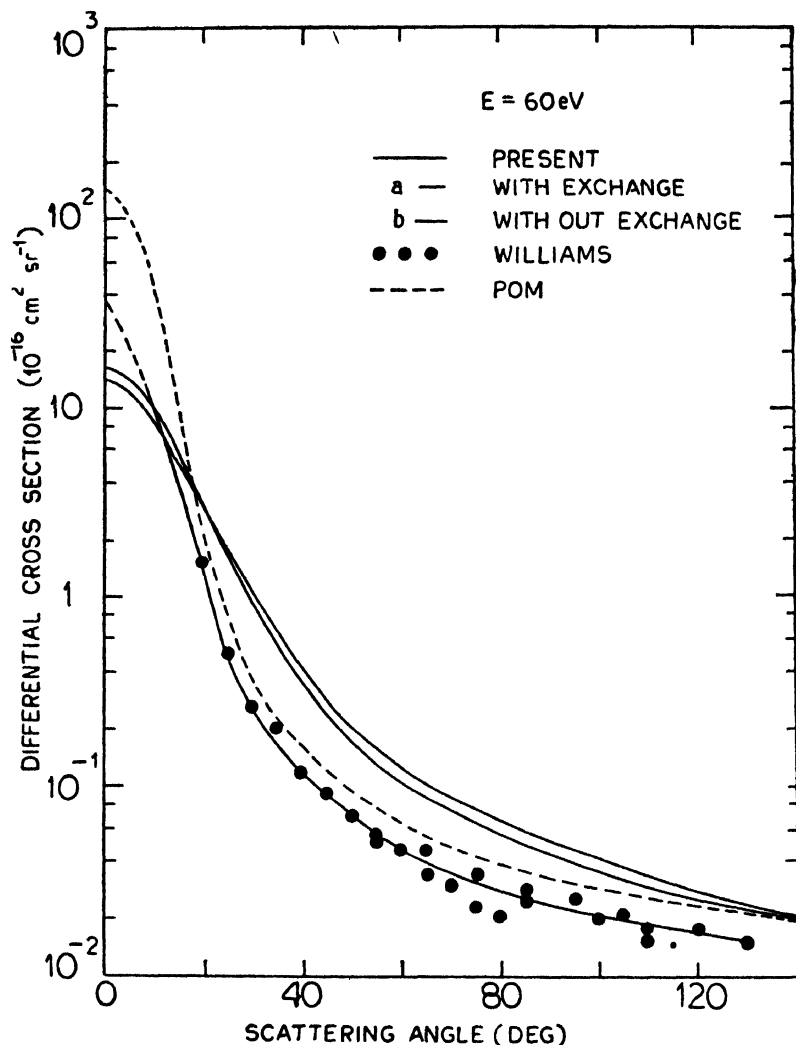


Figure 3.

In our method we have neglected the effect of higher order terms. The effect of polarization is also appreciable for the alkali atoms. This effect has not been taken into account explicitly in our method. Considering all these points, we think that the present result is expected to be reliable at large scattering angle and at the incident energies $E > 20$ eV. The inclusion of the higher order terms and polarization may improve the results appreciably. The disagreement

between the present results and the measured values at 60 eV in the large scattering angle is not understood.

The measurement of the differential cross-section is in the early stage. More rigorous theoretical attempts should be made to determine the exact behaviour of the cross-section.

B. Total cross-section

Figure 4 represents our results (with exchange) for the elastic integrated cross-sections along with Williams (1976) experimental results and other theoretical values upto 60 eV incident energy. Our value of the cross section at 10 eV overestimates the experimental value and it is very close to the POM value.

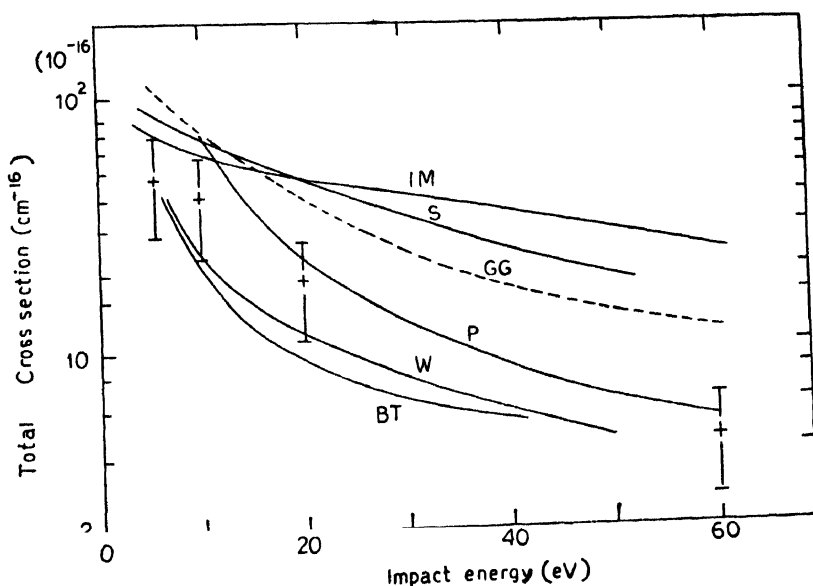


Figure 4.

But at 20, 30, 50 and 60 eV incident energies our values are close to the experimental values and they are within the experimental error range. Our POM values are always greater than those of experiment though there is a qualitative agreement between the two. The results of Burke and Taylor (1969) and Walters (1973) who have used the close coupling method and the Glauber method respectively underestimate the experimental values whereas the results of Sarkar *et al* (1973) (Modified Eikonal Approximation) and McDowell (First-Born approximation) overestimate the experimental findings. In comparison to other theoretical findings our results agree well with the experiment.

Table 1. Total elastic cross section in units of πa_0^2 in e^- -Li atom collisions at incident energies 10–200 eV. The symbol $a \pm b$ denotes $a \times 10 \pm b$.

Energy (eV)	Total elastic cross section (πa_0^2)	
	with exchange	without exchange
10.0	8.3186+1	6.9458+1
20.0	2.6337+1	2.3383+1
30.0	1.4568+1	1.3488+1
50.0	7.5109+0	7.2058+0
60.0	6.0343+0	5.8376+0
100.0	3.3785+0	3.3177+0
150.0	2.1825+0	2.1568+0
200.0	1.6135+0	1.5992+0

In table 1 we have given the elastic integrated cross-sections from 10 to 200 eV incident energies. Lastly we conclude by warranting further experimental and theoretical investigations.

APPENDIX I

The expression for the double scattering term of the direct scattering amplitude is given by

$$f^D = \frac{1}{8\pi^4} \int \phi_f^*(\mathbf{r}_2) \int d^3\mathbf{k}'' \frac{\langle \mathbf{k}_f | V | \mathbf{k}'' \rangle \langle \mathbf{k}'' | V | \mathbf{k}_i \rangle}{k''^2 - k_i^2 - i\epsilon} \phi_i(\mathbf{r}_2) d\mathbf{r}_2 \quad (\text{I.1})$$

$$\phi_f^*(\mathbf{r}_2) \phi_i(\mathbf{r}_2) d\mathbf{r}_2 \int \frac{d\mathbf{k}''}{q_1^2 q_2^2 (k''^2 - k_i^2 - i\epsilon)} [1 - e^{i\mathbf{q}_1 \cdot \mathbf{r}_2} - e^{i\mathbf{q}_2 \cdot \mathbf{r}_2} + e^{i\mathbf{q}_2 \cdot \mathbf{r}_2}] \quad (\text{I.2})$$

where

$$\mathbf{q} = \mathbf{k}_i - \mathbf{k}_f$$

$$\mathbf{q}_1 = \mathbf{k}'' - \mathbf{k}_f$$

$$\mathbf{q}_2 = \mathbf{k}_i - \mathbf{k}''.$$

Performing integrations over $d\mathbf{r}_2$ and $d\mathbf{k}''$ one gets finally

$$f^D = -32\pi [B^2 \lambda_2 X_1(\lambda_2) + 2AB \{X_1(\lambda_3) + 2\lambda_3^2 X_2(\lambda_3)\} - 6A^2 \lambda_1 X_2(\lambda_1) - 4A^2 \lambda_1^3 X_3(\lambda_1)] \quad (\text{I.3})$$

where

$$X(\lambda) = \frac{1}{\lambda^2 k_i (q^2 + \lambda^2)} \arctan(\lambda_2 / 2k_i)$$

and

$$\lambda_1 = 1.3, \quad \lambda_2 = 5.4, \quad \lambda_3 = 3.5.$$

X_1 , X_2 and X_3 are the 1st, 2nd and 3rd derivatives of X .

APPENDIX II

The double scattering term for the exchange scattering amplitude g^D may be written as

$$g^D = I_1 + I_2 + I_3 + I_4 \quad (\text{II.1})$$

where,

$$I_1 = \frac{1}{2\pi^3} \int \phi_f^*(\mathbf{r}_1) e^{-i\mathbf{k}_f \cdot \mathbf{r}_2} \frac{1}{r_2} \frac{\phi_i(\mathbf{r}_2) e^{i\mathbf{k}'' \cdot \mathbf{r}_1} d\mathbf{k}'' d\mathbf{r}_1 d\mathbf{r}_2}{|\mathbf{k}'' - \mathbf{k}_i|^2 (k''^2 - k_i^2 - i\epsilon)} \quad (\text{II.2})$$

$$I_2 = \frac{1}{2\pi^3} \int \phi_f^*(\mathbf{r}_2) e^{-i\mathbf{k}_f \cdot \mathbf{r}_2} \frac{1}{r_{12}} \frac{\phi_i(\mathbf{r}_2) e^{i\mathbf{k}'' \cdot \mathbf{r}_1} d\mathbf{k}'' d\mathbf{r}_1 d\mathbf{r}_2}{|\mathbf{k}'' - \mathbf{k}_i|^2 (k''^2 - k_i^2 - i\epsilon)} \quad (\text{II.3})$$

$$I_3 = -\frac{1}{2\pi^3} \int \phi_f^*(\mathbf{r}_2) e^{-i\mathbf{k}_f \cdot \mathbf{r}_2} \frac{1}{r_2} \frac{\phi_i(\mathbf{r}_2) e^{i(\mathbf{k}_i - \mathbf{k}'') \cdot \mathbf{r}_1 + i\mathbf{k}'' \cdot \mathbf{r}_1}}{|\mathbf{k}'' - \mathbf{k}_i|^2 (k''^2 - k_i^2 - i\epsilon)} d\mathbf{k}'' d\mathbf{r}_1 d\mathbf{r}_2 \quad (\text{II.4})$$

$$I_4 = \frac{1}{2\pi^3} \int \phi_f^*(\mathbf{r}_2) e^{-i\mathbf{k}_f \cdot \mathbf{r}_2} \frac{1}{r_{12}} \frac{\phi_i(\mathbf{r}_2) e^{i(\mathbf{k}_i - \mathbf{k}'') \cdot \mathbf{r}_1 + i\mathbf{k}'' \cdot \mathbf{r}_1}}{|\mathbf{k}'' - \mathbf{k}_i|^2 (k''^2 - k_i^2 - i\epsilon)} d\mathbf{k}'' d\mathbf{r}_1 d\mathbf{r}_2. \quad (\text{II.5})$$

The type integrals required for solving I_1 , I_2 , I_3 and I_4 are given below :

$$A_1 = \int d\mathbf{r}_2 e^{-\alpha_1 r_1 - \alpha_2 r_2 - i\mathbf{k}_f \cdot \mathbf{r}_2} \frac{1}{r_2} \int d\mathbf{k}'' \frac{e^{i\mathbf{k}'' \cdot \mathbf{r}_1}}{|\mathbf{k}'' - \mathbf{k}_i|^2 (k''^2 - k_i^2 - i\epsilon)} d\mathbf{r}_1 \quad (\text{II.6})$$

$$= \frac{32\pi^4}{k_i(k_f^2 + \alpha_2^2)(k_i^2 + \alpha_1^2)^2} \left[\alpha_1 \arctan \left(\frac{\alpha_1^2 - k_i^2}{2\alpha_1 k_i} \right) - k_i \right] \quad (\text{II.7})$$

$$A_2 = \int e^{-\alpha_1 r_1 - \alpha_2 r_2} \frac{1}{r_{12}} \frac{e^{-i\mathbf{k}_f \cdot \mathbf{r}_2 + i\mathbf{k}'' \cdot \mathbf{r}_1}}{|\mathbf{k}'' - \mathbf{k}_i|^2 (k''^2 - k_i^2 - i\epsilon)} d\mathbf{r}_1 d\mathbf{r}_2 d\mathbf{k}'' \quad (\text{II.8})$$

$$= \frac{16\alpha_2\pi^4}{k_i} \int_0^1 x dx Y_1, \quad (\text{II.9})$$

where

$$Y_1 = \frac{\partial Y}{\partial \mu^2} \quad (\text{II.10})$$

and

$$= \frac{2}{\mu} \left[(Q^2 + \gamma^2) \left\{ \frac{k_i(\gamma^2 + k_i^2 - \Lambda^2)}{4k_i^2\gamma^2 + (\gamma^2 - k_i^2 + \Lambda^2)} \right\} - \frac{\gamma}{Q^2 + \gamma^2} \tan^{-1} \frac{\gamma^2 - k_i^2 - \Lambda^2}{2k_i\gamma_1} \right] \quad (\text{II.11})$$

where

$$\mu^2 = x\alpha_2^2 + x(1-x)k_f^2$$

$$\Lambda = xk_f$$

$$\gamma = \mu + \alpha_1;$$

$$\begin{aligned} A_3 &= \int e^{-\alpha_1 r_1 - \alpha_2 r_2} \frac{1}{r_2} \frac{e^{-i\mathbf{k}_f \cdot \mathbf{r}_2 + i(\mathbf{k}_i - \mathbf{k}'). \cdot \mathbf{r}_2 + i\mathbf{d} \cdot \mathbf{r}_1}}{|\mathbf{k}'' - \mathbf{k}_i|^2 (k''^2 - k_i^2 - i\epsilon)} d\mathbf{r}_1 d\mathbf{r}_2 d\mathbf{k}'' \quad (\text{II.12}) \\ &= 16\pi^4 \left[\frac{2\alpha_1}{k_i^2 + \alpha_1^2} Z - \frac{2\alpha_1}{k_i^2 + \alpha_1^2} X - \frac{N'}{2N} X + \frac{N'\beta - 2N\beta'}{N(k_i^2 + \alpha_1^2)(\beta^2 + N)} \right] \end{aligned} \quad (\text{II.13})$$

where

$$Z = \frac{1}{k_i(k_f^2 + \alpha_2^2)(k_i^2 + \alpha_1^2)} \arctan \left(\frac{\alpha_2^2 - k_i^2 + q^2}{2k_i\alpha_2} \right) \quad (\text{II.14})$$

and

$$X = \frac{2}{k_i^2 + \alpha_1^2} \cdot \frac{1}{N^{\frac{1}{2}}} \arctan \left(\frac{N^{\frac{1}{2}}}{\beta} \right) \quad (\text{II.15})$$

with

$$N = q^2(k_i^2 + \alpha_1^2)(k_f^2 + \alpha_2^2) + (\alpha_2^2 - \alpha_1^2)^2 k_i^2$$

$$\beta = \alpha_1(k_i^2 + \alpha_2^2) + \alpha_2^2(k_i^2 + \alpha_1^2)$$

$$N' = \frac{\partial N}{\partial \alpha_2}$$

$$\beta' = \frac{\partial \beta}{\partial \alpha_2}$$

$$\begin{aligned} A_4 &= \int e^{-\alpha_1 r_1 - \alpha_2 r_2} \frac{1}{r_{12}} \frac{e^{-i\mathbf{k}_f \cdot \mathbf{r}_2 + i(\mathbf{k}_i - \mathbf{k}'). \cdot \mathbf{r}_2 + i\mathbf{k} \cdot \mathbf{r}_1}}{|\mathbf{k}'' - \mathbf{k}_i|^2 (k''^2 - k_i^2 - i\epsilon)} d\mathbf{r}_1 d\mathbf{r}_2 d\mathbf{k}'' \quad (\text{II.16}) \end{aligned}$$

$$= \frac{8\pi^4}{k_i^2} \int_0^\infty \frac{k dk \epsilon (k_i^2, k^2)}{(k^2 + \alpha^2)^2} \left[\frac{1}{\sqrt{c}} \left(-\frac{b'}{b} + \frac{a'}{a} \right) + \frac{c'}{2c^{3/2}} \ln \left(\frac{b}{a} \right) \right] \quad (\text{II.17})$$

with

$$\epsilon(k_i^2, k^2) \gtrless 1, 0, -1 \quad \text{according as } k_i^2 \gtrless k^2$$

and

$$a = \sqrt{c} \left\{ q^2 - \frac{2k_id}{(k+k_i)^2} + \frac{k_i^2 c}{(k+k_i)^2} \right\}^{\frac{1}{2}} - \frac{k_i c}{(k+k_i)^2} + d$$

$$\sqrt{c} \left\{ q^2 - \frac{2k_id}{(k-k_i)^2} + \frac{k_i^2 c}{(k-k_i)^2} \right\} - \frac{k_i c}{(k-k_i)^2} + d \quad (\text{II.18})$$

$$c = \left\{ (k^2 + q^2 + \alpha_2^2) - |q| \cos \theta \left(\frac{k^2 + k_i^2}{k_i} \right) \right\}^2 + \left\{ |q| \sin \theta \left(\frac{k^2 - k_i^2}{k_i} \right) \right\}^2$$

$$d = q^2 \left(\frac{k^2 + k_i^2}{k_i} \right) - |q| \cos \theta (k^2 + q^2 + \alpha_2^2)$$

where θ is the scattering angle.

Acknowledgment

One of us (SG) is thankful to University Grants Commission, India for a Teacher's Fellowship.

References

- Burke P G and Taylor A J 1969 *J. Physics* **B 2** 2382
- Daskhan M and Ghosh A S 1978 (to be published)
- Ghosh A S 1977 *Phys. Rev. Letters* **38** 1065
- Ghosh A S 1978 (to be published)
- Guha S and Ghosh A S 1979 (to be published)
- Inokuti M and McDowell M R C 1974 *J. Phys.* **B7** 2382
- Mathur K C, Tripathi and Joshi S K 1972 *Phys. Rev.* **A5** 746
- Sarkar K, Saha B C and Ghosh A S 1973 *Phys. Rev.* **A8** 236
- Walters H R J 1973 *J. Physics* **B6** 1003
- Williams W, Trajmar S and Bazinis D 1976 *J. Physics* **B9** 1529

A new method of estimation of limiting solid volume and related properties of simple non-polar liquids

B K Sharma

Department of Physics, Regional College of Education,
Bhubaneswar-751007 (Orissa)

Received 5 October 1978

Abstract. A simple theoretical method has been suggested for the evaluation of melting point limiting solid volume, melting temperature and heat of fusion of simple non-polar substances in terms of characteristic parameters of liquid state. The calculated values are in close agreement with experimental data and those reported by earlier workers.

1. Introduction

In the theory of melting, limiting molar volume of solid at melting point (or triple point as the case may be) has been found to be a useful tool of study of several thermodynamic properties of liquids (Yosim and Owens 1963, Kanno 1972, Lennard-Jones and Devonshire 1939, Eyring *et al* 1967, 1959, 1963, 1964, Mansoori and Canfield 1969, Tuerpe and Keeler 1967). So far, hardly any significant effort has been made to estimate such an important parameter on theoretical basis. Hence its evaluation is very important. Such a study is essential for a correct understanding of the conceptual framework and mechanism of melting process and related thermodynamic properties. We propose, in this paper, much needed analytical method of estimating limiting solid volume V_s of simple non-polar liquids in terms of characteristic volume V^* . We compute V_s and other melting-point properties in the case of small (slightly polarizable), symmetrical (non-polar), and slightly non-spherical molecules in condensed phase.

2.1. Calculation of V_s

In a recent publication, Sharma and Bhatnagar (1975) have suggested an effective method to compute characteristic volume V^* of simple non-polar and slightly non-spherical molecules in liquid state in terms of critical constants of liquids. Hence, V^* of any simple non-polar liquid bears a certain ratio to its critical volume V_c given by (Sharma and Bhatnagar 1975)

$$V^* = a V_c \quad (1)$$

where $a = (p_c V_c / RT_c)$ is the critical state compressibility factor, p_c , V_c and T_c are critical constants and R is the universal gas constant.

In view of the complicated nature of thermal atomic vibrations in liquid state (Singwi and Sjolander 1960), the coordination number Z in instantaneous liquid structure is not constant. At the melting point, the intermolecular distance in the liquid remains nearly the same as for the solid, thereby retaining the lattice pattern. However, the number of nearest neighbours Z of a typical molecule may be slightly decreased (Einstein and Gingrich 1942). As the temperature increases Z steadily decreases approximately to 4 at the critical point (Mikolaj and Pings 1967, Marchi and Eyring 1963). The variation in Z is roughly proportional to density of the liquid, with temperature having a smaller effect (Pings 1968), in agreement with analysis by Melrose (1966). In recent publications Sharma (1976a, 1976b) has proposed that Z is a function of compression, density and thermodynamic state of the liquid. The coordination number Z is assumed to vary inversely on molar volume thereby decreasing with increase of temperature. At absolute zero temperature, Z assumes maximum value in the lattice with minimum molar volume of hard core, referred to as the characteristic volume V^* .

Diffraction studies (Einstein and Gingrich 1942, Gingrich and Thompson 1962, Henshaw 1957) show that although liquid retains some aspect of short range order, considerable degree of disorder due to distortion or randomness of the instantaneous arrangement of molecules is inherent in liquid lattice structure. It is proposed that as temperature increases, the liquid lattice is so distorted as to lower the value of Z . Hence, the effective coordination number Z' in expanded liquid region at any temperature may be written as

$$Z' = ZA(V_s/V) \quad (2)$$

in which

$$A = ae \quad (3)$$

where Z is the coordination number at absolute zero temperature, V_s is the molar volume of unexpanded solid at melting point, V is the molar volume of liquid at any reference temperature T and pressure p , A is the proportionality constant introduced earlier (Sharma 1976b) and e is the base of the natural logarithms.

The present proposal of equation (2) is in close qualitative and quantitative agreement with experiment (Marchi and Eyring 1963, Mikolaj and Pings 1967, Pings 1968, Fisher 1964, Melrose 1966) throughout the whole liquid range of temperature from melting point T_m to critical temperature T_c .

Following the lattice theory, when geometric factors of the lattice at absolute zero and melting points are assumed equal, we can easily obtain an expression relating molar volumes with molecular diameters as

$$(V_s/V^*) = (\sigma/\sigma^*)^3 \quad (4)$$

where σ^* is the hard core diameter and σ is the nearest neighbour distance of the lattice.

Due to complex thermal atomic vibrations in liquids (Singwi and Sjolander 1960), not necessarily confined to their particular equilibrium lattice position by virtue of loose liquid lattice as compared to solid, σ is not necessarily equal to the equilibrium molecular diameter σ_0 . However, the ratio (σ/σ_0) may be close to unity for liquids (Eyring *et al* 1941). Hence, we introduce the approximation as

$$\sigma = B\sigma_0 \quad (5)$$

where B is a constant close to unity for most liquids.

For simple liquids the limiting value of molecular diameter σ_0 in terms of σ^* is given by (Lennard-Jones and Devonshire 1939)

$$\sigma_0 = 2^{1/6}\sigma^* \quad (6)$$

From equations (4)–(6), we obtain

$$(V_s/V^*) = 2^{\frac{1}{2}}B^3 = 2^{\frac{1}{2}}(\sigma/\sigma_0)^3 \quad (7)$$

We follow afore mentioned inverse dependence of Z on molar volume and obtain an alternative expression of Z' for simple liquids by introducing the approximation given by

$$\sigma_0^3 Z' = \sigma^3 Z. \quad (8)$$

Using equations (2), (7) and (8) we can now write the desired expression for V_s for the solid phase at the melting point as

$$V_s = CV^* \quad (9)$$

in which

$$C = 2^{\frac{1}{2}}B^3 \quad (10)$$

$$B = (Z'/Z)^{1/3} = A^{1/3}. \quad (11)$$

The validity of equation (9) has been tested for several simple, slightly polarizable non-polar liquids for which experimental data were available. Our calculated values of V_s in comparison with those reported in literature (Moelwyn-Hughes 1965 and Eyring *et al* 1967) are shown in Table 1. The agreement is extremely good. The calculated values of V^* were obtained by using equation (1) from the experimental data on α and V_c quoted from Lange (1967), and Kobe and Lynn (1953). The values of V^* and V_s are constants characteristic of the liquid.

Table 1. Comparison of calculated and observed values of V_s (values of V_c , V^* and V_s are given in cc mol⁻¹)

Liquid	a	V_c	V^* calc.	V_s calc.	V_s exptl.
Ne	0.296	41.7	12.34	14.04	14.03
Ar	0.292	75.3	21.99	24.68	24.61
Kr	0.290	92.1	26.71	29.77	29.66
N ₂	0.292	90.1	26.31	29.53	29.31
Xe	0.290	118.8	34.45	38.40	37.10
CH ₄	0.290	99.4	28.71	32.00	30.94
O ₂	0.292	74.4	21.72	24.38	23.77
H ₂	0.306	65.0	19.89	23.39	23.31
He	0.305	57.8	17.63	20.66	21.18
Hg	0.294	40.1	11.80	13.32	14.14

2.2. Calculation of T_m

The modified configurational partition function for a mole of molecules of the liquid is given by (Sharma and Bhatnagar 1976c)

$$Q_N = Q_N^{comb} \left(\frac{2\pi mKT}{h^2} \right)^{3/2 Nc^*} (q^3 g V^*)^{Nc^*} (\tilde{V}^{1/3} - 1)^{3Nc^*} \exp \left(\frac{NC^*}{\tilde{V} \tilde{T}} \right) \quad (12)$$

where $\tilde{V} = (V/V^*)$ is the reduced volume, $\tilde{T} = (T/T^*)$ is the reduced temperature, V^* is the characteristic volume, T^* is the characteristic temperature, Q_N^{comb} is the combinatorial partition function independent of temperature, m is the molecular mass, $3C^*$ is the number of external degrees of freedom, h is Planck's constant, k is Boltzmann constant, N is Avogadro's number, g is the geometric factor depending on the type of lattice and q^{3N} is the communal entropy of factor of liquids.

We write the reduced equation of state for the liquid system obtained from equation (12) as

$$\frac{\tilde{p}}{\tilde{T}} = \frac{\tilde{V}^{1/3}}{(\tilde{V}^{1/3} - 1)} - \frac{1}{\tilde{V} \tilde{T}} \quad (13)$$

where $\tilde{p} = (p/p^*)$ is the reduced pressure and p^* is the characteristic pressure.

Equation (13) is identical with those obtained by Flory *et al* (1964, 1965) and Sharma and Bhatnagar (1975).

Using equation (13) the characteristic parameters are given by (Sharma and Bhatnagar 1975)

$$C^* = 6a(1 - a^{1/3})/(3 - 4a^{1/3}), \quad (14)$$

$$T^* = T_c(3 - 2a^{1/3})/6a(1 - a^{1/3})^2, \quad (15)$$

$$p^* = C^*RT^*/V^*. \quad (16)$$

All the parameters V^* , C^* , T^* and p^* are constants characteristic of the liquid and are independent of temperature.

The experimental data refer to ordinary pressure p and may be considered to hold for zero pressure without any appreciable error. At the zero pressure limit, the melting temperature T_m using equation (13) is given as

$$T_m = T^*(\tilde{V}^{1/3} - 1)/\tilde{V}^{4/3}. \quad (17)$$

To extend the use of equation (17) for calculating the values of T_m for liquids the effect of distortion of lattice with temperature has to be considered. At the melting point, the crystal lattice of the solid breaks down and the solid melts to form a liquid.

The lattice distortion parameter which takes into account the distortion taking place in the liquid lattice is given by (Sharma 1976b)

$$\delta = \alpha Z_c(V_s/V) \quad (18)$$

where Z_c is the critical state coordination number assumed to be 4 for simple liquids (Eyring and Marchi 1963, Sharma 1976b).

Accordingly, the proposed equation correlating T_m with \tilde{V} and T^* is given as

$$T_m = T^*\delta(\tilde{V}^{1/3} - 1)/\tilde{V}^{4/3}. \quad (19)$$

The calculated values of δ and T_m along with experimental values of T_m are presented in Table 2. The experimental data on liquid molar volume V at

Table 2. Comparison of calculated and experimental values of T_m (values of T_c , T_m and T^* are given in K and those of V in cc mol⁻¹)

Substance	V	δ calc.	T_c	T^* calc.	T_m calc.	T_m exptl.
Neon	16.18	1.04	44.5	375.4	25.52	24.57
Argon	28.34	1.02	150.7	1270.0	81.06	83.78
Nitrogen	31.95	1.08	126.1	1064.0	59.40	63.14
Krypton	34.33	1.01	209.4	1765.0	110.60	116.00
Xenon	42.69	1.04	289.8	2422.0	141.80	161.30

melting temperature T_m for liquids composed of inert gases were taken from Cook (1961) and those for nitrogen from those reported by Fuller *et al* (1959). The calculated values of V^* and V_s utilized for calculating T_m were taken from table 1. The values of T^* were calculated by using equation (15). The experimental values of a and T_c utilized were taken from Lange (1967) and Kobe and Lynn (1953). It is seen from table 2 that the agreement between calculated and experimental values of T_m is fair. The value of factor δ is near unity for simple liquids.

2.3. Calculation of heat of fusion

We now apply the model calculations for evaluating entropies and heats of fusion of crystals which are composed of molecules with spherically symmetrical force field and thus examine their melting behaviour.

Kirkwood (1950) defined communal entropy ΔS_0 in terms of configurational integrals as

$$\Delta S_0 = k \ln(Q_N/Q_{s0}) \quad (20)$$

where Q_N is the configurational integral (12) which contains all configurations, crystalline, fluid and intermediate, which the N particles can assume. Q_{s0} is the single-occupancy configurational integral which allows only one particle in each of the cells centered on the crystal lattice and does not include communal entropy factor q^{3N} .

The single-occupancy configurational integral obtained from equation (12) may be written as

$$Q_{s0} = D(\bar{V}_s^{1/3} - 1)^{3NC^*} \exp(NC^*/\bar{V}_s \bar{T}), \quad (21)$$

in which

$$D = Q_N^{comb} (2\pi mkT/h^2)^{3NC^*/2} (gV^*)^{NC^*}, \quad (22)$$

$$\bar{V}_s = V_s/V^*. \quad (23)$$

We have employed the configurational partition function (12) for calculating entropy ΔS_f^0 and the heat of fusion ΔH_f^0 in terms of communal entropy ΔS_0 . The communal entropy ΔS_0 arises from the sharing of volume since the entire volume of the liquid is accessible to every molecule.

The equation of entropy S is given by

$$S = k \ln Q_N + kT(\partial \ln Q_N / \partial T)_v. \quad (24)$$

The equation of heat of fusion can be written as

$$\Delta H_f^0 = Tm(\Delta S_f^0 + \Delta S_0) \quad (25)$$

in which

$$\Delta S_f^0 = S_1 - S_0 = 3C^*R \ln[(\tilde{V}^{1/3} - 1)/(\tilde{V}_s^{1/3} - 1)] \quad (26)$$

$$\Delta S_0 = C^*R \left\{ 3 \ln[(\tilde{V}^{1/3} - 1)/(\tilde{V}_s^{1/3} - 1)] + \frac{1}{\tilde{T}} \left(\frac{1}{\tilde{V}} - \frac{1}{\tilde{V}_s} \right) \right\}. \quad (27)$$

From equations (19) and (25)–(27) we obtain the desired equation for heat of fusion as

$$\Delta H_f^0 = U^* \{ 6\tilde{T} \ln[(\tilde{V}^{1/3} - 1)/(\tilde{V}_s^{1/3} - 1)] - (V - V_s)/V_s \tilde{V} \} \quad (28)$$

where the characteristic energy U^* is given by (Sharma 1977)

$$U^* = p^*V^* = C^*RT^*. \quad (29)$$

The calculated values of ΔH_f^0 for a few simple non-polar substances in comparison with experimental values (Cook 1961, Fuller *et al* 1959) and those obtained by Yosim and Owens (1963) are shown in table 3. The values of ΔS_f^0 and ΔS_0 are also shown. It may be seen from table 3 that only a fraction of the communal entropy ΔS_0 appears across the melting transition. The communal entropy change is only a small fraction of about 0.25 of the entropy of fusion ΔS_f^0 . Our results are in qualitative agreement with Alder and Wainwright (1962) and Alder and Hoover (1967) who suggest that the communal entropy does appear somewhere between the perfect gas and the close-packed solid, but only gradually.

Table 3. Comparison of calculated and experimental heats of fusion of crystals composed of inert gases and nitrogen (values of C^* are given in molecule⁻¹, U^* and ΔH_f^0 in cal mol⁻¹, ΔS_f^0 and ΔS_0 in cal K⁻¹)

Substance	C^*	U^*	ΔS_f^0	ΔS_0	ΔH_f^0		
					Present work	Yosim & Owens (1963)	exptl.
Neon	0.590	440.2	2.67	0.66	85.15	65.5	80.1
Argon	0.573	1447.0	2.69	0.64	270.70	269.9	280.8
Krypton	0.564	2176.0	2.87	0.74	400.10	365.4	390.7
Nitrogen	0.573	1209.0	1.76	0.39	127.60	—	172.4
Xenon	0.564	2735.0	2.33	0.59	413.90	602.7	548.5

Data not available.

The estimated values of C^* , T^* and U^* were taken from our earlier publication (Sharma 1977) and those of T_m , V_1 from table 2. It may be seen from the table 3 that the agreement is fair. Our calculations show better results than

those obtained by Yosim and Owens (1963) in all systems considered except Xenon. This is not surprising since the estimated values of V_s and T_m for Xenon utilized to evaluate ΔH_f^0 differ from experimental values by about 3.5%. However, agreement would be better if experimental values of V_s and T_m were utilized.

3. Conclusion

An inspection of tables 1-3 reveals that the agreement between the calculated and observed values of V_s , T_m and ΔH_f^0 is very good in most of the substances in view of the crudeness of the model, approximations. Additionally, the present theoretical approach is convenient and involves few parameters. The estimation of various melting point properties requires the knowledge of critical constants and molar volume of the liquid at the melting point. The values of ΔH_f^0 are obtained from the estimated values of several parameters such as V^* , V_s , C^* , T^* , U^* and T_m of liquid state. This is a distinct advantage of the present theoretical treatment. However, the estimated values of all these parameters are limited by the accuracy of experimental values of critical constants. It is possible that these values may be of less than the desired accuracy.

Acknowledgment

The author is very grateful to Professor W. G. Hoover, Lawrence Radiation Laboratory, University of California, Livermore and Dr. D. Henderson, IBM Research Laboratories, San Jose, California, for their helpful and informative correspondence.

References

- Alder B J and Hoover W G 1967 *J. Chem. Phys.* **46** 686
- Alder B J and Wainwright T E 1962 *Phys. Rev.* **127** 359
- Cook G A 1961 *Argon, helium and the rare gases* (New York : Interscience)
- Einstein A and Gingrich N S 1942 *Phys. Rev.* **62** 261
- Fisher I Z 1964 *Statistical theory of liquids* (Chicago : University Press) pp 80
- Flory P J and Abe A 1965 *J. Am. Chem. Soc.* **87** 1833, 1838
- Flory P J, Orwoll R A and Vrij A 1964 *J. Am. Chem. Soc.* **86** 3507, 3515
- Gingrich N S and Thompson C W 1962 *J. Chem. Phys.* **36** 2398
- Glasstone S, Laidler K J and Eyring H 1941 *Theory of rate processes* (New York : McGraw-Hill) pp 481
- Henshaw D G 1957 *Phys. Rev.* **105** 976
- Kanno H 1972 *Bull. Chem. Soc. Japan* **45** 2687
- Kirkwood J G 1950 *J. Chem. Phys.* **18** 380
- Kobe K A and Lynn R E 1953 *Chem. Rev.* **52** 117, 200
- Lange N A 1967 *Handbook of Chemistry* (New York : McGraw-Hill) pp 1669-1674
- Lennard-Jones J E and Devonshire A F 1939 *Proc. R. Soc.* **A169** 317; **A170** 464
- Lu W C, John M S, Ree T and Eyring H 1967 *J. Chem. Phys.* **46** 1075
- Mansoori G A and Canfield F B 1969 *J. Chem. Phys.* **51** 4958 4967

- Marchi R P and Eyring H 1963 *J. Chem. Educ.* **40** 562
- Melrose J C 1966 *Ind. Eng. Chem. Fundamentals* **5** 224
- Mikolaj P G and Pings C J 1967 *J. Chem. Phys.* **46** 1401 1412
- Moelwyn-Hughes E A 1965 *Physical Chemistry* (London : Pergaman) pp 748
- Pings C J 1968 *Physics of simple liquids* eds H N V Temperley, J S Rowlinson and G S Rushbrooke (Amsterdam : North Holland) pp 440-441
- Ree T, Fuller E J and Eyring H 1959 *Proc. Natl. Acad. Sci.* **45** 1594
- Ree T S, Ree T and Eyring H 1964 *J. Phys. Chem.* **68** 1163 3262
- Sharma B K 1976a *Indian J. Pure Appl. Phys.* **14** 992
- Sharma B K 1976b *Indian J. Pure Appl. Phys.* **14** 1022
- Sharma B K 1977 *Indian J. Pure Appl. Phys.* **15** 633
- Sharma B K and Bhatnagar H L 1976c *Indian J. Pure Appl. Phys.* **14** 107
- Sharma B K and Bhatnagar H L 1975 *Indian J Pure Appl. Phys.* **13** 328
- Singwi K S and Sjolander A 1960 *Phys. Rev.* **119** 863
- Tuerpe D R and Keeler R N 1967 *J. Chem. Phys.* **47** 4283
- Yosim S J and Owens B B 1963 *J. Chem. Phys.* **39** 2222

Photodetachment cross section of negative hydrogen

M Daskhan*, K Roy and A S Ghosh

Department of Theoretical Physics,

Indian Association for the Cultivation of Science, Calcutta-700032

Received 8 November 1978, revised 2 May 1979

Abstract. The modified eikonal wave function has been used for continuum functions of the negative hydrogen ion. This function was combined with twenty-parameter bound state wave function to calculate the bound-free absorption cross sections of the negative hydrogen ion using the length and velocity alternatives for the dipole operator. It is found that the trend of our curves is very similar to those of experimental photodetachment results of Smith and Burch (1959a, b) though there is a considerable disparity at intermediate wavelengths between ours and the experimental. A comparison has also been made with the theoretical results of Doughty *et al* (1966) and those of Bell and Kingston (1967) and it is seen that our curves agree well in nature with those of Doughty *et al*.

1. Introduction

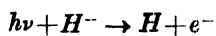
The photodetachment process of ground state atoms and ions by ultraviolet stellar radiation is a primary physical process. A great effort has been devoted to obtain accurate observations and to calculate accurate reaction rates for atomic processes. It is now possible to make detailed quantitative interpretations and to obtain results which are of very general astrophysical importance. Since the discovery of the stability of the negative ion of hydrogen by Bethe (1930) and Hylleraas (1930) and the recognition of its astrophysical importance by Wildt (1939), attempts have been made to determine the electron affinity of hydrogen with as high a precision as possible. The photodetachment cross-section of negative hydrogen ion also has been studied extensively both theoretically and experimentally. A large number of theoretical investigations have been carried out on the bound-free and free-free stimulated electron transitions of this system. Chandrasekhar and his associates have published a series of papers from 1942 upto 1958 (see Chandrasekhar 1958 for the complete reference list) on the bound-free absorption coefficient of negative hydrogen ion by quantum calculation. They have used increasingly more accurate two electron wave functions for the bound state, and have also investigated the effect of the static central

* R. K. Mission Residential College, Narendrapur, 24 Parganas, West Bengal.

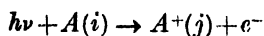
field on the free-state (Chandrasekhar and Elbert 1958). Geltman (1962) has evaluated the above mentioned absorption coefficient using a set of successively improved bound and free state wave functions. Three successively improved version of the free-state P wave-function viz. plane wave, radial correlation and full correlation version have been used. An alternative method has been employed by Doughty *et al* (1966). They have used Hartree-Fock eigenfunction expansions for the continuum waves with successive inclusion of all states upto and including the $3d$ state of atomic hydrogen. Bell and Kingston (1967) have attempted the same work by employing the method of polarized orbitals (Temkin and Lamkin 1961, Sloan 1964) to obtain a representation of the singlet P -wave continuum functions of the negative hydrogen ion, and to make an allowance for the effect of polarisation. These functions were combined with twenty and seventy parameter bound state wave functions in their calculation. The methods used by the above mentioned authors are rigorous and lengthy. For the continuum wave functions, one does require to solve the integro-differential equation with the help of a computer. Hence we are seeking for a simpler method which will give reliable results though not very challenging. This necessarily forces us to do some further approximation. The modified eikonal method is found to be very suitable for electrons (positrons)-atoms (molecules) scattering (Bhattacharyya and Ghosh 1975, 1976, Saha *et al* 1973a, b) for intermediate and high energies. Being encouraged by our previous results, we applied our modified eikonal wave function to calculate the continuous absorption coefficient of negative hydrogen ion. The continuum wave function takes account of static and polarization potential. The effect of exchange has also been included in the calculations. The method is expected to be valid for short and moderately long wave length of the incident photon.

2. Theory

A photon of energy $h\nu$ colliding with a negative hydrogen ion forming a hydrogen atom and ejecting an electron i.e.



is a process similar to photoionization process



A and A^+ being neutral atom and positive ion respectively. The fundamental relation governing the photoionization process is

$$E = h\nu - E_{ij}$$

where E is the kinetic energy of the ejected photoelectron and E_{ij} is the work function of the atom. In this section, the basic theory to calculate the photoionization cross section is discussed.

The cross section for photoionization of a system in state i by an unpolarized photon beam of energy $h\nu$ leaving the system in a final state j consisting of photoelectrons of energy ϵ plus ion in state j is given by (Bates 1946)

$$\sigma_{ij}(\epsilon) = (4\pi^2\alpha a_0^2/3g_i)(\epsilon + I_{ij}) |M_{ij}|^2 \tag{1}$$

where α is the fine structure constant, a_0 is the Bohr radius. g_i is the statistical weight of the initial discrete state, and the ionization energy I_{ij} and the photoelectron energy ϵ are expressed in Rydbergs. The matrix element, expressed in Rydberg atomic units, is given by (Bethe and Salpeter 1957)

$$|M_{ij}| = \frac{1}{(E_j - E_i)^2} \sum_{m_i} \sum_{m_j} | \langle jm_j | \sum \exp(i\mathbf{k}_\nu \cdot \mathbf{r}_\mu) \Delta_\mu | im_i \rangle |^2 \tag{2}$$

the summation over m_i, m_j being the sum over the degenerate initial and final substates respectively, \mathbf{r}_μ is the position coordinate of the μ^{th} electron, \mathbf{k}_ν is the propagation vector of the photon ($|\mathbf{k}_\nu| = 2\pi\nu/c$), and the wave functions are normalized. Upto this point the theory is essentially exact. For incident photon energies below several keV, the $\exp(i\mathbf{k}_\mu \cdot \mathbf{r}_\mu)$ term in the matrix element, equation (2) can be approximated. This is done by noting that the major concentration of wave function amplitude is around a distance from the nucleus, \mathbf{r}_μ , of the order of Bohr radius. Thus for photon energies below several keV, $(\mathbf{k}_\nu \cdot \mathbf{r}_\mu)$ is small enough so that $\exp(i\mathbf{k}_\nu \cdot \mathbf{r}_\mu)$ can be well approximated by unity. Thus the approximation simplifies the matrix element considerably and is known as the dipole approximation. The matrix element M_{ij} can then be written

$$|M_{ij}|^2 = \sum_{m_i} \sum_{m_j} | \langle jm_j | \sum_\mu \mathbf{r}_\mu | im_i \rangle |^2 \tag{3}$$

Further, we can deduce

$$|M_{ij}|^2 = \frac{4}{(E_j - E_i)^2} \sum_{m_i} \sum_{m_j} | \langle im_i | \sum_\mu \Delta_\mu | jm_j \rangle |^2 \tag{4}$$

as

$$E_j - E_i = I_{ij} + \epsilon. \tag{5}$$

Equation (4) is known as the dipole-velocity form of the matrix element, while equation (3) is called the dipole-length form.

A third, formally equal, form of the dipole matrix element can be derived as

$$|M_{ij}|^2 = \frac{16Z^2}{(E_j - E_i)^4} \sum_{m_i} \sum_{m_j} | \langle im_i | \sum_\mu (\mathbf{r}_\mu/r_\mu^3) | jm_j \rangle |^2 \tag{6}$$

(Z being the number of protons in the nucleus of the target) which is known as

the dipole-acceleration form of the matrix element. Thus we have three alternative formally equal forms of the dipole matrix element. We emphasize that using exact wave functions, equations (3), (4) and (6) are equal. Of course, for atomic systems other than hydrogen, exact wave functions are not available. In that case the results of using the various expressions for the dipole matrix element can differ considerably from each other. To conclude, we note that, as a practical matter, it is only the dipole-length and dipole-velocity expressions that are usually computed and compared, hence it is followed in our work also.

The twenty parameter bound state wave function of the form

$$\psi_i = Ne^{-\frac{1}{2}\alpha u} \sum_{l,m,n,t} a_l u^l s^m t^n, \quad u = r_{12}, \quad s = r_1 + r_2 \quad \text{and} \quad t = r_1 - r_2$$

(α and a_l are constants) given by Hart and Herzberg (1957) has been used in the present calculation to represent the negative hydrogen bound state wave function. The continuum wave function is considered as given below :

$$\psi_j = (N/(2\pi)^{\frac{1}{2}}) \{ \phi(\mathbf{r}_1) F(\mathbf{r}_2) + \phi(\mathbf{r}_2) F(\mathbf{r}_1) \},$$

$\phi(\mathbf{r})$ represent a hydrogen atom in its ground state, $F(\mathbf{r})$ being the wave function of the ejected electron.

The modified eikonal wave function (Glauber 1959) for $F(\mathbf{r})$ has been considered as

$$F(\mathbf{r}) = \exp[ikZ - (i/v) \int_{-\infty}^{\infty} U(b, Z') dZ'] \quad 1$$

(\mathbf{k} and \mathbf{v} being the initial momentum and velocity of the incident particle respectively) where $r^2 = b^2 + z^2$, b being the impact parameter, and U is the combination of static potential as well as polarization potential given by Temkin and Lamkin (1961)

Using ψ_i and ψ_j in equation (3) and in equation (4) we have calculated the length and velocity matrix elements correspondingly and thus the photo-detachment cross section has been determined.

3. Results and Discussion

The dipole length and velocity matrix elements have been calculated to evaluate the required cross sections. For the evaluation of matrix element four dimensions of the integrals are possible to perform analytically whereas two dimensions are left for numerical integration. The numerical integration has been evaluated on a highspeed computer (Burroughs 6700). For the method of numerical integration Gauss-Laguerre method has been adopted, there is an extra integral occurring in the calculation of potential part which also has been computed numerically by Gauss-Legendre method of integration.

For bound state wave function of negative hydrogen we considered only a 20-parameter wave function as we have seen that the results using a 20-parameter bound state wave function (Chandrasekhar 1958) are substantially the same as those following from an 11-parameter function (Henrich 1944), leading to the tentative conclusion that still more elaborate bound state functions will give no more appreciable improvement. A calculation by John (1960) using exchange approximation wave functions for the free state resulted in appreciably improved agreement with experiment. Hence without increasing the number of parameters in the bound state wave function of H^- , we have given more attention to the free state wave function.

In the Figure 1 we exhibit the length and velocity bound-free absorption cross section curves. The theoretical results of Bell and Kingston (1967) and of Doughty *et al* (1966) and the experimental values of Smith and Burch (1959a, b)

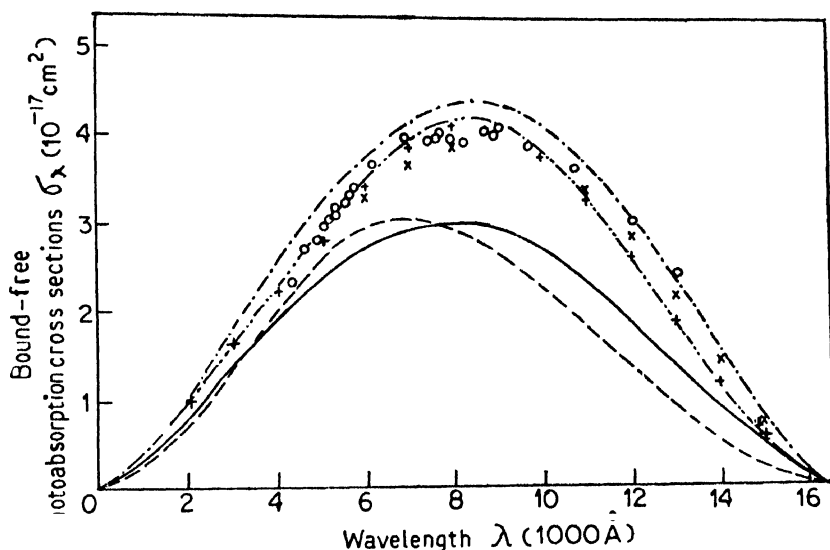


Figure 1 The bound-free H^- ion photoabsorption cross section :

- Calculated using 20-parameter bound function and modified eikonal free-function in the velocity form.
- Calculated using 20-parameter bound function and modified eikonal free-function in the length form.
- · - · - Calculated using 70-parameter bound function and polarised-orbital free-function (Bell and Kingston 1967) in the length formulation.
- · · · - Calculated using 70-parameter bound function and polarized-orbital free-function (Bell and Kingston 1967) in the velocity formulation.
- + + + Calculated using 70-parameter bound function and close-coupling free-function (Doughty *et al* 1966) in the length formulation.
- × × × Calculated using 70-parameter bound function and close-coupling free-function (Doughty *et al* 1966) in the velocity formulation.
- o o o Experimental measurement by Smith and Burch (1959a, b).

have been included for comparison. A comparison of our results, with the corresponding results of Bell and Kingston and those of Doughty *et al* shows that there is considerably disparity both when the length as well as velocity formulations of the dipole matrix element are employed. The disparity with the measured values is about 25% at the peak in the cross section against wave length curve and is not unexpected. The discrepancy between the present results and the measured or other theoretical results can be understood from the following reasons. In the calculation of photoionization cross section, one has to take care of exchange effect, electron correlation and the distortion of the residual atom. This may be done in several approximate ways. In our calculation we have not taken into account electron correlation. Moreover, in the case of atomic distortion we have included here only the adiabatic polarization effect. We have omitted the dynamic polarization potential (non-adiabatic) in the sense of Callaway *et al* (1968). The exchange polarization potential (Bell and Kingston 1967) is also expected to play an important role here. The inclusion of these effects may influence the cross section appreciably. The best over all agreement with experiment is obtained with the 'velocity curve'. The same feature has also been pointed out by Chandrasekhar (1945), Geltman (1962) and Doughty *et al* (1966), but in the results of Bell and Kingston (1967) the agreement is better with the length curve whereas the velocity curve overestimates the experimental values. Clearly our velocity curve exhibits the same shape as that obtained experimentally, being significantly low. Our curves agree fairly well with the measured values and the theoretical curves upto $\lambda = 5000 \text{ \AA}$. Above this wave length, our values underestimate the cross-sections to some extent. Our results, however, agree qualitatively with the measured values. The present results have shown appreciably improvement over those obtained by Chandrasekhar (not shown in the figure) using the first Born approximation. Our agreement is in fairly good with the conclusions of Doughty *et al* who were able to reproduce the shape of the experimental curve by using their velocity calculations. Similar to Doughty *et al* and dissimilar to Bell and Kingston our length and velocity curves almost coincide at lower wave length. After $\lambda = 3000 \text{ \AA}$ onwards our length curve goes above our velocity curve and at $\lambda = 8000 \text{ \AA}$ length curve crosses the velocity curve and it sharply comes down onwards. The velocity curve goes over the length curve after having a crossing with it and it has a flat peak between $\lambda = 6000 \text{ \AA}$ and $\lambda = 10500 \text{ \AA}$, very similar nature as experiment, and then comes down slowly.

Finally, we like to mention that the present method is very simple and does not involve much computer time.

Acknowledgments

The authors gratefully acknowledge the financial support of the Indian Space Research Organisation (ISRO), Bangalore.

References

- Bates D R 1946 *Monthly Not. Roy. Astron. Soc.* **106** 423
Bell K L and Kingston A E 1967 *Proc. Phys. Soc.* **90** 895
Bethe H A 1930 *Ann. Phys. (Leipzig)* **5** 325
Bethe H A and Salpeter E E 1957 *Quantum mechanics of one—and two—electron atoms* Berlin, Springer-Verlag
Bhattacharyya P K and Ghosh A S 1975 *Phys. Rev.* **A12** 1881
Bhattacharyya P K and Ghosh A S 1976 *Phys. Rev.* **A14** 1587
Callaway J, LaBahn R W, Pu R T and Duxlor W M 1968 *Phys. Rev.* **168** 12
Chandrasekhar S 1945 *Astrophys. J.* **102** 223
Chandrasekhar S 1958 *Astrophys. J.* **128** 114
Chandrasekhar S and Elbert D D 1958 *Astrophys. J.* **128** 633
Doughty N A, Fraser P A and McEachran R P 1966 *Monthly Not. Roy. Astron. Soc.* **132** 255
Geltman S 1962 *Astrophys. J.* **136** 935
Glauber R J 1959 *Lectures in Theoretical Physics* New York Interscience publishers
Hart J F and Herzberg G 1957 *Phys. Rev.* **106** 79
Henrich L R 1944 *Astrophys. J.* **99** 59
Hylleraas E A 1930 *Z. Physik* **65** 209
John T L 1960 *Monthly Not. Roy. Astron. Soc.* **121** 41
Saha B C, Sarkar Kalpana and Ghosh A S 1973 *J. Phys. B.* **6** 2303
Saha B C, Sarkar Kalpana and Ghosh A S 1973 *Proc. Indian Acad. Sci.* **A39** 382
Sloan I H 1964 *Proc. Roy. Soc.* **A281** 151
Smith S J and Burch D S 1959a *Phys. Rev. Letts.* **2** 165
Smith S J and Burch D S 1959b *Phys. Rev.* **116** 1125
Temkin A and Lamkin J C 1961 *Phys. Rev.* **121** 788
Wildt R 1939 *Astrophys. J.* **89** 295

Calculation of scattering amplitudes by the eikonal approximation method for a modified Gaussian potential

Sachindra Nath Upadhyay

Department of Mathematics, Presidency College, Calcutta

Received 17 November 1978, revised 22 February 1979

Abstract. We are considering here the scattering of a nucleon in a potential field. The successive terms of the scattering amplitudes for a potential of the type $Ae^{-\sigma r^2}/r$ (i.e. Modified Gaussian potential) have been calculated with the help of the eikonal method. The first and second order terms of the series for the scattering amplitudes have been shown graphically and a comparison is made with the results for a potential of the Yukawa type.

1. Introduction

The most direct information about the nature of forces between the interacting particles is obtained from the study of collisions. So the study of the scattering phenomena is an important subject matter in quantum mechanics.

The eikonal approximation was originally introduced in quantum scattering theory by Molière (1947), and it has been considerably developed later by Glauber (1959).

It is a semi-classical method and is a useful approximation technique when the de-Broglie wave length $\lambda = h/p$ of the incident particle is sufficiently short compared with the distance in which the potential varies appreciably.

The method has been quite useful in discussing the Scattering of very fast particles by smooth potentials.

Detailed analysis of the scattering amplitudes with a Yukawa or a superposition of two Yukawa potentials is available in the texts on quantum scattering theory (Joachain 1975).

In the present discussions we take the potential in the form, viz, $V = \frac{Ae^{-\sigma r^2}}{r}$, where A is the constant of potential. The space dependence of the potential is slightly different from that of Yukawa but this model also enables to derive results compatible with observations. We shall apply the eikonal method to obtain the different terms of the series for the scattering amplitude. Our discussions will be confined to high energy non-relativistic potential scattering so that $K/(\alpha)^{1/2} \gg 1$ (the short wave length condition) and $|A|/E \ll 1$.

2. General form of the approximations

Let us consider the scattering of a spinless particle of mass m by a real potential $V(\mathbf{r})$. The wave function ψ for a particle of energy E is a solution of the equation (excluding the time part $e^{-iEt/\hbar}$).

$$[\nabla^2 + K^2]\psi(K, \mathbf{r}) = U(\mathbf{r})\psi(K, \mathbf{r}) \quad (1)$$

where

$$U(\mathbf{r}) = \frac{2mV(\mathbf{r})}{\hbar^2}$$

and

$$K^2 = \frac{2mE}{\hbar^2}$$

Then the solution of the equation (1) can be written as (Lippmann-Schwinger equation)

$$\psi_{\mathbf{K}_i}(\mathbf{r}) = (2\pi)^{-3/2} \exp(i\mathbf{K}_i \cdot \mathbf{r}) + \int G_0(\mathbf{r}, \mathbf{r}') U(\mathbf{r}') \psi_{\mathbf{K}_i}(\mathbf{r}') d\mathbf{r}' \quad (2)$$

where \mathbf{K}_i is the incident wave vector and the Green's function $G_0(\mathbf{r}, \mathbf{r}')$ is given by

$$\begin{aligned} G_0(\mathbf{r}, \mathbf{r}') &= -\frac{1}{4\pi} \frac{\exp\{iK|\mathbf{r}-\mathbf{r}'|\}}{|\mathbf{r}-\mathbf{r}'|} \\ &= -(2\pi)^{-3} \lim_{\epsilon \rightarrow 0+} \int d\mathbf{K}' \frac{\exp\{i\mathbf{K}' \cdot (\mathbf{r}-\mathbf{r}')\}}{K'^2 - K^2 - i\epsilon}. \end{aligned} \quad (3)$$

Since the potential varies slowly over the scale of the incident wave-length, we can factor out the free incident plane wave from the wave function $\psi_{\mathbf{K}_i}(\mathbf{r})$, so that

$$\psi_{\mathbf{K}_i}(\mathbf{r}) = (2\pi)^{-3/2} \exp\{i\mathbf{K}_i \cdot \mathbf{r}\} \phi(\mathbf{r}) \quad (4)$$

where $\phi(\mathbf{r})$ is a slowly varying function (modulating function) when $K/(\alpha)^{1/2}$ is large.

From the equations (2) and (4), we find that $\phi(\mathbf{r})$ satisfies the equation,

$$\phi(\mathbf{r}) = 1 - (2\pi)^{-3} \int d\mathbf{R} \int d\mathbf{K}' \frac{\exp\{i(\mathbf{K}' - \mathbf{K}_i) \cdot \mathbf{R}\}}{(K'^2 - K^2 - i\epsilon)} U(\mathbf{r}-\mathbf{R}) \phi(\mathbf{r}-\mathbf{R}) \quad (5)$$

where we have set $\mathbf{R} = \mathbf{r} - \mathbf{r}'$.

Introduce the new variable

$$\mathbf{P} = \mathbf{K}' - \mathbf{K}_i$$

where \mathbf{K}' being the integration variable from equation (3) and write

$$\phi(\mathbf{r}) = 1 - I(\mathbf{r}). \quad (6)$$

so that

$$I(\mathbf{r}) = (2\pi)^{-3} \int d\mathbf{R} \int d\mathbf{P} \frac{\exp(i\mathbf{P} \cdot \mathbf{R})}{2\mathbf{K}_t \cdot \mathbf{P} + P^2 - i\epsilon} U(\mathbf{r} - \mathbf{R}) \phi(\mathbf{r} - \mathbf{R}). \quad (7)$$

Since the product $U\phi$ is slowly varying, this integral is dominated by small values of P/K . We may therefore expand the quantity $(2\mathbf{K}_t \cdot \mathbf{P} + P^2 - i\epsilon)^{-1}$ in powers of P/K as (Schiff 1956).

$$\frac{1}{2\mathbf{K}_t \cdot \mathbf{P} + P^2 - i\epsilon} = \frac{1}{2KP_z + P^2 - i\epsilon} = \frac{1}{(2KP_z - i\epsilon)} \left(1 - \frac{P^2}{2KP_z - i\epsilon} + \dots \right) \quad (8)$$

where Z -axis is chosen in the direction of the incident wave vector \mathbf{K}_t and from the equation (7) we obtain

$$I(\mathbf{r}) = I^{(1)}(\mathbf{r}) + I^{(2)}(\mathbf{r}) + \dots \quad (9)$$

where $I^{(1)}(\mathbf{r})$, $I^{(2)}(\mathbf{r}) \dots$ are the successive terms when the equation (8) is put in equation (7).

The correction terms $I^{(2)}(\mathbf{r})$ etc. appearing in equation (9) is not only small with respect to $I^{(1)}(\mathbf{r})$ is also small with respect to one, for $K/(\alpha)^{\frac{1}{2}} \gg 1$ and $|A|/E \ll 1$. (Byron Jr, Joachain and Mund 1973).

We therefore replace $I(\mathbf{r})$ by $I^{(1)}(\mathbf{r})$ in equation (6). So,

$$\phi(\mathbf{r}) = \phi^{(1)}(\mathbf{r}). \quad (10)$$

Therefore, the corresponding value of the quantity $\phi^{(1)}(\mathbf{r})$ is given by

$$\phi^{(1)}(x, y, z) = 1 - \frac{i}{2K} \int_0^\infty U(x, y, z - Z) \phi^{(1)}(x, y, z - Z) dZ \quad (11)$$

whence

$$\phi^{(1)}(x, y, z) = \exp \left\{ -\frac{i}{2K} \int_{-\infty}^z U(x, y, z') dZ' \right\} \quad (12)$$

Therefore the approximate wave function $\psi_E(\mathbf{r})$ which is known as the eikonal wave function is given by

$$\psi_E(\mathbf{r}) = (2\pi)^{-3/2} \exp \left\{ i\mathbf{K}_t \cdot \mathbf{r} - \frac{i}{2K} \int_{-\infty}^z U(x, y, z') dZ' \right\} \quad (13)$$

and the scattering amplitude

$$f_E = -\frac{1}{4\pi} \int d\mathbf{r} \exp(i\mathbf{\Delta} \cdot \mathbf{r}) U(\mathbf{r}) \exp \left\{ -\frac{i}{2K} \int_{-\infty}^z U(x, y, z') dz' \right\} \quad (14)$$

where $\mathbf{\Delta} = \mathbf{K}_i - \mathbf{K}_f$ is the wave vector transfer.

We adopt cylindrical co-ordinate system and decompose the vector \mathbf{r} as

$$\mathbf{r} = \mathbf{b} + Z\hat{n} \quad (15)$$

where \mathbf{b} is an "impact parameter" vector and the cylindrical co-ordinate system has been chosen with the direction of \hat{n} (unit vector) perpendicular to ∇ .

Therefore from (14) we have

$$f_E = \frac{\Lambda}{2\pi i} \int d^2\mathbf{b} \exp(i\mathbf{\Delta} \cdot \mathbf{b}) [\exp\{i\chi(K, \mathbf{b})\} - 1] \quad (16)$$

where

$$\chi(K, \mathbf{b}) = -\frac{1}{2K} \int_{-\infty}^{\infty} U(\mathbf{b}, Z) dZ \quad (17)$$

is the eikonal phase-shift function.

For the potential having cylindrical symmetry, we have from (16)

$$f_E = \frac{K}{i} \int_0^{\infty} db b J_0(\Delta b) [\exp\{i\chi(k, b)\} - 1]. \quad (18)$$

By expanding the quantity $\exp\{i\chi(K, b)\}$ in powers of χ and hence in powers of potentials in equation (18). We get the eikonal scattering series

$$f_E = \sum_{n=1}^{\infty} f_{E_n}$$

where

$$f_{E_n} = -\frac{(i)^{n+1}}{n!} K \int_0^{\infty} J_0(\Delta b) [\chi(K, b)]^n b db \quad (19)$$

is the n -th order term of the eikonal series.

3. Evaluation

From equation (19), the n -th order term of the eikonal series

$$f_{E_n} = -\frac{(i)^{n+1}}{n!} K \int_0^{\infty} J_0(\Delta b) [\chi(K, b)]^n b db. \quad (20)$$

Here the reduced potential

$$U(r) = A'e^{-\alpha r^2}, \quad A' = \frac{2mA}{\hbar^2}$$

From equation (17)

$$\begin{aligned} \chi(K, b) &= -\frac{1}{2K} \int_{-\infty}^{\infty} U(b, Z) dZ \\ & \quad [Z^2 = r^2 - b^2] \\ &= -\frac{A'}{K} \int_b^{\infty} \frac{e^{-\alpha r^2}}{\sqrt{r^2 - b^2}} dr \\ &= -\frac{A'}{2K} e^{-\alpha b^2/2} K_0(\alpha b^2/2) \end{aligned} \quad (21)$$

(Watson 1962). Where K_0 is the modified Bessel function of order zero. Therefore,

$$f_{E_n} = -\frac{(i)^{n+1}}{n!} K \int_0^{\infty} J_0(\Delta b) \left\{ -\frac{A'}{2K} e^{-\alpha b^2/2} K_0(\alpha b^2/2) \right\}^n b db \quad (22)$$

So that the terms of the eikonal scattering series are alternately real and imaginary. Thus

$$f_{E_1} = -\frac{A'}{2} \int_0^{\infty} J_0(\Delta b) e^{-\alpha b^2/2} K_0(\alpha b^2/2) b db \quad (23)$$

$$f_{E_2} = \frac{i A'^2}{2! 4K} \int_0^{\infty} J_0(\Delta b) \left\{ e^{-\alpha b^2/2} K_0(\alpha b^2/2) \right\}^2 b db \quad (24)$$

$$f_{E_3} = \frac{A'^3}{3! 8K^2} \int_0^{\infty} J_0(\Delta b) \left\{ e^{-\alpha b^2/2} K_0(\alpha b^2/2) \right\}^3 b db. \quad (25)$$

Now equation (23) can be evaluated by expanding $J_0(\Delta b)$. After some calculations we obtain (Erdelyi *et al* 1954)

$$f_{E_1} = -\frac{A'}{2\alpha} \left[1 - \frac{\Delta^2}{6\alpha} + \frac{\Delta^4}{60\alpha^2} - \frac{\Delta^6}{840\alpha^3} + \frac{\Delta^8}{15120\alpha^4} - \dots \right]$$

Now the collision being elastic, $\Delta = 2K \sin \theta/2$, where θ is the angle of scattering.

$$f_{E1} = -\frac{1}{\sqrt{\alpha}} \cdot \frac{A'}{\sqrt{\alpha}} \cdot \frac{1}{2} \left[1 - \frac{2}{3} (K/\sqrt{\alpha})^2 \sin^2 \theta/2 + \frac{4}{15} (K/\sqrt{\alpha})^4 \sin^4 \theta/2 \right. \\ \left. - \frac{8}{105} (K/\sqrt{\alpha})^6 \sin^6 \theta/2 + \frac{16}{945} (K/\sqrt{\alpha})^8 \sin^8 \theta/2 \dots \right] \quad (26)$$

It is not possible to evaluate the other integrals in suitable closed forms. We use numerical methods for their evaluation.

From equation (24)

$$f_{E2} = \frac{i}{\sqrt{\alpha}} \cdot \left(\frac{A'}{\sqrt{\alpha}} \right)^2 \cdot \frac{h}{8(K/\sqrt{\alpha})} \left[\frac{(I_0 + I_n)}{2} + \sum_{k=1}^{n-1} I_k \right] \quad (27)$$

where, $\sqrt{\alpha}b = h$, is the length of the interval and I_k , is the value of the integrand at the k -th point of division. Similarly f_{E3} and other higher terms of the series (22) can be evaluated.

3. Results and Discussion

With the help of the above method we can find the different terms of the approximate scattering wave function (oikonal wave function) and the corresponding terms of the scattering amplitudes provided the value of the constant of potential is assumed. The contribution of the various terms of the scattering amplitudes are shown in Table 1 for different values of the wave number ($K = 1, 2, 3, 4, 5$

Table 1. The number in the parentheses indicate the power of 10.

K	θ (degrees)	$\sqrt{\alpha} f_{E1} $	$\sqrt{\alpha} f_{E2} $	$\sqrt{\alpha} f_{E3} $
1	0	5.00 (-1)	2.24 (-1)	1.16 (-1)
	30	4.80 (-1)	2.20 (-1)	1.15 (-1)
	60	4.42 (-1)	2.12 (-1)	1.13 (-1)
	90	4.08 (-1)	2.02 (-1)	1.10 (-1)
2	0	5.00 (-1)	1.12 (-1)	2.91 (-2)
	30	4.19 (-1)	1.06 (-1)	2.81 (-2)
	60	2.64 (-1)	9.30 (-2)	2.63 (-2)
	90	1.52 (-1)	7.50 (-2)	2.40 (-2)
3	0	5.00 (-1)	7.35 (-2)	1.29 (-2)
	30	3.40 (-1)	6.25 (-2)	1.21 (-2)
	60	1.70 (-1)	4.75 (-2)	1.04 (-2)
	90	6.50 (-2)	3.20 (-2)	8.73 (-3)
4	0	5.00 (-1)	5.30 (-2)	7.27 (-3)
	30	2.53 (-1)	4.48 (-2)	6.52 (-3)
	60	6.92 (-2)	2.65 (-2)	5.09 (-3)
	90	3.04 (-2)	1.61 (-2)	3.90 (-3)
5	0	5.00 (-1)	4.48 (-2)	4.60 (-3)
	30	1.80 (-1)	2.93 (-2)	3.95 (-3)
	60	6.50 (-2)	1.60 (-2)	2.78 (-3)
	90	1.63 (-2)	9.00 (-3)	2.00 (-3)

in units $\sqrt{\alpha}$ and various scattering angles. Also $|A'|/\sqrt{\alpha}$ is taken to be of the order of one.

For $K = 1$ and $1/\sqrt{\alpha} = 2 \times 10^{-13}$ cm, the energy of the incident nucleon $E \sim 20$ MeV.

The value of $\sqrt{\alpha} |f_{E1}|$ and $\sqrt{\alpha} |f_{E2}|$ are also plotted graphically against θ where $|A'|/\sqrt{\alpha} \sim 1$.

We thus find that with the help of the eikonal method it is possible to calculate the scattering amplitudes for a potential of the form $(Ae^{-\alpha r^2}/r)$.

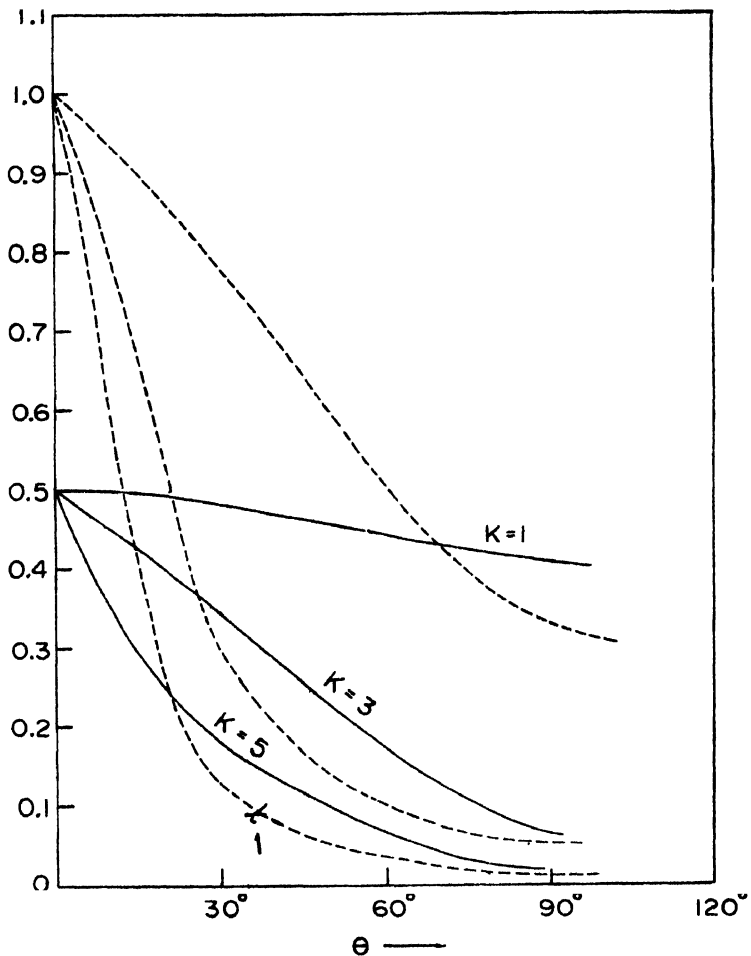


Figure 1. Graphs for $|f_{E1}|$.

The solid curves represent the ordinary $Y = \sqrt{\alpha} |f_{E1}|$ for the present potential and the dotted curves $Y = |f_{E1}|$ for the Yukawa potential (in units of "a" the range of the potentials).

From the graphs in Figure 1 and Figure 2 we see that as the energy increases the slope decreases rapidly. But it is more rapid for the Yukawa potential of the form $U_0 e^{-r/r_0}$, where $U_0 \sim 1$.

From this nature of the graphs we may say that the spreading of the curve over angles is more pronounced in the case of the modified Gaussian potential than in the case of the Yukawa potential.

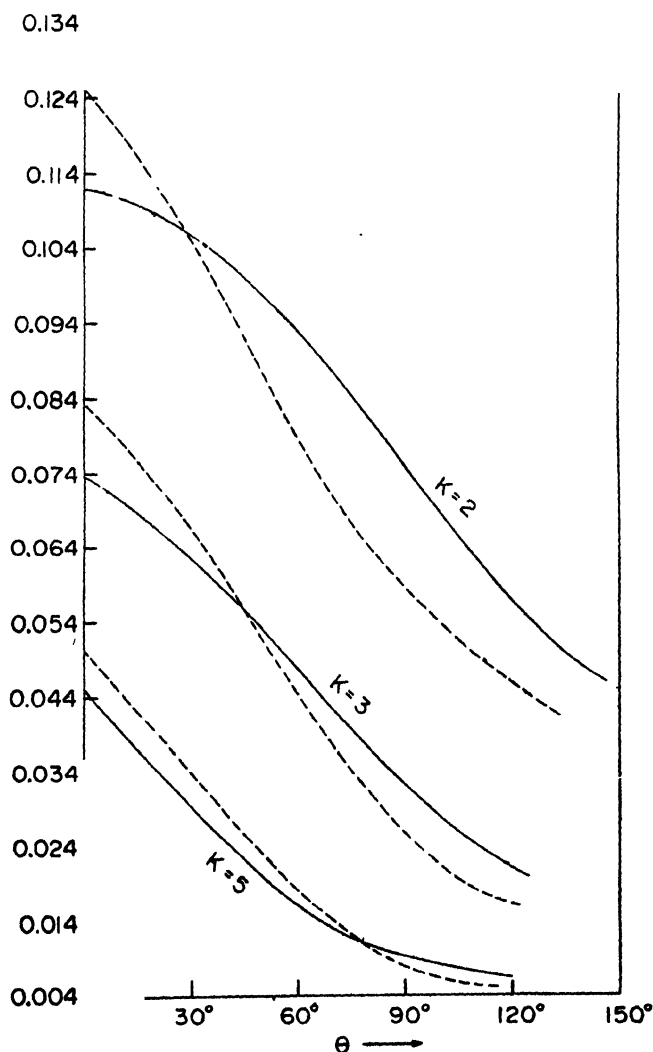


Figure 2. Graphs for $|f_{E2}|$.

The solid curves represent the ordinate $Y = \sqrt{\alpha} |f_{E2}|$ for the present potential and the dotted curves $Y = |f_{E2}|$ for the Yukawa potential (in units of " α " the range of the potentials).

It also seem that the interaction energy is more spread out over angles in the former than in the case of the latter.

Acknowledgment

I am indebted to Dr. S. C. Ganguli, Professor of Mathematics, Presidency College, Calcutta for his kind suggestion and valuable guidance.

References

- Byron Jr F N, Joachain C J and Mund E H 1973 *Phys. Rev.* **D8** 2622
- Erdelyi A, Magnus W, Oberhettinger F and Tricomi F G 1954 *Tables of integral transforms.* (McGraw-Hill New York) Vol. I, p 331
- Glauber R J 1959 in *Lectures in Theoretical Physics*, eds W E Brittin and L G Dunham (Inter Science Publication, New York) Vol. I, p 315
- Joachain C J 1975 *Quantum Collision Theory* (North Holland Publishing Company, Amsterdam), Chapter 9
- Moliere G 1947 *Z. Naturforsch* **2A** 133
- Schiff L I 1956 *Phys. Rev.* **103** 443
- Watson G N 1962 *A treatise on the theory of Bessel functions* (Cambridge University Press, 2nd Edition) p 172

Joule heating of the ionosphere

P N Khosa

Regional Engineering College, Kashmir

and

R N Singh

Institute of Technology, Banaras Hindu University, Varanasi-5

Received 20 July 1978, revised 1 March 1979

Abstract. A study of the joule heating of the ionosphere with a dominant bias on equatorial heating has been carried out. The heating produced by perpendicular and parallel components of electric field have been computed and it is shown that parallel electric fields although small and sporadic are very effective in heating the electron component of the plasma. The flow of electrojet current due to the inhibition of Hall current in the equatorial E -region of the ionosphere is likely to perturb the plasma and give rise to longitudinal oscillations. The interaction of these longitudinal oscillations with ion correlations makes the plasma more resistive (Oberman *et al* 1962). The perturbational heating due to the collisional damping of these longitudinal oscillations has been discussed and it has been shown that they can largely account for the observed thermal non equilibrium in this region of the ionosphere.

1. Introduction

The lower region of the ionosphere is a seat of various energy sources. The generation and dissipation of these energies result into the general heating of the lower ionospheric region. Considerable electric field is produced by the flow of electrojet current through the highly conducting E -region of the ionosphere. The magnitude of the electric field and conductivity determines the heating of the ionospheric region. Joule heating of the equatorial and auroral regions has been studied by a number of workers (Cole 1962, 1971; Kato 1962, 1963; Singh and Misra 1967a, b; Roes and Walker 1968). The joule heating studies have shown that the ionospheric region around 100 km becomes non thermal and the electron temperature T_e becomes greater than the gas temperature T_0 . The probe measurements of electron temperature in ionospheric region around 100 km (Aono *et al* 1961, Spencer *et al* 1965) have shown the existence of thermal non equilibrium. The discrepancy between the calculated and measured values of $(T_e - T_0)$ can be accounted for only in terms of additional sources of heat in the equatorial and auroral electrojet regions. The joule heating produced by

perpendicular component of electric field in the electrojet region has been studied and has been found to be insufficient for explaining the observed thermal non equilibrium (Cole 1962, 1971; Kato 1962, 1963). Jacchia *et al* (1966) have shown that the increased electron temperature in the electrojet region is correlated with the geomagnetic perturbation index. This correlation and the nature of electrojet current carrying layer led us to invoke the role of perturbed state of the ionospheric plasma in the joule heating.

We have considered the onset of electrostatic oscillations and their damping to account for the observed heating of the electrojet region.

The possibility of the existence of parallel component of electric field in equatorial and auroral zone has been discussed both theoretically and experimentally by several workers (Fried *et al* 1966, Block and Falthammar 1968, Kelley *et al* 1970, Muhleisen *et al* 1971, Knight 1973, Zimuda *et al* 1974, Lemaire and Schorer 1974, Murphy *et al* 1974). Mozer and Fahleson (1970) analyzing the results of a previously reported rocket borne experiment designed to measure the electric field over the auroral zone found that a parallel electric field of 10 mv/m (with a maximum uncertainty of 20%) existed during the first 180 seconds of the flight whereas no parallel field was detected towards the end of the flight. These authors also reported that the electron temperature arising from Joule heating was found to be 1000°K above the ambient temperature during first few minutes of the flight. We have, therefore, studied the role of transient parallel electric fields in explaining the observed sporadic electron temperature rise of a thousand degrees above the ambient temperature.

2. Joule heating of the lower ionosphere

The ionospheric plasma is permeated by a static magnetic field. The positive z direction of the rectangular co-ordinate system used is taken from south to north and the positive y direction from west to east. The magnetic field is taken along positive z direction. In this configuration the electronic conductivity tensor (the ions have been considered to be stationary) is defined as

$$\begin{bmatrix} \delta_1 & \delta_2 & 0 \\ -\delta_2 & \delta_1 & 0 \end{bmatrix} \quad (1)$$

$$\nu_0 \mathbf{I}$$

where δ_0 , δ_1 and δ_2 represent the components of tensor conductivity and are known as the longitudinal conductivity, the Pederson conductivity and the Hall conductivity respectively. These are given by

$$\begin{aligned} \delta_0 &= N_e q^2 / m_e \nu \\ \delta_1 &= N_e q^2 \nu / m_e (\nu^2 + \omega_{ce}^2) \\ \delta_2 &= N_e q^2 \omega_{ce} / m_e (\nu^2 + \omega_{ce}^2) \end{aligned} \quad (2)$$

where N_e is the free electron density; m_e the mass of the electron; ν the electron-neutral collision frequency; ω_{ce} the electron cyclotron frequency; and q the electron charge.

The current density \mathbf{J} can be expressed in terms of different components of the electric field and the conductivity tensor as

$$J_i = \delta_{ik} E_k \quad (3)$$

where summation over repeated indicies is implied. With the help of equation (3) the Joule dissipation is expressed as

$$\mathbf{J} \cdot \mathbf{E} = J_i E_i = \delta_{ik} E_i E_k. \quad (4)$$

We now assume the electrostatic field to lie in the $(y-z)$ plane. Equation (4) with this simplification is written as

$$\mathbf{J} \cdot \mathbf{E} = E^2 [\delta_1 \sin^2 \beta + \delta_0 \cos^2 \beta]. \quad (5)$$

In equation (5) $E \sin \beta$ represents the East-West electric field and $E \cos \beta$ the parallel electric field. The heat generated by Joule dissipation is shared by the ambient plasma particles. The electrons being lighter gain maximum energy from the heat source in the beginning and thereafter lose energy to heavier particles in subsequent collisions. The equilibrium electron temperature in this heating process is governed by the corresponding energy balance equation. For electrons we write the energy balance equation as

$$\frac{d}{dt}(3/2 N_e K T_e) = \mathbf{J} \cdot \mathbf{E} - \frac{3}{2} \delta \nu N_e K (T_e - T_0) \quad (6)$$

where δ is the fractional energy loss parameter of electrons to neutral particles. With the help of equations (2) and (5) we rewrite equation (6) as

$$\frac{d}{dt}(T_e - T_0) + \delta \nu (T_e - T_0) = \frac{2q^2 E^2 \nu}{3K m_e} \left[\frac{\sin^2 \beta}{\omega_{ce}^2 + \nu^2} + \frac{\cos^2 \beta}{\nu^2} \right] \quad (7)$$

The solution of equation (7) with the initial condition $t = 0$, $T_e = T_0$ is obtained and is written as

$$(T_e - T_0) = \frac{2q^2 E^2}{3m_e K \delta} [1 - \exp(-\delta \nu t)] \left[\frac{\sin^2 \beta}{\omega_{ce}^2 + \nu^2} + \frac{\cos^2 \beta}{\nu^2} \right] \quad (8)$$

2.1. Heating of the ionosphere by perpendicular electric field

In the E -region of the equatorial ionosphere the electric field configuration in most situations is transverse to the magnetic field lines although occasionally

a parallel electric field may also exist. In order to obtain Joule heating due to perpendicular component of electric field we put $\beta = 90^\circ$ so that equation (8) can be written as

$$T_e - T_0 = \frac{2q^2 E_\perp^2 [1 - \exp(-\delta \nu t)]}{3K m_e \delta (\omega_{ce}^2 + \nu^2)} \quad (9)$$

where E_\perp is the electric field perpendicular to the magnetic field. In the E -region of the equatorial ionosphere the Hall current which flows at right angles to \mathbf{B} and \mathbf{E} polarizes the medium and produces an additional electric field E_p which is sufficient for inhibiting the Hall current. The strength of E_p at the time of complete Hall current inhibition is given by the condition that the Pederson current due to E_p should be balanced by the Hall current due to E_\perp i.e.,

$$\delta_2 E_\perp = \delta_1 E_p \quad (10)$$

or,

$$E_p = \delta_2 / \delta_1 E_\perp. \quad (11)$$

The total electric field responsible for producing Joule heating in equatorial E -region of the ionosphere is the vector sum of the two electric fields E_\perp and E_p . Using the conductivity dependent value of polarisation electric field we rewrite equation (9) as

$$T_e - T_0 = \frac{2E_\perp^2 q^2 [1 + \delta_2^2 / \delta_1^2] [1 - \exp(-\delta \nu t)]}{3m_e K \delta (\omega_{ce}^2 + \nu^2)} \quad (12)$$

The electron temperature in the electrojet region is governed by various parameters appearing in equation (12). The electric field E_\perp and the ratio δ_2 / δ_1 play an important role in controlling the rise of electron temperature. Using a constant value of $E_\perp = 2 \times 10^{-3}$ v/m and the plasma parameters characteristic of this region ($\omega_{ce} = 5 \times 10^6$ sec $^{-1}$, $\nu = 10^5$ sec $^{-1}$ and $\delta = 10^{-3}$), we have calculated the electron temperature variation with time for different values of (δ_2 / δ_1) . The values of δ_2 / δ_1 have been taken from the reported work of Suguira and Cain (1966). This ratio which governs the magnitude of the polarization field set up due to Hall current inhibition is found to range between 20 and 30 at an altitude around 105 km. It is essentially this large value of the polarization field in this region which drives the electrojet current. We find that the electron temperature increases with increase of time and attains a saturation value. The maximum electron temperature corresponding to saturation is characterized by the δ_2 / δ_1 ratio. The electron temperature is higher corresponding to higher values of (δ_2 / δ_1) as shown in Figure 1. The fact that electron temperature attains saturation after sometime shows that some sort of a thermodynamic equilibrium must be established between the rate at which the electron component receives heat energy from the electric field and the rate at which the energy is lost by the electrons to the ambient neutral particles through binary collisions.

The ratio (δ_2/δ_1), the electrojet current and the electric field are known to vary with height. Therefore, we considered these variations and with the help

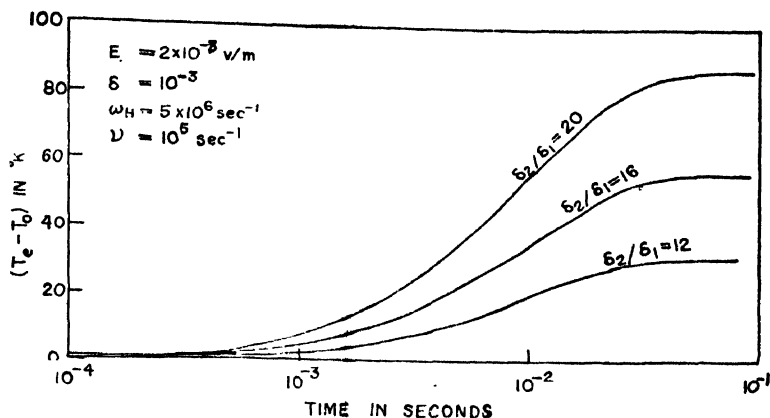


Figure 1. Variation of electron temperature with perturbation time.

of equation (12) we have obtained the height profile of electron temperature. For the sake of clarity we have shown in figure 2a the electric field values obtained from measured electrojet current and the conductivity profile that we have used in this calculation. The height variation of E shown in curve 2 of figure 2a has been obtained with the help of measured current density and Cowling conductivity profiles (Singh and Misra 1967a, b). The other curve-I in figure 2a showing height variation of electric field is taken from the recent measurements of Subaraya *et al* (1972). The electron temperatures corresponding to these profiles are shown in figure 2b. The other curve in figure 2b corresponds to a constant value of $E = 1$ mv/m which is in fair agreement with various probe measurements. We find that the maximum value of $(T_e - T_0)$ is of the order of 50°K .

2.2. Heating of the ionosphere by parallel component of the electric field

One of the most debated and controversial questions in the ionospheric-magnetospheric physics is the possible existence of parallel fields. There has been increasing evidence in the recent past based on theoretical arguments and experimental observations about their existence. Recent measurements of Muhleisen *et al* (1971) have shown that such fields with strengths ranging upto 5 mv/m do exist in the equatorial ionosphere during the interaction of sudden bursts of solar plasma with the magnetosphere. The theoretical possibility of their existence has been discussed in the recent past (Knight 1973). Field aligned currents are known to flow in ionosphere-magnetosphere coupled system. These currents give rise to transverse magnetic field. In response to the interaction between the geomagnetic field and the solar wind plasma together with its

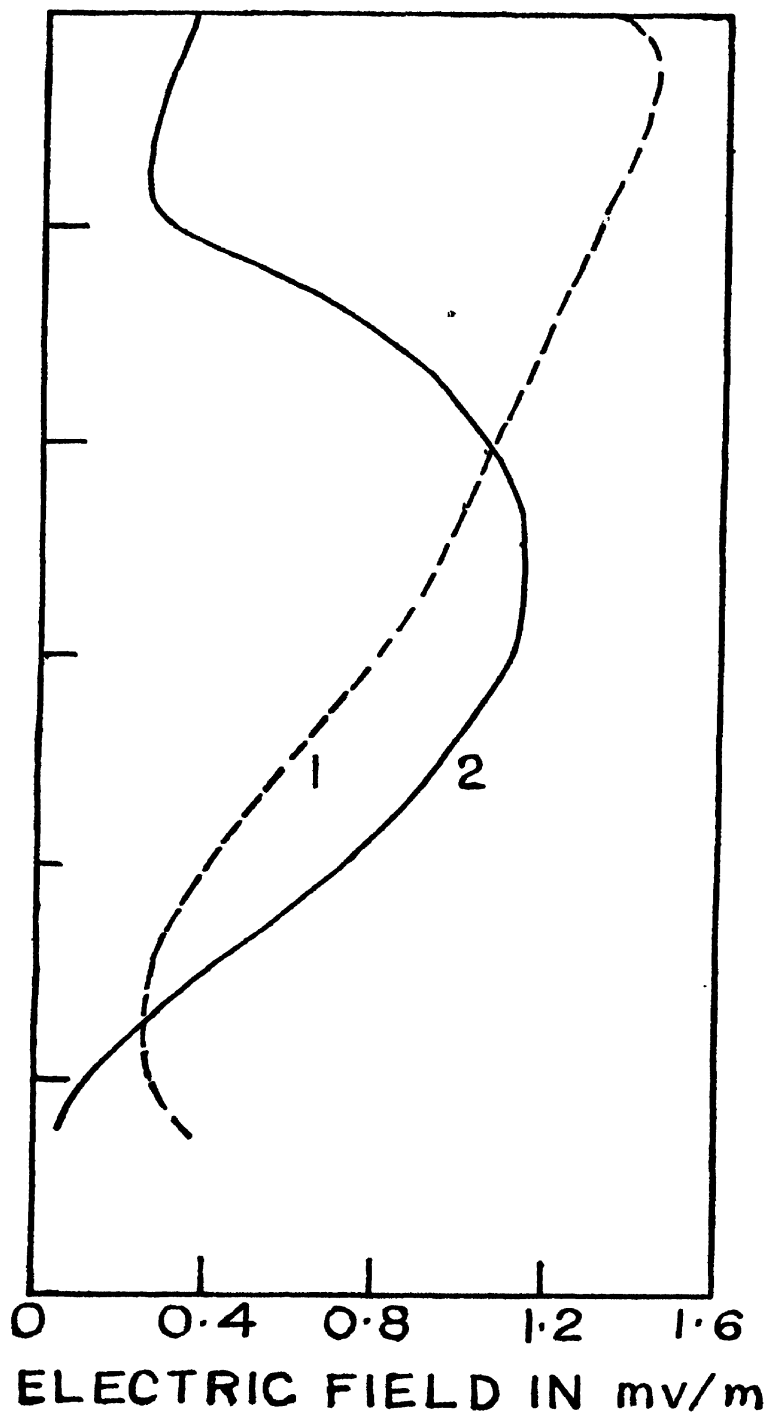


Figure 2(a). Height profile of electric field

variability the transverse magnetic fields generated by the field aligned currents are likely to undergo a change. The motion of the transverse magnetic fields of the field aligned currents can lead to an induced electric field parallel to the geomagnetic field (Zmuda *et al* 1974, Lemarie and Scherer 1974). Recently the parallel component of the electric field arising due to the time variation of the field aligned currents in the magnetosphere has been obtained theoretically by Murphy *et al* (1974). In order to study the heating of the ionosphere due to a possible parallel electric field we put $\beta = 0$ in equation (8) to obtain the steady state rise in electron temperature which can be written as

$$T_e - T_0 = 2E_{11}^2 q^2 / 3m_e K \delta \nu^2. \quad (13)$$

In order to obtain the heating of the electron component of the ionosphere we use the following plasma parameters

$$\delta = 10^{-3} \quad \text{and} \quad \nu = 10^5 \text{sec}^{-1}.$$

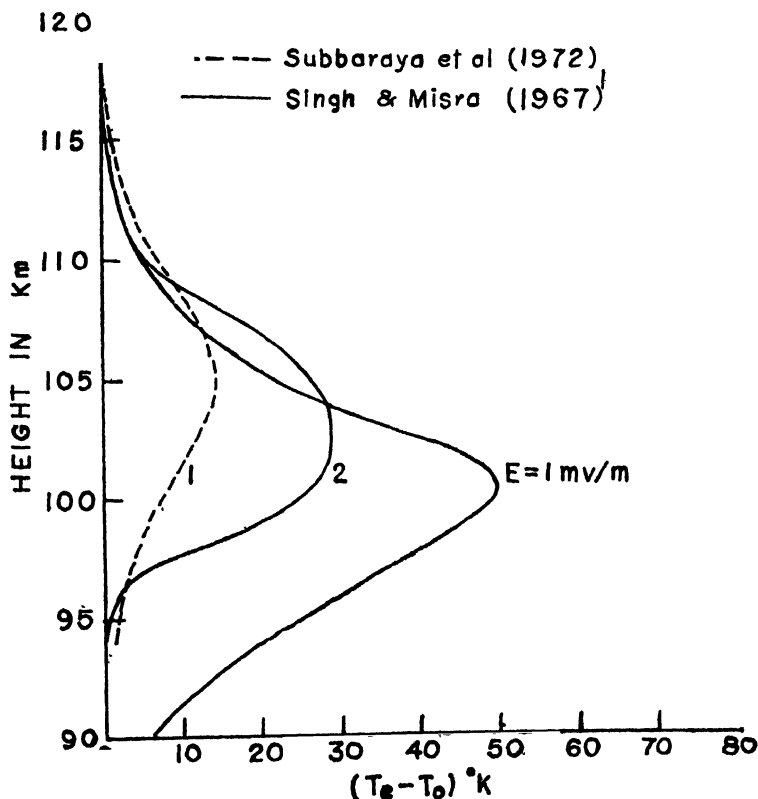


Figure 2(b). Height profile of electron temperature.

The variation of the electron temperature with the different values of the parallel electric field is shown in figure 3. The rise in electron temperature is found to

depend strongly on the magnitude of the parallel electric field. Although for electric field amplitudes larger than 2 mv/m in this region of the ionosphere non linear effects are likely to set in. We find that there can be significant heating due to Joule dissipation of the parallel electric fields in the lower ionosphere.

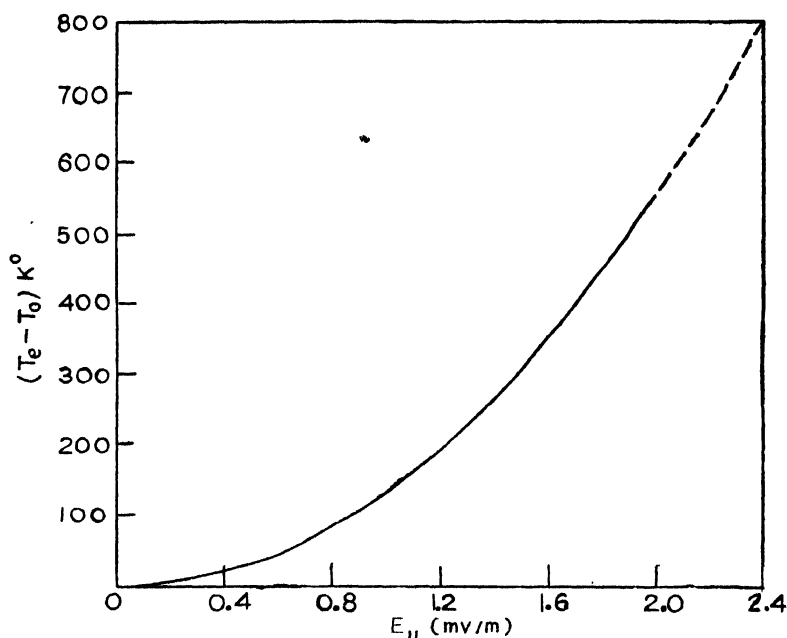


Figure 3. Heating of electrojet region by parallel field

It is therefore suggested that the measurement of the parallel electric fields in the equatorial and auroral ionosphere at the time of sudden bombardment of the solar plasma should accompany of a simultaneous measurement of the electron temperature in order to establish the correlation between the two effects.

3. Possible heating of equatorial electrojet by electrostatic oscillations

The plasma in the equatorial electrojet region is in a turbulent state supposedly due to the inhibition of Hall current, evolution of gradient drift instability and various other non linear effects. In response to these perturbations the electron velocities form vortex patterns and reach values comparable to the mean electrojet drift speed. The role of two stream plasma instabilities in this region has been discussed by Farley (1963) and Buneman (1963). It was shown that the plasma in this region sustains large amplitude electrostatic waves. Following these predictions the large amplitude waves were measured (Gdalevich 1964, Imanyitov *et al* 1964, Imanyitov and Skvartz' 1964). The ionospheric plasma

in the equatorial electrojet is weakly ionized plasma which is being perturbed by the magnetic fluctuations, induced electric fields and the wind system. The resulting small scale electrostatic oscillations give rise to a resonance in the charged particles and damp out giving rise to an additional source of heat in this region. The energy balance equation which accounts for this additional source is thus written as

$$\frac{3}{2} N_e K \frac{dT_e}{dt} = (\mathbf{E} \cdot \mathbf{J})_{static} + (\mathbf{E} \cdot \mathbf{J})_{quasi static} - \frac{3}{2} \delta \nu K N_e (T_e - T_0). \quad (14)$$

In order to calculate the contribution of the electrostatic waves to electron heating we use the Boltzmann transport equation which, in the case of an originally homogeneous plasma can be written as

$$\frac{\partial f}{\partial t} + \frac{q\mathbf{E}}{m} \cdot \nabla_v f = (\partial f / \partial b)_{coll} \quad (15)$$

For small amplitude electrostatic oscillations travelling in the z direction we write

$$\mathbf{E} = E_0 \hat{k} \sin(\omega t + kz') \quad (16)$$

where \hat{k} is a unit vector pointing in z direction. Substituting equation (16) in equation (15) and linearising we obtain the differential equation satisfied by the first order perturbation in the distribution function which can be written as

$$\frac{\partial f_1}{\partial t} + \frac{qE_0}{m_e} \sin(\omega t + k'z) \cdot \frac{\partial f_0}{\partial v_z} + v f_1 = 0. \quad (17)$$

We now assume that the original distribution function f_0 is Maxwellian so that

$$f_0 = N_e \exp(-v^2/a^2) / \pi^{3/2} a^3 \quad (18)$$

where $a^2 = 2kT_0/m_e$. We have assumed that the distribution function of the heavy particle component of the plasma remains unaffected and as such continues to remain Maxwellian. In presence of the electrostatic oscillations a small anisotropy will appear in the electron velocity distribution function in the direction of the impressed electric field. From equation (18) we obtain by differentiation

$$\frac{\partial f_0}{\partial v_z} = -\frac{2v_z}{a^2} f_0. \quad (19)$$

Using equation (19) we integrate equation (17) with the initial condition that at $t = 0$, $f_1 = 0$ to obtain

$$f_1 = \frac{2qE_0v_zf_0}{m_e a^2(\omega^2 + \nu^2)} [\nu \sin(\omega t + k'z) - \omega \cos(\omega t + k'z) - \nu e^{-\nu t} \sin k'z + \omega e^{-\nu t} \cos k'z]. \quad (20)$$

The current density can now be written as

$$J_z = q \int v_z f_1 d^3v. \quad (21)$$

Equation (21) with the help of equation (20) is integrated to give

$$J_z = \frac{N_e q^2 E_0}{m_e(\omega^2 + \nu^2)} [\nu \sin(\omega t + k'z) - \omega \cos(\omega t + k'z) - \nu e^{-\nu t} \sin k'z + \omega e^{-\nu t} \cos k'z]. \quad (22)$$

If we put $k' = 0$ in equation (22) we obtain the current density arising due to localized electric field oscillations of the type $\mathbf{E} = \mathbf{E}_0 \sin \omega t$ which can be written as

$$J_z = \frac{N_e q^2 E_0}{m_e(\omega^2 + \nu^2)^{\frac{1}{2}}} \sin(\omega t - \psi) + \frac{N_e q^2 \omega E_0}{m_e(\omega^2 + \nu^2)} e^{-\nu t} \quad (23)$$

where $\psi = \tan^{-1}(\omega/\nu)$. Equation (23) can be rewritten as

$$J_z = \delta_{eff} E_0 \sin(\omega t - \psi) + \delta_t E_0 \quad (24)$$

where

$$\delta_{eff} = \frac{\delta_0(\omega^2 + \nu^2)^{\frac{1}{2}}}{\omega} \quad (25)$$

and

$$\delta_0 = N_e q^2 \nu / m_e(\omega^2 + \nu^2).$$

Using equation (25) we have studied the variation of δ_{eff}/δ_0 with angular frequency ω corresponding to different values of ν (figure 4). The effective conductivity of the plasma turns out to be considerably higher as compared to δ_0 . Further, the value of δ_t decreases exponentially with perturbation time and is reduced to zero for large values of t (figure 5).

Joule heating of the ionosphere

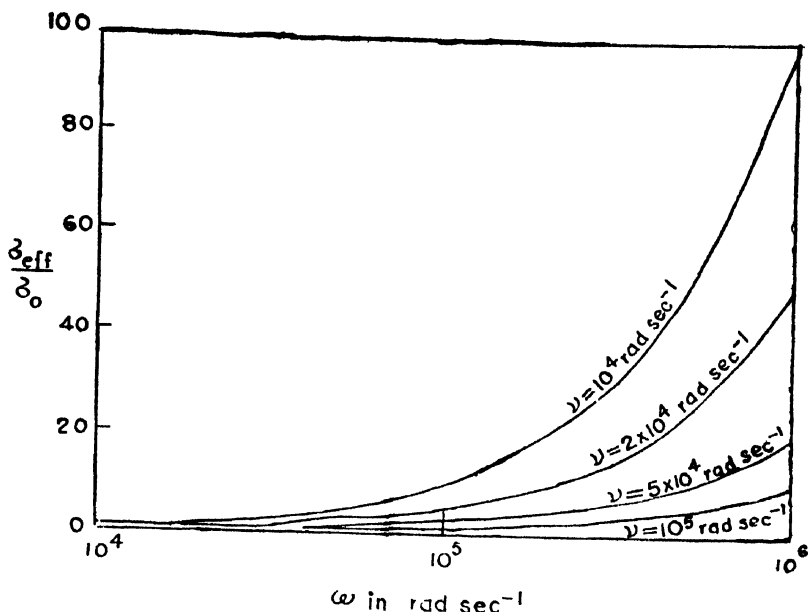


Figure 4. Variation of δ_{eff}/δ_0 with angular frequency for different values of collision frequency.

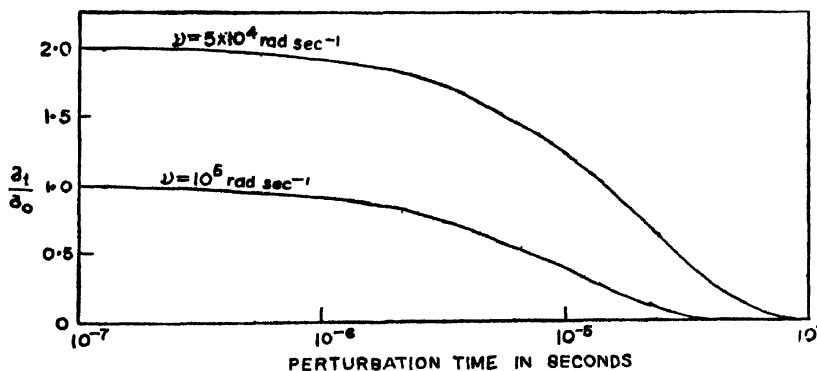


Figure 5. Variation of δ_i/δ_0 with perturbation time.

From equation (22) we can write

$$\begin{aligned}
 (E \cdot J)_{quasi-static} &= \frac{N_e q^2 E_0^2}{2m_e(\omega^2 + \nu^2)} [\nu\{1 - \cos(2\omega t + 2k'z)\} - \omega \sin(2\omega t + 2k'z)] \\
 &\quad - 2\nu e^{-\nu t} \sin(\omega t + k'z) \sin k'z + 2\omega e^{-\nu t} \sin(\omega t + k'z) \cos k'z.
 \end{aligned}
 \tag{26}$$

Using equation (26) we can write the energy balance equation (14) as

$$\begin{aligned} & \frac{3}{2} N_e K \frac{d}{dt} (T_e - T_0) + \frac{3}{2} \delta \nu N_e K (T_e - T_0) \\ &= (\mathbf{E} \cdot \mathbf{J})_{static} + \frac{N_e q^2 E_0^2}{2 m_e (\omega^2 + \nu^2)} [\nu - \nu \cos(2\omega t + 2k'z) - \omega \sin(2\omega t + 2k'z) \\ & \quad - 2\nu e^{-\nu t} \sin(\omega t + k'z) \sin k'z \\ & \quad + 2\omega e^{-\nu t} \sin(\omega t + k'z) \cos k'z]. \end{aligned} \quad (27)$$

Equation (27) is integrated with the initial condition that $(T_e - T_0) = 0$ at $t = 0$. We thus obtain for

$$(\delta \nu < \nu)$$

$$\begin{aligned} T_e - T_0 &= \frac{2q^2 E_0^2 [1 - \exp(-\delta \nu t)] [1 + \delta^2 / \delta_1^2]}{3 k m_e \delta (\omega_{ce}^2 + \nu^2)} + \frac{q^2 E_0^2}{3 k m_e (\omega^2 + \nu^2)} \\ & \times \left[\frac{1 - \exp(-\delta \nu t)}{\delta} - \frac{\nu}{4\omega^2 + \delta^2 \nu^2} \{ \delta \nu \cos(2\omega t + 2k'z) \right. \\ & \quad - \delta \nu \cos 2k'z \exp(-\delta \nu t) + 2\omega \sin(2\omega t + 2k'z) \\ & \quad - 2\omega \exp(-\nu \delta t) \sin^2 k'z \} \\ & \quad \left. - \frac{2\omega \cos(2\omega t + 2k'z) + 2\omega \cos 2k'z \exp(-\delta \nu t)}{4\omega^2 + \delta^2 \nu^2} \{ \delta \nu \sin(2\omega t + 2k'z) - \delta \nu \sin 2k'z \exp(-\delta \nu t) \right. \\ & \quad \left. + \frac{(2\omega \cos k'z - 2\nu \sin k'z)}{(\omega^2 + \nu^2)} \{ \nu \exp(-\delta \nu t) \sin k'z \right. \\ & \quad \left. + \omega \exp(-\delta \nu t) \cos k'z - \nu \sin(\omega t + k'z) \exp(-\nu t) \right. \\ & \quad \left. - \omega \cos(\omega t + k'z) \exp(-\nu t) \} \}. \end{aligned} \quad (28)$$

Taking $\nu = 10^5$ rad sec⁻¹, $\delta = 10^3$ and $\omega = 5 \cdot 10^3$ rad sec⁻¹, and $\omega_{ce} = 5 \times 10^6$ rad/sec and using equation (28) we find that the electron temperature due to the dissipation of electrostatic waves increases and after about 6×10^{-2} sec attains more or less a steady value. This behaviour of the electron temperature in response to electrostatic oscillations can be explained in terms of the energy relaxation time. For the chosen plasma model the energy relaxation time (10^{-2} sec) is large as compared to the time period of the longitudinal field

($\approx 10^{-3}$ sec). Therefore, the plasma does not get time to relax so that the temperature settles at some steady value. The rise in electron temperature obtained from equation (28) corresponding to different values of E_0 has been tabulated below :

No.	E_0 (mv/m)	$(T_e - T_0)^\circ\text{K}$
1	1.0	95
2	1.5	226
3	2.0	374

The heating of the electron component is found to be strongly dependent on the amplitude of the electrostatic oscillations. Large amplitude electrostatic waves have been detected in the ionosphere at higher altitudes (Scarfi *et al* 1965, Gdalevich 1964, Imyanitov *et al* 1964). It is likely that energy dissipated by collisional damping of these waves in the lower ionosphere may account for the observed non thermal equilibrium in the electrojet region.

4. Results and conclusion

We have obtained the heating of the electron component in the electrojet region and found that whereas the heating by the observed perpendicular component of the electric field can account for a temperature rise of about 50°K , the heating due to the collisional damping of small amplitude longitudinal oscillations could account for an electron temperature rise of about 300°K . The most potent mechanism, however, has been found to be the Joule dissipation due to parallel electric fields. We have seen that this mechanism can account for a sporadic temperature rise of the electron component of a thousand degrees above the ambient temperature or even more as sometimes observed (Mozar and Fahlson 1970). This has led us to conclude that future electron temperature measurements should be carried out simultaneously with the measurement of a possible parallel electric field in order to establish the identity of these parallel fields in the Joule heating mechanism of the ionosphere.

References

- Aono Y, Hirao K and Miyazaki S 1961 *J. Radio Res. Labs. (Japan)* **8** 453
 Block L P and Falthammar 1963 *J. Geophys. Res.* **73** 4807
 Buneman O 1963 *Phys. Rev. Letters* **10** 285
 Cole K D 1962 *Aust. J. Phys.* **15** 223
 Cole K D 1971 *Planet. Space-Sci.* **19** 59
 Farley D T Jr 1963 *J. Geophys. Res.* **68** 6083
 Fried B D, Kaufman A N and Sachs D L 1966 *Phys. Fluids* **9** 292
 Gdalevich G L 1964 *Artificial Earth Satellites* **17** 42
 Imyanitov I M, Gdalevich G L and Shvartz Ya M 1964 *Artificial Earth Satellites* **17** 66

212 *P N Khosa and R N Singh*

- Imyanitov I M and Shvartz Ya M 1964 *Artificial Earth Satellites* **17** 59
- Jacchia L G, Slowey J and Verniani F 1966 *Sp. rep.* 218 *Smithsonian Institution Astrophysical Observatory*
- Kato S 1962 *Planet Space Sci.* **9** 939
- Kato S 1963 *Planet Space Sci.* **11** 1297
- Kolley M C, Mozer F S and Fahleson U V 1970 *Planet Space Sci.* **18** 847
- Knight S 1973 *Planet Space Sci. (G.B.)* **21** 741
- Lemaire J and Scherer M 1974 *Planet Space Sci. (G.B.)* **22** 1485
- Mozer F S and Fahleson U V 1970 *Planet Space Sci.* **18** No. 11
- Muhleisen R, Fischer H J and Hoffman H 1971 *Zeitschrift fur Geophysik* **37** 1055
- Murphy C H, Wang C S and Kim J S 1974 *J. Geophys. Res.* **79** 2901
- Oberman C, Ron A and Dawson J 1962 *Phys. Fluids* **5** 1514
- Rees M H and Walker J C G 1968 *Annales de Geophysique Tome* **24**
- Scarf F L, Crook G M and Fredricks R W 1965 *J. Geophys. Res.* **70** 3045
- Singh R N and Misra K D 1967a *Nature* **214** 375
- Singh R N and Misra K D 1967b *J. Geomag. Geoelec.* **19** 143
- Spencer N W, Brace L H, Carignan G R, Tacusch D R and Nieman H 1965 *J. Geophys. Res.* **90** 2665
- Subbaraya B H, Muraliknishna P, Sastry T S G and Prakash S 1972 *Planet. Space Sci.* **20** 47
- Sugiura M and Cain J C 1966 *J. Geophys. Res.* **71** 1869
- Zmuda A J, Potemra T A and Armstrong J C 1974 *J. Geophys Res. (U.S.A.)* **79** 4222

Meridional neutral air winds and its effects on F_2 -region of the ionosphere during quiet and magnetically disturbed periods

B Singh

Applied Physics Section, Institute of Technology,
Banaras Hindu University, Varanasi-221005

and

R P Singh

Department of Physics, Electronics & Radio, Physics Section,
Banaras Hindu University, Varanasi-221005

Received 29 August 1978, revised 27 February 1979

Abstract. Diurnal variation of neutral air wind profile for quiet and magnetically disturbed periods both for low and mid latitudes have been computed and compared with the experimentally evaluated wind features. Theoretically evaluated wind features have been used to explain D_{st} variation of f_oF_2 .

1. Introduction

The critical frequency of F_2 -region shows a marked diurnal, seasonal and latitudinal variations in electron density and height of the layer which are not in agreement with the variation on basis of simple Chapman theory. These anomalous behaviour were explained earlier by Yonezawa (1959) and Rishbeth *et al* (1963) in terms of loss and diffusion processes but no satisfactory explanation could be given until the advent of neutral air winds (King and Kohl 1965) which are produced by solar heating of the upper atmosphere. To understand the mid-latitude behaviour of F_2 -region, equation of motion and continuity equations have been solved simultaneously and patterns of neutral air winds have been computed (Kohl *et al* 1968), Bailey *et al* (1969) and Cho and Yeh (1970). It is rather well known that during quiet periods these winds to a large extent are responsible for the observed behaviour of the thermosphere. During magnetically disturbed periods however the nature and dynamics of F_2 -region becomes much more complex and no exact mechanism has been proposed which can explain the observed structure and movements of neutral and ionised components of the atmosphere.

In the present paper we have studied the morphology of F_2 -region at low latitudes. The neutral air wind pattern both during quiet and magnetically

disturbed periods have been computed and compared with the available experimental and theoretical results. It is qualitatively shown that neutral wind may explain the ionospheric behaviour at low latitudes during disturbed periods.

2. Numerical evaluation of wind pattern :

The horizontal neutral air winds are caused by pressure gradients which are produced by the heating effects of EUV radiations. The speed and direction of neutral air winds are mainly governed by collisions between ions and neutrals and coriolis force, which is produced due to the rotation of the earth. The other forces which govern the neutral air winds are viscous and gravitational force. To compute the neutral wind pattern the equation of motion of neutrals, including the effect of above mentioned forces, is written as

$$\frac{\partial \mathbf{U}}{\partial t} = -\frac{1}{\rho} \nabla p_n + \frac{\mu}{\rho} \frac{\partial^2 \mathbf{U}}{\partial z^2} - \nu_{nt}(\mathbf{U} - \mathbf{V}) - 2\boldsymbol{\Omega} \times \mathbf{U} + \mathbf{g} \quad (1)$$

where \mathbf{U} is neutral wind velocity

$V_t = \frac{(\mathbf{U} \cdot \mathbf{B})\mathbf{B}}{B^2}$ is the projection of \mathbf{U} along \mathbf{B} .

\mathbf{B} geomagnetic field

$\boldsymbol{\Omega}$ earth's angular velocity

\mathbf{g} acceleration due to gravity

μ coefficient of viscosity

ν_{nt} neutral ion collision frequency

ρ neutral mass density.

In equation (1) we have considered viscous force caused by vertical gradient in the neutral wind velocity because the viscous force caused by horizontal gradient in wind velocity is negligible.

To evaluate meridional and zonal wind pattern separately we use the cartesian co-ordinate system such that x axis points towards south, y axis points towards east and z axis points vertically upwards. The x (meridional) and Y (zonal) components of wind velocity are governed by the following equation :

$$\frac{\partial U_x}{\partial t} = -\frac{1}{\rho} \frac{\partial p_n}{\partial x} + \frac{\mu}{\rho} \frac{\partial^2 U_x}{\partial z^2} - \nu_{nt} \frac{N_n}{N_t} (U_x - V_x) + 2\Omega U_y \sin \phi$$

and

$$\frac{\partial U_y}{\partial t} = -\frac{1}{\rho} \frac{\partial p_n}{\partial y} + \frac{\mu}{\rho} \frac{\partial^2 U_y}{\partial z^2} - \nu_{nt} \frac{N_n}{N_t} (U_y - V_y) - 2\Omega (U_x \sin \phi + U_z \cos \phi) \quad (2)$$

where ϕ is the geographical latitude. To evaluate $\frac{\partial p_n}{\partial x}$ and $\frac{\partial p_n}{\partial y}$ numerically, we assume that the neutral density distribution follows barometric law. Using barometric law and the definition of gas pressure $p_n = N_n k T_n$, we can write meridional and zonal pressure gradients as (Stubbe and Chandra 1970)

$$\frac{\partial p_n}{\partial x}(z, t) = \rho_n(z) T_n(z) \int_{z_0}^z \frac{g(z')}{T_n^2(z')} \frac{dT_n(z')}{dx} dz'$$

and

$$\frac{\partial p_n}{\partial y}(z, t) = \frac{2.16 \times 10^{-5}}{\cos \phi} \rho_n(z) T_n(z) \int_{z_0}^z \frac{g(z')}{T_n^2(z')} \frac{dT_n(z')}{dy} dz'. \quad (3)$$

To evaluate these pressure gradients the height variation of neutral density and temperature alongwith the latitudinal variation of temperature has to be known. If we assume that the latitudinal variation of temperature at various heights remains constant and the height variation of temperature at any one latitude (say mid latitude) is known then the height variation of neutral temperature for different latitudes are easily calculated. In the present calculation we have used Jacchia (1970) model for winter months. According to this model the neutral density and temperature at 90 Km. height remains constant over the whole globe. Also the minimum temperature T_c at any point on the globe and the exospheric temperature T_∞ are taken as

$$T_c = 383^\circ + 3.32^\circ F_{10.7}$$

and

$$T_\infty = 498^\circ + 3.38^\circ F_{10.7} \quad (4)$$

where $F_{10.7} = 100 \text{ watt m}^{-2} \text{ Hz}^{-1}$ is taken to be the intensity of solar radiation at 10.7 cm wavelength. The integration, in determination of pressure gradients has been carried out in the height range 90–300 Km.

To study neutral wind pattern in steady state condition we must evaluate the contribution of viscous force and collisional force alongwith Coriolis force. We have seen that the vertical gradient of height variation of horizontal wind velocity is small and thus the contribution of viscous force is neglected in the present calculation. Further the neutral-ion collision frequency for $(0, 0^+)$ is taken as (Rishbeth 1972).

$$\nu_{ni} = 9.3 \times 10^{-16} N_i \left(\frac{T_n}{1000} \right)^{0.87}$$

where $N_i(m^{-3})$ is the ion number density and neutral and ion temperatures and masses are assumed to be equal. Using this procedure meridional and zonal wind pattern for quiet periods have been computed.

For computations during magnetically disturbed periods we note that the pressure distribution, during high magnetic activity, changes due to preferential heating at high latitudes. The change in temperature with K_P index, empirically suggested by Roemer (1971) is written as

$$\Delta T = (21.4 \sin \phi + 17.9)K_P + 0.03K_P$$

where ϕ is the geographic latitude. Using the above relation and atmospheric model, the diurnal variation of neutral air wind pattern for low and mid latitude have been computed.

3. Neutral wind pattern at low and mid latitudes

The computed neutral wind pattern for winter months are shown in figures (1) and (2). From the figure (1) we find that at low latitude the wind remains poleward throughout the whole day during quiet time. Calculation has been made with and without coriolis force and it is found that apart from ion drag

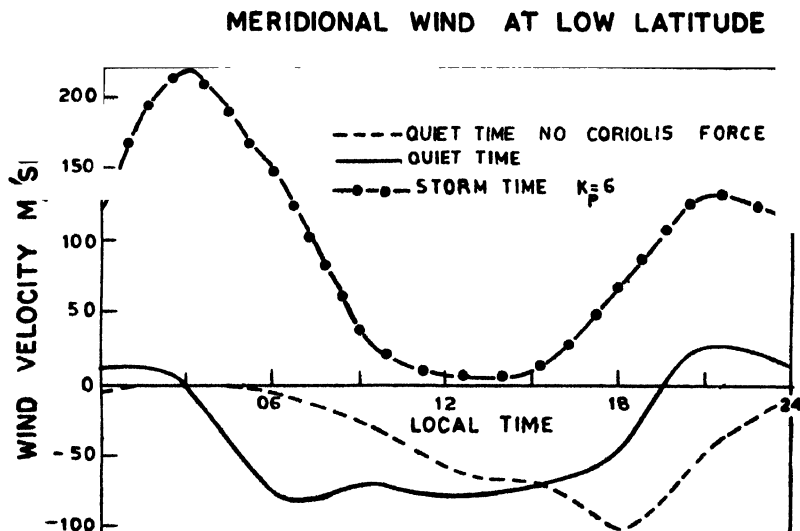


Figure 1. Showing the diurnal wind pattern at low mid latitudes during quiet and magnetically disturbed periods (+ve equatorward, -ve poleward).

coriolis force is also playing an important role and meridional wind is controlled by the zonal winds. For a few hours in the mid-night wind becomes equatorward, although its magnitude is very small. This pattern of wind is found to be quite different from mid-latitude winds which remains equatorward during night-time and poleward during daytime. The day-time wind in mid-latitude which are poleward are of comparable magnitude to that of equatorward wind

in the night which is not the case in summer months. In summer, night-time winds are strong and equatorward and poleward winds are known to be small in magnitude in day hours (Goisler (1966), Rishbeth (1968), Cho and Yeh (1970)).

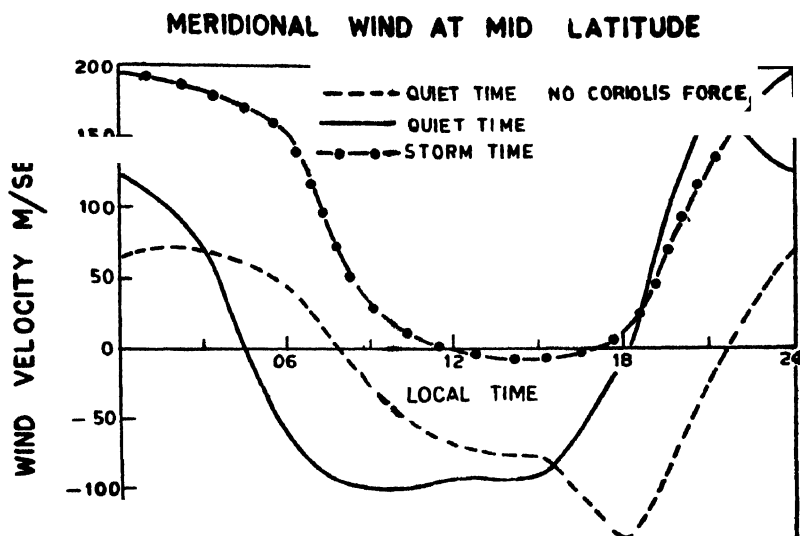


Figure 2. Same as figure 1 but for mid latitudes.

Recently Behnke and Harper (1973) have made measurements of neutral winds at low latitudes by incoherent scatter technique. It would be worthwhile to compare the measured wind and wind calculated on the basis of satellite drag method. In figure 3 we have compared theoretically calculated wind and

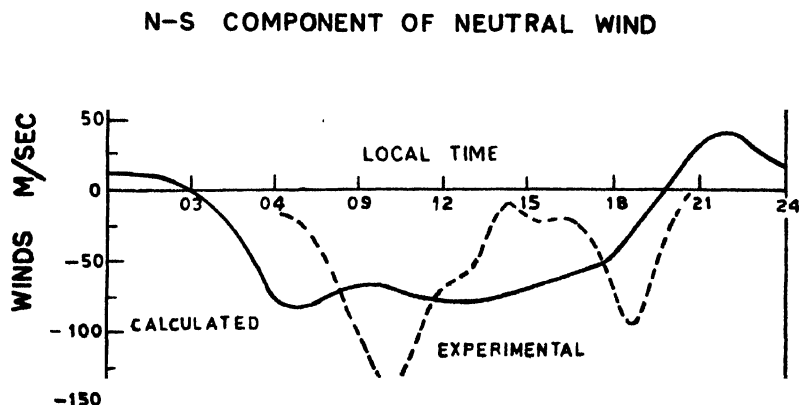


Figure 3. A comparison of theoretically calculated wind and experimentally measured wind at a low mid latitudes.

experimentally measured wind. We find that both the winds remain poleward almost throughout the day. Bohnke and Harper (1973) have discussed their results and concluded that wind will not be equatorward even during night hours. Contrary to this calculated wind however shows equatorward wind in midnight though it is of small magnitude.

The storm time wind has been plotted in the same figure along with quiet time wind. It is seen that during disturbed conditions winds are always equatorward. During the magnetic storms due to preferential heating at high latitude the temperature distribution is altered which is such that it augments the equatorward wind and reverses the poleward wind to equatorward in the daytime. This type of behaviour of neutral air winds during magnetic storm has been invoked by Evans (1970), Jones and Rishbeth (1971), Obayashi (1972) to explain the increase in peak density. Equatorward wind raises the ionisation to higher height of low loss which consequently give rise to increase in electron density and height of the layer. This fact will be discussed in detail in the next section.

4. Effects of neutral winds on the ionosphere

The neutral air wind drives the ionisation along the geomagnetic field direction and produces plasma drift in vortical and horizontal direction which is responsible for the observed features of F_2 region. Rajaram and Rastogi (1968) have studied the D_{st} variation of f_oF_2 and have shown that f_oF_2 shows asymmetric behaviour at a pair of stations on the same longitudes. For example the f_oF_2 variation during magnetically disturbed periods are shown in figure 4 which corresponds to Pacific and American zones at low-mid latitudes. In Pacific zone at Maui (dip 40°N) there is negative type of variation of f_oF_2 while at a station Rarotonga exactly at the same latitude (dip 40°S) but in opposite hemisphere there is increase in critical frequency. This shows that at a pair of station at the same longitude but in opposite hemisphere during main phase of the magnetic storm opposite effects are observed. This behaviour may be qualitatively explained in terms of neutral winds which during winter and on normal days remains poleward for all the time and moves the ionisation down the fields in a region of greater loss rate. Contrary to this on disturbed days the wind is of small magnitude as shown in figure 1, which is not capable of transporting the ionisation. Thus during winter positive storm effects may be observed while in opposite hemisphere equatorward component of neutral wind will be of larger magnitude and can transport the ionisation away. Therefore, during winter months D_{st} variation shows enhancement in electron density and in summer months there is depletion of electron density in the opposite hemisphere due to horizontal transport of ionisation which will give rise to negative storm effect.

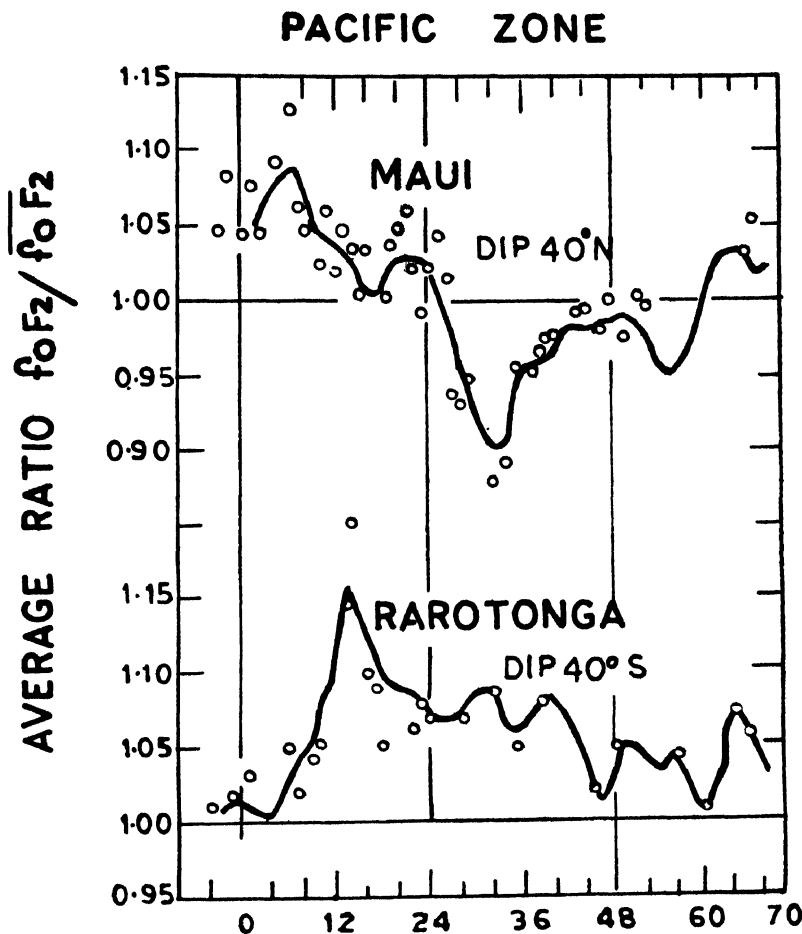


Figure 4. D_{st} variation of f_oF_2 in Pacific zone at a pair of stations in northern and southern hemisphere at the same longitude. Figure clearly shows the opposite variations at two stations on second day of magnetic storm. (After Rajaram and Rastogi 1968).

5. Conclusions

The meridional winds which are caused by solar heating are the main cause of the morphology of mid-latitude and low-latitude ionosphere. Apart from the mid-latitude where winds are undoubtedly effective and capable of explaining almost all the observed features, it appears that their effect is quite significant even at low latitudes and they can explain the ionospheric changes during disturbed conditions.

Acknowledgment

We gratefully acknowledge the help provided by Professor R. N. Singh and R. G. Rastogi (P. R. L., Ahmedabad). One of the authors (B.S.) is very much thankful to C.S.I.R. for financial assistance.

References

- Bailey G J, Moffett R J and Rishbeth H 1969 *J. Atmos. Terr. Phys.* **31** 253
Behnke R A and Harper R M 1973 *J. Geophys. Res.* **78** 8222
Cho H R and Yeh K C 1970 *Radio Science* **5** 881
Evans J V 1970 *J. Atmos. Terr. Phys.* **32** 1629
Eccles D, King J W and Kohl H J 1971 *J. Atmos. Terr. Phys.* **33** 1371
Geisler J E 1966 *J. Atmos. Terr. Phys.* **28** 703
Jones K L and Rishbeth H 1971 *J. Atmos. Terr. Phys.* **33** 391
Jacchia L G 1970 *Smithson Astrophys. Obs. Spec. Report* No. 313
King J W and Kohl H 1965 *Nature Lond.* **206** 699
Kohl H, King J W and Eccles D 1968 *J. Atmos. Terr. Phys.* **30** 1733
Obayashi T 1972 *Planet Space Sci.* **19** 503
Rajaram G and Rastogi R G 1968 *J. Atmos. Terr. Phys.* **32** 659
Rishbeth H, Lyon A J and Peart M 1963 *J. Geophys. Res.* **68** 2559
Rishbeth H 1968 *J. Atmos. Terr. Phys.* **30** 63
Rishbeth H 1972 *J. Atmos. Terr. Phys.* **34** 1
Roemer M 1971 *Space Research XI* 965 *Akademic Verlag, Berlin*
Stubbe P and Chandra S 1970 *J. Atmos. Terr. Phys.* **32** 1909
Yonezawa T 1959 1959 *J. Atmos. Terr. Phys.* **15** 89

Vapour absorption spectra of 4,7-dichloroquinoline in the near ultraviolet region

Nitish K Sanyal, S L Srivastava and Mrs Ananda Devi

Department of Physics, University of Gorakhpur, Gorakhpur 273001.

Received 15 November 1978

Abstract. The present communication presents a report on the investigations on the electronic absorption bands of 4, 7-dichloroquinoline appearing in the region (3222-2925 Å) in vapour phase. The 0, 0 band has been chosen at 3209 Å. The observed spectrum has been explained in terms of six 384, 555, 624, 1326, 1453 and 1507 cm^{-1} excited state fundamental vibrational frequencies.

1. Introduction

From the structural point of view, quinoline may be considered as a naphthalene molecule where one methine group ($=\text{CH}-$) in naphthalene has been replaced by ($=\text{N}-$) group at position 1. As observed from the structure, the nitrogen atom of the ring will have a lone pair of electrons and due to this, quinoline molecule is expected to give rise a weak $n-\pi$ transition in addition to the $\pi-\pi$ transition. The electronic and vibrational spectra of quinoline has been studied by Singh *et al* (1969) and by Wait *et al* (1970) for the first time. Studies on the electronic absorption spectra of monosubstituted quinolines (Shashidhar *et al* 1967, 1970, 1973) are also available. The present work on 4,7-dichloroquinoline has been undertaken with a view to study the effect of substitution of the ortho-para directing and strongly interacting groups on the electronic transitions of quinoline. Only one band system having limited number of the bands in the region (3222-2925 Å) has been observed. On the basis of the shift of the 0,0 band together with the strong appearance of the C-C stretching vibration, it has been concluded that it is a $\pi-\pi$ system. The $n-\pi$ system could not be traced, because on substitution, it shifts towards the shorter wavelength where the absorption intensity being very large prevents experimental observations.

2. Experimental

Pure chemicals obtained from M/S Koch Light Laboratories (England) were used as such without further purification. The absorption spectra was photographed on Hilger medium quartz spectrograph. The path length of the absorbing column was varied from 0.5 meter to 2 meter whereas the temperature was changed from 25°C to 100°C. The best experimental condition was obtained

at one meter path length of the absorption tube maintained at about 50°C. The bands listed in the table 1 in general are broad and diffuse and as such the accuracy for such bands is of the order of $\pm 15 \text{ cm}^{-1}$. The 0, 0 band of the system has been chosen at 31153 cm^{-1} . The system has been analysed in terms of six excited state 384, 555, 624, 1326, 1453 and 1507 cm^{-1} fundamental modes. In spite of several attempts for obtaining the fundamentals of the ground state no such band has been obtained.

Table 1. Analysis of the near ultraviolet absorption spectra of 4, 7-dichloroquinoline vapours

Intensity	Position of the bands in Å	Position of the bands in cm^{-1}	Separation from the 0, 0 band	Assignment
msb	3222.0	31028	0—125	0—125
msb	3209.0	31153	0,0	0, 0 band
msb	3200.0	31241	0+88	0+88
wb	3170.0	31537	0+384	0+384
wb	3154.0	31697	0+555	0+555
wb	3146.0	31777	0+624	0+624
wb	3114.6	32098	0+945	0+384+555
wb	3097.3	32277	0+1120	0+2×555
msb	3078.0	32479	0+1326	0+1326
msb	3066.0	32606	0+1453	0+1453
msb	3061.0	32660	0+1507	0+1507
wb	3015.4	33153	0+2000	0+555+1453
wb	2957.4	33804	0+2649	0+2×1326
wb	2941.0	33992	0+2839	0+1326+1507
wb	2925.1	34177	0+3024	0+2×1507

msb = medium strong and broad, wb = weak and broad.

3. Discussion

Quinoline, the parent molecule belongs to C_s point group in which all the forty five modes of vibrations are distributed in $31a'$ and $14a''$ on substitution of the two chlorine atoms at 4 and 7 position the symmetry of the molecule is maintained. In view of the C_s symmetry of the molecule, the electronic transition in question becomes $A' \rightarrow A'$ which is an allowed one. As a consequence of the allowed transition, it is expected to have a strong 0, 0 band towards the longer wavelength side of the band system. Thus 0, 0 band has been assigned at 3209.0 Å .

Except the 0, 0 band, the other bands where the major part of the intensity of the absorption is concentrated are at 32479, 32606 and 32660 cm^{-1} . These bands involve excited state fundamental frequencies 1326, 1453 and 1507 cm^{-1} respectively. Out of the three, the two vibrations 1326 and 1507 cm^{-1} has been found to be excited upto two quanta. The higher quanta of the vibration 1453 cm^{-1} could not be located with certainty because of the weak intensity. However, one combination has been observed. These three vibrations are assigned as the C-C stretching motion of the type a' which is the characteristic of the ring. These vibrations will correspond to intense Raman bands at 1371, 1469 and 1571 cm^{-1} in quinoline and at 1379, 1460 and 1579 cm^{-1} in naphthalene.

The weak fundamental at cm^{-1} has been traced upto two quanta. Further the presence of this fundamental explains some other bands of the system in combination with other fundamentals. The vibration corresponding to this has been traced around 670 cm^{-1} in some methyl quinolines (Shashidhar *et al* 1967) and at 720 cm^{-1} in quinoline (Wait *et al* 1970) in the excited state. Hence on the basis of the magnitude of this vibration it has been concluded that this vibration is mass dependent and only because of this its magnitude has been reduced by a large amount on substitution of two chlorine atoms. In view of the assignment proposed for methyl quinolines this vibration has been assigned as in plane skeletal deformation mode of the type a' .

Out of the other two remaining fundamentals 384 and 624 cm^{-1} , the 384 cm^{-1} band has been assigned to central C-C distortion mode and the 624 cm^{-1} to C-Cl stretching mode.

References

- Amma R A, Singh S N and Nair K P R 1969. *Ind. J. Pure Appl. Phys.* **7**
Wait S C and Mc Nerney J C 1970. *J. Mol. Spectroscopy* **34**, 56.
Shashidhar M A and Suryanarayana Rao. K 1967. *Ind. J. Phys.* **41** 299
Shashidhar M A and Suryanarayana Rao K 1970. *Ind. J. Pure Appl. Phys.* **8** 178
Shashidhar M A and Suryanarayana Rao K 1973. *Ind. J. Pure Appl. Phys.* **11** 371

Electronic transition moment variation in ($B^2\Sigma-X^2\Sigma$) band system of YO

A P Walvekar and T S Mukundan

Bangalore University Bangalore

Received 6 December 1978

Abstract. ρ -values have been evaluated by the methods I and II suggested by Walvekar, the results computed by the two methods are compared. It is found that the method II gives better results and preferable to method I from theoretical considerations. Hence the expression for $R_e(r)$, the electronic transition moment for YO ($B-X$) band system is given as

$$R_e(r) = \text{Constant}(1 - 0.5073r).$$

1. Introduction

The object of the present investigation is to put the available experimental data to rigorous test in the light of the recent theoretical developments with reference to the behaviour of the electronic transition moment (R_e) variation with internuclear separation r . The Yttrium Oxide YO ($B-X$) band system has been chosen for study because of its astrophysical interest.

The vibrational transition probability $q_{v'v''}$ of an electronic transition occurring in the intensity expression is given by the square of the overlap integral,

$$q_{v'v''} = \left| \int \psi_{v'} R_e(r) \psi_{v''} dr \right|^2 \quad (1)$$

The theoretical methods of obtaining arrays of $q_{v'v''}$ depend upon the evaluation of the integral in the above expression under a variety of approximations. One of the approximations is to take an average of $R_e(r)$ on the assumption that it is a slow variable over the possible range of r -values. (Herzberg 1950). Some workers have attempted to represent $R_e(r)$ by empirical quadratic functions of ' r ', thinking that its negligence might lead to large errors. Fraser (1954) developed the \bar{r} -Centroid concept in order to determine the relation of $R_e(\bar{r})$ with $\bar{r}_{u'v''}$. This formulation assumes the dependence of the electronic wave functions and hence of R_e on the internuclear distance ' r '. Once this assumption is made, then it becomes necessary to evaluate integral (1) with R_e under the integral (Herzberg 1950, Chamberlain 1961). This aspect has been studied by Walvekar (1976) one of the authors of the present paper and a method has been developed

by him to evaluate the ρ -Coefficient that occurs in the expression for R_e . This method is found by Walvekar (1976) to give better result for the constant ' ρ ' in the case of BaO ($1\Sigma-1\Sigma$) band system. This aspect has been studied here for YO ($B-X$) band system.

2. Theoretical Results

Franck-Condon factors have been evaluated for the YO bands by the Bates (1949) numerical integration method. The molecular constants needed for the purpose are taken from the compilation of Herzberg (1950). The $\bar{r}_{v'v''}$ -Centroids were evaluated by the numerical integration method by the method of Nicholls and Jermain (1956). Using these results the coefficient ' ρ ' that occurs in the expression for R_e is evaluated by the method suggested by Walvekar (1975). This method depends on the assumption that R_e is a function of $\bar{r}_{v'v''}$ and is taken outside the integral (1) for the evaluation of ρ . Next ' ρ ' value is again evaluated by the method suggested by Walvekar (1976) by taking R_e inside the integral. For the purpose of evaluation of ' ρ ', R_e variation is assumed to be of linear form as suggested by Murthy and Murthy (1976). The experimental integrated intensities that are used for the purpose of evaluation are due to Murthy and Murthy (1976). These results are entered in Table 1.

Table 1.

Observation	Band	$\bar{r}_{v'v''}$ -Centroids	F.C. Factor	ρ_{mn}	ρ with R_e	
					outside	inside
1	0, 0	1.80929	0.791482			
2	0, 1	1.89452	0.184705	$\rho_{1, 2}$	-0.3949	-0.5395
3	1, 0	1.73402	0.178508			
4	1, 1	1.82190	0.424134	$\rho_{3, 4}$	-0.5338	-0.5109
5	1, 2	1.89782	0.313729	$\rho_{4, 5}$	-0.44729	-0.5371
6	2, 1	1.74982	0.294908			
7	2, 2	1.82592	0.152086	$\rho_{6, 7}$	-0.17889	-0.4420
Average					-0.3886	-0.5075

$\rho_{m,n}$ indicates the result obtained by using the observations m and n .

Murthy and Murthy (1967) have evaluated the values of $\bar{r}_{v'v''}$ -Centroids and F.C. factors and our values agree with theirs.

The method suggested by Walvekar (1977) has been used to study the equivalence of the two methods based on the definition of two $\bar{r}_{v'v''}$ -Centroids. The results necessary for the purpose are evaluated and entered in Table 2.

Table 2.

Band	$\bar{\rho} \int \psi_v' \psi_v'' dr$	$\rho \int \psi_v' r \psi_v'' dr$	ρ average — ρ actual	
			Outside	Inside
0, 0	-6.28782	-8.207655		
0, 1	+3.185234	+4.157766	0.0063	0.0322
1, 0	-2.880642	-3.760173		
1, 1	-4.672072	-6.09857	0.1389	0.0036
1, 2	+4.17962	+5.455761	0.0586	0.0298
2, 1	-3.71704	-4.851956		
2, 2	-2.781385	-3.6306108	0.2096	0.0653

For calculating the results given in columns (2) and (3) of Table 2 the respective average ' ρ ' values from Table 1 have been used. The results in column (4) and (5) of Table 2 represent the difference between the ρ average and ρ actual values taken from Table 1.

3. Conclusion

It is found from the results in Table 1 that with the introduction of R_e inside the integral, though the ρ -value varies from band to band, this variation is small. This is evident from the $\rho_{ave.} - \rho_{act.}$ values entered in Table 2. The individual values come closer to the average value of -0.5073 . Hence there is an improvement in the results over those evaluated by the other method. This is in agreement with the observation of Walvekar (1976) for the BaO-band system. The second point that needs to be stressed is that \bar{r} -Centroid concept should lead to the same result of ρ irrespective of the method used. But that is not so. On the basis of the definition of \bar{r}_v -Centroids the values of $\rho \bar{r}_v \int \psi_v' \psi_v'' dr$ and $\rho \int \psi_v' r \psi_v'' dr$ should be the same. But the results entered in Table 2 show that they are not. This aspect has been studied by Walvekar (1977) previously in the case of BaO and BO- α -band systems. Our observation in the case of YO is fully in agreement with his. Apart from that even the values of ' ρ ' evaluated by the two methods should be the same. But they differ. Method II suggested by Walvekar (1976) involves no approximations and hence it is preferable. Hence the expression for $R_e(r)$ for YO ($B-X$) system of bands is

$$R_e(r) = \text{Constant}(1 - 0.5073r).$$

Acknowledgment

Authors are grateful to Prof. K. N. Kuchela, Professor and Head of the Department of Physics, Bangalore University for his keen interest shown in the above work and providing facilities. Hence our thanks are due to him.

References

- Bates D R 1949 *Proc. Roy. Soc.* **196A** 217
Chamberlain J W 1961 *Physics of the Aurora and Air Glow* Academic Press
Fraser P A 1954 *Can. J. Phys.* **32** 515
Herzberg G 1950 *Spectra of Diatomic Molecules* D Van Nostrand
Murthy N S and Murthy B N 1967 *Proc. Phys. Soc.* **90** 881
Murthy B N and Murthy N S 1976 *Ind. J Pure & Appl. Phys.* **14** 218
Nicholls R W and Jarman W R 1956 *Proc. Phys. Soc. (Lond.)* **69A** 253
Walvekar A P 1975 *Ind. J. Phys.* **49** 124
Walvekar A P 1976 *Ind. J. Phys.* **50** 394
Walvekar A P 1977 *Ind. J. Phys.* **51B** 267

Parametric excitation of acoustic waves in piezoelectric solid state magnetoplasma*

S Guha⁺ and P K. Son⁺

School of Studies in Physics, Vikram University, Ujjain 456010, India.

Received 12 September 1978

Abstract. The effect of a large transverse magnetostatic field on parametrically excited acoustic waves has been investigated for the case of piezoelectric semiconductors. The analysis is based on the hydrodynamic model of a plasma under the collision dominated regime for $kl \ll 1$. In a magnetoplasma ($\omega_c \sim \omega_p$) the condition of instability gets modified and is obtained at a lower value of the high frequency oscillatory electric field. Numerical analysis has been made for n -InSb at 77°K when the crystal is irradiated with a near infra red laser (e.g. 10.6 μm CO₂ laser). The magnetostatic field ($B_0 \sim 10.0$ tesla) reduces the threshold electric field to less than half its value in the absence of B_0 .

1. Introduction

The parametric excitation of low frequency acoustic waves in piezoelectric semiconductors was first investigated by Kaw (1973) in the absence of magnetic field. Later Sundaram *et al* (1974) studied the same problem using kinetic approach. The above analyses were made for homogeneous semiconductor-plasmas when a high frequency oscillatory electric field propagating longitudinally interacts with the comparatively low frequency acoustic wave. It has been shown by Kaw (1973) that the coupling between the acoustic waves and the plasma waves is better at higher values of the wave number k and low values of the oscillatory electric field is sufficient for instability. Pantell and Soohoo (1970) have studied analytically the amplification of acoustic waves in the presence of a dc electric field as well as an oscillatory electric field in a piezoelectric semiconductor when the frequencies of both the oscillatory electric field and the acoustic wave are small in comparison with the electron collision frequency and obtained the gain constants for the regions $kl \ll 1$ and $kl \gg 1$, where l is the electron mean free path. They have shown that the modulation on the electromagnetic wave is transferred to the acoustic wave with a considerable gain factor, depending on the semiconductor. Houck *et al* (1967) have shown experimentally

* Work partially supported by U.G.C., India under the Research Project, "Instabilities in Solid State Plasmas".

⁺ Present address : Department of physics, Ravishankar University, Raipur 492 010

(using inductive (direct electromagnetic) generation and a piezoelectric transducer as a detector for acoustic waves) that an external alternating field generates coherent acoustic waves in a metal when a large magnetic field is present. Nishikawa and Liu (1976) have discussed in detail the theory of coupled-mode parametric excitation by a homogeneous pump in plasma. The purpose of this paper is to investigate analytically the effect of a large transverse dc magnetic field \mathbf{B}_0 on parametric excitation of acoustic wave in piezoelectric semiconductors. The magnetic field \mathbf{B}_0 is taken so large that the electron cyclotron frequency ω_c is comparable to the electron plasma frequency ω_p and the medium becomes a magnetoplasma. The doped semiconductors— n -GaAs, n -InSb etc. are ideal systems in this respect (Platzman and Wolff 1973). We have applied the established method of Bers and Briggs (Baynham and Boardman 1970) to examine the nature of instability and analytically it has been seen that the system supports absolute instability. The present analysis further reveals that the instability of the acoustic wave can be caused at smaller values of k and E_0 in the presence of a large transverse magnetic field. The growth rate $|\Omega_i|$ as well as the phase velocity v_ϕ of the unstable mode have also been obtained analytically. The results have been discussed for the case of n -InSb at 77°K.

2. Dispersion relation

We use hydrodynamic model of a homogeneous infinite semiconductor-plasma. A high frequency oscillatory electric field $\mathbf{E}_0 \cos \omega_0 t$, uniform in space, is applied parallel to the wave vector \mathbf{k} (along x -axis) and the dc magnetic field \mathbf{B}_0 is taken normal to \mathbf{k} (along z -axis). We neglect the non-uniformity of the high frequency oscillatory electric field under the dipole approximation when the excited acoustic and electron-plasma waves have wavelengths which are very small compared to the scale length of electromagnetic-field variation (Kaw 1973). We have also assumed $\omega_0 (\approx \omega_p) \gg \nu$, where ν is the electron collision frequency.

We start with the following basic equations :

$$\frac{\partial \mathbf{v}_0}{\partial t} + \nu \mathbf{v}_0 = \frac{e}{m} (\mathbf{E}_0 \cos \omega_0 t + \mathbf{v}_0 \times \mathbf{B}_0) \quad (1)$$

$$\rho \frac{\partial^2 u}{\partial t^2} = c \frac{\partial^2 u}{\partial x^2} - \beta \frac{\partial E}{\partial x} \quad (2)$$

$$\frac{\partial E}{\partial x} = \frac{en}{\epsilon} - \frac{\beta}{\epsilon} \frac{\partial^2 u}{\partial x^2} \quad (3)$$

$$\frac{\partial n}{\partial t} + v_0 \frac{\partial n}{\partial x} + n_0 \frac{\partial v}{\partial x} = 0 \quad (4)$$

$$\frac{\partial \mathbf{v}}{\partial t} + (\mathbf{v}_0 \cdot \nabla) \mathbf{v} = \frac{e}{m} (\mathbf{E} + \mathbf{v} \times \mathbf{B}_0) - \frac{k_B T}{mn_0} \nabla n - \nu \mathbf{v}. \quad (5)$$

The equations and the notations used are explained by Kaw (1973) except the additional terms necessary to incorporate the effect of transverse dc magnetic field B_0 ; k_B is the Boltzmann's constant.

We assume that the acoustic wave has a frequency such that $\Omega \ll \omega_0$ and the perturbations are proportional to $\exp[i(kx - \Omega t)]$. The transverse acoustic wave is propagating in such a direction of the crystal that it produces longitudinal electric field; for example in *n*-InSb if \mathbf{k} is taken along (011) and \mathbf{u} is along (100), the electric field induced by the wave is a longitudinal field.

Using equations (2) and (3) we obtain

$$\left(\Omega^2 - \frac{c}{\rho} k^2 - \frac{\beta^2 k^2}{\epsilon \rho} \right) u = \frac{\beta e}{\epsilon \rho} n. \quad (6)$$

Differentiating equation (4) with respect to time and using equations (1) and (2), we obtain

$$\begin{aligned} \frac{\partial^2 n}{\partial t^2} + \omega_R^2 n + \nu \frac{\partial n}{\partial t} + \frac{n_0 e \beta}{m \epsilon} k^2 u + i \mathbf{k} \cdot \mathbf{v}_0 \left(\frac{\partial n}{\partial t} - n_0 \frac{\partial v}{\partial x} \right) + i k n_0 \omega_c v_y \\ = i k n \left(\frac{e}{m} E_0 \cos \omega_0 t - \omega_c v_0 y \right) \end{aligned} \quad (7)$$

where $\omega_c = -eB_0/m$, the electron cyclotron frequency; $\omega_R^2 = \omega_p^2 + k^2(k_B T/m)$, ω_p being the electron plasma frequency given by $\omega_p^2 = (n_0 e^2/m\epsilon)^{\frac{1}{2}}$, $\epsilon = \epsilon_0 \epsilon_l$, ϵ_l being the lattice dielectric constant and ϵ_0 is the absolute permittivity.

Under collision dominated regime ($\nu \gg \Omega$, $\mathbf{k} \cdot \mathbf{v}_0$), we obtain from equation (7)

$$\frac{\partial^2 n}{\partial t^2} + \bar{\omega}_R^2 n + \nu \frac{\partial n}{\partial t} + (n_0 e \beta / m \epsilon) k^2 u = -i k n \bar{E} \quad (8)$$

where

$$\bar{\omega}_R^2 = \omega_R^2 [1 + \omega_c^2 / (\nu^2 + \omega_c^2)]$$

and

$$\bar{E} = \frac{e}{m} E_0 \cos \omega_0 t - \omega_c v_0 y.$$

Equation (8) can now be resolved into two components (fast and slow) by writing $v = v_{fa} + v_{sl}$ and $n = n_{fa} + n_{sl}$ (suffixes *fa* and *sl* represent the fast and the slow component respectively). Hence one obtains

$$\frac{\partial^2 n_{fa}}{\partial t^2} + \nu \frac{\partial n_{fa}}{\partial t} + \bar{\omega}_R^2 n_{fa} = -i k n_{sl} \bar{E} \quad (9)$$

and

$$(\bar{\omega}_R^2 - i \Omega \nu^2 n_{sl} + \frac{n_0 e \beta}{m \epsilon} k^2 u = -i k n_{fa} \bar{E} \quad (10)$$

n_{fa} have components at frequencies $(\Omega \pm \omega_0)$. Thus from equation (9) one gets

$$n_{fa} = -ikn_s l \bar{E} [1/\{\bar{\omega}_R^2 - (\Omega + \omega_0)^2 - i(\Omega + \omega_0)\nu\} + 1/\{\bar{\omega}_R^2 - (\Omega - \omega_0)^2 - i(\Omega - \omega_0)\nu\}]. \quad (11)$$

Assuming $\omega_0 \approx \bar{\omega}_R (\approx \omega_p)$ and $\Omega \ll \omega_0$, we obtain from equation (11)

$$n_{fa} = i \frac{kn_s l \bar{E}}{\omega_R^2} \left[\frac{\bar{\omega}_R}{\Omega + \delta + i\nu} - \frac{\bar{\omega}_R}{\Omega - \delta + i\nu} \right] \quad (12)$$

where $\delta = \omega_0 - \bar{\omega}_R$.

Using equations (6) and (12) in equation (10), we get

$$\begin{aligned} & \left[\Omega^2 - \frac{c}{\rho} k^2 - \frac{\beta^2 k^2}{\epsilon \rho} \right] \left[\bar{\omega}_R^2 - i\Omega\nu - \frac{k^2 \bar{E}^2}{\omega_R^2} \left(\frac{\bar{\omega}_R}{\Omega + \delta + i\nu} - \frac{\bar{\omega}_R}{\Omega - \delta + i\nu} \right) \right] \\ & = -\omega_p^2 \frac{\beta^2 k^2}{\epsilon \rho}. \end{aligned} \quad (13)$$

Equation (13) represents the general dispersion relation of the acoustic wave for the region $kl \ll 1$ for piezoelectric semiconductors in the presence of a transverse dc magnetic field. When $B_0 = 0$, equation (13) becomes analogous to equation (9) of Kaw (1973).

3. Results and discussion

From equation (13) it is noticed that for $\beta = 0$, we obtain the usual equation $\Omega^2 = (c/\rho)k^2$ for the sound wave in an elastic medium. When the high frequency oscillatory electric field $\bar{E}_0 = 0$, we find $\bar{E} = 0$ and equation (13) reduces to

$$\Omega^2 - \frac{c}{\rho} k^2 - A \left[1 - \frac{\omega_p^2}{\bar{\omega}_R^2 - i\Omega\nu} \right] = 0 \quad (14)$$

where

$$A = K^2 k^2 v_s^2, \quad v_s^2 = c/\rho, \quad K^2 = \beta^2/\epsilon c;$$

v_s being the acoustic velocity. Equation (14) represents the damped acoustic wave and is analogous to equation (10) of Kaw (1973) with $\beta \neq 0$, and $B_0 \neq 0$. It is clear that the presence of the high frequency oscillatory electric field is a necessary condition to obtain the instability of the acoustic wave. Let us take $\bar{E}_0 \neq 0$, then equation (13) can be written as

$$[\Omega^2 - k^2 v_s^2 - A] \left[\bar{\omega}_R^2 - i\Omega\nu - \frac{2k^2 \bar{E}^2 \delta}{\omega_R(\nu^2 + \delta^2)} \right] + A\omega_p^2 = 0. \quad (15)$$

In order to obtain analytical information from equation (15), we rewrite it as

$$\Omega^2 - k^2 v_s^2 - A + A \omega_p^2 \left[\bar{\omega}_R^2 - i\Omega\nu - \frac{2k^2 E^2 \delta}{\bar{\omega}_R(\nu^2 + \delta^2)} \right]^{-1} = 0 \quad (16)$$

Assuming $\bar{\omega}_R^2 \gg i\Omega\nu$, equation (16) reduces to

$$\Omega^2 - k^2 v_s^2 - \frac{A}{G} (G - \omega_p^2) + i\Omega\nu \frac{A}{G} = 0 \quad (17)$$

where

$$G = \bar{\omega}_R^2 - \frac{2k^2 E^2 \delta}{\bar{\omega}_R(\nu^2 + \delta^2)}.$$

It can be shown that the solution of equation (17) supports the existence of absolute instability for which we apply the established method due to Bers and Briggs (Baynham and Boardman 1970). Accordingly there must exist a complex frequency with $\Omega_i > 0$ at which two roots from opposite halves of the complex k plane will merge. In order to show that this condition can be achieved in our problem we rewrite equation (17) in the following form

$$D_1 k^4 + D_2 k^2 + D_3 = 0 \quad (18)$$

where

$$D_1 = 2\sqrt{2}(1 + K^2)v_s^2 e^2 E_0^2 / (m^2 \omega_p \nu),$$

$$D_2 = \frac{2\sqrt{2}e^2 E_0^2 \Omega^2}{m^2 \omega_p \nu} - \omega_p^2 (2 - K^2)v_s^2$$

and

$$D_3 = -2\omega_p^2 \Omega^2.$$

Equation (18) yields

$$k^2 = -D_3/2D_1 \pm (D_2^2/4D_1^2 - D_3/D_1)^{\frac{1}{2}}. \quad (19)$$

These roots will coalesce at

$$k_m = \pm (|D_2|/2D_1)^{\frac{1}{2}} \quad (20)$$

when

$$D_2^2/4D_1 - D_3 = 0 \quad (21)$$

provided that D_2 is negative, which is possible in our case (for $\omega_p \gg \Omega$).

Substituting the values of D_1 and D_2 in equation (20), and assuming $K^2 \ll 1$, $k^2(k_B T/m) \ll \omega_p^2$, we obtain

$$k_m = \pm \left[\frac{\omega_p^3 m^2 \nu}{2\sqrt{2}e^2 E_0^2} - \frac{\Omega^2}{2v_s^2} \right]^{\frac{1}{2}} \quad (22)$$

The solution of equation (21) yields (for $\Omega = \Omega_r + i\Omega_i$ and separating the real and imaginary parts).

$$\Omega_i = \pm \left[\frac{v_s^2 \omega_p^3 \nu m^2}{\sqrt{2} e^2 E_0^2} \right] \quad (23)$$

and

$$\Omega_r = \sqrt{2} \Omega_i \quad \text{or} \quad 0. \quad (24)$$

Thus these two roots coalesce in the complex k -plane with $\Omega_i > 0$ at a value of k_m given by equation (22). Thus the system supports the existence of absolute instability. The growth rate of the unstable mode is given by $|\Omega_i|$.

With this established fact at our disposal we now proceed to obtain the threshold electric field and the growth rate $|\Omega_i|$ of the unstable mode.

From equation (17) we get

$$\Omega = -i \frac{\nu}{2} \frac{A}{G} \pm \frac{1}{2} \left[-\nu^2 \frac{A^2}{G^2} + 4 \left\{ \frac{A}{G} (G - \omega_p^2) + k^2 v_s^2 \right\} \right]^{\frac{1}{2}} \quad (25)$$

which yields

$$\Omega_i = -\frac{\nu}{2} \frac{A}{G} \quad (26)$$

provided that

$$4 \left\{ \frac{A}{G} (G - \omega_p^2) + k^2 v_s^2 \right\} - \nu^2 \frac{A^2}{G^2} \quad (27)$$

The acoustic wave will be unstable when $G < 0$

$$\text{i.e.} \quad \overline{\omega_R^2} - \frac{2k^2 \overline{E}^2 \delta}{\overline{\omega_R}(\nu^2 + \delta^2)} < 0. \quad (28)$$

This condition can be satisfied only when

$$(a) \quad \delta > 0 \quad \text{i.e.} \quad \omega_0 > \omega_R, \quad (29)$$

and

$$(b) \quad \frac{2k^2 \overline{E}^2 \delta}{\overline{\omega_R}(\nu^2 + \delta^2)} > \overline{\omega_R^2}. \quad (30)$$

Optimization of (30) with respect to δ yields $\delta = \nu$ (Nishikawa and Liu 1976). Thus the threshold value of the high frequency oscillatory electric field E_0 necessary for the instability ($\Omega_i > 0$) is obtained from (30) as

$$E_0 > \frac{m}{ek} \omega_R^{3/2} \left(1 + \frac{\omega_c^2}{\omega_c^2 + \nu^2} \right)^{3/4} \nu^{\frac{1}{2}} \left(1 - \frac{\omega_c^2}{\omega_0^2} \right) \quad (31)$$

where equation (1) is used to obtain v_{0y} as

$$v_{0y} = \frac{\omega_c}{\nu - i\omega_0} v_{0x} \quad (32)$$

with

$$v_{0x} = \frac{\nu - i\omega_0}{m(\nu - i\omega_0)^2 + \omega_c^2} E_0. \quad (33)$$

From equation (31) one can notice that at $B_0 = 0$, the necessary value of E_0 reduces to

$$E_0 > (\omega_R^3 \nu)^{\frac{1}{2}} \frac{m}{ek} \quad (34)$$

which is different from that of Kaw (1973) as he solved equation (9) (Kaw 1973) using binomial expansion whereas we have solved the dispersion relation algebraically without any such expansion.

Our next object is to obtain the value of E_0 necessary for the instability (with $\Omega_i > 0$) in the magnetoplasma ($\omega_c \sim \omega_p \gg \nu$). Under such circumstance condition (31) yields

$$E_0 > 2^{3/4} \left(1 - \frac{\omega_c^2}{\omega_0^2}\right) (\omega_R^3 \nu)^{\frac{1}{2}} \frac{m}{ek}. \quad (35)$$

Comparing the expressions (34) and (35) we get for instability

$$(E_0)_{B_0 \neq 0} / (E_0)_{B_0 = 0} = 2^{3/4} \left(1 - \frac{\omega_c^2}{\omega_0^2}\right). \quad (36)$$

From equation (36) we observe that in a magnetoplasma ($\omega_c \sim \omega_p \sim \omega_0$), the value of the high frequency oscillatory electric field E_0 necessary for the instability can be reduced appreciably in comparison to the unmagnetized semiconductor-plasmas.

To obtain the growth rate $|\Omega_i|$ and the phase velocity $v_\phi (= \Omega_r/k)$ of the unstable mode we use equation (25) which yields

$$|\Omega_i| = \frac{\nu}{2} \frac{A}{|G|} \quad (37)$$

and

$$v_\phi = \frac{1}{2k} \left[4 \left\{ A \left(1 - \frac{\omega_p^2}{|G|}\right) + k^2 v_s^2 \right\} - \nu^2 \frac{A^2}{G^2} \right]^{\frac{1}{2}}. \quad (38)$$

Let us now apply the analytical results to the case of a semiconductor like n -InSb at 77K. The physical constants used for numerical calculations are :

- Carrier concentration $n_0 = 10^{22} \text{m}^{-3}$,
- Effective mass of electron $m = 0.014 m_0$,
- lattice dielectric constant $\epsilon_l = 18.0$,
- acoustic velocity $v_s = 4.0 \times 10^3 \text{m} \cdot \text{sec}^{-1}$
- electron collision frequency $\nu = 3.5 \times 10^{11} \text{sec}^{-1}$
- density of n -InSb $\rho = 5.8 \times 10^3 \text{kg} \cdot \text{m}^{-3}$
- piezoelectric constant $\beta = 0.054 \text{cm}^{-2}$,
- m_0 being the free electron mass.

For $k = 5 \times 10^6 \text{m}^{-1}$, the value of E_0 is found from (34) to be $\sim 3.54 \times 10^5 \text{V} \cdot \text{m}^{-1}$ at $B_0 = 0$. Such an electric field can be obtained by irradiating the crystal with a $10.6 \mu\text{m}$ CO_2 laser with $\omega_0 \sim \omega_p$. For n -InSb magnetoplasma with $B_0 \sim 10.0$ Tesla, we observe from (36) that at the same value of k , $(E_0)_{B_0 \neq 0} / (E_0)_{B_0 = 0} \sim 0.4$. Thus one may infer from this that the parametric excitation of an acoustic wave can easily be observed in a magnetoplasma with a much lower value of the high frequency oscillatory electric field even at a lower value at k satisfying the condition $kl \ll 1$.

The heating of the electrons due to the electric field E_0 enters only through the thermal corrections for dispersion electron-plasma wave. We have assumed $kl \ll 1$ and $\omega_p \gg \nu$; therefore, $k\lambda_D \ll 1$ where λ_D is the Debye wave length. Thus one can assume $k^2(k_B T/m) \ll \omega_p^2$; whence ω_R becomes equal to ω_p in the long wavelength region.

For the chosen parameters it can further be shown that

$$(\nu A/G)^2 \ll 4\{A(1 - \omega_p^2/|G|) + k^2 v_s^2\}$$

which satisfies condition (27) and consequently the phase velocity v_ϕ is obtained as

$$v_\phi = \frac{1}{k} \{A(1 - \omega_p^2/|G|) + k^2 v_s^2\}^{\frac{1}{2}}. \quad (39)$$

Calculations show that $A(1 - \omega_p^2/|G|) \ll k^2 v_s^2$ and hence the phase velocity of the unstable acoustic wave is found to be nearly equal to the acoustic velocity v_s in the crystal. The corresponding growth rate $|\Omega_i|$ is found to be of the order of 10^3sec^{-1} . The growth rate at $B_0 \neq 0$ is slightly smaller than that at $B_0 = 0$.

Acknowledgment

One of the authors (PKS) is very much thankful to the Council of Scientific and Industrial Research, India for awarding a Senior Research Fellowship.

References

- Baynham A C and Boardman A D 1970 *Adv. Phys.* **19** 575 (663-6)
Houck J R, Bohm H V, Maxfield B W and Wilkins J W 1967 *Phys. Rev. Letters.* **19** 224.
Kaw P K 1973 *J. Appl. Phys.* **44** 1497.
Nishikawa K and Liu C S 1976 *Advances in Plasma Physics* eds A Simon and W. B. Thompson (New York: Wiley), Vol 6 14-22.
Pantell R H and Sohoo J. 1970 *J. Appl. Phys.* **41** 441.
Platzman P M and Wolff P A 1973 *Waves and Interactions in Solid State Plasmas* (New York: Academic Press), 90.
Sundaram A K, Kaw P K and Sharma S K 1974 *Pramana* **2**, 304.

Charge sheath around electrodes immersed in plasma

G P Gupta* and R N Singh

Applied Physics Section, Institute of Technology,
Banaras Hindu University, Varanasi-221005

Received 8 December 1978

Abstract. Assuming an appropriate velocity distribution function for the sheath region and considering a sharply bounded ion sheath we have solved Poisson equation and have studied the temporal and spatial variation of electrode potential. An expression for sheath thickness has been derived by equating the space charge limited ion current and random ion current. The temporal and spatial variation of steady state sheath thickness and its variation with d.c. bias potential have been computed. The diagnostic role of electrodes immersed in plasma has been discussed.

1. Introduction

The change in impedance of electrodes immersed in ionized gas led to the recognition of charge-sheath formation around electrodes. In the study of discharge phenomena on laboratory scale the charge-sheath formation played a dominant role and was approximately accounted in the interpretation of experimental results (Huddleston and Leonard 1965, Swift and Schwar 1970). The advent of space age simulated the conditions of a giant moving electrode (space vehicle) into extended and weakly ionized gas (the ionosphere). The first experiment with space vehicle was carried out by Jackson (1952) and the diagnostic features of antennas immersed in plasma were outlined by subsequent workers (Jastrow and Pearse 1957, Jackson and Pickar 1957, Jackson and Kane 1959, 1960, Rose and Clark 1961, Kane *et al* 1962). The role of sheath formation around an electrode immersed in ionospheric plasma was fully developed by above workers. The data thus obtained were analysed by accounting for the shape and size of the sheath.

The intent of the present paper is to bring out systematic time evolution of sheath around an electrode immersed in weakly ionized and tenuous ionospheric plasma. The ionospheric plasma is a tenuous plasma for which electron temperature is comparable to the ion temperature. This permits the use of well known Langmuir theory (1924) for ionospheric plasma. Using this theory the time evolution of floating potential on the electrode has been obtained by integrating the appropriate Poisson equation. The computed results have been compared

* Present address : Plasma Physics Section, Bhabha Atomic Research Centre,
Bombay 400 085

with the work of Anderson and Walsh (1971) which assumes the presence of free streaming ions. On the other hand we have assumed the ions to be immobile under electrostatic forces and they constitute current only due to thermal motion. Our formulation predicts larger steady state floating potential on the electrode. The spatial variation of floating potential on the electrode has been calculated. An expression for sheath thickness has been derived by equating the random ion current and the space charge limited current. The dependence of sheath thickness with electron density and dc bias has been studied.

2. Charge sheath formation

When an unbiased electrode is immersed in a plasma, the lighter plasma particles (electrons) collide with the electrode more often as compared to the heavier plasma particles (ions), the latter having less thermal velocity than that of electrons. As a result of this process a floating potential negative with respect to plasma potential is built-up on the surface of the electrode in contact with the plasma. As soon as the negative potential develops on the electrode, the electrons flow is reduced and the flow of ions continues to increase till an equilibrium state is reached. In the equilibrium state, the region around the electrode deficient in electrons is called an ion-sheath. The plasma sheath whose thickness is of the order of Debye length shields the entire plasma from the effect of negative potential on the immersed electrode. In the steady state condition there exists a difference between the 'floating potential' of the electrode and the plasma potential. This difference of potential results into a space charge field near the sheath-plasma boundary. The nature of sheath depends on the shape, size and material of the electrode, and also on the plasma parameters such as electron density, collision frequency and temperature of the plasma. The magnitude and frequency of the biasing potential also brings in interesting changes in observed features of charge sheath around electrodes. The charge sheath are broadly classified as; D.C. sheath and R.F. sheath.

3 Kinetic theory of DC plasma sheath

The size and shape of sheath around an electrode depend on the kinetics of the plasma particles, the density, temperature of the plasma particles and inter-particle collisions. It is difficult to account for all these details in the analysis of sheath formation, therefore, simplifying assumptions are often times made. The thickness of sheath is small therefore the sheath region is considered to be collisionless and characterised by Maxwell-Boltzmann distribution function. An infinitely conducting and perfectly absorbing plane electrode is assumed to be situated at $x = 0$ and the region $x \leq 0$ filled with neutral plasma. The dynamics of the electrons in the plasma is governed by the electric field described by a scalar potential $\phi(x, t)$. The distribution function of the electron component

in the plasma is thus written as

$$f(\mathbf{r}, \mathbf{v}, t) = n_0 \left(\frac{m_e}{2\pi k T_e} \right)^{3/2} \exp \left[-\frac{\frac{1}{2} m_e v^2 + e\phi(x, t)}{k T_e} \right], \quad (1)$$

where k is Boltzmann's constant, and n_0 is the number density of electrons at points where the electric potential vanishes. The average electron number density at a point x in the sheath is given by

$$\begin{aligned} n_e(x, t) &= \int f(\mathbf{r}, \mathbf{v}, t) d\mathbf{v}, \\ &= 4\pi n_0 \left(\frac{m_e}{2\pi k T_e} \right)^{3/2} \exp \left(\frac{e\phi}{k T_e} \right) \int_0^\infty v^2 \exp \left(-\frac{m_e v^2}{2k T_e} \right) dv, \end{aligned}$$

which, on simplification, gives

$$n_e(x, t) = n_0 \exp \left[\frac{e\phi(x, t)}{k T_e} \right]. \quad (2)$$

At any time t , the electron current density, $j_e(x, t)$, is obtained by integrating $-ev_x f(\mathbf{r}, \mathbf{v}, t)$ over a region $v_x \geq 0$ of the velocity space. We obtain

$$j_e(x, t) = -e \int f(\mathbf{r}, \mathbf{v}, t) v_x d\mathbf{v}. \quad (3)$$

Substituting for $f(\mathbf{r}, \mathbf{v}, t)$ and evaluating the integral, the expression for current density is written as

$$j_e(x, t) = -n_0 e \left(\frac{k T_e}{2\pi m_e} \right)^{1/2} \exp \left[\frac{e\phi(x, t)}{k T_e} \right]. \quad (4)$$

The positive values of v_x are taken while evaluating the integral in equation (3) because the electrode has been assumed to be perfectly absorbing. The sheath is formed due to transport of electrons and the ions being massive and moving randomly are held up at certain distance from the electrode. This situation is contrary to the Bohm criterion generally applicable in the case of dense plasma with $T_e \gg T_i$ and biased electrodes. Therefore, we assume a sharp boundary for ion sheath of density n which is formed around the electrode and is equal to ambient density n_0 . Since the sheath-thickness is small compared with the dimensions of the electrode, the potential $\phi(x, t)$ at any time t is described by one dimensional Poisson's equation.

$$\frac{\partial^2 \phi(x, t)}{\partial x^2} = -\frac{e}{\epsilon_0} (n_i - n_e). \quad (5)$$

Substituting for n_e from equation (2) and writing $n_i = n_0$, we rewrite equation (5) as

$$\frac{\partial^2 \phi(x, t)}{\partial x^2} = -\frac{en_0}{\epsilon_0} \left[1 - \exp \left(\frac{e\phi}{kT_e} \right) \right]. \quad (6)$$

In order to solve this equation for temporal variation of potential distribution, we define dimensionless variables

$$X = x/\lambda_D, \\ \Phi(X, t) = -\frac{e\phi(x, t)}{kT_e}, \quad (7)$$

where $\lambda_D = (\epsilon_0 kT_e / n_0 e^2)^{1/2}$ is the well known Debye length. Using these variables equation (6) simplifies to

$$\frac{\partial^2 \Phi}{\partial X^2} = [1 - \exp(-\Phi)]. \quad (8)$$

In order to obtain the spatial and temporal behaviour of $\Phi(X, t)$ it is essential to impose appropriate boundary conditions. In this case we assume that the potential and its gradient vanish as $x \rightarrow -\infty$. Integrating equation (8) with respect to X and applying this asymptotic condition, we obtain

$$-\left(\frac{\partial \Phi}{\partial X} \right)^2 = 2[\Phi + \exp(-\Phi) - 1]. \quad (9)$$

Putting $x = 0$ in equation (9), we obtain an expression for the potential gradient at the electrode at time t :

$$\frac{\partial \Phi(0, t)}{\partial X} = 2^{1/2} \{ \Phi(0, t) + \exp[-\Phi(0, t)] - 1 \}^{1/2}. \quad (10)$$

From Gauss law the electric field of a plane, infinite and conducting electrode is known to be independent of x and is written as

$$-\frac{\partial \phi}{\partial x} = \frac{\sigma}{\epsilon_0}, \quad (11)$$

where σ is surface charge density which results due to differential mobility of electrons and ions. According to Langmuir theory of sheath formation the random ion current density reaching the fixed electrode can be approximated as (Hoegy and Brace 1961).

$$j_i = n_0 e \left(\frac{kT_i}{2\pi m_i} \right)^{1/2}, \quad (12)$$

where e , m_i and T_i are the charge, mass and temperature of ion respectively and n_0 is ambient ion density. The surface charge density on the electrode is obtained with the help of equations (4) and (12).

$$\sigma(0, t) = \int_0^t \left\{ n_0 e \left(\frac{kT_i}{2\pi m_i} \right)^{\frac{1}{2}} - n_0 e \left(\frac{kT_e}{2\pi m_e} \right)^{\frac{1}{2}} \exp \left[\frac{e\phi(0, t)}{kT_e} \right] \right\} dt \quad (13)$$

Substituting for $\sigma(0, t)$ in equation (11) and rearranging in terms of dimensionless parameters we rewrite equation (11) as

$$\frac{\partial \Phi(0, t)}{\partial X} = -\frac{1}{\lambda_D} \left(\frac{kT_i}{2\pi m_i} \right)^{\frac{1}{2}} \int_0^t \left[1 - \alpha \left(\frac{T_e}{T_i} \right)^{\frac{1}{2}} \exp(-\Phi) \right] dt, \quad (14)$$

where

$$\alpha = \left(\frac{m_i}{m_e} \right)^{\frac{1}{2}}.$$

The linear relation between $\phi(0, t)$ and t is obtained by differentiating equations (10) and (14) with respect to t and equating their right hand sides. The resulting expression is written as

$$\frac{\partial \Phi(0, t)}{\partial t} = \frac{2^{\frac{1}{2}}}{\lambda_D} \left(\frac{T_i}{T_e} \right)^{\frac{1}{2}} \left(\frac{kT_i}{2\pi m_i} \right)^{\frac{1}{2}} \frac{[(T_e/T_i)^{\frac{1}{2}} \alpha \exp(-\Phi) - 1][\phi + \exp(-\Phi) - 1]^{\frac{1}{2}}}{[1 - \exp(-\Phi)]}. \quad (15)$$

Rearranging equation (15) we equate for a dimensionless parameter

$$\tau = \Lambda_{pi} t = \pi^{\frac{1}{2}} \left(\frac{T_e}{T_i} \right)^{\frac{1}{2}} \int_0^{\phi(0, t)} \frac{[1 - \exp(-\phi)] d\phi(0, t)}{[\alpha(T_e/T_i)^{\frac{1}{2}} \exp(-\phi) - 1][\phi + \exp(-\phi) - 1]^{\frac{1}{2}}}, \quad (16)$$

where $\Lambda_{pi} = (n_0 e^2 / m_i \epsilon_0)^{\frac{1}{2}}$ is ion plasma frequency. The analytical solution of equation (16) is not possible, therefore, the temporal variation of floating potential on the electrode has been obtained by numerical integration of equation (16). Further, the spatial variation of the time varying electrode potential is obtained by integrating equation (9) with respect to X and using the asymptotic condition at $x = -\infty$,

$$X = \frac{1}{2^{\frac{1}{2}}} \frac{\int_{\Phi(0, t)}^{\Phi(X, t)} d\Phi(X, t)}{[\phi + \exp(-\Phi) - 1]^{\frac{1}{2}}}. \quad (17)$$

The analytical solution of the integral in equation (17) is not possible, therefore, the computed results from equation (16) have been used to evaluate equation (17) and study the variation of floating potential within the sheath and plasma regions. Figure 1 shows the variation of floating potential with dimensionless.

parameter $\tau = \Lambda_D t$. The results obtained by this procedure are compared with the results reported by Anderson and Walsh (1971). We find that for small values of τ the Anderson and Walsh's formulation gives higher potential at the electrode (dotted curve in figure 1) and for certain value of τ the two formulations

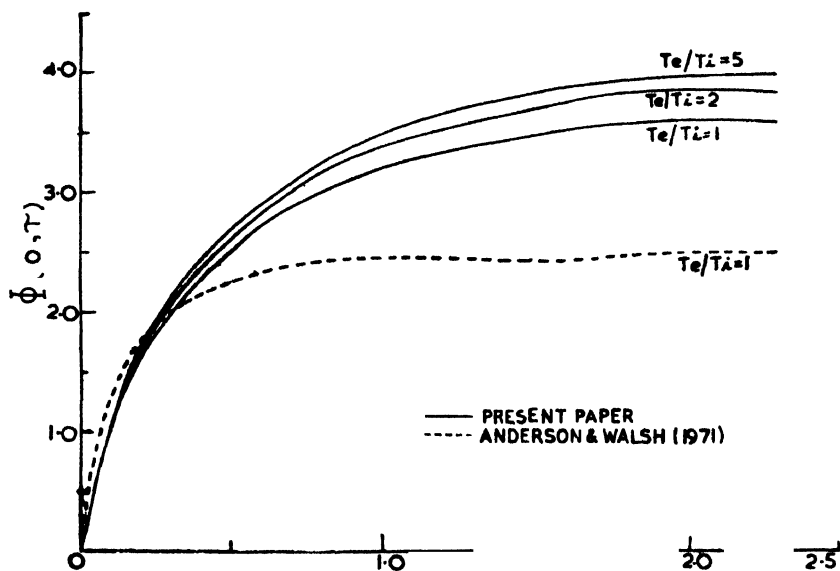


Figure 1. Variation of dimensionless electrode potential $\Phi(0, \tau)$ with τ for different T_e/T_i and $\alpha^2 = 1836$.

give same potential as shown by intersection of the two curves. Our formulation gives higher electrode potential for higher τ values. Therefore, we find that the time required for the floating potential to reach a steady state value is different for the two formulations. The most important effect of assuming the ions to be immobile is to enhance the floating potential on the electrode. Further it is seen that the steady state potential on the electrode is reached in a comparatively longer time. Within the framework of Langmuir's theory the effect of electron and ion temperature ratio on steady state electrode potential and rate of rise of electrode potential have been displayed in figure 1. The higher T_e/T_i ratio is found to establish a higher steady state potential on the electrode. The rate of rise of steady state potential is seen to increase rather slowly with increasing T_e/T_i . The spatial variation of the electrode potential for different values have been shown in figure 2. The potential at the electrode $x/\lambda_D \rightarrow 0$ is maximum and is found to decrease with increasing value of x/λ_D . At a fixed distance from the electrode the potential is seen to increase with increasing time. After certain time the steady state spatial and temporal distribution of electrode potential is reached. For very large values of x/λ_D and τ the potential variation curves

asymptotically approach the plasma potential. At a given time the electrode potential is seen to decrease faster than the potential distribution obtained by Anderson and Walsh (1971). The assumption of streaming ions (Anderson and Walsh 1971) seems to result into a higher plasma potential for large values of x/λ_D whereas the assumption of immobile ions asymptotically approaches to a comparatively lower plasma potential.

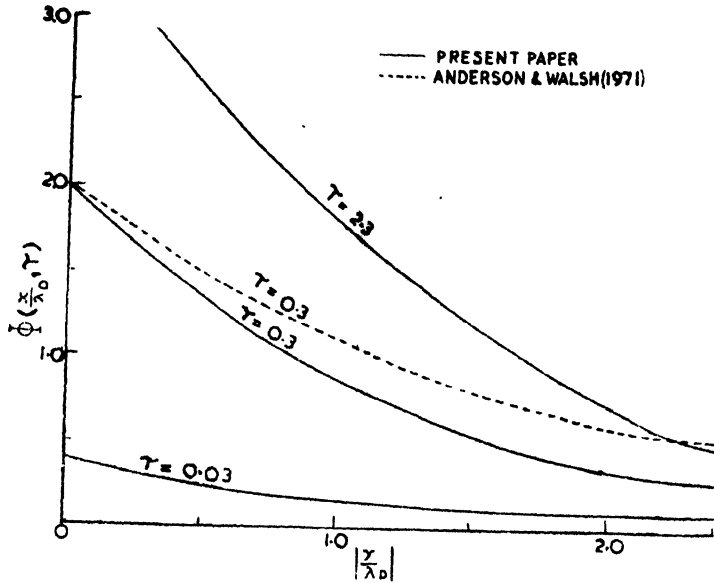


Figure 2. Variation of dimensionless potential $\Phi(x/\lambda_D, \tau)$ with $|x/\lambda_D|$ for different values of τ and $\alpha^2 = 1836$.

4. Steady state sheath thickness

4.1. Sheath around floating electrode

The ion sheath round an electrode is formed due to the flow of electrons toward the electrode. In a time sequence the electrode becomes negatively charged and holds ions around the electrode at a finite distance. The thickness of the ion sheath is governed by two forces acting on the sheath in opposite directions. These are thermal random motion and space charge limited movement encountering the thermal motion which govern the thickness of the ion sheath. The well known space charge limited ion current density for planar diode is written as

$$j_i = \frac{4e_0}{9} \left(\frac{2e}{m_i} \right)^{\frac{1}{2}} \frac{\phi_p^{3/2}}{S^2}, \quad (18)$$

where ϕ_p is equilibrium potential of the electrode and S is thickness of ion sheath. Equating the random ion current density and space charge limited current density we obtain an expression for the sheath thickness.

$$S = \left[\frac{4\epsilon_0}{9} \left(\frac{4\pi e}{kT_e} \right)^{\frac{1}{2}} \frac{\phi_p^{3/2}}{n_0 e} \right]^{\frac{1}{2}}. \quad (19)$$

This expression gives the sheath thickness variation as function of temperature and plasma density. With the help of equation (19) the sheath thickness has been computed and its variation with n_0 for different values of $T_e = T_i = T$ have been shown in figure 3. The steady state electrode potential for $T_e = T_i = T$ has been used from figure 1. Other parameters remaining constant the sheath

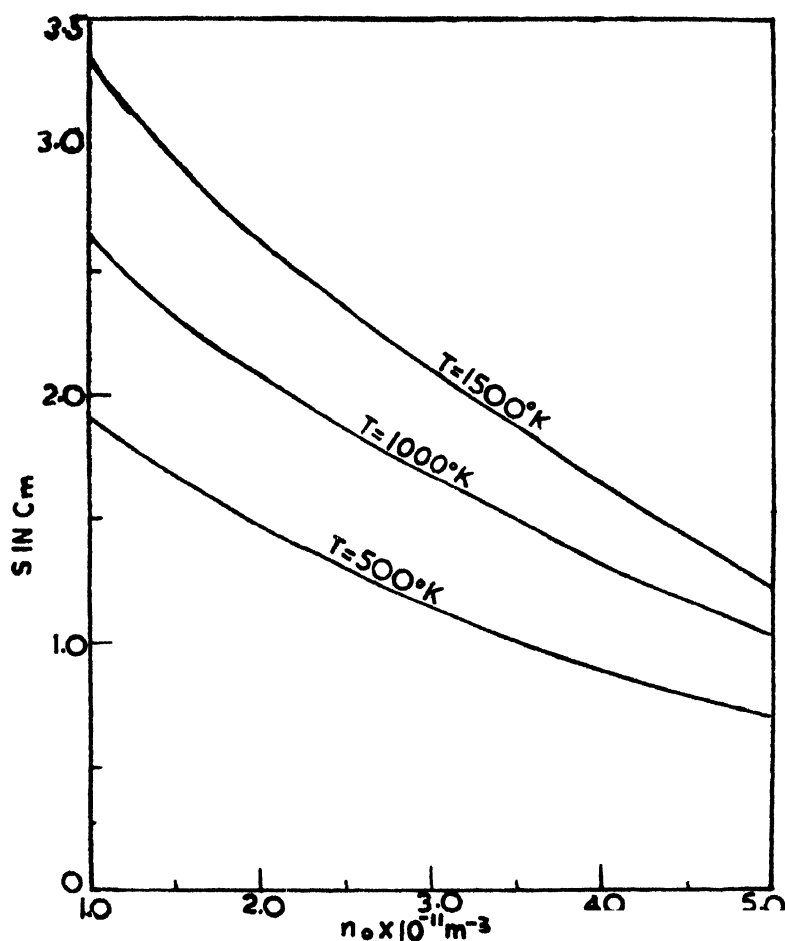


Figure 3. Variation of sheath thickness S with electron number density for different electron temperatures.

thickness has direct dependence on the steady state electrode potential. The temporal variation of ϕ_p depicted in figure 1 shows that the sheath thickness gradually increases with time and attains a steady state thickness.

4.2. Sheath around biased electrode

The potential distribution of a biased electrode highly depends on the size and shape of the electrode. So far we considered the physical features of sheath around a thin, flat and an infinite electrode. We now consider a thin cylindrical electrode which is most appropriate for diagnostic purposes. The potential distribution on the electrode, the electron density of the plasma and the temperature of the ambient plasma govern the effective impedance of the electrode. In a negatively biased electrode the sheath characteristics are chiefly governed by the magnitude of the bias potential. For certain applied d.c. potential the sheath around the electrode collapses and thereafter the electron density becomes uniform right up to the surface of the electrode (Wasserstrom *et al* 1965). The complete collapse of the sheath takes place at comparatively higher bias voltage. Therefore, as an approximation we assume that the ion sheath around the electrode is a thin sharply bounded cylindrical region and that there are no electrons within this region. This sharp ion sheath boundary is assumed to be at plasma potential. The electrode immersed in a plasma conforms to a configuration of a concentric cylinder. We proceed now to evaluate the electric field at the sheath boundary. The capacity of the electrode immersed in plasma is written as

$$C = \frac{2\pi\epsilon_0}{\ln(R/R_0)} F/m, \quad (20)$$

where

R = Sheath radius

R_0 = electrode radius

$\epsilon_0 = 8.9 \times 10^{-12} F/m$.

Let the electrode be biased negatively. The total charge on the electrode is

$$Q = 2\pi\epsilon_0 V / \ln(R/R_0) \text{ Coulombs/m},$$

where V = electrode bias potential in volts. The electric field at the sheath boundary is

$$E_s = - \left(\frac{\partial V}{\partial R} \right)_s = - V / [R \ln(R/R_0)] \text{ volts/m}. \quad (21)$$

For small bias potentials the ion sheath is of such a dimension that the total positive charge in the sheath equals the negative charge on the electrode. Such a charge distribution limits the electric field of the electrode within the inner

edge of the ion sheath. The polarization field arising from the electron deficiency is given by

$$E_p = \frac{(R^2 - R_0^2)n_0 e}{2R\epsilon_0} \text{ volts/m,} \quad (22)$$

where n_0 is ambient electron density/m³ and e is electronic charge in Coulombs. The size of the sheath is small therefore the electric field must be continuous over the sheath region. Now equating equations (21) and (22) we obtain

$$2\epsilon_0 V = n_0 e (R^2 - R_0^2) \ln(R/R_0). \quad (23)$$

Using this equation we have computed the thickness of the sheath with the magnitude of the bias potential in the case of a cylindrical electrode as shown in figure 4. The thickness of the sheath is seen to vary with the ambient electron

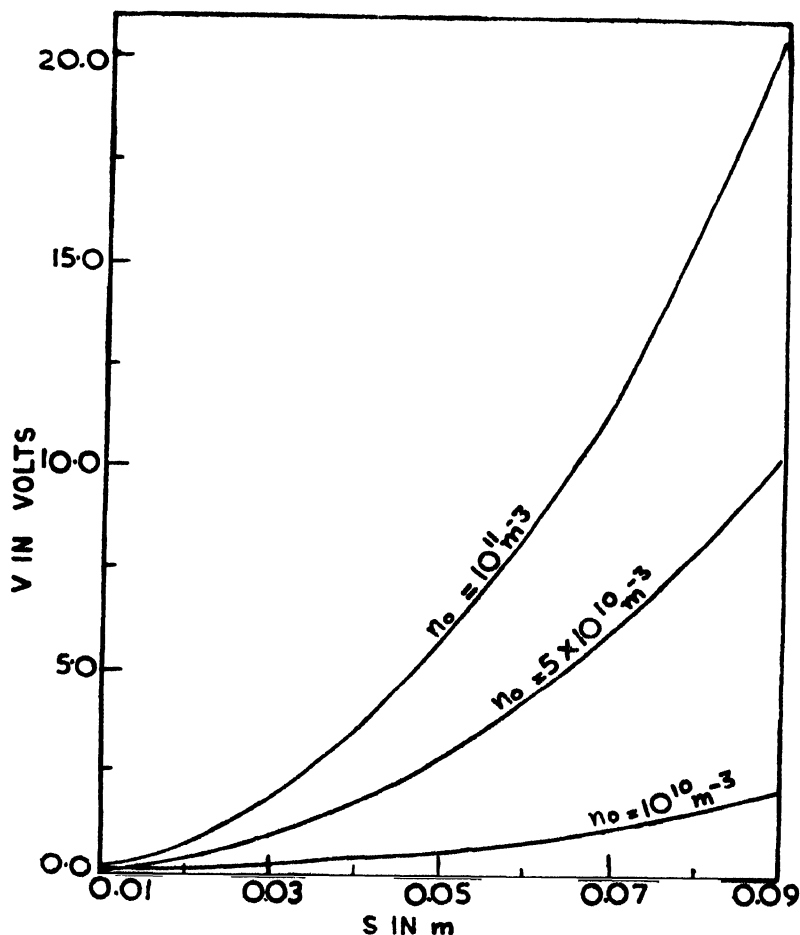


Figure 4. Sheath variation with d.c. bias potentials for plasma with different electron number density.

density. The high negative bias potential is seen to decrease the thickness of the sheath around the electrode which in turn changes the capacitance of the electrode system.

5. Conclusion

We have seen that the basic assumptions regarding plasma kinetics and microscopic behaviour result into significant change in the measurable parameters. Plasma sheath formation and its temporal and spatial variation are also governed by simplifying assumptions. Relaxing only one feature from the work of Anderson and Walsh (1971) we have shown the various consequential changes. Its effect on the bias electrode has been shown. The correct knowledge of these features would be helpful in using plasma immersed probes for diagnostic of ionospheric and space plasmas.

Acknowledgment

One of us (GPG) is thankful to the CSIR, New Delhi, for the award of post-doctoral fellowship.

References

- Anderson N and Walsh G R 1971 *Int. J. Electronics* **31** 217
- Hoogy W R and Brace L H 1961 *Sci. Report JS-1, Space Phys. Res. Lab., University of Michigan, USA*
- Huddleston R H and Leonard S L 1965 *Plasma Diagnostic Techniques* Academic Press, New York, London
- Jackson J E 1952 *NRL Rept.* 3909
- Jackson J E and Kane J A 1959 *NRL Rept.* 5345
- Jackson J E and Kano J A 1960 *J. Geophys. Res.* **65** 2209
- Jackson J E and Pickar A D 1957 *NRL Rept.* 4940
- Jastrow R and Pearse G A 1957 *J. Geophys. Res.* **62** 418
- Kane J A, Jackson J E and Whale H A 1962 *NASA Tech. Note D-1098*
- Langmuir I 1924 *Gen. Elec. Rev.* **27** 449
- Rose D J and Clark M 1961 *Plasmas and Controlled Fusion* John Wiley & Sons, New York p 195
- Swift J D and Schwar M J R 1970 *Electrical Probes for Plasma Diagnostics* Am Elsevier London
- Wasserstrom E C, Su C H and Probstein R F 1965 *Phys. Fluids* **8** 56

Letters to the Editors

Ultra-violet absorption spectrum of 2-aminopyrimidine

P V Shanbhag, M A Shashidhar and K Suryanarayana Rao

Physics Department, Karnatak University, Dharwad-580003, Karnataka

Received 1 November 1978, revised 5 February 1979

The electronic absorption spectrum of 2-aminopyrimidine was photographed in the vapour state on Hilger large Quartz Spectrograph using absorption lengths varying from 10 to 150 cms and temperature from 0° to 150°C.

The spectrum of the molecule lies approximately in the region 2745-3045 Å and consists of narrow bands which are degraded to the red. From the structural point of view 2-aminopyrimidine belong to C_s point group and the transition is an allowed $A'-A'$ transition with the transition moment lying in the plane of the molecule. The bands observed correspond to the ${}^1B_1 \leftarrow {}^1A_1$ transition of pyrimidine around 3200 Å.

The spectrum has been analysed with the help of the Raman and Infra-red data available in the literature (Spinner 1962, Lafai and Lebas 1970), and also with the help of the analyses of the corresponding spectrum of pyrimidine (Lord *et al* 1957, Simmons and Innes 1964, Innes *et al* 1969), 4- and 5-methyl pyrimidine (Shashidhar and Rao 1975, Shashidhar 1974) and 2-chloropyrimidine (Shashidhar and Rao 1976). The study of the effect of temperature on the band system has facilitated the choice of the band at 33622 cm^{-1} as the 0, 0 band of the system. Most of the bands could be accounted for in terms of two ground state fundamentals 406 and 608 cm^{-1} and five upper state fundamentals 376, 578, 726, 927 and 1019 cm^{-1} and two sequence intervals 113 and 162 cm^{-1} . The ground state fundamentals 406 and 608 cm^{-1} corresponding to the excited state fundamentals 376 and 578 cm^{-1} respectively are assigned to the modes ν_{6a} and ν_6 . The excited state fundamentals 376 cm^{-1} forms progressions and occurs in combination with other modes and is the most prominent feature of the spectrum. The excited state fundamentals 726, 927 and 1019 cm^{-1} are progression forming and they respectively correspond to the modes ν_{12} , ν_1 and ν_{6a} . Of the observed sequence intervals -113 and -162 cm^{-1} , 113 cm^{-1} may probably represent the 1-1 transition of ν_{16a} as suggested by Innes *et al* and -162 cm^{-1} the 1-1 transition of some other fundamental. Confirmation for this assignments of ν_{16a} sequence is obtained in this case from the identification of the corresponding 0-2 and 2-0 band from the 0, 0 band.

Table 1 gives only the prominent absorption bands of 2-aminopyrimidine and their assignments.

Table 1 Assignments of the prominent absorption bands of 2-aminopyrimidine

Wave number (cm ⁻¹) band Intensity	Assignments
33010 w	0, 0 - 608
33216 w	0, 0 - 406
33459 mw	0, 0 - 162
33509 w	0, 0 - 113
33622 s	0, 0
33998 ms	0, 0 + 376
34200 w	0, 0 + 578
34348 mw	0, 0 + 726
34366 mw	0, 0 + 2 × 376
34549 mw	0, 0 + 927
34581 mw	0, 0 + 578 + 376
34648 mw	0, 0 + 1019
34717 w	0, 0 + 726 + 376
34739 w	0, 0 + 3 × 376
34918 w	0, 0 + 927 + 376
35033 w	0, 0 + 1019 + 376
35086 w	0, 0 + 2 × 726
35123 w	0, 0 + 4 × 376
35278 w	0, 0 + 927 + 726
35458 w	0, 0 + 2 × 927
35501 w	0, 0 + 5 × 376
35634 w	0, 0 + 2 × 1019
35788 w	0, 0 + 3 × 726

References

- Innes K K, Meseolney H D, Simmons J D and Tilford S G 1969 *J. Mol. Spectr.* **31** 16
 Lafaix A J and Lobas J M 1970 *Spectrochim. Acta*. **26A** 1243
 Lord R C, Marston A L and Miller F A 1957 *Spectrochim. Acta* **9** 113
 Simmons J D and Innes K K 1964 *J. Mol. Spectro.* **29** 435
 Spinner E 1962 *J. Chem. Soc.* 3119
 Shashidhar M A 1974 *Indian J. Pure Appl. Phys.* **12** 726
 Shashidhar M A and Rao Suryanarayana K 1975 *Ind. J. Phys.* **49** 128
 Shashidhar M A and Rao Suryanarayana K 1976 *Indian J. Pure Appl. Phys.* **14** 689

On the virial coefficients of H_2O

S Singh

Department of Physics, Banaras Hindu University, Varanasi-221005.

Received 29 January 1979

The macroscopic properties of fluids are intimately related with the potential energy of group of molecules as a function of their mutual separation and orientation. Consequently, substantial improvements in the quantitative understanding of molecular forces between nonspherical molecules, and also improvements in the predicted behaviour of fluids, can be made provided the angle-dependence of the interactions is treated carefully. An investigation of the virial coefficients of the equation of state of a gas of nonspherical molecules furnishes valuable informations on molecular interactions and thus provides the possibility of evaluating many properties of the system having functional relation with these interactions. A systematic study of this kind is very necessary in the field of intermolecular forces and molecular liquids and recently has been made by us (Singh 1975, Singh and Singh 1976, 1977, Singh 1977). On the assumption that the dilute gas transport coefficients are less sensitive to the long-range angle-dependent interaction than the virial coefficients, we have explained the viscosity, second and third virial coefficients of a system of nonspherical molecules of arbitrary symmetry with the same set of force parameters.

The treatment of polar fluids has received much attention in the last few years. At least three different empirical potentials have been proposed over the years for calculating the molecular properties of polar fluids. The most common one is the Stockmayer 12-6-3 potential (Hirschfelder *et al* 1964) which is the Lennard-Jones potential augmented by dipole-dipole interaction. Another potential which has been proposed by Monchick and Mason (1961) considers the relative orientation of the molecules to remain fixed during a collision. Still another potential is the *preaveraged potential* of ours (Singh and Singh 1971, 1972) in which the angle-dependent parts of the interaction is represented by an averaged potential. The deciding factor which determines the appropriate potential has to do with the relative times for rotation and translation (collision). This has, however, been suggested but not demonstrated yet. In a previous paper (Singh and Singh 1977; referred to as I) we have applied the latter two potentials in the treatment of microscopic properties of polar gases. The second and third virial coefficients of NH_3 and CH_3F have been calculated using the

force parameters determined from the viscosity data. The transport and equilibrium properties of H_2O play a key role in many field such as Oceanography, Limnology, hydraulics, biochemistry and physical chemistry, therefore, its calculation will be of considerable importance. Adopting the procedure as outlined in I we report here the calculation of second and third virial coefficients of H_2O .

The pair and three-body interactions which are needed for the calculation of second and third virial coefficients can be written as

$$u(1, 2) = \phi_{12}(r_{12}) + v_{12}(r_{12}, \omega_1, \omega_2)$$

$$u(1, 2, 3) = \sum_{j>i=1}^3 u(i, j) + V(1, 2, 3).$$

The meaning of the symbols and the functional form of these interactions are summarized elsewhere (Stogryn 1969, 1970; Singh and Singh 1976).

The contribution of the different branches of the interaction to virial coefficients has been evaluated using the perturbation scheme as outlined in I in which tensor forces are taken as perturbation of the pair central potential. The values of the dipole and quadrupole moments and anisotropic polarizability available from independent measurements have been used in the calculation. The viscosity data have been used to determine the force parameters σ and ϵ/k and the second virial coefficient data the shape parameter D . The potential parameters obtained are given in table 1 together with other parameters used in the calculation. Using these parameters the contribution of the various interactions to the second virial coefficient has been evaluated. It has been found that all the branches of anisotropic interactions contribute significantly at all the temperatures investigated here. The calculated values are compared with the values obtained from the experimental data in table 2. It can be seen that the agreement between theory and experiment is better when the preaveraged potential is used.

For the potential parameters reported in table 1 we have evaluated the additive and nonadditive contributions to the third virial coefficient of H_2O for many values of T^* . From the calculation we find that at low temperatures

Table 1. Potential parameters used in virial coefficients calculation

Preaveraged model			Unaveraged model			$\mu \times 10^{18} \text{ } \alpha \text{ (}\text{\AA}^3\text{)}$		K	$\odot_{zz} \times 10^{26} \text{ esu cm}^2$	$\odot_{xx} \times 10^{26} \text{ esu cm}^2$
$\sigma(\text{\AA})$	$\epsilon/k(K)$	D	$\sigma(\text{\AA})$	$\epsilon/k(K)$	αD					
3.295	215	-0.25	2.710	506	-0.24	1.85	1.48	0.1351	-0.13(a)	2.63(a)

(a) Verhoeven and Dymanus (1970)

Table 2. Comparison of calculated and experimental second Virial coefficient

$T(K)$	$-B(T)$ (cm ³ /mole)		
	Exptl.	Calc.	
		Preaveraged	Unaveraged
423	338.0	332.6	301.5
523	153.1	152.0	150.0
573	116.8	116.6	116.9
623	92.0	95.6	104.5
723	59.1	59.8	71.0

all branches of pair and triplet interactions contribute substantially. However, at low temperatures the contributions of first order additive induction interaction and second-order nonadditive dispersion interaction are small. Figure 1 compares the calculated and experimental third virial coefficients. Experimental data which are given in the figure by dotted lines are due to Kell *et al* (1968). The values of third virial coefficient for the unaveraged and preaveraged potentials are given in the figure by dashed and full lines, respectively. It can be seen that the agreement between theory and experiment is not good for any method. Calculated values are always greater than the experimental values. But the values obtained at low temperatures for preaveraged method is closer to the experimental values than that of unaveraged method values. At temperatures above 500 K the unaveraged potential method give values which are closer to experiment than those predicted by the preaveraged potential. In I, however, we have found that the agreement between the calculated and experimental third virial coefficients of NH_3 and CH_3F is very satisfactory when preaveraged method is followed.

The structure of solid and liquid states of H_2O are known to have tetrahedral geometry (Eisenberg and Kauzmann 1969) which is interpreted as a consequence of the presence of strong orientational hydrogen bond. The hydrogen binding interaction dominates all other interactions at liquid and higher densities. From this it appears to us that the hydrogen binding interaction is always present in all the three states of H_2O and that the importance of this interaction increases with the density. In other words, the hydrogen binding interaction has strong many body character and that the potential function derived from the properties of one density cannot predict the property of the system at any other density unless a proper account for the hydrogen binding interaction is made. There-

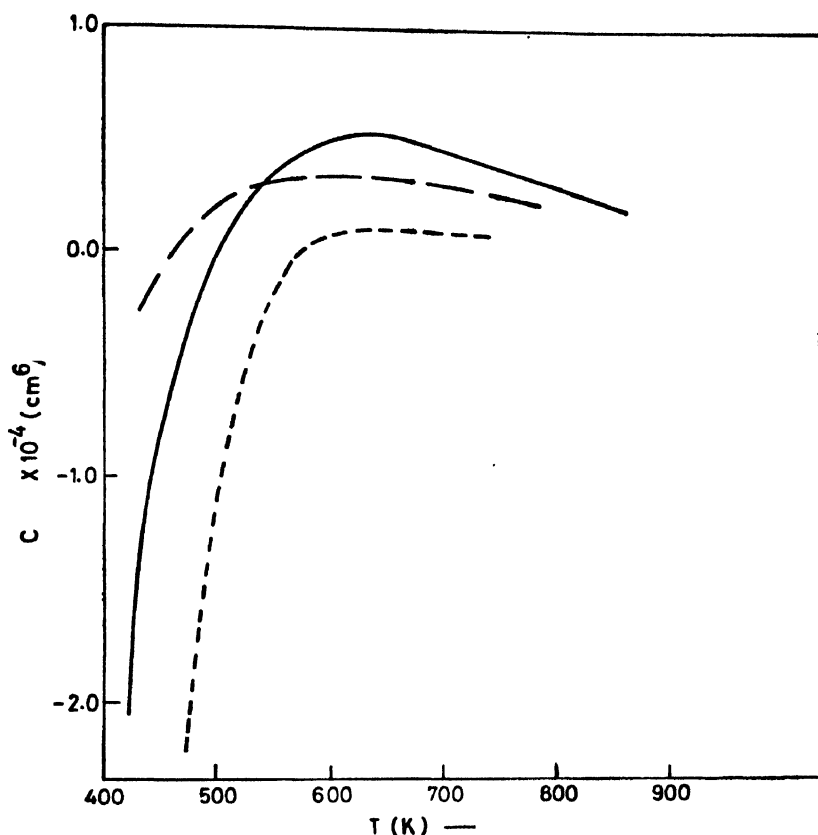


Fig. 1. Comparison of observed and calculated values of the third virial coefficient of H_2O . Dotted curve represents experimental values, full and dashed lines, respectively, represent the values calculated by the method of preaveraged and unaveraged and unaveraged potentials.

fore, the difference between the calculated and experimental third virial coefficients of H_2O may be attributed to hydrogen-binding interaction present in the cluster of three molecules. This interaction seems to be attractive for the most of the interior angles of triangle formed by the interacting molecules and the effect of this interaction on the third virial coefficient is opposite and larger than that of other three-body nonadditive interactions. As a result when a proper account of hydrogen-binding interaction will be taken in the calculation of third virial coefficient of H_2O the theory and experiment may agree satisfactorily.

Acknowledgment

The author wishes to thank Dr. Y. Singh for the helpful discussions and encouragement.

References

- Eisemberg D and Kauzmann 1969 *The structure and properties of water* (London: Oxford University Press)
- Hirschfelder J O, Curtiss C F and Bird R B 1964 *Molecular Theory of Gases and Liquids* (New York: John Wiley)
- Kell G S, McLaurins G E and Whalley E 1968 *J. Chem. Phys.* **48** 3805
- Monchick L and Mason E A 1961 *J. Chem. Phys.* **35** 1676.
- Singh S and Singh Y 1971 *J. Phys.* **B4** 776; 1972 **B5** 2039.
- Singh S and Singh Y 1976 *Physics* **83A** 339;
1977 *ibid* **87A** 209, 344
- Singh S 1977 *Physica* **89A** 219, *Ind. J. Phys.* **51A** 65
- Singh Y 1975 *Molec. Phys.* **29** 155
- Stogryn D E 1969 *J. Chem. Phys.* **50** 4967;
1970 *ibid* **52** 3671
- Verhoeven J and Dymanus 1970 *J. Chem. Phys* **52** 3222

Potential constants and centrifugal distortion constants of IOF_5 , ReOF_5 and OsOF_5

V Sengodan and K G Srinivasacharya

Department of Physics, FSG College of Arts and Science (Autonomous)
Coimbatore 641014, Tamilnadu.

Received 12 March 1979

A set of potential constants of the general valence type are evaluated for the molecules IOF_5 , ReOF_5 and OsOF_5 using the recent vibrational frequencies. The potential constants thus obtained are used to calculate the centrifugal distortion constants for the first time. The molecules belong to C_{4v} symmetry having eleven fundamental frequencies which are distributed into different species as $\Gamma_{\text{vib}} = 4A_1 + 2B_1 + 1B_2 + 4E$. Smith *et al* (1965) have assigned the vibrational frequencies of IOF_5 using Raman and Infrared spectra and carried out the normal co-ordinate analysis. Recently Holloway *et al* (1971) have assigned the frequencies relating to ReOF_5 and OsOF_5 . Further, the assignments relating to IOF_5 have been revised by them. In the present investigation the potential constants are evaluated using these recent vibrational frequencies. The symmetry co-ordinates and structural parameters used in the calculation are taken from references (Smith *et al* 1965, Holloway *et al* 1971, Sutton 1958).

The general valence force constants are obtained using Wilsons F-G matrix method and are presented in Table 1. It is observed that the equatorial stretching potential constant (f_r) is less than the corresponding axial stretching potential constant (f_R). Most of the interaction constants assume zero values in all the cases. In Table 1 the values obtained by Mohan (1977) by kinetic constant method are indicated for comparison and a fair agreement between the two values is observed.

The theory of centrifugal distortion constants has been developed by Kivelson and Wilson (1952, 1953) and has been further modified by Cyvin *et al* (1968). The method due to Cyvin *et al* is employed in the present investigation in evaluating the centrifugal distortion constants (τ 's). The τ elements are found to satisfy the following relations.

$$\tau_{xxxx} = \tau_{yyyy}, \tau_{xxzz} = \tau_{yyzz}, \tau_{zzzz} = \tau_{zzzz}$$

$$\text{and } 2\tau_{xyxy} = \tau_{xxzz} - \tau_{zzzz}.$$

The centrifugal stretching coefficients which are linear combinations of τ elements are also calculated and are reported in Table 2. Since all the molecules

are symmetric top, the centrifugal stretching coefficients R_5 , R_6 and δ_J vanish. It is noted that D_J is positive for all the molecules. This indicates that the centrifugal force about any given axis will always tend to increase the moment of inertia about that axis which in turn decreases the effective rotational constants. The centrifugal distortion constants are useful for the microwave analysis of these molecules.

Table 1. Potential Constants (m dyn/Å)

Force constants	IOF ₅	ReOF ₅	OsOF ₅
f_D	7.1410 (7.2742)	9.0253 (8.5477)	8.5573 (8.1964)
f_R	4.6911 (5.0742)	4.7637 (5.5688)	4.6477 (5.2164)
f_r	4.5333 (4.4097)	4.7100 (4.7505)	4.6159 (4.6699)
f'_{rr}	0.1579 (0.0653)	0.0537 (-0.0464)	0.0318 (0.0304)
f_α	0.2412 (0.4131)	0.4410 (0.1896)	0.4540 (0.2212)
f_β	0.3261 (0.2520)	0.5911 (0.3167)	0.5282 (0.3020)
f_γ	0.3859 (0.2417)	0.2644 (0.1845)	0.2634 (0.1518)
$f'_{\beta\beta}$	0.0230 (0.0123)	0.2247 (-0.1246)	0.1857 (-0.1528)
$f'_{\gamma\gamma}$	0.0230	0.2247	0.1857
$f_{\alpha\alpha}$	-0.0639 (-0.0036)	0.1285 (0.0843)	0.1452 (0.0743)
$f_{\beta\gamma}$	0.0602	0.0180	0.0120

Table 2. Centrifugal stretching coefficients (KHz)

Coefficient	IOF ₅	ReOF ₅	OsOF ₅
D_J	0.18035	0.12522	0.20052
D_K	-0.15551	-0.83256	-0.84545
D_{JK}	0.05192	0.77032	0.75240

R_5 , R_6 , $\delta_J = 0$ for symmetric top molecules.

Acknowledgment

The authors are thankful to the management and Professor D.K.P. Varadarajan, Principal, P.S.G. College of Arts & Science (Autonomous) for their kind encouragement.

References

- Cyvin S J *et al* 1968 *Z. Naturf.* **23a** 1649
Holloway J H *et al* 1971 *J. Chem. Phys.* **54** 4305
Mohan S 1977 *Bull. Soc. Chim. Belg.* **86** 531
Kivelson D and Wilson E B 1952 *J. Chem. Phys.* **20** 1575; *ibid* 1953 **21** 1229
Smith D F and Begum G M 1965 *J. Chem. Phys.* **43** 2001
Sutton L E 1958 *Chem. Soc. (London) Spec. Publ.* **11**.

New bands of $A^2\pi-X^2\Sigma^+$ system of BeCl

M P Varma and B L Jha

Department of Physics & Mathematics, Indian School of Mines, Dhanbad 826004

Received 2 April 1979

The band spectrum of BeCl molecule has been reported in emission, absorption and microwave discharge by different workers. Only one band system ($A^2\pi-X^2\Sigma^+$) has so far been attributed to this molecule. Colin *et al* (1972) carried out the rotational analysis of (0-0), (1-0), (1-1) and (2-1) bands of this system and reported the vibrational and rotational constants for the upper ($A^2\pi$) and lower ($X^2\Sigma^+$) states. Subbaram *et al* (1975) using microwave discharge through BeCl in presence of rare gas observed the $\Delta v = -2$ sequence in addition to earlier reported sequences of the $A^2\pi-X^2\Sigma^+$ system.

In an attempt to develop other band systems of this molecule the spectra of this molecule was excited in a microwave discharge. Specpure sample of anhydrous BeCl₂ obtained from M/s Fluka, Switzerland was placed in an electrodeless quartz tube of about 25 cm in length and 1.5 cm in diameter. The discharge was established by a C-type antenna of Philips model M.W/127 microwave oscillator operating at 2450 MHz and rated for the maximum output of 260 watt. Continuous evacuation of the discharge tube with vacuum pump and a power output of 120 watt were found adequate to maintain the bluish colour discharge. Photographs of the spectra were taken with Carlzeiss medium quartz spectrograph at a dispersion of 15 Å/mm at 3300 Å. An exposure of about 2 minutes was sufficient to develop the bands.

The spectrogram reproduced in Figure 1, reveals the existence of seven new red degraded bands extending from $\lambda\lambda 3375-3407$ Å in addition to all other previously reported bands of BeCl. Analysis of the observed bands was carried out as discussed by Herzberg (1950). It was found that the new bands form the $\Delta v = +2$ sequence of $A^2\pi-X^2\Sigma^+$ system of BeCl. The band heads data of these bands are given in table 1 along with their vibrational assignments.

The band heads are represented by the vibrational scheme :

$$\begin{aligned} \nu_{R1} = & 28029.58 + 813.32(v' + \frac{1}{2}) - 1.96(v' + \frac{1}{2})^2 \\ & - 840.33(v'' + \frac{1}{2}) + 8.71(v'' + \frac{1}{2})^2 - 6.48(v' + \frac{1}{2})(v'' + \frac{1}{2}) \end{aligned}$$

which agrees well with the vibrational scheme, for R_1 heads, given by Novikov *et al* (1960).

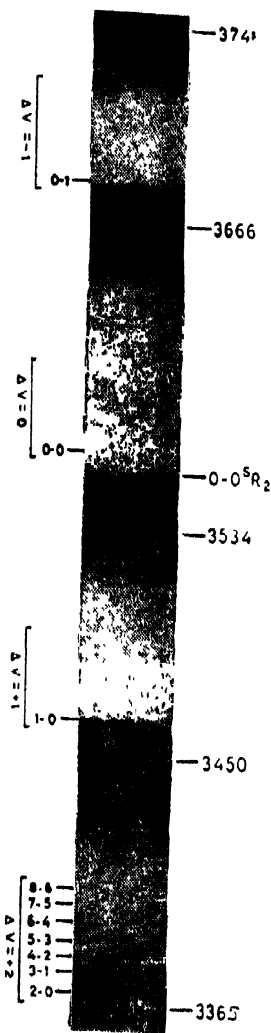


Figure 1

Table 1. Band head data of new bands with vibrational assignments.

Vib. assignments	Wave length in Å	Intensity on a scale of 10	$\nu_{ob.} - \nu_{cal.}$
2-0	3374.72	2	-0.83
3-1	3379.96	3	+1.35
4-2	3385.43	3	+0.14
5-3	3390.42	3	+1.86
6-4	3395.76	4	+0.61
7-5	3401.47	4	-1.01
8-6	3407.43	4	+1.40

References

- Colin R, Carleer M and Prevot F 1972 *Cand. J. Phys.* **50** 171
 Fredrickson and Hogan M E 1934 *Phys. Rev.* **46** 454.
 Herzberg G 1950 *Molecular Spectra and Molecular Structure I. Spectra of Diatomic*
 (D Van Nostrand & Co Inc New York)
 Novikov M M and Tuni Taskii L N 1960 *Opt. Spectrosc.* **8** 396.
 Subharam K V, Vasudeo R and Jones W E 1975 *Opt. Soc. Amer.* **65**. 318

RKRV Franck-Condon factors and r -centroids for the $(D^2\Sigma^+ - X^2\Sigma^+)$ transition of AlO

V M Mummigatti and B G Jyoti

Department of Physics, Karnatak University, Dharwar -580003

Received 25 March 1978, revised 6 December 1978

In view of the discovery (Donald and Innes 1969, Singh 1975) of some more electronic states of AlO molecule, the band system previously referred as due to $C^2\Sigma^+ - X^2\Sigma^+$ transition is now being referred to as $D^2\Sigma^+ - X^2\Sigma^+$. Franck-Condon (FC) factors and r -centroids for this transition, using approximate Morse and less appropriate RKR potential are available (Fraser and Jarman 1953, Kushwaha and Asthana 1972, Tawde and Tulasigeri 1972), only for 15 bands out of the 21 already reported by Krishnamachari *et al* (1966). A number of new bands belonging to this transition have been reported (Prasad and Narayan 1969). The purpose of the present paper is to report the FC-factors and r -centroids for the said transition for all the bands observed, using wavefunctions appropriate to a more realistic RKR potential. For this purpose the turning points required to construct the potential energy curves for the $D^2\Sigma^+$ and $X^2\Sigma^+$ states of AlO are obtained by the standard method (Singh and Jain 1972).

In the present study, four successive turning points are taken at a time and the potential energy, $U(r)$, is recorded at equal intervals of 0.01 Å for each vibrational quantum number. Ordinates of wavefunctions are determined by inserting these $U(r)$ values in Wu's (1952) expression and the corresponding FC-factors and r -centroids are computed accordingly. The results are given in Table 1.

It is expected that the FC-factors and r -centroids reported here, when taken in conjunction with intensities of the bands, yield valuable information regarding the electronic transition moment as a function of internuclear distance.

The authors acknowledge the financial assistance by U.G.C., New Delhi, to one of them (V.M.M.).

Table 1

$\rho' \rho''$	FC-factors	r-centroids Λ	$\rho' \rho$	FC-factors	r-centroids Λ
1, 0	2.1897×10^{-1}	1.6712	4, 2	1.1137×10^{-1}	1.6314
0, 1	3.6971×10^{-1}	1.7122	4, 3	8.1471×10^{-2}	1.6745
0, 2	2.7871×10^{-1}	1.7513	4, 4	7.2181×10^{-2}	1.7156
0, 3	1.0523×10^{-1}	1.7974	4, 5	4.1888×10^{-2}	1.7566
1, 0	3.0152×10^{-1}	1.6392	4, 7	2.1775×10^{-2}	1.8408
1, 2	7.7721×10^{-2}	1.7232	4, 8	1.2221×10^{-2}	1.9028
1, 3	2.7972×10^{-1}	1.7625	5, 3	5.1242×10^{-2}	1.6416
1, 4	1.9501×10^{-1}	1.8086	5, 4	4.9787×10^{-2}	1.6865
1, 5	6.4213×10^{-2}	1.8709	5, 5	4.3781×10^{-2}	1.7258
2, 0	2.2672×10^{-1}	1.6082	5, 6	1.9797×10^{-2}	1.7668
2, 1	1.0123×10^{-1}	1.6502	6, 3	4.1899×10^{-2}	1.6112
2, 4	1.5666×10^{-1}	1.7737	6, 4	3.9741×10^{-2}	1.6539
2, 5	2.4771×10^{-1}	1.8196	6, 5	3.0128×10^{-2}	1.6981
2, 6	1.3677×10^{-1}	1.8817	6, 6	2.7743×10^{-2}	1.7358
3, 0	1.3192×10^{-1}	1.5801	6, 7	1.0101×10^{-2}	1.7768
3, 1	5.1241×10^{-2}	1.6193	7, 4	1.1841×10^{-2}	1.6210
3, 2	4.0181×10^{-2}	1.6614	7, 5	1.1132×10^{-2}	1.6640
3, 4	1.0123×10^{-1}	1.7455	7, 6	1.0002×10^{-2}	1.7091
3, 6	2.1712×10^{-1}	1.8308	7, 7	9.9472×10^{-3}	1.7457
3, 7	2.1081×10^{-2}	1.9817	7, 8	9.1218×10^{-3}	1.7867
			8, 7	9.2187×10^{-3}	1.7199
			8, 8	9.0013×10^{-3}	1.7565

References

- McDonald J K and Innes K K 1969 *J. Mol. Spectry* **32** 501
 Frasher P A and Jarman W R 1953 *Proc. Phys. Soc.* **66A** 1153
 Krishnamachari S L N G, Narasimham N A and Mahaveer Singh 1966 *Can. J. Phys.* **44** 2513
 Kushwaha V S and Asthana B P 1972 *Indian J. Pure and Appl. Phys.* **10** 347
 Prasad S C and Narayan M K 1969 *Indian J. Pure and Appl. Phys.* **7** 413
 Singh M 1975 *J. Phys. (B)* **8** 308
 Singh N L and Jain D C *Proc. Phys. Soc.* 1972 **79** 274
 Tawde N R and Tulasigeri V G 1972 *J. Phys. (B)* **5** 1681
 Wu Ta You *Proc. 1952 Phys. Soc.* **65** 965

ERRATUM

Indian Journal of Physics Vol. **52B**, 1978, No. 4

p. 252, Fig. 15(ii) caption should read

“(a) Relative cross-section for the excitation of the Cs line $\lambda = 8512 \text{ \AA}$ (dark circles) and $\lambda = 5184 \text{ \AA}$ Mg line (light circles) against $1/v$, (b) Term scheme of the quasimolecule ($\text{Mg}^+ \text{Cs}$)”

instead of “Sputtering yield..... 75 \AA .”

p. 252 Fig. 16 caption should read

“sputtering yield S of Ag crystals as a function of energy of the colliding ions Ar^+ . Experimental points are compared with theory for three values of X_0 60 \AA ; $-\cdot-\cdot-$ 90 \AA ; $—$ 75 \AA .”

instead of “Experimental set up pattern”

page 255 under References

line 3, read Barwig P instead of Barwing P.

after line 7 add Bhattacharya R. S.,

Mukherjee D. K., Basu D. and Karmohapatro S. B. (1975) *Japan J. Appl. Phys.* **14**, 1591.

Biquadratic coupling in antiferromagnetic lattices

K G Chakraborty

Department of Physics, Basirhat College, 24-Parganas, West Bengal

Received 30 September 1977

Abstract. The sensitivity of Neel temperature to biquadratic coupling is studied. The method of Green function is applied to a two-sublattice antiferromagnet with both bilinear and biquadratic interactions. The higher order Green functions are decoupled by means of extended forms of Author's decoupling approximations previously introduced in ferromagnetic cases. It is seen that as the biquadratic coupling parameter increases from 0 to 1, the Neel temperature decreases by about 50% for a spin-1 BCC lattice. Numerical estimate is made for some wellknown antiferromagnetic compounds.

1. Introduction

The thermodynamics properties of a Heisenberg ferromagnet in the presence of biquadratic exchange were studied by a molecular-field approximation (Lines 1967, Brown 1971, Nauciel-Bloch *et al* 1972), a Green function approximation (Chadha 1974, Chakraborty 1974, 1975, 1976, 1977, Biogala 1975, Alder *et al* 1976, Kumar and Sharma 1976) and by Husimi Temperley model (Tanaka and Maunari 1976). From all these observations it has been found that the presence of biquadratic exchange affects the statistical mechanical properties of the system significantly. The occurrence of first order transitions and the new tri-critical points shed much light on the behaviour of magnetic systems (Chakraborty 1977). Although the quantitative verification of the theoretical predictions is not possible, the results have been found to correspond to definite experimental situations. One such example, namely, the occurrence of a first order transition in UO_2 has been already mentioned. Furthermore, the theoretical results regarding the steepness of the magnetization curves correspond to the observed behaviour.

In this paper we investigate the influence of an isotropic biquadratic exchange on Neel transitions in a two sublattice antiferromagnet, and present the numerical estimates with reference to the antiferromagnetic compounds KMnF_3 , MnO and NiO . It may at once be realized that the aspects of phase transitions in an antiferromagnetic lattice involve a good deal of complexities when a biquadratic term is included due to the fact that one has to distinguish in this case

two quadrupolar parameters corresponding to two sublattices which are not in general, equal in magnitude. If λ and μ are two sublattices then the bilinear order parameter and the quadrupolar order parameter are to be defined by

$$m_\lambda = \langle S_{\lambda i}^z \rangle, \quad m_\mu = \langle S_{\mu j}^z \rangle$$

$$B_\lambda = \langle (S_{\lambda i}^z)^2 \rangle - \frac{1}{2}S(S+1)$$

$$B_\mu = \langle (S_{\mu j}^z)^2 \rangle - \frac{1}{2}S(S+1).$$

It may be noted that although $m_\lambda = -m_\mu = m$ (say) such type of equality cannot be imposed on B_λ and B_μ consequently, one finds many different phase transitions occurring in the system and it is not easily possible to study them. We present here a discussion of the special case where $B_\lambda = B_\mu = 0$, which implies that our discussion concerns only with the dipolar transition or the usual Neel transition and with the study of sensitivity of Neel temperature to biquadratic exchange.

2. Mathematical Formalities

The Hamiltonian for a two sublattice antiferromagnet in the presence of biquadratic exchange may be written as

$$H = J \sum_{i,\Delta} S_{1,i} \cdot S_{2,i+\Delta} + J \sum_{j,\Delta} S_{1,j+\Delta} \cdot S_{2,j} \\ + \alpha J \sum_{i,\Delta} (S_{1,i} \cdot S_{2,i+\Delta})^2 + \alpha J \sum_{j,\Delta} (S_{1,j+\Delta} \cdot S_{2,j})^2. \quad (1)$$

The spontaneous magnetization in two sublattices is assumed to be in opposite direction ($+ZE$ and $-ZE$). The symbols 1 and 2 are sublattices and i is a lattice, site $\vec{\Delta}$ is a nearest neighbour vector.

The equation of motion for the Green function $G_{Ai}, B_j(E)$ is obtained as (Chakraborty 1976)

$$EG_{Ai}, B_j(E) = \delta_{AB}\delta_{ij} \frac{\langle S_{Ai}^z \rangle}{\pi} + 2J \sum_{\Delta} \ll (S_{Ai}^+ S_{c,i+\Delta}^z - S_{Ai}^z S_{c,i+\Delta}^+); S_{Bj}^- \gg \\ + 2\alpha J \sum_{\Delta} \ll [Q_{c,i+\Delta} \Phi_{Ai}^+ - Q_{Ai} \Phi_{c,i+\Delta}^+ + \frac{1}{2} \Phi_{c,i+\Delta}^- S_{Ai}^+ S_{Ai}^+ \\ - \frac{1}{2} \Phi_{Ai}^- S_{c,i+\Delta}^+ S_{c,i+\Delta}^+ + \frac{1}{2} (L_{c,i+\Delta} - L_{Ai})]; S_{Bj}^- \gg \quad (2)$$

where

$$\Phi^{\pm}_{Ai} = S^z_{Ai} S^{\pm}_{Ai} | \cdot S^{\pm}_{Ai} S^z_{Ai}$$

$$Q_{Ai} = \langle (S^z_{Ai})^2 \rangle$$

$$L_{Ai} = S^z_{Ai} S^{+}_{Ai} S^{+}_{c, i+\Delta} S^{-}_{c, i+\Delta} + S^{\pm}_{Ai} S^z_{Ai} S^{-}_{c, i+\Delta} S^{+}_{c, i+\Delta}$$

To decouple the bilinear Green functions we follow the arguments of Leo and Liu (1967). We extend the decoupling of the Author (Chakraborty 1976b) to the present case. The result is

$$\begin{aligned} & \ll S^z_{Ai} S^{+}_{c, i+\Delta}; S^{-}_{Bj} \gg \\ & = \langle S^z_{Ai} \rangle \{ 1 - a(1+\lambda) \langle S^{-}_{Ai} S^{+}_{Ai} \rangle \} \ll S^{+}_{c, i+\Delta}; S^{-}_{Bj} \gg \\ & + a \langle S^z_{c, i+\Delta} \rangle (1+\lambda) \langle S^{-}_{Ai} S^{+}_{c, i+\Delta} \rangle \ll S^{\pm}_{Ai}; S^{-}_{Bj} \gg. \end{aligned} \quad (3)$$

The five-spin biquadratic Green functions are first decoupled by RPA to three-spin Green functions which we decouple on the basis of the Author's method of decoupling (Chakraborty 1976a).

$$\begin{aligned} & \ll \Phi^{+}_{Ai}; S^{-}_{Bj} \gg \\ & = \frac{\langle S^z_{Ai} \rangle}{\delta} [1 + \lambda_1] \langle S^{-}_{Ai} S^{+}_{Ai} \rangle \\ & + \lambda_2 \langle S^{-}_{Ai} S^{+}_{Ai} \rangle^2 \ll S^{+}_{Ai}; S^{-}_{Bj} \gg \end{aligned} \quad (4)$$

The ground state requirements to be used here are:

(i) For spin $-\frac{1}{2}$ case

$$1 + \lambda_1 \langle S^{-}_{Ai} S^{+}_{Ai} \rangle + \lambda_2 \langle S^{-}_{Ai} S^{+}_{Ai} \rangle^2 = 0 \quad (5)$$

(ii) For any spin S , the bilinear exchange constants is modified by the factor

$$1 + 2\alpha S(S-1).$$

3. Energy Spectrum and Neel Temperature

Using the decoupling approximations mentioned above and Fourier transforming one gets the energy spectrum as

$$E_k = D(0)[1 - \gamma^2(k)] \quad (6)$$

where

$$\begin{aligned} D_A(k) = 2m_A J(k) & \left[1 - \frac{1}{2}\alpha - \frac{a(1+\lambda)}{N} \sum_{k'} F_{CA}(k') \right. \\ & \left. + \frac{a(1+\lambda)}{N} \sum_{k'} \gamma(k') F_{CA}(k') \right] \end{aligned} \quad (7)$$

$$J(k) = ZJ\gamma(k) - J \sum_{\Delta} \exp(i\mathbf{K} \cdot \Delta). \quad (8)$$

We have assumed

$$B_{Ai} = B_{e, i+\Delta} = 0 \quad (9)$$

also we have utilized the symmetric relations

$$D(k) = D^1(k) = \gamma(k)D(0) = -D_2(k) \quad (10)$$

$$m_1 = -m_2 = m \text{ (say)}. \quad (11)$$

The symbol $F_{CA}(k)$ is the Fourier transform of F_{Aa} , $c_e = \langle S^-_{Aa} S^+_{Ce} \rangle$.

It is a straight forward procedure to derive the expression for Neel temperature. We do not describe here the details which will be found in a recent paper of the Author (Chakraborty 1976c). The final result is

$$\tau_N(\alpha) = \frac{k_B T_N}{ZJ} = \frac{C_0}{I_0} [1 - \frac{1}{2}\alpha - \alpha C_0(1+\lambda)] \times \left[1 + \frac{\alpha C_0(1+\lambda)}{1 - \frac{1}{2}\alpha - \alpha C_0(1+\lambda)} \left(\frac{I_0 - 1}{I_0} \right) \right] \quad (12)$$

where

$$I_0 = \frac{2}{N} \sum_k \frac{1}{1 - \gamma^2(k)}, \quad C_0 = 2/3S(S+1).$$

For $\alpha = 0$, equation (12) reduces to that of Lee and Liu (1967). As α increases, T_N decreases gradually. In figure 1, we have plotted $T_N(\alpha)/T_N(0)$ against α which shows that as α increases from 0 to 1, T_N for a spin-1 BCC lattice decreases by about 50%.

4. Numerical Estimates

We shall make some numerical estimates for some well-known antiferromagnetic compounds where both the bilinear and biquadratic interactions are present.

1. KMnF_3

For this compound one finds $S = 5/2$, $T_N = 88^\circ\text{K}$ and $Z = 6$. Along with these data if one chooses $J/k_0 = 3.6^\circ\text{K}$, $\alpha = .02$, one finds that equation (12) is satisfied. These values of J/k_0 and α may be compared with those obtained by Joseph (1965) from the high temperature match of the susceptibility data. Joseph's results are: $J/k_B = 4.02^\circ\text{K}$, $\alpha = .015$. Srivastava (1976) performed a rigorous calculation of biquadratic superexchange and found that for KMnF_3 , the values of the interaction parameters are $J/k_B = 4^\circ\text{K}$, $\alpha = .01$. We, therefore, see that equation (12) is able to reproduce the numerical estimate for KMnF_3 fairly accurately.

2. *MnO*

MnO has the NaCl structure at high temperatures but undergoes rhombohedral structural distortion at the Neel temperature 120°K . One has for this compound $S = 5/2$, $Z = 8$. Rodbell *et al* (1963) estimated $\alpha = .05$ and $J/k_B = 3^\circ\text{K}$. If we now substitute this value of α in equation (12) we obtain $J/k_B \simeq 15^\circ\text{K}$ which thus differs markedly from the value obtained by Rodbell *et al* (1963). On the otherhand, if one uses the value of J/k_B of Rodbell *et al* in

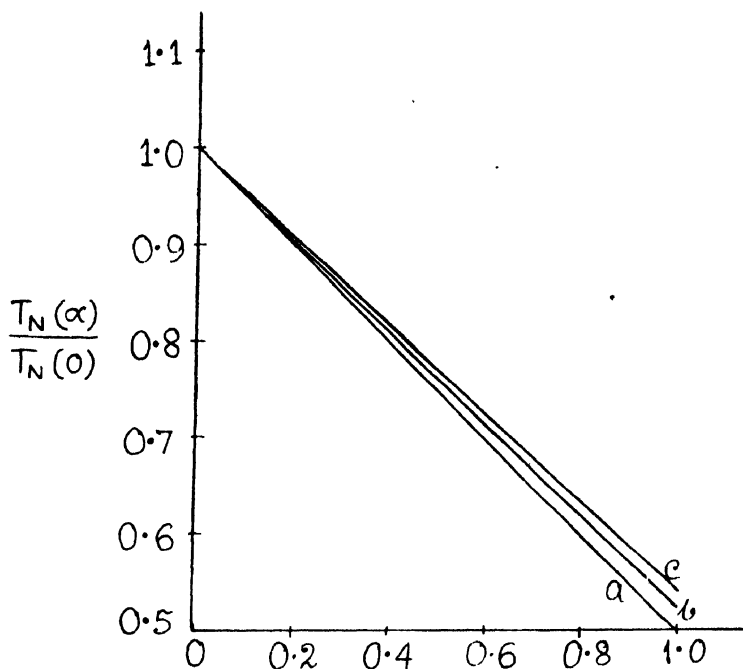


Figure 1. The sensitivity of Neel temperature to biquadratic coupling for a bcc antiferromagnet is shown considering several spin values. Curves a, b, c correspond to spin-1, spin-3/2 and spin-2 respectively.

equation (12) the value of α turns out to be much larger than the value estimated by Rodbell *et al*. It may, however, be appreciated that since MnO undergoes a first order phase transition at Neel temperature it should have a large α so that it crosses the critical value (Chakraborty 1977b).

3. *NiO*

This compound possesses a BCC structure with $S = 5/2$ and undergoes an antiferromagnetic transition at 523°K . Using the value of obtained by Rodbell *et al* ($\alpha = .04$) one finds $J/k_B \simeq 180^\circ\text{K}$. This value may be compared with the theoretical value obtained by Kanamori (1964) which is $J/k_B \simeq 150^\circ\text{K}$.

References

- Alder J, Oitmaa J and Stewart A M 1976 *J. Phys. C.* **9** 2011
Biegala L 1976 *Phys. Status Solidi (b)* **75** 333
Chadha G 1973 *Lett. Nuovo Cimento* **7** 163
Chakraborty K G 1974 *Z. Physik* **268** 179
——— 1975 *Indian J. Phys.* **49** 455
——— 1976a *J. Phys. C.* **9** 1499
——— 1976b *J. Phys. C.* **9** 4411
——— 1976c *Indian J. Phys.* **50** 553
——— 1977 *J. Phys. C.* **10** 297
Kamamori J 1963 in *Magnetism*, ed. by Rado G T and Suhl H Vol. 1, p 127
Kumar V and Sharma K C 1976 *Solid State Comm.* **20** 1167
Lee K H and Liu S H 1967 *Phys. Rev.* **159** 390
Rodbell D S, Jacobs I S, Owen J and Harris E A 1963 *Phys. Rev. Letters* **11** 10
Srivastava K N 1976 *Phys. Lett.* **56A** 399
Tanaka M and Mannari I 1976 *J. Phys. Soc. Japan* **41** 741

The effect of anharmonicity on the optical properties of silver and thallium halides

Vinod Kumar*, L K Bansal and S C Goyal

Department of Physics, Agra College, Agra-282002

Received 13 December 1977

Abstract. In the present study the value of the volume derivatives of the Szigeti effective charge in silver and thallium halides have been predicted using a phenomenological lattice theory of the elastic dielectric. The calculated values of $\frac{V}{e^*} \left(\frac{de^*}{dV} \right)$ have been utilised to evaluate the values of the Gruneisen constant parameter of these solids which are found in excellent agreement with the experimental results. The behaviour of the silver and thallium ions in their anharmonic optical properties has also been critically discussed.

1. Introduction

On the basis of the macroscopic theory of the dielectric constants, Szigeti (1950) has proved that during optical vibrations of the ionic lattices, the ionic charge is substantially modified. The effective ionic charge, thus obtained, is a measure of the deformations produced in the electron clouds while the ion vibrates. The experimental values of the Szigeti effective charge e_s are found to be less than unity in all the crystals. The thallium halides have the slightly larger values of e_s than for most of the alkali halides. However, both silver and thallium halides have the low value of the fractional ionic character in both Phillips (1970) and Goyal (1976) ionicity scales. These studies are limited to the harmonic approximations. On the other hand the measured values of the volume derivatives of the dielectric constants by Samara (1968), Lowndes (1970, 1972) which are related to anharmonic behaviour, have nearly equal values in all the silver, thallium and alkali halides and thus these halides under the stress do not show any distinguishable nature in their behaviour. Several theoretical attempts by Goyal *et al* (1974) and Bakhshi *et al* (1976) have been made in the past to explain the harmonic properties of the silver and thallium halides, however, anharmonic behaviour of these solids has not been analysed extensively (Aggarwal and Szigeti 1970). Therefore, it is necessary to analyse the Szigeti relation and other related properties in the cases of silver and thallium halides under the stress with an appropriate sophisticated model.

*Department of Physics, B.S.A. College, Mathura (India).

Recently, V. Kumar *et al* (in press) have described a phenomenological lattice model of elastic dielectric of NaCl and CsCl structure type solids based on the Srinivasan (1968) lattice theory. The theory has explained successfully the volume derivatives of the static dielectric constant of the silver and thallium halides. In the present study, we extend the earlier study to obtain the values of the volume derivatives of the effective charge e_s which are used to evaluate the Gruneisen parameter ν_{T0} and to analyse the role of anharmonicity in the optical properties of the silver and thallium halides.

2. Calculation and results

The expression for the effective charge e_s ($= e^*/e$) given by the Szigeti (1950) is

$$\epsilon_0 - \epsilon_\infty = \frac{4\pi}{9v} \frac{e_\infty^2}{\mu \omega_{T0}^2} e_s^2 e^2 \quad (1)$$

where v is the volume of the unit cell, ϵ_0 and ϵ_∞ are the static and high frequency dielectric constants respectively, μ is the reduced mass per ion pair, ω_{T0} is the characteristic transverse optic mode frequency. The temperature independent volume derivative of the equation (1) gives the expression for the Gruneisen parameter ν_{T0} associated with transverse optic mode phonon as

$$\begin{aligned} \nu_{T0} &\equiv - \frac{V}{\omega_{T0}} \left(\frac{\partial \omega_{T0}}{\partial V} \right)_T \\ &= \frac{1}{2} - \frac{V}{e_s} \left(\frac{\partial e_s}{\partial V} \right) - \frac{V}{\epsilon_\infty} \left(\frac{\partial \epsilon_\infty}{\partial V} \right) \left[\frac{\epsilon_\infty}{\epsilon_\infty + 2} + \frac{\epsilon_\infty}{2(\epsilon_0 - \epsilon_\infty)} \right] \\ &\quad + \frac{\epsilon_0}{2(\epsilon_0 - \epsilon_\infty)} \frac{V}{\epsilon_0} \left(\frac{\partial \epsilon_0}{\partial V} \right) \end{aligned} \quad (2)$$

The evaluation of the ν_{T0} require the values of ϵ_0 , ϵ_∞ , $\frac{\partial \epsilon_\infty}{\partial V}$, $\frac{\partial \epsilon_0}{\partial V}$ and $\frac{\partial e_s}{\partial V}$. The values of ϵ_0 and ϵ_∞ for the halides under study have been measured by Lowndes and Martin (1969). The lattice theory of elastic dielectric by Srinivasan (1968) has been used to obtain the values of the volume derivatives of the ϵ_0 , ϵ_∞ and e_s . Within the frame work of simple lattice theory by Kumar *et al* (1979) the Szigeti effective charges e_s is obtained in the following form.

$$e_s = 1 + \frac{Y_2 f}{K_2 + f} \quad (3)$$

where y_2 , K_2 are the shell charge and the spring constant of the negative ion

respectively, f is the short range force constant. The volume derivatives of the effective charge viz. $\frac{1}{e_s} \left(\frac{\partial e_s}{\partial V} \right)$ is obtained with the help of equation (1) in the following form :

$$\frac{1}{e_s} \left(\frac{\partial e_s}{\partial V} \right) = \left(1 - \frac{e}{e^*} \right) \frac{1}{3V} (C_1 + 2A_1 - 2B_1) \frac{1}{f} \left(\frac{K_2}{K_2 + f} \right) \quad (4)$$

where $f = A_1 + 2B_1$.

The basic equations of the shear modulus and the dielectric constant for the evaluation of the model parameters are given below :

NaCl structure

$$C_{11} - C_{12} = \frac{e^2}{4a^4} \left[-5.3380 + A_1 + B_1 + \frac{A_2 + 7B_2}{2} \right] \quad (5a)$$

$$C_{44} = \frac{e^2}{4a^4} \left[2.5560 + B_1 + \frac{A_2 + 3B_2}{2} \right] \quad (6a)$$

$$A_1 = \frac{4a^3}{e^2} \left[\frac{d^2 \phi_1(r)}{dr^2} \right]_{r=a}$$

$$B_1 = \frac{4a^3}{e^2} \left[\frac{1}{r} \frac{d\phi_1(r)}{dr} \right]_{r=a}$$

$$C_1 = \frac{4a^3}{e^2} \left[r \frac{d^3 \phi_1(r)}{dr^3} \right]_{r=a} = \frac{A_1^2}{B_1} \quad (7a)$$

$$A_2 = \frac{4a^3}{e^2} \left[\frac{d^2 \phi_2(r)}{dr^2} \right]_{r=a\sqrt{2}} \quad (8a)$$

$$B_2 = \frac{4a^3}{e^2} \left[\frac{1}{r} \frac{d\phi_2(r)}{dr} \right]_{r=a\sqrt{2}} \quad (9a)$$

CsCl structure :

$$C_{11} - C_{12} = \frac{e^2}{4a^4} \left[-1.2211 + \frac{B_1}{2} + \frac{A_2}{2} \right] \quad (5b)$$

$$C_{44} = \frac{e^2}{4a^4} \left[-0.3505 + \frac{A_1 + 2B_1}{6} + \frac{B_2}{2} \right] \quad (6b)$$

$$A_1 = \frac{16a^3}{e^2} \left[\frac{d^2\phi_1(r)}{dr^2} \right]_{r=a\sqrt{3}}$$

$$B_1 = \frac{16a^3}{e^2} \left[\frac{1}{r} \frac{d\phi_1(r)}{dr} \right]_{r=a\sqrt{3}}$$

$$C_1 = \frac{16a^3}{e^2} \left[r \frac{d^3\phi_1(r)}{dr^3} \right]_{r=a\sqrt{3}} = \frac{A_1^2}{B_1} \quad (7b)$$

$$A_2 = \frac{8a^3}{e^2} \left[\frac{d^2\phi_2(r)}{dr^2} \right]_{r=2a} \quad (8b)$$

$$B_2 = \frac{8a^3}{e^2} \left[\frac{1}{r} \frac{d\phi_2(r)}{dr} \right]_{r=2a} \quad (9b)$$

The expressions for the optical vibrational frequency at zone centre and the Lorentz-Lorenz relation in the frame work of simple shell model of Woods *et al* (1960) are given below—

$$\frac{3}{4\pi} \frac{\epsilon_\infty - 1}{\epsilon_\infty + 2} = \frac{y_2^2}{K_2 + f} \quad (10)$$

$$1 - \omega_{To} \left(\frac{\epsilon_0 - \epsilon_\infty}{4\pi} \right)^{\frac{1}{2}} \frac{3}{\epsilon_\infty + 2} \left(\frac{\mu V}{e^2} \right)^{\frac{1}{2}} = - \frac{y_2 f}{K_2 + f} \quad (11)$$

The short range next nearest neighbour interaction potential $\phi_2(r)$ is considered to be of vander Waal's type i.e. $\phi_2(r) = -\frac{C}{r^6} - \frac{D}{r^8}$. The parameters A_2 and B_2 are evaluated with the help of equations (8-9) using the recent values of the van der Waal's coefficients from Bakshi *et al* (1977). The values of the parameters A_1 , B_1 and C_1 are evaluated with the help of equations (5-7) using the constants given in the V. Kumar *et al* (in press). The shell model parameters y_2 , K_2 are evaluated using the relations (10) and (11) with the help of the optical data from Lowndes and Martin (1969). The experimental values of $\left(\frac{e_s}{e} \right)$ are also taken from Lowndes and Martin (1969). The all determined model parameters are used to evaluate the magnitude of $\frac{1}{e_s} \left(\frac{\partial e_s}{\partial V} \right)$ with the help of equation (4) and are displayed in the table.

Table 1.

Crystals	$\frac{V}{e_s} \left(\frac{\partial e_s}{\partial V} \right)$	$A \quad \frac{V}{e_\infty} \left(\frac{\partial e_\infty}{\partial V} \right)$	$B \quad \frac{V}{e_0} \left(\frac{\partial e_0}{\partial V} \right)$	$(\nu_{T_0})_{cal}$	$(\nu_{T_0})_{Exp}$
AgCl	0.2362	-1.1474	10.5616	6.31	5.0 ± 1.0
AgBr	0.3366	-1.3793	10.1614	5.95	5.6 ± 1.1
TlCl	0.2873	-1.3518	5.6454	3.81	3.9 ± 0.8
TlBr	0.3415	-1.6735	5.3703	3.83	3.8 ± 0.8

$$\text{where } A = \left[\frac{e_\infty}{e_\infty + 2} + \frac{e_\infty}{2(e_0 - e_\infty)} \right] ; \quad B = \left(\frac{e_0}{e_0 - e_\infty} \right)$$

It is striking to note from the table that the values of the volume derivatives of the effective charge in the cases of silver and thallium halides are nearly same and are very close to the values of this parameter for the alkali halides obtained by Barron and Batana (1969) using the deformation dipole model. Thus present study reveals that the values of the effective charge of the silver, thallium and alkali halides like the experimental measured values of the volume derivative of the static dielectric constant by Samara (1968), Lowndes *et al* (1970) and Lowndes (1972) do not show any remarkable distinction between them. The above observations strongly suggest that under the stress silver and thallium ions play an important role in bringing out the similar behaviour with alkali halides. The large contribution of these ions may be due to the presence of the *d*-core level in the optical spectra (Van Vechten 1969) of the silver and thallium halides. That is why the effect of anharmonicity on the optical properties of the silver and thallium halides is significant in comparison to other simple ionic solids like alkali halides. Which is also evident from the larger values of the Gruneisen constant parameter in these solids than for alkali halides (Ramji Rao 1975).

The theoretically predicted values of $\frac{V}{e_s} \left(\frac{\partial e_s}{\partial V} \right)$ for the silver and thallium halides are used to evaluate the values of ν_{T_0} with the help of equation (2). The values of the $\frac{V}{e_\infty} \left(\frac{\partial e_\infty}{\partial V} \right)$ and $\frac{V}{e_0} \left(\frac{\partial e_0}{\partial V} \right)$ of those solids are taken from the V. Kumar *et al* (in press) and of the other parameters from Lowndes and Martin (1969). The calculated values of the ν_{T_0} are also given in the table. It is worth noting here that the calculated values of ν_{T_0} are in excellent agreement with the experimental values, which further support the predicted low values of the $\frac{V}{e_s} \left(\frac{\partial e_s}{\partial V} \right)$ for these halides.

References

- Aggarwal K G and Szigeti B 1970 *J. Phys.* **C3** 1097
- Bakshi P S, Goyal S C and Jai Shanker 1976 *Indian J. Pure and App. Phys.* **14** 598
- Bakshi P S, Goyal S C and Jai Shanker 1976 *Indian J. Pure and App. Phys.* **14** 1017
- Bakshi P S, Goyal S C and Jai Shanker 1977 *J. Nucl. Ing. Chem.* **39** 546
- Barron T H K and Batana A 1969 *Phil. Mag.* **20** 619
- Goyal S C 1976 *Solid State Comm.* **20** 269
- Goyal S C, Aggrawal L D and Verma M P 1974 *Phys. Rev.* **B10** 779
- Kumar V and Goyal S C *Indian J. Phys.* (in press)
- Lowndes R P and Martin D H 1969 *Proc. Roy. Soc.* **A308** 473
- Lowndes R P and Martin D H 1970 *Proc. Roy. Soc.* **A316** 351
- Lowndes R P 1972 *Phys. Rev.* **B6** 4667
- Ramji Rav A 1975 *J. Phys. Soc. Japan* **38** 1080
- Szigeti B 1950 *Proc. Roy. Soc.* **A204** 51
- Samara G A 1968 *Phys. Rev.* **165** 969
- Srinivasan R 1968 *Phys. Rev.* **165** 1041
- Van Vechten J A 1969 *Phys. Rev.* **182** 891
- Woods A D B, Cochran W and Brockhouse B N 1960 **119** 980

Electron paramagnetic resonance of Mn^{2+} in $\text{NaH}_2\text{PO}_4 \cdot 2\text{H}_2\text{O}$ single crystals

Vimal Kumar Jain

Department of Physics, Indian Institute of Technology, Kanpur 208016

Received 21 November 1978

Abstract. The electron paramagnetic resonance of Mn^{2+} doped in $\text{NaH}_2\text{PO}_4 \cdot 2\text{H}_2\text{O}$ single crystals has been studied at X-band and at 300 K. Mn^{2+} substitutes for Na^+ ions in the lattice and charge compensation takes place at remote sites. The spectrum is satisfactorily described by a spin-Hamiltonian appropriate for Mn^{2+} in a rhombic crystalline field.

1. Introduction

Electron paramagnetic resonance (EPR) studies require the presence of unpaired electron in the sample to be studied. In general, these are not present in the pure material but can be introduced by doping with paramagnetic substances such as the transition elements or by radiation damage. Among all the ions which exhibit EPR spectrum d^5 and f^7 ions (S -state ions) are particularly interesting when one is concerned with the local symmetry of the environment of the ion. In fact, all sublevels of S -state are generally observed in low magnetic fields for the two reasons: (a) the zero-field splitting is zero to the first-order and (b) only higher-order effects permit lifting of the degeneracy of the fundamental states (6S and 8S). Therefore, a detailed study of the paramagnetic resonance spectra of S -state ions in diamagnetic crystals gives information about the environment around the paramagnetic ion.

Sodium dihydrogen orthophosphate ($\text{NaH}_2\text{PO}_4 \cdot 2\text{H}_2\text{O}$) belongs to a group of not very numerous crystal hydrates with small number of water molecules. The possibility of introducing the ions of transition elements into the crystal have not been studied previously. In this paper we report the EPR of Mn^{2+} in $\text{NaH}_2\text{PO}_4 \cdot 2\text{H}_2\text{O}$ single crystals at 300 K. The present study has been undertaken to understand the nature of crystalline field in the vicinity of Mn^{2+} and to study the probable lattice defects in the crystal.

2. Crystal Structure

The crystal structure of $\text{NaH}_2\text{PO}_4 \cdot 2\text{H}_2\text{O}$ has been determined by Bartl *et al* (1976). Sodium dihydrogen orthophosphate crystallizes in orthorhombic symmetry

with space group $P2_12_12_1 (D_2^4)$. The unit cell having the dimensions $a = 7.275 \text{ \AA}$, $b = 11.384 \text{ \AA}$, and $c = 6.604 \text{ \AA}$ contains four formula units. For the space group operation $P2_12_12_1$, all the atoms and molecules are in general position. The sodium atoms in the structure is surrounded by a distorted octahedron of oxygens. Out of six oxygens, four comes from phosphate radical and two from water molecules. The site symmetry of the $[\text{NaO}_4(\text{H}_2\text{O})_2]^+$ complex is C_1 .

3. Experimental

Single crystals of $\text{NaH}_2\text{PO}_4 \cdot 2\text{H}_2\text{O}$ doped with Mn^{2+} were grown at room temperature by slow evaporation of an aqueous solution of sodium dihydrogen orthophosphate to which manganese phosphate was added (1% by weight). The experiments were performed on a Varian V-4502 EPR spectrometer, operating at X-band microwave frequency region and using a 9-in. magnet and 100 kHz field modulation. As a reference for magnetic field strength, the resonance line of DPPH with $g = 2.0036$ was used. The magnetic field at the DPPH resonance was measured with the help of a Varian F-8A fluxmeter and the frequency of the proton signal was measured by a Systronic Type 701 frequency counter. The crystals were mounted on quartz rods. The angular variation studies were done using a Varian E-229 goniometer.

4. Results and Discussion

Mn^{2+} has $3d^5$ configuration and accordingly the Hund's rule ground state is $^6S_{5/2}$. In a crystalline field of low symmetry the ground state is split into three Kramers doublets. An external magnetic field lifts the degeneracy of the doublets, producing six energy levels. The EPR spectrum of a given Mn^{2+} centre should consists of five anisotropic fine structure transitions ($\Delta M = \pm 1$). The nuclear spin of ^{55}Mn (natural abundance 100%) is $5/2$. Therefore, the total hyperfine structure consists of six lines ($\Delta m = 0$) of equal intensity for each fine structure transition.

For an arbitrary orientation of the crystal, the EPR spectrum consists of a number of lines corresponding to allowed and forbidden transitions. The angular variation studies reveal the presence of two magnetically inequivalent but otherwise identical Mn^{2+} complexes. The principal axes of the manganese complexes were located by searching the direction corresponding to extrema in the spread of the spectrum. The z axis is defined as the direction of greatest separation of the hyperfine group of lines. The y axis is perpendicular to the z axis and the group of lines show least separation in this direction. The x axis is perpendicular to the z and y axes and the group of lines show intermediate separation in this direction. The spectrum taken at 300 K with magnetic field along the principal z axis of one set of equivalent Mn^{2+} complexes is shown in figure 1. The z axes of two complexes makes an angle of 40° with each other in the ab

plane. The z axis lies at 20° to the a axis in the ab plane. The y axis is directed along the c axis. The linewidth in the EPR spectrum of Mn^{2+} in $\text{NaH}_2\text{PO}_4 \cdot 2\text{H}_2\text{O}$ is ~ 8 Gauss. The angular variation studies indicate that the observed spectrum has orthorhombic symmetry. Since EPR in general does not distinguish between

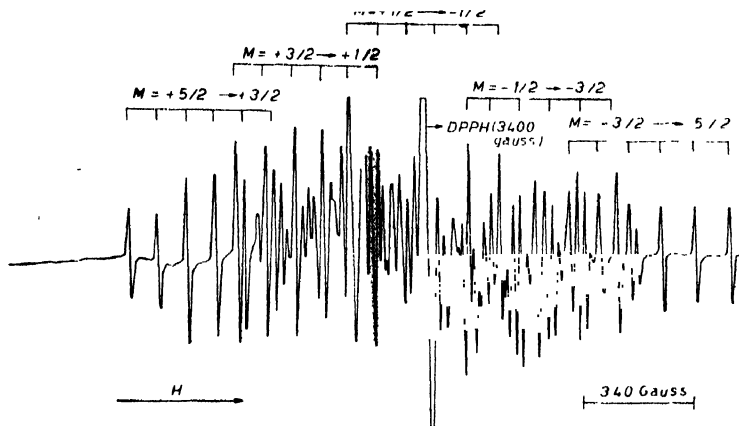


Figure 1. EPR spectrum of $\text{NaH}_2\text{PO}_4 \cdot 2\text{H}_2\text{O} : \text{Mn}^{2+}$ single crystals at 300 K; with H parallel to the z axis of one of the magnetic complexes of Mn^{2+} .

orthorhombic and lower symmetries (Bowers and Owens 1955), and as the symmetry of general position is C_1 , the crystal field symmetry at the Mn^{2+} site may be either orthorhombic or more probably lower.

The spectra observed at room temperature have been analysed using the spin-Hamiltonian approximate to Mn^{2+} in orthorhombic (or lower) symmetry.

$$\mathcal{H} = \beta(g_x H_x S_x + g_y H_y S_y + g_z H_z S_z) + D[S_z^2 - (1/3)S(S+1)] \\ + E(S_x^2 - S_y^2) + (a/6)[S_x^4 + S_y^4 + S_z^4 - (1/5)S(S+1) \times \\ \times (3S^2 + 3S - 1)] + (A_x S_x I_x + A_y S_y I_y + A_z S_z I_z).$$

The first term represent the Zeeman splitting due to the external magnetic field, where β is the Bohr magneton and g_x , g_y , and g_z are the components of the g -factor along the principal axes of the crystalline field. The D and E terms represent the Stark (zero-field) splitting in fields of axial and lower symmetries, respectively. The fourth term represents the cubic part of the crystalline field. The hyperfine interaction between the nuclear and electronic spin is represented by the A term.

Magnetic field measurements were made for the allowed lines with H along and z axis and x axis, respectively. No measurements could be made for H parallel to the y axis since the lines got mixed up and consequently the various fine structure transitions could not be distinguished. Therefore, it was necessary to assume that $A_x = A_y$ and $g_x = g_y$ in the calculations (the hyperfine and g tensors are normally isotropic for the Mn^{2+} ion). Using the expressions for the

resonance field positions given by Pandey and Upreti (1971) upto third-order perturbation for the above spin-Hamiltonian the best-fit parameters are obtained. It was found that the contribution to the line positions from the fourth-order perturbation term is negligibly small and must therefore not be considered. The Hamiltonian parameters of Mn^{2+} at 300 K are :

$$\begin{aligned} g_z &= 2.0098 \pm 0.0005, & g_x (= g_y) &= 2.0092 \pm 0.0005, \\ D &= 164 \pm 1 \times 10^{-4} \text{ cm}^{-1}, & E &= -34 \pm 2 \times 10^{-4} \text{ cm}^{-1}, \\ a &= -3.5 \pm 1 \times 10^{-4} \text{ cm}^{-1}, & A_z &= -88.5 \pm 0.5 \times 10^{-4} \text{ cm}^{-1}, \\ A_x (= A_y) &= -88.8 \pm 0.5 \times 10^{-4} \text{ cm}^{-1}. \end{aligned}$$

The sign of the parameters are only relative. The relative signs of the parameter D and A_z were obtained by comparing the second-order shifts in the separation between hyperfine components for the various electronic transitions (Low 1960). The sign of D is then obtained by assuming A_z to be negative as in all the materials the sign of A_z has been found to be negative (Abragam and Bleaney 1970). The sign of the parameter E results from the sign of D and the choice of the x and y axes.

The g value, which deviate slightly from the free spin value, shows a small anisotropy. The anisotropy of g is within the experimental error. The facts that the crystal field parameters have non-zero values, and that g departs from the free spin value, show that the ground state is not exactly ${}^6S_{5/2}$. Because of this, g may show an anisotropy, though it is very difficult to observe experimentally. The deviation from free spin value may be attributed to the effects of covalent bonding (Abragam and Bleaney 1970) although it is difficult to extract any meaningful covalency parameter out of it.

The hyperfine coupling constant is very close to isotropic and any anisotropy is within the experimental error. The isotropic interaction is presumed to result from the polarization of the s shell by the d electrons, since the d orbitals themselves have zero density at the nucleus. The zero-field splitting parameters D and E have non-zero values. The ratio $E/D \sim 0.48$ indicate strong rhombic distortion of the site. This is expected because of the low symmetry of the Mn^{2+} site.

It can be seen from the crystal structure that there are two cation sites (Na^+ and P^{5+}) available to Mn^{2+} ion for substitution. The ionic radii of Na^+ , P^{5+} and Mn^{2+} are 0.97 Å, 0.35 Å and 0.80 Å respectively (West 1975-76). Because of the large differences in the ionic radii and the valence states of the two ions, Mn^{2+} does not properly fit in at the P^{5+} site. On the other hand it fits in well at the Na^+ site as the ionic radii of the two ions are nearly equal and there is only a small difference in their valence states. The introduction of Mn^{2+} in place of Na^+ in the lattice causes a charge imbalance. The neutrality of the crystal can, however, be maintained by simultaneously introducing an equal number of negative charge defects. In $\text{NaH}_2\text{PO}_4 \cdot 2\text{H}_2\text{O}$, the positive ion vacancy

is the easiest defect to form that satisfy this requirement. As a result, Mn^{2+} addition will be accompanied by the introduction of an equal number of positive ion vacancies. The excess charge of vacancy will produce an extra contribution to the crystal field at the Mn^{2+} position and the direction of the z axis is expected to be along the Mn^{2+} -vacancy direction. For example, in $\text{NaCl}:\text{Mn}^{2+}$ single crystals the direction of z axis is along the Mn^{2+} -vacancy direction (Watkins 1959, Shrivastava and Venkateswarlu 1966). Further, as a result of local charge compensation the symmetry of Mn^{2+} site in NaCl is decreased and gives rise to tetragonal and orthorhombic spectra (Watkins 1959, Shrivastava and Venkateswarlu 1966). It is also interesting to note that the spectra of trivalent lanthanide ions substituting for Ca^{2+} ions in CaF_2 are observed with cubic symmetry, or with tetragonal or trigonal symmetry. In the first case charge compensation is taking place at remote sites; in the second an extra F^- ion occupies the nearest vacant interstitial site, and in the third it is presumed that an O^{2-} ion replaces an F^- ion on one apex of the immediate cube of fluorine (Abragam and Bleaney 1970). A comparison of the direction of Na-Na (vacancy) with the direction of z axis of Mn^{2+} in $\text{NaH}_2\text{PO}_4 \cdot 2\text{H}_2\text{O}$ indicate that the z axis does not lie along the Na-Na (vacancies) direction. This indicates that charge compensation is probably taking place at remote sites as observed in $\text{Ga}_2\text{O}_3:\text{Mn}^{2+}$ (Folen 1965) and in monoclinic $(\text{NH}_4)_2\text{SeO}_4$ doped with Mn^{2+} (Jain and Venkateswarlu 1979). The effect of vacancy association to lower the symmetry as observed in $\text{NaCl}:\text{Mn}^{2+}$ and $\text{CaF}_2:\text{R}^{3+}$ (R is lanthanide ion) could not be detected in $\text{NaH}_2\text{PO}_4 \cdot 2\text{H}_2\text{O}:\text{Mn}^{2+}$, because the symmetry of Mn^{2+} site is already lower and a further lowering of the symmetry does not affect the symmetry of the EPR spectrum. Therefore, only very little information about the lattice defects in crystals of lower symmetries can be obtained by EPR in contrast to crystals of higher symmetries where valuable information about the lattice defects can be obtained by EPR.

Acknowledgment

The author is thankful to the CSIR, New Delhi for financial assistance and to Professor Putcha Venkateswarlu for helpful discussions.

References

- Abragam A and Bleaney B 1970 *Electron Paramagnetic Resonance of Transition Ions*, (Clarendon, Oxford) Ch 5 7
 Bartl H, Catti M and Ferrariss G 1976 *Acta Crystallogr.* **B32** 987
 Bowers K D and Owen J 1955 *Rept. Prog. in Phys.* **18** 304
 Folen V J 1965 *Phys. Rev.* **139** 1961
 Jain V K and Venkateswarlu P 1979 *J. Chem. Phys.* **70** 5168
 Low W 1960 *Paramagnetic Resonance in Solids* Solid State Phys. Supp 2 (Academic Press, New York)
 Pandey S D and Upreti G C 1971 *Ferroelectrics* **2** 155
 Shrivastava K N and Venkateswarlu P 1966 *Proc. Ind. Acad. Sci.* **63A** 284
 Watkins G D 1959 *Phys. Rev.* **113** 79
 West R C 1975-76 *Handbook of Chemistry and Physics* (CRC Press, Cleveland, OH) 56th Ed. F-209.

Interband Faraday rotation in germanium at the L point*

B K Ray

Department of Physics, Indian Institute of Technology, Kharagpur-721302

Received 16 January 1978, revised 6 September 1978

Abstract. Using the theory of Faraday effect in solids developed by Roth, the theoretical values of the transmission and the polar reflection Faraday rotation due to the valence to conduction band transition at the L point for Ge-type material, are calculated. The calculated values of the transmitted Faraday rotation for Ge do not give the positive rotation near the low frequency region. The theoretical spectrum of the polar reflection Faraday rotation in Ge is compared qualitatively with the experimental spectrum of InSb, as experimental results in Ge are not available and the knowledge of the band parameters at the L point for InSb is inadequate.

1. Introduction

Boswarva and Lidiard (1962) suggested that the positive rotation near the low frequency region in Ge is due to the direct transition at the L point ($L_3 \leftrightarrow L_1$). However, later they pointed out their own error (Boswarva and Lidiard 1964) and stated that some contribution from the L point transition probably occurs in Ge, GaAs and GaSb but that this is qualitatively unimportant in determining the frequency dependence of Faraday rotation. Further, the sign of rotation depends upon the change in balance between the contributions from electrons in the light valence states and from electrons in heavy valence states at the Γ point. But according to our calculations (Ray 1976), the positive rotation near the low frequency region is due to all the transitions in the Brillouin zone and not just due to any one transition. Pidgeon *et al* (1964) performed an experiment to determine the effect of uniaxial strain on Faraday rotation in Ge. They concluded from their experiment that the direct transition at the L point give significant contribution to the Faraday rotation in Ge on the low frequency side of the direct gap. Because of these controversies we devote the present work to the theoretical study of the interband Faraday rotation spectrum based on the theory given by Roth (1964), in the energy range near the valence to conduction band energy gap at the L point which we call interband Faraday rotation at the L point.

* Part of the thesis submitted at the Department of Physics, Tufts University, Medford, Massachusetts, U.S.A., for the partial fulfillment of the requirements for the degree of Doctor of Philosophy.

We start with a short analysis of the energy surfaces at the L point including the theoretical expressions for the band parameters. We then use this analysis to obtain expressions for Faraday rotation in terms of these band parameters. Since at the L point the detailed knowledge of the valence band parameters in Ge is lacking some approximations are introduced for their estimation. The calculation for Ge shows that the L point transition does not give the positive rotation at the low frequency region contrary to expectation (Boswarva and Lidiard 1962, Pidgeon *et al* 1964) but instead gives a negative singularity near the energy gap. Since no transmission experiment is possible in this energy range, the polar reflection Faraday rotation spectrum is calculated. In the absence of experimental results in Ge, the calculated spectrum, is compared qualitatively with the experimental InSb spectrum (Lax and Nishina 1961), as the energy band structure of InSb is very similar to Ge at the L point. As the knowledge of the band parameters of InSb at the L point is even worse than that of Ge, theoretical spectrum of InSb is not possible to predict.

2. The form of the energy surface at the L point

The effective mass Hamiltonian for a set of degenerate states i, j near a band edge, in the presence of a magnetic field represented by the vector potential A is given by (Luttinger and Kohn 1955, Luttinger 1956)

$$D_{ij} = D_{ij}^{ab} P_a P_b \quad (2.1)$$

where

$$D_{ij}^{ab} = (1/2m)\delta_{ij}\delta_{ab} + (1/m^2)\sum_n \frac{(P_a)_{in}(P_b)_{nj}}{E_0 - E_n} \quad (2.2)$$

The repeated indices α and β are summed over x, y, z . The summation over n is over all those states of the unperturbed problem not belonging to the degenerate set i, j at the band edge, E_0 is the energy of the degenerate set, E_n the energy of the n th unperturbed state, $(p_a)_{in}$ are just the momentum matrix elements between the different bands evaluated at the degeneracy point and $P_a = p_a + (e/c)A_a$ is the kinetic momentum.

At the L point band edge (Callaway 1964) in the absence of spin orbit coupling there are two degenerate space functions belonging to the representation L_3 , which transforms like x' and y' respectively under operations of the point group at the L point. Here the prime system is such that the z' is in (111) direction and x' and y' axes are in $(2\bar{1}1)$ and $(0\bar{1}1)$ directions respectively.

Let us consider the following functions

$$\begin{aligned}
 \theta &= x'p_{x'} + y'p_{y'} \\
 \phi &= y'p_{x'} - x'p_{y'} \\
 \psi_1 &= z'x' \\
 \psi_2 &= z'y' \\
 \psi_1' &= (1/\sqrt{2})(x'p_{x'} - y'p_{y'}) \\
 \psi_2' &= -(1/\sqrt{2})(y'p_{x'} + x'p_{y'}) \\
 \psi_1'' &= p_{x'}x' \\
 \psi_2'' &= p_{y'}y'.
 \end{aligned} \tag{2.3}$$

These functions are such that under the operations of the point group at the L point (Callaway 1964), θ transforms as the one dimensional basis function belonging to the representation L_1 , ϕ transforms as the one dimensional basis function belonging to the representation L_2 and $\psi_1, \psi_2; \psi_1', \psi_2'; \psi_1'', \psi_2''$; transforms as the two dimensional basis functions belonging to the representation L_3 . Now to calculate the L point matrix elements of the effective mass Hamiltonian we use the prime system but for convenience omit the primes. Also for calculating the matrix elements we remember that the scalar product of two functions having the same transformation properties is nonzero while with different transformation properties is zero.

2.1. The effective mass $D_{xx}^{\alpha\beta}$ of an electron at the L_3' band in the absence of spin orbit coupling

Writing $p_x|x\rangle$ in terms of functions of equation (2.3) it is evident that $D_{xx}^{\alpha\alpha}$ is nonzero only due to the contributions from L_1 and L_3 bands. Thus

$$D_{xx}^{\alpha\alpha} = (1/2m) + (1/m^2) \left\{ \sum_n (a_n^2/E_{3',1n}) + \sum_n (b_n^2/E_{3',3n}) \right\} \tag{2.4}$$

where,

$$\frac{1}{2}(\theta|L_{1n}) = a_n$$

and

$$(1/\sqrt{2})(\psi_1'|L_{3n}^1) = (1/\sqrt{2})(\psi_2'|L_{3n}^2) = b_n \tag{2.5}$$

L_{nm}' denotes the n th basis function of the n th band belonging to the representation L_m and $E_{L_{mn}}$ denotes the energy of the n th L_m band with

$$E_{3',mn} = E_{L_3'} - E_{L_{mn}} \tag{2.6}$$

Writing

$$a^2 = (1/m^2) \sum_n a_n^2 / E_{s', 1n} \quad (2.7)$$

and

$$b^2 = (1/m^2) \sum_n b_n^2 / E_{s', 2n} \quad (2.8)$$

we get

$$D_{xx}^{xx} = (1/2m) + (a^2 + b^2).$$

Similarly writing $p_y|x$ in terms of the functions of equation (2.3) it is evident that D_{xx}^{yy} is nonzero only due to the contributions from the L_2 and L_3 bands, therefore

$$\begin{aligned} D_{xx}^{yy} &= (1/2m) + (1/m^2) \left\{ \sum_n \frac{c_n^2}{E_{s', 2n}} + \sum_n \frac{b_n^2}{E_{s', 3n}} \right\} \\ &= (1/2m) + (c^2 + b^2) \end{aligned}$$

where

$$c_n = (1/2)(\phi | L_{2n}) \quad (2.9)$$

$$c^2 = (1/m^2) \sum_n c_n^2 / E_{s', 2n}. \quad (2.10)$$

The form of $p_z|x$ shows that D_{xx}^{zz} is nonzero only due to the contribution from the L_3 band, therefore

$$\begin{aligned} D_{xx}^{zz} &= (1/2m) + (1/m^2) \sum_n d_n^2 / E_{s', 3n} \\ &= (1/2m) + d^2 \end{aligned}$$

where

$$d_n = (\psi_1'' | L_{3n}^1) = (\psi_2'' | L_{3n}^2) \quad (2.11)$$

$$d^2 = (1/m^2) \sum_n d_n^2 / E_{s', 3n}. \quad (2.12)$$

Looking at the form of $p_x|x$ and $p_y|x$ we easily see that

$$\begin{aligned} D_{xx}^{xy} &= 0 = D_{xx}^{yx} \\ D_{xx}^{xz} &= (1/m^2) \sum_n (b_n \cdot d_n^*) / E_{s', 3n} \\ &= (b \cdot d^*) \end{aligned}$$

and

$$D_{xx}^{zx} = (b^* \cdot d).$$

Exactly in a similar way we get the expressions for the other components of the effective mass,

2.2. The effective mass of an electron $D_{ij}^{\alpha\beta}$ at the L_3' band with spin orbit coupling

When we introduce the spin orbit interaction we choose a basis set in which the spin orbit operator is diagonal. We take the following four states as the states of the L_3' band

$$\phi_1 = (1/\sqrt{2})(x+iy)\alpha$$

$$\phi_2 = (1/\sqrt{2})(x+iy)\beta$$

$$y_3 = (1/\sqrt{2})(x-iy)\alpha$$

$$y_4 = (1/\sqrt{2})(x-iy)\beta$$

where α and β are the spin states. Then

$$D_{11}^{xx} = A = D_{11}^{yy}$$

$$D_{11}^{zz} = C$$

$$D_{11}^{xy} = iF = D_{11}^{yx}$$

$$D_{11}^{xz} = 0 = D_{11}^{zx} = D_{11}^{yz} = D_{11}^{zy}$$

where A , C and F are given by

$$A = \frac{1}{2} (a^2 + 2b^2 + c^2 + 1/m) \quad (2.13)$$

$$C = \frac{1}{2} (2d^2 + 1/m) \quad (2.14)$$

and

$$F = \frac{1}{2} (a^2 - 2b^2 + c^2). \quad (2.15)$$

From the form of ϕ_1 and ϕ_2 we see that the effective mass $D_{22}^{\alpha\beta}$ is exactly the same as $D_{11}^{\alpha\beta}$. Also the effective masses $D_{33}^{\alpha\beta}$ and $D_{44}^{\alpha\beta}$ are exactly the same and these can be obtained from that of $D_{11}^{\alpha\beta}$ by replacing i by $-i$, and that

$$D_{13}^{xx} = B$$

$$D_{13}^{xy} = -iB = D_{13}^{yx}$$

where

$$B = \frac{1}{2} (a^2 - c^2). \quad (2.16)$$

The expressions for the other components of the effective mass may be obtained in a similar way. Here we have neglected the spin orbit splitting of the L_3 bands, which does not contribute if it is far away from L_3 band. Also there is no spin orbit splitting of the L_1 and L_2 bands.

2.3. The effective mass Hamiltonian of the L_3' band with spin orbit coupling

In the calculation of the effective masses D_{ij}^{ab} we have not taken into account of the presence of the spin orbit energy $H_{s.o.}$. The spin orbit operator being diagonal in the set of states for the L_3 band, we take

$$(H_{s.o.})_{11} = (H_{s.o.})_{44} = 0$$

and

$$(H_{s.o.})_{22} = (H_{s.o.})_{33} = -\Delta.$$

Finally, therefore the nonzero matrix elements of the effective mass Hamiltonian for the L_3' band with spin orbit coupling is given by,

$$\begin{aligned} D_{11} &= A(P_x^2 + P_y^2) + CP_z^2 + iF[P_x, P_y] \\ &= D_{44}^* \\ D_{22} &= A(P_x^2 + P_y^2) + CP_z^2 + iF[P_x, P_y] - \Delta \\ &= D_{33}^* \\ D_{13} &= B\{(P_x^2 - P_y^2) - i(P_x P_y + P_y P_x)\} + (b.d^*)(P_x + iP_y)P_z \\ &\quad + (b^*.d)P_x(P_x + iP_y) \\ &= D_{31}^* = D_{24} = D_{42}^* \end{aligned}$$

In the presence of the magnetic field \mathbf{H} we have,

$$\mathbf{P} \times \mathbf{P} = \frac{e\hbar\mathbf{H}}{ic}$$

Using this we get,

$$\begin{aligned} D_{11} &= P + R \\ D_{44} &= P - R \\ D_{22} &= P + R - \Delta \\ D_{33} &= P - R - \Delta \end{aligned}$$

where

$$P = A(P_x^2 + P_y^2) + CP_z^2 \quad (2.17)$$

and,

$$R = e\hbar\mathbf{H}_z F/c \quad (2.18)$$

In the presence of the magnetic field \mathbf{H} the Hamiltonian will contain a term due to the spin splitting, which will be equal to $g_0\beta\mathbf{S}\cdot\mathbf{H}$, where $g_0 = 2$, the free

electron g -factor and β is the Bohr magneton. Substituting $S = g_0 \beta \mathbf{S} \cdot \mathbf{H}$, we can write the secular determinant giving the magnetic energy levels as

$$\begin{array}{cccc}
 P+R+S_{11}-E & S_{12} & Q+S_{13} & S_{14} \\
 S_{21} & P+R+S_{22}-\Delta-E & S_{23} & Q+S_{24} \\
 Q^*+S_{31} & S_{32} & P-R+S_{33}-\Delta-E & S_{34} \\
 S_{41} & Q^*+S_{42} & S_{43} & P-R+S_{44}-E
 \end{array} = 0 \quad (2.19)$$

where

$$Q = B(P_x - iP_y)^2 + (b \cdot d^*)(P_x + iP_y)P_z + (b^* \cdot d)P_z(P_x + iP_y) \quad (2.20)$$

Writing D_{ij} in the form

$$D_{ij} = D_{ij}^{(S)} + D_{ij}^{(A)}$$

where the superscripts (S) and (A) denote the symmetric and antisymmetric parts of D_{ij} , the g -factor for the pair of bands (i, j) may be defined (Roth 1960) as

$$\beta \mathbf{S}_{\alpha\beta} \cdot \mathbf{g} \cdot \mathbf{H} = D_{ij}^{(A)} + g_0 \beta \mathbf{S}_{ij} \cdot \mathbf{H}. \quad (2.21)$$

The subscripts α and β denote the pseudo spin states. For H parallel to z axis equation (2.21) reduces to

$$\beta(S_z)_{\alpha\beta} g_{zz} H_z = D_{ij}^{(A)} + g_0 \beta(S_z)_{ij} H_z$$

and the diagonal elements of S reduces to either $g_0 \beta H_z/2$ or $-g_0 \beta H_z/2$ and all the off diagonal elements vanish. Calling the g -factor corresponding to the pair (1, 4) and (2, 3) as g_1 and g_2 respectively we obtain,

$$R + g_0 \beta H_z/2 = g_{1zz} \beta H_z/2 = H_1$$

$$-R + g_0 \beta H_z/2 = g_{2zz} \beta H_z/2 = H_2.$$

The energy levels in this case are obtained from

$$\begin{array}{cccc}
 P+H_1-E & 0 & Q & 0 \\
 0 & P-H_2-\Delta-E & 0 & Q \\
 Q^* & 0 & P+H_2-\Delta-E & 0 \\
 0 & Q^* & 0 & P-H_1-E
 \end{array} = 0 \quad (2.22)$$

From equation (2.22) it can be shown that in the absence of the magnetic field ($H = 0$) the states are two fold degenerate separated by a distance Δ at the band edge. The states ϕ_1 and ϕ_4 have energy $E_{L_3'}$ and the states ϕ_2 and ϕ_3 have $E_{L_3'} - \Delta$.

In the presence of the magnetic field ($H \neq 0$) these degeneracies are lifted up.

2.4. The g -factors of the L_3' bands : g_{1v}, g_{2v}, g'_{1v} and g'_{2v}

To calculate the g -factors we take the field H in any general direction and use the approximation that $E \ll \Delta$ and $S_{ij} \ll \Delta$ for $i \neq j$. Calling the g -factor corresponding to the pair of bands 1 and 4 to be g_{1v} , we obtain from equation (2.19) using the definition (2.21)

$$\beta S_{aa} \cdot g_{1v} \cdot H = R + g_0 \beta S_{11} \cdot H \quad (2.23)$$

and

$$\beta S_{aa} \cdot g_{1v} \cdot H = 0 + g_0 \beta S_{14} \cdot H. \quad (2.24)$$

From equations (2.23) and (2.24) with a little inspection we see that the only nonzero components of g_{1v} is given by,

$$g_{1vzz} \beta / 2 = e \hbar F / c + g_0 \beta / 2. \quad (2.25)$$

Exactly in a similar manner, the g -factor corresponding to 2 and 3 bands g_{2v} , has only one nonzero component given by,

$$g_{2vzz} \beta / 2 = -e \hbar F / c + g_0 \beta / 2. \quad (2.26)$$

Now let us consider a tensor g' which is equal to the contribution to the g -factor from the L_{11} band, which is the conduction band at the L point. Therefore g' will be given by

$$\beta S_{ij} \cdot g' \cdot H = D_{ij}'^{(A)}(L_{11})$$

where $D_{ij}'^{(A)}$ is the contribution to $D_{ij}^{(A)}$ from the L_{11} band.

Following a similar method as for the determination of the components of g , we find the only nonzero components of g'_{1v} and g'_{2v} to be given by

$$g'_{1vzz} = 4mF' \quad (2.27)$$

and

$$g'_{2vzz} = -4mF' \quad (2.28)$$

where F' is the contribution to F only from the L_{11} band i.e.

$$F' = a_1^2 / 2m^2 E_{s',11} \quad (2.29)$$

2.5. The effective mass of an electron at the L_1 band in the absence of spin orbit coupling

For L_{11} band from the transformation properties of different functions as discussed previously we have

$$D^{xx} = 1/2m + a_1^2/m^2 E_{11,s'} = D^{yy}$$

where

$$a_1 = \frac{1}{2} (L_{11} | \theta).$$

Since $p_{y'}$ transforms as $L_3'^1$, and p_y as $L_3'^2$, we have,

$$D^{xy} = 0 = D^{yx}.$$

As p_z transforms as L_3' , we obtain

$$D^{zz} = 1/2m + (1/m^2) \sum_n \frac{f_n^2}{E_{11,2'n}} = 1/2m + f^2$$

where,

$$f_n = (L_{11} | p_z | L_{2'n})$$

and

$$f^2 = (1/m^2) \sum_n f_n^2 / E_{11,2'n}.$$

Using the fact that p_x , p_y and p_z transform as $L_3'^1$, $L_3'^2$, and L_2' respectively, we obtain

$$D^{xz} = 0 = D^{zx} = D^{yz} = D^{zy}.$$

2.6. The effective mass Hamiltonian of the L_1 band with spin orbit coupling

When we introduce the spin orbit interaction we take the basis functions as, ϕ_1, ϕ_4 corresponding to energy $E_{L_3'}$, and ϕ_2, ϕ_3 corresponding to energy $E_{L_3'} - \Delta$ of the L_3' bands, and

$$\phi_c = L_{11}\alpha$$

$$\phi_{c'} = L_{11}\beta$$

for L_{11} band corresponding to energy $E_{L_{11}}$, and $L_{2'n}\alpha$ and $L_{2'n}\beta$ corresponding

to energy $E_{L_{2'n}}$ of $L_{2'n}$ band, α and β being the spinors. With these one obtains the following

$$D_{cc}^{xx} = \frac{1}{2m} + (2E_{11,3'} + \Delta) \alpha_1^2 / 2m^2 E_{11,3'} (E_{11,3'} + \Delta)$$

$$= D_{cc}^{yy} = D_{c'e'}^{xx} = D_{c'e'}^{yy}$$

$$D_{cc}^{zz} = \frac{1}{2m} + f^2 = D_{c'e'}^{zz}$$

$$D_{cc}^{xy} = -i\alpha_1^2 / 2m^2 E_{11,3'} (E_{11,3'} + \Delta)$$

$$= D_{cc}^{yx} = D_{c'e'}^{xy} = D_{c'e'}^{yx}$$

$$D_{cc}^{xz} = 0 = D_{cc}^{zx} = D_{c'e'}^{xz} = D_{c'e'}^{zx}$$

$$D_{cc}^{yz} = 0 = D_{cc}^{zy} = D_{c'e'}^{yz} = D_{c'e'}^{zy}.$$

It is evident from the form of the states ϕ_c and $\phi_{c'}$, that all matrix elements $D_{cc'}^{\alpha\beta}$ and $D_{c'e'}^{\alpha\beta}$ are zero.

The matrix elements of the effective mass Hamiltonian are given by

$$D_{cc} = L(P_x^2 + P_y^2) + MP_z^2 - iN[P_x, P_y]$$

$$D_{c'e'} = L(P_x^2 + P_y^2) + MP_z^2 + iN[V_x, P_y]$$

$$D_{cc'} = 0 = D_{c'e}$$

where

$$L = 1/2m + \alpha_1^2 (2E_{11,3'} + \Delta) / 2m^2 E_{11,3'} (E_{11,3'} + \Delta)$$

$$M = 1/2m + f^2$$

$$N = \alpha_1^2 \Delta / 2m^2 E_{11,3'} (E_{11,3'} + \Delta).$$

In the presence of the magnetic field using the relation $\mathbf{P} \times \mathbf{P} = \frac{e\hbar\mathbf{H}}{ic}$, and noting that the Hamiltonian will contain a term due to electron spin interaction with the magnetic field, which is equal to $g_0\beta\mathbf{S} \cdot \mathbf{H} = S$, the secular determinant giving the magnetic energy levels is

$$L(P_x^2 + P_y^2) + MP_z^2 - \frac{e\hbar}{c} NH_z + S_{cc} - E, S_{cc'} = 0 \quad (2.30)$$

$$\left| \begin{array}{cc} L(P_x^2 + P_y^2) + MP_z^2 - \frac{e\hbar}{c} NH_z + S_{cc} - E & S_{cc'} \\ S_{c'e} & L(P_x^2 + P_y^2) + MP_z^2 + \frac{e\hbar}{c} NH_z + S_{c'e} - E \end{array} \right|$$

2.7. The g -factor of the L_1 (conduction) band : g_c, g'_{1c}, g'_{2c}

Exactly as for the L_3' band, to calculate the g -factor g_c for the pair (c, c') of L_{11} band we take the field H in any general direction, and obtain from equation (2.30) using the definition (2.21)

$$\beta S_{\alpha\alpha} \cdot g_c \cdot H = - \frac{e\hbar N H_z}{\mu} + g_0 \beta S_{cc} \cdot H \quad (2.31)$$

and

$$\beta S_{\alpha\beta} \cdot g_c \cdot H = 0 + g_0 \beta S_{cc} \cdot H. \quad (2.32)$$

With a little examination we see from equations (2.31) and (2.32) that the only nonzero components of g_c are given by,

$$g_{czz} = g_0 - 2a_1^2 \Delta / m E_{11,3'} (E_{11,3'} + \Delta)$$

$$g_{czz} = g_0 = g_{cyy}.$$

Similarly as for L_3' band we define for L_{11} band g_c' to be equal to the contribution to g_c from one of the L_3' bands. Since there are two degenerate pairs corresponding to L_3' bands there should be two g_c' . g'_{1c} corresponds to the pair of bands 1 and 4 with energy $E_{L_3'}$ and g'_{2c} corresponds to the pair 2 and 3 with energy $E_{L_3'} - \Delta$, then the only nonzero components are given by,

$$g'_{1czz} = -2a_1^2 / m E_{11,3'}$$

$$g'_{2czz} = -2a_1^2 / m (E_{11,3'} + \Delta).$$

The above expressions for the g -factors can be expressed in terms of the transverse effective mass (m_c) of the L_{11} band. We have,

$$\begin{aligned} 1/2(m_c)_t &= D^{xx} = D^{yy} \\ &= 1/2m + a_1^2 / m^2 E_{11,3'} \end{aligned}$$

or

$$2a_1^2 / m E_{11,3'} = (m / (m_c)_t - 1). \quad (2.33)$$

Therefore,

$$g_{czz} = g_0 - \frac{1}{(E_{11,3'} + \Delta)} (m / (m_c)_t - 1)$$

$$g'_{1czz} = -(m / (m_c)_t - 1)$$

$$g'_{2czz} = \frac{E_{11,3'}}{(E_{11,3'} + \Delta)} (m / (m_c)_t - 1)$$

3. Faraday rotation due to the interband transitions at the L points

It is seen (Roth 1961, Ray 1976) that the conductivity tensor component $\sigma_{xy}^{(ib)}$ due to interband transition consists essentially of two parts, first is the contribution from Zeeman interaction of a band electron and the second is the contribution from the change in matrix element due to the presence of the magnetic field. In this section we calculate separately the two contributions to Faraday rotation.

3.1. Contribution arising from Zeeman interaction

We obtain the contribution from Zeeman interaction when we put $n' = n''$ in the expression for $\sigma_{xy}^{(ib)}$ for interband transitions (equation (3.1) in Ray 1966). Evaluating the matrix elements at the L point band edge and expressing them in terms of the g -factors at the same band edge, since the only nonzero components of g' at the L point is g'_{zz} , the conductivity tensor component $\sigma_{xy}^{(ib)}$ may be written as

$$\sigma_{xy}^{(ib)} = \frac{e^2 \hbar}{6\sqrt{2}\pi(mE_g)^{\frac{1}{2}}} \left(\frac{\mu}{m}\right)^{3/2} [g_{cz} g'_{cz} - g_{vz} g'_{vz}]_{k=0} F_2(w/E_g)$$

Here we have evaluated the sum over k corrected for the low frequency behavior as is done by Roth (1964) and $F_2(x)$ is given by

$$F_2(x) = \frac{1}{x} \left\{ \frac{1}{(1-x)^{\frac{1}{2}}} - \frac{1}{(1+x)^{\frac{1}{2}}} \right\} -$$

Let us now write

$$\sigma_{xy}^{(ib)} = \sigma_{1xy} + \sigma_{2xy}$$

where σ_{1xy} is the contribution due to the transition from the pair of bands 1 and 4 with energy $E_{L_3'}$ to the L_{11} band with energy $E_{L_{11}}$ and σ_{2xy} is the contribution due to the transition from the pair of bands 2 and 3 with energy $E_{L_3'} - \Delta$ to L_{11} band with energy $E_{L_{11}}$. Therefore, using the values of the g -factors calculated in section 2 we have,

$$\sigma_{1xy} = \frac{e^2 \hbar}{6\sqrt{2}\pi(mE_g)^{\frac{1}{2}}} (\mu/m)^{3/2} \left\{ g_0 - \frac{2a_1^2 \Delta}{mE_g(E_g + \Delta)} \left(-\frac{2a_1^2}{mE_g} \right) - (g_0 + 4mF)(4mF') \right\} F_2(w/E_g)$$

where $E_g = E_{11,s'}$. Assuming that the effect of the band L_{11} is large compared to other bands we get,

$$F \cong F' = -a_1^2/2m^2E_g.$$

Using this relation and equation (2.33) we obtain

$$\sigma_{1xy} = -\frac{e^2\hbar}{6\sqrt{2}\pi(mE_g)^{\frac{1}{2}}} \frac{E_g}{(E_g+\Delta)} (\mu/m)^{3/2} \left(\frac{m}{(m_c)_t} - 1\right)^2 F_2(w/E_g)$$

Exactly in a similar way

$$\sigma_{2xy} = -\frac{e^2\hbar}{6\sqrt{2}\pi m(E_g+\Delta)^{\frac{1}{2}}} \frac{E_g}{(E_g+\Delta)} (\mu/m)^{3/2} \left(\frac{m}{(m_c)_t} - 1\right)^2 \times F_2\{\omega/(E_g+\Delta)\}.$$

Let us take θ_1 and θ_2 to be the contribution to the rotation from σ_{1xy} and σ_{2xy} respectively, then using relation between the rotation and conductivity tensor component σ_{xy} (relation (1.1) in Ray 1976) we can write θ_1 and θ_2 in the form

$$\theta_1 = \theta_{01} H F_2(w/F_g) \quad (3.1)$$

and

$$\theta_2 = \theta_{02} H F_2\{\omega/(E_g+\Delta)\} \quad (3.2)$$

where

$$\theta_{01} = -20.68 \frac{\sqrt{E_g}}{n(E_g+\Delta)} (\mu/m)^{3/2} (m/(m_c)_t - 1)^2$$

and,

$$\theta_{02} = -20.68 \frac{E_g}{n(E_g+\Delta)^{3/2}} (\mu/m)^{3/2} (m/(m_c)_t - 1)^2$$

To evaluate the reduced effective mass μ we have to use the relations

$$\mu = \mu_t^{2/3} \cdot \mu_l^{1/3} \quad (3.3)$$

where, μ_t and μ_l are the transverse and longitudinal reduced effective masses, and

$$m/\mu_t = (3/2)(m/(m_c)_t - 1) \quad (3.4)$$

$$m/\mu_l = m/(m_c)_t + (E_{11,s'}/E_{31,s'}) (m/(m_c)_t - 1) - 1. \quad (3.5)$$

In deriving equation (3.4) we have assumed that the contribution to A as defined by equation (2.13) from L_{11} band to be large compared to any other band, and in deriving equation (3.5) we assumed that there is only one L_s band which we call L_{31} and that $d_1 \cong a_1$, since d_1 is not known. This equations (3.3) to (3.5)

give the reduced effective mass μ , which has to be used in equations (3.1) and (3.2) to get θ_{01} and θ_{02} .

3.2. Contribution arising from change in matrix element

In terms of effective masses $D_{ij}^{\alpha\beta}$ as defined by equation (2.2) and $D_{ij}^{\alpha\beta}(n'')$, contribution to $D_{ij}^{\alpha\beta}$ from n'' band only we can write the contribution to the conductivity tensor arising from the change in matrix element (from equation (3.2) of Ray 1976) as

$$\sigma_{xy}^{(tb)} = e^2 \hbar \epsilon_{\alpha\beta\gamma\delta} \sum_{i,j,n''} \left[f_{in''} \left\{ D_{ij}^{\alpha\gamma} + \frac{\delta_{\alpha\gamma} \delta_{ij}}{2m} \right\} \right. \\ \left. \left\{ D'_{ji}{}^{\delta\beta}(n'') - \frac{\delta_{\delta\beta} \delta_{ji}}{2m} \right\} \right] \sum_k \frac{1}{(E_{in''}^2 - w^2)}$$

We now assume that the contribution from the pair of valence bands (1, 4) and (2, 3) can be considered independently of each other. With this approximation all the nondiagonal $D_{ij}^{\alpha\beta}$ for both the pairs (1, 4) and (2, 3) are neglected and $D_{ii}^{\alpha\beta} \neq 0$ only when $\alpha = \beta$ or $\alpha, \beta = x, y$ when $\alpha \neq \beta$. To calculate the matrix elements we need to evaluate the above equation, the basis functions ϕ_1, ϕ_2, ϕ_3 , and ϕ_4 are used for L_3' band and the basis functions ϕ_c and $\phi_{c'}$ are used for the L_1 band. In evaluating the matrix elements of the L_3' band we take into account the interaction of the L_3' band with L_{11} and L_{31} bands only, and for calculating the matrix elements of the L_1 band we consider the interaction of the L_{11} band with L_3' and L_2' bands only. Let σ_{3xy} and σ_{4xy} be the contribution to the conductivity tensor due to the transitions from the pair (1, 4) of the L_3' band to L_1 band and from the pair (2, 3) of the L_3' to L_1 band respectively and θ_3 and θ_4 the corresponding contributions to Faraday relation. With the above approximations and the approximation $d_1 \cong a_1$, and using the relation (2.33) one gets

$$\theta_3 = \theta_{03} Hf(w/E_g) \quad (3.6)$$

$$\theta_4 = \theta_{04} Hf\{w/(E_g + \Delta)\} \quad (3.7)$$

where

$$\theta_{03} = - \frac{41.36(\mu/m)^{3/2}}{n\sqrt{E_g}} \frac{m/(m_c)\epsilon - 1}{\epsilon - 1} \\ \times \left[(m/(m_c)_1 + 7) - \frac{E_{11,3'}}{E_{31,3'}} (m/(m_c)\epsilon - 1) \right] \\ \theta_{04} = - \frac{41.36(\mu/m)^{3/2}}{n\sqrt{E_g + \Delta}} \cdot \frac{E_g}{E_g + \Delta} (m/(m_c)\epsilon - 1) \\ \times \left[(m/(m_c)_1 + 7) - \frac{E_{11,3'}}{E_{31,3'} + \Delta} (m/(m_c)\epsilon - 1) \right]$$

and,

$$f(x) = \frac{1}{x} [\sqrt{1+x} - \sqrt{1-x}] - 1$$

θ_{03} and θ_{04} are in deg/cm-KG. and E_g and Δ are in eV and $f(x)$ is appearing here due to sum over k corrected for the low frequency behavior (Ray 1976).

3.3 Conclusion

Equations (3.1), (3.2), (3.6), and (3.7) give the contributions to the Faraday rotation due to the interband transitions at the L point. For Ge, $\theta_{01} = -12.47$, $\theta_{02} = -11.88$, $\theta_{03} = -8.82$ and $\theta_{04} = -7.98$. The values of the band parameters used are the cyclotron resonance values (Dresselhaus, Kip and Kittel 1955) and the values of the band gaps used are the ultraviolet reflectivity measurement values of Burst *et al* (1962). The values used are

$$m/(m_e)_t = 0.6; \quad m/(m_e)_t = 12; \quad \Delta = 0.2 \text{ eV};$$

$$E_{11,3'} = 2.1 \text{ eV}; \quad \text{and} \quad E_{31,3'} = 5.7 \text{ eV}.$$

Thus from our calculations we see that the L point transitions for Ge do not account for the positive rotation at the low frequency region as was concluded by Pidgeon *et al* (1964), but instead give a new negative singularity near the L point energy gap.

4. Contribution to the polar reflection faraday rotation due to the interband transitions at the L point

The usual method of measuring the Faraday rotation in transmitted light is not possible in a semiconductor in the frequency range where it becomes opaque. However, the Faraday rotation also occurs on reflection from a semiconductor near the absorption band with a magnetic field normal to the surface and has been observed by Lax and Nishina (1961) in InSb near the L point transition energy range. This is known as polar reflection Faraday effect, in nonferromagnetic materials, and should be observable in Ge near the L point energy gap. To examine the validity of our calculations for Ge we evaluate the theoretical polar reflection Faraday rotation spectrum near the above energy range in this section.

From macroscopic theory of Faraday effect one can get (Argyres 1955) easily the polar reflection Faraday rotation θ_r to be given by

$$\theta_r = \frac{4\pi}{w} \text{Im} \left\{ \frac{\sigma_{xy}}{N(N^2-1)} \right\} \quad (4.1)$$

where Im means imaginary part and N is the complex refractive index of the medium given by

$$N = n + ik. \quad (4.2)$$

If the medium is nonabsorbing, $\sigma_y / N(N^2 - 1)$ is real and the rotation of the relected beam vanishes.

Let us take θ_{1r} , θ_{2r} , θ_{3r} and θ_{4r} to be the contributions to the polar reflection Faraday rotation from σ_{1xy} , σ_{2xy} , σ_{3xy} and σ_{4xy} as calculated in section 3 due to the interband transitions at the L point. Then from the expressions for σ_{ixy} , $i = 1$ to 4 and equation (4.1) we obtain

$$\begin{aligned} \theta_{1r} &= \theta_{01r} H[n_0 F'_{2i}(w/E_g) + k_0 F'_{2r}(w/E_g)] \\ \theta_{2r} &= \theta_{02r} H[n_0 F'_{2i}(w/(E_g + \Delta)) + k_0 F'_{2r}\{w/(E_g + \Delta)\}] \\ \theta_{3r} &= \theta_{03r} H[n_0 f'_{1i}(w/E_g) + k_0 f'_{1r}(w/E_g)] \\ \theta_{4r} &= \theta_{04r} H[n_0 f'_{1i}\{w/(E_g + \Delta)\} + k_0 f'_{1r}\{w/(E_g + \Delta)\}] \end{aligned}$$

where, $F'_2(x) = F_2(x)/x$, and $f'_1(x) = f_1(x)/x$. $F'_{2r}(x)$ and $F'_{2i}(x)$ are the real and imaginary parts of $F'_2(x)$, $f'_{1r}(x)$ and $f'_{1i}(x)$ are the real and imaginary parts of $f'_1(x)$.

$$\begin{aligned} n_0 &= (n+1)/2\{(n+1)^2 + k^2\} + (n-1)/2\{(n-1)^2 + k^2\} - n/(n^2 + k^2) \\ k_0 &= k[1/2\{(n+1)^2 + k^2\} + 1/2\{(n-1)^2 + k^2\} - 1/(n^2 + k^2)] \\ \theta_{0ir} &= 0.0039n\theta_{0i}/E_g \quad \text{for } i = 1 \text{ and } 3 \\ \theta_{0ir} &= 0.0039n\theta_{0i}/(E_g + \Delta) \quad \text{for } i = 1 \text{ and } 4. \end{aligned}$$

We note here that the "effective gap" as discussed in Ray (1976) does not have any contribution to the polar reflection Faraday rotation, since $\sigma_{xy}/N(N^2 - 1)$ is real in this case.

Using the expression for θ_{ir} , $i = 1$ to 4, we calculate the polar reflection Faraday rotation spectrum near the L point energy gap for Ge and this is shown in figure 1. The values of n and k used are those of Philipp and Taft (1959). The calculated values of θ_{0ir} , $i = 1$ to 4 for Ge are, $\theta_{01r} = -0.0925$, $\theta_{02r} = -0.0814$, $\theta_{03r} = -0.0654$, and $\theta_{04r} = -0.0521$. The values of the band parameters and band gaps used are given in section 3.3. One important point to note here is that the contribution from Zeeman term predominates and is responsible for the qualitative feature of the spectrum, whereas the contribution from change in matrix element is small and may be neglected.

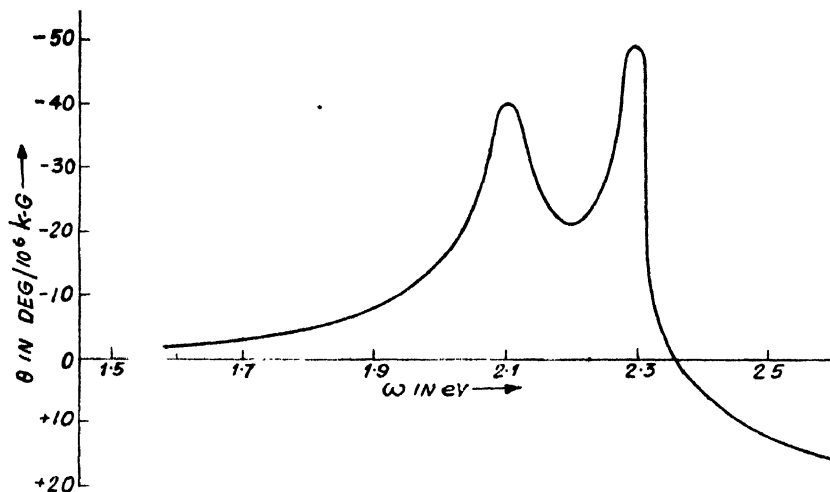


Figure 1. The theoretical polar reflection Faraday rotation of Ge as function of ω at 77°K.

5. Discussion

As there are no experimental results of polar reflection Faraday effect in Ge near the L point energy gap, it is not possible to assess the validity of our calculations at the present moment. However, a measurement of the polar reflection Faraday rotation spectrum in Ge near the above energy range will not only indicate the range of applicability of the present model, which satisfactorily explained the interband Faraday effect in semiconductors (Ray 1976) and inter-valence band Faraday effect in Ge (Ray 1978), but also might enable us to evaluate the unknown valence band parameter δ_1 , which we have taken approximately equal to α_1 .

There exists an experimental result (Lax and Nishina 1961) for the polar reflection Faraday effect in InSb, but the band parameters at the L point of this material is not known well enough to enable us to evaluate the theoretical spectrum. Since the energy band structure of InSb at the L point is very similar to that of Ge it is heartening to note the similarity between the theoretical curve for Ge and the experimental curve of InSb, including the order of magnitude of the rotation. We notice, however, two dissimilarities, namely, that the theoretical curve predicts negative rotation whereas the experimental curve shows positive rotation, and that there is a change in sign in the theoretical curve on the higher frequency side of the band gaps. The first discrepancy could be due to the opposite convention of sign used by Lax and Nishina (1961). (These authors did not specify the sign convention used by them. The sign convention used by the present author is the same as that used by Argyres (1955)). and the

second may be due to the noninclusion of the background rotation in the theory. For InSb it could be reasonable to try to fit the experimental curve with the theoretical expressions given in section 4 treating the unknown band parameters as variable parameters. The values of the unknown band parameters for the best fit should at least give an approximate idea of their magnitudes. This should also be true for other III-V compounds having the Ge-type band structure at the L point.

Acknowledgment

The author wishes to thank Professor L. M. Rath for her guidance.

References

- Argyres P N 1955 *Phys. Rev.* **97** 334
Boswarva I M and Lidiard A B 1964 *Proc. Roy. Soc. (London)* **A278** 588
Boswarva I M and Lidiard A B 1962 *Proc. Int. Conf. on the Physics of Semiconductors, Exeter*, p 308
Burst D, Phillips J C and Bassani F 1962 *Phys. Rev. Lett.* **9** 94
Callaway J 1964 *Energy band theory* (Academic Press, New York)
Dresselhaus G, Kip A F and Kittel C 1955 *Phys. Rev.* **98** 368
Lax B and Nishina Y 1961 *J. Appl. Phys. (Suppl.)* **82** 2128
Luttinger J M 1956 *Phys. Rev.* **102** 1030
Luttinger J M and Kohn W 1955 *Phys. Rev.* **97** 869
Philipp H R and Taft E A 1959 *Phys. Rev.* **113** 1002
Pidgeon C R, Sumner C J, Arai T and Smith S D 1964 *Proc. Int. Conf. on the Physics of Semiconductors*, Paris, p 289
Ray B K 1978 *Indian J. Phys.* **52A** 335
Ray B K 1978 *Indian J. Phys.* **50** 818
Roth L M 1964 *Phys. Rev.* **A133** 542
Roth L M 1960 *Phys. Rev.* **118** 1534

Electron paramagnetic resonance study of Mn^{2+} doped $\text{Zn}(\text{ClO}_4)_2 \cdot 6\text{H}_2\text{O}$

R Dayal*

Department of Physics, Indian Institute of Technology,
Kanpur 208016, U.P.

Received 6 December 1978

Abstract. The EPR investigations of Mn^{2+} doped $\text{Zn}(\text{ClO}_4)_2 \cdot 6\text{H}_2\text{O}$ have been made between 300 K and liquid nitrogen temperature. Mn^{2+} replaces Zn^{2+} at trigonal sites in the crystal and shows the characteristic thirty line hyperfine spectrum for the magnetic field H along the crystallographic c -axis at room temperature. Hyperfine forbidden transitions are observed for H off the c -axis. The observed line-widths show normal behaviour. The temperature variation study indicates the possibility of a distortion in the crystal field at the Mn^{2+} site at 284 ± 2 K.

1. Introduction

Electron paramagnetic resonance study of $\text{Zn}(\text{ClO}_4)_2 \cdot 6\text{H}_2\text{O} : \text{Mn}^{2+}$ at room temperature was first reported by Fritz and Yarmus (1968) who used the experimental arrangements in which the static magnetic field H could be kept parallel to the microwave magnetic field H_1 as well as in the conventional perpendicular orientation. Their main interest was to obtain the relative signs of the spin-Hamiltonian parameters directly by comparing the spectra for these two configurations and to observe the normally forbidden transition ($\Delta M = \pm 1$, $\Delta m = \pm 1$) in the parallel field case. These transitions are observed with H parallel to H_1 due to the breakdown of the selection rules normally forbidding them. The purpose of the present EPR study is to observe hyperfine forbidden transitions in the perpendicular field case at room temperature, to find out the relation in the linewidths of different groups and to investigate any possible phase transitions in this system as it belongs to a series of isomorphous compounds $\text{M}(\text{ClO}_4)_2 \cdot 6\text{H}_2\text{O}$ ($\text{M} = \text{Mg}, \text{Zn}, \text{Fe}, \text{Co}, \text{Ni}$ and Mn) which show phase transitions (Dozsi and Keszthelyi 1966 and Chaudhuri 1975). We have recently reported the studies of EPR and phase transitions in Mn^{2+} doped Mg perchlorate hexahydrate (Dayal *et al* 1978a) Fe, Co and Ni perchlorate hexahydrates (Dayal *et al* 1979a) and Cd perchlorate hexahydrate (Dayal *et al* 1979b, Dayal 1977) crystals.

* Present Address : Department of Physics, Aligarh Muslim University, Aligarh 202001.

Crystal Structure

The crystal structure of $\text{Zn}(\text{ClO}_4)_2 \cdot 6\text{H}_2\text{O}$ (henceforth to be referred to as ZnPH) was determined by West (1935). ZnPH possesses $\text{Mg}(\text{ClO}_4)_2 \cdot 6\text{H}_2\text{O}$ (MgPH)-type structure. However, there is a little difference in the structure of ZnPH and MgPH . In ZnPH , there exists an indefiniteness in the periodicity in the plane normal to the crystallographic c -axis. This was first reported by West (1935) and has been studied recently by Ghosh and Ray (1977). ZnPH crystallizes in pseudohexagonal form with orthorhombic space group C_{2v}^7 . The orthorhombic unit cell contains two molecules and its dimensions (Ghosh and Ray 1977) are

$$a = 7.715 \text{ \AA}, \quad b = a\sqrt{3}, \quad c = 5.22 \text{ \AA}.$$

Surrounding each Zn^{2+} there are six water molecules arranged on the face centres of a cube, one of whose body diagonals is along the crystallographic c -axis. There is a slight extension of the cube along this axis giving the configuration a trigonal symmetry in the pseudohexagonal crystal. The configuration about the second Zn^{2+} in the unit cell is obtained from the first by a 60° rotation about the c -axis. If Mn^{2+} replaces Zn^{2+} in ZnPH and trigonal symmetry is exact, the spectra of the two ions in the unit cell will coincide.

3. Experimental details

ZnPH is prepared by dissolving zinc carbonate in dilute perchloric acid. Crystals of $\text{ZnPH} : \text{Mn}^{2+}$ are grown by slow evaporation of aqueous solution inside a desiccator containing concentrated sulphuric acid. The crystals grow in the form of long slender hexagonal prisms (1010) with end faces not identifiable. They are hygroscopic and were therefore coated with 1:1 mixture of paraffin oil and petroleum jelly before proceeding for EPR study. The EPR spectra are recorded using an X-band Varian V-4502 spectrometer with 100 kHz field modulation and a 9-inch electromagnetic. DPPH is used as a standard field marker taking $g_{\text{DPPH}} = 2.0036$. Temperature variation is done with the help of a Varian V-4540 variable temperature accessory. A copper constantan thermocouple placed at the surface of the crystal and a Leeds and Northrup standard potentiometer give temperature measurements with an accuracy of $\pm 1\text{K}$.

4. Results and discussions

A. Room temperature study

The EPR study of Mn^{2+} doped ZnPH at room temperature has been made with magnetic field H in the ac and ab planes. The principal axes of the Mn^{2+} complexes are located by studying the angular variation of the spectra in these crystallographic planes and getting the extrema in the total width of the spectra,

The total width of the EPR spectrum is maximum for H parallel to the c -axis and the spectrum consists of characteristic 30 lines of the allowed hyperfine transitions ($\Delta M = \pm 1$, $\Delta m = 0$) of Mn^{2+} . Angular variation of this spectrum in the ac plane shows that the total width of the spectrum decreases when H is off the c -axis and attains a secondary maximum for H parallel to the a -axis. Angular variation study in the ab plane shows that the spectrum is nearly symmetric about the c -axis. From these studies, it may be concluded that Mn^{2+} goes substitutionally at Zn^{2+} sites in $ZnPH$ and is thus surrounded by water octahedron stretched along the c -axis. The c -axis is the principal z -axis.

The angular variation of the EPR spectrum may be presented by the spin-Hamiltonian (Burley 1964)

$$\begin{aligned} \mathcal{H} = & g_{\parallel} \beta H_z S_z + g_{\perp} \beta (H_x S_x + H_y S_y) + D \left(S_z^2 - \frac{35}{12} \right) \\ & - \frac{7}{36} (a - F) \left[S_z^4 - \frac{95}{14} S_z^2 + \frac{81}{16} \right] + A S_z I_z + \frac{1}{2} B (S_+ I_- + S_- I_+) \\ & + Q' \left[I_z^2 - \frac{35}{12} \right] - \gamma \beta_n H_z I_z - \gamma \beta_n [H_x I_x + H_y I_y] \end{aligned}$$

where g is the splitting factor, β is the Bohr magneton, H is the steady magnetic field, S is the spin angular momentum operator, D and F are axial crystal field splitting parameters with second and fourth degree terms; ' a ' is the cubic field parameter, A and B are hyperfine constants parallel and perpendicular to z -axis, Q' is the quadrupole interaction parameter, γ , β_n and I are the nuclear gyromagnetic ratio, nuclear magneton and nuclear spin operators respectively. The z -axis is chosen along the crystallographic c -axis. The values of the spin-Hamiltonian parameters obtained are

$$\begin{aligned} g_{\parallel} &= 2.0026 \pm 0.0010, & g_{\perp} &= 2.0005 \pm 0.0010 \\ D &= 125.50 \pm 1.0 \text{ G}, & (a - F) &= 10.2 \pm 1.0 \text{ G} \\ A &= -93.50 \pm 1.0 \text{ G}, & B &= -94.0 \pm 2.00 \text{ G} \end{aligned}$$

The signs of the parameters are relative. These values agree with those obtained by Fritz and Yarnus (1968).

The hyperfine forbidden transitions ($\Delta M = \pm 1$, $\Delta m = \pm 1$) are observed between the lines of the allowed central hyperfine sextet ($M = 1/2 \rightarrow -1/2$) when the magnetic field H is off the c -axis. These are shown in figure 1 for H

at 30° from the c -axis in the ac plane. The separation of the hyperfine forbidden doublets is given by

$$\Delta H = \frac{17B^2}{2H_0} + \left(\frac{2\gamma\beta_n}{g\beta} \right) H_0 - \left[\left(Q' - \frac{4B^2D}{H_0^2} \right) (3 \cos^2\theta - 1) + \frac{25A^2}{2H_0^2} \right] (2m+1)$$

$$H_0 = -\frac{h\nu}{g\beta}$$

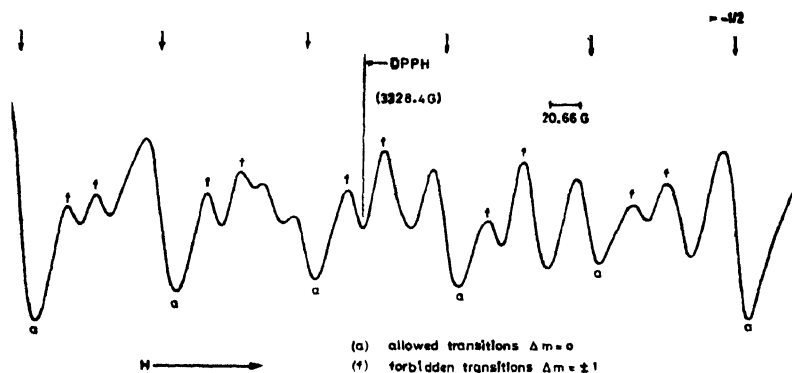


Figure 1. Hyperfine forbidden ($\Delta M = \pm 1$, $\Delta m = \pm 1$) doublets between $M = +1/2 \rightarrow -1/2$ transition for H making an angle 30° from the c -axis in the ac plane in $\text{Zn}(\text{ClO}_4)_2 \cdot 6\text{H}_2\text{O} : \text{Mn}^{2+}$. Allowed transitions of other groups ($M = \pm 3/2 \rightarrow \pm 1/2$) overlap with these doublets.

where γ is the gyromagnetic ratio of the Mn^{55} nucleus, θ is the angle between the principal z -axis and H lying in the ac plane and $m = -5/2$ for doublet occurring between $m = -5/2$ and $m = -3/2$ allowed transitions, and ν is the frequency of microwave radiation. Using the above equation and doublet separation in the spectrum for H at 30° from the c -axis, the value of Q' and

$\frac{\gamma\beta_n}{g\beta}$ have been obtained as

$$Q' = -0.001 \text{ G}$$

$$\frac{\gamma\beta_n}{g\beta} = 0.36 \times 10^{-3}.$$

The value of $\frac{\gamma\beta_n}{g\beta}$ for Mn^{55} nucleus determined here agrees fairly well with that

obtained by other workers (Srivastava and Venkateswarlu 1966, Upreti 1972). The linewidths in the EPR spectrum are very much sensitive to Mn^{2+} concentration in ZnPH . Also the EPR lines of the central hyperfine sextet ($M = +1/2 \rightarrow -1/2$) have smaller width than those of the outer sextets involving larger quantum numbers M . This is the usual behaviour and has been explained by Vanier (1964).

B. Temperature variation study

We have studied the temperature dependence of the principal z-axis spectrum so as to detect any change in the crystal field symmetry at Mn^{2+} site. Such changes are best observed along the principal axes (Müller and Berlinger 1971).

As the temperature is lowered, the total width of the spectrum does not change much. The principal axes also do not change their orientation until 284 K. At about 284 ± 2 K, some distortion is observed in the line shapes of the groups ($M = \pm 5/2 \longleftrightarrow \pm 3/2$). This distortion gradually increases with

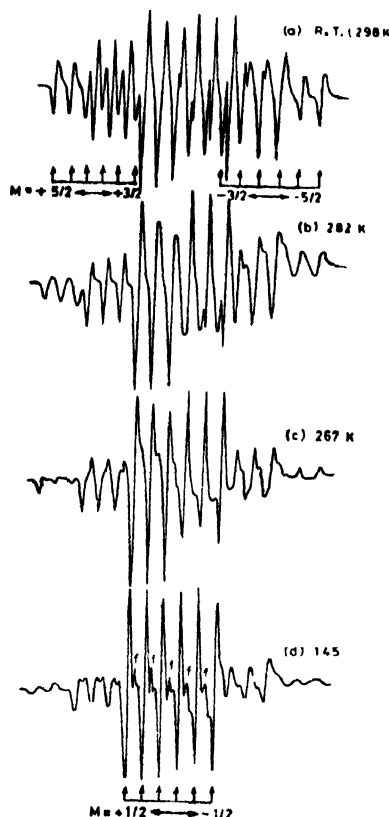


Figure 2. A comparison of the EPR spectra of Mn^{2+} in $\text{Zn}(\text{ClO}_4)_2 \cdot 6\text{H}_2\text{O}$ for H parallel to the c -axis at different temperatures. 'f's indicate hyperfine forbidden transitions.

further decrease in temperature. Figure 2 shows a comparison of the spectra recorded at various temperatures for the magnetic field H parallel to the c -axis. A gradual distortion in the line shapes of the groups ($M = \pm 5/2 \longleftrightarrow \pm 3/2$) with temperature is clearly seen in figure 2.

At lower temperatures, hyperfine forbidden transitions ($\Delta M = \pm 1$, $\Delta m = \pm 1$) between the central allowed transitions ($M = 1/2 \rightarrow -1/2$) appear even for H parallel to the c -axis as seen from figure 2(d). The intensity of these transitions is more for lower temperatures. This indicates that the principal z -axis is no longer parallel to the c -axis at lower temperatures.

From the line shape distortions and the appearance of the hyperfine forbidden transitions even for H parallel to the c -axis, it seems that there occurs some change in the crystal field symmetry at about 284 ± 2 K and it goes on increasing with the fall of temperature. Further studies are needed to check the possibility of a phase transformation in the crystal around this temperature.

Acknowledgments

I thank Professor Putcha Venkateswarlu and Professor D. Ramachandra Rao, Department of Physics, IIT, Kanpur, Dr. M. D. Sastry, Bhabha Atomic Research Centre, Trombay, Bombay and Dr. S. D. Pandey, P.P.N. College, Kanpur for helpful discussions. I also thank Dr. M. V. Ramanaiah, Bhabha Atomic Research Centre, Trombay, Bombay for extending the facilities to record some of the spectra in his laboratory. The help from Dr. A. V. Jain, Department of Physics, IIT Kanpur for low temperature work is gratefully acknowledged. Thanks are also due to the National Bureau of Standards, Washington (D.C.) and Indian National Science Academy, New Delhi for financial assistance through research grants.

References

- Burley S P 1964 *Aust. J. Phys.* **17** 537
- Chaudhuri B K 1975 *Solid State Comm.* **16** 767
- Dayal R 1977 *Ph.D. Thesis, Indian Institute of Technology, Kanpur*
- Dayal R, Ramachandra Rao D and Venkateswarlu P 1978a *Can. J. Phys.* **56** 1175
- Dayal R, Ramachandra Rao D and Venkateswarlu P 1979a *J. Mag. Res.* **36** 99
- Dayal R, Ramachandra Rao D and Venkateswarlu P 1979b *J. Chem. Phys.* **70** 2487
- Dezsi I and Keszthelyi L 1966 *Solid State Comm.* **4** 511
- Fritz I J and Yarmus L 1968 *Phys. Rev.* **173** 445
- Ghosh Minakshi and Ray Siddharth 1977 *Z. Kristall.* **145** 146
- Müller K A and Berlinger W 1971 *Phys. Rev. Lett.* **26** 12
- Shrivastava K N and Venkateswarlu P 1966 *Proc. Ind. Acad. Sci.* **A63** 311
- Upreti G C 1972 *Phys. Stat. Solidi (b)* **54** 387
- Vanier J 1964 *Canad. J. Phys.* **42** 494
- West C D 1935 *Z. Kristall.* **91A** 480

An ultrasonic pulse echo apparatus and velocity of compressional ultrasound in polymer glass

A Kanrar and U S Ghosh

Department of Magnetism

and

S N Bhattacharyya and B M Mandal

Department of Physical Chemistry,

Indian Association for the Cultivation of Science,

Jadavpur, Calcutta 700032.

Received 3 October 1978

Abstract. An ultrasonic pulse echo apparatus for the measurement of the velocity of ultrasonic waves and hence elastic constants in solids has been set up. The apparatus can be used for both the conventional pulse echo technique and coherent pulse/CW technique. Velocity of longitudinal ultrasonic waves in polymer glass (polystyrene) under different degrees of polymerization has been studied with the apparatus.

1. Introduction

The ultrasonic pulse echo (Truell *et al* 1969) and the continuous wave (Bolef and De Klerk 1963) techniques are the most suitable methods for the determination of the velocity of ultrasonic waves in solids and hence their elastic properties. De Klerk (1965) developed a coherent pulse/CW technique which combines both the pulse echo and the continuous wave (CW) techniques and thus utilizes the advantages of both the techniques in a more convenient way for measuring the acoustical wave velocity in solids rapidly. The instrument that we have set up is aimed at measuring the velocity of longitudinal and transverse acoustic waves of frequency 8 MHz in solids by coherent pulse/CW technique. The experimental set up presented here has the advantage that it can be readily converted into pulse echo technique to measure the velocity of acoustic waves in solids, both compressional and transverse where the former method cannot be adopted owing to large ultrasonic attenuation in some solids. We have used the pulse echo technique to measure the velocity of longitudinal acoustic wave of frequency 8 MHz in polymer glass in which large ultrasonic attenuation renders the coherent pulse/CW technique inapplicable. The specimens used are, (i) Polystyrene, (ii) Polystyrene + 10^{-3} Molar AIBN, (iii) Polystyrene + 10^{-2} AIBN, where AIBN stands for Azo-bis-isobutyronitrile and acts as initiator. The purpose is to see

whether the presence of initiator at different concentrations which correspondingly decreases the molecular weight from that of the pure sample causes any detectable change in ultrasonic wave velocities and hence elastic constants.

2. Experimental

Principle of coherent pulse/CW technique

It can be shown (Bolef and Menes 1960) that if the sample, the transducer and the bond is considered as a composite mechanical resonator, the acoustic wave velocity v in the sample can be written as,

$$v = 2l(\nu_{n+1} - \nu_n) = 2l\Delta\nu$$

neglecting the mass correction due to the transducer. Here ν_n and ν_{n+1} are the two successive mechanical resonance frequencies, $\Delta\nu$ is the average frequency separation between them and l is the length of the sample.

The coherent pulse/CW technique which is based on interference principle (De Klerk 1965) can be employed to measure $\Delta\nu$. In this technique, short duration r.f. pulses are generated by coupling the output of r.f. signal generator to a gated power amplifier. This short duration pulse of the carrier frequency excites a piezo-electric crystal of quartz which is cemented to the specimen under test. A single transducer is used both for transmitting and receiving purposes. The acoustic pulse travels down to the specimen and is reflected back from the end surface of the specimen to the transmitting quartz crystal. The successive echoes are then converted into electric pulses by the transducer and are then fed into the input of an amplifier. A low level continuous r.f. signal

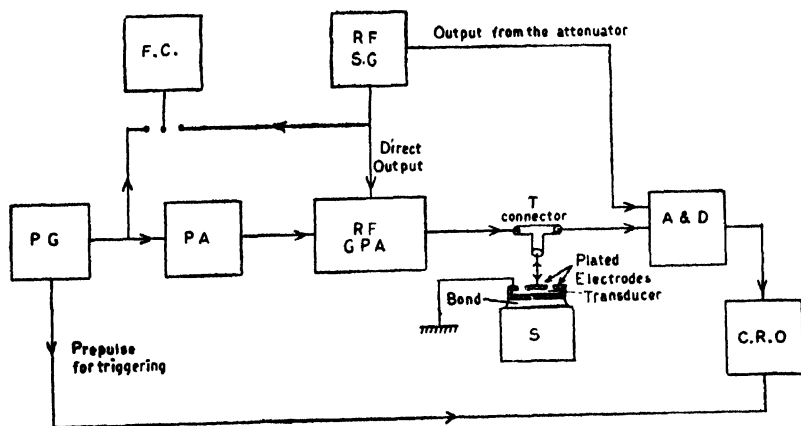


Figure 1.

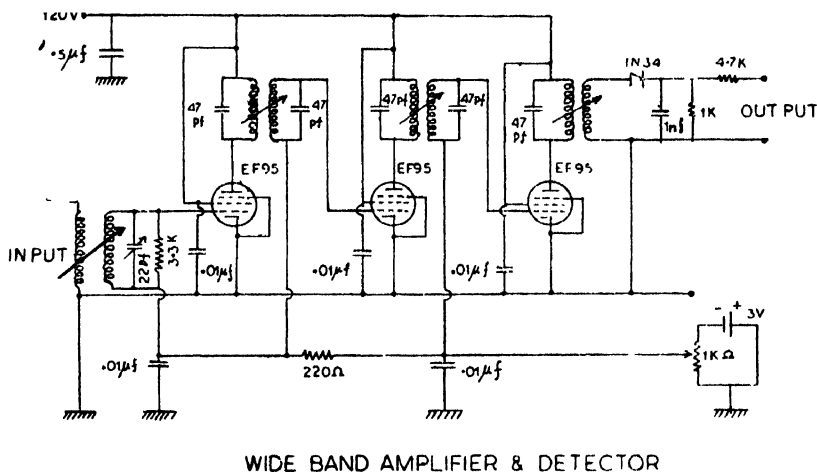
F. C.-Frequency Counter, RFS,G-Radio Frequency Signal Generator, P. G.-Pulses Generator

P. A.-Pulse Amplifier, RFG. P, A,-Radio Frequency Gated Power Amplifier

A&D Amplifier and Detector, s-Sample

Instrumentation :

Block diagram of the complete instrument is shown in figure 1. The instrumentation is basically the same as used by Sinha and Ghatak (1972) with some modifications in the circuitry of pulse amplifier and receiver keeping in view with the availability of components and better performance. These two circuits are shown separately in figures 3 and 4 respectively. The circuitry for the gated power amplifier is based on the same principle as used by De Klerk (1965) and is exactly the same as used by Sinha and Ghatak (1972) for their ultrasonic measurement purpose.

**Figure 4.**

Pulses of about 12 V and of 0.5μ sec duration are obtained from a PM5711 Philips Pulse Generator. Since a higher amplitude pulse is necessary to gate the power amplifier, a pulse amplifier as shown in figure 3 is used. The initial positive going pulse from the pulse generator is used to trigger the schmitt trigger circuit, the output of which is ~ 60 volt. It is then fed to the input of the one shot multivibrator and the large positive going pulse which is ~ 130 volt is obtained at the output without any appreciable distortion. A cathode follower has been used to have low output impedance. This positive going pulse is then applied for gating the power amplifier which provides enough power to excite the quartz transducer. The frequency of the r.f. can be changed by changing the frequency of the standard signal generator (Systronics No. 1101). The repetition rate of the pulsed r.f. can be changed by changing the repetition rate of the pulse generator. Since the measurement has been done for a fixed frequency, a simple transformer coupled type wide band amplifier is designed as shown in figure 4. It has three stages, staggered tuned so that the overall gain is uniform and is more than 60 db with a bandwidth of 2 MHz centered round

(a)

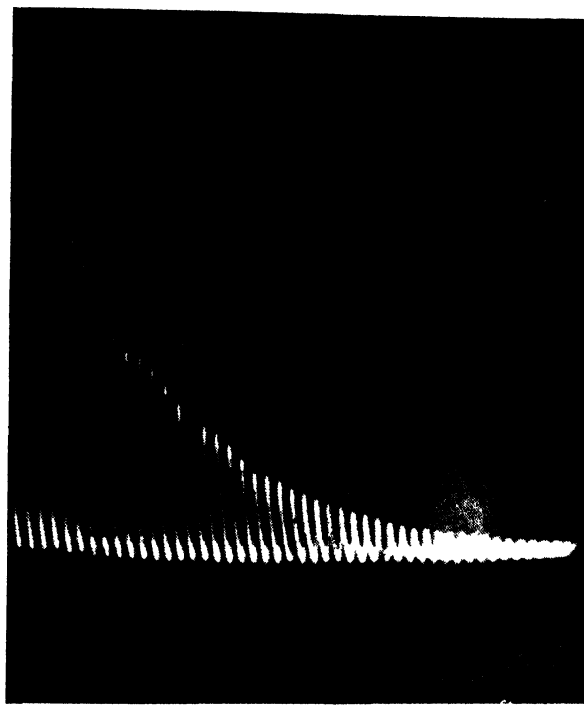
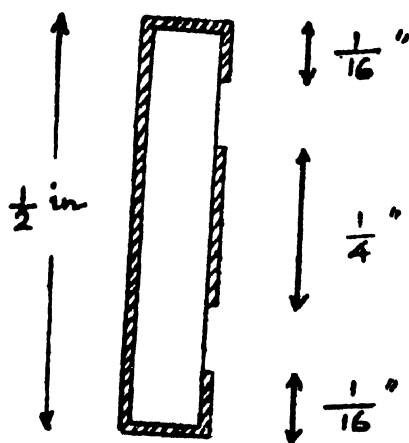


Figure 2: Photograph of coherent pulses/CW signals in aluminium sample. Fig. (a) shows the 'in phase' condition between the pulse echo and the CW signals (resonance).



HALF - SECTIONAL
VIEW

Fig. 5b The edge as shown is coated, so that the back is electrically connected with the outer ring of the front.

(b)

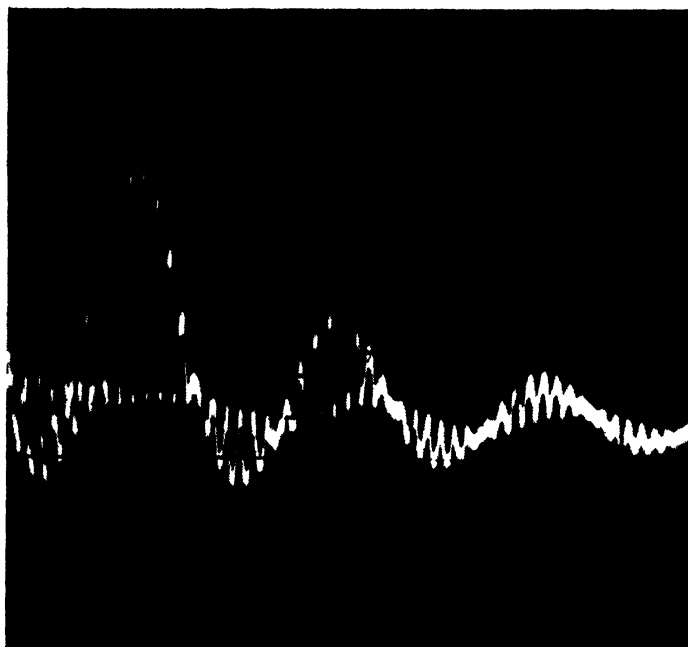
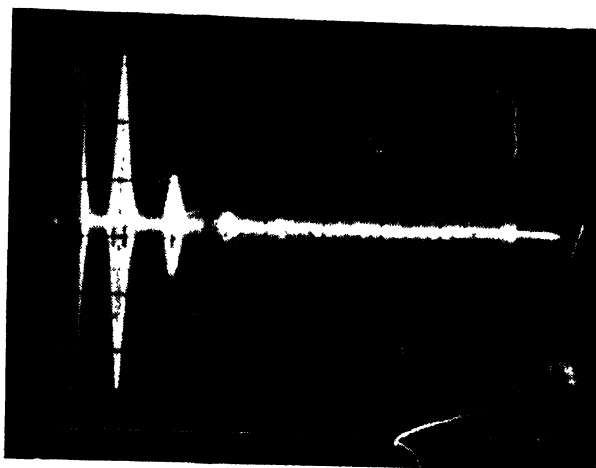


Figure (b) shows the 'out of phase' condition between the CW and pulse signals (out of resonance).

(a)



(b)

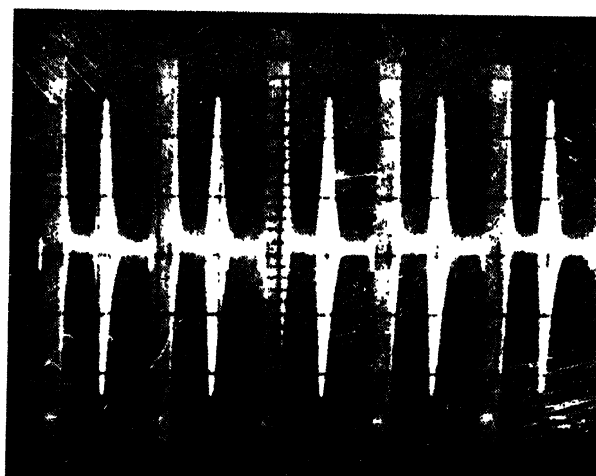


Figure 6: Oscillograms of echo pattern in polystyrene glass in simple pulse echo technique. **Figure 6 (a)** shows the pattern before the pulse superposition method is applied. **Figure 6 (b)** shows the pattern during the 'in phase' condition when pulse superposition method is applied.

obtained from the same signal generator via an attenuator is then mixed with the pulse echo signal as shown in figure 1. Since the wave that traverses through the sample suffers phase change, interference between the two signals will occur. Constructive interference between the two signals will occur when the phase difference between them is $r\pi$ radians, where r is even integer. Destructive interference will occur for all other phase differences, maximum occurring when r is an odd integer. By adjusting the level of continuous wave signal to that of the early echoes and by changing the frequency of the r.f. signal generator, successive mechanical resonance frequencies corresponding to a phase difference of $r\pi$ radians between the pulse echo and CW signals are obtained. The envelop of the resultant echo pattern is exponential at the *in-phase* condition as shown in figure 2a. The slightly non-exponential character in the echo envelope of figure 2a is due to non parallelism of the sample. When the CW and the pulse

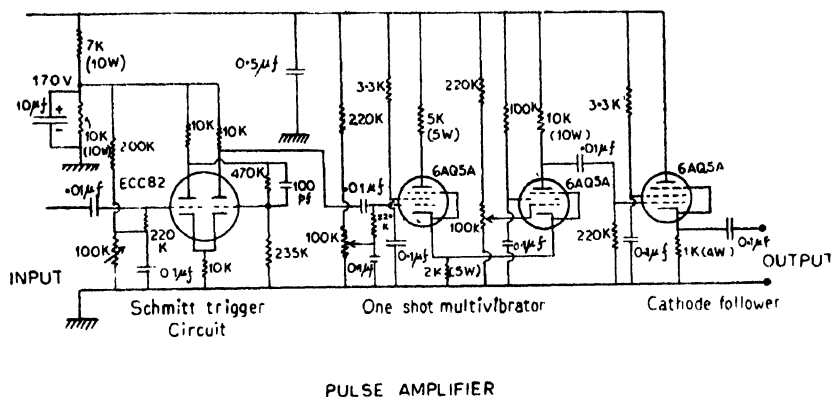


Figure 3.

signals are out of phase, a sinusoidal modulation signal appears on the pulse echo envelope as shown in figure 2b. Oscillograms of figure 2 have been taken using a X-cut quartz crystal of fundamental frequency 8 MHz bonded to a cylindrical rod of aluminium of 2 cm in length and 1.5 cm in diameter.

Principle of pulse echo technique :

With the variable attenuator disconnected, that is, with the absence of the low level continuous r.f. signal which mixes with the pulse echo signal causing interference, a normal pulse echo pattern is obtained on the time base sweep. The repetition rate of the r.f. pulses are then adjusted to cause of superposition of echoes and the repetition rate frequency is measured by means of an electronic counter to yield the velocity of the wave in the sample. This is what is known as pulse superposition method (Mcskimin 1961).

8 MHz. The amplifier is followed by a diode detector IN34 and the final video-visualization of the resulting pattern were obtained on a C.R.O.

For coherent pulse/CW technique, the frequency counter (Ec, Fc 731) is connected with the signal generator to measure the successive mechanical resonance frequencies. For pulse echo technique, the variable r.f. attenuator is disconnected from the amplifier and the frequency counter is connected with the pulse generator to measure the repetition rate of the pulsed r.f.

A reflection type sample holder which includes the transducer bonded to the sample has been used and its design is almost the same as that used by Sinha, and Ghatak (1972).

The transducer is of quartz crystal, having fundamental frequency 8 MHz $\frac{1}{2}$ inch in diameter, gold plated, wrap-around type as shown in figure 5.

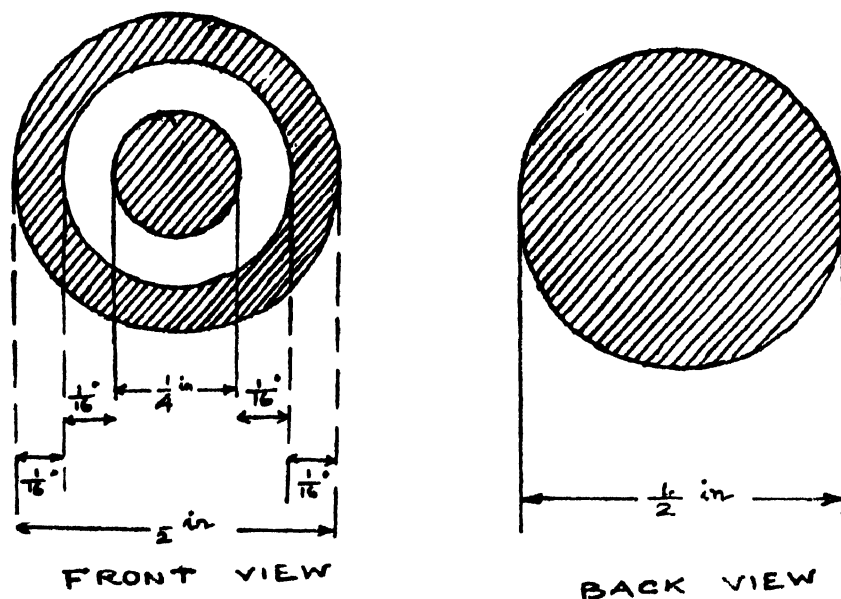


Figure 5: Cross sectional view of the transducer.

Figure 5 (a) The shaded portions in the diagrams is gold coated.

Preparation of the samples

Three samples for polystyrene were used in this study. Sample I was prepared by thermal polymerization of styrene (inhibitor free) at 60°C. Samples II and III were prepared at 60°C using azobisisobutyronitrile (AIBN) as initiator. The AIBN concentrations used were 10^{-3} mole/litre and 10^{-2} mole/litre respectively for sample II and III. It is a common knowledge in free radical polymerization that the molecular weight of the polymer decreases with increasing initiator concentration, the thermal uncatalysed polymerization yielding the

highest molecular weight. It is therefore expected that the molecular weights of the sample used in this study will follow the order sample I > Sample II > Sample III.

The samples are first cut in cylindrical shape with about 1 cm in length (given later in the table 1) and 1.5 cm in diameter. The cutting is such that the two surfaces are rendered parallel. They are initially ground in the grinding wheel with 325 carborundum powder and then finally with 600 alundum powder on a ground glass top. Extreme precautions are taken to make the surfaces scratch free. They are then polished on a polishing machine fitted with a rotating wheel covered with felts on which are sprayed chromium and magnesium powder. The polishing process is done alternatively with chromium and magnesium powder for several times until the surfaces appear perfectly polished. The final touch of polishing was done with chamois leather.

2. Results and discussion

Using X-cut quartz crystal and fundamental frequency 8 MHz, measurements were done on (i) Polystyrene only without any initiator, (ii) Polystyrene + 10^{-3} Molar AIBN as initiator, (iii) Polystyrene + 10^{-3} Molar AIBN as initiator. The ultrasonic attenuation in the samples are very high as is evident in figure (6a) taken for polystyrene only. The attenuation increases with increase of initiator concentration. Because of this high ultrasonic attenuation which results in only a few numbers of echoes, pulse echo technique has been used to measure acoustical wave velocity in these samples.

Longitudinal ultrasonic waves of frequency 8 MHz were generated in the samples by using X-cut quartz crystal which is bonded to the specimens under test with an extremely thin film of Dow Corning 200 silicone oil having viscosity of $\sim 30,000$ es at 25°C .

In the pulse superposition method (Meskinnin 1961) that we have used in the present measurement the repetition rate frequency of the pulse generator is critically adjusted so that the 1st echo of the 2nd pulse superposes on the 3rd echo of the 1st pulse and the amplitude of the summed echoes is made a maximum. This simple 'in phase' condition is attained in our experiment without the use of amplifier which has a tendency to slightly distort the pulse shape thus affecting the accuracy of the experiment. Oscillograms showing the 'in phase' condition is shown in the figure (6b).

Repeated measurements were taken on the same specimen to evaluate reproducibility and influence of the film used.

From the table 1, it is apparent that the presence of the initiator which decreases the degree of polymerization does affect the velocity of compressional ultrasound in polymer glass although the variation is small. The velocity of

compressional ultrasound in polymer glass decreases with the decrease of average molecular weight or size of the polymer molecule. It is known that the modulus of elasticity of polymer increases with the average molecular weight and the curve gradually plateaus off as the degree of polymerization attaining high values (Schmidt and Marlies 1948). The molecular densities of the polymer remaining the same at the high degree of polymerization in this case, the velocity of acoustic wave in the polymer samples should also follow the same behaviour as the modulus of elasticity with respect to average molecular weight. This is exactly what we observe in our present case.

Table 1

Sample	Length of the sample (cm)	Average round trip time (in μ sec)	Velocity in the sample
1) Polystyrene	0.941	9.1492	2.057×10^5 cm/sec
2) Polystyrene + 10 ⁻³ Molar AIBN	0.928	9.1338	2.032×10^5 cm/sec
3) Polystyrene + 10 ⁻² Molar AIBN	1.048	10.4330	2.009×10^5 cm/sec

For transverse waves, successful measurements have not yet been achieved with the present arrangement. Both silicone oil and solol (phenyl salicylate) were tried as bond but the attempts failed to detect any echoes. Determination of both compressional (v_c) and transverse (v_t) velocities will lead to the values of Lamé's constant λ and μ from the following relations,

$$v_c = \left[\frac{\lambda + 2\mu}{\rho} \right]^{\frac{1}{2}} \quad (1)$$

and

$$v_t = (\mu/\rho)^{\frac{1}{2}} \quad (2)$$

where ρ is the density of the solid. These two elastic constants completely define the elastic properties of an isotropic solid.

Acknowledgments

The authors thank Dr. S. K. Sinha of Saha Institute and Dr. S. K. Ghatak of I.I.T., Kharagpur for their valuable suggestions during the development of this work. They gratefully acknowledge the valuable assistance of Dr. A. Chatterjee of Bose Institute and Dr. A. K. Bhadra of C.G.C.R.I. They would also like to thank Dr. (Mrs.) C. Basu for her assistance in the construction of the sample holder.

References

- Bolef D I and De Klerk J 1963 *IEEE Trans.* **UL-10** 20
Bolef D I and Menes M 1960 *J. App. Phys.* **31** 1010
De Klerk J 1965 *Rev. Sci. Instr.* **63** 1540
Ghatak S K and Sinha S K 1974 *Indian J. Phys.* **48** 66
Moskimin H J 1961 *J. Acoust. Soc. Am.* **33** 12
Schmidt A X and Marlies C A 1948 *Principles of high polymer theory and practice* McGraw Hill, New York, Chapter 2
Truell R, Elbaum C and Chick B 1969 *Ultrasonic Methods in Solid State Physics* Academic Press New York

Hot-electron conduction in cadmium selenide

D Mukhopadhyay

Department of Electronics and Telecommunication Engineering,
Jadavpur University, Calcutta-700032.

Received 2 August 1977, revised 7 June 1978

Abstract. The hot-electron conductivity characteristics of cadmium selenide have been calculated using a displaced Maxwellian distribution function. It is found that polar-optical phonon scattering plays the dominant role in determining the mobility at both 300 and 77 K. The mobility at 300 K does not show any appreciable change upto a field of about 15 kV/cm. At 77 K, on the other hand, hot-electron conduction sets in at a field of about 1 kV/cm. The effect of the coupling constants for the different scattering mechanisms on the high-field mobility has been discussed. Marked non-linearity of the high-field conductivity characteristics at 77 K suggests the possibility of efficient harmonic generation in this material.

1. Introduction

For calculation of the current conduction in semiconductors under high field condition one has to solve the Boltzmann equation taking the various scattering mechanisms into account. The Boltzmann equation can be written as

$$\frac{\partial f}{\partial t} = \sum_j \frac{\partial f}{\partial t} \quad (1)$$

where f is the distribution function of the electron system. The subscripts F and j refer to the change of the distribution function due to the applied electric field and due to the j th collision process respectively.

The complications involved in the solution of the Boltzmann equation with polar optical phonon scattering which is neither randomizing nor elastic, can be avoided if one assumes that the carrier concentration in the sample is large enough for carrier-carrier scattering to predominate in both the momentum and the energy exchange processes. Intercarrier collisions do not change the total momentum or energy of the electron system, it only tends to equalise the momentum and energy of the carriers (Stratton 1958). Under this condition all the carriers have the same drift velocity and the distribution function becomes a displaced Maxwellian distribution function given by

$$f = [\hbar^3 / (2\pi m^* k_B T_e)^{3/2}] \exp[-\hbar^2 |k - d|^2 / 2m^* k_B T_e] \quad (2)$$

where $\hbar = h/2\pi$, h being the Planck's constant, m^* is the effective mass of the electrons and T_e is the electron temperature. \mathbf{d} is the common displacement of the electrons in the momentum space and \mathbf{k} is the momentum wave vector for the electron system.

For electron-electron collision to be dominant in both the momentum and energy exchange processes, the carrier concentration for most of the common semiconductors should be in the range of 1×10^{16} to $1 \times 10^{17} \text{ cm}^{-3}$ (Stratton 1958). For the displaced Maxwellian distribution function to be established what is more important is that the momentum be randomized and this is achieved at a carrier concentration one order lower. This explains the good agreement of the theoretical calculations based on the displaced Maxwellian distribution function with the experimental results in samples having a carrier concentration one or two orders lower than that required for the predominance of intercarrier scattering in the momentum and energy exchange processes (Nag 1972). Moreover, the calculations based on the displaced Maxwellian distribution function have the inherent accuracy associated with the method of variation of parameters.

It is now well established that the hot electron conduction characteristics of many semiconductors can be explained by calculations based on the displaced Maxwellian distribution function. It is to be noted that recently numerical techniques, such as Monte-Carlo simulation or the method of iterative integrations, have been developed to study the high-field conduction in semiconductors. Although these methods are supposed to be more accurate in solving the problem, the analytic simplicity of the displaced Maxwellian approach coupled with the closed form results offers distinct advantages.

Hot electron conductivity characteristics of both elemental (Barrie and Burgees 1962) and compound (Glicksman and Hicinbothem Jr. 1963, Butcher and Fawcett 1965, Mukhopadhyay and Nag 1972, Guha 1970) semiconductors have been studied by using a displaced Maxwellian distribution function for the electrons. The results are in good agreement with the experimental values and with other numerical calculations based on the Monte Carlo technique or the method of iterative integration (Nag 1972). The hot-electron microwave conductivity characteristics which are more sensitive to the choice of the distribution function have also been calculated with the displaced Maxwellian distribution function (Kopetz and Potzl 1968, Mukhopadhyay and Nag 1969a, 1969b) and microwave results also show good agreement with experiment.

Though the hot-electron conductivity characteristics of most of the elemental and III-V compound semiconductors have been studied extensively, little attention has been paid to the conductivity characteristics of II-VI compound semiconductors. It is the purpose of this paper to calculate the expected high-field

The explicit expressions for relaxation times are given by

$$\tau_{mac}^{-1} = (8/3)A[E_1^2/\hbar^4\rho C_L^2](m^*k_B T_L)^{3/2}(T_e/T_L)^{1/2}$$

$$\tau_{mps}^{-1} = (1/3)A[e^2 K_m^2/\hbar^2\epsilon_0\kappa_0](m^*k_B T_L)^{1/2}(T_e/T_L)^{-1/2}$$

$$\tau_{mimp}^{-1} = (1/24)A[N_i Z^2 e^4/\epsilon_0^2 \kappa_0^2 m^{*1/2}](k_B T_e)^{-3/2} L_{BH}$$

$$\tau_{mpo}^{-1} = (2/3)N_0\Omega_0 Z_m$$

$$\tau_{Eac}^{-1} = (16/3)A(m^{*5/2}E_1^2/\hbar^4\rho)(k_B T_e)^{1/2}(1 - T_L/T_e)$$

$$\tau_{EPo}^{-1} = (2/3)N_0\Omega_0\gamma Z_E$$

where

$$A = (1/\pi)(2/\pi)^{1/2}$$

E_1 is the deformation potential constant for the acoustic phonons, ρ is the density of the materials and C_L is the velocity of the longitudinal acoustic waves. T_L and T_e are the lattice and electron temperature, respectively. $\kappa_m^2 = P^2/\epsilon_0\kappa_0\rho C_L^2$, is the dimensionless electromechanical coupling constant, P being the piezo-electric constant of the material. N_i is the concentration of ionized impurities, Z is the degree of ionization and is unity for singly ionized impurities.

$$L_{BH} = \ln(1+B) - B/(1+B)$$

$$B = 24\epsilon_0\kappa_0 m^*(k_B T_e)^2/n\hbar^2 e^2,$$

n being the carrier density,

$$N_0 = [\exp(\gamma_L) - 1]^{-1}$$

is the thermal equilibrium number of phonons,

$$\gamma_L = \theta_D/T_L, \quad \gamma = \theta_D/T_e.$$

θ_D being the Debye temperature,

$$\Omega_0 = 2eE_0(2\pi m^*k_B T_e)^{-1/2}$$

$$E_0 = (m^*ek_B\theta_D/4\pi\epsilon_0\hbar^2)[\kappa_\alpha^{-1} - \kappa_0^{-1}]$$

is the characteristic field for polar optical phonon scattering, K_0 and K_α are respectively the dc and optical dielectric constant of the material and ϵ_0 is the free space permittivity.

$$Z_m = (\gamma/2)\exp(\gamma/2)[(e^{x_0}-1)K_0(\gamma/2) + (e^{x_0}+1)K_1(\gamma/2)]$$

$$Z_E = \exp(\gamma/2)[(e^{x_0}-1)K_0(\gamma/2)]$$

$x_0 = \gamma_L - \gamma$ and K_0 and K_1 are the modified Bessel function of the second kind of zeroeth and first order respectively.

3. Results and Discussion

To obtain the velocity-field characteristics, one has to solve the equations (5) and (6) for F and d for different assumed values of the electron temperature T_e .

These equations have been solved using the values of the parameters listed in table 1. The piezoelectric constant, P^2 for which no experimental value is available has been assumed to be $0.3103 \text{ C}^2/\text{m}^4$, the value corresponding to that of cadmium sulphide (Saitoh 1966). Two different assumed values for the velocity of longitudinal acoustic waves, $4.3 \times 10^5 \text{ cm/sec}$ and $5.0 \times 10^5 \text{ cm/sec}$, have been

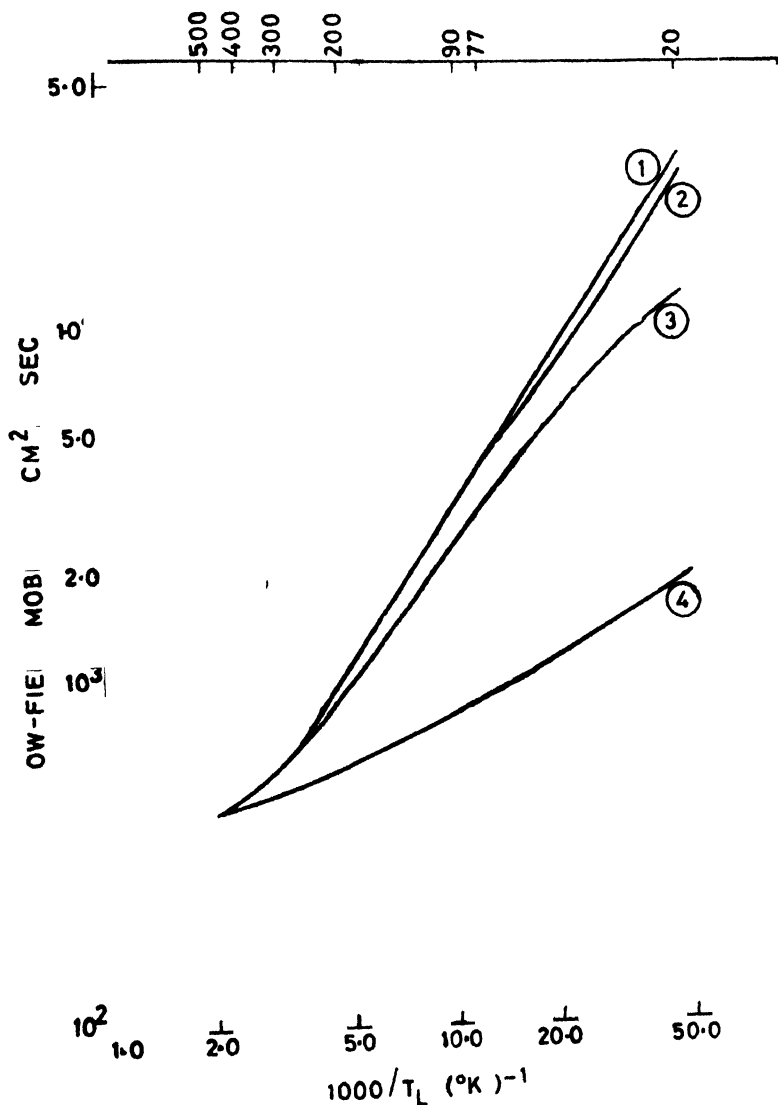


Figure 1. The variation of the low-field mobility with inverse of lattice temperature for different values of the ionized impurity concentration. $E_1 = 18 \text{ eV}$, $K_m^2 = 0.0261$.
 (1) $N_i = 0$, (2) $1 \times 10^{15} \text{ cm}^{-3}$, (3) $1 \times 10^{16} \text{ cm}^{-3}$, (4) $1 \times 10^{17} \text{ cm}^{-3}$.

used for calculations, the values corresponding to those of cadmium sulphide and zinc oxide respectively (Nag 1972). It is to be noted that the velocity of the longitudinal acoustic waves affects both the deformation potential and the piezoelectric scattering. The values of the electromechanical coupling constant, K_m^2 for the above two values of C_1 are 0.035 and 0.026 respectively. The value for the acoustic deformation potential coupling constant E_1 was carried as a parameter and two values, 10 eV and 18 eV were used in the calculation.

We have plotted in figure 1, the values of the low-field mobility against the inverse of lattice temperature for different values of the ionized impurity concentration. It is found that the ionized impurity scattering is unimportant except at temperatures below 77K for impurity concentration upto $1 \times 10^{16} \text{ cm}^{-3}$. For an ionized impurity concentration of $1 \times 10^{17} \text{ cm}^{-3}$, the mobility values are much lower and the mobility is predominantly determined by impurity scattering and such samples may be termed as *impure* so far as lattice scatterings are concerned.

Figure 2 shows the variation of mobility with the applied electric field for different values of ionized impurity concentration at lattice temperatures of 300K and 77K. It is found that there is no perceptible change in mobility

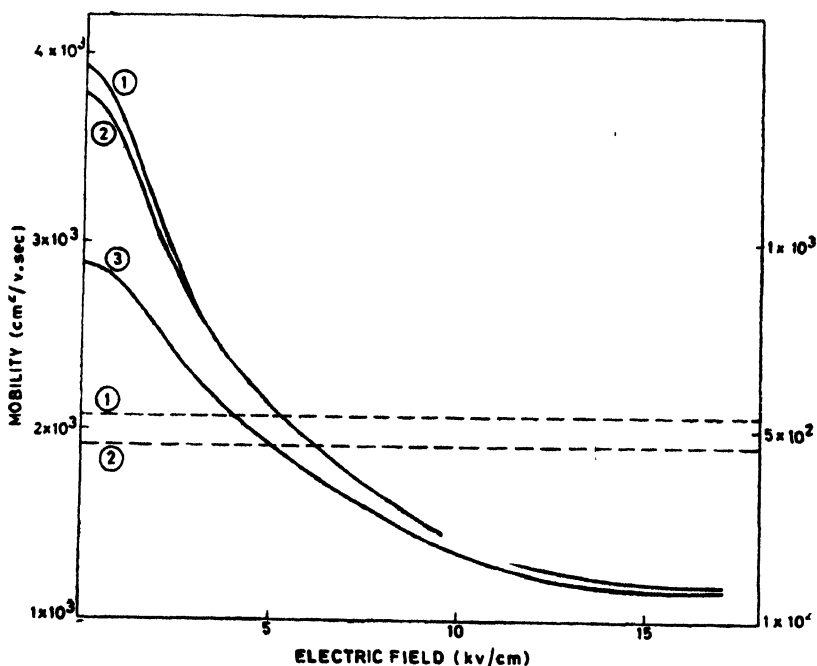


Figure 2. Variation of mobility with applied electric field for different values of ionized impurity concentration at 300 and 77 K. $E_1 = 18 \text{ eV}$, $K_m^2 = 0.0353$
 ——— 77 K, (1) $N_i = 0$, (2) $1 \times 10^{15} \text{ cm}^{-3}$, (3) $1 \times 10^{16} \text{ cm}^{-3}$
 - - - 300 K, (1) $N_i = 0$, (2) $1 \times 10^{17} \text{ cm}^{-3}$

at 300K upto a field of 15 kV/cm. Hence hot-electron effects are not expected to be observed in cadmium selenide at 300K. At 77K on the other hand the mobility gets reduced from its low-field values by a factor of about 3 at a field around 15 kV/cm. Hot-electron effect thus become increasingly prominent at lower lattice temperatures. This is also expected because at lower lattice temperature the mobility value is higher and the power input to the electron system which is proportional to μF^2 increases at lower lattice temperatures. The electron system thus gains energy at a much higher rate at low lattice temperature than at high lattice temperature. The thermal energy of the lattice system also becomes lower at lower temperature and the deviation from the Maxwellian distribution function of the energy distribution function of the electrons increases. It is this non-Maxwellian nature of the energy distribution function for the electron system which gives rise to the hot-electron effects.

The effect of impurity scattering is also found to affect the hot electron characteristics at 77K. The value of the mobility at any field normalized by

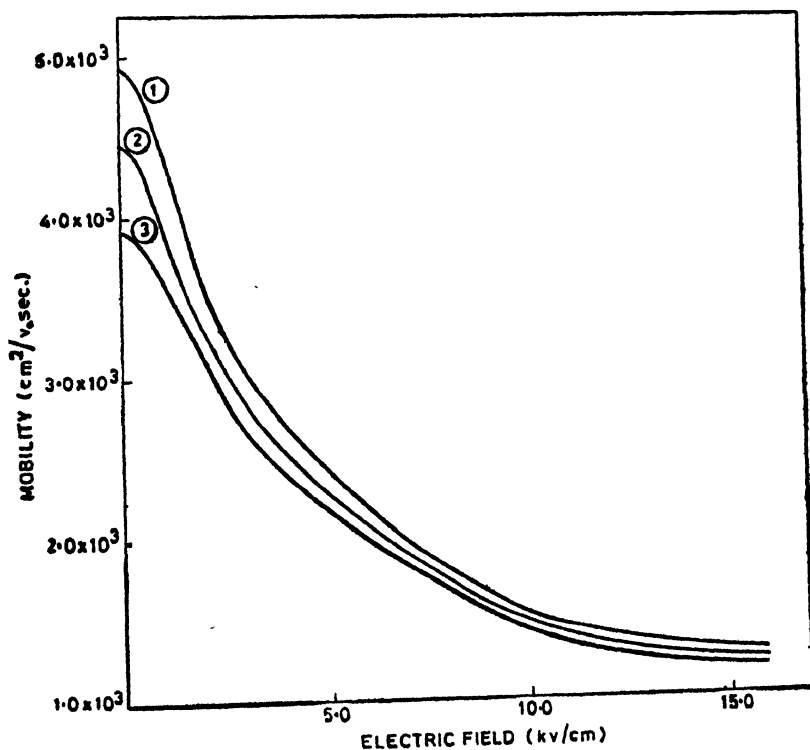


Figure 3. Variation of mobility with applied electric field at 77 K for different values of deformation potential and electromechanical coupling constant.

(1) $E_1 = 10$ eV, $K_m^2 = 0.0261$, (2) $E_1 = 18$ eV, $K_m^2 = 0.0261$,

(3) $E_1 = 18$ eV, $K_m^2 = 0.0353$

its low field mobility becomes higher for higher values of the impurity concentration. At 300K, on the other hand, impurity scattering does not play any role in determining the mobility or its field dependence for impurity concentrations below $1 \times 10^{16} \text{ cm}^{-3}$.

Figure 3 shows that effect of the electromechanical coupling constant and the acoustic deformation coupling constant on the mobility-field characteristics at 77K. It is found that the mobility at any field becomes lower for higher values of either of these coupling constants. This is expected because a higher value of the coupling constant means greater coupling with the phonon system and more frequent collisions.

To have an idea about the extent of nonlinearity in the velocity-field characteristics, we have plotted in figure 4, the drift velocity divided by the low-field mobility against the applied electric field at 77 K. Referring to figure 4, we find that the mobility starts decreasing at an applied electric field around 1 kV/cm and beyond that it shows a marked nonlinearity upto a field of about 6 kV/cm. Beyond this field, the characteristic is almost linear with a slope of about 0.2. The velocity tends to saturation beyond a field of 18 kV/cm, the saturated velocity at 77K being $2.4 \times 10^7 \text{ cm/sec}$.

It is also found that except in the near saturation region, this characteristic shown in figure 4, can be represented fairly accurately in the low-field and in the

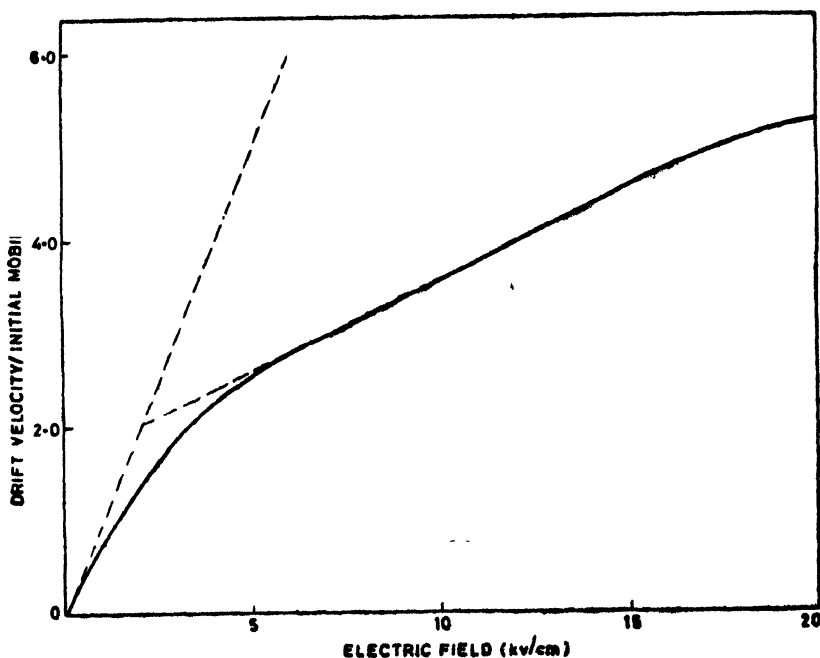


Figure 4. Variation of the ratio of drift velocity to the low-field mobility with applied electric field at 77 K. The two dashed lines have slopes 1 and 0.2.

high-field regions by two straight lines having slopes of 1.0 and 0.2 respectively. These two straight lines intersect at a field value of 2 kV/cm and the characteristic is markedly nonlinear in this region. The presence of this large amount of non-linearity in the hot-electron characteristics suggests that cadmium selenide may be efficiently used for second harmonic generation at 77 K under a bias field around 2 kV/cm. Studies in this direction are in progress and will be reported in future.

4. Conclusions

From the above study of the hot electron conduction characteristics of cadmium selenide one can conclude that

- i) Polar-optical phonon scattering is the predominant scattering mechanism in determining the high-field conduction characteristics of cadmium selenide at both 300 K and 77 K.
- ii) There is no reduction in mobility upto a field of about 15 kV/cm at 300 K. The mobility at 77 K, on the other hand, starts decreasing at a field around 1 kV/cm, showing the onset of the hot-electron region,
- iii) The effect of ionized impurity scattering at 77 K is to reduce the mobility at all values of the applied electric field. At 300 K, ionized impurity is unimportant for impurity concentrations below $1 \times 10^{16} \text{ cm}^{-3}$.
- iv) Both the mobility values and the field-dependence of mobility depend on the choice of the coupling parameters for various scattering mechanism.
- v) There is a marked non-linearity in the hot-electron characteristic at a field around 2 kV/cm. This nonlinearity can be utilized for second harmonic generation under hot-electron condition at 77 K.

Acknowledgment

The author is grateful to B. R. Nag for useful discussions and to J. S. Chatterjee for his encouragement.

References

- Barrie R and Burgess R R 1962 *Canad. J. Phys.* **40** 1056
 Butcher P N and Fawcett W 1965 *Proc. Phys. Soc.* **86** 1205
 Glicksman M and Hicinbotham (Jr) W A 1963 *Phys. Rev.* **129** 1572
 Guha S 1970 *Phys. Rev.* **B2** 4971
 Kopetz H and Potzl H W 1968 *Electron Letts* **4** 79
 Mukhopadhyay D and Nag B R 1969a *Electron. Letts.* **5** 20
 ——— 1969b *Electron. Letts.* **5** 359
 ——— 1969c *Ind. J. Pure Appl. Phys.* **7** 616
 ——— 1972 *Phys. Stat. Sol. (b)* **49** K41
 Nag B R 1972 *Theory of Electrical Transport in Semiconductors* (Pergamon Press)
 Rode D L 1970 *Phys. Rev.* **B2** 1012
 Saitoh M 1966 *J. Phys. Soc. Japan* **21** 2540
 Stratton R 1958 *Proc. Roy. Soc. (A)* **246** 406

Effect of dielectric functions on calculation of lattice dynamics of hexagonal metal

S P Singh and S S Kushwaha

Department of Physics, Banaras Hindu University, Varanasi-221005

Received 11 July 1978, revised 11 September 1978

Abstract. Phonon dispersion relations in beryllium along the three symmetry directions have been determined by means of a two parameter model pseudopotential with different types of screening functions. It is observed that the calculated frequencies using the screening function of Vashishta and Singwi compared well with the recent experimental data on phonon dispersion relations of beryllium.

1. Introduction

In recent years significant work has been done on the lattice dynamics of simple cubic metals using pseudopotential technique. The review of such work is given by Joshi and Rajagopal (1968). Hexagonal close-packed metals, however, received comparatively lesser attention. Roy and Venkataraman (1967) developed matrix elements for studying the lattice dynamics for hcp magnesium from First Principle Pseudopotential theory for the first time. Since then there have been several interesting calculations on the phonon dispersion relations of hcp metals with varied degree of success.

Two basic ideas enter the pseudopotential calculations. They are : (i) pseudo- or model potentials, and (ii) dielectric functions. Several forms of model potential and dielectric functions have been used in the past. In recent years although the significant advances have been made to calculate the correlation energy of electrons in metals (Hubbard 1957, 1958, Goldart and Vosko 1966, Moriarty 1970, 1972a, 1972b), no exact solution of this problem has been made so far. Nevertheless, Singwi and co-workers (1970) have tried to solve this problem as exactly as they could. The latest work on the dielectric screening in the metallic density range is due to Vashishta and Singwi (1972), who have presented a self-consistent treatment of correlations in the homogeneous electron liquid. Their expression is an improvement over the earlier work of Singwi and co-workers (1970). The modification consists in allowing for the change of the pair correlation function in an external weak field via the density derivative

of the equilibrium pair correlation function. The new expression for $f(q)$ is defined by

$$f_{VS}(q) = \left(1 + an \frac{\partial}{\partial n}\right) f'(q)$$

$f'(q)$ is the local field correlation term due to Singwi *et al* (1970), n is the electron density and a is a parameter. Above expression can be conveniently expressed in terms of two constants A and B . Thus

$$f_{VS}(q) = A(1 - e^{-4Bt^2})$$

where $t = \frac{q}{2k_F}$, k_F is the Fermi momentum.

The motivation behind the present work is therefore to test the validity of the latest and most appropriate screening function of Vashishta and Singwi (1972) and also to see the effect of other popular screening functions (Goldart and Vosko 1966 Singwi *et al* 1970) on phonon frequencies of hcp beryllium. Although the screening function of Goldart and Vosko (1966) suffers from a serious lacuna regarding the negative value of pair correlation function, it is still being used by theoretical workers for study the lattice dynamical properties of metals. For this purpose a suitable two parameter model pseudopotential (Kushwaha and Rajput 1970) which has been used quite successfully for studying the lattice dynamical properties of cubic metals (Kushwaha and Rajput 1970, Kushwaha 1973), is chosen by the authors.

2. Theoretical Calculation

The total energy of the system of ions and electrons is separated into two components :

$$E = E^C + E^E \quad (1)$$

where E^C , the electrostatic energy, represents the direct Coulombic interaction between the point ions of charge $+Ze$ immersed in a uniform compensating negative charge E^E , the so called band structure energy, represents the ionic interaction viz. conduction electrons. The ion-core exchange term is insignificant because of the smallness of the core-size for Be, and therefore neglected in the present case.

The phonon dynamical matrix is therefore expressed as consisting of two terms viz. $DC_{\alpha\beta}(q)$ due to electrostatic energy E^C between the point ions and $DE_{\alpha\beta}(q)$ due to band-structure energy E^E :

$$D_{\alpha\beta}(q) = DC_{\alpha\beta}(q) + DE_{\alpha\beta}(q). \quad (2)$$

The phonon-dispersion relation between frequency ω and wave vector q are a Bravais lattice can be easily obtained using the secular determinant in the following way

$$|D(q) - \omega^2 I| = 0 \quad (3)$$

I is the unit matrix ω is the angular frequency and $D(q)$ is a 6×6 dynamical matrix usually written as

$$D(q) = \begin{pmatrix} D(q \ KK) & D(q \ KK') \\ D^*(q \ KK') & D(q \ KK) \end{pmatrix} \quad (4)$$

where $D(q \ KK)$ and $D(q \ KK')$ are 3×3 sub-matrices and $D^*(q \ KK')$ is the complex conjugate of $D(q \ KK')$. The expressions for the Coulombic contribution to the dynamical matrix are obtained following the method of Cochran (1963). The corrected expressions as used here are as follows:

$$\begin{aligned} D^C_{\alpha\beta}(q \ KK) = & \frac{4\pi Z^{*2}e^2}{n\Omega_0 m} \left[\sum_{\mathbf{h}} \frac{(\mathbf{g}_{\mathbf{h}} + \mathbf{q})_{\alpha} (\mathbf{g}_{\mathbf{h}} + \mathbf{q})_{\beta}}{|\mathbf{g}_{\mathbf{h}} + \mathbf{q}|^3} \exp \left(-\frac{|\mathbf{g}_{\mathbf{h}} + \mathbf{q}|^2}{4\eta^2} \right) \right. \\ & \left. - \sum_{\mathbf{h}}' \frac{\mathbf{g}_{\mathbf{h}\alpha} \mathbf{g}_{\mathbf{h}\beta}}{|\mathbf{g}_{\mathbf{h}}|^3} \exp \left(-\frac{|\mathbf{g}_{\mathbf{h}}|^2}{4\eta^2} \right) (1 + \cos(\mathbf{g}_{\mathbf{h}} \cdot \mathbf{R}_{KK'})) \right] \\ & + \frac{(Z^*e)^2}{m} \sum_{\mathbf{l} \neq 0} (\exp(i\mathbf{q} \cdot \mathbf{R}(\mathbf{l} \ K))^{-1}) \left[\left\{ \frac{\text{erfc}(\eta |\mathbf{R}(\mathbf{l} \ K)|)}{|\mathbf{R}(\mathbf{l} \ K)|^3} \right. \right. \\ & + \frac{2\eta}{\sqrt{\pi}} \frac{\exp(-\eta^2 |\mathbf{R}(\mathbf{l} \ K)|^2)}{|\mathbf{R}(\mathbf{l} \ K)|^2} \left. \right\} \delta_{\alpha\beta} - \frac{\{\mathbf{R}(\mathbf{l} \ K)\}_{\alpha} \{\mathbf{R}(\mathbf{l} \ K)\}_{\beta}}{|\mathbf{R}(\mathbf{l} \ K)|^3} \\ & \times \left\{ \frac{3 \text{erfc}(\eta |\mathbf{R}(\mathbf{l} \ K)|)}{|\mathbf{R}(\mathbf{l} \ K)|^3} + \frac{6\eta}{\sqrt{\pi}} \frac{\exp(-\eta^2 |\mathbf{R}(\mathbf{l} \ K)|^2)}{|\mathbf{R}(\mathbf{l} \ K)|^2} + \frac{4\eta^3}{\sqrt{\pi}} \right. \\ & \times \exp(-\eta^2 |\mathbf{R}(\mathbf{l} \ K)|^2) \left. \right\} - \frac{(Z^*e)^2}{m} \sum_i \left[\left\{ \frac{\text{erfc}(\eta |\mathbf{R}(\mathbf{l} \ KK')|)}{|\mathbf{R}(\mathbf{l} \ KK')|^3} \right. \right. \\ & + \frac{2\eta}{\sqrt{\pi}} \frac{\exp(-\eta^2 |\mathbf{R}(\mathbf{l} \ KK')|^2)}{|\mathbf{R}(\mathbf{l} \ KK')|^2} \left. \right\} \delta_{\alpha\beta} - \frac{\{\mathbf{R}(\mathbf{l} \ KK')\}_{\alpha} \{\mathbf{R}(\mathbf{l} \ KK')\}_{\beta}}{|\mathbf{R}(\mathbf{l} \ KK')|^3} \\ & \left. \left\{ \frac{3 \text{erfc}(\eta |\mathbf{R}(\mathbf{l} \ KK')|)}{|\mathbf{R}(\mathbf{l} \ KK')|^3} + \frac{6\eta}{\sqrt{\pi}} \frac{\exp(-\eta^2 |\mathbf{R}(\mathbf{l} \ KK')|^2)}{|\mathbf{R}(\mathbf{l} \ KK')|^2} \right. \right. \\ & \left. \left. + \frac{4\eta^3}{\sqrt{\pi}} \exp(-\eta^2 |\mathbf{R}(\mathbf{l} \ KK')|^2) \right\} \right] \end{aligned} \quad (5)$$

for $K=K'$

$$\begin{aligned}
Dc_{\alpha\beta}(\mathbf{q} \mathbf{K} \mathbf{K}') = & \frac{4\pi Z^{*2}e^2}{n\Omega_0 m} \sum_{\mathbf{g}_h} \left[\frac{(\mathbf{g}_h + \mathbf{q})_\alpha (\mathbf{g}_h + \mathbf{b})_\beta}{|\mathbf{g}_h + \mathbf{q}|^2} \exp\left(-\frac{|\mathbf{g}_h + \mathbf{q}|^2}{4\eta^2}\right) \right. \\
& \times \exp(-i(\mathbf{g}_h + \mathbf{q}) \cdot \mathbf{R}_{\mathbf{K}\mathbf{K}'})] + \frac{(Z^*e)^2}{m} \sum_i \left[\left\{ \frac{\text{erfc}(\eta |\mathbf{R}(\mathbf{1} \mathbf{K} \mathbf{K}')|)}{|\mathbf{R}(\mathbf{1} \mathbf{K} \mathbf{K}')|^3} \right. \right. \\
& + \frac{2\eta}{\sqrt{\pi}} \frac{\exp(-\eta^2 |\mathbf{R}(\mathbf{1} \mathbf{K} \mathbf{K}')|^2)}{|\mathbf{R}(\mathbf{1} \mathbf{K} \mathbf{K}')|^2} \left. \left. \right\} \delta_{\alpha\beta} - \frac{\{\mathbf{R}(\mathbf{1} \mathbf{K} \mathbf{K}')\}_\alpha \{\mathbf{R}(\mathbf{1} \mathbf{K} \mathbf{K}')\}_\beta}{|\mathbf{R}(\mathbf{1} \mathbf{K} \mathbf{K}')|^2} \right. \\
& \times \left\{ \frac{3}{|\mathbf{R}(\mathbf{1} \mathbf{K} \mathbf{K}')|^3} \text{erfc}(\eta |\mathbf{R}(\mathbf{1} \mathbf{K} \mathbf{K}')|)} + \frac{6\eta}{\sqrt{\pi}} \frac{\exp(-\eta^2 |\mathbf{R}(\mathbf{1} \mathbf{K} \mathbf{K}')|^2)}{|\mathbf{R}(\mathbf{1} \mathbf{K} \mathbf{K}')|^2} \right. \\
& \left. \left. + \frac{4\eta^3}{\sqrt{\pi}} \exp(-\eta^2 |\mathbf{R}(\mathbf{1} \mathbf{K} \mathbf{K}')|^2) \right\} \right] \exp(i\mathbf{q} \cdot \mathbf{R}(\mathbf{1} \mathbf{K} \mathbf{K}')). \quad (6)
\end{aligned}$$

for $\mathbf{K} \neq \mathbf{K}'$. The matrix elements corresponding to the band structure part of the energy involve model pseudopotential and the dielectric function. The change in the band structure energy caused by a periodic distribution of wave vector \mathbf{q} is calculated by expanding the structure factor and retaining terms upto second order in the amplitudes of the normal coordinates. These expressions are as follows :

$$\begin{aligned}
D\varepsilon_{\alpha\beta}(\mathbf{q} \mathbf{K} \mathbf{K}) = & -\frac{4\pi Z^{*2}e^2}{n\Omega_0 m} \left[\sum_{\mathbf{g}_h} \frac{(\mathbf{g}_h + \mathbf{q})_\alpha (\mathbf{g}_h + \mathbf{q})_\beta}{|\mathbf{g}_h + \mathbf{q}|^2} F_N(|\mathbf{g}_h + \mathbf{q}|) \right. \\
& \left. - \sum_{\mathbf{g}_h \neq 0} \frac{\mathbf{g}_h \alpha \mathbf{g}_h \beta}{|\mathbf{g}_h|^2} F_N(|\mathbf{g}_h|) (1 + \cos(\mathbf{g}_h \cdot \mathbf{R}_{\mathbf{K}\mathbf{K}})) \right] \quad (7)
\end{aligned}$$

$$D\varepsilon_{\alpha\beta}(\mathbf{q} \mathbf{K} \mathbf{K}') = -\frac{4\pi Z^{*2}e^2}{n\Omega_0 m} \sum_{\mathbf{g}_h} \frac{(\mathbf{g}_h + \mathbf{q})_\alpha (\mathbf{g}_h + \mathbf{q})_\beta}{|\mathbf{g}_h + \mathbf{q}|^2} F_N(|\mathbf{g}_h + \mathbf{q}|) e^{-i\mathbf{q} \cdot \mathbf{R}_{\mathbf{K}\mathbf{K}'}} \quad (8)$$

where \mathbf{g}_h is a reciprocal lattice vector and $F_N(q)$ is the normalized energy-wave-number characteristic given by

$$F_N(q) = -\left(\frac{\Omega_0 q^2}{2\pi Z^{*2}e^2} \right) F(q)$$

Z^* is the effective valence, Ω_0 is the atomic volume and $F(q)$ is the energy-wave-number characteristic given by

$$F(q) = -\frac{\Omega_0 q^2}{8\pi e^2} \frac{|\omega^0(q)|^2}{e^*(q)} \frac{e^*(q)-1}{\{1-f(q)\}} \quad (9)$$

where $\omega^0(q)$ is the Fourier transform of the present model potential

$$\omega^0(\mathbf{r}) = -\frac{Ze^2}{r} + \left(\frac{Ze^2}{r} + \beta \right) e^{-\alpha r}$$

where α and β are two parameters, which have been determined using the following two equations

$$\frac{E}{N} = -E_b - E_i \quad (10)$$

and

$$\Omega_0[\partial(E/N)/\partial\Omega_0] = -\Omega_0 P = 0 \quad (11)$$

E_b is the binding energy per atom of the metal and E_i is the ionization energy of each ion. Knowing the experimental values of these energies, we find the values of parameters. The experimental values of the binding energy for Be is 0.122 Ry, while the ionization energies is 1.37 Ry. By slight adjustment of these parameters we can bring the calculated curves with the measurements within experimental errors. The values of α and β obtained in the present work are given in Table 2. $\epsilon^*(q)$, the modified Hartree dielectric function, is given by

$$\epsilon^*(q) = [1 + \{1 - f(q)\}\{\epsilon(q) - 1\}] \quad (12)$$

$\epsilon(q)$ is the static Hartree dielectric function and $f(q)$ function takes into account for the exchange and correlation effects amongst the conduction electrons. In Hartree's approximation, which includes neither exchange nor correlation effects, $f(q)$ is zero. Hubbard (1957, 1958), who made the first attempt to incorporate the effect of exchange between electrons of parallel spin obtained the following expression for $f(q)$

$$f(q) = \frac{q^2}{2(q^2 + \xi k_F^2)} \quad (13)$$

where ξ is a function of electron density. The parameter ξ is calculated using the following expression

$$\xi = \frac{1}{\{1 + 0.153(\pi a_0 k_F)^{-1}\}}$$

a_0 being the Bohr radius.

For Be, the value of ξ is found to be 1.911.

3. Results and discussion

The axial ratio ($c/a = 1.597$) of this metal departs from the ideal value 1.632, although the departure is not very large. Previously the lattice dynamics of this metal has been studied by many workers (Schmunk *et al* 1962, Dowames *et al* 1965, Gupta and Dayal 1965, Motzbower 1967, Kushwaha 1971, Bose *et al* 1973, Upadhyay and Verma 1973, Rajput and Kushwaha 1973) using force-constants model. Sahni *et al* (1966) calculated the phonon frequencies of Be for the first time using the pseudopotential technique. Later on, Koppel and Maradudin (1967) studied the phonon frequencies of this metal along [0001]

direction applying the first principle pseudopotential technique and obtained a good results with experiments. The phonon frequencies of Be were also calculated by Brovman *et al* (1968) using the pseudopotential approach. The calculated frequencies for the longitudinal modes were higher almost by a factor of two. Gilat *et al* (1969) used optimum model potential (Shaw 1967) for this purpose. The comparison of their calculated results for phonon frequencies with the observed ones showed very unsatisfactory agreement. Prakash and Joshi (1970) computed phonon frequencies of Be using the single OPW electron matrix element and the dielectric function of Singwi *et al* (1970) along $[0001]$ and $[01\bar{1}0]$ directions. A good agreement between calculated and experimental phonon frequencies except for the TO and LO branches in the $[01\bar{1}0]$ direction was obtained. Also the calculated LO branch lies above the TO(11), while the experimental measurements show that the situation is just reverse. Subse-

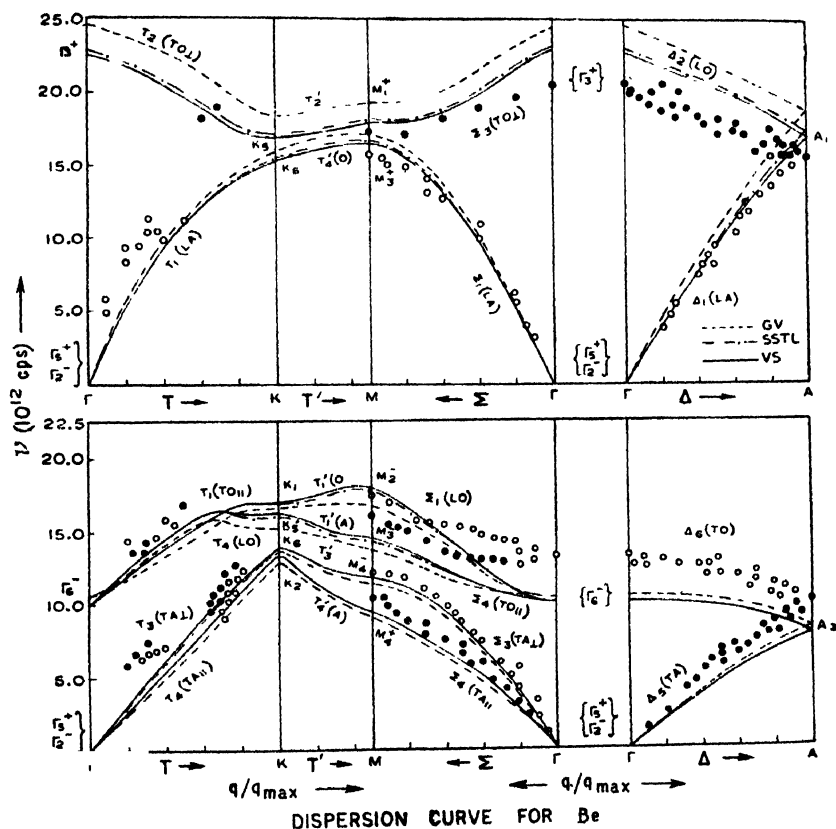


Figure 1. Phonon dispersion relations for Be. The experimental data are sampled from Schmunk *et al* (1962) for the Δ and Σ directions and from Schmunk (1966) for the T direction. The graphs are separated into two diagrams for clarity, as explained in the text. The computed results are shown by broken curves (dotted lines), solid lines (full curves) and chain lines.

quently, King and Cutler (1970) calculated phonon dispersion relations of Be with the exchange approximations for the conduction-band-core exchange due to Slater (1951), Kohn and Sham (1965) and Hartree-Fock. It was observed that although the Slater approximation with its inherent limitations such as (i) overestimating the exchange potential, and (ii) wrong behaviour in the limit of large internuclear separations, it nevertheless gives best agreement with the measured dispersion relations for Be. It was concluded by Bortoni *et al* (1973, 1975) that although the inclusion of three body forces gives the correct ordering of the phonon branches along $[01\bar{1}0]$ direction in the case of Be, they do not change the results of two body theory appreciably in most of hcp metals. These authors used the $f(q)$ function proposed by Singwi *et al* (1970). Recently, Maurya and Srivastava (1975) studied the phonon frequencies along symmetry directions using Toya's theory with his own screening factor and with the modified suggested by Boffey. It was observed by these authors that the screening factor of Boffey played significant role in controlling the vibrational frequencies of beryllium.

In the present case we have made detailed studies of phonon dispersion relations of Be using a two parameter model potential (Kushwaha and Rajput 1970) and three important dielectric functions as mentioned earlier. The calculated results are depicted in figure 1 along with the recent experimental results (Schmunk 1966, Schmunk *et al* 1962). The relevant physical data on which the present calculations are based are given in Tables 1 and 2.

Table 1. Various Physical Constants* used in calculations. Whenever not otherwise specified, the units are a.u.

$a(\text{\AA})$	$c(\text{\AA})$	k_F	Ω_0	$m(\text{at.wt.})$	$\eta(\text{\AA}^{-1})$	Z^{**}
2.2810	3.5770	1.0289	54.36	9.013	0.7672	2.1244

*Gilat *et al* (1969)

**Shaw (1968)

Table 2. Numerical values of the parameters.

A^a	B^a	A^b	B^b	α (a.u.)	β (a.u.)
0.8419	0.3346	0.8883	0.3483	5.099	29.11

Vashishta and Singwi (1972)

Singwi *et al* (1970)

Our computed results obtained with the screening function of Vashishta and Singwi (1972) show very good agreement for all the modes except for optic modes for low wave vectors. Our frequencies are comparable with the frequencies obtained by Prakash and Joshi (1970). Their TO(\perp) branch shows a divergence of about 14% from its corresponding experimental frequencies at M point of

the Brillouin-zone. The results of King and Cutler (1970) are also comparable with our results but they are based on an unsatisfactory exchange function of Slater (1951). This fact has already been explained earlier. Although the computed results of Bertoni *et al* (1973, 1975) are in better agreement with the experimental data, the theory has its own limitations. It is based on the idea of third order perturbation theory. The evaluation of the total electron energy to third order in the electron ion pseudopotential is a difficult task and involves heavy computational work. These authors have compared their results with the computed frequencies based on second order perturbation theory and have discussed the importance and limitations of three body forces.

Acknowledgments

The authors feel pleasure to acknowledge the encouragement rendered by Professors G. S. Verma and P. Krishna. One of us (S.P.Singh) also thanks C.S.I.R. (India) for providing the financial assistance during the course of present research work.

References

- Bertoni C M, Bortoloni V, Calandra C and Nizzoli F 1973 *Phys. Rev. Lett.* **31** 1466
 Bertoni C M, Bisi O, Calandra C and Nizzoli F 1975 *J. Phys. F. Metal Phys.* **5** 419
 Brovman E G, Kagan Y and Kholas A 1968 *Inelastic Scatt. of Neutrons (IAEA, Vienna)* **1** 165
 Bose G, Gupta H C and Tripathi B B 1973 *J. Phys. Soc. (Japan)* **34** 1006
 Cochran W 1963 *Proc. Roy. Soc. (London)* **A276** 308
 Dewames R E, Wolfram T and Lehman G W 1965 *Phys. Rev.* **188** A717
 Geldart D J W and Vosko S H 1966 *Cand. J. Phys.* **44** 2137
 Gilat G, Rizzi G and Cubiotti G 1969 *Phys. Rev.* **186** 971
 Gupta R P and Dayal B 1965 *Phys. Stat. Solidi* **8** 115
 Hubbard J 1957 *Proc. Roy. Soc. (London)* **A240** 539
 Hubbard J 1958 *Proc. Roy. Soc. (London)* **A243** 336
 Joshi S K and Rajagopal A K 1968 in *Solid State Physics* edited by F Seitz and D Turnbull (Acad. Press, Inc. New York) **22** 159
 King F W and Cutler P H 1970 *Phys. Rev.* **B2** 1733
 King F W and Cutler P H 1970 *Phys. Lett.* **31A** 150
 Kohn W and Sham L J 1965 *Phys. Rev.* **140** A1133
 Koppel J V and Maradudin A A 1967 *Phys. Lett.* **24A** 244
 Kushwaha S S 1971 *Phys. Lett.* **37A** 193
 Kushwaha S S 1973 *Phys. Stat. Sol. (b)* **59** 285
 Kushwaha S S and Rajput J S 1970 *Phys. Rev.* **B2** 3943
 Maurya J R and Srivastava R S 1975 *J. Phys. F. Metal Phys.* **5** 2256
 Metzbowser E A 1967 *Phys. Stat. Solidi* **20** 681
 Moriarty J A 1970 *Phys. Rev.* **B1** 1363
 Moriarty J A 1972a *Phys. Rev.* **B6** 1239
 Moriarty J A 1972b *Phys. Rev.* **B3** 4445
 Prakash S and Joshi S K 1970 *Phys. Rev.* **B1** 1468
 Rajput J S and Kushwaha S S 1973 *J. Phys. F. Metal Phys.* **3** 1531
 Roy A P and Venkataraman G 1967 *Phys. Rev.* **156** 769
 Sahni V C, Venkataraman G and Roy A P 1966 *Phys. Lett.* **23** 633
 Schunk R E 1966 *Phys. Rev.* **149** 450
 Schunk R E, Brugger R M, Randolph P D and Strong K A 1962 *Phys. Rev.* **128** 562
 Singwi K S, Sjolander A, Tosi M P and Land R H 1970 *Phys. Rev.* **B1** 1044
 Shaw R W Jr 1968 *Phys. Rev.* **174** 769
 Shaw R W Jr and Harrison W A 1967 *Phys. Rev.* **163** 604
 Slater J C 1951 *Phys. Rev.* **81** 385
 Upadhyay J C and Verma M P 1973 *J. Phys. F. Metal Phys.* **3** 571
 Vashishta P and Singwi K S 1972 *Phys. Rev.* **B6** 875

Letters to the Editors

Application of the shell model to the pressure dependence of the dielectric constants of alkali halides

O P Sharma*, H P Sharma and Jai Shanker

Department of Physics, Agra College, Agra-282002

Received 7 June 1977, revised 7 December 1978

The shell model originally proposed by Dick and Overhauser (1958) (herein after referred to as DO) has been widely used to describe the dielectric behaviour of ionic solids (Hanson and Lawson 1959, Havings 1960). The equations of motion of shell and cores of the ions lead to a relation between the pressure derivatives of low and high frequency dielectric constants (Havings 1960) which can provide a better test of the shell model theory. The reliable experimental data on the dielectric constants and their pressure derivatives are now available for alkali halides (Lowndes and Martin 1969, 1970). It is found that the expression for the strain derivatives of dielectric constants derived by Havings on the basis of the simple shell model is not satisfied with the experimental data. An obvious improvement in the shell model analysis can be made by considering the deformability of the shell. This can be incorporated in terms of the exchange charge polarization model developed by DO. This model gives

$$\frac{-1}{\epsilon_{\infty}+2} \frac{3V}{4\pi} \left[\frac{(n_+e-D)^2}{k_+} + \frac{(n_-e+D)^2}{k_-} - \left[\frac{n_+e-D}{k_+} - \frac{n_-e+D}{k_-} \right]^2 \right] \times \left(\frac{1}{A} + \frac{1}{k_+} + \frac{1}{k_-} \right)^{-1} \quad (1)$$

where n and k are the shell model parameters representing the shell charge and spring constant respectively. A is the short range force constant and D is the exchange charge polarization parameter introduced by DO. Differentiating equation (1) with respect V we obtain

$$\frac{9V}{4\pi(\epsilon_{\infty}+2)^2} \frac{d\epsilon_{\infty}}{dV} + \frac{\epsilon_{\infty}-1}{\epsilon_{\infty}+2} \frac{3}{4\pi} = - \frac{2D}{A} [(s-1)e-D] - [(s-1)e-D]^2 \frac{1}{A^2} \quad (2)$$

* Present address : P.G. College, Ambah (M.P.).

where $D' = \frac{dD}{dV}$ and $A' = \frac{dA}{dV}$. The Szigeti (1950) effective charge parameter s appearing in equation (2) is now given by

$$s-1 = \frac{D}{e} + \frac{1}{e} \left[\frac{n_+e-D}{k_+} - \frac{n_-e+D}{k_-} \right] \left(\frac{1}{A} + \frac{1}{k_+} + \frac{1}{k_-} \right)^{-1} \quad (3)$$

We calculate D from equation (3) taking experimental values of s from (Lowndes and Martin 1969) and using revised data of the shell model parameters (Dick 1966). The short range force constant between nearest neighbours for NaCl type crystals can be expressed as (Born and Huang 1954)

$$A = 2[\phi''(r) + 2\phi'(r)/r] \quad (4)$$

where $\phi'(r)$ and $\phi''(r)$ are respectively the first and second order derivatives of the short range repulsive potential $\phi(r)$ with respect to interionic separation r .

Using the Born-Mayer exponential form $B \exp\left(-\frac{r}{\rho}\right)$ for $\phi(r)$, we can find the following expression for A'

$$A' = -\frac{1}{6r^2} \frac{dA}{dr} = -\frac{B \exp(-r/\rho)}{3r^2\rho} \left[\frac{2}{r\rho} + \frac{2}{r^2} - \frac{1}{\rho} \right] \quad (5)$$

Values of A and A' are calculated (table 1) from equations (4) and (5), respectively, taking the repulsive parameters B and ρ from Tosi (1964). Now equation (2) can be used to evaluate D' taking A , A' and D from table 1 and using experimental data on $V \frac{d\epsilon_\infty}{dV}$ from Sharma *et al* (1976). By differentiating equation (3) with respect to V , one can find

Table 1. Values of A (10^4 ergs/cm²), A' (10^{28} ergs/cm³), D (10^{-10} e.s.u.) and D' (10^{14} e.s.u./cm³).

Crystal	A	A'	D	D'
LiF	9.02	-1.25	-0.29	0.12
NaF	6.25	-0.59	-0.38	0.09
NaCl	4.92	-0.33	-0.50	0.13
NaBr	4.04	-0.23	-0.63	0.14
KCl	3.86	-0.19	-0.50	0.14
KBr	3.56	-0.16	-0.62	0.14
KI	2.97	-0.11	-0.75	0.12
RbCl	3.97	-0.19	-0.34	0.09

$$\frac{ds}{dV} = \frac{D'}{e} + \frac{A'\mu + A\mu'}{e(1+A\lambda)} - \frac{A\mu A'\lambda}{e(1+A\lambda)^2} \quad (6)$$

where

$$= \frac{n_+e - D}{k_+} - \frac{n_-e + D}{k_-} \quad (7)$$

$$\lambda = \frac{1}{k_+} + \frac{1}{k_-} \quad (8)$$

and

$$\mu' = -\lambda D' \quad (9)$$

Values of $\frac{V}{s} \left(\frac{ds}{dV} \right)$ obtained from equation (6) are listed in table 2. A method for evaluating $\frac{V}{s} \left(\frac{ds}{dV} \right)$ based on the deformation dipole model (DDM) of Hardy (1960, 1962) and Mitskevitch (1964) has been suggested by Lowndes and Martin (1970). Values of $\frac{V}{s} \left(\frac{ds}{dV} \right)$ obtained from the DDM are also included in table 2 the sake of comparison. The positive values of $\frac{V}{s} \left(\frac{ds}{dV} \right)$ have the physical significance that the effective charge decreases when the crystal is compressed under hydrostatic pressure. This seems to be physically plausible since the ionic distortions are expected to increase under compressive stress, thereby decreasing the effective charge of the ions.

It should of course be remarked here that in deriving equation (3) two types of polarizations viz. the exchange charge polarization and the short range interaction polarization have been considered. DO have argued that both these effects are responsible to reduce the magnitudes of the ionic charges. Accordingly one can write

$$\frac{ds}{dV} = \left[\left(\frac{ds}{dV} \right)_{\text{exchange}} \right] + \left[\left(\frac{ds}{dV} \right)_{\text{short range}} \right] \quad (10)$$

In fact the contribution $\left[\left(\frac{ds}{dV} \right)_{\text{exchange}} \right]$ arising from the exchange charge polarization is just equal to $\frac{D'}{e}$ and hence the contribution $\left[\left(\frac{ds}{dV} \right)_{\text{short range}} \right]$ from the short range interaction polarization can be estimated from equation (10). Values of $\left[\left(\frac{ds}{dV} \right)_{\text{exchange}} \right]$ and $\left[\left(\frac{ds}{dV} \right)_{\text{short range}} \right]$ thus calculated have

been listed in table 2. It is informative to observe from there that the contribution from the exchange charge polarization towards $\frac{V}{s} \left(\frac{ds}{dV} \right)$ is substantially larger than that from the short range interaction polarization. It is also interesting to note that values of $\frac{V}{s} \left(\frac{ds}{dV} \right)$ based on DDM generally lie between

$$\left[\frac{V}{s} \left(\frac{ds}{dV} \right) \text{ exchange} \right] \text{ and } \left[\frac{V}{s} \left(\frac{ds}{dV} \right) \text{ short range} \right].$$

Table 2. Values of the strain derivative of the Effective Charge Parameter.

Crystal	$\frac{V}{s} \left(\frac{ds}{dV} \right)$			
	Present study	From the Deformation Dipole model	$\left[\frac{V}{s} \left(\frac{ds}{dV} \right) \text{ Exchange} \right]$	$\left[\frac{V}{s} \left(\frac{ds}{dV} \right) \text{ Short range} \right]$
LiF	0.85	0.50	0.52	0.33
NaF	0.78	0.50	0.57	0.21
NaCl	2.11	0.96	1.62	0.49
NaBr	2.66	1.07	2.17	0.49
KCl	2.55	0.82	2.25	0.30
KBr	3.01	1.09	2.66	0.35
KI	3.81	1.29	2.93	0.88
RbCl	1.91	0.81	1.63	0.28

References

- Born M and Huang K 1954 *Dynamical Theory of Crystal Lattice* (Oxford, Glarendon Press)
 Dick B G and Overhauser A W 1958 *Phys. Rev.* **112** 90
 Dick B G 1966 *Phys. Rev.* **145** 609
 Hanlon J E and Lawson A W 1959 *Phys. Rev.* **113** 472
 Hardy J R 1960 *Phil. Mag.* **6** 27
 Hardy J R 1962 *Phil. Mag.* **7** 663
 Havinga E E 1960 *Phys. Rev.* **119** 1193
 Lawndes R P and Martin D H 1969 *Proc. Roy. Soc.* **A308** 473
 Lowndes R P and Martin D H 1970 *Proc. Roy. Soc.* **A216** 351
 Mitskevitch V V 1964 *Soviet Phys. Solid State* **5** 2568
 Sharma H P, Jai Shanker and Verma M P 1976 *J. Phys. Chem. Solids* **37** 1077
 Szigeti B 1950 *Proc. Roy. Soc.* **A204** 51
 Tosi M P 1964 *Solid State Physics* **16** 1

On the probable radiative and other two-body decays of the upsilon and the tests of QCD

Sankari Saha and P Mukhopadhyay

Department of Physics, Jadavpur University, Calcutty 700032

Received 29 January 1979

This note concerns itself with the feasibility of occurrences in nature of the recently suggested probable radiative and other two-body decays of the upsilon. It has been discussed in this note that the radiative decays of the upsilon offer the most convenient platform for the tests of QCD as they are *not* suppressed by the pseudo-dimension rule which, however, kills some of the non-radiative decay channels.

Recently the radiative and other probable two-body non-radiative decay modes of the upsilon, $\nu(9500)$, have been investigated by Brodsky *et al* (1978) and Randa *et al* (1978). It may be mentioned here that Brodsky *et al* (1978) have advocated that the radiative decays $\nu \rightarrow X\gamma$ (where X is a pseudo-scalar hadron) can offer a convenient platform for the quantitative tests of the Quantum Chromodynamics (QCD). In this note we have shown that the radiative decays $\nu \rightarrow X\gamma$ are completely allowed by the pseudo-dimension rule (Mukhopadhyay 1975, 1978) which, however, guillotines some of the theoretically expected non-radiative decay channels. It may be recalled that Brodsky *et al* (1978) have also recommended the decays $\nu \rightarrow Xe^+e^-$ (which occurs via the off-mass-shell photon) for the quantitative tests of the QCD along with the decays $\nu \rightarrow X\gamma$ (as mentioned above) for the same purpose. In this note we have pointed out that the decays $\nu \rightarrow Xe^+e^-$ stand the risk of being suppressed by the pseudo-dimension rule (Mukhopadhyay 1975, 1978). We have, therefore, emphasized in this note that for the quantitative tests of QCD the most suitable decays are $\nu \rightarrow X\gamma$ which, as already mentioned, have been strongly advocated Brodsky *et al* (1978). In this note we have also emphasized the fact that the coupled-channel analysis (which is necessary for the identification of the hadronic modes) for ν -decay will be simpler than expected due to pseudo-dimension rule which kills some of the non-radiative two-body as well as many-body decay modes for the particle concerned.

The pseudo-dimension rule (Mukhopadhyay 1975, 1978) reads: All the allowed decays of an unstable particle must be governed by *one and only one* of the following two constraints

$$d_u \geq D \quad (1a)$$

and

$$d_u \leq D \quad (1b)$$

where d_u is the magnitude of the pseudo-dimension of the field of the unstable particle and D is the sum of the magnitudes of the pseudo-dimensions of the fields of the particles constituting a decay mode. The magnitudes of the pseudo-dimensions, denoted by d , of free fields are given by the following relations (Mukhopadhyay 1975, 1978).

$$d = 3J \text{ for fields having } J \neq 0, J \text{ being the actual spin} \quad (2a)$$

$$d = 1 \text{ for fields having } J = 0 \quad (2b)$$

$$d = 2 \text{ for the photon.} \quad (2c)$$

As equations (2a)–(2c) refer to free fields, therefore, the quantity D appearing in relations (1a) and (1b) refers to a decay mode *not* occurring through subreactions which necessitate interacting fields. For this reason, the selection rule stated above concerns itself, for example, with the 3π mode but *not* with the quasi two-body mode $\rho\pi$ (which results from the subreactions associated with the 3π mode) in $\phi(1020)$ -decay.

To demonstrate how the pseudo dimension rule for particle decays, discussed above, reduces the number of theoretically expected but unobserved decay modes of unstable particles, we consider the example of the decays of the $\omega(783)$. The observed decays $\omega(d_u = 3) \rightarrow 2\pi(D = 2)$, $3\pi(D = 3)$, $\pi^0\gamma(D = 3)$, $e^+e^-(D = 3)$, indicate that the ω -decay is governed by the constraint $d_u \geq D$, since $d_u = 3$, which follows from equation (2a) as the decaying particle ω is a spin-one particle and for the 2π mode $D = d_\pi + d_\pi = 1 + 1 = 2$ as $d_\pi = 1$ given by equation (2b). For the $\pi^0\gamma$ mode, $D = d_\pi + d_\gamma = 1 + 2 = 3$ since $d_\gamma = 2$ as evident from equation (2c) and for the e^+e^- mode $D = d_{e^+} + d_{e^-} = 3/2 + 3/2 = 3$ as $d = 3/2$, for a spin $-\frac{1}{2}$ particle which follows from equation (2a). As stated above, the pseudo-dimension rule demands that one and the same constraint must be valid for all the allowed decays (*not* occurring through subreactions) for a given unstable particle. Since the constraint $d_u \geq D$ is found to be valid in the observed decays of ω , therefore, the same constraint must be satisfied by all other allowed decays of the particle concerned. It is interesting to note that for the decay of ω theoretically expected decay modes $\pi^0\mu^+\mu^-(D = 4)$, $\pi^+\pi^-\gamma(D = 4)$, $3\gamma(D = 6)$ clearly fail to satisfy the constraint $d_u \geq D$ as $d_u = 3$ for ω and it is gratifying to note that these modes have not been seen so far (Particle Data Group 1978). Also, the observed decays $\psi(3100, d_u = 3) \rightarrow e^+e^-(D = 3)$, $\mu^+\mu^-(D = 3)$, $4\pi(D = 4)$, $5\pi(D = 5)$, $6\pi(D = 6)$, $7\pi(D = 7)$ and $\psi'(3685, d_u = 3) \rightarrow e^+e^-(D = 3)$, $\mu^+\mu^-(D = 3)$, $\psi(3100)\eta(D = 4)$, $\psi(3100)\pi\pi(D = 5)$, $5\pi(D = 5)$ suggest that both $\psi(3100)$ -decay and $\psi'(3685)$ -decay are governed by the constraint $d_u \leq D$ according to which the modes $\pi\pi(D = 2)$, $K\bar{K}(D = 2)$ are forbidden (and as such should be suppressed) for the decays of the particles concerned. Needless to mention that the $\pi\pi$ and $K\bar{K}$ modes have not been seen (Particle Data Group 1978) in the decays of the $\psi(3100)$ and $\psi'(3685)$ inspite of the fact that the decays $\psi(3100) \rightarrow \pi\pi$, $K\bar{K}$ and $\psi'(3685) \rightarrow \pi\pi$, $K\bar{K}$ have non-vanishing QED amplitudes.

We now examine in the light of the pseudo-dimension rule the feasibility of occurrences of the theoretically expected modes (Randa *et al* 1978, Brodsky *et al* 1978), $\pi\gamma$, $\eta\gamma$, $\eta'\gamma$, $K\bar{K}$, $D(1865)\bar{D}(1865)$, $F\bar{F}$, $K^*\bar{K}$, $D^*\bar{D}$, $F^*\bar{F}$, $\eta\omega$, $\eta'\omega$, $\eta'\phi$, $\rho\pi$, etc. in the ν -decay. According to the pseudo-dimension rule, apart from the already observed pure leptonic modes e^+e^- , $\mu^+\mu^-$ (Particle Data Group 1978), either the decays $\nu(d_u = 3) \rightarrow K\bar{K} (D=2)$, $D(1865)\bar{D}(1865) (D=2)$, $F\bar{F} (D=2)$, $\eta\gamma (D=3)$, $\eta'\gamma (D=3)$, $\pi\gamma (D=3)$, etc. governed by the constraint $d_u \geq D$ or the decays $\nu(d_u = 3) \rightarrow \eta\gamma (D=3)$, $\eta'\gamma (D=3)$, $\pi\gamma (D=3)$, $\eta\omega (D=4)$, $\eta'\omega (D=4)$, $\eta\phi (D=4)$, $\eta'\phi (D=4)$, $\rho\pi (D=4)$, $K^*\bar{K} (D=4)$, $D^*(1865)\bar{D}(1865) (D=4)$, $F^*\bar{F} (D=4)$, etc. governed by the constraint $d_u \leq D$ will be allowed. To know precisely which one of the two constraints, given by relations (1a) and (1b), will be valid in ν -decay, the identifications of its hadronic modes (which will determine the sign of the inequality in the appropriate constraint) are necessary. It is clear, however, that some of the non-radiative two-body decays will be suppressed whether $d_u \geq D$ or $d_u \leq D$ is found to be the appropriate constraint in ν -decay. The most striking point is that the radiative decays $e \rightarrow X\gamma$ (where X is a pseudo-scalar hadron) will not be suppressed (by virtue of the presence of the equality signs in both the constraints) whichever constraint will eventually turn out to be valid in ν -decay. However, the decays $\nu(d_u = 3) \rightarrow Xe^+e^- (D=4)$ stand the risk of being suppressed if in future it is found that e -decay is controlled by the constraint $d_u \geq D$ according to which the mode Xe^+e^- is forbidden. The situation, then, will be very similar to $\omega(783)$ -decay where the appropriate constraint is $d_u \geq D$ which forbids the expected modes like $\pi^0 e^+e^- (D=4)$, $\pi^0 \mu^+\mu^- (D=4)$ as discussed earlier. From what has been discussed so far it is clear that the radiative decays like $e \rightarrow X\gamma$ will offer the most convenient platform for the quantitative tests of the QCD as the decays concerned will not be suppressed by the pseudo-dimension rule. Needless to mention that a decay, if it is even partially suppressed by any selection rule, cannot be chosen for the quantitative tests of any theoretical formulation whatsoever. It may not be out of place if we mention that the coupled-channel analysis for the hadronic modes in ν -decay will be simplified due to the pseudo-dimension rule which will suppress some of the non-radiative decays.

Acknowledgments

One of us (S.S.) is thankful to the University Grants Commission (India) for awarding her a Research Fellowship.

References

- Brodsky S J, Coyne D G, DeGrand T A and Horgan R R 1978 *Phys. Letts.* **73B** 203
- Mukhopadhyay P 1975 *Ind. J. Phys.* **49** 668
- Mukhopadhyay P 1978 *Acta. Phys. Pol.* **B9** 71
- Particle Data Group 1978 *Review of Particle Properties*
- Randa J and Donnachie A 1978 *J. Phys.* **G4** 1261

On the electronic absorption spectra of 3-chloro-para-toluidine

Prakash V Shanbhag, M A Shashidhar and K Suryanarayana Rao

Department of Physics, Karnatak University, Dharwar-580 003

Received 1 December 1977, revised 25 July 1978

In continuation of our work on the ultra-violet absorption spectra of some substituted benzenes, the electronic absorption spectra of 3-chloropara-toluidine has been recorded in the vapour phase on a Hilger-Littrow spectrograph with 10 to 150 cm cells at temperatures ranging from 0 to 150°C. The accuracy of measurements has been estimated to be $\pm 5 \text{ cm}^{-1}$ for sharp bands and $\pm 10 \text{ cm}^{-1}$ for broad or diffuse bands. The spectrum lies approximately in the region 3120-2760 Å. The bands—observed corresponds to the $A_{1g}-B_{2u}$ transition of benzene. It is analysed with the help of the infra-red data of 3-chloro-para-toluidine (Sharma and Dwivedi 1976) and also with the help of the analysed spectra of aniline (Ginsburg and Matsen, 1945), toluidines (Biswas 1953) and other substituted anilines (Harnath and Sroeramanurthy, 1957, Shashidhar and Rao, 1966).

Table 1. Fundamental frequencies (cm^{-1}) of 3-Chloro-para-toluidine

Infrared	Ultra-violet absorption		Nature of the mode
	Ground state	Excited state	
236 w	228 m	155 w	$\delta(\text{C-C-C})$
316 ms	323 w	278 s	$\beta(\text{C-Cl})$
402 ms	410 w	383 m	$\delta(\text{C-C-C})$
575 vs	—	450 s	$\phi(\text{C-C-C})$
788 s	783 w	703 s	$\nu(\text{C-C})$
996 ms	—	971 m	$\phi(\text{C-C-C})$
1211 w	—	1169 m	$\nu(\text{C-CH}_3)$
1295 s	—	1259 m	$\nu(\text{C-N})$

vs = very strong, s = strong, ms = medium strong, m = medium, w = weak;
 δ = nonplanar ring deformation, ϕ = planar ring deformation, ν = stretching,
 β = in-plane bending

The study of temperature effect on the band system has facilitated the choice of the band at 32936 cm^{-1} as the 0,0 band of the system. Most of the observed bands could be accounted for in terms of four ground state fundamentals 228, 323, 410, and 783 cm^{-1} and eight excited state fundamentals 155, 278, 383, 450, 703, 971, 1169 and 1259 cm^{-1} .

The fundamentals obtained in the present work for 3-chloro-*para*-toluidine and their probable assignments are given in table 1 together with the infra-red data for this molecule.

References

- Guha Biswas U G 1953 *Ind. J. Phys* **36** 603
 Harnath P B V and Sreeramamurthy K 1957 *Ind. J. Phys* **31** 577
 Nathen Ginsburg and Matsen F A 1945 *J. Chem. Phys* **13** 167
 Sharma S N and Dwivedi C P D 1976 *Ind. J. Phys.* **50** 25
 Shashidhar M A and Rao Suryanarayana K 1966 *Ind. J. Phys.* **40** 53

Indian J. Phys. **53A**, 554-557 (1979)

Correlation between ionic radii, nuclear charges and ionization potentials

Jai Shankor

Department of Physics, Agra College, Agra-282002

and

S C Agrawal

Department of Physics, C. L. Jain College, Firozabad, Agra

Received 4 July 1978

The sizes of ions have played a prominent role in the development of the theory of ionic crystals (Pauling 1960, Tosi 1964). The ionic radii derived by Pauling (1960) correspond to free state for the reasons discussed at length by Fumi and Tosi (1964) and more recently by Jai Shankor and Agarwal (1977). Several interesting correlations between Pauling's ionic radii and other properties such as nuclear charges and ionization potentials have been investigated and widely used (Kordes 1961, Ahrens 1952). In fact, the correlation between ionization potential and ionic sizes has been successfully used by Ahrens to revise the

Pauling's radii and to predict the radii of ions for which data were not available. The ionic radii so obtained have been very useful in the studies on crystallography and mineralogy (Shannon and Prewitt 1969).

Recent electron density measurements (Sysio 1969) as well as theoretical studies (Tosi 1964) reveal that the sizes of ions in crystals are significantly different from Pauling's radii. The cation radii derived from electron density maps are larger and those for anions are smaller than the corresponding values reported by Pauling. In fact the Madelung potential existing in crystals is negative at the cation site and positive at the anion site and is thus responsible for the loosening of cations and the tightening of anions in the crystalline state relative to free state. It is desirable to investigate whether the new data on crystalline state radii exhibit some relationship with nuclear charges and ionization potentials. In the present letter we show that correlations consistent with earlier studies of Kordos and Ahrens are satisfied fairly well with the recent values of crystalline state radii of ions in alkali halides and alkaline earth chalcogenides.

The concept of ionic radii has been very useful in understanding the nature of short range repulsive interactions in ionic crystals (Pauling 1960, Tosi 1964). Pauling, in fact, derived the ionic radii from effective nuclear charges using the relation

$$\frac{Z_- - S_-}{Z_+ - S_+} \quad (1)$$

where r_+ and r_- are the radii of isoelectronic cation and anion, Z_{\pm} and S_{\pm} are, respectively, the nuclear charges and size screening parameters for the two types of ions. The utility of equation (1) is limited by the fact that the determination of size screening parameters for multielectron ions is a complicated task. Kordos therefore proposed for a pair of isoelectronic ions the following relation

$$\frac{r_+}{r_-} = K \sqrt{\frac{Z_-}{Z_+}} \quad (2)$$

We consider 8 crystals composed of isoelectronic ions. These are NaF, KCl, RbBr and CsI from the family of alkali halides, and MgO, CaS, SrSe and BaTe from the family of alkaline earth chalcogenides. The data on ionic radii and nuclear charges are given in table-1. The crystalline state values of ionic radii have been taken from Sysio (1969) for alkali halides and from Jai Shanker and Agrawal (1977) for alkaline earth chalcogenides. It is remarkable to note from table 1 that K remains nearly constant within a family of crystals. Mean value of K is 0.96 for alkali halides and 0.79 for alkaline earth chalcogenides. The utility of relation (2) is that one can quickly estimate ionic radii using the mean

Table 1. Input data and values of K .

Crystal	r_+ (Å)	r_- (Å)	Z_+	Z_-	K
NaF	1.15	1.23	11	9	1.03
KCl	1.49	1.67	19	17	0.94
RbBr	1.63	1.80	37	35	0.93
CsI	1.86	2.05	55	53	0.92
MgO	0.85	1.25	12	8	0.83
CaS	1.15	1.68	20	16	0.77
SrSe	1.32	1.80	38	34	0.78
BaTe	1.51	1.98	56	52	0.79

value of K . The ionic radii based on the mean value of K are given in table 2. These radii agree well with the corresponding values given in table 1. The maximum deviation is for Na^+ ion where the calculated radius (1.07 Å) differs from the input value by 0.08 Å. It is pertinent to mention here that Jennison and Kunz (1976) have obtained recently the radii for Na^+ and F^- ions in NaF crystal using the local orbitals Hartree-Fock method. These are in good agreement with our calculated values (table 2).

Table 2. Calculated values of ionic radii and interionic separation R .

Crystal	R (Å)	r_+ (Å)	r_- (Å)
NaF	2.31	1.07 (1.06 ^a)	1.24 (1.25 ^a)
KCl	3.14	1.49	1.65
RbBr	3.43	1.65	1.78
CsI	3.83	1.86	1.97
MgO	2.10	0.82	1.28
CaS	2.83	1.17	1.66
SrSe	3.11	1.33	1.78
BaTe	3.50	1.52	1.98

(a) Jennison and Kunz (1976)

Sizes of ions exhibit interesting correlation with ionization potentials. It was shown by Ahrens (1952) that Pauling's radii satisfy the following relation

$$r_+ = \frac{K'}{I^2} \quad (3)$$

where I is the ionization potential. It is interesting to investigate how far equation (3) is obeyed by new data on crystalline state radii. We observe from table 3 that K' is different for alkali halides and alkaline earth chalcogenides but is nearly same within a family of crystals. The mean value of K' is 28.7 for alkali halides and 167 for alkaline earth chalcogenides.

Table 3. Ionic radii and ionization potentials.

Crystals	r_+ (Å)	I (Volts)	K'
NaF	1.15	5.12	30.2
KCl	1.49	4.34	28.1
RbBr	1.63	4.18	28.5
CaI	1.86	3.89	28.2
MgO	0.85	15.03	192
CaS	1.15	11.87	162
SrSe	1.32	11.03	161
BaTe	1.51	10.00	151

We may thus conclude that empirical equations (2) and (3) represent fairly well the correlations between crystalline state radii of ions, nuclear charges and ionization potentials.

References

- Ahrens L H 1952 *Geochim. Cosmochim. Acta* **2** 155
 Fumi F G and Tosi M P 1964 *J. Phys. Chem. Solids* **25** 31
 Jai Shanker and Agarwal S C 1977 *J. Phys. Chem. Solids* **38** 91
 Jennison D R and Kunz A B 1976 *Phys. Rev.* **B13** 5597
 Kordes E 1961 *Z. Kristallogr.* **115** 169
 Pauling L 1960 *The Nature of the Chemical Bond* (Ithaca: Cornell University Press)
 Shannon R D and Prewitt C T 1969 *Acta Crystallogr.* **B25** 2374
 Sysio P A 1969 *Acta Crystallogr.* **B25** 2374
 Tosi M P 1964 *Solid State Physics* **16** 1

Indian J. Phys. **53A** 557-559 (1979)

Crystal data on MgNbCuO_4

P D Deshpande and D K Kulkarni

Department of Physics, Institute of Science, Nagpur-440001

and

V V Deshpande

Department of Chemistry, Institute of Science, Nagpur-440001

Received 2 August 1978

In continuation of our earlier work (Deshpande *et al* 1976, Deshpande *et al* 1978) on ternary oxides we report here the crystal structure of MgNbCuO_4 which is

Table 1. Crystallographic data of MgNbCuO_4

$1/d^2$ observed	$1/d^2$ calculated	$h\ k\ l$	$1/d^2$ observed	$1/d^2$ calculated	$h\ k\ l$
0.02049	0.02047	1 0 0	0.7335	0.7310	3 5 0
0.05067	0.05052	0 0 1	0.7863	0.7873	0 6 0
0.07268	0.07242	0 0 1	0.8083	0.8083	0 0 4
0.1090	0.1080	1 2 0	0.8379	0.8357	3 3 3
0.1310	0.1324	2 0 1	0.8786	0.8743	4 5 0
0.1686	0.1694	2 2 0	0.9389	0.9390	6 0 2
0.1820	0.1814	3 0 0	0.9781	0.9777	2 2 4
0.1980	0.1968	0 3 0	1.028	1.0256	1 3 4
0.2310	0.2345	3 0 1	1.070	1.0713	2 6 2
0.2816	0.2840	2 0 2	1.136	1.1358	4 0 4
0.2984	0.3058	2 1 2	1.195	1.1916	6 0 3
0.3154	0.3103	1 2 2	1.217	1.2135	6 1 3
0.3335	0.3292	2 3 1	1.272	1.2737	0 7 2
0.4031	0.4005	0 4 1	1.308	1.3064	3 7 1
0.4323	0.4318	2 4 0	1.351	1.3506	0 2 5
0.4516	0.4547	0 0 3	1.400	1.3997	0 8 0
0.4753	0.4752	1 0 3	1.426	1.4262	3 6 3
0.4968	0.4970	1 1 3	1.450	1.4497	4 7 1
0.5333	0.5341	3 4 0	1.479	1.4803	1 3 5
	0.5336	5 1 0	1.502	1.5011	5 6 2
0.5567	0.5584	2 1 3	1.550	1.5468	1 7 3
0.5886	0.5941	5 1 1	1.560	1.5574	8 3 1
	0.5846	3 4 1	1.580	1.5833	3 8 0
0.6339	0.6389	3 0 3	1.631	1.6327	6 2 4
0.6537	0.6515	0 3 3	1.643	1.6432	7 3 3
0.6785	0.6775	4 4 0	1.646	1.6440	3 3 5
0.7115	0.7138	5 0 2	1.658	1.6598	9 0 0

Orthorhombic

 $a = 6.990 \pm 0.005 \text{ \AA}$, $b = 6.761 \pm 0.005 \text{ \AA}$ and $c = 4.448 \pm 0.005 \text{ \AA}$.

not synthesized so far. It is assumed that Nb^{5+} ions would replace Ta^{5+} ions in MgTaCuO_4 completely since both of them have nearly the same ionic radii Ta^{5+} ions has 0.68 Å and Nb^{5+} ion 0.70 Å (Ahrens 1952) and equal valencies. But in the case of MgNbCuO_4 three different crystal structures are possible viz :

- (i) the MgTaCuO_4 structure due to the substitution of Ta^{5+} ions by those of Nb^{5+} ,
- (ii) spinel structure as all the three cations fulfil the conditions favourable (Romeijn 1953) for formation of such a structure, and
- (iii) any structure other than (i) or (ii) owing to energy conditions of the concerned cations. In view of these possibilities it was of interest to study the structure of MgNbCuO_4 .

The compound has been prepared for the first time, by oxide method (Economos 1955) in a similar way as described in our earlier work (Deshpande 1976). It has been analysed by powder method using Debye-Scherrer camera of diameter 114.6 mm with filtered copper radiation. The pattern showed a single phase and complete absence of the reflections due to the reacting oxides. All the observed reflections could be indexed on the basis of an orthorhombic unit cell with $a = 6.990 \pm 0.005 \text{ \AA}$, $b = 6.761 \pm 0.005 \text{ \AA}$ and $c = 4.448 \pm 0.005 \text{ \AA}$. All these dimensions were computed from the singly dependent reflections with two indices having zero value. The crystallographic observations on the compound are included in Table 1.

Our results clearly indicate that MgNbCuO_4 does not crystallise into a spinel structure. Similarly the crystal structure of this compound is different from that of MgTaCuO_4 as the extinction conditions are different for these compounds though they crystallise into the same crystal system and Bravais lattice.

References

- Ahrens L H 1952 *Geo-Chim. Cosmochim Acta* **2** 155
Deshpande P D, Kulkarni D K and Khandekar P V 1976 *Curr. Sci.* **45** 447
Deshpande P D, Kulkarni D K and Deshpande V V 1978 *Ind. J. Chem.* **A16** 154
Economos G 1955 *J. Amer. Cer. Soc.* **38** 241
Romeijn F C 1953 *Philips Res. Rep.* **8** 304

Indian J. Phys. **53A**, 559-562 (1979)

X-ray study of L-isoleucine HCl, L- β -phenylalanine HCl and DL-methionine 2HCl

B Khawas

Division of Agricultural Physics,
Indian Agricultural Research Institute, New Delhi 110012

Received 1 November 1978

Although the crystal structures of amino acids and their hydrochlorides have been studied in detail, there seems no data on the crystal structures of the title compounds. As it is extremely difficult to prepare single crystals for these without resort to extraordinary techniques, polycrystalline mass for either of the compounds were obtained from a saturated solution in conc. hydrochloric acid by evaporation at a temperature about 50°C .

Table 1. Powder data with indices for *L*-isoleucine HCl

$d_{obs}\text{\AA}$	$d_{cal}\text{\AA}$	hkl	I^*
15.93	15.97	001	m
12.54	12.54	011	vs
6.76	6.71	030	w
6.28	6.25	022	vs
5.34	5.32	003	m
4.35	4.32	122	s
4.17	4.17	033	vs
3.99	4.02	050	s
	3.99	004	
3.90	3.91	014	m
	3.90	051, 132	
3.75	3.74	141	w
3.65	3.65	043	m
3.36	3.36	060	m
3.29	3.28	061, 114	vs
3.19	3.19	005	w
2.99	2.99	200	vw
2.94	2.94	201	vw
2.82	2.82	221, 105	vs
2.67	2.66	006	s
2.63	2.64	016	vw
2.55	2.56	171	m
2.48	2.48	081	m
2.40	2.40	082, 250	vw
2.36	2.36	126, 164	vw
2.33	2.33	074, 173, 224	w
2.28	2.28	007	vw
2.23	2.23	090, 260	vw
2.14	2.14	075	vs
	2.13	225	
2.01	2.01	0, 10, 0	m
1.96	1.96	028, 320	vw
1.93	1.93	312	vw
1.89	1.89	118, 067	vw
1.76	1.76	324	vw
1.73	1.73	0, 11, 3	vw
1.68	1.68	0, 12, 0	w
1.64	1.64	0, 12, 2; 076; 335	w
1.55	1.55	2, 11, 1; 0, 3, 10; 336	w
1.45	1.45	2, 11, 4; 0, 0, 11	vw

*m—medium, s—strong, w—weak, vs—very strong, vw—very weak, vvw—very very weak.

Table 2. Powder data with indices for *L*- β -phenylalanine HCl

15.64	15.70	010	vs
10.91	10.91	100	vw
9.09	8.96	110	w
7.83	7.85	020	w
6.42	6.38	120	vw
5.51	5.45	200	s
5.30	5.34	011	m
	5.23	030	
5.01	5.04	101	s
4.72	4.72	130	m
4.50	4.48	220	s
4.23	4.24	121	m
3.91	3.92	040	s
3.82	3.82	211	m
3.76	3.77	230	s
3.63	3.64	300	vw
	3.63	131	
3.52	3.52	221	w
3.29	3.30	320	m
3.15	3.15	231	m
	3.14	050	
3.10	3.10	141	m
2.98	2.99	330	m
2.85	2.86	321	vw
	2.84	002	
2.73	2.73	400	m
	2.72	250	
2.54	2.55	160	vw
2.49	2.49	212	s
2.42	2.42	430, 341	m
2.37	2.38	350	
2.24	2.24	440, 302, 070	w
2.20	2.20	170	m
	2.19	351	
2.10	2.10	520	vw
2.04	2.04	051	w
1.98	1.97	521	vvw

Powder photographs were taken using 11.48 cm. camera and CuK_α radiation. The photographs were indexed following standard procedures (Lipson 1949).

L-isoleucine HCl: A probable unit cell is: $a = 5.987$, $b = 20.11$, $c = 15.97$ Å. Suggested space group is $P2_122$ with $Z = 8$; $D_{\text{calc}} = 1.16$, $D_{\text{meas}} = 1.18$ gm/c.c.

L- β -phenylalanine HCl: A probable unit cell is: $a = 10.91$, $b = 15.70$, $c = 5.689$ Å. Suggested space group is $P222_1$ with $Z = 4$; $D_{\text{calc}} = 1.37$, $D_{\text{meas}} = 1.40$ gm/c.c.

Table 3. Powder data with indices for *DL*-methionine 2HCl

$d_{obs}\text{\AA}$	$d_{calc}\text{\AA}$	hkl	I
13.39	13.32	010	vs
9.77	10.05	001	w
6.66	6.66	020	w
	6.54	110	
4.98	5.03	002	s(br)
	4.98	120	
4.67	4.70	012	m
4.19	4.18	102	s
3.99	4.01	022	m
	3.99	112	
3.83	3.82	130	s
3.76	3.76	200	m
3.60	3.61	210	vs
3.34	3.35	003	m
	3.33	040, 032	
3.11	3.11	221	vw
3.01	3.01	202	w
2.87	2.87	230	s
2.77	2.78	042	w
2.58	2.57	051	vw
2.49	2.49	240, 232	m
2.38	2.38	104	w
2.28	2.28	321	w
2.17	2.17	250	vw
2.13	2.13	331, 160, 322	vw
2.03	2.03	062	vvw
1.96	1.96	162	vvw
1.88	1.88	400	vvw
1.84	1.84	170	vvw
1.81	1.81	171	vvw
1.64	1.64	361	vw
1.59	1.59	423	vw

DL-methionine 2HCl: A probable unit cell is: $a = 7.516$, $b = 13.32$, $c = 10.05$ Å. Suggested space group is $P2_122$ with $Z = 4$; $D_{calc} = 1.46$, $D_{meas} = 1.49$ gm/cc.

The indexed powder data are given in tables 1, 2 and 3 below.

Reference

Lipson H 1949 *Acta Cryst.* **2** 43

Unit cell and space group of L- β -phenylalanine 2HCl

B Khawas

Division of Agricultural Physics,
Indian Agricultural Research Institute, New Delhi-110012

Received 1 November 1978

Pure L- β -phenylalanine, obtained from British Drug Houses Ltd., U.K. crystallises as fibre crystals of its dihydrochloride from conc. hydrochloric acid after pro-

Table 1. Powder data with indices for L- β -phenylalanine 2HCl

d_{obs} Å	d_{cal} Å	hkl	I^*
15.64	15.75	100	m
14.14	14.10	001	vs
6.97	7.05	002	m
6.26	6.18	102	w
5.57	5.57	202	vw
5.31	5.25	300	w
4.99	4.99	202	m
4.65	4.65	103	vw
4.34	4.34	211	w
	4.30	012	
4.22	4.25	203	m
	4.22	112	
3.91	3.94	400	s
	3.89	212	
3.72	3.72	311	w
	3.71	303	
3.51	3.52	004, 104	s
3.41	3.41	113	vw
3.15	3.15	500, 501	m
2.96	2.96	014, 114	vw
2.82	2.82	005	m
	2.81	412	
2.71	2.71	020	w
2.62	2.63	600	w
2.49	2.49	404, 504, 503	w(br)
2.38	2.38	602, 305	vw
2.35	2.35	006, 023	vw
2.33	2.32	206	vw
2.18	2.18	612, 315	vw
2.04	2.04	224, 324	vw
1.97	1.97	800, 107	vvw
1.94	1.94	424	vvw

* m—medium, s—strong, w—weak, vs—very strong, vw—very weak,
vvw—very very weak.

Table 2. Fibre pattern data of *L*- β -phenylalanine 2HCl : Zero and first layer line.

d_{obs} Å	d_{cal} Å	hkl	
14.14	14.10	001	s
6.97	7.05	002	s
6.26	6.18	102	m
4.99	4.99	202	s
4.65	4.65	103	w
4.44	4.47	201, 302	w
3.92	3.94	400	s
3.51	3.52	004, 104	vs
3.32	3.32	303	vw
3.15	3.15	500, 501	m
2.86	2.87	403	w
2.81	2.82	005	s
2.50	2.49	404, 504, 503	vw
2.38	2.38	305, 602	w
2.35	2.35	006	m
5.21	5.14	110	m
4.92	4.88	111	w
4.73	4.77	111	vw
4.34	4.34	211	vw
4.22	4.22	112	s
3.88	3.89	212	s
3.57	3.58	311	w
3.42	3.41	113	vw
3.19	3.19	410	w
2.82	2.81	412	w
2.73	2.73	501, 511	vw
2.64	2.63	512, 511	w
2.54	2.53	413	vw

longed evaporation at a temperature about 50°C. No work on these crystals has yet been reported.

Powder photographs and a fibre pattern were taken using 11.48 cm. camera and CuK α radiation. The photographs were indexed following standard procedures (Zsoldos 1958). A probable unit cell is : $a = 15.86$, $b = 5.431$, $c = 14.19$ Å, $\beta = 96^\circ 23'$. Suggested space group is $P2_1$ with $Z = 4$; $D_{calc} = 1.30$, $D_{meas} = 1.33$ gm/c.c.

The indexed powder and fibre data are given respectively in tables 1 and 2 below.

References

Zsoldos L 1958 *Acta Cryst.* **11** 835

Chiral $SU(4) \times SU(4)$ breaking : masses and coupling constants of pseudoscalar mesons

T N Tiwari and C V Sastry

Department of Mathematics, Regional Engineering College,
Rourkela-769008.

and

(Mrs.) Saroj Sharma

Department of Physics, D. N. College,
Meerut-250002

and

N C Giri

Department of Physics, Government College, Rourkela-769002.

Received 16 January 1978, revised 18 November 1978

Abstract. Expressions for the masses of the pseudoscalar mesons π , K , D , F and X are obtained in the $(4, 4^*) \oplus (4^*, 4)$ model of broken $SU(4) \times SU(4)$ chiral symmetry. Then the application of the PCAC hypothesis gives two new relations among the masses and coupling constants of these mesons. These relations are used to predict the masses of the charmed mesons D and F : $m_D \approx 1.98$ GeV and $m_F \approx 2.04$ GeV, which are quite close to the reported experimental values. We estimate also the values of the symmetry breaking parameters and find that $\epsilon_8/\epsilon_0 \approx -0.038$, $\epsilon_{15}/\epsilon_0 \approx -1.57$.

1. Introduction

Ever since its introduction by Gell-Mann more than a decade ago (Gell-Mann 1962, 1964), the chiral $SU(3) \times SU(3)$ symmetry has played a very fruitful role as an approximate theory for the study of strong interactions. Since the formulation of an exact theory of strong interactions has not so far been possible, it is essential to exploit as fully the available approximate theories like chiral symmetry as we can. Moreover, as the chiral symmetry holds only approximately for the strong interactions, it is important to know the $SU(3) \times SU(3)$ structure of the symmetry breaking part of the Hamiltonian density in order to extract the maximum possible information from this theory. In this connection, the most popular as well as the most successful model of chiral $SU(3) \times SU(3)$ symmetry breaking is the $(3, 3^*) \oplus (3^*, 3)$ representation of $SU(3) \times SU(3)$, which was proposed by Gell-Mann and others (Gell-Mann *et al* 1968, Glashow and Weinberg 1968) nearly a decade ago.

The chiral $SU(3) \times SU(3)$ symmetry has been further generalized on theoretical grounds and it has been proposed that the strong interaction Hamiltonian

is invariant under the larger group $SU(4) \times SU(4)$ except for a symmetry breaking term which turns out to be of the order of 20%. The form of this symmetry breaking term is assumed to be the $(4, 4^*) \oplus (4^*, 4)$ representation of $SU(4) \times SU(4)$. This generalized model was no more than a mere theoretical curiosity till a few years ago. But after the recent experimental discovery of the new particles ψ and ψ' and the new quantum number 'charm', the chiral $SU(4) \times SU(4)$ symmetry and the $(4, 4^*) \oplus (4^*, 4)$ model of the chiral symmetry breaking have assumed a new importance in the physics of strong interactions.

In this paper we apply the $(4, 4^*) \oplus (4^*, 4)$ model in Section (2) to obtain the expressions for the masses of ordinary and charmed pseudoscalar mesons. Then we apply the hypothesis of partial conservation of axial-vector currents (PCAC) in Section (3) to obtain two new relations, involving charmed particles, among the masses and coupling constants of the pseudoscalar mesons. The numerical estimations of the symmetry breaking parameters have been made in Section (4). In the final Section (5) we compare the two relations among the masses and coupling constants with the available experimental data. We also predict there the masses of the charmed mesons D and F and find that the predicted values are remarkably close to the recently reported experimental values and other theoretical estimates.

2. Masses of pseudoscalar mesons

Some years ago Cicogna, Strocchi and Vergara-Caffarelli analysed the consequences of $SU(3) \times SU(3)$ symmetry breaking (Cicogna *et al* 1972) and discussed in detail the results which follow simply from the $(3, 3^*) \oplus (3^*, 3)$ representation of chiral symmetry breaking. In this analysis the approach was as general as possible and no reference was made to a Lagrangian model, such as the σ -model, or to a semiclassical approximation. The analysis of Cicogna and coworkers (1972) showed that some of the results obtained previously by using specific models are, in fact, model-independent and follow simply from the assumption of $(3, 3^*) \oplus (3^*, 3)$ form of symmetry breaking. In the present paper our approach is similar to that of Cicogna *et al* (1972), but we assume the $(4, 4^*) \oplus (4^*, 4)$ representation for the symmetry-breaking piece of the Hamiltonian in order to accommodate the more recently discovered particles. So the basic assumptions of that paper are briefly discussed in this section.

The theoretical approach most suitable for the discussion of the spontaneous breakdown of symmetries in quantum field theory is the functional method. For simplicity Cicogna and coworkers (1972) considered the case in which the field theory is described by a Lagrangian of the form

$$L(x) = L_{free}(x) + L_{int}(x) + d_i \phi_i(x), \quad (1)$$

where $L_{free}(x) + L_{int}(x) = L_{inv}(x)$ is invariant under the given group G , d_i are constants, and $\phi_i(x)$ are the basic local fields in terms of which the Lagrangian

is constructed. The breaking of chiral symmetry is assumed to be linear and is represented by the term $d_i \phi_i(x)$ in equation (1). In fact, a linear breaking in the Lagrangian or Hamiltonian density is the basic assumption of the Gell-Mann-Oakes-Renner model (Gell-Mann *et al* 1968) as well as the Glashow-Weinberg model (Glashow *et al* 1968) of $SU(3) \times SU(3)$ breaking.

Adopting the same point of view of linear symmetry breaking in the present paper, we assume that the strong interaction Hamiltonian is given by

$$H = H_0 + H',$$

with

$$H' = \epsilon_0 u_0 + \epsilon_8 u_8 + \epsilon_{15} u_{15}. \quad (2)$$

Here H_0 is $SU(4) \times SU(4)$ invariant and H' , which breaks this symmetry, is assumed to transform as the $(4, 4^*) \oplus (4^*, 4)$ representation of $SU(4) \times SU(4)$. This form of H' is based on the requirement that the isospin, hypercharge and charm be conserved. Here u_i ($i = 0, 1, 2, \dots, 15$) are the wellknown scalar densities, while ϵ_0 , ϵ_8 and ϵ_{15} are the symmetry breaking parameters.

Following the functional method for the treatment of the spontaneous breakdown of symmetries, as mentioned above, Cicogna *et al* (1972) obtained the second-order Ward identity in the form

$$m_i^2 [G^a, \lambda]_t = [G^a, \epsilon]_t. \quad (3)$$

Here m_i^2 is the squared mass of the pseudoscalar meson i , G^a are the generators of the meson fields and

$$\lambda = \lambda_i \hat{u}_i, \quad \epsilon = \epsilon_i \hat{u}_i, \quad (4)$$

where \hat{u}_i is the unit vector in the direction i and λ_i are the vacuum expectation values of \hat{u}_i :

$$\lambda_i = \langle 0 | \hat{u}_i | 0 \rangle. \quad (5)$$

We note that equation (3) is the generalisation of the contents of Goldstone's theorem. In the limit $\epsilon \rightarrow 0$, the 'modes' i , for which $[G^a, \lambda]_t$ is different from zero, correspond to Goldstone bosons. To identify these Goldstone bosons, we should know the behaviour of λ as $\epsilon \rightarrow 0$.

Making use of the symmetry breaking Hamiltonian of equation (2) along with the appropriate generators for the pseudoscalar mesons in the Ward identity of equation (3), we get the following expressions for the squared masses of the pseudoscalar mesons in terms of symmetry breaking parameters:

$$\begin{aligned} & \frac{1}{\sqrt{2}} \epsilon_0 + \frac{1}{\sqrt{3}} \epsilon_8 + \frac{1}{\sqrt{6}} \epsilon_{15}, \\ & \frac{1}{\sqrt{2}} \lambda_0 + \frac{1}{\sqrt{3}} \lambda_8 + \frac{1}{\sqrt{6}} \lambda_{15} \end{aligned} \quad (6.1)$$

$$m_{K^0} = \frac{\frac{1}{\sqrt{2}} \epsilon_0 - \frac{1}{2\sqrt{3}} \epsilon_8 + \frac{1}{\sqrt{6}} \epsilon_{15}}{\frac{1}{\sqrt{2}} \lambda_0 - \frac{1}{2\sqrt{3}} \lambda_8 + \frac{1}{\sqrt{6}} \lambda_{15}} \quad (6.2)$$

$$m_{D^0} = \frac{\frac{1}{\sqrt{2}} \epsilon_0 + \frac{1}{2\sqrt{3}} \epsilon_8 - \frac{1}{\sqrt{6}} \epsilon_{15}}{\frac{1}{\sqrt{2}} \lambda_0 + \frac{1}{2\sqrt{3}} \lambda_8 - \frac{1}{\sqrt{6}} \lambda_{15}} \quad (6.3)$$

$$m_{F^0} = \frac{\frac{1}{\sqrt{2}} \epsilon_0 - \frac{1}{\sqrt{3}} \epsilon_8 - \frac{1}{\sqrt{6}} \epsilon_{15}}{\frac{1}{\sqrt{2}} \lambda_0 - \frac{1}{\sqrt{3}} \lambda_8 - \frac{1}{\sqrt{6}} \lambda_{15}} \quad (6.4)$$

$$m_{X^0} = \frac{\sqrt{2} \epsilon_0 - \frac{\sqrt{3}}{\sqrt{2}}}{\frac{1}{\sqrt{2}} \lambda_0 - \frac{\sqrt{3}}{\sqrt{2}} \lambda_{15}} \quad (6.5)$$

3. Two new relations

Now we invoke the PCAC hypothesis in the form

$$\partial^\mu A_\mu^i(x) = f_i m_i^2 \phi_i(x), \quad (7)$$

where f_i , m_i^2 and $\phi_i(x)$ are the coupling constant, squared mass and the local meson field, respectively, of the meson i . Combining equations (7) and (3) we get the following expression for the coupling constant f_i :

$$f_i = -i[G^\alpha, \lambda]_i. \quad (8)$$

Taking the appropriate generators G^α for various pseudoscalar mesons, we obtain the following expressions for the coupling constants:

$$f_\pi = \frac{1}{\sqrt{2}} \lambda_0 + \frac{1}{\sqrt{3}} \lambda_8 + \frac{1}{\sqrt{6}} \lambda_{15}, \quad (9.1)$$

$$f_K = \frac{1}{\sqrt{2}} \lambda_0 - \frac{1}{2\sqrt{3}} \lambda_8 + \frac{1}{\sqrt{6}} \lambda_{15}, \quad (9.2)$$

$$f_D = \frac{1}{\sqrt{2}} \lambda_0 + \frac{1}{2\sqrt{3}} \lambda_8 - \frac{1}{\sqrt{6}} \lambda_{15}, \quad (9.3)$$

$$f_F = \frac{1}{\sqrt{2}} \lambda_0 - \frac{1}{\sqrt{3}} \lambda_8 - \frac{1}{\sqrt{6}} \lambda_{15}, \quad (9.4)$$

$$f_X = \frac{1}{\sqrt{2}} \lambda_0 - \frac{\sqrt{3}}{\sqrt{2}} \lambda_{15}. \quad (9.5)$$

From equations (9.1)-(9.4) one easily obtains the relation

$$f_F - f_D = f_K - f_\pi \quad (10)$$

Combining the corresponding relations of equations (6) and (9) one gets the following relations :

$$f_\pi m_\pi^2 = \frac{1}{\sqrt{2}} \epsilon_0 + \frac{1}{\sqrt{3}} \epsilon_8 + \frac{1}{\sqrt{6}} \epsilon_{15}, \quad (11.1)$$

$$f_K m_K^2 = \frac{1}{\sqrt{2}} \epsilon_0 - \frac{1}{2\sqrt{3}} \epsilon_8 + \frac{1}{\sqrt{6}} \epsilon_{15}, \quad (11.2)$$

$$f_D m_D^2 = \frac{1}{\sqrt{2}} \epsilon_0 + \frac{1}{2\sqrt{3}} \epsilon_8 - \frac{1}{\sqrt{6}} \epsilon_{15}, \quad (11.3)$$

$$f_F m_F^2 = \frac{1}{\sqrt{2}} \epsilon_0 - \frac{1}{\sqrt{3}} \epsilon_8 - \frac{1}{\sqrt{6}} \epsilon_{15}, \quad (11.4)$$

$$f_X m_X^2 = \frac{1}{\sqrt{2}} \epsilon_0 - \frac{\sqrt{3}}{\sqrt{2}} \epsilon_{15}. \quad (11.5)$$

In equation (11), we have five relations in terms of three unknown parameters ϵ_0 , ϵ_8 and ϵ_{15} . Eliminating these parameters, we can get *two* independent relations among the squared masses and coupling constants of the ordinary and charmed pseudoscalar mesons. These two new relations are

$$f_D m_D^2 + f_F m_F^2 = f_K m_K^2 + f_X m_X^2, \quad (12)$$

$$f_\pi m_\pi^2 + 2f_F m_F^2 = f_X m_X^2 + 2f_K m_K^2. \quad (13)$$

It is possible to obtain eighteen more similar relations among the masses and coupling constants π , K , D , F and X mesons, although these relations will not be independent of the two relations given in equations (12) and (13). Two more such relations are :

$$f_\pi m_\pi^2 + f_F m_F^2 = f_K m_K^2 + f_D m_D^2, \quad (14)$$

$$f_\pi m_\pi^2 + f_X m_X^2 = 2f_D m_D^2. \quad (15)$$

4. Symmetry breaking parameters

The symmetry breaking parameters ϵ_0 , ϵ_8 and ϵ_{15} can be estimated directly from the equations (11.1)–(11.5) if we make the assumption of an exact $SU(4)$ for the coupling constants. Since the experimental masses of the mesons π , K and D are well established, the solution of equations (11.1)–(11.3) gives

$$\epsilon_0 = \frac{1}{\sqrt{2}} (f_D m_D^2 + f_K m_K^2), \quad (16.1)$$

$$\epsilon_8 = -\frac{2}{\sqrt{3}} (f_K m_K^2 - f_\pi m_\pi^2), \quad (16.2)$$

$$\epsilon_{15} = -\frac{1}{\sqrt{6}} (3f_D m_D^2 - f_K m_K^2 - 2f_\pi m_\pi^2). \quad (16.3)$$

Using the simplifying assumption $f_\pi \approx f_K \approx f_D$ ($SU(4)$ invariance of the vacuum) and the experimental result $f_\pi \approx 90$ MeV, along with the experimental masses of π , K and D , we get from equations (16.1)–(16.3),

$$\begin{aligned} \epsilon_0 &= 0.237 \text{ GeV}^3, \\ \epsilon_8 &= -0.0234 \text{ GeV}^3, \\ \epsilon_{15} &= -0.373 \text{ GeV}^3, \end{aligned} \quad (17)$$

which give

$$\frac{\epsilon_8}{\epsilon_0} = -0.0985, \quad \frac{\epsilon_{15}}{\epsilon_0} = -1.574. \quad (18)$$

The values given in equation (18) are almost the same as the recent predictions of Gounaris and Sarantakos (1977) who obtained $\epsilon_8/\epsilon_0 = -0.099$ and $\epsilon_{15}/\epsilon_0 = -1.57$. Moreover from equation (17) we find that $|\epsilon_8| \ll |\epsilon_{15}| \approx 1.57|\epsilon_0|$, which shows that the $SU(4) \times SU(4)$ breaking is not much stronger than the $SU(4)$ breaking.

On the other hand, if we take the experimental value 1.28 for f_K/f_π in equations (11.1) and (11.2) and use the weaker assumption $f_D \approx f_F$ in equations (11.3) and (11.4), then solving these four equations for $f_\pi = 90$ MeV, we get the following estimates for the symmetry breaking parameters and the coupling constants :

$$\begin{aligned} \epsilon_0 &= 0.202 \text{ GeV}^3, \\ \epsilon_8 &= -0.0305 \text{ GeV}^3, \\ \epsilon_{15} &= -0.173 \text{ GeV}^3, \\ f_D/f_\pi &\approx f_F/f_\pi \approx 0.49. \end{aligned} \quad (19)$$

From equation (19), we get

$$\epsilon_8/\epsilon_0 = -0.151, \quad \epsilon_{15}/\epsilon_0 = -0.859. \quad (20)$$

These values differ from those given in equation (18) since those values were obtained under the assumption of an exact $SU(4)$ symmetry for the decay constants, while under the weaker assumption used here we find that f_D/f_π and f_F/f_π differ appreciably from unity.

5. Discussion

The two new relations given in equations (12) and (13) cannot be compared with the experimental data directly, since many of the coupling constants appearing in them are not well established experimentally. However, if we make the simplifying assumption

$$f_\pi \approx f_K \approx f_D \approx f_F \approx f_X, \quad (21)$$

and use the above mentioned experimental values for the masses of π , K and X mesons, then equations (12) and (13) predict the following numerical estimates for the masses of the charmed D and F mesons:

$$m_D = 1.98 \text{ GeV}, \quad m_F = 2.04 \text{ GeV}. \quad (22)$$

We notice that this value of m_D is fairly close to the experimental value $m_D = 1.865 \text{ GeV}$. Moreover, the value of m_F roughly agrees with the previous estimates of 1.975 GeV (Do Rujula *et al* 1975) and is remarkably close to the recently reported experimental value $m_F = (2.030 \pm 0.060) \text{ GeV}$ (Brandelik *et al* 1977). On the basis of the measured near-equality of f_π and f_K , we may reasonably expect the assumptions of equation (21) and the predictions based upon it to hold within an accuracy of 10–20%. From this point of view, the close agreement of the predicted values of m_D and m_F of equation (22) with the experimental data is quite remarkable. Moreover, the assumption of the approximate equality of the coupling constants is consistent with equation (10) obtained earlier and has been predicted earlier on theoretical grounds by several authors (see, for example, Ueda 1976).

Finally we note that although it is quite possible that while $f_K \approx f_\pi$ and $f_D \approx f_F$, which follow from only an approximate $SU(3)$ symmetry, that f_D/f_π is not at all close to unity. For example, if we take $f_K \approx f_\pi$, $f_D \approx f_F$ and use the experimental masses of π , K , D and F mesons in equation (14), we obtain $f_D/f_\pi \approx 0.37$. The estimates for f_D/f_π made by other authors also show wide variations from the value unity. For example, Singer (1976) finds $f_D/f_\pi = 2.790$, while Quigg and Rosner (1977) estimate $f_D/f_\pi = 0.3$ in their phase space model.

Acknowledgments

We are thankful to Mr. K. Maharana for helpful discussions. One of us (T.N.T.) is grateful to the University Grants Commission for a Senior Research Fellowship, during the tenure of which most of the work reported here was performed.

References

- Brandelik R 1977 *DESY preprint* 77/44
Cicogna G, Strocchi F and Vergara Caffarelli R. 1972. *Phys. Rev.* **D6** 301
De Rujula A, Georgi H and Glashow S. L. 1975 *Phys. Rev.* **D12** 147
Gell-Mann M 1962 *Phys. Rev.* **125** 1067
Gell-Mann M 1964 *Physics* **1**, 63
Gell Mann M, Oakes R J and Renner B 1968 *Phys. Rev.* **175** 2195
Glashow S and Weinberg S 1968 *Phys. Rev. Lett.* **20** 224
Gounaris G J and Sarantakos S B 1977 *Nuovo Cimeto* **39A**, 554
Quigg C and Rosner J 1977 *FERMILAB preprint* No 77/40 *THY*
Singer M 1976 *Phys. Rev.* **D14** 2349
Ueda Y 1976 *I.C.T.P. preprint* No IC/76/16

The dielectric properties of cadmium iodide crystals*

A M Fernandez and O N Srivastava

Department of Physics, Banaras Hindu University, Varanasi 221005

Abstract. The dielectric constant (ϵ_r) for different CdI_2 polytypes is different. While high period polytypes exhibit values in the range of 60-190, the parent 4H structure exhibits values in the range of about 15-30. Both increasing periodicity and increasing disorder increase the ϵ_r value. It is also possible, in the absence of disorder, to characterize a particular polytype by means of its ϵ_r value.

1. Introduction

The phenomenon of polytypism has been widely investigated in the last two-three decades, the attention being particularly paid towards understanding the growth mechanism of polytypic crystals. A complete understanding of the growth process will eventually lead to the *controlled growth of polytypes*. This is of immense technological importance since, different polytypes of the same substance, differing widely in their crystallographic characteristics and hence possessing distinctly different physical properties, could be usefully harnessed in the fabrication of application devices. It may be mentioned here that different polytypes can be obtained from initial ones by inducing phase transformations in them. Thus phase transformations are important in themselves in that they represent a means of obtaining other polytypes by controlled methods.

CdI_2 is one such polytypic substance. Being an insulating material with a wide band gap (Connell *et al* 1968), its property of interest would naturally be the dielectric one. We chose to study the variation, if any, in the dielectric constant (ϵ_r) of different CdI_2 polytypes. In an extensive study spread over 70 specimens, it has been established that different polytypes possess different dielectric constants (Fernandez and Srivastava 1975).

2. Experimental

The CdI_2 crystals used were grown from aqueous solutions in the manner of Mitchell (1956). Suitable hexagonal shaped crystal platelets were chosen and tested for identification. 15° α -axis oscillation X-ray diffraction photographs were taken to identify their structures (Srivastava 1964).

* Presented at the International Symposium on Solid State Physics, Calcutta 1977.

Measurements of the dielectric constant were made with a systronics LCR Bridge Type 921, at a frequency of 10 KHz with the capacitance in series. No loss factor was observed which means that every ϵ_r value quoted is the equivalent of the real part of the complex dielectric constant, since the imaginary part, related to the loss, is zero.

3. Results

As mentioned earlier, our investigations over 60-70 crystals have established the fact that CdI_2 polytypes have dielectric constants higher than that of the parent 4H structure. The dielectric constants for several long period polytypes have been found to lie between 60 and 190 whereas the 4H parent structure has a value in the range of about 15 to 30. In particular, *both increasing polytype periodicity and increasing disorder increase the dielectric constant* (Fernandez and Srivastava 1977). Table 1 gives a list of polytypes listed in their increasing

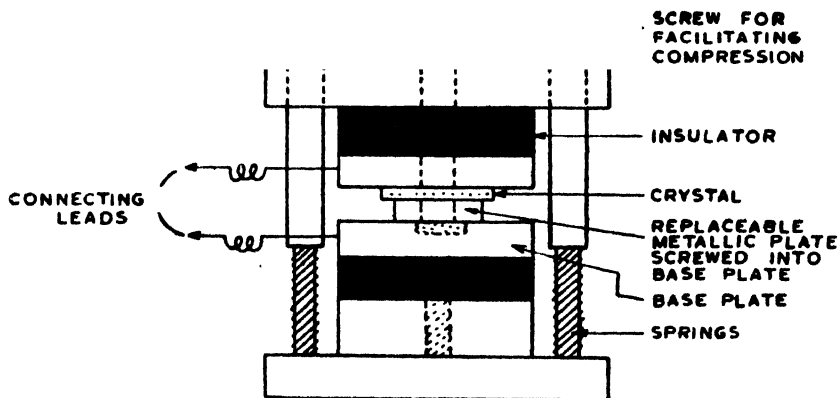


Figure 1. Triangular jig assembly initially employed for dielectric constant measurements.

Table 1

Sl. No.	Before transformation		After transformation	
	Structure	ϵ_r	Structure	ϵ_r
1.	16H (ordered)	68	—	—
2.	20H+D	90	4H+D	74
3.	32H+D	114	4H	21
4.	34H+D	156	4H	24
5.	66R } 108R }	181	4H	27

$D \Rightarrow$ Disorder

order of periodicity, with their respective ϵ_r values. The transformed structures are given alongside. It should be mentioned here that most of the structures exhibited varying amounts of disorder. This is denoted by D in the table.

As can be seen, the dielectric constants increase with the increasing periodicity of the polytype. For a crystal exhibiting syntactic coalescence of two very high period polytypes, namely $66R$ and $108R$, the ϵ_r value is as high as 181.

All these polytypes were made to undergo phase transformations (of the type nH (or nR) \rightarrow $4H$ which can be induced by vacuum annealing treatment at temperatures ranging between 250° and 280°C) (Tiwari and Srivastava 1972, Rai and Srivastava 1974) and the transformed $4H$ structures exhibited dielectric constant values in the expected range. This procedure helped in making an unambiguous distinction of the dielectric behaviour of the polytypic crystal in comparison to the corresponding $4H$ structure. It should be pointed out that there is a range for the values of ϵ_r for $4H$. This probably arises from somewhat differing growth conditions which may result in different densities of as-grown imperfections for different $4H$ crystals.

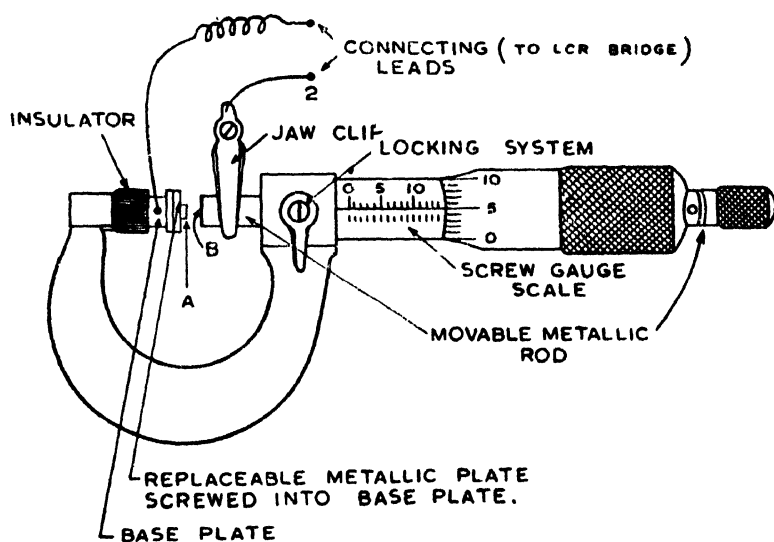


Figure 2. Screw gauge jig assembly employed for dielectric constant measurement. The crystal is mounted between A and B.

As stated earlier, several of the CdI_2 polytypic crystals exhibited varying amounts of disorder existing in conjunction with the order (e.g., see figure 3). The disorder is manifested by the presence of a continuous streak connecting the various 10. l spots on the X-ray diffraction photograph and arises from random stacking faults. In order to determine the influence of the disorder alone on

the dielectric constant, an extensive search was made for crystals exhibiting disorder only. Such a disordered $4H$ structure found in the present investigation is shown in figure 4. For this crystal, $\epsilon_r = 67$, which is higher than the normal value for ϵ_r ($4H$). Another such example was found in the transformed $4H$ structure of an initially disordered $20H$ polytype (No. 2, Table 1), where the disorder still existed after annealing (figure 5). The transformed crystal gave an ϵ_r value of 74.

A comparison of the original negatives of these two disordered $4H$ structures showed them to be possessing almost the same amount of disorder and their ϵ_r values (67 and 74) are seen to be comparable, too. The first crystal was annealed in a way similar to that employed for the polytypic crystals and transformed to an ordered $4H$ structure. The intensity of the continuous streak (depicting disorder) was found to have completely disappeared and the crystal gave an ϵ_r value of 36, in the range of ϵ_r ($4H$).

Based on these results, it can be said that disorder tends to increase the dielectric constant and that two identical structures exhibiting comparable degrees of disorder will have the same dielectric constant values to the first order of approximation.

For the unambiguous characterisation of a particular polytype with a specific dielectric constant value, one should have more than one polytypic crystal corresponding to the *same periodicity and structure*. It is not easy to get such cases as often, the structures (layer sequences) vary, even when the periodicities remain the same. In our search, however, two different crystals having identical periodicities and structures were encountered (Their photographs are shown in figure 6).

Based on considerations of the intensity sequence, it was concluded that these belonged to the structural series $(22)_n11$ with $n = 3$, i.e. they were $14H$ structures (Mitchell 1956). Both existed in syntactic coalescence with ordered $4H$ structures. Their dielectric constants were measured separately and gave values of 62 and 64, respectively. Table 2 summarises the data.

Together with the ordered structures, a slight disorder is also present which is indicated by the faint streak running parallel to the c axis in the X-ray diffraction photographs (figure 6). This, however, would not affect the value of the dielectric constant to the first order of approximation.

In order to get further confirmation of the fact that these crystals could be characterised by a common ϵ_r value of 63, they were made to undergo the $nH \rightarrow 4H$ transformation. Both crystals transformed to order $4H$ structures and their ϵ_r values were 15 and 14, respectively (in the expected range).



Figure 3. a -axis 15° oscillation x -ray diffraction photograph of the 20H polytype of CdI_2 . The presence of superposed disorder is indicated by the streak joining the 10, l row of spots on the first layer line. The first intense spot towards the centre on the 10, l row corresponds to 10.50, and is marked in the figure.

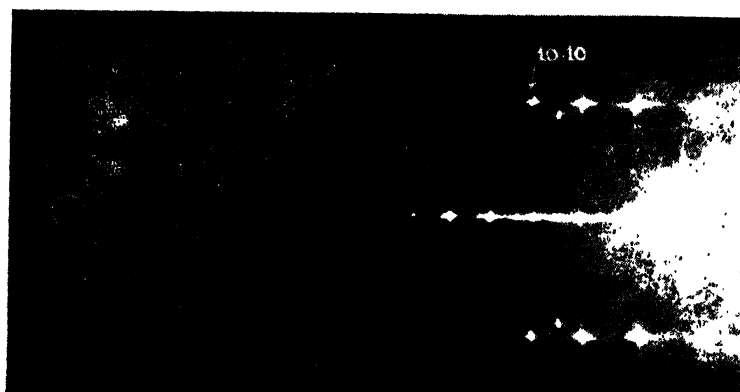


Figure 4. a -axis 15° oscillation x -ray diffraction photograph showing a 4H parent structure with a high degree of disorder superposed on it, as indicated by the broad streak joining the 4H spots on the first layer line. The first intense spot towards the centre on the 10, l row (first layer line) corresponds to 10.10.

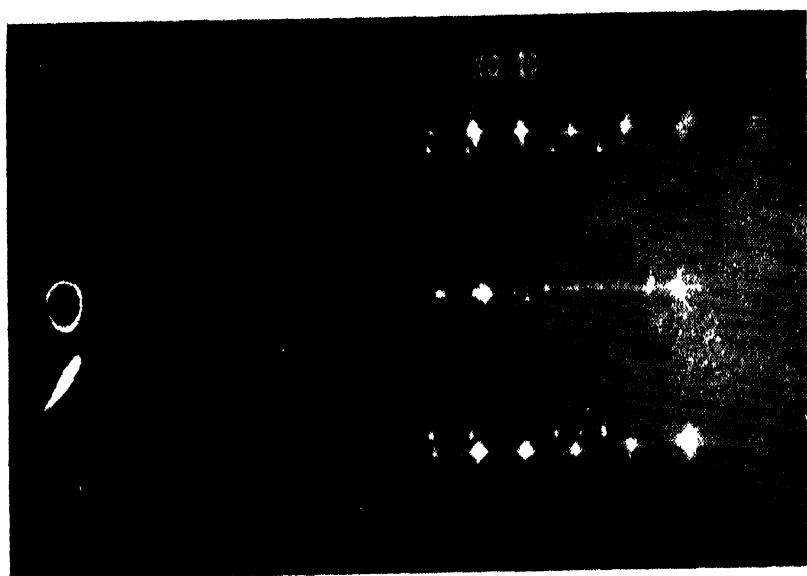


Figure 5. *a*-axis 15° oscillation *a* ray diffraction photograph showing the 4H parent structure obtained by annealing the 20H polytypic crystal (No. 2, Table I). Notice the presence of the streak parallel to the c^* axis indicating the presence of superposed disorder. The streak was clearly visible in the original negative but has dimmed somewhat on print.

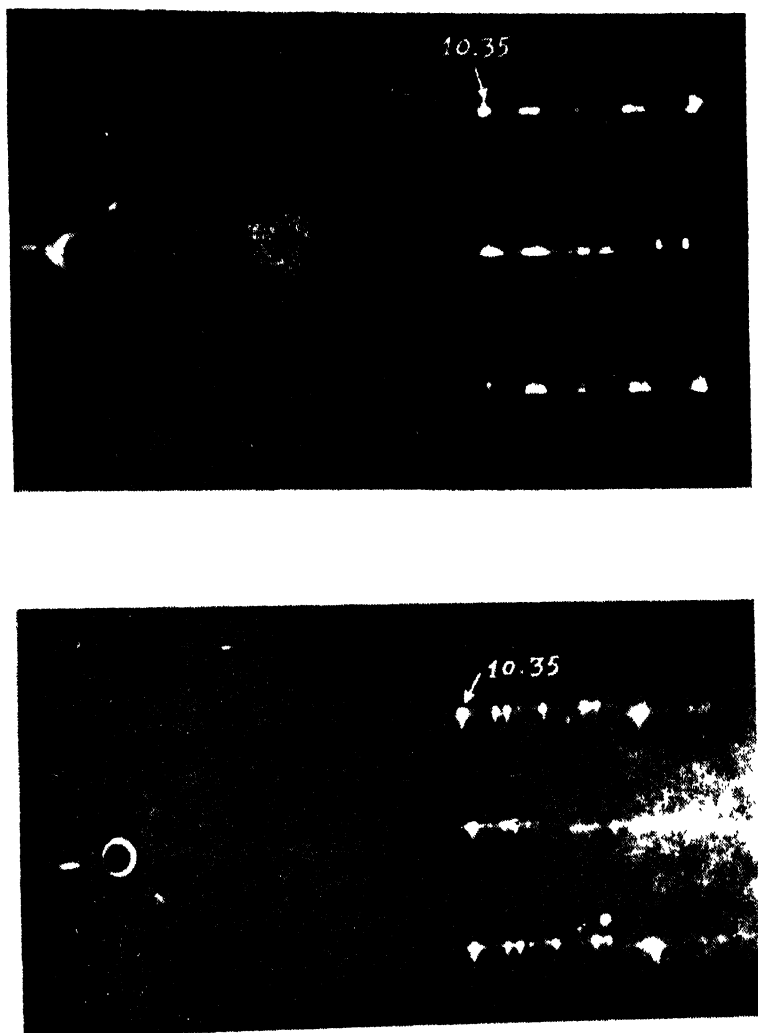


Figure 6. *a*-axis 15° oscillation *x*-ray diffraction photographs of the two 14H polytypes of CdI_2 . The faint streak joining the 10. *l* row of spots indicates the presence of a slight disorder. The first intense spot towards the centre on the 10. *l* row (first layer line) in each photograph corresponds to 10.35.

Table 2

Sl. No.	Before transformation		After transformation	
	Structure	ϵ_r Value	Structure	ϵ_r Value
1	$\left\{ \begin{array}{c} 14H \\ 4H \end{array} \right\}$	62	4H	15
2	$\left\{ \begin{array}{c} 14H \\ 4H \end{array} \right\}$	64	4H	14

Thus two identical ordered polytypic structures can be characterised by a particular ϵ_r value (Fernandez and Srivastava 1977).

4. Discussion

Our basic result states that different polytypes exhibit different values of dielectric constant and that polytypic structures exhibit high ϵ_r values while 4H parent structures exhibit values in the low range of 15-30. A possible explanation is suggested in terms of the occurrence of stacking faults and their effect on the orientation polarizability of the CdI_2 crystals.

As is well known, the dielectric behaviour arises due to various polarization effects such as the electronic, atomic (or ionic), orientational and interfacial polarizations.

This may be expressed as (Zaky and Hawley 1970)

$$\alpha = \alpha_e + \alpha_i + \alpha_o + \alpha_p$$

where α is the total polarizability. The dielectric constant depends on α as

$$\epsilon_r = 1 + \frac{N\alpha}{\epsilon_0}$$

and would change if any of the 4 component polarizabilities changed.

For solids, unlike liquids, the orientational polarization is usually absent. Only in special cases, where there exists sufficient freedom for the dipoles to orient themselves with the field, does the orientational part come into play and contribute to the dielectric constant.

In CdI_2 polytypes, since the structure consists of close-packed iodine layers, with the close-packed Cd layers sandwiched in between them, there is no room for the molecular units to rotate or turn over on application of the field (Smyth 1955). It is thus expected that in the 4H basic polytype, the sole polarization effects would be due to the electronic and ionic contributions. A polytype, however, results from the occurrence of ordered stacking faults in the parent 4H structure. The stacking fault regions, being bordered by partial dislocations,

would present local regions in the crystal where the dipoles would have freedom of turning and rotating with the field and thus would contribute to the orientational polarizability. The polytypes would, therefore, exhibit higher values of ϵ_r than the parent 4H structure.

We have seen that a high degree of disorder also influences the dielectric constant rather seriously. This is expected since dielectric constant represents an averaged out-effect of polarizations. Also, the disorder arises due to the presence of random stacking faults in the crystal. Therefore, regardless of whether the stacking faults are ordered (polytypic crystal) or disordered (disordered crystal), the orientational polarizability associated with stacking faults increases the dielectric constant. However, whereas in the ordered situation, the polytypic crystal can be characterized by a particular dielectric constant value, the same is not true for a disordered crystal, since in this case the degree of disorder associated with it cannot be easily evaluated.

Further studies concerning the effect of *intrapolytypic* transformations (Rai *et al* 1976) (of the type nH_1 (or nR_1) \rightarrow nH_2 (or nR_2)) on the dielectric constant are under progress and results would be forthcoming.

Acknowledgment

One of the authors (AMF) expresses her deep sense of gratitude to CSIR, New Delhi for financial support.

References

- Connell G A N, Wieting T, Wilson J A and Yoffe A D 1968 *IX Int. Conf. on the Physics of Semiconductors Moscow. Proceedings*, Vol. 1, 414-419
- Fernandez A M and Srivastava O N 1975 *J. Appl. Cryst.* **8** 645
- Fernandez A M and Srivastava O N 1977 *J. Appl. Cryst.* **10** 32
- Mitchell R S 1956 *Z. Kristallogr.* **108** 296
- Rai A K and Srivastava O N 1974 *J. Appl. Cryst.* **7** 240
- Rai A K, Tiwari R S and Srivastava O N 1976 *Phys. Stat. Sol. (a)* **35** 719
- Smyth C P 1955 *Dielectric Behaviour and Structure*, U.S.A. McGraw-Hill Book Company, Inc.
- Srivastava O N 1964 *Ph. D. Thesis*, Banaras Hindu University
- Tiwari R S and Srivastava O N 1972 *J. Appl. Cryst.* **5** 347
- Zaky A A and Hawley R 1970 *Dielectric Solids* London: Routledge and Kegan Paul

Bonds in solids : unified treatment*

Shri Kant Dubey

Department of Physics

Banaras Hindu University, Varanasi-221005

Received January 1977, revised 1 November 1978 and 17 April 1979

Abstract. In the present work the author has presented a quantum mechanical unified approach to bonds in solids. Technique used is the two particle two-time Green function method. Interactions taken into account are overlap, Coulombian, quadrupolar interactions and coupling of electronic states with thermal excitations. The result obtained gives, under various limiting conditions corresponding type of bonds, i.e., metallic, covalent, ionic and van der Waals bonds. In addition, the author has been able to obtain, from present approach, criterion of superconductivity in metals; superfluidity in liquid Helium and the Mott-transition. It has been shown that when bonding between same type of atoms is considered, semiconductors are differentiated from metals by the predominance of the quadrupolar interaction. Superfluidity has been shown to occur in liquid He³ due to Cooper pairing and in He⁴ due to collective effect only.

1. Introduction

A unified treatment of bonds is given here. It is formulated in tight-binding approximation where, in general, there are two types of atoms *A* and *B* and the system is at certain finite temperature. As the solidification starts, electrons of atoms interact with each other resulting in different types of bonds under various conditions. The analysis of this process is made in two electron approximation by using two-particle Green's function introduced for quantized fields by Schwinger (1951). This two particle Green's function is superior to one-particle one in discussing the nature of states (Haydock and Mookerjee 1974). Restriction is made to two times only and method of its calculation is the same as described by Zubarev (1960).

The Hamiltonian of the system is defined as :

$$H = \sum_{l\sigma} \epsilon_{l\sigma} a_{l\sigma}^+ a_{l\sigma} + \sum_{l'k} V_{lk} a_{l\sigma}^+ a_{l'\sigma} + \sum_{l'k'm'n} v_{lk'm'n} a_{l\sigma,1}^+ a_{k\sigma,2} a_{m\sigma,4}^+ a_{n\sigma,4} \\ + \sum_s \hbar \omega_s b_s^+ b_s + \sum_{l's} V_{ls} a_l a_l^+ (b_s + b_s^+). \quad (1)$$

* Presented at the International Symposium on Solid State Physics, Calcutta, 1977.

If last two terms (the phonon energy term and electron-phonon interaction term) are made zero, the above Hamiltonian reduces to the general form defined by Hubbard (1963). Values of indices l, k, m, n, \dots etc. take values i_A, l_A, m_A, \dots and j_B, q_B, n_B, \dots etc. where suffixes A and B represent sites corresponding to atoms A and B respectively. ϵ_l represents energy of l -th state minus chemical potential. V_{lk} is two centre overlap potential. v_{lkmn} represents four-centre interaction and takes different values as

$$I_A = v_{i_A i_A' i_A'} \quad I_B = v_{j_B j_B j_B'}, \quad t_{AB} = v_{i_A i_A' j_B j_B'}, \quad Q_{AB} = v_{i_A i_A' j_B j_B'}$$

where primes on indices denote different states at the same site, I represents Coulombian interaction at the same site, t represents Coulombian interaction between different sites and Q denotes quadrupolar interaction.

2. Theory

Double-time two-electron Green function is defined as

$$G_{i_A j_B}(t, t') = \ll a_{i_A}(t) a_{j_B}(t'); a_{j_B}^\dagger(t') a_{i_A}^\dagger(t') \gg \quad (2)$$

where a_i^\dagger, a_i are usual fermion creation and destruction operators. The expression for Fourier transform of above Green function is obtained after calculation to be ($\hbar = 1$)

$$G_{i_A j_B}(E) = \frac{1}{E - \epsilon_{AB} - \Sigma_{AB}(E)} + \text{terms containing propagators not returning to the original site and being negligible} \quad (3)$$

where

$$\begin{aligned} \epsilon_{AB} = & \epsilon_{i_A \sigma} + \epsilon_{j_B \sigma} + \pi_{AB}(E) + \Delta_{AB}^{su} + \eta_{AB}^{ph} + \lambda_{1A}(E) + \lambda_{1B}(E) \\ & + \lambda_2(E) + \lambda_3(E) + \lambda_{4A}(E) + \lambda_{4B}(E) \end{aligned} \quad (4)$$

$$\begin{aligned} \pi_{AB}^Q(E) = & \sum_{i_A, j_B'} \left(\sum_{i_A} Q_{AB}^2 \frac{\langle n_{i_A} (1 - n_{i_A}) \rangle}{E - \epsilon_{i_A} + \epsilon_{i_A'} - M_{AB}(E)} \right. \\ & \left. + \sum_{j_B} Q_{AB}^2 \frac{\langle n_{j_B} (1 - n_{j_B'}) \rangle}{E - \epsilon_{j_B} + \epsilon_{j_B'} - M_{i_A B}(E)} \right) \end{aligned} \quad (5)$$

$$\begin{aligned} M_{AB}(E) = & \epsilon_{i_A} + \epsilon_{j_B} + \sum_{i_A, i_A'} (I_A \delta_{i_A i_A'} + \sum_{j_B} t_{AB}) \langle n_{i_A'} \rangle \\ & + \sum_{j_B, j_B'} (I_B \delta_{j_B j_B'} + \sum_{i_A} t_{AB}) \langle n_{j_B'} \rangle \\ & + \sum_s \sum_{\mu = i_A, j_B} V_{\mu s}^2 \left\{ \frac{(1 + 2n_s) D_{2\mu} + \omega_s}{D_{2\mu}^2 - \omega_s^2} \right\} \end{aligned} \quad (6)$$

$$\Delta_{AB}^{su} = \sum_{\mu=(i_A, j_B)} \sum_{\nu=(l_A, m_B)} \langle n_{\mu\nu} \rangle p_2^\mu (I_A \delta_{\mu\nu} + \sum_{\beta=(A'B')} t_{AB})$$

$$\left[1 + p_2^\mu \omega_s V_{\mu s} \left(\frac{1}{D_{i_\mu^2} - \omega_s^2} \right) \right] \quad (7)$$

$$\eta_{AB}^{ph} = \sum_s \sum_{\mu=(i_A, j_B)} V_{\mu s^2} \left[(1 + 2\eta) \frac{D_{1\mu}}{D_{1\mu^2} - \omega_s^2} + \frac{\omega_s}{D_{1\mu^2} - \omega_s^2} \right] \quad (8)$$

$$\bar{E} = c_{i_A \sigma} + c_{j_B \sigma} + \langle V_{i_A \rho_A} \rangle + \langle V_{j_B m_B} \rangle$$

$$+ \left(\langle V_{j_B \rho_A} \rangle \frac{\langle G_{i_A \rho_A} \rangle}{\langle G_{i_A j_B} \rangle} - \langle V_{i_A m_B} \rangle \frac{\langle G_{j_B m_B} \rangle}{\langle G_{i_A j_B} \rangle} \right)$$

$$+ \sum_{i_A'} \langle n_{i_A'} \rangle I_A \delta_{i_A' l_A} + \sum_{i_A, i_A'} t_{AB} \langle n_{i_A'} \rangle + \sum_{i_B, j_B'} I_B \delta_{i_B m_B} + \sum_{j_B, j_B'} t_{AB} \langle n_{j_B'} \rangle \quad (9)$$

$$D_{1\mu}^{\mu=(i_A, j_B), \nu=(l_A, m_B)} = \langle V_{\mu\nu} \rangle + (c_{\mu} - c_{\mu}') \cdot D_{1\mu}^{\mu=(i_A, j_B)} - D_{1\mu} - p_2^\mu \sum_{\mu''} (I_A \delta_{\mu\nu} + \sum_{\beta=(l_A' m_B')} t_{AB}) \cdot \langle n_{\mu''} \rangle \quad (10)$$

$$D_{2i_A} = c_{i_A'} + c_{i_A'}^p + c_{i_A''} - c_{i_A'} + c_{j_B} - c_{j_B'} \quad (11)$$

$$D_{2j_B} = c_{j_B} - c_{j_B'} + c_{j_B''} - c_{j_B'} + c_{i_A} - c_{i_A'}$$

$$\lambda_{1A}(E) = C \sum_{l_A \pm i_A} \left\{ \frac{V_{l_A l_A}}{e^{l_A j_B}} \frac{V_{l_A l_A}}{e^{l_A j_B}} + \sum_{n_A \pm i_A, j_A} \frac{V_{l_A l_A}}{e^{l_A j_B}} \frac{V_{l_A n_A}}{e^{n_A j_B}} V_{n_A l_A} + \dots \right\}$$

$$= \lambda_{1A}^1(E) + \lambda_{1A}^2(E) + \dots \quad (12)$$

$$\lambda_{1B}(E) = C \sum_{m_B \pm j_B} \left\{ \frac{V_{j_B m_B}}{e^{l_A m_B}} \frac{V_{m_B j_B}}{e^{l_A m_B}} + \sum_{m_B \pm j_B, q_B \pm m_B j_A} \frac{V_{j_B m_B}}{e^{l_A m_B}} \frac{V_{m_B q_B}}{e^{q_B j_B}} V_{q_B j_B} + \dots \right\}$$

$$= \lambda_{1B}^1(E) + \lambda_{1B}^2(E) + \dots \quad (13)$$

$$\lambda_3(E) = C \sum_{l_A \pm i_A} \frac{V_{j_B l_A}}{e^{l_A l_A}} \left(\frac{V_{i_A l_A}}{G_{i_A j_B}} + V_{i_A j_B} \right) + \sum_{l_n \pm i_A, n_A \pm l_A, i_A} \sum_{m_B \pm j_B} \frac{V_{j_B l_A}}{e^{l_A l_A}}$$

$$\times \frac{V_{l_A m_B}}{e^{l_A m_B}} \left(\frac{Z_{i_A n_A}}{G_{i_A i_n}} + V_{n_A j_B} \right) + \dots = \lambda_2^1(E) + \lambda_2^2(E) + \dots \quad (14)$$

$$\begin{aligned}
\lambda_3(E) = & C \sum_{m_B \pm j_B} \frac{V_{i_A m_B}}{e'_{j_B m_B}} \left(\frac{Z_{j_B m_B}}{G_{i_A j_B}} - V_{m_B i_A} \right) \\
& + \sum_{\substack{n_B \pm j_B \\ q_B \pm m_B, j_B}} \frac{V_{i_A m_B}}{e^1_{j_B m_B}} \frac{V_{m_B i_A}}{e^2_{l_B j_B}} \left(\frac{\omega_{j_B m_B}}{G_{i_A j_B}} - V_{q_B i_A} \right) \\
& \lambda_3^1(E) + \lambda_3^2(E) + \dots
\end{aligned} \quad (15)$$

$$\begin{aligned}
\lambda_{4A}(E) = & \sum_{N>2} \lambda_{4A}^N(E) = \sum_{N>2} \sum_{\substack{l_A \pm i_A \\ n_A \pm l_A, i_A \\ t_A \pm n_A, l_A, i_A \\ v_A = \mu_A, \dots, t_A, n_A, l_A, i_A}} \\
& \left(V_{j_B i_A} - V_{j_B i_A} \frac{V_{i_A l_A}}{e_{l_A j_B}} \right) \frac{V_{i_A n_A}}{e^1_{i_A l_A}} \frac{V_{n_A t_A}}{e^2_{i_A n_A}} \dots \frac{V_{\mu_A \nu_A}}{e_{i_A \mu_A}^{N-1}} \frac{V_{\nu_A j_B}}{e_{i_A \nu_A}^N}
\end{aligned} \quad (16)$$

$$\begin{aligned}
\lambda_{4B}(E) = & \sum_{N>2} \lambda_{4B}^N(E) = \sum_{N>2} \sum_{\substack{m_B \pm j_B \\ q_B \pm m_B, j_B \\ X_B \pm q_B, m_B, j_B \\ \eta_B \pm \xi_B, \dots, X_B, q_B, m_B, j_B}} \\
& \times \left(V_{i_A m_B} - V_{i_A j_B} \frac{V_{j_B m_B}}{e_{i_A m_B}} \right) \frac{V_{m_B q_B}}{e'_{j_B m_B}} \frac{V_{q_B \xi_B}}{e^2_{j_B q_B}} \dots \frac{V_{\xi_B \eta_B}}{e_{j_B \xi_B}^{N-1}} \frac{V_{\eta_B l_A}}{e_{j_B \eta_B}^N} \Bigg\} \quad (17)
\end{aligned}$$

$$\begin{aligned}
e_{l_A \nu_B}^u &= [E - \epsilon_{l_A q_B} - \lambda_{1A}^{n-1}(E) - \lambda_{1B}^{n-1}(E) - (\lambda_2^{n-1}(E) - \lambda_3^{n-1}(E))] \gamma \\
e_{\mu\nu}^{n\mu\nu} &= [E - \epsilon_{\mu\nu} - \lambda_{1\alpha}^{n-1}(E)] \\
\mu = (i_A, j_B) & \quad \alpha = (A, B) \\
\tau = (t_A, \lambda_B) &
\end{aligned} \quad (18)$$

$$\begin{aligned}
e_{\mu} &= E - \epsilon_{\mu\sigma} - \prod_{\alpha}^s (E) \quad \alpha = (A, B) \quad \alpha = (A, B) \quad \alpha = (A, B) \\
\mu = (i_A, j_B) & \quad \alpha = (A, B) \quad \alpha = (A, B) \quad \alpha = (A, B) \\
\nu = (t_A, \lambda_B) &
\end{aligned}$$

$$C = 1 + \sum_{i_{A'}} F_{i_{A'}} (I_A \delta_{i_A l_A} + \sum_{i_A} t_{AB}) + \sum_{j_{B'}} F_{j_{B'}} (I_B \delta_{j_B m_B} + \sum_{j_B} t_{AB}) \simeq 1.$$

The term p_2 appearing in (7) gives the probability (concentration) with which the incoming electron gets scattered without affecting the Coulombian coupling existing before interaction. \bar{E} given by (9) is the first order energy expression and it has been used in calculating value of D 's given by (10), (11).

Series $\lambda_{1A}(E)$ and $\lambda_{1B}(E)$ defined by (12) and (13) are Anderson-series (Anderson 1958). When these diverge, the state at the corresponding atom becomes extended. In the reverse case of convergent series localized state is formed. Using this Andor-criteria it can be said that for propagating states series $\lambda_2(E)$, $\lambda_3(E)$, $\lambda_{4A}(E)$ and $\lambda_{4B}(E)$ should also diverge. When only series $\lambda_{4A}(E)$ or $\lambda_{4B}(E)$ diverges and others do not, the state at the corresponding site has the form of resonance state.

3. Explanation of bonds

Let us restrict to case of ordered solids. It implies that each series is considered to diverge. Also, since the solid is ordered one, only the first term in the series $\lambda_{1A}(E)$, $\lambda_{1B}(E)$, $\lambda_2(E)$, $\lambda_3(E)$ is sufficient for making the state propagating one. Rest terms and series $\lambda_{4A}(E)$ and $\lambda_{4B}(E)$ are neglected because of being higher order.

3.1 Covalent Bond

Let us consider identical atom case. The expression for energy, by making denominator of (3) zero, is obtained to be

$$E - \epsilon_{i_A\sigma} - \epsilon_{j_A\sigma} - \Delta_A^{s4} - \eta_A^{ph} - \sum_{i_A, i_A'} \frac{2Q^2}{E - \epsilon_{i_A} + \epsilon_{i_A''} - M_{AB}(E)} \frac{V^2_{i_A i_A'}}{E - \epsilon_{i_A} + \epsilon_{i_A''} - M_{i_A'}(E)} = 0. \quad (19)$$

Making use of Block expansion

$$\sum_{i_A, i_A'} V_{i_A i_A'} = \epsilon_{k\sigma} \exp\{i\mathbf{k} \cdot (\mathbf{R}_{i_A} - \mathbf{R}_{i_A'})\}$$

in the above equation, we get an equation in second order of $\epsilon_{k\sigma}$ showing existence of two (groups of) pseudoparticles-bands corresponding to two roots $\epsilon_{k_1\sigma}$ and $\epsilon_{k_2\sigma}$ of $\epsilon_{k\sigma}$. Evaluating selfconsistently at unperturbed value of energy

$$E = \epsilon_{i_A\sigma} + \epsilon_{j_A\sigma}, \quad \text{one gets the difference}$$

$$\epsilon_{k_2\sigma} - \epsilon_{k_1\sigma} = 2 \left[\frac{2Q^2}{\epsilon_{i_A'} - \epsilon_{i_A} + \epsilon_{j_A'} - \epsilon_{j_A} + 2 \sum_{i_A, i_A'} (I_A + \sum_{i_A} t_A) < n_{i_A'} >} - \Delta_A^{s4} - \eta_A^{ph} \right] \quad (20)$$

It expresses value of gap between two pseudoparticle bands.

To calculate order of magnitude of gap, let us substitute in (20) approximate expressions for I_A , t_A and Q_A given by

$$I_A = \frac{1}{N} \cdot \frac{2}{R}, \quad t_A = \frac{1}{N} \cdot \frac{1}{2R}, \quad Q_A = -\frac{1}{N} \cdot \frac{1}{R^3}$$

where N is number of particles and R is interatomic distance neglect Δ^{s4} term by considering p_2 very small and evaluate at $T = 0$; we get

$$\epsilon_{\kappa_2\sigma} - \epsilon_{\kappa_1\sigma} = 2 \times n_c \times (n_v - 1) \quad (1/R^6)(27 \cdot 2)^2 \\ (\epsilon_{i_{A'}} - \epsilon_{i_A}) + (n_v - 1) \left(\frac{2}{R} + \frac{n_c}{2R} \right) 27 \cdot 2 \quad \text{ev. (21)}$$

where n_c is coordination number and n_v is valence. Energy gaps of C (Diamond), C (Graphite) Si and Ge have been calculated by use of (24). Values of R have been taken from Pauling (1960) and $(\epsilon_{i_{A'}} - \epsilon_{i_A})$ values from ionization potential data given by Kothari and Rao (1970). Results obtained are respectively 6.05, 0.008, 0.79, 0.63 ev. Comparison of these estimates with other calculations (Kittle 1971) shows very good agreement. Also, it predicts correctly the smaller gap in Si, Ge (i.e., semiconducting behaviour) and larger gap in diamond.

3.2. Metallic Bond

If we make the quadrupolar term in (20), zero, as is the case in metals because of close packing of atoms, we get

$$\epsilon_{\kappa_2\sigma} - \epsilon_{\kappa_1\sigma} = -2[\Delta_A^{s4} + \eta_A^{ph}] \quad (22)$$

which gives the result of overlapping bands (negative gap). Polyvalent metals have both spin electrons, therefore lower band is completely filled and we get the above case of overlapping bands (cf. Mott and Davies (1971)). Monovalent metals have only one valence electron so that lower band is filled half only giving, thus, the case of incomplete Wilson band (Wilson 1931). This agreement, hence, gives proof of the object.

Superconductivity

When the term p_2 representing the probability of uncoupled Coulombian interaction is not small, Δ_A^{s4} is not negligible. If, in addition, we have conditions

$$\bar{D}_{1A}^2 - \omega^2 \quad \text{and} \quad p_2 \omega_s V_{iAs} - \bar{D}_{1A}^2 - \omega_s^2 > 1. \quad (23)$$

The term Δ_A^{s4} comes out to be negative at temperatures where

$$|\Delta_A^{s4}| > |\eta_A^{ph}|. \quad (24)$$

We, then, get from (22) a small positive band gap. The second condition of (23) has the effect of making the Coulombian term, present in Δ^{s4} expression, negative i.e. attractive. Thus, showing formation of Copper-pairs followed by the effect of band gap i.e., BCS effect (Bardeen *et al* 1957) and, hence, it shows agreement at microscopic scale.

Comparison between Covalent and Metallic bond

A comparison of the results of section 3.1 and 3.2 gives a new result that covalent bond is differentiated from metallic bond by the presence of quadrupolar interaction in the former and absence of it in the latter. The effect of quadrupolar term, which being due to directional character of bonds, has been though known in chemical explanations, it was not recognised in quantum mechanical theories of covalent bond. The present study overcomes it.

3.3 Ionic Bond

In this case A and B atoms are different. After similar procedure the band gap is obtained, at $T = 0$, to be

$$\epsilon_{\kappa_2\sigma} - \epsilon_{\kappa_1\sigma} = \frac{1}{\alpha} |\beta(\beta-2)|^{\frac{1}{2}} \quad (25)$$

where

$$\begin{aligned} \alpha &= \frac{\epsilon_1 + \epsilon_2}{\epsilon_1 \epsilon_2} & \beta &= \frac{c^0 [\alpha < V_{AB}^2 >]}{c_1 \epsilon_2 - c^0 < V_{AB} >} \\ \left. \begin{aligned} \epsilon_1 &= \epsilon_{iA\sigma} - \epsilon_{mB\sigma} - \sum_{j_{B'}} (I_B | \sum_{j_B} t_{AB}) < n_{j_{B'}} > \\ \epsilon_2 &= \epsilon_{j_{B\sigma}} - \epsilon_{lA\sigma} - \sum_{i_{A'}} (I_A | \sum_{i_A} t_{AB}) < n_{i_{A'}} > \end{aligned} \right\} \quad (26) \end{aligned}$$

In ionic solids difference in ionization potentials is very high. As a result ϵ^0 and therefore β comes out to be large giving large band gap. Thus, it yields Wilson criteria of large gap for ionic solids. The band gap given by (25) comes out to be large when β is large and negative, or when β is positive with $(\beta-2) > 1$. For $\beta = 0$ and 2, gap comes out to be zero and for β positive, gap becomes imaginary. Hence, for values of β positive and ≤ 2 one has non-ionic bond case as in alloys and $\beta = 0$ case is the metallic limit of bond between identical atoms. This result presents clear differentiation for ionic bonds, in addition, to showing the agreement.

Mott Transition

If the distance between A and B atoms in ABO compound is changed the contribution to t_{AB} is changed. It has the effect of changing ϵ^0 because of variation in ϵ_1 and ϵ_2 . If these values are so adjusted that value of β comes in between 0 and 2, the band gap disappears and one gets transition from non-metallic to metallic case. Similarly in vice-versa case transition from metallic to non-metallic one. This is Mott-transition (cf. Mott and Davies 1971), the theory of which was enunciated by Mott in 1949. This gives a microscopic agreement.

3.4 Van der Waals Bond

For inert gas atoms, overlap terms $V_{i_A l_A}$ etc. are zero. Restricting to identical atoms case we get, for this case, the expression

$$G_{i_A j_A}(E) = \frac{1}{E - \epsilon_{i_A \sigma} - \epsilon_{j_A \sigma} - \Delta^{s4} - \pi_A} \quad (27)$$

with

$$\pi_A = \sum_{i_A, i_{A'}} \sum_{j_A, j_{A'}} \frac{2Q^2}{(\epsilon_{i_A} - \epsilon_{i_{A'}}) + (\epsilon_{j_{A'}} - \epsilon_{j_A})} \quad (28)$$

The relation (28) of perturbed energy agrees with the relation obtained by London (1930), and, hence, proves the object.

Superfluidity

As the term Δ^{s4} is due to strongly correlated electrons (with probability p_2), its presence gives rise to a superfluid component where atoms are strongly correlated. It exists in the system together with the normal component having probability $p_1 = 1 - p_2$. The term $V_{i_A s}$ in Δ^{s4} is inversely proportional to mass, therefore, we get that presence of such effect is most probable in He. It is the two fluid model of London (1941). When in Δ^{s4} conditions (23) are also obeyed, one gets Copper-pairs which are obtained to be more probable in He^3 than He^4 because of the term $V_{i_A s}$. It is in agreement with results of Bruekner *et al* (1960), Pitaiveskii (1959), Emery and Sessler (1960). The above, hence, supports the theory.

4. Conclusions

This analysis, thus, presents a successful unification of theories of bonds in solids which, in addition, goes to the depth of explaining microscopic effects like superconductivity, superfluidity and Mott Transition. Also, new results for resonance state, covalent bond and ionic bond have been obtained. The implication of

Δ^{54} term in ionic crystals is not discussed here. This is hoped that such phenomena as very long range order, observed from direct lattice imaging experiments to hold upto distances as large as 1300 Å (Dubey *et al* 1977), will be explained by the inclusion of it as it contains contribution due to phonons also. Its theory will be given separately.

Acknowledgment

The author is grateful to Professor D. K. Rai and Dr. Y. Singh for useful discussions. He is also indebted to Professor D. L. Bhattacharya and Prof. J. Nagehouthury for generous help. Research is supported by C.S.I.R.

References

- Anderson P W 1958 *Phys. Rev.* **109** 1492
Bardeen J Cooper L N and Schrieffer J R 1957 *Phys. Rev.* **108** 1175
Brueckner K A Soda T Anderson P W and Morel P 1960 *Phys. Rev.* **118** 1442
Dubey W and Singh G and Van Tanderloo G 1977. *Acta Cryst.* **A33**, 276
Emergy V J and Sessler A M 1960 *Phys. Rev.* **119**, 43
Haydock R and Mookerjee A 1974. *J. Phys.* **C7** 3001
Hubard J 1963. *Proc. Soc. (London)* **A 276**, 238 ; 1964. *ibid.* **A 281**, 401
Kittel C 1971. *Introduction to the Solid State Physic*, 4th Ed., Wiley and Sons.
Kothari L S and Rao. C N R 1970. *Basic Physical and Chemical Data East-West Press, Delhi*
Landau L D 1941. *J. Phys. U.S.S.R.* **5**, 71
London F 1930. *Z Phys.* **63**, 245.
Mott. N F 1949. *Proc. Phys. Soc.*, **62**, 415
Mott N F and Davis S A 1971. *Electronic Processes in Non-Crystalline Materials*, Clarendon Press, Oxford
Pauling L 1960. *The Nature of Chemical Bonds*, 3rd ed., Cornell University Press
Pitaevskii L P 1959. *Zh. Eksp. Teor. Fiz.*, **37**, 1974. *English Translation*. 1960, *Soviet Phys. JEPT*, **10** 1267
Schwinger J 1951. *Proc. Nat. Acad. Sci. (USA)* **37**, 452
Wilson A H 1931. *Proc. Roy. Soc. A* **133**, 458
Zubarev D N 1960. *Usp. Fiz. Nauk.* **71**, 71 ; *English translation, Soviet Phys. USPEKHI* **3** 320

On the properties of degenerate semiconductors*

D K Roy and R Y Thakur

Department of Physics, Indian Institute of Technology,
Hauz Khas, New Delhi-110029

Received January 1977, revised 27 December 1978

Abstract. Despite the fact that degenerate semiconductors ($N_i = 10^{18}$ - 10^{20} /c.c) have established themselves as a distinct group of solids due to their various technological applications, the concepts upon which their physics rests are still open to questions. An attempt to reformulate their physics has been made in this article. Since shallow impurity states disappear above a particular doping in such samples, impurity bands can not be formed due to overlapping of impurity electron wavefunctions, as believed previously. Even prior to such a phenomenon, the band broadening may also be shown to be insignificant, as the ions are situated at relatively larger distances compared to the impurity Bohr radius. Employing Thomas-Fermi and Hulthen potentials, the binding energy of shallow states as a function of doping has been computed first to establish the futility of the impurity band concept. As in the heavy doping condition (above 10^{18} /c.c) the impurity ions are highly screened by mobile carriers, they may ideally be regarded to perturb electron's energy in an otherwise perfect crystal. In other words, Rayleigh-Schrodinger's perturbation theory may be regarded as the most appropriate tool in describing the behaviour of carriers in such samples. Using these ideas, several physical parameters concerning heavily doped semiconductors e.g., the percentage of ionization of impurities, the Fermi level position, the temperature and pressure gradients of energy gaps etc. have been derived and reported in this paper.

1. Introduction

The interest in the study of heavily doped semiconductors was spurred by the invention of tunnel diodes in 1958. Prior to this discovery, devices contained impurities upto about 10^{17} /c.c. only. At such and lower concentrations, shallow states are localized in the forbidden gap. Interaction amongst different impurity states then is negligibly small. But with subsequent rise in the doping level, the average distance between impurity atoms decreases and the wavefunctions of electrons bound to neighbouring impurity centres begin to overlap. This has been believed to lead to the impurity band formation and the resulting decrease in the carrier ionization energy. It has been argued that the activation energy reduces to zero with the merger of the top of the impurity band with the conduction band edge (in case of donor doping). With rise in the doping concentration,

* Presented at the Internative Symposium on Solid State Physics, Calcutta, 1977.

the Fermi level too maintains its steady drift towards the band edge and ultimately penetrates the allowed band. The higher density of carriers produced by heavy doping requires the application of the Fermi-Dirac statistics. Such a gas of particles has, therefore, been termed as degenerate and, as such, heavily doped semiconductors are often identified with degenerate semiconductors. Normally, they are doped in the range of 10^{18} to 10^{20} per c.c.

In the sections to follow, we shall prove the futility of impurity band concept and establish the applicability of Rayleigh-Schrodinger's perturbation theory in describing electrons' motion in heavily doped samples. Then, mathematical expressions for (i) the density of states, (ii) the Fermi level, (iii) the percentage of ionization of impurity centres and, (iv) the temperature and the pressure coefficients of energy gaps in such a sample shall be derived. All these parameters are known to have important physical significance.

2. Impurity band and ionisation energy

The variation in activation energy with doping was experimentally observed by Pearson and Bardeen (1949) and later by Debye and Conwell (1954). They expressed the dependence by the following empirical relations :

$$E_i(N_d) = E_i(0) - \beta N_d^{1/3} \quad (1)$$

where N_d represents the donor conc., $E_i(0)$, the ionization energy under low doping condition and β , a const. This expression clearly suggests the existence of a critical delocalization concentration at which the activation energy vanishes. ESR (Fehér 1959 Mackawa and Kinoshita 1965) and spin-lattice relaxation studies (Sundorfs and Holcomb 1964) have subsequently confirmed such a prediction.

Although, Pearson and Bardeen (1949) and later Castellani and Seitz (1951) had clearly remarked that the variation of the activation energy with doping is due to the electrostatic screening of charged ions by mobile carriers, it has been the prevalent belief that the ionization energy vanishes owing to the merger of the upper edge of the impurity band with the conduction band edge (for donor doping), as already mentioned. The chances of impurity band formation due to the overlap of bound electron wavefunctions can be shown to be insignificant before Mott transition or carrier delocalization, because the impurity atoms are situated at relatively larger distances compared to the impurity Bohr radius. Beyond this transition too, the formation of such a band is impossible because of the non-existence of bound electron wavefunctions.

To obtain expressions for the impurity Bohr radius and the critical electron

concentration at which the impurity states disappear, we represent electron potential energy by its familiar form,

$$V(r) = -\frac{A_s}{r} \cdot \exp(-\lambda r) \quad (2)$$

where

$$A_s = \frac{e^2}{\epsilon}, \quad \lambda^2 = \frac{4\pi n e^2}{\epsilon k_0 T}$$

e = electronic charge, ϵ = static dielectric const., n = electron conc., k_0 = Boltzmann const., T = absolute temperature. Following Bohr, one may then write

$$m^* V^2 = \frac{\partial}{\partial r} \left\{ -\frac{A_s}{r} \cdot \exp(-\lambda r) \right\} = \frac{A_s}{r^2} (1 + \lambda r) \exp(-\lambda r) \quad (3)$$

But from quantization condition, we have,

$$m^* v r = n \hbar. \quad (4)$$

Comparing (3) and (4), one gets the transcendental equation involving r in the form,

$$\frac{m^* A_s r}{n^2 \hbar^2} \cdot (1 + \lambda r) = \exp(\lambda r). \quad (5)$$

This equation may then be solved to obtain the impurity Bohr radius a_H as a function of doping. Consequently one obtains for carrier ionization energy,

$$E_i = -\frac{n^2 \hbar^2}{2m^* a_H^2} \left[1 - \frac{2}{1 + \lambda a_H} \right] \quad (6)$$

The effect of carrier screening on the binding energy may also be incorporated by Hulthén's potential described by,

$$V_H(r) = -\frac{e^2 \lambda \exp(-\lambda r)}{\epsilon(1 - e^{-\lambda r})}. \quad (7)$$

The expressions for impurity Bohr radius and the ionization energy obtained by using (7) are,

$$a_H = -\frac{\hbar^2}{m^* e^2 \lambda^2} \left[\frac{(1 - e^{-\lambda a_H})^2}{a_H^2 e^{-\lambda a_H}} \right] \quad (8)$$

and

$$E_i = -\frac{e^2 \lambda e^{-\lambda a_H}}{1 - \exp(-\lambda a_H)} \left[1 - \frac{\lambda a_H}{2} \frac{1}{(1 - e^{-\lambda a_H})^2} \right] \quad (9)$$

respectively.

The first impurity Bohr radius and the electron binding energy have been computed as functions of doping concentrations employing Yukawa and Hulthen models. The results are shown in figures 1 and 2. It may be noticed that the impurity Bohr radius first increases with increase in doping until it suddenly blows up at the delocalization conc. The nature of variation of carrier ionization energy with doping has also been found of the type described by Pearson and Bardeen (1949) and later by Debye and Conwell (1954) on the basis of their experimental findings.

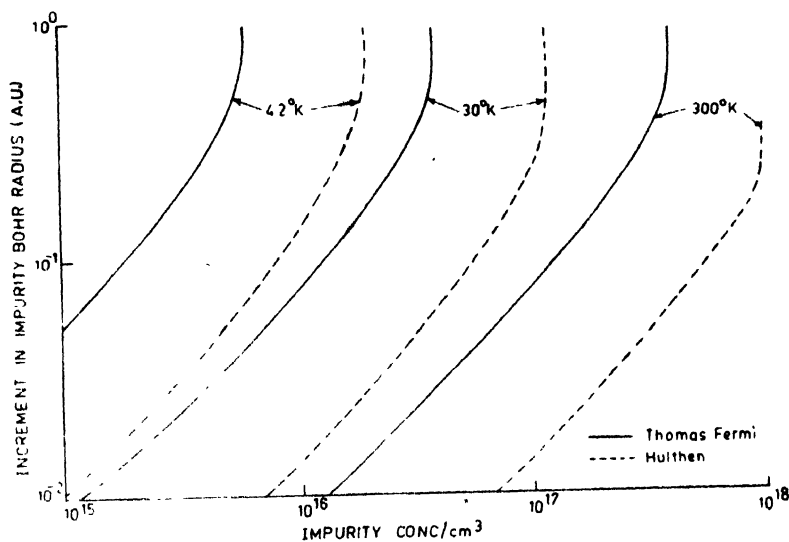


Figure 1. Impurity Bohr radius as a function of doping conc.

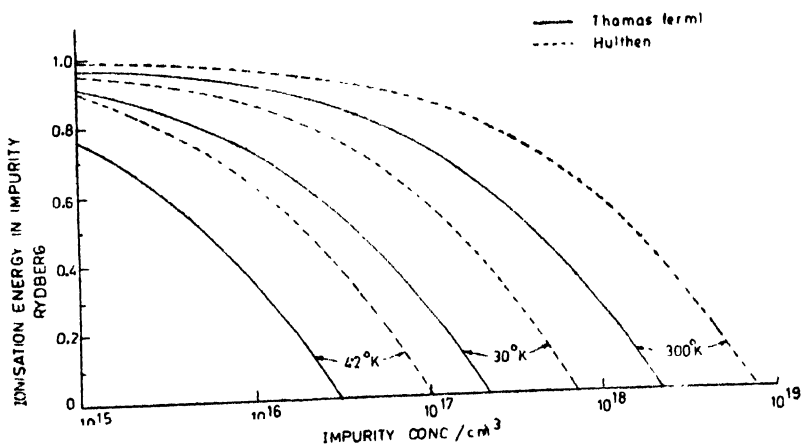


Figure 2. Electron binding energy as a function of doping conc.

3. Electronic density of states

The energy spectrum of carriers in heavily doped specimen was obtained by Kane (1963) and Bonch-Bruovich (1966). Kane believed that due to the existence of unusually large number of attractive impurities in certain regions of the crystal, bound states are formed in the forbidden band due to the fluctuations in impurity density. The deeper a level exists, the lower is the probability of its formation. Thus, the density of states was shown to decline in a gaussian manner, within the band gap and to retain its usual parabolic form deep inside the band. The approach of Bonch-Bruovich is also similar to that of Kane's but the former employs Green's function technique to solve the problem.

As both these workers regarded the impurity contribution to the electrons' potential energy to exceed their average value, they both questioned the applicability of the perturbation theory at the band edge. It may, therefore, be remarked that they failed to appreciate the weakness of attraction between screened ions and the free electrons. We just established in the earlier section that due to large scale screening of ions by mobile electrons, bound electron states disappear above a particular concentration. Realizing the weakness of this electron-ion interaction Roy and George (1975) obtained the energy spectrum of carriers employing perturbation theory. The corresponding density of states function relative to the first order band edge has been obtained to be,

$$\rho(E) = \frac{m^*}{2\pi^2\hbar^2} \left[1 - \left\{ \left(\frac{m^*E}{\hbar^2} - \frac{\lambda^2}{8} \right) + \frac{\lambda^2}{\hbar^4 N \Omega \lambda} \right\}^{\frac{1}{2}} \right] \quad (10)$$

We have also obtained this function employing the two band model (Thakur 1978). The result is,

$$\rho(E) = \frac{m}{\sqrt{2}\pi^2\hbar^2} \left[1 - \left\{ G^4 + \frac{8mG^2E}{\hbar^2} + \frac{16m^2|V_G|^2}{\hbar^4} \right\}^{\frac{1}{2}} \right] \times \left\{ \left(G^2 + \frac{4mE}{\hbar^2} \right) - \sqrt{G^4 + \frac{8mG^2E}{\hbar^2} + \frac{16m^2|V_G|^2}{\hbar^4}} \right\}^{\frac{1}{2}} \quad (11)$$

where, G stands for the average reciprocal lattice vector length and $|V_G|$, for half the energy gap of the semiconductor. The density of states function com-

puted for Te doped GaAs obtained by using (10) and (11) has been shown in figure 3.

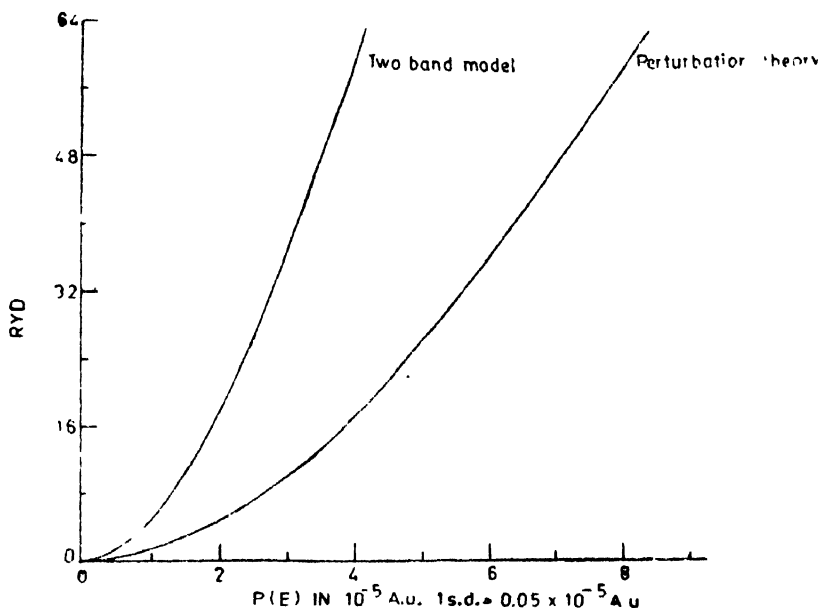


Figure 3. Density of States function *vs.* energy.

4. Fermi level

This is one of the most important parameters characterizing a degenerate semiconductor. The semiconductor specimen has been taken to be degenerate only when the Fermi level penetrates the main band. Its estimation was difficult on the conventional theory because the band edges of degenerate semiconductors were not sharp. This may be ascertained by a number of theoretical approaches. One, that is based upon the use of the uncertainty relation, utilizes the fact that the maximum spread in the electron energy at absolute zero is the Fermi energy of the material. If the free electron concentration be N_t , the minimum volume accessible to each electron will be $2/N_t$ where the factor 2 accounts for two possible spin orientations. Hence, the maximum momentum uncertainty product is,

$$\Delta p_x \Delta p_y \Delta p_z = \frac{4\pi}{3} (\Delta p)^3 = \frac{\hbar^3}{\Delta V} = \frac{\hbar^3 N_t}{2}$$

or,

$$\Delta p = \hbar k_F = \hbar \left(\frac{3N_t}{8\pi} \right)^{1/3}. \quad (12)$$

But, the $E-k$ relation of electrons in heavily doped semiconductors as given by Roy and George (1975) is,

$$E = \frac{\hbar^2 k^2}{2m^*} - \frac{4\pi N_t A_s^2}{\lambda N \Omega} \cdot \frac{m^*}{\hbar^2} \cdot \frac{1}{(\lambda^2 + 4k^2)} \quad (13)$$

where E is measured with reference to the first order band edge. Substituting k_F for k in (13), we have for the Fermi energy the expression,

$$E_{F0} = \frac{\hbar^2}{2m^*} \left(\frac{3N_t}{8\pi} \right)^{2/3} - \frac{4\pi A_s^2 N_t m^*}{\Omega \lambda N \hbar^2} \left\{ \frac{1}{\lambda^2 + 4 \left(\frac{3N_t}{8\pi} \right)^{2/3}} \right\} \quad (14)$$

But, the second order band edge has been obtained to be,

$$|e_2| = \frac{4\pi A_s^2 N_t m^*}{\Omega \lambda^3 \hbar^2 N} \quad (15)$$

Thus, the Fermi energy as measured from the new band edge reduces to,

$$\begin{aligned} E_{F0} &= E'_{F0} + |e_2| \\ &= \frac{\hbar^2}{2m^*} \left(\frac{3N_t}{8\pi} \right)^{2/3} + \frac{4\pi A_s^2 m^* N_t}{\Omega \lambda^3 \hbar^2 N} - \frac{4\pi A_s^2 m^* N_t}{\Omega \lambda \hbar^2 N} \left\{ \frac{1}{\lambda^2 + 4(3N_t/8\pi)^{2/3}} \right\} \end{aligned} \quad (16)$$

On purely free electron approximation (as in metals) the Fermi level should have been given by the first term in (16). But due to higher doping (larger N_t), the third term is smaller than the second one, leading to a larger value of the Fermi energy than is expected on the metallic behaviour of the sample under consideration.

The Fermi level E_F may also be obtained from the relation,

$$n = N_t = \int_0^\infty \rho(E) f(E) dE \quad (17)$$

where $f(E)$ stands for the Fermi-Dirac distribution function. The transcendental equation (17) has been solved by the method of successive bisection to determine the Fermi level position (Thakur 1978). To calculate this parameter at any arbitrary higher temperature, we have made use of the following expression (Ziman 1972) :

$$E_F = E_{F0} - \frac{\pi^2}{6} (k_0 T)^2 \left[\frac{\partial}{\partial E} \ln \rho(E) \right]_{E=E_{F0}} \quad (18)$$

Figures 4 and 5 show the dependence of the Fermi level in Ge on impurity concentration and temperature. The concentration required for degeneracy is found to obey the following empirical relation,

$$N_{deg} = CT^{3/2} \quad (19)$$

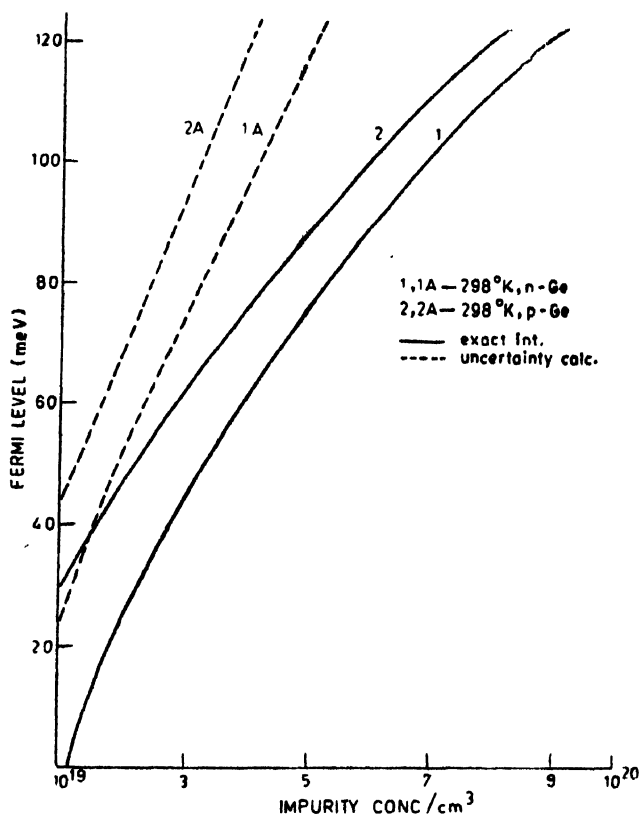


Figure 4. Fermi level vs. impurity conc.

where C is a material dependent constant. To test our results, we have computed peak voltages of tunnel diodes and have plotted them alongside experimental values (Meyerhofer *et al* 1962) (figure 6).

As long as the Fermi level is below the band edge, the electrons in an n -type sample behave as free carriers and the presumptions of complete ionization is valid. But the moment the Fermi energy penetrates the main band, electrons occupying states below the former are unable to take part in conduction process as freely as when they are above it. This gives rise to an impression that the degree of ionization of donors has decreased. To be able to calculate the percentage of ionization we presume that carriers occupying states above the Fermi level are capable of taking part in conduction, while those below it are completely

immobilized. The density of electrons not taking part in conduction may then be written as,

$$n_a = \int_0^{E_F} \rho(E)f(E)dE. \quad (20)$$

The fraction f_i of carriers ionized is then given by,

$$f_i = \left\{ 1 - \frac{n_a}{N_t} \right\}. \quad (20a)$$

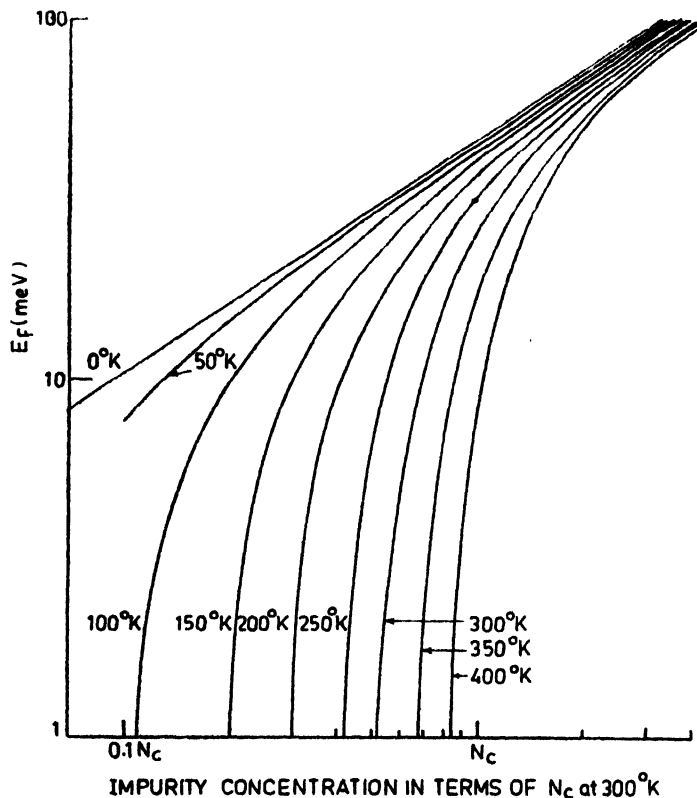


Figure 5. Fermi level vs. temperature.

The figure 7 shows the plot of f_i as a function of N_t .

The computed Fermi energy values may also be used, amongst other things, to compute the diffusivity-mobility ratio in heavily doped semiconductors, which is known to rise with increase in doping.

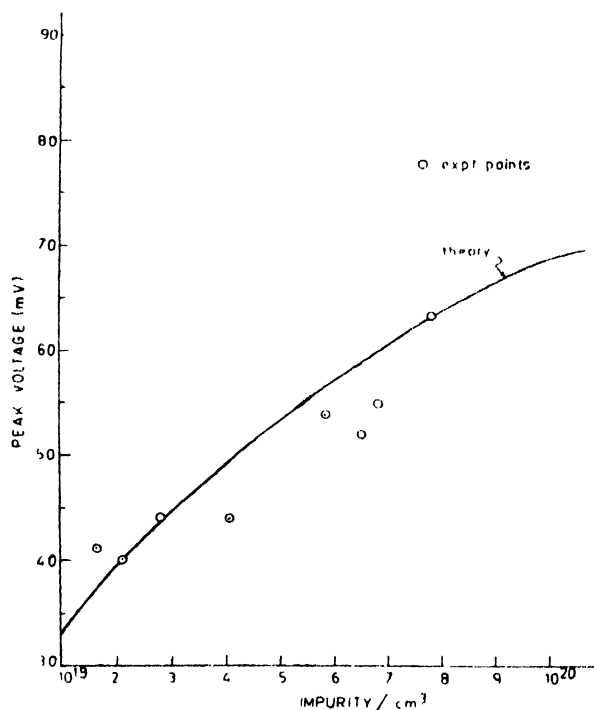


Figure 6. Tunnel diode peak voltages vs. doping conc.

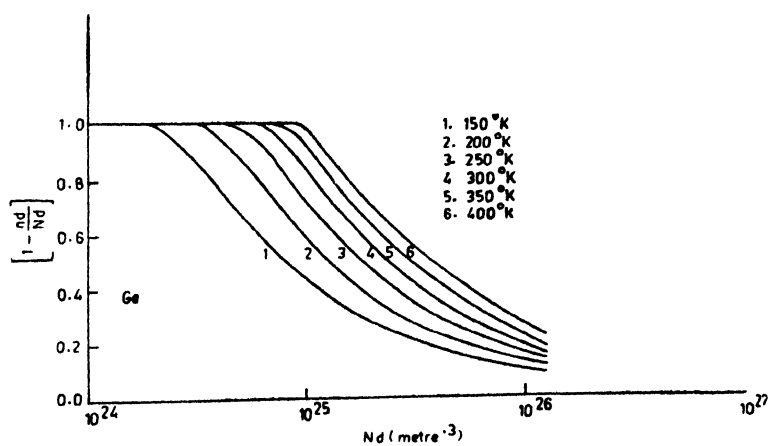


Figure 7. Fraction of carriers ionized at different temperatures and impurity conc.

5. Effect of temperature

The effect of temperature on the band edge may be incorporated by considering the effect of thermal vibrations upon the Yukawa potential (eq. 2). Representing the displacement of the impurity ion from its mean position by u_i , the altered impurity potential may be written in the form,

$$v(r') = v(r - u_i) = v(r) - u_i \frac{\partial v(r)}{\partial r}. \quad (21)$$

The electron Hamiltonian then modifies to,

$$H = H_0 + v(r) - u_i \frac{\partial v(r)}{\partial r} \quad (22)$$

where $v(r)$ represents the correction to electron energy due to the presence of impurity atoms at the lattice sites and $-u_i \frac{\partial v(r)}{\partial r}$ takes into account the effect of thermal vibrations of ions. For the problem under consideration, we examine only,

$$-u_i \frac{\partial v(r)}{\partial r} = -u_i \left[\frac{\lambda A_s}{r} e^{-\lambda r} + \frac{A_s}{r^2} e^{-\lambda r} \right] = H_1 \text{ (say)} \quad (23)$$

This perturbing term causes a shift in the conduction band edge which when evaluated by employing Rayleigh-Schrodinger's perturbation theory works out to be,

$$E_{2t} = - \frac{4m^* \pi A_s^2 N_i}{\Omega N \hbar^2 \lambda} \sum_q |U_q|^2 \quad (24)$$

where U_q is the amplitude of oscillation in the q -th mode. Making use of the classical expression for the energy of a simple harmonic oscillator, we write,

$$|U_q|^2 = \frac{\bar{\epsilon}_q}{MN\omega_q^2} \quad (25)$$

where

$$\bar{\epsilon}_q = (\bar{n}_q + \frac{1}{2}) \hbar \omega_q \quad (26)$$

is the average energy of the q -th mode and

$$\bar{n}_q = \frac{1}{\exp\left(\frac{\hbar \omega_q}{k_0 T}\right) - 1} \quad (27)$$

From (25) and (27), we get,

$$\sum_q |U_q|^2 = \sum_q \frac{(\bar{n}_q + \frac{1}{2})\hbar}{MN\omega_q}. \quad (28)$$

Since the total number of modes is $3N$ and the fraction of modes with frequency in the range between ω and $\omega + d\omega$ is,

$$D(\omega)d\omega = \frac{3\omega^2}{\omega_D^3} \cdot d\omega. \quad (29)$$

We may now rewrite equation (28) as,

$$\sum_q |U_q|^2 = \frac{3N}{NM} \int_0^{\omega_D} \left[\frac{1}{e^{\hbar\omega/k_0T} - 1} + \frac{1}{2} \right] \frac{\hbar 3\omega^2 d\omega}{\omega \cdot \omega_D^3}. \quad (30)$$

Putting $Z = \frac{\hbar\omega}{k_0T}$, we get,

$$\sum |U_q|^2 = \frac{9\hbar^2 T^2 I}{M k_0 \theta^3} \quad (31)$$

where

$$I = \int_0^{\theta/T} \left[\frac{1}{e^Z - 1} + \frac{1}{2} \right] Z \cdot dZ \quad (32)$$

and θ is the Debye temperature related to the Debye frequency ω_D through $\theta = \frac{\hbar\omega_D}{k_0}$. Now, combining (24) and (31), we get,

$$E_{2t} = E_{ca} = - \frac{36m^* \pi A S^2 N_i T^2 I}{\Omega N M L \omega_D^3}. \quad (33)$$

The contribution of the host lattice to the temperature coefficient of energy gaps may also be obtained by assuming that the electron-phonon interaction changes the structure factor of the crystal. We express the Fourier transform of the crystal potential $\Sigma v_a(r-l)$ by,

$$V_G = \sum_l e^{-iGR_l} \int e^{-iGr} v_a(r) d^3r = S_G V_a(G) \quad (34)$$

where

$$V_a(G) = \frac{1}{\Omega} \int e^{-iGr} v_a(r) d^3r \quad (35)$$

and

$$S_G = \frac{1}{N} \sum_{\mathbf{l}} e^{-iG\mathbf{R}_\mathbf{l}}. \quad (36)$$

At a finite temperature,

$$\mathbf{R}_\mathbf{l} = \mathbf{l} + \mathbf{u}_\mathbf{l} = \mathbf{l} + \sum_{\mathbf{q}} [U_{\mathbf{q}} e^{i\mathbf{q} \cdot \mathbf{l}} + U_{\mathbf{q}}^* e^{-i\mathbf{q} \cdot \mathbf{l}}] \quad (37)$$

so,

$$\begin{aligned} S_G &= \frac{1}{N} \sum_{\mathbf{l}} \exp(-iG \cdot \mathbf{l}) \prod_{\mathbf{q}} \exp[-iG \cdot \{U_{\mathbf{q}} e^{i\mathbf{q} \cdot \mathbf{l}} + U_{\mathbf{q}}^* e^{-i\mathbf{q} \cdot \mathbf{l}}\}] \\ &\simeq \prod_{\mathbf{q}} [1 - |G \cdot U_{\mathbf{q}}|^2] = \exp(-2W). \end{aligned} \quad (38)$$

Combining (34) and (38), we find,

$$V_G(T) = V_G(G) \exp[-2W(G, T)]. \quad (39)$$

This equation indicates that the effect of temperature may be incorporated through the Debye-Waller factor $\exp(-2W)$ which upon simplification may be rewritten as,

$$e^{-2W} = \exp[-\sum_{\mathbf{q}} |G \cdot U_{\mathbf{q}}|^2]. \quad (40)$$

Combining (31) and (40), we get,

$$W = \frac{9G^2 \hbar^2 T^2 I}{2Mk_0 \theta^3}. \quad (41)$$

Since the Debye-Waller factor $e^{-2W} [= 1 - 2W]$ is not very different from unity, we may express $E_{\mathbf{q}}$ as,

$$E_{\mathbf{q}}(T) = E_{\mathbf{q}0} - E_{\mathbf{t}}(T) = E_{\mathbf{q}0} - \frac{9E_{\mathbf{q}0} G^2 \hbar^2 T^2 I}{Mk_0 \theta^3}. \quad (42)$$

At higher temperatures the upper limit of I is small and it gives $I \sim \theta/T$. Therefore,

$$E_{\mathbf{ca}}(T)_{\text{high } T} = - \frac{36m^* \pi A_S^2 N_{\mathbf{t}} T}{\Omega N \lambda M k_0 \theta^2}$$

and

$$E_{\mathbf{t}}(T)_{\text{high } T} = - \frac{9G^2 \hbar^2 E_{\mathbf{q}0} T}{Mk_0 \theta^2}.$$

But below Debye temperature θ_D , the integral I cannot be evaluated analytically. Numerical methods are then employed to estimate its value. We note that owing to the zero-point energy of the lattice, $I \sim \frac{1}{4} \frac{\theta^2}{T^2}$, at lower temperatures. So,

$$\frac{E_{ca}}{T \rightarrow 0} = - \frac{9m^* \pi A s^2 N_i}{\Omega N M k_0 \lambda \theta} \quad (45)$$

and

$$\frac{E_i}{T \rightarrow 0} = - \frac{9G^2 \hbar^2 E_{g0}}{4 M k_0 \theta} \quad (46)$$

The results of our calculations of the temperature coefficient of energy gaps have been given in table 1.

Table 1. Calculation of temperature gradient of conduction band edge for degenerate semiconductors.

semi- conductors	intrinsic dE_i/dT in $\text{ev/K} \times 10^{-4}$		impurity contribution dE_{ca}/dT in $\text{ev/K} \times 10^{-4}$
	Expt. ^(a)	Theory (equation 44)	
Si	-4.4	-5.83	-0.51
Ge	-4.6	-4.01	-0.26
GaSb	-3.5	-5.33	-0.105
InAs	-3.5	-3.37	-0.062
InSb	-2.7	-1.07	-0.03

(a) N B Hannay 1959 *Semiconductors* p 451 Reinhold Publishing Corporation, New York.

6. Effect of pressure

An increase in the applied pressure produces a change in the internal energy of the crystal in accordance with Gruneisen's (1926) relation,

$$\left(\frac{\partial U}{\partial P} \right)_V = \frac{V}{\gamma} \quad (47)$$

where V is the volume of the crystal and γ is known as Gruneisen's constant. Since the thermal energy of the crystal manifests itself in the form of lattice vibrations, it is quite natural to presume that the pressure is also equally capable of inducing its own component of lattice vibrations. Denoting the consequent

lattice displacement by u_i' , the perturbing term to the crystal Hamiltonian may then be written as,

$$-u_i' \frac{\partial V(r)}{\partial r} = -u_i' \left[\frac{\lambda A_s}{r} e^{-\lambda r} + \frac{A_s}{r^2} e^{-\lambda r} \right]. \quad (48)$$

The second order energy correction due to this perturbing term is given by,

$$E_{ca}(P) = - \frac{4\pi m^* A_s^2 N_i}{\Omega \lambda \hbar^2 N} \sum_q |U_q'|^2. \quad (49)$$

But from Grunisen's expression,

$$- \frac{V\beta B_s}{C_p'} = V \left(\frac{\partial P}{\partial U} \right), \quad (50)$$

where β = coefficient of volume, expansion, B_s = adiabatic bulk modulus, and C_p' = molecular specific heat at constant pressure. Therefore, from (47), we get,

$$U = \frac{M c_p}{\beta B_s} P = \sum_q M \omega_q^2 |U_q'|^2 \quad (51)$$

where c_p is the specific heat at constant pressure and U_q' corresponds to the amplitude of oscillation in the q -th mode. Denoting the mean square frequency by $\bar{\omega}^2$, we obtain from (51),

$$\bar{\omega}^2 \sum_q |U_q'|^2 = \frac{c_p P}{\beta B_s}. \quad (52)$$

Combining (49) and (52), and taking $\bar{\omega}^2 = 1/5\omega_D^2$, we get,

$$\frac{\partial E_{ca}}{\partial P} = \frac{20m^* \pi A_s^2 c_p N_i}{\Omega N \lambda \beta B_s k_0^2 \theta_D^2}. \quad (53)$$

The contribution by the host lattice on the intrinsic band edge may then be computed in a manner discussed in the earlier section. Substituting for $\sum_q |U_q'|^2$ from (52) in (40), we get,

$$W = \frac{G^2 c_p P}{2\beta B_s \bar{\omega}^2}. \quad (54)$$

The pressure dependence of the intrinsic band edge may, therefore, be expressed as,

$$E_g(P) = E_{g0} \exp(-2W)$$

i.e.,

$$E_g(P) = E_{g0} - \frac{E_{g0} G^2 c_p P}{\beta B_s \bar{\omega}^2}. \quad (55)$$

Substituting again for $\bar{\omega}^2 = 1/5\omega_D^2$, we finally get,

$$E_g(P) = E_{g0} - \frac{5E_{g0} G^2 c_p P}{\beta B_s \omega_D^2}. \quad (56)$$

The table 2 summarizes the results of our calculations of pressure gradients of energy gaps.

Table 2. Calculation of pressure gradient of conduction band edge for degenerate semiconductors.

Semi-conductors	intrinsic dE_c/dP in ev/bar $\times 10^{-6}$		impurity contribution dE_c/dP in ev/bar $\times 10^{-6}$ for $N_i/N = 1/100$ (equation 53)
	Expt. ^(b)	Theory (equation 56)	
Ge	-14.2	-12.2	-0.392
GaAs	-10.7 ~ -11.7	-10.48	-0.138
InP	- 8.5	-11.5	-0.142
InAs	- 9.6	- 3.15	-0.187

(b) Y F Tsay and S S Mitra 1974 *Phys. Rev.* **B10** 1476

7. Conclusions

We noticed that the bound electronic states introduced by substitutional impurity atoms gradually lose their binding strengths with increased doping due to large scale screening of impurity ions by mobile carriers. The impurity concentration at which carriers become totally free is known as the delocalization concentration and this phenomenon has been referred to as the Mott transition in semiconductors. Random distribution of impurity centres in the semiconductor was previously believed to lead to Gaussian or exponential tails of the density of states function into the gap, owing to the formation of the so-called impurity bands. By establishing the fact that bound electronic states disappear in the heavily doped semiconductor, irrespective of the distribution of impurity centres within the specimen, we have shown that the impurity bands cannot be formed, as previously believed. However, these arguments are only applicable to shallow impurity states. The concept of impurity bands for deep level impurities continues to enjoy its usual significance. As the carrier energy in the heavy doping case is only slightly perturbed due to the introduction of impurity centres,

we have also re-established the applicability of the perturbation theory in describing the behaviour of carriers in such samples. Two band model has also been used for the computation of the density of states function as the perturbation theory is only able to predict the effect of doping only on the majority carrier band edge. The former treatment clearly shows that the doping affects the minority carrier band edge also. The Fermi level in degenerate semiconductors, which was difficult to conceive upon conventional theory, has been computed by using uncertainty relations and by direct integration method. Our results have been checked by computing the tunnel diode peak voltages and comparing them with experimental results. A reasonably good agreement has been noticed. The partial ionization of carriers has also been computed by taking the exact form of the density of states function and assuming that carriers only above the Fermi energy take part in conduction. The effects of temperature and pressure on the band edges have also been computed.

Acknowledgments

R. Y. Thakur would like to thank the authorities of U.G.C. for granting him the teacher fellowship under the faculty improvement programme to carry out research work as described in this paper to fulfill partially the requirements of Ph.D. at I.I.T., Delhi. We would also like to thank P. N. Roy and P. N. Singh for their valuable suggestions and criticisms.

References

- Bonch-Bruевич V L 1966 *Semiconductors and Semimetals* **1** 101
 Castellan G W and Seitz F 1951 *Semiconducting Materials* Butterworths Scientific Publications, London
 Debye P P and Conwell E M 1954 *Phys. Rev.* **93** 693
 Feher G 1959 *Phys. Rev.* **114** 1219; Maekawa S and Kinoshita N 1965 *J. Phys. Soc. Japan* **20** 1447
 Gruneisen E 1926 *Handbuch der Physik* (H Geiger and K Saheel ed.) **10** p 1 Springer Verlag, Berlin
 Kane E O 1963 *Phys. Rev.* **131** 79
 Meyerhofer D, Brown G A and Sommers H S 1962 *Phys. Rev.* **126** 1329; Minton R M and Glicksman R 1964 *Solid State Electronics* **7** 491
 Pearson G L and Bardeen J 1949 *Phys. Rev.* **75** 865
 Roy D K and George P J 1975 *Indian J. Phys.* **49** 589
 Sundorfs R K and Holcomb D F 1964 *Phys. Rev.* **136** A810
 Thakur R Y 1978 *The Heavily Doped Semiconductors Ph.D. Thesis, IIT, Delhi*
 Ziman J M 1972 *Principles of the Theory of Solids* University Press, Cambridge

Relaxation spectrum of deformed (Al + 21 % Zn) alloy

T H Youssef and F A Saadallah

Metal Physics Unit, National Research Centre, Dokki, Cairo, Egypt

Received 18 August 1978

Abstract. Annealing of deformed Al-21% Zn was studied in the temperature range from room temperature upto 823 K. The results showed the existence of four annealing stages viz., recovery, polygonization, recrystallization and formation of Al_3Fe precipitates; as in the case of annealing of pure Al. The addition of zinc lowered the temperature range, as well as decreased the activation energy of the recovery, polygonization, and recrystallization stages. This was attributed to the easy zinc binding with annealed defects.

1. Introduction

In a previous work, Attia and Saadallah (1966) studied the isochronal annealing spectrum of deformed aluminium in the temperature range from room temperature to 500°C, and found that it is consisted of four stages of different characteristics.

The present investigation is an attempt to extend that work, to throw some light on the effect of adding zinc (in solid solution) on the annealing spectrum of Al. In particular to clarify the influence and interaction of solute zinc atoms on annealed lattice defects.

This study is found worthwhile since most of the previous work (Kelly *et al* 1963, Fabian *et al* 1974) on Al-Zn alloys were focussed on ageing reactions and pre-precipitation.

2. Experimental work and results

The alloy used was prepared from pure Al and Zn, in a specially designed furnace. Spectroscopic analysis of the ingots showed that its composition contained 0.25 Fe, 0.002 Mg and 0.004 Cu wt%.

The ingots were homogenized at 300°C for four hours. Then the samples were deformed to 50% reduction in area by drawing at room temperature such that the final shape of the deformed specimens were rods of diameter 0.9 cm, and wires of diameter 0.5 mm, for hardness, and stress-strain experiments respectively.

Homogenization and annealing experiments were carried-out in an evacuated silica tube ($\approx 10^{-5}$ mm Hg) inserted into a suitable furnace of high thermal capacity. The furnace temperature was controlled to within $\pm 1^\circ\text{C}$.

To investigate the relaxation spectrum of the deformed alloy, room temperature runs of automatic stress-strain curves, at constant strain rate (10 mm./min) were traced for wires annealed isochronally. The deformed wires were given heat pulses for 5 min. At temperature successively increasing in steps of 25°C. From the stress-strain curves the change in, ultimate tensile stress (U.T.S.) limit of proportionality (L.P.), 0.2% proof stress (0.2% P.S.) and the maximum elongation % (Max. Elong.%) were calculated. Also the V.H.N. was measured for polished rods under the same annealing conditions.

Typical sets of curves relating the variations of the above properties with isochrone temperatures for annealing time of 5 min. are shown in figure 1. It

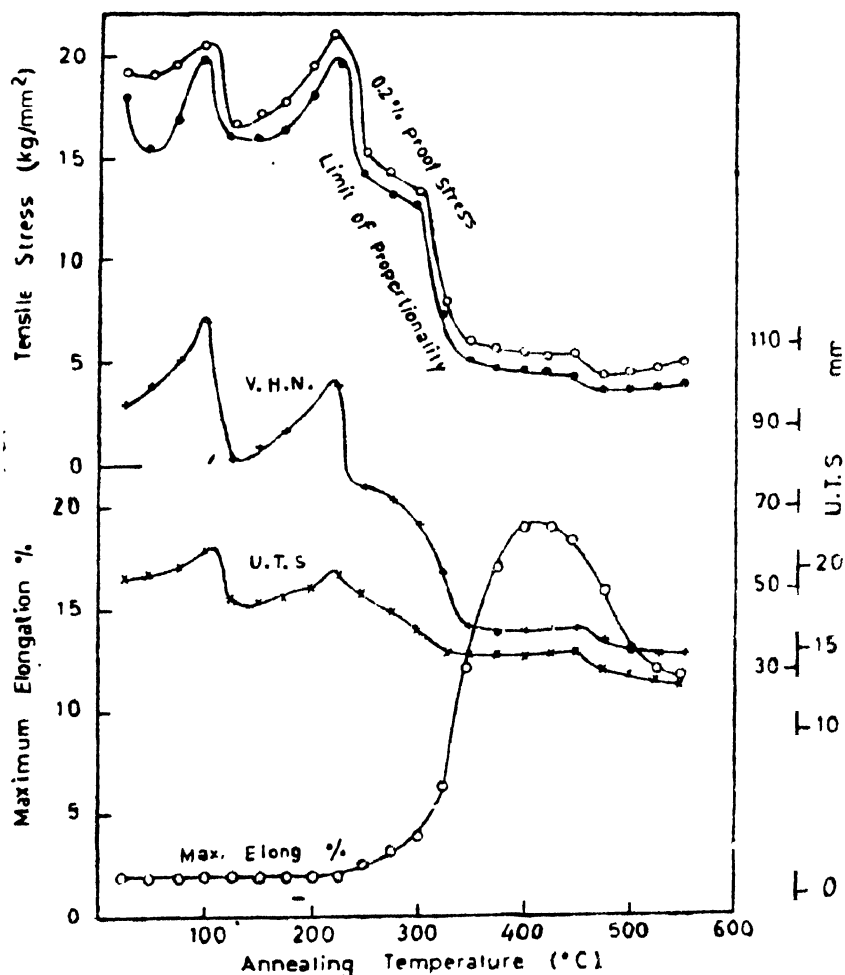


Figure 1. Isochronal annealing curves for Al-21% Zn samples deformed to 50% reduction in area and annealed for 5 minutes at temperatures increasing in steps of 25°C.

is clear that, there exists four annealing stages in the temperature ranges: 25°–125°C, 125°–275°C, 275°–400°C and above 400°C respectively. The first and second annealing stages were presented as peaks in U.T.S., L.P., 0.2% P.S. and the V.H.N., the third annealing stage was characterized by an enormous increase in the Max. Elong.%, while a drop occurred in the other calculated properties. The fourth stage of annealing appeared as a drop in all properties.

For the sake of comparison and to facilitate the analysis, the different relaxation stages were further studied by isochronal annealing using different annealing times at similar increasing temperatures. When the stage taking place at high temperatures was to be studied, the deformed specimens were given isochrone pre-anneals for 5 min. at the temperature boundary between any two stages. This treatment was found experimentally sufficient to eliminate the fraction of the properties change annealed out in the foregoing stage without causing any change in the coming one. Figure 2, shows typical sets of normalized annealing curves for the different properties calculated. It is clear from this figure that there is a shift in the peak temperatures with annealing time. From this shifting the energy activating each stage could be calculated by assuming that the time to observe a fraction of relaxation is proportional to $\exp(E/kT)$, where E is the energy activating per particle; K , is Boltzmann's constant, and T , is the absolute temperature.

Figure 3 shows activation energies for the different isochrone stages of properties. From this figure the activation energy calculated corresponding to the four annealing stages were found to be 0.42, 0.79, 1.10 and 2.00 eV respectively.

3. Discussion

It is generally accepted that on deformation, the alloy will contain beside zinc atoms, vacancies and dislocations. On annealing these defects will be annihilated on reaching sufficient thermal energy.

3.1. First annealing stage

It is generally accepted (Damask *et al* 1963) that vacancies migrate by annealing and trap zinc atoms forming vacancy-zinc pairs distributed randomly in the matrix. Those pairs are rendered mobile and migrate to dislocations, pin them (Maddin *et al* 1955, Richard *et al* 1959-60), leading to observed increase in the properties at the beginning of this stage. This is confirmed by reported activation energy, i.e., 0.42 eV, which is of the order of vacancy-Zinc migration in Al-Zn alloys (Fabian *et al* 1974).

Apart from these dislocation localities pinned by vacancy-zinc pairs, there exist dislocation segments that become relatively free to move in, glide or climb.

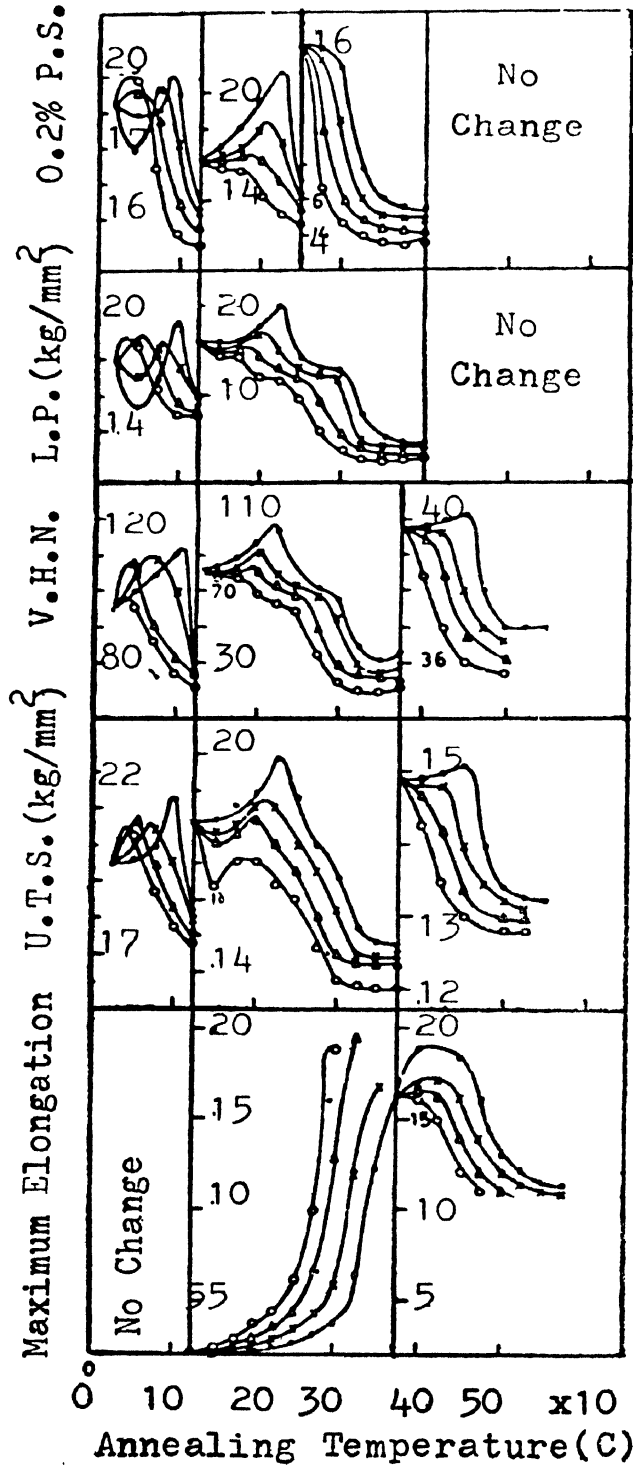


Figure 2. Typical sets of normalized isochronal curves for Al-21% Zn deformed to 50% reduction in area and annealed for 5, 10, 30 and 60 minutes.

The mobility of these segments will be associated with some rearrangement mechanisms causing decrease in the properties at the end of this stage.

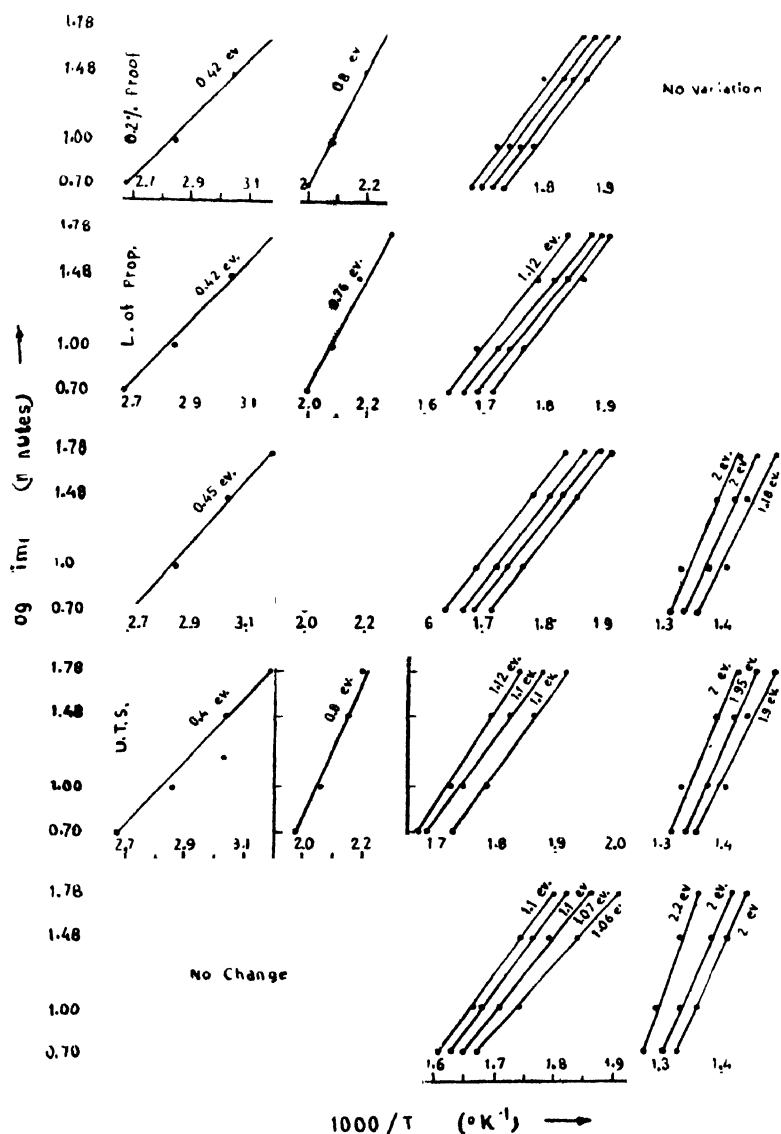


Figure 3. Typical sets of curves showing times and temperatures to calculate energies activating the four annealing stages, taken from figure 2.

3.2. Second annealing stage

It might be assumed that dissociation of vacancy-zinc pairs (Ceresara *et al* 1965), to vacancy and zinc atoms would take place. The zinc atoms will have

enough energy to form aggregates around dislocations and provide another impedance to dislocation motion (Smallman 1970). Due to this there is rise in the sample hardness and properties in this stage.

Migration of liberated vacancies will enable dislocations to climb. Recovery in this stage might be thus inferred to dislocation rearrangement in the form of polygonization and formation of sub-boundary (Fujita 1969). This is confirmed by the calculated activation energy (≈ 0.79 eV) which agrees with that previously (Matuki *et al* 1973) for subgrain boundary diffusion in Al-Zn alloy.

3.3. Third annealing stage

Sub-boundaries formed in the second annealing stage, on further annealing will migrate by self-diffusion leading to recrystallization and grain growth. This is achieved because of,

- (A) observed decrease in hardness and enormous increase in ductility.
- (B) the activation energy calculated, i.e., 1.1 eV, which agrees with that calculated previously for self-diffusion in Al-Zn alloys (Hilliard *et al* 1959, Kelly *et al* 1963).
- (C) the microstructure shown in figure 4 for sample annealed in this stage.

3.4. Fourth annealing stage

This stage is characterized by the growth of precipitates of globular shape (figure 5). It is similar to those previously reported by Al-Zn containing iron as impurity (Greaves *et al* 1971).

These precipitates might be Al_3Fe , since there exists iron impurity in the used alloy (0.25% Fe), as well as the temperature energy of this stage is quite equal to that needed for the formation of Fe-Al_3 precipitates (Donnelly *et al* 1964). The activation energy required for such precipitates formation was 2.0 eV which agrees with that quoted for its formation (Attia *et al* 1967).

Acknowledgment

The authors wish to express their deep gratitude to Professor R. Kamel, Head of Physics Department, Faculty of Science, Cairo University for his interest and stimulating discussions.

References

- Attia E A and Saadallah F A 1966 *Z. Metallkunde* **57** 769
- Attai E A, Sultan S A and Ahmed H A 1967 *J. Phys. Soc. Japan* **22** 767
- Ceresara S, Federighi T and Pieragostini F 1965 *Phys. Stat. Solidi* **11** 779



Figure 4. Microstructure showing recrystallization mechanism in sample cold-worked, then isochronally annealed at 300 °C for 30 minutes.

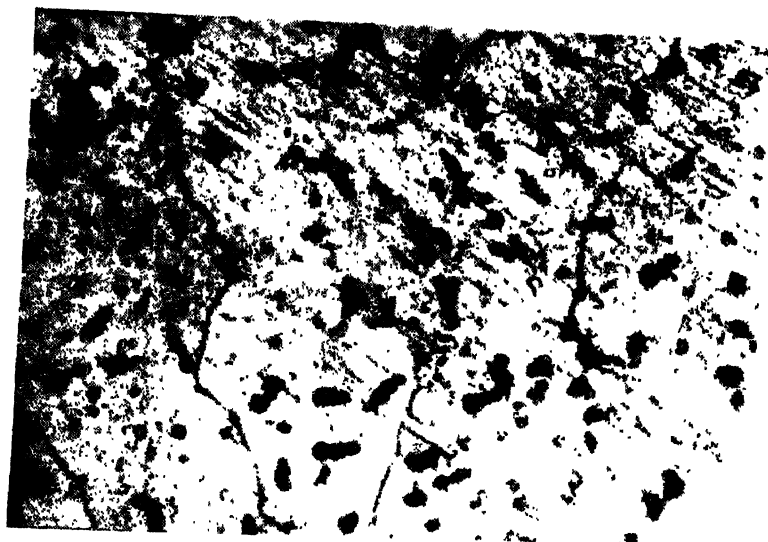


Figure 5. Microstructure showing FeAl_3 precipitates in sample cold-worked, then isochronally annealed at 400 °C for 30 minutes.

- Damask A C and Dienes G J 1963 *Point Defects in Metals* London, Gordon and Breach
- Donnelly W D and Rudee M L 1964 *Trans. AIME* **230** 1481
- Fabian H G and Löffler H 1974 *Phys. Stat. Sol. (a)* **21** 551
- Fujita H 1969 *J. Phys. Soc. Japan* **26** 1437
- Greaves R H and Wrighton H 1971 *Practical Microscopical Metallography* Chapman and Hall Ltd
- Hilliard J E, Averbach B L and Cohen M 1959 *Acta Met.* **7** 86
- Kelly A and Nicholson R B 1963 *Prog. Mat. Sci.* **10** 149
- Maddin R and Cottrell A H 1955 *Phil. Mag.* **46** 375
- Matuki K and Yauada M 1973 *J. Japan Inst. Met. (Japan)* **37** 448
- Richard T L and Pugh S F 1959-60 *J. Inst. Met.* **88** 141
- Smallman R E 1971 *Modern Physical Metallurgy* 3rd Ed London Butterworths

Spherulitic growth of BaWO_4 and SrWO_4 in gels

S K Arora and K Sangwal

Department of Physics, Sardar Patel University, Vallabh Vidyanagar 388120, Gujarat State, India.

Received 19 September 1978

Abstract. Growth of the crystals of barium tungstate and strontium tungstate by using modified gel technique has been described. Microtopographical investigations on the grown crystals have been made to reveal growth mechanism. The experiments on growth help one to safely distinguish experimental conditions conducive to the growth of spherulites on the one hand and perfect single crystals on the other. In order to obtain better and purer products one has necessarily to do away with the impurities of the gel solution and to use relatively greater concentrations of anions than that of cations.

1. Introduction

In ideal crystal growth theories, simplifying assumptions are made about the state of the medium from which crystals form although no account is taken of the medium at all in respect of non-polar crystals (Sheftal 1958). The multitudinous effects of the medium are mostly studied by experiment. Change of the medium has been known to bring about fantastic changes in the morphology which is characteristic of all crystals (Doremus *et al* 1958, Fisher 1954). Some crystals grow as whiskers, dendrites and spherulites. Whisker and dendritic growth invariably occurs in metals and alloys, whereas cellular and spherulitic growth is encountered with some inorganic materials and is a frequent feature of organic polymers (Strickland-Constable 1968). Such features are generally found to have been grown under conditions of high value of entropy and large supersaturation (Laudise 1970). They are typical and anomalous types of growth and a satisfactory elucidation of the factors which govern and control them is one of the difficult problems in the theory of crystal growth. Their growth mechanism has not been sufficiently understood because of the experimental difficulties, to a considerable extent, in the detection and investigation of the structure of small nuclei from which they develop. Work is, therefore, needed to characterize their microtopographical development, and the present paper is an attempt to do the same.

2. Experimental : Crystallisation apparatus and growth procedures

Gel technique, as modified by Patel *et al* (1972, 1973) has been successfully employed for growing good quality single crystals of BaSO_4 , SrSO_4 , BaWO_4 ,

SrWO₄, KClO₄, etc. in this laboratory. The double tube system used for crystal growth has the additional advantage of providing greater lateral diffusion of impurity ions too in the gel volume. It may be mentioned that for growing BaWO₄/SrWO₄ crystals, BDH Analar grade chemicals of BaCl₂/SrCl₂, Na₂WO₄ and acetic acid were used.

The as-available commercial grade sodium silicate was dissolved in double distilled water to give a resulting specific gravity of 1.05 to which was then added 2M acetic acid necessary to obtain resultant solution of 7.5 pH value. Na₂WO₄ solution was then poured in the vertically held tube and aqueous solution of BaCl₂/SrCl₂ (as the case may be, for growing crystals of BaWO₄/SrWO₄) was placed over the set gel in the crystallisation beaker while using the single tube system. On the other hand, these two solutions were separately introduced in the two vertical tubes and some amount of distilled water was placed above the set gel while employing the double tube system.

The crystals were found to have grown in the tube as well as in the beaker as shown in figure 1. Evidently, the nucleation density is tremendously large. Crystals were photographed after harvesting them out from the beaker and are shown in figure 2 (BaWO₄) and figure 3 (SrWO₄). These three dimensional spherulitic crystals with a few tree-leaf like ones were of the average size of 3 mm. across. Growth experiments were carried out between 20°-40°C by placing the crystallization beaker in a toluene-regulated water bath wherein the temperature could be controlled within $\pm 0.5^\circ\text{C}$. but no change in size, quality or morphology of the crystals was noticed. Influence of gel pH and of the change in concentration of nutrients has already been studied (Arora 1973). It was found that a relatively larger concentration of tungstate ions (employing M/2 or more of Na₂WO₄ solution) and relatively lower cation concentration (employing M/10 or less of BaCl₂/SrCl₂ solution) could favour the growth of more perfect or optically transparent crystals. In figures 2 and 3, clearer crystals were obtained with higher WO₄⁻² ion concentration and opaque ones with higher Ba⁺²/Sr⁺² ion concentration.

3. Observation and Discussion

Attention may be drawn to the fact that all the crystals displayed in figures 2 and 3 are not good single crystals but for the leaf-shaped ones. So far as the mechanism by which they grow is concerned, it may be noted that layer mechanism seems applicable. This is favourably supported by and evidenced to figure 4 where two dimensional piling and spreading of growth layers, which were initiated at the edges, can be observed.

In general, the larger leaf-shaped crystals and also the spherulitic ones which grew by using greater molarity of BaCl₂/SrCl₂ solution than that of Na₂WO₄ solution were milkywhite and almost opaque in appearance. On the other hand,

the smaller ones which grew by using greater molarity of Na_2WO_4 solution than that of $\text{BaCl}_2/\text{SrCl}_2$ solution were comparatively translucent to transparent. Figures 5 and 6 are the microphotographs of a large spherulite and a small one respectively. It can be seen that the smaller, more translucent spherulite (figure 6) consists of single crystalline fibres radiating from a heterogeneous extended source whereas only some inner portion of the larger spherulite (figure 5) exhibits that kind of feature; the outer half of these nearly opaque spherulites appears to have been grown by concentric banding and agglomeration process. Figure 7 is a similar picture of a nearly translucent spherulite, as observed between crossed polarisers, which seems to have grown by concentric banding of crystalline needles radiating from a central point source. The fact, however, is that all these spherulites are spherically symmetrical aggregates of single crystals.

We have been sure that the spherulites are not due to faster precipitation or attainment of rapid supersaturation because they were formed with very dilute nutrients too; they simply became more transparent with less concentrated solutions. The authors are inclined, therefore, to support Shubnikov's (1957) view that $E_s < E_k$ for their formation from a group of nuclei localised at a point, where E_s is the surface energy of a spherulite and E_k is the total energy of a crystal.

With a view to ascertaining the cause of origin and development of the spherulites, the purity of the mother liquor, that is, the as-available commercial grade solution of sodium meta-silicate, was suspected first. It was thought that spherulitic formation arises, as in the case of some igneous rocks (Bowen 1956), due to certain impurities. In order to minimize the suspended inherent impurities, such as Na, K, Si, etc. present in gel solution, decantation followed by high speed centrifugation was done and then the pure sodium meta-silicate solution thus obtained was treated, as usual, for obtaining appropriate density and pH values, etc., and thence for crystal growing. It is interesting to note that the 'pure' gel solution of specific gravity 1.05 and pH 7.5 produced perfect single crystals; a few of them are displayed in figure 8 (BaWO_4). It may be mentioned that since the crystals grow in a relatively strain-free environment, the density of dislocations in these gel-grown crystals as reported already (Patel and Arora 1977) was remarkably low; the few dislocations were created only accidentally.

It logically follows that the abnormal growths, such as spherulites, can be prevented in gels by removing the fine suspended impurities of sodium meta-silicate solution. It may be worth-while to note here that filtration was always avoided because using even micro-pore filter papers certain additional unwanted impurities got introduced in the gel solution.

To confirm the above conception further, some quantity of aqueous solution of CaCl_2 and/or KCl/NaCl was deliberately trickled down along with the aqueous



Figure 1. The Crystallization beaker having an exceedingly large number of nucleation centres in sodium meta silicate gel.

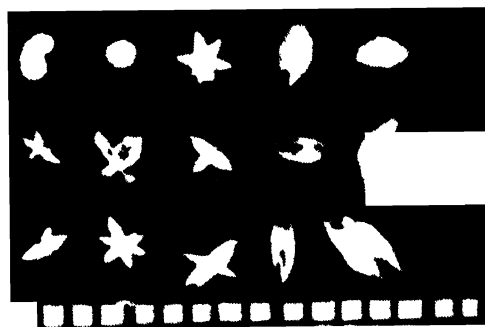


Figure 2. Crystals of BaWO_4 obtained in impure gel. Scale in mm

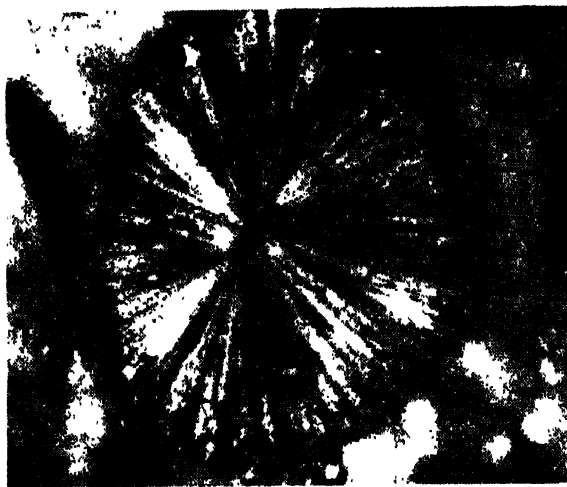


Figure 7. Clear BaWO₄ spherulite between crossed polarisers as observed under a Polarising Microscope, $\times 410$



Figure 8. Single crystals of BaWO₄ grown in pure gel. Scale in mm.

solution of BaCl₂/SrCl₂ in the vertically held tube (solution of Na₂WO₄ was not disturbed) and it was found that once again poor spherulites, instead of perfect single crystals, had grown in the 'pure' mother liquor. This indicates beyond doubt a great contribution of impurities in the gel itself to the development of anomalous growths. This matches well with the view of Palatnik and Kosevich (1967) that dust particles might cause spherulitic growth.

4. Conclusions

1. Crystal growth in gels proceeds by two dimensional piling and spreading of growth layers arisen from some crystal edges and corners.
2. Relatively greater concentration of WO₄⁻² ions produces clearer spherulites while greater Ba⁺²/Sr⁺² ion concentration produces opaque spherulites.
3. Certain impurities present inherently in sodium meta-silicate have been held responsible for the spherulitic generation.
4. Gel growth experiments can be conducted which produce dendrites or spherulites on the one hand and perfect single crystals on the other.

References

- Arora S K 1973 *Ph.D. Thesis*, 'Studies on Crystal Growth and Defects of some Tetragonal Tungstates', Sardar Patel University, Vallabh Vidyanagar
- Bowen N L 1956 *The Evaluation of the Igneous Rocks*, Dover Publication, Inc., New York
- Doremus R H, Roberts B W and Turnbull D 1958 *Growth and Perfection of Crystals* John Wiley and Sons, Inc., New York
- Fisher H 1954 *Elektrolytische Abscheidung und Elektrokristallization von Metallen*, Springer, Berlin
- Laudise R A 1970 *The Growth of Single Crystals*, Prentice-Hall, Inc., New Jersey
- Palatnik L S and Kosevich V N 1961 *Growth of Crystals (in Russian)*, Vol. V 167
- Patel A R and Arora S K 1973 *J. Crystal Growth* **18** 199
- Patel A R and Arora S K 1977 *Ind. J. Pure and Applied Phys.* **14** 971
- Patel A R and Bhat H L 1972 *J. Crystal Growth* **12** 288
- Sheftal N N 1958 *Growth of Crystals*, Vol III, Consultants Bureau, Inc., New York, p. 5
- Shubnikov A. 1957 *Sov. Phys. Crystallogr.* **2** 422
- Shubnikov A 1957. *Sov. Phys. Crystallogr.* **2** 578
- Strickland-Constable R F 1968 *Kinetics and Mechanism of Crystallization*, Academic Press, London

Alkali hydride molecules and their properties

S V Kulkarni and L K Sharma

Department of Applied Physics, Government Engineering College,
Jabalpur-482011

Received 1 November 1978, revised 13 February 1979

Abstract : In the present paper, we discuss the applicability of two new potential energy functions for evaluating the bulk properties of alkali hydride molecules. The properties discussed are rotational constant (α_e), anharmonicity constant ($\omega_e x_e$) and binding energy (D_e). Certain features of the repulsive term associated with the potential functions have been discussed. The riddle of universal potential energy function has also been discussed in connection with LiH molecule.

1. Introduction

In view of the considerable importance of the empirical potential energy functions in representing the true potential energy curves of various diatomic molecules, a knowledge of internuclear potential curves is of fundamental importance. The importance lies in a wide variety of fields ranging from gas kinetics to stellar structure. In particular the recent increased interest in astrophysical problems has emphasised the need for accurate potential curves governing the interaction of two atoms in either ground or excited states.

The aim of the present paper is two fold. First is to suggest a new repulsive term and secondly to discuss the importance of the proposed repulsive term in the potential energy function for alkali hydride molecules. This is particularly helpful as the dominant contribution to potential energy function comes from the Coulomb and repulsive part only. In the light of lack of reliable polarizability values of H ion and also of the feebleness of the Van der Waals constant for alkali hydride molecules, we have avoided the inclusion of these forces in the potential to save the reliability of the function. These facts have been demonstrated and discussed in connection with Rittner potential (Varshni and Shukla 1963).

Other authors (Das and Saxena 1970, Dass and Kachhava 1977) too have emphasised this fact and have thus avoided the inclusion of these forces.

2. Evaluation of α_e , $\omega_e x_e$ and D_e

For the present investigation we consider two potential functions both containing

the Coulomb and the repulsive terms only. In general the potential energy function may be written as

$$U(\gamma) = -\frac{e^2}{\gamma} + V(\gamma), \quad (1)$$

where the first term on the right hand side represents the Coulombian and the second term the repulsive forces. In this paper we discuss the following forms for the repulsive part :

$$V(r) = C \frac{\exp(-\gamma r^2)}{\gamma^2} \quad (2)$$

$$V(r) = A \frac{\exp(-br^2)}{r^{5/2}} \quad (3)$$

The two unknown parameters C and γ in (2) and A and b in (3) can be easily evaluated using the following conditions of equilibrium (Herzberg 1955) :

$$\left(\frac{dU}{d\gamma} \right)_{r=r_e} = 0$$

Table 1. Various values of α_e , $\omega_e x_e$ and D_e for different alkali hydride molecules calculated from potential (1) with repulsive part (2)

Molecules	α_e (cm ⁻¹)			$\omega_e x_e$ (cm ⁻¹)			D_e (Kcal/Mole)		
	Experi- mental	Calcu- lated	Percen- tage error	Experi- mental	Calcu- lated	Percen- tage error	Experi- mental	Calcu- lated	Percen- tage error
LiH	0.2132	0.1955	- 8.27	23.20	18.530	-20.12	165.1	152.35	-7.71
NaH	0.1353	0.1082	-20.02	18.58	14.120	-28.39	150.3 ±4.6	135.55	-9.81
KH	0.081	0.0711	-13.43	15.23	16.658	-18.47	127.2 ±3.5	117.98	-7.24
RbH	0.072	0.0085	-15.48	14.44	11.134	-21.64	119.6 ±4.6	113.21	-5.33
CsH	0.057	0.0538	- 5.45	13.70	10.638	-16.82	115.4 ±6.4	108.46	-6.01
Average percentage error			12.53			21.08			7.22

and

$$\left(\frac{d^2U}{d\gamma^2}\right)_{\gamma=r_e} = k_e$$

where k_e is the force constant.

Utilizing the well-known relations obtained by Varshni (1957), the values of α_e , $\omega_e x_e$ and D_e have been computed for various alkali hydride molecules. These values are listed in Table 1 and Table 2. The various experimental data used have been taken from Gray (1972).

Table 2. Various values of α_e , $\omega_e x_e$ and D_e for different alkali hydride molecules calculated from potential (1) with repulsive part (3)

Molecules	α_e (cm ⁻¹)		$\omega_e x_e$ (cm ⁻¹)		D_e (Kcal/mole)	
	Calculated	Percentage error	Calculated	Percentage error	Calculated	Percentage error
LiH	0.2683	25.88	25.211	8.66	144.65	-12.38
NaH	0.1368	1.15	16.700	-15.31	132.34	-11.94
KH	0.0834	-3.01	12.716	-11.07	116.33	-8.54
RbH	0.0709	-1.46	11.855	-16.57	111.90	-6.43
CsH	0.0618	8.47	11.134	-12.94	107.39	-6.93
Average percentage error		7.99		12.91		9.24

3. Discussion

Out of the two potential functions considered here, the P.E. function with repulsive part (3) is found to be highly satisfactory. The increase in the power of in the denominator of the repulsive term has reduced the average percentage errors for α_e and $\omega_e x_e$ by 4.54 and 8.12 respectively. It is worth mentioning here that a further increase in the power of γ in the denominator of the repulsive term will only deteriorate the results. Hence the applicability of a repulsive term like $(\exp(-kr^2)/r^n)$ when $n \geq 3$ may be safely ruled out.

Thus the present study clearly indicates the important part that the repulsive term plays on the form of the potential function for better reproduction of various properties. It also paves the way for further exploration of a still better form of the repulsive term within the limitations discussed here. This may pay rich dividends particularly in connection with alkali hydride molecules as the experimental data available for these molecules are meagre.

The question of obtaining a universal potential energy function has been discussed by Fallon *et al* (1960a, b), Singh and Jain (1962). We now discuss

the suitability of potential with repulsive term (2) as a universal potential function for the LiH molecule.

Now putting

$$C = \exp(y\gamma_e^2)\gamma_e e^{21/2(y\gamma_e+1)}$$

in equation (1) with $V(r)$ taken from equation (2), we got

$$U(\gamma) = \frac{e^2}{\gamma} \left[-1 + \frac{\exp\{-H(\gamma^2 - \gamma_e^2)\}}{2(y\gamma_e + 1)} \left(\frac{\gamma_e}{\gamma} \right) \right] \quad (4)$$

Further substitution of appropriate values of e , y and γ_e in (4) yields

$$U(\gamma) = \frac{116177}{\gamma} \left[-1 + 1.016 \frac{\exp(-0.3405\gamma)}{\gamma} \right] + (53287) \quad (5)$$

where $U(\gamma)$ is in cm^{-1} and γ in \AA . The second term in (5) has been included to shift the P.E. curve so as to coincide it with the corresponding experimental curve at $\gamma = \gamma_e$.

Figure 1 compares the potential energy curves obtained by Fallon *et al* (1960a, b) and that obtained by equation (5). The agreement between the two curves is satisfactory.

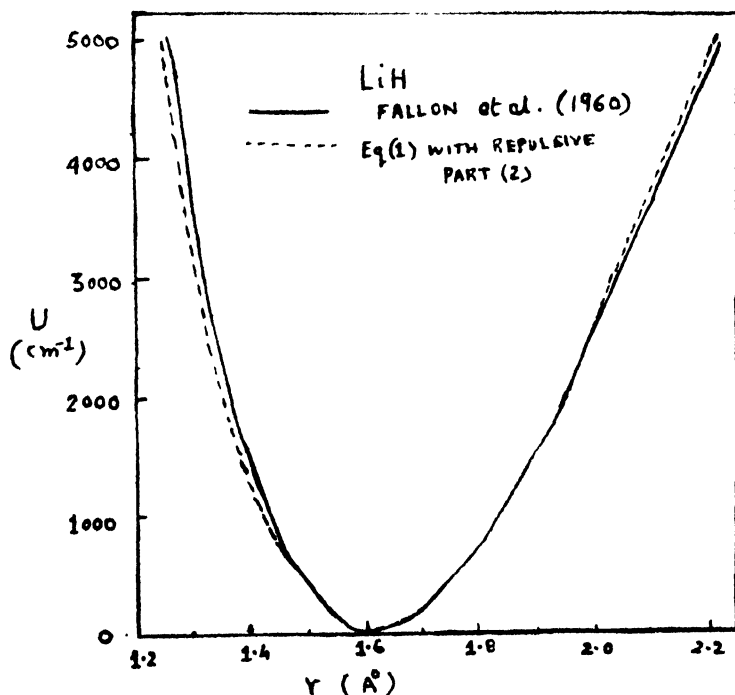


Figure 1. Potential energy curves for the ground state of LiH molecule.

Acknowledgments

The authors are grateful to Prof. N. L. Jain for encouragement. One of them (S.V.K.) is thankful to the C.S.I.R. for the award of a junior fellowship.

References

- Dass Lachhman and Saxena S C 1970 *Proc. Ind. Nat. Sci. Acad.* **36** 31
Dass Lachhman and Kachhava C M 1977 *Proc. Ind. Nat. Sci. Acad.* **43** 110
Fallon R J, Vanderslice J T and Mason E A 1960a *J. Chem. Phys.* **32** 1453
Fallon R J, Vanderslice J T and Mason E A 1960b *J. Chem. Phys.* **33** 944
Gray E 1972 *American Institute of Physics Hand Book* (Third Edition)
Herzberg G 1955 *Molecular Spectra and Molecular Structure-I, Spectra of Diatomic Molecules*
D Van Nostrand Company Inc (NY)
Singh N L and Jain D C 1962 *Proc. Phys. Soc. (London)* **79** 274
Varshni Y P 1957 *Rev. Mod. Phys.* **29** 664
Varshni Y P and Shukla R C 1963 *Rev. Mod. Phys.* **35** 130

Energy contributions to the second-order shear elastic constants of dilute Au-Ni alloys.

B P Barua* and S K Sinha

Saha Institute of Nuclear Physics, Calcutta-700009

Received 1 November 1978, revised 22 March 1979

Abstract.. Nickel concentration dependence data of Golding *et al* in the shear elastic constants of Au-Ni alloys are analysed using the pseudo-potential approach. Depending on the increase of the nickel content in the alloys, the band-structure energy contributions increase for both the shear elastic constants C' and C . It is found that the contributions to C' and C in the dilute Au-Ni alloys from the gold-gold ion-core repulsive interactions and the band-structure effects are of equal magnitudes.

1. Introduction

The elastic constants of the single crystal gold-nickel alloys for different nickel concentrations have been measured by Golding *et al* (1967) using the ultrasonic pulse-superposition method. They observed that the shear elastic constants C' and C increase linearly with nickel concentration when the concentration is low, and non-linearly when the concentration of nickel is high, and analysed these features of the experimental results in terms of Fuchs model (Fuchs 1936). In the Au-Ni alloys it is expected that the ion-core repulsive interaction will make larger contribution to the elastic constants as compared to the electrostatic contribution, because the atomic sizes of Au and Ni are significantly different as revealed by the X-ray studies (Flinn *et al* 1963). The above analysis corroborated these ideas, and achieved a good fit not only with the experimental data in the elastic constants, but also with the trends of variation of the enthalphy and the entropy of mixing with the alloy composition. However, the contributions to the above properties from the band-structure effects could not be evaluated in their analysis. The band-structure contributions account for the effects of the conduction electrons and in fact, their magnitudes may very well be comparable to the electrostatic contributions.

It is now possible to calculate the electrostatic, the band-structure and the ion-core repulsive contributions to the elastic constants of the simple metals (Suzuki *et al* 1968, Thomas 1973, Soma and Hiki 1974) using the pseudopotential formalism (Harrison 1966). Also it has recently been indicated by Cain (1976)

* On deputation from Chittagong College, Chittagong, Bangladesh.

how these calculations can be extended to analyse the elastic constants of dilute alloys like Cu-Al. In this paper we present a similar analysis of the elastic constants of the dilute Au-Ni alloys when the nickel concentration is low. In section 2, the calculations and results are presented and in section 3 the results are discussed.

2. Calculations and Results

Following Cain (1976) we first calculate the contributions of different energy effects to the shear elastic constants in pure gold. We then extend the results to include the effects of Ni concentration in dilute Au-Ni alloys. In the pseudo-potential theory the total energy of a noble metal at $T = 0^\circ\text{K}$ can be written as the sum of four energy terms (Moriarty 1972) :

$$E = E_{fe} + E_{es} + E_{bs} + E_{oi} \quad (1)$$

where E_{fe} is the free electron energy, E_{es} is the electrostatic (or Ewald) energy, E_{bs} is the band-structure energy and E_{oi} is the exchange energy between the ion cores. These energies can be written in parametric form such that the E_{fe} contains one adjustable parameter, E_{bs} contains two parameters for the Harrison model (Cohen and Heine 1970) and E_{ob} contains two parameters if the Born-Mayer form is assumed. The Fuchs second-order shear elastic constants C' and C can be defined in terms of the total energy of the crystal as

$$C' = \frac{3}{4} \frac{\partial^2 E}{\partial \epsilon^2} \quad \text{and} \quad C = \frac{3}{4} \frac{\partial^2 E}{\partial \gamma^2}$$

where ϵ and γ are the two volume-conserving shear defined by Thomas (1973). The usual forms (Thomas 1973) of E_{fe} , E_{es} , E_{bs} and E_{oi} are chosen in this calculation. The free electron energy depending only on the volume of the crystal remains unchanged during the volume conserving deformations, and hence it does not contribute to C' and C . It contributes only to the bulk modulus. The five adjustable parameters of the total energy expression have been obtained by fitting them with the experimental values of the two elastic constants C' and C , the bulk modulus, the lattice constant and the binding energy of gold. In calculating the band-structure energy and its derivatives, the energy-wave-number characteristic and its derivatives have been summed over the nearest 354 reciprocal-lattice vectors. The contributions to the electrostatic energy and the overlap energy to the shear elastic constants C' and C have been taken from the works of Cousins (1967). The results of such calculation (Barua and Sinha 1978) for the shear elastic constants of gold are shown in table 1, where the contributions of each energy term to the total value have been shown separately.

Table 1. Calculated lattice energy contributions to the Fuchs second order shear elastic constants in units of 10^{12} dynes/cm²

Elastic constant	M_{es}	M_{bs}	M_{ol}	Total
C'	+0.0180	-0.0267	+0.1707	+0.1620
C	+0.1614	-0.5148	+0.8074	+0.4540

For low nickel concentrations we can now write (Cain 1976) :

$$M = M_{es}(1-2\xi x) + M_{bs}(1+b_1x) + M_{ol}(1-\alpha x) \quad (2)$$

where M is either C' and C , x is the nickel concentration, ξ , b and α are adjustable parameters whose values can be chosen as described below. The particular forms chosen for the changes in M_{es} and M_{ol} in equation (2) are based on the following reasons: The electrostatic contribution depends on the square of the effective ionic charge (Heine and Weaire 1970). Since the ionic charge is compensated by the conduction electrons in the atomic volume, the effective ionic charge can be taken as the conduction electron density.

Following Golding *et al* (1967) the conduction electron density has been taken as $1-\xi x$ ($=n(x)$, say), where

$$\begin{aligned} n(x) &= 1-\xi x & \text{for } 0 \leq x \leq 0.4 \\ &= 0.6 & \text{for } 0.4 \leq x \leq 1.0. \end{aligned} \quad (3)$$

Neglecting $\xi^2 x^2$ term, we get the expression for change in M_{es} in equation (2). Cain (1976) has considered ξ to be equal to the excess valence of the solute while analysing the Cu-Al alloys and has used $\xi = -2$. Following Golding *et al* (1967) we, however, interpret $n(x)$ as equal to the conduction electron charge density and take $\xi = 0.3$ since this is more reasonable in terms of Friedel's model (1964) of the alloys. The value $\xi = 0.3$ implies that, near $x = 0$, the conduction electron density decreases slowly. The value of ξ will, however, be different for different solvent-solute pairs. While considering the overlap contribution it is reasonable to assume that for dilute Au-Ni alloys, Au-Au interactions are predominant. Therefore, following Golding *et al* (1967) and neglecting Au-Ni and Ni-Ni interactions we have chosen $\alpha = 2.0$. For the band-structure energy, the constants of proportionality is given by b so that the different elastic constants have different proportionality constants b_i . Hence, for constant lattice parameter, the change of modulus with respect to the concentration x is obtained from (2) as :

$$\frac{\partial M}{\partial x} = -2\xi M_{es} + b_1 M_{bs} - \alpha M_{ol}. \quad (4)$$

Using the calculated values of M_{es} and M_{ob} from table 1 and the experimental values of $\left. \frac{\partial M}{\partial x} \right|_x$ from Golding *et al* (1967) we obtain the band structure contributions, $b_1 M_{bs}$, from equation (4). These values are shown in tables 2 and 3.

Table 2. Changes in the lattice energy contributions to the Fuchs shear elastic constant C' for Au-Ni dilute alloys, gold being the solvent.

Composition (at. fraction Ni)	$\left. \frac{\partial M}{\partial x} \right _x$	$-2\xi M_{es}$	$b_1 M_{bs}$	$-\alpha M_{ol}$
0.0295	-0.014	-0.011	+0.338	-0.341
0.0972	-0.009	-0.011	+0.343	-0.341
0.2420	-0.007	-0.011	+0.345	-0.341
0.4242	-0.006	-0.011	+0.358	-0.341

Table 3. Changes in the lattice energy contributions to the Fuchs second order shear elastic constants C for Au-Ni dilute alloys, gold being the solvent.

Composition (at. fraction Ni)	$\left. \frac{\partial M}{\partial x} \right _a$	$-2\xi M_{es}$	$b_2 M_{bs}$	$-\alpha M_{ol}$
0.0295	-0.065	-0.097	+1.646	-1.614
0.0972	-0.063	-0.097	+1.648	-1.614
0.2420	-0.052	-0.097	+1.659	-1.614
0.4242	-0.003	-0.097	+1.708	-1.614

3. Discussion

The present analysis of the nickel concentration dependence data of Golding *et al* (1967) reveals (see tables 2 and 3) that the magnitude of the band-structure contribution to C is an order of magnitude greater than that to C' . Similar trends were also observed by Cain (1976) in the α -phase Cu-Al alloys. Also the band-structure energy contributions to the shear elastic constants C' and C of the dilute Au-Ni alloys increase for increasing concentrations of nickel. In fact, $b_1 M_{bs}$ gives the concentration dependence of the strain derivative of the band structure energy. This may serve as an additional useful data in a general analysis of the concentration dependence of the electron energy bands in dilute alloys. It is also noted that the overlap contributions to C' and C are dominant compared to the electrostatic contributions for different nickel concentrations, as anticipated by Golding *et al* (1967). However, the overlap contributions and the band-structure contributions to the shear elastic constants C' and C turn out to be almost of equal magnitudes in this case.

We, however, note that the above general trends have only qualitative significance because, the results in table 1 are calculated at $T = 0^\circ\text{K}$, and the experimental data for $\left.\frac{\partial M}{\partial x}\right|_x$ are taken at room temperature. The introduction of temperature dependence in the pseudopotential formalism is still quite complicated.

Acknowledgment

The authors wish to thank Prof. A. K. Saha for his interest in this work.

References

- Barua B P and Sinha S K 1978 *J. Appl. Phys.* **49** 3967
 Cain L S 1976 *Phys. Rev.* **B14** 833
 Cohen M L and Heine V 1970 in *Solid State Physics* (Edited by H. Ehrenreich, F. Seitz and D. Turnbull) Vol. 24 p 56 (Academic Press, New York)
 Cousins C S G 1967 *Proc. Phys. Soc. (London)* **91** 235
 Flinn P A, Averbach B I and Cohen M 1953 *Acta. Met.* **1** 664
 Friedel J and Daniel E 1964 in *Proceedings of the Ninth International Conference on Low Temperature Physics, Columbus, Ohio* (edited by J. G. Daunt, D. V. Edwards, F. J. Milford and M. Yaqub) Vol. 2 Plenum Press, Inc., New York, 1965
 Fuohs K 1963 *Proc. Roy. Soc. (London)* **A153** 622
 Golding B, Moss S C and Averbach B L 1967 *Phys. Rev.* **158** 637
 Harrison W A 1966 *Pseudopotentials in the Theory of Metals* (Benjamin, New York)
 Heine V and Weaire D 1970 in *Solid State Physics* (Edited by H. Ehrenreich, F. Seitz and D. Turnbull) Vol. 24 p 261 (Academic Press, New York)
 Moriarty J A 1972 *Phys. Rev.* **B6** 1239
 Soma H and Hiki Y 1974 *J. Phys. Soc. (Japan)* **37** 544
 Suzuki T, Granato A V and Thomas Jr. J F 1968 *Phys. Rev.* **175** 766
 Thomas Jr. J F 1973 *Phys. Rev.* **B7** 2385

CESR studies of high T_c A-15 Nb_3Ge films in normal and superconducting states

S N Ekbote, S K Gupta and A V Narlikar

National Physical Laboratory, New Delhi.

Received 27 September 1979

Abstract. For the first time CESR has been studied for a superconducting material. It is shown that the conditions are favourable, and the critical parameters are suitable for observation of CESR in thin films of Nb_3Ge having high T_c of 22.65 K. The samples have been systematically investigated in the temperature range of 400 K to 4.2 K and thus the CESR has been studied both in the normal and superconducting states. The behaviour of the line observed gives the direct support to the idea of pairing of conduction electrons in superconducting transition.

1. Introduction

The conduction electron spin resonance (CESR) in superconductors was discussed first by Azbel and Lifshits (1957) who suggested that the paramagnetic resonance in a bulk superconductor was improbable. However, Kaplan (1965) argued that, subject to the omission of surface scattering, CESR in thin superconducting films should be experimentally feasible provided the normal state of the films also exhibit CESR. Immediately thereafter Shultz *et al* (1966) indeed could succeed in observing CESR in the normal state of Al but they could not study it in the superconducting state for the obvious reason that the resonance field they used exceeded the critical field of Al.

In this paper we report for the first time, CESR studies of thin films of superconducting Nb_3Ge in the normal and superconducting states. It is well established that the observation of CESR in metals is difficult due to several reasons (Altshuter *et al* 1964). Superconductors above the critical temperature T_c are normal metals and consequently observing CESR in them necessitates overcoming all those difficulties discussed by Altshuter *et al*. The main critical parameters are the film thickness d and the spin-lattice relaxation time τ of the material. The one obvious constraint is that $d < \delta$, where δ is the skin depth. Below the critical temperature when a metallic material becomes superconducting more conditions are to be satisfied for CESR. Firstly, the thickness should be less than the penetration depth λ so that the constraint imposed by the Meissner effect is overcome and the applied field can 'see' the superconductor. Secondly, H_{C2} of the film should be large enough so that the application of the

magnetic field required for the observation of CESR does not destroy the superconducting state. Unfortunately, even in Gd doped La alloys, this has been ignored, and all the reported EPR studies therefore are almost in the normal state of the material (Davidov *et al* 1973, Aleskooviskii *et al* 1977). Regarding the other critical parameter, namely τ , according to Elliott's theory (1954), due to their relatively strong spin-orbit interaction the observation of CESR is considered difficult in heavy metals, and consequently in pure metals of transition series, such as Nb, V and Ta which readily become superconducting the possibility of observing CESR in them has not yet been properly explored. However, it is well established that for A-15 compounds of the above elements, the spin-orbit interaction parameter λ_{S_0} is drastically low, and therefore, observation of CESR in these compounds is plausible. In this connection as pointed out by Monod (1977), it is worth mentioning that a satisfactory theory of CESR, particularly applicable to heavy metals, is still lacking and the role of spin-orbit interaction is not yet fully established, as CESR has now been observed in heavy elements such as Pd and Au (Beunen and Monod 1978).

In view of above, thin films of A-15 compounds which are noted for high T_c and H_{C_2} become the most appropriate choice for the study of CESR in normal and superconducting states. In particular, we have selected thin films of Nb₃Ge with the highest T_c of 22.65 K, and H_{C_2} exceeding 300 kOe (Robert 1978).

2. Experimental

Thin films of Nb₃Ge of thickness $d \approx 2000$ Å, sputtered deposited on alumina and having A-15 structure were systematically investigated for CESR using the Varian V-4502, x-band ESR spectrometer using 100 kc/s magnetic field modulation. The spectra at liquid air temperature and above room temperature upto 400 K were obtained using Varian variable temperature accessories, V-4547. Temperature of the sample was measured using a 36 gauge copper-constantan thermocouple inserted in the sample cavity. The Varian V-4545A cavity with proper accessory was used for recording the spectra at the liquid helium temperature. In liquid helium work, the sample was pasted on the narrow wall of the cavity. The upper critical magnetic field for this film is more than 300 kOe whereas for resonance study we used the magnetic field up to 10 kOe only, and thus its superconducting state is not quenched at helium temperature. The g values were measured with respect to DPPH standard and the line width measurements were accurate upto ± 0.1 Oe.

3. Results and Discussion

Above discussed conditions for observing CESR are satisfactorily met in Nb₃Ge films of thickness $d \approx 2000$ Å. The estimated skin depth $\delta \approx 4000$ Å, while the penetration depth in the superconducting state is $\lambda \approx 5000$ Å. These values as pointed out by Kaplan (1965) favour the observation of CESR.

In Figure 1 the resonance absorption signals are shown at different temperatures. It is clear that at all temperatures except the helium temperature of

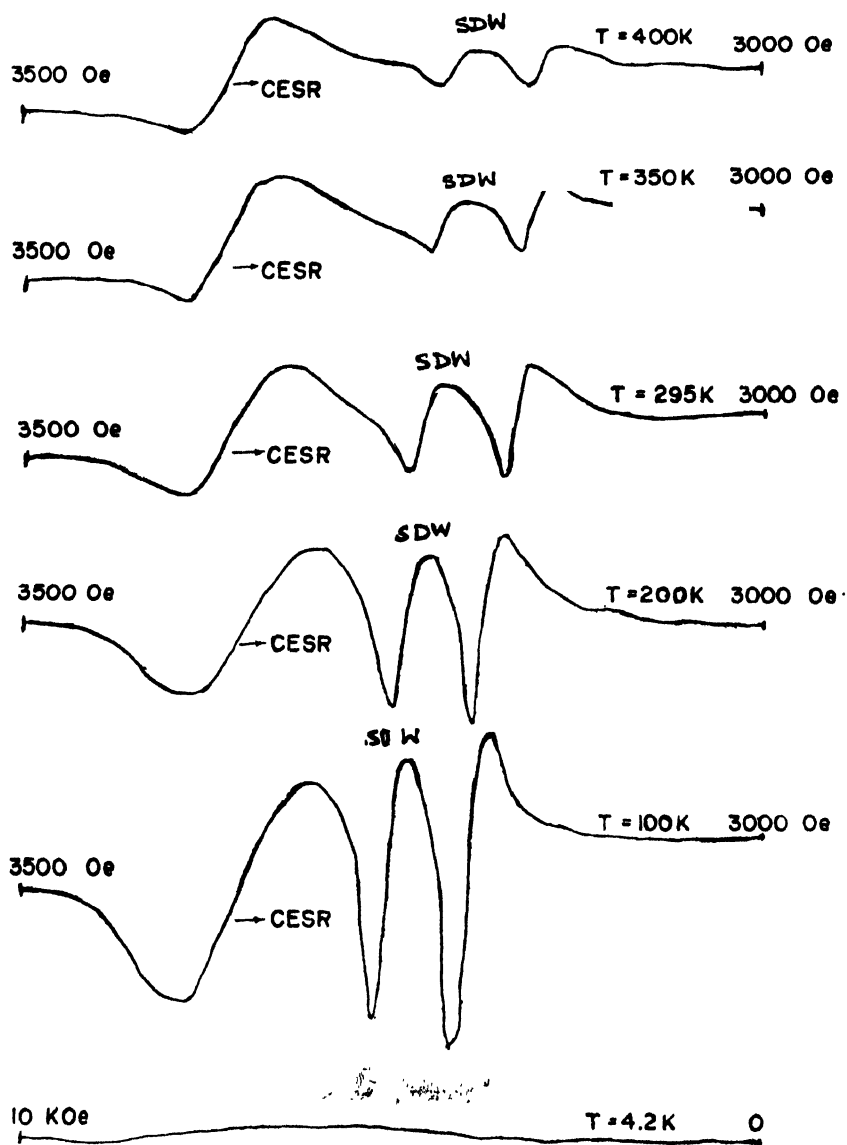


Figure 1 Electron spin resonance spectra of Nb₃Go at various temperatures showing CESR and SDW signals.

4.2 K, one resonance signal at $g \approx 2$ is present along with two more signals towards low field side. The signal for $g \approx 2$ is attributed to the CESR. The

values of line width, signal height and g -factor for this line at different temperatures are given in Table 1.

Table 1.

S.No.	Temperature K	g -value	Line width* ($\frac{1}{2}\Delta H_{pp}$ Oe)	Peak to peak height I cm
1	400	2.022	18.5	2.8
2	350	2.022	18.5	3.0
3	295	2.022	18.8	3.2
4	200	2.022	19.5	3.8
5	100	2.022	20.0	5.2
6	4.2	—	—	—

* $\frac{1}{2}\Delta H_{pp}$ = Peak to peak half line width.

As it is known, the CESR signal should be near $g = 2$, i.e. close to 2.003, the free electron g value. Moreover, other properties of CESR are also nearly satisfied by the same signal. It is known that the line width ($\frac{1}{2}\Delta H_{pp}$), and g value should be nearly invariant with temperature for CESR which is evident from the data of Table 1. Small temperature dependence observed in I is entirely reasonable as pointed out by Monod (1978) in CESR for Pd. Also, the observed line is isotropic. These features provide a reasonable ground to believe that the line is due to CESR. Besides, the observed data is found to fit well in the Elliott relation (Beunen and Monod 1978) which further substantiates the above contention. It may be mentioned that the X-ray diffraction and X-ray fluorescence studies made by Ekbote *et al* (1978) on these films revealed neither any second phase nor they could detect the presence of any para or ferromagnetic impurities. These results beyond reasonable doubt establish the CESR line in the normal state of Nb_3Ge .

The observation at 4.2 K is very interesting. The results show that in the superconducting state at 4.2 K, the CESR signal as well as the other two signals are no longer observed. This, in our opinion, is the most direct manifestation of superconducting state which is characterised by pairing of electrons of opposite spins and momenta located close to the Fermi surface. The disappearance of the CESR line, is contrary to the suggestion of Kaplan (1965). Since $T_c = 22.65 \gg 4.2$ K, for these films, the number density of unpaired electrons at 4.2 K, at the Fermi surface is expected to be low. This, thus, confirms the pairing of electrons in the superconducting state, an outcome of the BCS theory. Thus, the line in the normal state is due to the electrons in the conduction band which are taking

part in superconductivity. As regards to the other two lines observed in the present study, whose intensity varies considerably as compared to CESR, their origin is believed to be in the occurrence of spin density waves present in the conduction band. The occurrence of spin density waves in a high T_c superconductor is of extraordinary importance, having far reaching implications. The behaviour of these lines is a subject of separate communication to be published later.

4. Conclusion

The very first study of CESR in a superconductor is reported. Thin films of Nb_3Ge having high T_c of 22.65 K exhibit CESR in the normal state. On cooling below T_c , the line disappears in agreement with the idea of pairing, characteristic of the superconducting state. The presence of spin density waves in the conduction band is also indicated.

Acknowledgments

The authors are indebted to Dr. J. E. Evetts and Dr. R. Somekh of the University of Cambridge, U.K. for providing the sputtered samples of Nb_3Ge . One of us (A.V.N.) is thankful to Professor J. Buttet at the Swiss Federal Institute of Technology in Lausanne for the stimulating discussion and for making helpful suggestions. The authors thank the Director National Physical Laboratory for provision of facilities and Dr. G. D. Sootha for cooperation. This work was funded by the Department of Science and Technology.

References

- Aleskevich N E, Garferlin A, Kocheloav B I and Khavakhasvyan 1977 *Soviet, Phys. JETP* **45** 799
- Altshuler S A and Kozyor B M, Eds 1964 *Electron Paramagnetic Resonance* p 253 Academic Press, New York and London.
- Azbel M Ya and Lifshits I M 1957 *Zh. EKSP, Teoret. Fiz.* **33** 792
- Beuneu F and Monod P 1978 *Phys. Rev.* **B18** 2422
- Davidov D, Chelkowski A, Rettori C, Orbach R and Maple M B 1973 *Phys. Rev.* **B7** 1029
- Ekbote S N, Gupta S K, Nagpal K C and Narlikar A V 1978 *Proc. Nucl. Phys. and Solid State Phys. Symposium Bombay*
- Elliott R J 1954 *Phys. Rev.* **96** 266
- Kaplan J I 1965 *Phys. Lett.* **19** 266
- Monod P and Hurdequint H 1977 *Transition Metal* published by The Institute of Physics Techno House, Bristol
- Monod P 1978 *J. de Physique* **39** C6 1472
- Robert B W 1978 *Nat. Bur. Stand. (U.S.) Tech. Note* 983 4
- Schutz S, Dunifer D and Latham C 1966 *Phys. Letts.* **32** 192

Letters to the Editors

Debye-Waller factor of copper

S Tolpadi

Department of Physics, Indian Institute of Technology, Kharagpur

Received 7 June 1978, revised 6 December 1978

The theory of Paskin (1957) regarding the temperature variation of X-ray Debye temperature was modified (Tolpadi 1975, 1977) so as to include the additional anharmonic effect due to phonon-phonon interaction. The temperature variation of the lattice specific heat was recently investigated (Tolpadi 1979) by introducing a simple two parameter modified Debye model which includes the effect of lattice dispersion. The present calculation based on this two parameter model shows that the lattice dispersion and crystal anharmonicities must be taken into account in the study of the temperature variation of the Debye-Waller factor.

The exponent $2W$ of Debye-Waller formula for a monatomic lattice of cubic symmetry is given by (James 1954, Willis and Pryor 1975).

$$2W = \frac{16\pi^2 \text{Sin}^2 \theta}{3N m \lambda^2} \int_0^{\nu_D} \left(\frac{h\nu}{e^{h\nu/kT} - 1} + \frac{1}{2} h\nu \right) \frac{g(\nu)d\nu}{\omega^2} \quad (1)$$

where the symbols have their usual meaning.

For a Debye crystal equation (1) can be written as

$$2W = \frac{12h^2 \text{Sin}^2 \theta}{mk\lambda^2} \left\{ \frac{I(x)}{x^2 T} \right\} \quad (2)$$

where

$$I(x) = \frac{1}{x} \int_0^x \frac{tdt}{e^t - 1} + \frac{x}{4} \quad \text{and} \quad x = \frac{\theta}{T} = \frac{h\nu_D}{kT},$$

θ being the Debye temperature.

The comparison between theory and experiment is usually made by evaluating the temperature parameter Y_1 (James 1954, Owen and Williams 1947)

$$Y_1 = \frac{12h^2}{mk} \left[\frac{I(x_0)}{x_0^2 T_0} - \frac{I(x)}{x^2 T} \right] \quad (3)$$

where I_0 , x_0 and I , x refer to temperatures T_0 and T respectively

The effect of lattice dispersion on the Y_1 parameter can be included as follows. A good approximation for the dispersion relation is a sine curve (Barber and Martin 1959, Hewat 1972, Tolpadi 1979) which can be written as

$$\nu(q) = \nu_0 \sin(\pi q/2q_0) \quad (4)$$

where

$$\nu_0 = (2\nu_D/\pi).$$

The frequency distribution function corresponding to the dispersion relation given in equation (4) is given by

$$g(\nu) = \frac{36N\nu_0\{\sin^{-1}(\nu/\nu_0)\}^2}{\pi^2(\nu_0^2 - \nu^2)^{\frac{1}{2}}} \quad (5)$$

Substituting equation (5) in (1) we can show that the Y_1 parameter with the inclusion of lattice dispersion is given by

$$Y_1 = \frac{12h^2}{mk} \left[\frac{F(t_0)}{x_0^2 T_0} - \frac{F(t)}{x^2 T} \right] \quad (6)$$

where $t_0 = (2x_0/\pi)$, $t = (2x/\pi)$ and the integral F can be shown to be equal to

$$F(t_0) = \frac{2t_0}{\pi} \int_0^{\pi/2} \frac{\phi^2}{\sin \phi} \left\{ \frac{1}{e^{t_0 \sin \phi} - 1} + \frac{1}{2} \right\} d\phi \quad (7)$$

James (1954) has tabulated the integral I . We have reevaluated the integral I at closer intervals and the data is given in table 1. Hewat (1972) has calculated the integral F only in the limit $t_0 \rightarrow 0$, the value being $2 \ln 2$. In the present work F has been calculated by a numerical method as a function of t and the results are given in Table 1.

Table 1. The value of the integrals I and F as a function of t .

t	0.0	0.1	0.2	0.3	0.4	0.5	0.6	0.7	0.8	0.9
I	1.0000	1.0003	1.0011	1.0025	1.0044	1.0069	1.0100	1.0135	1.0177	1.0233
F	1.3863	1.3874	1.3895	1.3929	1.3977	1.4038	1.4113	1.4201	1.4303	1.4417
I	1.0275	1.0332	1.0394	1.0462	1.0534	1.0611	1.0694	1.0781	1.0872	1.0970
F	1.4544	1.4584	1.4637	1.5001	1.5178	1.5366	1.5566	1.5777	1.5999	1.6232
I	1.1069	1.1175	1.1284	1.1398	1.1516	1.1638	1.1764	1.1893	1.2027	1.2164
F	1.6475	1.6728	1.6991	1.7264	1.7545	1.7836	1.8135	1.8442	1.8754	1.9072
I	1.2304	1.2448	1.2596	1.2746	1.2900	1.3056	1.3216	1.3378	1.3543	1.3711
F	1.9403	1.9740	2.0084	2.0435	2.0792	2.1155	2.1524	2.1898	2.2277	2.2662
t	4.0	4.5	5.0	5.5	6.0	7.0	8.0	9.0	10.0	11.0
I	1.3881	1.4769	1.5709	1.6693	1.7713	1.9839	2.2052	2.4326	2.6644	2.8995
F	2.3051	2.5063	2.7166	2.9340	3.1568	3.6144	4.0826	4.5574	5.0365	5.5185

It was recently shown that a two parameter lattice dynamical model (Tolpadi 1979) which includes the effect of dispersion gives a good agreement between the calculated and observed specific heat. The two parameters of the model which refer to the zone boundary averages of transverse and longitudinal vibration frequencies, are calculated by solving the frequency determinant of the cubic crystal in the $\lambda \rightarrow \infty$ limit (Betts *et al* 1956) along the directions (100), (110), (111), (210), (211) and (221). A linear relation between ν and q is assumed and the zone boundary frequencies are calculated by considering the relevant values of the zone boundary wave vector. A six direction approximation (Betts *et al* 1956) is used to calculate the average transverse and longitudinal Debye temperatures. If $\theta_t = yT$ and $\theta_l = zT$ refer to the transverse and longitudinal Debye temperatures of the crystal the Y_1 parameters given in equations (3) and (6) can be written as

$$Y_1 = \frac{12h^2}{mk} \left\{ \frac{2}{3} \left(\frac{I(y_0)}{y_0^2 T_0} - \frac{I(y)}{y^2 T} \right) + \frac{1}{3} \left(\frac{I(z_0)}{z_0^2 T_0} - \frac{I(z)}{z^2 T} \right) \right\} \quad (8)$$

$$Y_1 = \frac{12h^2}{mk} \left\{ \frac{2}{3} \left(\frac{F(2y_0/\pi)}{y_0^2 T_0} - \frac{F(2y/\pi)}{y^2 T} \right) + \frac{1}{3} \left(\frac{F(2z_0/\pi)}{z_0^2 T_0} - \frac{F(2z/\pi)}{z^2 T} \right) \right\} \quad (9)$$

The effect of the crystal anharmonicity on the temperature variation of the Y_1 parameter can be calculated by assuming that the variation of the Debye temperature $\theta = xT$ is given by (Paskin 1957)

$$\theta^2 = x^2 T^2 = x_0^2 T_0^2 \{1 + 2\alpha\gamma_T(T_0 - T)\} \quad (10)$$

where α is the volume expansion coefficient and γ_T is the Gruneisen parameter (Gruneisen 1926). In equation (10) if the isobaric Gruneisen parameter γ_p is considered instead of γ_T we get the combined effect of anharmonicity due to volume expansion and phonon-phonon interaction (Tolpadi 1975, 1977).

The zone boundary transverse and longitudinal average Debye temperatures θ_t and θ_l of copper are 335.3 K and 663.6 K respectively. The average Debye temperature is therefore = 444.8 K. The isobaric Gruneisen parameter γ_p was taken from an earlier paper (Tolpadi 1975) and γ_T is taken as 1.96. Assuming the reference temperature $T_0 = 293$ K, the Y_1 parameter calculated from equation (6) for one parameter model by applying both the anharmonic corrections is given in figure 1. Y_1 parameter is also calculated for the two parameter model from equations (8) and (9) by assuming that the temperature variation of the Debye temperatures θ_t and θ_l are given by relations similar to equation (10). These results are given in figure 1 and compared with the experimental data of Owen and Williams (1947). It is found that instead of a single parameter model, the two parameter model which includes the effect of lattice dispersion and both

the crystal anharmonicities due to volume expansion and self energy effect gives results in good agreement with the experimental data.

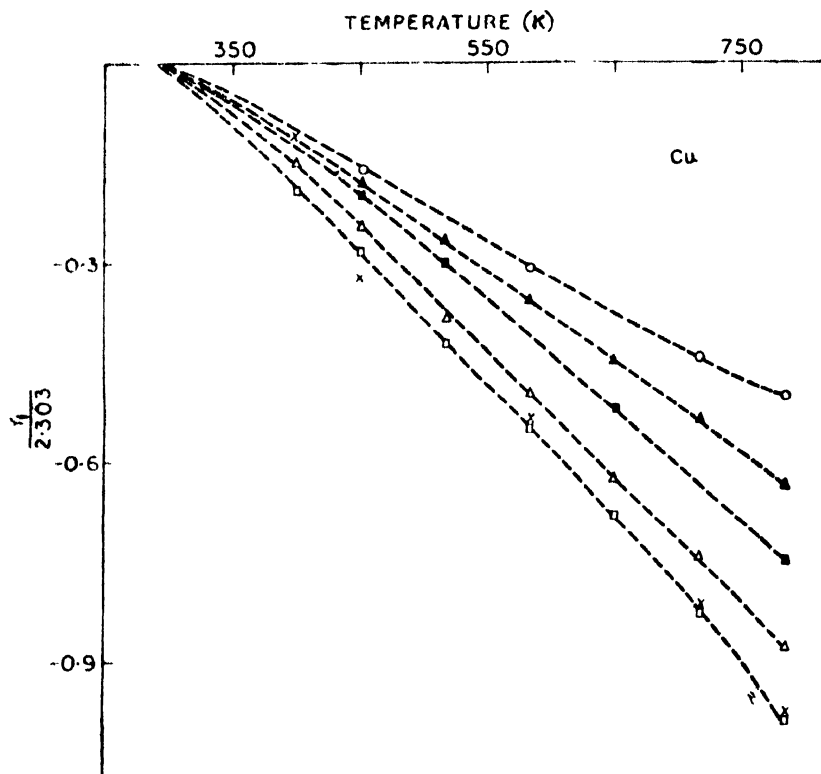


Figure 1. Temperature variation of the Debye-Waller factor of Cu using a two parameter (TPM) and a one parameter model (OPM). ■ - ■ with dispersion and isobaric anharmonicity (OPM), O - O Harmonic crystal without dispersion (TPM), ▲ - ▲ Isothermal anharmonicity without dispersion (TPM), Δ - Δ with dispersion and isothermal anharmonicity (TPM), □ - □ with dispersion and isobaric anharmonicity (TPM), × × experimental data.

References

- Barber S W and Martin B 1959 *J. Phys. Chem. Solids* **9** 198
 Gruneison E 1926 *Handbuch der Physik* **10** (Springer-Verlag, New York)
 Hewat A W 1972 *J. Phys. C. Solid State Phys.* **5** 1309
 James R W 1962 *The Optical Principles of the Diffraction of X-rays* (Bell and Sons Ltd. London)
 Owen E A and Williams R W 1947 *Proc. Roy. Soc.* **188A** 509
 Paskin A 1957 *Acta Cryst.* **10** 667
 Tolpadi S 1975 *Solid St. Commun.* **16** 937
 Tolpadi S 1976 *Physica* **81B** 315
 Tolpadi S 1977 *Indian J. Phys.* **51A** 181
 Tolpadi S 1979 *Ind. J. Pure Appl. Phys.* **17** 635
 Willis B T M and Pryor A W 1975 *Thermal Vibrations in Crystallography* (Cambridge Univ. Press London)

Improved digital solar aspect sensor for space Vehicles

G K M Thurtupalli

Apple Project, ISRO Satellite Centre, Peenya, Bangalore-58

Received 1 November 1978

Digital solar aspect sensors are used to measure the attitude with respect to the sun, of spin axis as well as three-axis stabilized satellites, sounding rockets and balloons. They are also used for attitude measurement of ground based optical instruments.

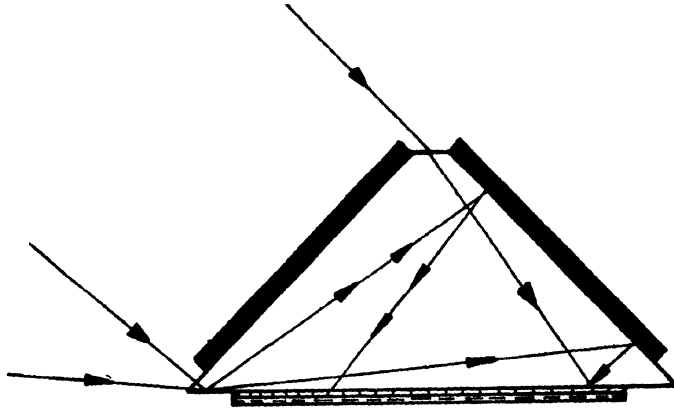
The system fundamentally consists of a quartz block, whose front surface facing the sun is made opaque except for a narrow entrance slit, while to the lower surface a reticle of binary or gray code consisting of 8-9 bits is fixed. Behind the reticle for each bit one P-N silicon photocell is attached. The linear image of the sun produced by the narrow slit is projected onto the P-N silicon cell via the grey code pattern. This produces different light patterns detected by the cells, depending on the inclination angle between sunlight and sensor normal. The field of view of such system is controlled by the width of the rectangular quartz block and is normally limited to $\pm 45^\circ$. To cover the 2 steradians, often required, three to four sensors are to be used.

Based on the principles of refraction and total internal reflection in a quartz piece, a conceptual design to increase the field of view (approximately 80°) without loss of angular resolution of the system is shown schematically in figure 1a-b.

Instead of a conventional rectangular quartz block a trapezoidal block is selected and usual narrow slit 1 is made on the short face A of the trapezium. Slit 2 and 3 of different widths and parallel to slit 1 are made of the faces B and D at the positions shown in the figure 1a. Reticle (gray/binary code) with light sensing elements are mounted on face C, faces B and D are made fully reflective by depositing suitable metallic films.

The angles between faces B-C/C-D are chosen to correspond to the critical angle for quartz. For light rays incident on face C at angles greater than this angle, total internal reflection takes place and the rays are totally reflected from surface C to impinge on face B/D. At this point, the rays are further reflected back from faces B/D finally to reach the sensing elements via mask, mounted on face C.

Light rays, incident at angles less than the critical angle, passes through slit '1' and for angles greater than this light rays passes through slit 2/3. However, all these rays finally pass through the same gray code mask and sensing elements. The light rays passing through each of the three slits can easily be



Figures 1a and 1b

- Metallic film
 ||||| Grey Binary Code Mask
 ---- Light sensing elements
 (Ray tracing is shown for positive angles only similar symmetrical system holds for opposite angles).

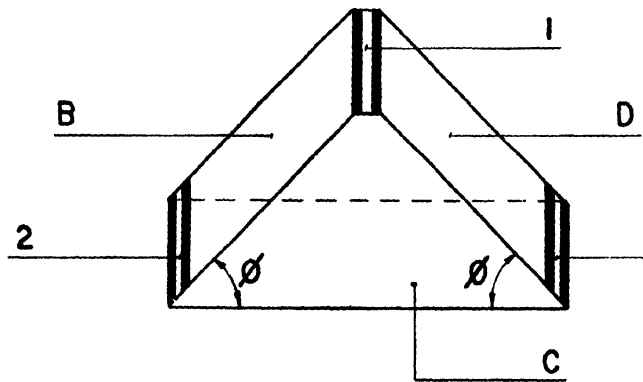


Figure 1b

identified from the pulse height of the output generated from the sensing elements as the widths of the three slits are different. This way wider angular field of views, covering a range of approx. $\pm 80^\circ$ can easily be achieved at no loss of any appreciable angular resolution.

The present system is equivalent to two conventional rectangular systems, this should result in considerable reduction in weight together with space economy and these are of utmost importance for space vehicles.

Acknowledgment

The author gratefully acknowledges the technical assistance of Shri K. C. Navada and grateful to Prof. U. R. Rao, Director, ISRO-Satellite centre, for the encouragement offered in bringing out this paper.

Electric and magnetic properties of potassium nickel periodate

(Miss) P Bose

Department of Magnetism, Indian Association for the Cultivation of Science,
Jadavpur, Calcutta 700032

Received 22 March 1979

A sample of polycrystalline potassium nickel periodate $[\text{KNiFO}_6]$ has been prepared by the Inorganic Chemistry Department of the Association in which nickel has been suggested by them, from their investigations, to exist in tetravalent form with trivalent nickel as substitutional impurity. As a consequence it may be expected that the sample would show appreciable electrical conductance (the situation being suitable for phonon assisted hopping of carriers) and interesting magnetic behaviour. The electric and magnetic properties of this sample have, therefore, been investigated within the temperature range 100°K to 300°K . The electrical measurements were performed with both pellets (obtained by pressure) and with powders pressed in a specially designed holder. The magnetic measurements were, however, made with powdered samples packed in sealed glass ampoules.

The electrical conductivity has been found to be of the order of 10^{-11} at 100°K and increasing to that of 10^{-7} at 300°K . The actual temperature variation of conductivity is shown in figure 1 where $\log \frac{1}{R} T$ has been plotted against T^{-1} (R is the resistance of the sample and T the temperature in degree Kelvin). It is observed therefrom that the resulting curve is a straight line from about 160°K to 300°K and below 160°K it deviates from linearity. The linear portion of the curve obviously then follows a relation of the type $\sigma = \frac{A}{T} e^{-q/kT}$ where σ is the electrical conductivity, q is the activation energy involved in hopping and contains both carrier activation energy and mobility activation energy, A , a constant and the rest of symbols have their usual significances. The value of q has been obtained to be ~ 0.1 e volt.

The material has been found to be appreciably paramagnetic and the temperature variation of its susceptibilities (χ) has been graphically represented in figure 1, where χ has been plotted against $1/T$. From 300°K downwards χ initially increases very feebly and thereafter at a faster rate following a linear relationship till $\sim 166^\circ\text{K}$ whereafter it decreases and ultimately attains a temperature independent value. The magnetic moment at 300°K has been obtained to be 1.25 Bohr magneton increasing to a value 1.8 Bohr magneton at $\sim 170^\circ\text{K}$

thereafter decreasing to 1.2 Bohr magneton at $\sim 90^\circ\text{K}$. The temperature variations of μ (magnetic moment) as well as of the product χT are shown in figure 2 where both μ and χT have been plotted against T .

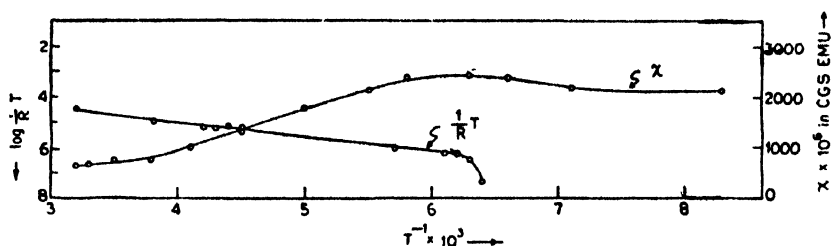


Figure 1. Temperature variations of conductivity ($1/R$) and magnetic susceptibility (χ).

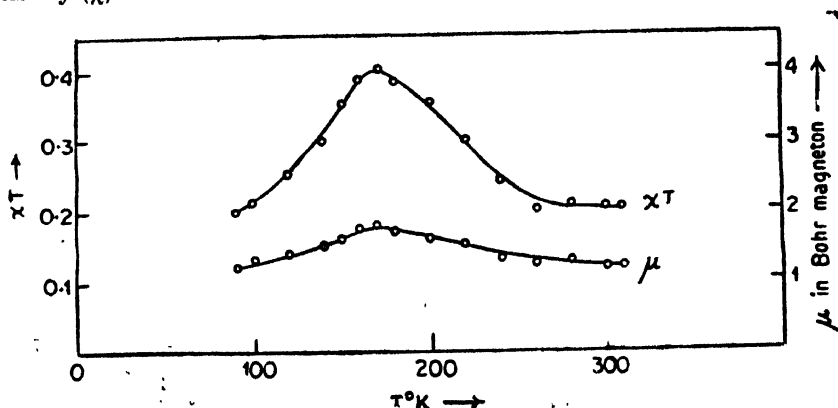


Figure 2. Temperature variation of :
i) magnetic moment (μ) in Bohr magneton, and
ii) χT (T , temperature in $^\circ\text{K}$).

It is obvious from above that while its electrical behaviour is understood in view of the existence of substitutional trivalent nickel impurity, the appreciable paramagnetism (especially its moment value) is not however very well understood. Further, it appears that there might be some sort of a change in the sample at low temperatures below about 160°K but the nature of this change is not understood. Therefore to clarify these points a thorough investigation of its various behaviours including magnetic, electric and dielectric combined with structural and spectroscopic studies have been undertaken and the results of these will be published in due course.

Acknowledgment

The author wishes to thank Dr. K. Nag of the Inorganic Chemistry Department for the kind presentation of the sample and for some useful discussion and to Sri A. K. Dutta for his kind interest in the work.

Monovacancy resistivity in noble metals

K N Khanna

Department of Physics, V. S. S. D. College, Kanpur

Received 2 May 1979, revised 18 June 1979

In a previous paper (Khanna 1978), the theoretical calculations of monovacancy resistivity have been carried out in alkali metals in the frame work of pseudopotential approach. The purpose of this paper is to extend the calculations for noble metals. The expression of monovacancy resistivity can be written as (Shyu *et al* 1971)

$$\rho_v = \frac{3\pi\Omega}{V_F^2 \hbar e^2} \langle |V(q)|^2 \rangle$$

where

$$\langle |V(q)|^2 \rangle = \frac{1}{4K_F^4} \int_0^{2K_F} |V(q)|^2 q^3 dq$$

where V_F is the fermi velocity and $V(q)$ is the screened pseudopotential matrix element. Thus a proper dielectric function for noble metals is needed. The noninteracting band scheme of Prakash and Joshi (1971) as modified by Singh and Prakash (1973) for dielectric function of d -band metal is applied in the computation. The model pseudopotentials of Upadhyaya *et al* (1976), Upadhyaya and Sharma (1977) and Hemkar and Kumar (1978) have been employed in the present calculations. Before presenting the calculated values of monovacancy resistivity let us consider the experimental work on the lattice vacancies in noble metals using various techniques. The most commonly accepted technique is the quenching method. Simmons and Balluffi (1963) have reported the following values of monovacancy resistivity in noble metals by using this method; $\rho_v = (1.5 \pm 0.3) \mu\Omega \text{ cm/at}\%$ (Cu), $\rho_v = (1.3 \pm 0.7) \mu\Omega \text{ cm/at}\%$ (Ag) and $\rho_v = (1.5 \pm 0.3) \mu\Omega \text{ cm/at}\%$ (Au). This process which combine equilibrium and quenching data, can be objected on the grounds of vacancy losses during quenching process. Siegel (1966) measured the electrical resistivity at 4.2°K of lattice vacancies in gold using combined resistivity measurements and transmission electron microscopy on quenched and annealed gold and obtained $\rho_v = (1.8 \pm 0.4) \mu\Omega \text{ cm/at}\%$. The same technique has been applied by Cotterill (1961) for gold ($\rho_v = 2.4 \pm 0.4 \mu\Omega \text{ cm/at}\%$) at 78°K. Furthermore, Ascoli *et al* (1970) reported the values of ρ_v which are four times higher than the results of Simmons and

Balluffi (1963). This strong discrepancy between equilibrium and quenching data was thought due to failure of Matthiessen's rule which holds between 4.2°K and 70°K. It is to be noted that Zett's *et al* (1969) did not find appreciable deviation from Matthiessen's rule in measuring the resistivities in quenched gold and platinum at 4.2°K and 303°K. However, the reason for this discrepancy is not fully understood at present.

By using the expression for monovacancy resistivity, the calculations were performed for various model potentials and the results are displayed in Table 1.

Table 1. Monovacancy resistivity of noble metals in the units of $\mu\Omega$ cm/at%

Metal	Experi- mental values	Theoretical values obtained by using the model potential of				
		Upadhyaya <i>et al</i>	Upadhyaya and Sharma	Hemkar and Kumar	Borchi and Gennaro	Moriarty
Cu	1.5 ± 0.3	1.09	1.44	—	3.21	3.20
Ag	1.3 ± 0.7	1.92	2.31	—	2.72	2.48
Au	$1.5 \pm 0.3(a)$ $1.8 \pm 0.4(b)$ $2.4 \pm 0.4(c)$	1.95	2.65	2.45	4.34	2.98

(a) Simmons and Balluffi

(b) Siegel

(c) Cotterill

Borchi and Gennaro (1970) have calculated the monovacancy resistivity for noble metals in pseudopotential formalism. They have not used the proper dielectric function. Their calculated values using Borchi and Gennaro (1970) potential and Moriarty model potential (1970) are also tabulated in table 1. They found a large discrepancy between the theoretical and experimental values. A perusal of table 1 shows that the present calculation gives ρ_v values more close to experiment than Borchi and Gennaro inspite of the fact that there is variation in available experimental results. A comparison in present theoretical values shows that for silver and gold, Upadhyaya *et al* model potential present a better agreement with Simmons and Balluffi and Siegel experimental values, for copper the better agreement is achieved for Upadhyaya and Sharma potential and the calculated value for gold using Hemkar and Kumar model potential shows a good agreement with Cotterill experimental value. The discrepancies between theory and experiment are not unexpected and arise from the neglected of lattice distortion and assumes the vacancy concentration is small so that one has essentially a collection of singly isolated vacancies.

Acknowledgment

The author is thankful to Prof. B. S. Bhargava, for providing departmental facilities and Swami Atmanandji for encouragement.

References

- Ascoli A, Guarini G and Queirolo G T 1970 *Crystal Lattice Defects* **1** 159
Borchi E and Gennaro S De 1970 *Letter Nuovo Cim.* **4** 365
Borchi E and Gennaro S De 1970 *Phys. Letter* **32A** 301
Cotterill R M J 1961 *Phil. Mag.* **6** 1351
Hemkar M P and Kumar M 1978 *Phys. Lett.* **65** 49
Khanna K N 1978 *Indian J. Phys.* **52A** 552
Moriarty J A 1970 *Phys. Rev.* **B1** 1363
Prakash S and Joshi S K 1971 *Phys. Rev.* **B4** 1770
Shyu W A, Gaspari G D, Wehling J H and Cords M 1971 *Phys. Rev.* **B4** 1802
Siegel R W 1966 *Phil. Mag.* **13** 359
Singh N and Prakash S 1973 *Phys. Rev.* **B8** 5532
Simmons R O and Balluffi R W 1963 *Phys. Rev.* **129** 1553
Upadhyaya J C, Kulshrestha O P and Gupta H C 1976 *Physica* **84B** 236
Upadhyay J C and Sharma O P 1977 *Solid State Comm.* **21** 149
Zetts J S, Gripshover J and Bass J 1969 *Phys. Lett.* **29A** 255

Indian J. Phys. **53A**, 641-643 (1979)

Surface layer effects on the spontaneous polarization of NH_4HSO_4

K Sambasiva Rao*, Rajendra P Nigam and Mrs A Bhanumathi

Microwave and Magnetic Resonance Laboratories,

Physics Department, Andhra University, Waltair

Received 10 July 1979

The surface layer effects on the spontaneous polarization can be studied by measuring the polarization of the compressed powders with different particle sizes. The compound ammonium bisulphate (NH_4HSO_4) was confirmed as a ferroelectric below -30°C and also found that the compound has got a defective

* Present address : Department of Physics, Andhra University Post Graduate Courses, Nuzvid-521201, A.P.

surface layer of thickness $40\mu\text{m}$ and its dielectric constant as 10 by the dielectric measurements at 1 MHz in the polycrystalline form (Sambasiva Rao and Bhanumathi 1978).

The spontaneous polarization and coercive field in the compound ammonium bisulphate in the single crystal form are measured (Pepinsky *et al* 1958) and the maximum values are estimated to be 0.8×10^{-6} coulomb/cm² and 1100 V/cm respectively. Also they found that the values of spontaneous polarization and coercive field are zero at -3°C and 119°C .

Hysteresis loops of the compressed powders of ammonium bisulphate were studied by using the ferroelectric loop tracer based on the compensation grounded sample scheme (Schubring *et al* 1964) in this laboratory. The measurements were made from -130°C to 0°C for powders with particle sizes in the range $105\text{--}710\mu\text{m}$. The samples used for the measurements of polarization are of the density 86% to that of a normal single crystal.

The variation of experimental values of the spontaneous polarization with temperature for five compressed powders of the particle size ranges $500\text{--}710\mu\text{m}$, $350\text{--}500\mu\text{m}$, $210\text{--}350\mu\text{m}$, $177\text{--}210\mu\text{m}$, and $105\text{--}177\mu\text{m}$, are shown in figure 1. The maximum value of coercive field is 1600 V/cm, the value is much higher than that of single crystal (Pepinsky *et al* 1958). It is clear from the figure that there are two transition temperatures in the compound, one at -3°C and the other is at -119°C , as observed in the single crystal measurement of ammonium bisulphate. The variation of the spontaneous polarization with temperature in the compressed powders is similar to that of a single crystal except at the second transition -119°C . At this temperature the decrease in spontaneous polarization is not so sharp in the single crystal. Also, the spontaneous polarization decreases with decreasing particle sizes similar to the particle size dependence on the dielectric constant (Sambasiva Rao and Bhanumathi 1978). Further, the broad peaks in powders and increase in broadening with the decrease in particle size may be noticed from the figure 1. The broadening may be caused by the difference in the properties of the surface and the bulk. It can be noticed from the figure that the compound (NH_4HSO_4) is ferroelectric in the temperature range -3°C and -119°C . The maximum value of the spontaneous polarization for the biggest particle size range ($500\text{--}710\mu\text{m}$) is about 1/30th of the single crystal value. For the smallest particle size range ($105\text{--}177\mu\text{m}$) the maximum value of the spontaneous polarization is about 1/48th of the single crystal value. The lowering of spontaneous polarization in powders as compared to single crystal may be attributed to the formation of a defective surface layer, which is due to the mechanical discontinuity in the periodic lattice. According to (Goswami 1969) this gives lower values of the dielectric constant and spontaneous

polarization at the surface than in the bulk resulting in the decrease of the dielectric constant and spontaneous polarization with decrease in particle size.

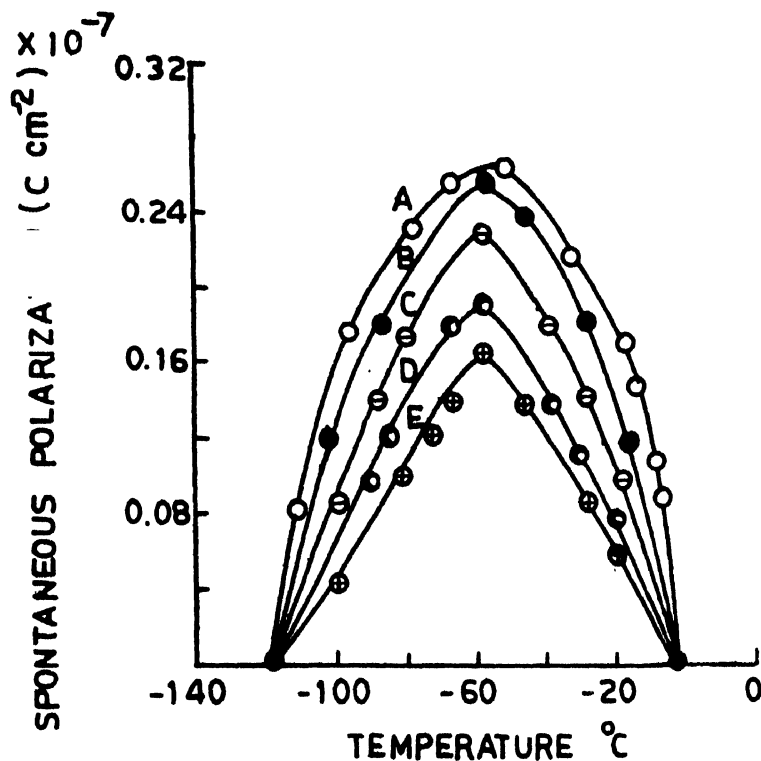


Figure 1. Spontaneous polarization as a function of temperature for five compressed powders of $(\text{NH}_4\text{HSO}_4)$. A. 500–710 μm ; B. 350–500 μm ; C. 210–350 μm ; D. 177–210 μm ; E. 105–177 μm .

Acknowledgment

One of the authors (K.S.Rao) wishes to thank U.G.C., New Delhi, for the financial help.

References

- Goswami A K 1969 *J. Appl. Phys.* **40** 619
- Pepinsky R *et al* 1958 *Phys. Rev.* **111** 1508
- Sambasiva Rao K and Bhanumathi A 1978 *Ind. J. Pure Appl. Phys.* (in press)
- Schubring N W *et al* 1968 *Rev. Sci. Instr.* **35** 1577

Comments on the microscopic theory of ferroelectric phase transition with transverse Ising model*

Suvra Ganguli and Bijay K Chaudhuri

Magnetism Department, Indian Association for the Cultivation of Science,
Calcutta-700032

Received 1 December 1978, revised 7 February 1979

KH_2PO_4 (KDP) and other isomorphous hydrogen bonded ferroelectrics have been extensively studied with a transverse Ising model (Bline and Zeks 1972). A microscopic treatment to consider the coupling between proton motion and the optic mode (OM) of the lattice was given by Kobayashi (1968). Brout *et al* (1966), however, showed that even the pure tunneling model (the transverse Ising model) gives rise to the soft-mode behaviour which was first theoretically put forward by Cochran (1960) and Anderson (1960). Brout *et al* (1966) and later Bline and Zeks (1972) (abbreviated as BBZ), however, used semiclassical equation of motion method to calculate the ferroelectric properties of KDP type crystals.

The purpose of this note is to show that the thermodynamic Green's function method which seems to be simpler than the procedure of BBZ using the Bloch equation gives rise to the same result as those of BBZ differing only by a factor $S(S+1)$. This controversy arises due to the use of quantum condition that the eigen value of S^2 is $S(S+1)$ while in the calculations of BBZ which is a semiclassical treatment such factor did not appear in the final results. Our calculated results obtained by RPA type decoupling of the Green's function should therefore be divided by $S(S+1)$ to make them equivalent to those of BBZ. It has also been shown that the simple RPA-type decoupling of the complex Green's function exhibits the most salient feature (the soft-mode behaviour) of ferroelectric transition in KDP type crystals.

The pseudospin Hamiltonian describing the ferroelectric characteristics in KDP family in presence of an external electric field \mathbf{E} has the form (for details see BBZ)

$$H = -2\Omega \sum_i S_i^x - \mu \mathbf{E} \cdot \sum_i \mathbf{S}_i - \sum_{ij} J_{ij} S_i^z S_j^z \quad (1)$$

where the parameters have the usual significances (BBZ).

* Content of this paper was accepted for presentation at the NPSP Symposium (1974) organized by DAE. Abstract No. SHA3 by (BKC).

We shall start with pseudo-spin Green's function (PGF) like $\ll S_i^m(t) | S_j^n(t') \gg$ defined by (Zubarev 1960)

$$\begin{aligned} \ll S_i^m(t) | S_j^n(t') \gg &= i\theta(t-t') \langle [S_i^m(t) - S_j^n(t')] \rangle \\ &+ i\langle S_i^m(t-t') \rangle \end{aligned} \quad (2)$$

where S_i^m are the m component of the pseudo spin \mathbf{S} ($m, n = x, y, z, \dots$), $\langle \dots \rangle$ denotes the statistical average of the enclosed product. The Fourier transform of the PGF satisfies the equation of motion viz.,

$$\omega \langle S_i^m | S_j^n \rangle = \frac{1}{2\pi} \langle [S_i^m, S_j^n] \rangle + K^{mn}(i, j, \omega) \quad (3)$$

where $K^{mn}(i, j, \omega)$ is the complex PGF viz.,

$$K^{mn}(i, j, \omega) = \ll [S_i^m, H] | S_j^n \gg \quad (4)$$

Using Bogolyubov-Tyablikov (1959) decoupling like

$$\ll AB | C \gg = A \ll B | C \gg$$

the nine equations of motion can be written as

$$\xi^{mn} G^{mn} = \eta^{mn} \quad (5)$$

where ξ^{mn} is a (9 × 9) matrix, η^{mn} and G^{mn} are column matrices

$$\xi^{mn} = \begin{pmatrix} \tau & 0 & 0 \\ 0 & \tau & 0 \\ 0 & 0 & \tau \end{pmatrix} \quad (5a)$$

where

$$\tau = \begin{pmatrix} \omega & -i\pi & 0 \\ i\pi & \omega & -i\theta \\ 0 & i\theta & \omega \end{pmatrix} \quad (5b)$$

Solution of τ gives the eigenfrequencies (energy spectrum with RPA)

$$\omega_1 = 0, \omega_{\pm}^2 = \pi^2 \pm \theta^2 \quad (6)$$

where

$$\begin{aligned} \pi &= \mu \mathbf{E} + \frac{1}{2} \langle J' \cdot S^z \rangle \\ \theta &= 2\Omega, J' = \sum_j J_{ij} \\ \langle S^z \rangle &= \langle S_i^z \rangle = \langle S_i^z \rangle \end{aligned} \quad (7)$$

Using Spectral theorem (Zubarev 1960) and the identity

$$\sum_{m=x'z'y} \langle (S^m)^2 \rangle = S(S+1)$$

we obtain

$$\langle S^z \rangle = \frac{\pi S(S+1)}{(\pi^2 + \theta^2)^{\frac{1}{2}}} \tanh \frac{\beta}{2} (\pi^2 + \theta^2)^{\frac{1}{2}} \quad (8)$$

and

$$\langle S^x \rangle = \frac{2\Omega S(S+1)}{(\pi^2 + \theta^2)^{\frac{1}{2}}} \tanh \frac{\beta}{2} (\pi^2 + \theta^2)^{\frac{1}{2}}. \quad (9)$$

These are the standard equations for studying ferroelectric behaviours obtained earlier by BBZ and Tokunaga and Matsubara (1966), but contains a multiplying factor $S(S+1)$ as mentioned earlier. To make our results identical to those of the earlier authors we define polarization by $\langle S^z \rangle / S(S+1)$ in our proceeding calculations. The energy spectrum shown in (6), however, do not show the soft mode behaviour. That is ω_+ does not freeze at T_c .

The microscopic behaviour of the ferroelectric phase transition in KDP as shown by Brout *et al* (1966) becomes clear if we consider fluctuations around the above mean field result which could be made by transforming the spin as

$$S_1^m(\mathbf{q}) = \sum_i S_1^m \exp i\mathbf{q} \cdot \mathbf{R}_i$$

and using the following decoupling viz.,

$$\ll AB|C \gg = \langle A \rangle \ll B|C \gg + \langle B \rangle \ll A|C \gg$$

The equation (5b) now transforms as

$$\tau(\mathbf{q}) = \begin{pmatrix} \omega & -i\pi & 0 \\ i\pi & \omega & i\Phi - i\theta \\ 0 & i\theta & \omega \end{pmatrix} \quad (10)$$

Equation (10) gives the eigen frequencies (energy spectrum) viz.,

$$\omega_{\pm}^2(\mathbf{q}) = (2\Omega)^2 + (\frac{1}{2}J' \langle S^z \rangle + \mu\mathbf{E})^2 - 2\Omega J(\mathbf{q}^2) \langle S^x \rangle \quad (11)$$

where

$$\Phi = J(\mathbf{q}) \langle S^x \rangle$$

$$J(\mathbf{q}) = \sum_{\mathbf{k}} J' e i\mathbf{q} \cdot (\mathbf{R}_l - \mathbf{R}_k).$$

In the limit $q \rightarrow 0$ one obtains the Cochran's mode instability for $T > T_c$.

$$\begin{aligned}\omega_{+,-}^2(0) &= 4\Omega^2 - 2\Omega J' < S^z > \\ &= 4\Omega^2 - 2\Omega J' \tanh \beta\Omega\end{aligned}$$

T_c is the transition temperature. For $T \rightarrow T_c$ we have $\omega_{+,-}^2(0) \sim (T - T_c)$. Calculating susceptibility from the Green's function $G^{zz}(q)$ and expanding around T_c we get divergence in the susceptibility viz., $\chi\alpha(T - T_c)^{-1}$. Plots of $< S^z >$, $< S^x >$ and $\omega_{+,-}(q)$ as a function of q give evidently the singularity at T_c as was shown elaborately by Cochran (1969) from lattice dynamical calculations.

Thus we see that simple RPA decoupling of the complex Green's functions are equivalent to the calculations of BBZ and are sufficient to describe the microscopic behaviour of phase transition in KDP even with pure tunneling model. Consideration of pseudo-spin lattice interaction is found to slightly modify the theoretical expressions of the eigen frequencies (Bline and Zeks 1972) by increasing the exchange constant. But the overall behaviour remains approximately the same. Further, consideration of higher order Green's function in our calculation does not improve the results and in this case expressions (8-9) also become complicated and different from those of BBZ. However, this method of our calculations may also be extended to explain the phase transition in the case of rochelle salt, PbHPO_4 , $\text{NH}_4\text{H}_2\text{PO}_4$ and in similar other crystals where two sublattice Ising model and asymmetric double well potential are used. All these results will be shown elsewhere.

References

- Anderson P W 1960 *Fizika Dielektrikov* (G I Skanovi edited) *Akad. Nauk SSSR Moscow*
 Blinc R and Zeks B 1972 *Adv. Phys.* **21** 693
 Bogolyubov N N and Tyablikov S V 1959 *Sov. Phys. Dokl.* **4** 604
 Brout R, Muller K A and Thomas II 1966 *Solid St. Commun.* **4** 507
 Cochran W 1960 *Adv. Phys.* **9** 387
 Cochran W 1969 *Adv. Phys.* **18** 157
 Kobayashi K K 1968 *J. Phys. Soc. Jpn.* **24** 497
 Tokunaga M and Matsubara T 1966 *Prog. Theo. Phys.* **35** 581
 Zubarev D N 1960 *Sov. Phys. Uspekhi* **3** 320

Structure of a sulfonamide drug-sulfisoxazole

Chandana Chatterjee, J K Dattagupta and N N Saha

Crystallography and Molecular Biology Division,
Saha Institute of Nuclear Physics, Calcutta-700009

Received 22 May 1979

The sulfonamides have still a significant role in the treatment of certain infections in spite of the wide use of antibiotics. Early pharmacological studies (Schnitzer *et al* 1946) of sulfisoxazole established that it was a rapidly absorbed and rapidly excreted sulfonamide with antibacterial activity equal to that of sulfadiazine. When a rapidly acting sulfonamide is indicated, sulfisoxazole is the one which is preferred over other sulfonamides (Weinstein 1966). In this communication, the results of our preliminary study of the crystal and molecule structure of sulfisoxazole are being reported. The ultimate object of this study is to understand the relationship between the structural features and pharmacological activities.

Single crystals of sulfisoxazole were obtained by slow evaporation of a solution of the compound in a mixture of water and alcohol at room temperature. The crystals were needle-shaped, the needle axis being parallel to *c*-axis. A crystal of dimensions $0.81 \times 0.13 \times 0.38$ mm was used and the unit cell dimensions were obtained from Weissenberg, oscillation and rotation photographs taken about *a*- and *c*-axes, using CuK_α radiation. The crystal data are given in Table 1.

Table 1. Crystal Data

$\text{C}_{11}\text{H}_{13}\text{N}_3\text{O}_3\text{S}$		
Molecular weight = 267.3	$a = 14.88 \text{ \AA}$	$\mu(\text{CuK}_\alpha) = 22.8 \text{ cm}^{-1}$
Orthorhombic	$b = 14.24 \text{ \AA}$	$\rho_{\text{obs}} = 1.40 \text{ gm/cc}$
Space group : Pbc _a	$c = 11.31 \text{ \AA}$	$\rho_{\text{calc}} = 1.48 \text{ gm/cc}$
$\lambda(\text{CuK}_\alpha) = 1.5418 \text{ \AA}$	$z = 8$	
Systematic absences :		
0 <i>kl</i> absent for <i>k</i> odd		
<i>hk</i> 0 absent for <i>h</i> odd		
<i>h</i> 0 <i>l</i> absent for <i>l</i> odd		

Three-dimensional intensity data were collected for layers *hk*0 to *hk*8 and 0*kl* using multiple-film equi-inclination technique. The intensities of 1357

spots were estimated visually and were corrected for spot shape and Lorentz and polarization factors. The intensity data from different layers were brought to the same scale by cross layer correlation method. The positions of the sulphur atoms in the unit cell were located from a three-dimensional Patterson synthesis. A 3-D Fourier synthesis computed with phases of the sulphur atoms revealed all the non-hydrogen atoms of the molecule. Refinement was carried out by the full-matrix least squares method using isotropic temperature factors.

Two cycles of refinement brought the discrepancy factor $R = \frac{\sum |F_o| - |F_c|}{\sum |F_o|}$ down to 0.22. Temperature factor of the oxygen atom O(1) was relatively high at this stage and a new peak for O(1) was chosen from the Fourier map which was more satisfactory from stereochemical consideration. After two cycles of further refinement R -value came down to 0.119. Atomic parameters and the intramolecular bond lengths and angles are given in Table 2 and 3 respectively. The atomic numbering scheme of sulfisoxazole molecule is shown in figure 2.

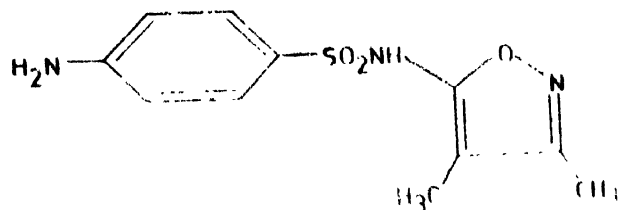


Figure 1. Sulfisoxazole molecule

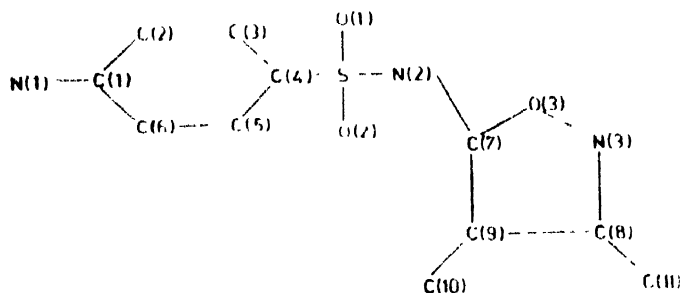


Figure 2. The atomic numbering scheme of sulfisoxazole

The two rings in the sulfisoxazole molecule are almost planar and the molecules are linked together by $\text{NH} \dots \text{N}$ and $\text{NH} \dots \text{OS}$ hydrogen bonds. 3-D packing of the molecules viewed down c -axis is shown in figure 3. Further refinement is in progress and a detailed paper will be published in due course.

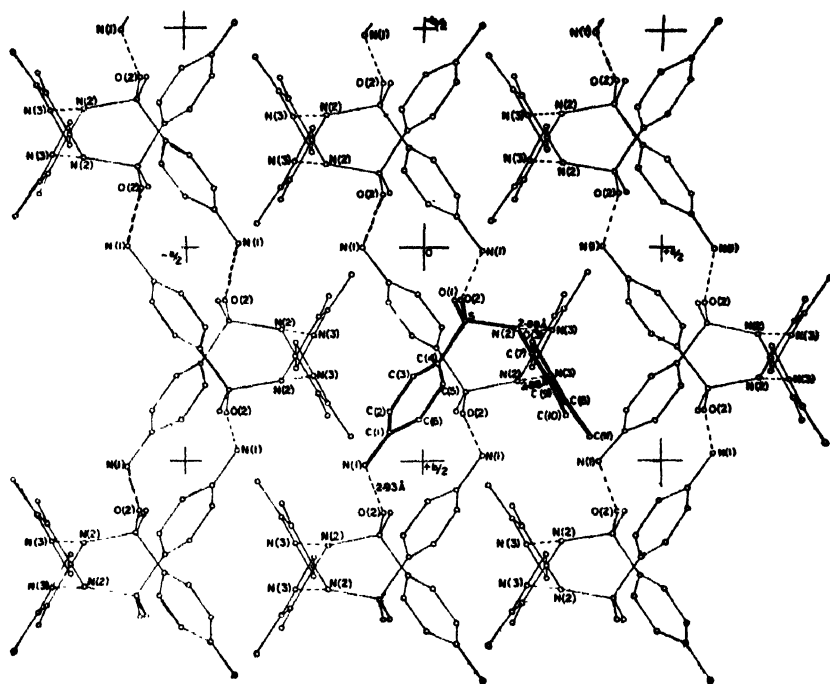


Figure 3. Projection of crystal structure down c .

Table 2. Fractional atomic co-ordinates together with the isotropic temperature factors

	x	y	z	$B(\text{\AA}^2)$
N(1)	-0.1191	0.5111	0.1084	5.0
C(1)	-0.0678	0.4291	0.1000	3.6
C(2)	-0.0100	0.4027	0.1905	3.6
C(3)	0.0374	0.3228	0.1816	3.6
C(4)	0.0315	0.2689	0.0806	2.6
C(5)	-0.0183	0.2965	-0.0116	4.0
C(6)	-0.0691	0.3800	-0.0027	4.4
S	0.0919	0.1654	0.0708	3.2
O(1)	0.0689	0.1227	-0.0362	4.5
O(2)	0.0833	0.1164	0.1793	4.8
N(2)	0.2013	0.1928	0.0690	3.2
C(7)	0.2339	0.2534	-0.0146	2.8
O(3)	0.2265	0.2239	-0.1265	3.8
N(3)	0.2674	0.2950	-0.1962	4.1
C(8)	0.2988	0.3566	-0.1258	3.4
C(9)	0.2766	0.3375	-0.0081	3.2
C(10)	0.3001	0.3935	0.0986	4.8
C(11)	0.3465	0.4387	-0.1692	4.7

Table 3. Intramolecular bond distances (Å) and bond angles (degrees)

N(1)-C(1)	1.40	N(1)-C(1)-C(2)	120.9
C(1)-C(2)	1.39	N(1)-C(1)-C(6)	118.8
C(2)-C(3)	1.34	C(6)-C(1)-C(2)	120.1
C(3)-C(4)	1.38	C(1)-C(2)-C(3)	119.9
C(4)-C(5)	1.34	C(2)-C(3)-C(4)	120.1
C(5)-C(6)	1.41	C(3)-C(4)-C(5)	121.1
C(6)-C(1)	1.36	C(4)-C(5)-C(6)	119.2
C(4)-S	1.73	C(5)-C(6)-C(1)	119.2
S-O(1)	1.40	C(3)-C(4)-S	119.7
S-O(2)	1.42	C(5)-C(4)-S	119.2
S-N(2)	1.67	C(4)-S-O(1)	107.4
N(2)-C(7)	1.37	C(4)-S-O(2)	108.5
C(7)-O(3)	1.34	O(1)-S-N(2)	109.3
O(3)-N(3)	1.42	O(2)-S-N(2)	102.3
N(3)-C(8)	1.27	O(1)-S-O(2)	120.9
C(8)-C(9)	1.40	N(2)-S-C(4)	107.9
C(8)-C(11)	1.45	S-N(2)-C(7)	120.0
C(9)-C(7)	1.36	N(2)-C(7)-O(3)	115.3
C(9)-C(10)	1.49	N(2)-C(7)-C(9)	133.2
		C(7)-O(3)-N(3)	105.5
		O(3)-N(3)-C(8)	107.5
		N(3)-C(8)-C(9)	112.0
		N(3)-C(8)-C(11)	121.5
		C(11)-C(8)-C(9)	126.4
		C(8)-C(9)-C(7)	103.4
		C(8)-C(9)-C(10)	127.8
		C(10)-C(9)-C(7)	128.7
		C(9)-C(7)-O(3)	111.5

Computations were carried out on the Burroughs B6700 computer using mainly the modified version of "X-ray arc" system for crystallography compiled by B. L. Vickory, D. Bright and P. R. Mallison of Agricultural Research Council University College of London.

Acknowledgment

The authors are thankful to Dr. (Mrs.) A. Podder and Dr. S. C. Bhattacharyya of the same laboratory for many helpful discussions.

References

- Schnitzer R J, Foster R H K, Ercoli N, Soo-Hoo G, Mangieri C N and Roe M D 1946 *J. Pharmac. exp. Ther.* **88** 47
 Weinstein L 1966 *The Pharmacological Basis of Therapeutics*, Ed. Goodman L S and Gilman A (The Macmillan Company, New York).

Crystal structure of phenylpropanolamine hydrochloride

A Podder, J K Dattagupta and N N Saha

Crystallography and Molecular Biology Division,
Saha Institute of Nuclear Physics,
92, Acharya Prafulla Chandra Road, Calcutta-700009

Received 5 June 1979

Phenylpropanolamine hydrochloride (propadrine) is a sympathomimetic drug. Barger and Dale (1910) synthesized a series of compounds having in common the phenethylamine grouping and with substituents at the α - or β -carbon atoms as well as in the benzene ring (Figure 1). Many of these amines mimicked the effect of stimulating the sympathetic nervous system and were termed as sympathomimetic amines (McLean 1960). Phenylpropanolamine hydrochloride is obtained by substitution of OH and CH_3 groups at α - and β -carbon atoms respectively. This drug molecule is also widely used for the treatment of nasal and sinus congestion, usually in combination with an antihistaminic drug.

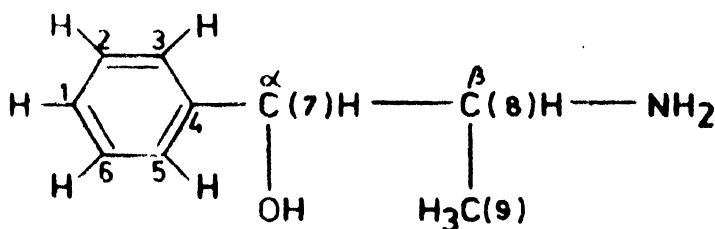


Figure 1. Phenylpropanolamine molecule with atomic numbering scheme.

The single crystals of phenylpropanolamine hydrochloride were obtained by slow evaporation of an aqueous solution of the compound at room temperature. Preliminary unit cell dimensions and systematic absences were determined from Weissenberg photographs while accurate cell parameters were obtained from diffractometer measurements. Crystal data is given in Table 1.

The observed systematic absences indicated that the possible space groups are $P2_1$ (non-centrosymmetric) and $P2_1/m$ (centrosymmetric). The statistical results of $\langle |E|^2 - 1 \rangle$, $\langle |E| \rangle$, and the $N(Z)$ distribution (Howells, Phillips and Rogers 1950) indicated that the space group is $P2_1$ with two molecules of phenylpropanolamine hydrochloride per asymmetric unit. The intensity data were collected on an automatic Stoe four-circle diffractometer using Ni-filtered CuK_α radiation and altogether 1658 reflections were measured in the $\theta/2\theta$ scanning mode.

Table 1. Crystal Data

*Phenylpropanolamine hydrochloride*Molecular Formula : $C_9H_{14}ClNO$

Mol. wt. : 187.7

 $a = 7.448 \text{ \AA}$ $b = 9.461 \text{ \AA}$ $c = 14.595 \text{ \AA}$ $\beta = 103.4^\circ$ *Monoclinic*Space group $P2_1$ $\rho_{calc} = 1.24 \text{ g.cm}^{-3}$ $\rho_{obs} = 1.25 \text{ g.cm}^{-3}$ $Z = 4$

The structure was determined by the heavy-atom method. The positions of the two chlorine atoms in the asymmetric unit were obtained from a three-dimensional Patterson synthesis and the remaining twenty two non-hydrogen atoms were derived from successive Fourier synthesis. The atomic parameters were refined by full-matrix least-squares method using isotropic temperature factors. The final R index was 12.3%. The positional and thermal parameters and the bond lengths and bond angles are given in Tables 2 and 3 respectively. The numbering scheme used is shown in figure 1. The crystal structure projected along b -axis is shown in Figure 2. Bond distances C(7)–C(8) and C(8)–C(9) in molecule B are rather long and are expected to improve with further refinement. The structure is stabilised by van der Waals forces and a network of hydrogen bonds where infinite chains of the molecules are connected via the chloride ions. One of the molecules in the asymmetric unit (Molecule B) has a maximally extended side chain but the other molecule has no such characteristic. The detailed paper after further refinement with anisotropic temperature factors will be published in due course. Computations were carried out on Burroughs B6700 computer using mainly the modified version of "X-ray are" program

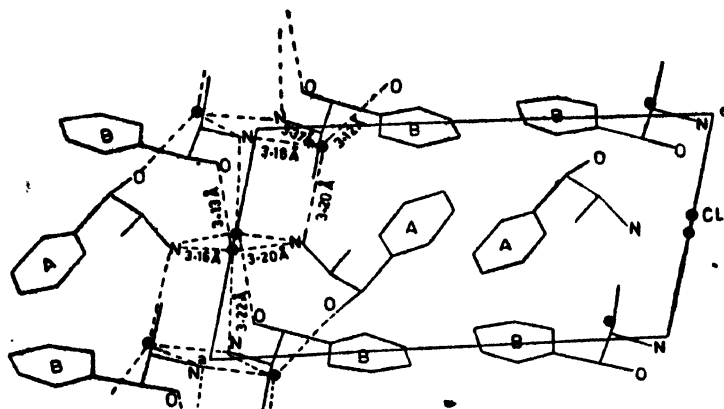


Figure 2. The crystal structure projected along y . Solid circles denote chloride ions.

system compiled by B. L. Vickery, D. Bright and P. R. Mallinson of Agricultural Research Council, University College, London.

Table 2. Fractional atomic co-ordinates together with isotropic temperature factors

Atom	Molecule A				Molecule B			
	<i>x</i>	<i>y</i>	<i>z</i>	<i>B</i> (Å ²)	<i>x</i>	<i>y</i>	<i>z</i>	<i>B</i> (Å ²)
CL	0.0883	0.7106	0.1491	3.2	0.5319	0.4959	0.0054	3.4
O	-0.1892	-0.4052	0.2608	4.2	-0.1396	0.1228	0.0754	3.4
N	-0.4872	-0.2476	0.1456	3.2	-0.0421	0.4066	0.0329	3.1
C(1)	0.3104	-0.4639	0.4334	4.9	0.0761	0.0692	0.4315	4.5
C(2)	0.3537	0.4553	0.3551	4.5	0.1024	-0.0137	0.3509	4.2
C(3)	-0.5035	-0.4853	0.3168	3.6	0.0417	0.3085	0.2594	3.6
C(4)	-0.4162	-0.3564	0.3474	3.1	-0.0481	0.1719	0.2457	2.9
C(5)	-0.4621	-0.2786	0.4245	4.2	-0.0808	0.2498	0.3227	3.4
C(6)	0.3965	-0.3420	0.4656	4.8	-0.0135	0.1979	0.4122	4.3
C(7)	-0.2707	-0.2875	0.3033	3.5	-0.1150	0.2309	0.1464	3.2
C(8)	-0.3482	-0.1842	0.2234	3.0	0.0344	0.3414	0.1256	3.1
C(9)	0.5604	-0.0503	0.2566	4.2	0.2258	0.2673	0.1237	3.9

Table 3. Intramolecular bond lengths (Å) and angles (degrees)

	Mol. A	Mol. B		Mol. A	Mol. B
O—C(7)	1.47	1.44	O—C(7)—C(4)	105.0	112.6
N—C(8)	1.48	1.48	O—C(7)—C(8)	106.3	107.3
C(1)—C(2)	1.47	1.47	N—C(8)—C(7)	113.6	108.0
C(2)—C(3)	1.43	1.40	N—C(8)—C(9)	106.8	109.0
C(3)—C(4)	1.41	1.42	C(4)—C(7)—C(8)	114.5	109.3
C(4)—C(5)	1.45	1.41	C(7)—C(8)—C(9)	113.3	112.2
C(5)—C(6)	1.46	1.38	C(3)—C(4)—C(7)	123.8	119.9
C(6)—C(1)	1.35	1.39	C(5)—C(4)—C(7)	115.4	119.2
C(4)—C(7)	1.53	1.52	C(3)—C(4)—C(5)	120.8	120.9
C(7)—C(8)	1.53	1.60	C(1)—C(2)—C(3)	114.7	120.4
C(8)—C(9)	1.57	1.59	C(2)—C(3)—C(4)	123.3	119.0
			C(4)—C(5)—C(6)	115.7	118.5
			C(5)—C(6)—C(1)	122.6	123.9
			C(6)—C(1)—C(2)	122.8	117.0

References

- Barger G and Dale H H 1910 *J. Physiol.* **41** 19
 Howells E R, Phillips D C and Rogers D 1950 *Acta Cryst.* **3** 210
 McLean R A 1960 *Medicinal Chemistry* pp 593, ed. A Burger, New York, Interscience Publishers

K-conversion coefficients of some transitions in the ^{152}Eu decay

K Venkata Ramaniah, A Ramanjaneyulu and K Venkata Reddy

Laboratories for Nuclear Research, Andhra University, Waltair 530003

Received 14 March 1979

The internal conversion electron spectrum of the 12.4 year ^{152}Eu has been studied for internal conversion coefficients of a few strong gamma transitions. The ^{152}Eu source was obtained as EuCl_3 in HCl solution from Atomic Energy Establishment, Harwell, England, made of enriched ^{151}Eu sample by neutron irradiation. Sources of 2 mm diameter on mylar foils of thickness $180 \mu\text{g}/\text{cm}^2$ are used for the conversion electron studies employing an intermediate-image beta ray spectrometer of the Siegbahn-Slatis type in its best performance conditions. K -conversion lines of the intense gamma transitions only are scanned. Initially the spectrometer was calibrated using standard conversion line energies. The exact conversion electron energies have been determined using the calibration. The intensities of the conversion lines are obtained from the area measurements. The conversion electron spectrum was scanned with different sources to obtain accurate data on electron line intensities.

The gamma-ray relative intensities due to Riedinger *et al* (1970) have been employed in determining the K -conversion coefficients. The gamma-ray and electron intensities have been normalised to the 344 keV transition. The theoretical α_K (E2) value for the 344 keV (0.031) from Hager and Seltzer (1968) tables has been used in calculating the α_K values of the remaining transitions. The conversion line intensities are listed in table 1 along with the values of Malmsten

Table 1. Conversion line intensities of some transitions in the decay of ^{152}Eu

Energy (keV)	Malmsten <i>et al</i> (1966)	Present work
244.7	53.0 (20)	73.60 (14)
344.2	72.0	100.00
443.9	1.2 (1)	1.666 (21)
778.8	1.9 (2)	2.866 (28)
867.3	1.0 (1)	1.333 (19)
964.0	2.9 (2)	4.066 (33)
1085.8	1.7 (2)	2.413 (25)
1112.8	2.0 (2)	2.860 (28)
1409.0	0.82 (6)	1.133 (20)

et al (1966). In table 2 the experimental values of Riedinger *et al* (1970) and Dzhelepov *et al* (1966) along with the present results are given and also the

Table 2. Experimental and theoretical *K*-conversion coefficients of some transitions in the decay of ^{152}Eu

Energy (keV)	Riedinger <i>et al</i> (1970)	Dzhelepov <i>et al</i> (1966)	Present work	Hager and Seltzer (1968)
244.7	0.080 (5)	0.088 (9)	0.0809 (34)	0.0798 (E2)
344.2	0.030	0.0308	0.031 (Th)	0.031 (E2)
443.9	0.0045 (4)	0.0055 (4)	0.0050 (3)	0.0049 (E1)
778.8	0.0017 (2)	0.0019 (1)	0.00191 (9)	0.0016 (E1)
867.3	0.0030 (3)	0.0029 (5)	0.00275 (13)	0.0029 (E2)
964.0	0.0023 (2)	0.0026 (1)	0.0024 (1)	0.0023 (E2)
1085.8	0.0026 (9)	0.0018 (3)	0.0020 (1)	0.0018 (E2)
1112.8	0.0017 (2)	0.0019 (1)	0.00179 (9)	0.0017 (E2)
1408.0	0.00046 (4)	0.00055 (3)	0.00045 (2)	0.00052 (E1)

experimental conversion coefficients are compared with the theoretical values calculated by Hager and Seltzer. The assigned multipolarities are given in the paranthesis.

References

- Dzhelepov B S, Zhukovskii N N and Maloyan A G 1966 *Bull. Acad. USSR Phys. Ser.* **30** 1322
 Hager R S and Seltzer E E 1968 *Nuclear Data A4*
 Malmsten G, Nilsson O and Andersson I 1966 *Arkiv. Fysik.* **33** 361
 Riedinger L L, Johnson N R and Hamilton J H 1970 *Phys. Rev.* **C2** 2358

**SOLAR ENERGY SOCIETY OF INDIA—
EASTERN REGIONAL CHAPTER**

**One Day Seminar On
SOLAR PHOTO CONVERSION DEVICES AND
THEIR APPLICATIONS**

Our present day energy needs are primarily met by fossil fuels. But increasingly higher demands of energy is likely to exhaust these within a few decades. Thus worldwide search for alternate and nonconventional sources of energy has begun. Photoconversion of Solar Energy constitutes a major thrust in this direction. The purpose of this Conference is to review the result of researches that are in progress on this topic in India. Moreover, the Seminar is intended to provide a platform where investigators can discuss their problems and new ideas and explore the possibilities of adopting measures for mutual co-operation on a long term basis.

The emphasis of the Conference will be on the following aspects :

- (a) Silicon, CdS/Cu₂S and thin film solar cells
- (b) Photo-electrochemical and photo-galvanic devices
- (c) Other types of solar cells
- (d) Storage and systems

The seminar will be held on the 29th November, Saturday, 1980 at Jadavpur University.

Registration fee for non-members, members and students are Rs. 25/-, 20/- and 10/- respectively.

Interested persons are cordially invited to attend the seminar.

For further information please contact

Prof. M. K. Mukherjee, Secretary
Dept. of Electronics & Tele-communication Engineering
Jadavpur University
Calcutta 700 032.

Angular dependence of polarization of the radiation following photoionization and photodissociation

Javed Husain

Department of Physics, Columbia University, New York, N.Y. 10027, U.S.A.

Received 12 June 1978, revised 6 December 1978

The measurement of the polarization of the light emitted by an aligned or oriented system provides useful information about its density matrix elements (e.g. Fofilov 1964, Case *et al* 1978). It is also well-known that the spatial distribution of the electrons in photoionization (Cooper and Zare 1969) and photofragments in photodissociation (Simons 1977) is asymmetric. Since spatial asymmetry and alignment or orientation are both intimately connected through the principle of angular momentum conservation, Caldwell and Zare (1977) recently demonstrated that the ions formed in photoionization are aligned. In an experiment involving the photoionization of Cd atoms by He II radiation they found ~ 5 and 10% polarizations in two transitions of Cd⁺. In 1968, Van Brunt and Zare pointed out that in some cases the fluorescence from photofragments is likely to be polarized. This has been observed to be true for the CN (Chamberlain and Simons 1975) and OH (Macpherson and Simons 1977) radicals. Most recently Grader *et al* (1977) have found that the emission of *Ll* transition radiation from the photoion of uranium is asymmetric, with the asymmetry being $\sim 6\%$. The observation of these effects leads us to the conclusion that the polarization of the radiation emitted by the photoion (or the photofragment) will also be asymmetric. Such an asymmetry has practical consequences for the size of the apertures that can be used in experimental situations. Corrections that need to be applied in these experiments are discussed in this letter.

We first derive an expression for the angular dependence of the polarization, $P(\theta)$. In order to do this we take recourse to the notation of Ferguson (1965).

Taking the alignment of the photoion or the photofragment to be along the *z*-axis the angular distribution of the radiation in the dipole approximation is given by

$$W(\theta, \phi) = \sqrt{4\pi a^2} | \langle b | 1 | \langle a | \rangle |^2 \sum_{k_n} (-1)^{b-a+k} \frac{1}{\sqrt{2}} W(1a, 1a; bk) \rho_{k_0}(a, a) \epsilon_{k_n}^{0*}(1 \ 1) Y_{k_n}(\theta, \phi). \quad (1)$$

Here a and b are the angular momenta of the initial and the final states of the ion or the photofragment, $\rho_{k_0}(a, a)$ is the density matrix, $\langle b | 1 | | a \rangle$ is the transition amplitude, $W(1a, 1a; bk)$ are the Racah coefficients and $c_{k_n}^0(1 1)$ are the radiation parameters given by

$$c_{k_0}^0(1 1) = \frac{9}{8\pi} (1 1, 1 -1 | k 0) \quad (2)$$

$$c_{k_{\pm 2}}^0(1 1) = \frac{9}{16\pi} (1 1, 1 1 | k 2) \quad (3)$$

where $(|)$ are Clebsch-Gordan coefficients.

The degree of polarization $P(\theta)$ is now given by

$$P(\theta) = \frac{W(\theta, 0^\circ) - W(\theta, 90^\circ)}{W(\theta, 0^\circ) + W(\theta, 90^\circ)} \quad (4)$$

Substitution of equations (1), (2) and (3) in equation (4) yields

$$P(\theta) = \frac{3\sqrt{5}W(1a 1a; b2)\rho_{20}(a, a)\sin^2 \theta}{10\sqrt{2}W(1a 1a; b0)\rho_{00}(a, a) + \sqrt{5}W(1a 1a; b2)\rho_{20}(a, a)(3\cos^2 \theta - 1)} \quad (5)$$

This result can be expressed in terms of the degree of alignment of the ion or photofragment,

$$A \equiv \frac{\rho_{20}}{\rho_{00}};$$

$$P(\theta) = \frac{3\sqrt{5}W(1a 1a; b2)\sin^2 \theta A}{10\sqrt{2}W(1a 1a; b0) + \sqrt{5}W(1a 1a; b2)(3\cos^2 \theta - 1)A} \quad (6)$$

For the sake of comparison of this result to the experiment of Grador, Oliver and Ebert (1977) we would like to express $P(\theta)$ in terms of β , the asymmetry parameter for the emission of radiation whose polarization is not detected. This can be done by choosing appropriate values for the radiation parameters in equation (1). The result of the calculation yields

$$W(\theta) = \frac{W_{tot}}{4\pi} (1 + \beta P_2^0(\cos \theta)) \quad (7)$$

where W_{tot} is the total cross-section and β is given by

$$\beta = \frac{3}{2} \hat{a}(-1)^{3a+b+1} W(1a 1a; b2)A.$$

Thus in terms of β , $P(\theta)$ becomes

$$P(\theta) = \frac{3\beta \sin^2 \theta}{2\sqrt{15}\hat{a}(-1)^{3a+b+1} W(1a \ 1a; b0) + \beta(3 \cos^2 \theta - 1)} \quad (8)$$

Consider now the $Ll \left(a = \frac{3}{2}, b = \frac{1}{2}\right)$ transition in the experiment of Grader, Oliver and Ebert (1977) with $\beta = 0.062$. We obtain

$$P(\theta) = \frac{3 \sin^2 \theta}{143.26 + 3 \cos^2 \theta}$$

Now a typical aperture subtends an angle of about 10° . This corresponds, for $\theta = 90^\circ$, to a change in the degree of polarization from its 90° value by 2.9%. This is a measurable change and needs to be taken into account.

Thus by analyzing existing experimental data we have demonstrated the need for applying corrections due to finite aperture size in experiments involving measurement of polarizations from excited photoions or photofragments. The average polarization measured from experiments is given by

$$\bar{P} = \frac{\int_{\text{aperture}} W(\theta, \phi) P(\theta) d\Omega}{\int_{\text{aperture}} W(\theta, \phi) d\Omega}$$

with $P(\theta)$ given by (5) or (6) and $W(\theta, \phi)$ by (7).

It is worth noting that equation (6) can be used for calculating the degree of alignment A from the measured value of the degree of polarization $P(\theta)$ at the angle θ . A or β can be conveniently obtained from equations (6) or (8) by measuring $P(\theta)$ at only one point. On the other hand the use of equation (7) requires two measurements for obtaining the value of A or β .

References

- Caldwell C D and Zare R N 1977 *Phys. Rev.* **A16** 255
 Case D A, McClelland G M and Herschbach D R 1978 *Molec. Phys.* **35** 541
 Chamberlain G A and Simons J P 1975 *J.C.S. Faraday II* **71** 2043
 Cooper J and Zare R N 1969 in *Lectures in Theoretical Physics*, Vol. 11C, edited by S. Geltman, K. Mahanthappa and N. Brittin, Gordon and Breach, New York, 317
 Feofilov P P 1964 *The Physical Basis of Polarized Emission*, Consultants Bureau, New York.
 Ferguson A T 1965 *Angular Correlation Method in Gamma-Ray Spectroscopy*, North-Holland, Amsterdam.
 Grader R J, Oliver A J and Ebert P J 1977 *Phys. Rev.* **A16** 2388
 Macpherson M T and Simons J P 1977 *Chem. Phys. Letters* **51** 261
 Simons J P, 1977 in *Gas Kinetic and Energy Transfer*, edited by P. G. Ashmore and R. J. Donovan, Chemical Society, London, 58
 Van Brunt R J and Zare R N 1968 *J. Chem. Phys.* **48** 4304

Vertical drift velocity in the topside F layer during Aug 7, 1972 flare

M P Singh

J. K. Institute of Applied Physics and Technology, University of Allahabad, Allahabad.

and

S N Ghosh

Department of Applied Physics, Calcutta University, Calcutta.

Received 22 November 1978

Abstract. In this paper vertical drift velocity during Solar Flare of 7 August, 1972 has been calculated for two electron density distributions namely (1) Chapman-like distribution and (2) exponential distribution. The results obtained thereof are compared with observed drifts obtained at Millstone Hill Observatory and predicted drifts by Mendillo and Evans (1973, 1974).

1. Introduction

It has been observed that during sunrise there is a marked upward, and during sunset downward drift in the upper atmosphere. These drifts are related with expansion and contraction of the *F* layer ionosphere (Evans 1969). Mendillo and Evans (1973, 1974) have reported for the first time that there is a large upward surge of electrons in the topside *F* layer during solar flare of August 1972. They have also obtained theoretically the values of the vertical drift velocity arising due to enhanced electron density and electron and ion temperatures and have found that the predicted vertical drift velocity is much larger as compared to the peak observed drifts. Mendillo and Evans have tried to explain this discrepancy on various convincing grounds. In this paper, we estimate the vertical drift velocity taking the different electron density models, namely, Chapman's distribution which is universally used and the exponential one which has been taken by Mendillo and Evans (1973, 1974) but with a different height gradient. The latter model has been in closer proximity with observed electron density than that of Mendillo and Evans.

Finally we have made a comparison of predicted and observed drift velocities and have tried to explain the discrepancy.

2. Theory

In the topside *F* layer a Chapman-like distribution of electron density is given by

$$N_z = N_F \exp \left[c \left(1 - \frac{z - z_F}{H} - e^{-\frac{z - z_F}{H}} \right) \right] \quad (1a)$$

where the constant c is either 1 or $\frac{1}{2}$ (Rishbeth 1971). On the other hand for exponential decay the distribution can be written as

$$N_Z = N_{Z_0} \exp \left[-\alpha \left(\frac{Z - Z_0}{H} \right) \right] \quad (1b)$$

where

N_F —electron density at *F* layer maximum having height Z_F

N_{Z_0} —electron density at the reference level Z_0

N_Z —electron density at level Z

Z_F, Z_0, Z —are all measured from the earth's surface.

H —Scale Height $= k(T_e + T_i)/m_i g$.

Expressing N_F in terms of N_{Z_0} , equation (1a) can be modified as

$$N_Z = N_{Z_0} \exp \left[-c \frac{Z - Z_0}{H} + e^{-\frac{Z - Z_F}{H}} - e^{-\frac{Z_0 - Z_F}{H}} \right] \quad (1c)$$

Let us assume that above some reference level Z_0 in the topside *F* layer the production and loss rates of electrons are each small and equal and the plasma temperature is constant with height. The total number of electrons above Z_0 will be obtained by integrating either equation (1b) or (1c) w.r.t. height within the limits Z_0 and ∞ . Let us suppose that it is given by $\beta N_{Z_0} H$ where the constant β depends upon the type of distribution taken. Again assuming that the temperature of the region increases uniformly so that scale height H , and electron density N_{Z_0} at the reference level, change at a constant rate, the total electron content in the topside *F* layer above Z_0 should change at a rate given by

$$\begin{aligned} \frac{d}{dt} \int_{Z_0}^{\infty} N_Z dZ &= \frac{d}{dt} (\beta N_{Z_0} H) \\ \beta N_{Z_0} \frac{dH}{dt} + \beta H \frac{dN_{Z_0}}{dt} \end{aligned} \quad (2)$$

This can be achieved if there is a flux of ionization through Z_0 having speed V_{Z_0} , so that

$$N_{Z_0} V_{Z_0} = \beta N_{Z_0} \frac{dH}{dt} + \beta H \frac{dN_{Z_0}}{dt} \quad (3)$$

The vertical drift velocity at the reference level is, therefore, given by

$$V_{Z_0} = \beta \frac{dH}{dt} + \beta \frac{H}{N_{Z_0}} \frac{dN_{Z_0}}{dt} \quad (4)$$

Similarly the velocity at any altitude above the reference level (topside *F* layer) is,

$$V_z = \beta \frac{dH}{dt} + \beta \frac{H}{N_z} \frac{dN_z}{dt}. \quad (5)$$

(a) *Chapman's Distribution*

For this distribution the time rate of the electron density is obtained by differentiating equation (1c) with time, i.e.

$$\begin{aligned} \frac{dN_z}{dt} = & \left[\frac{dN_{z0}}{dt} + N_{z0} \cdot \frac{dH}{dt} \left(\frac{Z-Z_0}{H^2} - \frac{Z-Z_F}{H^2} e^{-\frac{Z-Z_F}{H}} \right. \right. \\ & \left. \left. + \frac{Z_0-Z_F}{H^2} e^{-\frac{Z_0-Z_F}{H}} \right) \right] \times \\ & \times \exp \left[-c \left(\frac{Z-Z_0}{H} + e^{-\frac{Z-Z_F}{H}} - e^{-\frac{Z_0-Z_F}{H}} \right) \right]. \end{aligned} \quad (6)$$

Substituting values of N_z and $\frac{dN_z}{dt}$ from equations (1c) and (6) respectively in equation (5), we obtain

$$\begin{aligned} V_z = & \beta \frac{H}{N_{z0}} \frac{dN_{z0}}{dt} + \left[1 + c \left(\frac{Z-Z_0}{H} - \frac{Z-Z_F}{H} e^{-\frac{Z-Z_F}{H}} + \right. \right. \\ & \left. \left. + \frac{Z_0-Z_F}{H} e^{-\frac{Z_0-Z_F}{H}} \right) \right] \beta \frac{dH}{dt}. \end{aligned} \quad (7)$$

(b) *Exponential Distribution*

Starting with equation (1b) and proceeding as before we obtain,

$$\frac{dN_z}{dt} = \left[\frac{dN_{z0}}{dt} + \alpha \left(\frac{Z-Z_0}{H^2} \right) N_{z0} \frac{dH}{dt} \right] \exp -\alpha \left(\frac{Z-Z_0}{H} \right). \quad (8)$$

Substituting N_z and $\frac{dN_z}{dt}$ from equations (1b) and (8) in equation (5), we get

$$V_z = \beta \frac{H}{N_{z0}} \frac{dN_{z0}}{dt} + \left[1 + \alpha \left(\frac{Z-Z_0}{H} \right) \right] \beta \frac{dH}{dt}. \quad (9)$$

A comparison of the expressions (7) and (9) of the vertical drift velocity for the two models shows that the pressure term (1st term) is independent of height

while the thermal term (2nd term) is height dependent. The comparison also shows that the pressure term is same for two models while there is a marked difference for the thermal terms.

3. Application to solar flare of 7 August 1972

The electron density profiles were obtained by Mendillo and Evans (1973, 1974) during three consecutive runs each of 34 minutes before, during, and after the occurrence of maximum flare activity. In examining the topside profiles they have observed that electron densities were enhanced at all heights above the maximum ionization of the *F* layer. At the same time they observed a large upward drift at altitudes above 370 Km at the peak flare activity. They have observed that the solar flare has a growth time $\Delta t = 10$ min. and the following associated quantities at the reference level $Z_0 = 525$ Km.

$$N_{Z_0} = 11.8 \times 10^4 \text{ el./cm}^3$$

$$\Delta N_{Z_0} = 1.5 \times 10^4 \text{ el./cm}^3$$

$$T_e + T_i = 4860^\circ\text{K} \rightarrow H = 300 \text{ km}$$

$$\Delta(T_e + T_i) = 440^\circ\text{K} \rightarrow \Delta H = 24.7 \text{ km.}$$

The height of peak ionization density of *F* layer is taken as 296 Km.

Substituting the values of Z_0 , Z_F and H , the total electron content above the reference level Z_0 is

$$\begin{aligned} \int_{Z_0}^{\infty} N dz &= 1.85 N_{Z_0} H && \text{for Chapman distribution with } c = \frac{1}{2} \\ &= 1.01 N_{Z_0} H && \text{for Chapman distribution with } c = 1. \\ &= 0.63 N_{Z_0} H && \text{for experimental distribution with} \\ &&& \alpha = 1.6. \end{aligned}$$

giving the respective values of the proportionality constant β as 1.35, 1.01 and 0.63 respectively. The expressions of the vertical drift velocity then becomes

$$V_z = 64.5 + \left[1 + \frac{Z-525}{300} - \frac{Z-296}{300} e^{-\frac{Z-296}{300}} + \frac{229}{300} e^{-\frac{229}{300}} \right] 41.5 \text{ m/sec. (10a)}$$

for Chapman distribution with $c = 1$,

$$V_z = 118.0 + \left[1 + \frac{1}{2} \left(\frac{Z-525}{300} - \frac{Z-296}{300} e^{-\frac{Z-296}{300}} + \frac{229}{300} e^{-\frac{229}{300}} \right) \right] 76.0 \text{ m/sec. (10b)}$$

for Chapman distribution with $c = \frac{1}{2}$, and for exponential distribution we obtain

$$V_z = 40.0 + \left[1 + 1.6 \left(\frac{Z - 525}{300} \right) \right] 25.7 \text{ m/sec.} \quad (11)$$

Vertical drift velocity has been calculated for Chapman's distribution for $c = 1$ and $\frac{1}{2}$ and for exponential having $\alpha = 1.6$ at altitudes of 525, 600, 675 and 750 km. The drifts associated with thermal term together with the peak observed drifts have been given in figure 1 and table 1.

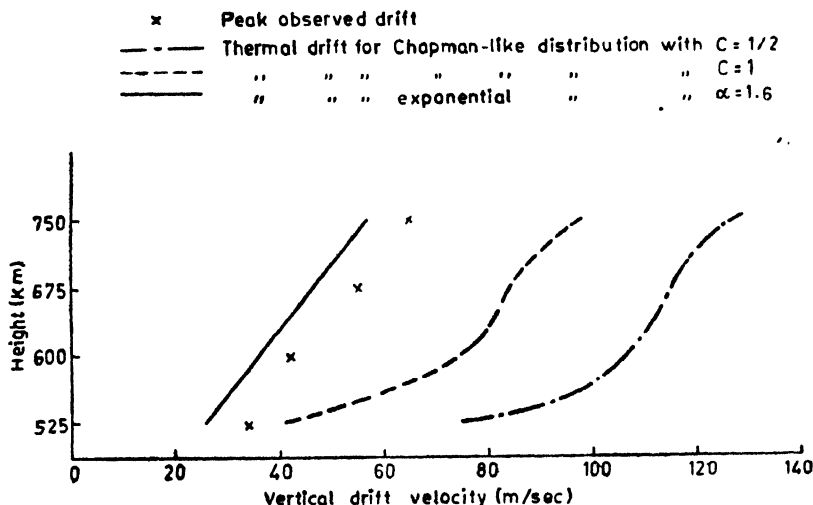


Figure 1. Comparison of observed drifts with those computed for Chapman's distribution and exponential decay.

Table 1. Vertical drift velocity during flare of 7 August 1972

Altitude (Km.)	Peak observed drifts (m/sec)	Predicted thermal drift (m/sec)		
		Chapman's distribution $c = 1$	$c = 1/2$	Exponential distributions $\alpha = 1.6$
525	34.2	41.5	76.0	25.7
600	42.4	75.2	107.0	35.9
675	55.1	84.1	115.3	46.2
750	64.7	97.6	127.5	56.5

4. Discussion

From figure 1 it is clear that the predicted thermal drift for exponential distribution with $\alpha = 1.6$ gives a good agreement with the peak observed drift. Specifically, the height gradient of the two is nearly equal. Large deviation in Chapman

distribution may be attributed to the disagreement in the electron density with the observed one (see table 2).

Table 2. Observed and calculated electron densities during flare 7 August 1972

Altitude (Km.)	Observed (cm ⁻³)	Chapman's distribution		Exponential decay	
		$c = 1$ (cm ⁻³)	$c = 1/2$ (cm ⁻³)	$\alpha = 1.0$ (cm ⁻³)	$\alpha = 1.6$ (cm ⁻³)
525	11.8×10^4	11.8×10^4	11.8×10^4	11.8×10^4	11.8×10^4
600	8×10^4	10.2×10^4	11.0×10^4	9.6×10^4	7.8×10^4
675	5.6×10^4	8.6×10^4	10.1×10^4	7.1×10^4	5.3×10^4
750	4.0×10^4	7.1×10^4	9.7×10^4	5.6×10^4	3.6×10^4

If we add some fraction (~ 7.5 m/sec) of the height independent drift (pressure-term) to the predicted thermal drift, we then should sought for an explanation for a constant term of 32.5 m/sec. In examining the possible causes for the upward surge, Mendillo and Evans (1973, 1974) have shown that the component of the cross field electrodynamic drift ($\mathbf{E} \times \mathbf{B}$) is downward having a value of about 10 m/sec at the *F* region (Rishbeth and Garriot 1969) and should essentially remain unchanged during flare at Millstone Hill Observatory (42.6°N, 71.5°W, 72° dip angle). Thus $\mathbf{E} \times \mathbf{B}$ drift which is height-independent and directed downward will cancel the large pressure term at least in part.

Mendillo and Evans (1973, 1974) have also pointed out that the possibility of a downward drift arising due to travelling ionospheric disturbance at the time of solar flare can not be ruled out. The third possibility of a less observed drift at the time of flare may be caused by the excess production of electrons above the reference level than its recombination. In establishing the relations of the vertical drift velocity, we have assumed that above the reference level the production and loss rates of electrons are each small and equal. However, if there is excess production of electrons than their loss at the time of flare, lesser number of electrons will be required to move upward in order to maintain hydrostatic equilibrium, which, in turn, shows that the actual velocity of electrons should be essentially lesser than that obtained theoretically. Mendillo *et al* (1974) have shown that of 3.79×10^{16} el/m² sudden increase in total electron content nearly 25% is contributed from regions above 375 Km. If the region above 525 Km is considered to have negligible electron production then to explain such a large change in the total electron content restricted to the 375–525 Km altitude range would be an impossibility. This is simply because one can not assume an abruptly larger value other than zero for the production rate of electron below 525 Km. The excess production rate of electrons, therefore, can also be thought to have an exponential nature decreasing with height.

Mendillo and Evans (1973, 1974) have calculated the predicted drift velocity assuming an exponential distribution having $\alpha = 1$ and have obtained

$$V_z = 63.8 + \left(1 + \frac{Z-525}{300}\right) \times 41.1 \text{ m/sec.} \quad (12)$$

Setting aside the larger pressure term even the predicted thermal term is large as compared to the peak observed drifts at all heights. For the cancellation of the large pressure term, they have significantly pointed out that

(1) the large scale height resulting from high summer day-time temperature may cause large vertical drifts even for small changes in N_{z0} , and

(2) inadequate time resolution for electron density changes at reference level may also produce considerable uncertainty.

For example, if one takes the growth time of the solar flare equal to 34 min. (the time for the individual run at Millstone Hill Observatory) instead of 10 min., the pressure term will lead to an upward drift of 19 m/sec instead of 64 m/sec.

Both the reasons seem to be untenable. The large scale height in summer day time should result in large upward drift if the physical process for lifting the ionosphere is the same as we have considered. The large scale height can not be considered to give erroneously high values of upward drifts.

As regards the second reason, inadequate time resolution for changes in the electron density at Z_0 will certainly result in wrong upward drift. To take $\Delta t = 34$ min is certainly not justified because the predicted thermal term will then reduce by a factor of 0.29 at all heights.

In the calculations we and Mendillo and Evans (1973, 1974) have taken equal growth times ($\Delta t = 10$ min) both for electron density and electron ion temperatures. However, from the figure of combined electron and ion temperature Δt can be roughly approximated to 20 min. instead of 10 min. This in turn, will reduce the predicted thermal drift, bringing the total calculated drift in close vicinity of the peak observed drift. Therefore the possibility of unequal growth times for electron and ion temperatures and electron density can not also be ignored.

References

- Evans J V 1971 *Radio Sci.* **6** 609
 Mendillo M and Evans J V 1972 AFCRL-TR-73-0686
 Mendillo M and Evans J V 1974 *Radio Sci.* **2** 197
 Mendillo M, Klobuchar J A, Fritz R B, da Rosa A V, Kersley L, Yeh K C, Flaherty B J, Ranganaswamy S, Schmid, P E, Evans J V, Schödel P J, Matsoukas D A, Koster J R, Webster A R and Chin P 1974 *J. Geophys.* **79** 665
 Rishbeth H and Garriot O K 1969 *Introduction to Ionospheric Physics*, Academic Press, New York
 Rishbeth H 1977 *Planet. Space Sci.* **19** 357

Probability of charge transfer in alpha particle-hydrogen atom collision

D Basu and D M Bhattacharya

Indian Association for the Cultivation of Science, Jadavpur, Calcutta-700032.

Received 17 November 1978

Abstract. The problem of charge transfer in alpha particle-hydrogen atom collision has been investigated in the atomic three state approximation taking into account the momentum transfer. The possible states in which the electron is considered to remain before and after the collision are the ground state of hydrogen atom and $1s$ and $2s$ states of singly ionised helium atom. Probabilities of charge transfer for fixed scattering angle 1.2° have been calculated and have been compared with the existing experiment.

1. Introduction

The experimental findings of Koever and Everhart (1966) for the process of charge transfer in alpha particle hydrogen atom collision, covering the energy range 2 KeV to 200 KeV, is of special interest because of the possibility of accidental resonance in the charge transfer process. Fite, Smith and Stebbings (1962) have earlier measured the total charge transfer cross section for this process in the energy range 0.1 KeV to 36 KeV. In the theoretical treatment of Bates and Lynn (1959) the authors have indicated a qualitative difference between the cases of accidental resonance process and symmetrical resonance process. The Charge transfer cross section in the former case falls to zero in the zero velocity limit, whereas, in the latter case it approaches infinity in the same limit. Basu *et al* (1967) have formulated the problem in a five state approximation neglecting the momentum transfer and have found that the general tendency of their theoretical curve for total charge transfer cross section, is to approach zero in the zero velocity limit as has been remarked by Bates and Lynn. The theoretical treatment of the problem by McCarroll and McElRoy (1962) employs two state approximation which includes only the initial state and ground state of singly ionised helium ion. McElRoy (1963) has extended the work by including along-with the ground state of hydrogen atom any one of the $2s$ and $2p$ states of singly ionised helium ion. His result of the total cross section near 30 KeV, where the experimental peak is observed, is too high and he affirms reliability of the results above 100 KeV. Schiff (1954) has made calculations for total charge transfer cross section using the Born approximation in the energy region from 100 KeV

to 1 MeV. Recently Malaviya (1969) and Rapp (1974) have investigated the problem and have calculated the total charge transfer cross section in alpha particle hydrogen atom collision.

In the present investigation we have considered the collision process in which the electron is initially in the ground state of the target atomic hydrogen and after the impact it either remains as such or is captured by the incoming alpha particle to form the singly ionised helium ion in the ground state or in the excited $2s$ state. The solution ψ of the time dependent Schrödinger equation represents the electron state at any instant. A trial wave function ψ_T which is formed by the linear combination of all possible states with time dependent coefficients is taken as an approximate solution of the Schrödinger equation. Using a variational method (1960) we minimise the variation integral and obtain a set of coupled differential equations. The solution of this set is equivalent to the solution of the Schrödinger equation. To determine the impact parameter p at a fixed scattering angle we follow Everhart *et al* (1955). We take the mass of the alpha particle to be three instead of four, for convenience of comparing our results with the experiment.

2. Theory

We consider that the alpha particle and the proton move with uniform velocities, with their centre of mass at rest. Initially the electron is bound to the proton in its ground state, $t = 0$ being the instant when the alpha particle and the proton are closest.

Let R be the position vector of the alpha particle relative to the proton and r_A, r_B and r the position vectors of the electron relative to the proton, the alpha particle and the centre of mass respectively. v is the velocity of the alpha particle relative to the hydrogen atom. The Hamiltonian in atomic units for the motion of the electron is given by

$$H = -\frac{1}{2} \nabla^2 - \frac{1}{r_A} - \frac{1}{r_B}$$

The variation integral which leads to the Schrödinger equation, $H\psi = \frac{i\partial\psi}{\partial t}$ is given by

$$I = -\frac{1}{2} \int \left[\bar{\psi} H \psi + \psi H \bar{\psi} - i \bar{\psi} \frac{\partial \psi}{\partial t} + i \psi \frac{\partial \bar{\psi}}{\partial t} \right] dv dt \quad (1)$$

We take, as an approximation to ψ , the trial wave function ψ_T ,

$$\psi_T = A_1(t)\psi_1 + B_1(t)\psi_1' + B_2(t)\psi_2',$$

ψ_1 is the 1s state of hydrogen atom and ψ_1' , ψ_2' are respectively the 1s and 2s states of singly ionised lithium ion. Replacing ψ by ψ_T and minimising the variation integral for small variations of \bar{A}_1 , \bar{B}_1 and \bar{B}_2 we get the following set of coupled differential equations

$$\left. \begin{aligned} \dot{A}_1 + g_{11}\dot{B}_1 + g_{12}\dot{B}_2 &= i[F_{11}A_1 + c_{11}B_1 + c_{12}B_2] \\ g_{11}'\dot{A}_1 + \dot{B}_1 &= i[c_{11}'A_1 + F_{11}'B_1 + F_{12}'B_2] \\ g_{21}'\dot{A}_1 + \dot{B}_2 &= i[c_{21}'A_1 + F_{21}'B_1 + F_{22}'B_2] \end{aligned} \right\} \quad (2)$$

$$\text{where } C_{mn} = G_{mn} + \frac{i}{2} g_{mn}, C_{mn}' = G_{mn}' + \frac{i}{2} g_{mn}'$$

in which

$$F_{mn} = \int \bar{\psi}_m \frac{2}{r_B} \psi_n dV = \bar{F}_{nm}$$

$$F_{mn}' = \int \bar{\psi}_m' \frac{1}{r_A} \psi_n' dV = \bar{F}_{nm}'$$

$$G_{mn} = \frac{1}{2} \int \bar{\psi}_m \left(\frac{1}{r_A} + \frac{2}{r_B} \right) \psi_n' dV = \bar{G}_{nm}'$$

$$g_{mn} = \int \bar{\psi}_m \psi_n' dV = \bar{g}_{nm}'$$

The matrix elements F_{mn} and F_{mn}' have been evaluated analytically.

$$F_{11} = 2 \left[\frac{1}{R} - \left(\frac{1}{R} + 1 \right) \exp(-2R) \right]$$

$$F_{11}' = \frac{1}{R} - \left(\frac{1}{R} + 2 \right) \exp(-4R)$$

$$F_{22}' = \frac{1}{R} - \left(\frac{1}{R} + \frac{3}{2} + R + R^2 \right) \exp(-2R)$$

$$F_{12}' = \sqrt{2} \left(\frac{8}{27} + \frac{8R}{9} \right) \exp(-3R - i\epsilon),$$

ϵ is the difference in the binding energies of the ground state and the excited state ($n = 2$) of singly ionised helium ion. The probabilities of scattering and charge transfer in different states of singly ionised helium ion are found by squaring the absolute values of the coefficients $A_1(t)$ and $B_n(t)$ at infinite time.

3. Numerical method and results

We solve the above set of eqs. (2) numerically by Runge-Kutta method. With the help of (2) it is seen that the unitarity of $\int \bar{\psi}_T \psi_T dV$ is preserved at all times and we employ this fact as a check on the solutions of the differential equations, at any instant. Those matrix elements which can not be evaluated analytically are determined following the method proposed by Chatterjee *et al* (1967) and are expressed as combinations of integrals in time, with coefficients of the form i^m , where m is an integer. The above integrals in time have been calculated numerically using the six point central difference method. The real and imaginary parts of the matrix elements are found to be either symmetric or antisymmetric in time.

In the figure we have compared our theoretical results of total charge transfer probability covering the energy range 7 KeV to 80 KeV, with the experimental results of Keever and Everhart. There is little oscillation in our theoretical curve, compared to the experimental curve. There is only one peak and one valley in our theoretical curve, whereas the experimental curve shows a number of peaks and valleys.

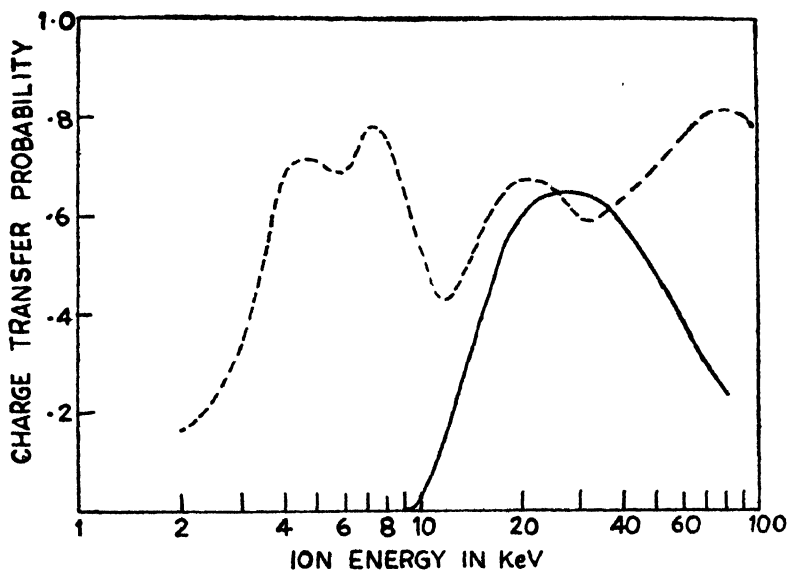


Figure 1. Charge transfer probability at 1.2° scattering angle in the Laboratory system.

———— Present theory
 ----- Keever and Everhart (experimental)

We plan to include in our future investigation, the accidental resonance states $2p_0$ and $2p_{\pm 1}$ of He^+ ion, in addition to the $2s$ state.

Acknowledgment

The authors are thankful to Prof. N. C. Sil, for many helpful discussions.

References

- Basu D, Bhattacharya D M and Chatterjee G 1967 *Phys. Rev.* **163** 8
Bates D R and Lynn N 1959 *Proc. Roy. Soc.* **A253** 141
Chatterjee G, Bhattacharya D M and Sil N C 1967 *Ind. J. Phys.* **41** 934
Everhart E, Stone G and Carbone R J 1965 *Phys. Rev.* **99** 1287
Fite W L, Smith A C H and Stebbings R F 1962 *Proc. Roy. Soc.* **A268** 527
Keever W C and Everhart E 1966 *Phys. Rev.* **150** 43
McCarroll R and McElRoy M B 1962 *Proc. Roy. Soc.* **A266** 422
McElRoy M B 1963 *Proc. Roy. Soc.* **A271** 542
Malaviya V 1969 *J. Phys.* **B2** 843
Rapp D 1974 *J. Chem. Phys.* **61** 3777
Schiff H 1954 *Can. J. Phys.* **32** 393
Sil N C 1960 *Proc. Phys. Soc.* **75** 194

A comparative study of Peacock, Heidborn and Muller's method and kinetic constant method for the solution of third order eigenvalue problem in molecular dynamics

P C Sarkar, G C Singh and U S L Srivastava

Department of Physics, St. Andrew's College, Gorakhpur (India) 273001

Received 21 February 1979

In view of the recent papers by Alix, Muller and Mohan (1975) and Sarkar and Singh (1976) establishing the equivalence of Peacock and Mullers (1968) L matrix approximation method and kinetic constant method (Thirugnanasambandam and Srinivasan) (1969), for the solution of second order secular equation in molecular vibrations, it is interesting to study whether similar equivalence holds in the (3×3) eigenvalue problem. In case of third order eigenvalue problem one has to calculate six distinct symmetry force constants with only three experimental frequencies. Calculation of symmetry force constants uniquely is not possible in such cases due to insufficient information.

Peacock, Heidborn and Muller (1969) have given the following explicit formulae for the approximate solution of the problem in third order secular equation in molecular vibration by an extension of their L matrix approximation method viz. $L_{12} = 0$, $L_{13} = 0$ and $L_{23} = 0$.

$$F_{11} = \left[\lambda_1 A + \lambda_2 G_{12}^2 + \frac{\lambda_3 G_{11} C^2}{\text{Det } G} \right] / G_{11} A$$

$$F_{12} = - \frac{(\lambda_2 G_{12} \text{Det } G + \lambda_3 B C)}{A \text{Det } G}$$

$$F_{13} = \frac{\lambda_3 C}{\text{Det } G}$$

$$F_{23} = - \frac{\lambda_3 B}{\text{Det } G}$$

$$F_{22} = \frac{\lambda_2 G_{11} \text{Det } G + \lambda_3 B^2}{A \text{Det } G}$$

$$F_{33} = \frac{\lambda_3 A}{\text{Det } G} \quad (1a-f)$$

where

$$\begin{aligned} A &= (G_{11}G_{22} - G_{12}^2) \\ B &= (G_{11}G_{23} - G_{12}G_{13}) \\ C &= (G_{12}G_{23} - G_{13}G_{22}) \end{aligned}$$

where the symbols have usual meanings.

Thirugnanasambandam and Mohan (1975), Thirugnanasambandam and Karunanidhi (1977) extended their kinetic constant method for the third order problem by generalising the constraint used for the second order problem viz.

$$\frac{F_{ij}}{F_{jj}} = \frac{K_{ij}(= G_{ij}^{-1})}{K_{jj}(= G_j^{-1})} \quad (2)$$

in particular for the third order problem this becomes :

$$\frac{F_{12}}{F_{22}} = \frac{K_{12}(= G_{12}^{-1})}{K_{22}(= G_{22}^{-1})} = -\frac{(G_{12}G_{33} - G_{23}G_{13})}{(G_{11}G_{33} - G_{13}^2)}$$

$$\frac{F_{13}}{F_{33}} = \frac{K_{13}(= G_{13}^{-1})}{K_{33}(= G_{33}^{-1})} = \frac{G_{12}G_{23} - G_{22}G_{13}}{G_{11}G_{22} - G_{12}^2}$$

and

$$\frac{F_{23}}{F_{33}} = \frac{K_{23}(= G_{23}^{-1})}{K_{33}(= G_{33}^{-1})} = -\frac{(G_{11}G_{23} - G_{12}G_{13})}{(G_{11}G_{22} - G_{12}^2)} \quad (3a, b, c)$$

Right hand side of (3a, b, c) are constants depending only on the masses and geometry of the constituent atoms and independent of frequency. Hence one can eliminate three of the symmetry force constants from the three equations as such one can calculate the force constants.

On the other hand from equations (1a-f) one obtains :

$$\frac{F_{12}}{F_{22}} = -\frac{(\lambda_2 G_{12} \text{Det } G + \lambda_3 BC)}{(\lambda_2 G_{11} \text{Det } G + \lambda_3 X^2)}$$

$$\frac{F_{13}}{F_{33}} = \frac{(G_{12}G_{23} - G_{13}G_{22})}{(G_{11}G_{22} - G_{12}^2)}$$

and

$$\frac{F_{23}}{F_{33}} = -\frac{(G_{11}G_{23} - G_{12}G_{13})}{(G_{11}G_{22} - G_{12}^2)} \quad (4a, b, c)$$

From (3a, b, c) and (4a, b, c) it is evident that excepting the constraint $\frac{F_{12}}{F_{22}}$ the other two constraints viz. $\frac{F_{13}}{F_{33}}$ and $\frac{F_{23}}{F_{33}}$ are identical. Thus one may conclude that use of the generalised constraints prescribed by kinetic constant method cannot lead to identical force constants obtained by using the Peacock, Heidborn and Mullers (1969) method.

Partly to verify our contention and partly to draw suitable conclusions, we are giving in table 1 ratios of the force constants $\left(\frac{F_{12}}{F_{22}}, \frac{F_{13}}{F_{33}}, \frac{F_{23}}{F_{33}}\right)$ calculated by these methods for twelve trigonal bipyramidal molecules of the type XY_5 . The relevant frequencies are listed in table 2.

Table 1. Ratios of symmetry force constants of some Trigonal Bi-pyramidal molecules of the type XY_5 .

System	$\frac{F_{12}}{F_{22}}$	$\frac{F_{13}}{F_{33}}$	$\frac{F_{23}}{F_{33}}$	m_x/m_y	Method
NbF ₅	0.3097	0.2689	0.1552	4.89	K
	0.3286	0.2689	0.1552		P
NbCl ₅	0.4245	0.3774	0.2180	2.62	K
	0.6101	0.3774	0.2180		P
NbBr ₅	0.5571	0.5096	0.2942	1.16	K
	0.8176	0.5096	0.2942		P
TaF ₅	0.1995	0.1694	0.0978	9.52	K
	0.2082	0.1694	0.0978		P
TaCl ₅	0.3020	0.2618	0.1511	5.10	K
	0.3853	0.2618	0.1511		P
TaBr ₅	0.4508	0.4029	0.2327	2.26	K
	0.5911	0.4029	0.2327		P
PF ₅	0.5063	0.4582	0.2645	1.63	K
	0.7177	0.4582	0.2645		P
MoF ₅	0.3039	0.2635	0.1522	5.05	K
	0.3346	0.2635	0.1522		P
GeCl ₅	0.4683	0.4202	0.2426	2.05	K
	0.6383	0.4202	0.2426		P
SnCl ₅	0.3794	0.3342	0.1929	3.35	K
	0.4917	0.3342	0.1920		P
AsF ₅	0.3491	0.3055	0.1764	3.94	K
	0.4511	0.3055	0.1764		P
VF ₅	0.4203	0.3734	0.2156	2.68	K
	0.5891	0.3734	0.2156		P

K = Kinetic constant method

P = Peacock, Heidborn and Mullers method

Table 2. Fundamental frequencies (in cm^{-1}) of some XY_5 type molecules

Molecules	ν_1	ν_2	ν_3	Ref.
NbF_5	726	253	226	a, b, c
NbCl_5	492 ⁺	180	54	a, b, c
NbBr_5	357 ⁺	119	67	a, b, c
TaF_5	713	245	213	a, b, c
TaCl_5	458 ⁺	181	54	a, b, c
TaBr_5	306 ⁺	110	70	a, b, c
PF_5	1022	533	300	d
MoF_5	730	250	203	e
GeCl_5	398	200	115	e
SnCl_5	359	160	89	e
AsF_5	811	372	130	d
VF_5	810	282	109	d

⁺ Estimated frequency.

a So S P 1975 *J. Mol. Struct.* **16** 311

b Kebert D L and Nyholm R S 1965 *J. Chem. Soc.* **28** 71

c Walton R A and Brisdon B J 1967 *Spectro. Chim. Acta* **28A** 2489

d Sleight H Holloway J H, Tyson J and Classen H 1970, *J. Chem. Phys.* **53** 2259

e Beattie I R, Gilson T, Livingstone K, Fawcett V. and Ozin G.A. 1967 *J. Chem. Soc.* **A712**

From table 1, it is found that the force constants (F_{12}/F_{22}) calculated by Peacock, Heidborn and Mullers (1969) method are slightly greater than those calculated by kinetic constant method. Furthermore the difference depends on the mass ratio m_x/m_y . The greater the mass ratio the smaller the difference, indicating that only in case of larger mass ratio the force constants calculated by these methods will be approximately equal.

Acknowledgment

The authors want to express their thanks to Dr. Y. B. Singh, Principal, St. Andrew's College, Gorakhpur and Dr. D. Sharma, Vice Chancellor, University of Indore for their interest and encouragement.

References

- Alix A J P, Muller A and Mohan N 1975 *J. Mol. Struct.* **27** 440
 Peacock C J and Muller A 1968 *J. Mol. Spectry* **26** 454
 Peacock C J, Heidborn U, and Muller A, 1969 *J. Mol. Spectry* **30** 338
 Sarkar P C and Singh G C Paper presented at the National Symposium on Mol. Spect. and atomic and Mol. Collision Processes July 30-Aug 1 (1976)
 Thiruganasambandam P, and Srinivasan G J 1969 *J. Chem. Phys.* **50** 2467

Infrared absorption spectra of 2, 4, 6-triaminopyrimidine

Nitish K Sanyal

Department of Physics, University of Gorakhpur, Gorakhpur-273001

and

R K Goel*

Department of Physics, D. N. College, Meerut-250002

and

S N Sharma

Analytical Physics Section, I.I.P. Dehradun-248005

Received 4 January 1979

Abstract. The infrared absorption spectra of 2, 4, 6-triamino-pyrimidine have been recorded on Perkin Elmer-521 spectrophotometer in the region 250-4000 cm^{-1} in KBr pellet and nujol mull. The spectra have been analysed assuming C_{2v} point group symmetry. Probable assignments to observed bands have been made and discussed and correlation with the fundamentals of pyrimidine has been made.

1. Introduction

Pyrimidine, cytosine and their derivatives are of considerable biological importance, even then very little spectroscopic studies are reported for them in literature (Ito *et al* 1956, Lord *et al* 1957, Simmons and Innes 1964, Sbrana *et al* 1966, Sarma 1974, Nejad and Stidham 1975, Goel *et al* 1976, Allenstein *et al* 1977, Job and Kartha 1977). As a part of our research project on *N*-heterocyclic molecules, we have recently studied the vibrational spectra of 2-mino-4-methyl pyrimidine and 5-methyl cytosine (Goel *et al* 1976), amino-methyl pyridines (Goel *et al* in press) and 3,6-dichloropyridazine (Goel *et al* 1979). In order to extend this work, the molecule 2,4,6-triaminopyrimidine has been undertaken at present for its vibrational studies. It is difficult to interpret the spectra of such molecules because of their high complexity and low symmetry. In absence of Raman spectra with depolarisation data and vapour phase infrared spectra the present assignment of observed bands is based mainly on the group frequency approach and on the analogy between the spectra of similar molecules.

*Address to whom all correspondence should be made.

2. Experimental details and results

Pure chemical obtained from M/S Tokyo Kasei Kogyo Co. Ltd., Tokyo, were used as such without further purification. The infrared absorption spectra have been recorded on Perkin Elmer 521 spectrophotometer in KBr pellet and Nujol mull in the region 250–4000 cm^{-1} . The spectrometer was calibrated by running the spectra of a thin sheet of polystyrene. The observed bands along with their intensities and their proposed assignment are presented in table 1. The fundamentals have also been correlated with the of pyrimidine- d_2 (Nejad and Stidham 1975) in table 1.

3. Results and Discussion

The structure of several pyrimidine compounds have been determined (Lancaster and Stoicheff 1956, Wheatley 1960) and in all cases the molecules were found to be planar. Assuming NH_2 groups as single mass points, the present molecule, 2,4,6-triaminopyrimidine would belong to C_{2v} point group symmetry and its 24 normal vibrations shall be distributed as $9A_1 + 8B_2 + 2A_2 + 5B_1$. Apart from these 24 vibrations there will be 18 group vibrations due to the substituents. All these vibrations are active in both, Raman and infrared, except those belonging to symmetry species A_2 , which are only Raman active.

3.1. Species A_1

One C–H stretching vibration 20a has been assigned at 3109 cm^{-1} in the present molecule. Out of the three X-sensitive stretching vibrations ν_2 , ν_{13} and ν_{7b} (B_2) only one at 1244 cm^{-1} has been observed in the present case and thus has been assigned to the C– NH_2 stretching mode. In substituted benzenes the frequency of one of the two ring modes ν_1 and ν_{12} decreases to $\sim 820 \text{ cm}^{-1}$ while the other remains at $\sim 1000 \text{ cm}^{-1}$. Recently Patel *et al* (1973) have shown that for different substituents as well as substitution at different positions in benzene, it is the potential energy distribution of the substituent sensitive mode that closely corresponds to ν_1 in benzene. We have assigned the very strong bands observed at 796 and 990 cm^{-1} to the vibrations ν_1 and ν_{12} respectively. These assignments are also in agreement with those proposed by Goel *et al* (1976) in 2-amino-4-methyl pyrimidine and Job and Kartha (1977) in case of 4- and 5-methyl pyrimidines.

The Raman line at 678 cm^{-1} in pyrimidine was assigned to ν_{8a} vibration of A_1 species by Simmons and Innes (1964) on the basis of rotational fine structure in the U.V. band spectrum and by Sbrana *et al* (1966) on the basis of the state of polarisation of the corresponding crystal i.r. band. A medium band at 580 cm^{-1} has been assigned to this mode in the present molecule. The ν_{8a} and ν_{19a} vibrations of A_1 species have been identified at 1550 and 1430 cm^{-1} respectively in the title compound. These vibrations were assigned at 1570 cm^{-1} and 1416 cm^{-1}

Table 1. Assignments of fundamental frequencies of 2, 4, 6-triamino-pyrimidine and comparison with those of pyrimidine

Symmetry Species	Vibration number	Pyrimidine ⁺ Wave number (cm ⁻¹)	2, 4, 6-Triamino Pyrimidine wave-number				Description of mode
			in KBr		in Nujol mull		
			cm ⁻¹	Int.	cm ⁻¹	Int.	
A ₁	20a	3074	3109	s	3109	ms	C-H Stretch
	2	3052	1244	vs	1240	sb	C-NH ₂ Stertch.
	13	3038					
	8a	1564	1550	vw	1569	sb	ring stretching
	19a	1398	1430	vs	1446	sb	ring stretching
	9a	1139	327	m	326	m	C-NH ₂ i.p.b
	12	1065	990	vs	980	vs	ring planar deform.
	1	992	796	vvs	796	vs	ring Stretching (breathing type)
	6a	678	580	m	578	mw	ring planar deformation
B ₂	7b	3086	1244	vs	1240	sb	C-NH ₂ stretch.
	8b	1568	1581	vsb	1570	sb	ring stretch
	19b	1466	1464	wb	—	—	ring stretch
	14	1370	1384	—	—	—	ring stretch
	3	1225	386	mw	386	m	C-NH ₂ in p.b.
	15	1159	1159	vw	1154	msb	C-H i.p.b.
	18b	1071	376	mw	376	m	C-NH ₂ i.p.b.
	6b	623	540	ms	540	s	Ring planar deformation
A ₂	16a	399	390	m	400	m	Ring non-planar def.
	17a	1870	—	—	—	—	—
B ₁	5	980	—	—	—	—	—
	11	811	780	sb	776	m	C-H o.p.b.
	10b	721	—	—	—	—	—
	4	708	719	ms	720	vs	ring o.p.b.
	16b	344	354	mb	354	mb	ring non-planar def.
					360		

Table 1 (Contd.)

Symmetry Species	Vibration number	Pyrimidino+ Wave number (cm ⁻¹)	2, 4, 6-Triamino Pyrimidine wave-number				Description of mode
			in KBr		in Nujol mull		
			cm ⁻¹	Int.	cm ⁻¹	Int.	
Group Vib.			3430	sb	3419	sb	N-H stretch asym.
			3319	sb	3309	sb	N-H stretch sym.
			1660	vw	1660	vvw	NH ₂ scissoring
			1134	vw	—	—	NH ₂ twisting
			1094	s	1092	msb	NH ₂ twisting
			1035	m	1039	m	NH ₂ twisting
			—	—	670	ms	NH ₂ wagging
			669	m	664	mw	NH ₂ wagging
			648	ms	649	s	NH ₂ wagging
			—	—	460	vw	2 × NH ₂ torsion
			—	—	446	vw	2 × NH ₂ torsion
			—	—	439	vw	2 × NH ₂ torsion
			419	vw	422	vw	2 × NH ₂ torsion
Other Vib.			2919	wb	—	—	$\nu_{19a} + \nu_{19b}$
					1652	sh	
					1640	sh	
					1580	vw	2 × ν_1
			1464	wb	—	—	$\nu_1 + \text{NH}_2 \text{ wag (669)}$
			370	vw	370	vw	$\nu_4 - \nu_{19b}$
			342	vvw	343	w	$\nu_{18} - \nu_4$
			334	vw	335	vw	$\nu_4 - \nu_3$
			316	vw	316	vw	NH ₂ twis. (1035)— ν_4
			301	vw	304	mw	$\nu_{8a} - \nu_2$
			—	—	290	vw	$\nu_{19a} - \nu_{18}$

*values from ref. Nejad & Stidham (1975)

w = weak, *vw* = very weak, *m* = medium, *ms* = medium strong, *s* = strong, *vs* = very strong, *sh* = shoulder, *mw* = medium weak, *wb* = weak & broad, *b* = broad, *i.p.b.* = in-plane bending, *o.p.b.* = out-of-plane bending.

in 2-amino-4-methyl pyrimidine (Goel *et al* 1976) and at 1570 and 1415 cm^{-1} in 5-methyl pyrimidine (Job and Kartha 1977).

3.2. Species B_2

The 1370 cm^{-1} Raman line of pyrimidine corresponding to ν_{14} vibration has been identified at 1384 cm^{-1} in the present molecule. This vibration was identified at 1340 cm^{-1} and 1353 cm^{-1} in 5-methyl pyrimidine (Job and Kartha 1977) and 2-amino-4-methyl pyrimidine (Goel *et al* 1976) respectively. The ν_{6b} vibration has been identified at 540 cm^{-1} in the present case. The bands in 2,4,6-triaminopyrimidine at 1581 and 1464 cm^{-1} have been assigned to correspond to ν_{6b} (1568) and ν_{10b} (1466) modes of pyrimidine.

The 1071 and 1225 cm^{-1} CH bending vibration ν_{18b} and ν_3 of pyrimidine found to be X-sensitive, which have been observed at 376 and 386 cm^{-1} in the present molecule. The band observed at 1159 cm^{-1} in the title compound has been assigned to the remaining B_2 C-H bending vibration ν_{15} .

3.3. Species A_2

As the vibrations of A_2 species are infrared inactive, they will either be absent in the infrared spectra or may occur very weakly. In the present case, the band observed at 390 cm^{-1} has been assigned to the out-of-plane bending vibration ν_{18a} . The vibration ν_{17a} is X-sensitive and C-NH₂ out-of-plane bending vibration generally lie around 200 cm^{-1} (Green *et al* 1971), thus it could not be observed in the present case.

3.4. Species B_1

The two ring bending vibrations ν_4 and ν_{10b} of the B_1 species appear in pyrimidine at 708 and 344 cm^{-1} respectively. The bands observed at 719 and 354 cm^{-1} in the present molecule have been assigned to these vibrations respectively. ν_4 was assigned at 725 cm^{-1} in 5-methyl pyrimidine (Job and Kartha 1977). As explained above, the C-NH₂ out-of-plane bending vibrations ν_6 and ν_{10b} could not be observed in the present case. The C-H out-of-plane bending vibration ν_{11} observed at 811 in pyrimidine has been identified at 780 cm^{-1} in the present case.

3.5. NH₂ Group vibrations

The present molecule has three NH₂ groups and each NH₂ group will involve one symmetric and one asymmetric N-H stretching vibrations. In the case of nearly all primary aromatic amines the two N-H stretching bands occur in the region 3300–3500 cm^{-1} (Bellamy 1959). The band around 3500 cm^{-1} has been assigned by a large number of workers (Singh and Singh 1969, Flett 1948, Sharma and Dwivedi 1976) as asymmetric and that appearing around 3400 cm^{-1} as symmetric stretching vibration. Out-of six N-H stretching vibration only two

could be indentified at 3430 and 3319 cm^{-1} in the present case. The broadness of bands shows that the three bands of each type which should have appeared at nearly equal frequencies, could not be resolved. Goel *et al* (1976) assigned these bands at 3420 and 3314 cm^{-1} respectively in 5-methyl cytosine. The NH_2 scissoring mode has been suggested to lie in the region 1590–1650 cm^{-1} (Bollamy 1959, Rao 1963). Out of three NH_2 scissoring mode only one has been identified at 1660 cm^{-1} in the present case.

The NH_2 twisting frequency lies around 1060 cm^{-1} . Goel *et al* (1976) have assigned this mode at 1030 cm^{-1} in 2-amino-5-methyl pyrimidine and Sharma and Dwivedi (1975) at 1083 cm^{-1} in 2-fluoro-5-methyl aniline. In view of these assignments, the bands observed at 1035, 1094 and 1134 cm^{-1} in the present molecule, have been assigned to this mode corresponding to three NH_2 groups. Similarly the three bands observed at 648, 669 and 670 (*nujol*) cm^{-1} have been identified as three NH_2 wagging modes. This finds support from the work of Goel *et al* (1976), Sharma and Dwivedi (1975) and Evans (1960).

NH_2 torsional mode lies below the region under study. But as done by Evans (1960) in case of aniline, the bands observed between 422–460 cm^{-1} have been assigned to the first overtone of NH_2 torsional modes.

Acknowledgment

One of the authors (RKG) is thankful to University Grants Commission, New Delhi for financial assistance.

References

- Allenstein E, Kiemle P, Woldin J and Podszum W 1977 *Spectrochim Acta* **33A** 189
 Bellamy L J 1959 *Infrared Spectra of Complex Molecules*, John Wiley & Sons Inc., New York
 Evans J C 1960 *Spectrochim Acta*. **16** 428
 Flett N St C 1948 *Trans. Faraday Soc.* **44** 767
 Goel R K, Sanyal Nitish K and Srivestava S L 1976 *Indian J. Pure Appl. Phys.* **18** 842
 Goel R K, Sharma S. D, Kansal K P and Sharma S N (in Press) *Indian J. Pure Appl. Phys.*
 Goel R K and Sharma S N 1979 *Indian J. Pure Appl Phys* **17** 630
 Green J H S, Harrison D J and Kynaston W 1971 *Spectrochim Acta* **27A** 793
 Ito M, Shimada R, Kuraishi T and Mizushima W 1956 *J. Chem. Phys.* **25** 597
 Job V A and Kartha S B 1977 *Proc. Indian Acad. Sci* **85A** 476
 Lancaster J E and Stoicheff B P 1956 *Canad. J. Phys.* **34** 1016
 Lord R C, Marson A J and Miller F A 1957 *Spectrochim Acta* **9** 113
 Nejad F M and Stidham H D 1975 *Spectrochim. Acta*. **31A** 1433
 Patel N D, Kartha V B and Narsimham N A 1973 *J. Molec. Spectrosc.* **48** 185
 Rao C N R 1963 *Chemical Application of Infrared Spectroscopy Academic Press Inc., New-York.*
 Sarma Y A, 1974 *Spectrochim Acta* **30A** 1801
 Shrana G, Adameri G and Califano S 1966 *Spectrochim Acta*, **22** 1831
 Sharma S N and Dwivedi C P D 1976 *Indian J. Phys.* **50** 25
 Sharma S N and Dwivedi C P D 1975 *Indian J. Pure Appl. Phys.*, **13** 570
 Singh S N and Singh N L 1969 *Indian J. Pure Appl. Phys.* **7** 250
 Simmons J D and Innes K K 1964 *J. Molec. Spectrosc.* **13** 435
 Wheatley P J 1960 *Acta Cryst.* **13** 80

Vibrational analysis of monomeric trihalides of scandium subgroup

V Sengodan and K G Srinivasacharya

Post-Graduate Department of Physics, PSG College of Arts and Science,
Coimbatore-641014, Tamil Nadu

Received 2 January 1979

Abstract. The kinetic constant postulate is applied to evaluate a fresh set of potential constants in the case of monomeric trihalides of Scandium subgroup, using recent vibrational frequencies (Krasnov 1967). The calculated kinetic and potential constants are used to evaluate other molecular constants namely compliance constants, mean amplitudes of vibration, Coriolis coupling constants, shrinkage constants and centrifugal distortion constants. The calculated mean amplitudes of vibration are compared with the experimental values (Akishin *et al* 1959a, 1959b). The compliance constants, Coriolis coupling constants and the centrifugal distortion constants for these molecules are reported here for the first time.

1. Introduction

This is in continuation of our systematic studies on the evaluation of potential constants and other molecular constants using kinetic constant method (Srinivasacharya *et al* 1978) for Scandium subgroup trihalide monomers. The molecules belong to the D_{3h} point group of the planar symmetrical XY_3 type. The six normal modes of vibrations of this model are classified as one totally symmetric (A'_1), two doubly degenerate (E') and one non-totally symmetric (A''_2).

2. Evaluation of kinetic and potential constants

Based on the method already discussed in our earlier paper (Srinivasacharya *et al* 1978), the kinetic and potential constants are evaluated for the Scandium subgroup trihalide monomers. The general expressions for the kinetic constants of the molecules are given below.

$$K_r = (2\mu_x + \mu_y)/\mu_y(3\mu_x + \mu_y)$$

$$K_{rr} = \mu_x/2\mu_y(3\mu_x + \mu_y)$$

$$K_x = -2K_{xx} = (3\mu_x + 2\mu_y)/9\mu_y(3\mu_x + \mu_y)$$

$$-K'_{rx} = 2K_{rx} = \mu_x/\sqrt{3}\mu_y(3\mu_x + \mu_y)$$

$$K_{op} = 1/3(3\mu_x + \mu_y).$$

where K_r , K_a and K_{op} are the stretching, bonding and out of plane bending kinetic constants and others are interaction constants. Here μ_x , μ_y are the reciprocal masses of the X (Sc, Y or La) and Y (F, Cl, Br or I) atoms respectively.

3. Compliance constants

The compliance constants are also evaluated for these molecules based on the procedure given by (Decius 1963).

4. Mean square amplitudes

The symmetrized mean square amplitude matrices (Σ'_s) are obtained for the temperatures 298 K, 500 K and 1000 K using the equation (Cyvin 1968) $\Sigma = L\Delta L'$. The Σ'_s are used to obtain the mean amplitudes of both bonded and non-bonded atom pairs.

5. Coriolis coupling constants

The Coriolis coupling constants which may be determined experimentally can however be evaluated from a reliable set of force constants and the values can be used for detailed interpretation of vibrational spectra. The Coriolis matrix elements G^{α}_{ij} ($\alpha = x, y, z$) are obtained by the vector method (Meal and Polo 1956) and are given below.

$$E' \times E'$$

$$G^z_{33} = (3/2)\mu_x$$

$$G^z_{44} = (9/2)\mu_x$$

$$G^z_{34} = \sqrt{3}[(3/2)\mu_x + \mu_y]$$

$$A''_2 \times E'$$

$$G^y_{2,3a} = -G^x_{2,3b} = \sqrt{6/2}(3\mu_x + \mu_y)$$

$$G^y_{2,4a} = -G^x_{2,4b} = 3\sqrt{2/2}(\mu_y + 3\mu_x)$$

The Coriolis coupling constants, ζ_{ij} are evaluated from the relation

$$\zeta^{\alpha} = L^{-1}G^{\alpha}(L')^{-1}.$$

6. Shrinkage effect

The Bastiansen-Morino shrinkage effect for these molecules are evaluated for 298 K, 500 K and 1000 K in terms of symmetrised mean square amplitudes of vibration matrices Σ'_s .

7. Centrifugal distortion constants

Cyvin *et al* (1968) have reformulated the theory of centrifugal distortion by introducing certain new elements $T_{\alpha\beta}'$ s instead of partial derivatives of inertia

tensor components $J_{\alpha\beta'\delta}$ (Kivelson and Wilson 1952, 1953). The quantities $t_{\alpha\beta\gamma\delta}$ are obtained using Cyvin's relation and hence $b_{\alpha\beta\gamma\delta}$ values are evaluated. The centrifugal stretching coefficients D_J , D_K , D_{JK} , R_δ , R'_δ and δ_J are obtained by the linear combination of the b'_δ . The values of the centrifugal distortion constants are useful for the microwave analysis of these molecules.

8. Results and discussion

The evaluated kinetic and force constants are listed in tables 1 and 2 respectively. The individual force constants (both in plane and out of plane) are obtained using the following redundancy conditions, $f_\alpha + 2f_{\alpha\alpha} = 0$, $f'_{n\alpha} + 2f_{r\alpha} = 0$. The calculated force constant values reproduce the vibrational frequencies accurately.

From tables 1 and 2 it is noted that all the kinetic constants in general increase as the mass of the Y atom increases for the same X atom, whereas in

Table 1. Kinetic constants (amu)

Molecule	$\frac{K_r}{K_{rr}}$	$\frac{K_\alpha}{-K_{\alpha\alpha}}$	$-\frac{K'_{r\alpha}}{K_{r\alpha}}$	K_{op}
ScF ₃	15.4599 1.7704	3.0420 1.5210	2.0440 1.0220	2.7929
ScCl ₃	27.1521 4.1544	5.1106 2.5553	4.7968 2.3984	3.5117
ScBr ₃	57.4964 11.2198	10.2836 5.1418	12.9538 6.4769	4.2072
ScI ₃	89.0669 18.9183	15.5886 7.7943	21.8406 10.9203	4.4683
YF ₃	16.5266 1.2370	3.3978 1.6989	1.4286 0.7143	3.8595
YCl ₃	29.0229 3.2190	5.7344 2.8672	3.7178 1.8589	5.3817
YBr ₃	60.5011 9.7175	11.2848 5.6424	11.2238 5.6119	7.2075
YI ₃	92.6161 17.1438	16.7710 8.3855	19.8006 9.9003	8.0094
LaF ₃	17.1577 0.9214	3.6080 1.8040	1.0643 0.5321	4.4905
LaCl ₃	30.3347 2.5631	6.1714 3.0857	2.9608 1.4804	6.6934
LaBr ₃	63.0671 8.4345	12.1406 6.0703	9.7448 4.8724	9.7752
LaI ₃	95.9206 15.4915	17.8732 8.9366	17.9018 8.9509	11.3071

Table 2. Force Constant_i (*m* dyne/Å)

Molecule	f_r $-f_{rr}$	f_a $-f_{aa}$	$-f'_{rx}$ f_{rx}	$f_{\theta\theta}$
ScF ₃	5.3252 0.0716	0.1260 0.0630	0.0846 0.0423	0.1114
ScCl ₃	3.2769 0.0478	0.0772 0.0386	0.0724 0.0362	0.0671
ScBr ₃	2.8645 0.0745	0.0668 0.0334	0.0842 0.0421	0.0558
ScI ₃	2.1809 0.0716	0.0451 0.0226	0.0632 0.0316	0.0412
YF ₃	4.6477 0.0188	0.1106 0.0553	0.0466 0.0233	0.0957
YCl ₃	3.0888 0.0343	0.0710 0.0355	0.0460 0.0230	0.0622
YBr ₃	2.7594 0.0779	0.0602 0.0301	0.0598 0.0299	0.0515
YI ₃	2.0329 0.0585	0.0418 0.0209	0.0494 0.0247	0.0383
LaF ₃	3.8034 0.0169	0.0894 0.0447	0.0264 0.0132	0.0811
LaCl ₃	2.8772 0.0070	0.0664 0.0332	0.0318 0.0159	0.0568
LaBr ₃	2.5963 0.0511	0.0578 0.0289	0.0464 0.0232	0.0520
LaI ₃	1.8564 0.0291	0.0446 0.0223	0.0446 0.0223	0.0375

the case of force constants a reverse trend is observed except in the case of interaction constants f_{rr} , f'_{rx} and f_{rx} . As the mass of the X atom increases for the same Y atom, the kinetic constants show an increase except the interaction constants K_{rr} , K'_{rx} and K_{rx} which show a reverse trend, whereas all the force constants show a decrease.

From table 2, it is apparent that the stretching force constant f_r decreases as the mass of the Y atom increases i.e.

$$f_r(\text{X-F}_3) > f_r(\text{X-Cl}_3) > f_r(\text{X-Br}_3) > f_r(\text{X-I}_3).$$

This is in accordance with the decrease in the electronegativity and increases in the atomic radii from F to I.

The calculated compliance constants are given in table 3. The compliance constants in general increase as the mass of the X atom increases for the same Y atom and also increase as the mass of the Y atom increases for the same X

Table 3. Compliance constants ($\text{\AA}/\text{m dynes}$)

Molecule	C_r C_{rr}	C_a $-C_{aa}$	C'_{ra} $-C_{ra}$	C_{op}
ScF ₃	0.1899 0.1567	3.5840 1.7920	0.0844 0.0422	8.9804
ScCl ₃	0.3116 0.0013	4.9428 2.9714	0.1942 0.0971	14.9006
ScBr ₃	0.8625 0.0028	7.0272 3.5136	0.3022 0.1511	17.9115
ScI ₃	0.4777 0.0065	10.5010 5.2505	0.4402 0.2201	24.2728
YF ₃	0.2161 0.0009	4.0414 2.0207	0.0604 0.0302	10.4531
YCl ₃	0.3270 0.0021	6.3410 3.1705	0.1404 0.0702	16.0730
YBr ₃	0.3705 0.0067	7.6396 3.8198	0.2412 0.1206	19.4305
YI ₃	0.5006 0.0077	11.0978 5.5489	0.3928 0.1964	26.1355
LaF ₃	0.2635 0.0009	4.9850 2.4925	0.0516 0.0258	12.3305
LaCl ₃	0.3493 0.0001	6.7534 3.3767	0.1118 0.0559	17.5907
LaBr ₃	0.3909 0.0050	7.8278 3.9139	0.2066 0.1033	19.2289
LaI ₃	0.5519 0.0021	10.3464 5.1732	0.3672 0.1836	26.6531

atom. From table 3 it is found that the compliance constants C_r are in the order of

$$C_r(\text{Sc-Y}_3) < C_r(\text{Y-Y}_3) < C_r(\text{La-Y}_3)$$

and also

$$C_r(\text{X-F}_3) < C_r(\text{X-Cl}_3) < C_r(\text{X-Br}_3) < C_r(\text{X-I}_3)$$

which supports the trend of variation in the strength of chemical bonding.

The presently evaluated mean amplitude of vibration at three temperatures are reported in table 4 along with the experimental values (Akishin *et al* 1959a, 1959b). From table 4 it can be noted that the calculated mean amplitude values for few molecules at 1000 K are in good agreement with the experimental values. However, in some cases the calculated values do not agree well with the observed values. A similar trend was also observed by (Phongastha 1977). It is found that the mean amplitudes of vibration for non-bonded atom pairs are greater than those of bonded atom pairs at the three temperatures. It can also be seen from table 4 that the mean amplitude of vibration increases as the temperature increases.

Table 4. Mean amplitudes of vibration (\AA)

Temp	ScF ₃	ScCl ₃	ScBr ₃	ScI ₃	YF ₃	YCl ₃	YBr ₃	YI ₃	LaF ₃	LaCl ₃	LaBr ₃	LaI ₃
298K	0.0400	0.0436	0.0439 *	0.0485	0.0403	0.0429	0.0428	0.0483	0.0424	0.0434	0.0432	0.0497
500K	0.0432	0.0504	0.0527	0.0595	0.0444	0.0501	0.0524	0.0604	0.0477	0.0519	0.0534	0.0627
1000K	0.0540	0.0671	0.0717	0.0819	0.0568 0.0540* (0.057)	0.0683 0.0680* (0.069)	0.0722 0.0670* (0.073)	0.0841 0.0620* (0.085)	0.0622 0.0500+ (0.063)	0.0705 0.1180+ (0.074)	0.0740 0.0920+ (0.075)	0.0876 0.1220+ (0.089)
298K	0.0764	0.0899	0.0935	0.1115	0.0810	0.0937	0.0983	0.1157	0.0887	0.0971	0.1004	0.1138
500K	0.0920	0.1130	0.1196	0.1436	0.0983	0.1180	0.1259	0.1550	0.1088	0.1227	0.1287	0.1467
1000K	0.1255	0.1577	0.1682	0.2026	0.1347 0.1530* (0.137)	0.1650 0.2800* (0.168)	0.1772 0.2500* (0.181)	0.2105 0.2700* (0.214)	0.1468 0.2600+ (0.152)	0.1715 0.5200+ (0.174)	0.1812 0.3700+ (0.185)	0.2070 0.4200+ (0.211)

* observed values from (Akishin 1959a) + observed values from ref (Akishin 1959b)
The values in the parentheses are from (Phongsatha 1977)

The evaluated Coriolis coupling constants, shrinkage effect and centrifugal stretching coefficients are listed in tables 5, 6 and 7 respectively.

Table 5. Coriolis Coupling coefficients

Molecule	ζ_{33}^z	ζ_{34}^z	$\zeta_{2,3a}^{\nu}$	$\zeta_{2,4a}^{\nu}$
	$= -\zeta_{44}^z$		$= -\zeta_{2,3b}^z$	$= -\zeta_{2,4b}^z$
ScF ₃	0.3880	0.9216	0.8331	0.5532
ScCl ₃	0.5419	0.8404	0.8782	0.4782
ScBr ₃	0.7273	0.6864	0.9293	0.3692
ScI ₃	0.8098	0.5877	0.9512	0.3080
YF ₃	0.2427	0.9701	0.7882	0.6156
YCl ₃	0.3743	0.9274	0.8289	0.5595
YBr ₃	0.5742	0.8187	0.8868	0.4623
YI ₃	0.6817	0.7317	0.9171	0.3987
LaF ₃	0.1703	0.9854	0.7651	0.6439
LaCl ₃	0.2769	0.9609	0.7991	0.6012
LaBr ₃	0.4633	0.8860	0.8552	0.5186
LaI ₃	0.5782	0.8160	0.8883	0.4601

Table 6. Shrinkage effect (Å)

Molecule	298K	500K	1000K
	δ	δ	δ
ScF ₃	0.00399	0.00619	0.01195
ScCl ₃	0.00514	0.00829	0.01630
ScBr ₃	0.00566	0.00924	0.01826
ScI ₃	0.00735	0.01211	0.02402
YF ₃	0.00409	0.00650	0.01271
YCl ₃	0.00504	0.00824	0.01630
YBr ₃	0.00566	0.00935	0.01858
YI ₃	0.00738	0.01225	0.02440
LaF ₃	0.00441	0.00712	0.01364
LaCl ₃	0.00510	0.00840	0.01667
LaBr ₃	0.00539	0.00894	0.01779
LaI ₃	0.00673	0.01120	0.02233

Table 7. Centrifugal stretching coefficients (KH_2)

Molecule	D_J	D_K	$-D_{JK}$
ScF_3	3.1799	2.7840	5.8071
ScCl_3	0.4575	0.3972	0.8346
ScBr_3	0.0733	0.0640	0.1342
ScI_3	0.0266	0.0235	0.0491
YF_3	2.4771	2.1617	4.5337
YCl_3	0.3441	0.3005	0.6301
YBr_3	0.0538	0.0470	0.0985
YI_3	0.0208	0.0183	0.0383
LaF_3	1.8569	1.6257	3.4956
LaCl_3	0.2734	0.2395	0.5016
LaBr_3	0.0451	0.0396	0.0829
LaI_3	0.0138	0.0119	0.0251

It is observed from table 5 that

$$\zeta_{33}^z = -\zeta_{44}^z, \quad (\zeta_{33}^z)^2 + (\zeta_{34}^z)^2 = 1, \\ (\zeta_{2,3a}^y)^2 + (\zeta_{2,4a}^y)^2 = 1 \quad \text{and} \quad 2(\zeta_{2,3a}^y)^2 - 1 = \zeta_{33}^z$$

are satisfied for all the molecules. The Coriolis coupling constants are useful in vibration-rotation interaction studies. From table 6 it can be noted that the shrinkage effect increases as the temperature increases.

It is observed from table 7 that the centrifugal stretching coefficients are very sensitive to the mass of the molecules. The centrifugal stretching coefficients decrease as the mass of the molecule increases. Since these molecules are planar symmetric top, Dowling's (1961) sum rule is found to be satisfied and also the centrifugal stretching coefficients R_5 , R_6 and δ_J vanish.

9. Conclusion

Thus using kinetic constant method all the molecular constants are evaluated for Scandium subgroup trihalide monomers. The molecular constants evaluated presently are quite reasonable and a systematic set of molecular constants are obtained.

Acknowledgment

The authors wish to thank the management and Professor D K P Varadarajan, Principal, PSG College of Arts and Science for their kind encouragement.

References

- Akishin P A *et al* 1959a *Kristallografiya* **4** 194
Akishin P J *et al* 1959b *Nauchn. Dokl. Vysshei Shkoly Khimiya* **1** 229
Cyvin S J 1968 *Molecular vibrations and Mean square amplitude*, Universitetsforlaget, Oslo and Elsevier Amsterdam.
Cyvin S J *et al* 1968 *Z. Naturf.* **23a** 1649
Decius J C 1963 *J. Chem. Phys.* **38** 241
Dowling M 1961 *J. Molec. Spectry.* **6** 550
Kivelson D and E B Wilson Jr 1952 *J. Chem. Phys.* **20** 1575
Kivelson D and E B Wilson Jr 1953 *J. Chem. Phys.* **21** 1220
Krasnov K S 1967 *Teplofizika Vysokikh Temperatur* **5** 715
Meal J H and Polo S R 1956 *J. Chem. Phys.* **24** 1119
Phongsatha A 1977 *Thesis No. 18 The University of Trondheim, Norway*
Srinivasacharya K G *et al* 1978 *Spectroscopy Letters* **11** No. 8 625

Rotational isomerism of some aliphatic esters

R Das, S Chattopadhyay and G S Kastha

Department, of Optics

Indian Association for the Cultivation of Science, Jadavpur, Calcutta-700032.

Received 5 February 1979

Abstract. The PCILO method of ground state energy calculation has been used for conformational studies of the molecules of the methyl esters of formic acid, acetic acid, cyanoacetic acid, mercaptoacetic acid, 2 chloropropionic acid and chloro-oxalic acid; conclusions therefrom have been compared with the experimental results available from the published literature. Only in the case of monomethyl oxalate chloride the liquid phase Laser Raman spectra and infrared absorption spectra have been recorded. The energy difference of the two rotamers of methylecyanoacetate has been experimentally determined in the present investigation.

1. Introduction

Though experimental studies on the rotational isomerism in aliphatic carboxylic esters and their derivatives have been reported in the literature, only a few theoretical calculations on their rotameric properties have been published. Consequently, the conformational characteristics of these molecules have not been reasonably established in most cases. In order to provide the necessary data, semiempirical computations of the conformational properties of some of the esters of formic acid, acetic acid, propionic acid and oxalic acid have been carried out and the results of these have been compared with the experimental observations, wherever available. Since for the molecules of methylecyanoacetate and monomethyl oxalate chloride, complete experimental data are not available, Raman and infrared studies have been made for the required comparison. The relevant results have been discussed in the present paper.

2. Experimental

Chemically pure methylecyanoacetate and monomethyl oxalate chloride procured from Fluka A.G. were further purified by repeated distillation under reduced pressure before being used in the investigation. The Raman spectra of monomethyl oxalate chloride in the liquid phase at 298°K were obtained with a recording grating spectrometer using 4880 Å radiations from an Argon-ion Laser for excitation. The liquid phase Raman spectra of methyl-cyanoacetate at different temperatures between 298-370°K were obtained with the same instrument. The infrared absorption spectra of monomethyl oxalate chloride in the liquid phase at 298°K were obtained with a Beckman 20Å spectrophotometer.

3. Method of Calculations

Perturbative configuration interaction with localised orbital (PCILO) method have been used for the calculations of the ground state energies of the different configurations of the molecules. The details of the method used are the same as given by Bhaumik and Kastha (Bhaumik *et al* 1977). The stable conformers were identified from the positions of the minima of the potential energy surface and the values of the energy differences between the conformers were determined from these energy minima.

4. Results and discussions

From the present calculations of the ground state energies of the molecules of methyl esters of formic acid, acetic acid, cyanoacetic acid, mercaptoacetic acid, 2-chloropropionic acid and chloro-oxalic acid, it has been found that in each case, the O-CH₃ bond remains fixed in *cis*-position with respect to C=O bond and all the rotameric forms, in these molecules, arise from orientations of the atoms or groups of atoms about the C-C bonds in them. This inference drawn from the present calculations by the PCILO method is in full agreement with the conclusions from the available experimental results (Charles *et al* 1973, Som and Mukherjee 1975, 1976, Das *et al* 1977, 1978). The rotation about the C-O bond being of minor importance in relation to rotameric forms, only the theoretical observations relating to different configurations arising from the rotations about other internal axes are discussed in the following paragraphs.

Methyl formate and methyl acetate

In each of the molecules of methyl formate and methyl acetate, ground state energy versus dihedral angle curve computed by the PCILO method shows only one minimum indicating the presence of only one stable rotameric configuration round the C-C bond. These conclusions are in accord with the experimental reports (Curb 1959, George *et al* 1972, Wilmschurst 1957) for both the molecules and the *ab initio* calculation for methyl formate (John *et al* 1977).

Methylcyanoacetate, methyl mercaptoacetate and methyl 2-chloropropionate :

The study of Raman and infrared spectra of methylcyanoacetate molecule have been reported previously by a number of authors. According to Charles *et al* (1973) this molecule exists as two rotamers, *cis* and *gauche*, about the C-C axis, while Sinha (1974) pointed out that a larger number of rotamers arising from the rotations about both the C-C and C-O axes might be present. The results of the present calculations show the existence of only the *cis* and *gauche* forms about the C-C bond and this is in agreement with the former view. The value of the energy difference between the two rotamers has been calculated by the PCILO method and also by CLASSICAL method. From these calculations, it is found that the *cis* form is less stable than the *g* form by about 360 cal/mole.

Charles *et al* from infrared measurements obtained a value of 1 Kcal/mole for the value of the energy difference *cis* being the more stable form. This has also been determined in the present investigation by studying the temperature dependence of the intensity-ratio of the Raman bands at 900 cm^{-1} and 850 cm^{-1} assigned to the C-C stretching modes of vibration of the two rotamers. A value of about 400 cal/mole has been obtained which is very near to the previously measured value. It might be noted that the change of relative

Table 1. Raman shifts and infrared bands of monomethyl oxalate chloride

Raman shift $\Delta_{\text{cm}^{-1}}$	Infrared bands cm^{-1}	Assignments
181 (w)		R(CoCl)
243 (w)		δ (C-C-Cl)
304 (m)		δ (C-O-C)
353 (m)		δ (C-C-O)/ δ (C-C = O)
	480 (m)	δ (O = C-Cl)
500 (s)		π (C = O)
577 (m)	570 (w)	δ (O = C-O)
795 (vs)	790 (sb)	ν (C-Cl)
898 (s)	890 (m)	} ν (O-CH ₃)
932 (m)	930 (m)	
995 (m)	985 (s)	} ν (C-C)
1013 (m)	1015 (s)	
1150 (w)	1150 (m)	} R(CH ₃)
1190 (w)	1200 (s)	
		O \parallel ν (C-O)
1273 (m)	1270 (sb)	} δ (CH ₃)
	1435 (s)	
1456 (m)	1460 (sb)	} ν (C = O)
1755 (v.s)	1770 (v.s)	
1786 (s)		} ν (C-H)
2852 (m)	2850 (w)	
2987 (v.s.)	2975 (m)	
	3015 (w)	
3037 (wb)		

stability of the forms due to change of state may be the reason of this difference of theoretical and experimental values.

The PCILO method was also applied to the calculation of energy of the different configurations of the molecules of methyl mercapto acetate, but the results were not satisfactory. So computation of the conformational energy was made by using the CLASSICAL method. According to the experimental results (Das *et al* 1978), this molecule exists in the *cis* and *gauche* configurations, about the C-C axis, but these results did not provide any information about their relative stability. The present theoretical calculations show the existence of the *cis* and *gauche* rotamers for this molecule and the two forms are predicted to be of nearly the same energy.

In the case of methyl 2-chloropropionate also, Raman and infrared studies (Das *et al* 1977) revealed the presence of three rotameric forms, but the relative energy difference between the different rotamers could not be measured experimentally. The present calculation by the PCILO method indicate the existence of one *cis* and two *gauche* conformers, one of the *gauche* rotamers g_1 , is the most stable form, while the *cis* conformer is the least stable, the energy difference between them being ~ 1 Kcal/mole. The second *gauche* form g_2 is higher in energy than the most stable form by about 300 cal/mole. This is qualitatively in agreement drawn from the experimental results mentioned above.

Monomethyl oxalate chloride : In the molecules of oxalyl halides, there are controversies as to whether these molecules are capable of existing in different rotameric forms around the C-C axis. Kagarise *et al* (1951), Kagarise (1966) concluded that the molecules of oxalyl chloride can have a number of rotameric forms, while from experimental results in oxalyl halides Ziomek *et al* (1953) and Hencher *et al* (1965) did not consider this to be probable. Similarly in the molecule of dimethyl oxalate (Wilmschurst 1966), the vibrational spectrum has been assigned on the assumption of the presence of only one molecular form. The present molecule of monomethyl oxalate chloride has a structure intermediate between oxalyl chloride and dimethyl oxalate and there are no reports on its conformational forms. To investigate this point the Raman and infrared spectra of the molecule have been recorded and the experimental results have been analysed. In monomethyloxalate chloride, the Raman and infrared spectra show four bands in the region $890-1020\text{ cm}^{-1}$, all of them appearing as bands of either strong or medium intensity. But in each of the similar molecules of oxalyl chlorides and dimethyl oxalate the bands in the corresponding region are rather weak. Ziomek *et al* and Wilmschurst *et al* interpreted these bands as combinations or overtones and suggested that these molecules exist in only one stable configuration, while Saksena *et al* assigned these bands to fundamental vibrations and suggested rotational isomerism in these molecules. In the present case of monomethyl oxalate chloride molecule, these bands being of appreciable intensity

can, in no way, be ruled out as combinations or overtones and has, therefore been treated as fundamentals.

In ester molecules, two fundamental frequencies due to C-C and H₃C-O stretching modes for each single configuration are, generally expected, in the frequency region 900-1050 cm⁻¹. The presence of four vibrational bands in the aforesaid region in both Raman and the infrared spectra of monomethyl oxalato chloride, therefore indicates the existence of more than one conformer in the molecule. Following the assignments made in dimethyl oxalate (Wilmschurst 1966), the higher two of the frequencies in the region have been attributed to the C-C stretching modes, and the two lower frequencies have been assigned to the O-CH₃ stretching modes of vibration. The present calculations by PCILO method predict the existence of two rotamers trans and cis of which the former one is more stable than the latter one by about 600 cal/mole.

References

- Bhaumik D and Kastha G S 1977 *Indian J. Phys.* **51B** 202
 Charles S W, Jones G I L and Owen N L 1973 *J. Chem. Soc. Part II (Trans Farad)* **69** 1454
 Curl R F 1959 *J. Chem. Phys.* **30** 1520
 Das R and Nandy S K 1977 *Indian J. Phys.* **52B** 85
 Das R and Chattopadhyaya S 1978 *Indian J. Pure Applied Phys.*, **16** 482
 George W O, Hassid D V and Maddams W F 1973 *J. Chem. Soc., Perkin II* 952
 Hencher J L and King G W 1965 *J. Mol. Spectry.*, **16** 158
 John I G and Randon L 1977 *J. Mol. Structure* **36** 133
 Kagarise R E 1953 *J. Chem. Phys.* **21** 1615
 Saksena B D and Kagarise R E 1951 *J. Chem. Phys.* **19** 987
 Sinha D 1974 *Can. J. Chem.* **52** 3054
 Som J and Mukherjee D K 1975 *Indian J. Pure Appl. Phys.* **13** 348
 Som J and Mukherjee D K 1976 *Indian. J. Pure Appl. Phys.* **14** 15
 Wilmschurst J K 1957 *J. Mol. Spectry.* **1** 201
 Wilmschurst J K 1966 *J. Mol. Spectry.* **21** 48
 Ziomek J S, Meister A G, Cleveland E F and Decker C E 1953 *J. Chem. Phys.* **21** 90

Book Review

Lecture Notes in Physics, Volume 34 : One Dimensional Conductors,
Edited by J. Ehlers, K. Hepp and H. A. Weidenmuller. Publishers :
Springer-Verlag, 1975, \$ 13.80.

The present volume 34 under the well-known series entitled *Lecture Notes on Physics* records the Conference proceedings on the exciting topic of one dimensional (1D) conductors, which has recently drawn wide-spread attention of both theoretical and experimental physicists. The Conference was organized by the Low Temperature Division of the German Physical Society in Co-operation with the University of the Saarland in July 1974. Altogether 24 papers by noted workers in this field were presented at this Conference covering several aspects of the 1D conductors.

In this Conference volume the introduction and survey of the literature by the editor Dr. H. G. Schuster give an up-to-date account on 1D conductors. For a long time 1D electrical conductor described as a single ionic chain with electrons hopping along had been a mathematical fiction and a number of startling predictions were made by theorists. Recently, it has become possible to do experimental measurements on the physical properties of compounds which behave like 1D conductors and this has revived considerable interest on this subject. Typically, KCP ($K_2Pt(CN)_4Br \cdot 0.3.3H_2O$) and TTF-TCNQ (tetra-thiofulvalinum tetracyanoquinodimethan) are the two most prominent representatives of 1D conductors, for which specific requirements must be met for the chemical preparation. Due to their extremely anisotropic electrical conductivity with nearly metallic like conduction in one dimension these compounds are called 1D conductors. On lowering the temperature in the range of 50–100°K, the electrical conductivity along the main axis, drops suddenly indicating a phase transition, and this is associated with a lot of interesting problems, namely, structural Peierls-transition, Frohlich-superconductivity and Frohlich-mode, Fluctuations etc. In the present proceedings, these problems have been given due considerations which are really interesting and exciting too. Another appealing aspect of these 1D conductors is that they may be compared to exactly solvable 1D models.

We thank the Organizers as well as the Publishers for bringing out such an important and helpful volume dealing with a very current research topic of fundamental interests. We also eagerly await the future proceedings covering other important aspects such as the role of impurities, the possibility of copper-pair superconductivity, magnetic properties etc.

S.P.S.G.

Effective Interactions and Operators in Nuclei

Edited by B. R. Barrett, Springer-Verlag, 1975.

This book contains the invited talks presented at an International Topical Conference held at the University of Arizona in Tucson from June 2 to 6, 1975. The coverage of material in the talks was planned quite comprehensively so as to bring together all the developments of the subject till the time of the conference. There being no other major development since then, the book remains quite useful as a source of nearly up-to-date informations on the subject of effective interactions and operators.

Theoretical understanding of effective interactions for the valence nucleons is invariably based on the degenerate perturbation theory and the initial groundwork was laid down by Bloch and Horowitz. More recently Brandow has made significant contributions by drawing attention to the so-called 'folded diagrams'. The first article in the present book is by Brandow in which he has very commendably reviewed the perturbation theory of effective interactions. There are two more alternative derivations based on the time-dependent perturbation theory and these are described in the next two articles by Johnson (the approach of Johnson-Baranger) and Ratcliff (the Ratcliff-Kuo approach).

The article by Sauer discusses an important practical question, namely how best to choose the single-particle basis wavefunctions for the computation. Major computational details of the G -matrix are then discussed in the papers by Becker and Barrett.

The problem of convergence of the perturbation expansion is discussed in the articles by Goode and Weidenmüller.

Two papers, one by Talmi and the other by Schiffer attempt to relate experimental data directly to effective interaction matrix elements. However, Talmi's paper contains only his old published results.

Several alternative approaches to the effective interaction have been developed in recent years and some of these have been refreshingly covered in this conference. The article by French, reviewing his statistical approach, the method of Pado approximation for the calculation of effective interaction by Schucan and the review of density-dependent potential given by Negele deserve mention.

To justify fully the title of the conference Ellis discusses the calculation of effective operators other than the Hamiltonian using the quadrupole operator for illustration.

The conference summary by Kirson is illuminating. It brings out clearly the distinctive features of the three approaches to the perturbation theory, the question of convergence, choice of basis etc. It also rightly evaluates the "new phenomenology" of the Skyrme-type density-dependent interactions.

This book, as mentioned earlier, will be helpful and instructive to anyone wishing to specialise on effective interactions.

M.K.P.

Electroluminescence

Editor : J. I. Pankove. (Topics in Applied Physics, Volume 17; Springer-Vörlag).

Electroluminescence is a very attractive topic in applied physics from the practical stand point. EL devices have a variety of applications. The present volume makes one aware of the fact that though the field is more than fifty years old, much progress remains to be achieved in the field of application development as well as in fundamental studies. The six reviews making up this volume have been written by scientists of long expertise in their respective fields. While the qualities of the reviews are generally high, few of the authors have provided guidelines for further advancement in fundamental studies.

In the first chapter Pankove introduces the readers to the field of electroluminescence with all its variety of phenomena. Tairov and Vodekov in their review discuss group IV indirect gap materials but they confine their discussion mainly to broad band semiconductor SiC well known for its high luminescence efficiency. In the third chapter Dean reviews the group III-V materials from which the commercially available light emitting devices (LEDs) are generally made. This is a good review and ends with a discussion of future prospects of III-V materials as LEDs. Efficient visible luminescence materials of II-VI compounds as sources of LEDs have been discussed by Park and Shin in the fourth chapter. Discussion on Zn and Cd Chalcogenides and alloy of II-VI materials in this chapter is of great interest because of their excellent luminescence properties in the whole visible and near UV range.

Chalcopyrite type semiconductor based devices are new members of LEDs family. In the fifth chapter Wagner explores the possibility of their more extensive commercial exploitation.

In the concluding chapter Inoguchi and Mito discuss the electroluminescence by means of phosphor films and its future prospect in the field of information display.

As one goes through the book one feels assured that the volume will amply serve the expectation of the editor to educate the newcomers in this field of Physics and also to provide specialists with useful references.

T.N.M.

Polarization Nuclear Physics

Edited by D. Fick, Springer-Verlag, 1974.

This book has been published in the *Lecture notes on Physics* series and consists of the proceedings of a meeting held at Ebermannstadt on October 1-5, 1973, on the occasion of the 70th birthday of Professor Rudolf Fleischmann, one of the earliest proponents of the field of nuclear polarization physics. The publication contains nine full-length papers delivered at the conference together with a one-page remark by H. A. Weidenmüller on the organization of the material. The papers, as they appear, bear considerable evidence of an almost total absence of editing by the editor. The remarks by Weidenmüller properly belongs next to the preface but the reader would be amused to find it interposed somewhere in the middle of the book.

All the papers are written with a fairly comprehensive list of references but some of them do little more than cataloguing of the different methods. Needless to say, intelligent readers, even if they be beginners to whom these papers were primarily addressed according to the preface, will not comprehend the subject from those papers and will have to work their way through only with the help of the original references or other review articles. The paper on nucleon-nucleon force gives a standard review of the subject but unfortunately it scrupulously avoids any reference to polarisation in two-nucleon physics although the coverage of the latter topic would have justified more its inclusion in a book on polarization nuclear physics. Approximately half of the papers are good and also serve well the pedagogic purpose mentioned in the preface.

M.K.P.

Nuclear Optical Model Potential

Edited by S. Boffi and G. Passatore, No. 55 of Lecture Notes in Physics, Published by Springer-Verlag, 1976.

The book contains a few articles on optical model potential as discussed in a symposium in Pavia, Italy in 1976. It discusses many interesting aspects of optical model but it omits a few other important work and recent references.

S.M.

Materials Reference Series II : Mechanical Properties, Vol. 1, 1975

Edited by F. H. Wohlbier, Trans. Tech. S. A., Switzerland.

The book under review is a periodic compilation, issued in two volumes in a year under Materials Reference Series II, of reported data and new observations on the mechanical properties of a wide range of technologically and fundamentally important materials namely, Ferrous and non-Ferrous metals and alloys, Ionic, semiconducting, Ceramic and Composite materials. The defect data on these materials are compiled in 'Materials Reference Series I : Diffusion and

Defect Data', which is also an upto-date and comprehensive reference book to the materials scientists. The purpose of the series is to provide ready reference data on these materials of importance to the materials scientist who 'needs to be informed continually of the new developments in the field', and the volumes in the two series have undoubtedly filled this purpose. Since for the technologically important materials knowledge on the mechanical properties is considered to be the most vital one in relating strength and hardness of materials, this volume as well as the forthcoming ones will naturally prove to be extremely useful and serve the purpose of standard reference books to a large number of research workers engaged in the fundamental and applied works on the development of new materials with improved properties. The editor and the publishers are to be thanked for bringing out such a well-arranged offset production of the series covering the topics of a large number of published research papers in this field.

S.P.S.G.

The Mathematical Theory of Electricity and Magnetism

The Macmillan Co. of India Ltd. Price Rs. 49-50.

The book appears to be self-contained insofar as it supplied almost all the mathematical pre-requisites. It starts with a chapter on vector analysis, other mathematical topics being discussed before they are needed. Some topics are briefly treated in the appendices.

Although the mathematization of electromagnetic phenomena is useful, the use of terminologies like "equivalence class of displacements" etc. is not helpful in stimulating interest in the study of the subject. Such use should, therefore, be avoided so that the book may be readable by the students of mathematics as well as of physics. A discussion of the units and dimensions is of much importance in the theory of electromagnetism. The particular system of units employed should be explicitly mentioned whenever necessary to avoid confusion and a table showing the numerical relationships among different systems of units should be incorporated.

There appears to be a discrepancy between the preface and the table of contents on the one hand and the actual contents in the book on the other. For example, the preface says that "some of the interdisciplinary subjects that have grown out of the fusion of electromagnetic fields and of piezoelectricity and electro-fluid mechanics are also briefly treated". But apart from the conventional treatment of electromagnetic wave in anisotropic media, no such discussion appears in the book. Again, the table of contents shows five appendices. But appendices IV and V appears to be mission. Finally, it may be mentioned that a large number of misprints has crept into the book.

It is expected that the book will serve as a useful literature to meet the needs of the students of physical sciences, if these limitations are removed.

G.B.

Environmental Radiation Measurements (NORP Report No. 50):
National Council on Radiation Protection and Measurements,
7910 Woodmont Avenue, Washington D.C. 20014 (1976 VI+246
pages). Price not stated.

The report by National Council of Radiation Protection and Measurement, entitled *Environmental Radiation Measurements* is mainly divided in three parts. The first part consists of the information on the properties of the radionuclide deposition and of radiation fields in the environment. The next part or the bulk of the report deals with the methods of their measurement with special emphasis on the estimation of the dose delivered to man. The last part contains a critical assessment of the limitations of the present knowledge in investigating the long term trends of redistribution of natural and man made radioactivity and emphasises the extreme importance of continuous monitoring of radiation fields due to different natural and manmade sources at the national and international level, analyse the data and obtain objective conclusions regarding the slow but continuous changes in environmental radioactivity.

The philosophy behind the entire book is that, due to the increased development of nuclear power, and the increased need of radiation in medical, agricultural industrial, research and other essential fields man's interaction with radiation is increasing; this is unavoidable. At the same time the population at large must be protected from incurring damages due to radiation. The change due to radiation can be divided in two categories in general. One is somatic and another genetic. It is the second category of danger that makes the subject so important, because the genetic damage may not be confined to a single person, or to a single generation, but the deleterious effects of radiation can manifest itself after several generations. This is an unseen danger. Man's increasing use of radiation energy changes the environment i.e., altering the danger level. Hence, a constant vigilance in the measurement of background level of radiation is a part of modern civilization. Naturally, the instrumentation part, analysis or the data obtained and the overall deficiency of the entire programme needs careful consideration. This book has served this purpose quite efficiently. This being a publication by N.C.R.P., the authors had the advantage of having a large amount of data to make the book successful. By avoiding too many technicalities, the authors have made the book useful, readable and understandable to persons of various disciplines like physics, chemistry, engineering and medicine. The report will serve as a guide book to the people engaged in radiation protection and radioactive waste disposal. To those teaching or developing postgraduate level courses in radiation biophysics, this report will be an invaluable aid. On the whole, the National Council of Radiation Protection and Measurement deserves our gratitude for providing such a good book on a most important subject. This book is must for all science libraries.

B. Bagchi and R. K. Poddar

Dye Lasers

Edited by F. P. Schdffer.

The book is a compilation of review articles on various aspects of principles, operation, applications and progress in dye lasers during the last four years.

The first chapter which deals with the principles of dye laser operation is very lucidly presented and is very helpful for beginners in the field. The articles on structure and properties of laser dye gives one a multitude choise of dye system and their limitations. The various applications of dye lasers in different field is well discussed by T. W. Hansch. The last chapter is devoted to the informations of progress made in the field of dye lasers and laser dyes during the last four years (1973 to 1977). The complete treatment of various aspects of dye laser will help immensely both beginners and those who are already working in this highly active field.

R.K.M.

Green's Functions for Solid State Physicists

By S. Doniach and E. H. Sondheimer. W. A. Benjamin Inc., pp. 226, \$ 12.00.

The Green's function technique has recently become the most powerful technique in manybody problem. There are few books on this subject notably that of Abrikosov and Kadanoff which deal mainly with the mathematical aspects of the subject with a few applications. But in solid state physics, specially for the disordered system whether one deals with lattice dynamics, energy bands or magnetism, the Green's function method has become the darling of the theoretical physicists. And therefore, this book of Doniach and Sondheimer is a welcome addition to the theoretical solid state physicists.

The book starts with an example of lattice in the Harmonic Oscillator and the authors develop most of the preliminary results of the Green's function through this example. His development of the temperature Green's function, although very concise, is really very lucid. The chapters on the anharmonicity and electrons in the presence of many impurities and on magnetism are well written, but the main drawback is their compactness which may be suitable for readers who have already some knowledge of Green's function theory. In short the book, although deals only with few subjects, is well written and is very suitable for readers (having already a little knowledge of the Green's function's method) who want to learn how to apply Green's function method to the Solid State theory.

S.C.

Integrated Optics

Edited by T. Tamir, Springer-Verlag Berlin Heidelberg, New York, 1975, pp. XI+315 \$ 32.80.

The *Integrated Optics* is the seventh volume of a series of publications on *Topics in Applied Physics*. This new technology is the outcome of researches in various scientific disciplines and is still in developing stage. Integrated Optics may be called the miniature counterpart of microwave device and when properly developed, it may open immense possibilities in communications at optical frequencies. No doubt, the discovery of laser has given a vigorous impetus for fast developing of this technology.

This monograph consists of six chapters contributed by five authors. The introductory chapter gives a historical survey of the development of this technology during the last fifteen years with its immediate and future prospects. In the second chapter is given, in detail, the theory of dielectric thin film wave guide which is the backbone of optical communications. Chapter 3, discusses the design and construction of passive components like prism and grating couplers which are required to couple the laser beam to the thin film wave guides. The active components like modulation, switches, photodetection etc. have been discussed in Chapter 4. Modulation of light waves has been considered from two view points : (i) variation of intensity, phase, polarization and frequency, (ii) modulation effected by electro optic, magneto optic and acousto optic processes. Relative merit of both the methods have been compared. In Chapter 5, the various methods (Sputtering, plasma polymerization, spinning and dipping, etc.) of film depositions on substrates for the fabrication of passive structure from amorphous materials, have been described. The importance of semiconductors for fabrication of various components for totally integrated optics has been discussed in detail in Chapter 6. GaAs has been found to be the only semiconductor in which all the functions of light generation, guiding, coupling, modulation and detection are possible. It is hoped that GaAs will play in integrated optics the same role that silicon does in integrated electronics.

Each chapter is followed by large number of upto date references.

The monograph will be particularly useful to research workers in thin film optics, microelectronics semiconductors, communication engineering etc.

Essential Relativity

By W. Rindler, Springer-Verlag, 2nd Edition, 1977, pp. 284, Price \$ 29.80.

The special and the general theory of relativity as well as the application of the general theory of relativity to the cosmological problem constitute the subject matter of the book. The treatment is lucid and at many points there are illuminating the critical discussions. The book will surely be of help to students taking up relevant courses.

The author spell out the purpose of the book as *to make relativity come alive conceptually*. Perhaps he has succeeded in doing this to a considerable degree. The reviewer however wonders whether this is an objective fit to be aimed at. After all our concepts are largely derived from our macroscopic world experience and very often carry the imprint of newtonian physics and euclidean geometry. To cite an example, a conceptual picture of Riemannian geometry in terms of the geometry of two dimensional surfaces is apt to lead to the not very welcome ideal that the *curvature* implied the existence of additional dimensions. Instances may be multiplied and one may feel that in many spheres of modern physics, it is better not to emphasise on *conceptions*.

It is rather unfortunate that there is no consideration of the deduction of field equations from a Variational principle. In a book published in 1977, one misses also any mention of tachyons and superlight velocities.

On the whole however the book is a welcome addition to the literature on the subject at the student level.

A.K.R.

Solid State Laser Engineering

Vol. 1, by W. Koechner.

The book as the name suggests us mainly directed to the practicing scientist or engineer who is interested in the design or use of solid state lasers.

Chapter 1 of the book discuss the fundamental concepts. Second chapter deals with the properties of most important solid-state laser mediums i.e., Ruby, Nd : YAG; Nd : Glass. Third and fourth chapter discuss the regenerative laser oscillator and amplifier and contain many useful graphs and tables useful to the designer. In chapters 5, 6, 7 optical resonator, pump-system and heat removal system are discussed. Chapters 8, 9, 10 describes how the laser output may be changed in power, frequency and pulsewidth by Q-switching. Non-linear devices and mode-locking.

Chapter 11 discusses the design of different lasers used in different application. Finally Chapter 12 gives the information that is useful to prevent the damage of the optical components.

The subject matter is presented clearly and is particularly useful to the student of laser physics who are interested also in designing the laser.

R.K.M.

Table of Laser in lines Gases and Vapours

By R. Beck, W. English and K. Gurra.

This catalog contains 4347 laser lines in gases and vapours reported up to April 1977, along with the operating conditions under which emission has been achieved. This complete listing will save the time of worker active in this field in finding the laser lines of his interest.

R.K.M.

Interplanetary Dust and Zodiacal Light

Lecture Notes in Physics, 48. Edited by H. Elsasser and H. Fechtig, (Springer-Verlag, Berlin) 1976, p. 493.

This volume containing Proceedings of the International Astronomical Union Colloquium No. 31 at Heidelberg between June 10 and 13, 1975, can be unreservedly recommended to all those working in the areas related to interplanetary dust and zodiacal light.

The section on zodiacal light has 19 papers devoted to observations from space, demonstrating the great advances made in observing techniques of the phenomenon which could not be observed with sufficient accuracy from the mountain-based stations. Other important topics covered include the measurements of interplanetary dust from satellites and space probes, the properties of cometary dust, the relationship between interplanetary dust and meteors. The theoretical problems relating to the physical properties and the possible sources of interplanetary dust together with the dynamics of dust particles are covered in a number of papers.

One of the important results to emerge from the colloquium was the density distribution of dust particles (varying inversely as the distance from the sun) derived from the observations of the zodiacal light with space probes. New results were reported on the spectral characteristics of the zodiacal light. No new light was, however, shed on the nature of the interplanetary dust and its chemical composition.

It is clear from the Proceedings that the subject is highly active and with more observations forthcoming from spacecrafts there will be a wealth of new information added. Hopefully, this will provide some clues about the origin of the interplanetary dust. The volume is neatly produced and is well worth having in a library which caters for research workers.

S.M.C.

Dynamics of Solids and Liquids by Neutron Scattering

Edited by S. W. Lovesey and T. Springer, Published by Springer-Verlag (Topics in Current Physics, Vol. 3), Berlin 1977.

The book under review, covering various aspects of research in condensed systems using inelastic neutron scattering, has come to be written almost 15 years since the publication of an earlier book entitled *Thermal Neutron Scattering* edited by P. A. Egelstaff. The latter book dealt with various aspects of neutron scattering and served to introduce basic techniques and theory of neutron scattering with application to solids, liquids, molecular systems and magnetic materials. Higher fluxes in several reactors in United States and Western Europe, combined with improved instrumentation and new techniques have made it possible to look at subtler and new phenomena in a variety of systems. The number of researchers in the West has enormously increased. The periodic International Atomic Energy Agency Conferences on Neutron Scattering and recent meetings like the Gatlinburg conference on "Neutron Scattering" and Potten meeting on "New Techniques in Neutron Diffraction" have all brought out a large amount of new information. It is therefore appropriate that review books summarising topics covered by such meetings and other publications be written periodically.

There are six review articles in the book each written by experts in the field. To back it all up, there is a comprehensive 'Introduction' by S. L. Lovesey. One may say that this introduction is an abridged version of the excellent book 'Theory of Thermal Neutron Scattering' by W. Marshall and S. L. Lovesey. Based on certain master equations, the chapter deals with various aspects of neutron scattering bringing under perview concepts such as correlation functions, phonons, magnetic excitations etc. This chapter helps to link the various other chapters together.

During the last ten years or so, the high flux reactors at Brookhaven National Laboratory (BNL), USA and Oak Ridge National Laboratory (ORNL), USA have been utilised very successfully in obtaining rich information on lattice dynamical aspects. In addition to conventional lattice dynamical studies in complex crystals like rutile, studies relating to soft modes and to phonon anomalies have been of major interest. The chapter on 'Phonons' by H. G. Smith and N. Wakabayashi deals mostly with the work from ORNL in superconducting materials like the transition metal carbides and related compounds, layered compounds like graphite, MoS_2 etc. It would have been appropriate to include the recent interesting work on low concentration defect modes and the extensive work on the quasi-one-dimensional systems KCP, TTF-TCNQ etc., where both BNL and ORNL have made notable contributions. Although the review covers experiments in which the authors have had a part, notably work originat-

ing in other research centres is somewhat not covered and hence the review is not extensive.

The next chapter on 'Phonons and Structural Phase Transitions' by B. Dorner and R. Comes is a useful chapter wherein certain basic concepts are discussed and illustrated with suitable examples. This chapter, I believe, is not meant to be an exhaustive review. Correlation of intensity of scattering to the dimensionality of the scattering system is highlighted. Description of X-ray and neutron scattering techniques discussed in this chapter could have formed part of 'Introduction' as there is a certain amount of commonness with the other chapters also.

It is but natural that one recollects the various NATO school proceedings and other books published recently while commenting on these two chapters. 'Soft Modes in Ferroelectrics and Antiferroelectrics', 'Structural Phase Transitions and Soft Modes', 'Anharmonic Lattices, Structural Transitions and Melting', 'Dynamical Properties of Solids' Vol. I and II etc. are some of them. These two chapters under review would but touch the fringe of the developments in the subject discussed in these books.

J. W. White discusses in the chapter devoted to 'Dynamics of Molecular Crystals, Polymers and Adsorbed Species', the nature of information obtained by incoherent scattering in a variety of polymers, molecular systems and adsorbed species on various substrates. Study of adsorbed species are carried out by experiments, —still in their infancy—, which are rather difficult owing to the penetration of neutrons into the substrate and the resulting scattering. This chapter serves as an introduction to researchers in study of various disciplines like catalysis, physisorption etc. involving surface phenomena. Both structural and dynamical information can be derived and this is illustrated with examples from recent studies.

T. Springer discusses in a chapter entitled 'Molecular Motion and diffusion in solids, in particular Hydrogen in metals', the problem of diffusion of hydrogen in metals and alloys, rotational motions of hydrogenous molecules like CH_3^+ and NH_4^+ in solids and of rotation and diffusion of molecules in liquids and liquid crystals. These studies are based on quasi-elastic neutron scattering into small energy changes in the range of 10^{-3} to 10^{-6} μeV . This chapter may be considered a companion to the treatise on 'Quasi-electric Neutron Scattering for Investigation of Diffusional Motion in Solids and Liquids' by T. Springer. Studies involving hydrogen in concentration range of 1% or less need high flux neutron sources. However, the other studies can be conveniently carried out in medium flux reactors. High resolution back scattering experiments have revealed quantum tunnelling transitions in the range of a few μeV . Several illustrative examples are provided.

R. D. Mountain's article on 'Collective Modes in Classical Monoatomic Liquids' is theoretically biased. Coherent neutron scattering studies and computer simulation provide information on collective modes. In this chapter the author reviews various theoretical approaches like the memory function models, conventional and general hydrodynamics to the study of correlated motions in liquids. Experimental data on the liquids helium, neon, argon and rubidium are discussed in relation to these theoretical models.

The last article by S. W. Lovesey and J. M. Loveluck is devoted to magnetic scattering. As the authors themselves have pointed out this chapter is of very restricted nature as far as inelastic magnetic neutron scattering is concerned. Brief discussions of magnons in ionic systems, quasi-one dimensional systems, layered magnetic systems, metals etc. are outlined. It is hoped that a book on neutron scattering from magnetic systems will be forthcoming to do justice to this vast field.

To conclude, the overall impression is that the book is well written by competent experts in various fields where neutron scattering has contributed to our understanding of the solid state and liquid state systems. The chapters, although written by different authors, have adequate coherence. The book gives an over-view of the state of the art to a beginner and an active researcher. To provide further information, the chapters are provided with sufficient references to other theoretical and experimental papers. In these days of exploding information and rapid obsolescence such ventures are necessary, useful and therefore welcome; the publishers and the editors deserve a word of appreciation.

K.R.R.

Ultrashort Light Pulses : Picosecond Techniques and Applications

(Topics in Advanced Physics, Volume 18), Edited by S. L. Shapiro,
Springer-Verlag : Berlin, Heidelberg, New York, 1977.

This is an excellent book to be commended to every scientist interested in direct temporal studies of extremely rapid events. Ultrashort light pulses have now become a basic research tool in physics, chemistry and biology. Many fundamental processes as free decay of molecular vibrations and orientational fluctuation in liquids, phonon decay and exciton migration in solids, growth and decay of plasmas in gases and solids, various intermolecular transfer and intramolecular relaxation processes have been and are being studied by pico-second light pulses together with ultrafast optical and electronic devices. Ultrashort pulses and their interaction with matter will, no doubt, remain a frontiers area in science and technology for many years to come. Publication of this volume at this time is therefore most welcome.

The book begins with an introduction by Shapiro who first gives a historical overview of the arts and sciences of measuring brief time interval and then discusses the origin of picosecond techniques and their advantages. Following this overview, Brodley in the second chapter describe various methods of ultrashort pulse generation and their measurement. This is a well written chapter. Various modelocked lasers are described and important measurements on the saturable absorbers are analysed in terms of laser operation. Techniques for producing pulses at other frequencies by harmonic generation is discussed. In the following chapter Ippen and Shank describe picosecond detection techniques. In the first half of this chapter they discuss measurement of pulse characteristics and emphasize that a combination of nonlinear correlation techniques can provide reliable information about the duration, shape and dynamic spectral behaviour of picosecond laser pulses. In the latter part Ippen and Shank describe various techniques for measuring picosecond events. Pump and probe technique, time resolved technique with continuously operated systems, light gating techniques and streak camera technique are described in detail.

In the fourth chapter Auston makes a point of discussing picosecond nonlinear optics and handles them with masterly expertise. The power available from modelocked lasers and laser amplifier system makes many higher order nonlinear effects observable. This discussion of transient stimulated Raman scattering and transient self focussing is excellent. Discussion of device application, particularly picosecond electronics, is captivating. His handling of other nonlinear effects is generally well.

The last three chapters are on the application of ultrashort light pulses for understanding various rapid processes in Physics, Chemistry and Biology.

In von-der-Linde's chapter, measurements of decays of excitons, phonons, polaritons, plasmas, molecular vibrations and coherent phenomena are described. Modelocked laser pulses, unlike traditional infrared and Raman Spectroscopy, permit novel and direct information of vibrational relaxation. Ultrafast light pulse experiments also have led to information on diffusion, conduction and recombination processes in very dense electron-hole plasma. Picosecond techniques eliminate competing processes and yield quantitative values of multiphoton absorption cross section and true multiphoton spectra. Interesting picosecond excitation experiments regarding excitonic molecules and Bose condensation of such molecules have been discussed and importances of further work in this field stressed.

In chapter 6, Eisenthal has presented a very carefully written review on picosecond relaxation processes in Chemistry. With the advent of ultrafast light pulses, a revolutionary breakthrough has occurred in the investigation of ultrafast molecular processes. In this review Eisenthal has discussed the rapid processes through which a molecule on excitation to some excited state dissipates its energy. He has successfully covered wide spectrum of molecular processes like intermolecular singlet-singlet and triplet-triplet energy transfer; molecular orientational relaxation in liquids resulting in Optical Kerr effect, induced dichroism and transient grating; photo dissociation and the cage effect in liquids. He has also reviewed recent works on electron transfer phenomena like electron photoejection and solvations excited state charge transfer and internal conversion and intersystem crossing.

In a complex biosystem such as photosynthetic apparatus, close proximity of molecules leads to rapid excitation transfer. Rapid rearrangement of molecular side chain or the molecule itself is often the part of a biophysical process. Picosecond measurements therefore are expected to find wide application in many areas of life sciences. In the concluding chapter, Compillo and Shapiro have reviewed the recent picosecond relaxation measurements in this interesting field of science. We now know that rhodopsin, a protein involved in visual perception, on light absorption forms one of the intermediate species prelumirhodopsin in less than 6 ps., also in the reaction center of the primary step in photosynthesis possibly occurs within 10 ps. The possibility of picosecond experiment in biology is immense and a rapid expansion of effort in this direction is expected.

Thus one finds that almost the whole of frontier area of picosecond pulse research is covered making this an outstanding book. The totality of coverage provide plenty of interesting reading and an invaluable reference source. The high standard of the book's production make it an extremely satisfying volume.

T.N.M.

Essentials of Computer Programming in Fortran IV

By N. N. Biswas, Radiant Books, Bangalore 560006, India, pp. xii+125, Price Rs. 16/- (1975).

The need of computers for overall progress of a nation is now well recognized. In this context computer programming has assumed great importance. A number of books written on the subject are often found not very suitable for a beginner who wants to learn programming in a short span of time by self-study. In this respect the above book is much welcome.

The book, based on IBM 360 computers, is well-written in a short volume. It consists of 9 chapters : Number Representation, Arithmetic Operations and Expressions, Relational Operators and Logical Expressions, Reading and Printing, Arrays, Control and Decision Statements, The DO Loop, Subprograms and Illustrated Programs. The essentials of computer programming in Fortran IV language are illustrated in a simple and useful way throughout these chapters, which are brief and to the point with some interesting examples worked out. Flow Chart, Mathematical Function Subprograms, and Useful Forms of Statements given in the 3 appendices will be found to be helpful in writing a program. In fact the book, which is quite inexpensive, will serve as a guide for beginners.

A few words may be added for further improvement of the book. The meaning of the word Fortran may be emphasized in connection with higher level languages discussed in p. 52-53. In chapter 8 on Subprograms it needs to be mentioned that Subroutines are also subprograms and are often called as Subroutine Subprograms. Hence in p. 92, it is better to put the name function before the word subprogram. It is worthwhile to state that the Mathematical Function Subprograms (in appendix B) are also known as Library Functions. The solutions of some of the important Problems given at the end of each chapter may be supplied at the end of the book. The errors (or misprints) crept in through oversight, such as ALG10(X) in p. 21, .ONT. in p. 29, COBAL in p. 52, A(26) etc. in p. 98, i_4 in p. 107, full stop (.) after a number of sentences in p. 92-93, and page number on p. 89, should be corrected. Finally, the quality of the paper and printing may be improved to some extent.

S.C.S.

Progress in Electro-Optics

Edited by Ezio Camatini (Plenum Press, New York and London), pp. i-xiii, 1-213, ten chapters.

This volume contains articles on recent developments in the field of electro-optics by well-known workers. The topics examined may be broadly subdivided into three sectors: (1) Types of display devices, (2) circuit techniques and (3) display module costs.

In the first chapter a brief account of the historical development of electro-optics is given by A. Kastler. In the second chapter O. S. Heavens discusses some fundamentals of electro-optics like propagation in isotropic, anisotropic and gyrotropic media, Pockels effect, Kerr effect and several non-linear optical phenomena. Some new developments in hologram are reviewed by W. E. Koch in the third chapter. The topics include radar range acquisition by holography, use of incoherent radiation in hologram radar and parallel processing aspects of synthetic aperture technique. In the fourth chapter on Holography by Shadow Casting, H. J. Culfield discusses the present state of the art of coded aperture imaging and surveys some possible problems for future research. In the two following chapters C. H. Grooch describes techniques of displaying information based on liquid-crystal electro-optical phenomena and light-emitting diodes. The possibilities of applications of gas discharge devices for data displays form the subject of chapter seven written by G. F. Weston, while the present state of the digital laser beam deflection technique for alphanumeric and graphic displays is dealt with by U. J. Schmidt in chapter eight. Methods of deposition of thin films, which are useful components in electro-optical devices, are described in chapter nine by E. Ritter, who also discusses properties of thin film and their applications in displays. In the last chapter, P. B. Page deals with different aspects of display device circuits and their impact on system economics.

At the end of each chapter a large number of up to date references are given. The wide and neat coverage of the topics will be very useful to research workers in this field of great current interest.

S.B.B.